

Marina Gavrilova et al. (Eds.)

LNCS 3980

Computational Science and Its Applications – ICCSA 2006

International Conference
Glasgow, UK, May 2006
Proceedings, Part I

1
Part I

 Springer

Commenced Publication in 1973

Founding and Former Series Editors:

Gerhard Goos, Juris Hartmanis, and Jan van Leeuwen

Editorial Board

David Hutchison

Lancaster University, UK

Takeo Kanade

Carnegie Mellon University, Pittsburgh, PA, USA

Josef Kittler

University of Surrey, Guildford, UK

Jon M. Kleinberg

Cornell University, Ithaca, NY, USA

Friedemann Mattern

ETH Zurich, Switzerland

John C. Mitchell

Stanford University, CA, USA

Moni Naor

Weizmann Institute of Science, Rehovot, Israel

Oscar Nierstrasz

University of Bern, Switzerland

C. Pandu Rangan

Indian Institute of Technology, Madras, India

Bernhard Steffen

University of Dortmund, Germany

Madhu Sudan

Massachusetts Institute of Technology, MA, USA

Demetri Terzopoulos

University of California, Los Angeles, CA, USA

Doug Tygar

University of California, Berkeley, CA, USA

Moshe Y. Vardi

Rice University, Houston, TX, USA

Gerhard Weikum

Max-Planck Institute of Computer Science, Saarbruecken, Germany

Marina Gavrilova Osvaldo Gervasi
Vipin Kumar C.J. Kenneth Tan
David Taniar Antonio Laganà
Youngsong Mun Hyunseung Choo (Eds.)

Computational Science and Its Applications – ICCSA 2006

International Conference
Glasgow, UK, May 8-11, 2006
Proceedings, Part I

 Springer

Volume Editors

Marina Gavrilova
University of Calgary, Canada
E-mail: marina@cpsc.ucalgary.ca

Oswaldo Gervasi
University of Perugia, Italy
E-mail: ogervasi@computer.org

Vipin Kumar
University of Minnesota, Minneapolis, USA
E-mail: kumar@cs.umn.edu

C.J. Kenneth Tan
OptimaNumerics Ltd., Belfast, UK
E-mail: cjtan@optimanumerics.com

David Taniar
Monash University, Clayton, Australia
E-mail: david.taniar@infotech.monash.edu.au

Antonio Laganà
University of Perugia, Italy
E-mail: lag@unipg.it

Youngsong Mun
SoongSil University, Seoul, Korea
E-mail: mun@computing.soongsil.ac.kr

Hyunseung Choo
Sungkyunkwan University, Suwon, Korea
E-mail: choo@ece.skku.ac.kr

Library of Congress Control Number: 2006925086

CR Subject Classification (1998): F, D, G, H, I, J, C.2-3

LNCS Sublibrary: SL 1 – Theoretical Computer Science and General Issues

ISSN 0302-9743
ISBN-10 3-540-34070-X Springer Berlin Heidelberg New York
ISBN-13 978-3-540-34070-6 Springer Berlin Heidelberg New York

This work is subject to copyright. All rights are reserved, whether the whole or part of the material is concerned, specifically the rights of translation, reprinting, re-use of illustrations, recitation, broadcasting, reproduction on microfilms or in any other way, and storage in data banks. Duplication of this publication or parts thereof is permitted only under the provisions of the German Copyright Law of September 9, 1965, in its current version, and permission for use must always be obtained from Springer. Violations are liable to prosecution under the German Copyright Law.

Springer is a part of Springer Science+Business Media
springer.com

© Springer-Verlag Berlin Heidelberg 2006
Printed in Germany

Typesetting: Camera-ready by author, data conversion by Scientific Publishing Services, Chennai, India
Printed on acid-free paper SPIN: 11751540 06/3142 5 4 3 2 1 0

Preface

This five-volume set was compiled following the 2006 International Conference on Computational Science and its Applications, ICCSA 2006, held in Glasgow, UK, during May 8–11, 2006. It represents the outstanding collection of almost 664 refereed papers selected from over 2,450 submissions to ICCSA 2006.

Computational science has firmly established itself as a vital part of many scientific investigations, affecting researchers and practitioners in areas ranging from applications such as aerospace and automotive, to emerging technologies such as bioinformatics and nanotechnologies, to core disciplines such as mathematics, physics, and chemistry. Due to the sheer size of many challenges in computational science, the use of supercomputing, parallel processing, and sophisticated algorithms is inevitable and becomes a part of fundamental theoretical research as well as endeavors in emerging fields. Together, these far-reaching scientific areas contributed to shaping this conference in the realms of state-of-the-art computational science research and applications, encompassing the facilitating theoretical foundations and the innovative applications of such results in other areas.

The topics of the refereed papers span all the traditional as well as emerging computational science realms, and are structured according to the five major conference themes:

- Computational Methods, Algorithms and Applications
- High-Performance Technical Computing and Networks
- Advanced and Emerging Applications
- Geometric Modeling, Graphics and Visualization
- Information Systems and Information Technologies

Moreover, submissions from 31 workshops and technical sessions in areas such as information security, mobile communication, grid computing, modeling, optimization, computational geometry, virtual reality, symbolic computations, molecular structures, Web systems and intelligence, spatial analysis, bioinformatics and geocomputations, are included in this publication. The continuous support of computational science researchers has helped ICCSA to become a firmly established forum in the area of scientific computing.

We recognize the contribution of the International Steering Committee and sincerely thank the International Program Committee for their tremendous support in putting this conference together, the near 800 referees for their diligent work, and the IEE European Chapter for their generous assistance in hosting the event.

We also thank our sponsors for their continuous support without which this conference would not be possible.

Finally, we thank all authors for their submissions and all invited speakers and conference attendants for making the ICCSA Conference truly one of the premium events on the scientific community scene, facilitating exchange of ideas, fostering new collaborations, and shaping the future of computational science.

May 2006

Marina L. Gavrilova
Oswaldo Gervasi

on behalf of the co-editors
Vipin Kumar
Chih Jeng Kenneth Tan
David Taniar
Antonio Laganà
Youngsong Mun
Hyunseung Choo

Organization

ICCSA 2006 was organized by the Institute of Electrical Engineers (IEE)(UK), the University of Perugia (Italy), Calgary University (Canada) and Minnesota University (USA).

Conference Chairs

Vipin Kumar (University of Minnesota, Minneapolis, USA), Honorary Chair
Marina L. Gavrilova (University of Calgary, Calgary, Canada), Conference

Co-chair, Scientific

Oswaldo Gervasi (University of Perugia, Perugia, Italy), Conference Co-chair,
Program

Steering Committee

Vipin Kumar (University of Minnesota, USA)

Marina L. Gavrilova (University of Calgary, Canada)

Oswaldo Gervasi (University of Perugia, Perugia, Italy)

C. J. Kenneth Tan (OptimaNumerics, UK)

Alexander V. Bogdanov (Institute for High Performance Computing
and Data Bases, Russia)

Hyunseung Choo (Sungkyunkwan University, Korea)

Andres Iglesias (University of Cantabria, Spain)

Antonio Laganà (University of Perugia, Italy)

Heow-Pueh Lee (Institute of High Performance Computing, Singapore)

Youngsong Mun (Soongsil University, Korea)

David Taniar (Monash University, Australia)

Workshop Organizers

Applied Cryptography and Information Security (ACIS 2006)

Sherman S.M. Chow (New York University, USA)

Joseph K. Liu (University of Bristol, UK)

Patrick Tsang (Dartmouth College, USA)

Duncan S Wong (City University of Hong Kong, Hong Kong)

Approaches or Methods of Security Engineering (AMSE 2006)

Haeng Kon Kim (Catholic University of Daegu, Korea)

Tai-hoon Kim (Korea Information Security Agency, Korea)

Authentication, Authorization and Accounting (AAA 2006)
Haeng Kon Kim (Catholic University of Daegu, Korea)

Computational Geometry and Applications (CGA 2006)
Marina Gavrilova (University of Calgary, Calgary, Canada)

Data Storage Devices and Systems (DSDS 2006)
Yeonseung Ryu (Myongji University, Korea)
Junho Shim (Sookmyong Womens University, Korea)
Youjip Won (Hanyang University, Korea)
Yongik Eom (Seongkyunkwan University, Korea)

Embedded System for Ubiquitous Computing (ESUC 2006)
Tei-Wei Kuo (National Taiwan University, Taiwan)
Jiman Hong (Kwangwoon University, Korea)

4th Technical Session on Computer Graphics (TSCG 2006)
Andres Iglesias (University of Cantabria, Spain)
Deok-Soo Kim (Hanyang University, Korea)

GeoComputation (GC 2006)
Yong Xue (London Metropolitan University, UK)

Image Processing and Computer Vision (IPCV 2006)
Jiawan Zhang (Tianjin University, China)

**Intelligent Services and the Synchronization in Mobile
Multimedia Networks (ISS 2006)**
Dong Chun Lee (Howon University, Korea)
Kuinam J Kim (Kyonggi University, Korea)

**Integrated Analysis and Intelligent Design Technology
(IAIDT 2006)**
Jae-Woo Lee (Konkuk University, Korea)

Information Systems Information Technologies (ISIT 2006)
Youngsong Mun (Soongsil University, Korea)

Information Engineering and Applications in Ubiquitous Computing Environments (IEAUCE 2006)

Sangkyun Kim (Yonsei University, Korea)

Hong Joo Lee (Dankook University, Korea)

Internet Communications Security (WICS 2006)

Sierra-Camara José Maria (University Carlos III of Madrid, Spain)

Mobile Communications (MC 2006)

Hyunseung Choo (Sungkyunkwan University, Korea)

Modelling Complex Systems (MCS 2006)

John Burns (Dublin University, Ireland)

Ruili Wang (Massey University, New Zealand)

Modelling of Location Management in Mobile Information Systems (MLM 2006)

Dong Chun Lee (Howon University, Korea)

Numerical Integration and Applications (NIA 2006)

Elise de Doncker (Western Michigan University, USA)

Specific Aspects of Computational Physics and Wavelet Analysis for Modelling Suddenly-Emerging Phenomena in Nonlinear Physics, and Nonlinear Applied Mathematics (PULSES 2006)

Carlo Cattani (University of Salerno, Italy)

Cristian Toma (Titu Maiorescu University, Romania)

Structures and Molecular Processes (SMP 2006)

Antonio Laganà (University of Perugia, Perugia, Italy)

Optimization: Theories and Applications (OTA 2006)

Dong-Ho Lee (Hanyang University, Korea)

Deok-Soo Kim (Hanyang University, Korea)

Ertugrul Karsak (Galatasaray University, Turkey)

Parallel and Distributed Computing (PDC 2006)

Jiawan Zhang (Tianjin University, China)

Pattern Recognition and Ubiquitous Computing (PRUC 2006)

Jinok Kim (Daegu Haany University, Korea)

Security Issues on Grid/Distributed Computing Systems (SIGDCS 2006)

Tai-Hoon Kim (Korea Information Security Agency, Korea)

Technologies and Techniques for Distributed Data Mining (TTDDM 2006)

Mark Baker (Portsmouth University, UK)

Bob Nichol (Portsmouth University, UK)

Ubiquitous Web Systems and Intelligence (UWSI 2006)

David Taniar (Monash University, Australia)

Eric Pardede (La Trobe University, Australia)

Ubiquitous Application and Security Service (UASS 2006)

Yeong-Deok Kim (Woosong University, Korea)

Visual Computing and Multimedia (VCM 2006)

Abel J. P. Gomes (University Beira Interior, Portugal)

Virtual Reality in Scientific Applications and Learning (VRSAL 2006)

Oswaldo Gervasi (University of Perugia, Italy)

Antonio Riganelli (University of Perugia, Italy)

Web-Based Learning (WBL 2006)

Woochun Jun Seoul (National University of Education, Korea)

Program Committee

Jemal Abawajy (Deakin University, Australia)
Kenny Adamson (EZ-DSP, UK)
Srinivas Aluru (Iowa State University, USA)
Mir Atiqullah (Saint Louis University, USA)
Frank Baetke (Hewlett Packard, USA)
Mark Baker (Portsmouth University, UK)
Young-Cheol Bang (Korea Polytechnic University, Korea)
David Bell (Queen's University of Belfast, UK)
Stefania Bertazzon (University of Calgary, Canada)
Sergei Bespamyatnikh (Duke University, USA)
J. A. Rod Blais (University of Calgary, Canada)
Alexander V. Bogdanov (Institute for High Performance Computing
and Data Bases, Russia)
Peter Brezany (University of Vienna, Austria)
Herve Bronnimann (Polytechnic University, NY, USA)
John Brooke (University of Manchester, UK)
Martin Buecker (Aachen University, Germany)
Rajkumar Buyya (University of Melbourne, Australia)
Jose Sierra-Camara (University Carlos III of Madrid, Spain)
Shyi-Ming Chen (National Taiwan University of Science and Technology,
Taiwan)
YoungSik Choi (University of Missouri, USA)
Hyunseung Choo (Sungkyunkwan University, Korea)
Bastien Chopard (University of Geneva, Switzerland)
Min Young Chung (Sungkyunkwan University, Korea)
Yiannis Cotronis (University of Athens, Greece)
Danny Crookes (Queen's University of Belfast, UK)
Jose C. Cunha (New University of Lisbon, Portugal)
Brian J. d'Auriol (University of Texas at El Paso, USA)
Alexander Degtyarev (Institute for High Performance Computing
and Data Bases, Russia)
Frederic Desprez (INRIA, France)
Tom Dhaene (University of Antwerp, Belgium)
Beniamino Di Martino (Second University of Naples, Italy)
Hassan Diab (American University of Beirut, Lebanon)
Ivan Dimov (Bulgarian Academy of Sciences, Bulgaria)
Iain Duff (Rutherford Appleton Laboratory, UK and CERFACS, France)
Thom Dunning (NCSA and University of Illinois, USA)
Fabrizio Gagliardi (Microsoft, USA)
Marina L. Gavrilova (University of Calgary, Canada)
Michael Gerndt (Technical University of Munich, Germany)
Osvaldo Gervasi (University of Perugia, Italy)
Bob Gingold (Australian National University, Australia)
James Glimm (SUNY Stony Brook, USA)

Christopher Gold (Hong Kong Polytechnic University, Hong Kong)
Yuriy Gorbachev (Institute of High Performance Computing
and Information Systems, Russia)
Andrzej Goscinski (Deakin University, Australia)
Jin Hai (Huazhong University of Science and Technology, China)
Ladislav Hluchy (Slovak Academy of Science, Slovakia)
Xiaohua Hu (Drexel University, USA)
Eui-Nam John Huh (Seoul Women's University, Korea)
Shen Hong (Japan Advanced Institute of Science and Technology, Japan)
Paul Hovland (Argonne National Laboratory, USA)
Andres Iglesias (University of Cantabria, Spain)
Peter K. Jimack (University of Leeds, UK)
In-Jae Jeong (Hanyang University, Korea)
Chris Johnson (University of Utah, USA)
Benjoe A. Juliano (California State University at Chico, USA)
Peter Kacsuk (MTA SZTAKI Research Institute, Hungary)
Kyung Wo Kang (KAIST, Korea)
Carl Kesselman (USC/ Information Sciences Institute, USA)
Daniel Kidger (Quadrics, UK)
Haeng Kon Kim (Catholic University of Daegu, Korea)
Jin Suk Kim (KAIST, Korea)
Tai-Hoon Kim (Korea Information Security Agency, Korea)
Yoonhee Kim (Syracuse University, USA)
Mike Kirby (University of Utah, USA)
Dieter Kranzmueller (Johannes Kepler University Linz, Austria)
Deok-Soo Kim (Hanyang University, Korea)
Vipin Kumar (University of Minnesota, USA)
Domenico Laforenza (Italian National Research Council, Italy)
Antonio Laganà (University of Perugia, Italy)
Joseph Landman (Scalable Informatics LLC, USA)
Francis Lau (The University of Hong Kong, Hong Kong)
Bong Hwan Lee (Texas A&M University, USA)
Dong Chun Lee (Howon University, Korea)
Dong-Ho Lee (Institute of High Performance Computing, Singapore)
Sang Yoon Lee (Georgia Institute of Technology, USA)
Tae-Jin Lee (Sungkyunkwan University, Korea)
Bogdan Lesyng (ICM Warszawa, Poland)
Zhongze Li (Chinese Academy of Sciences, China)
Laurence Liew (Scalable Systems Pte, Singapore)
David Lombard (Intel Corporation, USA)
Emilio Luque (University Autònoma of Barcelona, Spain)
Michael Mascagni (Florida State University, USA)
Graham Megson (University of Reading, UK)
John G. Michopoulos (US Naval Research Laboratory, USA)
Edward Moreno (Euripides Foundation of Marilia, Brazil)

Youngsong Mun (Soongsil University, Korea)
 Jiri Nedoma (Academy of Sciences of the Czech Republic, Czech Republic)
 Genri Norman (Russian Academy of Sciences, Russia)
 Stephan Olariu (Old Dominion University, USA)
 Salvatore Orlando (University of Venice, Italy)
 Robert Panoff (Shodor Education Foundation, USA)
 Marcin Paprzycki (Oklahoma State University, USA)
 Gyung-Leen Park (University of Texas, USA)
 Ron Perrott (Queen's University of Belfast, UK)
 Dimitri Plemenos (University of Limoges, France)
 Richard Ramaroson (ONERA, France)
 Rosemary Renaut (Arizona State University, USA)
 René S. Renner (California State University at Chico, USA)
 Paul Roe (Queensland University of Technology, Australia)
 Alexey S. Rodionov (Russian Academy of Sciences, Russia)
 Heather J. Ruskin (Dublin City University, Ireland)
 Ole Saastad (Scali, Norway)
 Muhammad Sarfraz (King Fahd University of Petroleum and Minerals,
 Saudi Arabia)
 Edward Seidel (Louisiana State University, USA and Albert-Einstein-Institut,
 Potsdam, Germany)
 Jie Shen (University of Michigan, USA)
 Dale Shires (US Army Research Laboratory, USA)
 Vaclav Skala (University of West Bohemia, Czech Republic)
 Burton Smith (Cray, USA)
 Masha Sosonkina (Ames Laboratory, USA)
 Alexei Sourin (Nanyang Technological University, Singapore)
 Elena Stankova (Institute for High Performance Computing and Data Bases,
 Russia)
 Gunther Stuer (University of Antwerp, Belgium)
 Kokichi Sugihara (University of Tokyo, Japan)
 Boleslaw Szymanski (Rensselaer Polytechnic Institute, USA)
 Ryszard Tadeusiewicz (AGH University of Science and Technology, Poland)
 C.J. Kenneth Tan (OptimaNumerics, UK and Queen's University
 of Belfast, UK)
 David Taniar (Monash University, Australia)
 John Taylor (Streamline Computing, UK)
 Ruppa K. Thulasiram (University of Manitoba, Canada)
 Pavel Tvrdik (Czech Technical University, Czech Republic)
 Putchong Uthayopas (Kasetsart University, Thailand)
 Mario Valle (Swiss National Supercomputing Centre, Switzerland)
 Marco Vanneschi (University of Pisa, Italy)
 Piero Giorgio Verdini (University of Pisa and Istituto Nazionale di Fisica
 Nucleare, Italy)
 Jesus Vigo-Aguar (University of Salamanca, Spain)

Jens Volkert (University of Linz, Austria)
Koichi Wada (University of Tsukuba, Japan)
Stephen Wismath (University of Lethbridge, Canada)
Kevin Wadleigh (Hewlett Packard, USA)
Jerzy Wasniewski (Technical University of Denmark, Denmark)
Paul Watson (University of Newcastle Upon Tyne, UK)
Jan Weglarz (Poznan University of Technology, Poland)
Tim Wilkens (Advanced Micro Devices, USA)
Roman Wyrzykowski (Technical University of Czestochowa, Poland)
Jinchao Xu (Pennsylvania State University, USA)
Chee Yap (New York University, USA)
Osman Yasar (SUNY at Brockport, USA)
George Yee (National Research Council and Carleton University, Canada)
Yong Xue (Chinese Academy of Sciences, China)
Igor Zacharov (SGI Europe, Switzerland)
Xiaodong Zhang (College of William and Mary, USA)
Aledander Zhmakin (SoftImpact, Russia)
Krzysztof Zielinski (ICS UST / CYFRONET, Poland)
Albert Zomaya (University of Sydney, Australia)

Sponsoring Organizations

Institute of Electrical Engineers (IEE), UK
University of Perugia, Italy
University of Calgary, Canada
University of Minnesota, USA
Queen's University of Belfast, UK
The European Research Consortium for Informatics and Mathematics (ERCIM)
The 6th European Framework Project "Distributed European Infrastructure
for Supercomputing Applications" (DEISA)
OptimaNumerics, UK
INTEL
AMD

Table of Contents – Part I

Workshop on Computational Geometry and Applications (CGA 2006)

Upper Bound on Dilation of Triangulations of Cyclic Polygons <i>Narayanasetty Amarnadh, Pinaki Mitra</i>	1
Optimal Guard Placement Problem Under L-Visibility <i>Debabrata Bardhan, Sasanka Roy, Sandip Das</i>	10
Visibility Maps of Segments and Triangles in 3D <i>Esther Moet, Christian Knauer, Marc van Kreveld</i>	20
Non-euclidean Metrics and Chordal Space Structures <i>José Andrés Díaz Severiano, César Otero Gonzalez, Reinaldo Togores Fernandez, Cristina Manchado del Val</i>	30
Algorithms for Rectangular Covering Problems <i>Stefan Porschen</i>	40
Backward Error Analysis in Computational Geometry <i>Di Jiang, Neil F. Stewart</i>	50
Reply to “Backward Error Analysis...” <i>Lutz Kettner, Kurt Mehlhorn, Sylvain Pion, Stefan Schirra, Chee Yap</i>	60
Two Map Labeling Algorithms for GIS Applications <i>Marina L. Gavrilova</i>	61
Surface Reconstruction from Large Point Clouds Using Virtual Shared Memory Manager <i>Josef Kohout, Michal Varnuška, Ivana Kolingerová</i>	71
Computing Terrain Multi-visibility Maps for a Set of View Segments Using Graphics Hardware <i>Narcis Coll, Marta Fort, Narcis Madern, J. Antoni Sellarès</i>	81
Fast Intersections for Subdivision Surfaces <i>Aaron Severn, Faramarz Samavati</i>	91

A β -Shape from the Voronoi Diagram of Atoms for Protein Structure Analysis
Jeongyeon Seo, Donguk Kim, Cheol-Hyung Cho, Deok-Soo Kim 101

Reduction of the Search Space in the Edge-Tracing Algorithm for the Voronoi Diagram of 3D Balls
Youngsong Cho, Donguk Kim, Hyun Chan Lee, Joon Young Park, Deok-Soo Kim 111

Routing Properties of the Localized Delaunay Triangulation over Heterogeneous Ad-Hoc Wireless Networks
Mark D. Watson, J. Mark Keil 121

A Speculative Approach to Clipping Line Segments
Frank Dévai 131

An Efficient Algorithm for Mobile Guarded Guards in Simple Grids
Adrian Kosowski, Michał Małafiejski, Paweł Żyliński 141

Approximation of Optimal Moving Paths of Huge Robot Reclaimer with a 3D Range Finder
Kwan-Hee Lee, Hyo-Jung Bae, Sung-Je Hong 151

Fault Tolerant Guarding of Grids
Adrian Kosowski, Michał Małafiejski, Paweł Żyliński 161

Tunable Bounding Volumes for Monte Carlo Applications
Yuan-Yu Tsai, Chung-Ming Wang, Chung-Hsien Chang, Yu-Ming Cheng 171

A Data Hiding Algorithm for Point-Sampled Geometry
Yu-Ming Cheng, Chung-Ming Wang, Yuan-Yu Tsai 181

An Algorithm for Rendering Vertexes and Edges of Polyhedron with High Order Geometric Continuity
Xiaolin Lu 192

Workshop on Virtual Reality in Scientific Applications and Learning (VRSAL 2006)

SimVIZ – A Desktop Virtual Environment for Visualization and Analysis of Protein Multiple Simulation Trajectories
Ricardo M. Czekster, Osmar Norberto de Souza 202

Immersive Molecular Virtual Reality Based on X3D and Web Services <i>Oswaldo Gervasi, Sergio Tasso, Antonio Laganà</i>	212
Yeast Naked DNA Spatial Organization Predisposes to Transcriptional Regulation <i>Oriane Matte-Tailliez, Joan Hérisson, Nicolas Ferey, Olivier Magneau, Pierre Emmanuel Gros, François Képès, Rachid Gherbi</i>	222
Interactive Real-Time 3D Visualization of Grid Portal for Quantum Mechanics <i>Sung-Wook Byun, Yun-Kyoung Lee, Chang-Sung Jeong</i>	232
Development of a Virtual Reality Bicycle Simulator for Rehabilitation Training of Postural Balance <i>Nam-Gyun Kim, Yong-Yook Kim, Tae-Kyu Kwon</i>	241
Virtual Reality Edutainment: Cost-Effective Development of Personalised Software Applications <i>Maria Virvou, Konstantinos Manos, George Katsionis</i>	251
3D Panoramic Mosaicking to Suppress the Ghost Effect at Far-Range Scene for Urban Area Visualization <i>Jaechoon Chon, Eihan Shimizu, Ryosuke Shibasaki</i>	261
VR Based Knowledge Transfer in Medical Technology and Techniques <i>Wolfram Schoor, Rüdiger Mecke, Martina Rehfeld</i>	268
A Diagnostic Model Using a Clustering Scheme <i>Seong Baeg Kim, Kyoung Mi Yang, Cheol Min Kim</i>	278
Ontology-Based Edutainment System <i>Cheol Min Kim, Hye Sun Kim, Seong Baeg Kim</i>	288
Workshop on Visual Computing and Multimedia (VCM 2006)	
A Fast Video Encoding Algorithm by Skipping the Operations on Zero-Valued DCT Coefficients <i>Kook-Yeol Yoo</i>	298
Efficient Block Matching for Ray-Space Predictive Coding in Free-Viewpoint Television Systems <i>Gangyi Jiang, Feng Shao, Mei Yu, Ken Chen, Tae-Young Choi</i>	307

New Approach to Complexity Reduction of Intra Prediction in
Advanced Multimedia Compression
Mei Yu, Gangyi Jiang, Shiping Li, Fucui Li, Tae-young Choi 317

Reduction of Mode Decision Complexity in H.264/AVC Using Adaptive
Selection of Reference Frame and Intra Prediction Mode
Woongho Lee, Jungho Lee, Ik-hwan Cho, Dongseok Jeong 326

3D Visualization for Tele-medical Diagnosis
Sun K. Yoo, Jaehong Key, Kuiwon Choi 335

Content Based Image Retrieval Based on a Nonlinear Similarity Model
Guang-Ho Cha 344

**Technical Session on Web Based Learning
(WBL 2006)**

Simple and Powerful Interactive E-Learning System Using VXML:
Design and Implementation of Web and PSTN Linked Efficient
Learning System
Jeong-Hoon Shin, Kwang-Seok Hong 354

A Web-Based Tool for Entity-Relationship Modeling
Ferran Prados, Imma Boada, Josep Soler, Jordi Poch 364

Reusable Learning Objects (RLOs) for Computer Science Students
Birim Balci, Mustafa Murat Inceoglu 373

WebQuest Markup Language (WQML) for Sharable Inquiry-Based
Learning
Sebastian Fleissner, Yuen-Yan Chan, Tsz Hon Yuen, Victor Ng 383

**Technical Session on Computer Graphics
(TSCG 2006)**

Practical Boolean Operations on Point-Sampled Models
Xujia Qin, Weihong Wang, Qu Li 393

Dynamic Brush Stroke Generation for an Impressionist Effect
Youngsup Park, Kyunghyun Yoon 402

Image-Based 3D Face Modeling from Stereo Images
Kyongpil Min, Junchul Chun 410

Perception-Guided Simplification for Real Time Navigation of Very Large-Scale Terrain Environments <i>Sheng Li, JunFeng Ji, XueHui Liu, GuoPing Wang, EnHua Wu</i>	420
3D Building Reconstruction from LIDAR Data <i>Yuan Luo, Marina L. Gavrilova</i>	431
Efficient Computation of Elliptic Gabriel Graph <i>Changhee Lee, Donguk Kim, Hayong Shin, Deok-Soo Kim</i>	440
Systematic Sampling in Image-Synthesis <i>Mateu Sbert, Jaume Rigau, Miquel Feixas, Laszlo Neumann</i>	449
History-Based Selective Boolean Operations for Feature-Based Multi-resolution Modeling <i>Sang Hun Lee, Kunwoo Lee, Sungchan Kim</i>	459
Path Finding Method for Various Applications <i>Jaesung Song, Manseung Seo, Masahiko Onosato</i>	469
Natural-Textured Mesh Stream Modeling from Depth Image-Based Representation <i>Seung Man Kim, Jeung Chul Park, Kwan H. Lee</i>	480
Workload Characterization in Multiplayer Online Games <i>Pedro Morillo, Juan Manuel Orduña, Marcos Fernández</i>	490
Delaunay-Based Polygon Morphing Across a Change in Topology <i>Xiaqing Wu, John K. Johnstone</i>	500
Jittering Reduction in Marker-Based Augmented Reality Systems <i>Monica Rubio, Arturo Quintana, Hebert Pérez-Rosés, Ricardo Quirós, Emilio Camahort</i>	510
Workshop on Modeling Complex Systems (MCS 2006)	
A Bias-Variance-Complexity Trade-Off Framework for Complex System Modeling <i>Lean Yu, Kin Keung Lai, Shouyang Wang, Wei Huang</i>	518
A Neural Network Strategy for 3D Surface Registration <i>Heng Liu, Jingqi Yan, David Zhang</i>	528

Parallel Hierarchical Methods for Complex Systems Optimization <i>Ewa Niewiadomska-Szynkiewicz</i>	537
Numerical Modelling of Coastal Currents <i>Lale Balas, Asu İnan, İpek Yıldız</i>	547
A Novel Model for Bacterial Foraging in Varying Environments <i>W.J. Tang, Q.H. Wu, J.R. Saunders</i>	556
Stochastic Modeling of Cytoplasmic Reactions in Complex Biological Systems <i>Preetam Ghosh, Samik Ghosh, Kalyan Basu, Sajal Das, Simon Daeﬂer</i>	566
Modelling of Complex Cryptographic Systems in Terms of Simple Cellular Automata <i>Amparo Fúster-Sabater, Pino Caballero-Gil, Maria Eugenia Pazo-Robles</i>	577
Modeling Supply Chain Complexity Using a Distributed Multi-objective Genetic Algorithm <i>Khalid Al-Mutawah, Vincent Lee, Yen Cheung</i>	586
Different Responses of Two Types of Class II Neurons for Fluctuated Inputs <i>Ryosuke Hosaka, Yutaka Sakai, Tohru Ikeguchi, Shuji Yoshizawa</i>	596
Branching Method for Computation of Probability of Given Data Stream Transmission <i>Mikhail Y. Murzin, Alexey S. Rodionov</i>	605
An Agent-Based Approach to Immune Modelling <i>Dimitri Perrin, Heather J. Ruskin, John Burns, Martin Crane</i>	612
Comparison of Homogeneous and Heterogeneous Motorised Traffic at Signalised and Two-Way Stop Control Single Lane Intersection <i>Puspita Deo, Heather J. Ruskin</i>	622
A New Algorithm for Complex Stochastic Boolean Systems <i>Luis González</i>	633

Theoretical Steps Towards Modelling Resilience in Complex Systems <i>Cathy Hawes, Chris Reed</i>	644
Collaborative Multidiscipline/Multiscale Analysis, Modeling, Simulation and Integration in Complex Systems: System Biology <i>Thomas J. Wheeler</i>	654
Workshop on Structures and Molecular Processes (SMP 2006)	
On the Structuring of the Computational Chemistry Virtual Organization COMPCHEM <i>Antonio Laganà, Antonio Riganelli, Osvaldo Gervasi</i>	665
Computing Molecular Energy Surfaces on a Grid <i>Loriano Storchi, Francesco Tarantelli, Antonio Laganà</i>	675
Electronic States in Three Dimensional Quantum Dot/Wetting Layer Structures <i>Marta Markiewicz, Heinrich Voss</i>	684
A Web Based Application to Fit Potential Energy Functionals to ab Initio Values <i>Leonardo Arteconi, Antonio Laganà, Leonardo Pacifici</i>	694
Dynamic Load-Balancing for the STEM-II Air Quality Model <i>J. Carlos Mouriño, María J. Martín, Patricia González, Ramón Doallo</i>	701
New Molecular Mechanism of Dextran Extension in Single Molecule AFM <i>Igor Neelov, David Adolf, Tom McLeish</i>	711
Atom-Bond Additive Potentials for Benzene-Rare Gas Clusters <i>Margarita Albertí, Antonio Laganà, Fernando Pirani, Massimiliano Porrini, David Cappelletti</i>	721
A Simplified Myoglobin Model for Molecular Dynamics Calculations <i>Federico Filomia, Noelia Faginas Lago</i>	731
Parallel Calculation of Propane Bulk Properties <i>Alessandro Costantini, Antonio Laganà, Fernando Pirani</i>	738

Ab-Initio Multi-reference Study of a Bistable Spiro Molecule <i>Wissam Helal, Benoît Bories, Stefano Evangelisti, Thierry Leiminger, Daniel Maynau</i>	744
On the Algorithm of Calculation of the Equilibrium Gas-Phase Concentration at the Particle Surface in the Kinetic Models of Aerosol Dynamics <i>Elena N. Stankova</i>	752
Study of the Passage of an H ⁺ Ion Along a Carbon Nanotube Using Quantum Wavepacket Dynamics <i>Dimitris Skouteris, Antonio Laganá</i>	757
Workshop on Specific Aspects of Computational Physics and Wavelet Analysis for Modelling Suddenly-Emerging Phenomena in Nonlinear Physics, and Nonlinear Applied Mathematics (PULSES 2006)	
Invariance Properties of Practical Test-Functions Used for Generating Asymmetrical Pulses <i>Stefan Pusca</i>	763
Simulating Superradiant Laser Pulses Using Partial Fraction Decomposition and Derivative Procedures <i>Theodora Toma, Stefan Pusca, Cristian Morarescu</i>	771
Simulating Delayed Pulses in Organic Materials <i>Bogdan Lazar, Andreea Sterian, Stefan Pusca, Viorel Paun, Cristian Toma, Cristian Morarescu</i>	779
Wave Propagation of Shannon Wavelets <i>Carlo Cattani</i>	785
Finite Element Analysis of the Thermoforming Manufacturing Process Using the Hyperelastic Mooney-Rivlin Model <i>Pierpaolo Carlone, Gaetano Salvatore Palazzo</i>	794
Analysis of Compatibility with Experimental Data of Fractal Descriptions of the Fracture Parameters <i>Dan Iordache, Stefan Pusca, Ghiocel Toma, Viorel Paun, Andreea Sterian, Cristian Morarescu</i>	804

Inner Potential of Generating Pulses as a Consequence of Recurrent Principles and Specific Computing Architecture <i>Cristian Morarescu</i>	814
Phenomenological and State Coefficients in Viscoanelastic Medium of Order One (with Memory) <i>Vincenzo Ciancio, Francesco Farsaci, Antonino Bartolotta</i>	821
Analysis of Singularities by Short Haar Wavelet Transform <i>Armando Ciancio, Carlo Cattani</i>	828
Spatial Aspects of Interaction Between High-Energy Pulses and Waves Considered as Suddenly Emerging Phenomena <i>Alexandru Toma, Stefan Pusca, Cristian Morarescu</i>	839
Noise Level Estimation Using Haar Wavelet Packet Trees for Sensor Robust Outlier Detection <i>Paolo Mercorelli, Alexander Frick</i>	847
A Theoretical Multiscale Analysis of Electrical Field for Fuel Cells Stack Structures <i>Carlo Cattani, Paolo Mercorelli, Francesco Villecco, Klaus Harbusch</i>	857
Workshop on Geocomputation (GC 2006)	
Tangent-Linear Models by Augmented LL-Parsers <i>Uwe Naumann, Andre Vehreschild</i>	865
GIS-T Web Services: A New Design Model for Developing GIS Customized ITS Application Systems <i>Xiaolin Lu</i>	875
An Algorithm on Extraction of Saline-Alkalized Land by Image Segmentation Based on ETM ⁺ Image <i>Li Jianping, Zhang Bai, Zhang Shuqing, Wang Zongming</i>	885
GIS Web Service Using Context Information in Mobile Environments <i>Xun Li, Woochul Shin, Li Li, Sang Bong Yoo</i>	895
The System for Predicting the Traffic Flow with the Real-Time Traffic Information <i>Mi-Gyung Cho, Young Jung Yu, SungSoo Kim</i>	904

Versioning Based Spatial Record Management Technique for Non-blocking Search Operations of Moving Objects
Ho Seok Kim, Hee Taek Kim, Myung Keun Kim, Gyoung Bae Kim, Hae Young Bae 914

A Wavelet Packets Watermarking Algorithm Based on Chaos Encryption
Jin Cong, Yan Jiang, Zhiguo Qu, Zhongmei Zhang 921

Workshop on Pattern Recognition and Ubiquitous Computing (PRUC 2006)

On a Face Recognition by the Modified Nonsingular Discriminant Analysis for a Ubiquitous Computing
Jin Ok Kim, Kwang Hoon Jung, Chin Hyun Chung 929

Rapid Determination of Compound Rifampicin Tablets Using Near Infrared Spectroscopywith Artificial Neural Network
Weiliang Guo, Qingfan Meng, Jiahui Lu, Chaojun Jiang, Yanchun Liang, Lirong Teng 938

An Efficient Search Algorithm for High-Dimensional Indexing Using Cell Based MBR
Bo-Hyun Wang, Byung-Wook Lee 946

Bimanual Hand Tracking
Hye-Jin Kim, Keun-Chang Kwak, Jaeyeon Lee 955

On a Feature Extraction by LMCUH Algorithm for a Ubiquitous Computing
Jin Ok Kim, Jun Yeong Jang, Chin Hyun Chung 964

Autoregressive Models of Speech Signal Variability in the Speech Commands Statistical Distinction
Victor Krasheninnikov, Andrey Armer, Natalia Krasheninnikova, Valery Derevyankin, Victor Kozhevnikov, Nikolay Makarov 974

u-Table: A Tabletop Interface for Multiple Users
Jangho Lee, Jee-In Kim 983

Implementation of Embedded System for Intelligent Image Recognition and Processing
Taikyeong Jeong, Jinsuk Kang, Yeon Sung Choi 993

Workshop on Data Storage Devices and Systems (DSDS 2006)

A Software Reproduction of Virtual Memory for Deeply Embedded Systems <i>Keun Soo Yim, Jae Don Lee, Jungkeun Park, Jeong-Joon Yoo, Chaeseok Im, Yeonseung Ryu</i>	1000
Block-Level Storage Security Architectures <i>Shichao Ma, Jizhong Han, Zhensong Wang</i>	1010
An Intelligent Garbage Collection Algorithm for Flash Memory Storages <i>Long-zhe Han, Yeonseung Ryu, Tae-sun Chung, Myungho Lee, Sukwon Hong</i>	1019
Design and Implementation of a Security Framework Based on the Object-Based Storage Device Standard <i>Kwangsun Ko, Gu Su Kim, June Kim, JungHyun Han, Ungmo Kim, Young Ik Eom</i>	1028
A Snappy B+-Trees Index Reconstruction for Main-Memory Storage Systems <i>Ig-hoon Lee, Junho Shim, Sang-goo Lee</i>	1036
An Approximate Analytic Performance Model of Object-Based Storage <i>Qun Liu, Dan Feng</i>	1045
OASIS: Implementation of a Cluster File System Using Object-Based Storage Devices <i>Young-Kyun Kim, Hong-Yeon Kim, Sang-Min Lee, June Kim, Myoung-Joon Kim</i>	1053
G-SCAN: A Novel Real-Time Disk Scheduling Using Grouping and Branch-and-Bound Strategy <i>Taeseok Kim, Eungkyu Song, Yunji Koh, Youjip Won, Kern Koh</i>	1062
A New Key Management Scheme for Distributed Encrypted Storage Systems <i>Myunghjin Lee, Hyokyung Bahn, Kijoon Chae</i>	1072

Technical Session on Technologies and Techniques for Distributed Data Mining (TTDM 2006)

WSRF Services for Composing Distributed Data Mining Applications on Grids: Functionality and Performance <i>Domenico Talia, Paolo Trunfio, Oreste Verta</i>	1080
On Mining 2 Step Walking Pattern from Mobile Users <i>John Goh, David Taniar</i>	1090
Effect of Similar Behaving Attributes in Mining of Fuzzy Association Rules in the Large Databases <i>Zahra Farzanyar, Mohammadreza Kangavari, Sattar Hashemi</i>	1100

General Tracks

The Study on Three Stages in Retinal Mechanism <i>Sung-Kwan Je, Kwang-Baek Kim, Jae-Hyun Cho, Ewi-Young Cha</i>	1110
Curvature Monotony Condition for Rational Quadratic B-spline Curves <i>Zhong Li, Lizhuang Ma, Dereck Meek, Wuzheng Tan, Zhihong Mao, Mingxi Zhao</i>	1118
Estimation of Input Ranking Using Input Sensitivity Approach <i>Sanggil Kang, Steve Morphet</i>	1127
A Collaborative Design Environment <i>Wuzheng Tan, Lizhuang Ma, Zhihong Mao, Zhong Li</i>	1134
Towards a High Integrity XML Link Update in Object-Relational Database <i>Eric Pardede, J. Wenny Rahayu, David Taniar</i>	1146
Various Types of Attacks and Solutions Regarding Secure Remote User Access over Insecure Networks <i>Eun-Jun Yoon, Kee-Young Yoo</i>	1156
Revealing Statistical Independence of Two Experimental Data Sets: An Improvement on Spearman's Algorithm <i>Bogdan Badea, Adriana Vlad</i>	1166

Parallelizable Computational Technique for Singularly Perturbed
Boundary Value Problems Using Spline
Rajesh Kumar Bawa 1177

Author Index 1183

Table of Contents – Part II

Workshop on Information Systems Information Technologies (ISIT 2006)

Efficient Algorithm for the Extraction of Association Rules in Data Mining <i>Pinaki Mitra, Chitrita Chaudhuri</i>	1
A Robust Digital Fingerprinting Mechanism for Digital Copyright Protection <i>Sangkuk Kim, Heejun Yoon, Hwamook Yoon, Wongoo Lee</i>	11
SoapFS: A Multiplatform File System <i>Víctor J. Sosa, Rodolfo Pazos, Juan G. González, Santos Cáceres, Laura Cruz, Mario Guillen</i>	18
An Application-Independent Multimedia Adaptation Framework for the Mobile Web <i>Sungmi Chon, Younghwan Lim, Kyujung Kim</i>	28
Effort Prediction Model Using Similarity for Embedded Software Development <i>Kazunori Iwata, Yoshiyuki Anan, Toyoshiro Nakashima, Naohiro Ishii</i>	40
A Component Cohesion Metric Applying the Properties of Linear Increment by Dynamic Dependency Relationships Between Classes <i>Misook Choi, Jongsuk Lee, Jongsung Ha</i>	49
The Maximum Capacity and Minimum Detectable Capacity of Information Hiding in Digital Images <i>Fan Zhang, Xianxing Liu, Jie Li, Xinhong Zhang</i>	59
BEAST: A Buffer Replacement Algorithm Using Spatial and Temporal Locality <i>Jun-Ki Min</i>	67
Performance Evaluation of the Flow-Based Router Using Intel IXP2800 Network Processors <i>Jaehyung Park, Myoung Hee Jung, Sujeong Chang, Su-il Choi, Min Young Chung, Byung Jun Ahn</i>	77

Robust 3D Face Data Acquisition Using a Sequential Color-Coded Pattern and Stereo Camera System <i>Ildo Kim, Sangki Kim, Sunjin Yu, Sangyoun Lee</i>	87
Robust Design of Face Recognition Systems <i>Sunjin Yu, Hyobin Lee, Jaihie Kim, Sangyoun Lee</i>	96
Transmission Rate Prediction of VBR Motion Image Using the Kalman Filter <i>Won Kim, Hyo-Jong Jang, Gye-Young Kim</i>	106
A Modeling and Similarity Measure Function for Multiple Trajectories in Moving Databases <i>Choon-Bo Shim, John Kim</i>	114
Distributed Processing of Context-Aware Authorization in Ubiquitous Computing Environments <i>Young-Chul Shim</i>	125
An Evaluation and Analysis for IP VPN Model in IPv6 Transition Environment <i>Hyung-Jin Lim, Dong-Young Lee, Tae-Kyung Kim, Tai-Myoung Chung</i>	135
Hybrid Storage Design for NC-94 Database Within the Parametric Data Model Framework <i>Seo-Young Noh</i>	145
A Unified Index for Moving-Objects Databases <i>Jaekwan Park, Bonghee Hong, Kyoungghan An, Jiwon Jung</i>	155
A Semantic Context-Aware Access Control in Pervasive Environments <i>Hyuk Jin Ko, Dong Ho Won, Dong Ryul Shin, Hyun Seung Choo, Ung Mo Kim</i>	165
Design and Implementation of an Index Structure Using Fixed Intervals for Tracing of RFID Tags <i>Sungwoo Ahn, Bonghee Hong, Chaehoon Ban, Kihyung Lee</i>	175
GARPAN: Gateway-Assisted Inter-PAN Routing for 6LoWPANs <i>Ali Hammad Akbar, Ki-Hyung Kim, Won-Do Jung, Ali Kashif Bashir, Seung-Wha Yoo</i>	186
Design and Performance Analysis of Multimedia Teachware Making System Using 2D Barcode <i>Duckki Kim, Youngsong Mun</i>	195

A Traffic Conditioning Algorithm for Enhancing the Fairness Between TCP and UDP Flows in DiffServ <i>Sungkeun Lee, Sunbok Goh, Moonsuk Jang</i>	204
Adaptive Mode Switching for Internetworking of MANET and WLAN Based on HMIPv6 <i>Hyewon K. Lee, Gukboh Kim, Youngsong Mun</i>	214
Automated Keyword Extraction Using Category Correlation of Data <i>Young-Ho Woo, Do-Hyun Nam, Tai-Sung Hur, Young-Bae Park, Woong Huh, Yo-Seop Woo, Hong-Ki Min</i>	224
On Cognitive Role of Negative Schema <i>Kang Soo Tae, Samuel Sangkon Lee</i>	231
Qualitative Method-Based the Effective Risk Mitigation Method in the Risk Management <i>Jung-Ho Eom, Sang-Hun Lee, Hyung-Jin Lim, Tai-Myoung Chung</i>	239
A Real-Time Web Contents Adaptation for Mobile User <i>Youn-Sik Hong, Ki-Young Lee</i>	249
STMPE: An Efficient Movement Pattern Extraction Algorithm for Spatio-temporal Data Mining <i>Dong-Oh Kim, Hong-Koo Kang, Dong-Suk Hong, Jae-Kwan Yun, Ki-Joon Han</i>	259
Return on Security Investment Against Cyber Attacks on Availability <i>Byoung Joon Min, Seung Hwan Yoo, Jong Ho Ryu, Dong Il Seo</i>	270
An Approach for Document Fragment Retrieval and Its Formatting Issue in Engineering Information Management <i>Shaofeng Liu, Chris A. McMahon, Mansur J. Darlington, Steve J. Culley, Peter J. Wild</i>	279
Minimum Cost Multicast Routing Based on High Utilization MC Nodes Suited to Sparse-Splitting Optical Networks <i>Sang-Hun Cho, Tae-Jin Lee, Min Young Chung, Hyunseung Choo</i>	288
Refinement Method of Post-processing and Training for Improvement of Automated Text Classification <i>Yun Jeong Choi, Seung Soo Park</i>	298

An Implementation of the Vectorizing-Based Automatic Nesting Software *NST*
Tae-Jung Lho, Dong-Joong Kang, Am-Suk Oh, Jang-Woo Kwon, Suk-Tae Bae, Kang-Hyuk Lee 309

A Resource Balancing Scheme in Heterogeneous Mobile Networks
Sangjoon Park, Youngchul Kim, Hyungbin Bang, Kwanjoong Kim, Youngsong Mun, Byunggi Kim 319

Fast BU Process Method for Real Time Multimedia Traffic in MIPv6
Wongil Park, Byunggi Kim 330

Network Intrusion Detection Using Statistical Probability Distribution
Gil-Jong Mun, Yong-Min Kim, DongKook Kim, Bong-Nam Noh 340

Network Anomaly Detection Based on Clustering of Sequence Patterns
Sang-Kyun Noh, Yong-Min Kim, DongKook Kim, Bong-Nam Noh 349

A Routing Protocol for Throughput Enhancement and Energy Saving in Mobile Ad Hoc Networks
HyoJin Kim, SeungJae Han, JooSeok Song 359

Spatial Indexing Based on the Semi-approximation Scheme of MBR
Jongwan Kim, SeokJin Im, Sang-Won Kang, Chong-Sun Hwang 369

Workflow Clustering Method Based on Process Similarity
Jae-Yoon Jung, Joonsoo Bae 379

Distributed, Scalable and Reconfigurable Inter-grid Resource Sharing Framework
Imran Rao, Eui-Nam Huh, SungYoung Lee, TaeChoong Chung 390

Scalable Mobile Internet Servers: Selecting Useful Images from the Web for Mobile Services
DaeHyuck Park, Maria Hong, Euisun Kang, Seongjin Ahn, YoungSong Mun, YoungHwan Lim 400

A Macro Mobility Handover Performance Improvement Scheme for HMIPv6
Kyunghye Lee, Younghwan Lim, Seongjin Ahn, Youngsong Mun 410

Cost Evaluation of Differentiated QoS Model in Mobile IPv6 Networks <i>Misun Kim, Youngsong Mun</i>	420
Proactive Self-healing System for Application Maintenance in Ubiquitous Computing Environment <i>Jeongmin Park, Giljong Yoo, Chulho Jeong, Eunseok Lee</i>	430
An Approach to Developing Domain Architectures Based on Variability Analysis <i>Mikyeong Moon, Keunhyuk Yeom</i>	441
A Technical Assessment of SoC Methodologies and Requirements for a Full-Blown Methodology <i>Du Wan Cheun, Tae Kwon Yu, Soo Ho Chang, Soo Dong Kim</i>	451
Context-Aware Home Network Environment on Grid (CAHE-G) <i>Seung-Hwan Jung, Tae-Dong Lee, Chang-Sung Jeong</i>	462
An Efficient Binding Update Scheme in HMIPv6 <i>Jaeduck Oh, Youngsong Mun</i>	471
A Scheduling Algorithm for Parallel Tasks in Peer-to-Peer Systems <i>Jeong Woo Jo, Jin Suk Kim</i>	480
Automatic Configuration of IPv6 Tunneling in a Dual Stack Host <i>Jaewook Lee, Jahwan Koo, Jinwook Chung, YoungSong Mun, YoungHwan Lim, Seung-Jung Shin, Seongjin Ahn</i>	487
Estimation of Link Speed Using Pattern Classification of GPS Probe Car Data <i>Seung-Heon Lee, Byung-Wook Lee, Young-Kyu Yang</i>	495
Storing and Querying of XML Documents Without Redundant Path Information <i>Byeong-Soo Jeong, Young-Koo Lee</i>	505
Route Optimization Problems with Local Mobile Nodes in Nested Mobile Networks <i>Young Beom Kim, Young-Jae Park, Sangbok Kim, Eui-Nam Huh</i>	515
Design of Network Aware Resource Allocation System for Grid Applications <i>Jonghyoun Choi, Ki-Sung Yu, Jongjin Park, Youngsong Mun</i>	525

Traffic Groomed Multicasting in Sparse-Splitting WDM Backbone Networks <i>Yeo-Ran Yoon, Tae-Jin Lee, Min Young Chung, Hyunseung Choo</i>	534
2-Way Text Classification for Harmful Web Documents <i>Youngsoo Kim, Taekyong Nam, Dongho Won</i>	545
Integration of a Structural Index with a Structural Join for Accelerating Path Queries <i>Jongik Kim, SooCheol Lee, Oh-Cheon Kwon</i>	552
Workshop on Mobile Communications (MC 2006)	
Thin-Client Computing for Supporting the QoS of Streaming Media in Mobile Devices <i>Joahyoung Lee, Dongmahn Seo, Yoon Kim, Changyeol Choi, Hwangkyu Choi, Inbum Jung</i>	562
MPLS Alternate Path Restoration with Guaranteed Bandwidth <i>Kil-Hung Lee, Jae-Soo Kim</i>	572
A Study on the WBTC and NBTC for CDMA Mobile Communications Networks <i>Sun-Kuk Noh</i>	582
A Secure Multicast Routing Protocol for Ad Hoc Networks with Misbehaving Nodes <i>Young-Chul Shim</i>	591
Seamless and Reliable Mobile Multicast Mechanism in Next Generation Networks <i>Choonsung Rhee, Sunyoung Han</i>	601
Adaptive Selection of MIPv6 and Hierarchical MIPv6 for Minimizing Signaling Cost <i>Younghyun Kim, Youngsong Mun</i>	611
DIASCOPE: Distributed Adaptation System Using Cooperative Proxies in Ubiquitous Network <i>Seunghwa Lee, Eunseok Lee</i>	621
A Novel Method for Energy-Efficient Clustering in Wireless Sensor Networks <i>Sung-Hyup Lee, Gi-Won Park, You-Ze Cho</i>	631

iSCSI Multi-connection and Error Recovery Method for Remote Storage System in Mobile Appliance <i>Shaikh Muhammad Allayear, Sung Soon Park</i>	641
Distributed Coordination and QoS-Aware Fair Queueing in Wireless Ad Hoc Networks <i>Muhammad Mahbub Alam, Md. Mamun-or-Rashid, Choong Seon Hong</i>	651
Lightweight Bindings for Mobile Routers <i>Youngjin Ahn, Tae-Jin Lee, Hyunseung Choo</i>	661
A Balanced Deployment Algorithm for Mobile Sensor Networks <i>Kil-Woong Jang, Byung-Soon Kim</i>	671
A Merging Clustering Algorithm for Mobile Ad Hoc Networks <i>Orhan Dagdeviren, Kayhan Erciyas, Deniz Cokuslu</i>	681
Context-Aware Cross Layered Multimedia Streaming Based on Variable Packet Size Transmission <i>Hyung Su Lee, Hee Yong Youn, Hyedong Jung</i>	691
Adaptive Mobile Checkpointing Facility for Wireless Sensor Networks <i>Sangho Yi, Junyoung Heo, Yookun Cho, Jiman Hong</i>	701
NeMRI - Based Multicasting in Network Mobility <i>Moonseong Kim, Tae-Jin Lee, Hyunseung Choo</i>	710
Improving TCP Throughput and Fairness over Multi-rate IEEE 802.11 Wireless LANs <i>Seon-Don Lee, Dong-Hee Kwon, Woo-Jae Kim, Young-Joo Suh</i>	720
Local Source Routing Based Route Optimization in Nested Mobile Networks <i>Yunkuk Kim, Sinam Woo, Sangwook Kang, Woojin Park, Sunshin An</i>	730
An Efficient Movement Management Method of Mobile Node in Mobile IPv6 <i>Chungsoo Shin, Byunggi Kim, Youngsong Mun</i>	740
Homogeneous 2-Hops Broadcast in 2D <i>Gautam K. Das, Sandip Das, Subhas C. Nandy</i>	750

A Study on the Transportation Period of the EPG Data Specification in Terrestrial DMB
Minju Cho, Jun Hwang, Gyung-Leen Park, Junguk Kim, Taeuk Jang, Juhyun Oh, Young Seok Chae 760

Cluster-Based Certificate Chain for Mobile Ad Hoc Networks
GeneBeck Hahn, Taekyoung Kwon, SinKyu Kim, JooSeok Song 769

Optimization of Base Stations Positioning in Mobile Networks
Surgwon Sohn, Geun-Sik Jo 779

Design of Maximum Remaining Energy Constrained Directed Diffusion Routing for Wireless Sensor Networks
An Kyu Hwang, Jae Yong Lee, Byung Chul Kim 788

A Timestamp-Based Optimistic Concurrency Control for Handling Mobile Transactions
Ho-Jin Choi, Byeong-Soo Jeong 796

Effects of PRF and Slot Interval on the Data Throughput of PPM-Based Ultra Wide-Band Systems in Multi-path Channels
Sungbin Im, Taehyung Park 806

Hierarchical Cluster Configuration Scheme for Scalable Ad Hoc Networks
Keun-Ho Lee, Chong-Sun Hwang 816

A Route Optimization Via Recursive CoA Substitution for Nested Mobile Networks
Young Beom Kim, Kang-Yoon Lee, Hyunchul Ku, Eui-Nam Huh 827

Energy-Aware Routing Algorithm Using Backup Route for Ad-Hoc Networks
Se-Won Jung, Chae-Woo Lee 837

Mitigating Broadcast Storms in Stateless Address Auto-configuring MANETs
Shoaib Mukhtar, Ali Hammad Akbar, Shafique Ahmad Chaudhry, Won-Sik Yoon, Ki-Hyung Kim, Suk-Kyo Hong 847

Routing with Maximum EDPs and Wavelength Assignment with Path Conflict Graphs
Won Jin Yoon, Duk Hun Kim, Min Young Chung, Tae-Jin Lee, Hyunseung Choo 856

Workshop on Authentication, Authorization and Accounting (AAA 2006)

Energy Conserving Security Mechanism for Wireless Sensor Network <i>Md.Abdul Hamid, Md. Mustafizur Rahman, Choong Seon Hong</i>	866
Inter-domain Security Management to Protect Legitimate User Access from DDoS Attacks <i>Sung Ki Kim, Byoung Joon Min</i>	876
An Authentication Scheme Between Wireless LAN and Mobile IPv6 During Handover <i>Youngsong Mun, Miyoung Kim</i>	885
Mechanism of the Secure MAP Discovery in Hierarchical MIPv6 <i>Jonghyoun Choi, Youngsong Mun</i>	895
An Efficient Authentication Mechanism for Fast Mobility Service in MIPv6 <i>Seung-Yeon Lee, Eui-Nam Huh, Yang-Woo Kim, Kyesan Lee</i>	905
An Improved Fingerprint-Based Remote User Authentication Scheme Using Smart Cards <i>Youngkwon Lee, Taekyoung Kwon</i>	915
Route Optimization with AAA in Network Mobility <i>KwangChul Jeong, Tae-Jin Lee, Sungchang Lee, Hyunseung Choo</i>	923
Verifier-Based Home Network Security Mechanism <i>Hoseong Jeon, Min Young Chung, Jaehyoun Kim, Hyunseung Choo</i>	934
VO Authentication Framework in Grid Environment Using Digital Signature <i>Seung-Hyeon Lee, Byung-Sun Choi, Jae-Seung Lee, Ki-Young Moon, Jae-Kwang Lee</i>	945
Confidence Value Based Multi Levels of Authentication for Ubiquitous Computing Environments <i>He Zheng, Jin Kwak, Kyungho Son, Wansuk Lee, Seungjoo Kim, Dongho Won</i>	954

Workshop on Modelling of Location Management in Mobile Information Systems (MLM 2006)

An Efficient Mobility Management Scheme for Hierarchical Mobile IPv6 Networks
Zheng Wan, Zhengyou Wang, Zhijun Fang, Weiming Zeng, Shiqian Wu 964

The Verification of Linearizer for Wibro PAM
Inn-yeal Oh, Hyung-joon Jeon 974

Automatic Location Detection System for Anomaly Traffic on Wired/Wireless Networks
Ki-Sung Yu, Won-Hyuk Lee, Sung-Jin Ahn, Jin-Wook Chung 982

Road Boundary Extraction Using Shadow Path Reconstruction in Urban Areas
Kong-Hyun Yun, Hong-Gyoo Sohn, Joon Heo 989

Photograph Database for Highway Facility Management in Mobile Mapping System
Jeong Hyun Kim, Dong-Hoon Jeong, Byung-Guk Kim 996

High Speed Codebook Searching Algorithm for the CELP Vocoder in the Internet-Based Environment
So Yeon Min, Eun Sook Cho, Chul Jin Kim 1003

Algorithm and Structure to Cancel Signal Distortion in ATSC Digital TV System
Hyung Joon Jeon, Inn Yeal Oh 1009

Mobility Management for INS in 3G Mobile Networks
Dong Chun Lee 1017

Detection Methods for Executive Compressed Malicious Codes in Wire/Wireless Networks
Seung-Jae Yoo, Kwiam J. Kim 1025

Workshop on Intelligent Services and the Synchronization in Mobile Multimedia Networks (ISS 2006)

A Dynamic QoS Management Scheme in B3G Networks
Sangjoon Park, Youngchul Kim, Jongmyung Choi, Jongchan Lee, Kwanjoong Kim, Byunggi Kim 1033

Stereo Matching Strategy for 3-D Urban Modeling <i>Choung-Hwan Park, Hong-Gyoo Sohn, Yeong-Sun Song</i>	1043
Protection Structure Building for Malicious Traffic Protecting in Intranet Systems <i>SiChoon Noh, Eun Jee Song, Dong Chun Lee</i>	1051
A Transaction Processing Model for Performance Analysis in Multilevel-Secure Database Systems <i>Sukhoon Kang, Seok Soo Kim, Geuk Lee</i>	1060
Temporal Land Information System (TLIS) for Dynamically Changing Cadastral Data <i>Joon Heo, Jeong Hyun Kim, Seoungpil Kang</i>	107
A Study on the Pitch Extraction Detection by Linear Approximation of Sub-band <i>Keun Wang Lee, Kwang Hyoung Lee, So Yeon Min</i>	1074
Hybrid Queuing Scheme to Reduce Call Blocking in Multimedia Mobile Networks <i>Hong-Jin Kim, Sok-Pal Cho, Dong Chun Lee</i>	1082
General Tracks	
A Study for Monitoring Technique for Home Server Based on Web Camera <i>Jong-Geun Jeong, Byung-Rae Cha</i>	1090
New Algorithms for the Unsplittable Flow Problem <i>Krzysztof Walkowiak</i>	1101
Performance Evaluation of the Parallel Packet Switch with a Sliding Window Scheme <i>Chia-Lung Liu, Chiou Moh, Chin-Chi Wu, Woei Lin</i>	1111
A Simple and Efficient RWA Algorithm Based on Priority of Edge Disjoint Paths <i>Soon-Bin Yim, Min Young Chung, Hyunseung Choo, Tae-Jin Lee</i>	1121
Performance Improvement of TCP over Optical Burst Switching Networks with Drop Policy <i>SuKyoung Lee, LaeYoung Kim, JooSeok Song</i>	1131

A New Size-Based Burst Assembly Scheme for OBS Switches
SeoungYoung Lee, InYong Hwang, HongShik Park 1140

The E-Textile Token Grid Network with Dual Rings
Nenggan Zheng, Zhaohui Wu, Lei Chen, Yanmiao Zhou 1149

A MAC Protocol Using Separate Wakeup Slots for Sensor Network
Jinsuk Pak, Jeongho Son, Kijun Han 1159

A Study on L2/OPN Design for Grid High Performance Network
Min-Ki Noh, Joon-Min Gil, Ki-Sung Yoo, Seong-Jin Ahn 1169

Reasoning Technique for Extended Fuzzy ALCQ
Yanhui Li, Baowen Xu, Jianjiang Lu, Dazhou Kang 1179

Reducing Delivery Delay in HRM Tree
Sang-Seon Byun, Chuck Yoo 1189

Data Analysis and Utilization Method Based on Genetic Programming
 in Ship Design
*Kyung Ho Lee, Yun Seog Yeun, Young Soon Yang, Jang Hyun Lee,
 June Oh* 1199

An Evolutionary and Attribute-Oriented Ensemble Classifier
Chien-I Lee, Cheng-Jung Tsai, Chih-Wei Ku 1210

A Study of the Evaluation Function and the Clustering Algorithm for
 Semantic Web Environment
Je-Min Kim, Young-Tack Park 1219

A Divergence-Oriented Approach for Web Users Clustering
*Sophia G. Petridou, Vassiliki A. Koutsonikola, Athena I. Vakali,
 Georgios I. Papadimitriou* 1229

Author Index 1239

Table of Contents – Part III

Workshop on Approaches or Methods of Security Engineering (AMSE 2006, Sess. A)

A Security Requirement Management Database Based on ISO/IEC 15408 <i>Shoichi Morimoto, Daisuke Horie, Jingde Cheng</i>	1
Development of Committee Neural Network for Computer Access Security System <i>A. Sermet Anagun</i>	11
C-TOBI-Based Pitch Accent Prediction Using Maximum-Entropy Model <i>Byeongchang Kim, Gary Geunbae Lee</i>	21
Design and Fabrication of Security and Home Automation System <i>Eung Soo Kim, Min Sung Kim</i>	31
PGNIDS(Pattern-Graph Based Network Intrusion Detection System) Design <i>Byung-kwan Lee, Seung-hae Yang, Dong-Hyuck Kwon, Dai-Youn Kim</i>	38
Experiments and Hardware Countermeasures on Power Analysis Attacks <i>ManKi Ahn, HoonJae Lee</i>	48
Information System Modeling for Analysis of Propagation Effects and Levels of Damage <i>InJung Kim, YoonJung Chung, YoungGyo Lee, Eul Gyu Im, Dongho Won</i>	54
A Belt-Zone Method for Decreasing Control Messages in Ad Hoc Networks <i>Youngrag Kim, JaeYoun Jung, Seunghwan Lee, Chonggun Kim</i>	64
A VLSM Address Management Method for Variable IP Subnetting <i>SeongKwon Cheon, DongXue Jin, ChongGun Kim</i>	73
SDSEM: Software Development Success Evolution Model <i>Haeng-Kon Kim, Sang-Yong Byun</i>	84

A Robust Routing Protocol by a Substitute Local Path in Ad Hoc Networks
Mary Wu, SangJoon Jung, Seunghwan Lee, Chonggun Kim 93

Power Efficient Wireless LAN Using 16-State Trellis-Coded Modulation for Infrared Communications
Hae Geun Kim 104

The Design and Implementation of Real-Time Environment Monitoring Systems Based on Wireless Sensor Networks
Kyung-Hoon Jung, Seok-Cheol Lee, Hyun-Suk Hwang, Chang-Soo Kim 115

Ontology-Based Information Search in the Real World Using Web Services
Hyun-Suk Hwang, Kyoo-Seok Park, Chang-Soo Kim 125

An Active Node Set Maintenance Scheme for Distributed Sensor Networks
Tae-Young Byun, Minsu Kim, Sungho Hwang, Sung-Eok Jeon 134

Intelligent Information Search Mechanism Using Filtering and NFC Based on Multi-agents in the Distributed Environment
Subong Yi, Bobby D. Gerardo, Young-Seok Lee, Jaewan Lee 144

Network Anomaly Behavior Detection Using an Adaptive Multiplex Detector
Misun Kim, Minsoo Kim, JaeHyun Seo 154

Applying Product Line to the Embedded Systems
Haeng-Kon Kim 163

Enhanced Fuzzy Single Layer Learning Algorithm Using Automatic Tuning of Threshold
Kwang-Baek Kim, Byung-Kwan Lee, Soon-Ho Kim 172

Optimization of Location Management in the Distributed Location-Based Services Using Collaborative Agents
Romeo Mark A. Mateo, Jaewan Lee, Hyunho Yang 178

Design of H.264/AVC-Based Software Decoder for Mobile Phone
Hyung-Su Jeon, Hye-Min Noh, Cheol-Jung Yoo, Ok-Bae Chang 188

Transforming a Legacy System into Components
Haeng-Kon Kim, Youn-Ky Chung 198

Pseudorandom Number Generator Using Optimal Normal Basis <i>Injoo Jang, Hyeong Seon Yoo</i>	206
Efficient Nonce-Based Authentication Scheme Using Token-Update <i>Wenbo Shi, Hyeong Seon Yoo</i>	213
An Efficient Management of Network Traffic Performance Using Framework-Based Performance Management Tool <i>Seong-Man Choi, Cheol-Jung Yoo, Ok-Bae Chang</i>	222
A Prediction Method of Network Traffic Using Time Series Models <i>Sangjoon Jung, Chonggun Kim, Younky Chung</i>	234
An Obstacle Avoidance Method for Chaotic Robots Using Angular Degree Limitations <i>Youngchul Bae, MalRey Lee, Thomas M. Gatton</i>	244
Intersection Simulation System Based on Traffic Flow Control Framework <i>Chang-Sun Shin, Dong-In Ahn, Hyun Yoe, Su-Chong Joo</i>	251
A HIICA(Highly-Improved Intra CA) Design for M-Commerce <i>Byung-kwan Lee, Chang-min Kim, Dae-won Shin, Seung-hae Yang</i>	261
Highly Reliable Synchronous Stream Cipher System for Link Encryption <i>HoonJae Lee</i>	269
Recognition of Concrete Surface Cracks Using ART2-Based Radial Basis Function Neural Network <i>Kwang-Baek Kim, Hwang-Kyu Yang, Sang-Ho Ahn</i>	279
Hybrid Image Mosaic Construction Using the Hierarchical Method <i>Oh-Hyung Kang, Ji-Hyun Lee, Yang-Won Rhee</i>	287
Workshop on Applied Cryptography and Information Security (ACIS 2006)	
Public Key Encryption with Keyword Search Based on K-Resilient IBE <i>Dalia Khader</i>	298
A Generic Construction of Secure Signatures Without Random Oracles <i>Jin Li, Yuen-Yan Chan, Yanming Wang</i>	309

A Separation Between Selective and Full-Identity Security Notions for Identity-Based Encryption <i>David Galindo</i>	318
Traceable Signature: Better Efficiency and Beyond <i>He Ge, Stephen R. Tate</i>	327
On the TYS Signature Scheme <i>Marc Joye, Hung-Mei Lin</i>	338
Efficient Partially Blind Signatures with Provable Security <i>Qianhong Wu, Willy Susilo, Yi Mu, Fanguo Zhang</i>	345
A Framework for Robust Group Key Agreement <i>Jens-Matthias Bohli</i>	355
BGN Authentication and Its Extension to Convey Message Commitments <i>Yuen-Yan Chan, Jin Li</i>	365
New Security Problem in RFID Systems “Tag Killing” <i>Dong-Guk Han, Tsuyoshi Takagi, Ho Won Kim, Kyo Il Chung</i>	375
A Model for Security Vulnerability Pattern <i>Hyungwoo Kang, Kibom Kim, Soonjwa Hong, Dong Hoon Lee</i>	385
A New Timestamping Scheme Based on Skip Lists <i>Kaouthar Blibech, Alban Gabillon</i>	395
A Semi-fragile Watermarking Scheme Based on SVD and VQ Techniques <i>Hsien-Chu Wu, Chuan-Po Yeh, Chwei-Shyong Tsai</i>	406
New Constructions of Universal Hash Functions Based on Function Sums <i>Khoongming Khoo, Swee-Huay Heng</i>	416
Analysis of Fast Blockcipher-Based Hash Functions <i>Martin Stanek</i>	426
Application of LFSRs for Parallel Sequence Generation in Cryptologic Algorithms <i>Sourav Mukhopadhyay, Palash Sarkar</i>	436
Provable Security for an RC6-like Structure and a MISTY-FO-like Structure Against Differential Cryptanalysis <i>Changhoon Lee, Jongsung Kim, Jaechul Sung, Seokhie Hong, Sangjin Lee</i>	446

Design and Implementation of an FPGA-Based 1.452-Gbps Non-pipelined AES Architecture <i>Ignacio Algreto-Badillo, Claudia Feregrino-Urbe, René Cumplido . . .</i>	456
--	-----

Workshop on Internet Communications Security (WICS 2006)

Security Weaknesses in Two Proxy Signature Schemes <i>Jiqiang Lu</i>	466
A Proposal of Extension of FMS-Based Mechanism to Find Attack Paths <i>Byung-Ryong Kim, Ki-Chang Kim</i>	476
Comparative Analysis of IPv6 VPN Transition in NEMO Environments <i>Hyung-Jin Lim, Dong-Young Lee, Tai-Myoung Chung</i>	486
A Short-Lived Key Selection Approach to Authenticate Data Origin of Multimedia Stream <i>Namhi Kang, Younghan Kim</i>	497
Weakest Link Attack on Single Sign-On and Its Case in SAML V2.0 Web SSO <i>Yuen-Yan Chan</i>	507
An Inter-domain Key Agreement Protocol Using Weak Passwords <i>Youngsook Lee, Junghyun Nam, Dongho Won</i>	517
A Practical Solution for Distribution Rights Protection in Multicast Environments <i>Josep Pegueroles, Marcel Fernández, Francisco Rico-Novella, Miguel Soriano</i>	527
Audit-Based Access Control in Nomadic Wireless Environments <i>Francesco Palmieri, Ugo Fiore</i>	537

Workshop on Optimization: Theories and Applications (OTA 2006)

Cost – Time Trade Off Models Application to Crashing Flow Shop Scheduling Problems <i>Morteza Bagherpour, Siamak Noori, S. Jafar Sadjadi</i>	546
--	-----

The ASALB Problem with Processing Alternatives Involving Different Tasks: Definition, Formalization and Resolution <i>Liliana Capacho, Rafael Pastor</i>	554
Satisfying Constraints for Locating Export Containers in Port Container Terminals <i>Kap Hwan Kim, Jong-Sool Lee</i>	564
A Price Discrimination Modeling Using Geometric Programming <i>Seyed J. Sadjadi, M. Ziaee</i>	574
Hybrid Evolutionary Algorithms for the Rectilinear Steiner Tree Problem Using Fitness Estimation <i>Byounghak Yang</i>	581
Data Reduction for Instance-Based Learning Using Entropy-Based Partitioning <i>Seung-Hyun Son, Jae-Yearn Kim</i>	590
Coordinated Inventory Models with Compensation Policy in a Three Level Supply Chain <i>Jeong Hun Lee, Il Kyeong Moon</i>	600
Using Constraint Satisfaction Approach to Solve the Capacity Allocation Problem for Photolithography Area <i>Shu-Hsing Chung, Chun-Ying Huang, Amy Hsin-I Lee</i>	610
Scheduling an R&D Project with Quality-Dependent Time Slots <i>Mario Vanhoucke</i>	621
The Bottleneck Tree Alignment Problems <i>Yen Hung Chen, Chuan Yi Tang</i>	631
Performance Study of a Genetic Algorithm for Sequencing in Mixed Model Non-permutation Flowshops Using Constrained Buffers <i>Gerrit Färber, Anna M. Coves Moreno</i>	638
Optimizing Relative Weights of Alternatives with Fuzzy Comparative Judgment <i>Chung-Hsing Yeh, Yu-Hern Chang</i>	649
Model and Solution for the Multilevel Production-Inventory System Before Ironmaking in Shanghai Baoshan Iron and Steel Complex <i>Guoli Liu, Lixin Tang</i>	659

A Coordination Algorithm for Deciding Order-Up-To Level of a Serial Supply Chain in an Uncertain Environment <i>Kung-Jeng Wang, Wen-Hai Chih, Ken Hwang</i>	668
Optimization of Performance of Genetic Algorithm for 0-1 Knapsack Problems Using Taguchi Method <i>A.S. Anagun, T. Sarac</i>	678
Truck Dock Assignment Problem with Time Windows and Capacity Constraint in Transshipment Network Through Crossdocks <i>Andrew Lim, Hong Ma, Zhaowei Miao</i>	688
An Entropy Based Group Setup Strategy for PCB Assembly <i>In-Jae Jeong</i>	698
Cross-Facility Production and Transportation Planning Problem with Perishable Inventory <i>Sandra Duni Ekşioğlu, Mingzhou Jin</i>	708
A Unified Framework for the Analysis of M/G/1 Queue Controlled by Workload <i>Ho Woo Lee, Se Won Lee, Won Ju Seo, Sahng Hoon Cheon, Jongwoo Jeon</i>	718
Tabu Search Heuristics for Parallel Machine Scheduling with Sequence-Dependent Setup and Ready Times <i>Sang-Il Kim, Hyun-Seon Choi, Dong-Ho Lee</i>	728
The Maximum Integer Multiterminal Flow Problem <i>Cédric Bentz</i>	738
Routing with Early Ordering for Just-In-Time Manufacturing Systems <i>Mingzhou Jin, Kai Liu, Burak Eksioğlu</i>	748
A Variant of the Constant Step Rule for Approximate Subgradient Methods over Nonlinear Networks <i>Eugenio Mijangos</i>	757
On the Optimal Buffer Allocation of an FMS with Finite In-Process Buffers <i>Soo-Tae Kwon</i>	767
Optimization Problems in the Simulation of Multifactor Portfolio Credit Risk <i>Wanmo Kang, Kyungsik Lee</i>	777

Two-Server Network Disconnection Problem <i>Byung-Cheon Choi, Sung-Pil Hong</i>	785
One-Sided Monge TSP Is NP-Hard <i>Vladimir Deineko, Alexander Tiskin</i>	793
On Direct Methods for Lexicographic Min-Max Optimization <i>Włodzimierz Ogryczak, Tomasz Śliwiński</i>	802
Multivariate Convex Approximation and Least-Norm Convex Data-Smoothing <i>Alex Y.D. Siem, Dick den Hertog, Aswin L. Hoffmann</i>	812
Linear Convergence of Tatônnement in a Bertrand Oligopoly <i>Guillermo Gallego, Woonghee Tim Huh, Wanmo Kang, Robert Phillips</i>	822
Design for Using Purpose of Assembly-Group <i>Hak-Soo Mok, Chang-Hyo Han, Chan-Hyoung Lim, John-Hee Hong, Jong-Rae Cho</i>	832
A Conditional Gaussian Martingale Algorithm for Global Optimization <i>Manuel L. Esquivel</i>	841
Finding the Number of Clusters Minimizing Energy Consumption of Wireless Sensor Networks <i>Hyunsoo Kim, Hee Yong Youn</i>	852
A Two-Echelon Deteriorating Production-Inventory Newsboy Model with Imperfect Production Process <i>Hui-Ming Wee, Chun-Jen Chung</i>	862
Mathematical Modeling and Tabu Search Heuristic for the Traveling Tournament Problem <i>Jin Ho Lee, Young Hoon Lee, Yun Ho Lee</i>	875
An Integrated Production-Inventory Model for Deteriorating Items with Imperfect Quality and Shortage Backordering Considerations <i>H.M. Wee, Jonas C.P. Yu, K.J. Wang</i>	885
A Clustering Algorithm Using the Ordered Weight Sum of Self-Organizing Feature Maps <i>Jong-Sub Lee, Maing-Kyu Kang</i>	898

Global Optimization of the Scenario Generation and Portfolio Selection Problems <i>Panos Parpas, Berç Rustem</i>	908
A Generalized Fuzzy Optimization Framework for R&D Project Selection Using Real Options Valuation <i>E. Ertugrul Karsak</i>	918
Supply Chain Network Design and Transshipment Hub Location for Third Party Logistics Providers <i>Seungwoo Kwon, Kyungdo Park, Chulung Lee, Sung-Shick Kim, Hak-Jin Kim, Zhong Liang</i>	928
A Group Search Optimizer for Neural Network Training <i>S. He, Q.H. Wu, J.R. Saunders</i>	934
Application of Two-Stage Stochastic Linear Program for Portfolio Selection Problem <i>Kuo-Hwa Chang, Huifen Chen, Ching-Fen Lin</i>	944
General Tracks	
Hierarchical Clustering Algorithm Based on Mobility in Mobile Ad Hoc Networks <i>Sulyun Sung, Yuhwa Seo, Yongtae Shin</i>	954
An Alternative Approach to the Standard Enterprise Resource Planning Life Cycle: Enterprise Reference Metamodeling <i>Miguel Gutiérrez, Alfonso Durán, Pedro Cocho</i>	964
Static Analysis Based Software Architecture Recovery <i>Jiang Guo, Yuehong Liao, Raj Pamula</i>	974
A First Approach to a Data Quality Model for Web Portals <i>Angelica Caro, Coral Calero, Ismael Caballero, Mario Piattini</i>	984
Design for Environment-Friendly Product <i>Hak-Soo Mok, Jong-Rae Cho, Kwang-Sup Moon</i>	994
Performance of HECC Coprocessors Using Inversion-Free Formulae <i>Thomas Wollinger, Guido Bertoni, Luca Breveglieri, Christof Paar</i>	1004
Metrics of Password Management Policy <i>Carlos Villarrubia, Eduardo Fernández-Medina, Mario Piattini</i>	1013

Using UML Packages for Designing Secure Data Warehouses <i>Rodolfo Villarroel, Emilio Soler, Eduardo Fernández-Medina, Juan Trujillo, Mario Piattini</i>	1024
Practical Attack on the Shrinking Generator <i>Pino Caballero-Gil, Amparo Fúster-Sabater</i>	1035
A Comparative Study of Proposals for Establishing Security Requirements for the Development of Secure Information Systems <i>Daniel Mellado, Eduardo Fernández-Medina, Mario Piattini</i>	1044
Stochastic Simulation Method for the Term Structure Models with Jump <i>Kisoeb Park, Moonseong Kim, Seki Kim</i>	1054
The Ellipsoidal l_p Norm Obnoxious Facility Location Problem <i>Yu Xia</i>	1064
On the Performance of Recovery Rate Modeling <i>J. Samuel Baixauli, Susana Alvarez</i>	1073
Using Performance Profiles to Evaluate Preconditioners for Iterative Methods <i>Michael Lazzareschi, Tzu-Yi Chen</i>	1081
Multicast ω -Trees Based on Statistical Analysis <i>Moonseong Kim, Young-Cheol Bang, Hyunseung Choo</i>	1090
The Gateways Location and Topology Assignment Problem in Hierarchical Wide Area Networks: Algorithms and Computational Results <i>Przemyslaw Ryba, Andrzej Kasprzak</i>	1100
Developing an Intelligent Supplier Chain System Collaborating with Customer Relationship Management <i>Gye Hang Hong, Sung Ho Ha</i>	1110
The Three-Criteria Servers Replication and Topology Assignment Problem in Wide Area Networks <i>Marcin Markowski, Andrzej Kasprzak</i>	1119
An Efficient Multicast Tree with Delay and Delay Variation Constraints <i>Moonseong Kim, Young-Cheol Bang, Jong S. Yang, Hyunseung Choo</i>	1129
Algorithms on Extended (δ, γ) -Matching <i>Inbok Lee, Raphaël Clifford, Sung-Ryul Kim</i>	1137

SOM and Neural Gas as Graduated Nonconvexity Algorithms <i>Ana I. González, Alicia D’Anjou, M. Teresa García-Sebastian, Manuel Graña</i>	1143
Analysis of Multi-domain Complex Simulation Studies <i>James R. Gattiker, Earl Lawrence, David Higdon</i>	1153
A Fast Method for Detecting Moving Vehicles Using Plane Constraint of Geometric Invariance <i>Dong-Joong Kang, Jong-Eun Ha, Tae-Jung Lho</i>	1163
Robust Fault Matched Optical Flow Detection Using 2D Histogram <i>Jaechoon Chon, Hyongsuk Kim</i>	1172
Iris Recognition: Localization, Segmentation and Feature Extraction Based on Gabor Transform <i>Mohammadreza Noruzi, Mansour Vafadoost, M. Shahram Moin</i>	1180
Optimal Edge Detection Using Perfect Sharpening of Ramp Edges <i>Eun Mi Kim, Cherl Soo Park, Jong Gu Lee</i>	1190
Eye Tracking Using Neural Network and Mean-Shift <i>Eun Yi Kim, Sin Kuk Kang</i>	1200
The Optimal Feature Extraction Procedure for Statistical Pattern Recognition <i>Marek Kurzynski, Edward Puchala</i>	1210
A New Approach for Human Identification Using Gait Recognition <i>Murat Ekinçi</i>	1216
Author Index	1227

Table of Contents – Part IV

Workshop on Ubiquitous Web Systems and Intelligence (UWSI 2006)

Message Transport Interface for Efficient Communication Between Agent Framework and Event Service <i>Sang Yong Park, Hee Yong Youn</i>	1
An Ontology-Based Context Model in a Smart Home <i>Eunhoe Kim, Jaeyoung Choi</i>	11
Service Mobility Manager for OSGi Framework <i>Seungkeun Lee, Intae Kim, Kiwook Rim, Jeonghyun Lee</i>	21
A Ubiquitous Workflow Service Framework <i>Joohyun Han, Yongyun Cho, Eunhoe Kim, Jaeyoung Choi</i>	30
Self Organizing Sensor Networks Using Intelligent Clustering <i>Kwangcheol Shin, Ajith Abraham, Sang Yong Han</i>	40
Searching and Selecting Web Services Using Case Based Reasoning <i>Olivia Graciela Fragoso Diaz, René Santaolaya Salgado, Ismael Solís Moreno, Guillermo Rodríguez Ortiz</i>	50
Fuzzy Logic Based Propagation Limiting Method for Message Routing in Wireless Sensor Networks <i>Sang Hoon Chi, Tae Ho Cho</i>	58
Content Delivery with Spatial Caching Scheme in Mobile Wireless Networks <i>Backhyun Kim, Iksoo Kim</i>	68
Higher Education Web Information System Usage Analysis with a Data Webhouse <i>Carla Teixeira Lopes, Gabriel David</i>	78
A User Management System for Federated Databases Using Web Services <i>Fuyu Liu, Erdogan Dogdu</i>	88

A Dynamic Evaluation Framework for Mobile Applications <i>Anders Magnus Andersen, Torab Torabi</i>	98
SOAM: An Environment Adaptation Model for the Pervasive Semantic Web <i>Juan Ignacio Vazquez, Diego López de Ipiña, Iñigo Sedano</i>	108
Implementing the MPEG-21 Adaptation Quality of Service in Dynamic Environments <i>Marios C. Angelides, Anastasis A. Sofokleous, Christos N. Schizas</i>	118
A Middleware Architecture Determining Application Context Using Shared Ontology <i>Kugsang Jeong, Deokjai Choi, Soo Hyung Kim, Gueesang Lee</i>	128
Context-Aware Regulation of Context-Aware Mobile Services in Pervasive Computing Environments <i>Evi Syukur, Seng Wai Loke</i>	138
Designing and Implementing Physical Hypermedia Applications <i>Cecilia Challiol, Gustavo Rossi, Silvia Gordillo, Valeria De Cristófolo</i>	148
Replicated Ubiquitous Nets <i>Fernando Rosa-Velardo, David de Frutos-Escrig, Olga Marroquín-Alonso</i>	158
Design of a Shared Ontology Used for Translating Negotiation Primitives <i>Joaquín Pérez, Maricela Bravo, Rodolfo Pazos, Gerardo Reyes, Juan Frausto, Víctor Sosa, Máximo López</i>	169
A Web Page Ranking Method by Analyzing Hyperlink Structure and K-Elements <i>Jun Lai, Ben Soh, Chai Fei</i>	179
Efficient Scheduling by Incorporating Bin Packing with Limited and Weighted Round Robin for Bluetooth <i>Eung Ju Lee, Hee Yong Youn</i>	187
ECA Rule Component for Timely Collaboration of Web-Based Distributed Business Systems <i>DongWoo Lee, Seonghoon Lee, Yongjin Lee</i>	197
Dynamic Approach for Integrating Web Data Warehouses <i>D. Xuan Le, J. Wenny Rahayu, Eric Pardede</i>	207

Location Aware Business Process Deployment <i>Saqib Ali, Torab Torabi, Hassan Ali</i>	217
A Framework for Rapid Development of RFID Applications <i>Youngbong Kim, Mikyeong Moon, Keunhyuk Yeom</i>	226
Workshop on Ubiquitous Application and Security Service (UASS 2006)	
A Flexible DRM System Considering Ubiquitous Environment <i>Jong Hyuk Park, Sangjin Lee, Byoung-Soo Koh</i>	236
User Centric Intelligent IPMPS in Ubi-Home <i>Jong Hyuk Park, Jungsuk Song, Sangjin Lee, Byoung-Soo Koh, In-Hwa Hong</i>	245
The Design and Development of a Secure Keystroke System for u Business <i>Hangbae Chang, Kyung-Kyu Kim, Hosin Lee, Jungduk Kim</i>	255
Linkability of a Blind Signature Scheme and Its Improved Scheme <i>Jianhong Zhang, Tao Wei, Jian Yu Zhang, Wei Zou</i>	262
A Noble Structural Model for e-Learning Services in Ubiquitous Environment <i>Minseong Ju, Seoksoo Kim, Yeong-Deok Kim, Sukhoon Kang</i>	271
Backward Channel Protection Method for RFID Security Schemes Based on Tree-Walking Algorithms <i>Wonjoon Choi, Byeong-hee Roh</i>	279
Design of the Configurable Clothes Using Mobile Actuator-Sensor Network <i>Bo-Hee Lee, Kyu-Tae Seo, Jung-Shik Kong, Jin-Geol Kim</i>	288
Hash-Based RFID Security Protocol Using Randomly Key-Changed Identification Procedure <i>Jia Zhai, Chang Mok Park, Gi-Nam Wang</i>	296
Counting-Based Distance Estimations and Localizations in Wireless Sensor Networks <i>Oh-Heum Kwon, Ha-Joo Song</i>	306

Self Re-encryption Protocol Providing Strong Privacy for Low Cost RFID System <i>Jeong Su Park, Su Mi Lee, Eun Young Choi, Dong Hoon Lee</i>	316
Authentication for Single/Multi Domain in Ubiquitous Computing Using Attribute Certification <i>Deok-Gyu Lee, Seo-Il Kang, Dae-Hee Seo, Im-Yeong Lee</i>	326
Improving the CGA-OMIPv6 Protocol for Low-Power Mobile Nodes <i>Ilsun You</i>	336
Tracking Illegal System Access in a Ubiquitous Environment – Proposal for ATS, a Traceback System Using STOP <i>Gwanghoon Kim, Soyeon Hwang, Deokgyu Lee</i>	344
Real-Time Intrusion Detection in Ubiquitous Networks with a String-Based Approach <i>Bo Zhou, Qi Shi, Madjid Merabti</i>	352
A Security Model for Home Networks with Authority Delegation <i>Jin-Bum Hwang, Jong-Wook Han</i>	360
An Efficient Key Distribution for Ubiquitous Environment in Ad-Hoc Network Using Broadcast Encryption <i>Deok-Gyu Lee, Jang-Su Park, Im-Yeong Lee, Yong-Seok Park, Jung-Chul Ahn</i>	370
Distributed Certificate Authority Under the GRID-Location Aided Routing Protocol <i>JiHyung Lim, DaeHun Nyang, Jeonil Kang, KyungHee Lee, Hyotaek Lim</i>	380
An Efficient Hierarchical Group Key Management Protocol for a Ubiquitous Computing Environment <i>Sangjin Kim, Taewook Ahn, Heekuck Oh</i>	388
Efficient User Authentication and Key Agreement in Ubiquitous Computing <i>Wen-Sheng Juang</i>	396
Single Sign-On and Key Establishment for Ubiquitous Smart Environments <i>Yuen-Yan Chan, Sebastian Fleissner, Joseph K. Liu, Jin Li</i>	406
A Light Weight Authentication Protocol for Digital Home Networks <i>Ilsun You, Eun-Sun Jung</i>	416

Smart Home Microcontroller: Telephone Interfacing <i>Chee-Seng Leong, Bok-Min Goi</i>	424
SPAD: A Session Pattern Anomaly Detector for Pre-alerting Intrusions in Home Network <i>Soo-Jin Park, Young-Shin Park, Yong-Rak Choi, Sukhoon Kang</i>	432
Home Gateway with Automated Real-Time Intrusion Detection for Secure Home Networks <i>Hayoung Oh, Jiyoung Lim, Kijoon Chae, Jungchan Nah</i>	440
The Performance Analysis of UWB System for the HD Multimedia Communication in a Home Network <i>Chul-Yong Uhm, Su-Nam Kim, Kyeong-Hoon Jung, Dong-Wook Kang, Ki-Doo Kim</i>	448
Extraction of Implicit Context Information in Ubiquitous Computing Environments <i>Juryon Paik, Hee Yong Youn, Ung Mo Kim</i>	456
Convergence of Context-Awareness and Augmented Reality for Ubiquitous Services and Immersive Interactions <i>Jae Yeol Lee, Gue Won Rhee, Hyun Kim, Kang-Woo Lee, Young-Ho Suh, Kwangsoo Kim</i>	466
An Adaptive Fault Tolerance System for Ubiquitous Computing Environments: AFTS <i>Eung Nam Ko</i>	475
Design and Implementation of Middleware for Context-Aware Service Discovery in Ubiquitous Computing Environments <i>Kyu Min Lee, Hyung-Jun Kim, Ho-Jin Shin, Dong-Ryeol Shin</i>	483
A Dynamic Channel Allocation Mechanism in Cellular Mobile Networks for Ubiquitous Environments Based on Time Constraints <i>SeongHoon Lee, DongWoo Lee, Donghee Shim, Dongyoung Cho, Wankwon Lee</i>	491

Workshop on Embedded System for Ubiquitous Computing (ESUC 2006)

Performance Analysis of Task Schedulers in Operating Systems for Wireless Sensor Networks <i>Sangho Yi, Hong Min, Junyoung Heo, Boncheol Gu, Yookun Cho, Jiman Hong, Jinwon Kim, Kwangyong Lee, Seungmin Park</i>	499
---	-----

Wireless Sensor Networks: A Scalable Time Synchronization <i>Kee-Young Shin, Jin Won Kim, Ilgon Park, Pyeong Soo Mah</i>	509
A New Cluster Head Selection Scheme for Long Lifetime of Wireless Sensor Networks <i>Hyung Su Lee, Kyung Tae Kim, Hee Yong Youn</i>	519
Two-Dimensional Priority Scheduling Scheme for Open Real-Time Systems <i>Pengliu Tan, Hai Jin, Minghu Zhang</i>	529
An Enhanced Dynamic Voltage Scaling Scheme for Energy-Efficient Embedded Real-Time Control Systems <i>Feng Xia, Youxian Sun</i>	539
Adaptive Load Balancing Mechanism for Server Cluster <i>Geunyoung Park, Boncheol Gu, Junyoung Heo, Sangho Yi, Jungkyu Han, Jaemin Park, Hong Min, Xuefeng Piao, Yookun Cho, Chang Won Park, Ha Joong Chung, Bongkyu Lee, Sangjun Lee</i>	549
Design and Performance Analysis of a Message Scheduling Scheme for WLAN-Based Cluster Computing <i>Junghoon Lee, Mikyung Kang, Euiyoung Kang, Gyungleen Park, Hanil Kim, Cheolmin Kim, Seongbaeg Kim, Jiman Hong</i>	558
A Method for Efficient Malicious Code Detection Based on Conceptual Similarity <i>Sungsuk Kim, Chang Choi, Junho Choi, Pankoo Kim, Hanil Kim</i>	567
A Minimized Test Pattern Generation Method for Ground Bounce Effect and Delay Fault Detection <i>MoonJoon Kim, JeongMin Lee, WonGi Hong, Hoon Chang</i>	577
Efficient Exponentiation in $GF(p^m)$ Using the Frobenius Map <i>Mun-Kyu Lee, Howon Kim, Dowon Hong, Kyoil Chung</i>	584
A Dual-Channel MAC Protocol Using Directional Antennas in Location Aware Ad Hoc Networks <i>DoHyung Han, JeongWoo Jwa, HanIl Kim</i>	594
A Power-Efficient Design Employing an Extreme Condition Detector for Embedded Systems <i>Hyukjun Oh, Heejune Ahn, Jiman Hong</i>	603

An Efficient Delay Metric on RC Interconnects Under Saturated Ramp Inputs <i>Ki-Young Kim, Seung-Yong Kim, Seok-Yoon Kim</i>	612
Low Power Microprocessor Design for Embedded Systems <i>Seong-Won Lee, Neungsoo Park, Jean-Luc Gaudiot</i>	622
History Length Adjustable <i>gshare</i> Predictor for High-Performance Embedded Processor <i>Jong Wook Kwak, Seong Tae Jhang, Chu Shik Jhon</i>	631
Workshop on Information Engineering and Applications in Ubiquitous Computing Environments (IEAUCE 2006)	
Security Engineering Methodology Based on Problem Solving Theory <i>Sangkyun Kim, Hong Joo Lee</i>	639
Design and Implementation of an Ontology Algorithm for Web Documents Classification <i>Guiyi Wei, Jun Yu, Yun Ling, Jun Liu</i>	649
Automatic Test Approach of Web Application for Security (AutoInspect) <i>Kyung Cheol Choi, Gun Ho Lee</i>	659
A Scenario-Based User-Oriented Integrated Architecture for Supporting Interoperability Among Heterogeneous Home Network Middlewares <i>Min Chan Kim, Sung Jo Kim</i>	669
Session Key Agreement Protocol for End-to-End Security in MANET <i>Jeong-Mi Lim, Chang-Seop Park</i>	679
Process-Oriented DFM System for Ubiquitous Devices <i>Yongsik Kim, Taesoo Lim, Dongsoo Kim, Cheol Jung, Honggee Jin</i>	687
A Study on the Application of BPM Systems for Implementation of RosettaNet Based e-Logistics <i>Yong Gu Ji, Chiwoo Park, Minsoo Kim</i>	697
Information Security Management System for SMB in Ubiquitous Computing <i>Hangbae Chang, Jungduk Kim, Sungjun Lim</i>	707

A Study on the Development of Usability Evaluation Framework
(Focusing on Digital TV)
Hong Joo Lee, Choon Seong Leem, Sangkyun Kim 716

**Workshop on Component Based Software
Engineering and Software Process Model
(CBSE 2006)**

Designing Aspectual Architecture Views in Aspect-Oriented Software
Development
*Rogelio Limón Cordero, Isidro Ramos Salavert,
José Torres-Jiménez* 726

Process and Techniques to Generate Components in MDA/CB-PIM for
Automation
Hyun Gi Min, Soo Dong Kim 736

An Ontology Definition Framework for Model Driven Development
Yucong Duan, Xiaolan Fu, Qingwu Hu, Yuqing Gu 746

An AHP-Based Evaluation Model for Service Composition
Xiaoqin Xie, Kaiyun Chen 756

Construction of Quality Test and Certification System for Package
Software
Ha-Yong Lee, Hae-Sool Yang, Suk-Hyung Hwang 767

Design of an On-Line Intrusion Forecast System with a Weather
Forecasting Model
*YoonJung Chung, InJung Kim, Chulsoo Lee, Eul Gyu Im,
Dongho Won* 777

Goal Programming Approach to Compose the Web Service Quality of
Service
*Daerae Cho, Changmin Kim, MoonWon Choo, Suk-Ho Kang,
Wookey Lee* 787

Healthcare Home Service System Based on Distributed Object Group
Framework
Chang-Sun Shin, Chung-Sub Lee, Su-Chong Joo 798

A Learning Attitude Evaluation System for Learning Concentration on
Distance Education
Byungdo Choi, Chonggun Kim 808

A Calculation Method for Direction Based Handover Rate in Cell Based Mobile Networks <i>Mary Wu, Chonggun Kim</i>	818
The Classification of the Software Quality by Employing the Tolerance Class <i>Wan-Kyoo Choi, Sung-Joo Lee, Il-Yong Chung, Yong-Geun Bae</i>	828
Components Searching System Using Component Identifiers and Request Specifics <i>Jea-Youn Park, Gui-Jung Kim, Young-Jae Song</i>	835
Software Architecture Generation on UML <i>Haeng-Kon Kim</i>	844
Distributed Programming Developing Tool Based on Distributed Object Group Framework <i>Chang-Won Jeong, Dong-Seok Kim, Geon-Yeob Lee, Su-Chong Joo</i>	853
A Study on Automatic Code Generation Tool from Design Patterns Based on the XMI <i>Young-Jun Seo, Young-Jae Song</i>	864
Design of Opportunity Tree for Organization's Process Strategy Decision-Making Based on SPICE Assessment Experience <i>Ki Won Song, Haeng Kon Kim, Kyung Whan Lee</i>	873
SUALPPA Scheme: Enhanced Solution for User Authentication in the GSM System <i>Mi-Og Park, Dea-Woo Park</i>	883
Design of Mobile Video Player Based on the WIPI Platform <i>Hye-Min Noh, Sa-Kyun Jeong, Cheol-Jung Yoo, Ok-Bae Chang, Eun-Mi Kim, Jong-Ryeol Choi</i>	893
Discovering Patterns Based on Fuzzy Logic Theory <i>Bobby D. Gerardo, Jaewan Lee, Su-Chong Joo</i>	899
Metrics Design for Software Process Assessment Based on ISO/IEC 15504 <i>Sun-Myung Hwang, Hee-Gyun Yeom</i>	909

A Quantitative Evaluation Model Using the ISO/IEC 9126 Quality Model in the Component Based Development Process <i>Kilsup Lee, Sung Jong Lee</i>	917
Component Specification Model for the Web Services <i>Haeng-Kon Kim, Eun-Ju Park</i>	927
A Data-Driven Approach to Constructing an Ontological Concept Hierarchy Based on the Formal Concept Analysis <i>Suk-Hyung Hwang, Hong-Gee Kim, Myeng-Ki Kim, Sung-Hee Choi, Hae-Sool Yang</i>	937
Web-Document Filtering Using Concept Graph <i>Malrey Lee, Eun-Kwan Kang, Thomas M. Gatton</i>	947
Development of Integrated DAO Pattern Applying Iterator Pattern <i>Seong-Man Choi, Cheol-Jung Yoo, Ok-Bae Chang</i>	955
A Coupling Metric Applying the Characteristics of Components <i>Misook Choi, Seojeong Lee</i>	966
Software Process Improvement Environment <i>Haeng-Kon Kim, Hae-Sool Yang</i>	976
A Design Technique of CBD Meta-model Based on Graph Theory <i>Eun Sook Cho, So Yeon Min, Chul Jin Kim</i>	985
Description Technique for Component Composition Focusing on Black-Box View <i>J.H. Lee, Dan Lee</i>	994
XML Security Model for Secure Information Exchange in E-Commerce <i>Kwang Moon Cho</i>	1003
Design and Implementation of B2Bi Collaboration Workflow Tool Based on J2EE <i>Chang-Mog Lee</i>	1012
Traffic-Predicting Routing Algorithm Using Time Series Models <i>Sangjoon Jung, Mary Wu, Youngsuk Jung, Chonggun Kim</i>	1022
A Study on Software Architecture Evaluation <i>Gu-Beom Jeong, Guk-Boh Kim</i>	1032

RFID-Based ALE Application Framework Using Context-Based Security Service <i>Jungkyu Kwon, Mokdong Chung</i>	1042
A Study on the Standard of Software Quality Testing <i>Hye-Jung Jung, Won-Tae Jung, Hae-Sool Yang</i>	1052
Scene Change Detection Using the Weighted Chi-Test and Automatic Threshold Decision Algorithm <i>Kyong-Cheol Ko, Oh-Hyung Kang, Chang-Woo Lee, Ki-Hong Park, Yang-Won Rhee</i>	1060
Design Opportunity Tree for Schedule Management and Evaluation by COQUALMO <i>Eun Ser Lee, Sang Ho Lee</i>	1070
CTL Model Checking for Boolean Program <i>Taehoon Lee, Gihwon Kwon, Hyuksoo Han</i>	1081
General Tracks	
Grid Service Implementation of Aerosol Optical Thickness Retrieval over Land from MODIS <i>Yincui Hu, Yong Xue, Guoyin Cai, Chaolin Wu, Jianping Guo, Ying Luo, Wei Wan, Lei Zheng</i>	1090
Revocation Scheme for PMI Based Upon the Tracing of Certificates Chains <i>M. Francisca Hinarejos, Jordi Forné</i>	1098
Nailfold Capillary Microscopy High-Resolution Image Analysis Framework for Connective Tissue Disease Diagnosis Using Grid Computing Technology <i>Kuan-Ching Li, Chiou-Nan Chen, Chia-Hsien Wen, Ching-Wen Yang, Joung-Liang Lan</i>	1107
EFH: An Edge-Based Fast Handover for Mobile IPv6 in IEEE 802.11b WLAN <i>Sangdong Jang, Wu Woan Kim</i>	1116
An Extendible Hashing Based Recovery Method in a Shared-Nothing Spatial Database Cluster <i>Yong-Il Jang, Ho-Seok Kim, Soon-Young Park, Jae-Dong Lee, Hae-Young Bae</i>	1126

A Quantitative Justification to Partial Replication of Web Contents <i>Jose Daniel Garcia, Jesus Carretero, Felix Garcia, Javier Fernandez, Alejandro Calderon, David E. Singh</i>	1136
Content Distribution Strategy Using Web-Cached Multicast Technique <i>Backhyun Kim, Iksoo Kim</i>	1146
Load Distribution Strategies in Cluster-Based Transcoding Servers for Mobile Clients <i>Dongmahn Seo, Joahyoung Lee, Yoon Kim, Changyeol Choi, Hwangkyu Choi, Inbum Jung</i>	1156
Safety of Recovery Protocol Preserving MW Session Guarantee in Mobile Systems <i>Jerzy Brzeziński, Anna Kobusińska</i>	1166
Author Index	1175

Table of Contents – Part V

Workshop on Parallel and Distributed Computing (PDC 2006)

Resource Demand Prediction-Based Grid Resource Transaction Network Model in Grid Computing Environment <i>In Kee Kim, Jong Sik Lee</i>	1
A CGM Algorithm Solving the Longest Increasing Subsequence Problem <i>David Semé</i>	10
Computer Assisted Source-Code Parallelisation <i>Peter J. Vidler, Michael J. Pont</i>	22
A Template Language for Agent Construction <i>Li Xiaohong, Feng Zhiyong, Li tie, Lv Li</i>	32
Efficient Parallel Processing for K -Nearest-Neighbor Search in Spatial Databases <i>Yunjun Gao, Ling Chen, Gencai Chen, Chun Chen</i>	39
An Adaptive Mobile System Using Mobile Grid Computing in Wireless Network <i>Jehwan Oh, Seunghwa Lee, Eunseok Lee</i>	49
Comparison of Allocation Algorithms for Mesh Structured Networks with Using Multistage Simulation <i>Leszek Koszalka, Dominik Lisowski, Iwona Pozniak-Koszalka</i>	58
The Election Problem in Asynchronous Distributed Systems with Bounded Faulty Processes <i>SeongHoon Park</i>	68
Improving the Genetic Algorithms Performance in Simple Assembly Line Balancing <i>Seren Özmehmet Tasan, Semra Tunali</i>	78
Reformulation and Solution Approaches for an Integrated Scheduling Model <i>Herbert Jodlbauer, Sonja Reitner, Andreas Weidenhiller</i>	88

Safety of a Client-Based Version Vector Consistency Protocol of Session Guarantees <i>Jerzy Brzeziński, Cezary Sobaniec, Dariusz Wawrzyniak</i>	98
A New I/O Architecture for Improving the Performance in Large Scale Clusters <i>L.M. Sánchez García, Florin D. Isaila, Félix García Carballeira, Jesús Carretero Pérez, Rolf Rabenseifner, Panagiotis Adamidis</i>	108
Performance Modeling of a Fully Adaptive and Fault-Tolerant Wormhole Switching Strategy in 2-D Mesh <i>Farshad Safaei, Mahmood Fathy, Ahmad Khonsari, Mohamed Ould-Khaoua</i>	118
Parallelization of Simulations for Various Magnetic System Models on Small-Sized Cluster Computers with MPI <i>Frank Schurz, Dietmar Fey, Dmitri Berkov</i>	129
A New Reflective and Reliable Context-Oriented Event Service Architecture for Pervasive Computing <i>Sung Keun Song, Hee Yong Youn, Ungmo Kim</i>	139
X-Torus: A Variation of Torus Topology with Lower Diameter and Larger Bisection Width <i>Huaxi Gu, Qiming Xie, Kun Wang, Jie Zhang, Yunsong Li</i>	149
Feedback Vertex Sets in Rotator Graphs <i>Chiun-Chieh Hsu, Hon-Ren Lin, Hsi-Cheng Chang, Kung-Kuei Lin</i>	158
Efficient Longest Common Subsequence Computation Using Bulk-Synchronous Parallelism <i>Peter Krusche, Alexander Tiskin</i>	165
Simulation of Internet Transport Protocols for High Bandwidth-Delay Networks <i>Junsoo Lee</i>	175
Performance Evaluation of Parallel Systems Employing Roll-Forward Checkpoint Schemes <i>Gyung-Leen Park, Hee Yong Youn, Junghoon Lee, Chul Soo Kim, Bongkyu Lee, Sang Joon Lee, Wang-Cheol Song, Yung-Cheol Byun</i>	185

A Purely Distributed Approach for Coupling Scientific and Engineering Applications <i>Vicente Berbegall, L.A. Drummond, Gumersindo Verdú, Vicente Vidal</i>	192
A Monitoring and Visualization Tool and Its Application for a Network Enabled Server Platform <i>Raphael Bolze, Eddy Caron, Frederic Desprez, Georg Hoesch, Cyril Pontvieux</i>	202
Parallel Hash Join Algorithms for Dynamic Load Balancing in a Shared Disks Cluster <i>Aekyung Moon, Haengrae Cho</i>	214
Workshop on Security Issues on Grid/Distributed Computing Systems (SIGDCS 2006)	
Towards Reliable and Trustworthy Cooperation in Grid: A Pre-evaluating Set Based Trust Model <i>Xiangli Qu, Jingwei Zhong, Xuejun Yang</i>	224
A Spreading MIMO-OFDM Transmission Scheme for Wireless Mobile Environment <i>Sang Soon Park, Tae Jin Hwang, Juphil Cho, Heung Ki Baik</i>	236
A Security Auditing Approach Based on Mobile Agent in Grid Environments <i>Zhenghong Xiao, Changqin Huang, Fuyin Xu</i>	243
XML-Signcryption Based LBS Security Protocol Acceleration Methods in Mobile Distributed Computing <i>Namje Park, Howon Kim, Kyoil Chung, Sungwon Sohn, Dongho Won</i>	251
Optimization of a Simulation for 300mm FAB Semiconductor Manufacturing <i>DongSik Park, Youngshin Han, Chilgee Lee</i>	260
Performance Analysis Using the Two Kinds of Receiving Gain of Smart Antenna in IS20001X System <i>Sungsoo Ahn, Minsoo Kim, Jungsuk Lee</i>	269
An Improved Popescu's Authenticated Key Agreement Protocol <i>Eun-Jun Yoon, Kee-Young Yoo</i>	276

SVM Based False Alarm Minimization Scheme on Intrusion Prevention System <i>Gil-Han Kim, Hyung-Woo Lee</i>	284
Lightweight Wireless Intrusion Detection Systems Against DDoS Attack <i>Hyung-Woo Lee</i>	294
One-Time Password Authentication Scheme Using Smart Cards Providing User Anonymity <i>Eun-Jun Yoon, Kee-Young Yoo</i>	303
Loss Reduction in Distribution Networks Using Cyclic Best First Search <i>Sang-Yule Choi, Myong-Chul Shin, Jae-Sang Cha</i>	312
Short-Term Power Demand Forecasting Using Information Technology Based Data Mining Method <i>Sang-Yule Choi</i>	322
A Design of the Flexible Mobile Agents Based on Web <i>Yun Ji Na, Il Seok Ko, Gun Heui Han</i>	331
A Sales Agent Using Case-Based Reasoning and Rule-Based Reasoning for E-Commerce System <i>Yun Ji Na, Il Seok Ko, Jong Min Kwak</i>	338
A New Ciphering Method Associated with Evolutionary Algorithm <i>Fouzia Omary, Abdelaziz Mouloudi, Abderrahim Tragha, Abdelghani Bellaachia</i>	346
Power Distribution Automation System Using Information Technology Based Web Active Database <i>Sang-Yule Choi</i>	355
Workshop on Image Processing and Computer Vision (IPCV 2006)	
Alternative Target Density Functions for Radar Imaging <i>Askin Demirkol</i>	365
A Novel Image Restoration Algorithm Based on High-Dimensional Space Geometry <i>Wenming Cao, Mei-fen Xie, Shoujue Wang</i>	375

A Fast Image Retrieval System Based on Color-Space and Color-Texture Features <i>Chuen-Hornq Lin, Kai-Hung Chen, Yung-Kuan Chan</i>	384
Generation of Dynamic Heart Model Based on 4D Echocardiographic Images <i>Michał Chlebiej, Paweł Mikołajczak, Krzysztof Nowiński, Piotr Ścisto, Piotr Bala</i>	394
Object-Based Image Retrieval Using Dominant Color Pairs Between Adjacent Regions <i>Ki Tae Park, Young Shik Moon</i>	404
Real-Time Vision Tracking Algorithm <i>Edgar R. Arce-Santana, Jose M. Luna-Rivera, Daniel U. Campos-Delgado, Ulises Pineda-Rico</i>	412
Efficient Method to Perform Isomorphism Testing of Labeled Graphs <i>Shu-Ming Hsieh, Chiun-Chieh Hsu, Li-Fu Hsu</i>	422
Camera Motion Parameter Estimation Technique Using 2D Homography and LM Method Based on Projective and Permutation Invariant Features <i>JeongHee Cha, GyeYoung Kim</i>	432
Automatic Generation Technique of Three-Dimensional Model Corresponding to Individual Vessels <i>Na-Young Lee, Gye-Young Kim, Hyung-Il Choi</i>	441
Modulating Energy Distribution of Reflected Light Based on Images <i>Zhanwei Li, Guolin Duan, Jizhou Sun, Lijuan Sun, Xinran Lv</i>	450
Workshop on Integrated Analysis and Intelligent Design Technology (IAIDT 2006)	
Aerodynamic Analysis on the Supersonic Separation of Air-Launching Rocker from the Mother Plane <i>Young Mu Ji, Young Shin Kim, Jae Woo Lee, Young Hwan Byun, Jun Sang Park</i>	457
Effect of Grid Resolution on the Statistics of Passive Scalar in an Injection-Driven Channel <i>Yang Na, Dongshin Shin, Seungbae Lee</i>	467

Test of Large Eddy Simulation in Complex Flow with High Schmidt Number <i>Yang Na, Seungmin Lee</i>	476
High-End Modeling and Simulation of Cookoff of HMX-Based Energetic Materials <i>Jack Jai-ick Yoh</i>	484
Multiobjective Optimization Using Adjoint Gradient Enhanced Approximation Models for Genetic Algorithms <i>Sangho Kim, Hyoung-Seog Chung</i>	491
Development of Automated Generation Algorithm for Skipped Surface in Die Design <i>Sang-Jun Lee, Seoung-Soo Lee, Jong-Hwa Kim, Yoon-Jung Kwon</i>	503
Development of Requirement Driven Design Concept Selection Process in Aerospace System <i>Hyeong-Uk Park, Mee-Young Park, Seung-Jin Lee, Jae-Woo Lee, Yung-Hwan Byun</i>	512
A TMO-Based Tele-operation Model: Supporting Real-Time Applications in Grid Environments <i>Chulgoon Kim, Karpjoo Jeong, Hanku Lee, MoonHae Kim, KumWon Cho, Segil Jeon, Jaehoon Ahn, Hyunho Ju</i>	522
Design Trade-Offs and Power Reduction Techniques for High Performance Circuits and System <i>Taikyeong T. Jeong, Anthony P. Ambler</i>	531
Cavitation Flow Analysis of Axisymmetric Bodies Moving in the Water <i>Changjin Lee, Doyoung Byun</i>	537
Workshop on Approaches or Methods of Security Engineering (AMSE 2006, Sess. B)	
Design and Implementation of Semantic Web Search System Using Ontology and Anchor Text <i>Nam-deok Cho, Eun-ser Lee</i>	546
Design Progress Management for Security Requirements in Ubiquitous Computing Using COQUALMO <i>Eun Ser Lee, Sang Ho Lee</i>	555

Web Document Classification Using Changing Training Data Set <i>Gilcheol Park, Seoksoo Kim</i>	565
Study on Contents Protection in M-Learning Environment <i>Jaekoo Song, Mingyun Kang, Seoksoo Kim</i>	575
Design of Security Session Reuse in Content-Based Load Distribution Server <i>Seoksoo Kim, Kunhee Han</i>	584
Design of POC System in Ubiquitous Environment <i>Seoksoo Kim, Gilcheol Park</i>	591
The Performance Evaluation of OFDM/HL-16QAM System for Optimizing Image Transmission Quality in Wireless Fading <i>Jae-min Kwak, Yang-sun Lee, Sung-eon Cho</i>	600
Reliable Evaluations of URL Normalization <i>Sung Jin Kim, Hyo Sook Jeong, Sang Ho Lee</i>	609
Enhanced Misuse Case Model: A Security Requirement Analysis and Specification Model <i>Sang-soo Choi, So-yeon Kim, Gang-soo Lee</i>	618
An Analysis of Policy Provisioning Complexity in Accordance with the Application Attributes of the Policy-Based Network <i>Hyung-Jin Lim, Moonseong Kim, Dong-Young Lee, Tai-Myoung Chung</i>	626
Privacy Preserving Unsupervised Clustering over Vertically Partitioned Data <i>D.K. Tasoulis, E.C. Laskari, G.C. Meletiou, M.N. Vrahatis</i>	635
Process Development Methodology for U-Integrated Management System <i>Seong-Man Choi, MalRey Lee, Cheol-Jung Yoo, Ok-Bae Chang</i>	644
A Study on Agent-Based Integrated Security Management System for Managing Heterogeneous Firewall Systems <i>Dong-Young Lee, Hyung-Jin Lim, Tai M. Chung</i>	655
Optimization of Fuzzy Rules: Integrated Approach for Classification Problems <i>Yunjeong Kang, Malrey Lee, Yongseok Lee, Thomas M. Gatton</i>	665

A Cooperation Model Using Reinforcement Learning for Multi-agent <i>Malrey Lee, Jaedeuk Lee, Hye-Jin Jeong, YoungSoon Lee, Seongman Choi, Thomas M. Gatton</i>	675
Development of Network Event Analysis Algorithm Applying Association Rule <i>Seakjae Han, Wooyoung Soh</i>	682
A New Secure Oblivious Transfer Protocol <i>Soon-gohn Kim, Heau-jo Kang</i>	690
Analysis of Security Session Reusing in Distribution Server System <i>Tai-hoon Kim, Seoksoo Kim, Hee-Un Park, Myoung-sub Kim</i>	700
Clustered OFDMA in the Multi-path Fading Channel <i>Kyujin Lee, Kyesan Lee</i>	708
Distribution Antenna Diversity System According to Adaptive Correlation Method for OFDM-DS/CDMA in a Frequency Selective Fading Channel <i>Kyesan Lee, Euinam Huh</i>	717
 General Tracks	
MIDAS: Detection of Non-technical Losses in Electrical Consumption Using Neural Networks and Statistical Techniques <i>Íñigo Monedero, Félix Biscarri, Carlos León, Jesús Biscarri, Rocío Millán</i>	725
Hyperbolic Voronoi Diagram <i>Zahra Nilfroushan, Ali Mohades</i>	735
Effects of Confinement on Chemical Reaction Equilibrium in Nanoporous Materials <i>William R. Smith, Martin Lísal, John K. Brennan</i>	743
Multi-channel Estimation in Multiple Antenna MB-OFDM UWB System for Home Entertainment Network <i>Myung-Sun Baek, So-Young Yeo, Byung-Jun Jang, Young-Hwan You, Hyoung-Kyu Song</i>	752
Compiler-Optimized Kernels: An Efficient Alternative to Hand-Coded Inner Kernels <i>José R. Herrero, Juan J. Navarro</i>	762

Noise Subspace Fuzzy C-Means Clustering for Robust Speech Recognition <i>J.M. Górriz, J. Ramírez, J.C. Segura, C.G. Puntonet, J.J. González</i>	772
Using Box-Muller with Low Discrepancy Points <i>Tim Pillards, Ronald Cools</i>	780
A Fast Integration Method and Its Application in a Medical Physics Problem <i>Shujun Li, Elise de Doncker, Karlis Kaugars, Haisen S. Li</i>	789
Payment in a Kiosk Centric Model with Mobile and Low Computational Power Devices <i>Jesús Téllez Isaac, José Sierra Camara, Antonio Izquierdo Manzanares, Mildrey Carbonell Castro</i>	798
Survivable Mechanism for IEEE 802.11 WLAN Improvements <i>Flavio E. de Deus, Ricardo Staciarini Puttini, Luis Molinaro, Joseph Kabara, Luis Javier García Villalba</i>	808
Proposal of a System for Searching and Indexing Heterogeneous Vulnerabilities Databases <i>Robson de Oliveira, Fabio Buiati, Luis Javier García Villalba, Daniel Almendra, L. Pulcineli, Rafael de Sousa, Cláudia Jacy Barenco Abbas</i>	819
Performance Analysis of Dynamic Host Isolation System in Wireless Mobile Networks <i>Hyuncheol Kim, Seongjin Ahn, Junkyun Choi</i>	829
Meta-model Driven Collaborative Object Analysis Process for Production Planning and Scheduling Domain <i>Chang Ouk Kim, Jun-Geol Baek, Jin Jun</i>	839
Response Against Hacking and Malicious Code in P2P <i>Wongoo Lee, Sijung Kim, Bonghan Kim</i>	851
Two Efficient and Secure Authentication Schemes Using Smart Cards <i>Youngsook Lee, Junghyun Nam, Seungjoo Kim, Dongho Won</i>	858
Location-Aware Agent Using Data Mining for the Distributed Location-Based Services <i>Jaewan Lee, Romeo Mark A. Mateo, Bobby D. Gerardo, Sung-Hyun Go</i>	867

An Empirical Development Case of a Software-Intensive System Based on the Rational Unified Process <i>Kilsup Lee</i>	877
Color Preference and Personality Modeling Using Fuzzy Reasoning Rule <i>Am-Suk Oh, Tae-Jung Lho, Jang-Woo Kwon, Kwang-Baek Kim</i>	887
The Development of Reliability Verification Tool of RFID Tag for Effective Product Control Systems <i>Ki-Uk Kim, Hyun-Suk Hwang, Bong-Je Kim, Su-Hwan Jeong, Chang-Soo Kim</i>	895
Avoidance of State Explosion Using Dependency Analysis in Model Checking Control Flow Model <i>Sachoun Park, Gihwon Kwon</i>	905
Design and Implementation of Web Usage Mining System Using Page Scroll <i>IL Kim, Bong-Joon Choi, Kyoo-Seok Park</i>	912
A Security Architecture for Adapting Multiple Access Control Models to Operating Systems <i>Jung-Sun Kim, SeungYong Lee, Minsoo Kim, Jae-Hyun Seo, Bong-Nam Noh</i>	922
Rotor Design for the Performance Optimization of Canard Rotor/Wing Aircraft <i>Jae-Woo Lee, Kwon-Su Jeon, Min-Ji Kim, Yung-Hwan Byun, Chang J. Kim, Yung H. Yu</i>	932
Process Decomposition and Choreography for Distributed Scientific Workflow Enactment <i>Jae-Yoon Jung, Wookey Lee, Suk-Ho Kang</i>	942
Adaptive Multi-carrier Direct-Sequence CDMA System Using Fast-Frequency-Hopping <i>Kyesan Lee, Gigan Lee</i>	952
Object Modeling for Mapping XML Document Represented in XML-GDM to UML Class Diagram <i>Dae-Hyeon Park, Chun-Sik Yoo, Yong-Sung Kim, Soon-Ja Yeom</i>	958
A Two-Phase Local Server Security Model Based on XML Certificate <i>Yong-Hwa Kim, Jin-Sung Kim, Yong-Sung Kim, Jang-Sup Shim</i>	968

Integrated Object Modeling for Web-Based XML Application Documents <i>Chun-Sik Yoo, Jin-Sung Kim, Yong-Sung Kim, Jang-Sup Shim</i>	979
Model of Generating SMIL Document Using Temporal Scripts of Animation Component <i>Chun-Sik Yoo, He-Jue Eun, Yong-Sung Kim, Jang-Sup Shim</i>	990
Marginal Bone Destructions in Dental Radiography Using Multi-template Based on Internet Services <i>Yonghak Ahn, Oksam Chae</i>	1001
The Band Selection Algorithm in Supervised Classification Using Mixed-Pixels and Canonical Correlation Analysis <i>Hoon Chang, Hwan-Hee Yoo, Hong Sok Kim</i>	1010
Domain Analysis for Components Based Developments <i>Ha-Jin Hwang</i>	1018
Author Index	1029

Upper Bound on Dilation of Triangulations of Cyclic Polygons

Narayanasetty Amarnadh and Pinaki Mitra

Department of Computer Science & Engineering,
Indian Institute of Technology, Guwahati, India
{amarnadh, pinaki}@iitg.ernet.in

Abstract. Given a planar graph G , the dilation between two points of a Euclidean graph is defined as the ratio of the length of the shortest path between the points to the Euclidean distance between the points. The dilation of a graph is defined as the maximum over all vertex pairs (u,v) of the dilation between u and v . In this paper we consider the upper bound on the dilation of triangulation over the set of vertices of a cyclic polygon. We have shown that if the triangulation is a fan (i.e. every edge of the triangulation starts from the same vertex), the dilation will be at most approximately 1.48454. We also show that if the triangulation is a star the dilation will be at most 1.18839.

1 Introduction

Given set S of n points in the plane (not all collinear), a triangulation $T(S)$ of S is a planar subdivision of the convex hull of S into triangles with vertices from S . $T(S)$ is a maximal planar subdivision i.e. no edge connecting two vertices can be added to $T(S)$ without destroying its planarity. Any triangulation of S has at most $2n - 2 - k$ triangles and $3n - 3 - k$ edges, where k is the no points on the convex hull of S . In this paper we consider the upper bound on triangulations of cyclic polygons. A cyclic polygon is a convex polygon whose vertices lie on a circle. Fan triangulation of a cyclic polygon is obtained when every edge of triangulation originates from the same vertex. Star triangulation of a cyclic polygon is obtained by joining every vertex to the center of the circumscribing circle assuming the center is inside the polygon.

Research has been done on dilation ratios of certain types of triangulations. Chew [1] shows that the rectilinear Delaunay triangulation has dilation at most $\sqrt{10}$. Dobkin *et al.*[2] showed that the Euclidean Delaunay triangulation can be bounded from above by $(1+\sqrt{5})\pi/2 \approx 5.08$. This bound was further improved to $2\pi / (3\cos(\pi/6)) \approx 2.42$ by Keil and Gutwin [5]. A more comprehensive survey of results on the graph theoretic dilation of planar and general graphs can be found in Eppstein's survey [4]. Surprisingly, very few results are known about triangulations which actually achieve optimum graph theoretic dilation. In his thesis Mulzer [3], investigates the structure of the minimum dilation triangulations for a regular polygon, but beyond that is not much known.

In this paper we consider cyclic polygons, i.e., polygons whose vertices are on the boundary of a circle. The work is an extension of some results claimed in [6]. We

prove results related to the upper bound on the maximum dilation of two different types of triangulations. Our paper is organized as follows. In section 3 we describe the Fan triangulation and then prove the upper bound on the dilation. In section 4 we describe the star triangulation and the corresponding upper bound on the dilation. In section 5 we show some experimental results. Finally in section 6 we conclude by summarizing our result and stating some directions for future research.

2 Definitions and notations

1. Dilation: Given a planar point set S , a triangulation of S is a maximal set of non-intersecting edges connecting points in S . Given a triangulation T of S , for any two points $u, v \in S$, the ratio between the shortest path distance $\pi_T(u, v)$ and the Euclidean distance $|uv|$ is called the dilation between u and v with respect to T , which we shall denote by $\delta_T(u, v)$. Formally, the dilation is defined as follows:

$$\delta_T(u, v) = \begin{cases} 1 & \text{if } u = v, \\ \pi_T(u, v) / |uv| & \text{if } u \neq v \end{cases}$$

The Graph theoretic dilation of T is defined as the maximum dilation over all the vertex pairs (u, v) of T . Formally we define it as:

$$\delta(T) = \max_{u, v \in S} \delta_T(u, v)$$

2. Cyclic Polygon: It is a convex polygon whose vertices are on the boundary of a circle.

3. Fan Triangulation: It is a triangulation of a cyclic polygon in which all vertices are joined to exactly one vertex, known as the point of origin.

4. Star Triangulation: It is triangulation of a cyclic polygon in which all vertices are joined to the center of the circumscribing circle (assuming the center is within the polygon).

3 Upper Bound on Fan Triangulation of a Cyclic Polygon

Given a cyclic n -gon, what is the triangulation that minimizes the dilation? Can we find a good upper bound for the dilation? The trivial upper bound for dilation is $\pi/2$. This is achieved without any triangulation. We can do slightly better and show that, if the triangulation is a fan (i.e. every edge of the triangulation starts from the same vertex), the dilation will be at most approximately 1.48454. In case of fan triangulation the shortest path between the pair of points of maximum dilation can exist in two ways.

1. Via the point of origin of Fan triangulation (shown in Figure 1(a)).
2. Path containing the sides (minimum no of sides) of the cyclic polygon (shown in Figure 1(b)).

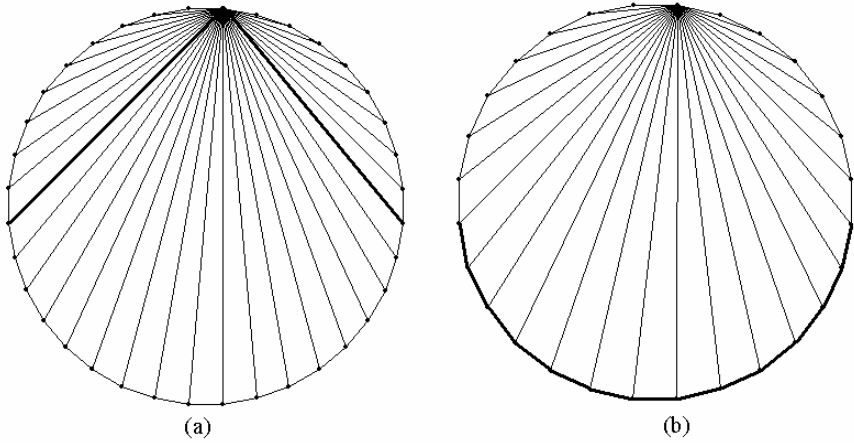


Fig. 1. (a) The shortest path between the points of maximum dilation via vertex of origin of Fan triangulation. (b) The shortest path between the points of maximum dilation via sides of a cyclic polygon.

Let A and B be any two points on a circle. Then the sum of the lengths of the included sides of the inscribed angle of the arc AB is maximum when those two sides are equal i.e. let C be any point on arc AB , then $AC+BC$ is maximum when $AC=BC$ and C lies is equidistant from AB . Figure 2 illustrates this fact.

Let C be any point on the circle, then there exists unique pair of points A, B such that $AC=BC$ and $AC + BC$ equals length of the minor arc AB . In other words, for a given point C there exists unique pair of vertices A, B such that $AC+BC$ is maximum

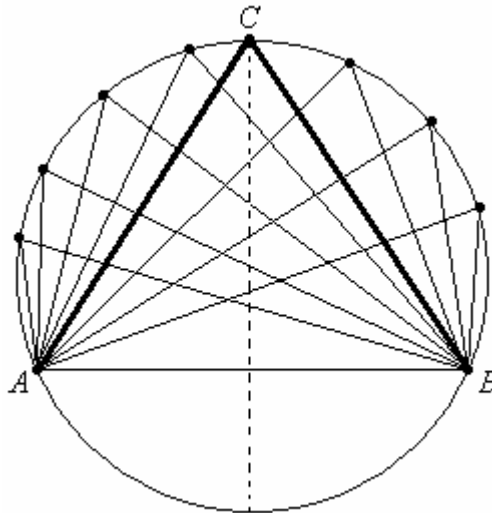


Fig. 2. The dark line indicates where sum of the included sides of the inscribed angle of arc AB is the maximum

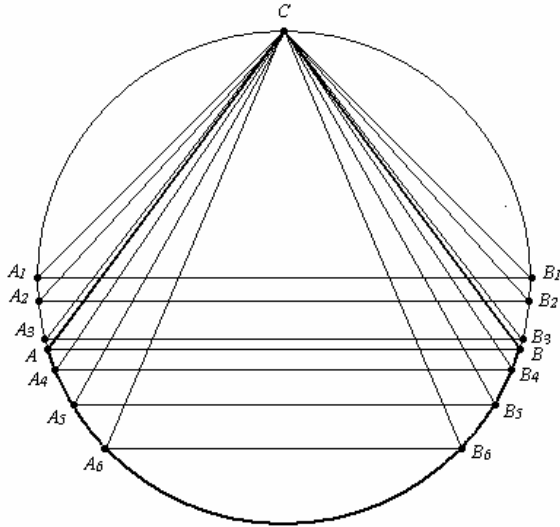


Fig. 3. This illustrates the situation defined in Lemma 3.1 Minor arc AB equals AC+BC

and this equals length of the minor arc AB. Figure 3.depicts this situation. If we consider any pair of vertices A_i, B_i above A and B, then $A_iC + B_iC$ is smaller than the length of the arc A_iB_i (arc not containing C). Similarly when we consider any pair of vertices A_i, B_i below A and B, then $A_iC + B_iC$ is greater than the length of the arc A_iB_i (arc not containing C).

Given a point C on a circle, by performing Fan triangulation over the set of points on the circle with respect to C, maximum dilation occurs between the pair of points A,B where the two points are equidistant from C and the length of the arc AB(arc not containing C) equals AC+BC. Let this dilation be denoted by MAX_DIL_F.

Lemma 3.1. MAX_DIL_F is equal to approximately 1.484534.

Proof. Please refer to Figure 4 for an illustration. $MAX_DIL_F = l/k = 2a/k$.

We know $a = b$. From $a + b = 2a = l$ and $l = 2r\theta$ we have $a = r\theta$. Since $\sin \theta = k/2r$ we have $k = 2r \sin \theta$. Therefore $MAX_DIL_F = (a + b) / k = 2a / k = 2r\theta / 2r \sin \theta = \theta / \sin \theta$.

Since $k/2a = \sin(\theta/2)$ we have $2a/k = 1/\sin(\theta/2)$. Also we know $MAX_DIL_F = 2a/k = \theta / \sin \theta$. Thus we have $\theta / \sin \theta = 1/\sin(\theta/2)$. Therefore $\sin(\theta/2) = \sin \theta / \theta \Rightarrow \sin(\theta/2) = 2 \sin(\theta/2) \cos(\theta/2) / \theta \Rightarrow \theta/2 = \cos(\theta/2)$. Solving by bisection method we get $\theta/2 \approx 0.739085133215$ rad. Thus $\theta \approx 1.47817026643$ rad.

Putting the above value of θ in MAX_DIL_F we get $MAX_DIL_F = \theta / \sin \theta \approx 1.484534$. **Q.E.D**

Lemma 3.2. The maximum dilation of Fan triangulation of a cyclic polygon is always less than MAX_DIL_F i.e. MAX_DIL_F is the upper bound on the dilation of Fan triangulation of a cyclic polygon.

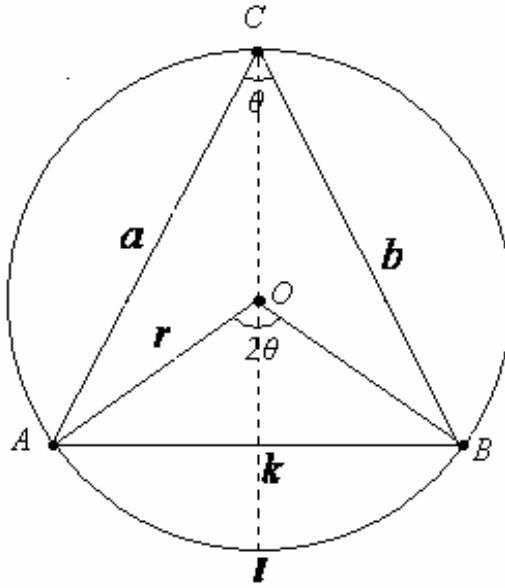


Fig. 4. MAX_DIL_F occurs between points A, B

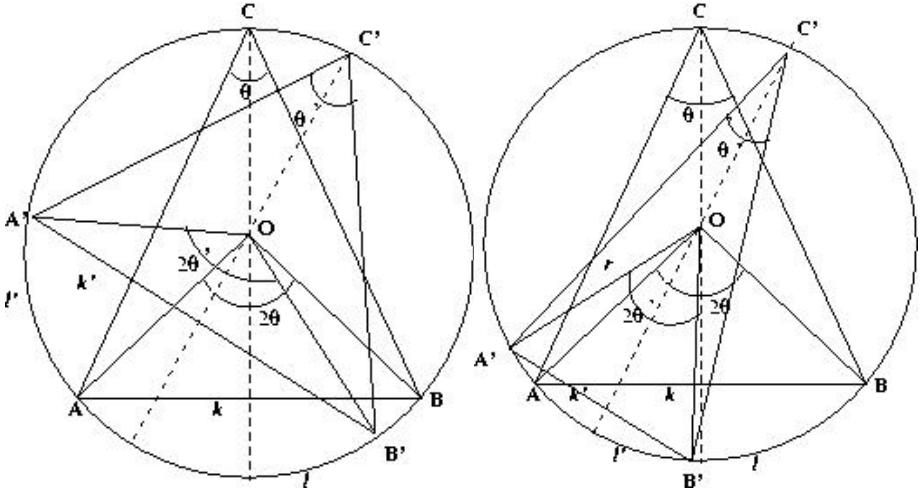


Fig. 5.(a) Case when $l' > l$ (b) Case when $l' \leq l$

Proof. Let DIL_F be the dilation of Fan triangulation between two arbitrary vertices A' , B' of a cyclic polygon. Please refer to Figure 5(a) and 5(b) for illustrations. Let $2\theta'$ be the angle subtended by the two points A' and B' at the centre of the circle and k' be the length of the chord $A'B'$ and let l' be the length of the arc $A'B'$. Now we have the following two cases:

Case 1: $l' > l$ as in Fig. 5(a)

$$\begin{aligned} \text{DIL_F} &= \text{MIN}(l', A'C' + B'C') / k' \\ &\leq \text{MIN}(l', A'C' + B'C') / k' \\ &\leq \text{MIN}(l', AC + BC) / k' \\ &= \text{MIN}(l', 1) / k' = l / k' < l / k = \text{MAX_DIL_F} \end{aligned}$$

Case 2: $l' \leq l$ as in Fig. 5(b)

$$\begin{aligned} \text{DIL_F} &= \text{MIN}(l', A'C' + B'C') / k' \\ &= l' / k' \\ &= 2r \theta' / 2r \sin \theta' \\ &= \theta' / \sin \theta' \end{aligned}$$

Now $\theta' \leq \theta \Rightarrow \theta' / \sin \theta' \leq \theta / \sin \theta = \text{MAX_DIL_F}$. This is because $x / \sin x$ is a monotonically increasing function in the interval $[0, \pi/2]$.

Thus in both the cases $\text{DIL_F} \leq \text{MAX_DIL_F}$.

Q.E.D

Thus we have established the following theorem:

Theorem 3.1. *The upper bound on the dilation of Fan triangulation of a cyclic polygon is approximately 1.484534.*

4 Upper Bound on Dilation of Star Triangulation of a Cyclic Polygon

Let C, the center of the circumscribing circle of the cyclic polygon be inside the polygon. In a Star triangulation of such a cyclic polygon, the maximum dilation occurs between a pair of vertices A, B where the length of the arc equals twice the radius of the circumscribing circle of the cyclic polygon. Let us denote this dilation by MAX_DIL_S .

Lemma 4.1. *MAX_DIL_S is equal to approximately 1.18839.*

Proof. Please refer to Figure 6 for an illustration. $\text{MAX_DIL_S} = l / k = 2r / k$.

We know $l = r\theta$. Also $\sin(\theta/2) = k/2r$ we have $k = 2r \sin(\theta/2)$. Therefore $\text{MAX_DIL_S} = l / k = r\theta / 2r \sin(\theta/2) = \theta / 2 \sin(\theta/2)$.

From $l = r\theta = 2r$ we have $\theta = 2$ rad. Putting the value of θ in MAX_DIL_S we get $\text{MAX_DIL_S} = 1 / \sin 1 \approx 1.18839$.

Q.E.D

Lemma 4.2. *The maximum dilation of Star triangulation of a cyclic polygon is always less than MAX_DIL_S i.e. MAX_DIL_S is the upper bound on the dilation of Star triangulation of a cyclic polygon.*

Proof. Let DIL_S be the dilation of Star triangulation between two arbitrary vertices A', B' of a cyclic polygon. Please refer to Figure 7(a) and 7(b) for illustrations. Let θ' be the angle subtended by the two points A' and B' at the centre of the circle and k' be the length of the chord A'B' and let l' be the length of the arc A'B'. Now we have the following two cases:

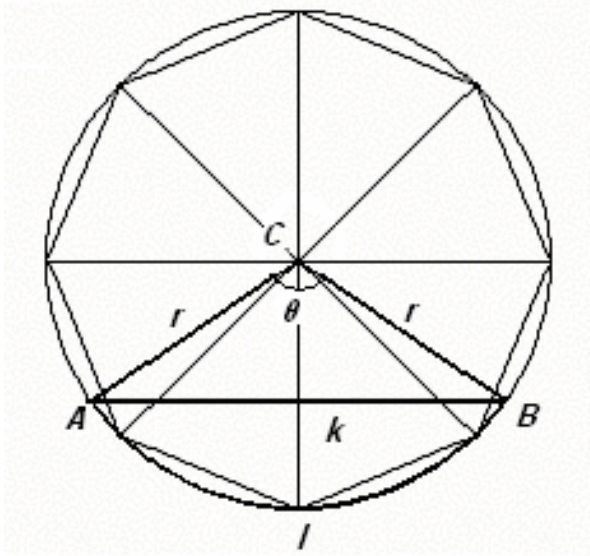


Fig. 6. Illustrates Star triangulation. A, B are the points on the circle where the maximum dilation occurs.

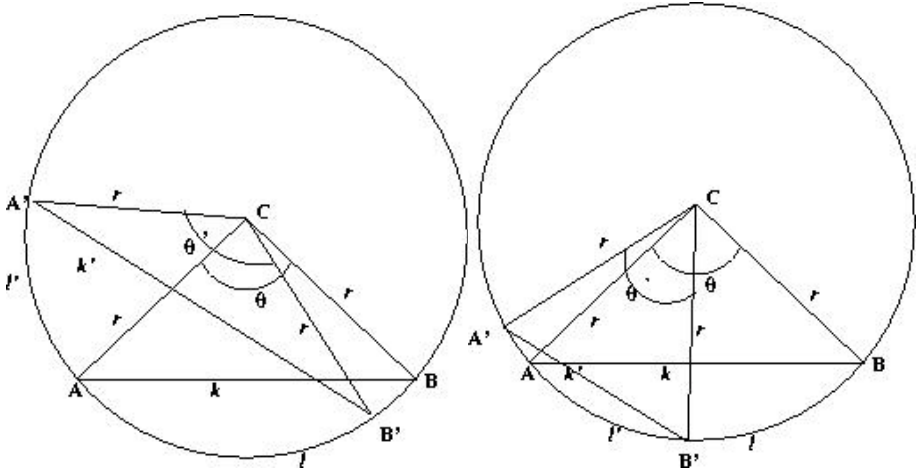


Fig. 7. (a) Case when $l' > 2r$ (b) Case when $l' \leq 2r$

Case 1: $l' > 2r$ as in Fig. 7(a)

$$\begin{aligned} \text{DIL}_S &= \text{MIN}(l', 2r) / k' \\ &= 2r / k \\ &= 2r / 2r \sin(\theta'/2) \\ &= 1 / \sin(\theta'/2) \end{aligned}$$

Since $l' = r \theta' > 2r \Rightarrow \theta' > 2 = \theta$.

Thus $DIL_S = 1 / \sin(\theta'/2) < 1 / \sin(\theta/2)$, since $1 / \sin x$ is a monotonically decreasing function in the interval $[0, \pi/2]$. Therefore $DIL_S < MAX_DIL_S$.

Case 2: $l' \leq 2r$ as in Fig. 7(b)

$$\begin{aligned} DIL_S &= MIN(l', 2r) / k' \\ &= l' / k' \\ &= r \theta' / 2r \sin(\theta'/2) \\ &= \theta' / 2 \sin(\theta'/2) \end{aligned}$$

Now $\theta' \leq \theta \Rightarrow \theta' / 2 \sin(\theta'/2) \leq \theta / 2 \sin(\theta/2) = MAX_DIL_S$. This is because $x / \sin x$ is a monotonically increasing function in the interval $[0, \pi/2]$.

Thus in both the cases $DIL_S \leq MAX_DIL_S$. **Q.E.D**

Thus we have established the following theorem:

Theorem 4.1. *The upper bound on the dilation of Star triangulation of a cyclic polygon is approximately 1.18839.*

5 Experimental Results

We verified the correctness of the results of our proof experimentally using java programming. Figure 8 shows the graph of our experimental results.

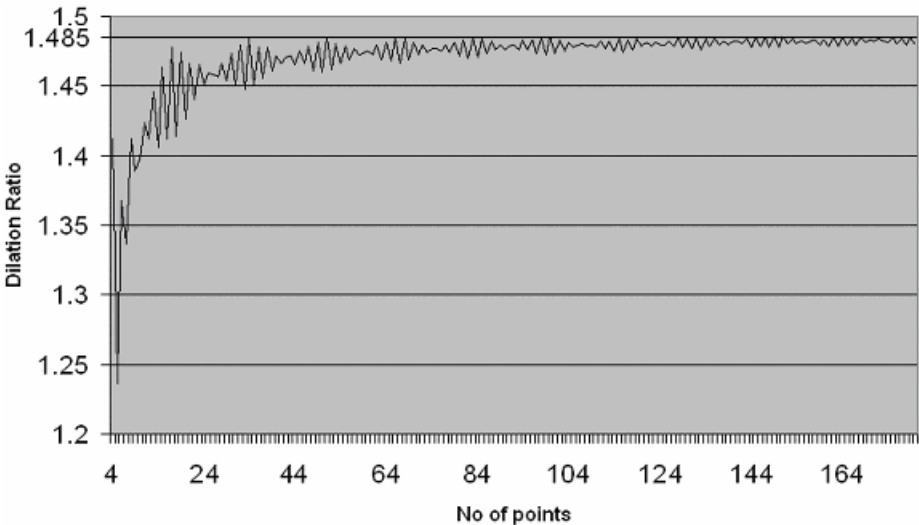


Fig. 8. Graph of Dilation Ratios of Fan triangulation over different Cyclic polygons

6 Conclusion

In this paper we have shown the upper bound on the dilation of Fan and Star triangulation of a cyclic polygon. The most interesting open problem concerns the design of a good spanner for arbitrary convex polygons. Another open problem

concerns the design of a spanner having dilation better than that of Delaunay triangulation of point sets.

References

- [1] L.P. Chew. There are planar graphs almost as good as the complete graph. *Journal of Computer and System Sciences*, vol. 39,1989, pp. 205-219.
- [2] D.P. Dobkin, S.J. Friedman and K.J.Supowit. Delaunay graphs are almost as good as complete graphs. *Discrete and Computational Geometry*, vol. 5, 1990, pp. 399-407.
- [3] W. Mulzer. *Minimum dilation triangulations for the regular n -gon*. Diploma Thesis. Freie universitat Berlin. 2004.
- [4] D. Eppstein. Spanning trees and Spanners, in J.R. Sack and J Urrutia, editors, *Handbook of computational Geometry*, elsevier, 1999, pp. 425-465.
- [5] J.M. Keil and C.A. Gutwin. The Delaunay triangulation closely approximates the complete Euclidean graph. *Proceedings of the 1st Workshop on Algorithms and Data Structures*. LNCS 382, 1989, pp. 47-56.
- [6] <http://www.cs.ubc.ca/nest/beta/tpsg/>

Optimal Guard Placement Problem Under L-Visibility

Debabrata Bardhan¹, Sasanka Roy², and Sandip Das³

¹LSI Logic India Pvt. Ltd., Kolkata - 700 091, India

²Indian Statistical Institute, Kolkata - 700 108, India

³Institut de Mathematiques, Universite de Bourgogne, Dijon - 21078, France

Abstract. Two points a and b in the presence of polygonal obstacles are L -visible if the length of the shortest path avoiding obstacles is no more than L . For a given convex polygon Q , Gewali et al. [4] addressed the guard placement problem on the exterior boundary that will cover the maximum area exterior to the polygon under L -visibility. They proposed a linear time algorithm for some given value of L . When the length L is greater than half of the perimeter, they declared that problem as open. Here we address that open problem and present an algorithm whose time complexity is linear in number of vertices of the polygon.

1 Introduction

Two points a and b are said to be *visible* if the line segment joining them is not obstructed by any other objects. A point p on a given polygon guards the polygon P if every point u of P is visible from point p . Sometimes a single guard may not be able to see the entire polygon. Chvatal [2] established in *Art Gallery theorem* that $\lfloor n/3 \rfloor$ guards are always sufficient and occasionally necessary to cover a simple polygon with n vertices. Since then a tremendous amount of research on *Art Gallery problem* has been carried out [6, 7, 8].

Guard placement problems have also been pursued by allowing interesting variations on the standard notion of visibility [7]. A guard can be considered as a robot that can sense any movement or sound in its *territory* and can able to reach the source of problem in short time. The *territory* of a guard can be defined as the region, such that for each point u in that region, there exists a path from u to guard at p avoiding obstacle whose distance is bounded by a constant c . In other words, each point in the region is L -visible from p with length L is equal to c . Here the constant c can be considered as the power of the robot. Similar concept of L -visibility was introduced in [1, 5]. We shall use the term *obstacle* to refer a region whose interior is forbidden in considering a path between two points. The complement of the set of a obstacle is the free space.

Given a convex polygon Q , here we would like to place a guard on the boundary that can guard the outer boundary of the polygon and can able to reach at trouble point for rescue within a fixed amount of time. This trouble point may be the source of attack or an accident on the guarded region. Given that the

distance between trouble point and guard avoiding the polygonal obstacle Q is bounded by a fixed length L , objective is to maximize the area of the guarded zone on the outer boundary of the polygon. We also identify the possible location of guard p on the boundary so as to guard the region.

Linear time algorithms for computing the visibility polygon under standard visibility was studied in [3]. Computation of visibility region from a given point inside/outside under L -visibility have been reported in [4]. They proposed a linear time algorithm for locating the position of a guard on the boundary of a restricted class of polygons that will maximize the outer visibility region under L-visibility. But they keep the constraint that the value of L is strictly less than half of the perimeter of the given convex polygon. They declared the problem of placing guard on convex polygon boundary under L -visibility for any general value of L as open.

External L-visibility problem is to compute the area outside the boundary of the polygon guarded by a guard posted at p under L-visibility. An optimization problem is to identify the location p on boundary of the polygon P such that the external guarded area is maximum. Considering P as convex, Gewali et al. in [4], made a conjecture regarding this problem. Their technique for generating the *Steiner points* for identification of guard location for optimum solution fails. In next section, we describe the technique for generating the *Steiner points*. Here we will consider the length L is greater than the length of half of the perimeter of the given convex polygon and the *Steiner points* generated here are completely different than that of [4]. Next we show that these *Steiner points* are possible locations of the guard on the boundary of a convex polygon Q , that maximizes the area of the territorial region, considering Q as an obstacle. In section 3, we propose an algorithm that can detect the location of a guard on boundary of the polygon that maximizes the guarded area. The time complexity of the algorithm is $O(n)$, where n is the number of vertices of the polygon.

2 Computation of the Territory of a Guard

Let Q be a convex polygon. The vertices are v_0, v_1, \dots, v_{n-1} in clockwise order and the edge (v_i, v_{i+1}) is denoted by e_i with length l_i and the angle between e_{i-1} and e_i as shown in Fig. 1(a), referred to as *sector angles* at v_i and are denoted by θ_i and θ'_i . Consider a placement of a guard at a point p on e_i having visibility limited by length L and L is greater than half of the perimeter of Q .

An *apex point* a is a point on the territory of the guard such that the shortest paths from p to a avoiding obstacle Q in both clockwise and anti clockwise directions are distinct and their lengths are equal to L . Note that for a placement of guard on the boundary of Q and for given length L (\geq half of the perimeter of Q), the apex point is unique. These paths from p to a pass through vertices of Q and the nearest vertices of polygon Q from a along these paths are called *supporting vertices*. Let v_c and v_a be two supporting vertices for apex point a in clockwise and anti clockwise directions and α_c and α_a are the angles formed by joining line segments $v_c a$ and $v_a a$ with edge e_c and e_a respectively as shown in

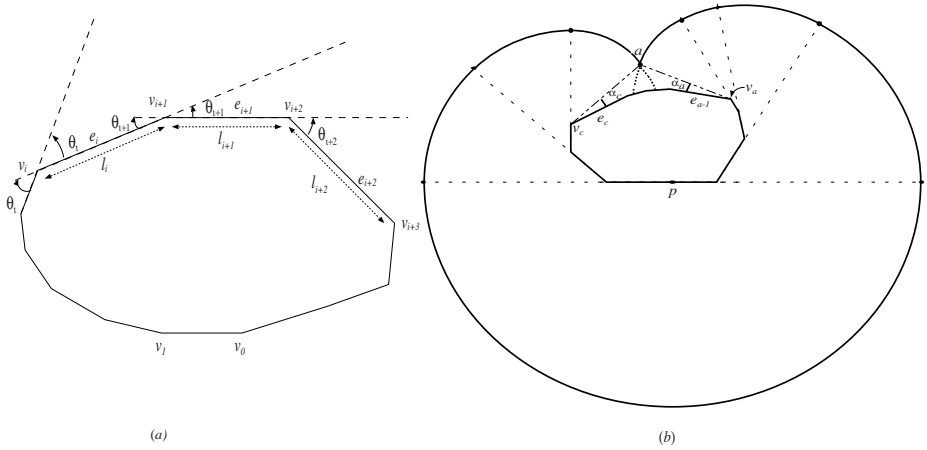


Fig. 1. (a) Vertices, edges and sector angles of a convex polygon and (b) Territory of a guard located at p

Fig. 1(b). Those two angles α_c and α_a are termed as *supporting angles* in clockwise and anti clockwise directions for the guard placed at point p at the boundary of Q . The observations below help to generate an algorithm for finding apex point at a given position of guard for a fixed length L .

Observation 1. α_c and α_a must be less than or equal to the sector angles at v_c and v_a respectively.

Proof. If the sector angle at v_c is less than supporting angle α_c , then there always exists a point say u on path from p to v_c on e_{c-1} such that path from u to a is a line segment (see Fig.2). So, the length of the line segment ua must be less than the distance from u to a via vertex v_c . \square

Observation 2. If a point a outside the convex polygon Q is an apex point, then the location of guard on the boundary of Q that generates the apex point a can be identified uniquely.

Proof. Locate the point p on the convex hull formed by the vertices of Q along with the point a such that the length of path along the convex hull from p to a

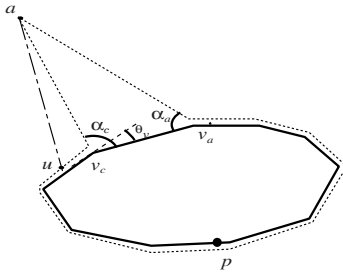


Fig. 2. Illustrating the proof of Observation 1

in clockwise and anti clockwise direction are same. As a is an apex point, such a point p on the boundary of Q must exist and it is unique. \square

Observation 3. *For a given length L and a supporting vertex say v_c in clockwise direction (resp. v_a in anti clockwise direction), an apex point can be identified uniquely where sector angle θ_c at v_c (resp. θ_a at v_a) is equal to α_c (resp. α_a).*

Proof. Extend the line segment e_{c-1} in the direction to v_c and this half line is denoted by l . The points of intersection by the extended lines of edges e_c, e_{c+1}, \dots on l are marked by p_c, p_{c+1}, \dots respectively. Note that the distance of the intersection points p_c, p_{c+1}, \dots from v_c are in increasing order.

If the apex point a whose sector angle at v_c is equal to α_c ($=\theta_c$) lies within the interval $[p_i, p_{i+1}]$ on l , then the supporting vertices for that apex point are v_c and v_{i+1} . Let L_i (res. L_{i+1}) be the length of half of the perimeter of convex hull formed by vertices of the polygon along with point p_i (res. p_{i+1}). Therefore L_i (res. L_{i+1}) is the distance of apex point from the guard when the apex is at point p_i (res. p_{i+1}). Here L_i (res. L_{i+1}) is considered as the length of the visibility of p_i (res. p_{i+1}) from the guard.

Again, from observation 1, if the value of L lies between L_i and L_{i+1} and apex point is on half line l , then the apex point must be on interval $[p_i, p_{i+1}]$. So, the sum of the distances from apex point to two of its supporting vertices can be determined by computing the distance of two supporting vertices along the perimeter of Q in appropriate direction. This generates an ellipse with foci at two supporting vertices, and intersection point with l defines the apex point. \square

The above observation leads to the following lemma.

Lemma 1. *For placement of the guard at a given point p on the boundary of Q , the corresponding apex point can be computed in $O(n)$ time.*

Proof. Follows from similar arguments as in the proof of observation 3. \square

Let a guard be located at point p on Q that generates an apex point with supporting vertices v_c and v_a in clockwise and anti clockwise directions respectively. p is a *Steiner point* whenever the sector angle at v_c is equal to α_c or the sector angle at v_a is equal to α_a .

Lemma 2. *Possible number of Steiner points are at most $2n$.*

Proof. For a given supporting vertex in clockwise direction, we can identify the apex point and the corresponding supporting vertices in anti clockwise direction using the method described in observation 3 and that generates the location of guard uniquely. So, consider all the vertices as supporting vertices in clockwise direction and anti clockwise direction with $\alpha_c = \theta_c$ or $\alpha_a = \theta_a$, we can generate at most $2n$ *Steiner points*. \square

Lemma 3. *All Steiner points can be identified in $O(n)$ time.*

Proof. Consider v_1 be the supporting vertex in clockwise direction with sector angle θ_1 at v_1 is equal to the supporting angle α_c in clockwise direction. From observation 3, we can identify the apex point and the location of guard in $O(n)$ time and will report the supporting vertex v_a in anti clockwise direction. Now two pointers pt_1 and pt_2 are set at v_1 and v_α . After computing point for these instance, move pointer pt_1 towards v_2 . So, we are looking for next *Steiner point* whose supporting vertex at clockwise direction is at v_2 with sector angle θ_2 at v_2 is equal to supporting angle in clockwise direction. Obviously its supporting angle in anti clockwise direction must be at v_α or at some vertex in clockwise direction of v_α . That vertex can be detected by shifting pointer pt_2 by one by one vertices of the polygon Q in clockwise direction. Note that, each shift and check takes constant amount of time. This process is continued by shifting pointer pt_1 , one by one until it reaches v_n and pt_2 will move from v_α to $v_{\alpha+1}, \dots, v_n, v_1, \dots, v_\alpha$. Hence the lemma follows. \square

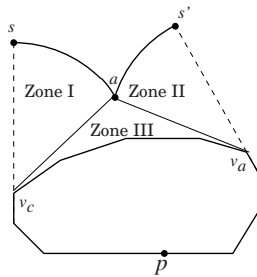


Fig. 3. Type I-III zones for guard located at p

Below, we introduce three types of zones on territory of guard for comparing the territorial area for different location of guard on boundary of Q . Let s and s' be two points on the extended lines of edge e_{c-1} in the direction towards v_c and e_a in the direction towards v_a respectively, such that the shortest distance from s and s' to p avoiding obstacle Q , is equal to L . We partition the territory of guard p , bounded by line segments sv_c and $s'v_a$ as follows (Fig. 3):

Type I Zone: area bounded by arc sa and line segments sv_c and av_c .

Type II Zone: area bounded by arc $s'a$ and line segments $s'v_a$ and av_a .

Type III Zone: territory on the triangular region $\Delta av_c v_a$.

Let d_c denotes the length of the path p to v_c along the boundary of the polygon Q in clockwise direction. Similarly we can compute d_a , the length of the path p to v_a in anti clockwise direction. Therefore the area of *Type I* and *Type II* zones are $(L - d_c)^2 \frac{\alpha_c}{2}$ and $(L - d_a)^2 \frac{\alpha_a}{2}$ respectively where α_c and α_a are their respective supporting angles. Note that, in case of *Steiner points*, one of these two supporting angles must be equal to the respective sector angle. We can compute the *Type III* zone by computing the difference of the area of the triangle $\Delta av_c v_a$ and the area of the intersection region $\Delta av_c v_a \cap Q$. Again while

computing the *Steiner points* and their supporting vertices v_c and v_a , we can store information of the area of the intersection region $\Delta av_c v_a \cap Q$ with same time complexity by subtracting area of triangle region $\Delta v_c v_{c+1} v_a$ while moving pointer pt_1 from v_c to v_{c+1} and adding region $\Delta v_a v_{a+1} v_c$ while moving pointer pt_2 from v_a to v_{a+1} for fixing supporting vertex at anti clockwise direction.

Therefore we can conclude the following lemma using the same technique for locating *Steiner points* as described in proof of Lemma 3.

Lemma 4. *Area of Type I-III zones for $2n$ Steiner points can be computed in $O(n)$ time.*

A set S of size $3n$ consists of n vertices and at most $2n$ *Steiner points*. Following lemma indicates that the guard must be anchored at one of those points on S that maximizes the territorial region under L-visibility.

Lemma 5. *An optimal location of guard must be at one of those points in S that maximize the outer visibility region under L-visibility.*

Proof. Let p_m be a point on an edge e of Q which is not in S . We can always find two neighbors p_l and p_r on left and right side of p_m respectively on the same edge e such that there is no point of S is in interval $[p_l, p_m]$ and are equal distance apart from p_m . Observe that the supporting vertices of apex points are same for guards located at p_l , p_m and p_r . We will claim that p_m cannot be an optimum location as the sum of areas of the territory for guards placed at p_l and p_r are greater than twice the area of the zone guarded by a guard placed at p_m . We denote $\mathcal{A}(p_m)$, $\mathcal{A}(p_l)$ and $\mathcal{A}(p_r)$ as the territories for the guard placed at p_m , p_l and p_r respectively. Let θ_i and d_i be sector angle and shortest distance of vertex i from the anchor point p_m avoiding obstacle Q . Apart from *Type I-III* zones and a half circle of radius L , a territory is constituted by the sum of areas $(L - d_i)^2 \frac{\theta_i}{2}$ for all vertices of Q not in *Type I-III* zones and this sum is denoted by $R(p_m)$ for guard located at p_m . Hence $\mathcal{A}(p_m)$ is equal to the sum of a half

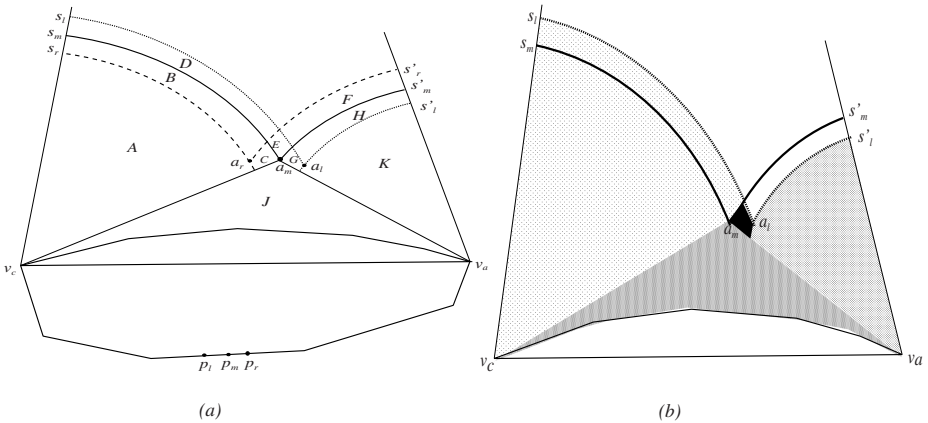


Fig. 4. Illustrating the proof of Lemma 5

circle of radius L along with region $R(p_m)$ and *Type I-III* zones formed for that placement. Note that, the vertices of the polygon Q in *Type I-III* zones for guard at p_m are same for the guard located at p_l and p_r .

For any vertex v_i , not in *Type I-III* zones, let the shortest distance from v_i to p_m avoiding obstacle Q be d_i . Let v_i is in between p_m and v_c at clockwise direction of p_m . Let its distance from p_l is $d_i - \epsilon$ and hence its distance from p_r is $d_i + \epsilon$.

From simple algebraic inequality $2(L - d_i)^2 \frac{\theta_i}{2} < ((L - d_i - \epsilon)^2 + (L - d_i + \epsilon)^2) \frac{\theta_i}{2}$ we can conclude that, $2R(p_m) < R(p_l) + R(p_r)$. Below we prove that the same result holds good for *Type I-III* zones also and hence follows the lemma.

Suppose v_c and v_a are the supporting vertices in clockwise and anti clockwise direction. a_l , a_m and a_r are the apex corresponding to the guards located at p_l , p_r and p_m respectively and they are on a ellipse with foci at v_c and v_a .

Here apex point for guard located at point p is not in the *Type III* Zone generated by guard located at any point other than p . We further partition *Type I-III* Zones generated by the guards located at p_l , p_m and p_r as follows (fig. 4(a)).

- A: Region formed by extended arc $s_r a_r$ with line $s_r v_c$ and $a_m v_c$
- B: Region bounded by arc $s_r a_r$, $s_m a_m$, $a_r s'_r$ and line $s_r s_m$
- C: Region bounded by arc $a_r s'_r$, $s_m a_m$, $s_r a_r$ and line $v_c a_m$.
- D: Region bounded by arc $s_l a_l$, $s_m a_m$, $a_r s'_r$ and line $s_l s_m$.
- E: Region bounded by arc $a_r s'_r$, $s_l a_l$, $s_m a_m$, and arc $a_m s'_m$.
- F: Region bounded by arc $a_r s'_r$, $s'_m a_m$, $s_l a_l$ and line $s'_r v_a$.
- G: Region bounded by arc $s'_m a_m$, $a_l s_l$, $a_l s'_l$ and line $a_m v_a$.
- H: Region bounded by arc $s'_m a_m$, $a_l s_l$, $a_l s'_l$ and line $s'_m s'_l$.
- K: Region bounded by arc $a_l s'_l$ and line $a_m v_a$, $s'_l v_a$.

Consider R_l as a *Type I-III* zones generated by guard located at p_l . Note that the region R_l have an area equal to the area formed by the distinct regions A, B, C, D, E, G, J, K all together (Fig. 4(b)). Similarly *Type I-III* zones generated by guard located at point p_r , say R_r have an area equal the area formed by the regions A, J, K, H, G, F, E, C all together.

As we observed that $2(L - d_i)^2 \frac{\theta_i}{2} < ((L - d_i - \epsilon)^2 + (L - d_i + \epsilon)^2) \frac{\theta_i}{2}$, and the extended line segment $v_c a_m$ intersect arc $s_l a_l$ in its interior, we can conclude that $area(A) + area(A \cup B \cup C \cup D \cup E \cup G) > 2 \cdot area(A \cup B \cup C)$ and $area(K) + area(C \cup E \cup F \cup G \cup H \cup K) > 2 \cdot area(G \cup H \cup K)$ where, $area(R)$ indicates the area of the region R . So, the sum of area of regions R_l and R_r is greater than twice the area formed by region A, B, C, K, G, H, J . \square

We can compute the maximal covering area and the location of the guard by considering each point of S as guard location. We can compute the area in $O(n)$ time for each guard location. As the cardinality of set S is of order n , we can detect the maximal cover area and the location of guard in $O(n^2)$ time. In order to compute the maximal cover area efficiently, we like to study the functions for computing the cover area for given location of the guard.

3 Placement of Guard for Maximizing Territory Region

Now we redefine the vertices of the polygon Q by considering all $3n$ points of set S on the boundary of Q as its vertices. Therefore, the vertices of Q are $v_0, v_1, \dots, v_{3n-1}$ in clockwise direction with edges $e_i = (v_i, v_{i+1})$ having length l_i . Here the angle of the polygon at original Steiner vertices are equal to π and the sector angles are equal to Zero. Note that, when L is strictly greater than half of the perimeter, apex point cannot be on the boundary of the polygon. Therefore, the supporting vertices do not belong to the original *Steiner points*.

Suppose the guard is placed on the boundary of the polygon Q at a location x distance apart from a vertex v_i of the polygon Q in the clockwise direction. Let $\mathcal{A}_i^+(x)$ and $\mathcal{B}_i^+(x)$ denote the cover areas outside the polygon Q excluding *Type I-III* zones and the area in *Type I-III* zones respectively. Similarly, when the guard is located on the boundary of the polygon Q at a location x distance apart from v_i in anti clockwise direction we define $\mathcal{A}_i^-(x)$ and $\mathcal{B}_i^-(x)$ as the cover area outside the polygon Q excluding *Type I-III* zones and the cover area in *Type I-III* zones respectively.

Let v_i and v_{i+1} are two adjacent vertices in Q and v_{i+1} is in clockwise direction of v_i . The supporting vertices for apex point for guard located at any point on edge $e_i = (v_{i+1}, v_i)$ are same and let those points be v_c and v_a in clockwise and anti clockwise direction respectively. Therefore, any value of x within the range $[0, l_i]$, the guard must be located in the interval $[v_{i+1}, v_i]$ on the boundary of the polygon Q . In that case, $\mathcal{A}_i^+(x)$ and $\mathcal{B}_i^+(x)$ are smooth functions of x within the range $[0, l_i]$. Consider $0 \leq x \leq l_i$ and then $\mathcal{A}_i^+(x)$ can be expressed as follows.

$$\begin{aligned} \mathcal{A}_i^+(x) &= \frac{\pi L^2}{2} + \frac{\theta_{i+1}}{2}(L - l_i + x)^2 + \frac{\theta_{i+2}}{2}(L - l_i - l_{i+1} + x)^2 + \dots \\ &\quad + \frac{\theta_{c-1}}{2}(L - l_i - l_{i+1} - l_{i+2} - \dots - l_{c-2} + x)^2 + \frac{\theta_i}{2}(L - x)^2 \\ &\quad + \frac{\theta_{i-1}}{2}(L - l_{i-1} - x)^2 + \dots + \frac{\theta_{a+1}}{2}(L - l_{i-1} - l_{i-2} - \dots - l_{a+1} - x)^2 \end{aligned}$$

where θ_i is the sector angle at vertex v_i of the polygon Q .

This expression can be viewed as a function of distance x from v_i with $0 \leq x \leq l_i$ and can be expressed as: $\mathcal{A}_i^+(x) = a_i^+x^2 + b_i^+x + c_i^+$ where a_i^+ , b_i^+ and c_i^+ are considered as constant and

$$\begin{aligned} a_i^+ &= \frac{1}{2}\{\theta_{c-1} + \theta_{c-2} + \dots + \theta_{i+1} + \theta_i + \theta_{i-1} + \dots + \theta_{a+1}\} \\ b_i^+ &= \{\theta_{i+1}(L - l_i) + \theta_{i+2}(L - l_i - l_{i+1}) + \theta_{i+3}(L - l_i - l_{i+1} - l_{i+2}) + \dots + \\ &\quad \theta_{c-1}(L - l_i - l_{i+1} - \dots - l_{c-2})\} - \{\theta_i L + \theta_{i-1}(L - l_{i-1}) + \theta_{i-2}(L - l_{i-1} - \\ &\quad l_{i-2}) \dots + \theta_{a+1}(L - l_{i-1} - l_{i-2} - \dots - l_{a+1})\} \\ c_i^+ &= \frac{1}{2}\{\pi L^2 + \{\theta_{i+1}(L - l_i)^2 + \theta_{i+2}(L - l_i - l_{i+1})^2 + \theta_{i+3}(L - l_i - l_{i+1} - l_{i+2})^2 + \\ &\quad \dots + \theta_{c-1}(L - l_i - l_{i+1} - l_{i+2} - \dots - l_{c-2})^2\} + \{\theta_i(L)^2 + \theta_{i-1}(L - l_{i-1})^2 + \\ &\quad \theta_{i-2}(L - l_{i-1} - l_{i-2})^2 \dots + \theta_{a+1}(L - l_{i-1} - l_{i-2} - \dots - l_{a+1})^2\} \end{aligned}$$

Observe that, if the location of guard is expressed as x distance apart in anti clockwise direction from vertex v_{i+1} and x is within range $[0, l_i]$, then supporting vertices for apex point in clockwise and anti clockwise directions are same v_c and v_a respectively. In that case $\mathcal{A}_i^+(x)$ is same as $\mathcal{A}_{i+1}^-(l_i - x)$ for $0 \leq x \leq l_i$.

Therefore equating the coefficient of equal powers of x of both functions we get, $a_i^+ = a_{i+1}^-$; $b_i^+ = -b_{i+1}^- - 2.l_i.a_{i+1}^-$ and $c_i^+ = c_{i+1}^- + l_i.b_{i+1}^- + l_i^2.a_{i+1}^-$. Therefore a_{i+1}^- , b_{i+1}^- and c_{i+1}^- can be computed from a_i^+ , b_i^+ and c_i^+ in constant time.

Let $v_{c'}$ and $v_{a'}$ are the supporting vertices for guard located on interval $[v_i, v_{i-1}]$. If v_i does not represent an original *Steiner point* then the guard located at any point between v_i and v_{i-1} have the same supporting vertices for guard located at interval $[v_i, v_{i+1}]$, that is v_c and v_a in clockwise and counter clockwise directions respectively. The supporting vertices can be identified by the pointer attached to Steiner vertex at v_i . Therefore $\mathcal{A}_i^-(x)$ can be expressed as

$$\mathcal{A}_i^-(x) = a_i^- x^2 + b_i^- x + c_i^- \quad (1)$$

where,

$$\begin{aligned} \mathcal{A}_i^-(x) = & \frac{\pi L^2}{2} + \frac{\theta_i}{2}(L-x)^2 + \frac{\theta_{i+1}}{2}(L-l_i-x)^2 + \frac{\theta_{i+2}}{2}(L-l_i-l_{i+1}-x)^2 + \dots \\ & + \frac{\theta_{c'-1}}{2}(L-l_i-l_{i+1}-l_{i+2}-\dots-l_{c'-2}-x)^2 + \frac{\theta_{i-1}}{2}(L-l_{i-1}+x)^2 + \dots + \\ & \frac{\theta_{a'+1}}{2}(L-l_{i-1}-l_{i-2}-\dots-l_{a'+1}+x)^2 \end{aligned}$$

therefore,

$$\begin{aligned} a_i^- &= \frac{1}{2}\{\theta_{c'-1} + \theta_{c'-2} + \dots + \theta_{i+1} + \theta_i + \theta_{i-1} + \dots + \theta_{a'+1}\} \\ b_i^- &= \{\theta_{i-1}(L-l_{i-1}) + \theta_{i-2}(L-l_{i-1}-l_{i-2}) + \theta_{i-3}(L-l_{i-1}-l_{i-2}-l_{i-3}) + \\ & \theta_{a'+1}(L-l_{i-1}-\dots-l_{a'+1})\} - \{\theta_i L + \theta_{i+1}(L-l_i) + \theta_{i+2}(L-l_i-l_{i+1}) + \\ & \dots + \theta_{c'-1}(L-l_i-l_{i+1}-\dots-l_{c'-2})\} \\ c_i^- &= \frac{1}{2}[\pi L^2 + \{\theta_{i+1}(L-l_i)^2 + \theta_{i+2}(L-l_i-l_{i+1})^2 - \theta_{i+3}(L-l_i-l_{i+1}-l_{i+2})^2 + \\ & \dots + \theta_{c'-1}(L-l_i-l_{i+1}-l_{i+2}-\dots-l_{c'-2})^2\} + \{\theta_i(L)^2 + \theta_{i-1}(L-l_{i-1})^2 + \\ & \theta_{i-2}(L-l_{i-1}-l_{i-2})^2 \dots + \theta_{a'+1}(L-l_{i-1}-l_{i-2}-\dots-l_{a'+1})^2\}] \end{aligned}$$

Lemma 6. *Covered area excluding Type I-III zones for guard located at each vertices can be computed in $O(n)$ time.*

Proof. From the expressions of a_i^- , b_i^- , c_i^- and a_i^+ , b_i^+ , c_i^+ , we express:

$$\begin{aligned} a_i^- &= a_i^+ - \frac{1}{2}\{\theta_{c-1} + \theta_{c-2} + \dots + \theta_{c'}\} + \frac{1}{2}\{\theta_a + \theta_{a-1} + \dots + \theta_{a'+1}\} \\ b_i^- &= \{\theta_a(L-l_{i-1}-\dots-l_a) + \theta_{a-1}(L-l_{i-1}-\dots-l_{a-1}) + \dots + \theta_{a'+1}(L-l_{i-1}- \\ & \dots-l_{a'+1})\} + \{\theta_{c'}(L-l_i-\dots-l_{c'-1}) + \theta_{c'+1}(L-l_i-l_{i+1}-\dots-l_{c'}) + \dots + \\ & \theta_{c-1}(L-l_i-l_{i+1}-\dots-l_{c-2})\} - b_i^+ - 2\theta_i L \\ c_i^- &= c_i^+ - \frac{1}{2}[\theta_{c'}(L-l_i-l_{i+1}-\dots-l_{c'-1})^2 + \theta_{c'+1}(L-l_i-l_{i+1}-\dots-l_{c'})^2 + \\ & \dots + \theta_{c-1}(L-l_i-l_{i+1}-\dots-l_{c-2})^2] + \frac{1}{2}[\theta_{a'+2}(L-l_{i-1}-l_{i-2}-\dots-l_{a'+2})^2 + \\ & \dots \theta_{a+1}(L-l_{i-1}-l_{i-2}-\dots-l_{a+1})^2] \end{aligned}$$

If v_i is not an original *Steiner point*, then a and a' are the same points, and similarly, c and c' are the same points. Hence, we can compute a_i^+ , b_i^+ , c_i^+ from a_i^- , b_i^- , c_i^- in constant time. But we need to compute the above expressions for computing a_i^+ , b_i^+ , c_i^+ when v_i is actually representing a *Steiner point*.

Note that, while computing the supporting vertices of an original *Steiner points*, we also can keep the information of distances from *Steiner points* to its

supporting vertices. Observe that, each terms in the expressions of a_i^- , b_i^- , c_i^- involves the individual length of edges from $v_{c'}$ to v_c and v_a to $v_{a'}$ in clockwise directions, the sector angles on those vertices and distances from *Steiner point* to its supporting vertices along the boundary of the polygon. Furthermore, those lengths, edges and angles are only considered for that particular *Steiner point* and for different Steiner points, those terms are completely different. Therefore at most $O(n)$ such terms are involved all total in computing a_i^+ , b_i^+ , c_i^+ from a_i^- , b_i^- , c_i^- for all values of i ($0 \leq i \leq 3n$). As we have seen, a_{i+1}^- , b_{i+1}^- and c_{i+1}^- can be computed from a_i^+ , b_i^+ and c_i^+ in constant time, hence the lemma follows. \square

Theorem 1. *Location of the guard on the boundary of convex polygon that yield the maximum territorial region can be computed in $O(n)$ time.*

Proof. Proof follows mainly from Lemmata 3, 4, 5 and 6. \square

References

1. B. Aronov, A.R. Davis, T.K. Dey, S.P. Pal and D.C. Prasad, *Visibility with reflection*, Proc. of the 11th ACM symposium on computational geometry, pp. 316-325, 1995.
2. V. Chvatal, *A combinatorial theorem in plane geometry*, Journal of combinatorial Theory SER B, vol. 18, pp. 39-41, 1975.
3. H. ElGindy and D. Avis, *A linear time algorithm for computing the visibility polygon from a point*, Journal of Algorithms, vol. 2, pp. 186-197, 1981.
4. L. Gewali, R. Venkatasubramanian and D. Glasser, *Algorithms for Computing Grazing Area*, unpublished results, <http://www.egr.unlv.edu/~laxmi/>.
5. S. Ntafos, *Watchman routes under limited visibility*, Computational Geometry: Theory and Application, vol. 1, pp. 149-170, 1992.
6. J. O'Rourke, *Art Gallery Theorems and Algorithms*, Oxford University Press, 1987.
7. J. R. Sack and J. Urrutia, *Handbook of computational geometry*, North-Holland, Elsevier Science B. V., Netherlands, 2000.
8. T. Shermer, *Recent results in Art Galleries*, Proceedings of the IEEE, pp. 1384-1399, 1992.

Visibility Maps of Segments and Triangles in 3D*

Esther Moet¹, Christian Knauer², and Marc van Kreveld¹

¹ Department of Information and Computing Sciences, Universiteit Utrecht,
P.O.Box 80.089, 3508 TB Utrecht, The Netherlands

{`esther`, `marc`}@`cs.uu.nl`

² Institute of Computer Science, Freie Universität Berlin,
Takustraße 9, D-14195 Berlin, Germany
`christian.knauer@inf.fu-berlin.de`

Abstract. Let T be a set of n disjoint triangles in three-dimensional space, let s be a line segment, and let t be a triangle, both disjoint from T . We consider the visibility map of s with respect to T , i.e., the portions of T that are visible from s . The visibility map of t is defined analogously. We look at two different notions of visibility: strong (complete) visibility, and weak (partial) visibility. The trivial $\Omega(n^2)$ lower bound for the combinatorial complexity of the strong visibility map of both s and t is almost tight: we prove an $O(n^2 \log n)$ upper bound for both structures. Furthermore, we prove that the weak visibility map of s has complexity $\Theta(n^5)$, and the weak visibility map of t has complexity $\Theta(n^7)$. If T is a polyhedral terrain, the complexity of the weak visibility map is $\Omega(n^4)$ and $O(n^5)$, both for a segment and a triangle. We also present efficient algorithms to compute all discussed structures.

1 Introduction

Computations concerning visibility and the generation of shadows are important to obtain realistic images in computer graphics. Unfortunately, these computations can be very time-consuming. The *visibility map* of a point p with respect to a set T of n disjoint triangles in 3D, which we call a *3D scene*, is the set of maximally connected components on T that are visible from p . When projected onto a viewplane near p , the visibility map is a planar graph with $\Theta(n^2)$ vertices, edges, and faces [1, 2]. This graph is also referred to as the visibility map.

In this paper, we study the worst-case combinatorial complexity of the visibility map for a set S that consists of more than a single point; in particular, we consider the cases where S is a line segment or a triangle. The *strong visibility map* of S identifies the maximally connected components on T in which the points see *every* point of S , whereas the other points of T do not see all of S , i.e., they see S partly or not at all. The *weak visibility map* separates the points that see at least one point in S , and the points that do not see any point in S . An alternative way of looking at the weak visibility map is to consider S to

* This research was initiated during a visit of the first author to Freie Universität Berlin, which was supported by a Marie-Curie scholarship.

be a light source. Then the weak visibility map of S is equivalent to the set of maximally connected components on T that are illuminated; we will sometimes call the weak visibility map of S the *shadow map* of S .

With the results of Wang and Zhu [3], the weak visibility map of a triangle in a general 3D scene can be computed in $O(n^9)$ time and $O(n^7)$ space; to compute the same structure in a polyhedral terrain, the algorithm of [3] can be used to achieve a running time of $O(n^7)$ time and $O(n^5)$ storage. In this paper, we improve significantly on these previous results and show that our bounds are almost tight by giving lower bound constructions. For a line (segment), a collection of general results can be found in [4]. Both of the above papers use the detection of transparent and opaque topology changes to compute the parts of a 3D scene that are weakly visible from a given view element; these topology changes are generally known as EEE events [5, 6].

Recently, an $O(n^2 \log n)$ time algorithm was presented to compute the weak visibility map of an edge in a terrain on another edge [7]. One of the main topics related to our study is the aspect graph [5, 6, 8]. This graph corresponds directly to the more frequently used *viewpoint space partition* of \mathbb{R}^3 into three-dimensional cells such that the visibility map with respect to the scene is combinatorially the same throughout each cell. The *critical points* where the view of the scene changes combinatorially lie exclusively on *critical surfaces* called *reguli*; see [6] and Sec. 2. The above mentioned spatial subdivision is induced by a set of $O(n^3)$ of these critical surfaces, and therefore has complexity $O(n^9)$. However, it has been shown that its complexity is almost a linear factor less for polyhedral terrains [9, 10].

Table 1 gives a summary of our results. All displayed results are worst-case combinatorial complexities. We also present algorithms to compute the discussed structures within almost matching time bounds, i.e., in most cases computation is only an $O(\log n)$ factor worse than the worst-case complexity.

Table 1. Combinatorial complexities of the visibility map in a 3D scene for the two types of view elements under different models of visibility

	Strong	Weak (terrain)	Weak (general)	Section
Segment	$\Omega(n^2)$	$\Omega(n^4)$	$\Theta(n^5)$	3 & 4
Triangle	$O(n^2 \log n)$	$O(n^5)$	$\Theta(n^7)$	5

2 Preliminaries

In this paper, we consider sets of triangles in \mathbb{R}^3 with pairwise disjoint interiors. We call such a set T a *3D scene*, or simply *scene*. Without loss of generality, we assume that the vertical direction is the z -direction. A special case of a scene is a *polyhedral terrain*, or simply *terrain*, in which T is a piecewise-linear continuous function defined over the triangles of a triangulation in the xy -plane.

Given a scene T and two points $p, q \in \mathbb{R}^3$, we say that p *sees* q if the open line segment pq does not intersect the interior of any triangle in T , i.e., grazing contact of the line-of-sight with the edges of the triangles of T is permitted. In the case of terrains, two points can only be mutually visible if they both lie on or above the terrain. All our results, both the bounds on the worst-case complexities and the algorithms, hold when T contains degeneracies. However, to simplify argumentation, we only consider general position configurations in our proofs. This is no restriction; the worst-case complexities can be achieved by a 3D scene in general position, and in the presented algorithms, we can apply standard symbolic perturbation techniques [11].

The *regulus* $\mathcal{R}(l_1, l_2, l_3)$ for three lines l_1, l_2 , and l_3 , is the set of all lines that intersect l_1, l_2 , and l_3 , in this (or the inverse) order. A regulus has the following properties [12, §3]: (1) it is one ruling of either a hyperbolic paraboloid, or a hyperboloid of one sheet; (2) it is an algebraic surface of constant degree; (3) the projection of its boundary onto the xy -plane is a set of algebraic curves of constant degree; and (4) it can be partitioned into a constant number of xy -monotone parts. Let $\ell(s)$ denote the supporting line of a line segment s . For three edges e, f , and g of T , all lines that intersect e, f , and g , in this (or the inverse) order, lie in a subset of $\mathcal{R}(\ell(e), \ell(f), \ell(g))$. This set consists of at most three connected components [13], and is denoted by $\mathcal{R}(e, f, g)$. The critical points where the view of the scene changes combinatorially lie exclusively on these reguli [6]. Throughout this paper, we adopt an appropriate model of computation, i.e., we assume that computing various elementary operations on algebraic curves and surfaces of constant degree can be performed in constant time; for a discussion, see [14].

Let p be a point in \mathbb{R}^3 ; we denote by $\text{VP}(p, T)$ the *visibility polyhedron* of p with respect to T , i.e., the connected subset of \mathbb{R}^3 of all points that see p . If s is a low-dimensional simplex, for example, an edge e or a triangle t of T , then the *strong visibility polyhedron* of s , denoted by $\text{SVP}(s, T)$, is the set of points in \mathbb{R}^3 that see s completely. The subdivision of T induced by $\text{SVP}(e, T)$ is called the *strong visibility map* $\text{SVM}(s, T)$. The *weak visibility polyhedron* $\text{WVP}(s, T)$ is the set of points in \mathbb{R}^3 that see at least one point of s . The subdivision of T induced by $\text{WVP}(s, T)$ is the *weak visibility map* $\text{WVM}(s, T)$.

Let e be an edge of T , and let t be a triangle of T . In this paper, we study the worst-case combinatorial complexities of the following four structures: $\text{SVM}(e, T)$, $\text{WVM}(e, T)$, $\text{SVM}(t, T)$, and $\text{WVM}(t, T)$. We assume that e or t is a feature of T , but this is no restriction; if an arbitrary segment or triangle (1- or 2-simplex) $s \subset \mathbb{R}^3$ does not intersect any triangle in T , and lies above T in case T is a polyhedral terrain, then we can transform s into a feature s' of a 3D scene T' in $O(n \log n)$ time in such a way that the visibility map of s in T is essentially the same as the visibility map of s' in T' .

A trivial lower bound for the complexity of all four types of visibility maps is $\Omega(n^2)$, which is a lower bound for the visibility map of a single point [1]. The complexity of the *aspect graph* [8], which is $O(n^7)$ for any scene with n triangles, is an upper bound on both $\text{SVM}(s, T)$ and $\text{WVM}(s, T)$.

3 The Strong Visibility Map of an Edge

In this section, we are given a 3D scene T and an edge e of T . Since the triangles of T already induce $\text{SVP}(e, T)$, we analyze the complexity of $\text{SVP}(e, T)$ to obtain an almost tight $O(n^2 \log n)$ upper bound on the complexity of $\text{SVM}(e, T)$.

Definition 1. Let p be a point, and let s be a line segment, both in \mathbb{R}^3 . We define $\mathcal{P}(p, s)$ to be the set of points q for which there exists a ray starting at p that first passes through s and then through q . Similarly, $\mathcal{P}(s, p)$ is the set of points q for which there exists a ray starting at a point on s that first passes through p and then through q .

For two line segments $s_1 = p_1q_1$ and $s_2 = p_2q_2$, the (unbounded) region enclosed by $\mathcal{P}(s_1, p_2)$, $\mathcal{P}(p_1, s_2)$, $\mathcal{P}(q_1, s_2)$, and $\mathcal{P}(s_1, q_2)$ contains exactly the points p for which the triangle with base s_1 and apex p intersects the segment s_2 . For our purposes, if v is a vertex and e an edge of T , where v and e are not incident to each other, we represent the unbounded object $\mathcal{P}(e, v)$ by a large triangle, by clipping it with a vertical plane that lies beyond all features of T . Also, we clip and split $\mathcal{P}(v, e)$, and represent it by two triangles.

Definition 2. Given a 3D scene T and an edge $e = vw$ of T , we define $S(e, T)$ to be the following set of triangles:

$$S(e, T) = \{\mathcal{P}(v, f) \mid f \text{ edge of } T\} \cup \{\mathcal{P}(w, f) \mid f \text{ edge of } T\} \cup \\ \{\mathcal{P}(e, u) \mid u \text{ vertex of } T\} \cup \{t \mid t \text{ triangle of } T\}$$

$\mathcal{A}(S(e, T))$ is the arrangement induced by the triangles in $S(e, T)$.

The arrangement $\mathcal{A}(S(e, T))$ is induced by the $O(n)$ triangles of the set $S(e, T)$, and thus has complexity $O(n^3)$ overall. However, we can show that $\text{SVP}(e, T)$ is one cell of $\mathcal{A}(S(e, T))$, and thus has complexity $O(n^2 \log n)$ [15, 16]. A detailed proof of the following theorem is given in the full version of this paper [17].

Theorem 3. Let T be a 3D scene with n triangles, and let e be an edge of T . The strong visibility map $\text{SVM}(e, T)$ has complexity $\Omega(n^2)$ and $O(n^2 \log n)$.

The above argumentation directly gives a way to compute the strong visibility map. Given an edge e of T , we first generate the set $S(e, T)$ as defined in Definition 2. Next, we compute the cell c of $\mathcal{A}(S(e, T))$ that contains e . Finally, we compute the connected components of c on each triangle of T and output this set, which is $\text{SVM}(e, T)$. The first step trivially takes $O(n)$ time, the second step can be performed in randomized expected time $O(n^2 \log^3 n)$ by combining results of de Berg *et al.* [18] and Tagansky [16], and the third step can be carried out in $O(n^2 \log n)$ time in a fairly straightforward way. Thus, we have the following theorem.

Theorem 4. Let T be a 3D scene with n triangles, and let e be an edge of T . The strong visibility map $\text{SVM}(e, T)$ can be computed in $O(n^2 \log^3 n)$ randomized expected time.

4 The Weak Visibility Map of an Edge

The weak visibility region of an edge in a polygon with holes can have complexity $\Omega(n^4)$, as was shown by Suri and O'Rourke [19]. In their construction, an edge light source and two rows of segments with suitably placed gaps A and B produce a quadratic number of narrow light cones that all mutually intersect. These intersections of cones result in $\Omega(n^4)$ illuminated vertices of the visibility region; see Fig. 1(a) for a schematic illustration of this construction.

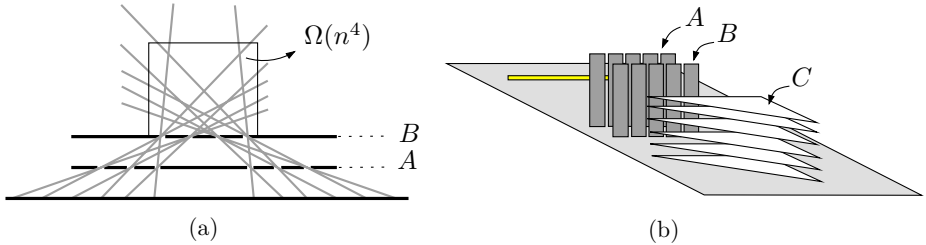


Fig. 1. (a) A schematic illustration of the lower bound construction for the weak visibility region of an edge in a polygon with holes [19]. (b) A schematic display of a 3D scene in which the weak visibility map of an edge has complexity $\Omega(n^5)$.

We can create the same construction with a polyhedral terrain, where the 2D situation described above is replicated on the xy -plane, such that a single triangle contains all the $\Omega(n^4)$ intersections of the light cones. Thus, we have the following lemma.

Lemma 5. *The weak visibility map of an edge in a polyhedral terrain can have $\Omega(n^4)$ vertices.*

For general scenes, we can improve this lower bound. By placing a linear number of triangles vertically above each other, we can replicate the triangle that contains $\Omega(n^4)$ vertices of the visibility map $\Omega(n)$ times. Note that the triangles in this stack should be spaced in such a way that the light can extend through to the back of the stack. Figure 1(b) shows a schematic display of the lower bound construction for general 3D scenes. Due to the vertically stacked triangles in C , this construction cannot be built as a polyhedral terrain.

Lemma 6. *The weak visibility map of an edge in a 3D scene with n triangles can have $\Omega(n^5)$ vertices.*

We prove upper bounds on the complexity of the weak visibility map of an edge, by proving bounds on the shadow map that an illuminating edge e induces onto different features of the 3D scene T . First, we prove a bound of $\Theta(n^2)$ for the complexity of the shadow map on *an edge* of T , and then $\Theta(n^4)$ for the complexity of the shadow map on *a triangle* of T . The latter, together with Lemma 6, implies that the complexity of the weak visibility map of an edge in a general 3D scene is $\Theta(n^5)$.

By the lower bound construction of Fig. 1(a), the shadow map restricted to an edge can have complexity $\Omega(n^2)$, since there can be a quadratic number of light cones that intersect the edge in distinct points. We can show that the illuminated portion of an edge is the union of a number of cells in an $O(n^2)$ size arrangement on this edge, induced by a quadratic number of reguli. The proof of the following lemma is given in the full version of this paper [17].

Lemma 7. *Let e and f be two edges of a 3D scene T with n triangles. If e acts as a light source, then the shadow that T casts on f has complexity $O(n^2)$.*

By the lower bound construction of Fig. 1(a), the shadow map on a triangle t of a 3D scene can have complexity $\Omega(n^4)$, which is tight. The proof of the following lemma is very similar to the one of Lemma 7; we now obtain an $O(n^4)$ arrangement induced by $O(n^2)$ algebraic curves on a triangle. This proof is also given in the full version of this paper [17].

Lemma 8. *Let T be a 3D scene with n triangles, let e be an edge of T , and let t be a triangle of T . If e acts as a light source, then the shadow that T casts on t has complexity $O(n^4)$.*

Putting together Lemmas 5, 6 and 8 yields the following theorem.

Theorem 9. *Let T be a 3D scene with n triangles, and let e be an edge T . Then $WVM(e, T)$ has complexity $\Theta(n^5)$ in the worst case. If T is a polyhedral terrain, then the complexity of $WVM(e, T)$ is $\Omega(n^4)$ and $O(n^5)$.*

To compute the shadow of T that is cast onto an edge f by the illuminating edge e , we use a sweep algorithm. We use an algorithm that is very similar to the $O(n^2 \log n)$ time algorithm that is described in [7]; however, we sweep the *illuminated* edge instead of the *illuminating* one. The reason for this adjustment is that, in this way, we immediately obtain the subdivision of f into illuminated and dark points, i.e., the shadow map of e on f . The analysis of [7] easily follows through for this new setting as well, which gives us the following lemma.

Lemma 10. [7] *Let T be a 3D scene with n triangles, and let e and f be two edges of T . We can compute the part of $WVM(e, T)$ restricted to f in $O(n^2 \log n)$ time.*

The shadow of T cast onto a triangle t of T by the illuminating edge e can be computed by a sweep algorithm as well. First, we need an extra lemma. Since two algebraic curves of constant degree in the plane have at most a constant number of intersections, it is easy to verify the lemma below (the proof is basically similar to the proof of Lemma 7 and the analysis in [7]).

Lemma 11. *Let e be an edge of a 3D scene T with n triangles, and let c be an algebraic curve of constant degree on a triangle t of T . If e acts as a light source, then the shadow that T casts on c has complexity $O(n^2)$ and can be computed in $O(n^2 \log n)$ time.*

The first step in computing the shadow map of an edge e on a triangle t is to generate the set $S(t)$ of curves of intersection of the reguli $\mathcal{R}(e, f, g)$ with t , for all ordered edge pairs (f, g) of T . Next, we compute the subdivision of t induced by $S(t)$, denoted by $\mathcal{A}(S(t))$. This arrangement can be computed in $O(n^4)$ randomized expected time [20], or in $O(n^4 \log n)$ time by a standard sweep algorithm. We execute the $O(n^2 \log n)$ algorithm that computes the shadow map on an algebraic curve *twice* for every curve c in $S(t)$; we compute curves c' and c'' that, symbolically, lie infinitesimally close to c on either side. By computing the shadow maps on c' and c'' we can determine whether the adjacent cells of $\mathcal{A}(S(t))$ are **illuminated** or **dark**. Since we have $O(n^2)$ curves in $S(t)$, the cell labelling takes $O(n^4 \log n)$ time. Therefore, we have the following theorem.

Theorem 12. *Let T be a 3D scene with n triangles, let e be an edge of T , and let t be a triangle of T . We can compute the part of the weak visibility map of e on t in $O(n^4 \log n)$ time. The weak visibility map $\text{WVM}(e, T)$ can be computed in $O(n^5 \log n)$ time.*

5 The Triangle Visibility Map

The Strong Visibility Map of a Triangle. Let e_1, e_2 , and e_3 be the edges of a triangle t of a 3D scene T . We define $S(t, T)$ to be the set $\bigcup_{i=1..3} S(e_i, T)$, where $S(e_i, T)$ is defined as in Definition 2. Let $\mathcal{A}(S(t, T))$ be the spatial subdivision induced by the triangles of $S(t, T)$. By a similar argumentation as in the proof of Theorem 4, we have:

Theorem 13. *Let T be a 3D scene with n triangles, and let t be a triangle of T . Then $\text{SVP}(t, T)$ and $\text{SVM}(t, T)$ have complexity $\Omega(n^2)$ and $O(n^2 \log n)$ and can be computed in $O(n^2 \log^3 n)$ randomized expected time.*

The Weak Visibility Map of a Triangle. For polyhedral terrains, the lower bound construction of Fig. 1(a) where the weak visibility map of an edge has $\Omega(n^4)$ vertices obviously yields the same lower bound for a triangle light source.

The upper bound of $O(n^5)$ on the complexity of the weak visibility map of an edge in a polyhedral terrain is also an upper bound for the triangle case. To verify this, suppose there is a point p in the weak visibility map of $\text{WVM}(t, T)$ for a given triangle t , and let q be a point on t that sees p . Then we can rotate the line-of-sight pq vertically upwards around p , until we obtain a free line-of-sight pq' , such that the point q' lies on one of the edges of t . Hence, $\text{WVM}(t, T) \subseteq \bigcup_{i=1..3} \text{WVM}(e_i, T)$. Trivially, it holds that $\text{WVM}(t, T) \supseteq \bigcup_{i=1..3} \text{WVM}(e_i, T)$. Because on every triangle of T , the complexity of $\bigcup_{i=1..3} \text{WVM}(e_i, T)$ is bounded from above by the complexity of the arrangement induced by three sets of $O(n^2)$ reguli, $\text{WVM}(t, T)$ is $\Theta(n^4)$ on a single triangle and $O(n^5)$ overall.

Theorem 14. *Let T be a polyhedral terrain with n triangles, and let t be a triangle of T . Then $\text{WVM}(t, T)$ has complexity $\Omega(n^4)$ and $O(n^5)$.*

In the remainder of this section, we show that $O(n^7)$, the complexity of the aspect graph restricted to a general 3D scene T , is a tight upper bound on the complexity of $\text{WVM}(t, T)$ for a triangle t ; we show this by extending the $\Omega(n^5)$ lower bound construction of Fig. 1(b). The basic idea of the extension is the following: first, we ‘replace’ A by a row giving $\Omega(n^2)$ gaps, which produces $\Omega(n^3)$ illuminated vertical planes, and thus we get $\Omega(n^6)$ illuminating vertical lines that each intersect $\Omega(n)$ triangles. In this way, we get a weak triangle visibility map with $\Omega(n^7)$ vertices. We describe this construction in more detail.

In order to construct a row with $\Omega(n^2)$ gaps that let the light that is emitted by t pass through without using more than $O(n)$ triangles, we first make the following observation. Each of the illuminated vertical planes of the lower bound of Fig. 1(b) is uniquely determined by two gaps: one in A and one in B . Besides the obvious restriction that the light source should be located on the opposite side of A than B , these illuminated planes do not depend on the location of the light source. Because we now have an extra degree of freedom, we have the opportunity to make $\Omega(n^2)$ gaps by building a grid G instead of the row A . This idea is illustrated in Fig. 2(a). The important fact here is that, if the holes in the grid degenerate to points, every hole has a unique x -coordinate.

If we allow enough distance between G and B , the holes in G basically act as point light sources, emitting cones of light. Now, just like in the old construction, each of the holes in G interacts with each of the gaps in B , producing $\Omega(n^3)$ illuminated vertical planes in total; see Fig. 2(b).

The total construction is illustrated schematically in Fig. 2(c). First, we have the illuminating triangle t , followed by the grid G , then the row of vertical slabs B , and finally the set C of vertically stacked triangles. To ensure that we indeed get $\Omega(n^6)$ illuminated vertical lines, we place a copy of G and B on the xy -plane such that they generate $\Omega(n^3)$ illuminated vertical planes from a different direction; the light source must be large enough to provide light for both constructions. This gives us another set of $\Omega(n^3)$ illuminated vertical planes,

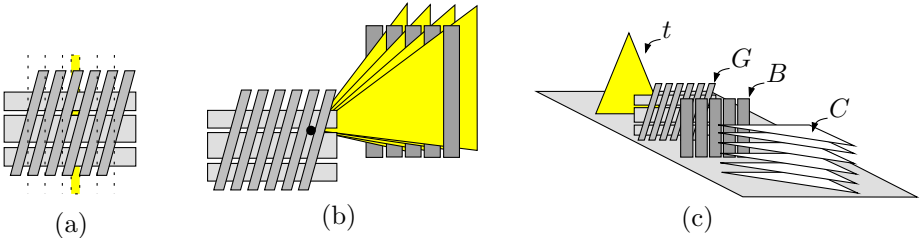


Fig. 2. a) A vertical grid with $\Omega(n^2)$ holes that allow light to pass through. (b) Every combination of a hole in the grid and a gap between two vertical slabs induces $\Omega(n)$ illuminated planes. (c) The total lower bound construction. The copy of G and B that induces another $\Omega(n^3)$ illuminated planes is not shown.

intersecting the $\Omega(n^3)$ planes that are produced by the first copy. Concluding, we have the following theorem.

Theorem 15. *Let T be a 3D scene with n triangles, and let t be a triangle of T . Then $\text{WVM}(t, T)$ has complexity $\Theta(n^7)$ in the worst case.*

We present an $O(n^7 \log n)$ time algorithm to compute $\text{WVM}(t, T)$. Take one triangle Δ from T and select and clip all triangles of T to the convex hull of t and Δ . This gives a set T' of triangles. Next, we compute the arrangement \mathcal{A} of all reguli $\mathcal{R}(e, f, g)$ on Δ , where (e, f, g) is an ordered triple of edges from triangles in $T' \cup t$. Choose a point p in some cell c in \mathcal{A} , and compute the arrangement \mathcal{E} of edges of T' projected onto the plane supporting t . Because \mathcal{A} corresponds directly to the aspect graph on Δ , the combinatorial structure of \mathcal{E} is the same for any point in c . It only changes when we move p in \mathcal{E} such that it crosses a regulus $\mathcal{R}(e, f, g)$ and enters a cell c' that is adjacent to c . The projected edges of e , f , and g must have had subedges that formed a triangle in \mathcal{E} , which collapses when p reaches $\mathcal{R}(e, f, g)$. When p enters c' , an inverted version of this triangle appears.

After computing \mathcal{E} for the point p in c , we compute for every cell in \mathcal{E} how many triangles of T' cover it, and store this information with the cell. We also maintain whether c lies inside or outside t ; recall that \mathcal{E} lies in the plane supporting t . Finally, we maintain a global count of the number of cells of \mathcal{E} that lie inside t and are not covered by any of the projected triangles. If for a cell c of \mathcal{A} the global count is zero, then c is completely in the shadow; c is illuminated if the global count is positive.

All of the above information can be updated when we go from cell c to a neighboring cell c' in $O(\log n)$ time, with the aid of a balanced binary search tree for each projected edge, which provides efficient access to \mathcal{E} . We have to make local changes to \mathcal{E} for the collapsing and appearing triangle, and we must determine the number of projected triangles that cover the new triangle in \mathcal{E} . This is the number of triangles that covered the collapsing triangle, plus or minus 1 or 3; this can be determined from the edges e , f , and g of T' . Since \mathcal{A} has $O(n^6)$ cells, the total update time if we traverse all cells of \mathcal{A} is $O(n^6 \log n)$. After we visited every cell of \mathcal{A} , we have computed the weak visibility map of t on Δ .

Theorem 16. *Let T be a 3D scene with n triangles, and let t be a triangle of T . The weak visibility map $\text{WVM}(t, T)$ can be computed in $O(n^7 \log n)$ time.*

6 Concluding Remarks

We presented lower and upper bounds on the combinatorial complexities of various types of visibility maps of edges and triangles in a 3D scene. As can be seen in Table 1, there are a few gaps left between lower and upper bounds. Finally, it would be interesting to look into output-sensitive algorithms to compute the different types of visibility maps.

References

1. McKenna, M.: Worst-case optimal hidden-surface removal. *ACM Trans. Graph.* **6** (1987) 19–28
2. O’Rourke, J.: 28. Visibility. In: *Handbook of disc. and comput. geom.* J.E. Goodman and J. O’Rourke, editors. CRC Press, Inc., Boca Raton, FL, USA (2004)
3. Wang, C., Zhu, B.: Three-dimensional weak visibility: Complexity and applications. *Theor. Comput. Sci.* **234** (2000) 219–232
4. Bern, M., Dobkin, D., Eppstein, D., Grossman, R.: Visibility with a moving point of view. In: *Proc. 1st ACM-SIAM Sympos. Discrete Algorithms.* (1990) 107–117
5. Plantinga, H., Dyer, C.R.: Visibility, occlusion, and the aspect graph. *Int. J. Comput. Vision* **5**(2) (1990) 137–160
6. Gigus, Z., Canny, J., Seidel, R.: Efficiently computing and representing aspect graphs of polyhedral objects. *IEEE Trans. Pattern Anal. Mach. Intell.* **13**(6) (1991) 542–551
7. Coll, N., Fort, M., Sellarès, J.: Approximate multi-visibility map computation. In: *Abstr. Europ. Workshop Comput. Geom.* (2005) 97–100
8. Koenderink, J.J., van Doorn, A.J.: The internal representation of solid shape with respect to vision. *Biological Cybernetics* **32** (1979) 211–216
9. de Berg, M., Halperin, D., Overmars, M., van Kreveld, M.: Sparse arrangements and the number of views of polyhedral scenes. *Internat. J. Comput. Geom. Appl.* **7** (1997) 175–195
10. Agarwal, P.K., Sharir, M.: On the number of views of polyhedral terrains. *Discrete Comput. Geom.* **12** (1994) 177–182
11. Edelsbrunner, H., Mücke, E.P.: Simulation of simplicity: A technique to cope with degenerate cases in geometric algorithms. *ACM Trans. Graph.* **9**(1) (1990) 66–104
12. Pottmann, H., Wallner, J.: *Computational Line Geometry.* Springer Verlag (2001)
13. Brönnimann, H., Everett, H., Lazard, S., Sottile, F., Whitesides, S.: Transversals to line segments in \mathbb{R}^3 . In: *Proc. 15th Canad. Conf. Comput. Geom.* (2003) 174–177
14. Heintz, J., Reico, T., Roy, M.F.: Algorithms in real algebraic geometry and applications to computational geometry. In J.E. Goodman, R. Pollack and W. Steiger, editors. *Discrete Comput. Geom.* (1991) 137–163
15. Aronov, B., Sharir, M.: Castles in the air revisited. *Discrete Comput. Geom.* **12** (1994) 119–150
16. Tagansky, B.: A new technique for analyzing substructures in arrangements of piecewise linear surfaces. *Discrete Comput. Geom.* **16** (1996) 455–479
17. Moet, E., Knauer, C., van Kreveld, M.: Visibility maps of segments and triangles in 3D. Technical Report UU-CS-2005-049, (Universiteit Utrecht)
18. de Berg, M., Dobrindt, K., Schwarzkopf, O.: On lazy randomized incremental construction. *Discrete Comput. Geom.* **14** (1995) 261–286
19. Suri, S., O’Rourke, J.: Worst-case optimal algorithms for constructing visibility polygons with holes. In: *Proc. 2nd Annu. ACM Sympos. Comput. Geom.* (1986) 14–23
20. Mulmuley, K.: *Computational Geometry: An Introduction Through Randomized Algorithms.* Prentice Hall, Englewood Cliffs, NJ (1993)

Non-euclidean Metrics and Chordal Space Structures

José Andrés Díaz Severiano, César Otero Gonzalez,
Reinaldo Togores Fernandez, and Cristina Manchado del Val

Geographical Engineering and Graphical Expression Techniques Dept.,
Civil Engineering Faculty, University of Cantabria, Spain
{diazja, oteroc, togoresr, manchadoc}@unican.es
<http://www.egicad.unican.es/>

Abstract. This paper proposes the use of the *stereographic projection* within the realm of Computational Geometry for the design of tree-dimensional space structures arising from planar power diagrams. In order that such structures (to which we apply the term *Chordal*) can approximate a broad catalogue of quadrics, it will be necessary to formulate this projection under *non-Euclidean metrics*.

1 Introduction

The correspondence that associates the *power diagrams* in E^d (d -dimensional spaces) with *convex polyhedra* in E^{d+1} is well known [2]; it is formulated taking into account that:

- a sphere's power function can be described as a hyperplane in a higher dimensional space; and that
- each hyperplane can be associated through polarity to a point, its pole.

Resorting to these simple considerations the edges of a power diagram can be made to correspond to the edges of a polyhedron: power diagrams in E^d are essentially the same as the boundaries of $(d+1)$ -polyhedra [1]. Although in the aforementioned reference the link among both spaces, E^d and E^{d+1} , are the paraboloids of revolution and the projection used is the cylindrical projection (see Fig. 1, left), it is confirmed [3] that it is possible to relate spheres, hyperplanes and points in space by means of other quadrics through central projections (Fig. 1, right and Fig. 2).

In order to extend this research line, we will start by describing the way in which the stereographic projection should be used to project a power diagram on a sphere (section 2.1) and the intimate connection of the resulting polyhedra with certain structural models (section 2.2). In section 2.3 we shall propose the algorithms for the design of those structures whose origin can be found in power diagrams, emphasizing in 2.4 the usefulness which the Möbius Transformations have proved to possess in the adequate disposition of generators in the plane. In section 3 we will expound an approximation to non-Euclidean geometries (this being the way chosen to demonstrate that the polyhedra obtained can also approximate other quadrics, besides the sphere). Finally, the conclusions of this paper will be exposed in section 4.

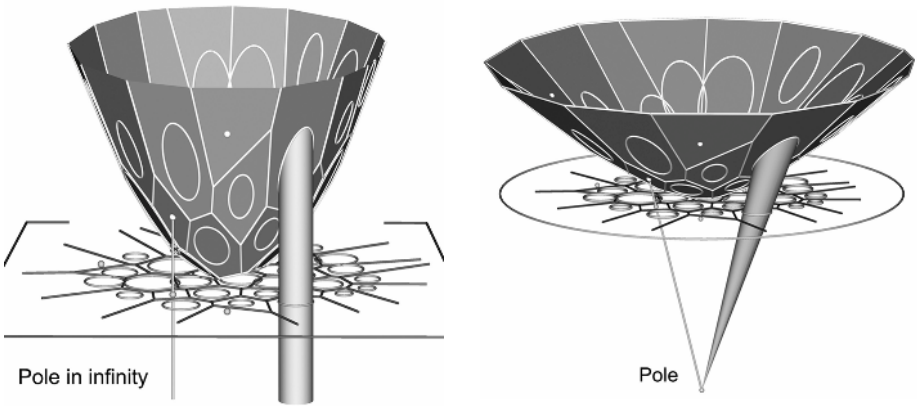


Fig. 1. Polyhedra that materialize the paraboloid of revolution and the hyperboloid of two sheets generated through cylindrical projection (*left*) and through central projection (*right*) of a power diagram

2 Structures Approximating the Sphere

2.1 Stereographic Projection of Power Diagrams

According to the considerations made in the introduction and the authority of the cited references, it is possible to enunciate that:

Proposition 1. The stereographic projection of every *power diagram* gives rise to a polyhedron whose faces are secant to the sphere (see Fig. 2), in such a way that:

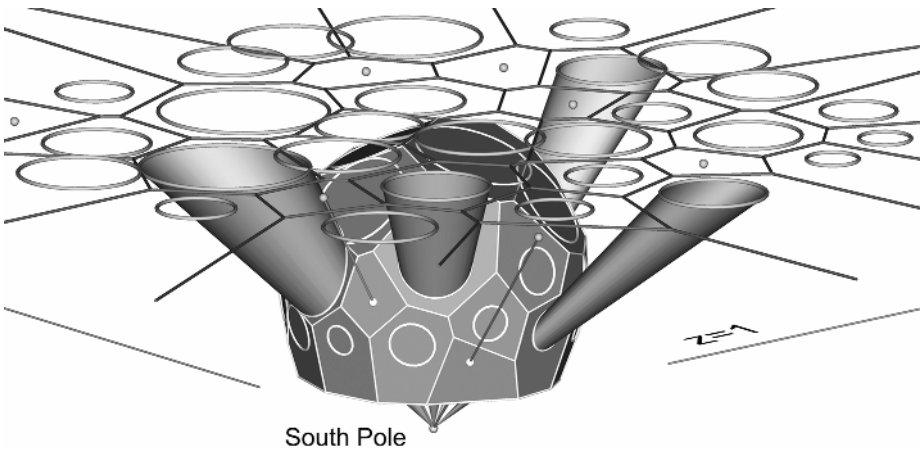


Fig. 2. Generation of a polyhedron that materializes the sphere through the stereographic projection of a power diagram

- the sections that generate each face of the polyhedron on the sphere correspond univocally with the circumferences in the diagram;
- the edges of the polyhedron turn out to be the projections of the radical axes that configure the planar subdivision of the plane (this fact was determinant in choosing the expression *Chordal Space Structures* to name the solutions arising from this proposal); and,
- the polyhedron's vertices coincide with the projections of the vertices of the power diagram (points where three or more radical axes coincide).

Let us consider such a polyhedron as a structure that *approximates* (in the sense of *materialization*) the sphere.

2.2 Interesting Models. Structural Correspondence

It is possible to materialize different geometric models (see Fig. 3, left) and identify them with a similar number of structural models (see Fig. 3, right) when an adequate selection of generators in the plane is made (see Table 1).

Table 1. Structural models and a description of the planar tessellations from which they arise

Structural Model	Size of the Generator	Layout of the Generator	Tessellation of the Plane	Geometric Model ¹
Geotangent Structure	Variable radius	Central symmetry and radial distribution ²	Power Diagram	Midscribed polyhedron
Panel Structure	Radius = 0	Variable	Voronoi Diagram	Circumscribed polyhedron
Lattice Structure	Radius = 0	Variable	Delaunay Triangulation	Inscribed Polyhedron

¹ General appearance of the structure in relation with the sphere it approximates.

² It is a packing of tangent circumferences.

If we consider the Voronoi diagrams as degenerated power diagrams and remember that the Delaunay triangulations are derived from the former by duality, it is possible to find a common origin for all these structures.

Proposition 2. For the purpose of characterizing all of the structures arising from Power Diagrams, we have proposed naming them [4] as *Chordal Space Structures*.

2.3 Algorithms for the Design of Chordal Space Structures

Algorithm 1. Design of a Geotangent Structure or a Panel Structure.

Data: a finite set S of circumferences s in E^2 .

1. Obtain the power diagram, PD , associated to S (see Fig. 4, left).
2. For each cell, $cell(s_i)$, of PD :
 - 2.1. Determine three points P_j of the circumference s_i .
 - 2.2. Obtain the stereographic projection (inversion) of points P_j on the sphere: P_j' .

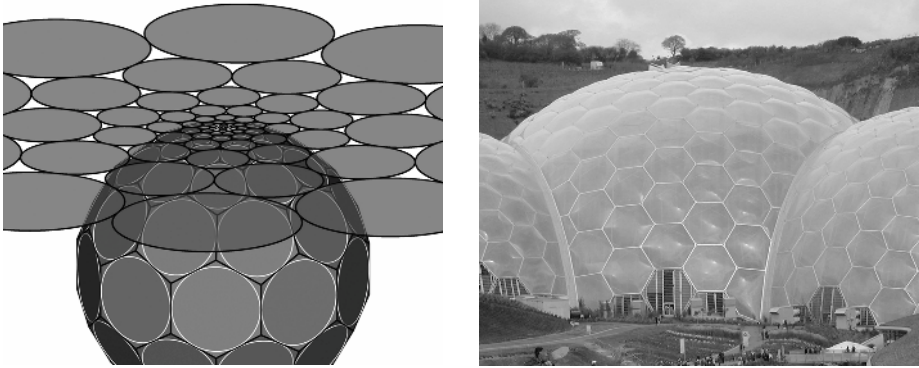


Fig. 3. *Left:* Geotangent structure; the sections that originate each face are tangent to all of its neighbors. *Right:* structures suggesting the panel typology. Eden Project, Cornwall, UK [5]. Other examples of the structures in Table 1, and the geometric models that sustain them in [4].

- 2.3. Define the equation of the plane α secant to the sphere that contains the points P_j' .
- 2.4. Materialize the face, *face* (s_i), of the approximating polyhedron: vertices V'_k of the face turn out to be the projection of the cell's vertices, *cell* (s_i), from the south pole of the sphere, at the point in which the projecting rays are sectioned by the plane α .

In the case any of the circumferences s has zero radius (*point-circle* P, [6]), the equation of the plane secant to the sphere will be substituted in step 2.3 by that of the plane that is tangent to the sphere in its inverse point P' .

Algorithm 2. Design of a Lattice Structure.

Data: a finite set S of generators s (zero radius circumferences) in E^2 .

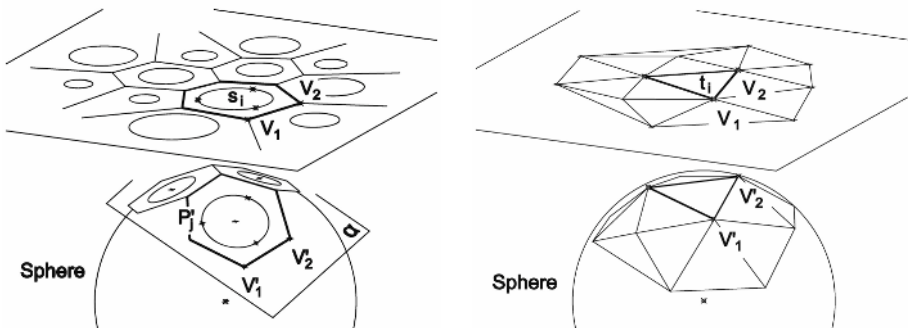


Fig. 4. Projection of the power diagram's cells (*left*) and the Delaunay's triangulation (*right*) on the approximated sphere

1. Obtain the Delaunay triangulation, DT , associated to S (see Fig.4, right).
2. For each of the triangles t_i in DT :
 - 2.1. Obtain the stereographic projection of vertices V_j of t_i on the sphere: V'_j .
 - 2.2. Join vertices V'_j and materialize the face of the polyhedron inscribed in the sphere.

2.4 Möbius Transformations and Layout of the Generators

Albeit the design procedure proposed in the preceding section guarantees obtaining panel structures and lattice structures from any cloud of generators contained in the reference plane, it seems opportune to propose a layout leading to a polyhedron that approximates the sphere with faces as similar as possible. It has been documented in [3] the way to attain this goal based on the extension of a *fundamental grid* to a plane in which:

- Euclidean metrics is substituted by elliptic metrics; and, in which
- the Möbius transformations are used.

3 Structures Approximating Other Quadrics

3.1 Preliminary Considerations: The Homologic Transformation

It is possible to generalize Proposition 1 and allow that the structures hereby defined materialize, not only the surface of a sphere, but even that of other quadrics. A first way for obtaining this has been presented in references [3] and [4]: it consists in applying a homologic transformation [7] to the polyhedron that approximates the sphere. However, after using the homologic transformation, the faces of the polyhedron are greatly distorted (Fig. 5). Thus, when the aim is to approximate a non-spherical quadric, it is necessary to find a way to compensate in length and area the polygons that delimit the structure.

We shall proceed to explore a second way for generalization that implies the use of non-Euclidean metrics, as intuitively this seems the way that can lead to a more

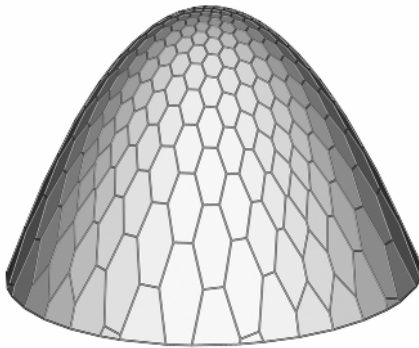


Fig. 5. Distortion of the faces' size after applying the homologic transformation



Fig. 6. Circular Limit III, xylography. M. C. Escher, 1959.

adequate layout of the generators in the plane (this supposition can be illustrated by any of Escher’s representations defined in hyperbolic geometry – see Fig. 6).

3.2 Spaces and Metrics

The same way we define the distance between two points $M_1(x_1, y_1, z_1)$ and $M_2(x_2, y_2, z_2)$, and the angle between two vectors OM_1 and OM_2 in the ordinary Euclidean space, it is also possible to formulate both magnitudes this other way:

$$d^2 = (x_2 - x_1)^2 + (y_2 - y_1)^2 - (z_2 - z_1)^2 \tag{1}$$

and

$$\cos \varphi = \frac{x_1 x_2 + y_1 y_2 - z_1 z_2}{\sqrt{x_1^2 + y_1^2 - z_1^2} \cdot \sqrt{x_2^2 + y_2^2 - z_2^2}} \tag{2}$$

The resulting space receives the name of *pseudo-Euclidean space* or *Minkowskian space* [8]. Unlike the common Euclidean space, pseudo-Euclidean space comprises segments of real length, zero length and purely imaginary length; likewise it includes spheres of three kinds: of real radius, of purely imaginary radius and of zero radius. The equations for these three spheres, when their centers coincide with the origin of coordinates, are shown in Fig. 7.

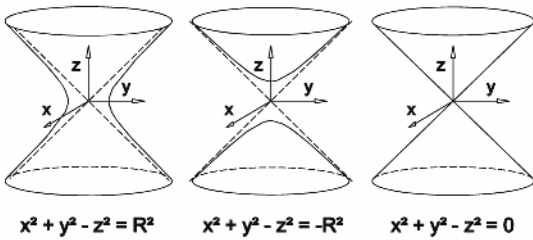


Fig. 7. Spheres in pseudo-Euclidean space: with real radius, with imaginary radius and with zero radius

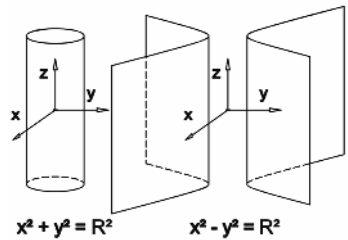


Fig. 8. Spheres in semi-Euclidean and semi-Minkowskian spaces

For this reason the real radius spheres in pseudo-Euclidean space have the appearance of *one sheet hyperboloids*, those with purely imaginary radius are represented as *hyperboloids of two sheets* and those with zero radius take the form of *cones of revolution*.

In addition to Euclidean and Minkowskian space [8], we are going to consider *semi-Euclidean space*, a three-dimensional space in which the distance d between two points $M_1(x_1, y_1, z_1)$ and $M_2(x_2, y_2, z_2)$ is given by:

$$d^2 = (x_2 - x_1)^2 + (y_2 - y_1)^2, \tag{3}$$

and *semi-Minkowskian space*, a three-dimensional space with metric:

$$d^2 = (x_2 - x_1)^2 - (y_2 - y_1)^2. \tag{4}$$

In these spaces *circular* and *hyperbolic cylinders* stand for *spheres* centered on the origin of coordinates (see Fig. 8).

3.3 Stereographic Projection in Non-euclidean Spaces

All those previously characterized spaces allow us to define the stereographic projection of the sphere associated to them. It concerns a projection that is always *conformal* (preserves angles) and *circular* (transforms circles in the plane into circles on the sphere, these understood in a broad sense as sections cut in the sphere by planes).

Continuing the line of work initiated in previous papers, Table 2 shows the relation between the coordinates of points in a plane with those of their homologous points on the sphere, when the former are stereographically projected.

Table 2. Relationship between the coordinates of points $P_i(x,y,1)$ of plane $z=1$ and its homologous $P'_i(X,Y,Z)$ on the sphere of radius 0.5 centered on point $(0,0,0.5)$. Projection pole: the coordinate system's origin (south pole of the sphere).

Euclidean Space ¹	
Sphere	$X^2 + Y^2 + (Z - 0.5)^2 = (1/2)^2 = 0.25$
Point on the sphere	$X = \frac{x}{1 + (x^2 + y^2)}$ $Y = \frac{y}{1 + (x^2 + y^2)}$ $Z = \frac{1}{1 + (x^2 + y^2)}$
Minkowskian Space ²	
Sphere	$X^2 + Y^2 - (Z - 0.5)^2 = (i/2)^2 = -0.25$
Point on the sphere	$X = \frac{x}{1 - (x^2 + y^2)}$ $Y = \frac{y}{1 - (x^2 + y^2)}$ $Z = \frac{1}{1 - (x^2 + y^2)}$
Minkowskian Space	
Sphere	$X^2 + Y^2 - (Z - 0.5)^2 = (1/2)^2 = 0.25$
Point on the sphere	$X = \frac{x}{1 + (x^2 - y^2)}$ $Y = \frac{y}{1 + (x^2 - y^2)}$ $Z = \frac{1}{1 + (x^2 - y^2)}$

¹ Making $y=0$ the expressions corresponding to the semi-Euclidean space are obtained.

² Making $y=0$ the expressions corresponding to the semi-Minkowskian space are obtained.

3.4 Domains of Definition

The stereographic projection of the previously presented spheres gives rise to the planar models proposed by Poincaré for the study of the Cayley-Klein geometries. Such models extend to the plane on which they are projected (in our case, the $z=1$ plane) in its totality. However, it is useful to consider those regions of the plane (circles of unit radius centered on the Oz axis) on which the upper semi-spheres are projected. The appearance of those *circles* or more properly speaking *cycles*, according to the spaces, is shown in Fig. 9.

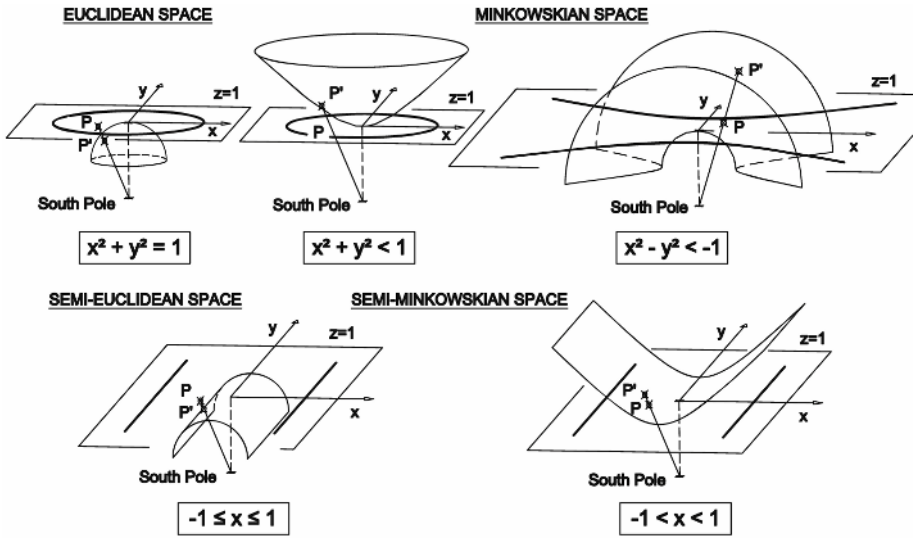


Fig. 9. Domains of definition for the planar models of the Cayley-Klein geometries generated by stereographic projection (their inner region is annotated)

Interest on the definition of these domains is double:

- it is within them that the power diagrams that will serve as starting point for a Chordal Structure design process will be defined (once generated half of the structure, it will be sufficient to apply the adequate symmetry to reconstruct the other half); and,
- the limits of these regions are, for some of these spaces, the points according to which the three-dimensional models' points in infinity are projected. Thus happens in the case of Minkowskian (for values equal to: $x^2+y^2=1$ and to: $x^2-y^2=-1$, according to the spheres) and semi-Minkowskian (for values equal to: $x=\pm 1$) spaces. This fact must be taken into account when programming the procedure.

3.5 Implementation of the Design Procedure

Arising from the definition given for non-Euclidean metrics, it is confirmed that the algorithms described in section 2.3 make the immediate generation of a complete catalogue of quadrics possible (Fig. 10). To achieve this it is only necessary to:

- use as the coordinates for the inverse points P'_i those shown in Table 2; and to
- deploy the generators within the domains of definition established in 3.4.

However, it is necessary to clarify an additional question: the one derived from the appearance adopted by the circles (stereographic projections of the planar sections of the different quadrics) on the planes that support the different geometries:

- They are *circles* in an Euclidean sense for the sphere and the hyperboloid of two sheets (their treatment does not present any difficulties) (Fig. 10, left).

- They are *parabolas* [8] for circular and hyperbolic cylinders, which may degenerate into pairs of parallel straight lines in the case in which the plane that sections the quadric is parallel to the cylinder's axis. Under this premise the triangulation and the discretization of the surface in bands is possible when the design process is initiated from degenerate Voronoi or power diagrams.
- They are *hyperbolas* for the single sheet hyperboloid. About the appearance that the power diagrams adopt in this case we cannot make any conclusive assertion (this remaining as a future line of research). However, triangulation does not pose any problems (see Fig. 10, right).

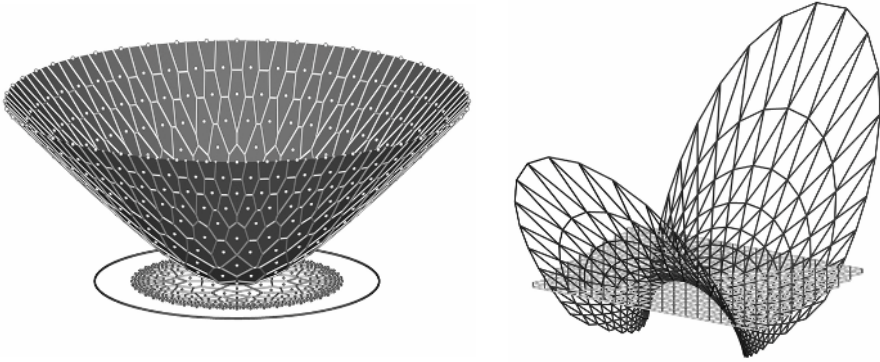


Fig. 10. Panel structure (*left*) and lattice structure (*right*) generated by the stereographic projection of a Voronoi diagram and a Delaunay triangulation, respectively

4 Conclusion

The intimate connection linking convex polyhedra with power diagrams through stereographic projection has been exploited in this paper to expound a unitary design procedure for *Chordal Space Structures*. Formulating this projection from the point of view of non-Euclidean metrics consolidates the line of research initiated in previous papers, since, at the same time:

- it simplifies the design tasks, making it possible to disregard the homologic transformation during the process of generating quadrics;
- it widens the catalogue of structures, as it makes it possible to approximate the one sheet hyperboloid and the circular and hyperbolic cylinders; and,
- it entices the search for new generator layouts that prove to be more auspicious for the attainment of surfaces with more uniform face sizes (laws of formation are already known that verify it for some of the quadrics – see Fig. 10, left).

Finally, may the illustrations in Fig. 11 serve as an example of the fact that our interest goes beyond the mere theoretical speculation, seeking with the use of these Computational Geometry resources a renewal of the design guidelines currently in force within the realm of Civil Engineering.

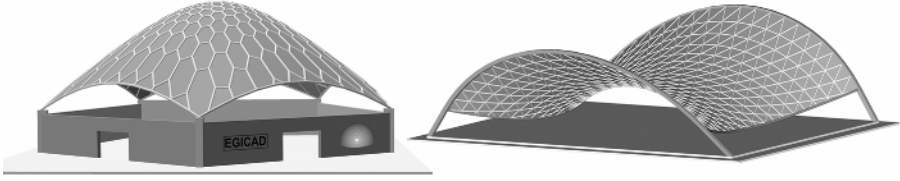


Fig. 11. Portions of quadrics used as space enclosures

References

1. Aurenhammer, F.: Power diagrams: properties, algorithms and applications. *SIAM Journal on Computing* archive, Vol. 16, N° 1. Publisher Society for Industrial and Applied Mathematics, Philadelphia (1987) 78–96
2. Aurenhammer, F.: Voronoi Diagrams – a survey of a fundamental geometric data structure. *ACM Computing Surveys*, Vol. 23, N° 3. ACM Press, New York (1991) 345–405
3. Díaz, J. A., Otero, C., Togoress, R. and Machado, C.: Power diagrams in the design of Chordal Space Structures. *The 2nd International Symposium on Voronoi Diagrams in Science and Engineering*. Seoul, Korea (2005) 93–104
4. Díaz, J. A., Togoress, R., and Otero, C.: *Chordal Space Structures: Computational Geometry Getting into Building and Civil Engineering*. Lecture Notes in Computer Science, Vol. 3045. Springer-Verlag, Berlin Heidelberg (2004) 158–167
5. <http://www.ivanweb.net/images/Mondo/Inghilterra/Cornowall/Eden/EdenProject01.jpg>
6. Pedoe, D.: *Geometry. A Comprehensive Course*. Dover Publications, New York (1988) 139
7. Preparata, F. P., and Shamos, M. I.: *Computational Geometry: An Introduction*. Springer-Verlag, New York (1985) 246–248
8. Yaglom, I. M.: *A simple non-Euclidean geometry and its physical basis. An elementary account of Galilean geometry and the Galilean principle of relativity*. Springer-Verlag, New York (1979)

Algorithms for Rectangular Covering Problems

Stefan Porschen

Institut für Informatik, Universität zu Köln, D-50969 Köln, Germany
porschen@informatik.uni-koeln.de

Abstract. Many applications like picture processing, data compression or pattern recognition require a covering of a set of points most often located in the (discrete) plane by rectangles due to some cost constraints. In this paper we provide exact dynamic programming algorithms for covering point sets by regular rectangles, that have to obey certain boundary conditions. The objective function is to minimize sum of area, circumference and number of patches used. This objective function may be motivated by requirements of numerically solving PDE's by discretization over (adaptive multi-)grids.

Keywords: rectangular covering problem, dynamic programming, integer grid, closure operator.

1 Introduction

We investigate a class of problems concerning covering grid points in the Euclidean plane by regular rectangles such that the overall area, the total circumference and the number of the rectangles used is minimized. Rectangular covering problems may arise for example in numerical analysis for solving partial differential equations by iterative multigrid methods [1, 8]. For that purpose the equations are discretized and computed on grids. According to the values of error estimation functions it has to be decided iteratively whether the lattice has to be refined in certain regions meaning to modify the lattice spacing accordingly. Refinement steps may require a covering of indicated regions by e.g. regular, i.e., axis parallel rectangles optimized subjected to some reasonable constraints. Such computations can efficiently be performed only by parallel machines, where the communication amount of cooperating processors assigned to different lattice regions should be minimized. The specific choice of objective function as stated above aims at taking into account requirements of such parallel environments. Other applications for rectangular covering problems may be picture processing [9, 10] and data compression.

However, in this paper we stress a more abstract computational point of view. We provide deterministic exact dynamic programming algorithm for solving rectangular covering problems, where the rectangles have to satisfy some conditions w.r.t. side length and boundary. There are numerous variants of related covering problems most of them concerning points distributed in the Euclidean plane [3, 5, 6]. On the other hand, there are also certain partition problems [2, 4], which could be related to partition variants of the problem at hand.

To fix the notation, let \mathbb{R}^2 be the Euclidean plane. For $z \in \mathbb{E}^2$ its coordinate values are $x(z), y(z)$. Let $L_\lambda = \mathbb{Z}e_x\lambda + \mathbb{Z}e_y\lambda$ be an axis-parallel integer grid embedded in \mathbb{R}^2 with lattice constant $\lambda \in \mathbb{R}_+$. (It may be convenient to set $\lambda = 1$ but in view of applications as mentioned above a lattice spacing parameter may be useful.) By translational invariance, w.l.o.g. it is sufficient to consider a bounded region of the first quadrant: $B := [0, N_x\lambda] \times [0, N_y\lambda] \subset \mathbb{E}^2$, for $N_x, N_y \in \mathbb{N}$. For $n \in \mathbb{N}$, we write $[n] := \{1, \dots, n\}$.

2 The Problem and Basic Concepts

Assume that a set $M = \{z_1, \dots, z_n\} \subseteq I_\lambda := B \cap L_\lambda$ for $n \in \mathbb{N}$ ($1 \leq n \leq N_x N_y$) of points is fixed where each $z_i \in M$ is represented by its coordinates: $z_i = (x_i, y_i)\lambda \in I_\lambda$. The task is to construct a covering of M by *regular*, i.e., axis parallel rectangles such that the sum of areas, circumferences as well as the number of rectangles used is minimized. (Rectangles $r \subset \mathbb{E}^2$ are considered as closed sets in the norm topology. This specifically means that points of M lying on the boundary of a rectangle r are also contained in r and thus are covered by r .) We impose a further constraint on a covering of M to be feasible: Each of its rectangles must have sides of length at least $k \in \mathbb{R}_+$ which is a given parameter with $0 < k < N\lambda$ ($N := \min\{N_x, N_y\}$). For rectangle r , let $\ell_x(r)$ resp. $\ell_y(r)$ denote the length of its x -parallel resp. y -parallel sides, let $a(r), u(r)$ be its area resp. circumference. Let ∂r denote the boundary of r consisting of its four sides $\partial_i r, i \in \{1, \dots, 4\}$. A rectangle $r \subset B$ is uniquely determined by its upper right $z_u := (x_u, y_u)$ and lower left $z_d := (x_d, y_d)$ diagonal points such that $r = [x_d, x_u] \times [y_d, y_u], \ell_x(r) = x_u - x_d, \ell_y(r) = y_u - y_d$. For a k -admissible rectangle r by definition holds $\ell_j(r) \geq k$ ($j \in \{x, y\}$). For some applications it may be required not to allow lattice points on the boundary of rectangles. This could be encountered by posing a minimal distance condition for points covered by a rectangle: Given $\varepsilon \geq 0$ then a rectangle r covering a set S of points is called ε -admissible if each point $z \in S \cap r$ has minimal euclidean distance ε to each part of the boundary ∂r of r . For $\varepsilon = 0$ there are no boundary restrictions for covered points. Let \mathcal{R} denote the set of all regular rectangles $r \subset B$ which can be placed in B each represented by its upper right and lower left diagonal points $(z_d(r), z_u(r)) \in B^2$. Given a set $M \subset I_\lambda$ of lattice points, by a (k, ε) -admissible rectangular covering of M we mean a set $R \subset \mathcal{R}$ of regular rectangles which are (k, ε) -admissible such that $M \subset \bigcup_{r \in R} r \cap I_\lambda$ and $\forall r \in R : r \cap M \neq \emptyset$. The totality of all (k, ε) -admissible rectangular coverings of M is denoted as $\mathcal{C}_{(k, \varepsilon)}(M) := \mathcal{C}(M) \subseteq 2^{\mathcal{R}}$, where the indices (k, ε) are omitted since these values are fixed in a given problem instance. For fixed $c \geq 1$ the objective function $w := w_c$ is defined by $w : \mathcal{R} \ni r \mapsto w(r) := a(r) + u(r) + c \in \mathbb{R}_+$. Extending to sets $R \subseteq \mathcal{R}$ we have $w(R) := a(R) + u(R) + c|R|$ where $a(R) := \sum_{r \in R} a(r), u(R) := \sum_{r \in R} u(r)$. Obviously, w satisfies the monotonicity property: $r_1 \subseteq r_2 \Rightarrow w(r_1) \leq w(r_2)$.

Definition 1. k -RECTANGULAR COVER (k -RC) is the following optimization problem: Given $N_x, N_y, k, c, \lambda, \varepsilon \geq 0$ such that $\varepsilon \ll \lambda/2, 0 < k < N :=$

$\min\{N_x, N_y\}\lambda$ and a finite set $M \subset I_\lambda$. Find a (k, ε) -admissible covering R_0 of M with $\text{opt}(k, M) := \min\{w(R) : R \in \mathcal{C}(M)\} = w(R_0)$. Such a covering R_0 is called optimal covering.

For fixed lattice spacing λ input instances consist of the point set and the boundary parameters k, ε for rectangles. According to the relation of the value of k to λ several problem classes arise as discussed now. For arbitrarily fixed k ($0 < k < N\lambda$, $N := \min(N_x, N_y)$) there is a largest $\nu(k) \in \mathbb{N}_0 : k = \nu(k)\lambda + \alpha(k)$, $0 \leq \alpha(k) < \lambda$, hence, $\nu(k) = \lfloor \frac{k}{\lambda} \rfloor$, $\alpha(k) = k - \nu(k)\lambda$. Thus, we have the following classes partitioning the given interval: $\nu(k) = 0 \Leftrightarrow 0 < k < \lambda$ is the first class and $\nu(k) = j \Leftrightarrow j\lambda \leq k < (j+1)\lambda$ corresponds to class $j+1$ for $j \in \{1, \dots, N-1\}$.

We now address the task to determine the smallest (k, ε) -admissible rectangle containing a given subset $S \subset M$ of the input set $M \subset I_\lambda$. To that end, consider the map

$$\rho : 2^M \setminus \{\emptyset\} \ni S \mapsto \rho(S) := (z_d(S), z_u(S)) \in I_\lambda^2$$

with $z_d(S) := (x_d(S), y_d(S))$ and $z_u(S) := (x_u(S), y_u(S))$ where $x_d(S) := \min_{z \in S} x(z)$, $y_d(S) := \min_{z \in S} y(z)$ and $x_u(S) := \max_{z \in S} x(z)$, $y_u(S) := \max_{z \in S} y(z)$ are the extremal coordinates of points in S . Hence, $\rho(S)$ in general contains no points of S or even M , but in any case lattice points. By the uniqueness of these values follows immediately that ρ is well defined. The unique ‘rectangle’ $r(S) := [x_d(S), x_u(S)] \times [y_d(S), y_u(S)]$ (which may be degenerated to a single point or a line segment) having $z_d(S), z_u(S)$ as its lower left and upper right diagonal points is called *rectangular base of S* . We may identify $r(S)$ and $\rho(S)$ which are related as stated above.

Lemma 1. $r(S)$ is w.r.t. to inclusion and also w.r.t. the objective function w the smallest rectangle containing $S \subseteq M$, $S \neq \emptyset$. \square

Of course, for arbitrary k, ε in general $r(S)$ is not (k, ε) -admissible. Thus we need a procedure transforming $r(S)$ into a (w.r.t. w smallest) (k, ε) -admissible rectangle containing $r(S)$. For convenience, we define $\bar{x} := y$ and $\bar{y} := x$, and use a data structure **point** storing the components $x(z), y(z)$ of each $z \in M$. M is assumed to be represented as a one-dimensional **array** of length $n = |M|$ containing objects of type **point**. Furthermore, suppose that M_j ($j \in \{x, y\}$) is an array in which the elements of M are sorted by *lexicographic j -order* \leq_j , that is $\forall z_1, z_2 \in M : z_1 \leq_j z_2 \Leftrightarrow : j(z_1) \leq j(z_2)$ and if $j(z_1) = j(z_2)$ then $\bar{j}(z_1) \leq \bar{j}(z_2)$, $j = x, y$. Hence, M_j is sorted by increasing j -coordinate values of the points. By construction of $r(S)$ holds $\ell_x(r(S)), \ell_y(r(S)) \in \mathbb{N}_0$ and $S \cap \partial_i r(S) \neq \emptyset, \forall i = 1, \dots, 4$. We can consider the x, y -parallel sides of r independently, so for each of them two cases have to be distinguished: a) $\ell_j(r(S)) \geq k, j \in \{x, y\}$, then we only have to enlarge each side of $r(S)$ at both ends by ε simultaneously, obviously resulting in a unique smallest (k, ε) -admissible rectangle containing S . b) There is $j \in \{x, y\} : \ell_j(r(S)) < k$. If $\gamma_j/\lambda := [\nu(k) - \ell_j(r(S))]/\lambda \in \mathbb{N}_0$, is odd then by extending $\ell_j(r(S))$ at both ends symmetrically by value $[\gamma_j + \alpha_j(k)]/2$ we simultaneously satisfy both the k - and ε -conditions, because by definition $\varepsilon < \lambda/2$. If γ_j/λ is even, we have to analyse the following subcases: (i): $\alpha(k)/2 \geq \varepsilon$, then symmetrically extending

$\ell_j(r(S))$ at both ends about $[k - \ell_j(r(S))]/2$, we also satisfy the ε -condition; the rectangle achieved in this way may contain a larger set $M \supset S' \supset S$. (ii): $\alpha(k)/2 < \varepsilon$. In case we can find a value j in the interval $I_j^- := [j_d(S) - \gamma_j, j_d(S)]$ such that there is no intersection with M on the corresponding grid line parallel \bar{j} , then choosing this as the new boundary part we satisfy the ε -condition at that side. Similarly, we proceed for the interval $I_j^+ := [j_u(S), j_u(S) + \gamma_j]$. These tests can be executed in linear time as follows: Compute all j -values corresponding to points in M falling in the range I_j^- and store them in array S_j^- . Do the same for I_j^+ storing the values in S_j^+ . For each $j \in S_j^-$, compute its *counterpart* $j + \gamma_j \in I_j^+$; storing them by increasing values in C_j^+ . Then merge arrays S_j^+, C_j^+ resulting into array B_j^+ and finally check if there is a gap inside, i.e., whether there is any value in I_j^+ not contained in B_j^+ , in which case obviously we can choose two new boundary parts parallel \bar{j} , s.t. at both the ε -conditions are fulfilled automatically. Realize that all these computations including the merge step can be done in $O(|S|)$ time because both arrays are sorted by increasing values. If there is no such choice we have to check if there can be chosen at least one boundary part not intersecting M . This can be done by first checking, whether there is any $j \in S_j^-$ having no counterpart in S_j^+ , and if the search yields no success then perform an analogous check for S_j^+ . This simply can be done by two assistant arrays R_j^-, R_j^+ of length $|I_j^-|, |I_j^+|$ having coordinate values as indices. More formally:

Algorithm (OPT1)

Input: rectangular base $r(S) := [x_d(S), x_u(S)] \times [y_d(S), y_u(S)]$, $S \subset M$

Output: w.r.t. w smallest (k, ε) -admissible rectangle

begin

$r_\delta(S)$ containing $r(S)$

for $j = x, y$ **do**

$\delta_j^d \leftarrow \delta_j^u \leftarrow 0, \gamma_j \leftarrow \nu(k) - \ell_j(S)$

if $\ell_j(r(S)) \geq k$ **then** $\delta_j^d \leftarrow \delta_j^u \leftarrow \varepsilon$

else if $\ell_j(r(S)) < k \wedge \alpha(k)/2 \geq \varepsilon$ **then** $\delta_j^d \leftarrow \delta_j^u \leftarrow [k - \ell_j(r(S))]/2$

else $(*\ell_j(r(S)) < k \wedge \alpha(k)/2 < \varepsilon*)$

if $\gamma_j/\lambda \bmod 2 = 1$ **then** $\delta_j^d \leftarrow \delta_j^u \leftarrow [\gamma_j + \alpha_j(k)]/2$

else $(*\gamma_j/2$ is even: compute arrays S_j^-, R_j^-, C_j^+*):

for all $z_i \in M_j : j_d(S) - \gamma_j \leq j(z_i) \leq j_d(S)$ **do**

if $\bar{j}_d(S) \leq \bar{j}(z_i) \leq \bar{j}_u(S)$ **then**

$S_j^-[i] \leftarrow j(z_i), R_j^-[j(z_i)] \leftarrow j(z_i), C_j^+[i] \leftarrow j(z_i) + \gamma_j$

od $(*$ compute arrays S_j^+, R_j^+*):

for all $z_i \in M_j : j_u(S) \leq j(z_i) \leq j_u(S) + \gamma_j$ **do**

if $\bar{j}_d(S) \leq \bar{j}(z_i) \leq \bar{j}_u(S)$ **then** $S_j^+[i] \leftarrow j(z_i), R_j^+[j(z_i)] \leftarrow j(z_i)$

end do

$(*$ merge S_j^+, C_j^+ into B_j^+*)

for all $j_i \in B_j^+$ **do** $(*$ check if there are two sides not intersecting $M*$)

if $j_{i-1} \notin B_j^+$ **then**

$\delta_j^d \leftarrow j_d(S) - j_{i-1} - \gamma_j + \alpha(k)/2, \delta_j^u \leftarrow j_{i-1} + \alpha(k)/2 - j_u(S)$


```

    break
  if  $j_{i+1} \notin B_j^+$  then
     $\delta_j^d \leftarrow j_d(S) - j_{i+1} - \gamma_j + \alpha(k)/2, \delta_j^u \leftarrow j_{i+1} + \alpha(k)/2 - j_u(S)$ 
    break
  end do
  if  $\delta_j^d = \delta_j^u = 0$  then (* check if there is one side not
    intersecting  $M^*$ )
    for all  $j \in S_j^-$  do (* check for  $S_j^-*$ *)
      if  $R_j^+[j + \gamma_j] = \text{nil}$  then
         $\delta_j^d \leftarrow x_d(S) - j + \max\{\varepsilon, \alpha(k)\}, \delta_j^u \leftarrow j + \gamma_j - x_u(S)$ 
        break
      end do
      if  $\delta_j^d = \delta_j^u = 0$  then
        for all  $j \in S_j^+$  do (* check for  $S_j^+*$ *)
          if  $R_j^-[j - \gamma_j] = \text{nil}$  then
             $\delta_j^d \leftarrow x_d(S) - j + \gamma_j, \delta_j^u \leftarrow j + \max\{\varepsilon, \alpha(k)\} - x_u(S)$ 
            break
          end do
          if  $\delta_j^d = \delta_j^u = 0$  then (* both sides intersect  $M^*$ )
             $\delta_j^d \leftarrow \delta_j^u \leftarrow \gamma_j/2 + \max\{\varepsilon, \alpha(k)/2\}$ 
          end do
        end do
      end do
    end do
  if  $\delta_j^d = \delta_j^u = 0$  then (* both sides intersect  $M^*$ )
     $\delta_j^d \leftarrow \delta_j^u \leftarrow \gamma_j/2 + \max\{\varepsilon, \alpha(k)/2\}$ 
  end do
 $r_\delta(S) \leftarrow [x_d(S) - \delta_x^d, x_u(S) + \delta_x^u] \times [y_d(S) - \delta_y^d, y_u(S) + \delta_y^u]$ 
end

```

Lemma 2. *Let (M, k) be an instance of k -RC. For each $S \in 2^M \setminus \{\emptyset\}$, let $r(S)$ be the rectangular base corresponding to $\rho(S)$ as defined in Lemma 1. Then Algorithm OPT1 correctly computes $r_\delta(S) \in \mathcal{R}(k, M)$ which, w.r.t. w , is a smallest (k, ε) -admissible rectangle containing S , i.e., $\text{opt}_1(k, S) := \min\{w(r); r \supseteq S, r \in \mathcal{R}(k, M)\} = w(r_\delta(S))$. In general, $r_\delta(S)$ is not unique. Algorithm OPT1 runs in $O(|S|)$ time. \square*

3 A Dynamic Programming Approach

A first reasonable time bound for k -RC can be achieved using dynamic programming on a pure set theoretical base. The idea is to construct under the constraints minimal rectangular coverings systematically for all subsets of a subset of M and for all reasonable cardinalities $|R| \in \{1, 2, \dots, n\}$ of coverings. For a fixed subset $\emptyset \neq S \subseteq M, |M| := n \in \mathbb{N}$, let $\text{opt}_j(k, S) := \min\{w(R); R \in \mathcal{C}(S), |R| = j\}$. Suppose there is a way for computing $\text{opt}_j(k, M), 2 \leq j \leq n$. Then $\text{opt}(k, M) = \min_{j \in [n]} \text{opt}_j(k, M)$ is the optimal value for k -RC with regard to the objective function.

Now suppose, for each subset $S \in 2^M \setminus \{\emptyset\}$, we have computed $\text{opt}_1(k, S) = w(r_\delta(S))$ as well as $\text{opt}_j(k, S), 2 \leq j \leq i - 1$. As induction step on that basis, for each fixed $\emptyset \neq S \in 2^M$, holds $\text{opt}_j(k, S) = \min\{w(r_\delta(T)) + \text{opt}_{j-1}(T'); \emptyset \neq T \in 2^S\}, \forall \emptyset \neq S \in 2^M, T' := S \setminus T$ forming the Bellman optimality equations

in our context. Of course, we touched too many subsets, needed are only those, having sufficient cardinality: $\mathcal{S}_j := \{S \in 2^M; |S| \geq j\}$, and given $S \in \mathcal{S}_j$, for computing $\text{opt}_j(k, S)$ it is sufficient to consider each element of $\mathcal{T}_j(S) := \{T \in 2^S \setminus \{\emptyset\}; |T| \leq |S| - (j - 1)\}$.

Before precisely stating the procedure, we explain the data structures used: Rectangles will be represented by their diagonal points in a data type **rectangle** storing objects of type **point**. Thinking of M as a sorted alphabet, each subset $S \subset M$ corresponds to a unique word over M , denoted $\text{word}(S)$ or S for short, thus 2^M may be sorted by the corresponding lexicographic order. For each S , there can be determined a unique index $\text{ind}(S)$ according to this order. A datatype **subset** is used for storing a rectangle and an integer. Then in a preprocessing step for each $S \subseteq M$ there can be defined **subset** A_S holding $\text{ind}(S)$ and also $r_\delta(S)$ such that it is possible to read each of them in constant time. We make use of two further container arrays $\text{Opt}_i, \text{Rect}_i$ for $i = 0, 1$, each sorted by increasing $\text{ind}(S)$. Two of each kind are needed, because during the algorithm they may be read and filled up alternately. The arrays $\text{Opt}_i, i = 0, 1$, shall store the intermediately computed $\text{opt}_j(k, S)$ -values. The other two arrays Rect_i of dynamic length have the task to hold at each index $\text{ind}(S)$ a set $R_0^{(j)}(S)$ for storing the intermediately computed rectangles covering S . These arrays are also (re-)used alternately. By the common order of these arrays the task of determining for a given set $T \subset M$ its array position is solved in $O(1)$ by referring to $A_S.\text{ind} = \text{ind}(S)$. Finally, we make use of two arrays $\text{Subs}_i, i = 0, 1$, of dynamic length. The first one shall store $\text{word}(T)$ and the second $\text{word}(T')$ for each subset T of the current $S \subset M$. These arrays may be sorted by lexicographic order.

Algorithm (k -RC)

Input: set of points in the plane M as array of **points**

Output: optimal covering value $\text{opt}(k, M)$, optimal covering $R_0(M)$

begin

compute arrays $M_j, j = x, y$, by lexicographic j -order

compute $r_\delta(M), w(r_\delta(M))$ by algorithm OPT1

if $n = |r_\delta(M) \cap I|$ **then** $\text{opt}(k, M) \leftarrow w(r_\delta(M)), R_0(M) \leftarrow \{r_\delta(M)\}$

else

$\text{opt}(k, M) \leftarrow \infty, R_0(M) \leftarrow \emptyset$

sort $2^M \setminus \{\emptyset\}$ by lexicographic order, thereby:

$\forall S \in 2^M \setminus \{\emptyset\}$: compute $r_\delta(S), \text{ind}(S)$ and fill A_S

$\forall S \in 2^M \setminus \{\emptyset\}$: $\text{Opt}_0[\text{ind}(S)] \leftarrow w(r_\delta(S)), \text{Rect}_0[\text{ind}(S)] \leftarrow \{r_\delta(S)\}$

$\text{opt}(k, M) \leftarrow \text{Opt}_0[\text{ind}(M)], \text{Rect}_0[\text{ind}(M)] \leftarrow \{r_\delta(M)\}$

if $n \geq 3$ **then**

for $j = 2$ **to** $n - 1$ **do**

for all $S \in \mathcal{S}_j := \{S \in 2^M \setminus \{\emptyset\}; j \leq |S|\}$ **do**

sort $2^S \setminus \{\emptyset\}$ by lexicographic order, thereby:

$\forall T \in 2^S \setminus \{\emptyset\}$: $\text{Subs}_0[\text{ind}(T)] \leftarrow \text{word}(T), \text{Subs}_1[\text{ind}(T)] \leftarrow \text{word}(T')$

$\text{Opt}_{(j-1) \bmod 2}[\text{ind}(S)] \leftarrow \infty$ ($*\text{opt}_j(k, S) \leftarrow \infty*$)

for all $T \in \mathcal{T}_j(S) := \{T \in 2^S \setminus \{\emptyset\}; 1 - j + |S| \geq |T|\}$ **do**

```

temp = w(rδ(T)) + Optj mod 2[ind(T')] (*optj-1(k, T')*)
if temp < Opt(j-1) mod 2[ind(S)] then
  Opt(j-1) mod 2[ind(S)] ← temp
  Rect(j-1) mod 2[ind(S)] ← {rδ(T)} ∪ Rectj mod 2[ind(T')]
end do (* now: Opt(j-1) mod 2[ind(S)] = optj(k, S)*)
end do
if Opt(j-1) mod 2[ind(M)] < opt(k, M) then
opt(k, M) ← Opt(j-1) mod 2[ind(M)], R0(M) ← Rect(j-1) mod 2[ind(M)]
end do
Opt(n-1) mod 2[ind(M)] ← ∞, Rect(n-1) mod 2[ind(M)] ← ∅
for all T ⊂ M : |T| = 1 do
  temp = w(rδ(T)) + Optn mod 2(ind(T')) (*optn-1(k, T')*)
  if temp < Opt(n-1) mod 2[ind(M)] then
    Opt(n-1) mod 2[ind(M)] ← temp
    Rect(n-1) mod 2[ind(M)] ← {rδ(T)} ∪ Rectn mod 2[ind(T')]
  end do (* now: optn(k, M) = min{w(rδ(T)) + optn-1(k, T'); T ∈ Tn(M)}*)
  if Opt(n-1) mod 2[ind(M)] < opt(k, M) then
    opt(k, M) ← Opt(n-1) mod 2[ind(M)], R0(M) ← Rect(n-1) mod 2[ind(M)]
  (* now: opt(k, M) = min{optn(k, M); n ∈ M}*)
end

```

Theorem 1. For input (M, k) with $n := |M|$, Algorithm k -RC correctly computes $\text{opt}(k, M) = \min_{i \in [n]} \text{opt}_i(k, M)$ and $R_0 \in \mathcal{C}(M)$ such that $\text{opt}(k, M) = w(R_0)$ in $O(n^2 3^n)$ time.

Proof. Let $n := |M|$. For proving correctness we first show that $\text{opt}(k, M) = \min_{i \in [n]} \text{opt}_i(k, M)$ holds true, where $(*)$: $\text{opt}_i(k, M) := \min\{w(R); R \in \mathcal{C}_i(M)\}$, $i \in [n]$ and $\mathcal{C}_i(M) := \{R \in \mathcal{C}(M); |R| = i\}$. In the second step it is verified that the dynamic program correctly computes $(*)$ by induction on $n \in \mathbb{N}$. Clearly, as disjoint union $\mathcal{C}(M) = \bigcup_{i \in \mathbb{N}} \mathcal{C}_i(M)$ ($|R| = 0$ is impossible). Obviously, we never need more covering components than there are elements in M , thus

$$\text{opt}(k, M) = \min_{i=1}^n \{w(R); R \in \mathcal{C}_i(M)\} = \min_{i \in [n]} \text{opt}_i(k, M)$$

Next, we have to show that the dynamic program will reproduce $\text{opt}_i(k, M)$, $1 \leq i \leq n \in \mathbb{N}$, as in $(*)$. First of all, by directly applying the above argumentation it is clear that we never have to take into consideration more covering components than there are elements in a set $S \subseteq M$ for finding $\text{opt}(k, S)$. Which means, for $|S| = j$ it suffices to compute $\text{opt}_l(k, S)$, $l \leq j$. In other words $\text{opt}_j(k, S)$ has to be computed only for all elements of $\mathcal{S}_j := \{S \in 2^M \setminus \{\emptyset\}; j \leq |S|\}$. In the same way it is clear that in the most inner loop of the algorithm it suffices to consider only $\mathcal{T}_j(S) := \{T \in 2^S \setminus \{\emptyset\}; 1 - j + |S| \geq |T|\}$, as then $|T'| = |S \setminus T| \geq j - 1$, $|S| \geq j$. Let us proceed by induction on n . By Lemma 2, $\text{opt}_1(k, S) = w(r_\delta(S))$ for each $\emptyset \neq S \subseteq M$, especially $\text{opt}_1(k, M) = w(r_\delta(M))$, $\forall |M| \in \mathbb{N}$, which is also the basis of the dynamic program. Now suppose that for each $|M| \leq n$ holds

$$\text{opt}_i(k, S) = \min\{w(r_\delta(T)) + \text{opt}_{i-1}(k, T'); T \in \mathcal{T}_i(S)\}$$

$\forall S \subseteq M, |S| \geq i, \forall i \in \{2, \dots, n\}$. Consider the case $|M| = n + 1$. Then for $S \subsetneq M$ we are ready by induction, because $|S| \leq n$. Moreover, by definition $\text{opt}_i(k, M) = \{w(R); R \in \mathcal{C}_i(M)\}$, for each $i \in \{2, \dots, |M|\}$. Thus, for each $S \subsetneq M, |S| \geq j$ and $|M| - |S| \geq i - j$, we have $R_1 \cup R_2 \in \mathcal{C}_i(M)$ whenever $R_1 \in \mathcal{C}_j(S), R_2 \in \mathcal{C}_{i-j}(S')$, hence

$$\begin{aligned} \text{opt}_i(k, M) &= \min_{S \subset M: i+|S|-|M| \leq j \leq |S|} \{w(R_1) + w(R_2); R_1 \in \mathcal{C}_j(S), R_2 \in \mathcal{C}_{i-j}(S')\} \\ &= \min_{S \subset M: i+|S|-|M| \leq j \leq |S|} \left(\min_{R \in \mathcal{C}_j(S)} w(R) + \min_{R \in \mathcal{C}_{i-j}(S')} w(R) \right) \\ &= \min_{S \subset M: i+|S|-|M| \leq j \leq |S|} (\text{opt}_j(k, S) + \text{opt}_{i-j}(k, S')) \end{aligned}$$

Now we state the following simple but helpful claim: For $S \subsetneq M$ and l with $i + |S| - |M| \leq l \leq |S|$ there is a $T \subset S$ such that

$$\text{opt}_i(k, M) \leq w(r_\delta(T)) + \text{opt}_{i-1}(k, T') \leq \text{opt}_l(k, S) + \text{opt}_{i-l}(S')$$

From this directly follows $\text{opt}_i(k, M) = \{w(r_\delta(T)) + \text{opt}_{i-1}(k, T'); \emptyset \neq T \subseteq M, |T| \leq n - i + 1\}$, which is what has been stated.

Finally, for proving the claim take an arbitrary fixed $S \subsetneq M$, then the case $l = 1$ is clear by setting $T = S$. For $|S| \geq l > 1$ by induction there is a $T_0 \subset S : |T_0| \leq |S| - l + 1$ with $\text{opt}_l(k, S) = w(r_\delta(T_0)) + \text{opt}_{l-1}(k, S \setminus T_0)$ hence

$$\text{opt}_l(k, S) + \text{opt}_{i-l}(k, S') = w(r_\delta(T_0)) + \underbrace{\text{opt}_{l-1}(k, S \setminus T_0) + \text{opt}_{i-l}(k, S')}_{\text{covering } S' \cup (S \setminus T_0) = M \setminus T_0}$$

thus $\text{opt}_{l-1}(k, S \setminus T_0) + \text{opt}_{i-l}(k, S') \geq \text{opt}_{i-1}(k, M \setminus T_0)$. Therefore the choice T_0 establishes the claim.

Addressing the running time only the else-part is of interest. First of all there is the preprocessing step consisting of sorting $2^M \setminus \{\emptyset\}$ thereby computing $r_\delta(S), \text{ind}(S)$. For fixed S computing $r(S)$ needs $O(|S|)$ time and from this according to Lemma 2 we can compute $r_\delta(S)$ also in $O(|S|)$ time which also holds for computing $\text{ind}(S)$, hence this step delivers an additive term of $O(n2^n)$. Next, there is the dominating part consisting of two nested loops. The inner loop considers all subsets $S \subset M$ such that $|S| = p \geq j$; for each p we have $\binom{n}{p}$ such sets. For each of which there is computed the body containing two further loops. In the first for each $S, |S| = p \geq j$, the set 2^S is constructed, and for each fixed $T \subset S$ corresponding $\text{word}(T)$ and $\text{word}(T')$ are computed needing $O(|S|)$ time thus yielding $O(p2^p)$. In the second loop each relevant $T \subseteq S$ is considered where all operations are of $O(1)$. Therefore and because of $\sum_{k=1}^{p-j+1} \binom{p}{k} \leq 2^p \leq p2^p$ it also contributes $O(p2^p)$. Hence, by the binomial theorem, we get for the inner loop $O(\sum_{p=j}^n \binom{n}{p} p2^p \leq n3^n)$. Finally, the outer loop is iterated less than n times leading altogether to $O(n^23^n)$ also dominating the bound of the preprocessing

step. The last step contains a loop of $O(n)$ iterations during each of which $O(n)$ time is needed for computing $\text{word}(T')$ thus it contributes additively $O(n^2)$ also dominated by $O(n^2 3^n)$ completing the proof. \square

4 Improving Time Bounds

In the discussion of the preceding section almost all subsets $S \in 2^M$ have been considered, but many of these subsets can be identified in the sense that they lead to the same rectangular base: $r(S) = r(S'), S, S' \in 2^M$.

Definition 2. A set $S \in 2^M \setminus \{\emptyset\}$ is called admissible rectangular subset of M if $r(S) \cap M = S$. Let $\mathcal{A}(M) \subset 2^M \setminus \{\emptyset\}$ denote the set of all admissible rectangular subsets of M . Given k , we define $\mathcal{A}_{\nu(k)}(M) := \{A \in \mathcal{A}(M) \mid \ell_x(r(A)) \geq \nu(k)\lambda, \ell_y(r(A)) \geq \nu(k)\lambda\} \subset \mathcal{A}(M) =: \mathcal{A}_0(M)$, for each $\nu(k) \in \{1, \dots, N-1\}$.

The next two useful results are shown in [7] (Proposition 2, Corollary 1).

Proposition 1. (i) $S_1 \sim_r S_2 \Leftrightarrow_{\text{def}} r(S_1) = r(S_2), \forall \emptyset \neq S_1, S_2 \in 2^M$ defines an equivalence relation on $2^M \setminus \{\emptyset\}$. We write $\mathcal{M} := [2^M \setminus \{\emptyset\}] / \sim_r$.

(ii) The map $\sigma : 2^M \ni S \mapsto \sigma(S) := r(S) \cap M \in 2^M$ ($r(\emptyset) := \emptyset$) is a closure operator (rectangular closure) having image $\sigma(2^M) = \mathcal{A}(M) \cup \{\emptyset\}$.

(iii) The sets $\mathcal{A}(M)$ and \mathcal{M} are isomorphic, let the corresponding bijection be denoted by $\mu : \mathcal{A}(M) \rightarrow \mathcal{M}$. Thus each $A \in \mathcal{A}(M)$ defines a class of subsets $\mu(A)$ called rectangular subset class. \square

Lemma 3. For $(M, k), \mathcal{A}(M)$ as above, $|\mathcal{A}(M)| \in O(|M|^4)$ (hence $|\mathcal{A}_i(M)| \in O(|M|^4), \forall i \in \{0, \dots, N-1\}$). \square

Lemma 4. Let (M, k) be an instance of k -RC. If, for each $S \in \mathcal{S}_j$ one replaces $\mathcal{T}_j(S)$ by the set $\hat{\mathcal{T}}_j(S) := \mathcal{T}_j(S) \cap \mathcal{A}_{\nu(k)}(M), j \in \{2, \dots, |M|\}$, in Algorithm k -RC, then it still works correctly.

Proof. We have to show that $(*) : \text{opt}_j(k, S) = \min\{w(r_\delta(T)) + \text{opt}_{j-1}(k, S'); T \in \hat{\mathcal{T}}_j(S)\}$ holds. By Theorem 1 we have $\text{opt}_j(k, S) = \min\{f_S^j(T); T \in \mathcal{T}_j(S)\}$ defining $f_S^j(T) := w(r_\delta(T)) + \text{opt}_{j-1}(k, S')$. Now we claim that for each $T \in \mathcal{T}_j(S)$ there is $A \in \hat{\mathcal{T}}_j(S) : f_S^j(A) \leq f_S^j(T)$, from which directly follows the lemma, because in that case we do not miss any relevant candidate computing $\text{opt}_j(k, S)$ as in $(*)$. To show the claim consider any $T \in \mathcal{T}_j(S)$; if $T \in \hat{\mathcal{T}}_j(S)$ we are ready by setting $A := T \Rightarrow f_S^j(A) = f_S^j(T)$. $T \in \mathcal{T}_j(S) \setminus \hat{\mathcal{T}}_j(S)$ implies $T \notin \mathcal{A}_{\nu(k)}(M)$, and we set $A := A(T) := r(T) \cap M \in \mathcal{A}(M)$, and obviously $w(r_\delta(T)) = w(r_\delta(A))$. Moreover, from Proposition 1, (ii), we obtain $S \setminus A \subseteq S \setminus T$, because $T \subseteq A(T)$, which in case $|S \setminus A| \geq j-1$ directly implies $f_S^j(A) \leq f_S^j(T)$. In the remaining case $|S \setminus A| < j-1$, we have

$$\begin{aligned} \text{opt}_{j-1}(k, S \setminus A) &= \text{opt}_l(k, S \setminus T) + \text{opt}_{j-1-l}(k, \emptyset) \\ &\leq \text{opt}_l(k, S \setminus T) + \text{opt}_{j-1-l}(k, \emptyset) \\ &\leq \text{opt}_{j-1}(k, S \setminus T) \end{aligned}$$

where the last inequality follows because $|S \setminus T| \geq j - 1$ and $\text{opt}_{j-1-l}(k, \emptyset)$ means the value of w for $j - 1 - l$ rectangles being smallest according to k , from which the claim and also the lemma follow. \square

Theorem 2. *For input (M, k) , k -RC can be solved in $O(|M|^{62^{|M|}})$ time.*

Proof. The correctness directly follows from Lemma 4. To verify the time bound first observe that from the proof of Theorem 1 follows that for the most inner loops instead of considering each element of $\mathcal{T}_j(S)$ we have to consider only those also being elements of $\mathcal{A}_{\nu(k)}(M)$. Thus, instead of $p2^p$, for fixed $S \subset M : |S| = p$, one obtains $\sum_{p=j}^n \binom{n}{p} p |\mathcal{A}_{\nu(k)}(M)| \leq n2^n |\mathcal{A}_{\nu(k)}(M)|$ and the outer loop never is iterated more than n times leading to another factor $n := |M|$. Finally, realizing $|\mathcal{A}(M)| \leq |\mathcal{B}_4(M)|$ due to Lemma 3 finishes the proof. \square

5 Concluding Remarks

We provided algorithms for covering a given set of n points in the plane by regular rectangles due to an objective function minimizing sum of areas, circumferences and number of rectangles used. A first dynamic programming approach yielding an appropriate covering algorithm of running time $O(n^2 3^n)$ could be improved to $O(n^6 2^n)$ by slight modifications exploiting the underlying rectangular structure.

References

1. P. Bastian, Load Balancing for Adaptive Multigrid Methods, SIAM Journal on Scientific Computing, 19 (1998) 1303-1321.
2. F. C. Calheiros, A. Lucena, C. C. de Souza, Optimal Rectangular Partitions, Networks 41 (2003) 51-67.
3. J. C. Culberson, R. A. Reckhow, Covering Polygons is Hard, Proceedings of the twenty-ninth IEEE Symposium on Foundations of Computer Science, 1988, pp. 601-611.
4. J. Hershberger, S. Suri, Finding Tailored Partitions, Journal of Algorithms 12 (1991) 431-463.
5. D. S. Hochbaum, Approximation Algorithms for NP-hard problems, PWS Publishing, Boston, Massachusetts, 1996.
6. S. Porschen, On Covering \mathbb{Z} -Grid Points by Rectangles, ENDM Vol. 8, 2001.
7. S. Porschen, On the Rectangular Subset Closure of Point Sets, Proc. CGA 2005, Lect. Notes in Comp. Sci., Vol. 3480, pp. 796-805, 2005.
8. S. J. Plimpton, B. Hendrickson, J. R. Stewart, A parallel rendezvous algorithm for interpolation between multiple grids, J. Parallel Distrib. Comput. 64 (2004) 266-276.
9. S. S. Skiena, Probing Convex Polygons with Half-Planes, Journal of Algorithms 12 (1991) 359-374.
10. S. L. Tanimoto, R. J. Fowler, Covering Image Subsets with Patches, Proceedings of the fifty-first International Conference on Pattern Recognition, 1980, pp. 835-839.

Backward Error Analysis in Computational Geometry

Di Jiang and Neil F. Stewart*

Département IRO, Université de Montréal,
CP6128, Succ. CentreVille, H3C 3J7, Canada
{jiangdi, stewart}@iro.umontreal.ca

Abstract. A recent paper, published in Algorithms—ESA2004, presented examples designed to illustrate that using floating-point arithmetic in algorithms for computational geometry may cause implementations to fail. The stated purpose was to demonstrate, to students and implementors, the inadequacy of floating-point arithmetic for geometric computations. The examples presented were both useful and insightful, but certain of the accompanying remarks were misleading. One such remark is that researchers in numerical analysis may believe that simple approaches are available to overcome the problems of finite-precision arithmetic. Another is the reference, as a general statement, to the inadequacy of floating-point arithmetic for geometric computations.

In this paper it will be shown how the now-classical backward error analysis can be applied in the area of computational geometry. This analysis is relevant in the context of uncertain data, which may well be the practical context for computational-geometry algorithms such as, say, those for computing convex hulls. The exposition will illustrate the fact that the backward error analysis does not pretend to overcome the problem of finite precision: it merely provides a tool to distinguish, in a fairly routine way, those algorithms that overcome the problem *to whatever extent it is possible to do so*.

It will also be shown, by using one of the examples of failure presented in the principal reference, that often the situation in computational geometry is exactly parallel to other areas, such as the numerical solution of linear equations, or the algebraic eigenvalue problem. Indeed, the example mentioned can be viewed simply as an example of an unstable algorithm, for a problem for which computational geometry has already discovered provably stable algorithms.

1 Introduction

This paper presents an exposition of how the combined backward/forward error analysis, from numerical analysis, relates to the study of robustness in computational geometry.

* The research of the second author was supported in part by a grant from the Natural Sciences and Engineering Research Council of Canada.

As stated in our principal reference [1], “. . . the algorithms of computational geometry are designed for a machine model with exact arithmetic. Substituting floating point arithmetic for the assumed real arithmetic may cause implementations to fail.” The authors of [1] go on to say that “due to . . . [a] . . . lack of examples, instructors of computational geometry have little material for demonstrating the inadequacy of floating point arithmetic for geometric computations, students of computational geometry and implementers of geometric algorithms still underestimate the seriousness of the problem, and researchers in our and neighboring disciplines, e.g., numerical analysis, still believe, that simple approaches are able to overcome the problem.” An incremental scan algorithm (which is related to Graham’s scan [2] and which we will refer to as *Graham_incremental*), for planar convex hulls, is then studied in some detail. In particular, examples are given which show the algorithm can fail, and an explanation is given for why it fails, when executed with floating-point arithmetic.

The examples given in [1] should indeed be useful to students and teachers of computational geometry, in order to illustrate what can go wrong, and why, when finite-precision arithmetic is used to solve geometric problems. Furthermore, [1] satisfies the criteria of classical experimental science [3, p. 147] in a way that is rare in computer science [4], in that it presents the results of experiments that are repeatable in every detail. In fact, we have implemented the *Graham_incremental* algorithm for example A1 of [1], and we confirm that the algorithm behaves exactly as described in [1] when applied to the data given there¹. Briefly, for example A1 of [1], *Graham_incremental* produces a completely spurious result.

There are, however, three misleading suggestions in the final sentence quoted above, and it would be unfortunate if they were communicated to students of computational geometry. One of these is the suggestion that the approaches of computational geometry and numerical analysis are somehow adversarial, since in fact they are complementary. Another is the suggestion that numerical analysts believe that they can “overcome” the problem of finite precision. This is not true. What *is* true, however, is that in the case where input data is uncertain and a stability result is available, a backward/forward error analysis, and often a pure backward error analysis, can deal with the problem in a fairly routine way, by showing that a stable algorithm overcomes the problem of finite precision *to whatever extent it is possible to do so*. Indeed, a stable algorithm provides us with a solution that is as good as the data warrants [5]. (Stability will be defined below in the context of a combined backward/forward analysis, but we will usually just refer to a backward error analysis, since this is usually sufficient.)

A third misleading remark in the passage from [1], quoted above, is the reference to the “inadequacy” of floating-point arithmetic for geometric computations, which is incorrect as a general statement. In fact, some algorithms using floating point will provide adequate solutions, while others will not, and a backward error analysis will permit us to recognize which algorithms are satisfactory.

¹ Published confirmation of experimental results is common in fields such as experimental physics, and it is satisfying to participate in this kind of process here.

On the other hand, it *is* true that we must begin by defining precisely what constitutes an *adequate*, or *inadequate*, solution to a geometric problem.

In this paper we will show that numerical robustness for the convex-hull problem is analogous to the case of linear equations, or the algebraic eigenvalue problem, and that when input data is uncertain, the difficulties documented in [1] fit exactly into the paradigm of the backward error analysis. We emphasize that this does not imply that research into other paradigms, including exact arithmetic and others, should not be vigorously pursued. Our only claim is that in the proper context (uncertain input data), the backward-error analysis is a useful approach, and it should not be neglected.

In Section 2 of the paper we will present a brief summary of how the backward error analysis is used in numerical linear algebra, and an illustration will be used to show that breakdowns of methods, of the sort described in [1] for the convex-hull problem, are quite typical in other fields. Then, in Section 3, a description of the combined backward/forward error analysis will be given, and applied to the planar convex-hull problem. These ideas were developed several decades ago, but work such as [5] and [6] is very much relevant today. As already mentioned, the first task is to define exactly what is meant by the “inadequacy” of a solution to the convex-hull problem. We are then in a position to do a *perturbation analysis* [6, Ch. 2] to examine the effects of perturbations of the input data (whether they are caused by original uncertainty or by subsequent application of a stable numerical algorithm). Finally, we discuss Fortune’s implementation of the Graham scan, which we will call *Graham_Fortune*. This implementation is numerically stable for the planar convex-hull problem, as proved in [7]. Indeed, a slight modification of the algorithm in [7, Sec. 4] will produce a sequence of points that lie on the topological boundary of their convex hull, and this convex set is the correct convex hull for points that have been relatively perturbed by a small amount. Thus, we can use a pure backward error analysis to affirm that *Graham_Fortune* provides a solution that is as good as we can hope for, given that the data is uncertain.

The situation for planar convex hulls is, therefore, closely analogous to the case of solving linear equations. In both cases there exist unstable algorithms (*Graham_incremental*, and Gaussian elimination without pivoting, respectively), and in both cases there exist stable algorithms (*Graham_Fortune*, and Gaussian elimination with total pivoting, respectively). Also, in both cases there exist examples for which unstable algorithms produce complete nonsense, and this with no warning that anything is amiss. In fact, the only breakdown in the analogy is that in the case of the convex-hull problem, with the error criterion used below as an illustration, the situation is much *better* than for solving linear equations. This is because the perturbation analysis, mentioned above, shows that the problem is *well-conditioned*, which is not always true for linear equations. Thus, whereas even a stable algorithm may produce an unsatisfactory answer for the problem $A\mathbf{x} = \mathbf{b}$ (if A is the Hilbert matrix, for example), a stable algorithm such as *Graham_Fortune* always produces a satisfactory answer for the convex-hull problem.

2 Backward Error Analysis for Linear-Equation Solvers

For linear equations, the problem is defined by the pair $[A, \mathbf{b}]$, and the solution is defined by \mathbf{x} such that $A\mathbf{x} = \mathbf{b}$. We proceed as follows:

- a. *Measuring error in the solution space.* A measure of the inadequacy of an approximate solution \mathbf{y} , for the problem $[A, \mathbf{b}]$, is the relative error $\frac{\|\mathbf{x} - \mathbf{y}\|}{\|\mathbf{x}\|}$, where $\|\cdot\|$ denotes any convenient vector norm.
- b. *Perturbation Analysis.* A simple argument shows that if δA is a matrix representing perturbation of the elements of A , and if $\delta \mathbf{b}$ is a vector representing perturbations of the elements of \mathbf{b} , then the solution \mathbf{y} of the perturbed problem $[A + \delta A, \mathbf{b} + \delta \mathbf{b}]$ satisfies (neglecting second-order terms):

$$\frac{\|\mathbf{x} - \mathbf{y}\|}{\|\mathbf{x}\|} \leq \|A\| \cdot \|A^{-1}\| \left\{ \frac{\|\delta A\|}{\|A\|} + \frac{\|\delta \mathbf{b}\|}{\|\mathbf{b}\|} \right\}, \quad (1)$$

where $\|\cdot\|$ is now used also to denote a matrix norm subordinate [6, p. 56] to the vector norm introduced above. The quantity $\|A\| \cdot \|A^{-1}\|$ is usually referred to as the *condition number* of the problem: for a trivial matrix like the identity it will be equal to 1, while for a Hilbert matrix of even moderate dimension it will be very large. The condition number represents the amount by which a given perturbation of the input data for $A\mathbf{x} = \mathbf{b}$ will be magnified in the solution. A problem with a low condition number is said to be *well-conditioned*, and a problem with a large condition number is said to be *ill-conditioned*. The two cases are illustrated by the lines linking problems to solutions in Figures 1 and 2, where P denotes the class of problems, and S denotes the class of solutions [8].

- c. *Stability proof.* The third step is to seek *stable* algorithms, that is, algorithms that produce a slightly incorrect solution to a slightly perturbed problem [5], as illustrated by the unfilled circles in Figures 1 and 2. (This describes a combined backward/forward error analysis; if the words “a slightly incorrect solution” can be replaced by “the exact solution”, so that there is no need for the unfilled circle in S , then we have a pure backward error analysis.) Gaussian elimination with total pivoting is stable for the problem $A\mathbf{x} = \mathbf{b}$. Such algorithms produce answers that are, for practical purposes, as good as the best answers we can hope for (*even using infinite precision*), if the “slight perturbation” is smaller than the uncertainty already in the data. Furthermore, by the perturbation analysis of step b, above, the size of the error in the solution can be estimated.

It should be observed that the concept of problem condition, and the corresponding perturbation analysis, are considered prior to any discussion of numerical methods [6, Ch. 2]. This reflects the central idea of the backward error analysis: if the elements of A contain uncertainty that may be as large as $\frac{\|\delta A\|}{\|A\|}$, and the elements of \mathbf{b} contain uncertainty that may be as large as $\frac{\|\delta \mathbf{b}\|}{\|\mathbf{b}\|}$, then

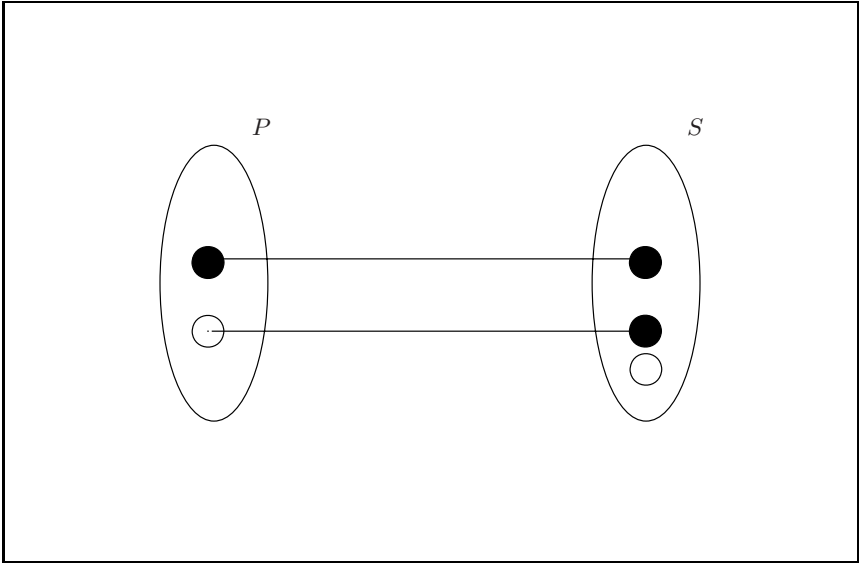


Fig. 1. Well-conditioned problem

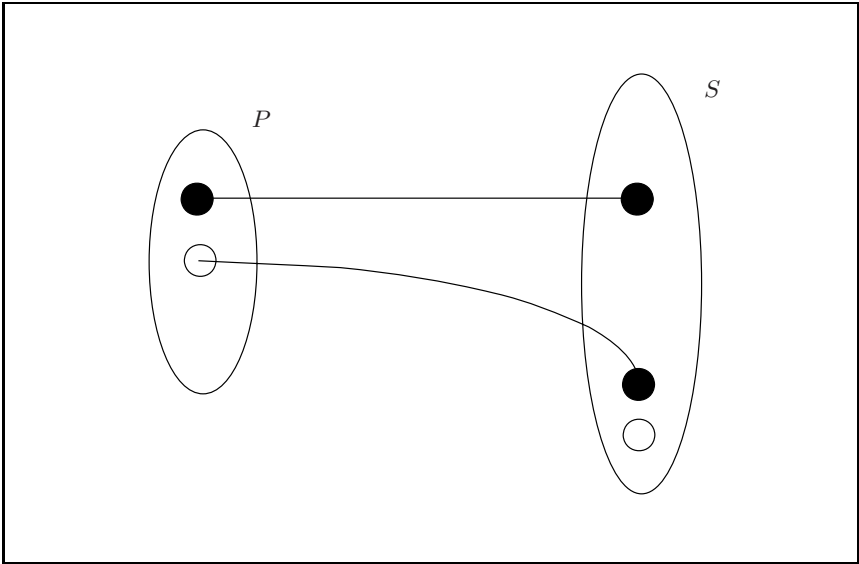


Fig. 2. Ill-conditioned problem

the relative error $\frac{\|\mathbf{x}-\mathbf{y}\|}{\|\mathbf{x}\|}$ may be as large as is indicated in (1). This means that even an exact, infinite-precision algorithm cannot help us avoid a large error in the solution, in the case of an ill-conditioned problem, because of the effects of

the inherent uncertainty in the data (see Figure 2). It also means, however, that if we can find an algorithm that produces a solution that is the exact solution, of a problem that differs from the given problem by an amount smaller than the inherent uncertainty in the data, then the algorithm has produced an answer that is as good as the data warrants [5].

We emphasize again that a stable algorithm does not necessarily produce an answer with small error: it only produces an answer with error on the order of that which we must accept in any event, due to data uncertainty (see Figure 2, where the unfilled circle in S indicates that the method has done a good job of solving the perturbed problem, but has nonetheless produced an answer with large error). The backward error analysis does not “overcome” the problem of numerical error: it merely allows us to identify algorithms that produce errors of the same order as those that we must accept anyway.

We conclude this section with the remark that computational geometry is by no means unusual in the fact that there are theoretically exact algorithms that produce nonsense when implemented in floating point arithmetic. For example, in the case of $A\mathbf{x} = \mathbf{b}$, suppose we attempt to solve the sequence of problems

$$\begin{bmatrix} \phi(\rho) & 1.0 \\ 1.0 & 0.0 \end{bmatrix} \begin{bmatrix} x_1 \\ x_2 \end{bmatrix} = \begin{bmatrix} 1.0 \\ 1.0 \end{bmatrix}, \quad \rho = 0.1, 0.2, \dots$$

where $\phi(\rho) = \rho^2 - 0.01$. For $\rho = 0.1$, the correct answer is $x_1 = 1.0$, $x_2 = 1.0$, but Gaussian elimination without pivoting, as implemented in the following program, returns the answer $x_1 = 0.0$, $x_2 = 1.0$. There is no division by zero, and no overflow or underflow occurs during the execution of the implemented algorithm. In the evaluation of $A[1][1]$, however, the first term on the righthand side of the assignment statement is shifted off the end of a register and ignored.

```

double rho = 0.1, phi = rho * rho - 0.01 ;
double A[2][2] = { {phi, 1.0} , {1.0, 0.0} } , b[2] = {1.0, 1.0} ;
double x[2] ;
/***** Triangulate A *****/
double mult = 1.0 / A[0][0] ;
A[1][1] = A[1][1] - mult * A[0][1] ;
b[1] = b[1] - mult * b[0] ;
/***** Back-substitute *****/
x[1] = b[1] / A[1][1] ;
x[0] = (b[0] - A[0][1] * x[1]) / A[0][0] ;
cout<<" The result is: "<<x[0]<<" "<<x[1]<<endl ;
/*****
The result is: 0 1

```

3 Backward Error Analysis for Planar Convex Hulls

We will now provide a parallel development for the problem of computing convex hulls of points in the plane. In this case the problem is defined [1] by a finite set

of vectors $S = \{\mathbf{a}_1, \dots, \mathbf{a}_n\}$, where each \mathbf{a}_i lies in the plane². An algorithm to compute the extreme points of S will normally select a subset $\{i_1, i_2, \dots, i_m\}$ of the indices $\{1, \dots, n\}$ and declare $\{\mathbf{a}_{i_1}, \dots, \mathbf{a}_{i_m}\}$ to be the solution, but since we are envisaging the possibility of uncertainty in the problem data, we will permit any non-empty finite set of vectors $Y = \{\mathbf{y}_1, \dots, \mathbf{y}_m\}$ as a solution, where each \mathbf{y}_i lies in the plane. It may be noted here that the use of convex-hull algorithms for problems with uncertain data is of real practical interest. For example, in [9] it was shown that Bézier curves and patches do not self-intersect (and adjacent patches do not have extraneous intersections) provided that the origin $\mathbf{0}$ is not an element of the convex hull of certain points depending directly on the Bézier control points. These points will typically contain uncertainty far greater than the perturbations introduced by the implementation of *Graham_Fortune* using even single-precision floating-point arithmetic, and use of this algorithm for this problem would therefore be entirely appropriate.

3.1 Step a: Measuring Inadequacy

If $\{\mathbf{v}_1, \dots, \mathbf{v}_k\}$ is a finite set of vectors in the plane, define $\text{conv}(\{\mathbf{v}_1, \dots, \mathbf{v}_k\}) \subseteq E^2$ to be the convex hull of the set of vectors. We will define the distance d between two distinct solutions Y^1 and Y^2 of the convex-hull problem to be infinite if for $i = 1$ or 2 the vectors in Y^i do not actually lie on the topological boundary of $\text{conv}(Y^i)$; otherwise, d is defined to be the Hausdorff distance between $\text{conv}(Y^1)$ and $\text{conv}(Y^2)$. Defining $d(Y^1, Y^1) = 0$, the distance d is a metric. Let $\{\mathbf{a}_{i_1}, \dots, \mathbf{a}_{i_m}\}$ be a set of points lying on the topological boundary of

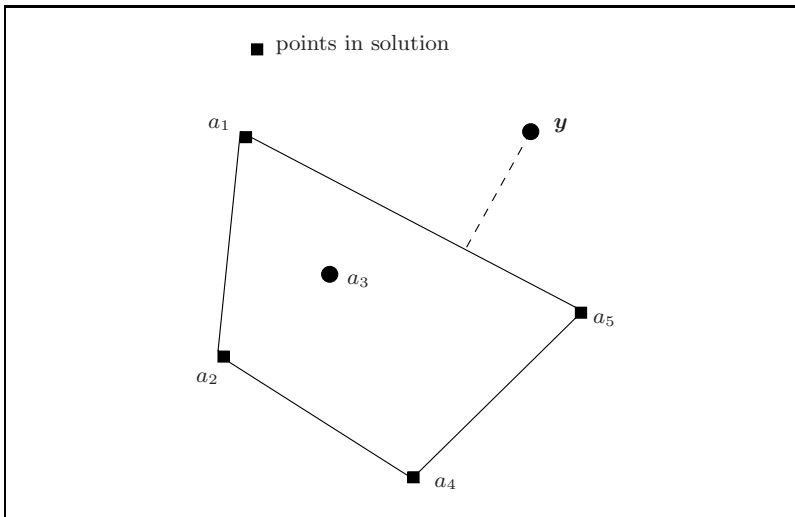


Fig. 3. Example convex-hull problem

² We denote the points by \mathbf{a} in order to increase the parallelism with Section 2.

$\text{conv}(\{\mathbf{a}_1, \dots, \mathbf{a}_n\})$, and such that $\text{conv}(\{\mathbf{a}_{i_1}, \dots, \mathbf{a}_{i_m}\}) = \text{conv}(\{\mathbf{a}_1, \dots, \mathbf{a}_n\})$. The error E in a solution Y is defined to be

$$E = d(\{\mathbf{a}_{i_1}, \dots, \mathbf{a}_{i_m}\}, Y)/M, \quad (2)$$

where M is a fixed upper bound for the absolute value of any coordinate of any point [7]. (Thus, as in [10], for a solution to be considered accurate, its points are required to actually lie on a convex polygon.) In Figure 3, the solution to the problem defined by $\{\mathbf{a}_1, \mathbf{a}_2, \mathbf{a}_3, \mathbf{a}_4, \mathbf{a}_5\}$ is $\{\mathbf{a}_1, \mathbf{a}_2, \mathbf{a}_4, \mathbf{a}_5\}$. The solution $Y = \{\mathbf{a}_1, \mathbf{a}_2, \mathbf{a}_3, \mathbf{a}_4, \mathbf{a}_5\}$ has infinite error, since \mathbf{a}_3 is not in the boundary of $\text{conv}(\{\mathbf{a}_1, \mathbf{a}_2, \mathbf{a}_3, \mathbf{a}_4, \mathbf{a}_5\})$, while $Y = \{\mathbf{a}_1, \mathbf{a}_2, \mathbf{a}_4, \mathbf{a}_5, \mathbf{y}\}$ has error as indicated by the dashed line.

It is possible to define other measures of distance between solutions of this problem, *e.g.*, we might penalize solutions with redundant points on the boundary of the convex hull.

We will use the simple criterion (2) to illustrate our point, which is that if we wish to prove rigorous theorems about the inadequacy of computed solutions, we must give a careful definition of inadequacy.

3.2 Step b: Perturbation Analysis

If the input data $\{\mathbf{a}_1, \dots, \mathbf{a}_n\}$ is uncertain, then the true problem that we wish to solve is defined by $\{\mathbf{a}_1 + \delta\mathbf{a}_1, \dots, \mathbf{a}_n + \delta\mathbf{a}_n\}$, where each $\delta\mathbf{a}_i$ is a vector in the plane. Suppose that $\frac{\|\delta\mathbf{a}_i\|_2}{\|\mathbf{a}_i\|_2} \leq \Delta$, $i = 1, \dots, n$, where $\|\cdot\|_2$ denotes the Euclidean norm. This means that the relative error in the computed solution could be as large as $\Delta\sqrt{2}$, due to the uncertainty in the input data alone, since the Hausdorff distance between $\text{conv}(\{\mathbf{a}_1, \dots, \mathbf{a}_n\})$ and $\text{conv}(\{\mathbf{a}_1 + \delta\mathbf{a}_1, \dots, \mathbf{a}_n + \delta\mathbf{a}_n\})$ has the achievable upper bound of $\Delta\sqrt{2}M$. Thus, if criterion (2) is used, $\sqrt{2}$ can be taken as a condition number for the problem of planar convex hulls.

In comparison with the linear-equations case, this is a very satisfying result: the problem of computing planar convex hulls is always well conditioned. (In this respect, the convex-hull problem is closer to the problem of computing the eigenvalues of a real symmetric matrix than to the problem of solving $A\mathbf{x} = \mathbf{b}$: the symmetric eigenvalue problem is also always well-conditioned [6, p. 93].)

3.3 Step c: Stability of Algorithms

Just as in the case of linear equations, there exist both unstable and stable algorithms for the planar convex-hull problem, when criterion (2) is used. In particular, it was shown in [1] that *Graham_incremental* is unstable. This algorithm should therefore not be used (just as we should not use Gaussian elimination without pivoting to solve $A\mathbf{x} = \mathbf{b}$). On the other hand, a slight modification of the *Graham_Fortune* algorithm of [7] is numerically stable, that is, the computed answer is such that it is the exact solution for a perturbed problem for which the relative perturbation bound in problem space is at most $O(n\epsilon)$, where ϵ is the relative error of floating-point arithmetic. The algorithm uses a function called *TriangleTest* [7], first to establish lists of candidates for upper and lower chains,

and secondly to decide whether or not to retain the *middle* point of possible triplets in these chains. The proof of stability depends on *both* uses of *TriangleTest* to show, for example, that slightly perturbed versions of the candidates for an upper convex chain satisfy the following condition: either they were retained and form part of an actual upper convex chain, or they were not retained but nonetheless lie above the line determined by the two points with minimum and maximum x -coordinate. The slight modification, referred to above, is to use the *a priori* bounds for finite-precision floating-point arithmetic to implement the test of a “left turn” in *TriangleTest* in a fail-safe way, so that an ambiguous point is considered to part of a “left turn”, and dropped from the computed convex hull. (This modified test is described in detail in [10], and a similar test was used for another purpose in [11]).

3.4 Consequence

The consequence of this well-conditioning and stability is this: not only is it true that a stable algorithm such as *Graham_Fortune* will always produce an answer that is scarcely more in error than we should expect because of data uncertainty (this conclusion follows from stability), it is true in addition that the actual error in the computed solution is small (this follows from well-conditioning). We are in the situation illustrated in Figure 1. The overall situation is illustrated in Figure 4, where p_1 is the true problem to be solved, p_2 is the problem presented to the method, and p_3 is the problem for which the method actually finds an exact solution. This is a pure backward error analysis, with a well-conditioned problem. Even if (2) were replaced by a criterion that rendered the problem ill-conditioned, however, it would remain true that the algorithm always produces

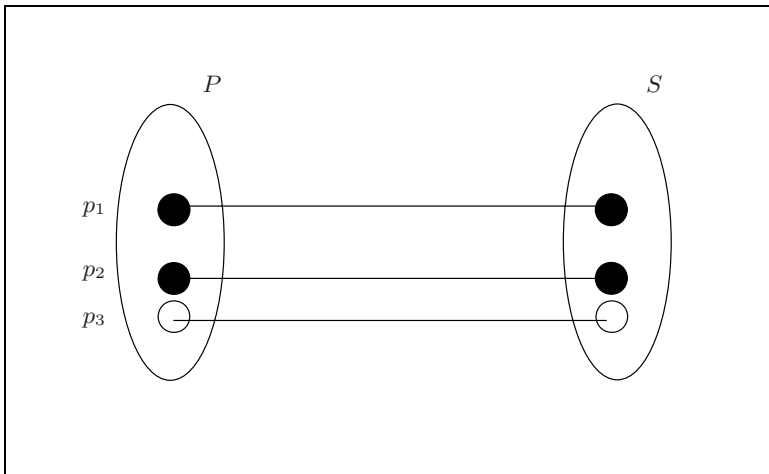


Fig. 4. Overall situation

an answer that is scarcely more in error than we should expect because of data uncertainty.

4 Conclusion

In order to prove theorems about the adequacy of numerical algorithms in computational geometry, we must define how to measure adequacy. Furthermore, in the case where data is uncertain, it is worthwhile to do a perturbation analysis, and seek stable solution methods. Carrying out these steps in the context of the planar convex-hull problem shows that the numerical difficulties described in [1] are unexceptional.

References

1. Kettner, L., Mehlhorn K., Pion, S., Schirra, S. and Yap, C. Classroom examples of robustness problems in geometric computations. *ESA '04: Proceedings of the 12th Annual European Symposium on Algorithms*. 702-713, Bergen, Norway, September 2004. Springer.
2. Graham, R. L. An efficient algorithm for determining the convex hull of a finite planar set. *Information Processing Letters*, 1:132-133, 1972.
3. Cohen, I. B. *Revolution in Science*. Harvard University Press, 1985.
4. Stewart, N. F. Science and computer science. *ACM Comp. Surveys* (27), No. 1, 39-41, 1995.
5. Kahan, W. M. A survey of error analysis. *IFIP '71*, North Holland, 1214-1239, 1971.
6. Wilkinson, J. H. *The Algebraic Eigenvalue Problem*. Clarendon Press, Oxford, 1965.
7. Fortune, S. Stable maintenance of point set triangulations in two dimensions. *Proceedings of the 30th annual IEEE Symposium on Foundations of Computer Science* Vol. 30, 494-499, 1989.
8. Hoffmann, C. M. and Stewart, N. F. Accuracy and semantics in shape-interrogation applications. *Graphical Models* 67, No. 5, 373-389, September 2005.
9. Andersson, L.-E., Peters, T. J. and Stewart, N. F. Selfintersection of composite curves and surfaces, *Computer Aided Geometric Design* 15, No. 5, 507-527, 1998.
10. Jaromczyk, J. W. and Wasilkowski, G. W. Computing convex hulls in a floating point arithmetic. *Computational Geometry* 4, 283-292, 1994.
11. Fortune, S. Numerical stability of algorithms for 2D Delaunay triangulations. *International Journal of Computational Geometry and Applications* (5), No. 1, 193-213, 1995.

Reply to “Backward Error Analysis . . .”

Lutz Kettner, Kurt Mehlhorn, Sylvain Pion, Stefan Schirra, and Chee Yap

We highly welcome the opportunity to comment on D. Jiang and N. F. Stewart’s paper in these proceedings. The paper refers to our ESA 2004 paper “Classroom Examples of Robustness Problems in Computational Geometry”. We quote from the introduction of the full version of our paper.¹

The algorithms of computational geometry are designed for a machine model with exact real arithmetic. Substituting floating-point arithmetic for the assumed real arithmetic may cause implementations to fail. Although this is well known, it is not common knowledge. There is no paper that systematically discusses what can go wrong and provides simple examples for the different ways in which floating-point implementations can fail. Due to this lack of examples, instructors of computational geometry have little material for demonstrating the inadequacy of floating-point arithmetic for geometric computations, students of computational geometry and implementers of geometric algorithms still underestimate the seriousness of the problem, and researchers in our and neighboring disciplines still believe that simple approaches are able to overcome the problem. In this paper, we study simple algorithms for two simple geometric problems, namely computing convex hulls and triangulations of point sets, and show how they can fail and explain why they fail when executed with floating-point arithmetic.

We believe that the paper and its companion web page will be useful in teaching computational geometry, and that even experts will find it surprising and instructive in how many ways and how badly even simple algorithms can be made to fail. The companion web page² contains all sources and allows the reader to perform our and further experiments. Numerical analysts are well aware of the pitfalls of floating point computation (G.E. Forsythe: Pitfalls in Computation, or Why a Math Book Isn’t Enough, Amer. Math. Monthly, 77, 931–956, 1970). Forsythe’s paper and many numerical analysis textbooks contain instructive examples of how popular algorithms, e.g., Gaussian elimination, can fail when used with floating point arithmetic. These examples have played a guiding role in the development of robust numerical methods. Our examples are in the same spirit, but concentrate on the geometric consequences of approximate arithmetic. While sophisticated machinery was developed for making numerical computations reliable over the past 50 years, a corresponding machinery for geometric computation does not yet exist to the same extent. However, significant progress was made over the past 15 years. Approaches to reliable geometric computing include the exact computation paradigm, approximate algorithms, and perturbation methods. In our recent courses on geometric computing, we have used the warning negative examples of our paper to raise student awareness for the problem and then discussed these approaches. D. Jiang and N.F. Stewart’s suggestion of backward analysis and the papers cited by them would be discussed under the heading approximate algorithms.

¹ <http://www.mpi-inf.mpg.de/~{mehlhorn}/ftp/ClassroomExamples.pdf>

² <http://www.mpi-inf.mpg.de/~{kettner}/proj/NonRobust/>

Two Map Labeling Algorithms for GIS Applications

Marina L. Gavrilova

Department of Computer Science,
University of Calgary, Calgary, AB, Canada
marina@cpsc.ucalgary.ca

Abstract. Driven by the industrial challenge of labeling maps for GIS applications, we investigate the problem of computing the largest convex partitioning of the map P such that the rectangular axis-parallel label L can be placed in it. The map region to be labeled is in general non-convex and may contain holes. Our main result is the new polygonal area removal (PAR) algorithm to identify the area within P where the center of the label L can be placed. We then derive a new and faster algorithm based on the sweep technique that determines the complete set of maximum inscribed rectangles (MIR) in P in the most common case when rectangle sides have an axis-parallel orientation. The set of all maximum inscribed rectangles is then post-processed to produce the best size/orientation combination of the final label placement depending on the specific requirements from the end users.

Keywords: map labeling for polygons with holes, polygonal area removal, sweep algorithm, set of maximum inscribed rectangles, GIS.

1 Introduction

The area of geomatics engineering covers surveying, remote sensing, geographic information systems and other topics concerning the capture and management of spatial information. In all of the above areas, problems related to limitations of two-dimensional representation of geographical information arise. One of those problems is known as the map labeling problem, whereas the given portion of the two-dimensional map shall be marked, or labeled, with the specific information. The question of how to find the appropriate representation and how to position it within the given area remains at a center of discussion of cartographers, GIS software developers, users and researchers alike.

The paper describes the solution developed at the request from the GIS research community and the industry. It is currently being tested in the industrial settings and incorporated in the commercial production. The problem in general settings is outlined below. Given a cartographic map, one need to compute a largest convex partitioning of the map area P such that the rectangular axis-parallel label L can be placed in it. The map region to be labeled is in general non-convex and may contain holes.

The solution to the problem involved both computational as well as conceptual issues. Computational issues arise from the need to process potentially very large data

files containing geographical information. The developed solution should be versatile, efficient in terms of the required memory and especially computational time, and should be easily implemented. Conceptual issues range from the pressing need for standardization and interoperability in GIS (Geographical Information Systems) to the conceptualization of space in the context of diverse spatial processes. The solution therefore should be easily integrated as part of the existing GIS software and be upgradeable. The mathematical aspects of the problem also shall not be neglected. The algorithm should be mathematically sound, as well as to provide a unique methodological approach to the problem. Having the above in mind, the solution to the problem was developed. Our main result is the novel and efficient polygonal area removal (PAR) algorithm to identify the area within P where the center of the label L can be placed. We then derive a new and faster algorithm based on the sweep-based technique that determines the complete set of maximum inscribed rectangles (MIR) in P in the case when rectangle sides have an axis-parallel orientation.

The paper is structured in the following way. In Section 2, the literature survey of articles pertaining to map labeling was conducted. Section 3 formally defines the general problem and presents the polygonal area removal algorithm for the generalized case. Section 4 describes the detailed solution to the sub-problem of determining the complete set of maximum inscribed rectangles for P in the case of axis-parallel polygonal edges. Section 5 estimates the algorithm complexity and discusses implementation. Section 6 provides the conclusion.

2 Relevant Research

In computational geometry area, the problem of inscribed sphere, a largest inscribed rectangle and other planar geometric shapes has been well known for the last few decades. The problem was recently restated as the problem of finding the maximum independent set in the intersection graph of n axis-parallel rectangles. Agarwal et.al. [1] gave a $(1+1/k)$ -factor algorithm with an $O(n \log n + n^{2k-1})$ time bound for the case of rectangles of unit height; and in the general case, Berman et. al. [3] gave a $\lfloor \log_k n \rfloor$ -factor algorithm with an $O(n^{k+1})$ time. The results were recently improved in Chan [4]. However, these algorithms are too expensive to be implemented in practice. Thus, an approximation technique should be used.

A number of variations of the above problem were also studied. Jiang et.al. [7] recently reported results on new bounds on map labeling with circular labels. A special case of map labeling problem with specific point location were considered by Roy et.al. [8]. Finding the connected components and a maximum clique of an intersection graph of rectangles in the plane was elegantly solved in Imai and Asano [6]. The algorithm for circular-arc graphs, which finds a maximum independent set and a minimum covering by disjoint completely connected sets or cliques was developed by Gupta et.al. [5].

The research was dictated by the needs of the GIS software developers, private companies working with cartographic applications and researchers concentrating on applied aspects of GIS. A comprehensive survey and analysis of models and efficient algorithms for rectangular maps can be found in [2], as a result of extensive project on

automated text placement on maps. The solution was modified to fit the specific applied problem of real-time map labeling for personal navigation in [10], and the problem of diagram placement on maps in [9].

The presented results are unique in a way that a specific problem dictated by the industry is addressed in a novel way. The solution developed is aimed at satisfying the requirements of the given problem as well as providing an elegant algorithmic approach that is also easy to implement and integrate with the given GIS database. We found no analogy to the given solution in the literature on map labeling in computational geometry or in cartography applications.

3 The General Problem of Map Labeling

Problem 1. Given a simple polygon P possibly with holes, and a rectangle R with sides r_x and r_y , determine whether R can be inscribed in P . If the outcome is positive, return the coordinates of the inscribed rectangle.

The developed algorithm proceeds by “cutting off” portions of the polygon P which can not contain the center of the inscribed rectangle. The edges of P are traced by an “eraser” in the form of the rectangle R . If there is an area left inside P that did not get to be removed, then the center of R can be positioned anywhere inside this area (see dark shaded area in the middle of P in Figure 1).

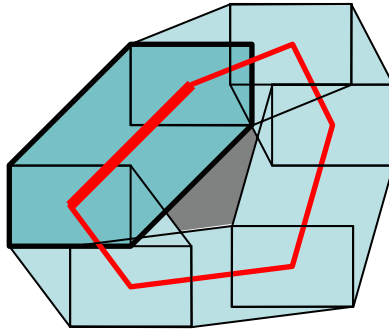


Fig. 1. The illustration to polygonal area removal algorithm – dark shaded area in the middle of the polygon is the algorithm outcome

In Figure 1, the polygon area removal algorithm is illustrated. For each edge e of P , a hexagon H_e is constructed such that the rectangle R that is being inscribed belongs entirely to this hexagon as well as lies inside the rectangle R . Next, the difference R without H_e is computed. The process continues for the next edge until the remaining (outcome) polygon is empty, then the algorithm stops, reporting “impossible to inscribe”. Otherwise, the next edge is considered, until hexagons for all edges have been removed from R . The remaining area within P that was not removed by the process is the algorithm outcome, i.e. the area where the center of the inscribed polygon R can be placed.

The following Lemma arises from the observations on algorithm performance:

Lemma 1. Consider the “erased” part P_e , i.e. the union of all H_e hexagons. Then the following statements are true: (1) any rectangle R whose center belongs to P_e intersects some edge of P ; and (2) for any rectangle R that intersects some edge of P , its center belongs to P_e .

Thus, it follows from the *Lemma 1* that if a rectangle R intersects with a side of P , then R 's center would have been “erased”. So, if R 's center belongs to the “un-erased” area of P , then R 's center belongs to P , and its sides don't intersect with P sides. Therefore, the complete R belongs to P . This proves the correctness of the algorithm.

Now, we have to prove that the algorithm will always find a solution whenever it exists. Assume that the solution exists and consider the inscribed rectangle R . From *Lemma 1*, it follows that its center does not belong to the “erased” part P_e . Therefore, it belongs to the “un-erased” area. Thus, we are guaranteed that the algorithm will arrive to this solution.

The algorithm complexity can be estimated as follows. Intersecting a hexagon with an N -side polygon takes $O(N)$. Consequently, the algorithm will run in $O(N^2)$ time.

4 Set of Maximum Inscribed Rectangles Algorithm

While the above algorithm is general and works for most of the cases, there is a very common situation when the rectangle edges (as well as hole inside this rectangle edges) are parallel to the coordinate axes. The development of a faster algorithm to handle such cases is of the highest priority to many R&D companies working in GIS and cartography areas. Thus, this section is devoted to the solution to the problem of determining the complete set of maximum inscribed rectangles for P for this most common type of polygons. The powerful sweep- based technique described below is utilized for this purpose. The method is now described in details.

Definition 1. Given an axis-parallel polygon P . A rectangle R_m inscribed in P is called a *maximum inscribed rectangle* (MIR) if there is no other inscribed rectangle Q such as R_m belongs to Q .

Lemma 2. Any inscribed rectangle R belongs completely to some maximum inscribed rectangle R_m .

Proof. It follows from the definition of the MIR. We can start increasing the size of R until it touches some sides of P and can not be increased any more. This “blown up” version constitutes a MIR, and it contains the initial rectangle R .

As follows from *Lemma 2*, the set of MIRs can be used to answer queries about inscribing rectangles of varying sizes into P . Indeed, once the set of MIRs has been computed, for a given query rectangle $R=(r_x, r_y)$, we determine if there's a MIR that is of same size as R or larger. If there is, then R can be inscribed into P .

Thus, the set of MIRs can be used to solve the following problem – for a fixed axis-parallel polygon P and a query rectangle R we should determine quickly whether R can be inscribed into P .

First of all, let us introduce a specific data structure to answer such queries. All MIRs are sorted by their increasing width. Then, for each MIR R_i in the list, we find

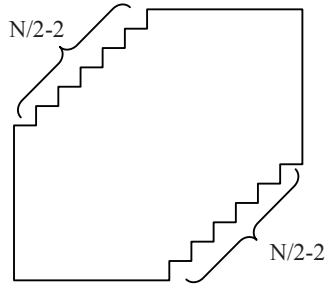


Fig. 2. $O(N^2)$ maximum number of inscribed rectangles

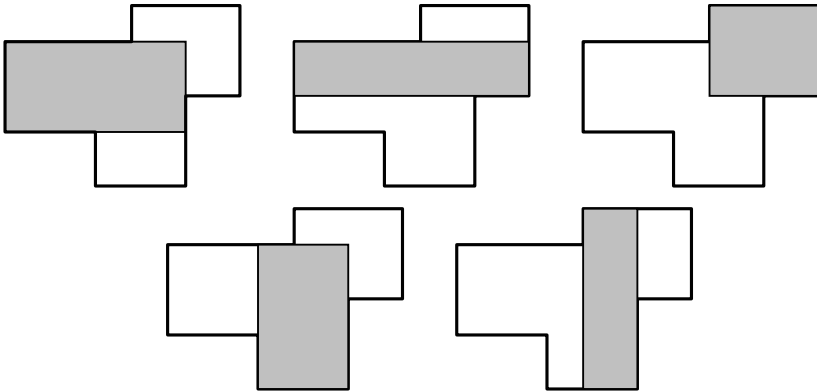


Fig. 3. Example: The set of all maximum inscribed rectangles

the highest MIR among the ones that lie to the right (i.e. are wider than R_i). Then, the query can be answered in $O(\log N)$ – first we find the first MIR R_i such that it is wider than the query R . Then, we compare R with the tallest MIR R_j that R_i references. If R fits in R_j , then it is reported as the answer.

Now, let us estimate the largest number of MIRs. Note that a polygon with N edges may contain up to $O(N^2)$ maximum inscribed rectangles, see Figure 2.

Finally, let us provide the solution to this problem.

Problem 2. Determine the complete set of maximum inscribed rectangles for P .

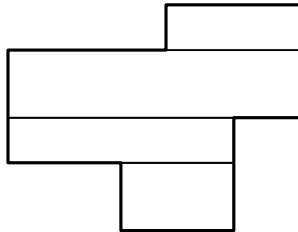


Fig. 4. Splitting R into horizontal polygons

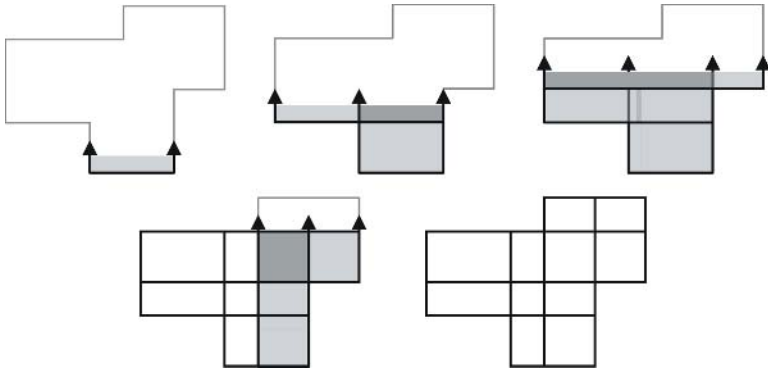


Fig. 5. Vertical sweep example

Algorithm description

1. Split P into a set of horizontal polygons, sorted in vertical direction (see Figure 4).
2. Process polygons one by one, starting from the bottom. Maintain the set of maximum inscribed rectangles.

Data structures

1. Queue Q – the set of horizontal segments sorted by the increasing y coordinate
2. Wavefront W – the set of “U-rectangles”. These are the U-shaped figures open from the top. Each U-rectangle is defined by the intersection of the maximum inscribed rectangle with the horizontal sweepline. Wavefront W is thus represented by a sorted set of segments. Each U-rectangle is defined by three segments – one at the bottom and two on the sides.
3. Output – the set of maximum inscribed rectangles.

Processing an event

An event is the addition of the next horizontal line segment taken from the queue Q . The eight possible cases of segment alignment depicted in Figure 6 below are possible:

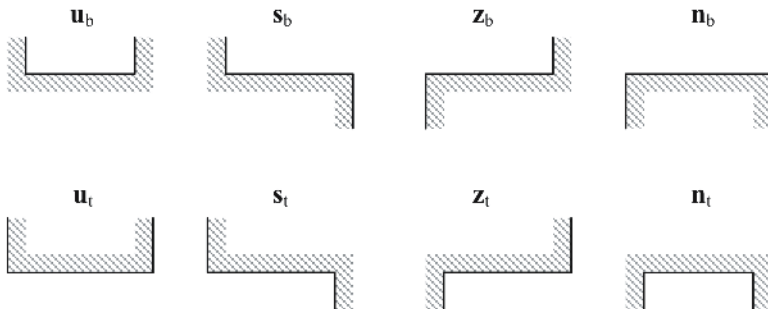


Fig. 6. Eight possible cases of segment alignment

In Figure 6 above, the hatched areas represent the “outside” of polygon P .

In each of the b-cases (“bottom” edges), one new U-rectangle is inserted into the wavefront.

u_b case. The U-rectangle is defined by the 3 segments being inserted (see Figure 7).



Fig. 7. Processing u_b event

s_b case. We find the nearest vertical segment to the right, and it defines the right side of the U-rectangle (see Figure 8 left).



Fig. 8. Processing s_b and z_b events

z_b case is similar to s_b , but to the left (see Figure 8 right).

n_b case. We find the nearest vertical segments to left and right, they define the sides of the U-rectangle (see Figure 9).



Fig. 9. Processing n_b event

For each of the t-cases (“top” edges), the set of U-rectangles in W is transformed.

First, we locate each rectangle that intersects with the horizontal segment being inserted. Then, the intersecting U-rectangle is “closed” from the top and added to the output. Finally, zero, one, or two new U-rectangles are inserted into the wavefront.

u_t case. The resulting maximum inscribed rectangle is shown in Figure 10.

There are four possible cases, where new U-rectangles are inserted from either side of the newly added segment S . The new U-rectangles are inserted as shown in Figure 11, depending on the relative positions of the inserted segment S and the U-rectangle R being closed. They “inherit” the base value of R and one of its “side” values. The other “side” value is taken from the neighboring segments of S . The new U-rectangle is only inserted if the “base” segment of the rectangle R intersects S along the x axis (see Figure 11).

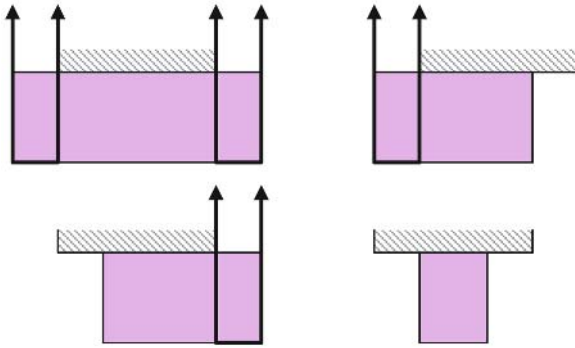


Fig. 10. Processing u_t event

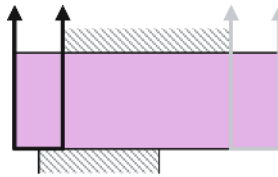


Fig. 11. Processing u_t event: only one new U-rectangle is inserted

In Figure 11, the right U-rectangle is not inserted because it does not have a “base”.
 s_t case. In this case, one or zero new U-rectangles are inserted. Again, the new rectangle is only inserted if it has a non-empty “base” (see Figure 12).

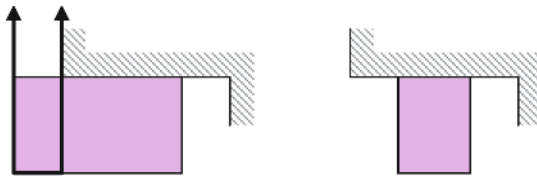


Fig. 12. Processing s_t event

z_t case is similar to s_t case.

n_t case. In this case, no new U-rectangles are inserted into the wavefront (see Figure 13). Thus, all possible cases have been considered above. The sweep algorithm stops when all horizontal segments have been processed.

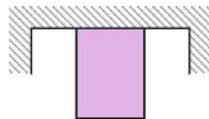


Fig. 13. Processing n_t event

5 Complexity Estimate

The complexity of the algorithm depends on the maximum number M of MIRs that can exist. Above, this number was estimated as $O(N^2)$. However, in most cases this number is just a constant. Processing an event involves considering each active U-rectangle, which is a part of some MIR. An event is processed in constant time. Thus, the total algorithm complexity is $O(MN)$.

After the set of all maximum inscribed rectangles was found, it is then subjected to post-processing to produce the best size/orientation combination of the final label placement depending on the specific requirements from the end users. For instance, if the label to be placed should have the shape that resembles most the square, such maximum rectangle can be picked from the set. Or, if the vertical orientation of the label is preferred to the horizontal one, all vertical maximum rectangles can be selected.

The algorithm prototypes were implemented in C# environment and runs under Windows operating system. The preliminary results on algorithm efficiency show the linear performance of the algorithm on the number of edges in the polygon R . The algorithm is currently goes through the industrial testing and production incorporation process.

6 Conclusions

The paper presents two novel and efficient algorithms for map labeling problem in GIS applications developed by the request from a research and development company working on mapping and cartography applications. We provided the general PAR algorithm to identify the area within P where the center of the label L can be placed based on the given label size R . We also derived the sweep-based $O(MN)$ algorithm that determines the complete set of maximum inscribed rectangles in P , which can be used to answer queries in $O(\log N)$ time. The algorithm prototype was implemented and is currently being tested in the industrial settings. The post-processing analysis of the resulting set of maximum polygons and matching the set characteristics to the requests from the end users presents an interesting topic for further investigation.

Bibliography

1. Agarwal, P.K., van Kreveld, M. and Suri, S. "Label placement by maximum independent set in rectangles," *Comput. Geometry: Theory Appl.* **11** (1998), pp. 209–218.
2. Bekos, M.A., Kaufmann, M., Symvonis, A. and Wolff, A. "Boundary labeling: Models and efficient algorithms for rectangular maps," In Janos Pach, editor, *Proc. 12th Int. Symposium on Graph Drawing (GD'04)*, Lecture Notes in Computer Science, New York, 29 September -- 2 October 2004. Springer-Verlag.
3. Berman, P., Bhaskar Das Gupta, S. Muthukrishnan, and Suneeta Ramaswami. Efficient approximation algorithm for tiling and packing problems with rectangles. *Journal of Algorithms*, 41(2):443-470, 2001
4. Chan, T. M. "A note on maximum independent sets in rectangle intersection graphs," *Information Processing Letters*, 89(1):19-23, 2004

5. Gupta, U.I., Lee, D.T. and Leung, J.Y.-T. "Efficient algorithms for interval graphs and circular arc graphs," *Networks* **12** (1982), pp. 459–467
6. Imai, H. and Asano, T. "Finding the connected components and a maximum clique of an intersection graph of rectangles in the plane," *J. Algorithms* **4** (1983), pp. 310–323.
7. Jiang, M., Bereg, S., Qin, Z. and Zhu, B. "New bounds on map labeling with circular labels," In Rudolf Fleischer and Gerhard Trippen, editors, *Proc. 15th Annual International Symposium on Algorithms and Computation (ISAAC'04)*, volume 3341 of *Lecture Notes in Computer Science*, pages 606-617, Hong Kong, 20-22 December 2004
8. Roy, S., Goswami, P. P., Das, S. and Nandy, S. C. "Optimal algorithm for a special point-labeling problem," *Information Processing Letters*, 89(2):91-98, 2004.
9. van Kreveld, M., Schramm, É. and Wolff, A. "Algorithms for the placement of diagrams on maps," In Dieter Pfoder, Isabel F. Cruz, and Marc Ronthaler, editors, *Proc. 12th Int. Symp. ACM GIS (GIS'04)*, pages 222-231
10. Zhang, Q. and Harrie, L. "Real-time map labelling for personal navigation," In *Proc. 12th Int. Conf. on Geoinformatics*, Gävle, Sweden, 7-9 June 2004.

Surface Reconstruction from Large Point Clouds Using Virtual Shared Memory Manager

Josef Kohout, Michal Varnuška, and Ivana Kolingerová

Centre of Computer Graphics and Data Visualization,
University of West Bohemia, Plzeň, Czech Republic
{besoft, miva, kolinger}@kiv.zcu.cz
<http://herakles.zcu.cz/>

Abstract. Surface reconstruction is a common problem in computer graphics. Given a set of points sampled from some surface, a triangle mesh interpolating or approximating the points is to be obtained. One of very often used techniques for solving this problem is the selection of surface triangles from the set of Delaunay tetrahedronization faces. In the case of large data, it is difficult to obtain the tetrahedronization due to its huge memory requirements. One of possible solutions is to use distributed computing. Here, we describe the newly developed VSM (Virtual Shared Memory) distributed toolkit and its utilization for the task of surface reconstruction. By our approach, we were able to process dataset having 1.4M points on 4xP4 interconnected via 100Mb Ethernet in 6 hours. About 5GB of memory was consumed during the reconstruction.

1 Introduction

The problem of surface reconstruction belongs to common tasks in today's computer graphics and therefore many algorithms have been developed during the last twenty years. The applications from many areas of human activities, such as CAD, archeology, medicine, architecture, e-commerce, etc., need to work with piecewise-linear approximations or interpolations of real object. One of the most used possibilities of model acquisition is to digitize the real object with some 3D scanner followed by the reconstruction of the obtained point cloud by a reconstruction algorithm.

Modern scanning devices are able to sample more than 10 millions of points and many algorithms which have been developed during last years are not usable to process so big amount of data in one piece. It holds, especially, for the algorithms based on Delaunay tetrahedronization which is often used as a supportive technique for the surface reconstruction.

This paper consists of seven sections. Section 2 contains the formal definition of the surface reconstruction task and gives a brief survey of existing methods. Section 3 briefly describes the CRUST algorithm which is based on Delaunay tetrahedronization and which was developed by Nina Amenta et al. [1]. This algorithm was chosen as a base for our approach. In Section 4, we describe our VSM (Virtual Shared Memory) toolkit which is used as a distributed core of our surface reconstructor. The description of the reconstructor itself is

given in Section 5 and the results of our experiments are presented in Section 6. Section 7 concludes this paper.

2 Surface Reconstruction

The problem of the surface reconstruction can be formulated as follows: Given a set of points P which are sampled from a surface S of a real object, $S \in E^3$, construct a surface S' so that the points of $P\{p_i, i = 1, 2, \dots, N\}$ lie on S . Let us note that the sampled points typically contain only 3D coordinates without other surface information (such as normal vectors). For the reconstruction output S' , structures such as triangle mesh (the most often used structure), Bezier patches or NURBS are used.

Many algorithms based on various approaches have been developed for the surface reconstruction problem. The importance of the task has grown in the last years as the devices used for points acquisition became cheaper and more applicable. Generally, the algorithms are based on warping, incremental surface construction, distance function methods and spatial subdivision. The description of these methods is out of the scope of this paper and can be found, e.g., in Mencl and Müllers [10] or in Bernardini and Rushmeiers papers [3]. We describe here only the main methods for large data reconstruction.

Typical real datasets, e.g. scans of statues [8], contain millions of points and, therefore, its processing (especially by a Delaunay based surface reconstructor) demands a lot of memory. For instance, in our implementation of the CRUST, we need at least 1GB of memory to process 250K of points. In practice, it is, however, often necessary to deal with even larger datasets; e.g., the model of Lucy has 14 millions of points.

As an application running under MS Windows operating system on 32-bits computer can use at most 2 GB, typical real datasets cannot be processed in an unmodified version in one step on one computer. We could use some kind of compressed data representation or out-of-core technique. Such an approach, however, would slow down the processing significantly. Therefore, the first possibility how to deal with large datasets is to reduce the number of points and reconstruct the surface from this smaller set. As it is necessary to store coordinates of all points, the reduction approach is useful up to about 130 millions of points (due to memory limitation).

Carr et al. [5] reduces the number of points and smoothes data using radial basis functions (RBF). Authors claim that their method is able to handle datasets with millions of points. According to the presented results, the processing, however, seems to be limited to datasets with about 3 millions due to the memory requirements needed for RBF. Let us note that the reconstruction of such a dataset would consume a couple of hours to be done.

Ivrissimtzis et al. [7] propose an interesting algorithm based on a learning neural network. The input dataset is randomly sampled and these samples are used as a training set for the initial neural mesh chosen as a tetrahedron. Other points are afterwards successively processed using this neural mesh. By the processing,

the neural mesh grows learning the geometry and the topology of the surface. When the algorithm stops, the surface is extracted from the neural mesh. A significant drawback with this approach is its time complexity (a couple of hours even for dataset with only 200K points).

Varnuška [12] finds for each point the nearest neighbour and merge these two points together. The process is repeated until the number of points is lower than some given threshold. Author suggests that if the information about merging was retained, it could be possible to insert removed points to the surface using LOD vertex expansion and so to improve the result. Indeed, it is possible for triangulations up to 10 mil. points (about 30 mil. triangles).

It is clear that the reconstructed surface obtained from a reduced dataset is just an approximation of the original surface. If the object to be reconstructed contains sharp edges or the ratio of the original size and the reduced size is high, reduction solutions may produce an incorrect surface. It is a serious problem if the reconstructed surface should be accurate; e.g., for the manufacturing process.

Another way was presented by Dey et al. in [6]. Their approach, which is based on Delaunay tetrahedrization, is built on the divide&conquer strategy. It subdivides the input dataset into several smaller groups whose min-max boxes overlap, reconstructs the surface using COCONE (Delaunay based reconstructor) in each group and then merges surfaces together. By this approach, the authors were able to handle 3.5 millions of points in 3 hours. Two problems appear: merging may not be an easy implementation task and, if the chosen overlapping of boxes is insufficient, the reconstructed surface may suffer from artefacts, especially for non-uniformly sampled points or noisy data.

Bernardini et al. [2] describe another algorithm dealing with large data. Their ball-pivoting algorithm is relatively simple but powerful approach. Starting from the seed triangle, the surface is incrementally grown by adding other triangles which are recognized using the ball pivoting around each edge. This approach was used, for example, for the reconstruction of the Michelangelo's Florentine Pieta (7.2M points). The main disadvantage of the algorithm is that it requires that the sampled points are equally sampled anywhere and surface normal in each point must be known.

3 CRUST Algorithm

We use already developed one-pass CRUST algorithm by Nina Amenta [1] for surface reconstruction. The main idea of this approach is that the surface triangles can be separated from the other triangles contained in Delaunay tetrahedrization (DT) of the input point set using the information from the Voronoi diagram. The geometrical properties of the Voronoi diagram (created by the dualization from DT) can be utilized using the concept of poles. The poles are some vertices of the Voronoi diagram with the following properties. The positive pole $p+$ is the farthest Voronoi vertex (VV) of the Voronoi cell of some point p , the negative pole $p-$ is the farthest VV on the other side of the plane, when we take the vector from p to $p+$ as the normal vector of such a plane, see Figure 1.

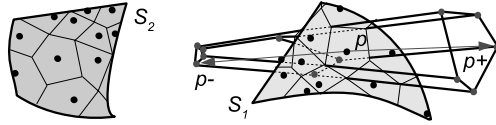


Fig. 1. S_1 , S_2 are two parts of some surface, black dots are the input points. The Voronoi cell for a point p is shown; p_+ and p_- are its positive pole and negative pole, respectively.

For a successfully sampled surface the Voronoi cells are very thin, the vector (p_+, p) is almost perpendicular to the surface and it is used as an estimation of the normal vector of p .

The set of surface triangles T , called CRUST, is selected from the set of triangles formed by the faces of all tetrahedra using the dual Voronoi edge of the tested triangle and estimated normal vectors in triangle's vertices. The set T may not form a manifold (e.g. some overlapping triangles may appear) hence the surface has to be extracted. The step of manifold extraction is not presented here, it can be found, e.g., in [13].

We choose this algorithm, because it is provably correct, clear to understand, it can be simply implemented and we can combine it with our distributed DT code. It produces good results for well sampled smooth data. A big advantage is that it is not very sensitive to changes in the sampling density.

4 VSM (Virtual Shared Memory)

In order to simplify the parallelization of the CRUST surface reconstructor, we developed a toolkit simulating the shared memory and offering data read-write operations and also means for synchronization between processors. We call this toolkit Virtual Shared Memory (VSM) manager. The main idea is that an application does not access data directly but through calls of appropriate functions of the VSM which provide a transparent access to local and remote data. Figure 2 shows a schema of the distributed computing under the VSM.

The idea to simplify the parallelization for parallel computers with distributed memory by the use of a hardware or software solution that simulates the shared memory is very old, it was proposed by Kai Li in [9], but it has become popular in recent few years. While the first works were mainly intended for the massive parallelism, recent solutions are dedicated to clusters of workstations. They differ in the level of abstraction that provide. Some of them allow users to continue to



Fig. 2. A distributed computing using the VSM

operate with traditional 32-bits pointers limiting them to access at most 2GB of total memory. Such systems are typically used by applications that are quite time consuming but do not require a big amount of memory. Other solutions overcome this drawback by introducing a generalized 64-bits long pointer, which either requires unnecessarily complicated changes in user source codes or the use of specialized compiler shipped within the solution (e.g., commercial systems Linda or Paradise). In [4], Bilas gives a nice survey of virtual shared memory systems and discusses problems with their performance.

The main part of our approach is the VSM library (briefly the VSM). It is an object library dynamically or statically linked to a user application. From the distributed point of view, there is a necessity to have two programs: master and worker. In the system, there is just one running instance of master program and any number of running instances of worker program. One instance runs, typically, on one computer. It is possible to start more instances on one computer but it degrades the performance of computation, except for the case that the user application introduces an intensive synchronization. The master program is responsible for the initialization of computation, which usually involves displaying of a setup dialog allowing the user to set parameters for the calculation, e.g., the name of data set, thresholds for filtering, etc. The worker program is dedicated for the calculation only and it cannot interact with the user. Very often master and worker programs are written according to the farmer-worker programming model. However, it is not a condition and both programs may implement the same algorithm, e.g., both participate to the construction of the Delaunay tetrahedrization.

4.1 Initialization of Distributed Computing

The master program is executed manually by the user and it calls the master initialization routine of VSM passing the minimal and maximal number of computers to be used for the computation and the name of configuration file as arguments. From the specified file, the VSM reads UNC or IP addresses of computers available in the cluster. For each such an address, the VSM attempts to contact a special utility, the VSM admin, running on the background of the appropriate computer and sends it the worker program (including all required binary and initialization files). Usually, the VSM admin is launched automatically by the operating system when it starts and terminated when it shutdowns. The utility stores the sent files onto the local disk and executes the worker program.

When the worker program starts, it calls the VSM worker initialization routine. This routine starts a listening thread responsible for receiving of all incoming requests and waits until the computation can start. The utility sends a confirmation to the computer from which the request came. When a sufficient number of workers, i.e., instances of worker program, run, the VSM master initialization routine assigns a unique number identification, starting from zero, to every instance. The master is always denoted by the zero value. Afterwards, it sends a message containing all addresses and identifications to every worker. Each worker establishes the connection with other workers. Now, everything is

prepared for the computation. Initiation routines finish and the execution of user code proceed.

At the beginning of computation, the application (both master and worker) calls the VSM to register data structures that should be distributed over computers. During the registration, it specifies a user unique identification of data type, the size of this type, references (pointers) used in this type and a maximal number of elements of this data type that can be created in the local memory. In our case, we register the data structure describing a tetrahedron and a triangle.

Typically, the application also calls the VSM to create synchronization primitives. Critical sections, events and barriers are supported. A barrier is used to synchronize work of a group of processors. When a processor reaches the barrier, it has to wait until all its counterparts reach this barrier. Barriers are an ideal choice for an algorithm divided into stages where one stage must be finished before the algorithm can proceed with next stage, e.g., the Delaunay tetrahedrization must complete before the CRUST may start.

The VSM offers the use of so-called atoms. An atom is an indivisible piece of data, usually very small, that is stored in the local memory of one computer but it is accessible from any computer. Typically, the application exploits atoms to exchange small pieces of data such as values of counters, names of input data sets, settings of computation, etc. An access to an atom is considered always as an atomic operation, i.e., only one processor may operate with the same atom at one moment. Besides standard read and write operations, the VSM supports also more sophisticated operations, e.g., the operation that modifies the atom only if its value matches a given mask, which is useful for low overhead synchronization.

4.2 Operations with “Shared” Data Structures

Whenever the application needs to allocate a new element of the registered data type, instead of calling standard allocation routine, e.g., `new` or `malloc`, it calls the `Add` operation provided by the VSM for this purpose. If the request cannot be handled locally (e.g., because of an insufficient amount of available memory), the VSM creates the element remotely, constructs its local version in the cache. In both cases, a traditional pointer, 32-bits long, is returned to the application. This is very important because it allows to programmers to continue using of standard pointers, which means that the content of an element of data structures can be read and modified in the same way as in the original sequential program and, therefore, there is no need to change source code. Internally, the element, indeed, is identified by a 64-bits number.

When the application wants to operate with the content of data element for read-only purpose, it has to call the `Get` operation passing the full identification or, if the element is stored locally or it is cached, the traditional pointer to the element as an argument. If it is necessary, the VSM retrieves the data from the appropriate owner and places it into the cache. Afterwards, it retrieves all refereed elements and updates 32-bits pointers in the structure to point to proper place.

If the application needs to modify the element, it calls the `Edit` operation. As simultaneous modification must be avoided, the VSM in this operation attempts

to get for the caller an exclusive access to this element, i.e., to lock the element. If the access cannot be granted, the application is suspended until the blocking application finishes modification of the element. In the case that the waiting would cause a deadlock, the Edit fails and the calling application has to return in the control flow to the stable state and to call CancelUpdate operation. The VSM then undoes all not confirmed changes and unlocks all elements. If no deadlock is detected, the application has to call from time to time the Update operation to confirm the changes and to unlock elements. Both operations also reorganize the cache and release memory that is no longer needed. After their call, any pointer provided to the application by the VSM is invalid and, therefore, it is needed to call either the Get or the Edit again.

The VSM offers similar functionality for arrays of elements. An item in the array is accessed via pointer that is returned from the Get or the Edit operations called, naturally, with an index to the array as an argument. Using the indexer operator supported by almost any object oriented programming language, arrays in the original sequential code by objects can be superseded with minimal effort.

The advantage of the proposed VSM approach is the simplicity of its programming interface, which opens a possibility to parallelize a sequential algorithm even by a person not focused on distributed computing. Primarily, 32-bits pointers are supported; their translations to 64-bits long identifiers and vice versa are for the user transparent. It minimizes the number of changes to be done in order to parallelize the algorithm. On the other hand, the provided higher level of abstraction introduces quite a big overhead, especially for hierarchical structures. It harms the efficiency of algorithm parallelized with the VSM.

5 Distributed CRUST

We exploited the VSM toolkit for the distributed computing of the CRUST surface reconstruction. The original sequential reconstructor is written in Borland Delphi 7.0 and it contains several tens thousands lines of source code. As the Delphi programming language does not offer the indexer operator, the parallelization of access to arrays distributed over processors, unfortunately, needs significant implementation effort. Therefore, not every data structure consuming a lot of memory is distributed at present (we plan it in a near future), which limits the size of largest data set to 6 millions of points. Currently, we managed to distribute major data, such as the Delaunay tetrahedronization or output triangular surface. As the coordinates of points are accessed frequently from many routines, we decided to duplicate them on every processor. It is not too limiting and it increases significantly speed of the processing.

At the beginning of the reconstruction (indeed, after the registration of data structures and initialization of the VSM system), each processor loads the whole input dataset into the local memory. Next, the processor determines which points to handle. For this purpose, we use a modified Mueller algorithm [11] that ensures

almost balanced workload. It is based on a recursive division of the summed-area table constructed from the 3D grid that covers the minmax box of the data and, in every cell, contains the number of points lying in this cell.

The master then constructs the auxiliary big simplex (tetrahedron in our case) containing all points inside its interior and it uses an atom and an event to submit 64-bit long identification of this simplex to workers. This first tetrahedron represents the initial Delaunay tetrahedronization. Points are inserted successively into the Delaunay tetrahedronization. In each step, a simplex containing the point to be inserted inside in its interior has to be found and this simplex and appropriate simplices in the neighborhood are modified in such a manner to incorporate current point and to ensure that the tetrahedronization is the Delaunay tetrahedronization. Naturally, processors insert their points simultaneously. When the insertion is finished, the master removes from the tetrahedronization any simplex having at least one vertex of the first auxiliary tetrahedron.

In our current version, only the computation of the Delaunay tetrahedronization is parallelized, all remaining parts of reconstruction run sequentially on master. Therefore, it is necessary to transmit huge amount of data, which is time consuming. We suppose to decrease the amount of required network traffic and to speed-up the processing significantly by a proper parallelization of the whole reconstruction algorithm.

6 Results and Observations

The largest dataset that we have processed using the described approach had 1.4M points and it was a part of the original Lucy model dataset. Its reconstruction ran on 4xP4 2.7 GHz interconnected via 100Mb Ethernet. About 5GB of memory was consumed and the computation took about 6 hours. Figure 3 shows the result of the process and compares it with the result of reconstruction from dataset reduced to 200K by decimation method described in [12]. As it can be seen, if the decimation technique is used, some details (e.g., brow or lips) are lost.

Other examples of reconstructed surfaces of real datasets are presented in Fig. 4. Let us note that although the time spent by the construction of the Delaunay triangulation grows almost linearly with the size of data set, the time consumed by the remaining parts of the surface reconstruction process depends also on the complexity of object (i.e., whether there is some noise,

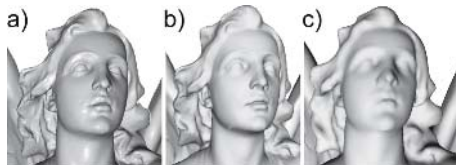


Fig. 3. The reconstruction of large dataset, a) the original from Stanford - point based rendering, b) by the distributed computation, c) by points decimation to 200K points




					
Points	137 062	Points	209 779	Points	437 645
Tetrahedra	935 304	Tetrahedra	1 322 057	Tetrahedra	3 041 391
Triangles	274 118	Triangles	419 500	Triangles	857 930
DT time	8 min 33 sec	DT time	9 min 5 sec	DT time	22 min 40 sec
Total time	1 hr 38 min	Total time	62 min 31 sec	Total time	2 hr 2 min

Fig. 4. Surface reconstruction of real data sets from Stanford and Cyberware

sharp edges, outliers, etc). Therefore, the reconstruction of a smaller dataset may take more time than the reconstruction of a larger dataset - see times for bone and club models.

Compared with the approach by Dey et al. [6] (as far as we know, the only one other approach that produces a surface interpolating the given points of large data using Delaunay tetrahedrization), our solution is supposed to be more robust (it does not suffer from artefacts that may appear in the surface reconstructed by Dey et al. algorithm). On the contrary, we require much larger time to process datasets. Let us, however, remind that at present, except for the construction of the Delaunay triangulation, the reconstruction runs on one computer only and, therefore, it has to communicate very often, which explains why the total time needed for the reconstruction is so large (i.e., several hours). As the reconstruction part in the serial version takes about 20% of Delaunay tetrahedrization time, the proper parallelization of the whole reconstruction would bring significant speed-up.

7 Conclusion

surface reconstruction algorithm based on the CRUST algorithm. Our approach is able to process large datasets that cannot be handled sequentially in one piece due to the memory limitation of sequential computers. Currently, only the computation of the Delaunay tetrahedrization, which is the most time and memory consuming step, is parallelized, all remaining parts of reconstruction run sequentially. Therefore, it is necessary to transmit huge amount of data, which significantly harms the efficiency of our approach, e.g., the processing of 1.4M data set required about 6 hours. As the computation of poles and normal vectors, extraction of surface triangles and the correction of wrong places are local operations, proper parallelization would bring a significant improvement. We intend to do it in our future work.

Acknowledgment

This work was supported by MSMT Czech Republic, Project No. LC 06008. The authors want to thank to the Cyberware and Stanford data repositories for real data and to prof. V. Skala for good working conditions.

References

1. N. Amenta, S. Choi, T. K. Dey, and N. Leekha. A simple algorithm for homeomorphic surface reconstruction. *Int. J. Comp. Geometry & Applications*, 12(1-2):125–141, 2002.
2. F. Bernardini, J. Mittleman, H. Rushmeier, C. Silva, and G. Taubin. The ball-pivoting algorithm for surface reconstruction. *IEEE Transactions on Visualization and Computer Graphics*, 5(4):349–359, 1999.
3. F. Bernardini and H. E. Rushmeier. The 3d model acquisition pipeline. *Comput. Graph. Forum*, 21(2):149–172, 2002.
4. A. Bilas. *Improving the Performance of Shared Virtual Memory on System Area Networks*. PhD thesis, 1998.
5. J. C. Carr, R. K. Beatson, B. C. McCallum, W. R. Fright, T. J. McLennan, and T. J. Mitchell. Smooth surface reconstruction from noisy range data. In *Proc. GRAPHITE*, pages 119–126. ACM Press, 2003.
6. T. K. Dey, J. Giesen, and J. Hudson. Delaunay based shape reconstruction from large data. In *Proc. of the IEEE Symp. on Parallel and Large-Data Vis. and Graphics*, pages 19–27. IEEE Press, 2001.
7. I. Ivrișsimtzis, W. Jeong, and H. P. Seidel. Using growing cell structures for surface reconstruction. In Myung-Soo Kim, editor, *Shape Modeling International 2003 (SMI 2003)*, pages 78–86, Seoul, Korea, May 2003. IEEE.
8. M. Levoy, K. Pulli, B. Curless, S. Rusinkiewicz, D. Koller, L. Pereira, M. Ginzton, S. Anderson, J. Davis, J. Ginsberg, J. Shade, and D. Fulk. The digital michelangelo project: 3d scanning of large statues. In *Proc. of ACM SIGGRAPH*, <http://www-graphics.stanford.edu/projects/mich>, pages 131–144, July 2000.
9. K. Li. *Shared virtual memory on loosely coupled multiprocessors*. PhD thesis, 1986.
10. R. Mencl and H. Müller. Interpolation and approximation of surfaces from three-dimensional scattered data points. In *Scientific Vis. Conf. (Dagstuhl)*, pages 223–232. IEEE/CS, 1997.
11. C. Mueller. Hierarchical graphics databases in sort-first. *Proceedings of IEEE Symposium on Parallel Rendering*, pages 49–57, 1997.
12. M. Varnuška. *Surface Reconstruction of Geometrical Objects from Scattered points*. PhD thesis, Dep. of Computer Science, University of West Bohemia, Pilsen, 2005.
13. M. Varnuška and I. Kolingerová. Improvements to surface reconstruction by crust algorithm. *SCCG 2003 Budmerice, Slovakia, Comenius University Bratislava*, pages 101–109, 2003.

Computing Terrain Multi-visibility Maps for a Set of View Segments Using Graphics Hardware*

Narcis Coll, Marta Fort, Narcis Madern, and J. Antoni Sellarès

Universitat de Girona, Spain
{coll, mfort, nmadern, sellares}@ima.udg.es

Abstract. A multi-visibility map is the subdivision of the domain of a terrain into different regions that, according to different criteria, encodes the visibility concerning a set of view elements. In this paper we present an approach for computing a discrete approximation of a multi-visibility map of a triangulated terrain corresponding to a set of view segments, for weak and strong visibility, by using graphics hardware.

1 Introduction

Visibility information of terrain areas is necessary in many Geographic Information Systems applications, such as path planning, mobile phone networks design and environmental modelling.

The visibility map is a structure that encodes the weak or strong visibility of a terrain concerning a view element (point, segment, triangle, etc.) belonging to or above the terrain. Visibility structures for several view elements, that we generically call multi-visibility maps, can be defined by combining the visibility map of such elements according to some operators, for example intersection, union or counting. Taking into account that the representation of a terrain is a rough approximation of the underlying terrain and that the combinatorial complexity of exact multi-visibility maps is too complex to compute them exactly, an approximation of a multi-visibility map is often considered sufficient.

Algorithms for computing the visibility map corresponding to a point are available in [3, 7, 8, 11]. There also exist some recent papers dealing with multi-segment visibility [5] and inter-region visibility [5, 12]. In [5] a multi-visibility map is approximated using an algorithm based on an approach that reconstructs an approximation of an unknown planar subdivision from information gathered from linear probes of the subdivision [4]. The multi-visibility map is obtained by repeatedly executing an algorithm that computes segment-segment visibility in an exact fashion: the visible parts of a segment on the terrain from a view segment.

* Partially supported by the Spanish Ministerio de Educación y Ciencia under grant TIN2004-08065-C02-02. Marta Fort is also partially supported by the Spanish Ministerio de Educación y Ciencia under grant AP2003-4305. Narcís Madern is also partially supported by the Ministerio de Educación y Ciencia under grant BES2005-9541.

The increasing programmability and high computational rates of graphics processing units (GPUs) make them attractive as an alternative to CPUs for general-purpose computing. Recently, different algorithms and applications that exploit the inherent parallelism and vector processing capabilities of GPUs have been proposed [16]. In computational geometry there exist several algorithms that have a fast hardware-based implementation [1, 6, 9, 10, 13, 14].

In this paper we address the problem of computing approximate multi-visibility maps for a terrain modelled by a TIN concerning a set of view segments, for weak and strong visibility. Since we consider discrete approximations of multi-visibility maps, it suffices to compute solutions on a grid covering the domain of the terrain. For computational purposes, we discretize the domain of the terrain into pixels. This discretization allows us to exploit graphics hardware capabilities. Our approach repeatedly uses the skewed projection for representing segment-segment visibility in a bounded two-dimensional space. Once again, the discretization into pixels of this two-dimensional space allows us to quickly compute segment-segment visibility using graphics hardware.

2 Preliminaries

We model a terrain as the graph of a *Triangulated Irregular Network* (TIN), $(\mathcal{T}, \mathcal{F})$, formed by a triangulation $\mathcal{T} = \{T_1, \dots, T_n\}$ of the domain D (in the xy -plane), and by a family $\mathcal{F} = \{f_1, \dots, f_n\}$ of linear functions such that: a) function $f_i \in \mathcal{F}$ is defined on triangle T_i , $i = 1..n$; b) for any pair of adjacent triangles T_i and T_j , f_i and f_j coincide in $T_i \cap T_j$. For any triangle $T_i \in \mathcal{T}$, $f_i(T_i)$ is a triangle in space called a *face* of the terrain, and the restriction of f_i to an edge or a vertex of T_i is called an *edge* or a *vertex* of the terrain.

A *view element* v (point, segment, triangle, etc.) is an element belonging to or above the terrain, i.e. its projection onto the xy -plane is contained in D , and for any point (x, y, z) of v , $z \geq z'$, where (x, y, z') is a point on the terrain. A point P on the terrain is: *visible* from a view point V if the interior points of the line segment VP with endpoints V and P lie above the terrain; *weakly visible* from a view segment or polygon v if P is visible at least from a point of v ; *strongly visible* from a view segment or polygon v if P is visible from any point of v .

The *visibility map* related to a view element v consists of a partition of the domain D into visible and non visible maximal connected regions. If a region is labelled as visible (non visible) then all points on the terrain whose vertical projection is in the region are visible (non visible) from v , considering weak or strong visibility.

Multi-visibility maps related to a set V of r view elements are defined combining the single visibility maps of such elements. A multi-visibility map is a subdivision of the domain D of the terrain into regions according to different visibility criteria. Typical multi-visibility maps are *union*, *intersection*, *counting* and *overlay*. Union yields domain portions visible from at least one view element; intersection yields domain portions visible from all the view elements; counting yields domain portions according to the cardinal of the set of view elements from

which a region is visible; overlay is obtained superimposing the visibility maps of all view elements and labelling each region in the resulting partition of the domain with the set of view elements from which that region is visible.

2.1 Graphics Hardware

The rendering pipeline [15] is divided into several stages. Each stage is implemented as a separate piece of hardware on the GPU. The input to the pipeline is a list of 3D geometric primitives, expressed as vertices, and the output is an image in the frame buffer ready to be displayed on a screen. A vertex defines a point, an endpoint of a line, a corner of a polygon, etc. The attributes associated to a vertex are 3D coordinates, color, texture coordinates, etc. The frame buffer is a collection of several hardware buffers, each of them corresponds to an uniform two dimensional grid, composed of cells called pixels. Each pixel in the frame buffer is a set of some number of bits grouped together into several buffers. There is a special buffer, the *Color buffer*, that mainly contains RGB color information. Arrays in GPU memory are called textures. The coordinates of a texture are used to access the values stored in textures. Textures are mainly used to store information that will be used in the per-fragment operations to decide or modify a pixel color. Usually the maximal size of a texture is 2048×2048 or 4096×4096 and at most 8 textures can be used simultaneously.

In the first stage of the pipeline per-vertex operations take place. Each input vertex is transformed depending on the point-of-view and the defined transformations, lighting calculations may also be performed to determine its color. The next stage is rasterization. The result of this stage is a fragment for each pixel location covered by a geometric primitive. Each of them corresponds to a pixel in the frame buffer with a depth value. The third stage, the fragment stage, computes the color for each pixel according to the fragments corresponding to it. Each fragment has to pass different tests and per-fragment operations before being placed into the frame buffer. Such operations can use values from global memory in the form of textures and include updating, blending, masking and other logical operations. Finally, the fragments that pass the tests and the operations of the previous stage are drawn or rendered on the screen with the appropriate color.

Logical operations are established by calling *glLogicOp* specifying the desired logical operation: *AND_LOGIC*, *OR_LOGIC*, etc. They are performed on the color of the incoming fragment and the previously stored pixel color. Information of a user defined rectangle of the color buffer can be transferred to the CPU in a summarized way with *getMinmax* or *getHistogram*. The minimum and maximum pixel colors contained in the rectangle are given by *getMinmax* and the number of occurrences of each color by *getHistogram*.

A fragment shader, also sometimes called pixel shader, is a programable function executed on a per-fragment basis. A fragment shader allows combination of fragment values, such as color and position on screen, with texture values to change the appearance of the pixels. Textures are sent as parameters to the fragment shader.

3 The Skewed Projection

Let v and s be two non coplanar segments in space parameterized by t and u in $[0, l_v]$ and $[0, l_s]$ where l_v and l_s are the lengths of v and s , respectively. Denote $T_{v,s}$ the tetrahedron determined by the endpoints of v and s .

For any point P in $T_{v,s} \setminus \{v, s\}$, let $\pi_{P,v}$ and $\pi_{P,s}$ be the planes determined by the point P and the segments v and s , respectively. Let $w_P = \pi_{P,v} \cap \pi_{P,s}$ be the unique line passing through P , v and s . Denote t_P, u_P the parameters of the points v_P and s_P where w_P intersects segments v and s , respectively.

Consider the continuous function, sk , that maps a point P in the tetrahedron $T_{v,s} \setminus \{v, s\}$ to the point $(t_P, u_P) \in [0, l_v] \times [0, l_s]$. Observe that all points of the segment whose endpoints are v_P and s_P are mapped to (t_P, u_P) . The map sk is essentially the restriction to the tetrahedron $T_{v,s} \setminus \{v, s\}$ of the *skewed projection* introduced in [17].

The skewed projection $sk(s')$ of a segment s' in $T_{v,s} \setminus \{v, s\}$ is a connected conic arc contained in $[0, l_v] \times [0, l_s]$. The conic is a hyperbola or a parabola and, in degenerate cases, a line or a point. Consequently, the skewed projection $sk(T)$ of the region bounded by a triangle T in $T_{v,s} \setminus \{v, s\}$ is a region of $[0, l_v] \times [0, l_s]$ bounded by three connected conic arcs, one per edge of T . It is not difficult to prove that the region $sk(T)$ can only be defined by: (a) three conic edges with three or four vertices, (b) two conic edges with two vertices (an edge is mapped to a point). In Figure 1a) we can see (in white) the skewed projection of a triangle that yields a region with three vertices, and in Figure 1b) we can see the skewed projection of a triangle yielding a region with four vertices.

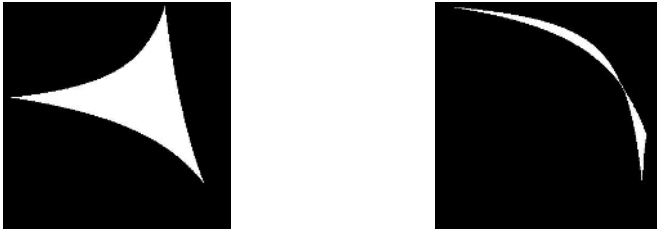


Fig. 1. a) Region with 3 boundary vertices b) Region with 4 boundary vertices

3.1 Extending the Skewed Projection

Let l be a segment in $T_{v,s} \setminus \{v, s\}$ coplanar with s . Then $sk(l) = \{(t_l, u)|u \in I \subset [0, l_s]\}$ is a vertical segment in $[0, l_v] \times [0, l_s]$, where t_l is the parameter of the point where v intersects with the plane through s and l . Let l be a segment in $T_{v,s}$ with an endpoint B in s . We know that $sk(l \setminus B) = \{(t_l, u)|u \in I \subset [0, l_s]\}$ and we continuously extend it to the whole segment l taking $sk(B) = (t_l, u_B)$, where u_B is the parameter of B in s . Let T be a triangle with a vertex B in s , and denote b the edge of T opposite to B . We can express T as the union of segments with endpoints in the edge b of T and B respectively. We extend the skewed

projection from $sk(T \setminus B)$ to the whole T by defining $sk(T) = \bigcup_{C \in b} sk(CB)$, so that $sk(B) = \{(t, u_B) | t \in I \subset [0, l_v]\}$ is an horizontal segment in $[0, l_v] \times [0, l_s]$.

In a similar way we can extend the skewed projection to the endpoint of a segment or to the vertex of a triangle located in v .

4 Segment-Segment Visibility Computation

Given a view segment v and a segment s on a face of the terrain, we want to compute the visible parts of s from v . We focus on the case in which v and s are non coplanar, so that they determine the tetrahedron $T_{v,s}$. The study of the simpler case in which v and s are coplanar is omitted due to space limitations.

To simplify computations we apply a preprocess in two stages. First we delete the subsegment of v not facing the front side of the face containing s . If s is an edge of the terrain, we delete the subsegment of v that does not face the front side of any of the two faces containing s . If the entire segment v is deleted, then s will be not visible at all from v . Otherwise, we take as view segment the part of v not deleted, that we still denote v . If segment v belongs to the terrain an equivalent study has to be done. This first step outputs two segments s and v whose faces do not block each others visibility.

The other parts of the terrain that may hide s must be contained in $T_{v,s}$. The second preprocessing stage allows us to determine these parts. Observe that the intersection of a face with $T_{v,s}$ is a convex polygon of constant complexity that can be easily triangulated. We find the faces intersecting $T_{v,s}$ by considering the m triangles of the triangulation \mathcal{T} of the domain D that intersect the projection of $T_{v,s}$ onto D [2]. In the worst case we have $m = O(n)$. Next we compute the polygons obtained intersecting these faces with $T_{v,s}$. Finally, we triangulate all these polygons obtaining a set F of triangles. Abusing language, the obtained triangles are still called faces. Clearly in the worst case is $|F| = O(m)$ and the total cost of the whole preprocess is $O(m)$.

After the preprocessing step: a) all parts of the view segment $v(s)$ face the front side of the face/s containing $s(v)$; b) we consider only the set F of triangular faces contained in $T_{v,s}$. Observe that may exist some triangle in F with a vertex in an endpoint of s or v .

A point of s is visible from a point of v if the segment connecting them does not go through any face. Segments holding this condition are called *non blocked* segments. Thus, by determining the set of non blocked segments we are able to obtain the visible parts of s from v . We use the skewed projection sk to map the triangular faces T of F to $[0, l_v] \times [0, l_s]$. Let $U = \bigcup_{T \in F} sk(T)$ be the union of the images of the faces of F under sk . Clearly, points in $\overline{U} = [0, l_v] \times [0, l_s] - U$ correspond to non blocked segments. Let $Y = \{(0, u) | u \in [0, l_s]\}$ and define the orthogonal projection of point $(t, u) \in [0, l_v] \times [0, l_s]$ onto Y by $pr_Y(t, u) = (0, u)$. The weakly visible parts of s , points that are visible from at least one point of v , are represented by $pr_Y(\overline{U})$, whereas the strongly visible parts of s , points that are visible from the whole segment v , are represented by $\underline{pr_Y(U)} = Y - pr_Y(U)$.

The computation of U can be performed exactly using a sweep line algorithm in worst-case time $O(|F|^2)$. However, U can be also approximately computed

with a simple algorithm by discretizing $[0, l_v] \times [0, l_s]$ into pixels and rendering each region $s(T)$ using graphics hardware. We use a parameter μ that defines the number of pixels per unit length, so that the number of pixels per row and per column are $\mu \cdot l_v$ and $\mu \cdot l_s$, respectively. All regions $sk(T)$ are drawn in white onto an initial black background. Final black points correspond to non blocked segments. In this way we avoid analytic computations and some robustness problems common in geometric algorithms.



Fig. 2. Black pixels represent non blocked lines. White pixels represent the union of the skewed projections. In the left vertical segment, the weakly visibles parts of segment s are painted black and the non visible ones in grey.

4.1 Rendering the Skewed Projection of a Triangle

We know that the skewed projection $sk(T)$ of a triangle T in $T_{v,s} \setminus \{v, s\}$ is a region of $[0, l_v] \times [0, l_s]$ bounded by: (a) three conic edges and three or four vertices, (b) two conic edges and two vertices. In a preprocessing step we split regions of type (a) into two or three parts in the following way. A region with four vertices is split into two regions: one formed by two edges and two vertices and another by three edges and three vertices. Regions formed by three vertices bounded by three non straight line edges are split into two regions by a vertical or horizontal line through one of its vertices. We denote \mathcal{R} the set of all the current regions. After the preprocessing stage each region $R \in \mathcal{R}$ can be described by a system I_R of quadratic or linear inequalities, with one inequality per edge.

To determine the part of $[0, l_v] \times [0, l_s]$ covered by $U = \bigcup_{R \in \mathcal{R}} R$ we use graphics hardware. We discretize $[0, l_v] \times [0, l_s]$ into pixels and we paint each region $R \in \mathcal{R}$ in white on an initially black background. To determine the pixels that correspond to a region R we consider a collection of geometric primitives \mathcal{C}_R whose union contains R , and a fragment shader whose input parameters are the coefficients of the system I_R . The fragment shader assigns white color to the fragments that fulfill I_R and black color to the others. Since the time required by the fragment shader is proportional to the number of fragments obtained by the rasterization of \mathcal{C}_R , we choose this region so that the number of fragments is reasonably small. We associate to each non straight convex edge e of R a rectangle R_e that has one side with endpoints in the vertices of e and its opposite parallel side tangent to e . We define \mathcal{C}_R as the union of the rectangles associated to the convex edges of R and, in case that R has three vertices, the straight triangle defined by the vertices of R (See Figure 3).

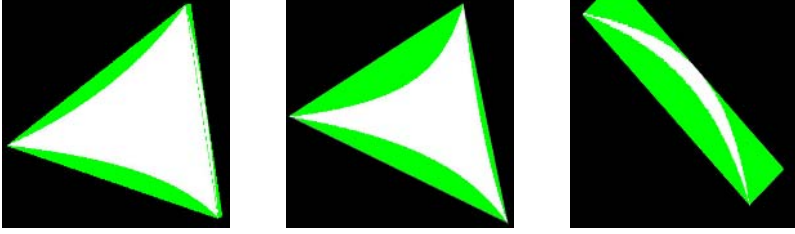


Fig. 3. In white the region determined by the conics, in green and white the region that we send to rasterize and that goes through the Fragment Shader

4.2 Computing the Visible Parts of a Segment

Once the union $U = \bigcup_{T \in F} sk(T)$ has been rendered in white. We compute $pr_Y(\overline{U})$ or $pr_Y(U)$ in order to determine the weakly or strongly visible parts of s from v , respectively. Since the OpenGL *getMinmax* function allows determination of the minimal and maximal pixel color (white is greater than black in RGB code) in a row of the screen, it can be used in order to compute $pr_Y(\overline{U})$ or $pr_Y(U)$. We obtain $pr_Y(\overline{U})$ by scanning through all the rows of the screen and considering that the projection of a row is white when the minimal color of its corresponding row is. Similarly we obtain $pr_Y(U)$ projecting into Y in black when the maximal color of the row is black. The result of the computation is stored in the CPU.

4.3 Acceleration

Tacking into account that we only need one bit of the color buffer per pixel to represent the union of skewed projections corresponding to one pair of segments (v, s) , we can simultaneously represent in the color buffer the unions corresponding to a collection of pairs of segments $(v, s_1), \dots, (v, s_k)$, with $1 \leq k \leq 24$. Then we use the per-fragment *logicOp*, specifying the *OR_LOGIC* operation, to merge the color of the already rendered fragments with the incoming one. Using the OpenGL *getHistogram* function, instead of the *getMinmax* function, we can compute the projections onto Y of the k pairs of segments (v, s_j) .

5 Discrete Multi-visibility Map Computation

In this section we present an algorithm for computing discrete multi-visibility maps relative to a set of view segments using a color code and according to the type of visibility chosen (weak or strong). We give a method to visualize the following types of multi-visibility maps: union, intersection, counting and overlay.

The domain of the terrain is discretized into a rectangular grid of size $H \times W$. This size is chosen according to a parameter μ' representing the number of grid points per unit length of the terrain domain. The grid is mapped into an unidimensional array \mathcal{A} of integers (8 bits) of length $4 \cdot H \cdot W$, in such a way that each grid element is mapped in 4 consecutive elements of \mathcal{A} . Next the array

is transferred from the CPU to a texture in the GPU that stores values of 32 bits (8 bits per 4 channels). Each 4 consecutive elements of \mathcal{A} are transferred to a texture value. Since only 8 textures can be used simultaneously, the maximal number of view segments is limited to $256 = 8 \cdot 32$.

In a first step, for each view segment we compute its discrete visibility map and we store it in array \mathcal{A} . The discrete visibility map for a view segment is obtained by scanning all the rows of the grid and computing, using the segment-segment-visibility algorithm, the visibility of the set of segments on the terrain that correspond to a row of the grid. Each one of these segments is obtained by first computing the intersection of a horizontal line and a triangle of the triangulation of the domain and then lifting the intersection into a segment on a triangle of the terrain. For each grid position we store visibility information in an index of \mathcal{A} . A bit suffices to represent the visibility: this bit is set to 1 when the grid position is visible and to 0 otherwise. In fact, to increase the computational efficiency, we simultaneously store the visibility information for up to 32 view segments in \mathcal{A} . In the case when we have more than 32 view segments, we need a new array for every 32 view segments or fraction.

Once all the visibility information is computed it is transferred to the GPU, then, by using a proper fragment shader, which has the textures as input parameters, we can visualize any multi-visibility map in a $H' \times W'$ window of the screen for any region of the terrain we are interested in. When in a texture we have k view segments, $1 \leq k \leq 32$, the fragment shader only uses the corresponding k bits of the texture values. Next we describe how the union, intersection and counting fragment shaders work.

The union fragment shader paints white a pixel corresponding to a position of the texture if it has some bit equal to 1 (visible) and black otherwise (not visible); the intersection fragment shader paints white a pixel corresponding to a position of the texture if it has all bits equal to 1 (visible) and black otherwise (not visible); the counting fragment shader paints each pixel in the appropriate color according to the number of bits equal to 1 of the corresponding position of the texture.

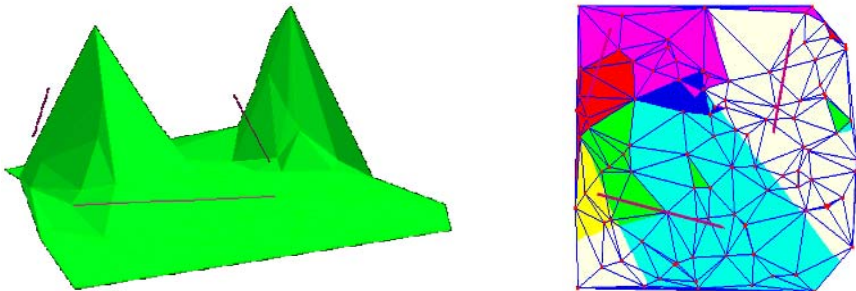


Fig. 4. a) Terrain and three view segments, v_1 on the left, v_2 on the right and v_3 on the front. b) The corresponding multi-visibility map: points visible from v_1 are painted red, from v_2 in green, from v_3 in blue, from v_1 and v_2 in yellow, from v_1 and v_3 in pink, from v_2 and v_3 in light blue and from v_1 , v_2 and v_3 in white.

It is not difficult to adapt our method to visualize the union, intersection and counting for a subset of view segments; the overlay of e view segments, assuming that we are able to distinguish 2^e colors; the special case of overlay that we describe next. Let $\mathcal{U} = \{V_1, ..V_g\}$ be a user specified collection of subsets of view segments such that $V_i \cup V_j \in \mathcal{U}$, $i, j = 1..g$. The terrain domain is subdivided into regions R_1, \dots, R_g, R_{g+1} of different colors, in such a way that the region R_i , $i = 1..g$, contains the points of the terrain that are visible from all the view segments of V_i , and region R_{g+1} contains the remaining points.

Moreover, without recomputing the information and only adapting the window to a specific region of the domain, we can visualize any multi-visibility map we are interested in.

6 Complexity Analysis

Given a terrain and a set of view segments, to analyze the cost of visualizing a discrete multi-visibility map on a grid of size $H \times W$ some important considerations have to be taken into account:

- The number of intersections between H lines and the n triangles of the domain is $O(nH)$ in the worst case. The maximal number of tetrahedra to be considered is $O(rnH)$, where r is the number of view segments.
- The faces of the terrain that intersect a tetrahedron are determined in $O(n)$ worst case time. Let c be the time needed to render the skewed projections of a triangle. Then, the total time expended in processing faces is $O(rn^2Hc)$.
- Let G be the time expended by the *getHistogram* function. Each cluster of 24 tetrahedra uses this function. Then, the total time expended by *getHistogram* is $O(rnH\frac{G}{24})$.
- Let M be the time of loading a texture of size $H \times W$ to the GPU. Each cluster of 32 view segments uses a texture. Then, the total time of loading textures is $O(r\frac{M}{32})$.
- The visualization of a region of a multi-visibility map in a $H' \times W'$ window can be done in constant time.

According to these considerations we obtain that the computational cost of visualizing a multi-visibility map is $O(rnH(nc + \frac{G}{24}) + r\frac{M}{32})$.

Since visualizing a multi-visibility map takes constant time, the time needed to visualize N additional multi-visibility maps is $O(N)$.

7 Conclusions and Future Work

We have presented a method for visualizing multi-visibility maps of a triangulated terrain concerning a set of view segments, for weak and strong visibility, using graphics hardware. We want to remark that our method can be easily parallelized. We have implemented the described algorithms and in our implementation parameters μ and μ' can be chosen by the user. Presently we are studying the best combinations of these parameters in order to reduce errors produced during the different discretizations. We are also working to extend our method to heterogeneous sets of view elements: segments, polygonal lines and polygonal regions.

Acknowledgements

We thank Teresa Paradinas for helping us to implement our algorithms.

References

1. P. K. Agarwal, S. Krishnan, N. H. Mustafa, S. Venkatasubramanian, Streaming Geometric Optimization Using Graphics Hardware. European Symposium on Algorithms, 544–555, 2003.
2. M.D. Berg, M.V. Kreveld, R.V. Oostrum, M. Overmars, Simple traversal of a subdivision without extra storage, *International Journal of Geographical Information Science*, Vol 11, 4(15):359–373,1997.
3. M. Bern, D. Dobkin, D. Eppstein, and R. Grossman., Visibility with a moving point of view, *Algorithmica*, 11:360–378, 1994.
4. N. Coll, F. Hurtado and J.A. Sellarès., Approximating planar subdivisions and generalized Vornoi diagrams from random sections, *19th European Workshop on Computational Geometry*, 27–30, 2003.
5. N. Coll, M. Fort and J.A. Sellarès. Approximate Multi-Visibility Map Computation, *Proc. 21th European Workshop on Computational Geometry*, 97–100, 2005.
6. Q. Fan, A. Efrat, V. Koltun, S. Krishnan, S. Venkatasubramanian: Hardware-Assisted Natural Neighbor Interpolation. Proc. 7th Workshop on Algorithms Engineering and Experimentation. ALENEX 2005.
7. L.DeFloriani,P.Magillo,VisibilityAlgorithmsonTriangulatedDigitalTerrainModels, *International Journal of Geographic Information Systems*, 8(1):13–41, 1994.
8. L. De Floriani, E. Puppo, P. Magillo, Applications of Computational Geometry to Geographic Information Systems, *Handbook of Computational Geometry, J.R. Sack, J. Urrutia (Eds.)*, Elsevier Science., 333–388, 1999.
9. K.E.HoffIII,J.Keyser,M.C.Lin,D.Manocha,T.Culver:FastComputationofGeneralized Voronoi Diagrams Using Graphics Hardware. SIGGRAPH, 277–286,1999.
10. V. Koltun, D. Cohen-Or, and Y. Chrysanthou, Hardware-Accelerated From-Region Visibility Using a Dual Ray Space, *Proc. 12th Eurographics Workshop on Rendering*, 204–214, 2001.
11. M.J. van Kreveld, Digital Elevation Models and TIN Algorithms, *Algorithmic Foundations of Geographic Information Systems, LNCS*, 1340::37–78, 1997.
12. M.J. van Kreveld, E. Moet, R. van Ostrum, Region inter-visibility in terrains, *Proc. 20th European Workshop on Computational Geometry*, 155–158, 2004.
13. S. Krishnan, N. H. Mustafa, S. Venkatasubramanian: Hardware-Assisted Computation of Depth Contours. *13th ACM-SIAM Symposium on Discrete Algorithms*, 558-567, 2002.
14. N. Mustafa, E. Koustsofiros, S. Krishnan, S. Venkatasubramanian: Hardware Assisted View-Dependent Planar Map Simplification. *Proc. of the 17th ACM Symposium on Computational Geometry (SoCG '01)*, 2001.
15. M. Segal, K. Akeley, The OpenGL Graphics System: A Specification, <http://www.opengl.org/documentation/specs/version2.0/glspec20.pdf>, 2004.
16. J. D. Owens, D. Luebke, N. Govindaraju, M. Harris, J. Krger, A. E. Lefohn and T. J. Purcell: A Survey of General-Purpose Computation on Graphics Hardware, *Eurographics 2005, State of the Art Reports*, 21–51, 2005.
17. J.W. Jaromczyk, and M. Kowaluk, Skewed projections with an application to line stabbing in \mathbb{R}^3 , In *Proc. 4th ACM Symp. on Comp. Geometry*, 362–370, 1988.

Fast Intersections for Subdivision Surfaces

Aaron Severn and Faramarz Samavati

Department of Computer Science,
University of Calgary

Abstract. Subdivision surface intersections can be costly to compute. They require the intersection of high resolution meshes in order to obtain accurate results, which can lead to slow performance and high memory usage. In this paper we show how the strong convex hull property can lead to a method for efficiently computing intersections at high resolutions. Consequently, the method can be used with any subdivision scheme that has the strong convex hull property. In this method, a bipartite graph structure is used to track potentially intersecting faces.

1 Introduction

Surface intersection is a common problem with a variety of applications. It is integral to algorithms for computing Boolean operations between surfaces, which are an essential tool in Computer Aided Geometric Design (CAGD). The somewhat simpler problem of detecting surface intersection is necessary for collision detection, which has a wide variety of applications in animation, simulations, video games, and other areas. Much work has been devoted to the surface intersection problem for analytical surfaces [4, 5, 18] and NURBS surfaces [10, 11, 12], however few previous works have attempted to solve this problem for subdivision surfaces. Subdivision surface intersection often involves subdividing the control meshes to a desired resolution and then applying a mesh intersection algorithm, without considering properties of subdivision [2].

Today, meshes and subdivision surfaces are used in high end modelling packages [1], animation production [3], and have become part of the MPEG4 standard [16]. Subdivision is considered to be a fundamental building block in digital geometry and mesh processing [19]. We can easily find many libraries and data sets for meshes that represent various kinds of objects. By applying subdivision schemes to these meshes we can create smoother surfaces, and it is also possible to include sharp features in the results. Efficient intersection of these surfaces makes it possible to apply Boolean operations on meshes, creating many useful and new objects from the current objects (Fig. 1). Consequently, computing intersections on the hierarchy of meshes resulting from subdivision is an important task. For low resolution meshes this problem can be solved efficiently using existing mesh intersection techniques. However, in order to produce high quality results we need to perform these intersections on high resolution meshes which can be slow and memory intensive. Subdivision schemes lead to exponential

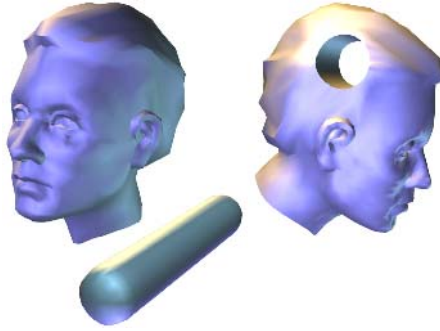


Fig. 1. Using subdivision surface intersection to compute a Boolean operation between two surfaces. The cylinder is subtracted from the man’s head.

growth of the number of faces in a mesh and only a few iterations of subdivision can lead to meshes that are difficult to intersect due to their size.

In this paper we present a method for efficiently computing the intersection between two subdivision surfaces. The operations can be performed with arbitrary precision, but our focus is on intersecting high resolution surfaces efficiently. We will not consider the case of self-intersecting surfaces. Our main contributions are a fast face intersection exclusion test derived from the strong convex hull property of subdivision surfaces, a bipartite graph construction that makes it possible to identify and track which faces do not need to be tested for intersection, and a complete subdivision surface intersection algorithm built from these two results. We have implemented and tested our algorithm for Loop and Catmull-Clark subdivision. Our exclusion method can also be used for the case where the vertices are sent to the limit position.

Our method could be applied to any subdivision scheme where the strong convex hull property of subdivision surfaces holds. The method can be used for any existing meshes without additional pre-processing steps and could fit into the framework of existing CAGD systems that use subdivision surfaces.

2 Previous Work

Much work has been done on computing intersections between various types of surfaces. Several techniques have been developed for intersecting trimmed NURBS surfaces. Methods involving symbolic and numerical techniques have been used to trim the resulting surfaces [12], as well as mostly symbolic methods involving exact algebraic number representation [10, 11]. Hohmeyer [8] gives a framework for robust surface intersection based on loop detection.

The work of Epstein et al. [4], Goldfeather et al. [5], and Rappoport and Spitz [18] on efficient rendering of constructive solid geometry (CSG) objects presents a different approach to the problem of computing Boolean operations. For such surfaces, intersection is a trivial problem.

Lin and Gottschalk [14] give an excellent survey of collision detection algorithms. Collision detection between subdivision surfaces was discussed as a part of character animation by DeRose et al. [3]. Bounding hierarchies are commonly used when intersecting meshes, some examples of these include Gottschalk et al. [6] and Zachmann [22]. Interference detection on subdivision surfaces has been considered in works by Wu and Peters [21] and Grinspun and Schröder [7].

Our work on intersecting subdivision surfaces is most closely related to that of Lanquetin et al. [13], who developed a method for intersecting subdivision surfaces using their control meshes and bipartite graphs to minimize the cost. It should be noted, however, that their method can incorrectly compute the intersection in some cases, as they explained in their paper. Our use of bipartite graphs was inspired by their work, although our graphs are constructed differently.

Biermann et al. [2] developed a technique for approximating Boolean operations on free-form solids bounded by subdivision surfaces. In their work, they intersected the surfaces by performing midpoint subdivision on the control meshes and using a standard mesh intersection technique based on spatial subdivision. Our intersection approach could be employed in their Boolean operations framework. Litke et al. [15] developed ways for trimming subdivision surfaces, such trimmed surfaces are produced naturally through surface intersections. Several different approaches for producing sharp features or creases have been described in the past [2, 9, 20], which can be produced from intersection curves.

3 Excluding Face Intersections

For the remainder of this paper, the neighbourhood of face f , denoted $N(f)$, refers to the vertices of face f and all vertices of faces that share at least one vertex with f . A child of face f refers to any face produced by the subdivision of f . The convex hull of a set of vertices V will be denoted $co(V)$.

3.1 Convex Hull Intersection

The strong convex hull property for subdivision surfaces states that, for any face f , the children of f will be contained within $co(N(f))$ (Fig. 2). This property holds where all masks' weights are positive. B-spline based subdivision schemes, including Loop, Catmull-Clark, polyhedral, and Doo-Sabin, are subdivision examples with this property. As a rare case, the convex hull property does not hold for Butterfly subdivision.

We can apply this property to the process of intersecting subdivision surfaces with the following observation. If C_1 and C_2 are control meshes of two subdivision surfaces and $f_1 \in C_1$ and $f_2 \in C_2$ are two arbitrary faces in those meshes, then the children of f_1 will be contained in $co(N(f_1))$ and the children of f_2 will be contained in $co(N(f_2))$. Therefore, if $co(N(f_1))$ does not intersect $co(N(f_2))$ we know that none of the children of f_1 will intersect any of the children of f_2 , no matter how often each surface is subdivided. We now state this formally.

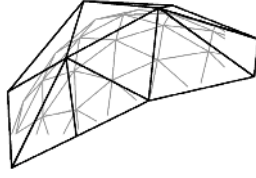


Fig. 2. The strong convex hull property illustrated for Loop subdivision. The fine mesh is contained within the convex hull of the coarse mesh.

Theorem 1. Let C_1^0 and C_2^0 be the control meshes of two subdivision surfaces, let C_1^i and C_2^i be the meshes resulting from subdividing C_1^0 and C_2^0 i times, and let $f_1^i \in C_1^i$ and $f_2^i \in C_2^i$ be two arbitrary faces produced from subdividing $f_1^0 \in C_1^0$ and $f_2^0 \in C_2^0$ i times respectively. If $co(N(f_1^0))$ does not intersect $co(N(f_2^0))$ then f_1^i does not intersect f_2^i .

This theorem gives us a strong condition for excluding the intersection of two faces. If $co(N(f_1^i))$ does not intersect $co(N(f_2^i))$ for $f_1^i \in C_1^i$ and $f_2^i \in C_2^i$ then we can exclude all children of f_1^i and f_2^i from intersection tests with each other. We show in our results that this can be applied to greatly reduce the number of face intersection tests when compared to other standard mesh intersection algorithms.

It should be noted that we do not need to compute any convex hulls in order to apply this result. If the distance between the convex hulls of the vertices of the neighbourhood is greater than zero then an exclusion has been detected, and this can be determined without computing the convex hulls. Rabbitz [17] gives an algorithm for computing the distance between two convex polyhedra using only the vertices of the polyhedra. If vertices of a non-convex polyhedra are given then the intersection is computed with the convex hull of those vertices. Since this algorithm takes only two sets of vertices as input it is well suited to our purposes. To determine if the children of faces $f_1 \in C_1$ and $f_2 \in C_2$ could potentially intersect, we can pass $N(f_1)$ and $N(f_2)$ to Rabbitz's algorithm.

Even though we have a relatively efficient way to test for intersection between $co(N(f_1))$ and $co(N(f_2))$, our experiments have found that this technique is only beneficial for extremely high resolution meshes. Although convex hulls are very good at reducing the number of face-face intersections performed, in most practical cases the expense of intersecting two convex hulls for each pair of faces results in a slower algorithm than a standard spatial subdivision approach. In order to make these ideas work at more practical resolution levels we need a much faster intersection exclusion test.

3.2 Alternate Intersection Tests

Any bounding volume around the convex hull can be used for excluding intersections. We have experimented with a variety of methods for bounding the convex hull of the neighbourhood of a face, including bounding spheres, oriented bounding boxes (OBBs), and axis-aligned bounding boxes (AABBs). A tight radius

for bounding spheres is hard to find and we have found that, with a larger radius, bounding spheres are not able to exclude enough face-face intersection tests. OBBs are very effective at excluding face-face intersection tests, however computing an OBB around the neighbourhood of a face is not trivial. OBBs are typically most effective when they can be pre-computed, but in our case they need to be computed on the fly each time a mesh is subdivided.

We have found that the best method of bounding the convex hull of the neighbourhood of a face, in terms of running time, is to use axis-aligned bounding boxes. For a face f , it is clear that the AABB of $N(f)$ will contain $co(N(f))$, which leads to the following corollary.

Corollary: Let C_1^0 and C_2^0 be the control meshes of two subdivision surfaces, let C_1^i and C_2^i be the meshes resulting from subdividing C_1^0 and C_2^0 i times, and let $f_1^i \in C_1^i$ and $f_2^i \in C_2^i$ be two arbitrary faces produced from subdividing $f_1^0 \in C_1^0$ and $f_2^0 \in C_2^0$ i times respectively. If an AABB containing all vertices of $N(f_1^0)$ does not intersect an AABB containing all vertices of $N(f_2^0)$ then f_1^i does not intersect f_2^i .

This results in a highly efficient exclusion test with a tight enough bound to exclude the majority of face-face intersection tests.

4 Graph Based Intersection

We use a dynamic bipartite graph to keep track of only the faces that remain from the convex hull exclusion. In other words, this graph helps us to find all potentially intersecting faces. Our graph, $G = (V_1, V_2, E)$, consists of two sets of vertices, V_1 and V_2 , and a set E of edges. Each vertex in V_1 represents a face in the control mesh C_1 and each vertex in V_2 represents a face in the control mesh C_2 . An edge $e \in E$ connects $v_1 \in V_1$ to $v_2 \in V_2$ if the faces represented by v_1 and v_2 could *potentially* intersect. We call this the *potential intersection graph*. Using our result from the previous section, this means that if an AABB around $co(N(v_1))$ intersects an AABB around $co(N(v_2))$ then v_1 and v_2 are connected by an edge. Otherwise, they are not. The vertex sets V_1 and V_2 form the two partitions of the graph. As we are not considering self-intersection, there will be no edges between two vertices of the same set since two faces from the same control mesh will not need to be tested for intersection.

Upon subdividing C_1 , each vertex of V_1 is split into n new vertices representing the new faces resulting from subdivision (in Loop or Catmull-Clark subdivision, for example, each vertex of V_1 is split into 4 vertices representing the 4 new faces resulting from the subdivision of each face). If an edge existed between $v_1 \in V_1$ and $v_2 \in V_2$ then edges will connect v_2 to each of the vertices resulting from splitting v_1 (Fig. 3). Subdivision of C_2 is handled the same way.

This dynamic graph structure is used to keep track of which faces need tested for intersection and which tests can be excluded. Each edge represents a face intersection test that has not yet been resolved. Using the quick exclusion test described in Sect. 3, we can eliminate many edges from the graph each time a control mesh is subdivided using the algorithm described in the next section.

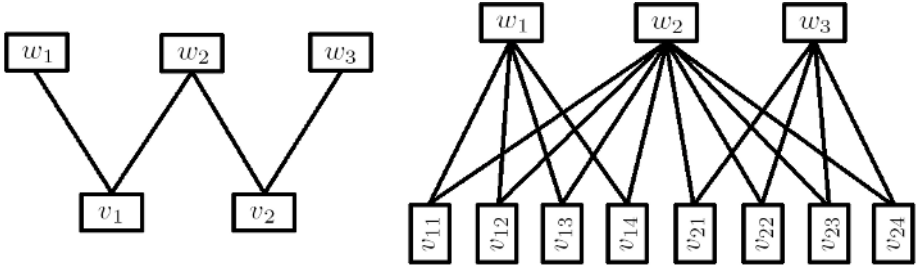


Fig. 3. A bipartite graph with potential intersections between v_1 and w_1 , v_1 and w_2 , v_2 and w_2 , and v_2 and w_3 (left). The same graph after subdividing one partition (right).

5 The Intersection Algorithm

We begin with the control meshes C_1^0 and C_2^0 of two subdivision surfaces and an integer n , the depth of subdivision at which the intersection will be computed. The choice of n will determine the accuracy of the intersection, with larger values leading to a more accurate intersection. Larger values of n will also lead to a slower intersection due to the exponential growth in the number of faces resulting from subdivision.

In the first step of the algorithm, we must compute an initial potential intersection graph G^0 , having the form described in Sect. 4. Since we begin with no previous information on whether or not any two faces of C_1^0 and C_2^0 intersect, we must test each face of C_1^0 with each face of C_2^0 . For each face $f_1^0 \in C_1^0$ and $f_2^0 \in C_2^0$ we compute $N(f_1^0)$ and $N(f_2^0)$ and then test if an AABB around $co(N(f_1^0))$ intersects an AABB around $co(N(f_2^0))$. If there is no intersection, we can conclude that there will be no intersections between the children of these faces. Otherwise we add an edge to G^0 from f_1^0 to f_2^0 (a potential intersection in further levels). Note that the construction of the AABBs is trivial since they depend only on the vertices of $N(f_1^0)$ and $N(f_2^0)$ respectively.

At this point we can use spatial subdivision to make the process of constructing the initial potential intersection graph more efficient. We compute the AABB of $co(N(f))$ for each face f of a control mesh and then place these in an axis-aligned hierarchical bounding box structure [22], one for each control mesh, where the leaf nodes are the AABBs. The initial graph can then be computed by intersecting the two bounding box trees, adding an edge whenever two leaf nodes intersect. This optimization is unnecessary for extremely coarse control meshes having few faces, but can be beneficial in other cases.

After computing the initial graph, we proceed in a loop where, for each iteration, both meshes are subdivided and then a new graph is created from the old one. The new graph G^{i+1} is created from G^i by splitting the vertices of G^i in the manner described in Sect. 4. This produces a much larger graph, but many of the edges can be removed using the intersection exclusion test once again. If there is an edge $e \in G^{i+1}$ from face f_1^i to face f_2^i then we compute $N(f_1^i)$ and $N(f_2^i)$ and test for intersection between an AABB around $co(N(f_1^i))$ and an AABB around $co(N(f_2^i))$. If they do not intersect edge e is removed from



Fig. 4. The intersection algorithm proceeds from left to right, subdividing and updating the graph at each iteration. Faces still in the graph are highlighted. Note that most faces are excluded at a low resolution.

G^{i+1} . We can further prune the graph by removing any isolated vertices that do not have any edges connected to them. The loop terminates when the desired subdivision depth has been reached (Fig. 4).

When the loop is complete we have two meshes, C_1^n and C_2^n , and a bipartite graph G^n , and we are ready to compute the final, precise intersection. To do this, we iterate over all edges of G^n and, if an edge connects f_1^n to f_2^n in the graph, we test f_1^n and f_2^n for real intersection.

One common method for producing a more accurate approximation to the limit surface after several applications of subdivision is to relocate the vertices of the mesh to the limit surface. Due to the fact that the limit surface is contained within the convex hulls of the neighbourhoods of the faces, this technique can be used with our algorithm before computing the real intersection without affecting the results of the computation.

6 Results

We have tested our algorithm on a wide variety of surfaces using both Loop and Catmull-Clark subdivision and have found that it leads to significant performance improvements, especially at high resolutions that are problematic in real applications. Table 1 gives a comparison of our method with a mesh intersection algorithm using spatial subdivision. The table gives the average number of face intersections that need to be performed for each algorithm. The number of subdivisions refers to the depth of subdivision at which the intersection is performed (the integer n in our algorithm). In the case of hierarchical bounding boxes, the control meshes were subdivided n times and the resulting surfaces were intersected. Fifty pairs of surfaces were intersected with the surfaces selected from a set of polygonal meshes. The meshes consisted of simple surfaces, such as cubes and spheres, as well as arbitrary topology surfaces such as animals and human heads. The number of faces in the coarse meshes varied from 24 to 3336. Notice that, if we subdivide only once, spatial subdivision outperforms our method in the case of Loop subdivision and performs almost equally as well with Catmull-Clark subdivision. However, when subdividing four times our method is nearly twice as efficient in excluding intersection tests for Loop subdivision, and three times as efficient for Catmull-Clark subdivision. Our method also performs well with non-intersecting surfaces. In such cases all faces are excluded at a low resolution and no tests need to be performed on the high resolution meshes.

Table 1. Average number of face-face intersection tests performed while intersecting 50 pairs of subdivision surfaces at various resolutions

Subdivisions (n)	1	2	3	4
Catmull-Clark subdivision				
Hierarchical bounding boxes	48850	137330	397056	1179298
Bipartite graph with AABB exclusion test	52462	100827	198595	396781
Bipartite graph with convex hull exclusion test	13463	19899	25602	37905
Loop subdivision				
Hierarchical bounding boxes	48667	127348	357738	1036631
Bipartite graph with AABB exclusion test	82805	152086	288928	554449
Bipartite graph with convex hull exclusion test	23031	29522	39620	65865

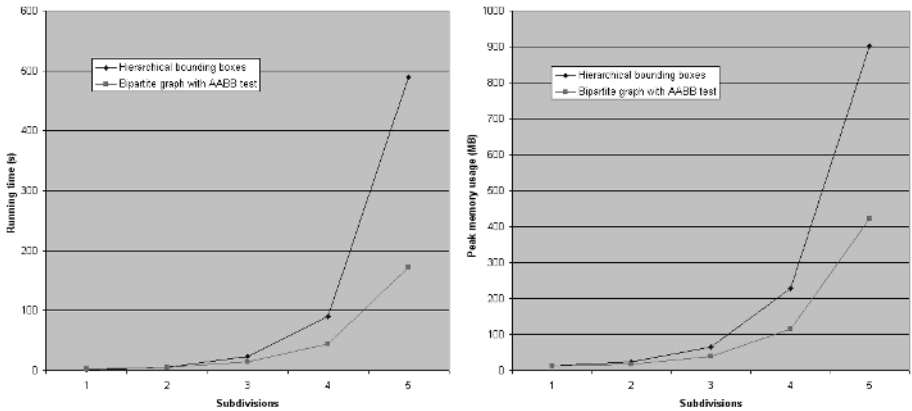


Fig. 5. A comparison of the running time (left) and peak memory usage (right) for a typical surface intersection at various subdivision depths using Loop subdivision. Two arbitrary topology surfaces, a dolphin (816 faces in the coarse mesh) and a duck (1818 faces in the coarse mesh) were used in the tests.

We have also included in the Table 1 the number of face-face intersection tests performed when using an exact convex hull intersection test to exclude faces from intersection. Clearly this gives a tighter bound than the AABB exclusion test, and this is reflected in the results. Using an exact convex hull test enormously reduces the number of face-face intersections that need to be performed. However, in practice, testing for intersection between two convex hulls is not fast enough for our purposes and leads to a slower algorithm.

We have experimented with a variety of different exclusion tests, including bounding spheres centred around faces, vertices, or edges, oriented bounding boxes, and exact convex hulls around face neighbourhoods, and we have found that most efficient method in terms of running time is the AABB test presented here. Figure 5 shows a comparison between the performance of our method and a hierarchical bounding box approach for a typical collision detection case

resolved to various subdivision depths. As the resolution gets higher, our method performs significantly better due to the reduction in face-face intersection tests.

Also in Fig. 5 is a comparison of peak memory usage. Our method leads to a large reduction in memory usage at higher resolutions since we only need to store information about faces that could potentially intersect. After several subdivision steps, most faces have been removed from the graph.

7 Conclusion

We have presented a method for computing the intersection of two subdivision surfaces with arbitrary precision that takes advantage of the strong convex hull property to produce an efficient algorithm. Our method can be used with any subdivision scheme where the strong convex hull property holds, and we have shown that it leads to a significantly more efficient intersection computation than existing methods for both Loop and Catmull-Clark subdivision. This method could be applied to improve the efficiency of several algorithms that involve intersecting subdivision surfaces, such as performing Boolean operations or collision detection.

Although we have investigated several intersection exclusion tests, it may be possible to find a more efficient test that improves these results. Our results indicate that many more face intersection tests could be excluded using the strong convex hull property if an appropriate exclusion test could be developed, however such a test must be quite quick in order to work effectively in this context. It is not clear if such a test exists and therefore merits further investigation.

References

1. ALIAS|WAVEFRONT: Maya. www.aliaswavefront.com (2002)
2. Biermann, H., Kristjansson, D., Zorin D.: Approximate Boolean operations on free-form solids. Proceedings of SIGGRAPH 2001 185–194
3. DeRose, T., Kass, M., Truong T.: Subdivision surfaces in character animation. Proceedings of SIGGRAPH 1998 85–94
4. Epstein, D., Gharachorloo, N., Jansen, F., Rossignac, J., Zoulos, C.: Multiple depth-buffer rendering of csg. Technical report, IBM Research Report (1989)
5. Goldfeather, J., Hultquist, J. P. M., Fuchs, H.: Fast constructive solid geometry in the pixel-powers graphics system. Proceedings of SIGGRAPH 1986 107–116
6. Gottschalk, S., Lin, M. C., Manocha D.: OBBTree: A hierarchical structure for rapid interference detection. Computer Aided Geometric Design **3(4)** (1986) 295–311
7. Grinspun, E., Schröder, P.: Normal bounds for subdivision-surface interference detection. Proceedings of the conference on Visualization 2001 333–340
8. Hohmeyer, M. E.: Robust and efficient intersection for solid modeling. PhD thesis, UC Berkeley (1992)
9. Hoppe, H., DeRose, T., Duchamp, T., Halstead, M., Jin, H., McDonald, J., Schweitzer, J., Stuetzle, W.: Piecewise smooth surface reconstruction Proceedings of SIGGRAPH 1994 295–302

10. Keyser, J., Krishnan, S., Manocha, D.: Efficient and accurate b-rep generation of low degree sculptured solids using exact arithmetic: I-representations. *Computer Aided Geometric Design* **16(9)** (1999) 841–859
11. Keyser, J., Krishnan, S., Manocha, D.: Efficient and accurate b-rep generation of low degree sculptured solids using exact arithmetic: II-computation. *Computer Aided Geometric Design* **16(9)** (1999) 861–882
12. Krishnan, S., Manocha, D.: An efficient surface intersection algorithm based on lower-dimensional formulation. *ACM Transactions on Graphics* **16(1)** (1997) 74–106
13. Lanquetin, S., Fofou, S., Kheddouci, H., Neveu, M.: A graph based algorithm for intersection of subdivision surfaces. *ICCSA 2003* **3** 387–396
14. Lin, M., Gottschalk, S.: Collision detection between geometric models: A survey. *Proceedings of IMA Conference on Mathematics of Surfaces* (1998)
15. Litke, N., Levin, A., Schröder, P.: Trimming for subdivision surfaces. *Computer Aided Geometric Design* **18(5)** (2001) 429–454
16. MPEG 4 Committee: MPEG 4 Standard. (2002)
17. Rabbitz, R.: Fast Collision Detection of Moving Convex Polyhedra. *Graphics Gems IV* (1994) 83–109
18. Rappoport, A., Spitz, S.: Interactive Boolean operations for conceptual design of 3-d solids. *Proceedings of SIGGRAPH 1997* 269–278
19. Schröder, P.: Subdivision as a fundamental building block of digital geometry processing algorithms. *Journal of Computational and Applied Mathematics* **149(1)** (2002) 207–219
20. Schweitzer, J. E.: Analysis and application of subdivision surfaces. PhD Thesis, University of Washington (1996)
21. Wu, X., Peters, J.: Interference detection for subdivision surfaces. *Computer Graphics Forum* **23(3)** (2004) 577–584
22. Zachmann, G.: Minimal hierarchical collision detection. *Proceedings of the ACM symposium on Virtual reality software and technology* (2002) 121–128

A β -Shape from the Voronoi Diagram of Atoms for Protein Structure Analysis

Jeongyeon Seo¹, Donguk Kim², Cheol-Hyung Cho², and Deok-Soo Kim^{1,2}

¹ Department of Industrial Engineering, Hanyang University,
17 Haengdang-Dong, Sungdong-Ku, Seoul, 133-791, South Korea
jyseo@voro noi . hanyang . ac . kr, dskim@hanyang . ac . kr

² Voronoi Diagram Research Center, Hanyang University,
17 Haengdang-Dong, Sungdong-Ku, Seoul, 133-791, South Korea
donguk@voro noi . hanyang . ac . kr, murick@voro noi . hanyang . ac . kr

Abstract. In this paper, we present a β -shape and a β -complex for a set of atoms with arbitrary sizes for a faster response to the topological queries among atoms. These concepts are the generalizations of the well-known α -shape and α -complex (and their weighted counterparts as well). To compute a β -shape, we first compute the Voronoi diagram of atoms and then transform the Voronoi diagram to a quasi-triangulation which is the topological dual of the Voronoi diagram. Then, we compute a β -complex from the quasi-triangulation by analyzing the valid intervals for each simplex in the quasi-triangulation. It is shown that a β -complex can be computed in $O(m)$ time in the worst case from the Voronoi diagram of atoms, where m is the number of simplices in the quasi-triangulation. Then, a β -shape for a particular β consisting of k simplices can be located in $O(\log m + k)$ time in the worst case from the simplices in the β -complex sorted according to the interval values.

Keywords: Voronoi diagram of spheres, α -shape, α -complex, β -shape, β -complex.

1 Introduction

The geometry of biological systems, such as the geometry of proteins, is a very important consideration when investigating the functions of these systems. Hence, one of the major geometric considerations in the study of biological systems is the accurate representation of the proximity among atoms.

Lee and Richards, in 1971, presented the definition of a solvent accessible surface which provided a theoretical foundation for analyzing the mass properties of protein [1]. In 1974, Richards defined a molecular surface using the concept of a Voronoi diagram of atom centers, which became the basis for most of the structural analysis for proteins [2]. Connolly later reported how to compute the molecular surface analytically and beautifully visualized the rendered molecular surface [3, 4]. Thereafter, the molecular surface has also been referred to as a Connolly surface.

Edelsbrunner and Mücke defined a new and powerful geometric construct called an α -shape as a transformation of the Voronoi diagram of a set S of points (or equivalently its topological dual structure called the Delaunay triangulation) [5] in various applications of reconstructing the shape from which S is produced.

However, α -shapes have limitations in their applications in biological systems mainly due to the fact that α -shapes do not account for the size variations among atoms at all. In general, the proximity among spheres is not necessarily identical to the proximity among the centers of the spheres [6, 7].

In order to incorporate the size differences among atoms, Edelsbrunner extended the α -shape to the *weighted* α -shape using the power diagram of the particles instead of the Voronoi diagram of the particle centers [8]. The weighted α -shape has been used in the reasoning of spatial structure for biological systems quite extensively [9, 10, 11, 12].

However, power diagrams are not suitable for biological systems which are based on Euclidean distance metric. The weighted α -shape has limitations as well even though they reflect the size variations of atoms at a certain level.

In this paper, we present the theory of β -shape which reflects the size difference among atoms in their full Euclidean metric. Then, the quasi-triangulation, which is the topological dual of the Voronoi diagram of atoms, is defined. Based on the quasi-triangulation which is the topological dual of the Voronoi diagram of atoms, particular β -shapes can be easily constructed by a simple search.

2 α -Shape and Weighted α -Shape

2.1 α -Shape

In this section, we briefly review the three-dimensional α -shape. Let S be a finite set of points in \mathbb{R}^3 and α be a real number with $0 \leq \alpha \leq \infty$.

An α -shape is identical to the boundary of the convex hull of S when $\alpha = \infty$. For $\alpha = 0$, the α -shape reduces to the point set S itself. In general, α -shapes can be concave and disconnected. α -shapes can contain two-dimensional patches of triangles and one-dimensional strings of edges. Its components can be even points. An α -shape is a subset of the Delaunay triangulation of S , and it may have handles and interior voids. Note that each instance of an α -shape for a given value of α can be easily located by checking whether each simplex in the Delaunay triangulation remains or not. They analyzed the conditions for each simplex in the Delaunay triangulation to survive for the α -shape for a given value of α and provided a simple table to efficiently compute the α -shape [5].

2.2 Weighted α -Shape

Since α -shapes do not properly account for the size variations among atoms, Edelsbrunner extended the α -shape concept to the *weighted* α -shape by using the power diagram of the atoms [8]. Note that the distance metric in the power diagram is the power distance. Hence, the weighted α -shape takes the

size variations among atoms at a certain level. However, it is always necessary to check if the minimum distance between the two atoms defining a bisector in the power diagram really allows for a spherical eraser to freely pass between the two atoms.

However, we want to point out that the power diagram, and therefore the weighted α -shape, do not fully incorporate the proximity information among atoms in the full fidelity of Euclidean metric. Fig. 1(a) shows a set of 2D atoms with different sizes and the power diagram defined on the atom set. Fig. 1(b) shows its counterpart for the Voronoi diagram of atoms where the distance is defined as the minimum Euclidean distance from a point to the boundary of atoms. The dotted circle in Fig. 1(a) is a tangent circle which is computed from the three atoms a_1 , a_2 and a_4 corresponding to a vertex in the power diagram. Note that the tangent circle intersects with the atom a_3 . On the other hand, the dotted tangent circle in Fig. 1(b) corresponds to the Voronoi vertex and is guaranteed to be intersection-free with any other atoms. Therefore, the largest empty circle in the atomic structure can be easily found from the Voronoi diagram. However, the same computation is not so clear with the power diagram and a global search seems necessary.

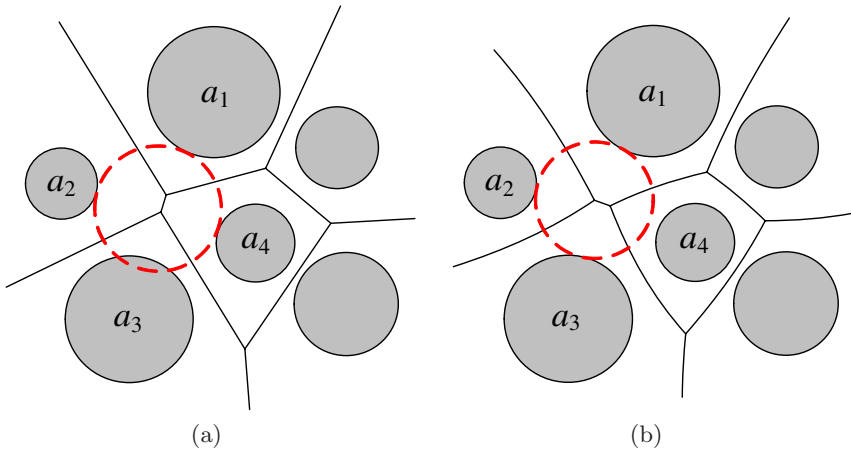


Fig. 1. Discrepancy between power diagram and Voronoi diagram

3 β -Hull and β -Shape

To fully incorporate the size differences of spheres in the definition of their proximity in Euclidean space, the concept of β -shape is proposed. We first introduce the concept of β -hulls and then extend it to β -shapes. Lastly, we propose a β -complex to compute any β -shape as a simple search from the β -complex. Being the generalization of the theory of α -shape, we will follow the presentation style of [5] for the sake of convenience in our presentation of this paper.

3.1 β -Hull

Conceptually, a β -hull is the generalization of an α -hull and can be similarly described. The point set, from which an α -hull is defined, is now replaced by a set of three dimensional spherical balls. As for the case of α -hulls, think of \mathbb{R}^3 filled with Styrofoam and some spherical rocks scattered around inside the Styrofoam. The radii of the spherical rocks vary. Then, carving out the Styrofoam with an omnipresent and empty spherical eraser with the radius of β will result in a β -hull. Since the eraser is omnipresent, there can be interior voids as well. The molecular surface used in biology quite a long time is indeed equivalent to the β -hull of the molecule [3, 4].

3.2 β -Shape

Suppose that we have a β -hull of an atom set A . Then, we straighten the surface of the β -hull by substituting straight edges for the circular ones and triangles for the spherical caps where the vertices are the centers of the atoms contributing the β -hull. Then, the straightened object is the β -shape of A . This is illustrated in Fig. 2.

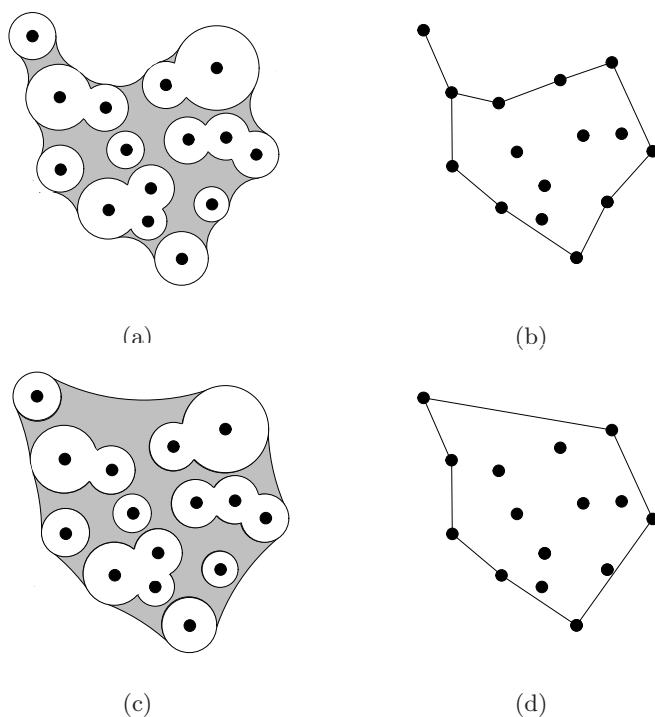


Fig. 2. β -hulls and β -shapes for a 2-dimensional atom set. (a) a set of 2-dimensional atoms and the β -hull corresponding to β_1 , (b) the β -shape of the atom set corresponding to β_1 , (c) and (d) the β -hull and β -shape of the same atom set corresponding to β_2 , where $0 \leq \beta_1 < \beta_2$.

The formal definition of β -shape follows. Let $A = \{a_i \mid i = 1, \dots, n\}$ be a finite set of three dimensional spheres a_i , which we call atoms, where $a_i = \{q \mid |q - c_i| \leq r_i\}$. Hence, each sphere is associated with a center c and a radius r . Let $C = \{c_i \mid i = 1, \dots, n\}$. For $0 \leq \beta \leq \infty$, a β -ball $b \in \mathbb{R}^3$ is an open ball with a radius β . Hence, a 0-ball is a point and an ∞ -ball is an open half space. A β -ball b is called *empty* iff $b \cap A = \emptyset$.

Definition 1. Suppose that b is a β -ball located at a particular location in three-dimensional space. Let $\widetilde{A}(b) = \{a \in A \mid b \cap A = \emptyset, a \cap \partial(b) \neq \emptyset\}$ and $\widetilde{C}(b) = \{c \mid a = (c, r) \in \widetilde{A}(b)\}$. Suppose Δ_b is the convex combination of elements in $\widetilde{C}(b)$. Then, the β -shape of $\mathcal{S}_\beta(A)$ of A is defined as a polytope bounded by a set $\{\bigcup_b \Delta_b, \text{ for all possible } b \text{ in the space}\}$ corresponding to a particular value of β .

A β -shape $\mathcal{S}_\beta(A)$ can be conveniently represented as sets of vertices, edges and faces. In other words, $\mathcal{S}_\beta(A) = (V^\beta, E^\beta, F^\beta)$ where $V^\beta = \{v_1^\beta, v_2^\beta, \dots\}$, $E^\beta = \{e_1^\beta, e_2^\beta, \dots\}$ and $F^\beta = \{f_1^\beta, f_2^\beta, \dots\}$ are sets of vertices, edges and faces of $\mathcal{S}_\beta(A)$, respectively. Note that $v_i^\beta \in V^\beta$ corresponds to the center c_i of an atom $a_i \in A$.

Fig. 3 shows different β -shapes computed by different probes from the atomic complex shown in Fig. 3(a). This example is a subset of a protein downloaded from PDB [13]. The model consists of 67 atoms (41 C's, 14 N's and 12 O's) and forms a secondary structure called an α -helix. Fig. 3(b) is a β -shape corresponding to a probe with a radius of infinity, i.e., $\beta = \infty$. On the other hand, Fig. 3(f) is the β -shape when $\beta = 0$ Å. Fig. 3(c) through (e) are the β -shapes corresponding to probe sizes of 5, 1.4 and 0.7 Å, respectively. When the probe reduces to a point (i.e, when $\beta = 0$), as shown in Fig. 3(f), the corresponding

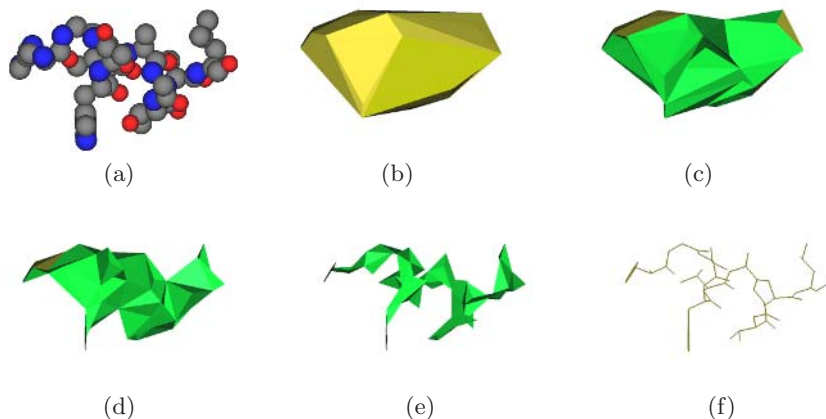


Fig. 3. The β -shapes computed by different probes from an atomic complex: (a) an atomic complex of a molecule consisting of 67 atoms (different colors denote different atoms) (b) The radius of probe β is infinity, i.e., $\beta = \infty$ Å (c) $\beta = 5$ Å (d) $\beta = 1.4$ Å (e) $\beta = 0.7$ Å and (f) $\beta = 0$.

β -shape results in a structure consisting of points, edges and/or triangles. Note that the intersection of two atoms transforms to an edge, and the simultaneous intersection among three atoms transforms to a triangle. When an atom is located far away from the other atom complex, it can even be reduced to an isolated point.

3.3 Quasi-triangulation

A Voronoi diagram $\text{VD}(A)$ for an atom set A is defined as follows. Associated with each atom $a_i \in A$, there is a corresponding *Voronoi region* VR_i for a_i , where $VR_i = \{p \mid \text{dist}(p, c_i) - r_i \leq \text{dist}(p, c_j) - r_j, i \neq j\}$, where $\text{dist}(p, q)$ denotes the Euclidean distance between points p and q . Then, $\text{VD}(A) = (V^V, E^V, F^V, C^V)$ is the Voronoi diagram for the given atoms and represented as $G^V = (V^V, E^V, F^V)$ where $V^V = \{v_1^V, v_2^V, \dots\}$, $E^V = \{e_1^V, e_2^V, \dots\}$, $F^V = \{f_1^V, f_2^V, \dots\}$ and $C^V = \{c_1^V, c_2^V, \dots, c_n^V\}$ are sets of Voronoi vertices, edges, faces, and Voronoi cells (or regions VR_i) respectively.

From the definition of a Voronoi diagram, a Voronoi vertex v^V is the center of an empty sphere tangent to four nearby atoms, while a Voronoi edge e^V is defined as a locus of points equi-distant from the surfaces of three surrounding atoms. In addition, a Voronoi face f^V is the surface defined by two neighboring atoms. Note that the face is always a hyperbolic surface and any point on the face is equi-distant from the surfaces of both atoms. For more details, readers are referred to [14, 15, 16].

Let a quasi-triangulation $\text{QT}(A)$ for an atom set A be defined as $\text{QT}(A) = (V^Q, E^Q, F^Q, C^Q)$, where $V^Q = \{v_1^Q, v_2^Q, \dots, v_n^Q\}$, $E^Q = \{e_1^Q, e_2^Q, \dots\}$, $F^Q = \{f_1^Q, f_2^Q, \dots\}$, and $C^Q = \{c_1^Q, c_2^Q, \dots\}$ denote the sets of vertices, edges, faces, and cells in the quasi-triangulation, respectively. Note that there is a one-to-one correspondence between a vertex v_i^Q and a generator atom $a_i \in A$.

A Voronoi diagram $\text{VD}(A)$ is mapped to a quasi-triangulation $\text{QT}(A)$ as follows.

- A Voronoi cell $c^V \in C^V$ is mapped to a vertex $v^Q \in V^Q$. The vertex v^Q corresponds to the center of a generator atom a_i corresponding to a Voronoi cell c^V .
- A Voronoi face $f^V \in F^V$ is mapped to an edge $e^Q \in E^Q$. The edge e^Q is a line segment bounded by two v^Q 's.
- A Voronoi edge $e^V \in E^V$ is mapped to a face $f^Q \in F^Q$. The face f^Q is a triangle bounded by three e^Q 's.
- A Voronoi vertex $v^V \in V^V$ is mapped to a cell $c^Q \in C^Q$. The cell c^Q is a tetrahedron bounded by four f^Q 's.

The dual structure $\text{QT}(A)$ is called a quasi-triangulation since it is not always a valid triangulation of \mathbb{R}^3 space. Recall that the topological duals of the Voronoi diagram of points and the power diagram are respectively called a Delaunay triangulation and a regular triangulation, and both triangulations are simplicial complexes which tessellate the convex hull of input points by a set of tetrahedra.

If they do intersect, then two tetrahedra in these triangulations intersect each other at a vertex, an edge, or a triangular face. In $\text{QT}(A)$, however, this property is not guaranteed.

Due to this non-simplicial complex nature of $\text{QT}(A)$, it is usually stored in a radial data structure for the corresponding Voronoi diagram of the atom set A [17]. Recently, a method has been proposed to directly store $\text{QT}(A)$ in a set of simple arrays called an interworld data structure [18]. The interworld data structure compactly stores the topology of $\text{QT}(A)$ without losing query efficiency.

4 β -Complex

Suppose that $\tilde{P} \subseteq A$ where $|\tilde{P}| = k + 1$ where k is the dimension of the space where \tilde{P} is defined. Let $b_{\tilde{P}}$ be the smallest open ball whose boundary $\partial b_{\tilde{P}}$ touches all atoms of \tilde{P} from outside. Hence, $2 \leq |\tilde{P}| \leq 4$ in the three-dimensional space since $1 \leq k \leq 3$. For $1 \leq k \leq 3$ and $0 \leq \beta \leq \infty$, define $G_{k,\beta}$ as the set of k -simplices $\sigma_{\tilde{P}} \in \text{QT}(A)$ for which $b_{\tilde{P}}$ is empty and $\rho_{\tilde{P}} < \beta$ where $\rho_{\tilde{P}}$ is the radius of $b_{\tilde{P}}$. Note that the vertices of $\sigma_{\tilde{P}}$ consists of the centers of appropriate atoms. Especially, $G_{0,\beta} = C$ for any value of β , where C is the set of atom centers.

A β -**complex** \mathcal{C}_β is defined as the set of either k -simplices $\sigma_{\tilde{P}}$ in $G_{k,\beta}$ or those k -simplices which bound $(k + 1)$ -simplices in \mathcal{C}_β . In addition, $G_{k,\beta} \subseteq \text{QT}(A)$.

Definition 2. $\mathcal{C}_\beta = \{\sigma_{\tilde{P}} \cup \sigma_{\tilde{P}'} \mid \sigma_{\tilde{P}} \in G_{k,\beta}, \tilde{P}' \subset \tilde{P}, 0 \leq k \leq 3\}$.

4.1 Classification of Simplexes

Each simplex in a β -complex \mathcal{C}_β may take one of the following three states depending on the value of β .

- **Singular:** The simplex belongs to the boundary of β -shape \mathcal{S}_β and does not bound any higher-dimensional simplex in β -complex \mathcal{C}_β .
- **Regular:** The simplex belongs to the boundary of β -shape \mathcal{S}_β and bounds higher-dimensional simplex in β -complex \mathcal{C}_β .
- **Interior:** The simplex does not belong to the boundary of β -shape \mathcal{S}_β .

In addition, a simplex can be one of the following three situations depending on the condition of the smallest possible tangent sphere Z which is simultaneously tangent to the atoms corresponding to the vertices of the simplex from outside.

- **unattached:** There is no intersection between Z and the atoms corresponding to the vertices of the simplex.
- **attached:** There is an intersection between Z and the atoms corresponding to the vertices of the simplex.
- **nottached:** All of the atoms corresponding to the simplex intersect each other. In this case, there is always an edge (or face in the higher dimensional case) regardless the value of β , and it is not even necessary to check if it is attached or unattached and hence we call this *nottached*.

Table 1. Intervals of β -values for β -complex

	singular	regular	interior
tetrahedron			$(\rho, \infty]$
edge or triangle, $\notin \partial\widetilde{\text{CH}}(A)$, unattached	$(\rho_{\tilde{P}}, \underline{\mu}_{\tilde{P}})$	$(\underline{\mu}_{\tilde{P}}, \overline{\mu}_{\tilde{P}})$	$(\overline{\mu}_{\tilde{P}}, \infty]$
$\notin \partial\widetilde{\text{CH}}(A)$, attached		$(\underline{\mu}_{\tilde{P}}, \overline{\mu}_{\tilde{P}})$	$(\overline{\mu}_{\tilde{P}}, \infty]$
$\notin \partial\widetilde{\text{CH}}(A)$, nottached	$[0, \underline{\mu}_{\tilde{P}})$	$(\underline{\mu}_{\tilde{P}}, \overline{\mu}_{\tilde{P}})$	$(\overline{\mu}_{\tilde{P}}, \infty]$
$\in \partial\widetilde{\text{CH}}(A)$, unattached	$(\rho_{\tilde{P}}, \underline{\mu}_{\tilde{P}})$	$(\underline{\mu}_{\tilde{P}}, \infty]$	
$\in \partial\widetilde{\text{CH}}(A)$, attached		$(\underline{\mu}_{\tilde{P}}, \infty]$	
$\in \partial\widetilde{\text{CH}}(A)$, nottached	$[0, \underline{\mu}_{\tilde{P}})$	$(\underline{\mu}_{\tilde{P}}, \infty]$	
vertex, $\notin \partial\widetilde{\text{CH}}(A)$	$[0, \underline{\mu}_{\tilde{P}})$	$(\underline{\mu}_{\tilde{P}}, \overline{\mu}_{\tilde{P}})$	$(\overline{\mu}_{\tilde{P}}, \infty]$
$\in \partial\widetilde{\text{CH}}(A)$	$[0, \underline{\mu}_{\tilde{P}})$	$(\underline{\mu}_{\tilde{P}}, \infty]$	

Then, the valid intervals of β values for each simplex are shown in the following table 1. Let $\text{CH}(A)$ denote the convex hull of whole atoms in the atom set A , and $\widetilde{\text{CH}}(A)$ denote the convex hull of the centers of all atoms in A . In addition, let $\widetilde{\text{CH}}(A)$ denote the polytope defined by the centers of atoms which contribute to $\text{CH}(A)$. When there is a cylindrical boundary between a pair of atoms in $\text{CH}(A)$, a corresponding edge is defined in $\widetilde{\text{CH}}(A)$ between the centers of the two atoms. When there is a triangular boundary for a triplet of atoms in $\text{CH}(A)$, a corresponding triangle is defined in $\widetilde{\text{CH}}(A)$ among the centers of the three atoms. Note that $\widetilde{\text{CH}}(A)$ is not identical to $\text{CH}(C)$ in general.

All simplices $\sigma_{\tilde{P}} \in \text{QT}(A)$ have their respective intervals according to the singular, regular or interior states in complex \mathcal{C}_{β} . $\sigma_{\tilde{P}}$ is a face of the β -shape \mathcal{S}_{β} iff β is contained in this interval. A regular simplex belongs to the boundary of the interior of β -shapes. In a β -complex, a regular simplex bounds some higher-dimensional simplexes while a singular simplex does not. The interior simplices triangulate the interior of β -shapes.

Given a quasi-triangulation $\text{QT}(A)$, therefore, the presented algorithm can compute β -complex in $O(m)$ time in the worst case, where m is the number of simplices in $\text{QT}(A)$. Once the simplicies in the β -complex are sorted according to their respective intervals, it is obvious that the β -shape of a particular value of β can be computed in $O(\log m + k)$ time in the worst case where the β -shape has k simplices.

4.2 Interpretations of Intervals: Edge Cases

Suppose that an edge $\sigma_{\tilde{P}} \in \text{QT}(A)$ is defined by the centers of two atoms $\tilde{P} = \{a_i, a_j\}$. Recall that $\rho_{\tilde{P}}$ the radius of Z which is an open ball $b_{\tilde{P}}$ whose boundary is tangent to the both atoms a_i and a_j .

Note that the edge $\sigma_{\tilde{P}}$ is shared by a number m of triangles which are higher dimensional simplexes. Each triangle t_{im} is then associated with the smallest open ball b_{im} which is tangent to the atoms corresponding to the vertices of

the triangle t_{im} . Then, let $\underline{\mu}_{\tilde{P}}$ be the radius of the smallest ball among all b 's. Similarly, $\overline{\mu}_{\tilde{P}}$ denotes the radius of the largest ball among all b 's.

The rules for the triangles and tetrahedra can be easily understood by extrapolating the explanations for the edges.

5 Discussions and Conclusions

The α -shape for a set of finite points in 3D is a well-known concept and it is extensively used in various applications such as structural biology, computer graphics, computational geometry, CAD, etc.

In this paper, we generalized the α -shape and α -complex (also their *weighted* counterparts as well) for a set of points to a β -shape and a β -complex for a set of spheres with arbitrary sizes. After computing the Voronoi diagram of spheres, we transform the Voronoi diagram to a quasi-triangulation which is the topological dual of the Voronoi diagram. Then, an analysis of intervals is done with the quasi-triangulation. From this analysis, a simple interval table is created which computes the β -complex as well as the β -shape.

Even though the quasi-triangulation may not be a complex, the presented algorithm computes β -complex from the Voronoi diagram of spheres in $O(m)$ time in the worst case, where m is the number of simplices in the quasi-triangulation. Then, the simplices in the β -complex are sorted for queries and this takes $O(m \log m)$ time. Then, the β -shape of a particular value of β can be computed $O(\log m + k)$ time in the worst case where the β -shape has k simplices.

The β -complex and β -shape can be used for various applications.

Acknowledgements

This research was supported by Creative Research Initiatives from the Ministry of Science and Technology, Korea.

References

1. Lee, B., Richards, F.M.: The interpretation of protein structures: Estimation of static accessibility. *Journal of Molecular Biology* **55** (1971) 379–400
2. Richards, F.M.: Areas, volumes, packing, and protein structure. *Annual Review of Biophysics and Bioengineering* **6** (1977) 151–176
3. Connolly, M.L.: Analytical molecular surface calculation. *Journal of Applied Crystallography* **16** (1983) 548–558
4. Connolly, M.L.: Solvent-accessible surfaces of proteins and nucleic acids. *Science* **221** (1983) 709–713
5. Edelsbrunner, H., Mücke, E.P.: Three-dimensional alpha shapes. *ACM Transactions on Graphics* **13**(1) (1994) 43–72
6. Kim, D.S., Kim, D., Sugihara, K.: Voronoi diagram of a circle set from Voronoi diagram of a point set: I. topology. *Computer Aided Geometric Design* **18** (2001) 541–562

7. Kim, D.S., Kim, D., Sugihara, K.: Voronoi diagram of a circle set from Voronoi diagram of a point set: II. geometry. *Computer Aided Geometric Design* **18** (2001) 563–585
8. Edelsbrunner, H.: Weighted alpha shapes. Technical Report UIUCDCS-R-92-1760, Department of Computer Science, University of Illinois at Urbana-Champaign, Urbana, IL (1992)
9. Edelsbrunner, H., Facello, M., Liang, J.: On the definition and the construction of pockets in macromolecules. *Discrete Applied Mathematics* **88** (1998) 83–102
10. Liang, J., Edelsbrunner, H., Woodward, C.: Anatomy of protein pockets and cavities: Measurement of binding site geometry and implications for ligand design. *Protein Science* **7** (1998) 1884–1897
11. Liang, J., Edelsbrunner, H., Fu, P., Sudhakar, P.V., Subramaniam, S.: Analytical shape computation of macromolecules: I. molecular area and volume through alpha shape. *PROTEINS: Structure, Function, and Genetics* **33** (1998) 1–17
12. Liang, J., Edelsbrunner, H., Fu, P., Sudhakar, P.V., Subramaniam, S.: Analytical shape computation of macromolecules: II. inaccessible cavities in proteins. *PROTEINS: Structure, Function, and Genetics* **33** (1998) 18–29
13. : (RCSB Protein Data Bank Homepage) <http://www.rcsb.org/pdb/>.
14. Kim, D.S., Cho, Y., Kim, D.: Euclidean Voronoi diagram of 3D balls and its computation via tracing edges. *Computer-Aided Design* **37**(13) (2005) 1412–1424
15. Kim, D.S., Cho, Y., Kim, D., Cho, C.H.: Protein structure analysis using Euclidean Voronoi diagram of atoms. In: *Proceedings of the International Workshop on Biometric Technologies (BT2004)*. (2004) 125–129
16. Kim, D.S., Cho, Y., Kim, D., Kim, S., Bhak, J., Lee, S.H.: Euclidean Voronoi diagrams of 3D spheres and applications to protein structure analysis. In: *Proceedings of the 1st International Symposium on Voronoi Diagrams in Science and Engineering (VD2004)*. (2004) 137–144
17. Cho, Y., Kim, D., Kim, D.S.: Topology representation for the Voronoi diagram of 3D spheres. *International Journal of CAD/CAM* **5**(3) (2005) in press.
18. Kim, D.S., Kim, D., Cho, Y., Sugihara, K.: Quasi-triangulation and interworld data struction in three dimensions. *Computer-Aided Design* (**submitted**) (2005)

Reduction of the Search Space in the Edge-Tracing Algorithm for the Voronoi Diagram of 3D Balls

Youngsong Cho¹, Donguk Kim¹, Hyun Chan Lee²,
Joon Young Park³, and Deok-Soo Kim⁴

¹ Voronoi Diagram Research Center, Hanyang University, Seoul, Korea
{ycho, donguk}@voronoi.hanyang.ac.kr

² Dept. of Industrial Engineering, Hongik University, Seoul, Korea
hclee@wow.hongik.ac.kr

³ Dept. of Industrial and Systems Engineering, Dongguk University, Seoul, Korea
jypark@dgu.edu

⁴ Dept. of Industrial Engineering, Hanyang University, Seoul, Korea
dskim@hanyang.ac.kr

Abstract. Voronoi diagram for 3D balls can be applicable to various fields in science and engineering. The edge-tracing algorithm constructs the Voronoi diagram in $O(mn)$ time in the worst-case where m and n are the numbers of edges and balls, respectively. The computation time of the algorithm is dominated by finding the end vertex of a given edge since all edges in the Voronoi diagram should be traced essentially. In this paper, we define the feasible region which a ball to define the end vertex of a given edge should intersect. Then, balls which do not intersect the feasible region are filtered out before finding an end vertex since they cannot define an end vertex. Therefore, we improve the runtime-performance of the edge-tracing algorithm via the feasible region.

Keywords: Voronoi diagram for balls, edge-tracing algorithm, feasible region.

1 Introduction

Voronoi diagram has been known as one of the central topics in many disciplines in science and engineering including computational geometry. Especially, the Voronoi diagram for 3D balls in the Euclidean distance metric, often called an *additively weighted Voronoi diagram* in the computational geometry community [1], can have more significant applications in various fields than its planar counterpart since most important geometric problems are 3D in nature. For example, the structural analysis of proteins or RNA's requires an efficient computational tool to analyze the spatial properties among atoms [2, 3, 4, 5].

While an ordinary Voronoi diagram for points has been extensively studied [1], Euclidean Voronoi diagram for 3D balls has not been sufficiently explored. There are only a few previous works on this Voronoi diagram [6, 7, 8, 9, 10, 11, 12].

Among them, the edge-tracing algorithm, recently reported on the full implementation, is a simple and powerful algorithm for constructing the whole Voronoi diagram [10, 13]. Starting from a valid initial Voronoi vertex, the edge-tracing algorithm follows Voronoi edges until the construction is completed. In the worst-case, the edge-tracing algorithm takes $O(mn)$ time where m and n are the numbers of edges and balls, respectively.

In the edge-tracing algorithm, the computation time is dominated by finding the end vertex of a given Voronoi edge. Note that an edge is always defined by three neighboring balls called *gate balls* and a vertex is defined as the center of the sphere tangent to four balls. Therefore, finding an end vertex of an edge is equivalent to finding a ball to define a tangent sphere, together with gate balls, corresponding to the end vertex of the given edge. In fact, this can be done by searching all of input balls except three gate balls. However, some balls may define no tangent sphere with gate balls or make a tangent sphere intersecting other balls such as a ball defining a start vertex of the given edge. If we filter out these balls, we can save the computation time for these balls.

In this paper, we present the feasible region which a ball to define an end vertex should intersect, to reduce the search space to find an end vertex. Then, balls which do not intersect the feasible region can be filtered out before finding an end vertex since they cannot define an end vertex. Therefore, we can improve the runtime performance of the edge-tracing algorithm via the feasible region.

This paper is organized as follows. In Section 2, we define the Voronoi diagram of 3D balls and briefly describe the edge-tracing algorithm to construct the diagram. In Section 3, we discuss the process to find an end vertex in detail. The feasible region for an end ball is defined in Section 4. We give the discussions on the experimental performance of the feasible region in Section 5. In Section 6, we conclude this paper with some future works.

2 Brief Review of Edge-Tracing Algorithm

In this section, we define the Voronoi diagram of 3D balls and briefly describe the edge-tracing algorithm to construct the Voronoi diagram in $O(mn)$ time in the worst-case.

2.1 Definition of Voronoi Diagram for 3D Balls

Let $B = \{b_1, b_2, \dots, b_n\}$ be a set of generators for a Voronoi diagram where b_i is a 3-dimensional spherical ball. Hence, $b_i = (c_i, r_i)$ where $c_i = (x_i, y_i, z_i)$ and r_i denote the center and the radius of a ball b_i , respectively. We assume that no ball is completely contained inside another ball even though intersections are allowed among balls. Associated with each ball b_i , there is a corresponding *Voronoi region* VR_i for b_i , where $VR_i = \{p \mid dist(p, c_i) - r_i \leq dist(p, c_j) - r_j, i \neq j\}$. Then, $VD(B) = \{VR_1, VR_2, \dots, VR_n\}$ is called a *Voronoi diagram* for B . In this paper, the ordinary L_2 -metric is used to define Euclidean Voronoi diagram.

As in the ordinary Voronoi diagrams, Voronoi regions are bounded by a set of faces, call *Voronoi faces*, where a Voronoi face is defined by two neighboring balls.

Note that a face is always a hyperboloid. A Voronoi face intersects another face to form a *Voronoi edge* which is a conic section. When Voronoi edges intersect, a *Voronoi vertex* is defined. Note that there is always one-to-one correspondence between a Voronoi vertex and a sphere tangent to neighboring balls defining the vertex. Hence a tangent sphere is always centered at the corresponding vertex. In that case, the tangent sphere is called *empty* since it never intersects or contains any other ball except at tangent points with its generating balls.

In this paper, we assume that the degree of a Voronoi vertex is always four which means that no five balls are cotangent to an empty tangent sphere. We also assume that a Voronoi edge is always a common intersection among three Voronoi faces and therefore only three balls define an edge. We call a spherical generator defining a Voronoi diagram a *ball* in this paper, while a *sphere* denotes a tangent sphere corresponding to a Voronoi vertex. For the convenience of notation, we will ignore the term *Voronoi* and call simply a *vertex*, *edge* or *face* unless it is necessary. Similarly, the term *Euclidean* will be also minimally used.

2.2 Overview of Edge-Tracing Algorithm

The edge-tracing algorithm first locates a true Voronoi vertex v_1 by computing an empty tangent sphere defined by four appropriate nearby balls. Provided that v_1 has been found, four edges e_1 , e_2 , e_3 , and e_4 emanating from v_1 can be easily identified and pushed into a stack called Edge-stack. Hence, those edges have v_1 as their starting vertices. After popping an edge from the stack, the algorithm computes the end vertex of the edge. Note that a vertex can be found by computing an appropriate empty tangent sphere from each of candidate balls plus three gate balls defining the popped edge.

If an appropriate empty tangent sphere is found, the center of the sphere becomes the end vertex of the popped edge. Once the end vertex of currently popped edge is found, it is also possible to compute three more edges emanating from this new vertex. Hence, when an edge is created, its end vertex is used as the start vertex of another three new-born edges. Note that these edges are also pushed into Edge-stack. By repeating this process until Edge-stack is empty, the computation of a Voronoi diagram of a connected edge graph is completed.

The process to trace an edge iterates m times where m is the number of edges. Each process is completed by finding the true end vertex of the given edge. This algorithm takes $O(mn)$ in the worst case. It is known that m is $O(n^2)$ in the worst case and $O(n)$ on the average for general ball set where n is the number of balls. For more details, readers are recommended to refer to [10].

3 Location of End Vertex of a Given Edge

In the edge-tracing algorithm, the process to trace an edge is completed by finding the end vertex of the edge. An edge is always defined by three gate balls and its end vertex are defined as the center of the sphere simultaneously tangent to gate balls and a ball, called an *end ball* b_e , in a set of input balls B . Therefore, finding the end vertex of an edge is equivalent to finding the end ball to define a

tangent sphere, together with gate balls, corresponding to the end vertex. Then, a ball in B except three gate balls may become the end ball. The set of these balls which consists of $n - 3$ balls is called a *set of candidate balls* B_c for an end vertex.

To find the end vertex of a given edge e , we can first consider a brute-force algorithm as follows. We first compute a sphere s_i tangent to gate balls and a ball b_i in B_c , and test the emptiness of s_i against $n - 4$ balls in $B_c \setminus \{b_i\}$. Note that only an empty tangent sphere can define an end vertex as its center. We may also find more than one empty tangent spheres. In that case, we select a tangent sphere with the closest center to v_s among them. This algorithm to find an end vertex of an edge takes $O(n^2)$ time in the worst-case since the emptiness of a tangent sphere defined by gate balls and a ball b_i among $n - 3$ balls of B_c is guaranteed by the intersection test against $n - 4$ balls in $B_c \setminus \{b_i\}$.

The above time complexity can be improved by one scanning of candidate balls based on an angular distance which is defined by the angle between a start vertex v_s and a candidate end vertex of a given edge. We first compute a sphere tangent to gate balls and each ball in B_c and an angular distance between v_s and a candidate end vertex as the center of the tangent sphere. Then, the end vertex is defined as the center of tangent sphere with the minimum angular distance. Therefore, we can find the end vertex of an edge in $O(n)$ time in the worst case and compute Voronoi diagram of balls in $O(mn)$ time in the worst case [10].

As discussed above, we examined all candidate balls to find the end vertex of an edge. However, there are some balls among them which may define a tangent sphere which intersects another balls such as a ball defining a start vertex of the given edge or define no tangent sphere to three gate balls simultaneously. If we filter out such balls from a set of candidate balls B_c before finding an end vertex, we can save the computation time for filtered balls. Therefore, filtering B_c may contribute largely to the improvement for the runtime-performance of the edge-tracing algorithm. Note that the number of edges to be traced cannot be reduced since we should trace all Voronoi edges in the Voronoi diagram due to essential characteristics of the edge-tracing algorithm.

4 Reduction of Search Space by Feasible Region

According to the definition of a Voronoi edge e , e is a set of equidistant points from gate balls. Let us consider a set S of spheres tangent to gate balls. Then, e can also be defined as the locus of centers of spheres in S . An edge e is oriented from a *start vertex* v_s to an *end vertex* v_e . The empty tangent spheres corresponding to v_s and v_e are called a *start tangent sphere* s_s and an *end tangent sphere* s_e , respectively. Two balls to define s_s and s_e together with gate balls are called a *start ball* b_s and an *end ball* b_e , respectively.

Note that s_s and s_e are also tangent to gate balls, that is, $s_s, s_e \in S$. Therefore, b_s and b_e intersect the union of tangent spheres in S . In this section, we define the subregion of this union, which b_e should intersect, called a *feasible region* R for b_e . Since the feasible region is defined differently according to Voronoi edges,

we classify Voronoi edges into two types: a *non-elliptic edge* and an *elliptic edge*. Therefore, parabolic, hyperbolic, and linear edges belong to the non-elliptic edges and circular and elliptic edges belong to elliptic edges.

4.1 Feasible Region in Non-elliptic Edge

Given three balls, b_{g_1} , b_{g_2} , and b_{g_3} , to define a non-elliptic edge, let us consider a set S of tangent spheres to these balls. Let a *center plane* P_c be a plane defined by centers of three balls. Then, the edge intersects P_c at a single point which corresponds to the center of a minimum tangent sphere s_{min} in S . Starting from s_{min} , we trace tangent spheres through the edge orientation. At last, we can arrive at a tangent sphere s_∞ with infinite radius. This time, we trace tangent spheres from s_{min} on the opposite orientation of the edge. Also, we can arrive at a infinite tangent sphere $s_{-\infty}$. Fig. 1(a) shows tangent spheres in S and the union of tangent spheres. As shown in the figure, this union is unbounded. The union of tangent spheres and the edge are symmetric around P_c , since the gate balls to define the edge are symmetric.

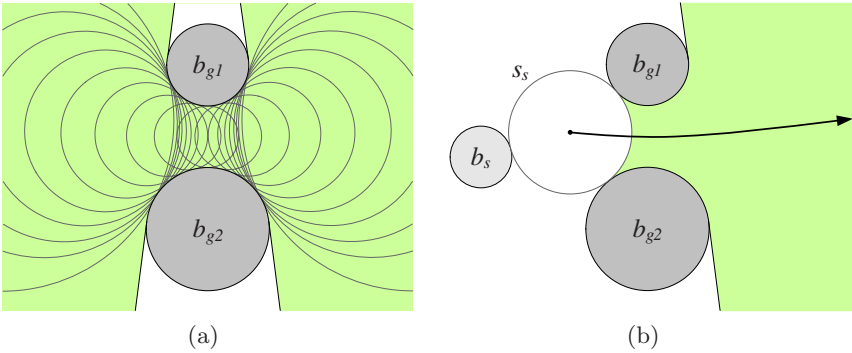


Fig. 1. Defining the feasible region in a non-elliptic edge. (In the figure illustrating its 2D analogy, only two gate balls are shown.) (a) the union of spheres tangent to gate balls, and (b) the feasible region to define an end vertex of a non-elliptic edge.

When we find an end vertex of a non-elliptic edge e in the edge-tracing algorithm, the gate balls and the start vertex v_s of e is already known. The start tangent sphere s_s corresponding to v_s of e is simultaneously tangent to the gate balls and a start ball b_s . Then, any ball in B except gate balls does not intersect s_s since s_s is an empty sphere. Let us consider a tangent sphere s whose center is near v_s on the opposite orientation of e . Then, s is not an empty tangent sphere any longer since it intersects b_s . In addition, e cannot arrive at the center of s by tracing on the edge orientation since e goes on the center of s_∞ which is not identical to $s_{-\infty}$. Therefore, s cannot define the end vertex of e . It means that we can consider only tangent spheres on the edge orientation from a start vertex as shown in Fig. 1(b). S_r denotes a set of tangent spheres in the interval $(s_s, s_\infty]$. Then, one of the centers of spheres in S_r may become the end vertex

and therefore an end tangent sphere s_e is an element of S_r , that is $s_e \in S_r$. It means that an end ball b_e , to define s_e together with gate balls, intersects the union of tangent spheres in S_r . We call the union the *feasible region*, R , of the end ball to define an end vertex of a non-elliptic Voronoi edge.

Let us observe a ball b_i intersecting the feasible region R as shown in Fig. 2(a). b_i defines a tangent sphere s_i . If s_i is empty, does this emptiness guarantee that b_i is a true end ball b_e ? However, the answer is NO, since there may be an arbitrary ball in the region between s_s and s_i and it can define closer tangent sphere to a start vertex than s_i such as b_j in Fig. 2(a). Therefore, we should check this region to guarantee that the center of s_i is a valid end vertex.

Suppose that there is no ball in the region defined between s_s and s_i as shown in Fig. 2(b). If s_i is empty, the center of s_i becomes a true end vertex. Otherwise, there is another ball b_j intersecting s_i as shown in Fig. 2(b). Then, b_j can define a closer tangent sphere s_j and its center becomes v_e . In this case, one of balls intersecting with s_i must define a true end vertex.

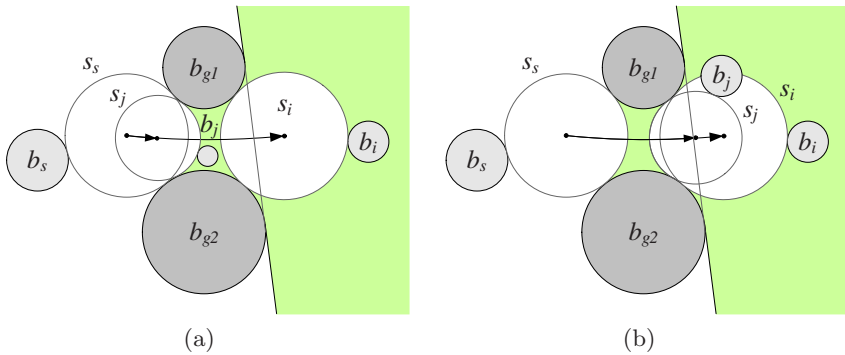


Fig. 2. Search of an end ball on the feasible region. (a) search on a front feasible region, and (b) search on a rear feasible region.

According to the position of a ball on the feasible region, we can construct the following strategy to find a true end vertex. Let a *gate plane* P_g be a plane which corresponds to an infinite tangent sphere s_∞ on the edge orientation. We divide the feasible region R into two subregion: *front feasible region* R_f and *rear feasible region* R_r according to P_g . To find an end vertex v_e , we first search balls intersecting R_f . If the closest tangent sphere s defined by one of them is completely included in R_f , s defines v_e . Otherwise, there is an end ball among balls intersecting s . If there is no ball intersecting R_f , we search balls intersecting R_r next. If there is a tangent sphere s by a ball intersecting R_r and it is empty, s defines v_e . If s is not empty, there should be an end ball b_e among balls intersecting s . If there is no ball intersecting R_f and R_r , the edge goes to infinity.

4.2 Feasible Region in Elliptic Edge

Given three gate balls, one of them may be completely included in the convex-hull of the other two balls. Then, these gate balls define an elliptic Voronoi edge. Let us consider spheres tangent to these gate balls. In Fig. 3(a), the whole spheres tangent to gate balls are shown on a center plane P_c and a edge plane P_e which an edge lies on. As shown in the figure, the union of spheres in a set of tangent spheres S is defined as a bounded region. And the union and the edge are also symmetric for P_c . Note that a circular Voronoi edge is defined by three gate balls whose centers are collinear.

As a non-elliptic edge, a start vertex v_s is the center of a start tangent sphere s_s defined by gate balls and a start ball b_s . Note that b_s intersects the union of tangent spheres since $s_s \in S$. In the elliptic edge, a ball intersecting the union always defines two tangent spheres while one or two tangent spheres may be defined in a non-elliptic edge. Therefore, b_s and gate balls also define two tangent spheres as shown in Fig. 3(b). In the figure, s_s is a tangent sphere corresponding to v_s and s'_s is the other sphere tangent to b_s . We assume that the elliptic edge starting from the center of s_s go to the center of s'_s . The tangent spheres in the interval (s'_s, s_s) always intersect the start ball b_s . Therefore, a ball to define the end vertex of an elliptic edge should intersect a sphere in the interval $(s_s, s'_s]$. The feasible region R for an elliptic edge can be defined as the union of sphere in the interval $(s_s, s'_s]$.

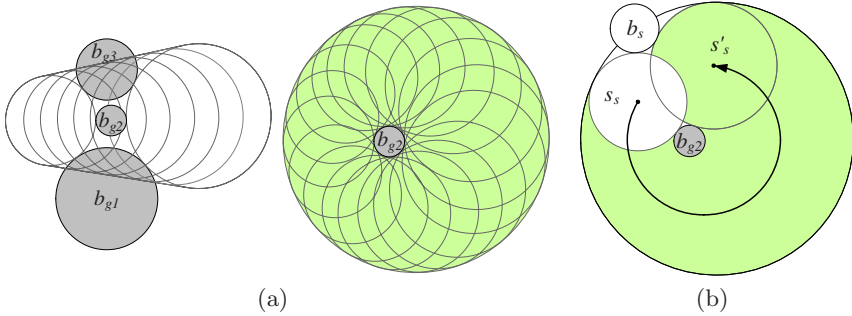


Fig. 3. Defining the feasible region in an elliptic edge. (a) the union of spheres tangent to gate balls, and (b) the feasible region to define an end vertex of an elliptic edge.

Suppose that a ball b_i intersecting the feasible region defines an empty tangent sphere s_i . There may be a ball b_j located in the region between s_s and s_i in the feasible region and b_j can define closer tangent sphere to a start vertex than s_i . Therefore, all balls in the region between s_s and s_i of the feasible region should be checked to guarantee that s_i defines an end vertex v_e as a candidate ball in the front feasible region for a non-elliptic edge.

To find an end vertex efficiently, we had better search the feasible region through an edge from its start vertex. During the search in the feasible region to trace an edge, we may find a candidate end vertex to guarantee a minimum angular distance. Then, this vertex becomes the end vertex without the search

of remaining the feasible region. This also makes the practical reduction of the search space for the end ball.

5 Experiment and Discussion

The Voronoi diagram for balls is applicable to various problems in science and engineering. Among them, problems associated with proteins can be efficiently solved via Voronoi diagram for atoms. In this paper, we use the structural data of proteins from Protein Data Bank which is a public repository of protein structural data [14]. The protein data has some unique characteristics. First, most proteins consist of six different types of atoms. Therefore, the differences in the atom radii are within a constant. In addition, m is $O(n)$ in the worst case for proteins since the number of immediate neighbor atoms for an atom is constant [15] where m and n are the numbers of Voronoi edges and atoms, respectively.

As mentioned in Section 3, the computation time of the edge-tracing algorithm is dominated by the process to find an end vertex. In the previous work [10], we computed angular distances for all input balls except three gate balls. In this case, the candidate ball set B_c defined by this full search consists of $n - 3$ balls. However, the feasible region can filter out balls which cannot define an end vertex. Therefore, the candidate ball set B_r defined by the feasible region only consists of balls intersecting the feasible region. In Fig. 4, the average numbers of balls in B_c and B_r are shown. The figure shows that about 60 % balls in B_c intersect the feasible region.

As discussed in the previous section, we do not need to search the rear feasible region for a non-elliptic edge if a true end vertex is defined by a ball in the front feasible region. The protein is a dense model because of its physicochemical properties. Therefore, we can expect that there are many balls intersecting the front feasible region. According to the experiments, the end balls of about 70 % non-elliptic edges intersect their front feasible regions and these front feasible regions also have 8 intersecting balls on the average. This means that we can find end vertices of 70 % non-elliptic edges by checking 8 balls per an edge on the average.

In addition, we actually count the number of balls to be searched for finding a valid end vertex. The set B_a of balls by defined by actual search is extremely small. For protein data in the paper, only 23 to 38 balls per an edge are searched on the average. To find an end vertex, we search candidate balls as follows. We first define a bucket as a minimum sized axis-aligned bounding box containing all input balls, and then divide the bucket into a number of elements by defining some axis-parallel planes. If a bucket element intersects a ball, the element and the ball have pointer to each other. We approximate the front and rear feasible region since it is not easy to compute intersection between a ball and a feasible region. The front feasible region is approximated by a sphere to completely enclose the region. The enclosing sphere passes through three tangent points between gate balls and a gate plane and its center lies on a center plane.

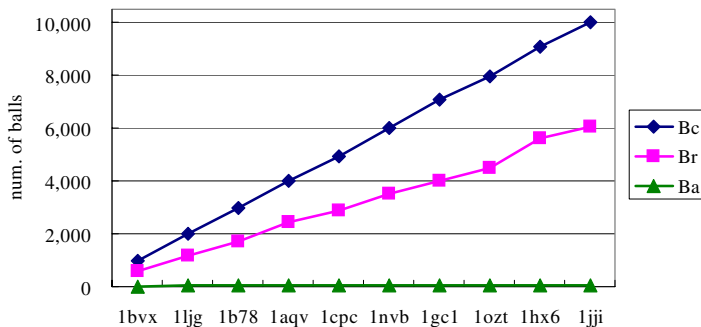


Fig. 4. The average numbers of balls in the candidate ball sets, B_c , B_r , and B_a , respectively defined by full search, the feasible region, and actual search for the end vertex of a given edge. Each protein data consists of many atoms as follows. (1bvx: 1,001, 1ljg: 2,002, 1b78: 2,990, 1aqv: 3,998, 1cpc: 4,921, 1nvb: 5,993, 1gc1: 7,080, 1ozt: 7,966, 1hx6: 9,091, 1jji: 10,032).

The rear feasible region is represented as the half-space of a gate plane. The balls intersecting the enclosing sphere for a front feasible region are searched first. If we cannot find the ball to define a true end vertex among them, we search balls in the half-space for the rear feasible region by propagating bucket elements.

6 Conclusion

The Voronoi diagram for 3D balls in the Euclidean distance metric can have significant applications in various fields since most important geometric problems are 3D in nature. The edge-tracing algorithm, recently reported on the full implementation, is a simple and powerful algorithm for constructing the whole Voronoi diagram which takes $O(mn)$ time in the worst-case where m and n are the numbers of edges and balls, respectively.

The computation time of the edge-tracing algorithm is dominated by finding the end vertex of a given Voronoi edge. In the previous work, a true end vertex was found by searching the whole balls except three gate balls to define a given edge. In this paper, we defined the feasible region for non-elliptic and elliptic edges. We could filter out balls which cannot define an end vertex before finding an end vertex. The feasible region showed the powerful filtering performance especially for dense models such as protein data. Therefore, we can improve the runtime performance of the edge-tracing algorithm via the feasible region.

Acknowledgements

This research was supported by Creative Research Initiative grant from the Ministry of Science and Technology, Korea.

References

1. Okabe, A., Boots, B., Sugihara, K., Chiu, S.N.: Spatial Tessellations: Concepts and Applications of Voronoi Diagrams. 2nd edn. John Wiley & Sons, Chichester (1999)
2. Goede, A., Preissner, R., Frömmel, C.: Voronoi cell: New method for allocation of space among atoms: Elimination of avoidable errors in calculation of atomic volume and density. *Journal of Computational Chemistry* **18**(9) (1997) 1113–1123
3. Kim, D.S., Cho, Y., Kim, D., Cho, C.H.: Protein structure analysis using Euclidean Voronoi diagram of atoms. In: Proceedings of the International Workshop on Biometric Technologies (BT2004). (2004) 125–129
4. Kim, D.S., Cho, C.H., Kim, D., Cho, Y.: Recognition of docking sites on a protein using β -shape based on voronoi diagram of atoms. *Computer-Aided Design* (2005) in printing.
5. Richards, F.M.: The interpretation of protein structures: Total volume, group volume distributions and packing density. *Journal of Molecular Biology* **82** (1974) 1–14
6. Aurenhammer, F.: Power diagrams: Properties, algorithms and applications. *SIAM Journal on Computing* **16** (1987) 78–96
7. Boissonnat, J.D., Karavelas, M.I.: On the combinatorial complexity of Euclidean Voronoi cells and convex hulls of d -dimensional spheres. In: Proceedings of the 14th Annual ACM-SIAM Symposium on Discrete Algorithms. (2003) 305–312
8. Gavrilova, M.: Proximity and Applications in General Metrics. PhD thesis, Department of Computer Science, The University of Calgary, Calgary, Canada (1998)
9. Gavrilova, M., Rokne, J.: Updating the topology of the dynamic Voronoi diagram for spheres in Euclidean d -dimensional space. *Computer Aided Geometric Design* **20**(4) (2003) 231–242
10. Kim, D.S., Cho, Y., Kim, D.: Euclidean Voronoi diagram of 3D balls and its computation via tracing edges. *Computer-Aided Design* **37**(13) (2005) 1412–1424
11. Luchnikov, V.A., Medvedev, N.N., Oger, L., Troadec, J.P.: Voronoi-Delaunay analysis of voids in systems of nonpherical particles. *Physical Review E* **59**(6) (1999) 7205–7212
12. Will, H.M.: Computation of Additively Weighted Voronoi Cells for Applications in Molecular Biology. PhD thesis, Swiss Federal Institute of Technology, Zurich (1999)
13. Cho, Y., Kim, D., Kim, D.S.: Topology representation for the Voronoi diagram of 3D spheres. *International Journal of CAD/CAM* **5**(3) (2005) in printing.
14. RCSB Protein Data Bank Homepage (2005) <http://www.rcsb.org/pdb/>.
15. Halperin, D., Overmars, M.H.: Spheres, molecules, and hidden surface removal. In: Proceedings of the 10th ACM Symposium on Computational Geometry. (1994) 113–122

Routing Properties of the Localized Delaunay Triangulation over Heterogeneous Ad-Hoc Wireless Networks

Mark D. Watson and J. Mark Keil

Department of Computer Science, University of Saskatchewan, Canada
mark.watson@usask.ca, keil@cs.usask.ca

Abstract. We explore the extremal properties of the Localized Delaunay Triangulation over networks with heterogeneous ranges. We find theoretical bounds on these properties and compare them with those found via experimentation.

1 Introduction

In a wireless network each device can be used as a router in the process of carrying a signal between two locations. Wireless networks are potentially extremely inconsistent due to new devices entering and exiting continually. As well, two devices could move apart and a pathway which had existed could be broken without changing the overall connectivity of the network. It is due to the rapid, continual change of the devices that we consider the networking to be “ad-hoc.”

The devices we consider are able to transmit over some range in an omnidirectional manner. This means that all devices within some range can receive the transmission. We only regard those devices which can both “see” (i.e. receive messages from) each other as being able to communicate [1].

Here, we explore the Localized Delaunay Triangulation [2] [3] [4]. This structure was identified as having a variety of excellent extremal properties over uniform range Ad-Hoc Wireless Networks. However, some current research in the field has moved towards networks without uniform ranges. We show that while in general the Localized Delaunay Triangulation is not a spanner, the 1-hop Localized Delaunay Triangulation over the Intersection Neighborhood has a spanning ratio of $O(j)$ where j is the ratio between the longest and shortest edges in the graph. Furthermore, we show the Localized Delaunay Triangulation may have $\Omega(n^2)$ edges and $\Omega(n^2)$ intersections, where n is the number of nodes in the graph. We contrast these results with those gathered from experimental trials conducted on a variety of graphs.

2 Geometric Modeling

A euclidean graph $G = (S, E)$ is a graph where the vertex set is a set of points S in the plane and the weight of any edge $e(u, v) \in E$ (where u and $v \in S$) is equal to the euclidean distance between u and v .

When modeling a wireless network, we use nodes to represent wireless devices and edges to signify that two nodes are capable of communication.

The Unit Distance Graph (UDG) is a euclidean graph G wherein two vertices are joined by an edge if and only if they are at distance one or less.

While easier to analyze, the UDG is too simple a structure to accurately (or adequately) model ad-hoc networks. The UDG assumes that each device has a uniform range, which is not a valid assumption. Not only do antennas vary in strength from one another, the range of a device may vary over time. To overcome this, we consider a structure that can model nodes with non-uniform ranges. Such networks are referred to as having *heterogeneous ranges*.

A Mutual Inclusion Graph (MIG) [5] is a graph G where each node $v \in G$ has an associated weight w_v where $1 \leq w_v \leq l$ where l is some bounded constant. Two nodes $u, v \in G$ are joined by an edge in G if and only if the distance between u and v is less than $\min(w_u, w_v)$. We see that in the MIG, edges only exist between nodes if they are each *mutually contained* within the other's range. These edges, then, are undirected.

For node v in graph G , the k -neighborhood of v is the set K of all nodes in G that are reachable from v via a path of k edges (or "hops"), where k is an integer $0 \leq k \leq n$, where n is the number of nodes in the graph. The k -neighborhood of v where $k = 1$, then, is the set of nodes containing v and immediate neighbors to v .

In graphs with varying-node ranges, like the MIG, there are cases where two nodes may be connected, but may not be mutually connected to a third node which lies between them. To handle this, we define two types of neighborhoods.

Given a graph G , the Union k -Neighborhood (UN) of two nodes $u, v \in G$ is the set of vertices that contains all the k -neighbors of either u or v . The Intersection k -Neighborhood (IN) of two nodes $u, v \in G$, is the set of vertices formed from the intersection of the k -neighborhood of u and the k -neighborhood of v . Any node w in the intersection neighborhood is said to be *co-visible* to u and v .

The Delaunay Triangulation of a set of points S in the plane is a Euclidean graph containing all points of S . For each pair of points $p, q \in S$, there exists an edge in the Delaunay Triangulation if and only if there exists a circle passing through both points which does not include any other points within S . The Delaunay Triangulation is a *spanner* of the complete Euclidean Graph.

Spanners have been of some interest in graph theory and geometry since their introduction by Chew [6]. The distance between two nodes, $u, v \in G$ is the total weight of the shortest path between u and v in G . We denote this value $d_G(u, v)$. A subgraph H is called a t -spanner for G with value t if for each $u, v \in G$, $d_H(u, v) \leq t \times d_G(u, v)$ [7]. This value t is known as the *stretch factor* of the subgraph H . Any graph with a constant stretch factor is a spanner.

Spanners are obvious candidates for routing algorithms because their short paths helps ensure that the network has a low cost for transmitting data. The Delaunay Triangulation is known to be a 2.42 spanner of the complete Euclidean graph[8] and is a planar graph. This prompted interest in it as a routing structure. Unfortunately, there is no known distributed method for generating a

Delaunay Triangulation, so researchers developed a similar structure, the Localized Delaunay Triangulation [2].

An edge wv is called k -localized Delaunay relative to a geometric graph G if the interior of any circle through u and v does not contain any vertex of V that is a k -neighbor in G of u or v .

Clearly, if k is allowed to equal n where $n = |V|$ and V is the set of vertices in G , then the Localized Delaunay Triangulation is equivalent to the Delaunay Triangulation of the given geometric graph.

3 Topographical Properties

Kapoor and Li [5] have redefined the Localized Delaunay Triangulation to take the concept of union and intersection neighborhoods into account.

At the end of their paper [5], Kapoor and Li present a number of open problems. Of particular interest is the problem of determining if the Localized Delaunay Triangulation over the Intersection Neighborhood was a spanner.

We are able to show that the $LDel^k(MIG)$ over the IN where $k \geq 2$ is not a spanner.

Theorem 1. *$LDel^k$ over the Intersection Neighborhood has stretch factor of at least $\min(2(k - 1), (n - 2)/2)$ when $k \geq 2$.*

Proof Idea. Figure 1 shows the method we employ for $k = 3$. For clarity, we have only shown the top half of the graph; The entire structure (aside from a and b) are mirrored below. All nodes, aside from i_1 , have a range of 2. Note that the node i_1 is initially hidden to both a and b so that in $LDel^1$ the path between a and b is of length 2. While i_1 breaks the Gabriel circle for a and b , it is not until $k = 3$ that the node becomes co-visible to a and b . When this happens, there is no longer a $LDel$ edge between them, and they are forced to use the long route around the graph. So while the initial cost was 2, the number grows to 8 in $LDel^3$. This is the structure for $k = 3$, It is possible to find a construct a similar structure for $k = 2$, or $k \geq 4$.

To prove the lower bound on the stretch factor in general we can construct paths with $k - 2$ nodes each of power two, from a to node i and likewise from b to node i . We place each node distance two from the one that proceeds it. However, to disrupt any circle through a and b we add similar paths from a to i_2 and from b to i_2 . Now edge ab cannot be included, and either path from a to b requires a walk through half of the graph. So the spanning factor is at least $2(k - 1)$.

We see that the stretch factor is tied to k , but it is clear that if k is larger than $(n - 2)/2$ (since half the nodes are used above and below the nodes a and b), then n becomes the limiting variable in the construction, and $LDel^n$ has a stretch factor of $\frac{n-2}{2}$.

Corollary 1. *$LDel^k(MIG)$ over the Intersection Neighborhood is not a $2(k-1)$ spanner for $k \leq \frac{n}{2}$.*

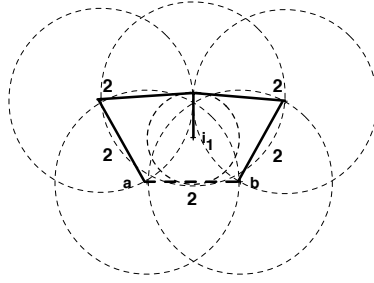


Fig. 1.

Having established a lower bound to the spanning of the Localized Delaunay Triangulation over the Intersection Neighborhood for k -hop neighborhoods when $k \geq 2$, we now turn to the 1-hop $LDEL$ of the Intersection Neighborhood over the MIG.

Lemma 1. *Given a MIG G , the shortest path in the $LDEL^1(G)$ over the IN between two points p and q , which are MIG neighbors, is at most distance j^2 , where j is the ratio between the largest and smallest edges in G and the closest pair in G are at unit distance.*

Proof. We now show via induction on the rank of d that the shortest path in the MIG between p and q is at most d^2 , where d is the distance between p and q .

Base Case: We consider the closest pair of co-visible points p and q . Then pq is a Delaunay Edge and the distance between them is at most l .

Inductive Hypothesis: For some edge in the MIG between two points p and q of length d , ($d < d^*$) the entire length of the shortest path can be assumed to be at most d^2 . Since the largest possible d is j , this is equivalent to a spanning ratio of j .

Inductive Step: Now we consider an edge pq in the MIG where the distance between p and q is d^* . If pq is an edge in $LDEL^1(G)$ the shortest path between p and q is of length d^* . Otherwise, we consider the general case where nodes p and q are co-visible but there is no empty circle that allows the creation of a Delaunay edge. Let r be the point visible from p and q such that $\angle prq$ is maximum. We know that $\angle prq \geq \frac{\pi}{2}$, it then creates two edges. See figure 2. We call the interior angle between edges b and c A .

By the cosine law $a^2 = b^2 + c^2 - 2bc \cos A$. Since angle A is greater than or equal to $\frac{\pi}{2}$, $\cos A$ is zero or negative, thus $a^2 \geq b^2 + c^2$. By the inductive hypothesis, the length of path between nodes p and q is less than or equal to $b^2 + c^2$ which we know is less than or equal to a^2 .

Therefore, the length of a path can be at most d^2 . The longest possible distance between two nodes co-visible nodes is j . Thus it follows that the spanning ratio of the one-hop Localized Delaunay Triangulation is no worse than j .

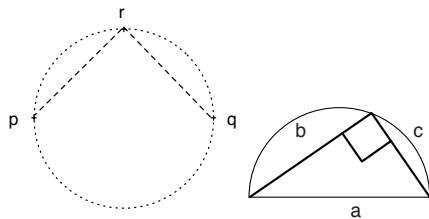


Fig. 2. Left: The nature of the recursion. Right: The angles.

4 Sparseness of the Localized Delaunay Triangulation

So far we have been concerned with the spanner properties of the Localized Delaunay Triangulation, but the sparseness properties are equally important, if routing is to be done.

Using the union neighborhood model identified by Kapoor and Li as a basis, Pinchasi and Smorodinsky [9], have analyzed the Localized Delaunay Graph over the Union Neighborhood. Importantly, their results can be applied to any geometric graph rather than just the MIG. For the two-hop Local Delaunay Triangulation (of the union neighborhood) of some geometric graph, there can only be $O(n \log n)$ edges and only $O(n^{3/2})$ edges for a one-hop graph. Their first proof is to show that self intersecting copies of a length 3 path (that is, 4 nodes and 3 edges, a “ P_3 ”) are forbidden in G .

As well, if a graph has a planar embedding, it has a linear number of edges, due to Kuratowski’s theorem:

Theorem 2. *A graph has a planar embedding if and only if it contains no subgraph which is homeomorphic to $K_{3,3}$ or K_5 [10].*

Pinchasi and Smorodinsky have shown that if a subgraph of a geometric graph consisting of the edges whose slopes are limited to fall within some constant range contains none of these forbidden subgraphs, then in general the graph has that sparseness property.

Showing that particular subgraphs are forbidden in the $LDel^1(MIG)$ over the IN graph would thus establish a bound on sparseness. Unfortunately, figure 3 gives examples of a P_3 and a C_4 that can be formed and are self-intersecting. Furthermore they require such a small difference in the angles of the edges (although those pictured have larger angles than are necessary) that Pinchasi and Smorodinsky’s angle restriction is of no benefit. Also, the difference in the size of ranges is not extreme, giving no real ability to link sparseness to l . Similar results were found when constructing the $K_{3,3}$ graph. Figure 4 shows a construction that generates a 1-hop Localized Delaunay Triangulation over the Intersection Neighborhood that has $K_{3,3}$ as a subgraph. In the figure, the a ’s have a range of two, the closest of the two of the b ’s unit range, and the other b has range two.

While in many cases the sparseness of the Localized Delaunay Triangulation over the Intersection Neighborhood may prove to be quite reasonable, we present a case where the number of edges is quadratic.

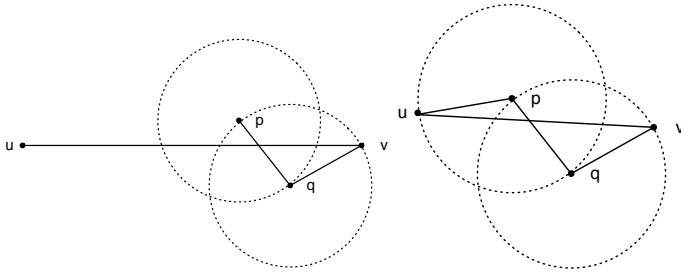


Fig. 3. Left: A self intersecting $P3$. Right: A self intersecting $C4$.

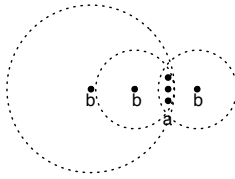


Fig. 4.

Theorem 3. *The 1-hop Localized Delaunay Triangulation over the Intersection Neighborhood has $\Omega(n^2)$ edges.*

Proof. We first cluster a set of $n/2$ nodes on the y-axis equally spaced in the interval $[-\epsilon, \epsilon]$. These nodes have a range equal to the largest range of nodes in the system, which we will show is equal to $3^{\frac{n-1}{4}} + \epsilon$. Now, on the x-axis we will place a node on either side, each at distance 1 from the center of the cluster. The range of the first node we place is $1 + \epsilon$, we then place successive nodes on each side at 3^i from the origin with range $3^i + \epsilon$ so that it can reach the central nodes. Note that these nodes will not see any of the nodes between them and the y-axis. We continue in this manner until all remaining nodes have been placed. Since a quarter of the nodes are on either side, the largest range is $3^{\frac{n-1}{4}} + \epsilon$.

A node u in the central cluster will be connected to a node v on the x-axis as the circle through u and v tangent to the y-axis is empty of any nodes both can see. Therefore each outer node has $n/2$ edges for a total of $\frac{n^2}{4}$. This graph has $\Omega(n^2)$ edges.

Theorem 4. *It is possible to construct a Mutual Inclusion Graph G such that the 1-hop Localized Delaunay Triangulation will have $\Omega(n^2)$ edge intersections, where n is the number of nodes in G .*

Proof. We begin by placing two evenly spaced rows of unit ranged nodes, one row above the other, such that each node is visible by every other node in the opposite row. Each row contains $n/4$ nodes. Given this, the 1-hop Localized Delaunay Triangulation over the Intersection Neighborhood forms a strip of $(n/2) - 2$ triangles for $\Omega(n)$ edges, $n/2 - 1$ of them being vertical.

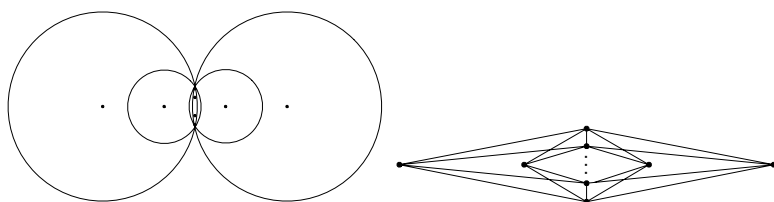


Fig. 5.

Just outside of the range of this structure, on both the left and right sides, we place a column of $n/4$ nodes, evenly placed and with a great enough range such that they all can see those in their row and those in the other. We place them such that the bottom node in each column is above the bottom row of nodes in the center and the top node below the top row. Again, there are $(n/2) - 2$ triangles for $\Omega(n)$ edges, $n/2 - 1$ of them being horizontal. Because of their configuration, a total $n/2 - 1$ edges will collide with $n/2 - 1$ edges going the other direction for a total of $\Omega(n^2)$ intersections.

5 Experimental Results

Given the above negative results, it seemed prudent to compare the theoretical results (many derived from unlikely arrangements) with experimental trials. A program was written that first generates a set of points placed via some programmed criterion and from this set the mutual inclusion graph is constructed. It can then generate the one-hop Localized Delaunay Triangulation over the Intersection Neighborhood, the regular (global) Delaunay Triangulation, and to find the respective spanning ratio of each as well as other information.

The first tests done were based on a uniform distribution. 200 nodes were randomly placed on a planar region of size 70×70 units, each node having a range uniformly selected between 1 and 10 units. As this was the most general case, it was performed the largest number of times, 50,000 individual tests were performed. The Uniform Distribution with Large Ranges (UD-LR) tests used

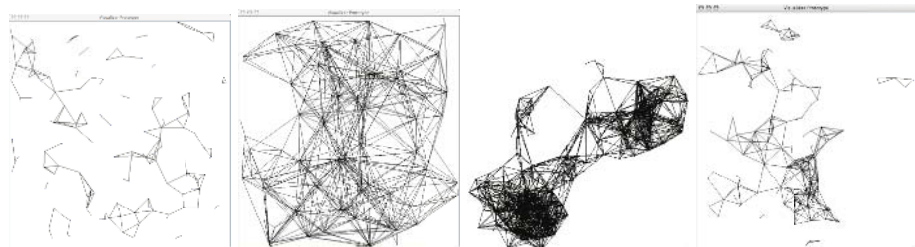


Fig. 6. Left: An example of a MIG generated using the Uniform Distribution. Middle Left: An example of a MIG generated using the UD-LR. Middle Right: An example of a MIG generated using the Dense Distribution. Right: a MIG generated using the Wider Distribution.

a uniform distribution as above, but the ranges for the nodes were uniformly selected from 1 to 40. Only 100 nodes were placed on the plane. Uniformly distributed graphs have been studied by other Computational Geometers working in Ad-hoc Wireless networking [11].

The uniform distribution leads to a very evenly spaced network. As a contrast, the Dense Distribution is based around a random walk, such that the termination point of each step is a new node and that each step is likely to be within range of the last node. The first node is placed in the center of the plane. Every node has a range uniformly selected from 1 to 10. After the first node is placed, the next node is placed between 0 and 3.5 units away in each the X and Y directions from the previous node. 200 nodes are placed into the plane. The Wider Distribution is almost identical, the difference is that each step in the random walk has a distance between 0 to 10 units. See figure 6 for examples of all the topologies.

5.1 Spanning

The spanning results of our experiments are summarized in table 1. Average Span is the average spanning ratio calculated from each Localized Delaunay Triangulation of that distribution. The second column shows what the max spanning ratio was for each distribution. The third column shows what the Standard Deviation of the spanning ratio was for each distribution.

Table 1. Spanning Results

Spanning Results on the 1-hop LDel			
Distribution	Average Span	Max Span	StdDev of Span
Uniform Distribution	1.24	1.45	0.06
UD-LR	1.34	1.54	0.03
Dense Distribution	1.36	1.53	0.03
Wider Distribution	1.32	1.53	0.04

In the more than 100,000 tests that were run, never did the Localized Delaunay Triangulation have a spanning ratio greater than $\frac{\pi}{2}$; the conjectured spanning ratio of the Delaunay Triangulation. This is a good result and confirms intuition that the LDel is a good spanner.

5.2 Sparseness and Intersections

Sparseness can be an important metric – ideally a graph shouldn't have too many edges as more edges are difficult to route over. We previously found that the number of edges in the 1-hop LDel over the IN was $\Omega(n \log l)$ edges, where n is the number of nodes. This was because the construction used to prove this used required an exponential increase in ranges until that limit was hit. If the range of nodes had no limit, the sparseness would be $\Omega(n^2)$. The number

Table 2. Sparseness and Intersection Results

Sparseness and Intersections								
Distribution	Av. No. MIG Edges	Av. No. Nodes	Av. No. LDel Edges	Av. No. DT Edges	Av. No. Unique Edges	Av. No. Intersections	Max No. Intersections	Std. Dev.
Uniform	243	158	219	457	26.84	12.82	43	5.43
UD-LR	650	93	235	264	35.85	33.77	111	13.52
Dense	1792	195	509	571	66.05	73.09	180	21.27
Wider	493	172	334	500	58.71	45.06	126	15.59

of intersections is also a measure of how easy it is to route information. The number of intersections was shown to be $\Omega(n^2)$.

The sparseness and intersection results of the experiments are summarized in table 2. The table displays specific data contrasting the 1-hop Localized Delaunay Triangulation and the global Delaunay Triangulation. Any node with no edges is removed. The table gives the average number of retained nodes, average number of LDel edges, the average number of edges in the Delaunay Triangulation over the same set of points, the average number of edges which occur are unique to the LDel, the average number of intersections in the LDel, the maximum in that given test, and the standard deviation of these intersections.

In practice the LDel is decently sparse, containing a number of edges proportional to the number of nodes in the graph. The Uniform Distribution is quite sparse and on average the MIG contains about the 1.5 times more edges than nodes. In such sparse graphs, the number of LDel edges is not considerably less than the MIG. The other distributions are quite dense. The Wider distribution has about $\frac{3}{5}$ as many edges, on average, as it's MIG.

As a whole, the intersection results are disappointing, though the standard deviation seems to imply that extremely bad results are fairly rare. As the UD is quite sparse, ensuring the network is connected may require a greater degree of intersections than with other distributions. In the case of the maximums, the UD-LR has more intersections than nodes. In denser structures, one can expect $\Omega(n)$ intersections and even the sparser structures yield a substantial number.

6 Conclusion

While much of earlier research in Ad-Hoc Wireless Routing had been done using networks where each node had a uniform range, this model was not particularly realistic. Structures that had seemed promising as a structure for routing may not be nearly as useful in an environment with heterogeneous ranges. A good candidate for routing was the Localized Delaunay Triangulation, which had been shown to have good spanning in the Unit Distance Graph domain.

The Localized Delaunay Triangulation of the Intersection Neighborhood is in general not a spanner, although if constrained to the 1-hop version, it is a

spanner with a theoretical stretch factor of j (where j is the ratio between the smallest and largest edge length) and an experimental stretch factor of ≈ 1.6 . Furthermore, the 1-hop LDel over the IN may have $\Omega(n^2)$ edges, as well as $\Omega(n^2)$ intersections.

References

1. Kuhn, F., Wattenhofer, R., Zhang, Y., Zollinger, A.: Geometric ad-hoc routing: Of theory and practice. In: Proc. 22nd ACM Int. Symposium on the Principles of Distributed Computing (PODC). (2003)
2. Li, X.Y., Calinescu, G., Wan, P.J.: Distributed construction of planar spanner and routing for ad hoc wireless networks. In: Proceedings IEEE INFOCOM 2002, The 21st Annual Joint Conference of the IEEE Computer and Communications Societies, New York, USA, June 23-27, 2002., IEEE (2002)
3. Li, X.Y., Song, W.Z., Wang, Y.: Efficient topology control for wireless ad hoc networks with non-uniform transmission ranges. ACM Wireless Networks **11**(3) (2005)
4. Li, X.Y.: Applications of computational geometry in wireless ad hoc networks. In Cheng, X., Huang, X., Du, D.Z., eds.: Ad Hoc Wireless Networking. Kluwer (2003) 1–68
5. Kapoor, S., Li, X.Y.: Proximity structures for geometric graphs. In: Algorithms and Data Structures, 8th International Workshop, WADS 2003, Ottawa, Ontario, Canada, July 30 - August 1, 2003, Proceedings. Volume 2748 of Lecture Notes in Computer Science., Springer (2003) 365–376
6. Chew, P.: There is a planar graph as good as the complete graph. In: Proceedings of the 2nd Symposium on Computation Geometry. (1986) 564–567
7. Peleg, D., Schaffer, A.A.: Graph spanners. Journal of Graph Theory **13**(1) (1989) 99–116
8. Keil, J.M., Gutwin, C.A.: Classes of graphs which approximate the complete euclidean graph. Discrete Computational Geometry **7** (1992) 13–28
9. Pinchasi, R., Smorodinsky, S.: On the delaunay graph of a geometric graph. In: ACM Symposium on Computational Geometry - SoCG'2004, Brooklyn, NY. (2004)
10. Kuratowski, K.: Sur le problème des courbes gauches en topologie. Fundamental Mathematics **15** (1930) 271–283
11. Bose, P., Morin, P., Stojmenovic, I., Urrutia, J.: Routing with guaranteed delivery in ad hoc wireless networks. Wireless Networks **7**(6) (2001) 609–616

A Speculative Approach to Clipping Line Segments

Frank Dévai

London South Bank University, London, UK
fl.devai@lsbu.ac.uk

Abstract. The Nicholl-Lee-Nicholl (NLN) algorithm for clipping line segments against a rectangular window in the plane (*Computer Graphics* **21**,4 pp 253–262) was proved to be optimal recently in terms of the minimum and maximum number of comparisons and the number of predicates used. A new algorithm is proposed that does not use predicates, but calculates intersections speculatively. Surprisingly, this approach not only leads to a much simpler algorithm, but also takes fewer operations in many cases, including the worst case. It is proved that the new algorithm never takes more operations than the optimal algorithm. Experimental results demonstrate that the new algorithm is 80% to 560% faster than long-established, widely known algorithms.

1 Introduction

Clipping is the extraction of the required portion of a two-dimensional image, or a three- or four-dimensional model, and belongs to the wider area of geometric intersection problems. In two dimensions the shape of the extracted portion is usually a rectangle with sides parallel to the coordinate axes. We restrict ourselves to computing the intersection of a line segment and a rectangular window, called the *window*, in two dimensions. This is a fundamental algorithm in computer graphics, and has attracted much attention in the literature [1, 2, 3, 4, 5, 6, 7, 8, 9].

Clipping line segments is a relatively simple operation, but it is repeated many times for many line segments in graphics systems. The performance analysis of such an algorithm for a set of line segments appears to be a complex task [2, 3, 7, 8] as it seems to be dependent on the size and the position of the window, the size of the line segments and their distribution in the plane. Experimental analysis has the difficulty that the probabilistic model used to generate random input data may not be realistic. We use *equivalence partitioning* [5] to analyse clipping algorithms independently of the probability distribution of the input and the size and the position of the window.

In Sect. 2 relevant previous work is discussed. It is argued that the evaluation of predicates by the Cyrus-Beck [2], Liang-Barsky [7] and the Nicholl-Lee-Nicholl (NLN) [8] algorithms is a potential source of inefficiency. In Sect. 3 a new paradigm for algorithm design, called *speculation*, is introduced. In Sect. 4

a new algorithm, called *clip-and-test* (C&T) is proposed that does not require the evaluation of any predicate, but speculatively computes intersections, and decides in at most two comparisons if they are valid. In Sect. 5 it is demonstrated that C&T is faster than existing algorithms. In Sect. 6 conclusions are offered.

2 Previous Work

All known line-clipping algorithms adopt a conservative approach in the sense that the information gathered in earlier steps is used [1, 3, 6, 10, 11, 12, 9]. For example, Skala [12] states: “The proposed algorithm is based on a simple rule: *Make tests first and then compute.*” The algorithm proposed by this paper is based on a radically different paradigm, which is the opposite of the above: *Compute intersections speculatively, then decide by simple tests if they are valid.*

The Cyrus-Beck [2] and the Liang-Barsky [7] algorithms use a parametric representation of the line segment, where the parameter value is 0.0 at the first endpoint (x_1, y_1) and 1.0 at the second endpoint (x_2, y_2) of the line segment. Let the bottom-left corner of the window represented by (x_L, y_B) and the top-right corner by (x_R, y_T) , and let t_E and t_L be the parameter values at the points where the line segment enters and leaves the window respectively. These values can be calculated as $t_E = (x_L - x_1)/\Delta x$ and $t_L = (y_T - y_1)/\Delta y$, where $\Delta x = x_2 - x_1$ and $\Delta y = y_2 - y_1$ by using the notations of Fig. 1.

Rotating the line segment in Fig. 1 counterclockwise around (x_1, y_1) initially $t_E < t_L$ holds, then when the line segment hits the top-left corner, $t_E = t_L$, and when the line segment leaves the top-left corner, $t_E > t_L$ will hold. Therefore the condition $t_E < t_L$ is an appropriate predicate to decide if the line segment intersects the window. Nicholl et al [8] use the predicate $(x_L - x_1)\Delta y < (y_T - y_1)\Delta x$, which is basically the same as the above—only rearranged to use multiplications instead of divisions. This minor change, however, has the side effect of the dependence of the predicate on the assumptions of $x_2 > x_1$ and $y_2 > y_1$. The NLN algorithm [8] was proved to be optimal recently [5], but it is rather complex—even its compact form takes four pages of C code.

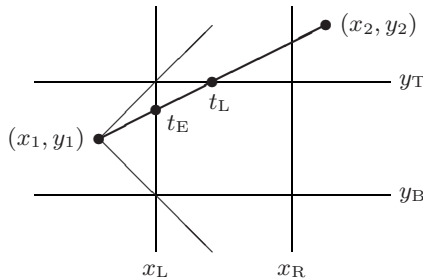


Fig. 1. Derivation of a predicate

3 A Paradigm for Efficient Algorithms

To develop a simpler and more efficient algorithm, let us abandon the model of computation based on predicates, and try to find useful patterns in efficient algorithms. For example, when sorting objects with integer keys, we can *speculate* on the final position of each object by using its key value, thus sorting N objects in $\Theta(N)$ time, and beating the $\Omega(N \log N)$ lower bound established by some concrete models of computation. The idea can also be generalized to non-integer keys: Distribute all the objects into $\Theta(N)$ groups with the help of the *floor* function. Then sorting each group, e.g., by insertion sort, the average run-time is $\Theta(N)$, assuming key values evenly distributed in a given range [13].

Often the floor and other operations, such as division and integer multiplication are excluded from models of computation because of their “unreasonable power”. In the above example it is not the “magic” power of floor, but the power of speculation that makes the algorithm fast. In particular, a good initial guess was obtained from the actual values of the keys, a readily available information, which, however, is not accounted for by the concrete model of computation used to establish a lower bound. The floor operation only facilitates speculation.

The next example does not use floor at all, and it is provided to demonstrate that we can get a practical and efficient algorithm even if the work done speculatively often has to be discarded. For primality testing we can guess an integer a as a *witness* to the fact that an input integer n is a composite, then use a test, such as Fermat’s test or the strong pseudoprime test [14, 15] to check to see if n is indeed a composite. If the test using a does not establish the fact that n is a composite, we discard a altogether, and make another guess. The Miller-Rabin algorithm, the most widely used method for primality testing, selects integers a at random in the interval $[2, n - 1]$, as at least three-quarters of the integers in this range are known to be witnesses for n [15].

The Miller-Rabin algorithm is known as a randomized algorithm, but it is also a prime example of a speculative algorithm. To demonstrate this, consider the numbers 2, 3, 5, and 7, which are a set of reliable witnesses with the property that every 32-bit composite integer has a witness in this set. If we want to test integers in the 32-bit range, we only need to try these four numbers in turn, which is still a speculative, but no longer a randomized algorithm. According to a conjecture by Alford et al [14] the smallest positive witness for any integer n is $c \log n \log \log n$ for some constant $c > 0$. If this conjecture is proved, it results in a deterministic speculative algorithm for primality testing.

The pattern we can observe in all the above examples is as follows: 1. *Guess* the possible outcome of some steps of the computation. 2. Do some further work according to the predicted outcome. 3. *Verify* the initial guess, and accept, reject or modify the work carried out in the second step. If the work carried out speculatively was discarded, the algorithm gambled and lost. However, it is possible to find algorithms that do not lose all the time.

4 The New Algorithm

The new algorithm, called *clip-and-test* (C&T) is formulated as follows. If $x_1 < x_L$ and also $x_2 < x_L$, the line segment is rejected. We do the same initial tests with the right-hand side, the bottom and the top of the window. If the line segment survives these tests, it is either completely inside the window, or its endpoints are in different regions of the subdivision induced by the four lines $y = y_B$, $x = x_L$, $y = y_T$ and $x = x_R$.

Suppose that endpoint (x_1, y_1) is in the left edge region as shown in Fig. 2. Then $x_2 \geq x_L$ must hold, otherwise the line segment is rejected. We speculatively assume that the intersection point (x, y) is on the left edge of the window, calculate y , and find out in at most two comparisons, $y < y_B$ and $y > y_T$, if we won or lost. Even if lost, we calculated one intersection point (A) instead of a predicate. If we won, however, we have already calculated intersection B. The pseudocode for this case is given as Fig. 3.

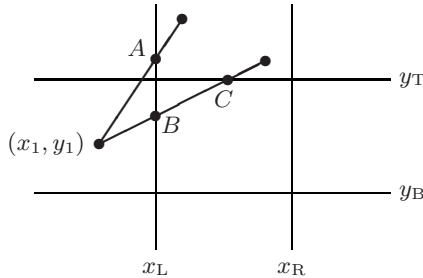


Fig. 2. Calculating intersections speculatively

```

procedure edge( $x_L, y_T, x_R, y_B, x_1, y_1, x_2, y_2$ )
   $y \leftarrow y_1 + (y_2 - y_1) \frac{x_L - x_1}{x_2 - x_1}$ ;
  if  $y > y_T$  or  $y < y_B$  then return nil;
  if  $y_2 > y_T$  then
     $x_2 \leftarrow x_1 + (x_2 - x_1) \frac{y_T - y_1}{y_2 - y_1}$ ;
     $y_2 \leftarrow y_T$ 
  else if  $y_2 < y_B$  then
     $x_2 \leftarrow x_1 + (x_2 - x_1) \frac{y_B - y_1}{y_2 - y_1}$ ;
     $y_2 \leftarrow y_B$ 
  if  $x_2 > x_R$  then
     $y_2 \leftarrow y_1 + (y_2 - y_1) \frac{x_R - x_1}{x_2 - x_1}$ ;
     $x_2 \leftarrow x_R$ 
  return ( $x_L, y, x_2, y_2$ )
end  $\triangleright$  edge
  
```

Fig. 3. Pseudocode for the edge regions

```

procedure corner( $x_L, y_T, x_R, y_B, x_1, y_1, x_2, y_2$ )
   $x \leftarrow x_1 + (x_2 - x_1) \frac{y_B - y_1}{y_2 - y_1}$ ;
  if  $x > x_R$  then return nil;
  if  $x < x_L$  then
     $y \leftarrow y_1 + (y_2 - y_1) \frac{x_L - x_1}{x_2 - x_1}$ ;
    if  $y > y_T$  then return nil;
     $x \leftarrow x_L$ 
  else
     $y \leftarrow y_B$ 
  if  $y_2 > y_T$  then
     $x_2 \leftarrow x_1 + (x_2 - x_1) \frac{y_T - y_1}{y_2 - y_1}$ ;
     $y_2 \leftarrow y_T$ 
  if  $x_2 > x_R$  then
     $y_2 \leftarrow y_1 + (y_2 - y_1) \frac{x_R - x_1}{x_2 - x_1}$ ;
     $x_2 \leftarrow x_R$ 
  return ( $x, y, x_2, y_2$ )
end  $\triangleright$  corner

```

Fig. 4. Pseudocode for the corner regions

If endpoint (x_1, y_1) is in the bottom-left corner region, conditions $x_2 \geq x_L$ and $y_2 \geq y_B$ must hold, or else the line segment is trivially rejected. We speculate that the intersection point (x, y) is on the bottom edge. Calculating x , we can again find out in two comparisons if our speculation pays. If not, there are two possibilities: if $x > x_R$, we simply reject the line segment, but if $x < x_L$, we repeat the gamble with the left edge of the window. If $y_2 > y_T$ we calculate the second intersection point with the top, and if still $x_2 > x_R$, with the right edge of the window. The pseudocode for this case is given in Fig. 4.

The pseudocodes given in Figures 3 and 4 are used in the other three edge and corner regions. For example, in the edge region below the window we use

$$s \leftarrow \text{edge}(y_B, x_L, y_T, x_R, y_1, x_1, y_2, x_2);$$

$$s.x_1 \leftrightarrow s.y_1; s.x_2 \leftrightarrow s.y_2$$

where $s.x_i$ and $s.y_i$, $i = \{1, 2\}$, denote the x and y coordinates of the endpoints of the line segment s returned by procedure `edge`, and the operator \leftrightarrow swaps the values of its operands. Finally if (x_1, y_1) is *in the window*, we speculate that the intersection point is on the top edge if $y_2 > y_T$, and on the bottom edge of the window if $y_2 < y_B$. In both cases if lost, the intersection is on the left or right edge, depending on the outcome of the comparisons $x'_2 > x_R$ and $x'_2 < x_L$. If $y_B \leq y_2 \leq y_T$, we know that the intersection point is on the right edge if $x_2 > x_R$, and on the left edge if $x_2 < x_L$. If none of the latter two conditions holds, the line segment is inside the window.

5 Analysis of the Algorithm

Using the notation of Sect. 4 if $x_1 < x_L$, we check to see if $x_2 < x_L$ also holds, and reject any line segment left to $x = x_L$ in two comparisons. From

here it follows that each element in the first column of the acceptance-rejection matrix [5] is 2. If $x_1 < x_L$ does not hold, we repeat the rejection test at the right-hand side of the window. We can reject any line segment right to $x = x_R$ in two additional comparisons, therefore each element in the right column is 3. If both $x_1 < x_L$ and $x_1 > x_R$ are false, but $y_1 < y_B$ and $y_2 < y_B$ are true, we reject any line segment in the bottom edge region in four comparisons. By similar reasoning any line segment in the top edge region can be rejected in five comparisons. If the line segment is inside the window, $x_L \leq x_1, x_2 \leq x_R$ and $y_B \leq y_1, y_2 \leq y_T$ must hold, hence trivial acceptance takes eight comparisons.

Therefore the acceptance-rejection matrix for the C&T method is $\begin{pmatrix} 2 & 5 & 3 \\ 2 & 8 & 3 \\ 2 & 4 & 3 \end{pmatrix}$.

C&T may calculate the intersections of the input line segment with the lines $y = y_B, x = x_R, y = y_T$ and $x = x_L$, called the *boundary lines*. Let k be the number of these intersections, $0 \leq k \leq 4$. An intersection is called *valid* if it is an endpoint of the output line segment; otherwise it is *invalid*. For simplifying the presentation we assume that the two endpoints of each line segment are disjoint, and that the input line segment never intersects a corner of the window (though the algorithm can handle such cases at no extra cost). In the worst case C&T calculates four intersection points as shown in Fig. 5. The evaluation of a predicate, however, costs about the same as calculating an intersection. Assuming the costs are the same, we can prove the following.

Theorem 1. *C&T takes less operations in the worst case than any algorithm using predicates to avoid invalid intersection calculations.*

Proof. As the first endpoint is in a corner region, any algorithm based on predicates needs one to decide if the line segment may enter the window at the vertical or the horizontal edge. A second predicate is required to decide if the line segment hits or misses the window at the other endpoint of the same edge. A third one is needed to check to see if the line segment leaves the window at the opposite vertical or horizontal edge [5]. To calculate the two intersections two more operations are required, which is five in total. C&T takes four. \square

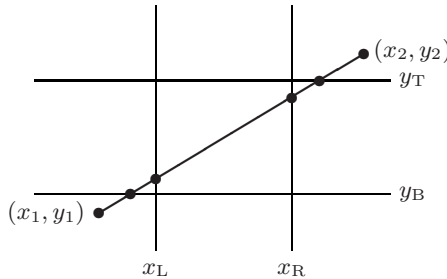


Fig. 5. A worst-case scenario

Lemma 1. *If an input line segment has exactly one valid intersection, it can only have at most one invalid intersection.*

Proof: If there is only one valid intersection, one endpoint of the line segment must be inside the window. If the line segment leaves the window intersecting a particular edge, it cannot possibly intersect the boundary line at the opposite edge. Assuming that the line segments leaves the window at the left edge, it can only intersect the boundary line either at the top or the bottom edge, but not both. The same argument applies for the other three window edges. \square

Theorem 2. *C&T never takes more operations than any algorithm based on the algebraic tree model of computation.*

Proof. We consider all the cases of valid and invalid intersections for all the possible values of k . Let i and j , respectively, be the number of invalid and valid intersections, $0 \leq i \leq 4$, $0 \leq j \leq 2$ and $i + j = k$. The possibilities are summarised in Table 1, where p is the lower bound on the number of predicates in the particular case [5], q is the number of intersections calculated by an optimal algorithm based on predicates, and finally r is the number of intersections calculated by the speculative algorithm C&T. In case $k = 0$ the output is decided by initial acceptance-rejection tests.

Table 1. The number of predicates eliminated by speculation (bottom line)

k	0	1	1	2	2	2	2	2	2	3	3	3	3	3	3	4	4	4	4	4	4
i	0	0	1	0	0	1	1	2	2	1	1	1	3	3	2	2	2	2	4	4	4
j	0	1	0	2	2	1	1	0	0	2	2	2	2	0	0	2	2	2	2	0	0
p	0	0	0	1	0	1	1	0	1	2	2	2	2	2	2	3	3	3	3	2	2
q	0	1	0	2	2	1	1	0	0	2	2	2	2	0	0	2	2	2	2	0	0
r	0	1	0	2	2	1	2	0	1	2	3	2	3	1	2	2	3	3	4	1	2
$p + q - r$	0	0	0	1	0	1	0	0	0	2	1	2	1	1	0	3	2	2	1	1	0

Case $k = 1$: If the intersection is valid, the first endpoint is either in the window or in an edge region. No predicate is required. If the intersection is invalid, the output is decided by acceptance-rejection tests.

Case $k = 2$: If both intersections are valid, (x_1, y_1) is in an edge, e.g., the left-edge region and if $y_2 > y_T$ or $y_2 < y_B$, the optimal algorithm needs a predicate to decide if the line segment hits the window, hence C&T wins. If $y_B \leq y_2 \leq y_T$, there is no need for a predicate to calculate the intersection with the right-hand side of the window, and C&T breaks even. If the (x_1, y_1) is in a corner region, and one intersection is valid and the other is invalid, C&T wins if it calculated the valid intersection first. If the invalid intersection was calculated first, C&T makes two intersection calculations instead of a predicate and an intersection calculation, and breaks even. If both intersections are invalid, laying on two parallel lines, e.g., $y = y_B$ and $y = y_T$, the case is decided by acceptance-rejection tests. If one intersection is on a vertical, and the other is on a horizontal line, C&T breaks even, calculating one intersection instead of a predicate.

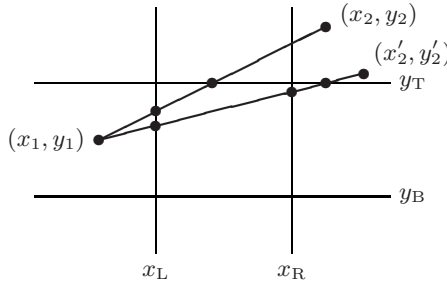


Fig. 6. Two possibilities for $k = 3$

Case $k = 3$: If two intersections are valid and one is invalid, C&T always wins. If endpoint (x_1, y_1) is in an edge region, algorithms based on predicates need two to decide if the top-left and the top-right corners of the window are above or below the line segment, then need to calculate the two valid intersection points. For the line segment with endpoint (x_2, y_2) in Fig. 6, C&T just calculates the two intersections, and wins by eliminating two predicate calculations as shown by the first column of Table 1 for $k = 3$. For (x'_2, y'_2) C&T “mistakenly” calculates the invalid intersection with the line $y = y_T$ instead of one predicate, but still wins by eliminating a second predicate calculation.

We have the same possibilities if the first endpoint is in a corner region—this is represented by the third and fourth columns of Table 1 for $k = 3$. If a valid intersection was calculated first, C&T never calculates the invalid one, and it wins by calculating only two intersections instead of two intersections and two predicates. If the invalid intersection was calculated first, C&T wins by calculating three intersections instead of two intersections and two predicates.

It follows from Lemma 1 that one valid and two invalid intersections are not possible, but three invalid intersections are possible. Assuming the first endpoint is in the bottom-left corner region, the following two cases are symmetric in the three other corner regions. If the line segment intersects $y = y_B$ at a point A right to the bottom-right corner of the window, C&T wins by evaluating one intersection instead of two predicates. If, however, the line segment intersects the line $y = y_B$ at a point A' left to the bottom-left corner of the window, and $x = x_L$ at a point B above the top-left corner of the window, C&T breaks even by calculating A' and B instead of two predicates.

Case $k = 4$: If two intersections are valid and two are invalid, any algorithm avoiding invalid intersection calculations needs at least three predicates [5] hence C&T always wins. If it calculates the two valid intersections first (e.g., when the first endpoint is in the bottom-left corner, and the line segment enters at the bottom, and leaves at the top edge) C&T spectacularly wins by calculating only two intersections instead of three predicates and two intersections.

If C&T calculates an invalid, followed by two valid intersections (e.g., when the first endpoint is in the bottom-left corner, and the line segment enters at the left, and leaves at the top edge) it wins by calculating three intersections instead of three predicates and two intersections. The third and fourth columns

of Table 1 for $k = 4$ represent the cases when (x_1, y_1) is in a corner region, and C&T calculates an invalid intersection first, e.g., with $y = y_B$.

It follows from Lemma 1 that one valid and three invalid intersections are not possible. Four invalid intersections, however, are possible. If the line segment intersects the boundary line $y = y_B$ beyond the bottom-right corner of the window, C&T wins by evaluating one intersection instead of two predicates. If the line segment intersects the boundary line $x = x_L$ above the top-left corner of the window, C&T breaks even by evaluating two intersections instead of two predicates. The bottom line of Table 1 completes the proof. \square

C&T was evaluated in timing experiments against the Cohen-Sutherland (CS), the Liang-Barsky (LB) and the NLN algorithms. All the code used in the experiments was written in the C language by the same person. Clock cycle counts obtained on a 166 MHz Pentium MMX processor are given in Table 2.

Table 2. Clock cycle counts

<i>region/algorithm</i>	CS	LB	NLN	C&T
top-left corner	71	109	48	26
left edge region	93	109	48	26
bottom-left corner	93	109	48	26
top edge region	69	424	113	59
window	93	469	89	88
bottom edge region	91	319	125	48
top-right corner	49	214	115	37
right edge region	71	214	115	37
bottom-right corner	71	214	115	37
<i>average</i>	78	242	91	43

Assuming the *average window* (a rectangle of width $a/3$ and height $b/3$ in the middle of an universe of width a and height b [4, 5]) all the regions in the equivalence partitioning have the same area. If all equivalence classes have the same number of line segments on average, we can average cycle counts over the equivalence classes. Note that this does not mean the assumption of evenly distributed input within the universe.

The optimal NLN algorithm takes more than twice as many clock cycles as C&T. As we have already seen in Sect. 2, the predicates used by the NLN algorithm depend on the assumptions $x_2 > x_1$ and $y_2 > y_1$. To handle this dependency the NLN algorithm needs 10 procedures, which are too complex to be implemented as macros.

Our reasoning about intersection calculations is also well supported by clock cycle counts. For example, clipping a line segment with the first endpoint in the left edge region and the second inside the window takes 206 clock cycles with the NLN, and 157 with the C&T algorithm on the above-mentioned platform. If the line segment with the same first endpoint misses the window, i.e., C&T loses, the counts are 226 for NLN, and 111 for C&T.

6 Concluding Remarks

Equivalence partitioning has been used to analyse clipping algorithms independently of the probability distribution of the input and the size and the position of the window. This is the reason why the paper only claims that the proposed algorithm—based on a new paradigm of algorithm design—theoretically never takes more operations than the optimal algorithm, even though in 12 cases out of 21 it actually takes less. The proposed algorithm was compared experimentally with three long-established and widely known algorithms, and was found 80% to 560% faster.

References

1. Blinn, J.F.: A trip down the graphics pipeline: Line clipping. *IEEE Computer Graphics & Applications* **11**(1) (1991) 98–105
2. Cyrus, M., Beck, J.: Generalised two- and three-dimensional clipping. *Computers & Graphics* **3**(1) (1978) 23–38
3. Day, J.D.: A new two dimensional line clipping algorithm for small windows. *Computer Graphics Forum* **11**(4) (1992) 241–245
4. Dévai, F.: An analysis technique and an algorithm for line clipping. In: Proc. 1998 IEEE Conference on Information Visualization, IV'98. (1998) 157–165
5. Dévai, F.: Analysis of the Nicholl-Lee-Nicholl algorithm. *Lecture Notes in Computer Science* **3480** (2005) 726–736
6. Duvanenko, V.J., Gyurcsik, R.S., W. E, R.: Simple and efficient 2D and 3D span clipping algorithms. *Computers & Graphics* **17**(1) (1993) 39–54
7. Liang, Y.D., Barsky, B.A.: A new concept and method for line clipping. *ACM Transactions on Graphics* **3**(1) (1984) 1–22
8. Nicholl, T.M., Lee, D.T., Nicholl, R.A.: An efficient new algorithm for 2-D line clipping: its development and analysis. *Comput. Graph.* **21**(4) (1987) 253–262
9. Slater, M., Barsky, B.A.: 2D line and polygon clipping based on space subdivision. *The Visual Computer* **10**(1) (1994) 407–422
10. Foley, J.D., van Dam, A., Feiner, S.K., Hughes, J.F.: *Computer Graphics: Principles and Practice*. Addison-Wesley (1996) (2nd ed in C).
11. Hearn, D., Baker, P.: *Computer Graphics with OpenGL*. 3rd edn. Prentice Hall (2004)
12. Skala, V.: An efficient algorithm for line clipping by convex polygon. *Computers & Graphics* **17**(4) (1993) 417–421
13. Knuth, D.E.: *Sorting and Searching*. Volume 3 of *The Art of Computer Programming*. Addison-Wesley, Reading, MA (1973)
14. Alford, W.R., Granville, A., Pomerance, C.: On the difficulty of finding reliable witnesses. *Lecture Notes in Computer Science* **877** (1995) 1–16
15. Rabin, M.O.: Probabilistic algorithms for testing primality. *Journal of Number Theory* **12** (1980) 128–138

An Efficient Algorithm for Mobile Guarded Guards in Simple Grids

Adrian Kosowski¹, Michał Małafiejski¹, and Paweł Żyliński^{2,*}

¹ Gdańsk University of Technology, Department of Algorithms and System Modeling

² University of Gdańsk, Institute of Mathematics

{kosowski, mima, buba}@sphere.pl

Abstract. A set of mobile guards in a grid is guarded if at any point on its patrol segment every guard can be seen by at least one other guard. Herein we discuss a class of polygon-bounded grids and simple grids for which we propose a quadratic time algorithm for solving the problem of finding the minimum set of mobile guarded guards (the MinMGG problem). Recall that the MinMGG problem is NP-hard even for grids every segment of which crosses at most three other segments. We also provide an $O(n \log n)$ time algorithm for the MinMGG problem in horizontally or vertically unobstructed grids. Finally, we investigate complete rectangular grids with obstacles. We show that if both the vertical and the horizontal sizes of the grid are larger than the number of obstacles k , $k + 2$ mobile guarded guards always suffice to cover the grid.

1 Introduction

The *guard problem in grids* was first formulated by Ntafos in 1986 [18]. A *grid* P is a connected union of vertical and horizontal segments, an example of which is shown in Fig. 1(a). A *grid segment* is a segment of the grid which is not strictly contained in any segment of the grid. A point $x \in P$ can see point $y \in P$ if the segment $\overline{xy} \subseteq P$. Ntafos established that a minimum set of guards covering all points in a 2D-grid of n grid segments consists of $(n - m)$ guards, where m is the size of the maximum matching in the intersection graph of the grid which can be found in $O(n^{2.5})$ time. The *intersection graph* G_P of a grid P is defined as follows: each vertex of G_P corresponds to a grid segment of P and two vertices are connected by an edge iff their corresponding segments cross; the intersection graph of the grid in Fig. 1(a) is shown in Fig. 1(b). In the case of 3D-grids, the problem of finding the minimum guard set is NP-hard [18].

The guard problem in grids is one of variations of the *art gallery problem* which was originally posed by Victor Klee in 1976 as the question of determining the minimum number of guards sufficient to see every point of the interior of an n -vertex simple polygon, and the first result was due to Chvátal [4] who proved that $\lfloor \frac{n}{3} \rfloor$ guards are occasionally necessary and always sufficient to cover a polygon with n vertices; see [20, 22] for more details.

* Supported by the KBN Grant No. 4 T11C 047 25.

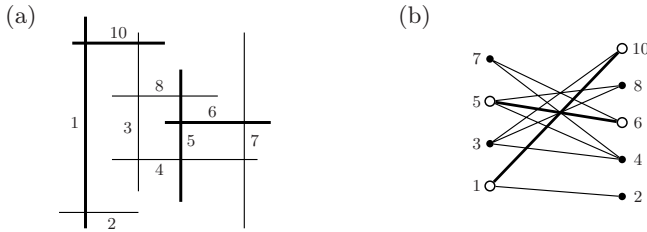


Fig. 1. (a) A minimum mobile guarded guard set and (b) its corresponding minimum total dominating set of the intersection graph

Guarded guards. The concept of *guarded guards* (or *weakly cooperative*, or *watched guards*) was proposed by Liaw and Lee in [13]. For a guard set S , we define the *visibility graph* $VG(S)$ as follows: the vertex set is S and two vertices v_1, v_2 are adjacent if they see each other. A set of guards S is said to be *guarded* if its visibility graph $VG(S)$ has no isolated vertices. The guarded guards problem for general simple polygons was completely settled by Michael and Pinciu [15], and independently by Żyliński [23], who proved that $\lfloor \frac{3n-1}{7} \rfloor$ is a tight bound. The guarded guards problem for orthogonal polygons was solved by Hernández-Peñalver [9], and by Michael and Pinciu [16], who proved the $\lfloor \frac{n}{3} \rfloor$ -bound to be tight. Combinatorial bounds for star-shaped, spiral and monotone polygons were given by Żyliński [23].

When speaking about grids, the minimum guarded guards problem in grids was solved by Małafiejski and Żyliński [14], who showed that a minimum coverage for a grid of n segments has exactly $(n - p_3)$ guarded guards, where p_3 is the size of the maximum P_3 -matching in the intersection graph of the grid. However, as they proved that the maximum P_3 -matching problem in bipartite planar graphs is NP-hard, the minimum guarded guards problem in grids turned out to be NP-hard as well.

Mobile guarded guards. In 1981, Toussaint introduced the idea of mobile guards in art galleries [2]: a *mobile guard* was constrained to patrol either along an edge of the polygon or along a straight line wholly contained within the polygon. Note that in the mobile guard problem we do not require that every point of a polygon is permanently covered, but we only need every point to be seen by at least one guard during his walk. Toussaint conjectured that except for a small number of polygons, $\lfloor \frac{n}{4} \rfloor$ edge guards are sufficient to guard a polygon, and this problem still remains open; for more details concerning mobile guards in polygons see [1, 3, 19, 20].

In this paper, we explore the problem of mobile guarded guards in grids. Specifically, each *mobile guard* is allowed to move along a grid segment, and then point x in a grid P is said to be seen by guard g iff there is a point $y \in g$ such that the segment $\overline{xy} \subseteq P$. Thus x is covered by the guard g if either $x \in g$ or x belongs to a grid segment crossing g . Now by the definition, a mobile guard corresponds to a vertex in the intersection graph G_P of grid P , and P is covered by a set of mobile guards S iff S dominates all vertices (grid segments) in graph

G_P , that is, every vertex of G_P is adjacent to at least one vertex in S . Thus there is a one-to-one correspondence between a minimum mobile guard set in grid P and a minimum dominating set in the intersection graph G_P . Consequently, if the *domination number* of G_P , denoted by $\gamma(G_P)$, is defined to be the cardinality of a minimum dominating set in graph G_P , then a minimum mobile guard set of grid P has $\gamma(G_P)$ mobile guards. This crucial fact was used by Katz *et al.* [10] who proved that the problem of finding the minimum number of mobile guards covering a grid is NP-hard.

In order to discuss the mobile guarded guards problem in grids, we have to modify the definition of cooperation. More precisely, a set of mobile guards S is *guarded* if the subgraph $G[S]$ in the intersection graph G of a grid induced by set S has no isolated vertices. The authors [11] observed that there is a one-to-one correspondence between a minimum mobile guard set in grid P and a minimum total dominating set in the intersection graph G_P . Recall that a dominating set D is a *total dominating set* if the subgraph induced by D has no isolated vertices, and the minimum cardinality of a total dominating set, denoted by γ_t , is called the *total domination number*.

REMARK 1.1. [11] *A minimum mobile guarded guard set of an n -segment grid has $\gamma_t(G)$ guards, where G is the intersection graph of the grid (see Fig. 1).*

Following this remark, Kosowski *et al.* [11] proved that the problem of finding the minimum number of mobile guarded guards covering a grid (the *MinMGG problem*) is NP-hard.

1.1 Our Results

Considering NP-hardness results, it seems natural to seek a non-trivial restricted class of grids for which the minimum mobile guarded guards problem can be solved in polynomial time. In the next section we discuss restricted classes of grids, that is, so-called *polygon-bounded* and *simple* grids [7], for which we propose a quadratic time algorithm for solving the MinMGG problem. The algorithm is based upon the property that horizontal and vertical grid segments may be covered independently, whereas the constructed guard set satisfies the condition of being guarded. We then explore *horizontally* and *vertically unobstructed grids* for which we propose an $O(n \log n)$ time algorithm for the MinMGG problem. Finally, we investigate *complete rectangular grids with obstacles*. We show that if both the vertical and the horizontal sizes of the grid are larger than the number of obstacles, $k + 2$ mobile guarded guards are always sufficient to cover a grid with k obstacles.

2 Polynomial Algorithms for Mobile Guarded Guards

The problem of determining the minimum number of mobile guarded guards required to cover a grid is NP-hard [11], there exist, however, certain classes of grids for which the optimum placement of guarded guards can be computed in polynomial time.

2.1 Basic Property

Before we characterise some of these classes, let us establish the following elementary property of a total dominating set in a bipartite graph.

PROPOSITION 2.1. *Let $G = (V_1 \cup V_2, E)$ be a bipartite graph. The problem of determining a minimum total dominating set $TD(G) \subseteq V_1 \cup V_2$ is equivalent to finding the solution to the following two independent problems:*

- (1) *Finding a minimum vertex set $TD_1(G) \subseteq V_1$ which dominates V_2 .*
- (2) *Finding a minimum vertex set $TD_2(G) \subseteq V_2$ which dominates V_1 .*

In particular, for any pair of minimum sets $TD_1(G)$ dominating V_2 and $TD_2(G)$ dominating V_1 , the set $TD_1(G) \cup TD_2(G)$ is a minimum total dominating set for G . On the other hand, if $TD(G)$ is a minimum total dominating set for G , the set $TD(G) \cap V_1$ is a minimum set dominating V_2 and the set $TD(G) \cap V_2$ is a minimum set dominating V_1 .

Proof. Due to space limits, the proof is omitted. □

Clearly, the above proposition has immediate application to the minimum mobile guarded guards problem in grids, since intersection graphs of grids are bipartite, as shown in [5].

COROLLARY 2.2. *To solve the MinMGG problem in a grid P , it suffices to find a minimum set of vertical segments covering all horizontal segments of P and a minimum set of horizontal segments covering all vertical segments of P .*

2.2 Polygon-Bounded Grids

A *complete rectangular grid* is a grid in which all endpoints of the grid segments are located on the boundary of a rectangle formed by four extremal grid segments (northernmost, westernmost, southernmost, easternmost). We assume that the set of intersections of segments of a rectangular grid is a subset of the integer point grid \mathbb{Z}^2 ; an example of a complete rectangular grid is shown in Fig. 2(a). The class of *polygon-bounded* grids is constructed as follows:

- (1) A grid consisting of a single segment is *polygon-bounded*.
- (2) A complete rectangular grid is *polygon-bounded*.
- (3) Any other grid P is *polygon-bounded* if it has induced polygon-bounded subgrids P_1 and P_2 such that $P = P_1 \cup P_2$ and $P_1 \cap P_2$ is a segment or a point.

Examples of polygon-bounded grids are presented in Fig. 3-4; the grid presented in Fig. 2(b) is not polygon-bounded as P_2 is not a complete rectangular grid. Thus a polygon-bounded grid can be thought of as a grid which consists of all segments cut off by an orthogonal polygon without holes from grid paper. Note that the class of polygon-bounded grids is a subclass of *simple grids* introduced by Gewali and Ntafos [7], but this we shall discuss later.

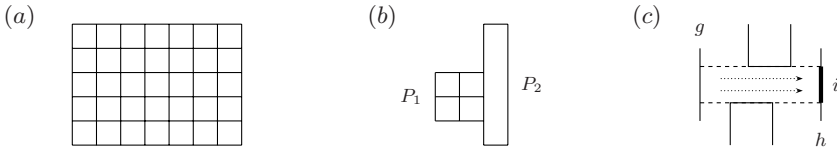


Fig. 2. (a) A complete rectangular grid. (b) Grid $P = P_1 \cup P_2$ is not polygon-bounded as P_2 is not complete rectangular. (c) The orthogonal projection i of g onto h with respect to the orthogonal hull.

Algorithm. Let H and S be arbitrary sets of segments. We say that H covers S if for any segment $p \in P$ there exists a segment $h \in H$ such that $p \cap h \neq \emptyset$. We will now construct an efficient algorithm for solving the MinMGG problem in polygon-bounded grids. Let polygon-bounded grid P consist of set S_H of horizontal grid segments and set S_V of vertical grid segments. The algorithm finds the minimum set of guards in grid P by determining the minimum set of horizontal grid segments of P covering S_V and the minimum set of vertical grid segments of P covering S_H (Corollary 2.2). We assume that the input of the algorithm is presented in the form of an n -vertex sequence describing the orthogonal hull of the polygon-bounded grid – this is important when speaking about complexity, as for example a complete rectangular grid can be described by four points, but can have arbitrary many (an exponential number of) grid segments.

THEOREM 2.3. *There exists a quadratic time algorithm solving the MinMGG problem for polygon-bounded grids.*

Proof. To simplify further considerations, we confine ourselves to the description of the algorithm for determining the minimum cover of horizontal grid segments with vertical grid segments (Corollary 2.2). Let P be a polygon-bounded grid. Segments g and h belonging to a set of segments S are regarded as *neighbouring in S* (with respect to grid P) if they are parallel, they both intersect with some grid segment s , and there is no segment in S which intersects with s between g and h . Now, let S_H be a set of horizontal segments, and suppose that S_H contains a segment g with exactly one neighbouring segment h in S_H with respect to grid P . Let us define the segment set $S'_H = (S_H \setminus \{g, h\}) \cup \{i\}$, where i is the orthogonal projection of g onto h with respect to the orthogonal hull of grid P , see Fig. 2(c) (note that i is connected by the definition of a polygon-bounded grid). Then S'_H has the following property.

REMARK 2.4. *Every minimum subset M of S_V covering S'_H also covers set S_H .*

Indeed, since all segments of S'_H are covered by $M \subset S_V$, some segment s of M intersects with i , and thus it intersects with segment h as well. Next, it is easy to see that s also intersects with g by the definition of a polygon-bounded grid. Hence s covers both g and h . The minimality of set M as a cover of S_H is a direct conclusion of M being a cover of S'_H , which is geometrically contained in S_H .

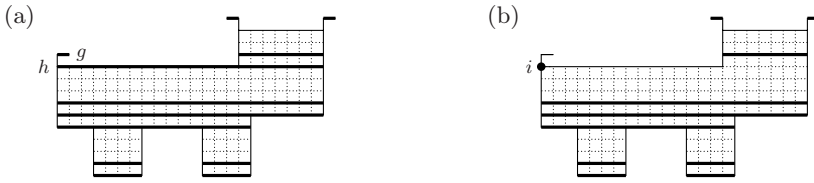


Fig. 3. (a) The initial set S in Step 1 of the algorithm (bold line). Segments g and h are replaced with segment (point) i (b).

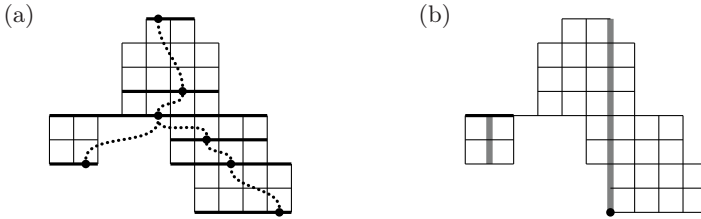


Fig. 4. (a) An illustration of the algorithm: a polygon-bounded grid P , the corresponding set S (bold line) and the neighbourhood graph $G(S)$ (edges drawn with a dotted line). (b) The resulting minimum set of vertical grid segments (gray lines) covering all horizontal line segments after Step 3.

The idea of the algorithm is first to construct a set of horizontal segments S whose minimum cover M with grid segments from S_V can be easily determined. By Remark 2.4, M will cover S_H as well.

1. Given a polygon-bounded grid P in the form of its orthogonal hull, create set S as shown in Fig. 3, by dissecting P into the minimum possible number of complete rectangular grids whose pairwise intersections are horizontal segments and selecting at most two segments from all such rectangular grids as elements of S .
2. Take any segment $g \in S$ with only one neighbour $h \in S$, and replace S with S' by applying the construction used when discussing Remark 2.4. Repeat Step 2 as long as S contains a segment with only one neighbour in S .
3. Construct the solution M by selecting one intersecting grid segment of S_V for every segment of S .

It remains to be shown that set M is a minimum set of segments covering S . Consider the graph $G(S)$ whose vertex set is the set S , in which two vertices are neighbours iff the corresponding segments of S are neighbours (with respect to grid P). At the end of Step 1 the graph $G(S)$ is a tree, see Fig. 4(a). Throughout Step 2, the modifications of set S result in the iterated removal of leaves and edges from $G(S)$, thus $G(S)$ remains a forest until the end of the algorithm. The algorithm proceeds to Step 3 when $G(S)$ has no leaves left, or equivalently – when $G(S)$ is a graph with no edges. Thus during Step 3 no two segments of S

are neighbouring (with respect to P), see Fig. 4(b). It transpires that a separate vertical guard is required to cover every segment in S .

The operating time of Step 1 of the algorithm is linear with respect to the number of sides n of the orthogonal hull of grid P , since the hull of P can always be decomposed into no more rectangles (intersecting only at horizontal segments) than it has horizontal sides. Set S and the relation of neighbourhood between segments can be represented in the form of the previously defined forest $G(S)$, whose size and order is bounded by $2n$. Step 2 consists of $O(n)$ iterations, each of which requires at most $O(n)$ time. Step 3 can be done in linear time. \square

2.3 Simple Grids

A grid is called a *simple grid* if all the endpoints of its segments lie on the outer face of the planar subdivision formed by the grid and if there exists $\epsilon > 0$ such that each of the grid segments can be extended by ϵ in both directions in such a way that its new endpoints still lie on the outer face, see [7] for more details. For example, the grid shown in Fig. 5(a) is simple, whereas the grid shown in Fig. 5(b) is not. Of course by the definition, a polygon-bounded grid is a simple grid.

It is easy to see that the algorithm discussed above can be directly applied for the MinMGG problem in simple grids with the only difference that now the initial set S during Step 1 consists of all horizontal segments (respectively, vertical segments), and the complexity of the algorithm is quadratic in the number of grid segments. Thus we have the following theorem.

THEOREM 2.5. *There exists a quadratic time algorithm solving the MinMGG problem for simple grids.* \square

2.4 Horizontally and Vertically Unobstructed Grids

A grid is called *vertically (horizontally) unobstructed* if it can be constructed by removing some set of horizontal (vertical) segments of the plane from a complete rectangular grid. An example of a vertically unobstructed grid is shown in Fig. 6(a). The problem of determining a minimum set of mobile guarded guards covering a vertically unobstructed grid or a horizontally unobstructed grid can also be solved in polynomial time. In the following, we shall present an $O(n \log n)$

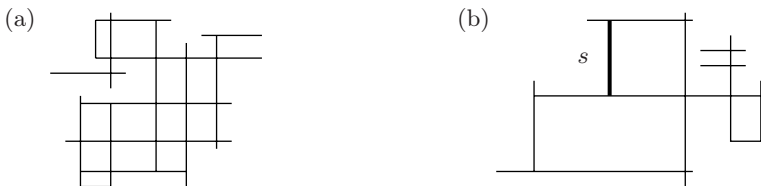


Fig. 5. (a) An example of a simple grid. (b) A grid which is not simple, as segment s can not be extended without destroying the property that all segment endpoints lie on the outer face.

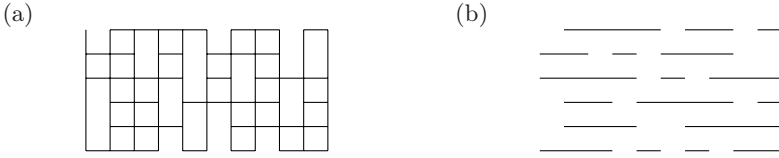


Fig. 6. (a) A vertically unobstructed grid P , (b) and its set of horizontal segments

algorithm which solves the problem for vertically unobstructed grids consisting of n segments.

Algorithm. For a given grid $P = S_H \cup S_V$, the algorithm returns a set of grid segments of P representing the positions of guards in some solution of $MinMGG(S)$, expressed as the union of the following sets:

1. A minimum set of horizontal segments $T \subset S_H$ such that the following inclusion of segments of the real line holds:

$$\bigcup_{s \in S_H} [[l(s)], [r(s)]] \subset \bigcup_{t \in T} [[l(t)] - 1/2, [r(t)] + 1/2]$$

($l(h)$ and $r(h)$ denote the horizontal coordinates of the left-hand and right-hand endpoints of segment h , respectively).

2. A set of vertical segments $W \subset S_V$ such that W covers all segments of S_H and the set of segments obtained from W by replacing any vertical segment of W with its nearest neighbour to the right, or by removing a segment from W , does not cover S_H .

By Corollary 2.2, both stages of the algorithm may be analysed separately. Stage 1 of the algorithm is equivalent to the solution to the problem of covering a sequence of points representing consecutive integers with a minimum subset of a given set of segments of the real line, see Fig. 6(b), and can be solved with a simple $O(n \log n)$ plane sweep algorithm. Stage 2 of the algorithm describes an $O(n \log n)$ greedy left-to-right sweep approach to the problem of covering S_H with a minimum number of segments from S_V . The correctness of this approach is intuitively obvious and can be proven by induction on the number of vertical segments of the grid. Thus we have

THEOREM 2.6. *There exists an $O(n \log n)$ time algorithm solving the MinMGG problem for horizontally (vertically) unobstructed grids.* \square

3 Final Remarks

Let us consider a complete rectangular grid P . If we put an *obstacle* b on a grid segment s of P then b blocks the visibility on s , that is, segment s is divided into two grid segments (we assume that an obstacle is never placed at a crossing). Consequently, a *grid* P with k *obstacles* is a complete rectangular grid in which we put k obstacles. Note that if obstacles are put only on horizontal



Fig. 7. (a) $mgg(n, k) \geq k + 2$. (b) The backbone of the grid.

(or vertical) grid segments, then the resulting grid is vertically unobstructed (or resp., horizontally unobstructed). Let $mgg(n, k)$ denote the maximum number of mobile guarded guards that are ever needed for an n -segment grid with k obstacles. Fig. 7 shows a class of grids with k obstacles that requires as many as $k + 2$ mobile guards guards. Notice that the exemplary grid requires $k + 2$ arbitrary and cooperative mobile guards as well. Thus we have $mgg(n, k) \geq k + 2$.

PROPOSITION 3.7. *If both the vertical and the horizontal sizes of the grid are larger than k , then $mgg(n, k) \leq k + 2$.*

Proof. Since the sizes of the grid are sufficiently large, it is possible to find a vertical grid segment and a horizontal grid segment in P which span from one of the sides of the rectangle bounding grid P to the opposite side (these segments are marked with bold lines in Fig. 7(b), and will be referred to as the *backbone* of the grid). We place guards in both grid segments of the backbone of the grid, leaving k guards still to be placed. The number of uncovered segments in P is at this point equal to at most k . Consider any connected partition D of the disjoint subgrid U of P consisting of all uncovered segments (one such partition is marked with dashed lines in Fig. 7(b)). Grid D must be connected to the backbone of P by some segment d (denoted by a dotted line in Fig. 7(b)). By placing guards in segment d and in all segments of D but one (leaving out a segment corresponding to one of the leaves in the spanning tree of the intersection graph of $D \cup \{d\}$), we obtain a cover of D with $|D|$ guards, and the set of guards is always connected to the backbone of P . By repeating this procedure for all connected partitions of U , we finally obtain a guarded guard cover of P using 2 guards along the backbone and $|U|$ guards to cover U , and $|U| + 2 \leq k + 2$. \square

Table 1. Guards in grids — a summary of all results

Guard Type	Number	Complexity	
stationary	$n - m$	P	[18]
cooperative	$n - 1$	P	[17]
guarded	$n - p_3$	NPH	[14]
mobile	γ	NPH	[10]
cooperative	γ_c	NPH	[11]
guarded	γ_t	NPH	[11]
– in polygon-bounded grids		$O(n^2)$	Thm. 2.3
– in simple grids		$O(n^2)$	Thm. 2.5
– in horizontally/vertically unobstructed grids		$O(n \log n)$	Thm. 2.6

References

1. A. Aggarwal, The Art Gallery Theorem: Its Variations, Applications, and Algorithmic Aspects, Ph.D. Thesis (Johns Hopkins University, 1984).
2. D. Avis, G.T. Toussaint, An optimal algorithm for determining the visibility of a polygon from an edge, *IEEE Trans. Comput.* C-30 (1981), 910-914.
3. I. Bjorling-Sachs, D.L. Souvaine, A tight bound for edge guards in monotone polygons, DIMACS Technical Report 92-52 (1992).
4. V. Chvátal, A combinatorial theorem in plane geometry, *J. Combin. Theory, Ser. B* 18 (1997) 39-41.
5. J. Czyżowicz, E. Kranakis, J. Urrutia, A simple proof of the representation of bipartite planar graphs as the contact graphs of orthogonal straight line segments, *Inf. Process. Lett.* 66 (1998), 125-126.
6. U. Finke, K. Hinchirs, Overlaying simply connected planar subdivisions in linear time, in: *Proc. of ACM SoCG'95*, 119-126.
7. L.P. Gewali, S. Ntafos, Covering grids and orthogonal polygons with periscope guards, *Computational Geometry: Theory and Applications 2* (1993) 309-334.
8. G. Hernández-Peñalver, Controlling guards, *Proc. of CCCG'94*, 387-392.
9. G. Hernández-Peñalver, Vigilancia vigilada en polígonos ortogonales, *Actas del VI Encuentro de Geometría Computacional* (1995), 198-205.
10. M.J. Katz, J.S.B. Mitchell, Y. Nir, Orthogonal segment stabbing, *Computational Geometry: Theory and Applications 30* (2005), 197-205.
11. A. Kosowski, M. Małafiejski, P. Żyliński, Weakly cooperative mobile guards in grids, Extended abstract in *Proc. of JCDCG* (2004), 83-84.
12. B.C. Liaw, N.F. Huang, R.C.T. Lee, The minimum cooperative guards problem on k -spiral polygons, *Proc. of CCCG'93*, 97-101.
13. B.C. Liaw, N.F. Huang, R.C.T. Lee, An optimal algorithm to solve the minimum weakly cooperative guards problem for 1-spiral polygons, *Inf. Process. Lett.* 52 (1994), 69-75.
14. M. Małafiejski, P. Żyliński, Weakly cooperative guards in grids, *Proc. of ICCSA'05*, LNCS Vol. 3480 (2005), 647-656.
15. T.S. Michael, V. Pinciu, Art gallery theorems for guarded guards, *Computational Geometry: Theory and Applications 26* (2003), 247-258.
16. T.S. Michael, V. Pinciu, Multiply guarded guards in orthogonal art galleries, LNCS Vol. 2073 (2001) 753-762.
17. T. Nierhoff, P. Żyliński, Note on cooperative guards in grids, *Annual CGC Workshop* (Neustrelitz, 2003).
18. S. Ntafos, On gallery watchman in grids, *Inf. Process. Lett.* 23 (1986), 99-102.
19. J. O'Rourke, Galleries need fewer mobile guards: a variation to Chvátal's Theorem, *Geometriae Dedicata* 14 (1983), 273-283.
20. J. O'Rourke, *Art Gallery Theorems and Algorithms* (Oxford University Press, 1987).
21. V. Pinciu, Connected guards in orthogonal galleries, LNCS 2669 (2003), 886-893.
22. J. Urrutia, Art Gallery and Illumination Problems, in: *Handbook on Computational Geometry* (Elsevier, Amsterdam 2000).
23. P. Żyliński, Watched guards in art galleries, accepted for: *Journal of Geometry*.
24. P. Żyliński, Cooperative Guards Problem – Combinatorial Bounds and Complexity, Ph.D. Thesis (Gdańsk University, 2005).

Approximation of Optimal Moving Paths of Huge Robot Reclaimer with a 3D Range Finder

Kwan-Hee Lee¹, Hyo-Jung Bae¹, and Sung-Je Hong²

¹ Mechanical and Electrical Engineering Team,
Research Institute of Industrial Science & Technology,
32 San Hyoja-Dong Pohang, 790-330, Republic of Korea
{kwanhee, hjbae}@rist.re.kr

² Dept. of Computer Science and Engineering,
Pohang University of Science and Technology,
31 San Hyoja-Dong Pohang, 790-784, Republic of Korea
sjhong@postech.ac.kr

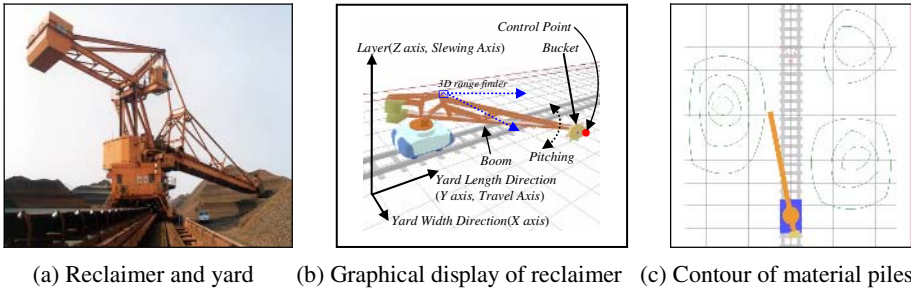
Abstract. This paper proposes a simple method for approximating the optimal moving paths of a huge robot reclaimer located in the outdoor material stock yard with emphasis on safety, energy consumption, and transfer time. The reclaimer is equipped with a 3D range finder to measure the shape of material piles in the yard, and the material yard is modeled into 3D space where 2D section of grid type is constructed in several layers. To define a safety function against moving between grids, a simplified Voronoi diagram that has a minimized extension error of vertex is used. In addition, the function of energy consumption and transfer time required when the control point of the reclaimer moves between 3D grids is defined. This is used as a cost evaluation factor of path optimization along with the safety function. The proposed method can be readily applied to low-performance industrial control devices.

1 Introduction

The reclaimer is an excavating machine designed to dig and scoop up from the piles of raw materials such as coal and iron-ores in the yard and transfer the materials to other factories. The actual size of the reclaimer is 25 meters high and 50 meters long, and it moves back and forth over the rail of about 1.2 km, carrying the materials to each unit factory (see Fig. 1 (a)). The traditional method of operating the reclaimer involved manning the reclaimer with the operator, traveling, slewing, and pitching by using an operation lever manually. The automatic reclaimer system is equipped with a 3D range finder which plays the role of human eyes, measuring the three dimensional mountainous shapes of the materials in the yard, and guiding the working process for the reclaimer. There are two main functions: automatic landing and excavation. The automatic landing function enables the reclaimer to land its digging bucket exactly on to the materials, using the distance information obtained from its 3D range finder. With its automatic excavation function, the automated reclaimer can perform assigned workloads based on weight without human intervention [4]. However, there are no

optimal traveling functions which can move the reclaimer from the current position to the next destination point for excavation. The optimal navigation function is very important for the unmanned automatic system of the reclaimer.

There are two methods for robot path planning. One way is to calculate the paths by using the known information on the terrain where the robot and the obstacles are located, and the other method is to let the robot gather information for itself on the obstacles and the terrain and let the robot use that information in planning its own paths.



(a) Reclaimer and yard (b) Graphical display of reclaimer (c) Contour of material piles

Fig. 1. Configuration of yard

If the information on the terrain is known, the *C-Space*[13, 16] approach capable of finding the shortest paths and a method of finding the safest paths using the Voronoi Diagram[1-3, 9-11] can be applied to the robot's path planning. However, since it is difficult to realize the Voronoi Diagram in the actual applications, the Voronoi Diagram calculated by a graphics hardware can be used in motion planning[11]. The *Variational Dynamic Programming Approach* proposed by Suh et al.[12] and the *Genetic Approach* by Chen et al.[8] offer the methods that simultaneously consider traveling distance and safety. These methods adopt a cost function expressed as the sum of the traveling distance that measures the goodness of paths and their safety.

For the terrains with unknown obstacles on them, sensors attached on a robot can be utilized for global path planning[7, 15, 17-19]. For global path planning for an autonomous mobile robot that does not consider optimization, the proposed method use sonar sensors[7], an omnidirectional stereo and a laser range finder[18], a sonar and 2D laser range finder[19] or a 3D laser range finder[17].

The shortest path does not necessarily mean the shortest time and minimum energy consumption for huge robots such as a reclaimer whose power consumption and traveling speed are not the same at its three axes. Moreover, for huge robots that require a considerable amount of energy, their energy efficiency needs to be controlled to improve their productivity. This paper proposes a simple hybrid method for approximating the optimal moving paths of a reclaimer whose power consumption and traveling speed are different at each axis in a 3D space such as a material yard whose terrain cannot be modeled in advance. Optimized in terms of moving path safety, energy consumption, and moving time, the proposed method can be readily applied to low-capacity industrial control devices.

2 Construction of Voronoi Diagram

The mound of material pile is approximated with the contour carrying intervals of specified heights. Since the maximum height of the material piles is 18m, up to 6 contours can be obtained from one material pile if the contour is extracted at an interval of 3m. Fig. 1 (c) shows this contour and the reclaimer in a 2-dimensional graphic. Each contour is composed of continuous cubic Bezier curve segments, and each curve segment is composed of 4 control points. Since this curve is a 3rd degree algebraic curve, whose bisector curve carries high degree of $2 \times 3^4 = 162$ at the maximum [6], it is difficult to mathematically obtain an accurate Voronoi Edge. In this study, we used a method of obtaining the polygon surrounding each curve segment and a method of approximating the Voronoi Diagram from the polygon set comprising line segments.

2.1 Approximation of Outer Polygon

Bajaj and Kim[2] presented an algorithm seeking the *characteristics*, *inner* and *outer* polygon with respect to the planar curved objects. This study considered only the convex-shaped planar curved object for the sake of simplification. The carrier polygon, therefore, not only automatically becomes a simple *carrier*, a *characteristic* and *inner* polygon, but it is very also effectively calculated to the linear time. In addition, the *outer* polygon can be obtained by the sum of points (OP_i), which is the intersection point of the line(TL_i) and the adjoining line (TL_{i+1}), both of which are the tangent lines of the vertex of each inner polygon.

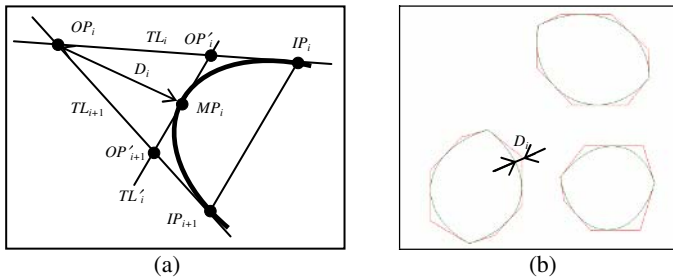


Fig. 2. (a) Creation of *outer* polygon. (b) *outer* polygons of curved objects

The *outer* polygon is a polygon that surrounds the outside of the curve segment. Therefore, there can be an error margin in the actual distance between the *outer* polygon and the curve segment. To reduce the error in the maximum distance between the *outer* polygon and the curve segment to less than D_ϵ , which is an allowable error, the following process is carried out. As shown in Fig. 2, if the minimum distance D_i (distance between OP_i and MP_i) is greater than the maximum tolerance D_ϵ of the *outer* polygon and the curve segment, the points OP'_i, OP'_{i+1} are added to the *outer* polygon set instead of OP_i repeatedly. Where OP'_i is the intersection point of TL_i and TL'_i , which is the tangent line of curve segment at MP_i , OP'_{i+1} is the intersection point of TL_{i+1} and TL'_i . Fig. 2 (b) shows the *outer* polygon created by this process.

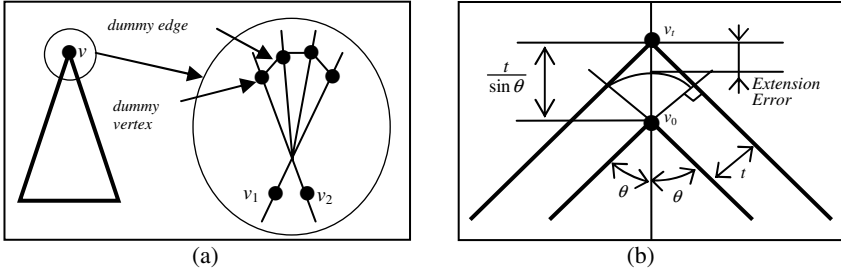


Fig. 3. (a) Vertex Cracking, (b) Error in object extension

2.2 Vertex Cracking

The simplest method of approximating the Voronoi Edge from the set of the non-overlapping convex polygon is to obtain the bisector line considering only the growth of each edge of the polygon. This is the *simplified Voronoi Diagram* proposed by Canny[1]. In this method, there is an *island* phenomenon that occurs because of the acute vertex which grows extremely fast compared with the growing speed of the adjoining edge. We used the *Vertex Cracking* technique to solve such problems. As shown in Fig. 3 (a), the *Vertex Cracking* technique is a method of inserting null edges (dummy edges) into each vertex to solve the problems that are caused by the acute vertex. In other words, it is a method of dividing vertex v into v_1 and v_2 , inserting a dummy vertex and a dummy edge between them.

2.3 Error Analysis

The exact Voronoi Diagram shows that each vertex grows into a circular arc. In the simplified Voronoi Diagram, however, each vertex grows in the convex polygonal arc composed of line segments as it undergoes the process of *Vertex Cracking*. Fig. 3 (b) shows growing errors on a vertex, where, $\theta \neq 0$. When the object grows by the time t , the extension error occurs from the vertex. The distance between the edge and the extended edge is always t . However, the distance between vertex v_0 and extended vertex v_1 is $\frac{t}{\sin \theta}$, when the inner angle created by the adjoining edge is 2θ . The extension error between the two growing vertices, therefore, can be defined as follows:

$$ExtensionError = \frac{t}{\sin \theta} - t = t \cdot \left(\frac{1}{\sin \theta} - 1 \right) \tag{1}$$

From formula (1), we can see that the errors related to the growth of a vertex are dependent upon the angle θ created by the two adjoining edges and the time t . We can also see that to approximate the Voronoi Diagram within the maximum extension error ε after comparing it with the actual Voronoi Diagram, many dummy edges must be inserted into the vertex of each polygon to make a polygonal arc.

The Voronoi edge is formed by the neighboring objects in the simplified Voronoi Diagram. Because more exact control path is required when the reclaimer moves between the narrowest adjacent piles, this paper analyzed the errors of Voronoi edges. Fig. 4 shows the composition of the yards where materials are piled.

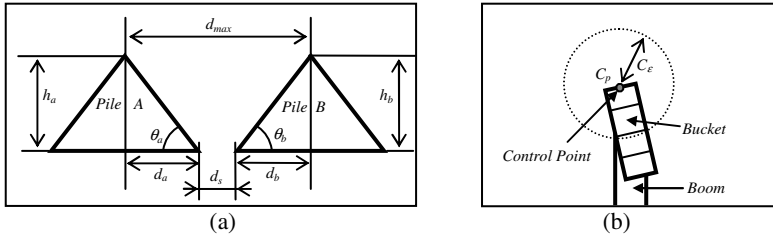


Fig. 4. (a) Correlations of the piles stacked in material yards, (b) Control error of control point

Fig. 4 (a) shows brief side views of the two adjoining material piles A and B stacked in the material yards. Each symbol carries the following meaning.

- θ_a, θ_b : The angle of repose of material pile A, B
- h_a, h_b : Maximum height of material pile A, B
- d_s : Maximum distance between the material pile A and B
- d_a, d_b : Width of material pile A, B
- d_{max} : Maximum distance between the vertex of material piles A and B

The maximum distance d_s between the material pile A and B is a safe distance provided to prevent the materials from being mixed with other ores in the yard. d_{max} (Maximum distance between the vertex of the material piles A and B) shown in Fig. 4 (a) is calculated as:

$$d_{max} = d_s + d_a + d_b = d_s + \frac{h_a}{\tan \theta_a} + \frac{h_b}{\tan \theta_b} \quad (2)$$

From Fig. 4, the maximum growing time that can be carried by each vertex of the outer polygon located on the top of the material pile A or B is less than d_{max} when the outer polygon is on the same adjoining height. If d_{max} is substituted in place of t in the extension error formula defined in formula (1) above, the following equation is created:

$$\varepsilon = d_{max} \cdot \left(\frac{1}{\sin \theta} - 1 \right), \quad \theta = \sin^{-1} \left(\frac{d_{max}}{\varepsilon + d_{max}} \right) \quad (3)$$

From formula (3), all items except the maximum extension error ε are constants decided according to the characteristics of the relevant material yard. From Fig. 4 (b), ε can be deduced on the basis of characteristics of the control motion of the reclaimer. As shown in Fig. 1 (b) and Fig. 4 (b), the Control Point (C_p), which is a reference point of moving control of the reclaimer, is on the tip of the scooping bucket. The Control Point (C_p) is the reference point used to calculate the inverse kinematics of the reclaimer. To accurately bring C_p to the targeted position by controlling the reclaimer's travel, slewing and pitching axes, highly accurate control systems are required. However, the actual reclaimer is not equipped with such systems. In general, if we assume the range of tolerance errors occurring from repetitions and control errors to be C_ε , the error that occurs by the vertex when the Voronoi Diagram is approximated should be less than this value. If ε is substituted by C_ε in the formula (3), the following formula is created:

$$\theta = \sin^{-1} \left(\frac{d_{max}}{C_\varepsilon + d_{max}} \right) \quad (4)$$

If the formula of a common material yard is $\theta_a = \theta_b = 38^\circ$, $h_a = h_b = 18\text{m}$, $d_s = 20\text{m}$, $C_\varepsilon = 3\text{m}$, θ is approximately 73° . Since the inner angle of each vertex of the polygon is 2θ , vertex cracking should be performed and the null edges inserted so that the inner angle of each vertex becomes 146° . Vertex cracking needs to be repeated the maximum of three times because 2θ will be $90^\circ + \theta$ for one vertex cracking.

3 Optimal Moving Path

3.1 Configuration of Safe Region

Fig. 5 shows the method of configuring layers and regions. First, the 3-dimensional space where the reclaimer and the material piles are situated is approximated into the n number of the layers, which is a 2-dimensional plane. Each layer has the contours that have the same height. Next, each layer is divided into rectangular forms with the width RU_x and length RU_y , respectively, further subdividing the layer into $RNx \cdot RNy$ regions each, where, RNx , RNy is the number of regions being divided in each axial direction. If the number of layers is RNz , the number of the entire divided regions will be $RNx \cdot RNy \cdot RNz$. Each divided rectangular form is defined as a region($REGION(x, y, z)$).

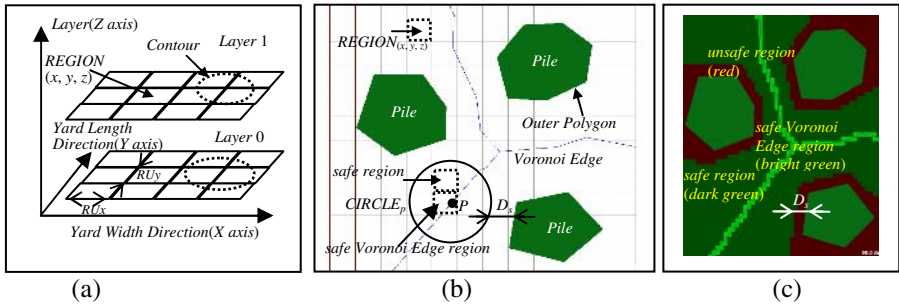


Fig. 5. (a) Configuration of *Layer* and *Region*, (b) and (c) Definition of *safe region*, *unsafe region* and *safe Voronoi Edge region*(where, D_s is predefined safe distance)

Each region may be classified into 3 types: *safe region*, *unsafe region*, and *safe Voronoi Edge region*. The *safe region* is an area where the control point of the reclaimer can move without any collision. The *unsafe region* is where the control point cannot move because of obstacles such as the material piles. The *safe Voronoi Edge region* is defined as a *safe region*, and it contains a Voronoi Edge within.(see Fig. 5(b)).

3.2 Computation of Cost Array

Cost Array is defined as $N \times N$ array $Cost[M][N]$, which includes the cost required to move the control point of the reclaimer from the $REGION(i, j, k)$ to $REGION(i', j', k')$. Because each region carries 2 inverse kinematics values whose posture directions are forward and backward [4], the formula is $N = RNx \cdot RNy \cdot RNz \cdot 2$. $Cost[\alpha][\beta]$ represents the cost required to move from the center point(CP_α) of $REGION(i_\alpha, j_\alpha, k_\alpha)$ to

the center point (CP_β) of $REGION(i_\beta, j_\beta, k_\beta)$. The value of *Cost Array* represents the function value of energy required for movement, for safety during the movement, and for the moving time described below.

3.2.1 Energy Function: $f_E(\alpha, \beta)$

Energy function $f_E(\alpha, \beta)$ indicates the energy value required when moving from region α to region β . Since the reclaimer has 3 axes: the travel axis (A_{Travel}), the slewing axis (A_{Slew}) and the pitching axis ($A_{Pitching}$), the energy function can be defined as follows:

$$f_E(\alpha, \beta) = A_{Travel}(\alpha, \beta) + A_{Slew}(\alpha, \beta) + A_{Pitching}(\alpha, \beta) \tag{5}$$

Assuming that the value of inverse kinematics at position α is $I_\alpha = (y_\alpha, \theta_\alpha, \delta_\alpha)$, and that at position β is $I_\beta = (y_\beta, \theta_\beta, \delta_\beta)$ – where, y denotes the value of the travel axis, θ is the angle of the slewing axis, and δ is the angle of the pitching axis, the energy required by each axis for movement can be approximated as follows:

$$\begin{aligned} A_{Travel}(\alpha, \beta) &= \left| y_\alpha - y_\beta \right| \cdot EC_{Travel} \\ A_{Slew}(\alpha, \beta) &= \left| \theta_\alpha - \theta_\beta \right| \cdot EC_{Slew} \\ A_{Pitching}(\alpha, \beta) &= \left| \delta_\alpha - \delta_\beta \right| \cdot EC_{Pitching} \end{aligned} \tag{6}$$

(Where, EC_{Travel} , EC_{Slew} and $EC_{Pitching}$ mean the value of energy consumption-constant resulting from the characteristics of each axis.)

3.2.2 Safety Function: $f_S(\alpha, \beta)$

Safety function $f_S(\alpha, \beta)$ can be approximated to the sum of safety values that can occur when moving between $REGION(i, j, k)$ and $REGION(i', j', k')$, which exist on the moving path of the control point. First, the safety value when moving between regions is defined as shown on Table 1.

Table 1. *SafetyTable* (state_u, state_v) value of moving between *REGIONS*: M_{ss} , M_{sv} , M_{vs} and M_{vv} are predefined constant values, M_{xy} means the value of state x to state y

<i>REGION</i>	<i>unsafe</i>	<i>safe</i>	<i>safe Voronoi Edge</i>
<i>unsafe</i>	∞	∞	∞
<i>safe</i>	∞	M_{ss}	M_{sv}
<i>safe Voronoi Edge</i>	∞	M_{vs}	M_{vv}

Based on *SafetyTable* shown on Table 1, $f_S(\alpha, \beta)$ is defined as follows:

$$f_S(\alpha, \beta) = \sum \text{SafetyTable}(\text{State of } REGION(i, j, k), \text{State of } REGION(i', j', k')) \tag{7}$$

(Where, $REGION(i, j, k)$ and $REGION(i', j', k') \in \text{Trajectory Set of Control Point}$ and $REGION(i', j', k')$ is next position of $REGION(i, j, k)$ on trajectory).

3.2.3 Time Function: $f_T(\alpha, \beta)$

Time Function $f_T(\alpha, \beta)$ is the time required for the reclaimer’s Control Point to move from region α to region β . This value becomes the maximum value of the moving time of each axis when travel, slewing, and pitching axes move together simultaneously. If

there exist an *unsafe region* on the trajectory of control point, $f_T(\alpha, \beta)$ will be ∞ . Accordingly, the following formula is created:

$$f_T(\alpha, \beta) = \text{MAX} \left(\frac{|y_\alpha - y_\beta|}{S_{Travel}}, \frac{|\theta_\alpha - \theta_\beta|}{S_{Slew}}, \frac{|\delta_\alpha - \delta_\beta|}{S_{Pitching}} \right) \quad (8)$$

(Where, S_{Travel} , S_{Slew} and $S_{Pitching}$ denote the moving speed of each axis.)

3.2.4 Calculation of Cost Array

$Cost[\alpha][\beta]$ required when the reclaimer's Control Point moves from region α to region β can be expressed as the function of $f_E(\alpha, \beta)$, $f_S(\alpha, \beta)$ and $f_T(\alpha, \beta)$.

$$Cost[\alpha][\beta] = f_C(\alpha, \beta) = f(f_E(\alpha, \beta), f_S(\alpha, \beta), f_T(\alpha, \beta)) \quad (9)$$

To simplify calculation, this paper used the following model.

$$Cost[\alpha][\beta] = f_E(\alpha, \beta) \cdot SF_{Energy} + f_S(\alpha, \beta) \cdot SF_{Safety} + f_T(\alpha, \beta) \cdot SF_{Time} \quad (10)$$

(Where, SF_{Energy} , SF_{Safety} and SF_{Time} are weighted value constants.)

The weighted value constant used in the above formula determines on which value of energy, safety, and time the priority should be placed when moving the reclaimer. When energy and safety are reflected as 2:1 and time is ignored, the formula will be $SF_{Energy} = 2$, $SF_{Safety} = 1$ and $SF_{Time} = 0$.

3.3 Optimal Path Search

It is difficult to mathematically calculate an optimal moving path that can be used on the 3-dimensional space; and even if it can be calculated, it is difficult to apply at industrial sites because of the complexity of implementation[11]. Considering these difficulties, this paper, proposes a method of approximating the optimal path through the use of the cost array calculated in the preceding section. Each element of the cost array calculated in the preceding section satisfies the condition of $Cost[\alpha][\beta] \geq 0$. Therefore, this problem can be solved by using the *shortest path search algorithm*. The shortest path search algorithm is an algorithm that finds the shortest path when the reclaimer attempts to move from position α to position β , and it is an algorithm that finds the shortest path only by comparing and adding up the array value [5]. If the shortest path search algorithm is applied to array $Cost[N][N]$, all *REGION* indexes λ_k of the lowest cost leading to index β from index α can be obtained. In addition, since a *REGION* indexed λ_k contains information on the posture of the reclaimer, not only the value of the optimal path, but also the value of each axis can be obtained simultaneously.

4 Experimental Results

Fig. 6 shows the comparison results of the motion characteristics according to the changes in $Cost$ Function $f_C(\alpha, \beta)$. The blue and red arrows in each figure indicates the direction of the control point of each reclaimer, with the blue indicating the starting point and red, the goal point. In each figure showing the comparison result of the motion characteristics, $f_S(\alpha, \beta)$ tends to move the control point according to Voronoi

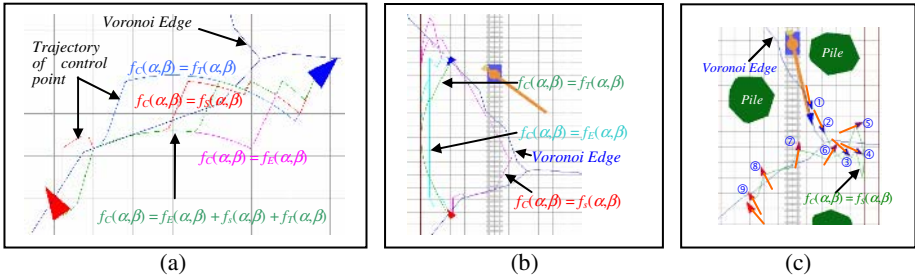


Fig. 6. Comparison of the motion characteristics varying according changes in $f_C(\alpha, \beta)$

Edge. $f_T(\alpha, \beta)$ shows the characteristics of attempting to enlarge the motion in one operation to reduce the overall moving time. $f_E(\alpha, \beta)$ shows a characteristic that is almost similar to that of $f_T(\alpha, \beta)$ because the saving of the moving time has a meaning similar to that of reducing overall moving energy. Fig. 6 (c) shows the changes in the posture direction of the reclaimer and the numbers of control sequences.

5 Conclusions

We discussed the method of searching the reclaimer's optimal moving path. The optimal moving paths of a robot such as a reclaimer can significantly reduce the risk of accidents, cost of energy and moving time compared to other "reasonable" paths [14]. At night time, the safe moving paths are preferred since a wide view cannot be secured from a remote place. In the case of urgent operations, the shortest moving time, not the shortest path, is more desirable. For normal operations, the optimal moving paths should be achieved in terms of safety, energy consumption, and moving time taking the operation conditions into consideration. Each of the proposed algorithms carries characteristics that can easily be applied at industrial sites. The proposed algorithm was successfully implemented for the reclaimer in the yards of Gwangyang Steelworks in Korea.

References

1. J. Canny, B. Donald, "Simplified Voronoi Diagrams", *Discrete & Computational Geometry*, Vol. 3, pp.219-236, (1988)
2. C. Bajaj, and M.-S., Kim, "Algorithms for Planar Geometric Models," *Proceeding of the 15th International Colloquium on Automata, Languages and Programming (ICALP 88)*, Tampere, Finland, *Lecture Notes in Computer Science*, Springer-Verlag, pp.67-81, (1988)
3. J. Canny, *The Complexity of Robot Motion Planning*, The MIT press, pp.128-147, (1987)
4. C.-T Choi, K.-H Lee, K.-T Shin, K.-S Hong, and H.-S Ahn, "Automatic Landing Method of a Reclaimer on the Stockpile", *IEEE Trans. on System, Man, and Cybernetics-Part C : Applications and Reviews*, VOL. 29, NO. 1, Feb., pp.308-314, (1999)
5. Sara Baase, "Computer Algorithms: Introduction to Design and Analysis", 2nd Ed., (1988)
6. R. Walker, "Algebraic Curves," Springer Verlag, New York, (1978)

7. J. G. Lee and H. Y. Chung, "Global Path Planning for Mobile Robot with Grid-Type World Model," *Robotics & Computer-Integrated Manuf.*, Vol. 11, No. 1, pp. 13-21, (1994)
8. Mingwu Chen and Ali M. S. Zalzal, "A Genetic Approach to Motion Planning of Redundant Mobile Manipulator Systems Considering Safety and Configuration", *Journal of Robotic Systems* 14(7), pp 529-544, (1997)
9. M. Foskey, M. Garber, M. C. Lin, D. Manocha, "A Voronoi-Based Hybrid Motion Planner for Rigid Bodies," *Intelligent Robotics and Systems*, Vol. 1, pp.55-60, (2001)
10. Osamu Takahashi and R. J. Schilling, "Motion Planning in a Plane Using Generalized Voronoi Diagrams," *IEEE Trans. on Robotics and Automation*, Vol. 5, No. 2, April, (1989)
11. K. Hoff, T. Culver, J. Keyser, MC Lin, D. Manocha, "Interactive motion planning using hardware-accelerated computation of generalized Voronoi diagrams," *Proc. IEEE Int. Conf. on Robotics & Automation*, pp. 2931-2937, (2000)
12. S.-H. Suh, K.G. Shin, "A variational dynamic programming approach to robot-path planning with a distance-safety criterion," *IEEE Journal of Robotics and Automation*, Vol. 4, No. 3, pp. 334-349, (1988)
13. K. Sun and V. Lumelsky, "Path planning among unknown obstacles: the case of a three-dimensional Cartesian arm," *IEEE Trans. on Robotics and Automation*, pp. 776-786, (1992)
14. Robert S. Alexander and Neil C. Rowe, "Path Planning by Optimal-Path-Map Construction for Homogeneous-Cost Two-Dimensional Regions," *IEEE Int. Conf. Robotics and Automation*, pp. 1924-1929, (1990)
15. V. J. Lumelsky, S. Mukhopadhyay and K. Sun, "Dynamic Path Planning in Sensor-Based Terrain Acquisition," *IEEE Trans. Robotics and Automation*, Vol. 6, No. 4, pp. 462-472, Aug., (1990)
16. T. Lozano-Perez, "Spatial planning: A configuration space approach," *IEEE Trans. Comput.*, Vol. C-32, pp.108-120. Feb., (1983)
17. H. Surmann, A. Nuechter and J. Hertzberg, "An autonomous mobile robot with a 3D laser range finder for 3D exploration and digitalization of indoor environments," *Robotics and Autonomous Systems*, pp. 181-198, (2003)
18. J. Miura, Y. Negishi and Y. Shirai, "Mobile Robot Map Generation by Integrating Omnidirectional Stereo and Laser Range Finder," *Proceedings of 2002 IEEE/RSJ Int. Conf. on Intelligent Robotics and Systems*, pp. 250- 255, (2002)
19. A. Aboshosha and A. Zell, "Robust mapping and path planning for indoor robots based on sensor integration of sonar and a 2D laser range finder," *IEEE 7th International Conference on Intelligent Engineering Systems*, (2003)

Fault Tolerant Guarding of Grids

Adrian Kosowski¹, Michał Małafiejski¹, and Paweł Żyliński^{2,*}

¹ Gdańsk University of Technology,
Department of Algorithms and System Modeling

² University of Gdańsk,
Institute of Mathematics
{kosowski, mima, buba}@sphere.pl

Abstract. In this paper we deal with one of the art gallery problems, namely the problem of fault tolerant guarding of grids, which is defined as the problem of finding two disjoint guard sets in a grid. Although determining the existence of such a structure is easy in general grids, the task of minimising the number of guards taken over both teams is shown to be NP-hard even for subcubic grids. Moreover, we propose a $6/5$ -approximation algorithm for solving the fault tolerant guard problem in grids.

Keywords: fault tolerant guards, packing factors, edge-colorable subgraph.

1 Introduction

A *grid* P is a connected union of segments of the plane, such that no three segments cross at one point. A grid with the imposed restriction that segments may only be horizontal or vertical is called *orthogonal*. A point $x \in P$ can see point $y \in P$ if the segment $\overline{xy} \subseteq P$, and a set of points S in the grid P is a *guard set* for P provided that for every point x in P there is a point g in S such that g sees x . In this paper, we explore an interesting variant of the *art gallery problem* [21, 23], where we consider the guarding of grids with independent teams of guards which are allowed to be placed only at intersections and no two guards can occupy the same place. The problem is motivated by power supply issues or camera sensor systems, where we backup the whole guarding system to ensure its reliability. In real life, it might happen that an ordinary guard set would become disabled (i.e. when considering system failures in closed circuit surveillance), thus leaving the grid uncovered. We wish to reduce this risk, and this can be done by using a *fault tolerant guard set*. Note that the considered problem is significantly different from another guarding model, in which the system of guards need only be resistant to the loss of an arbitrary single guard.

Problem definition. A set of guards S for a grid P is said to be *fault tolerant* if it can be decomposed into two disjoint sets S_1 and S_2 such that each of them

* Supported by the State Committee for Scientific Research (Poland) Grant No. 4 T11C 047 25.

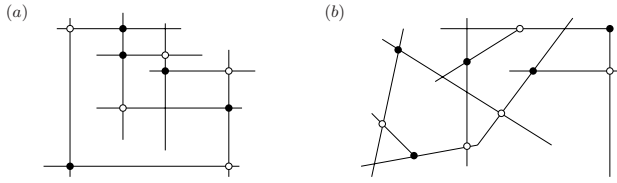


Fig. 1. A fault tolerant guard set S for (a) an orthogonal grid and (b) a general grid: $S = S_1 \cup S_2$ and each set S_i , $i = 1, 2$, is a guard set for the grid (black and white dots)

is a guard set for P ; an example of a fault tolerant guard set in a grid is shown in Fig. 1. Let us introduce the primary problem considered in this paper.

Fault Tolerant Guard Problem (FTG)

Instance: A grid P .

Question: Does a fault tolerant guard set exist in grid P ?

The minimisation version of problem FTG is defined with respect to the size of the set of guards forming the solution.

Minimum Fault Tolerant Guard Problem (MinFTG)

Instance: A grid P .

Question: Find the minimum fault tolerant guard set for grid P .

Our results. By the *degree* of a grid P , denoted by Δ_P , we mean the maximum number of segments crossed by a segment of grid P ; if $\Delta_P = 3$ then the grid is called *subcubic*. The main results of our paper for fault tolerant guarding of grids are briefly presented in Table 1. The results were obtained through reduction to the problem of finding the maximum 2-edge-colorable subgraph in a given graph (the *Max-2-ECS* problem for short) [7]. Recall that a graph G is *k-edge-colorable* if its edges can be colored with k colors in such a way that no two edges of the same color share a vertex.

Related work. The original *guard problem in orthogonal grids* was first formulated by Ntafos in 1986 [20], who established that a minimum set of guards covering all points in a 2D-grid of n segments consists of $(n - m)$ guards, where m is the size of the maximum matching in the intersection graph of the grid, and it can be found in $O(n^{2.5})$ time. The *intersection graph* G_P of a grid P is defined as follows: each vertex of G_P corresponds to a grid segment of P and two vertices are connected by an edge iff their corresponding segments cross. In the case of 3D-grids, the problem of finding the minimum guard set is NP-hard [20]. In [18, 19] the authors considered the concept of cooperative guards in grids. Let us recall that a guard set S is *cooperative* (or respectively, *weakly cooperative*) if its visibility graph is connected (respectively, has no isolated vertices) [16, 17]; the *visibility graph* of a set of guards S is the graph whose vertex set is S and two vertices are adjacent if they see each other. The authors [19] established that the problem of finding the minimum cooperative guards set can be solved in

Table 1. Our results, where n and t denote the number of grid segments and the number of crossings, respectively

Grid Type	Problem	Complexity
orthogonal	FTG	$O(n + t)$ Thm. 2.1
	MinFTG	$O(nt^2)$ Thm. 2.2
general	FTG	$O(n \log n + t)$ Thm. 3.2
	MinFTG	NP-hard Thm. 3.5 6/5-approx. Thm. 4.5

polynomial time for both two- and three-dimensional grids. For weakly cooperative guards, the authors [18] showed that a minimum coverage for an n -segment grid has exactly $(n - p_3)$ weakly cooperative guards, where p_3 is the size of the maximum P_3 -matching in the intersection graph of the grid, which implies that the minimum weakly cooperative guards problem in grids is NP-hard.

1.1 Packing Factors and Fault Tolerant Guarding of Grids

Let $G(V, E)$ be a graph, and let f and g be integer-valued functions on $V(G)$, $f, g : V(G) \rightarrow \mathbb{N}$. Then a spanning subgraph H of G is called an (f, g) -factor if $f(v) \leq \deg_H(v) \leq g(v)$ for all $v \in V(H)$; by $\deg_S(v)$ we denote the degree of a vertex v in a graph S . A special case holds if $f(v) = a$ and $g(v) = b$ for all $v \in V(G)$, and then an (f, g) -factor is referred to as $[a, b]$ -factor. Hence for example, an edge cover of G is equivalent to a $[1, \Delta]$ -factor of G , where Δ is the maximum degree in G .

Remark 1.1. *Let $G(V, E)$ be a graph, and let $a \geq 1$ be an integer. Then the problem of finding the $[a, \Delta]$ -factor of G with the minimum number of edges is equivalent to the problem of finding the $(0, g)$ -factor of G with the maximum number of edges, where $g(v) = \deg_G(v) - a$ for all $v \in V$.*

By node splitting method proposed by Tutte (see [10]) it is possible to transform the $(0, g)$ -factor into a perfect matching.

Remark 1.2. *The problem of finding the $(0, g)$ -factor of a given graph $G(V, E)$ with the maximum number of edges can be solved in $O(|V||E|^2)$ time.*

An H -packing of a graph G is a set $L = \{H_1, \dots, H_k\}$ of edge-disjoint subgraphs of G , where each graph from L is isomorphic to graph H . A natural generalization of the H -packing problem is the \mathcal{H} -packing problem, where \mathcal{H} is a family of graphs. In the \mathcal{H} -packing problem, for a graph G and an integer k , we ask whether there exists a set S of k edge-disjoint subgraphs of G such that every subgraph is isomorphic to an element of family \mathcal{H} . A special case holds if family \mathcal{H} consists of all $[1, \Delta]$ -factors of a graph G .

[1, Δ]-factor k -packing Problem (k -FP)

Instance: A connected graph G (k is fixed).

Question: Does there exist a set $\{F_1, \dots, F_k\}$ of edge-disjoint $[1, \Delta]$ -factors of G ?

This problem can also be considered in its minimisation version, with respect to the number of edges forming the sought $[1, \Delta]$ -factor.

Minimum $[1, \Delta]$ -factor k -packing Problem (Min- k -FP)

Instance: A connected graph G (k is fixed).

Question: Find a $[1, \Delta]$ -factor k -packing in G with the minimum number of edges or decide that one does not exist.

Before we discuss the relation between the fault tolerant guards problem in grids and the problem of $[1, \Delta]$ -factor packing, let us state an elementary property of a minimal $[1, \Delta]$ -factor k -packing.

Remark 1.3. Let $\mathcal{F} = \{F_1, F_2, \dots, F_k\}$ be a minimal (not necessarily minimum) $[1, \Delta]$ -factor k -packing of a graph. Then each of connected components of factor F_i , $i = 1, \dots, k$, is a star.

By the above remark, the Min- k -FP problem in a graph $G(V, E)$ is equivalent to the problem of finding a $[1, \Delta]$ -factor k -packing for which the sum of the numbers of connected components of a factor, taken over all factors of the packing, is the largest possible. This is an immediate consequence of the fact that a minimal factor with c connected components (stars) has $|V| - c$ edges, hence a factor k -packing with a total of s connected components has exactly $k|V| - s$ edges. Thus the Min- k -FP problem is equivalent to the problem of finding k edge-disjoint edge covers of graph G with the minimum number of edges, taken over all covers. As far as we know, this problem has not been studied before, while the problem of finding the maximum number of edge-disjoint edge covers was investigated in [13, 14].

Let us come back to fault tolerant guards. Throughout the paper, we assume that guards are restricted to be located at crossing of a grid (compare [20]). Recall that Ntafos [20] established that a guard set for a grid P is equivalent to a set of edges covering all vertices in the intersection graph G_P of grid P , that is, taking into account the definition of a factor packing, to the $[1, \Delta]$ -factor 1-packing. Consequently, it is easy to see that there is a one-to-one correspondence between a fault tolerant guard set for grid P and a solution to the $[1, \Delta]$ -factor 2-packing problem in intersection graph G_P . Thus we have

Remark 1.4. The FTG problem is equivalent to the 2-FP problem in the intersection graph of a grid.

Remark 1.5. The MinFTG problem is equivalent to the Min-2-FP problem in the intersection graph of a grid.

From now on, the number of grid segments will be denoted by n , and the number of crossings by t . A minimum degree of a given graph will be denoted by δ , and

maximum degree by Δ . The cardinality (i.e. the number of edges) of a factor F will be denoted by $|F|$. Finally, notice that the concept of $[1, \Delta]$ -factor k -packing problem can be generalized for \mathcal{F} -factors, where \mathcal{F} is an arbitrary family of connected graphs.

2 Fault Tolerant Guard Sets in Orthogonal Grids

In this section, we shall show that both the FTG problem and the MinFTG problem for orthogonal grids can be solved in polynomial time. The first result follows immediately from König’s Theorem [15] asserting that a bipartite graph G has a edge-disjoint set of k edge disjoint edge covers iff $\delta(G) \geq k$. As the intersection graph of any orthogonal grid is bipartite, and it can be constructed in $O(n + t)$ time [8], we get the following corollary.

Theorem 2.1. *The FTG problem in grids can be solved in $O(n + t)$ time.*

When considering the minimisation problem, König’s theorem can be generalised to show that a minimum $[1, \Delta]$ -factor k -packing (not only 2-packing) in a bipartite graph can be efficiently determined.

Theorem 2.2. *A minimum $[1, \Delta]$ -factor k -packing in a connected bipartite graph $G(V, E)$ with $\delta \geq k$ can be found in $O(|V||E|^2)$ time.*

Proof. Consider any bipartite graph $G(V, E)$ and its $[k, \Delta]$ -factor H with the minimum possible number of edges. On the one hand, the spanning subgraph of G formed by combining the edge sets of factors in any $[1, \Delta]$ -factor k -packing is a $[k, \Delta]$ -factor, and thus has not fewer edges than H . On the other hand, by König’s Theorem, graph H which is bipartite and of minimum degree at least k , has a $[1, \Delta]$ -factor k -packing. Therefore, the edge set of the minimum $[1, \Delta]$ -factor k -packing is the edge set of H . Since G is bipartite, taking into account Remarks 1.1 and 1.2, we obtain that the minimum $[k, \Delta]$ -factor H of G can be found in $O(|V||E|^2)$ time. Then by König’s Theorem, H can be decomposed into $[1, \Delta]$ -factors in $O(|V||E|^2)$ time. \square

Hence by the theorem above, we get

Theorem 2.3. *The MinFTG problem in grids can be solved in $O(nt^2)$ time.*

3 Fault Tolerant Guard Sets in General Grids

As the intersection graph of a general grid is not bipartite any more, we cannot make use of König’s Theorem. However, a correspondence between a fault tolerant guard set for a grid and an edge-disjoint set of two $[1, \Delta]$ -factors of the intersection graph of the grid remains the same, i.e., Remarks 1.4 and 1.5 remain valid for general grids. In the next, we will show that for all graphs the $[1, \Delta]$ -factor 2-packing problem can be solved in linear time, whereas its minimisation version is NP-hard even for 3-colorable subcubic planar graphs. These results

will imply polynomial solvability of the FTG problem and NP-hardness of the MinFTG problem in general grids.

Theorem 3.1. [13, 14] *A connected graph $G(V, E)$ has a $[1, \Delta]$ -factor 2-packing iff $\delta \geq 2$ and G is not a cycle of odd length; such a packing can be found in $O(|V| + |E|)$ time.*

Consequently, by Remark 1.4, and Theorem 3.1, we get that if there are no segments crossing exactly one other segment in an n -segment grid P and additionally, if n is even or at least one segment of the grid crosses at least 3 other segments, then grid P has a fault tolerant guard set. Thus we have

Theorem 3.2. *The FTG problem can be solved in $O(n \log n + t)$ time.*

Notice that the complexity of the algorithm for the FTG problem is determined by the problem of computing the intersection graph of a general grid [3]. Although determining the existence of a $[1, \Delta]$ -factor 2-packing is easy, the minimisation version of this problem is NP-hard even for 3-colorable subcubic planar graphs (the proof is omitted due to the limits of space).

Theorem 3.3. *The Min-2-FP problem is NP-hard in 3-colorable subcubic planar graphs.*

Let us recall that the following question: *Is every planar graph the intersection graph of a set of segments in the plane?*, posed by Scheinerman [22], still remains open. Up to now, there have been only some partial answers, see [2, 4, 5, 11], and one of them is as follows.

Theorem 3.4. [2] *Every 3-colorable subcubic planar graph G can be represented as the intersection graph of a general grid.*

Finally, by Remark 1.4, and Theorems 3.1-3.4, we get

Theorem 3.5. *The MinFTG problem is NP-hard even in grids in which every grid segment crosses at most three other segments.*

4 Approximation Algorithms for Fault Tolerant Guards

This section is devoted to approximation algorithms for the MinFTG problem in general grids. First notice that the result of Theorem 3.1 immediately provides a 2-approximation algorithm for the MinFTG problem in grids.

Theorem 4.1. *There exists a $O(n \log n + t)$ linear time 2-approximation algorithm for the MinFTG problem in grids.*

Proof. All we need is to observe that the set S constructed in the proof of Theorem 3.1 has no more than $2n - 2$ edges, while the minimum $[1, \Delta]$ -factor 2-packing in G consists of not fewer than n edges. Hence the presented algorithm is 2-approximate for the Min-2-FP problem, and by Remark 1.5, for the MinFTG as well. \square

When considering approximation algorithms in general graphs, it has to be observed that there is a strong relation between the Min-2-FP problem and the Max-2-ECS problem, and this we shall discuss next.

4.1 6/5-Approximation Algorithm for the MinFTG Problem

Let us recall that a graph G is *2-edge-colorable* if its edges can be colored with two colors in such a way that none two of edges in the same color share a vertex, and in the *Max-2-ECS* problem, we are interested in finding a maximum 2-edge-colorable subgraph of a given graph G [7].

Lemma 4.2. *If graph $G(V, E)$ has a minimal $[1, \Delta]$ -factor 2-packing of not more than $2|V| - s$ edges, then G contains a 2-edge-colorable subgraph of not fewer than s edges.*

Proof. As by Remark 1.3 a minimal factor 2-packing with $2|V| - s$ edges has s connected components, taken over two factors of the packing, we can create a subgraph of G induced by selecting exactly one edge from each connected component of each factor of G . This subgraph is obviously 2-edge-colorable. \square

Note that the lemma remains valid if we consider k -packing and k -edge-colorability, respectively.

Theorem 4.3. *Let $G(V, E)$ be a graph which has a $[1, \Delta]$ -factor 2-packing. Then G contains a 2-edge-colorable subgraph of not fewer than s edges iff G has a minimal $[1, \Delta]$ -factor 2-packing of not more than $2|V| - s$ edges. The equivalence is implied by the existence of an algorithm with $O(|V|^2)$ running time.*

Proof. (\Leftarrow) By Lemma 4.2.

(\Rightarrow) Let G be a connected graph with $\delta \geq 2$ and $\Delta \geq 3$, and let H be a 2-edge colorable spanning subgraph of G with the largest possible number $s^* \geq s$ of edges. Notice that the connected components of H must be cycles, paths or isolated vertices, and denote the number of paths and isolated vertices as p and i , respectively. Obviously, $s^* + p + i = |V|$. We will construct the two $[1, \Delta]$ -factors in the form of a subgraph S of G with edges labeled 1 and 2. First, let $S = H$, and create a labeling of the edges of S corresponding to some correct 2-edge-coloring of H . Next, consider all the connected components of H which are paths. The end vertices of the paths may never be adjacent to an end vertex of some other path, or to an isolated vertex in H , since this would mean that there exists a 2-edge-colorable subgraph of G with more edges than H , a contradiction. Hence, any end vertex v of a path P in H must be connected by some edge e in $G \setminus H$ to at least one vertex which is of degree 2 in H , or to the other end vertex of the same path P in H . In the former case (if v is not adjacent to the end vertex of the same path), add e to S and label it in such a way that v is incident to edges labeled 1 and 2. In the latter case, $C = P \cup \{e\}$ must be a cycle of odd length. Therefore at least one of the vertices of C must be of degree not less than 3 in G , and there must exist a vertex u in C such that some edge

f incident to u does not belong to C . Add edges $\{e, f\}$ to S and create a new labeling of the edges of C and edge f such that each vertex of C is adjacent to edges labeled 1 and 2. Once this process is complete, S has not more than $s^* + 2p$ edges, and all non-isolated vertices of S are adjacent to edges labeled both 1 and 2. Finally, by inserting into S two edges (labeled 1 and 2) for each isolated vertex of H , we obtain a $[1, \Delta]$ -factor 2-packing using not more than $s^* + 2p + 2i = 2|V| - s^* \leq 2|V| - s$ edges. \square

Theorem 4.3 can be constructively applied to reduce the Min-2-FP and Min-FTG problems to the Max-2-ECS problem when constructing approximation algorithms.

Corollary 4.4. *The existence of a polynomial time α -approximation algorithm for the Max-2-ECS problem implies the existence of a polynomial time $(2 - 1/\alpha)$ -approximation algorithm for the Min-2-FP problem (and consequently also for the MinFTG in the appropriate class of grids).*

Proof. Let A be an α -approximated solution for the Max-2ECS problem, and let OPT and OPT' be the optimal solutions for the Max-2ECS problem and the Min-2FP problem, respectively. By Theorem 4.3, we have $OPT' = 2|V| - OPT$. Moreover, Theorem 4.3 guarantees the existence of an approximated solution A' to Min-2FP with $2|V| - |A|$ edges. As $\frac{|OPT|}{|A|} \leq \alpha$, and $|OPT| \leq |V|$, we get

$$\frac{|A'|}{|OPT'|} = \frac{2|V| - |A|}{2|V| - |OPT|} \leq \frac{2|V| - \frac{1}{\alpha}|OPT|}{2|V| - |OPT|} = 1 + \frac{|OPT|(1 - \frac{1}{\alpha})}{2|V| - |OPT|} \leq 2 - \frac{1}{\alpha}.$$

The computational complexity of the inferred algorithm is determined by the complexity of the original algorithm and the $O(|V|^2)$ cost of post-processing. \square

As the existence of a $6/5$ -approximation algorithm with $O(|V|^2|E|^2)$ running time for the Max-2-ECS problem was shown in [7], by Remark 1.5 and Corollary 4.4, we get the following theorem.

Theorem 4.5. *There is a $6/5$ -approximation algorithm with $O(n^3)$ running time for the MinFTG problem in general grids.*

5 Final Remarks

A natural generalisation of the fault tolerant guard problem is k -fault tolerance. A set of guards S for a grid P is said to be k -fault tolerant if it can be decomposed into $k + 1$ disjoint sets S_1, \dots, S_{k+1} such that each of them is a guard set for P ; thus a 1-fault tolerant guard set is just fault tolerant. Clearly, a k -fault tolerant guard set is equivalent to the $[1, \Delta]$ -factor $(k + 1)$ -packing, and consequently, König's Theorem and Theorem 2.2 imply that both the problem of existence of a k -fault tolerant guard set (the k -FTG problem) in an orthogonal grid as well as its minimisation version (the Min - k -FTG problem) can be solved in polynomial time for arbitrary $k \geq 1$. However for general grids with $k \geq 2$, these

problems remain open, although one can easily prove that the $[1, \Delta]$ -factor k -packing problem is NP-complete for $k \geq 3$ by [12]. Hence it is interesting to ask whether the class of graphs representable as intersection graphs of general grids is sufficiently rich for the $[1, \Delta]$ -factor k -packing problem to be NP-complete when restricted to this class and with $k \geq 3$. We believe the answer to this question to be positive, thus we state the following conjecture.

Conjecture 5.1. *For $k \geq 2$, the k -FTG problem is NP-complete, and thus the Min- k -FTG problem is NP-hard.*

It is also worth noting the practical applications of the algorithms presented as auxiliary results in this paper. The $[1, \Delta]$ -factor 2-packing problem may be formulated in terms of constructing minimum edge-disjoint edge covers and as such has a number of applications, mainly in problems related to routing and subdivision of traffic in computer networks [1]. The closely related problem of finding a maximum 2-edge-colorable subgraph is motivated by call admittance issues in satellite based telecommunication, where parallel transmission is performed in two separate spaces, using Time Division Multiplexing and Frequency Division Multiplexing [7].

References

1. J. Bialogrodzki, Path Coloring and Routing in Graphs. In: *Graph Colorings*, Kubale M. ed., Contemporary Mathematics series 352, AMS (2004), Providence, Rhode Island, USA, 139–152.
2. N. de Castro, F.J. Cobos, J.C. Dana, A. Marquez, M. Noy, Triangle-free planar graphs as segment intersection graphs, *Proc. ISGD*, LNCS **1731** (1999), 341-358.
3. B. Chazelle, H. Edelsbrunner, An optimal algorithm for intersecting line segments in the plane, *Journal of the ACM* **39** (1992), 1-54.
4. J. Czyżowicz, E. Kranakis, J. Urrutia, A simple proof of the representation of bipartite planar graphs as the contact graphs of orthogonal straight line segments, *Information Processing Letters* **66** (1998), 125-126.
5. C. Dangelmayr, Intersection graphs of straight-line segments, 4th Annual CGC Workshop on Computational Geometry (Stels, 2004).
6. M. E. Dyer, A. M. Frieze, Planar 3DM is NP-complete, *Journal of Algorithms* **7** (1986), 174-184.
7. U. Feige, E. Ofek, U. Wieder, Approximating Maximum Edge Coloring in Multi-graphs, *Proc. APPROX*, LNCS **2462** (2002), 108-121.
8. U. Finke, K. Hinchirs, Overlaying simply connected planar subdivisions in linear time. In *Proc. ACM SoCG* (1995), 119-126.
9. M.R. Garey, D.S. Johnson, *Computers and Intractability: A Guide to the Theory of NP-completeness*, Freeman, New York (1979).
10. R.L.Graham, M.Groetschel, L.Lovasz, *Handbook of Combinatorics*, Vol.1, Elsevier (1995), 211-212.
11. I. B.-A. Hartman, I. Newman, and R. Ziv, On grid intersection graphs, *Discrete Mathematics* **87** (1991), 41-52.
12. I. Holyer, The NP-completeness of edge-colouring, *SIAM Journal of Computing* **10** (1981), 718-720.

13. D.P.Jacobs, R.E.Jamison, Complexity of recognizing equal unions in families of sets, *Journal of Algorithms* **37** (2000), 495-504.
14. K. Kawarabayashi, H. Matsuda, Y. Oda, K. Ota, Path factors in cubic graphs, *Journal of Graph Theory* **39** (2002), 188-193.
15. D. König, Über Graphen und ihre Anwendung auf Determinantentheorie und Mengenlehre, *Math. Ann.* **77** (1916), 453-465.
16. B.C Liaw, N.F. Huang, R.C.T. Lee, The minimum cooperative guards problem on k -spiral polygons, In *Proc. CCCG'93*, 97-101.
17. B.C. Liaw, R.C.T. Lee, An optimal algorithm to solve the minimum weakly cooperative guards problem for 1-spiral polygons, *Information Processing Letters* **52** (1994), 69-75.
18. M. Małafiejski, P. Żyliński, Weakly cooperative guards in grids, In *Proc. ICCSA'05*, LNCS **3480** (2005), 647-656.
19. T. Nierhoff, P. Żyliński, Cooperative guards in grids, 3rd Annual CGC Workshop on Computational Geometry (Neustrelitz, 2003).
20. S. Ntafos, On gallery watchmen in grids, *Information Processing Letters* **23** (1986), 99-102.
21. J. O'Rourke, *Art Gallery Theorems and Algorithms*, Oxford University Press (1987).
22. E. R. Scheinerman. Intersection classes and multiple intersection parameters of graphs, PhD thesis, Princeton University (1984).
23. J. Urrutia, *Art Gallery and Illumination Problems*, Handbook on Computational Geometry, Elsevier Science, Amsterdam (2000).

Tunable Bounding Volumes for Monte Carlo Applications

Yuan-Yu Tsai, Chung-Ming Wang, Chung-Hsien Chang, and Yu-Ming Cheng

Institute of Computer Science, National Chung-Hsing University, Taichung, 402, Taiwan
{cuckoo, cmwang, cschang}@cs.nchu.edu.tw,
ssmtt.cym@msa.hinet.net

Abstract. Luminaire sampling plays an important role in global illumination calculation using Monte Carlo integration. A conventional approach generates samples on the surface of the luminaire, resulting in rendered images with high variance of noise. In this paper, we present an efficient solid angle sampling technique using tunable bounding volumes for global illumination calculation. In contrast to the conventional approach, our technique derives samples from the solid angle subtended by the luminaire. In the construction process, we build a convex, frustum-like polyhedron as a bounding volume for a light source. Front-facing polygons of the bounding volume are then projected onto the unit hemisphere around the shaded point. These projected polygons represent the approximated solid angle subtended by the luminaire. The third step samples the projected spherical polygons on which a number of stratified samples are generated. We employ various types of light sources including ellipse, elliptic cylinder, elliptic cone and elliptic paraboloid. We perform our technique for Monte Carlo Direct Lighting and Monte Carlo Path Tracing applications. Under similar sample numbers, our technique produces images with less variance of noise compared to the conventional method. In addition, our technique provides roughly equal image quality in less execution time. Our approach is simple, efficient, and applicable to many types of luminaries for global illumination calculation.

1 Introduction

Developing efficient techniques for sampling on luminaires is important for global illumination calculation using Monte Carlo integration [2, 5, 6, 8, 9, 10, 11, 12, 16, 17, 18]. These algorithms determine the luminous radiance using a stochastic approach to evaluate the rendering equation [3]. Efficient sampling techniques can help reduce the variance of noise in the rendered images without sacrificing the rendering time and perhaps the sample numbers.

Previous approaches in deriving efficient sampling on luminaries have achieved some success, as summarized in Table 1. Some sampling techniques were presented using different probability density functions for two- and three-dimensional luminaries. Of these, the sampling technique using CWSA (Cosine-Weighted Solid Angle) is the most efficient since it employs the concept of importance sampling. This approach takes into account both the solid angle and the cosine factor, which are components of

the function being integrated in the rendering equation. However, this approach normally requires high-cost numerical computing [17] and therefore is of less interest.

Alternatively, SUDS (Sampling Uniformly in Directional Space) used by some sampling technique is an efficient approach since it considers, at least, the effect of the solid angle when designing the probability density function. However, this approach is not suitable for three-dimensional luminaires because solid angles subtended by three-dimensional luminaires are difficult to compute. Apparently, except for a spherical luminaire since it is entirely symmetric in three-dimensional space, constructing the solid angle for sampling is not easy. However, if we can efficiently approximate the solid angle subtended by the luminaire using a tight bounding volume for the luminaire instead of the luminaire itself, we may still take advantage of the SUDS approach. Obviously, the bounding volume should be as tight as possible and its shape as simple as possible so as to reduce potential overheads.

Table 1. Sampling techniques for luminaires

Luminaire Geometry	UD	VA	SUDS	CWSA
Triangle	[13][7][17][10]	N.S.	[18][1]	[14]
Rectangle	[7] [18][10]	N.S.	[17]	[17]
Polygon	[17][10]	N.S.	[17]	[17]
Disc	[7][17]	N.S.	[17]	N.A.
Sphere	[16][7]	[17][10]	[16][17][10]	[10][17]
Cylinder	[7][10]	N.A.	[19]*	N.A.
Cone	[7]	N.A.	N.A.	N.A.

1. UD (Uniform Density); 2. VA (Visible Area); 3. SUDS (Sampling Uniformly in Directional Space); 4. CWSA (Cosine-Weighted Solid Angle).

N.S.: No such cases for the planar luminaires.

N.A.: Not available.

*: only for the cosine factor.

In this paper, we propose such an efficient SUDS sampling technique for three-dimensional luminaires. For simplicity, we refer to our technique as solid angle sampling technique, or SA technique. The efficiency of our approach is due to employment of a tight bounding volume together with optimization, described later, for three-dimensional luminaires. Besides, the adoption of the bounding volume approach avoids numerical computing which is computationally expensive.

This paper is organized as follows: Section 2 describes a general view of SA technique. Section 3 derives bounding volumes with optimization for different types of luminaires. Section 4 presents experimental results, followed by conclusions and future work in section 5.

2 An Overview of the SA Technique

A conventional sampling approach generates sample points on the surface of the luminaire. The SA technique, however, generates samples on the solid angle subtended by the luminaire. This section presents a general overview of the SA technique.

Let l denote a luminaire, let p be a point on the surface of an arbitrary object on the scene, and let n be the unit normal vector at p . Let sal denote the solid angle subtended by the luminaire. From the definition of solid angle, sal is a bounded spherical area, which is the projection of l onto a unit hemisphere centered at p with a normal vector n . Clearly, sal depends on l, p, n , and the distance between l and p .

For a curved luminaire, sal is difficult to compute analytically, but sampling on a spherical triangle is possible [1]. This inspired us to adopt the bounding volume for a luminaire. If we could derive a tight bounding volume for a curved luminaire with non-curved boundaries, e.g., a convex polyhedron with small number of vertices, then we could handily approximate the solid angle subtended by the convex polyhedron.

Let HS be a unit hemisphere centered at P , and let Q be the set of n vertices of a polyhedron (denoted by V_1, V_2, \dots, V_n) i.e. $Q = \{ V_1, V_2, \dots, V_n \}$. Also, let V_c be the center of the polyhedron (see Fig. 1). The approximation of a solid angle can be realized by three processes; namely, the construction, the projection, and the sampling process.

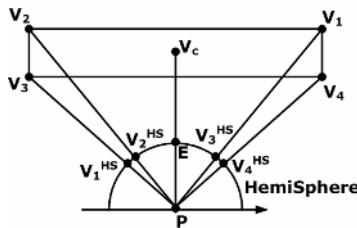


Fig. 1. An Illustration of the solid angle sampling technique

In the construction process, we employ a convex, frustum-like polyhedron as a bounding volume. Note that we must achieve a compromise between the tightness and the vertex numbers. On the one hand, we would like to construct a bounding volume as tight as possible to the luminaire. On the other hand, such a bounding volume will surely complicate the sampling and thus reduce the advantage we may get from the bounding volume approach. We will discuss the issues of finding an appropriate bounding volume in the next section. At this moment, we can simply assume that a bounding volume with n vertices, V_1, V_2, \dots, V_n , is available.

In the projection process, we intend to approximate the solid angle subtended by the luminaire. Because the bounding volume is convex, the back-facing polygons of the constructed bounding volume will always be contained inside the final convex hull. We project each front-facing polygon onto the hemisphere, which center is located at shaded point P and the direction of normal is from P to V_c . The projected polygons can be determined straightforward since V_i^{HS} is the intersection point between the hemisphere HS and a line passing through V_i and P .

After the projected polygon is constructed, we then applied a well-known stratified sampling technique for an arbitrary spherical triangle [1]. However, any generated sample S will need to be determined if it is inside the exact area of solid angle. This

can be done in combination to determine the geometric term using ray casting, with the ray origin at P and the ray direction parallel to the normalized vector from P to S .

It is worth mentioning that we need to consider the trade-off between the vertex numbers and the tightness of the bounding volume. Since we approximate the solid angle subtended by the luminaire, whether the generated samples are effective, i.e. inside the exact area of the solid angle, will be influenced by the degree of the tightness of the bounding volume. A tighter bounding volume, e.g. a polyhedron with many vertices, will result in more effective samples. On the contrary, such a polyhedron will consist of more spherical triangles, and increase the potential overhead for the sampling. Therefore, we must reach an efficient compromise between the tightness and the vertex numbers. We present below a number of polyhedra, each of which illustrates a different efficiency compromise.

3 Bounding Volumes for Different Luminaires

In this section, we propose methods to derive bounding volumes with optimization for various luminaires. We will derive bounding volumes for ellipse, elliptic cylinder, elliptic cone and elliptic paraboloid.

3.1 Elliptic, Elliptic Cylinder and Elliptic Cone Luminaire

Ellipse: Assume an ellipse has the major-axis, a , and the minor-axis, b . We generalize a minimal and orthogonal 2^n -sided polygon as a bounding volume for an ellipse with the restriction $n \geq 3$. The X and Y coordinates of each vertices can be represented as $a * \cos((\pi/2^{n-1}) * i) / \cos(\pi/2^n)$ and $b * \sin((\pi/2^{n-1}) * i) / \cos(\pi/2^n)$ separately, where $i = 1$ to 2^n . Fig. 2a shows a bounding volume with 8 vertices.

Elliptic Cylinder: An elliptic cylinder is constructed by the major-axis, a , the minor-axis, b , in the cross section, and a height h . We can replace the top and the bottom sides of the elliptic cylinder with two equivalent polygons for an ellipse. We then connect the corresponding vertices to construct the desired bounding volume. The bounding volume with 16 vertices is shown in Fig. 2b.

Elliptic Cone: It is apparent that a cone is constructed by two major-axes, a_1 and a_2 , two minor-axes, b_1 and b_2 and height, h . Therefore, we can replace the top and bottom sides of the elliptic cone with two different polygons, connect the corresponding vertices and then get the bounding volume. The bounding volume with 16 vertices is shown in Fig. 2c.

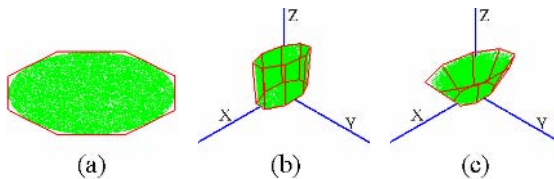


Fig. 2. Bounding volumes for (a) elliptic, (b) elliptic cylinder and (c) elliptic cone luminaires

3.2 Elliptic Paraboloidal Luminaire

Without lose of generality, we can define an elliptical paraboloid as a surface in three-dimensional space. The mathematical representation of an elliptical paraboloid can be represented as $Z/h = X^2/a^2 + Y^2/b^2$. In this equation, h is the height of the elliptical paraboloid, a is the length of the semi-major axis at $Z=h$, and b is the length of the maximal semi-minor axis at $Z=h$. The elliptic paraboloid is orthogonal in the XYZ coordinate systems. When the elliptic paraboloid is not orthogonal, we can always apply a transformation matrix containing translation and rotation vectors to produce the desired one.

For an arbitrary point $P(x, y, z)$ on an elliptic paraboloid, we can find an ellipse centered at $C'(0,0,h')$. Assume this ellipse is the orthogonal cross section of the elliptical paraboloid passing through $P(x, y, z)$. In this ellipse, we further indicate a' as the length of semi-major axis and b' as the length of semi-minor axis ($a' = a\sqrt{h'/h}$ and $b' = b\sqrt{h'/h}$). Finally, let θ be the angle between the vector $C'P$ and the unit X-axis vector. We can represent a point $P(x, y, z)$ on an elliptic paraboloid using $(w\cos\theta, w\sin\theta, h')$, where $w = ab/\sqrt{a^2\sin^2\theta + b^2\cos^2\theta}$.

We derive five types of bounding polyhedrons for the paraboloid, each with a different number of vertices but all with the minimum volume in their respective cases. We show approaches to develop these minimal bounding polyhedrons below.

8-Vertex Cuboid: The common bounding volume for a paraboloid is the 8-vertex cuboid, as shown in Fig. 3a. The volume of the paraboloid is $\pi abh/2$, while the volume of the 8-vertex cuboid is $4abh$. We define the volume ratio as the bounding volume over that of the paraboloid. The volume ratio for the 8-vertex cuboid is $8/\pi$.

8-Vertex Frustum: This bounding polyhedron is the 8-vertex frustum where the top and the bottom parts are rectangles with different lengths and widths (see Fig. 3b). The crucial issue is to determine four tangent planes around the frustum so that the resulting 8-vertex frustum has minimal volume. This can be done by considering the cross section of the paraboloid in X-Z and Y-Z plane.

12-Vertex Frustum: The third bounding polyhedron is the 12-vertex frustum where the top, the middle, and the bottom parts are rectangles with different lengths and widths. In particular, the length of the top and middle rectangles is $2a$ and the width is $2b$, while we need to derive the length and width of the bottom rectangle. Again,

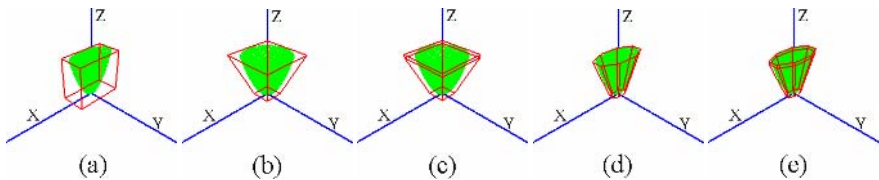


Fig. 3. Different bounding volumes for elliptic paraboloidal luminaire

the crucial issue in developing the minimal 12-vertex frustum is to determine four tangent planes around the frustum so that the resulting 12-vertex frustum has the minimal volume, as shown in Fig. 3c.

16-Vertex Frustum: The fourth bounding polyhedron is the 16-vertex frustum. This is an extension of the 8-vertex frustum where the top and the bottom parts are octagons, instead of rectangles, with different lengths and widths as shown in Fig. 3d. A 16-vertex frustum is definitely tighter than an 8-vertex frustum.

24-Vertex Frustum: The fifth bounding polyhedron is the 24-vertex frustum (see Fig. 3e). This is an extension of the 12-vertex frustum where the top, the middle, and the bottom parts are octagons, instead of rectangles, with different lengths and widths. Again, a 24-vertex frustum is definitely tighter than a 12-vertex frustum.

3.3 Summary

Tables 2 and 3 show the volume ratio. Table 2 shows the volume ratio equals one when n approaches infinity because the bounding volume is exactly the object itself. However, the volume ratio of paraboloid in Table 3 doesn't approach one unless we divide the paraboloid into many parts according to height.

Table 2. Volume ratios for a variety of bounding volumes

Object	Volume	Bounding Volume	Volume Ratio (while $n \rightarrow \infty$)
Disc(r)	πr^2	$2^n r^2 \tan(\frac{\pi}{2^n})$	1
Cylinder (r, h)	$\pi r^2 h$	$2^n r^2 \tan(\frac{\pi}{2^n})h$	
Cone (R, r, h)	$\frac{1}{3} \pi h (\frac{R^3 - Rr^2 + r^3}{R - r})$	$\frac{1}{3} 2^n \tan(\frac{\pi}{2^n})h (\frac{R^3 - Rr^2 + r^3}{R - r})$	
Ellipse (a, b)	πab	$2^n ab \tan(\frac{\pi}{2^n})$	
Elliptic Cylinder (a, b, h)	πabh	$2^n ab \tan(\frac{\pi}{2^n})h$	
Elliptic Cone (A, B, a, b, h)	$\frac{1}{3} \pi h (\frac{A^2 B - Aab + a^2 b}{A - a})$	$\frac{1}{3} 2^n \tan(\frac{\pi}{2^n})h (\frac{A^2 B - Aab + a^2 b}{A - a})$	

Table 3. Volume ratios of elliptic paraboloid for a variety of bounding volumes

Elliptic Paraboloid (a, b, h)	Bounding Volume	Volume Ratio (while $n \rightarrow \infty$)
8-Vertex Cuboid	$2^n abh \tan(\frac{\pi}{2^n})$	2
8-Vertex Frustum	$(2^n \tan(\frac{\pi}{2^n})) (\frac{2\sqrt{3} + 3}{12}) abh$	1.07735
12-Vertex Frustum	$(2^n \tan(\frac{\pi}{2^n})) (1 + \frac{8\sqrt{2}}{3} \cos \theta + 8 \cos^2 \theta - \frac{16 \cos^4 \theta}{3}) abh^*$	1.07180

*: $\theta = 17\pi / 12$

4 Results

We have implemented the proposed technique where the rendering algorithms we chose were Monte Carlo Direct Lighting (MCDL) and Monte Carlo Path Tracing (MCPT). We collected experimental results on a personal computer with a P4-1.6G MHz processor and 256 MB memory. We adopted four test scenes (Office, Room, Sball, Cornell Box) and rendered images at a resolution of 256 x 256 pixels. For simplicity, we adopted four types of luminaries in each scene, including elliptic paraboloid, elliptic cylinder, elliptic cone and ellipse. Nevertheless, our technique can also be applied to more regular shapes such as paraboloid, cylinder, cone and disc.

Fig. 4 shows images rendered with our technique in MCDL using 1 sample per pixel and 25 samples on luminaries. We also show a corresponding image using the conventional sampling method for comparison. For these comparisons, it is obvious that for equal sample numbers, our technique generates significantly better quality

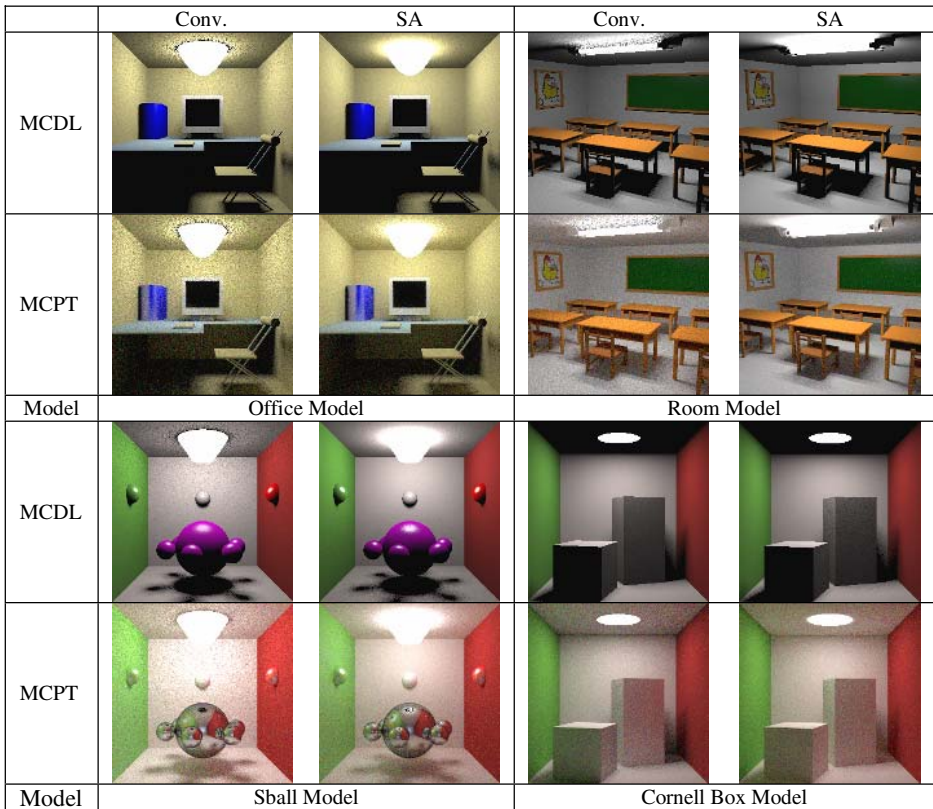


Fig. 4. A comparison of images rendered using our SA technique and the conventional method in MCDL and MCPT. All images for MCDL are generated using 1 sample per pixel and 25 samples on different types of luminaries; while all images for MCPT are generated using 25 samples per pixel and 1 sample on different types of luminaries.

pictures. A significant noise on the ceiling is shown for scenes with non-planar luminaire when using the conventional method. In contrast, noise does not appear in the images rendered with our technique. In addition, a rather obvious noise can also be visualized in the soft shadow regions when using the conventional method. In Cornell Box model, however, it is hard to detect any visual difference. This is due to the planar shape of the luminaire.

When employing our SA technique in MCPT (see Fig. 4), we utilize more samples on a pixel but fewer samples in the luminaire to avoid dispersion of the random directions in the secondary rays. Again, for these comparisons, it is obvious that for equal sample numbers, our technique generates significantly better quality pictures. A significant noise in the image is shown for scenes with non-planar luminaire when using the conventional method. In Cornell Box, the ceiling is now illuminated via the inter-reflection and thus the image is rendered with color. Nevertheless, once again, it is hard to detect any visual difference due to the planar shape of the luminaire.

Recall that our technique generates samples on the solid angle subtended by the luminaire, which is approximated by the convex spherical polygon. Thus, within the total sample number (TSN), some are fake samples (FS), which make no luminous contributions (assuming no blocked objects in the scene). Certainly, fake samples do not produce luminous contribution. Though they are generated from the convex spherical polygon, they are, in fact, not inside the precise solid angle subtended by the luminaire. We can define the efficient sample ratio (in percentage) as $ESR = 100\% \times (TSN - FS) / TSN$. Note that for a random sample, we can always cast a ray from the shaded point back to the luminaire to determine if it is a fake sample. Obviously, our technique will be more efficient if we can make the ESR as high as possible, since fake samples make no luminous contributions and cost computing time.

Table 4 compares ESR results of different luminaries for MCDL (1 sample per pixel and 25 samples per luminaire) and MCPT (4 samples per pixel and 25 samples per luminaire). For these comparisons, it is obvious that our technique (SA) produces significantly higher ESR values for the elliptic paraboloid, elliptic cylinder, and elliptic cone luminaire. The ESR values for our technique in MCDL and MCPT can be as high as 89%, compared to much smaller values (49%–65%) when using the conventional method. The relatively high ESR values explain the superiority of our technique. A particular situation occurs for the ellipse luminaire. Note that for any shaded point on the ceiling, no random samples make luminous contributions. This explains why the conventional method achieves only 85% of ESR . Obviously, the SA technique has slightly smaller values of ESR (84%) due to the approximation of solid angle.

Table 4. A comparison of efficient sample ratio between our SA technique and the conventional method

Algorithm	Elliptic Paraboloid (%)		Elliptic Cylinder (%)		Elliptic Cone (%)		Ellipse (%)	
	SA	Conv.	SA	Conv.	SA	Conv.	SA	Conv.
MCDL	89.5	63.1	89.8	49.5	90.0	57.0	84.7	85.9
MCPT	90.5	65.3	90.8	50.7	90.7	56.6	82.5	83.6

Table 5. A comparison of RMS error and execution time between our SA technique and the conventional method

	Office Model		Room Model		Sball Model		Cornell Box Model	
	SA	Conv.	SA	Conv.	SA	Conv.	SA	Conv.
MCDL	25.84	25.93	16.06	15.50	27.83	32.71	10.38	14.28
Time	142	297	1608	4073	210	420	98	155
MCPT	11.76	13.05	21.49	20.58	16.66	16.73	23.80	22.56
Time	4808	5040	4147	20604	1309	1971	768	868

For each test scene, we rendered a reference image using high sample rates. We then rendered images using our technique and the conventional method and compared the RMS errors with respect to the reference image. Table 5 presents the comparison of RMS error and execution time. For example, for MCDL in the room model, when the rendered images have similar RMS errors (around 16.0), our technique requires 1608 seconds, but the conventional method needs 4073 seconds. Compared to the conventional method, our technique is 1.58 ~ 2.53 times faster for MCDL and 1.04 ~ 4.96 times faster for MCPT. For these comparisons, it is obvious that our technique provides roughly equal image quality in less time.

5 Conclusions and Future Work

We have presented an efficient sampling technique for several kinds of curved luminaire, including disk, cylinder, cone, paraboloid, ellipse, elliptic cylinder, elliptic cone and elliptic paraboloid, and collected experimental results for Monte Carlo Direct Lighting and Monte Carlo Path Tracing applications. The basic rationale for the technique is that solid angles subtended by the luminaire can be efficiently approximated using various types of tight and tunable bounding volumes with optimization. The efficiency is due to the employment of the optimization so as to develop the bounding volumes with minimal volume. The approximated solid angle thus can be triangulated to a number of spherical triangles for sampling with high sample efficiency ratios. Experimental results indicate that the tighter the bounding volume is, the higher the efficiency ratio is. However, it doesn't mean that we can approximate the solid angle without limits. Tighter bounding volumes can get better efficiency ratios; however, the rendering time also increases when the number of vertices increases. The choice of bounding volume can be based on efficiency ratio. In our test, we choose the bounding volume where the efficiency ratio is near 90%. There may be another method to choose the bounding volume.

Urena [14] presented a cosine-weighted solid angle sampling method for a spherical triangle by an adaptive sampling approach. When using this method, the underlying variance is bounded and can be controlled to approach the minimum possible value. It might be worthwhile to investigate the potential benefits of applying the approach presented by Urena to sampling part of or all of the spherical triangles after the triangulation process. In addition, future experiments can be conducted on other applications by using other global illumination algorithms such as bi-directional path

tracing [5] or metropolis light transport [15], and by sampling other complex types of luminaries with solid angle approach such as helical or torus luminaries.

References

1. Arvo, J.: Stratified Sampling of Spherical Triangles. In: Mair, S. G. and Cook, R. (eds.): Proc. 22nd Annual Conference on Computer Graphics and Interactive Techniques (1995) 437–438
2. Heckbert, P. S.: Introduction to Global Illumination. In: Thomas, J. J. (eds.): Proc. 19th Annual Conference on Computer Graphics and Interactive Techniques (1992) Global Illumination Course
3. Kajiyaya, J. T.: The Rendering Equation. In: Evans, D. C. and Athay, R. J. (eds.): Proc. 13th Annual Conference on Computer Graphics and Interactive Techniques (1986) 143–150
4. Kolb, C., Hanrahan, P., and Mitchell, D.: A Realistic Camera Model for Computer Graphics. In: Mair, S. G. and Cook, R. (eds.): Proc. 22nd Annual Conference on Computer Graphics and Interactive Techniques (1995) 317–324
5. Lafortune, E.: Mathematical Model and Monte Carlo Algorithm for Physically based Rendering. Ph.D. thesis, Leuven University (1996)
6. Mood, A. M., Graybill, F. A. and Boes, D. C.: Introduction to the Theory of Statistics, McGraw-Hill, Singapore (1974)
7. Pattanaik, S. N. and Mudur, S. P.: Computation of Global Illumination in a Participating Medium by Monte Carlo Simulation. *The Journal of Visualization and Computer Animation* 4(3) (1993) 133–152
8. Rubinstein, R. Y.: Simulation and the Monte Carlo Method, John Wiley & Sons, New York (1981)
9. Shirley, P. and Wang, C.: Direct Lighting Calculation by Monte Carlo Integration. In: Brunt, P. and Jansen, F. W. (eds.): Proc. 2nd Eurographics Workshop on Rendering (1991) 54–59
10. Shirley, P., Wang, C. and Zimmerman, K.: Monte Carlo Techniques for Direct Lighting Calculation. *ACM Trans. Graph* 15(1) (1996) 1–36
11. Shirley, P.: Monte Carlo Methods in Rendering. In: Cunningham, S., Bransford, W. and Cohen, M. F. (eds.): Proc. 25th Annual Conference on Computer Graphics and Interactive Techniques (1998) Course Note 5: A Basic Guide to Global Illumination 9-1–9-26
12. Shreider, Y. A.: The Monte Carlo Method, Pergamon Press, New York (1996)
13. Turk, G.: Generating Random Points in Triangles. In: Glassner, A. S. (eds.) *Graphics Gems*, Academic Press, New York (1990) 24–28
14. Urena, C.: Computation of Irradiance from Triangles by Adaptive Sampling. *Comput. Graph. Forum* 19(2) (2000) 165–171
15. Veach, E. and Guibas, L. J.: Metropolis Light Transport. In: Owen, G. S., Whitted, T. and Mones-Hattal, B. (eds.): Proc. 24th Annual Conference on Computer Graphics and Interactive Techniques (1997) 65–76
16. Wang, C.: Physically Correct Direct Lighting for Distribution Ray Tracing. In: Kirk, D. (eds.) *Graphics Gems III*, Academic Press, New York (1992) 307–313
17. Wang, C.: The Direct Lighting Computation in Global Illumination Methods. Ph.D. Thesis, Indiana University (1993)
18. Zimmerman, K.: Direct Lighting Models for Ray Tracing with Cylindrical Lamps. In: Paeth, A. W. (eds.) *Graphics Gems V*, Academic Press, New York (1995) 285–289
19. Zimmerman, K.: Density Prediction for Importance Sampling in Realistic Image Synthesis. Ph.D. thesis, Indiana University (1998)

A Data Hiding Algorithm for Point-Sampled Geometry

Yu-Ming Cheng, Chung-Ming Wang, and Yuan-Yu Tsai

Institute of Computer Science, National Chung Hsing University, Taichung, 402, Taiwan
ssmtt.cym@msa.hinet.net, cmwang@cs.nchu.edu.tw,
cuckoo@cs.nchu.edu.tw

Abstract. We present a data hiding algorithm for point-sampled geometry. The basic idea is to consider every point of a model as a message point. We propose a Virtual Multi-Level Embed Procedure to embed information based on shifting the message point, the order of which is assigned by principal component analysis. We modify the message point by its virtual geometrical property, which leads to a change of the position of the orthogonal projection of the message point on the virtual base, the height of the virtual triangle, and the arc length of the virtual circle. Experimental results show that the proposed technique is efficient and secure, has high capacity and low distortion, and is robust against affine transformations. The technique has proven to be feasible in data hiding.

1 Introduction

The goal of data hiding is to conceal messages inside other, harmless messages in a way that does not allow any enemy to even detect that there is a second, secret message present [1], [2]. Whereas classical cryptography is about protecting the content of messages, data hiding, or steganography, is about concealing their very existence [1], [2], [3].

Protecting secret messages during transmission is an important issue with the development of internet technologies. In computer-based data hiding, images, audio files, documents, and even three-dimensional (3D) models may all serve as innocuous-looking hosts for secret messages. Recently, 3D models, including point-sampled geometries and 3D polygonal models, have attracted great interest since 3D hardware has become much more affordable than ever, allowing the wide use of such models [4], [5]. Unfortunately, traditional schemes of data hiding are not very well suited to 3D files. Especially in point-sampled geometries, the surface of a 3D object is only described by a set of sample points without further topological information. Preferred data hiding algorithms need to satisfy three basic requirements: security, high capacity, and low distortion. Performance is also an important trade-off attribute, especially when trying to recover hidden messages [6].

Unfortunately, research in data hiding has not kept pace with the advances of point-sampled geometries, even though some data hiding and watermarking schemes have been presented for conventional 3D polygonal models [7], [8], [9], [10]. Our proposed data hiding algorithm is inspired by the concepts proposed by [11], [12], [13],

[14]. This paper presents a high-capacity, low-distortion data hiding algorithm for point-sampled geometry which is efficient, secure, and robust against affine transformations. Because we only consider point information of point-sampled geometries, our approach is also well suited to 3D polygonal models, for which type we just discard topological information. We propose a Virtual Multi-Level Embed Procedure (VMLEP) that can embed at least three bits per point. In addition, a secret key is used on the VMLEP for more security. Experimental results show that the proposed technique is feasible in data hiding.

In next section, related work is described. In section 3, we present our algorithm. Experimental results are shown in section 4, followed by a brief conclusion in section 5.

2 Related Work

Several information hiding schemes for 3D models have been proposed either in the frequency domain or in the spatial domain. However, only a few watermarking approaches [15], [16] consider point-sampled geometry. Unfortunately, only one data hiding approach [14] for point-sampled geometry has been proposed. Due to the recent popularity of point-sampled geometry, it is important to develop appropriate data hiding algorithms that keep pace with this type of model. Since we are interested in maximizing capacity and assume no robustness requirements, we prefer to develop a technique based on a substitutive scheme in the spatial domain.

Wang and Cheng [13] proposed an efficient data hiding scheme for 3D triangle meshes. Their scheme is also a blind scheme in the spatial domain. First, they resolved the initial triangle for embedding by principal component analysis (PCA) [17]. Next, an efficient mesh traversal method was used to generate a sequence list of triangles, which will contain the hidden message. Finally, they embedded three bits per vertex for all vertices relying on three independent degrees of freedom. As a result, they exploit larger capacity in the 3D space than Cayre *et al.* [11], [12]. Their scheme is robust against translation, rotation, and scaling operations. Unfortunately, it needs a complex data structure for mesh traversal. In addition, their scheme requires information of edge connection. As a consequence, the scheme is suitable to 3D triangle meshes, but is not appropriate to point-sampled geometry. Our method, on the other hand, works in both cases. Without the help of mesh connectivity, we would need a more sophisticated method to decide the embedding sequence list. Furthermore, the embedding method must not distort the list. Consequently, we use PCA to decide the list, and we add a little advanced random noise to achieve higher capacity. Finally, embedding that relies on the angle between triangle planes is not still appropriate to point-sampled geometry, because such embedding can cause larger distortion for a larger radius. To solve this, we embed messages based on the arc length, which can efficiently avoid apparent distortion and yet still be useful for distortion control.

Research presented by Wang and Wang [14] seems to be the only source for data hiding on point-sampled geometries. Theirs also works in the spatial domain. Their scheme uses a PCA and symmetrical swap procedure (SSP). First, they directly project

every point into the first principal axis. Next, they divide the interval between n_{th} and $n+2_{th}$ points as two subsets. Finally, they embed one bit into each interval by shifting the $n+1_{th}$ point across the subinterval border of points n_{th} and $n+2_{th}$. It is robust against translation, rotation, and scaling operations. However, the data capacity in bits generally achieves only about half of the number of points in the cover models. This algorithm suffers two drawbacks in the areas of capacity and processing time. As to the first, the algorithm doesn't employ all the points of the cover models. Second, their scheme is inefficient; for example, for a model with around 35,947 points, the time required to embed data is approximately one minute. In contrast to this approach, our scheme can hide three bits per point. For a model with around 35,947 points, the time required to embed data is less than 0.7 second using our algorithm.

3 The Proposed Technique

This section describes the proposed algorithm for data hiding. Our algorithm consists of two separate procedures: an embedding procedure and an extraction procedure (see Fig. 1).

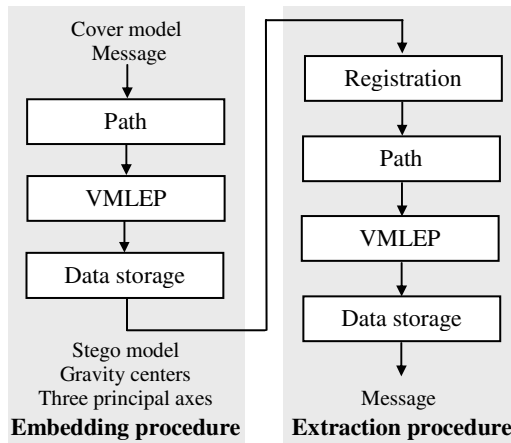


Fig. 1. An overview of the embedding and extraction procedures

3.1 Information Embedding

To embed information, we must choose a sequence list (called a *path* in the following). We adopt PCA to produce three principal axes of the 3D model. We then translate the original points' coordinate system to a new coordinate system. Obviously, the new coordinate system has a new origin, which is a gravity center of the 3D model; it also has three basis vectors, which are the three principal axes. The first principal axis is the C_{p1} -axis, the second principal axis is the C_{p2} -axis, and so on. Next, we sort points according to coordinate values of the C_{p1} -axis. For security

reasons, we employ a secret key to generate random sequence numbers for the embedding path.

Unfortunately, the problem arises when two or more points have almost the same abscissa on the C_{p1} -axis. For simplicity, we can just discard these points, without embedding a message, because the number of the discarded points is always relatively few for all points of a model. Since we do not embed a message on these points, they should not be shifted. During extraction, they should still have almost the same abscissas on the C_{p1} -axis. Consequently, we similarly discard these points, without extracting the message. In fact, we can also add advanced random noise (ARN) to these points to achieve higher capacity. To solve this problem, we advance shift these points which have almost the same abscissa on the C_{p1} -axis parallel to the direction of C_{p1} -axis depending on the ARN, which efficiently makes these points have different abscissas on the C_{p1} -axis. Finally, since the VMLEP is robust against affine transformations and it is impossible to distort the sequence list resolved by PCA, we easily maintain this path at the extracting procedure when we keep the secret key, three principal axes, and the gravity center of the cover model.

We consider every point of a model as a potential message point. To embed information in every message point, we propose a VMLEP, which includes *Sliding*, *Extending*, and *Arching*. In VMLEP, we embed the information by modifying the message point based on virtual geometrical properties; VMLEP guides the change of the position of the orthogonal projection of the message point on the virtual base, height of the virtual triangle, and arc length of the virtual circle.

First, we treat the gravity center of the cover model as a base point P_g and assume a base point P_x was extended from it; see equation 1.

$$P_x = P_g + p \times m \times \left(\frac{\overrightarrow{C_{p1}}}{|C_{p1}|} \right), \tag{1}$$

where $p \in \{-1, 1\}$ is the pseudo random number sequence (PRNS) generated from a known secret key. The m is the multiple of the unit vector of the first principal axis (C_{p1} -axis), which can resolve a virtual base. Furthermore, this m is somewhat similar to the secret key; for simplicity, we chose 0.001 as the m in the following experiments.

In the sliding level, we let every point of a cover model be a message point P_m , and assume a virtual triangle $\Delta P_g P_x P_m$. Each virtual triangle is easily treated as a two-state geometrical object. The position of the orthogonal projection of the virtual triangle summit P_m on the virtual edge $P_g P_x$ is denoted as P_s . Extending the QIM concept to triangles, the $P_g P_x$ interval is divided into two sets (B_0 and B_1), and both sets have α_s subsets. If $P_s \in B_0$, then we consider the triangle is in a “0” state; otherwise, $P_s \in B_1$, and the triangle is in a “1” state (see Fig. 2). To embed messages i ($i=0$ or 1) in the triangle, two cases occur:

- $P_s \in B_i$: No modifications are needed.
- $P_s \notin B_i$: P_m has to be shifted toward P_m' so that $P_s' \in B_i$.

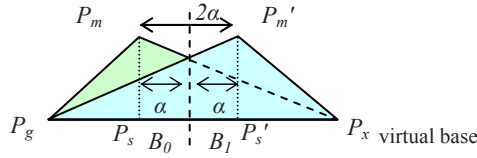


Fig. 2. Sliding level of the VMLEP

The $P_m \rightarrow P_m'$ mapping is a symmetry across the closest axis orthogonal to $P_g P_x$ that intersects the border of the closest subinterval belonging to B_i ; the shifted distance between P_m and the closest axis is denoted as α , which α conforms to equation 2:

$$\alpha \leq \frac{|P_s P_s'|}{4 \times \alpha_s} \tag{2}$$

Since we must keep the sequence list resolved by PCA after embedding procedure exactly the same as before, in the worst case two points may be shifted toward each other, which makes it possible for both points to change their order after their shift. To avoid this problem, we define the minimum distance of abscissa on the C_{pl} -axis between any two points as d and let the α_s conform to equation 3:

$$\alpha_s > \frac{|P_s P_s'|}{2 \times d} \tag{3}$$

By the way, we can certainly limit the shift distance for keep the path consistently. In addition, the $P_m \rightarrow P_m'$ mapping has to be invariant through affine transformations. We extend this partition of the virtual edge to the whole line defined by P_g and P_x . In this way, we can handle virtual triangles for which the projection of P_m falls out of the segment $P_g P_x$.

Similarly, we apply the same basic idea to the extending level and embed messages in the height of the virtual triangle $\Delta P_g P_x P_m$. First, let a point P_v and the line defined by P_v and P_x be orthogonal to line $P_g P_x$; we define the state of the virtual triangle by the position of the orthogonal projection of the virtual triangle summit P_m on the virtual edge $P_v P_x$, which position is denoted as P_e . In addition, we define β_r as the interval distance ratio and β as the interval distance. We also divide the $P_v P_x$ interval into two sets (see Fig. 3). We prefer to use the ratio of virtual base $P_g P_x$ to control movement of the message point here (see equation 4); in this way we can reverse affine transformations correctly.

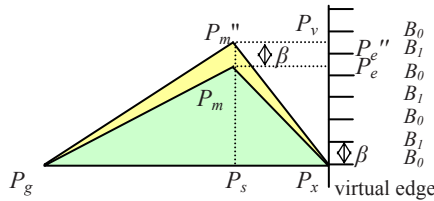


Fig. 3. Extending level of the VMLEP

$$\beta = \beta_r \times \left\lceil \frac{P_g P_x}{P_s P_x} \right\rceil \tag{4}$$

To embed messages i ($i=0$ or 1) in the virtual triangle, two cases occur:

- $P_e \in B_i$: No modifications are needed.
- $P_e \notin B_i$: P_m has to be shifted toward P_m'' so that $P_e'' \in B_i$.

This level leads to a change of the height of the virtual triangle; in other words, we can achieve this procedure by the following system of equations:

$$\begin{cases} \text{if } \left\lceil \frac{P_g P_m}{\beta} \right\rceil \bmod 2 \in B_i : \text{ No modifications are needed.} \\ \text{if } \left\lceil \frac{P_g P_m}{\beta} \right\rceil \bmod 2 \notin B_i : \overline{P_r P_m''} = \overline{P_r P_m} + p \times \beta \times \left(\frac{P_r P_m}{P_s P_m} \right), \end{cases} \tag{5}$$

where $p \in \{-1, 1\}$ is the PRNS generated from a known secret key. The shift of this level is perpendicular to the C_{p1} -axis, which should not change the abscissa on the C_{p1} -axis. Consequently, it is impossible to distort the sequence list resolved by PCA. Equally, the $P_m \rightarrow P_m''$ mapping has to be invariant through affine transformations. Finally, we apply the same concept to the arching level and embed messages in the arc length of the virtual circle. First, we assume a reference point P_r , which was simply extended from P_g by equation 6.

$$P_r = P_g + \left(\frac{\overline{C_{p2}}}{|C_{p2}|} \right) \tag{6}$$

Both virtual triangles $\Delta P_g P_x P_m$ and $\Delta P_g P_x P_r$ form two individual planes. We define the degree of the angle between the two planes as θ . Let E3 be a plane with the normal vector $\overrightarrow{P_g P_x}$ and P_m, P_s, P_m'' be the points on the same E3 plane (equation 7).

$$\overrightarrow{P_g P_x} \cdot (x - x_{P_m}, y - y_{P_m}, z - z_{P_m}) = 0 \tag{7}$$

Next, we assume that the point P_s is the center of a virtual sphere and the radius of it is $|\overrightarrow{P_g P_x}|$ (replaced by r in the following explanation). Based on the virtual sphere, we can obtain a virtual circle on the E3 plane, then an arc length resolved by the radius r and angle θ denoted as γ_d (see equation 8). In addition, we define γ_r as the arc interval length ratio, and γ_i as the arc interval length (see equation 9). For robust reasons, we use the ratio of the virtual base to control the γ_i here; in this way we can reverse affine transformations correctly. In this level, we can simply embed or extract our secret messages based on the γ_d . Using the arc length instead of the angle between virtual triangles $\Delta P_g P_x P_m$ and $\Delta P_g P_x P_r$ is more suitable for a larger radius and more useful for distortion control. Although we change the same angles, a larger radius leads to a larger distortion; in contrast, changing the same arc lengths always leads to analog distortions which are less than γ_i . We can obtain the real shift distance γ_d on this level by equation 10, where φ is the variation of angle introduced by the change of the arc length.

$$\gamma_d = 2 \times \pi \times r \times \frac{\theta}{360^\circ} \tag{8}$$

$$\gamma_i = \gamma_r \times \left\lceil \frac{P_g P_x}{P_s P_x} \right\rceil \tag{9}$$

$$\gamma_d = 2 \times r \times \cos \left(\frac{\pi - \varphi}{2} \right) \tag{10}$$

Similarly, we treat the γ_i as the interval length in this level and divide the arc length into two sets B_0 and B_1 . As a result, we can fine tune the γ_a by adding or subtracting the γ_i , which leads to the change of angle φ based on equations 7, 8, 9 and 11 (see Fig. 4 and 5).

$$\overline{P_s P_m} \cdot \overline{P_s P_m^{'''}} = |\overline{P_s P_m}| \cdot |\overline{P_s P_m^{'''}}| \cos \varphi = r^2 \cos \varphi, \text{ where } r = |\overline{P_s P_m}| = |\overline{P_s P_m^{'''}}| \quad (11)$$

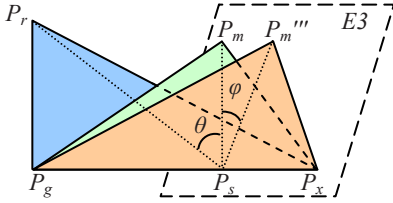


Fig. 4. Arching level of the VMLEP

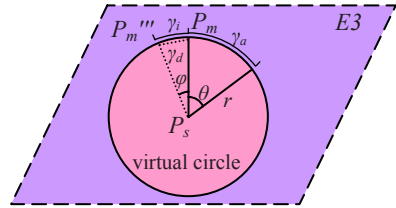


Fig. 5. Virtual circle used on arching level

To embed messages i ($i=0$ or 1) in the virtual circle, two cases occur:

$$\begin{cases} \text{if } \left\lfloor \frac{\gamma_a}{\gamma_i} \right\rfloor \bmod 2 \in B_i : \text{ No modifications are needed.} \\ \text{if } \left\lfloor \frac{\gamma_a}{\gamma_i} \right\rfloor \bmod 2 \notin B_i : \varphi = \left(\frac{360^\circ \times (\gamma_a + p \times \gamma_i)}{2 \times \pi \times r} \right) - \theta, \end{cases} \quad (12)$$

where $p \in \{-1, 1\}$ is the PRNS generated from a known secret key. For the path, the shift of this level is a circle round the C_{pI} -axis, which should not change the abscissa on the C_{pI} -axis. Consequently, it is also impossible to distort the sequence list resolved by PCA. Equally, the $P_m \rightarrow P_m'''$ mapping has to be invariant through affine transformations.

In fact, every method of these levels is not limited to embedding one bit per point. These methods really can partition more delicately to get a larger capacity; the real limitation is data representation precision. For instance, in the sliding level, when we divide the $P_g P_x$ interval into 2^s ($s \geq 1$) sets, we can embed s bits into each set.

Finally, the stego model is created. In addition, we keep three principal axes and the gravity center of the cover model to establish the same path during the extraction procedure. Furthermore, three principal axes and the gravity center of the stego model are retained to align the potentially attacked stego model during the registration process.

The VMLEP algorithm was developed to decrease distortion and increase capacity with respect to the human visual system (HVS). Considering distortion, the message point will be shifted toward the diagonal point in a box in the worst case.

3.2 Information Extracting

In order to guard against affine transformations and be able to extract the message correctly, the potentially attacked stego model and the original stego model have to be

aligned by a registration process. The new three principal axes and the gravity center of the potentially attacked stego model and the three principal axes and the gravity center of the original stego model have to be aligned using PCA, which leads to some affine transformations, i.e. translation, rotation, and scaling. After that, it produces the un-attacked stego model, which is the same as the original. In other words, if we suppose the stego model would not be attacked, we can just pass this processing step and not even keep the three principal axes and the gravity center of the original stego model anymore.

Since the remaining procedures of the algorithm are symmetrical, we easily extract the message using the method mentioned above if we have the help of the secret key, three principal axes, and the gravity center of the cover model.

4 Experimental Results

We implemented the proposed technique using C++ programming language. Results were collected on a personal computer with a Pentium IV 2GHz processor and 512 MB memory. The analyses of our steganographic system are based on the following four goals: increased capacity, invisibility, security, and complexity.

We assume no robustness requirements, except basic operations such as affine transformations. For simplicity, we hide three bits per point. Nevertheless, it is possible to hide more than three bits per point, which depends on the data representation precision.

Model details, distortion, and processing time are detailed in Tables 1 and 2. In a still image, a simple measure is used for distortion: the signal-to-noise ratio (SNR). This measure is dedicated to regularly sampled signals, which is not the case with 3D models. Some proposals have been made for 3D polygonal models based on the

Table 1. Results of point-sampled geometries, we chose 32 as the α_s , 0.01 as the β_r , and 0.02 as the γ_r

cover model	points	embedded messages (bits)	Distortion		time cost (sec)	
			RMS / bounding diagonal		embed	extract
teeth	116,604	349,812	5.427×10^{-5}		2.219	1.375
rabbit	67,038	201,114	5.902×10^{-5}		1.296	0.812
horse	48,485	145,455	1.957×10^{-5}		0.937	0.578
bunny	35,947	107,841	1.992×10^{-5}		0.688	0.437

Table 2. Results of 3D polygonal models, we chose 32 as the α_s , 0.01 as the β_r , and 0.02 as the γ_r

cover model	vertices	faces	embedded messages (bits)	Distortion		time cost (sec)	
				RMS / bounding diagonal		embed	extract
dragon	437,645	871,414	1,312,935	1.890×10^{-6}		8.344	5.234
venus head	134,345	268,686	403,035	3.201×10^{-5}		2.578	1.610
dinosaur	56,194	112,384	168,582	3.200×10^{-5}		1.079	0.672
rocker arm	40,177	80,354	120,531	5.482×10^{-5}		0.797	0.485

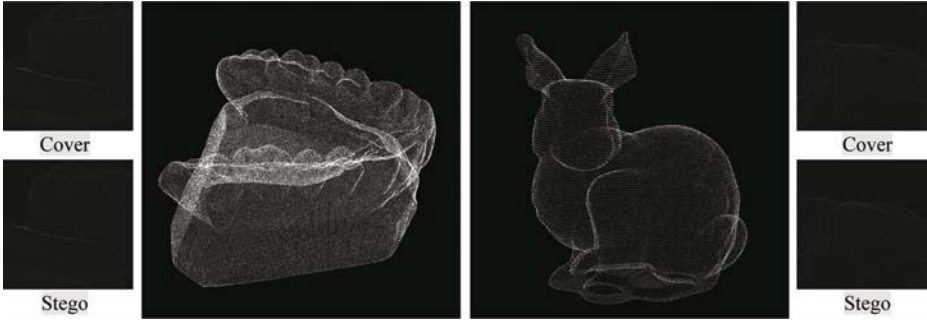


Fig. 6. From left to right, stego point-sampled geometries are listed in the following order: teeth and bunny. For a better comparison, we also show the close-up views.

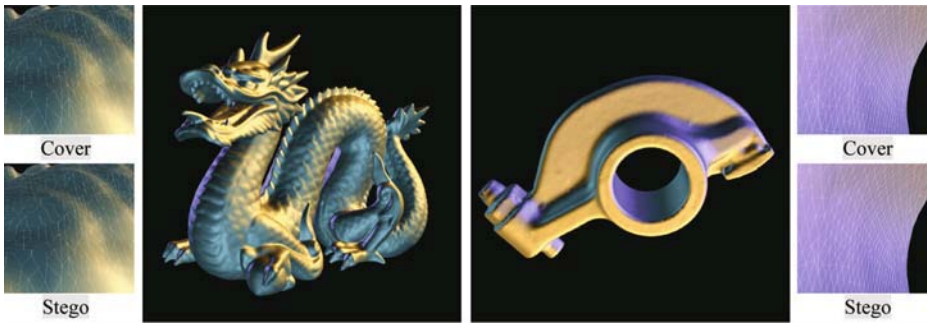


Fig. 7. From left to right, stego polygonal models are listed in the following order: dragon and rocker arm. For a better comparison, we also show the close-up views.

Hausdorff distance to handle meshes with different topologies. Since our scheme does not change the topology of 3D polygonal models, we use an estimation of the root mean square (RMS) to evaluate the distortion induced by the embedding process. Tables 1 and 2 demonstrate that our approach works well in 3D models. As expected, no errors are found in the recovered messages. The RMS values are small, indicating little distortion in quality for the stego models. As a result, we exploit the feature of 3D more: every point of a 3D model can be treated as a message point, and it can be represented by at least three bits in the three dimension space, which means the filling rate of our method approximates 300%. Visual results of the stego models are shown in Figures 6 and 7. The RMS values and visual appearance of images showed insignificant distortion for the models.

From the security point of view, finding the three principal axes and the gravity center of the cover model, getting the path over the model with secret key, and obtaining the p value of PRNS, m , α_s , β_r and γ_r are the challenges for an attacker. Just by looking at these issues, it is clear that our scheme is secure in the cryptographic sense. It is resistant against exhaustive search. Retrieving the message without the key is virtually impossible. This problem is NP-hard with respect to the number of points in

the model. Moreover, we embed the message in an undeterministic way, which makes any steganalysis difficult [18].

Finally, we estimate the complexity of our algorithm by giving execution times for various models, as shown in Tables 1 and 2. Clearly, the time cost is very low, despite the embedding and extracting processes. To create a path by our scheme only needs a little setup time to construct the three principal axes of the 3D model resolved by PCA. We can then sort points according to coordinate values of the C_{p1} -axis and generate random sequence numbers for the path by a secret key, which can improve security well. In sum, every message point sequence processed by VMLEP depends on the path. As a result, the processing time of our method increases linearly with message length.

5 Conclusion and Future Work

In this paper we have presented a data hiding algorithm for point-sampled geometry. Our technique provides data hiding with efficiency, security, high capacity, low distortion, and robustness against affine transformations. Because we just consider the point information of point-sampled geometry, our approach is well suited to point-sampled geometries and 3D polygonal models, for which type we discard topological information.

Our scheme is fast; for a model with around 48,485 points, the time required to embed data is less than one second, and it takes less than nine seconds even if the model has around 437,645 points. We believe that extracting the messages without assistance of the key is virtually impossible. This problem is NP-hard in the cryptographic sense. Since our VMLEP shifts message points with respect to the HVS, this process naturally leads to higher capacity and lower distortion. We have demonstrated the feasibility of our technique for steganographic applications.

Even though our approach already delivers good results, some further improvements are conceivable. The main limitation of this approach is machine precision errors when considering small models. Since the definitive capacity limit is reached when these errors occur, one could use other approaches to divide intervals or even use different approaches and rules to decide intervals for increased capacity or to avoid such errors. Another kind of improvement is to investigate how to preserve the quality of 3D models when embedding the message. It is also worth exploring the characteristics of the HVS in order to decrease visual degradation. Finally, future research has to further explore and analyze the relationship between message length, visual effect, and the resulting robustness.

References

1. Johnson, N. F., Jajodia, S.: Exploring Steganography: Seeing the Unseen. *IEEE Computer*, vol. 31, no. 2 (1998) 26-34
2. Petitcolas, F. A. P., Anderson, R. J., Kuhn, M. G.: Information Hiding - A Survey. in *Proc. IEEE Special Issue on Protection of Multimedia Content*, vol. 87, no. 7 (1999) 1062-1078

3. Katzenbeisser, S., Petitcolas, F.A.P.: *Information Hiding Techniques for Steganography and Digital Watermarking*. London: Artech House (2000)
4. Pauly, M., Keiser, R., Gross, M.: Multi-Scale Feature Extraction on Point-Sampled Surfaces. *Computer Graphics Forum*, vol. 22, no. 3 (2003) 281-289
5. Kobbelt L., Botsch, M.: A Survey of Point-Based Techniques in Computer Graphics. *Computers & Graphics*, vol. 28, no. 6 (2004) 801-814
6. Bayer P., Widenfors, H.: *Information Hiding - Steganographic Content in Streaming Media*. M.S. thesis, Deptment of Software Engineering and Computer Science, Blekinge Institute of Technology, Sweden (2002)
7. Ohbuchi, R., Masuda, H., Aono, M.: Watermarking Three-Dimensional Polygonal Models Through Geometric and Topological Modifications. *IEEE Journal on Selected Areas in Communications*, vol. 16, no. 4 (1998) 551-560
8. Praun, E., Hoppe, H., Finkelstein, A.: Robust mesh watermarking. in *Proc. SIGGRAPH* (1999) 49-56
9. Ohbuchi, R., Takahashi, S., Miyasawa, T., Mukaiyama, A.: Watermarking 3D Polygonal Meshes in the Mesh Spectral Domain. in *Proc. Graphics Interface* (2001) 9-17
10. Ohbuchi, R., Mukaiyama, A., Takahashi, S.: A Frequency-Domain Approach to Watermarking 3D Shapes. *Computer Graphics Forum*, vol. 21, no. 3 (2002) 373-382
11. Cayre, F., Macq, B.: Data Hiding on 3-D Triangle Meshes. *IEEE Trans. Signal Processing*, vol. 51, no. 4 (2003) 939-949
12. Cayre, F., Devillers, O., Schmitt, F., Maitre, H.: *Watermarking 3D Triangle Meshes for Authentication and Integrity*. Rapport de recherche 5223, INRIA (2004)
13. Wang, C. M., Cheng, Y. M.: An Efficient Information Hiding Algorithm for Polygon Models. *Computer Graphics Forum*, vol. 24, no. 3 (2005) 591-600
14. Wang, C. M., Wang, P. C.: Data Hiding Approach for Point-Sampled Geometry. *IEICE Transactions on Communications* E88-B, 1 (2005) 190-194
15. Cotting, D., Weyrich, T., Pauly, M., Gross, M.: Robust Watermarking of Point-Sampled Geometry. in *Proc. International Conference on Shape Modeling and Applications* (2004) 233-242
16. Ohbuchi, R., Mukaiyama, A., Takahashi, S.: Watermarking a 3D Shape Model Defined as a Point Set. In *Proc. of International Conference on Cyberwords* (2004) 392-399
17. Rencher, A.C.: *Methods of Multivariate Analysis*. 2nd ed. New York: Wiley (2002)
18. Cachin, C.: An Information-Theoretic Model for Steganography. In *Proc. of 2nd Information Hiding Workshop* (1998) 306-318

An Algorithm for Rendering Vertexes and Edges of Polyhedron with High Order Geometric Continuity

Xiaolin Lu

School of Information Technology, Zhejiang University of Finance & Economics,
Hangzhou 310012, China
luxiaolin@mail.hz.zj.cn

Abstract. The surface rendering for simultaneously connecting with several neighboring surfaces with high order geometric continuous is quite complicated in the computer graphics and CAGD. This paper proposed a new simple geometric algorithm for generating and rendering the smooth connecting surfaces for the vertexes and edges of the polyhedron. The rectangular Bézier surfaces are generated to connect the two adjacent planes, and the triangular Bézier surfaces are generated to connect its several neighboring surfaces with high order geometric continuity. The control net points of the connecting surfaces are calculated by the geometric drawing method according to the geometric continuity connection condition or the share common plane condition. All the surfaces and planes can be connected smoothly with G^2 geometry continuity in the polyhedron. The algorithm can be popularized to the situation of higher order geometric continuous connection easily.

1 Introduction

The connecting surface generating and rendering with high order geometric continuity is one of the most important contents in the computer graphics and the computer aided geometric design [1-6]. The traditional method for rendering the vertexes and edges of the polyhedron is the applying the circular cylindrical and spherical surfaces to polish and render the vertex and edges. However, it does not possess the property of geometric continuity. Another method is applying the Bézier surfaces to construct the smooth connection surfaces with the geometric continuity. Frequently, the algorithm for connecting surface rendering with the high order geometry continuous is very complicated [7,8]. The situation will be more complicated if the generated connecting surface must be simultaneously connected with several neighboring surfaces. For example, in order to polishing the vertexes of the cube, the smooth connecting surface is needed to connecting six neighboring surfaces in the same time.

In this paper, we present a new algorithm for generating and rendering the smooth connecting surfaces for the vertexes and edges of the polyhedron. We used the rectangular Bézier surface to connect the two adjacent planes, and then we used the triangular Bézier surface to connect its several neighboring surfaces with high order geometric continuity. The generated connecting surfaces are generated by the geometric drawing method based on the geometry continuity theorems. Therefore, the connecting surface

rendering for the vertexes and edges of the polyhedron with the high order geometry continuous become easily implemented in the CAD/CAGD systems.

2 Related Geometry Continuity Connection Theorems

Geometry continuity definition: Let $\Omega \subset R^2$ be a single bordered connected domain, it claims that two regular surfaces: $R = R(u, v) \in C^k(\Omega)$ and $R'(u', v') \in C^k(\Omega)$ are k order geometry continuity (G^k) at the common border CB, if there exist a formal parameter transforms [7,8]:

$$\begin{cases} u = u(s, t) \\ v = v(s, t) \end{cases} \quad \text{and} \quad \begin{cases} u' = u'(s, t) \\ v' = v'(s, t) \end{cases} \tag{1}$$

To make all the partial derivative that does not great than k is equal at the place of CB.:

$$\frac{\partial^{i+j} R(u(s,t), v(s,t))}{\partial s^i \partial t^j} \Big|_{(s,t) \in CB} = \frac{\partial^{i+j} R'(u'(s,t), v'(s,t))}{\partial s^i \partial t^j} \Big|_{(s,t) \in CB} \tag{2}$$

$0 \leq i+j \leq k.$

Theorem 1: Let two formal surfaces $R = (u, v)$, and $R' = (u', v')$, satisfy following condition at CB:

$$R = (0, v) = R'(0, v'), v = v'$$

The necessary and sufficient condition of G^k of S_0, S_1 is existed k order formal parameter transform:

$$\begin{cases} u' = u'(u, v) \\ v' = v'(u, v) \end{cases} \quad \text{and} \quad \begin{cases} u'(0, v) = 0 \\ v'(0, v) = v \end{cases}$$

To make:

$$\frac{\partial^{i+j} R(u,v)}{\partial u^i \partial v^j} \Big|_{u=0} = \frac{\partial^{i+j} R'(u'(u,v), v'(u,v))}{\partial u^i \partial v^j} \Big|_{u=0} \tag{3}$$

where $0 \leq i+j \leq k.$

Theorem 2: The necessary and sufficient condition of G^k for S_1, S_2 at the common border CB is that there existed a k order derivative formal parameter transform:

$$\begin{cases} u' = u'(u, v) \\ v' = v'(u, v) \end{cases} \quad \text{and} \quad \begin{cases} u'(0, v) = 0 \\ v'(0, v) = v \end{cases}$$

To make:

$$\frac{\partial^l R(u,v)}{\partial u^l} \Big|_{u=0} = \frac{\partial^{i+j} R'(u'(u,v), v'(u,v))}{\partial u^i \partial v^j} \Big|_{u=0} \tag{4}$$

$l=i+j; l = 0, \dots, k; v \in [0, 1]$

Theorem 3: The necessary and sufficient condition of Gk for S0,S1a at the common border CB is that there existed k order smooth $\{ \pi_i(v), q_i(v); i, j = 1, \dots, k \}$, where $p_i \neq 0$, to make:

$$\left. \frac{\partial^l R(u,v)}{\partial u^l} \right|_{u=0} = \frac{\partial^l}{\partial u^l} R' \left(\sum_{s=1}^l \frac{1}{s!} p_s(v) u^s, v + \sum_{s=1}^l \frac{1}{s!} q_s(v) u^s \right) \Big|_{u=0} \tag{5}$$

$l = 0, \dots, k; v \in [0, 1]$

From the theorem 1 to 3, we could deduce the special cases of the necessary and sufficient condition for G^0 to G^2 geometry continuity connection:

$$R'(0, v) = R(0, v) \tag{6}$$

$$\frac{\partial R'(0, v)}{\partial u'} = p_1 \frac{\partial R(0, v)}{\partial u} + q_1 \frac{\partial R(0, v)}{\partial v} \tag{7}$$

$$\begin{aligned} \frac{\partial^2 R'(0, v)}{\partial u'^2} &= p_1^2 \frac{\partial^2 R(0, v)}{\partial u^2} + 2 p_1 q_1 \frac{\partial^2 R(0, v)}{\partial u \partial v} + q_1^2 \frac{\partial^2 R(0, v)}{\partial v^2} \\ &+ p_2 \frac{\partial R(0, v)}{\partial u} + q_2 \frac{\partial R(0, v)}{\partial v} \end{aligned} \tag{8}$$

Rational triangle Bézier surface definition: In the affined coordinate space E^3 , n order rational triangular Bézier surface can be expressed as [9]:

$$B_n(u, v, w) = \frac{Q_n(u, v, w)}{\omega_n(u, v, w)} \tag{9}$$

Where:

$$Q_n(u, v, w) = \sum_{i+j+k=n} Q_{i,j,k} \omega_{i,j,k} B_{i,j,k}^n(u, v, w) \tag{10}$$

$$\omega_n(u, v, w) = \sum_{i+j+k=n} \omega_{i,j,k} B_{i,j,k}^n(u, v, w) \tag{11}$$

$$B_{i,j,k}^n(u, v, w) = \frac{n!}{i!j!k!} u^i v^j w^k \tag{12}$$

Let two rational triangular Bézier surfaces B^0 and B^1 as:

$$B^0 = B^0(u_0, v_0, w_0) = \frac{Q^{(0)}(u_0, v_0, w_0)}{\omega^{(0)}(u_0, v_0, w_0)} \tag{13}$$

$$B^1 = B^1(u_1, v_1, w_1) = \frac{Q^{(1)}(u_1, v_1, w_1)}{\omega^{(1)}(u_1, v_1, w_1)} \tag{14}$$

Where:

$$Q_{0,j,k}^{(0)} = Q_{0,j,k}^{(1)} \quad \forall j+k=n \tag{15}$$

$$Q^{(0)}(u_0, v_0, w_0) = \sum_{i+j+k=n} Q_{i,j,k}^{(0)} \omega_{i,j,k}^{(0)} B_{i,j,k}^n(u_0, v_0, w_0)$$

$$\begin{aligned} \omega^{(0)}(u_0, v_0, w_0) &= \sum_{i+j+k=n} \omega_{i,j,k}^{(0)} B_{i,j,k}^n(u_0, v_0, w_0) \\ Q^{(1)}(u_1, v_1, w_1) &= \sum_{i+j+k=n} Q_{i,j,k}^{(1)} \omega_{i,j,k}^{(1)} B_{i,j,k}^n(u_1, v_1, w_1) \\ \omega^{(1)}(u_1, v_1, w_1) &= \sum_{i+j+k=n} \omega_{i,j,k}^{(1)} B_{i,j,k}^n(u_1, v_1, w_1) \end{aligned}$$

G^0 connecting condition: if

$$B^{(0)}(0, v_0, w_0) = B^{(1)}(0, v_1, w_1) \Big|_{v_1=v_0} \tag{16}$$

It is called that B^0 and B^1 is G^0 continuity along their common border $u = 0$.

Let $t = v_0 = v_1$, then $w_0 = w_1 = (1 - t)$, equation (16)become:

$$B^{(0)}(0, t, 1 - t) = B^{(1)}(0, t, 1 - t) \tag{17}$$

from equation (13)and equation (14), we can get:

$$\frac{\sum_{j+k=n} Q_{i,j,k}^{(0)} \omega_{i,j,k}^{(0)} B_{i,j,k}^n(u_0, v_0, w_0)}{\sum_{j+k=n} \omega_{i,j,k}^{(0)} B_{i,j,k}^n(u_0, v_0, w_0)} = \frac{\sum_{j+k=n} Q_{i,j,k}^{(1)} \omega_{i,j,k}^{(1)} B_{i,j,k}^n(u_0, v_0, w_0)}{\sum_{j+k=n} \omega_{i,j,k}^{(1)} B_{i,j,k}^n(u_0, v_0, w_0)} \tag{18}$$

Let:

$$\begin{cases} Q_{0,j,k}^{(0)} = Q_{0,j,k}^{(1)} \\ \omega_{0,j,k}^{(0)} = \omega_{0,j,k}^{(1)} \end{cases} \quad \forall j+k=n \tag{19}$$

The equation (19)is the connection condition of G^0 for two rational Bézier surfaces B^0 and B^1 .The connection condition of G^1 :

$$\text{let } \vec{Z} = P_1 - P_0, \vec{a} = P'_2 - P'_1, \vec{b} = P'_0 - P'_1$$

from equation(9), the connection condition of G^1 for two rational Bézier surface:

(1) G^0 : same as (19)

$$(2)G^1: D_{\vec{Z}}B^{(0)}(0, t, 1 - t) = p_1(t)D_{\vec{a}}B^{(1)}(0, t, 1 - t) + q_1(t)D_{\vec{b}}B^{(1)}(0, t, 1 - t) \tag{20}$$

From the directional derivative equation (3)and (6), then the two sides of equation (20) become:

$$\begin{aligned} \text{Left} &= \frac{n}{\Omega} [\sum_{i+j+k=n-1} (E_1 - E_0) Q_{i,j,k}^{(0)} \omega_{i,j,k}^{(0)} B_{i,j,k}^{n-1}(0, t, 1 - t) \\ &\quad - C \sum_{i+j+k=n-1} (E_1 - E_0) \omega_{i,j,k}^{(0)} B_{i,j,k}^{n-1}(0, t, 1 - t)] \\ \text{Right} &= \frac{n}{\Omega} [\sum_{i+j+k=n-1} p_1(t)(E_2 - E_1) Q_{i,j,k}^{(1)} \omega_{i,j,k}^{(1)} B_{i,j,k}^{n-1}(0, t, 1 - t) \\ &\quad - C \sum_{i+j+k=n-1} p_1(t)(E_2 - E_1) \omega_{i,j,k}^{(1)} B_{i,j,k}^{n-1}(0, t, 1 - t) \\ &\quad + \sum_{i+j+k=n-1} q_1(t)(E_0 - E_1) Q_{i,j,k}^{(1)} \omega_{i,j,k}^{(1)} B_{i,j,k}^{n-1}(0, t, 1 - t) \\ &\quad - C \sum_{i+j+k=n-1} q_1(t)(E_0 - E_1) \omega_{i,j,k}^{(1)} B_{i,j,k}^{n-1}(0, t, 1 - t)] \end{aligned}$$

where:

$$\begin{cases} C = C(t) = Q^{(0)}(0, t, 1 - t) = Q^{(1)}(0, t, 1 - t) \\ \Omega = \Omega(t) = \omega^{(0)}(0, t, 1 - t) = \omega^{(1)}(0, t, 1 - t) \end{cases} \tag{21}$$

Let $p_1(t) = \alpha, q_1(t) = \lambda$ that:

$$\begin{aligned} Left &= \frac{n}{\Omega} \left[\sum_{i+j+k=n-1} (E_1 - E_0) Q_{i,j,k}^{(0)} \omega_{i,j,k}^{(0)} B_{i,j,k}^{n-1}(0, t, 1-t) \right. \\ &\quad \left. - C \sum_{i+j+k=n-1} (E_1 - E_0) \omega_{i,j,k}^{(0)} B_{i,j,k}^{n-1}(0, t, 1-t) \right] \\ Right &= \frac{n}{\Omega} \left[\sum_{i+j+k=n-1} \alpha (E_2 - E_1) Q_{i,j,k}^{(1)} \omega_{i,j,k}^{(1)} B_{i,j,k}^{n-1}(0, t, 1-t) \right. \\ &\quad - C \sum_{i+j+k=n-1} \alpha (E_2 - E_1) \omega_{i,j,k}^{(1)} B_{i,j,k}^{n-1}(0, t, 1-t) \\ &\quad + \sum_{i+j+k=n-1} \lambda (E_0 - E_1) Q_{i,j,k}^{(1)} \omega_{i,j,k}^{(1)} B_{i,j,k}^{n-1}(0, t, 1-t) \\ &\quad \left. - C \sum_{i+j+k=n-1} \lambda (E_0 - E_1) \omega_{i,j,k}^{(1)} B_{i,j,k}^{n-1}(0, t, 1-t) \right] \end{aligned}$$

Therefore:

$$(E_1 - E_0) Q_{i,j,k}^{(0)} \omega_{i,j,k}^{(0)} = \alpha (E_2 - E_1) Q_{i,j,k}^{(1)} \omega_{i,j,k}^{(1)} + \lambda (E_0 - E_1) Q_{i,j,k}^{(1)} \omega_{i,j,k}^{(1)} \tag{22}$$

$$(E_1 - E_0) \omega_{i,j,k}^{(0)} = \alpha (E_2 - E_1) \omega_{i,j,k}^{(1)} + \lambda (E_0 - E_1) \omega_{i,j,k}^{(1)} \tag{23}$$

We can get:

$$\begin{cases} Q_{1,j,k}^{(0)} = \frac{Q_{0,j+1,k}^{(1)} - \alpha e_{j,k} - \lambda e'_{j,k}}{\omega_{1,j,k}^{(0)}} \\ \omega_{1,j,k}^{(0)} = \omega_{0,j+1,k}^{(1)} - \alpha \Delta \omega_{j,k} - \lambda \Delta \omega'_{j,k} \end{cases} \tag{24}$$

Where:

$$\begin{cases} e_{j,k} = Q_{0,j,k+1}^{(1)} \omega_{0,j,k+1}^{(1)} - Q_{0,j+1,k}^{(1)} \omega_{0,j+1,k}^{(1)} \\ e'_{j,k} = Q_{1,j,k}^{(1)} \omega_{1,j,k+1}^{(1)} - Q_{0,j+1,k}^{(1)} \omega_{0,j+1,k}^{(1)} \\ \Delta \omega_{j,k} = \omega_{0,j,k+1}^{(1)} - \omega_{0,j+1,k}^{(1)} \\ \Delta \omega'_{j,k} = \omega_{1,j,k+1}^{(1)} - \omega_{0,j+1,k}^{(1)} \end{cases} \tag{25}$$

G¹ Connection Judgment Condition (share common plane condition): The necessary and sufficient condition of G¹ for two rational triangular Bézier surfaces B⁰ and B¹ is that:

$$\forall j + k = n - 1 \text{ make } [D_z B^{(0)}(0, t, 1 \uparrow t), D_a B^{(1)}(0, t, 1 \uparrow t), D_b B^{(1)}(0, t, 1 \uparrow t)]$$

share a common plane [7,8].

Figure 1 shows the G¹ connection judgment condition. The left picture shows that the two rational Bézier surfaces control triangular along the common border. The

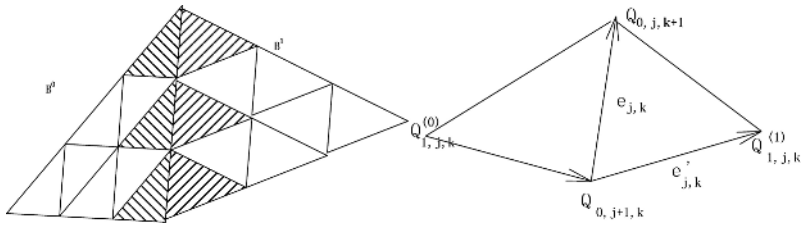


Fig. 1. The G^1 connection judgment condition: the neighboring two Bézier control triangular share the common plane along the common border

right picture shows a single cell vector relationship in G^1 connection between two triangular.

In the same way, we can deduce the G^2 and higher order geometry continuity connection condition between two rectangular Bézier surfaces.

3 Algorithm for Rendering Vertexes and Edges of Polyhedron

To polish the vertexes and edges of a polyhedron, the rectangle and triangle Bézier surfaces can be used as the connecting surfaces to render the smooth joining vertex and edges in the polyhedrons. For example, in the case of polishing the vertexes and the edges of a cube, the rectangular Bézier surface can be used to connecting the two adjacent planes smoothly and the triangular Bézier surface can be used to connect the three planes and three Bézier surfaces smoothly. All the surfaces and planes can be connection smoothly with high order geometry continuity as it shows in the figure 2.

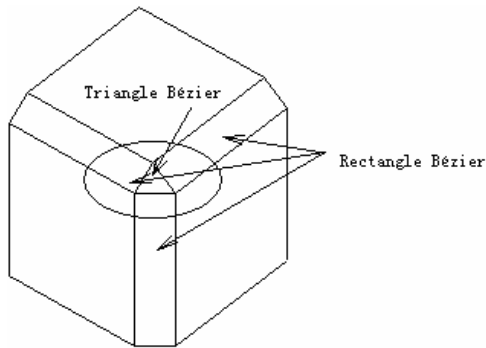


Fig. 2. Rendering the vertexes and edges of a cube by polishing by Bézier surfaces

From the theory and geometry meaning of the continuity connection conditions described in above section, the geometric meaning of the G^1 geometry continuity is that planes constructed by the first layer of the Bézier control net must be shared the same plane with its connected surfaces. The meaning of the G^2 geometry continuity is that the planes constructed by the first and second layer of the Bézier control net must be

shared the same plane with related connected surfaces. Therefore, we can draw out the control points from the shared planes conditions with simple calculation.

3.1 The Algorithm for Rendering the Vertexes and Edges with G^1 Geometry Continuity

Figure 3 shows the Bézier control net relationship to render the polyhedron vertex by three rectangular surfaces one triangular Bézier surfaces. The a, b, c are three planes of the cube. The e, f, g are three rectangular Bézier surfaces. They are used to construct the connecting surface between a and b, b and c, a and c respectively. The k is a triangular Bézier surface, which is used to construct a surface to connect all the planes and surfaces of a, b, c, e, f, g . The generated Bézier surfaces are connected with G^1 geometry continuity.

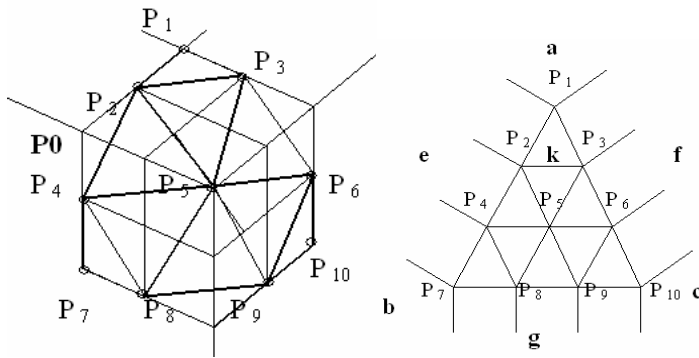


Fig. 3. Bézier control net relationship with G^1 connection in rendering vertexes and edges for the polyhedron connecting surface

G^1 Algorithm

- Step 1: The rectangular Bézier surface can be used to connecting the two adjacent planes smoothly.
- Step 2: Establishing the common border of the connecting surfaces: The parallel lines of the polyhedron edges are assumed as the common borders between e, f, g and a, b, c . The control net points P_1, P_7, P_{10} are used as the control net points of the triangular Bézier surfaces k .
- Step 3: Calculating the control net point of the rectangular Bézier surfaces e, f, g : Based on the G^1 connecting condition described in above section. For examples, we can calculate the control points $P_2, P_3, P_4, P_6, P_8, P_9$, by $P_2 = (P_1 + P_0)/2$; $P_4 = (P_7 + P_0)/2$. P_2 is the center point between P_1 and P_0 and P_0 is a point at the edges of the cube as shown in figure 3.
- Step 4: Calculating other the control net points of the triangular Bézier k : The $P_5 = (P_2 + P_3 + P_4 + P_6 + P_8 + P_9) / 6$, that is, P_5 is the center of the points. All the surfaces and planes can be connection smoothly with high order geometry continuity.

3.2 The Algorithm for Rendering the Vertexes and Edges with G^2 Geometry Continuity

In the same way, we present the algorithm for rendering the vertexes and edges with G^2 geometry continuity. Figure 4 shows the Bézier control net relationship to render the polyhedron vertex by three rectangular surfaces and one triangular Bézier surfaces. In the figure 4, the b, c are three planes of the cube. The e, f, g are three of four order rectangular Bézier surfaces. They are used to construct the connecting surface between a and b, b and c, a and c respectively. The k is a four order triangular Bézier surface, which is used to construct a surface to connect all the planes and surfaces of a, b, c, e, f, g . the generated Bézier surfaces are connected with G^2 geometry continuity.

G^2 Algorithm

- Step 1: The rectangular Bézier surface can be used to connecting the two adjacent planes smoothly.
- Step 2: Establishing the common borers of the connecting surfaces: The parallel lines of the edges are assumed as the common border between e, f, g and a, b, c . We can establish the control net points P_1, P_7, P_{10} of the triangular Bézier surfaces k .
- Step 3: Calculating the control net points of the rectangular Bézier surfaces e, f, g : Based on the G^1 connecting condition described in above section. We can calculate the control points $P_2, P_3, P_7, P_{10}, P_{12}, P_{14}$, by $P_2 = (P_1 + P_0)/2$; $P_7 = (P_{11} + P_0)/2$, that is P_2 is the center point between P_1 and P_0 . P_0 is a point at the edges of the cube.
- Step 4: Calculating the control net points P_4, P_6, P_{13} of the rectangular Bézier surfaces e, f, g by $P_4 = (P_2 + P_7)/2$ etc. that is P_4 is the center point between P_1 and P_2 . In the same way, we can get the P_6, P_{13} .
- Step 5: Calculating other the control net points P_5, P_8, P_9 of the triangular Bézier k : The $P_5 = (P_2 + P_3 - P_3)$. In the same way, we can get the P_8, P_9 . All the surfaces and planes can be connection smoothly with G^2 order geometry continuity.

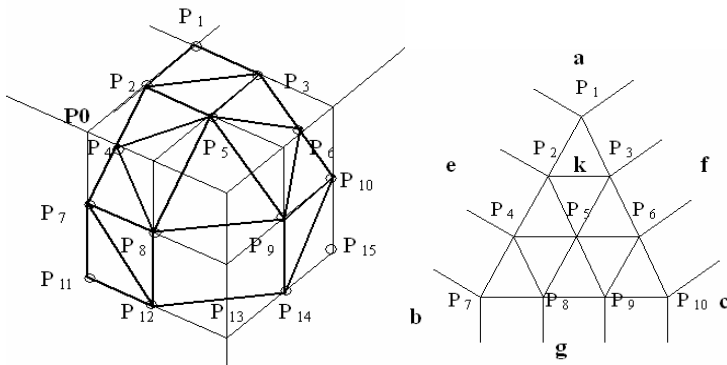


Fig. 4. Bézier control net relationship with G^2 connection in polyhedron vertex connecting surface rendering

In the similar way, we can construct the connection surfaces with G^3 and higher geometry continuity with five orders Bézier surface for rendering the vertex and edges of the polyhedrons. For example, the Bezier control net relationship in G^3 algorithm is shown in figure 5. The detail algorithm is similar to the G^1 and G^2 algothrnm.

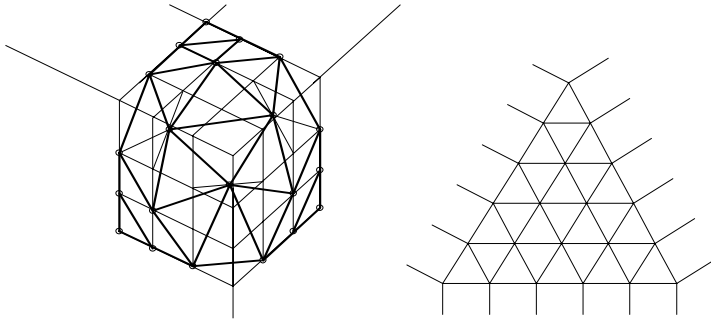


Fig. 5. Bézier control net relationship for vertex connecting surface rendering with G^3 connection in polyhedron

4 Numerical Experimental Results

We have used the algorithm to render the vertex of the cube and the vertex of tetrahedron respectively.

The figure 6 shows numerical experimental results of the polished cube and tetrahedron. We used eight rectangular five-order Bézier surfaces to connect the eight planes for polishing the eight edges of the cube. We use eight triangular five order Bézier surfaces to connect all of its neighboring surfaces in the eight vertexes of the cube (left picture in figure 6). All the surfaces and planes are connected smoothly with G^2 geometry continuity. We used the algorithm to render the edges and vertexes of a tetrahedron in the similar way (right picture in figure 6).

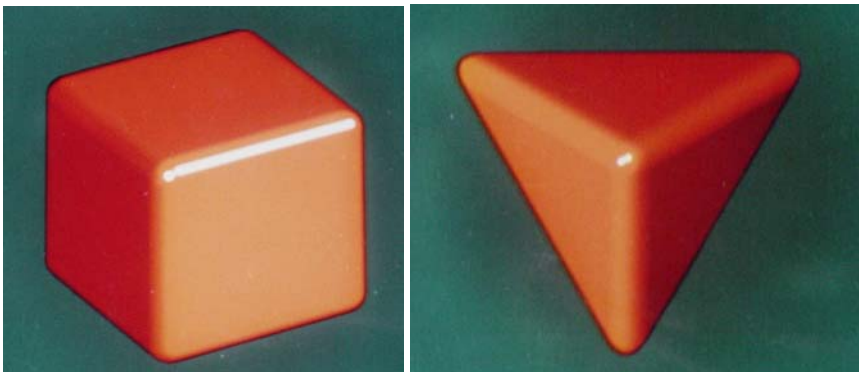


Fig. 6. The numerical experimental results of rendering the vertex and edges of a cube (left) and a tetrahedron (right) with G^2 continuity based on proposed algorithm

5 Conclusions and Future Work

This paper presents a new algorithm for generating and rendering the smooth connecting surfaces for the vertexes and edges of the polyhedron. The algorithm can be used to construct the connecting surfaces to polish and render the vertex and edges of the polyhedron with G^1 , G^2 and higher geometry continuity. The control net points of the connecting surfaces are calculated by the geometry drawing method according to the geometric continuity connection condition (share common plane condition), and it does not need complicated computation. The generated connecting Bézier surfaces can connect the neighboring surfaces with high order geometry continuity.

There are still many open problems in the algorithm. There are lots of the adjustable parameters in the connecting surfaces that can be used to review and change the generated connecting surfaces. Our further work will be focus on the research of the adjustable parameters to review and change the shape of the generated connecting surfaces.

References

1. Paul G. K., Dinesh K. P.: Continuous contact simulation for smooth surfaces. ACM Transactions on Graphics (TOG), Vol. 22 (1), (2003)106-129
2. Boehm W., Farin G., Kahmann J.: A survey of curve and surface methods in CAGD. CAGD 1, (1984)1-60
3. Barnhill R. E.: Surfaces in computer aided geometric design: a survey with new results. CAGD 2, (1985)1-17
4. Farin G.: Curves and Surfaces for CAGD (Fifth Edition). Morgan Kaufman Inc., (2001)
5. Nira Dyn, Micchelli C. A.: Piecewise polynomial spaces and geometric continuity of curves. Numerische Mathematik Vol. 54(3), (1989) 319 – 337
6. Veron M., G. Ris, and J. P. Musse: Continuity of biparametric surface patches. CAD 8, (1976) 267-273
7. Lu X., Ma L., He Z.: Investigation of G4 Connection Algorithm between Adjacent Bézier Patches. In: Proc. of Fourth International Conference on Computer-Aided Design and Computer Graphics, CAD/Graphics'95, SPIE Proceedings Vol.2644, (1995)209-215
8. Lu X., Ma L., He Z.: A Recursive G_n Joining Algorithm for Adjacent Bezier Patches. In: Proc. of the Fifth International Conference for Young Computer Scientists (ICYC'99), Nanjing, China, August, (1999) 939-939
9. Farin G.: Triangular Bernstein-Bézier Patches. CAGD. Vol.3, No. 1,(1986) 83-127

SimVIZ – A Desktop Virtual Environment for Visualization and Analysis of Protein Multiple Simulation Trajectories

Ricardo M. Czekster and Osmar Norberto de Souza

Laboratório de Bioinformática, Modelagem e Simulação de Biosistemas - LABIO,
PPGCC - FACIN, PUCRS, Av. Ipiranga, 6681. Prédio 16 - Sala 106, 90619-900,
Porto Alegre, RS, Brasil
osmarns@inf.pucrs.br

Abstract. *In silico* protein conformation simulation generates massive amounts of data which needs to be properly visualized and analyzed. We are applying Desktop Information-Rich Virtual Environments (*Desktop IRVE's*) techniques and concepts to aid multiple trajectory simulation analysis, improving user experience and developing a problem-solving environment to help the decision making process. We will present *SimVIZ*, a tool which integrates visualization to simulation analysis, improving previous knowledge about trajectories. This environment shows informative panels, Contact Maps, RMSD charts, the Ramachandran Plot and a Parallel Coordinate multidimensional visualization of simulation output in a single rendering scene. *SimVIZ* also opens multiple trajectories along with user associated information concerning many aspects of the simulation. *SimVIZ* is an integrated problem solving environment of multiple trajectories of protein simulations, offering various kinds of analysis and visualization tools used by the community to validate protein structures or to gather a better understanding of the protein folding process.

1 Introduction and Motivation

When performing *in silico* protein conformation simulation, it is very common to produce several trajectories, each one generated by a set of parameters, often generating different outputs. This brings a very intriguing challenge to visualization system designers: how to convey and extend available information on a rendering scene in a simple and meaningful manner.

Our approach is based on *Desktop IRVE's* [1], where the users associate information within a trajectory, step of simulation or amino acid. We are proposing a visualization-analysis environment offering numerous analysis options along with multidimensional visualization techniques for the simulation outputs.

The available visualization and analysis tools are mutually exclusive, meaning that specific tasks are done by specific software. Our idea is to build a single environment where this problem is minimized, so users can benefit from the analysis experience and improve their knowledge and decisions.

The environment, which we called *SimVIZ* (as in Simulation Visualization), is an attempt to integrate information visualization techniques with simulation trajectory analysis tools, aggregating and extending it with user information and insights about the events. A few protein visualization representations were implemented, and a protein *Contact Map* [2], the *Ramachandran Plot* [3] and *RMSD Plot (Root Mean Square Deviation)* [4, 5]. All graphics are drawn inside the scene, as well as their associated information (written on transparent panels).

This paper is divided as follows: Section 2 discuss the theoretical aspects such as visualization, virtual environments, simulation analysis and previous related works. Section 3 lists the modules and features of the environment and presents the achieved results, showing *SimVIZ* and its visualization/analysis combinations. Section 4 discusses final considerations and future perspectives.

2 Theoretical Aspects

Visualization serves multiple purposes, but the most important one is that it comprehends a series of tasks aiding the decision making process about data [6, 7]. Visualizing raw data is often easier when insightful images are being used to convey the results [8]. Among its benefits we can mention its effectiveness when representing data using interesting and relevant visual techniques [9].

2.1 Visualization and Desktop IRVE's

Schneiderman et al [10] introduced the concept of what is known as *Visual Information-Seeking Mantra*: Overview first, zoom and filter, details-on-demand. This is the main set of rules visual system designers should follow in order to build and implement meaningful information visualization software. Firstly, all data is displayed in the scene so users can overview it. Then, through zooming and filtering, users can remove irrelevant objects/data from the scene. Lastly, details-on-demand dictates that the system should indicate all the possible details about a certain object.

Another relevant aspect of visualization concerns the multidimensional nature of the data, varying from 1-dimensional (linear data), 2-dimensional (maps, sizes, temperatures), 3-dimensional (real world objects), temporal (data varying through time), multi-dimensional (defined by n -attributes) and tree (hierarchical data). Multidimensional visualization issues are a current topic of research, along with how users detects patterns and relations inside the data [10].

One popular multi-dimensional technique is known as *Parallel Coordinates* [11, 12]. Single 1-dimensional vertical lines are drawn in a rendering scene, representing an attribute of the data. Lines connect the attributes to create the final representation. This kind of visualization could be used to detect the variability throughout the dataset.

Another multidimensional visualization technique, known as *Glyphs* [13, 14], are iconic representations of attributes, highlighting patterns or anomalies within the data, when seen in totality. This approach has unique characteristics such

as positioning and deciding which icons or shapes will convey more meaning to each dimension.

IRVE's are a combination of a VE or *Virtual Environment* (a synthetic, spatial world seen from a first-person point of view) and *Information Visualization* [1, 6]. Its main objective is to enhance virtual worlds with abstract information. *Desktop IRVE's* are *VE's* executing in a desktop computer screen and without any specific equipments to be operated (as those of Virtual Reality, for instance). *Bowman et al* [1] defined the theoretical aspects when using *IRVE's*, such as concerns about abstract information positioning, association and classifications for text layout [1, 15].

2.2 Proteins and Multiple Simulation Trajectories Analysis

Proteins are biological macromolecules formed by amino acids and perform specific functions inside the cell [3]. Proteins are classified through their hierarchical structure: primary structure (the amino acid sequence), secondary structure (α -helix, β -sheet, turns, coils), tertiary structure (combinations of secondary structure elements, forming a three-dimensional structure) and quaternary (combinations of tertiary structures) [3].

In order to either refine structures or to study the protein folding process, simulation methods are used [4]. Simulation using the method of *Molecular Dynamics*, or *MD*, computes atomic trajectories by numerically solving Newton's equations of motion [16]. MD simulations are used for evaluation and quantification of protein folding as well as to search for energetically favorable structures.

MD can predict thermodynamical properties where experimental data does not exist, are hard or even uncertain to obtain. Another practical aspect is related to system equilibrium, by selecting which parameters will determine simulation abortion or continuation. These properties include energy, temperature, pressure and structural behaviour [4].

In the context of this work, we are using *AMBER* software as force field [17] and the software *ptraj* to process the output for *MD* simulations which will serve as input to our environment. This application, a command line tool distributed with *AMBER* toolkit, is used to extract trajectory information [17].

A simulation comprehends different phases, starting with initial parameters setup to output generation and analysis. The purpose is to calculate protein thermodynamical properties and atom positioning by extracting, filtering and interpreting the massive output from the simulation trajectory data. A distinctive list of software and tools are used to help interpretation and analysis, each one of them are responsible for specific tasks.

A common set of useful analysis are the *Ramachandran Plot* [3], the *Contact Map* [2] and the *RMSD (Root Mean Square Deviation) Plot* [4]. The *Ramachandran Plot* represents the ϕ and ψ angles that represent allowed or prohibited combinations of a conformation. This plot informs, for all amino acids, which conformations are possible and those structurally improbable.

On the other hand, the *Contact Map* is a map of amino acid distances, used to discover protein structure formation, informing the occurrence of con-

tacts among each other [2]. Finally, the *RMSD Plot* contains a distance between the atoms from the simulated conformation and a *Reference Structure* - *RS*, which is a structure used for comparison, often experimentally determined [4].

2.3 Related Works

This section discusses protein visualization tools, *IRVE*'s and trajectory analysis software. Among the most commonly open-source protein visualization tools used nowadays, we highlight *VMD* - *Visual Molecular Dynamics* [18] and *PyMOL* [19].

VMD [18] is a powerful tool for visualization and analysis of biological systems, such as proteins, nucleic acids and lipids. The software authors used *OpenGL* for graphical aspects. We emphasize scripting capabilities and plugins installation among its main features. This software can be used for molecular dynamics interactive studies and trajectory analysis.

PyMol [19] is a graphical presentation system for molecules, with a *Python* command line interpreter, mainly developed for real time visualizations and high quality images generation. Its main features include optimized three-dimensional structures visualization, eight different molecular representations, molecular superimposition and animation.

A sample of *VE* and Information Visualization, previous to *IRVE*'s, is *VDV* or *Virtual Data Visualizer* [20]. This *VE* is a toolkit for exploratory data visualization. *VDV* manipulates multiple data sources relying on *Glyphs* to inform data characteristics. This toolkit is a good example of *VE* and Information Visualization integration.

Another environment that is worth noticing is *PathSim Visualizer* [21], specific for analysis and visualization of pathogen agents simulation results. Its main objective is to associate relevant abstract information and annotations such as texts, links and audio to a rendering scene, intensifying user experiencing about data. Its major drawback is the fact that it solves particular pathogenic simulation problems.

3 The *SimVIZ* Environment

The goal of *SimVIZ* is to provide a coherent environment centered on visualization and simulation analysis. To achieve this intent, we implemented a basic protein viewer with four visualization formats: *Lines*, *Bonds*, *VDW* and *CPK*. *SimVIZ* allows changing lines and cylinders heights, widths and definition. Also, it is possible to change colors by amino acid name, by chain, by structure and by chemical element.

We divided the environment in three different phases: a) Data Input and Association, b) Data Processing, Extraction and Mapping and c) Data Presentation. In a), we are considering all input from the user, for example, a full trajectory and its output, as well as user interaction. The next phase comprehends some processing to build amino acid topology and extract relevant information

within data such as distances between amino acids and simple counting and statistics.

The final phase is responsible for determining which information is seen at the rendering scene and creating the visual elements such as charts, plots, abstract textual information and visual protein structure representations.

The *SimVIZ* data flow is described as follows: when a dataset is opened, containing a trajectory, the system iterates from the first to the last step, opening the coordinate file (*PDB*) [22] and the output file (*OUT*). After the reading process, we build all amino acid topology and run *STRIDE* [23] (get the ϕ , ψ and the secondary structure) for each conformation. Then, we calculate simple counting (number of amino acids and atoms) in order to build graphical mappings, presenting it in the rendering scene, according to user defined interface selections.

In addition to *RS* data, users can associate abstract information for the trajectory, to a given step of simulation and for each step, information related to single amino acids. This information is saved for further analysis. We also allow mapping of multiple *RMSD* files to the trajectory. *SimVIZ* will draw a single plot containing all files, defining different colors for each one.

The *SimVIZ* implementation is based on *Desktop IRVE's* concepts and characteristics to present abstract output simulation data and textual information concerning multiple trajectories. We used informative panels, textual output taxonomies and visual choices while adding charts, countings, statistics and different analysis plots, such as colors, fonts and transparencies.

As we mentioned before, besides the files we add to the scene such as *RMSD* and *RS*, users can associate abstract information in three elements: a) the trajectory (*world-fixed*), b) individual steps (*display-fixed*) and c) individual amino acids of individual steps (*object-fixed*) [1].

We also defined regions for textual abstract information containing simulation output data. The upper region in the rendering scene shows transparent information panels with *AMBER's* parameters for *Resource Use* and *Control Data*. This panels shows dynamic information, based on the current simulation step. The lower region shows the *Outputs* of *AMBER*, the energies, temperature and pressure for a given conformation.

The right side of the rendering scene lists all conformation amino acids and the secondary structure for each one, using *STRIDE's* one letter code. One relevant aspect is creation concerning the panels, the plots and the charts. They are all transparent, so users can still see the structural behavior along the simulation trajectory run. On the center, we show the rest of the charts, plots, countings and statistics. Also, we draw the *Ramachandran Plot*, the *Parallel Coordinates* and the *Contact Map*. Some visual results are shown in Section 3.2.

3.1 Implementation Details and Main Features

SimVIZ is implemented with C/C++ for the core, FLTK [24] for the Graphical User Interface and OpenGL [25] for graphics. To determine secondary struc-

ture formation throughout the trajectory and for the ϕ , ψ angles, we integrated *STRIDE* [23] on *SimVIZ*. We are combining the use of fonts for drawing the atoms and amino acids names with pure *OpenGL* text primitives and *PLIB*'s font library [26]. This library is very useful to represent diverse font types, colors and sizes.

The differential features for the environment are: opens multiple simulation trajectories; allows other relevant abstract information to be associated with the trajectory, the conformation and individual amino acids; offers simple, but useful representations formats such as *Lines*, *Bonds*, *VDW* and *CPK*; is integrated with *STRIDE*; colors by various options; scaling, rotating and translating; simulation controls (play, goto, stop); use a *Parallel Coordinates* multidimensional representation for output data; offers charts, *RMSD*'s plots, *Ramachandran Plot* and *Contact Maps* for all trajectory conformations as well as for *RS* (if added by users).

3.2 Experiment and Visual Results

In order to illustrate *SimVIZ*, we used a dataset containing 100 nanoseconds of a *MD* simulation trajectory for a small 33 amino acid protein known as Helical Hairpin (or *HH*). The protein structure with PDB code *1ZDB* is used as a Reference Structure (*RS*), for comparison. This study produced 100 coordinate files in PDB format, one for every 1 nanosecond, with 100 output files in the *OUT* format, containing analysis data for the simulation run.

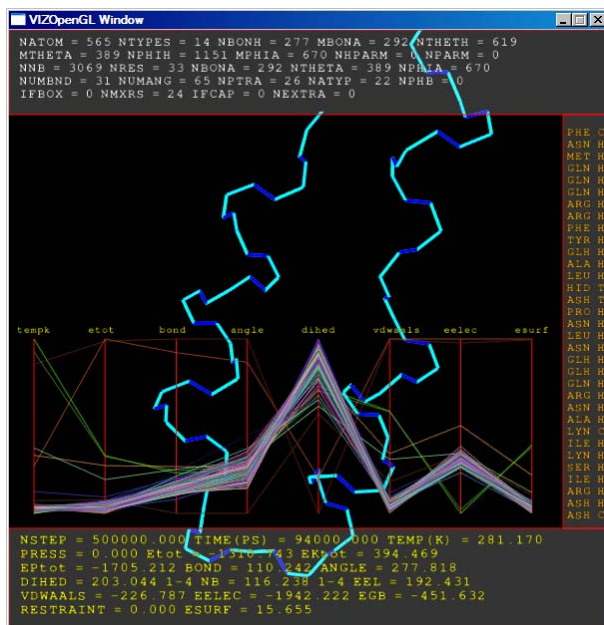


Fig. 1. Backbone conformation, amino acids, outputs and *Parallel Coordinates*

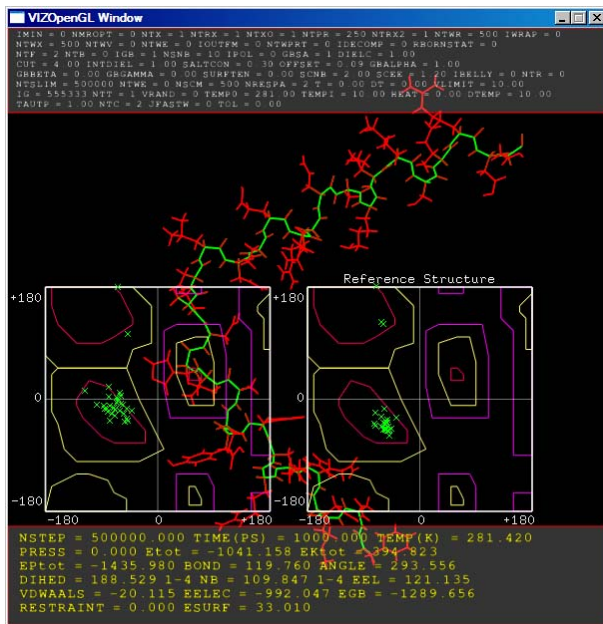


Fig. 2. All-atom conformation, parameters, outputs and the *Ramachandran Plot*

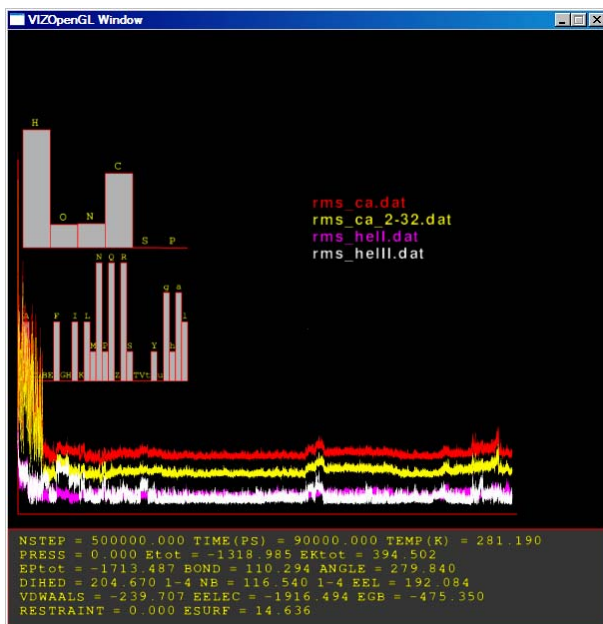


Fig. 3. *RMSD* data, outputs and counting

SimVIZ opens user produced AMBER output files, normally using *ptraj*'s options. The more details it provides, more information is presented and more reliable inferences can be drawn about the simulation run. The environment is prepared to open whatever output data is produced, to the memory limit.

An issue observed while implementing the environment is related to simultaneous visualization massive output data pertaining each conformation. To solve these occlusion problems, SimVIZ opens multiple trajectories, on multiple rendering windows. For example, if the same trajectory is opened twice, multiple analysis tools are presented, without occlusion, enhancing visualization and interpretation. Each new rendering window sets its own visual options, so users can view different analysis aspects on different windows, about different (or same) trajectories. These feature enhance and extend analysis possibilities, showing multiple kinds of information about the same trajectory.

We can see in the Figure 1 the protein conformation for a given simulation step containing, in the upper region, the *Resource Use*, in the lower region, the *Output*, in the right, the amino acid list plus the secondary structure, and, in the center of the rendering scene, the *Parallel Coordinates* for 8 dimensions of the output data and the conformation using the format *Lines*, for the backbone atoms only.

The all-atom conformation, colored by the *Backbone*, with the *Ramachandran Plot* and simulation parameters are shown in the Figure 2. The *Ramachandran Plot's* coloring follows the color selected for the conformation.

Figure 3 shows 4 files generated by *ptraj* containing *RMSD* data. The system assigns a different color for each file, with the corresponding subtitle. We are

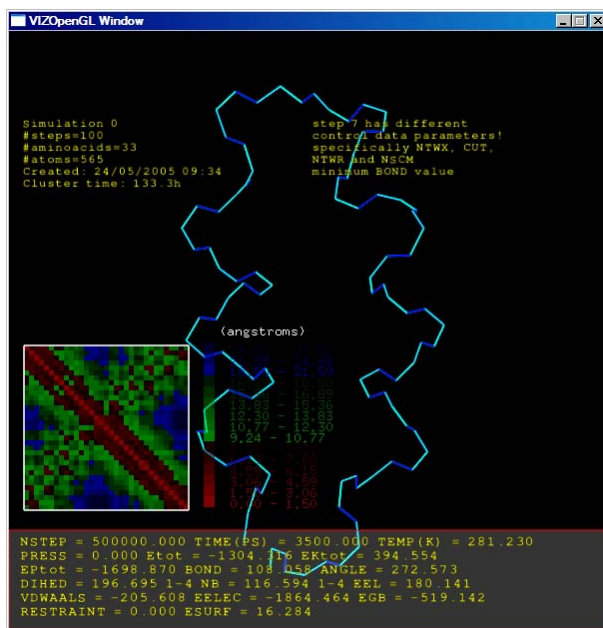


Fig. 4. Protein conformation, Contact Map, abstract textual information and outputs

showing the counting of amino acids and atoms with simulation output. In this example, the conformation is not presented at the scene, clearing the rendering window.

Figure 4 shows the conformation, the *Contact Map*, simulation output and abstract related information concerning the volume (on the upper left) and an individual step (on the upper right). The structure is designed as *Lines*, colored by chemical element.

4 Conclusions, Perspectives and Acknowledgements

There is a need in the structural biology community for high-quality, insightful visualization software. Visualization offers meaningful techniques to help researchers perform better analysis through visual inspection. On the other hand, there should be a concern about simulation quality when multiple trajectories are produced. This work is committed to this aspect, presenting a graphic platform where users can learn more about their simulation. We develop a simulation annotation environment, combining visualization and analysis features.

This work focused on visualization and analysis of related abstract information for improving previous knowledge about trajectories. Our next tasks includes adding more classic representations such as *Ribbons* and developing other user interaction techniques such as Semantic Zooming and 3D User Interfaces. We also intend to research about integrating other multidimensional visualization techniques such as *Glyphs*.

We thank FAPERGS and CAPES for financial support. Also Dr. Marcio Pinho and Regis Kopper for helpful discussions.

References

1. Bowman, D. A., North, C., Chen, J., Polys, N. F., Pyla, P. S., Yilmaz, U.: Information-rich virtual environments: theory, tools, and research agenda. VRST '03: Proceedings of the ACM symposium on Virtual reality software and technology, 2003, pp. 81-90.
2. Vendruscolo, M., Domany, E.: Efficient dynamics in the space of contact maps. *Folding and Design*, vol. 3(5), 329-336, 1998.
3. Branden, C., Tooze, J.: *Introduction to protein structure*. Garland, 1999.
4. Leach, A. R.: *Molecular Modeling: Principles and Applications*. Person Education, 2001.
5. van Gunsteren, W. F., Mark, A. E.: Validation of molecular dynamics simulation. *J. Chem. Phys.*, v. 108, p. 6109-6116, 1998.
6. Ware, C.: *Information Visualization: Perception for Design*. Morgan Kaufman, 2000.
7. Ma, Kwan-Liu: Visualization - A Quickly Emerging Field. *ACM SIGGRAPH Computer Graphics Quarterly*, 2004, vol. 38, number 1, pp. 4-7.
8. Vailaya, A., Bluvias, P., Kincaid, R., Kuchinky, A., Creech, M., Adler, A.: An Architecture for Biological Information Extraction and Representation. *Bioinformatics*, 2005, vol. 21, pp. 430-438.

9. de Oliveira, M. C. F., Levkowitz, H.: From visual data exploration to visual data mining: a survey IEEE Transactions on Visualization and Computer Graphics, vol. 9(3), 378–394, 2003.
10. Shneiderman, B.: The Eyes Have It: A Task by Data Type Taxonomy for Information Visualizations. VL '96: Proceedings of the 1996 IEEE Symposium on Visual Languages, 1996, pp. 336-343.
11. Inselberg, A., Dimsdale, B.: Parallel Coordinates: A Tool for Visualizing Multidimensional Geometry. Proceedings of IEEE Visualization, 1990, pp. 361-375.
12. Fua, Y. -H., Ward, M. O., A. Rundensteiner: Hierarchical Parallel Coordinates for Exploration of Large Datasets. VISUALIZATION '99: Proceedings of the 10th IEEE Visualization 1999 Conference (VIS '99), 1999.
13. Ribarsky, W., Ayers, E., Eble, J., Mukherjee, S.: Glyphmaker: Creating Customized Visualizations of Complex Data. Computer, 1994, vol. 27, number 7, pp. 57-64.
14. Ward, M. O.: A taxonomy of glyph placement strategies for multidimensional data visualization. Information Visualization, 2002, vol. 1, number 3, pp. 194-210.
15. Polys, N. F., Bowman, D. A.: Design and display of enhancing information in desktop information-rich virtual environments: challenges and techniques. Virtual Reality, 2005, vol. 8, pp. 41-54.
16. van Gunsteren, W. F., Berendsen, H. J. C.: Computer Simulation of Molecular Dynamics: Methodology, Applications and Perspectives in Chemistry. Angewandte Chemie International Edition in English, v. 29, p. 992.1023, 1990.
17. Pearlman, D. A., Case, D. A., Caldwell, J. W., Ross, W. S., Cheatham III, T. E., DeBolt, S., Ferguson, D., Seibel, G., Kollman, P.: AMBER, a package of computer programs for applying molecular mechanics, normal mode analysis, molecular dynamics and free energy calculations to simulate the structural and energetic properties of molecules. vol. 91, 1–41, 1995.
18. Humphrey, W., Dalke, A. and Schulten, K.: VMD - Visual Molecular Dynamics. J. Molec. Graphics, 1996, vol. 14, pp. 33-38.
19. DeLano, W. L.: The PyMOL Molecular Graphics System. DeLano Scientific, San Carlos, CA, USA. 2002.
20. van Teylingen, R., Ribarsky, W., van der Mast, C.: Virtual Data Visualizer. IEEE Transactions on Visualization and Computer Graphics, 1997, pp. 65-74.
21. Polys, N. F., Bowman, D. A., North, C., Laubenbacher, R., Duca, K.: PathSim visualizer: an Information-Rich Virtual Environment framework for systems biology. Web3D '04: Proceedings of the ninth international conference on 3D Web technology, 2004, pp. 7-14.
22. Berman, H. M., Westbrook, J., Feng, Z., Gilliland, G., Bhat, T. N., Weissig, H., Shindyalov, I. N., Bourne, P. E.: The Protein Data Bank. Nucleic Acids Research, 2000, vol. 28, pp. 235-242.
23. Frishman, D., Argos, P.: Knowledge-based protein secondary structure assignment. Proteins, vol. 23(4), 566–579, 1995.
24. Fast Light Toolkit (FLTK). Accessed on November, 2005. Available on <http://www.fltk.org/>
25. OpenGL - The Industry Standard for High Performance Graphics. Accessed on November, 2005. Available on <http://www.opengl.org/>
26. A Font Library for OpenGL. Accessed on November, 2005. Available on <http://plib.sourceforge.net/fnt/index.html>

Immersive Molecular Virtual Reality Based on X3D and Web Services

Oswaldo Gervasi¹, Sergio Tasso¹, and Antonio Laganà²

¹ Department of Mathematics and Computer Science, University of Perugia,
via Vanvitelli, 1, I-06123 Perugia, Italy
ogervasi@computer.org, sergio@unipg.it

² Department of Chemistry, University of Perugia,
via Elce di Sotto, 8, I-06123 Perugia, Italy
lag@dyn.unipg.it

Abstract. An immersive Molecular Virtual Reality environment in which the user interacts with a X3D virtual world using immersive devices and dynamic gestures is presented.

The user through the virtual world invokes a Web server to perform a real-time simulation and find a stable molecular structure.

The outcome of the simulation is the representation of the stable structure of the molecular system in the X3D world.

1 Introduction

The visualization of molecular structures is fundamental to chemical research because it helps the understanding of chemical processes. Some packages have been developed for this purpose (especially for biological and medical applications [1, 2, 3]) by combining advanced visualization tools with molecular structure and dynamics software. The integration of virtual with augmented reality technologies and molecular modeling systems (also called Molecular Virtual Reality, MVR[4]) has recently attracted increasing attention and dedicated environments and infrastructures have been based on it[5, 6].

The basic goal of our effort is to explore new technologies available on the World Wide Web and rely on Java applications to interact with the X3D[7] molecular world using immersive devices. These technologies allow also to present in real time the outcome of molecular processes by invoking related simulation packages.

In this paper we present a system developed in our laboratory that uses immersive devices (such as data gloves and an head-mounted display) and the X3D language. It allows to implement a MVR environment in which the researcher is able to explore molecular structures using *dynamic gestures*. The molecular properties are calculated using a popular molecular package, DL-POLY[8] invoked as a Web Service. The resulting system allows the researcher to connect to a virtual laboratory implemented as a Web site and access X3D applications. In this way the immersive devices can be used to both explore the molecular virtual world and invoke the relevant Web Services.

The ultimate goal of our research is the building of MVR systems based on Web technologies. Compared with other existing applications running on local workstations equipped with VR devices and based on specialized software (e.g.: OpenGL), our system combines the properties of a worldwide access from the Web and the meta-data handling capability. Moreover, being based on XML, it also opens new perspectives towards the integration with other software available on the network and the semantic use of the data handled.

The paper is organized as follows: in section 2 the Virtual Reality tools and the interaction between the external devices and programs are described; in section 3 the Web Service architecture adopted and the implemented Services are illustrated; in section 4 a prototype case study is sketched.

2 The VR Scenario

The Virtual Reality environment is based on a Web browser enabled to render an X3D world. The virtual world interacts with the immersive devices through Java Native Interface (JNI)[9] programs.

The interfaces between the immersive devices, the Web Services related to the simulation engines and the X3D virtual world are implemented in Java. The Java programs run both on the client side (to implement the X3D scripts and the programs handling the gloves and the motion trackers) and on the Web server (to implement the Web Services).

In the following subsections a detailed description of the components of the Virtual Reality scenario are given.

2.1 The X3D Virtual World

The X3D virtual world is implemented using the authoring tool X3D-Edit[10] and the browser Xj3D[11] to simulate the environment, while the molecular structure representations are produced dynamically by a Java application that converts the molecular structure information into objects of the corresponding X3D scene.

To render the molecular structure the user can select dynamically the following representations:

ball and sticks: balls of appropriate radius (proportional to the Van der Waals radius) and different colors are used to represent atoms and sticks to represent bonds between the atoms;

wire frame: only bonds (shown as thin wires) are represented;

space filling: atoms are represented as large balls of the proper radius (given by a scaled Van der Waals radius) and color, filling the internuclear space;

space filling and wire frame: a mixed use of *space filling* and *wire frame* representations is made.

colored wire frame: bonds are represented as colored wires of which one half has the color of one atom and the other half of the other atom.

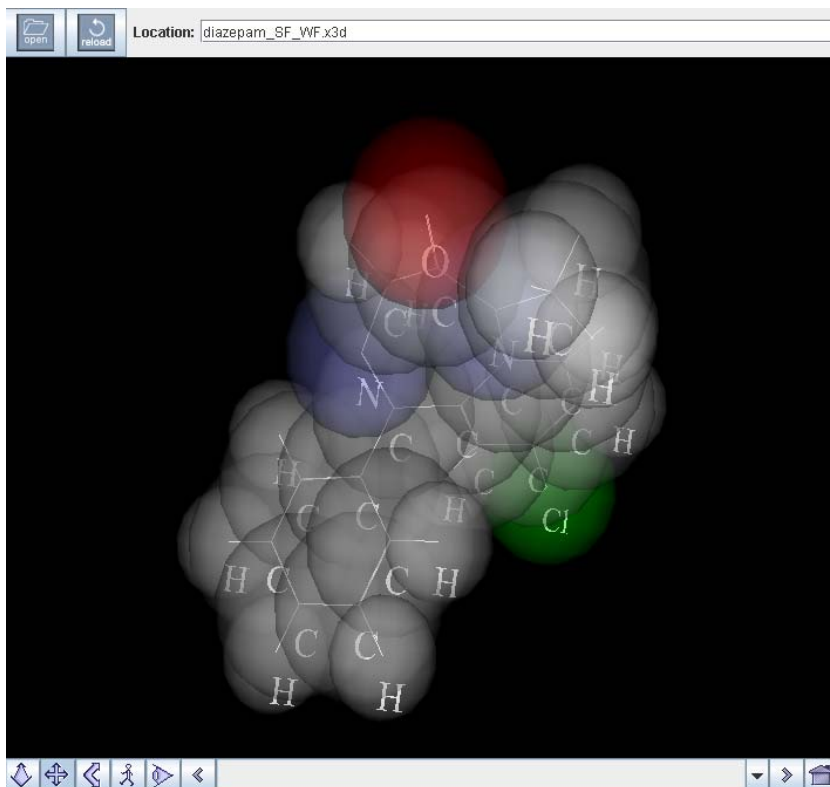


Fig. 1. The X3D world of the "space filling" and "wire frame" representations of the Diazepam molecule is shown on a Xj3D window. Atomic labels are also shown.

The user can also activate dynamically at run-time the following properties:

transparency: when a molecule is represented together with the solvent a variable degree of transparency can be applied to the latter;

labels: the chemical symbol of the atom is given in the same position of the corresponding ball (with a certain degree of transparency).

The atoms are colored by the element type. To this end the RASMOL CPK coloring scheme[12] was used. The scheme is based upon the colors of the popular plastic space-filling models developed by Corey, Pauling and later improved by Kultun[13].

Although in our application all the above listed representations can be used, most of our work has been carried using the space filling and wire frame ones (as an example the Diazepam molecule obtained from a Sybil MOL2 molecular structure file is given in fig.1).

The user interacts with the system thanks to a sensor associated with each atom of the molecule and with the label of each atom and bond of the molecular system. Each atom has the collision function enabled to control the

interaction with the avatar. In this way when the user makes a given gesture (say breaks a given portion of the molecule) the virtual world interprets it by showing again the result of the gesture (i.e.: an animation is activated to extract out the given portion of the molecule) and then showing the effect of the extraction on the represented molecule (by modifying atom positions and bonds). The new representation is obtained by invoking the Simulator Web Service and letting it produce the new spatial coordinates of the atoms and the active bonds.

2.2 The Immersive Technology

The increasing use of immersive devices in X3D benefits from the development of powerful relatively low cost PCs, the broadening of the network bandwidth, the development of new Web Services and the advances made by the Web3D Consortium[14] in X3D specifications. In particular the Web3D community has developed the Extensible Modeling and Simulation Framework (XMSF) devoted to integrate the X3D technologies and several Web technologies[15] and several laboratories have integrated immersive devices in the X3D worlds[16, 17]. The Web3D technologies have also been successfully exploited in scientific applications to implement powerful interactive 3D environments and to represent molecular systems[18, 19].

For our experiments we used the 5DT digital gloves[20], the Polhemus FastTrack[21] motion trackers and the 5DT HMD 800-26 Head Mounted



Fig. 2. A user during an immersive experience in the X3D virtual world

Display[22] in an X3D environment. A typical experimental set up of an immersive experience into the X3D virtual world to work on the Diazepam molecule is shown in fig.2.

To use the immersive devices shown in figure 2 the Scene Access Interface (SAI) has been invoked from the internal script environment of X3D (implemented in Java) and from the programs (written in JNI enabled to execute programs written in C++ to handle immersive devices).

2.3 The Gestures

To attach microscopic relevance to dynamic gestures a special language has been defined. This language sets a correspondence between digital data and physical action modes. For the glove we defined the following modes:

pointing forefinger, remaining fingers clenched: *Navigation mode.* This gesture activates the glove as a pointer device. The motion tracker information are used to move the avatar in the X3D virtual world.

clenched fist: *Exploration mode.* This gesture activates the glove as a rotator (i.e.: the objects rotate when the hand rotates). In this configuration the motion tracker information are used to rotate objects.

open hand: *Selection mode.* This gesture activates the selection of other objects (atoms) in the proximity of the object (atom) selected using the forefinger. In this configuration the relative position of the phalanges are used to widen (more open hand) or narrow (more clenched finger) the cone that will include the selected objects (atoms). The motion tracker information are used to move the avatar in the world, while the information of the glove are associated with the selection cone.

3 The Web Services Approach

Web Services are basically server functions which have published the interface mechanisms needed to access their capabilities.

The Web Service model implemented for our application sets a communication link between a world of MVR and a molecular real-time simulator. The service allows to set up the simulation (by interacting with the immersive tools and the MVR world) and run it by invoking a molecular simulation program. Moreover the service provides a parser in order to search and retrieve molecular configuration files from Databanks or Web sites. The molecular configuration files are then interpreted by the Web Service to produce the input file(s) for the molecular simulation program invoked.

The implemented Web Service is based on Java/SOAP[23] RPC (remote procedure call) technology. The model architecture implemented is shown in figure 3. The use of the Web Service has been made for the following reasons:

- To bypass security protections (firewall) often encountered on the path from the X3D client to the simulator host by using the standard HTTP port;
- To conform the application to the communication standards;

- To benefit of the communication facilities offered by the SOAP protocol (the analysis given by the SOAP parser in the communication allows the identification of the formats both at envelop and body level);
- To use a uniform model for the RPC and the return parameters;
- To supply further extensions to several simulator engines by specifying their URN (to be found in the UDDI[24] register servers).

The implemented Web Service has been written in the Java language with the help of remote procedure calls (RPC) because of the distributed nature of the application. The method calls on Java objects are translated to RPC calls. The service is managed at the transport level by SOAP protocol.

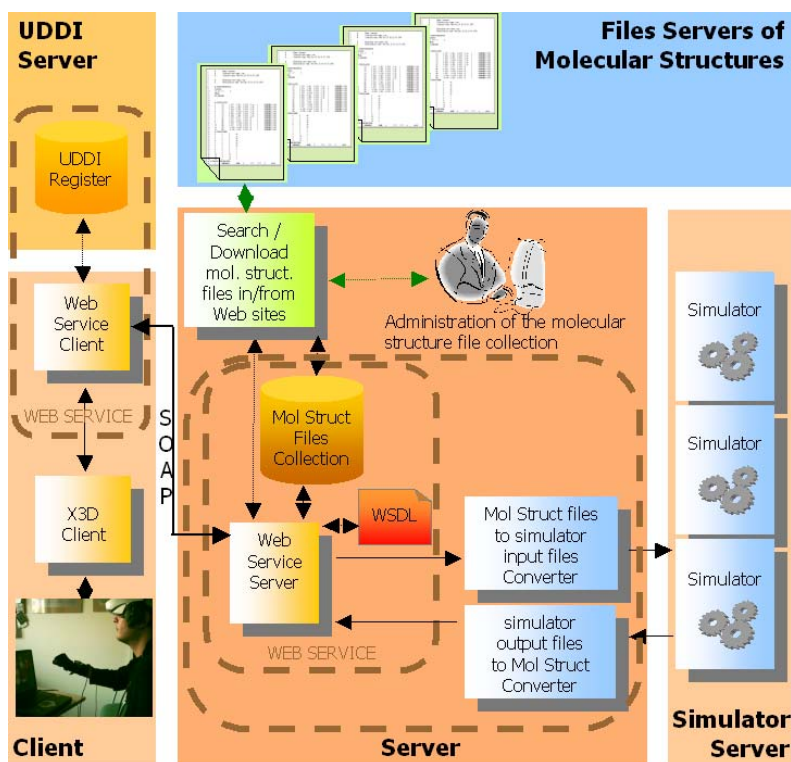


Fig. 3. Architecture of the Web Service implemented for making real-time simulations

3.1 The Simulation Engine

In this section the client and the server part of the Web Service are described.

The client part of the Web Service is directly invoked by the virtual reality world to search the location of a molecular dynamic simulator on a UDDI register. Through this location the Web Service client takes the Web Service description from the Web Service server. This information is stored on a Web

Services Description Language (WSDL)[25] document. The WSDL is a XML grammar that specifies the parameters and the constraints of the Web Service communications. The client code uses this information to build its request to the Web Service server invoking the method which executes the RPC call. This method builds the call by setting the destination URI and the remote method and by calling the Web Service as well. The client code waits then for the response and checks it to handle possible faults. At the end of this process it sends the output file describing the simulated molecular structure to the virtual reality application.

The server part of the Web Service manages the clients requests. When the server receives a client request through a SOAP message it analyzes the identifier of the molecule and searches its presence in the local database of molecular structures. If the requested file is not present in the local repository, the server invokes the Search Service of molecular structure files on the Internet. This service is described in detail in section 3.2. When the file is downloaded, it is stored in the local database for further needs. In any case the Web Service server runs a conversion program to generate the simulator input files and starts the simulation program (locally or on remote hosts using additional RPC calls).

At the end of the simulation another conversion program produces a molecular structure file from the simulator output files. Through the SOAP protocol, the Web Service server sends the molecular structure file in XML format to the X3D client to visualize the molecular structure in the virtual reality world.

3.2 Searching Molecular Configuration Files on the Web

When the user selects a molecular system for starting a simulation, the Web Service invokes an internal module to retrieve a suitable molecular structure file from Databanks. The related URL is kept in a repository list to be updated by the Administrator. For each new site of the list the Administrator must create an XML plug-in file that provides all information about the named Databank. The XML plug-in will allow the Web Service server to interact with the Databank server, using its specific dialect and specifying all necessary fields to perform the query.

For all Databank sites possessing the information, the Web Service server will automatically perform the query for searching and retrieving the requested file (transparently to the end-user) and pass the molecular structure file to the end-user client for building the X3D scene.

4 A Case Study

Using the above mentioned environment we have examined in detail the case of the solvation of benzene rings by considering a cluster formed by two C_6H_6 and a few Ar atoms. To begin with we collect from the Web the benzene configuration files (selecting one of the available common formats like PDB, Sybil Mol2, CML, MDL, etc, or invoking some offline programs like Openbabel[26] when the information are available in a different format). Then we position the benzene and the Ar atoms using the gloves in our laboratory space and let the related force field act on them.

We could also generate in the same way new molecules either by adding piece by piece their components already available on the Web or by taking some pieces out of that molecule. In this case not only one has to add (subtract) the position and the nature of the added (subtracted) atoms but she/he has also to add (subtract) the associated interaction components. Then since the new aggregate may not be stable also in this case, one has to run dynamical calculations to let the new aggregate adjust its structure under the effect of the force field at the chosen temperature.

In some of the virtual experiments we carried out the piling-up of the two benzene rings in presence of *Ar* atoms was studied. In particular we have considered the simple case in which two benzene rings are piled-up using positive ions[27] and are solvated by *Ar* atoms gradually added to the system.

To stabilize the pile up of the second benzene ring a K^+ ion is inserted between the two C_6H_6 . At this point a first thermalization is run. Afterwards, an increasing number of *Ar* atoms are added and the dynamics of the system as well as the isomeric variants produced are observed.

5 Conclusions

We have presented an X3D Molecular Virtual Reality environment in which the researcher is able to interact with it by using immersive devices and dynamic gestures. By using the gestures the researcher is able to modify the composition of the molecular system by adding or subtracting functions and the molecular properties of the new species are evaluated in real time by invoking a Web Service implementing the simulation environment. This has required the assemblage of an innovative approach coupling the management of immersive devices with Web Services and molecular dynamics packages.

The tests carried out show, even for the simple case study considered here, the validity of the chosen solution and the particular usefulness of the approach adopted for understanding the behavior of molecular systems.

Acknowledgments

Financial support from the *Fondazione Cassa di Risparmio di Perugia* and from the European Union through the COST action D23 (SIMBEX and ELCHEM working groups) is acknowledged. Thanks are also due to MASTER-UP srl, a Perugia University Spin-Off, for the logistic support.

References

1. QMOL package is developed by Jason Gans, Department of Molecular Biology & Genetics, Cornell University, Ithaca, NY, 14853; http://www.mbg.cornell.edu/Shalloway_Lab_QMOL.cfm
2. RasMol package: <http://www.umass.edu/microbio/rasmol/>

3. VMD, Visual Molecular Dynamics, is developed by the Theoretical and Computational Biophysics Group (TCBG), an NIH Resource for Macromolecular Modeling and Bioinformatics, Beckman Institute of the University of Illinois at Urbana-Champaign (UIUC); <http://www.ks.uiuc.edu/Research/vmd/>
4. Riganelli, A., Gervasi, O., Laganà, A., Alberti, M.: "A multiscale virtual reality approach to chemical experiments", Lecture Notes on Computer Science, 2658, 324-330 (2003)
5. Gervasi, O., Riganelli, A., Pacifici, L., and Laganà, A.: VMSLab-G: A Virtual Laboratory prototype for Molecular Science on the Grid. Future Generation Computer Systems 20(5) (2004) 717-726
6. Park, S.J., Lee, J., and Kim, J.I.: A Molecular Modeling System Based on Dynamic Gestures, VRSAL Workshop, LNCS 3480, (2005) 886-895.
7. The X3D specifications and the documentation are available at the Web3D Consortium Web site: <http://www.web3d.org/x3d>
8. Smith, W., and Forester, T.R., J. Molecular Graphics, 14 (1996) 136; http://www.dl.ac.uk/TCS/Software/DL_POLY/;
9. Liang S.: "The Java Native Interface: Programmer's Guide and Specification", Addison Wesley Longman, Inc. (June 1999); <http://java.sun.com/docs/books/tutorial/native1.1/>
10. The X3D-Edit authoring tool has been developed and released by the Web3D Consortium Web and is freely available for downloading at the URL: <http://www.web3d.org/x3d/content/README.X3D-Edit.html>
11. The Xj3D is a project of the Web3D Consortium focused on creating a toolkit for VRML97 and X3D content written completely in Java. The Web site is: <http://www.xj3d.org/>
12. See for example: [+http://info.bio.cmu.edu/Courses/BiochemMols/RasFrames/CPKCLRS.HTM+](http://info.bio.cmu.edu/Courses/BiochemMols/RasFrames/CPKCLRS.HTM)
13. Koltun, W. L.: "Precision Space-Filling Atomic Models", Biopolymers, 3, 665-679 (1965)
14. The Web3D Consortium is the organization that is promoting 3D and Virtual Reality through the World Wide Web. The Web3D Web site, that is a repository of an impressive amount of software packages, documentation, examples is: <http://www.web3d.org>;
15. The Extensible Modeling and Simulation Framework (XMSF) uses X3D and XML Web Services to enable a new generation of distributed simulations. <http://www.web3d.org/applications/vizsim/>, <http://www.movesinstitute.org/xmsf/xmsf.html>
16. Davies, R.A., John, N.W., MacDonald, J.N., and Hughes, K.H., "Visualization of Molecular Quantum Dynamics: A Molecular Visualization Tool with Integrated Web3D and Haptics", Proc. ACM Web3D Symposium, 2005
17. Behr, J., Ohne, P.D., Roth, M., "Utilizing X3D for Immersive Environments", Proc. ACM Web3D Symposium, 2004
18. Polys, N., "Stylesheet transformations for interactive visualization: towards a Web3D chemistry curricula", Proc. ACM Web3D Symposium, 2003
19. Riganelli, A., Gervasi, O., Laganà, A., and Froehlich, J., "Virtual Chemical Laboratories and Their Management on the Web", Lecture Notes in Computer Science, 3480, pp. 905-912 (2005)
20. Fifth Dimension Technology Inc.; see <http://www.5dt.com>
21. For info related to the 6 degree-of-freedom Polhemus motion tracker visit: <http://www.polhemus.com/fastrack.htm>

22. Info on the 5DT HMD 800 series are available at the <http://www.5dt.com/products/phmd.html>
23. SOAP, the Simple Object Access Protocol, is a W3C standard that provides a way to communicate between applications running on different operating systems, with different technologies and programming languages over Internet. See: <http://www.w3.org/2000/xml/Group/>
24. The Universal Description, Discovery and Integration (UDDI) protocol creates a standard interoperable platform that enables applications to find and use Web services over the Internet. See <http://www.uddi.org>
25. The *Web Services Description Language* (WSDL) specification is available at the World Wide Web Consortium URL: <http://www.w3.org/TR/wsdl>
26. Shah A.V., Walters W.P., Shah R., Dolata D.P.: "Babel a Tool for Converting Between Molecular Data Formats", Computerized Chemical Data Standards: Databases, Data Interchange, and Information Systems, , STP 1214, R. Lysakowski and C. E. Gragg, Eds., ASTM Philadelphia (1994); http://openbabel.sourceforge.net/wiki/Main_Page
27. Aguilar, A., Albertí, M., Laganà, A., Pacifici, L.: A Molecular dynamics study for isomerization of rare gas solvated (benzene)_n-alkaline ion heteroclusters, Chem. Phys., in press.

Yeast Naked DNA Spatial Organization Predisposes to Transcriptional Regulation*

Oriane Matte-Tailliez^{1,2}, Joan Hérisson², Nicolas Ferey², Olivier Magneau³,
Pierre Emmanuel Gros², François Képès⁴, and Rachid Gherbi²

¹ Inference and Learning, LRI, UMR CNRS 8326, Université Paris 11,
F-91405 Orsay Cedex, France
oriane.matte@lri.fr
<http://www.lri.ia/~oriane>

² Bioinformatics Team, LIMSI & IBISC CNRS, Genopole Evry &
³ VENISE transversal action on V&AR, LIMSI-CNRS,
BP 133, F-91403 Orsay Cedex, France

{herisson, ferey, magneau, gros, gherbi}@limsi.fr

⁴ Epigenomics project & Atelier de Génomique Cognitive, CNRS UMR 8071, Génopole,
Tour Evry2, 523 place des terrasses de l'Agora,
F-91034 Evry, France
Francois.Kepes@genopole.cnrs.fr

Abstract. This paper presents a new structural-based approach to explore spatial organization of naked DNA on a whole chromosome sequence and its biological features related to gene regulation. A 3D trajectory representation on full-length yeast chromosomes based on Bolshoy's conformation model is discussed. These trajectories are predicted by our visualizing system ADN-Viewer. Observations show interesting geometric properties of chromosomes dealing with variability of 3D structures and the fact that regions linearly distant could be spatially close. These new observed phenomena are correlated then with biological considerations. In particular, transcriptional co-regulation of the data of Lee *et al.*, 2002 are exploited. A characterization parameter (RLS), ratio of linear distance and 3D one, was computed for each couple of genes. The co-regulated genes are found to be either linearly distant and spatially close, or linearly close. The co-regulated genes arranged in 1D-clusters could be detected directly in raw data. But, our model offers new predictions of co-regulated genes thanks to 3D-clusters. Then, we concluded that yeast naked DNA spatial organization seems to predispose to transcriptional regulation.

1 Introduction

The amount, variety and complexity of the genomic data require the use of techniques allowing a total integrated exploration and analysis like Visualization increased by Virtual Reality [1,2,3]. Whereas the proteins are the subject of many works of modeling and visualization, still very little work has been done on the DNA except 3D graphical representation of DNA primary sequences [4,5] and transforming in matrix to reduce complexity. Several works are related to the analysis and understanding of

* This work was supported by LIMSI-CNRS and Génopole ®.

transcriptional regulatory networks through large scale studies, in *Saccharomyces cerevisiae* [6,7,8], but the 3D organization of genes implicated in these networks [8,9,10,11,12] are still mostly unknown. However, some works, using different techniques [13,9] tried to understand how the three-dimensional structure properties are implied in functional mechanisms and how 3D-structure is conserved in regulatory regions of genes [14]. A recent work [8] has showed that *Saccharomyces cerevisiae* possesses a periodic spatial organization genome in concordance with its transcriptional regulation network. For two others eukaryotes *C. elegans* and *D. melanogaster*, the genome architecture was shaped by regulatory intergenic DNA [9]. Communication between distal chromosomal elements is essential for control of many nuclear processes. Models proposed direct contact interactions [15] but long-range contacts were been still controversial until recently and Carter *et al.* [16] have provided the first direct evidence within the mouse genome.

In this paper, we address the exploring of relationships of *Saccharomyces cerevisiae* genome spatial organization and transcriptional regulation by 3D modeling and visualization approaches. Our aim is to determine whether the genome basic architecture (3D spatial organization of DNA resulting from conformational models) [17,18,19] presents a predisposition in favor of its transcriptional co-regulation as genes are known to be co-regulated by transcriptional factors. DNA is generally considered by its primary sequence (succession of bases A, T, G, C). A new way of studying this molecule is to increase such representation by its *in silico* spatial conformation information. We consider that co-regulated genes which are linearly very distant in the sequence may be spatially close. This implies a folding up and supercoiling, as well as a specific and conserved curvature in the final organization of the genome [8]. This folding up supporting a certain co-regulation of genes (in particular supporting the energy level) must have an intrinsic pattern in the primary sequence.

Existing tools for the investigation of such properties are very limited. The work carried out in this paper uses our software tools previously described [20,21]. Each *S. cerevisiae* chromosome was 3D reconstituted with ADN-viewer obtaining thus a spatial trajectory (3D coordinates for each base pair). From the data of this modeling, we propose other tools which make it possible to consolidate the idea of relation between spatial organization and genome regulation.

2 Materials and Methods

2.1 Virtual Reality Platform and 3D DNA Model

The LIMSI-CNRS laboratory, through its scientific and technological action VENISE (<http://www.limsi.fr/venise>), is equipped with a Virtual Reality platform, which is materialized today by 2 retro-projected stereoscopic screens of 2mx2m. One of the major scientific stakes of this action is the immersive visualization and exploration by the contents of genomic information.

The software ADN-Viewer used for the 3D prediction of the trajectory of DNA has been published in a previous work [20] and here, described briefly. ADN-Viewer is a powerful graphic software tool which allows visualization and virtual exploration of

any huge naked DNA sequence. In order to build the 3D structure of DNA, two kinds of input data are required: DNA sequence in textual format and a 3D conformation model that provides rotations and a vertical translation [20]. For each di-nucleotide, the rotation table provides 3 angular values (O_x, O_y, O_z). The translation is constant and represents the raise. Several prediction models of 3D conformation exist. The more widely used are [8,22] and [18] ones. ADN-Viewer is based on Bolshoy's model [22] because it is the only one that provides the algorithm of the 3D trajectory prediction. The visualization of DNA sequence is very fruitful but not enough and it is necessary to carry out quantitative studies on the DNA molecule and its contents (genes, introns, exons, transposons, etc.). The visualization of DNA content needs interfacing ADN-Viewer with annotated accessible genomic databases or databanks. ADN-Viewer allows the user to access all the annotated information of the database through a middleware [21] and to visualize them.

2.2 3D DNA Degree of Freedom Computation Algorithm

The DNA Degree of Freedom (DNADoF), as defined here below, makes it possible to determine the maximum 3D spatial aperture of any DNA segment (points of interest). Within a chromosome, the DNADoF of any point of interest is defined mathematically as the maximum angle at the cone's vertex of this point (see Figure 1). Moreover, this cone does not cut and does not contain the 3D trajectory of the chromosome. The DNADoF algorithm is based on the computation of a sphere centered on the point of interest. This sphere is digitalized and initialized to 0 value. Each 3D point of the trajectory is then projected on the sphere. Then we set the value of each sphere digit to 1 where a 3D point is projected. At this step, we have a sphere with 0 or 1 values. Now, the goal is to find, on the sphere, the largest circular area containing only contiguous 0 values. Indeed, this area represents the free-spatial field of a point of interest without intersecting the chromosome trajectory. In order to measure this area, a morphomath-based algorithm is performed. It iteratively "propagates" values 1 on the sphere. This propagation is performed until all sphere digits are set to values 1. If the number of iterations is N, it defines the DNADoF of the point of interest. Both projection and propagation processes are described below.

For the projection of the 3D DNA trajectory, the algorithm takes the 3D positions of the center of each nucleotides plate (P_i), and it computes the polar coordinates (ρ, θ, ψ) centered on this point. For each plate, the algorithm fills the projection sphere (S_i) in order to obtain the following result:

$$S_i(\theta, \psi) = \begin{cases} 1 & \text{for any nucleotide plate} \\ 0 & \text{elsewhere} \end{cases} \tag{1}$$

The propagation process is carried out from here using a simple dilation operation (morphomath) which consists in changing all '0' values into '1' values if these 0 are neighbors of value 1. In order to perform the propagation in a homogeneous way, it is

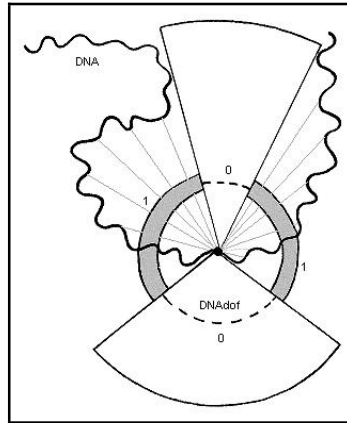


Fig. 1. An example illustrating the computation of the DNA Degree of Freedom (DNADoF). The figure represents the result obtained after running both projection and propagation processes (as defined in section 2.2). DNADoF determines here the largest 3D spatial aperture (cone angle) of the DNA point P within a DNA trajectory. The sphere centered on P has either values 0 (accessible) or value 1 (inaccessible).

necessary to use an identical angular sampling step (q) for the two angular variables θ and ψ . Finally, we define the DNADoF as follows:

$$\text{DNADoF} = 2.N.q \quad (2)$$

2.3 Datasets

Generation of co-regulation data. The data used to build the co-regulation pairs data set was 106 regulators studied by Chromatin Immunoprecipitation (ChIP) by Lee *et al.* [6]. Data were separated by regulator and by chromosome. Then, all possible co-regulated gene couples (pairs of genes adjacent to each other) for each regulator were computed.

3D-based distances of gene couples. Let RLS be the ratio of linear distance and spatial distance between two chromosome coordinates. The linear distance is the number of nucleotides between two coordinates, and the spatial one is the Euclidean distance in Angstrom between these two coordinates. In this study, we computed linear and spatial distances from the gravity center of each gene, and that for all gene pairs. The larger the RLS is, the spatially closer the considered two genes are. Linear distances between genes and other gene features were automatically collected with GenoMEDIA software [21].

3 Results and Discussion

3.1 Visualization of the Whole Chromosomes

The chromosomes 1, 2, 3 and 9 were modeled and visualized with ADN-Viewer (Figure 2). The visualization made it possible to notice that the chromosomes are

compacted structures and that there are zones of spatial proximity. The results show that the degree of apparent curvature varies by domain along the chromosomes, leading to compact zones and a relaxed one. The model clearly shows the circular behavior of the chromosomes, with two telomeres spatially closed, especially for the chromosome III. These results are in concordance with Dekker *et al.* work [23].

The above observations show that application of the Bolshoy *et al.* model is sufficiently accurate to allow rich comparisons between genome segments issued from various chromosomes, even if these chromosomes are from the same organism.

It suggested that the compactness of genomes may be achieved partly by the intrinsic curvature of naked DNA. It also showed that genomic DNA sequences display three-dimensional structures which are universally shared by most of them. It has given us a new image of many chromosomes, with two different feature: First, the quite universal pseudo-periodic of their compactness structure; second, the extreme variability of their local compactness.

Another interesting observation concerns the spatial availability of some zones. A good manner to measure this availability is to compute the DNADoF and to display its distribution along the chromosomes I, II, III, IX (Figure 3).

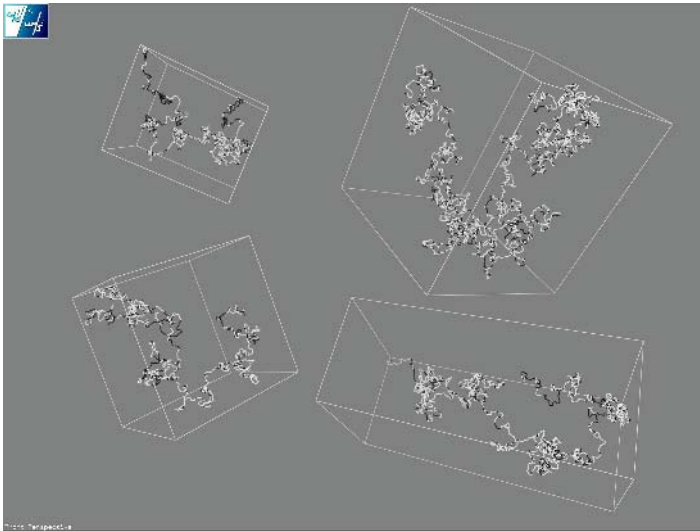


Fig. 2. Snapshots of ADN-Viewer for chromosomes I, II, III and IX. ORFs are in white color and intergenic regions in black

3.2 Distribution of the Co-regulated Genes Within the Topology in the Chromosome

Figure 4 shows the distribution of co-regulated pairs of genes and the number of transcription factors that regulate these pairs. Genes co-regulated by a high number of factors seem to be either clustered on the sequence, or linearly distant on the sequence but spatially close.

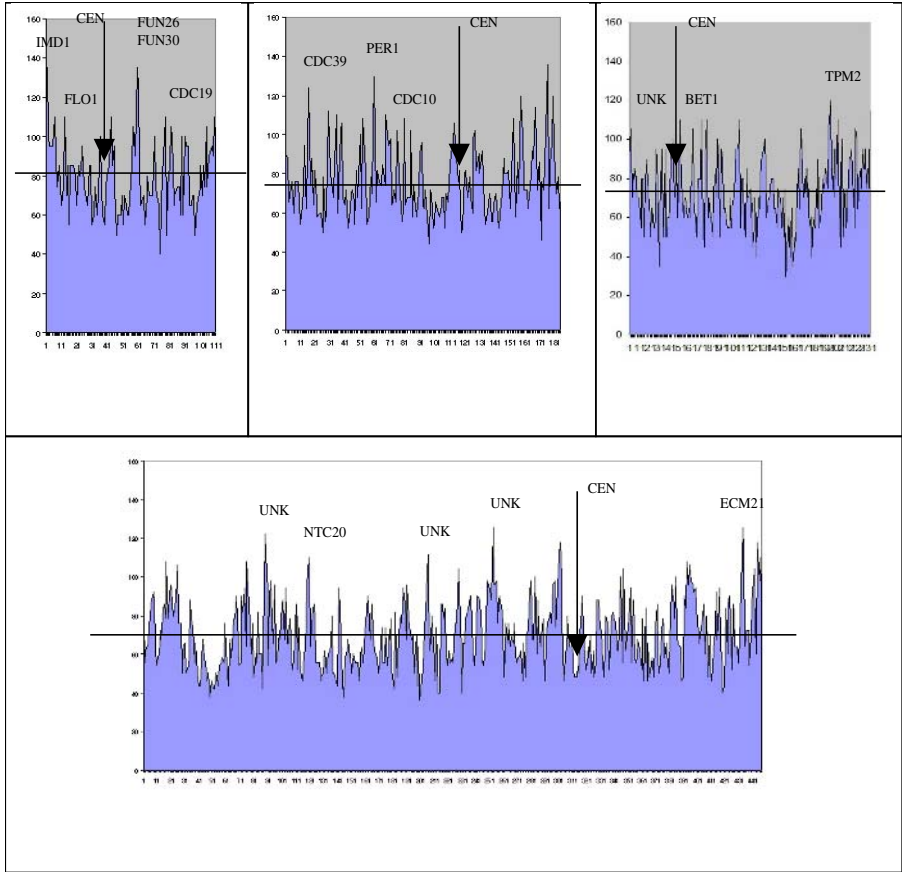


Fig. 3. DNADoF distribution along the chromosomes I, II, III, IX has similar profile. But it increases in a way inversely proportional to the chromosome size. For chromosome I and IX, the telomeres and subtelomeres are more accessible than central zones. For chromosome II, the left arm is accessible (telomere and subtelomere) while the right arm is only accessible at the telomere region.

We note (Table 1, column 3) that only a low level of spatially close genes is signaled to be co-regulated by [6]. Several explanations could be listed: First, the data of co-regulation are not exhaustive, and do not represent all the cellular conditions; second, the spatially close genes could interact physically to assume another biological process (recombination, duplication...). We noted on several cases that these juxtapositions correspond to duplication zones. Another evident explanation would be that these not co-regulated genes are 3D close relations because they are 1D close relations of genes 3D co-regulated, but they do not interact.

Chromosomes III and IX have approximately the same percentage of co-regulated genes among all regulated genes; see Column 1 (A+B+C, Figure 3, top). On the other

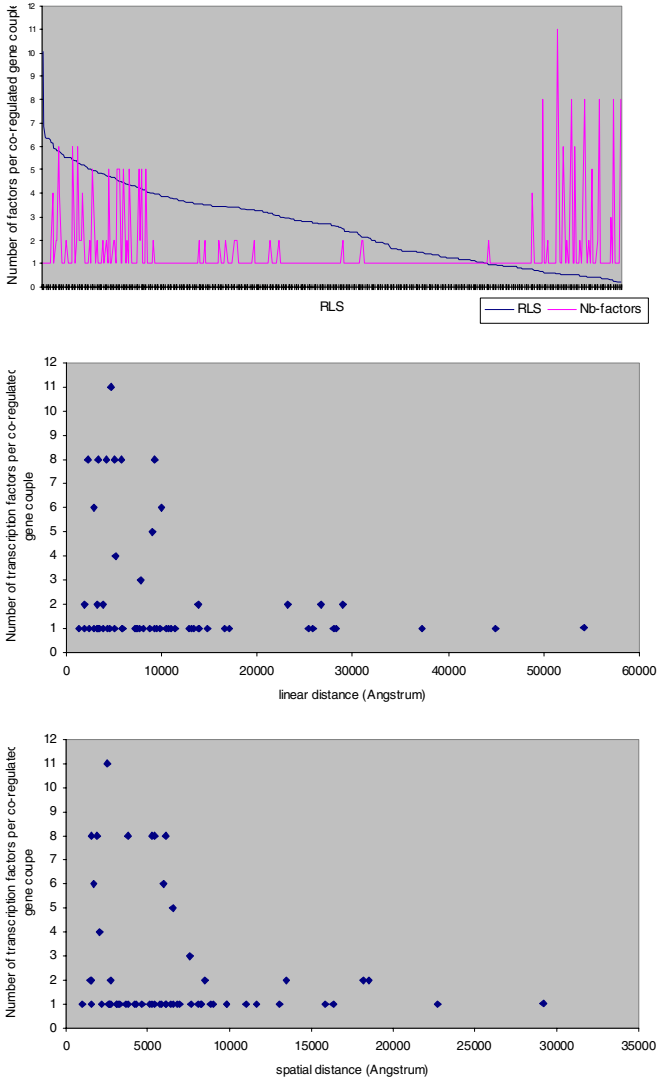


Fig. 4. The top graphic represents the number of transcription factors in function of RLS for each co-regulated gene couple (minimum of one transcription factor). RLS is the ratio between the linear distance (given in nucleotides) and the spatial distance (given in Angstroms). Spatial distance was computed from 3D-DNA model. Numbers of transcription factors by gene couple were generated from the data of Lee *et al.* [6]. Gene couples co-regulated by more than two transcription factors are linearly clustered (right of the figure) or on the contrary, linearly distant but spatially close (high RLS values, in the left of figure). In the lower graphics, for low values of RLS, the number of transcription factors that regulated gene pairs is inversely proportional to the linear distance and the spatial distance.

Table 1. Percentages of co-regulated genes with $R_{LS} > \text{mean} + \text{standard deviation}$. A, B and C correspond to the domains on the Figure 3 (top).

	co-regulated genes with $R_{LS} > \text{mean} + \text{stand_dev}$		
	/ all regulated (A+B+C)	/ co-regulated genes in 1-clusters (A+C)	/ all couple genes with $R_{LS} > \text{mean} + \text{stand_dev}$ (A+ other $R_{LS} > \text{mean} + \text{stand_dev}$)
Chr II	3.4%	64.4%	0.44%
Chr III	18%	54%	3.8%
Chr IX	17%	72%	3%

hand, there are five times less co-regulated genes compared with the two chromosomes previously quoted. Chromosome II has a size about three times higher than chromosomes III and IX. The small chromosomes are proportionally less compact than the large ones [20]. One measured a larger accessibility degree (mean) for these small chromosomes (data not shown), appears to be a valid explanation for the fact that the percentages of spatially closed co-regulated genes are higher.

The visualization represents a powerful technique to explore the features of the biological 3D structures. The goal of this paper was to mark the fact that there is a most probably relation between the intrinsic property of three-dimensional structure dictated by the nucleotidic primary sequence and the properties of genes including their regulation. If the genes are organized linearly [24], they are also organized spatially. Moreover, it has been shown that the chromosomes preserve their organization within the nucleus from generation to generation [25], which consolidates this assumption. The data of structure 3D resulting from our modeling were enriched by the regulation data of Lee *et al.* [6]. We noted that regulations are done on close groups of genes on the sequence (cluster) and other regulations touch very linearly distant but spatially close genes.

In chromosomes, we observed by a complementary representation in dynamical graphs (data not shown) that genes having the most relationships and spatially close together correspond to the sub-telomeric areas, known to be implicated in genome organization. Moreover, for chromosomes III and IX, telomeric or sub-telomeric areas were implied in this last kind of regulation. Among the co-regulations that gather distant areas, the genes controlled by a greater number of factors correspond to those which are known to have boundary sequences named “insulators” in their regulating sequence. On chromosome III, that concerns the areas HMR, HML and MAT. On chromosome IX, among genes implied, we found the cluster including HXT12 whose a member of the same family (HXT17) was placed on the chromosome XIV and supposed to be an insulator [26]. The combination of the properties of accessibility and

space proximity gives the areas more chance to meet, and the genes more chance to be co-regulated.

4 Conclusion

We have shown that the spatial conformation of naked DNA on full-length yeast chromosomes predispose to biological needs, in particular transcriptional co-regulation. Our results are not in discordance with the model of Cook [27,28] and Képès [12] pointing to mRNA transcription as a major architect of the prokaryotic genome structure. Besides, this work presents a first large scale validation of Bolshoy's model [22]. Our results on chromosome predicted 3D-structure could be discussed regarding other biological constraints of yeast (recombination, duplication, evolution, conservation of genetic information), showing that naked DNA intrinsic 3D-structure is of primordial importance for the functional organization of genome.

References

1. Rojdestvenski, I., Modjeska, D. and Pettersson, F.: Sequence World: A Genetics Database in Virtual Reality. International Conference on Information Visualization IEEE (2000) 513-517
2. Gilbert, D.R., Schroeder, M. and van Helden, J.: Interactive visualization and exploration of relationships between biological objects. Trends Biotech. 18 (2000) 487-494
3. Férey, N., Gros, P.E., Hérisson, J. and Gherbi, R.: Exploration by visualization of numerical and textual genomic data. J. Biol. Physics and Chem. 4 (2004) 102-110
4. Randic, M., Vracko, M., Nandy, A and Basak, S.C.: On 3-D graphical representation of DNA primary sequences and their numerical characterization. J. Chem. Inf. Comput. Sci. 40 (2000) 1235-1244
5. Li, C. and Wang, J.: On 3-D representation of DNA primary sequences. Comb. Chem. & High Throughput Screen 7 (2004) 23-27
6. Lee, T.I., Rinaldi, N.J., Robert, F., Odom, D.T., Bar-Joseph, Z., Gerber, G.K. *et al.*: Transcriptional regulatory networks in *Saccharomyces cerevisiae*. Science 298 (2002) 799-804
7. Guelzim, N., Bottani, S., Bourguin, P. and Képès, F.: Topological and causal structure of the yeast transcriptional regulatory network. Nature Genetics 31 (2002) 64-68
8. Képès, F.: Periodic Epi-organization of the Yeast Genome Revealed by the Distribution of Promoter Sites. J. Mol. Biol. 329 (2003) 859-865
9. Nelson, C., Hersh, B.M. and Carroll, S.B.: The regulatory content of intergenic DNA shapes genome architecture. Genome Biology 5 (2004) R25
10. Cremer, T. and Cremer, C.: Chromosome territories, nuclear architecture and gene regulation in mammalian cells. Nature Rev. Genet. 2 (2001) 292-301
11. Gerlich, D., Beaudouin, J., Kalbfuss, B., Daigle, N., Eils, R. and Ellenberg, J.: Global chromosome positions are transmitted through mitosis in mammalian cells. Cell 112 (2003) 751-764
12. Képès, F.: Periodic transcriptional organization of the E.coli genome. J. Mol. Biol. 340 (2004) 957-64
13. King, G.J.: Stability, structure and complexity of yeast chromosome III. Nucleic Acids Res. 21 (1993) 4239-4245

14. Jáuregui, R., Abreu-Goodger, C., Moreno-Hagelsieb, G., Collado-Vides, J. and Merino, E.: Conservation of DNA curvature signals in regulatory regions of prokaryotic genes. *Nucleic Acids Res.* 31 (2003) 6770-6777
15. de Bruin, D., Zaman, Z., Liberatore, R.A. and Ptashne, M.: Telomere looping permits gene activation by a downstream UAS in yeast. *Nature* 409 (2001) 109-113
16. Carter, D., Chakalova, L., Osborne, C.S., Dai, Y. and Fraser, P.: Long-range chromatin regulatory interactions in vivo. *Nature Genetics* 32 (2002) 623-626
17. Bolshoy, A., McNamara, P., Harrington, R.E. and Trifonov, E.N.: Curved DNA without A-A: Experimental estimation of all 16 DNA wedge angles. *Proc. Natl. Acad. Sci. USA* 88 (1991) 2312-2316
18. Cacchione, S., De Santis, P., Foti, D.P., Palleschi, A. and Savino, M.: Periodical polydeoxynucleotides and DNA curvature. *Biochemistry* 28 (1989) 8706-8713
19. Ponomarenko, M.P., Ponomarenko, J.V., Kel, A.E. and Kolchanov, N.A.: Search for DNA conformational features for functional sites. Investigation of the TATA box. *Proceedings of the International Pacific Symposium of Biocomputing (PSB)* (2000)
20. Gherbi, R. and Hérisson, J.: Representation and Processing of Complex DNA Spatial Architecture and its Annotated Content. *Proceedings of the International Pacific Symposium of Biocomputing (PSB)* (2002)
21. Gros, P-E., Férey, N., Hérisson, J. and Gherbi, R.: A Distributed Multimedia Database Visualization within an Immersive Environment for Bioinformatics. *Proceedings of the International Conference of Bioinformatics and Applications, Lauderdale, FL, USA.* (2004)
22. Shpigelman, A.S., Trifonov, E.N. and Bolshoy, A.: CURVATURE: Software for the analysis of curved DNA. *Comput. Appl. Biosci.* 9 (1993) 435-440
23. Dekker, J., Rippe, K., Dekker, M. and Kleckner, N.: Capturing Chromosome Conformation. *Science* 295 (2002) 1306-1311
24. Spellman, P.T. and Rubin, G.M.: Evidence for large domains of similarly expressed genes in the *Drosophila* genome. *J. Biol.* 1 (2002) 5
25. Weitzman, J.B.: Transcriptional territories in the genome. *J. Biol.* 1 (2002) 2
26. Meneghini, M.D., Wu, M. and Madhani, H.D.: Conserved histone variant H2A.Z protects euchromatin from the ectopic spread of silent heterochromatin. *Cell* 112 (2003) 725-736
27. Cook, R.C.: Predicting three-dimensional genome structure from transcriptional activity. *Nature Genetics* 32 (2002) 347-352
28. Cook, R.C.: Nongenic transcription, gene regulation and action at a distance. *J. Cell Sci.* 116 (2003) 4483-4491

Interactive Real-Time 3D Visualization of Grid Portal for Quantum Mechanics*

Sung-Wook Byun, Yun-Kyoung Lee, and Chang-Sung Jeong**

Department of Electronics Engineering, Graduate School, Korea University,
5-ka, Anam-Dong, Sungbuk-ku, Seoul, Korea
sungwook@snoopy.korea.ac.kr, apple7224@korea.ac.kr,
csjeong@charlie.korea.ac.kr

Abstract. This paper describes work-in-progress towards developing grid portal for quantum mechanics (QMWISE) featuring real-time 3D visualization. The goal of QMWISE project is to provide a powerful and convenient system for computational chemistry using grid technologies. In this paper, we propose an environment which enables computational chemists to calculate quantum mechanics problems and explore the result data through interactive real-time 3D visualization.

1 Introduction

In these days, computational chemistry is expected to play a major role in fields such as computer-aided chemistry, pharmacy, and biochemistry. Computational chemistry is used in a number of different ways. One particular important way is to model a molecular system prior to synthesizing that molecule in the laboratory. Although computational models may not be perfect, they are often good enough to rule out 90% of possible compounds as being unsuitable for their intended use. This is very important because synthesizing a single compound could require months of labor. A second use of computational chemistry is in understanding a problem more completely. There are some properties of a molecule that can be obtained computationally more easily than by experimental means. There are also insights into molecular bonding, which can be obtained from the results of computations that cannot be obtained from any experimental method. Computational chemistry now encompasses a wide variety of areas, which include quantum chemistry, molecular mechanics, molecular dynamics, Monte Carlo methods, Brownian dynamics, continuum electrostatics, reaction dynamics, numerical analysis methods, artificial intelligence, and others. Although these researches are essential for various part of science, they need a lot of resources.

* This work has been supported by KIPA-Information Technology Research Center, University research program by Ministry of Information Communication, Seoul Metropolitan and Brain Korea 21 projects in 2006.

** Corresponding author.

However, it is not easy to model a molecular structure. In order to obtain and analyze the properties of molecule, it needs a lot of annoying steps. For example, to optimize the proposed molecule, computational chemist should do as followings:

1. make a text-based input file
2. run a quantum mechanical calculation tool with input file under command prompt environment
3. check the result data frequently during calculation or wait until the calculation is finished
4. modify the result data with text editor to adapt them to visualization tool
5. explore 3D structure of result data with visualization tools such as Chem3D [1]
6. if the result is wrong, change input data value and calculate again

These steps make computational chemists not free while only one calculation is running. We have tried to solve this problem with grid technology.

In these days, grid technology is extending the horizons of computational chemistry, allowing aggregated computing resources to be harnessed in the solution of major problems [2]. We proposed workflow-based computational Grid portal for quantum mechanics (QMWISE) to provide a convenient and effective environment in order to ease the current quantum mechanical problems with grid technologies [3]. Providing Web-based interface makes users compute quantum mechanical problems and access to quantum mechanical calculation programs in any place that is connected to Internet. We described the architecture and user interface of QMWISE in Fig. 1. QMWISE system consists of the followings:

- a) Input Generator
translates user's input data into XML
- b) Data Broker
manages a lot of data efficiently
- c) Workflow Manager
generates workflow routines
- d) Data Viewer
shows the update data in real time
- e) Controller
controls calculation process

In this paper, we focus on an interactive visualization part of QMWISE, Data Viewer. Interactive visualization is the most powerful trend in visualization nowadays, in that it extends the visualization process by enabling users to ask questions of the data as their understanding of the situation evolves. Interactive visualization therefore enables the seeker to understand complex problems or phenomena, even when the questions themselves are not initially fully known.

Our goal is to make computational chemists sit on the desktop and be able to be free from their annoyance. The remaining sections of this paper describe the previous work of the computational chemistry visualization in grid computing in section 2, real-time 3D visualization of QMWISE system in section 3, the architecture of visualization part of QMWISE in section 4, usage scenario in section 5, finally, conclusion and future work.

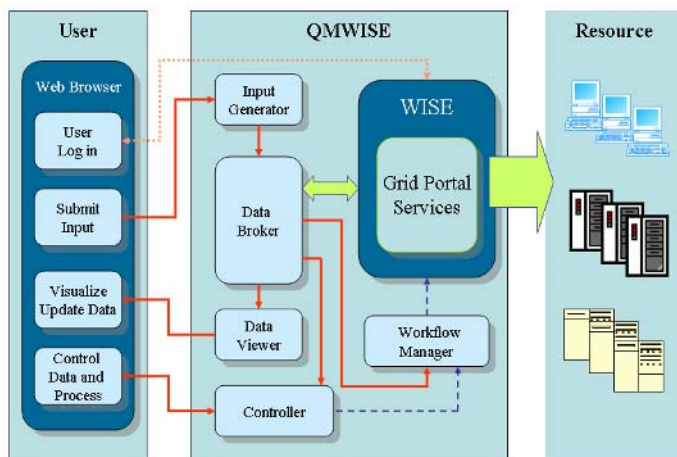


Fig. 1. The architecture of QMWISE

2 Previous Work

While a quantum mechanical calculation has been investigated long time, it is very difficult for computational chemists to see the three dimensional structure of data generated from calculation process in real time. Moreover, in order to analyze the results, a user has to use other tools that provide graphical environment when the process is finished. To overcome these problems, there were some efforts.

Grid-based portal featuring visualization is proposed by T. J. Jankun-Kelly et al [4]. They proposed Web-based visualization system which consists of three major components: (1) Web-based user interface to grid-enabled visualization services, (2) visualization Web application that tracks the exploration of visualization results, and (3) the portal application server that manages and coordinates the authentication for use of grid resources. Because they wanted to create platform-independent system, they used ECMAScript/Javascript and cookie for implementing Web application. However, despite of good attempt, it lacks interactivity and functionality.

In quantum mechanics, there are two major grid portal systems. Design and implementation of the intelligent scheduler for Gaussian Portal on quantum chemistry Grid (QC Grid) are investigated by T. Nishikawa et al [5]. QC Grid consists of a Web interface, a meta-scheduler, computing resources, and archival resources on grid infrastructure. The QC Grid user has a Web-based interface that does all operations such as uploading the input file, controlling the job, displaying job status, and getting results. Although QC Grid provides various functions for grid portal, however, it lacks the concept of visualization.

GAMESS Web portal services were proposed by Kim K. Baldrige et al [6]. They purposed development of computational chemistry Web portal. Initially, GAMESS portal was to isolate users from the complexities of the computational grid by providing a standard user interface for accessing input and output, running jobs on one of a variety of platforms without logging into those platforms, and the ability to transfer

data among various platforms. Also, the portal has facilities for processing the output of a particular run via visualization with their computational chemistry visualization and analysis tool, QMView.

QMView [7-9] program was designed to facilitate the visualization and interpretation of quantum mechanical data. Visualization of molecular system includes displaying properties such as the atomic structure of systems obtained by energy minimization, animation of the structural and orbital changes along a reaction paths, the illustration of dynamic vibrations of a molecule, or viewing large datasets of volumetric properties such as electron density or density difference distributions, molecular orbitals, and electronic potential maps.

QMView has a user-friendly interface that allows users to manipulate interactively many features of the molecular structure and property, including positioning and structure representation, via mouse-activated dialog boxes. Although the interface may allow input of results from any of the popularly used quantum mechanical software, they have focused GAMESS [10], a widely distributed quantum chemistry code. QMView has been designed with the special feature of working in distributed mode with GAMESS, the latter running on a supercomputer, the former running on a Silicon Graphics platform. Ancillary programs provide a method of obtaining output of graphic images in various media, including hardcopy, PostScript files, slide and video. Although QMView represents various functions to analyze the data effectively, GAMESS portal does not provide a unified environment like QC Grid.

At this point, we propose new Grid portal system with real-time 3D visualization for quantum mechanics.

3 Real-Time 3D Visualization

We have been developing an interactive visualization module meeting the following main objectives and requirements:

- 1) Real-time visualization
- 2) Interactive environment
- 3) Displaying necessary data from massive output data

3.1 Real-Time Visualization

In computational chemistry, it is difficult for a user to predict the time of calculation that may take a month. Moreover, a user cannot know if the calculation goes right till the process is completed. In order to remove wasting time innovatively, we suppose real time 3D visualization system. Our visualization system provides real-time update function. Through our visualization system, a user can see real-time 3D structure and various information of molecule which is being calculated. If a user know that the calculation is going wrong by watching real-time 3D visualization, users can stop the process immediately. Because we want to merge computation system and visualization system into Grid portal, we should implement visualization system in Web browser. That is the reason why we use Java3D API. Java3D API is a hierarchy of Java classes which serve as the interface to a sophisticated 3D graphics rendering and sound rendering system, and used for writing interactive 3D graphics applications and

applets. Java3D is also built upon Java, a language that focuses on portability and Web-based architectures [11].

3.2 Interactive Environment

The use of interactive visualization in our system provides an environment that enhances research productivity greatly by relying on 3D visualization through Web environment and facility of transforming 3D data by user's input. The use of 3D visualization increases productivity by at least 40% compared with conventional non-interactive methods [12]. In our system, a user can see the result information of calculation through DataViewer module in Web browser that provides various functions, such as 3D visualization, 3D animation of molecule, display of molecular properties, etc. What a user have to do is just moving and clicking the mouse where he is interested in. Java3D defines a set of classes that let the user use the mouse to easily pick an object in the 3D scene and to transform an object freely. Such features are especially useful for interactive visualization system.

3.3 Displaying Necessary Data from Massive Output Data

In quantum mechanics, calculations to obtain interesting properties of molecule are to solve differential equations. The goal of this process is to find out eigenvalues of matrix operations. These eigenvalues are the properties of newly-modeled molecules, and produced continuously at each calculation iterations until a specific condition is met. If initial condition of molecule is set wrong, the calculation may not be finished, and the result data may be produced infinitely.

The output data of calculation include many information such as molecular geometries using energy optimization, IR intensities, intrinsic reaction path, dynamic reaction coordinate, etc. However, it is reckless and impossible to fetch the all data in order to visualize some information. Hence, we need a specific module which has functions of filtering output data. For example, if a user wants to see the geometry change of molecule by this time, visualization system doesn't have to fetch the whole data which is produced. Visualization system chooses only coordinate parts of molecule from output data, then, produces a geometry animation, and shows it to a user.

3.4 Other Things

In the course of implementing and testing visualization system, several problems arise. At first, we implemented an algorithm which updates automatically when one cycle of iteration calculation process is finished. However, when the period of calculation iteration is very fast, the processing speed of visualization system cannot keep up with the update data. Also, when a user investigates the 3D structure of molecule, automatic update may let interesting data go out of sight. Thus, we modified the algorithm by dividing data into two categories - one is updated automatically, the other is manually. The former includes the progress of calculation, properties of molecules, etc. that is text-based. The latter includes 3D geometry, animation of geometries, etc. that is graphic-based. Hence, by pressing 'Update' button, a user can see recent data from calculation in real time.

4 Architecture of Visualization Part

In this section, we describe the architecture of DataViewer in detail (Fig. 2). DataViewer consists of two modules - Visualizer and Data Filter. Visualizer provides interactive 3D visualization environment, and communicates with Data Filter by user's interactive input. Data Filter receives messages from Visualizer, then pick out necessary data from huge output data through Data Broker, and returns them.

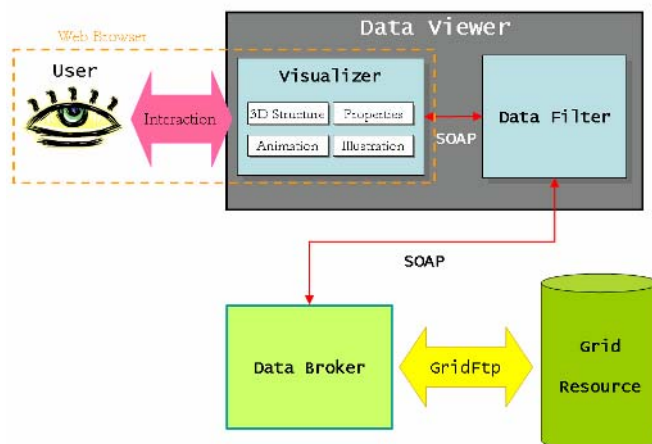


Fig. 2. The architecture of interactive real-time 3D visualization system of QMWISE

4.1 Visualizer

Visualizer focuses on visualizing necessary information mostly. Most computational chemists who uses quantum mechanical calculation tool want to see :

Real-time 3D atomic structure

Visualizer displays real-time 3D molecular structure which is generated from result data obtained from quantum mechanical calculations being processed. This structure can be able to translate, zoom, and rotate 3D geometry freely by mouse click. Also, by mouse pointing on a specific atom or bond of molecule, it can show properties of the atom or bond such as position, length, type, etc. As we mentioned above, 3D molecular structure should be updated manually. This is done by pressing 'Update' button.

Animation of the structural changes

Visualizer provides an animation of 3D molecular structure. This function is implemented by using scene graph structures of Java3D. Java3D's scene graph-based programming model provides a simple and flexible mechanism for representing and rendering scenes. The scene graph contains complete description of the entire scene. This includes the geometric data, the attribute information, and the viewing information needed to render the scene form a particular point of view. Hence, we adjust

changes of each atom's position from calculation iteration to each atom's position of transformation group in scene graph.

This animation function shows the progress of changes of molecular structure by that time. It also provides free transformation function like real-time 3D atomic structure.

Other properties

The illustration of dynamic vibrations of a molecule viewing and large datasets of volumetric properties such as electron density or density difference distributions, molecular orbitals, and electrostatic potential maps are being added to our system.

4.2 Data Filter

Data Filter provides a function of filtering output data. While Visualizer is embedded in user's Web browser, Data Filter is running on QMWISE server, thus, transmission of all data makes visualization system slow and heavy. By choosing the exact data for visualization, we can reduce data transmission time.

In QMWISE system, all internal data is changed to XML format. Data Broker manages input and output XML data of calculation process in QMWISE system. If Data Filter receives query from Visualizer by user interaction, it pick out appropriate data from Data Broker, then send them back to Visualizer. The communication protocol in this system is implemented by using SOAP (Simple Object Access Protocol).

5 Usage Scenario

To demonstrate the visualization part of QMWISE, we'll describe a typical scenario. In this scenario, a computational chemistry scientist named Kyoung wants to optimize the structure of the molecule which is designed by non-linear optics theory and calculate physical properties of the molecule. Kyoung first enters QMWISE URL into her Web browser. After logging onto the system, she submits the data of the molecule, such as geometry, charge, spin multiplicity, etc. The input data is translated into XML format by Input Generator, then, sent to Data Broker. Data Broker divides input data by a specific rule, and sends each data to Workflow Manager and grid resources. After Workflow Manager generates workflow routines according to user's input, and submits the workflow to WISE system, WISE system produces the result data by the workflow communicating with grid resources.

Now, Kyoung can see the 3D visualization of result data in real time through DataViewer (Fig. 3). Kyoung can explore the 3D data freely with rotating, moving, zooming the 3D data using mouse interaction. Also, she can see the properties of each atom of molecule through text panel in Web browser, such as position, bond length, type, etc. According to user's interaction Data Filter in Data Viewer selects the necessary data from Data Broker. If Kyoung wants to see the optimization process of molecule, she can press Animation Button in Web browser. Then, Data Viewer shows the animation of molecule by that time. By checking the result through 3D visualization in real time during calculating process, Kyoung can know if the calculation is going

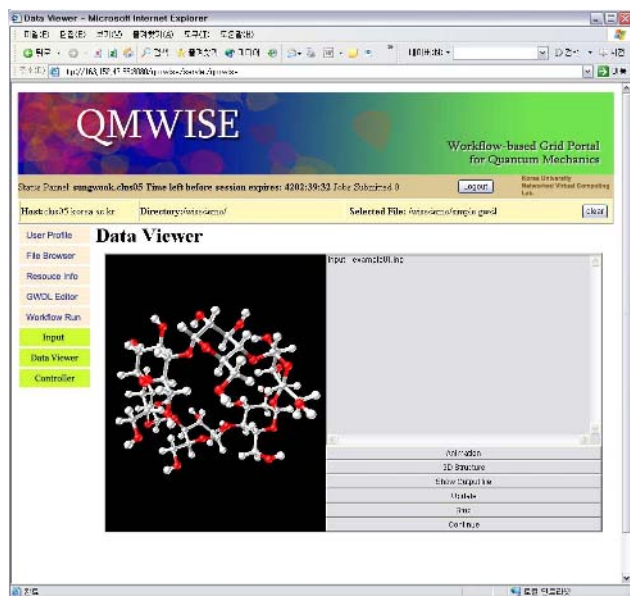


Fig. 3. The screenshot of real-time 3D visualization system of QMWISE

well or not easily. This feature helps a user save time. Also, providing an environment merging visualization system and grid portal, users don't get annoyed about using several tools separately to analyze the result data.

6 Conclusion and Future Work

In this paper, we propose interactive real-time 3D visualization of Grid portal for quantum mechanics. Our interactive visualization system provides a unified environment of computation and visualization simultaneously. This system is implemented using Java3D technology which enables to embed 3D graphic contents into Web browser. Java3D has a set of classes which help to make an interactive environment.

In QMWISE system, DataViewer module is used for interactive visualization. To increase efficiency, we divide Data Viewer into two parts - Visualizer and Data Filter, the former is used to visualize the real-time 3D data in user's Web browser, and the latter is used to pick out appropriate data from huge output data. By doing this, we can reduce the data transmission, and load of visualization system.

Our goal is to increase efficiency of computational chemistry scientists and provide a convenient environment for research by removing nuisance.

Now, our visualization system does not contain all the features that are provided by commercial visualization tools. We have a plan of adding various functions which are necessary for computational chemists.

References

1. <http://www.cambridgesoft.com/>
2. G.C. Fox and D GANNON, "Computational Grids", *IEEE Comput SciEng*, Vol. 3, pp. 74-77, 2001
3. Sung-Wook Byun, Yun-Kyoung Lee, Yong-Won Kwon, So-Hyun Ryu, and Chang-Sung Jeong, "Workflow-Based Grid Portal for Quantum Mechanics", *GCC 2004*, LNCS 3252, pp. 625-632, 2004
4. T.J. Jankun-Kelly, Oliver Kreylos, John Shalf, Kwan-Liu Ma, Bernd Hamann, Kenneth I. Joy, and E. Wes Bethel, "Deploying Web-based Visual Exploration Tools on the Grid", *IEEE Computer Graphics and Applications*, Vol. 23(2), pp. 40-50, IEEE Computer Society Press 2003.
5. T. Nishikawa, U. Nagashima, S. Sekiguchi, "Design and Implementation of Intelligent Scheduler for Gaussian Portal on Quantum Chemistry Grid", *ICCS 2003*, LNCS 2659, pp. 244-253, 2003 <http://www.gaussian.com/>
6. K. K. Baldrige, J. P. Greenberg, "Management of Web and Associated Grid Technologies for Quantum Chemistry Computation", *ICCS 2003*, LNCS 2660, pp. 111-121, 2003
7. K. K. Baldrige and J. P. Greenberg, "QMView: A computational chemistry three-dimensional visualization tool at the interface between molecules and mankind", *J. Mol. Graphics*, Vol. 13, pp. 63-66, 1995
8. K. K. Baldrige and J. P. Greenberg "QMview as a Supramolecular visualization tool in Supramolecular Chemistry", *J. Siegel, Ed.: Kluwer Academic Publishers*, pp. 169-177, 1995
9. K. K. Baldrige, J. P. Greenberg, S. T. Elbert, S. Mock, and P. Papadopoulos, "QMView and GAMESS: integration into the world wide computational grid", *Proceedings of the 2002 ACM/IEEE conference on Supercomputing*, pp. 1-25, 2002
10. M. W. Schmidt, K. K. Baldrige, J. A. Boatz, S. T. Elbert, M. S. Gordon, J. H. Jensen, S. Koseki, N. Matsunaga, K. A. Nguyen, S. Su, T. L. Windus, M. Dupuis, J.A. Montgomery, "General Atomic and Molecular Electronic Structure System", *J. Comput. Chem.*, Vol. 14, pp. 1347-1363, 1993 <http://www.msg.ameslab.gov/GAMESS/GAMESS.html> GAMESS program
11. Vormoor, O., "Quick and easy interactive molecular dynamics using Java3D", *Computing in Science & Engineering*, Vol. 3(5), pp. 98-104, Sept.-Oct. 2001
12. D. Hohl, R. Idaszak, R. O. Jones, "Quantum molecular modeling with simulated annealing-a distributed processing and visualization application", *Proceedings of the 1990 conference on Supercomputing*, pp. 816-825, 1990

Development of a Virtual Reality Bicycle Simulator for Rehabilitation Training of Postural Balance

Nam-Gyun Kim¹, Yong-Yook Kim², and Tae-Kyu Kwon¹

¹Division of Bionics and Bioinformatics, Chonbuk National University,
561-756 Jeonju-si, South Korea
{ngkim, kwon10}@chonbuk.ac.kr

²Center for Healthcare Technology Developments, Chonbuk National University,
561-756 Jeonju-si, South Korea
yykim@chonbuk.ac.kr

Abstract. Development of a virtual-reality training system based on an exercise bicycle and a personal-computer for rehabilitation of motor functions and balance capability in elderly patients has been described. The system can take three inputs from the bicycle: the pedaling speed, the direction of the handles, and the location of the center of pressure on the supporting base of the bicycle. These inputs allow user interactions with a virtual environment that increase motivation of the user. A series of experiments were conducted with three different visual feedback conditions: without visual feedback of balance information; with visual feedback of weight shift; or with visual feedback of the center of pressure. The assessment of balance parameters obtained from the experiments showed the improvement of balance capability on the bicycle. Especially, the visual feedback of weight shift most increased the effectiveness of the training. The findings suggest that the system might be used as a balance and motor function rehabilitation system with further objective measurements of balance ability of the patients in longer terms.

1 Introduction

Postural balance of human is maintained by a complex mechanism utilizing the functions of cerebellum, equilibrium, and other various organs. Today, number of traffic accidents keeps increasing due to an increase in the traffic volume. At the same time, the population of the elderly has been also increasing. Such increases in the traffic accidents and the populations of the elderly are some of the main causes of increased number of reported cases of injuries to central nervous system such as stroke, traumatic brain injury, and various ailments requiring balance rehabilitation [1-2]. Such a loss of ability in controlling postural balance results in many kinds of complications in rehabilitative treatments.

A study on the training or the diagnosis of the postural balance can be categorized into either a clinical assessment or an objective and quantitative assessment. A clinical assessment of postural balance has been used by many researchers who reported the effectiveness of different methods for assessing postural balance control by indexes based on clinical assessment [3]. However, such clinical methods leave a space for objective and quantitative assessment toward more complete analysis.

Objective and quantitative assessments have advantages in that it quantifies various parameters such as swaying directions and the magnitude of sway. Kamen et. al [4] developed an accelerometer-based system for the assessment of balance and postural sway. Kooij et. al reviewed and compared different methodological ways to identify and quantify balance control using force plate, tracking of body center of mass, and electromyography [5]. Different methods to estimate the center of mass during balance assessment has been reviewed by Lafond et. al [6]. However, most of previous works related to balance rehabilitation concentrated on training or assessment in standing posture and there has been much smaller number of researchers who worked on balance rehabilitation in sitting posture [7-9]. However, most of the balance rehabilitation in both standing and sitting posture have a shortage in stimulating all the senses required for rehabilitation of postural balance and generally make the subject feel monotonous during training and diagnosis session. Therefore, there is a great demand for a new rehabilitation training system that not only provides a simulative environment that can stimulate all the senses related to postural balance but also enables quantitative analysis of related factors.

In this study, a system that can draw more attentions and maximize training effect by simultaneously stimulating various senses that are related to balance and can assess the effect of the stimulation has been suggested overcoming the shortcomings of conventional rehabilitation training system giving an opportunity for more quantitative and objective assessment. Moreover, the new system that utilizes exercise bicycles tries to achieve not only balance rehabilitation in sitting posture but motor rehabilitation of lower limbs by providing bicycle exercise.

2 System Configuration

The new bicycle training system is shown in Fig. 1. The monitor displays a virtual environment generated by a reality engine composed of a personal computer with a high-performance graphic accelerating board and a 3D virtual environment generation software. The parameters that are related to the pedaling speed, the rotation angle of handlebars, and the force measurements from load cells are acquired in real time through an A/D converter. Then, the riding speed and the heading direction in the virtual environment are determined by the acquired parameters enabling the interactions with the virtual environment. Moreover, an automatic load control device attached to the flywheel of the bicycle applies appropriate load to the pedals depending on whether it is an uphill or a downhill in the virtual environment. Figure 2 shows the connections between the inputs and the outputs and the construction of the reality engine.

2.1 Hardware Configuration

Detection of Riding Speed. The speed in the virtual environment is determined by the readings from Hall Effect sensor shown in Fig. 3 using Eq. (1) where t is the time between the signals observed at the sensor, and k is a speed parameter.

$$v = \frac{k}{t} \quad (1)$$

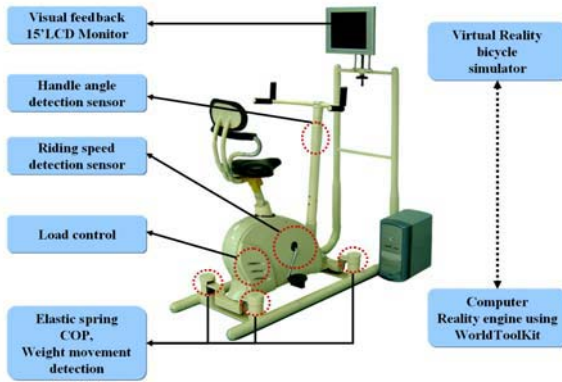


Fig. 1. Training system for postural control based on an exercise bicycle and a visual interface

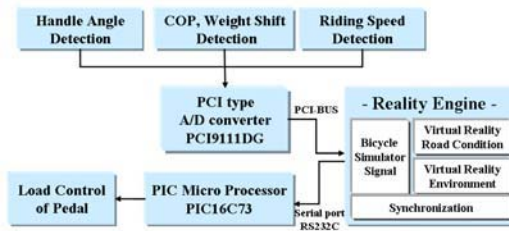


Fig. 2. Diagram of system connections

Detection of the Direction of Handlebar. The direction of the handlebar is measured using a one-turn potentiometer converter ($\pm 5V$ full scale). The analog voltage from the potentiometer converter was digitized by an analog-to-digital converter. In determining the heading direction of the handlebar, the middle value of the converter of the potentiometer is at $2.5V$ when they are heading in frontal direction. The direction of the handlebar is identified as the right direction whenever the output voltage from the converter is higher than $2.5V$, and the direction of the handlebars was determined to be left if it is lower than $2.5V$.

Springs at the Base. The springs attached to the virtual bicycle enables the rider to slightly pitch or rotate the bicycle by moving his or her weight so that the patient can feel the ride more realistic. The elasticity of the four springs shown in Fig. 4 were 11.22 kg/cm . The springs were chosen in full consideration of the weight of the bicycle and the rider. The springs were installed in front left, front right, rear left, and rear right parts of the supporting frame.

COP and Weight Shift Variation. Four load cells with maximum load of 100kg were installed below each spring to measure the load applied to the four locations at the base of the bicycle. The coordinate location of the center of pressure (COP) and the parameter of weight shift are calculated using Eq. (2~5) based on the inputs

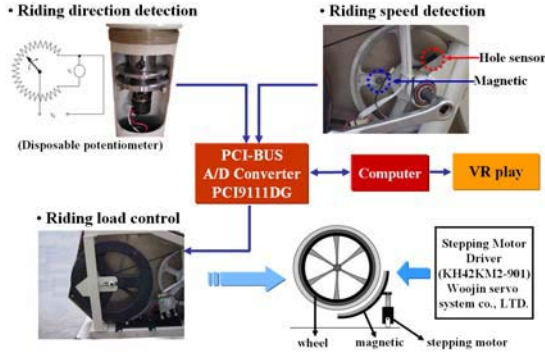


Fig. 3. Input devices of virtual reality bicycle for interactions with virtual environment

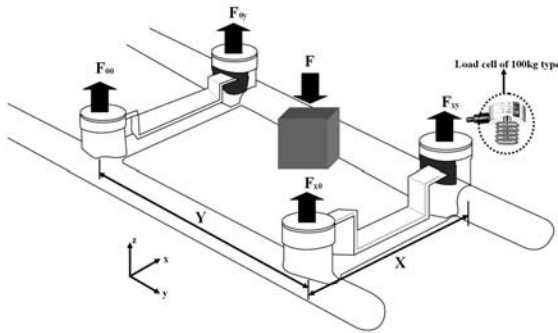


Fig. 4. Locations of the springs and the load cells at the base of the bicycle

from the load cells. The sum of vertical force is calculated using Eq. (2) and the distance of the center of pressure in x direction from the center of bicycle is calculated using Eq. (3) and the distance of the center of pressure in y direction is calculated using Eq. (4). The degree of weight shift in the right lateral direction is calculated using Eq. (5).

$$F_z = F_{00} + F_{x0} + F_{0y} + F_{xy} \tag{2}$$

$$COP_x = \frac{X}{2} \left[1 + \frac{(F_{0y} + F_{xy}) - (F_{00} + F_{x0})}{F_z} \right] \tag{3}$$

$$COP_y = \frac{Y}{2} \left[1 + \frac{(F_{xy} + F_{x0}) - (F_{00} + F_{0y})}{F_z} \right] \tag{4}$$

$$Weight\ shift = \left[\frac{F_z - (F_{0y} + F_{xy})}{F_z} \right] \times 100\% \tag{5}$$

2.2 Development of the Software for the System

The visuals of the virtual environment was developed using a 3D computer graphics tool [10]. The virtual environment included bicycle road, environmental images, and

surrounding objects. The design of a 3D environment was done with 3D computer graphics tool and the details of the 3D environment were generated using a 3D graphics library [11]. The programming of the interface between the virtual environment and the inputs from the A/D board was done with Visual C++ [12].

Figure 5 shows major subroutines and the order of the activation of the subroutines for the virtual environment with the initial screen. The virtual bike road is 6m wide two-way road with the whole length of 720m. The number of pixels corresponds to 1m was determined to be 20 at the bottom of the screen. Figure 6 shows the road with various objects such as trees, a rose garden, and a café.

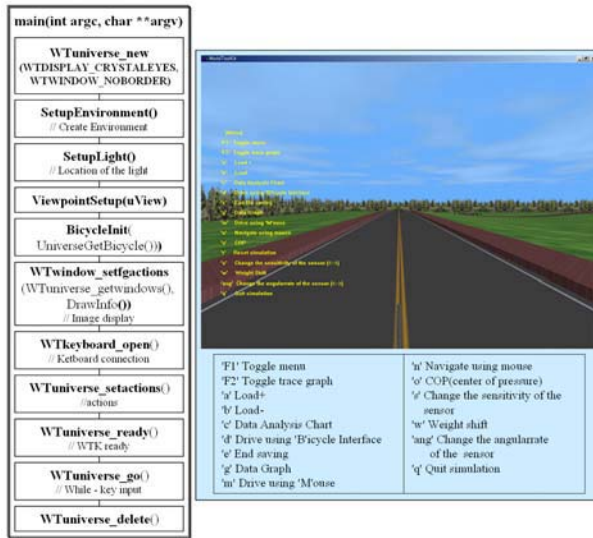


Fig. 5. Subroutines for the virtual road generation in the activation order and the initial screen with instructions

One can ride the bike under three different modes as shown in Fig. 7: without visual feedback of balance information (NVF); with visual feedback of weight shift (VFW); or with visual feedback of the center of pressure (VFC). In the NVF mode, only the pedaling speed and the handle direction are updated to the virtual environment. In the VFW mode, the weight shift information is represented as two bars on the screen. When the heights of the two bars are the same, the bike is in level condition. In the VFC mode, the location of COP is at the center when the heights of the two bars are same and the height of the bar is half of the full length. These visual feedbacks can give control and training of balance.

Assessment Routine. Figure 8 shows an assessment program for the evaluation of balance ability on the bicycle. The program was developed in LabView [13]. The program gives the maximum, the minimum, and the average values for various

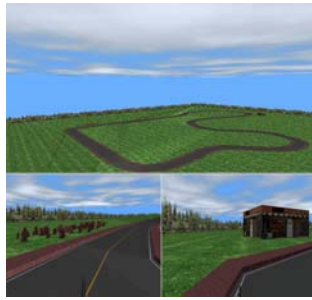


Fig. 6. Virtual road with a rose garden and a café

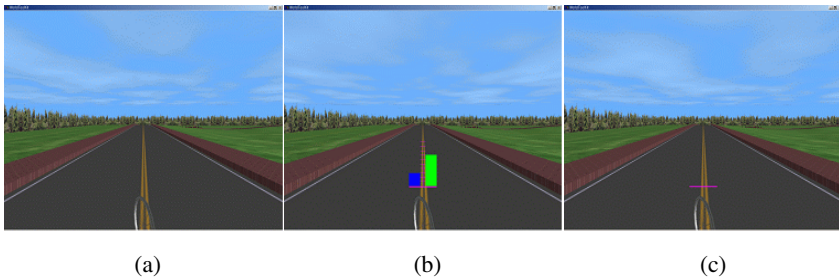


Fig. 7. Three different riding modes: (a) without visual feedback of balance (NVF); (b) with visual feedback of weight shift (VFW); (c) with visual feedback of the center of pressure (VFC)

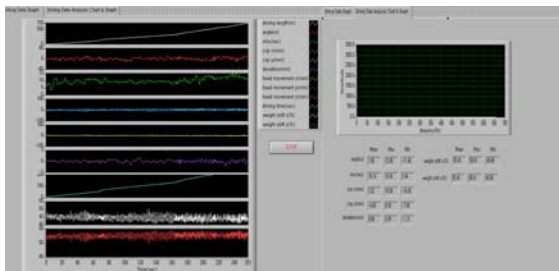


Fig. 8. Assessment window for training sessions

parameters such as the weight shift, the pedaling speed and the direction of the handlebar.

3 Experimental Method

One session of training consisted of riding the bicycle with three different modes of visual feedback modes in random order. The subject took five minutes of practice ride before the beginning of the session and one session was done per a day. A session

took about 50 to 60 minutes. The subject took ten sessions of training in ten days of time frame.

Motion Analysis. Figure 9 shows an opto-electric 3D motion analysis system [14] and a data acquisition and analysis system [15]. The markers with 6 degree of freedom (DOF) were attached to the locations marked as circles in Fig. 9 (b). The upper body sway was assessed from the calculation of the movement of the center of mass (COM) of the upper body during the ride of bicycle.

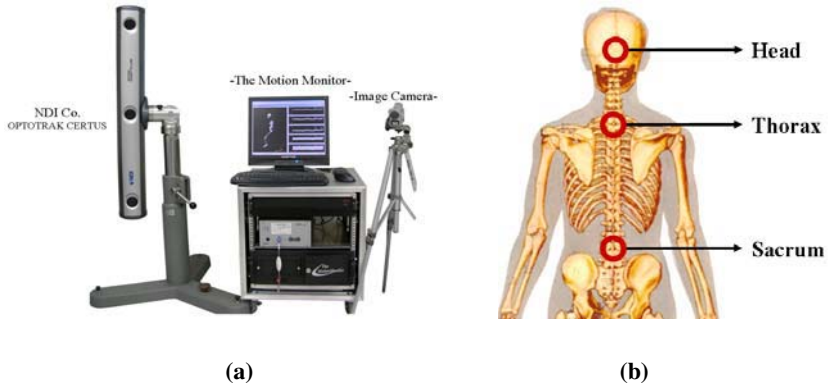


Fig. 9. Motion analysis for upper body sway (a) a 3D motion tracking system with a data acquisition system (b) the locations for 6 DOF markers

4 Results

After a series of training, the parameters obtained at the first session of the course of training were compared against the parameters obtained at the last session of the training.

Riding Time. The riding time here indicates the duration time of ride in completing the whole course of the virtual road that spans 720m. We can notice the duration time decreased after training as shown in Fig. 10. The reduced time with NVF mode suggest that the subject was paying more attention to balance when there was visual feedback of balance information.

Weight shift. The parameter of weight shift here indicates whether there is disproportion of weight in one side. This parameter indicates balanced weight when the value is close to 50%. Figure 11 shows that the weight shift decreased after training for three different modes of visual feedback. More decreased weight shift can be seen with visual feedback of weight mode. The weight shift decreased 1.08% with NVF mode, 1.28% with VFC mode, 1.51% with VFW mode. This suggests that the VFW is more effective in reducing the weight shift.

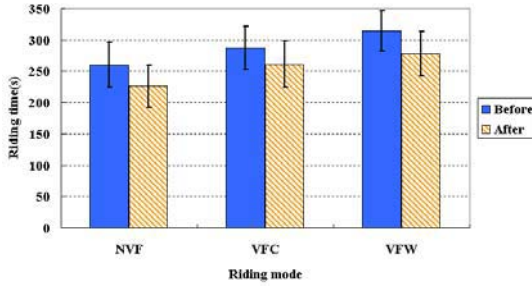


Fig. 10. Comparison of the duration of ride in completing the whole course of the virtual road

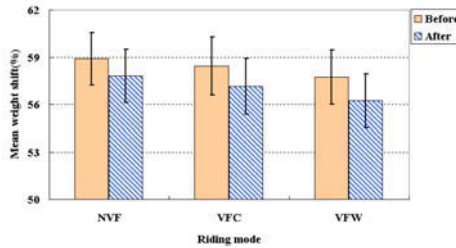


Fig. 11. Mean value of weight shift parameter before and after the training in different riding modes

The Area of COP Movement. The parameter of the area of COP movement indicates the swept area of the coordinate location of the COP. As shown in Fig. 12, the swept area of COP decreased by 3.29 cm² after training for NVF mode, by 15.87 cm² for VFW mode. This indicates that the subject was more successful in trying to maintain constant posture on the bicycle after the course of training.

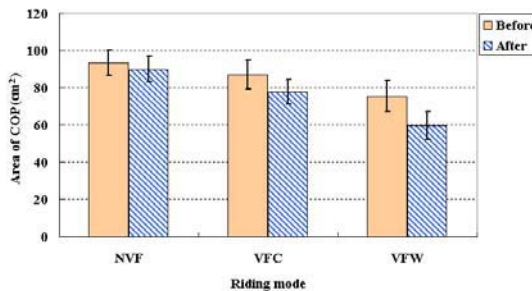


Fig. 12. Comparison of the swept area of the COP for different riding modes

Upper Body Sway. The parameter of the upper body sway indicates the combined swept area of the coordinate location of the COM of the three segments of the upper body. The three segments of the upper body is head, thorax, and lumbar. As shown in Fig. 13, the swept area of COP decreased by 210 cm² after training for NVF mode, by

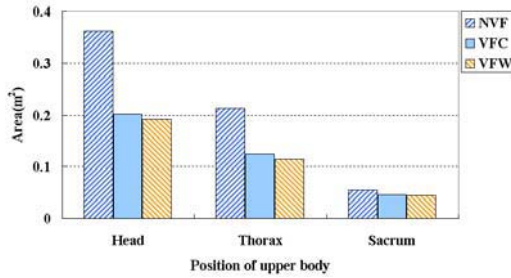


Fig. 13. Comparison of the sizes of swept areas by the movement of the COM of the upper body on a horizontal plane for different riding modes

117 cm² for VFW mode. This also indicates that the subject was more successful in trying to maintain constant posture on the bicycle after a course of training and visual feedback modes help maintaining constant posture.

5 Discussion

Development of a personal-computer based virtual-reality bicycle system has been presented. A series of training experiments performed for the validation of the effectiveness of the system suggested that the interactive quality of virtual environment increased active participation of the subject and the effect of the training. Especially, the experiments suggested that the visual feedback of weight shift is most effective among various visual feedback modes for increasing the effect of the balance training on the bicycle showing reduced weight shift and body sway after a course of training. In the other hand, the system was successful in assessing various parameters related to balance during the ride of the bicycle showing the possibility of the system to be used as a diagnosis tool for balance ability as well as a device for rehabilitating motor function. Further clinical studies are planned to find the effectiveness of the virtual bicycle system toward balance ability in standing posture and gait.

Acknowledgements

This research was supported by the Korean Ministry of Education & Human Resources Development through the Center for Healthcare Technology Development.

References

1. Shepard, N. T., Smithwheelock, M., Telian, S. A., Raj, A.: Vestibular and balance rehabilitation therapy, *Annals of Otolaryngology Rhinology and Laryngology* 102 (1993) 198-205.
2. Badke, M. B., Shea, T. A., Miedaner, J. A., Grove, C. R.: Outcomes after rehabilitation for adults with balance dysfunction, *Archives of Physical Medicine and Rehabilitation* 85 (2004) 227-233.
3. Horak, F. B.: Clinical assessment of balance disorders, *Gait and Posture* 6 (1997) 76-84.

4. Kamen, G., Patten, C., Du, C. D., Sison, S.: An accelerometry-based system for the assessment of balance and postural sway, *Gerontology* 44 (1998) 40-45.
5. van der Kooij, H., van Asseldonk, E., van der Helm, F. C. T.: Comparison of different methods to identify and quantify balance control, *Journal of Neuroscience Methods* 145 (2005) 175–203.
6. Lafonda, D., Duarteb, M., Princea, F.: Comparison of three methods to estimate the center of mass during balance assessment, *Journal of Biomechanics* 37 (2004) 1421–1426.
7. Preuss, R. A., Grenier, S. G., McGill, S. M.: Postural control of the lumbar spine in unstable sitting, *Archives of Physical Medicine and Rehabilitation* 86 (2005) 2309-2315.
8. Kerr, H. M., Eng, J. J.: Multidirectional measures of seated postural stability, *Clinical Biomechanics* 17 (2002) 555-557.
9. Butler, P. B.: A preliminary report on the effectiveness of trunk targeting in achieving independent sitting balance in children with cerebral palsy, *Clinical Biomechanics* 12 (1998) 281-293.
10. 3D Studio, Autodesk, Inc., San Rafael, CA, USA.
11. World Tool Kit, Engineering Animation, Inc., USA.
12. Visual C++, Microsoft, Inc., Redmond, WA, USA
13. LabVIEW, National Instruments Corp., Austin, TX, USA
14. Optotrak CERTUS, Northern Digital, Inc., Waterloo, Ontario, Canada
15. Motion Monitor, Innovative Sports Training, Inc., Chicago, IL, USA

Virtual Reality Edutainment: Cost-Effective Development of Personalised Software Applications

Maria Virvou, Konstantinos Manos, and George Katsionis

Department of Informatics,
University of Piraeus,
80 Karaoli & Dimitriou St., Piraeus, 18534
mvirvou@unipi.gr, konstantinos@kman.gr, gkatsion@kman.gr

Abstract. Virtual Reality edutainment can provide pleasant environments for educating students through VR-games. However, as a side effect, it may impose extra difficulties to students due to the complexity of VR-game user interfaces. Moreover, creating tutoring systems that combine teaching with the sophisticated environments of VR-games can be very complicated for instructional designers. Solutions to these problems have been given through VR-Multi-Author that provides a user-friendly authoring environment to instructional designers for the creation of personalised tutoring systems that perform student-player modelling and they operate as virtual reality adventure games. The common practice of modelling the student has been expanded to include domain-independent characteristics of players such as their level of game-playing competence on top of domain-dependent characteristics such as the level of knowledge of a student in a particular domain.

Keywords: virtual reality edutainment, authoring tools, educational games, user modelling, intelligent tutoring systems.

1 Introduction

One of the main aims of education is to engage students in learning. However, learning in a traditional way, such as in school classrooms may be very tiring for students who have to deal with many disciplines and learn in a fast way. In this respect, presentation of the teaching material plays an important role in stimulating students and keeping them alert. Therefore educational software researchers seek new technology means to improve the appeal and effectiveness of educational applications. However, there is a whole imposing culture of computer games that has not been exploited sufficiently yet for the purposes of education, although it is widely acknowledged that children and adolescents are fascinated by computer games. Indeed, a large number of research studies show that computer game playing is by far the most popular activity on the computer for children and adolescents (e.g. [2], [3], [8] and [10]). This is particularly the case for virtual reality adventure games that are very popular among children and adolescents.

Edutainment is meant to combine entertainment with education. Virtual Reality edutainment can be realised by VR-games that have been designed for educating

students. This kind of VR-edutainment can be very promising but it can also create problems for the people involved in the educational process. From the instructional designers' perspective, one problem is that combining educational systems with VR-games can be a complicated and difficult task that is hard to be repeated for multiple teaching domains. From the students' perspective, one problem is that the complex user interface of a VR-game may impose extra cognitive burden to that of learning the teaching syllabus. Indeed, educational games should be targeted to all kinds of students irrespective of their skill level in playing computer games; despite the great popularity of games there are still a lot of children that do not know how to play. Moreover, there must be underlying reasoning mechanisms in the educational game that may ensure individualised interaction based on the actions of the student-players, otherwise the game runs the risk of providing little educational benefit.

The technology of Intelligent Tutoring Systems (ITSs) may provide such reasoning mechanisms. ITSs are computer-based learning systems, which attempt to adapt to the needs of students. It is simple logic that response individualised to a particular student must be based on some information about that student; in ITSs this realisation led to student modelling, which became a core or even defining issue for the field [1]. Thus the combination of ITSs with the virtual reality environment of the games can render an educational application both highly adaptive to students' needs and attractive for them.

However, despite their nice features, few ITSs have seen widespread use, mainly because the development of ITSs is difficult, time-consuming and costly [4]. If this is the case for an ITS with a simple user interface then the difficulty of constructing a learning environment will be far greater if the ITS has to be combined with a demanding interface of a VR- game. The problem of constructing such sophisticated educational applications has been addressed in our research by the development of a knowledge-based authoring tool that can provide ITSs, which operate as VR adventure games. Knowledge-based authoring tools are meant to be used by instructors who wish to author their own ITSs on a certain domain. Murray [11] highlights the potential of ITS authoring tools in giving the instructional designer a combination of facilities to produce visually appealing, interactive screens and a deep representation of content and pedagogy. Authoring tools have to be used for multiple domains. However, there are no such authoring tools that can generate VR- edutainment applications.

The authoring tool that we have developed is called VR-Multi-Author. VR-Multi-Author provides an authoring environment to instructors who wish to create ITSs that operate through a VR- game. The targeted audience of the resulting educational games is school children of elementary school or secondary school. The resulting ITSs are able to provide individualised instruction that takes into account individual characteristics of students concerning their level and quality of knowledge of the domain being taught and their game playing skills that may affect their learning through the edutainment environments. In particular, the common practice of modelling the student has been expanded to include domain-independent characteristics of players such as their level of game-playing competence on top of domain-dependent characteristics such as the level of knowledge of a student in a particular domain. This is done because players of educational games should be modelled in two different aspects: their knowledge of the domain being taught and their competence level in playing the particular virtual reality adventure game. A student's game playing skill

may affect his/her overall performance that assesses the student's knowledge. For example, a novice player of virtual reality adventure games may not gain a good score because s/he may be lost while navigating through the game. This has to be known by the educational application that aims primarily at educating players so that the domain knowledge of the student-player is not underestimated. Moreover, in contrast with the level of domain knowledge of a student-player, the game playing skill level of a player is domain-independent. Therefore this information about a particular player may be reusable in many application domains. Thus it is stored in a separate part of the student model and can be used by all applications of different domains that are created using VR-Multi-Author.

2 Description of VR-Multi-Author

VR-Multi-Author operates at two levels, the authoring level and the game level. At the authoring level, human instructors can provide the domain-knowledge of their courses and thus create their own personalised educational games through the authoring tool. At the game level the created personalised educational games may be used by students who can learn while playing. VR-Multi-Author provides the facility for the construction of student-player modelling components for the resulting educational games, henceforth referred to as player modelling components.

2.1 Authoring Level

The authoring tool creates an integrated learning environment where multiple human instructors can contribute the respective domain knowledge of the lesson they teach. The resulting integrated environment is targeted to students of the same class of a school. Such students normally attend a variety of courses of different domains such as geography, biology, mathematics etc. In this way each student may play games for more than one course that s/he is being taught at school.

All domain-dependent data is given by the human instructor to the system during the authoring procedure which is illustrated in Figure 1. VR-Multi-Author provides a user-friendly environment where the author may create lessons to be presented to students and may provide a concept-map of the domain which is stored in the form of hierarchies in the knowledge-base about the domain.

The initial input to VR-Multi-Author which is given by each human instructional designer consists of domain knowledge concerning the topic to be taught. The domain knowledge consists of a description of key concepts of the domain, lessons and tests accompanying these lessons. At first, the domain has to be described in terms of hierarchies, which constitute the knowledge representation of HPR. Therefore the author has to decide what the main concepts of the lesson are, that may be represented in hierarchies. Then s/he may create hierarchies by giving data to a dialogue box of the system. After this input has been given, the tool constructs a knowledge base concerning the specific domain in the form of hierarchies. Then the author inserts facts that s/he wishes to be taught to students and which are relevant to the main concepts of the hierarchies. Finally, VR-Multi-Author may automatically construct tests that consist of questions relating to the factual knowledge of the domain.

Tests may consist of questions of multiple-choice questions, True/False questions or questions where the student has to type in the answer. All tests are part of the story of the virtual reality game. In all types of questions the instructor has the ability to associate erroneous answers with particular causes and explanations of errors so that these may be used by the system to give more detailed and informative feedback to players. Moreover, these explanations are recorded in each player’s profile, which is updated after each session of the player with the educational application.

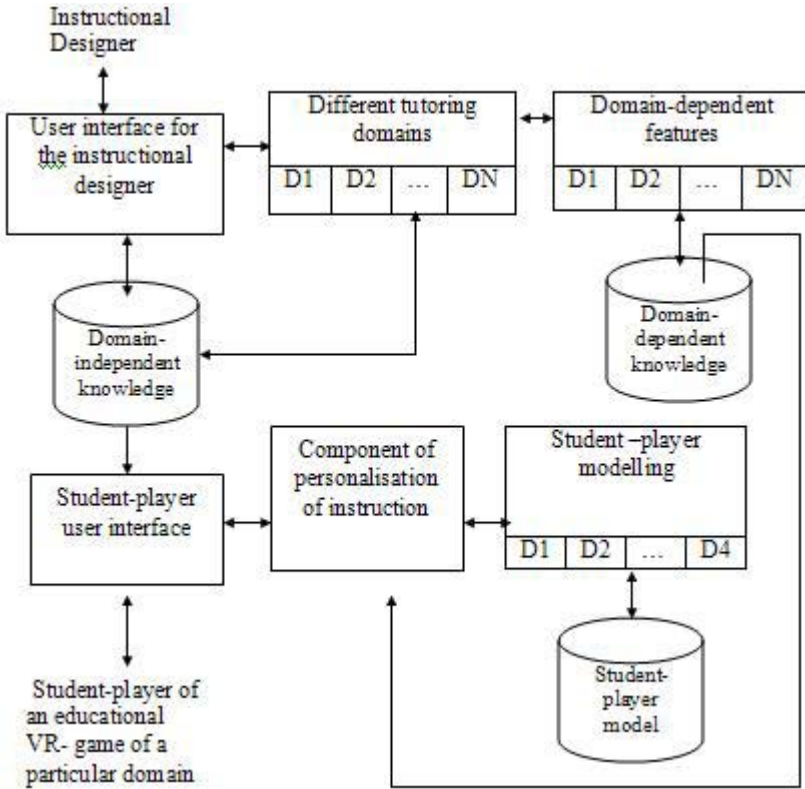


Fig. 1. Architecture of VR-Multiple-Author

2.2 Player-Student Level

The interaction of the student with the resulting educational applications is performed through a virtual reality game. The environment of the games generated by VR-Multi-Author is similar to that of the popular game called “DOOM” [7] which has many virtual theme worlds with castles and dragons that the player has to navigate through and achieve the goal of reaching the exit. In the case of VR-Multi-Author, questions to students are always asked by animated agents. Then, students may type their answer in a dialog box. In the resulting educational applications, the system communicates with the student via three types of animated agent, the virtual enemy, the virtual

advisor and the virtual companion. All three types of animated agent use synthesised voice as well as written messages.

The ultimate goal of a student-player, is to navigate through a virtual world and climb up the “mountain of knowledge”, which is at the end of the world. To navigate through the virtual world a player has to open closed doors, which are guarded by dragons. Examples of a virtual water world is illustrated in Figure 2. A guard dragon poses a question to the player from the domain of the particular educational application that has been created via VR-Multi-Author. If the player gives a correct answer then the dragon allows him/her to take the key to open the guarded door and the player receives full marks for his/her answer.



Fig. 2. Virtual water world

If the player gives an answer, which is not correct then the system performs error diagnosis so that it can find out what the cause of the error has been. The explanation of a mistake may be difficult for a system to spot. Hollnagel [5, 6] makes an important distinction between the underlying cause or genotype of an error and the observable manifestation or phenotype of the error. In addition, ambiguity may be a problem, since there may be different explanations of observed incorrect users' actions [9].

For example, a student may give an erroneous answer due to a typing or spelling error and may appear that the student does not know the answer in the domain being taught. If the system decides that the error has been due to a typing mistake then the error is considered superficial and the player receives some marks (although not full marks) for his/her answer. However, if a player types a totally irrelevant answer then this is considered a serious error and the player does not receive any marks at all. In cases where there is an ambiguity as to what the underlying cause of an error has been, the system consults the player's long-term model. For example, if a player has made an error that could either be a spelling mistake or a serious error then the long-term player model will resolve the ambiguity. If this player has been consistently

making a lot of spelling mistakes when s/he is typing answers to questions posed but s/he does not usually make serious errors, then the spelling mistake will be favoured as the most probable cause of the error and the player will be given the benefit of the doubt.

At times a player is given a key as a bonus, in which case s/he will not have to answer a question to get through a guarded door. In such cases the bonus-key is kept in the player's inventory list to be used by the player in a difficult situation where s/he does not know an answer posed to him/her by a dragon. As part of the adventure of the game the player may also come across certain objects where s/he may click on. These objects appear at random and give hints to students or guide them to read another part of the domain being taught. For example, Figure 3 illustrates a hint in the form of a blue ball in a virtual volcano world. However, these hints or the parts of the theory that are visited, are not immediately usable by the students, since they refer to questions that the students will have to answer at a location of the virtual world other than the one that they are currently at. Hence, the students will have to remember these hints or parts of the theory so that they may use them when the time comes. Educationally, these hints motivate students to read and memorise important parts of the theory.

The player modelling component observes the behaviour of student-players within the educational applications and examines the correctness of the players' answers in terms of the players' factual knowledge and reasoning that they have used. The diagnostic process is based on previous research in error diagnosis in the context of a single ITS-game for learning geography [14]. However, VR-Multi-Author extends significantly this research by creating an authoring tool that can generate ITS-games for multiple domains and provide an integrated environment where all the generated ITS-games can collect and exchange information among them about individual students.

3 Domain-Independent vs Domain-Dependent Player Modelling

Player features are permanently recorded in the long-term player model [12], [13]. The long-term player model represents the player's knowledge in the domain being taught, his/her game playing skill level and other features concerning his/her behaviour (e.g. how often s/he may be absent-minded etc.). This means that a particular student who is going to play in all available games has to log-in to identify himself/herself. Then each game contributes both domain-dependent and domain-independent information about the particular player to his/her individual long-term player model. Then in turn, the individual long-term player model may be used by all applications to resolve ambiguities about errors and to provide personalised advice.

For example, a student may be consistently facing navigation problems while s/he is moving through a virtual world. This is a domain-independent feature of the player, which remains the same in all the domain-applications that have resulted from VR-Multi-Author. This kind of feature is recorded in the long-term player model and is updated constantly in all domains. This feature is taken into account so that the particular student receives more automatic help on how to navigate through the world. On the other hand, when a student knows all the answers in a particular domain, this

is a domain-dependent feature concerning his/her level of knowledge in the particular domain. For example, a student's knowledge level in history does not relate with his/her knowledge level in Mathematics.

Domain-independent features mainly concern the player's level of game playing skill, which should not interfere with the player's level of knowledge in the domain being taught. There are also other domain-independent player features, such as the player's proneness in making typing mistakes, spelling mistakes, his/her level of concentration while playing etc. Some important features of students that concern their game playing skill are the following:

1. Virtual Reality User Interface Acquaintance

This feature measures the player's level of acquaintance with the Virtual Reality User Interface of the application. In this feature the system measures whether the player knows the functionality of user interface features such as the "Inventory", the "Tutor" etc., and how to read/answer the various questions which are presented in the relevant section of the screen. For example, supposing a case where a player faces a question that he cannot answer (s/he tried at least twice) and the player retreats and starts wandering around in the virtual world although there is a key inside the player's inventory, then this player is probably ignorant of his inventory's usage.

2. Navigational Effort

Not all users know how to play a 3D Virtual Reality Game. This feature measures how well the user can navigate through the Virtual World. This feature is calculated taking into account the frequency of occurrence of certain actions of the player inside a virtual world. Such actions are the character's bumping onto a wall (or other virtual items), aimless rotation around the same position, which shows that the player tries to find his/her way out of a point where s/he has been stuck, etc.

3. VR Environment Distractions

There are many cases when the Virtual Environment draws the player's attention so much that s/he may miss the main point of the educational game (which is learning a specific subject). This is the case in situations such as when a player finds a door, does not answer the riddle, goes back to the previous encountered tutor (angel), reads the hint, goes to the door, does not answer the riddle, goes again to the tutor etc. This behaviour shows that from the tutor to the door the player may have been so distracted that s/he forgot the hint.

However, naturally there are other domain-dependent errors, which may only be made in the corresponding domain game. For each domain there are pre-defined categories of error that the system knows about. These categories have been inserted into the system by the human tutor who acted as author of the particular domain application. For example, in an educational application about modern history, a student may have made 10 errors in questions concerning the period 1900-1945 and none in questions concerning the period 1850-1900. In this case, the system will record the fact that the student has a serious lack of knowledge about the particular history period and will compare this finding with the findings of previous interactions and future interactions to determine how the student is progressing.

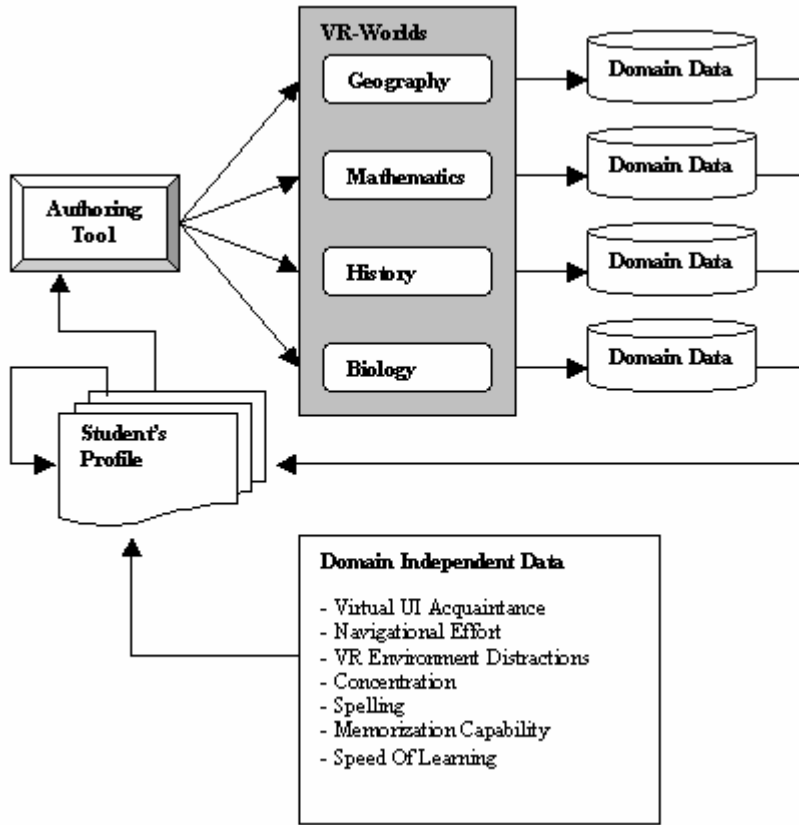


Fig. 3. Interaction of domain-dependent and domain-independent parts of player models

Domain dependent information about a player is kept separately in the corresponding domain application. On the other hand, domain independent information about each student is kept in the integrated learning environment so that it may be used and updated by all available domain applications. The interaction of these parts of the player model is illustrated in Figure 3.

4 Evaluation

VR-Multi-Author is a complex authoring tool that needs many experiments at many stages and levels to be evaluated thoroughly. First, it has to be used by instructors who wish to create their educational games and then it has to be used by students who are going to be taught some lesson through the educational games.

As an evaluation of VR-Multi-Author, the authoring tool was given to four human teachers that taught history, biology, spelling and mathematics respectively to the

same grade of a school. They were asked to construct educational games for the domains they taught by using the authoring tool. The human teachers created their lessons quite easily after they had been given a short training concerning the use of the tool. Then the generated educational games had to be evaluated by the respective students of the human teachers who participated in the experiment.

The experiment involved a class of 16 school children of 11-12 years old and the four human teachers that taught history, biology, spelling and mathematics respectively to this grade.

After the children had completed using the programs, the scores they had obtained and the errors they had made which were collected in their user protocols since all their actions, were given to their school teachers. Then the school teachers were asked to repeat the questions where students of both groups had originally given erroneous answers while they used the software. This test would reveal the degree to which students had learnt from their mistakes while they used the software. The players of the educational games remembered the correct answers to a high extent. This showed that the educational games had achieved their aim of being educationally effective as well as entertaining.

Finally both instructors and students were interviewed concerning the respective software they had used. These interviews revealed that instructors were quite happy authoring in the environment of VR-Multi-Author. Moreover, the players of the educational games were fascinated by the idea of a game in the classroom and they were certainly more enthusiastic about the software that they had used.

5 Conclusions

In this paper we presented VR-Multi-Author, a knowledge-based authoring tool for Intelligent Tutoring Systems that operate as virtual reality computer games, and focused on its player modelling capabilities. VR-Multi-Author models two broad categories of user characteristics: the domain dependent and the domain independent. Domain dependent features mainly concern the particular domain being taught. On the other hand, domain independent features concern the player's behaviour in the game irrespective of the content of questions being asked to him or her. In this way, domain-independent features may be used for modelling an individual student across many application domains and provide clear separation of the user's skills as a VR-game player from his /her competence level in the domain being taught.

We argued that a computer game, which aims to be used for educational purposes, has to have the ability to distinguish between a player's ability to play the game itself and a player's level of knowledge in the particular domain being taught. Players who are not familiar with the user interfaces of games should be given extra help in this respect and their level of domain knowledge should not be underestimated. Moreover, we discussed an issue that we consider important: the construction of an integrated learning environment where several game applications could co-exist and pass domain independent information about each player to each other.

References

1. Cumming G. & McDougall A.: Mainstreaming AIED into Education? *International Journal of Artificial Intelligence in Education*, Vol. 11, (2000), 197-207.
2. Cunningham, H.: Gender and computer games. *Media Education Journal*, 17, (1994).
3. Downes, T.: Playing with computer technologies in the home. *Education and Information Technologies*, 4, (1999) 65-79.
4. El-Sheikh E. & Sticklen, J.: Generating Intelligent Tutoring Systems from Reusable Components and Knowledge-Based Systems. In S.A. Cerri, G. Gouarderes and F. Paraguacu (Eds.): *ITS 2002, LNCS 2363*, (2002), 199-207.
5. Hollnagel, E. (1991). The Phenotype of Erroneous Actions: Implications for HCI Design. *Human-Computer Interaction and Complex Systems*, G. R. S. Weir and J.L. Alty (eds.), London Academic Press Ltd.
6. Hollnagel, E. (1993). The Phenotype of Erroneous Actions. *International Journal of Man-Machine Studies*, 39, 1-32.
7. Id Software (1993), *Doom - Virtual Reality Computer Game*, Id Software Company Texas.
8. Kirkman, C.: Computer experience and attitudes of 12-year-old students: implications for the U.K. national curriculum. *Journal of Computer Assisted Learning*, 9, (1993) 51-62.
9. Mitrovic, A., Djordjevic-Kajan, S., Stoimenov, L. (1996). INSTRUCT: Modeling students by asking questions. *User Modeling and User Adapted Interaction*, 6 (4), 273-302
10. Mumtaz, S.: Children's enjoyment and perception of computer use in the home and the school. *Computers and Education*, 36 (2001) 347-362.
11. Murray, T.: Authoring Intelligent Tutoring Systems: An analysis of the state of the art. *International Journal of Artificial Intelligence in Education*. 10 (1999) 98-129.
12. Rich, E.: User Modelling via Stereotypes. *Cognitive Science*. 3 (4) (1979) 329-354
13. Rich, E.: Users as Individuals: Individualizing User Models. *International Journal of Man-Machine Studies*. 18 (1983) 199-214
14. Virvou, M., Manos, C., Katsionis, G. & Tourtoglou, K.: VR-ENGAGE: A Virtual Reality Educational Game that Incorporates Intelligence In *IEEE International Conference on Advanced Learning Technologies* (2002), Kazan, Russia, September 16-19, 2002

3D Panoramic Mosaicking to Suppress the Ghost Effect at Far-Range Scene for Urban Area Visualization

Jaechon Chon¹, Eihan Shimizu², and Ryosuke Shibasaki¹

¹ Center for Spatial Information Science at the University of Tokyo, Cw-504 4-6-1 Komaba, Meguro-ku, Tokyo, Japan

{jcchon, shiba}@iis.u-tokyo.ac.jp

² Dept. of Civil Engineering, The University of Tokyo, Japan
shimizu@civil.t.u-tokyo.ac.jp

Abstract. 3D image mosaicking is useful for 3D visualization of the roadside scene of urban area by projecting 2D images to the 3D planes. When a sequence of images are filmed from a side-looking video camera passing far-range areas, the ghost effect in which same objects appear repeatedly occurs. To suppress such ghost effect, the far-range areas are detected by using the distance between the image frame and the 3D coordinate of tracked optical flows. The ghost effects are suppressed by projecting the part of image frames onto 3D multiple planes utilizing vectors passing the focal point of frames and a vertical slit. The vertical slit is calculated by utilizing the first and last frames of the far-range areas. We demonstrated algorithm that creates efficient 3D panoramic mosaics without the ghost effect at the far-range area.

1 Introduction

Environment visualization becomes popular gradually on Internet websites (or mobile systems) for tourism or virtual reality. So far, most of these websites provide still image-based visualization. Therefore, it is monotonous due to its fixed angle and viewpoint. Recently, panoramas have appeared to give more impressive visualization. Although the panorama enables the user to pan and zoom, the viewpoint of the panorama remains fixed. More impressive form of environment visualization is required to allow the user to view environment scenes from arbitrary viewpoints and angles. Three-dimensional Geographic Information System (3D GIS) data well meet the requirement.

A main approach for creating 3D GIS data is detailed 3D reconstruction of a scene [1-4]. Unfortunately, it is difficult to apply these detailed 3D surfaces to current Internet or mobile systems, because of their limited real-time transmission speeds. The image mosaicking technique is considered to be another efficient approach for environment visualization on websites. However, direct application of ordinary image mosaickings cannot create 3D sensation [5-8].

The goal of the 3D image mosaicking, our previous research [9,10], is to give 3D feeling for urban visualization on internet websites or mobile systems. The created 3D image mosaics are textured 3D vector data generated from a side-looking camera along a road in a city or town area. The 3D feeling can be obtained through watching

3D vectors and textured image slits. The 3D vectors and textured image slits give imagination of the global abstract and detail part of objects, respectively. The 3D image mosaicking uses a roadside scene acquired by a side-looking video camera as a continuous set of textured vertical planar faces named "multiple projection planes". The scene geometry is approximated to multiple vertical planes using sparsely distributed optical flows. These vertical planes are concatenated to create an approximate model on which the images could be back-projected as textures [9,10].

If the multiple projection planes are created around the far-range area in the same way around the close-range area, then the ghost effect will occur [11]. To suppress ghost effect, we proposed 3D panoramic mosaicking as on an expanded concept of the crossed-slits projection [7]. The far-range areas are detected by using the distance between the image frame and the 3D coordinate of the detected optical flows. The ghost effects are suppressed by projecting the part of image frames onto 3D multiple planes utilizing vectors passing the focal point of frames and a vertical slit. The vertical slit is calculated by utilizing the first and last frames of the far-range areas.

2 3D Image Mosaicking Using Multiple Projection Planes

The multiple projection planes around the close-range area involved a continuous set of vertical planes. The vertical plane for each frame was calculated from the sparsely distributed feature points belonging to a frame [12]. The least median of squares (LMedS) was applied to estimate the projection plane, which was calculated from the regression line, $Z = aX + b$, in (x,z) coordinates. During the estimation, only the feature points closer than D_{max} were used (Fig 1(a)). The distance D_{max} was defined as being 1.5 times the average distance between the focal point of the first frame and the feature points with 3D coordinates that appeared in the first and second frames, and was specified by trial and error. Assume that the outer covering of urban objects and the position of a side-looking and moving video camera are built like the thick curve and rectangles shown in Fig. 1(b). In this case, the multiple planes will be designed as a dotted curve in Fig. 1(b) and will be presented as linked planes in 3D space, as in Fig. 1(c).

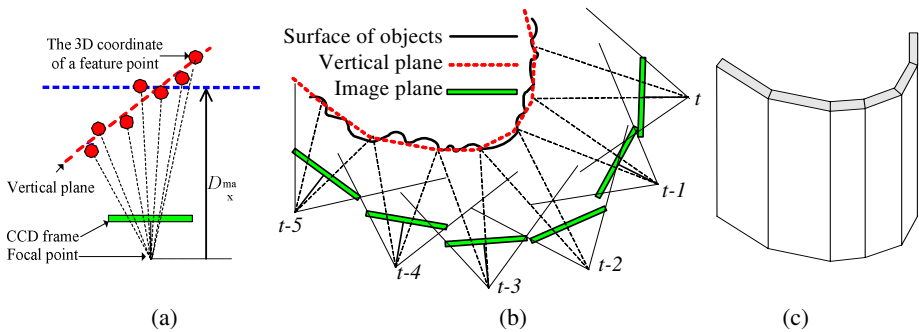


Fig. 1. Concatenation of vertical planes formed with the feature points of each frame; (a) The vertical plane of each frame, (b) multiple projection planes in 2D space, (c) multiple projection planes in 3D space

3 3D Panoramic Mosaicking Using Expanded Crossed-Slit Projection

In the case where the distance between one frame and a building exceeded the distance D_{max} , the frame was determined to be in the far-range area frame. For the far-range area frame, a virtual vertical plane was needed to create a multiple projection plane. The virtual vertical plane was calculated using the path of the camera and the two neighboring vertical planes in the close-range area. The terms P_t and P_{t+n} depicted in Fig. 2(a) represent the right-hand and the left-hand endpoints of the two neighboring vertical planes in the close-range area, respectively. The virtual vertical plane was designed in the same way as the camera path. The virtual vertical plane of Frame t+k was set as the line passing through Positions P_{t+k-1} and P_{t+k+1} . Position P_{t+k} was computed as follows:

$$P_{t+k} = P_t + \frac{l(k)(P_{t+n} - P_t)}{L}, \tag{1}$$

where $L = \sum_{i=t}^{t+n} |F_i - F_{i+1}|$ and $l(k) = \sum_{i=t}^{t+k} |F_i - F_{i+1}|$ are the lengths along the path of the transverse view camera from Frame t to Frame t+n and to frame t+k, respectively. The term F_{t+k} denotes the focal point of Frame t+k, where $k = 1 \dots n$.

If the same way used around close-range areas is directly applied to the virtual vertical planes to project images onto the virtual vertical planes as textures, then certain urban objects will appear repeatedly in a continuous set of textured planar faces (see Fig. 2) [13]. This is known as the "ghost effect". To reduce the ghost effect, we proposed the use of an expanded crossed-slits projection technique [7] (see Fig. 3(a)).

The technique determined Point p , as shown in Fig. 3(b). Point p is the point at the intersection of the virtual vertical plane with a ray passing through the focal point and a vertical slit, V. Vertical slit V was calculated using Frames B and C. Frame B is the final frame that includes Point P_t , and Frame C is the first frame that includes Point P_{t+n} . Vertical slit V was calculated by using two vectors, $\overrightarrow{P_t B}$ and $\overrightarrow{P_{t+n} C}$, as below

$$\begin{bmatrix} X_V \\ Z_V \end{bmatrix} = \begin{bmatrix} X_{P_t} \\ Z_{P_t} \end{bmatrix} + K_t \left(\begin{bmatrix} X_B \\ Z_B \end{bmatrix} - \begin{bmatrix} X_{P_t} \\ Z_{P_t} \end{bmatrix} \right) = \begin{bmatrix} X_{P_{t+n}} \\ Z_{P_{t+n}} \end{bmatrix} + K_{t+n} \left(\begin{bmatrix} X_C \\ Z_C \end{bmatrix} - \begin{bmatrix} X_{P_{t+n}} \\ Z_{P_{t+n}} \end{bmatrix} \right), \tag{2}$$

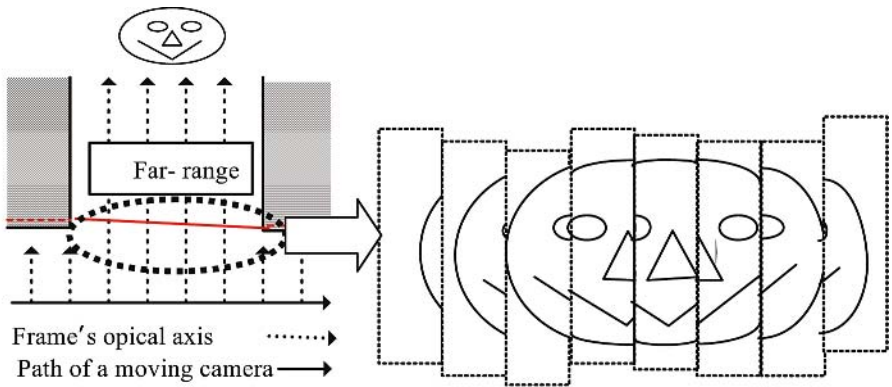
where $K_{t+n} = \frac{X_{P_t} + K_t(X_B - X_{P_t}) - X_{P_{t+n}}}{X_C - X_{P_{t+n}}}$ and

$K_t = \left(Z_{P_{t+n}} + \left(\frac{X_{P_t} - X_{P_{t+n}}}{X_C - X_{P_{t+n}}} \right) (Z_C - Z_{P_{t+n}}) - Z_{P_t} \right) / \left(Z_B - Z_{P_t} - \frac{(X_B - X_{P_t})(Z_C - Z_{P_{t+n}})}{X_C - X_{P_{t+n}}} \right)$ are the

proportionality coefficients. The point p on each virtual vertical plane was determined as an intersection point

$$\begin{bmatrix} X_p \\ Z_p \end{bmatrix} = k \left(\begin{bmatrix} X_F \\ Z_F \end{bmatrix} - \begin{bmatrix} X_V \\ Z_V \end{bmatrix} \right) + \begin{bmatrix} X_V \\ Z_V \end{bmatrix} \tag{3}$$

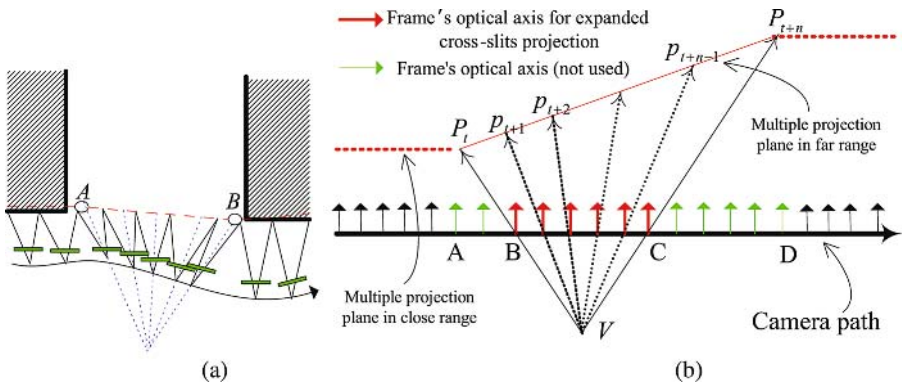
where F is the focal point of each frame, $k = \frac{aX_V + b - X_V}{Z_{F_i} - Z_V - a(X_{F_i} - X_V)}$ is a proportionality coefficient, and (a, b) represents the set of coefficients of the vertical plane of the frame.



(a) A camera passing an intersection area

(b) Ghost artifacts

Fig. 2. Ghost effect by applying the same way used in close-range areas to virtual vertical planes directly



(a)

(b)

Fig. 3. Concept of expanded crossed-slits projection technique in a far-range area

4 Experimental Results

We used Visual C++ 6.0 and OpenGL to realize our proposed method and to display the results in 3D space. We applied our method to a real sequential image taken from a moving train equipped with a side-looking video camera. The extracted and tracked feature points, and the calculated camera positions and orientations are shown in Fig. 4(a). In Fig. 4, the red and green points denote feature points belonging to the close- and far-range areas, respectively. The computed vertical planes in the close-range area and the virtual vertical planes in the far-range area are denoted by the white and green lines in Fig. 4(b), respectively. The multiple projection planes obtained using the panoramic mosaicking algorithm to obtain the virtual vertical planes (green line) are shown in Fig. 4(c).

Figure 5(a) shows the textured surface of multiple projection planes corresponding to the data shown in Fig. 5(b). It can be seen that the result around the far-range area includes the ghost effect. Most of the ghost effect disappeared in the results obtained when using the expanded crossed-slits projection algorithm, as shown in Fig. 5(b). Although the expanded crossed-slits projection algorithm was applied in this case, the result still included a partial ghost effect. Fig. 5(c) shows the results obtained from another viewpoint.

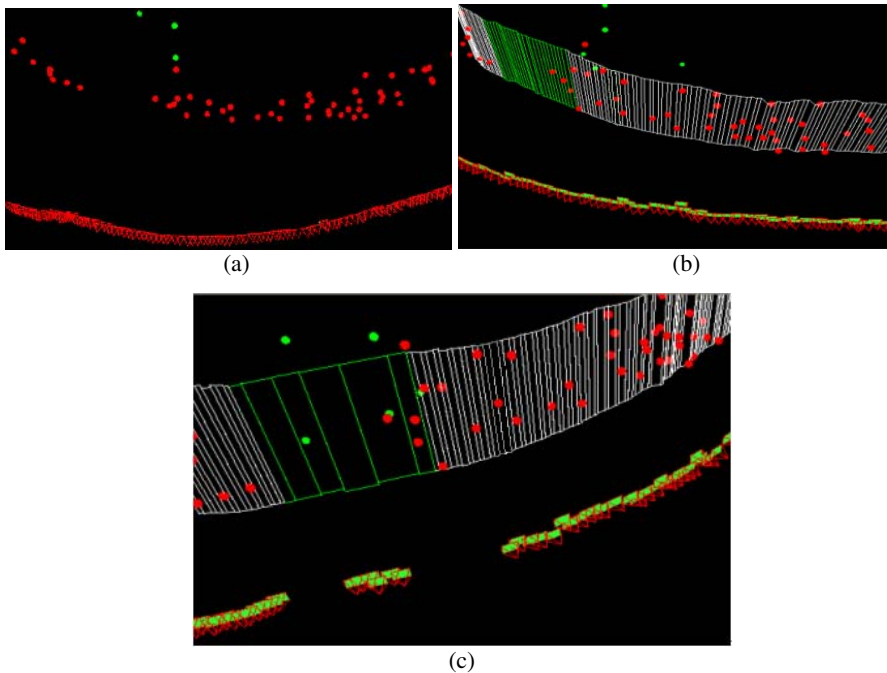


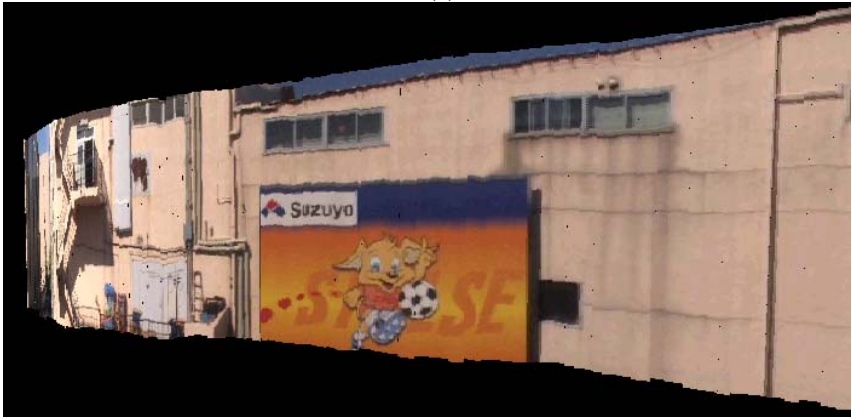
Fig. 4. The multiple projection planes around the far-range area



(a)



(b)



(d)

Fig. 5. Back-projection of images using multiple projection planes around the far-range area

4 Conclusions

When applying the 3D image mosaicking into frames capturing far-range areas, the ghost effect occurred in the created 3D image mosaics. To suppress the ghost effect, we proposed 3D panoramic mosaicking based on the crossed-slit projection. The ghost effects are suppressed by projecting the part of image frames onto 3D multiple

planes utilizing vectors passing the focal point of frames and a vertical slit. The vertical slit is calculated by utilizing the first and last frames of the far-range areas. We demonstrated algorithm that creates efficient 3D panoramic mosaics without the ghost effect at the far-range area.

Since the textured projection plane of each frame consists of four 3D coordinates and a part of the image, the results obtained by using the proposed method can be the form of MPEG-7 data [13]. Therefore, these results as next generation navigation data can be widely applied to 3D virtual visualization and games on websites, cellular phones, and PDAs.

References

1. Zhao, H. and R. Shibasaki, "A vehicle-borne urban 3D acquisition system using single-row laser range scanners," *IEEE Transaction onSMC Part B: Cybernetics*, vol.33, no. 4, 2003.
2. Fruh, C. and A.Zakhor, "Data processing algorithms for generating textured 3D building facade meshes from laser scans and camera images," *Proc. 3D Data Processing, Visualization and Transmission 2002*, Padua, Italy, 2002.
3. Pollefeys, M., R. Koch, M. Vergauwen, L. Van Gool, "Automated reconstruction of 3D scenes from sequences of images," *ISPRS Journal Of Photogrammetry And Remote Sensing*, vol. 4, no. 55, pp. 251-267, 2000.
4. Sato, T., M. Kanbara and N. Yokoya, " Dense 3D reconstruction of an outdoor scene by hundreds-baseline stereo using a hand-held video camera. In *IJCV*, vol. 47, no. 1/2/3, pp. 119-129, 2002.
5. Zomet, A., S. Pleeg and C. Arora, "Rectified Mosaicking: Mosaics without the Curl," *International Conference on Computer Vision and Pattern Recognition*, II: pp. 459-465, 2000.
6. Zhu, Z., A. R. Hanson and E. M. Riseman, "Generalized parallel-perspective stereo mosaics from airborne video," *IEEE Transactions on PAMI*, vol. 26, no. 2, pp. 226-237, 2004.
7. Zomet, A., D. Feldman, S. Peleg and D. Weinshall, "Mosaicking new views: the crossed-slits projection," *IEEE Transactions on PAMI*, vol. 25, no. 6, pp. 741-754, 2003.
8. Rom, A., G. Garg and M. Levoy, "Interactive Design of Multi-Perspective Image for Visualizing Urban Landscapes," *Proc. Visualization 2004*.
9. Chon, J., T. Fuse, and E. Shimizu, "Urban Visualization through Video Mosaics Based on 3D Multibaselines", *20th Congress of the International Society for Photogrammetry and Remote Sensing*, Istanbul, Turkey, 2004.
10. Chon, J., "3D image mosaicking using multiple projection planes", *The University of Tokyo*, Ph.D dissertation, 2005.
11. Uyttendaele, M., A. Eden and R. Skeliski, "Eliminating ghosting and exposure artifacts in image mosaics," *Proc. 2001 IEEE Computer Society Conference on CVPR 2001*, Vol. 2 , pp. 8-14,2001.
12. Chon, J., H. Kim, C. Ahn, and K. Kim, " The computation of the real-time CCD camera motion using correlation and system dynamic model," *IEEE International Conference on Mechatronics and Machine Vision in Practice*, Hong Kong, pp. 168-172, 2001.
13. MPEG-7 descriptions released in websites, <http://www.chiariglione.org/mpeg> , <http://mpeg7.nist.gov> , and <http://www.mpegif.com>

VR Based Knowledge Transfer in Medical Technology and Techniques

Wolfram Schoor¹, Rüdiger Mecke¹, and Martina Rehfeld²

¹ Fraunhofer Institute for Factory Operation and Automation (IFF),
Sandtorstrasse 22, 39106 Magdeburg, Germany
Phone: +49 391 4090147; Fax: +49 391 4090155

{wolfram.schoor, ruediger.mecke}@iff.fraunhofer.de

² FIT-Bildungs-GmbH,

Halberstädter Strasse 42, 39112 Magdeburg, Germany

m.rehfeld@fit-bildung.de

Abstract. This paper reports on an ongoing project's use of virtual reality (VR) technologies to support vocational training. Three-dimensional interactive VR models can be employed to support the innovative transfer of knowledge about complex equipment and special processes of neuromedical technology and neurobiology. The target group for the type of knowledge transfer in this project is specialized medical-technical staff members who, in basic and advanced training, have to develop competencies to properly perform immunohistochemical analyses with quality results. The project is developing and testing interactive 3-D scenarios that are expected to lead to new approaches to transferring declarative and procedural knowledge. In addition, project work is also dealing with issues of scene modeling, learning-based design and increased levels of interaction between users and trainees.

1 Introduction

The use of three-dimensional contents opens completely new possibilities for information exchange, presentation and knowledge transfer in virtual environments.

While three-dimensional and interactive representations of virtual prototypes are widespread in various domains of industry such as engineering and design, such model data is hardly being used at this time in basic and advanced vocational training. In the field of design, the added value of 3-D information can already dramatically increase the effectiveness of work in the prototype design phase. Planning mistakes can be detected early on since spatial correlations can be developed more easily (cf. [1]).

Knowledge transfer in virtual environments, likewise based on such interactive 3-D models, will be extremely important in the future. Virtual learning or work environments generated from 3-D model data of a real environment have fundamental advantages over the real environment (cf. [2]) such as the unlimited availability of the virtual learning or work environment, the capability to reverse learning actions (safely and without financial losses), the didactic reduction of

real facts to core contents by means of time lapse, slow motion, transparencies and sectional planes.

Hence, the use of such technologies in the educational and training sector provides great potentials. However, beyond geometry-based model description, advanced concepts for scenario management, didactics and user-based design have to be developed. The Fraunhofer IFF has core competencies in the innovative field of VR based training and VR based development, which have been built up in successfully completed industry projects [3], [4], etc.

In the project presented here and being worked on by several project partners, prototype virtual training modules are being developed and tested specifically for basic and advanced vocational training in the field of neuromedical technology and techniques. The use of VR technologies in this specific context is something completely new.

2 Basics of VR Based Systems for Knowledge Transfer

There are a multitude of fields of application for knowledge transfer using virtual learning environments; the forms of presentation that can be used are just as diverse though. The forms of presentation and the potentials for integrating a basic didactic concept in VR are gone into in more detail below. According to [5] there are three basic forms of VR presentation:

- *Immersive VR*: the trainee is completely integrated in the virtual world, e.g. CAVE [6], [7] or head-mounted displays [8] (cf. Figure 1a).

High acquisition costs, locational constraints of the technology and physiological restrictions on operating time (quick head, eye and hand fatigue) are currently points against commercial use of this form of presentation in the project.

- *Semi-immersive VR*: output devices such as vision stations, stereoscopic wall screens or 3-D displays [9] are used to fill most of the field of vision (cf. Figure 1b).

This form of presentation gives users a high level of immersion and falling hardware prices will make it increasingly important in the near future. It is however prohibitively expensive for basic and advanced training at educational institutions at this time.

- *Desktop VR*: the presentation takes place only in a certain area of the field of vision with less than 60 degree (cf. Figure 1c).

This is an extremely cost effective variant since existing interaction components can be used. 2-D input devices such as a keyboard or mouse are used for control, though their intuitive use in the 3-D environment is limited. Since

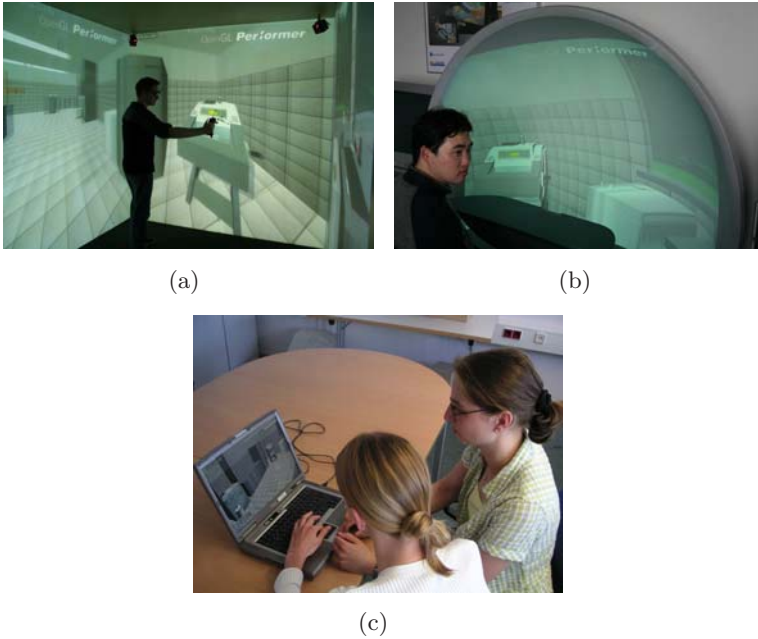


Fig. 1. a) Interactive VR scenario in the CAVE at the Fraunhofer IFF; b) on the Vision Station; and c) desktop VR training scenario on a laptop

current studies, e.g. [10], have been unable to detect any significant differences in the learning effect as a function of the presentation form selected and the costs for immersive/semi-immersive VR are so high, this project is geared toward inexpensive desktop VR.

Another aspect that can be inferred from current research is the substantial influence the type of presentation of learning content and the sensory organs addressed as well as the form of the sequential control have on the efficiency of knowledge transfer. The generative theory of multimedia learning ([11], [12]) states that their separate processing makes a combination of verbal and nonverbal representations of learning content more conducive to knowledge retention and retrievability. Accordingly, texts and images are complementary sources of information that can be separately reproduced as verbal and visual representations. Knowledge is transferred with comparatively little cognitive effort when the combination of text and image is expediently arranged [13]. When both representations of learning content have a local coherent presence, the networking of the verbal and visual patterns can sustainably boost the efficiency of knowledge transfer [12]. Studies conducted by [14] reveal that previously acquired knowledge, particularly when based on static images as the form of representation, can also be generalized as animations.

3 Development of VR Based Educational Modules for Neuromedical Technology

The VR training platform (VDT Platform) developed at the Fraunhofer IFF employs methods that support the most optimal knowledge transfer possible. A training module from the field of neuromedical technology is being implemented as a prototype.

3.1 Development System for Generating Virtual Learning Environments

The basic didactic conditions described were integrated in the design of the VDT Platform. The platform is a mixed form of the learning software types classified in [15]: presentation and visualization software, tutorial software and test software. It is being used as the basic software for generating 3-D scenarios in the project and being developed further. The complete system can be broken down into three categories according to [16].

The authoring system: The authoring system supports trainers when they are generating learning scenarios. The aim of the authoring system is to provide trainers (technical experts) a universal support that requires a minimum of level of knowledge of computer science.

The runtime system: The runtime system supports the actual training itself. It is scenario-independent and can be used for any scenario generated with the authoring system. One runtime instance is needed for each trainee.

The scenario data: The result of the work with the authoring system is a training scenario generated in the form of a scenario file containing the specific data for the concrete training exercise.

At first, a static 3-D scenario has to be generated, which represents all relevant real-world objects. Commercial modeling tools (3ds Max®) are largely used to generate the 3-D models. However, digitization that captures both geometry and surface texture can also be used [17]. The essential part is using the authoring system and expert knowledge to appropriately integrate the knowledge to be transferred in the static scenario and its modules. The Fraunhofer IFF has developed various modes of knowledge transfer and integrated them in the VR platform. Figure 2 is a schematic overview of the training modes based on [18].

The rectangular fields illustrate the time flow when a task or procedure is being completed. A task consists of procedures and procedures in turn consist of procedure steps. The building blocks outside the fields symbolize the task to be completed. While the discovery mode does not involve any specific task and can be used to easily query information and explore the scenario interactively, the presentation mode presents the ideal approach (broad arrows). Users can move freely and progressively view the ideal sequence of actions (see circles in Figure 2). The guided mode is similar to the presentation mode. However, users themselves have to complete the task while observing boundary conditions (barriers), yet they receive assistance from a text blended into the VR scene or by

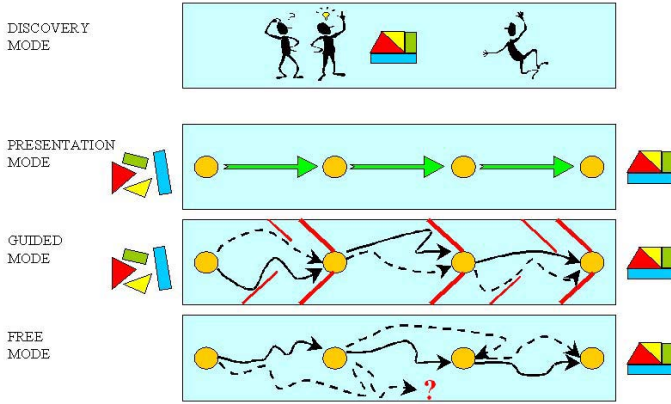


Fig. 2. Structure of different training modes from [19]

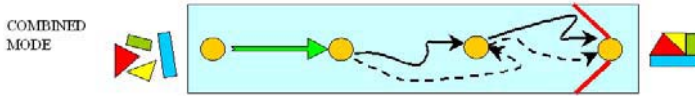


Fig. 3. Sample structure of the combined mode

using simplified action options (e.g. clicking to act). The free mode represents a higher level of user interaction, yet is the most difficult to handle since inexperienced users can easily experience disorientation and cognitive overload when they attempt to navigate the virtual 3-D environment (cf. [20]). When users put the sequences of action in VR into action in this mode, they have to tackle the current task independently without any assistance.

In addition to this, the project introduced a combined Mode (see Figure 3). The combined mode is made up of the other training modes and contextually combines the respective training modes and their advantages within one task. The advantage here, for example, is that users themselves have to complete difficult subtasks by acting actively (guided or free mode) and a clever change of modes ensures the trainee’s attention curve does not drop off as sharply as it would if the training modes were organized sequentially.

Another important aspect is the integration of conventional forms of learning contents such as texts, images, basic diagrams, etc. It does not always make sense to represent all information three-dimensionally. New methods are not generally better suited for knowledge transfer [21]. Thus, by reducing them to their core contents, many technical facts can also be adequately presented by concise text passages or diagrams. For this reason, conventional contents are reverted to here and there in the project and integrated in VR scenarios in appropriate places. Examples of such conventional learning contents are textual and diagrammatic technical specifications of equipment, which predominantly represent declarative knowledge (factual knowledge).

3.2 Virtual Learning Environment for Knowledge Transfer in Neuromedical Technology

The objective of the project is to develop and employ VR technologies as a model to support needs-based basic and advanced training for specialized medical-technical staff in the field of immunohistochemical analyses. To this end, a model analysis sequence was first specified, which provides the substantive focus for the project. This is a relatively complex sequence that begins with the removal of the brain from test animals and after several process steps ends when the image-based analysis of corresponding tissue sections is performed.

As a preliminary step to implementing it in the virtual work environment, the analysis sequence was first structured in four modules (cf. Figure 4). The first module, *perfusion*, involves fixing the tissue and then extracting the test preparations (brain). The subsequent *tissue processing* (second module) encompasses the post-fixation and production of tissue sections. The third module includes the actual *immunohistochemical reaction*. A successive application of special chemical substances and antibodies is employed to process the tissue sections for later analysis. The *analysis* of the tissue sections was implemented as a fourth module. For the sake of simplicity, the tissue processing module is chiefly dealt with here.

Initially, the primary objective is to transfer these modules to a virtual 3-D learning environment, taking into account the close correlation between the contents of the individual modules and its effects on the results of analysis. This is the rationale behind assigning the individual modules to different local work stations in a virtual lab (cf. Figure 5). This metaphor can be employed to represent both the specifics of the individual process steps per work station (spatial separation) and their relationship to the complete analysis sequence. As a result, trainees are enabled not only to work on the specific module (or process step) at

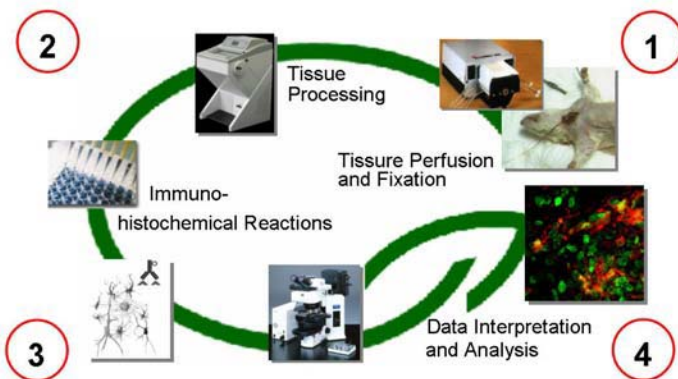


Fig. 4. Process steps and modules of an immunohistochemical analysis intended for implementation in a virtual learning environment

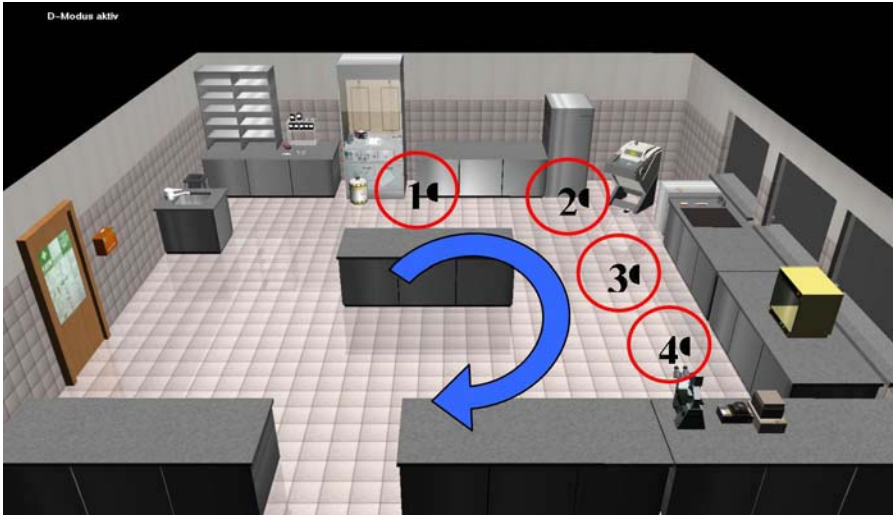


Fig. 5. Virtual lab as learning environment: The individual training modules (cf. Figure 4) are assigned to different work stations (numbered circles) and completed successively (in the direction of the arrow)



Fig. 6. Menu in the virtual scenario

any time but also to place the content into the overall context of the analysis. Users can use a menu superimposed over the VR scene (see Figure 6) to access the virtual work environment's individual components and functionalities at any time.

The sequence of training is structured as follows: An introduction familiarizes trainees with system handling and interaction and enables them to view project information. In order to better transfer this knowledge, users can explore the scenario in the discovery mode by navigating in the virtual scenario and exploring the environment. In this mode, for example, components and equipment in

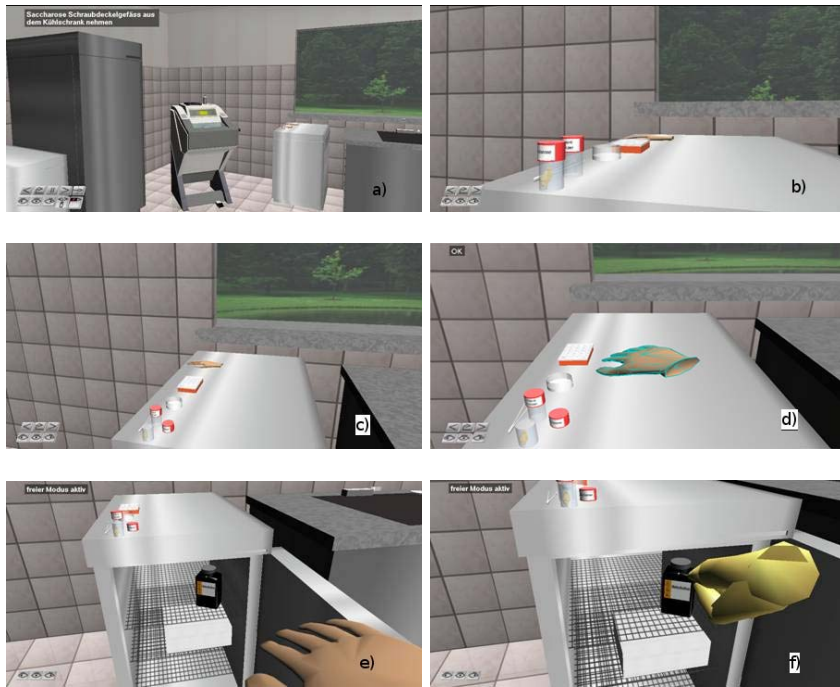


Fig. 7. Six procedure steps (a-f); opening refrigerator door in presentation mode and placing the screw-top container on the freezer (a-b), Unscrewing the top from the container (c) and putting on the protective gloves in guided mode (d) opening refrigerator door in guided mode (e) and taking methyl butane out in free mode (f)

the virtual environment can be "clicked on" and corresponding information (e.g. object name, function) is then blended into the scene as text.

After trainees have exited the introduction, they can use one of the four modules to begin the training. Under the point work preparation, every module provides the option of viewing the equipment/objects involved (e.g. automatic tissue sectioning machine, freezer, etc.) and work preparations as well as retrieving additional background information from linked text documents. The next step is guided learning, i.e. as part of a presentation the ideal approach to the subtask is presented step by step. Afterward, users can use active learning to directly interact with the virtual scene to consolidate and deepen their knowledge. The learning contents were selected beforehand in such a way that training modes generally teach simple operations with very little active effort (presentation mode). A high level of user interaction and autonomy is required to complete difficult subtasks though (cf. Figure 7f). The learning module can be completed by passing a test of both declarative and procedural knowledge. This might involve a multiple choice test of factual knowledge or independent completion of subtasks in the module.

Figure 7 presents the application of the combined mode (cf. Figure 3).

4 Conclusion and Outlook

This paper reported on an ongoing project that is dealing with the development and use of desktop VR based knowledge transfer in neuromedical technology. Current work has demonstrated that interactive training modules have great potential in the vocational training of specialized medical-technical staff, which can also be generalized for other special fields.

Initial field tests of VR based knowledge transfer are being conducted. They have proven that simple interactions between users and virtual work environments are possible in desktop VR without any problems. Initial trends in using VR to transfer knowledge in the field of neuromedical technology indicate that VR use definitely boosts knowledge transfer more than conventional educational methods. In order to validate these conclusions, plans have been made to let a group without any medical-technical background perform the real test sequence after they have completed the virtual training scenario and to compare the results with those from test persons who use conventional learning methods. The test results will be published in a follow-up study.

Acknowledgements

This research work is being supported by the BMBF grant 03I0422A and 03I0422B.

References

1. R. Kikinis, G. Langham, T. M. Moriarty, M. R. Moore, E. Alexander, M. Matsumae, W. E. Lorensen, P. M. Black, and F. A. Jolesz. Computer-assisted interactive three-dimensional planning for neurosurgical procedures. In *Neurosurgery*, volume 38, pages 640–651, 1996.
2. D. Dörner. *Problemlösungen als Informationsverarbeitung*. Kohlhammer, Stuttgart, 1987.
3. E. Blümel. Aktuelle Berufsausbildung - Visuell-Interaktives Trainieren an der Kernschiesmaschine. In *Giesserei-Rundschau*, volume 50, pages 250–251, 2003.
4. A. Hintze, M. Schumann, and S. Stüring. Interaktive Szenarien für die Ausbildung von Wartungs- und Instandhaltungspersonal. In *Simulation und Visualisierung 2000*, pages 225–237, Magdeburg, 2000.
5. L. Bernd. *Konzepte für den Einsatz von Virtueller und Erweiterter Realität zur interaktiven Wissensvermittlung*. PhD thesis, Technische Universität Darmstadt, Fachbereich Informatik, 2004.
6. C. Cruz-Neira, D. J. Sandin, T. A. DeFanti, R. V. Kenyon, and J. C. Hart. The Cave: Audio visual experience automatic virtual environment. *Commun. ACM*, 35(6):64–72, 1992.
7. C. Cruz-Neira, D. J. Sandin, and T. A. DeFanti. Surround-screen projection-based virtual reality: The design and implementation of the cave. In *SIGGRAPH '93: Proceedings of the 20th annual conference on Computer graphics and interactive techniques*, pages 135–142, New York, NY, USA, 1993. ACM Press.
8. I. Sutherland. A head-mounted three-dimensional display. In *Proceeding of the Fall Joint Computer Conference*, volume 33, pages 757–764, Arlington, 1968. AFIPS Conference Proceedings.

9. Fraunhofer Institute for Telecommunications. Free2c 3-d display. Company flier published at CeBIT, March 2005.
10. Randy Pausch, Dennis Proffitt, and George Williams. Quantifying immersion in virtual reality. In *SIGGRAPH '97: Proceedings of the 24th annual conference on Computer graphics and interactive techniques*, pages 13–18, New York, NY, USA, 1997. ACM Press/Addison-Wesley Publishing Co.
11. R. E. Mayer and R. Moreno. A split-attention effect in multimedia learning: Evidence for dual processing systems in working memory. In *Journal of Educational Psychology*, volume 90, pages 312–320, 1998.
12. Richard E. Mayer. *Multimedia Learning*. Cambridge University Press, New York, NY, USA, 2001.
13. B. Weidenmann. *Abbilder in Multimediaanwendungen*, volume 2. Weinheim: Psychologie Verlags Union, 1997.
14. W. Schnotz, W. J. Böckheler, H. Grzondziel, I. Gärtner, and M. Wächter. Individuelles und kooperatives Lernen mit interaktiven animierten Bildern. In *Zeitschrift für pädagogische Psychologie*, volume 12, pages 135–145, 1998.
15. H. Mandl, H. Gruber, and A. Renkl. Lernen mit dem Computer. Empirisch-pädagogische Forschung in der BRD zwischen 1970 und 1990, 1992.
16. A. Hintze, M. Schumann, and S. Stüring. Flexibles Modellieren von Maschinen und Anlagen in verteilten Umgebungen. In *The New Simulation in Production and Logistics*, pages 339–346. 9. ASIM-Fachtagung Simulation in Produktion und Logistik, 2000.
17. R. Mecke, D. Berndt, W. Schoor, and E. Trostmann. Generation of texturized 3-d models with high resolution using optical 3-d metrology. In *Optical 3-D Measurement Techniques VII*, volume 2, pages 3–12, 2005.
18. A. Hintze. Wissen erleben - Interaktives Lernen in virtuellen Welten. In *ASIM 17*, Magdeburg, 2003.
19. E. Blümel and K. Jenewein. Kompetenzentwicklung in realen und virtuellen Arbeitsumgebungen - Eckpunkte eines Forschungsprogramms. In *Virtual Reality und Augmented Reality zum Planen, Testen und Betreiben technischer Systeme*, pages 177–182, Magdeburg, 2005.
20. G. Haschke and M. Diener. Interaktives Lernen in der tierärztlichen Aus- und Weiterbildung am Beispiel der Veterinär-Physiologie. In *Pferdeheilkunde*, volume 15, pages 184–186, 1999.
21. C. J. Peimann. Kontextsensitive Visualisierung in multimedialen Lernprogrammen in der Medizin. In K. Dette, editor, *PC-Einsatz in der Hochschulausbildung*. Springer Verlag, 1992.

A Diagnostic Model Using a Clustering Scheme

Seong Baeg Kim, Kyoung Mi Yang, and Cheol Min Kim

Department of Computer Education, Cheju National University,
66 Jejudaehakno, Jeju, 690-756, Korea
{sbkim, kmyang, cmkim}@cheju.ac.kr

Abstract. It has been recognized that it is a challenging problem to deal with the situation where learners have diverse computing backgrounds and the learning content to be covered is also in the broad coverage. In the case, it's required to devise a sophisticated diagnostic model for applying a proper teaching-learning method. We have drawn a scheme which can be applied to that case efficiently by using clustering algorithms based on web technology. In our approach, we focus on finding out methods for classifying both learners and learning content on the web. To make classification and manipulation of learning content ease, we reorganize learning content in order to have discrete form by introducing the concept of the knowledge unit which is extracted from each topic. Also, to make classification and diagnostic ease, we develop questions to measure them and analyze each question using item response theory (IRT) on the web. From the experiment of students sampled using our method, we show that learners with various backgrounds and the learning content with distribution on the broad range can be categorized effectively into the groups with homogeneous property. Also, we describe how to apply our proposed scheme to the introductory courses at postsecondary level.

1 Introduction

In case of the presence of a broad spectrum regarding learning contents or learners, level-oriented education can be introduced. The idea behind level-oriented education is simple: students are assigned to different groups that reflect their level of comprehension of topics; students in each group are then presented with resources for learning that are commensurate with their level (each group is generally in a separate class or a different learning path in web-based learning, although this is not strictly necessary). However, it is unrealistic to apply level-oriented education to learning content and learners with broadly spread spectrum in the existing class without the help of an advanced e-learning technology like computing or web.

There are many literatures about how to assess learners. For example, Sly and Rennie [10] talk about a computer based tool to perform formative as well as summative assessment. Gayo-Avello and Fernández-Cuervo [11] provide some evidences about the effectiveness of self-assessment and self-learning. In this paper, we make learners diagnostic through web-based self-assessment. To make the diagnostic exact, we use item response theory (IRT) which could be easily computerized on the web and refer to Bloom's cognitive domain [2] in developing items and grasping the depth of

understanding. Specially, we intend to identify the depth of learner's understanding per subarea into which we classifies the learning content with distribution on the broad coverage.

Also, there has been research [4], [5], [6] on computing courses based on Bloom's taxonomy [2]. Lister and Leaney [4] focused on an introductory programming course and proposed the approach for teaching and grading the students in the course. Scott [6] developed test questions to test student mastery in an introductory programming course in C++. Oliver et al. [5] evaluated the six courses related to an IT degree using a difficulty metric called Bloom Rating. In our paper, we focused on introductory computer science courses for high school students at secondary level and freshmen at postsecondary level. We also used web-based e-learning technology and computerized adaptive test (CAT) based on item response theory [8], [9] in order to provide an efficient teaching-learning.

In our approach, the demands for the introductory courses will be changed according to the students' background in order to enable level-oriented education. In case of high schools, there are sometimes hundreds of students per each school who are required to take computer science courses. So, it's easy to see that there exist broad spread spectrums inside the courses. However, presently, classification has been in the size of 20 or 30 students per class at random without considering the characteristic of the broad spectrum. Also, in case of postsecondary level, we are targeting all students including the CS major, minor, and non-major. So, there exist much more broad spectrums inside the courses.

We infer that if our approach would be considered with the previous research together, the decrease in the drop rate would be significant in the courses. For example, if the approach of Lister and Leaney [4] can be applied to an introductory course after the classification of students and learning contents using our approach, then more efficient instruction could be given in the course. So, the relation between our work and their work is complementary at many cases.

2 Classifying the Learning Content

The first step required that we identify the learning content that students are expected to learn. Using Computing Curricula 2001 [1] and The ACM Model High School Computer Curriculum [7] criteria, we examined popular textbooks which are being used in high school computer science courses and introductory courses at postsecondary level. Then we classified the learning content into ten major subareas:

- processors
- memory types
- multimedia
- internet skills
- networking and communications
- security and intellectual property
- peripheral devices
- computing history
- information encoding
- operating systems

We came up with 186 discrete knowledge units that consist of the basic subjects or terms extracted from the learning content. During this process, in order to get the

appropriateness or validity of each knowledge unit extracted, we took some advices from peer teachers and professors about what knowledge units should be chosen and also used Cronbach alpha test to show the validity [12, 13, 14]. We then constructed a survey instrument that listed all 186 knowledge units, each of which the students had to evaluate according to the depth of understanding. Each student can mark one of five criteria per each knowledge unit. Also, it is possible to provide survey instruments of other criteria according to the judgment of instructor.

3 Analyzing/Applying the Results

In analyzing the results of the survey we attempted to assign a value to each of the 186 knowledge units that represented how well that knowledge unit was understood by the students. We used the following formula for this purpose, which can get easily the result through computing.

$$W_k = \frac{\sum_{i=1}^5 \frac{S_{ik}}{S} \times 100 \times i}{5} \quad (1)$$

Where W_k is the weighted value for the k th knowledge unit (k ranging over all knowledge units from 1 to 186), S is the total number of students, and S_{ik} is the number of students who marked the i th response (out of 5) for the k th knowledge unit. Notice the factor of i in the numerator; the responses are weighted by a factor corresponding to the number of that response. The factor 100 is used to normalize the results to a percentage.

After calculating the weighted values for the knowledge units, we need to classify them using a clustering technique. We define the new formula and algorithm for

Algorithm KUC(C, $n_{\text{partition}}$)

/ C = {w₁, ...w_n} and assume that C is sorted using W_k*

C_{copy} = C;

if the number of distinct values in C < n_{min_ku}, return

/ n_{min_ku} is a threshold */*

call BinaryDivide(C) to find the best cut, for C such that relaxation error is minimized

divide values in C based on the best cut

let the resultant sub-clusters be C₁ and C₂

n_{partition} = n_{partition} - 1

if (n_{partition} = 0) return

choose the one of sub-clusters C_i with maximum RE(C_i)

call KUC(C_i, n_{partition})

Algorithm BinaryDivide(C)

for h=1 to n-1

Let D be the partition with clusters C₁ and C₂

Compute relaxation error RE(D) for D

if RE(D) < MinRE then

MinRE = RE(D), cut = h / the best cut point */*

Return cut as the best cut

Fig. 1. Clustering Algorithms

classifying the knowledge units from clustering techniques [15] of numerical values. The relaxation error of C denoted by RE(C) is defined as the normalized difference between any weighted values of the knowledge units in C. C_k is the subcluster partitioned by BinaryDivide() algorithm. $p(w_i)$ is the occurring probability of w_i in C. RE(D) is the summation of RE(C) considering the frequency. Figure 1 shows the algorithm based on the formula defined.

$$RE(C) = \frac{1}{n} \sum_{i=1}^n \sum_{j=1}^n p(w_i)p(w_j) |w_i - w_j| \quad (2)$$

$$RE(D) = \sum_{k=1}^G P(C_k) RE(C_k) \quad (3)$$

4 A System for Classifying Learners

Once a categorization of learning content into the depth of understanding has been achieved, the next step is to classify learners appropriately. Again, there are various approaches that could be taken to determine what students need to learn. In our case, we tackled this problem with the help of the students themselves. Using this classification scheme as the basis for determining what students should know after completing a course or series of courses in computing, the task is to determine.

- What students already know, and
- The depth of their understanding.

In order to make this determination, we developed a set of examination questions based on the knowledge units in each subarea. To capture the depth of student understanding, we developed our questions referring to Bloom's taxonomy as our guide. There are six cognitive levels in this taxonomy: (1) knowledge, (2) comprehension, (3) application, (4) analysis, (5) synthesis, and (6) evaluation, each of which indicates an increasing degree of the grasp of a concept. For our purposes we use only the first five levels in determining the depth of student understanding of computing concepts at high school level. Also, we reflected the depth of understanding of the knowledge units we analyzed above.

Consider the subarea of memory types of being examined as an example. Typical knowledge units that might appear under this subarea are memory, main memory, cache, RAM, ROM, auxiliary memory, semiconductor, logic unit, and so on. Developing questions to determine at what cognitive level students understand these knowledge units is largely a matter of subjective opinion; we thus used Bloom's taxonomy as a guide in developing questions that are increasingly more difficult to answer and seem to capture the spirit of the taxonomy.

It can be seen that the questions progress from simple questions requiring rudimentary knowledge units to more complex questions that eventually require that students synthesize their knowledge of a number of knowledge units into a coherent answer, following the intent of Bloom's taxonomy. Questions at the lower cognitive levels may be true/false, whereas questions at progressively higher levels require more thought and need to be answered in the absence of clues. We tailored questions

by reflecting on useful tips from high school computer teachers, computer-related professors, and several high school students to be tested.

Following this example, we created the five questions of increasing cognitive difficulty for each of the ten subareas identified earlier, for a total of fifty questions. For each subarea we selected a set of five to ten knowledge units related to that subarea according to the depth of understanding we analyzed previously, and then we designed our questions to test the level of understanding of this knowledge unit.

5 Testing/Classifying the Students

Table 1 shows the results of our test. It was given to 127 eleventh grade students in a few high schools who had indicated that they planned to get computer-related jobs or study computer science at a college after graduation.

All were given fifty minutes to answer the fifty test questions. The rows of the table represent the subareas being tested; the columns represent the cognitive level of the question for each subarea. The two numbers in each table entry represent the percentage and number of students, respectively, who answered that question correctly. As we expected, the number of students who could answer a question decreased substantially as the cognitive level of the question became more difficult.

Now, we describe how to classify the students into the groups with homogenous property. We define the new formula and algorithm of learners similar to those of learning content mentioned earlier. The relaxation error of C denoted by RE(C) is defined as the normalized difference between any weighted test scores in C. C_k is the sub-cluster partitioned by BinaryDivide() algorithm. $p(T_i)$ is the occurring probability of T_i in C. T_i is the summation of subarea score t_{is} . RE(D) is the summation of RE(C) considering the frequency of the score.

$$RE(C) = \sum_{i=1}^n \sum_{j=1}^n \sum_{s=1}^a p(T_i)p(T_j) |t_{is} - t_{js}| \tag{4}$$

$$RE(D) = \sum_{K=1}^G P(C_K)RE(C_K) \tag{5}$$

By this point we have presented methods for (1) ascertaining what students should know at a certain point in their education, (2) segregating the material to be learned into groups based on how well students already understand it, and (3) categorizing students into levels based on their levels of understanding of this material.

What remains is to design learning experiences and resources that are appropriate for each of the levels identified in step 2 and 3. If students of all levels are restricted (by resource constraints) to the same classroom, this would work particularly well with e-learning like specially developed hypertext books [3], which are web-based, this would work particularly well with e-learning like specially developed hypertext books [3], which are web-based, active-learning resources that incorporate different learning paths for different levels of learners. Currently, our approach was applied to the field of computer science. However, it is possible to apply our approach to the other area courses (for example, English or Mathematics), where the distribution of learning contents or learners is on a broad spectrum.

Table 1. Percentage and Number of Students with Correct Answer

Subarea	Cognitive Level				
	1	2	3	4	5
Information encoding	86.6 (110)	25.2 (32)	18.9 (24)	7.1 (9)	0.00 (0)
Multimedia	70.9 (90)	27.6 (35)	32.2 (32)	24.4 (31)	11.8 (15)
Internet skills	67.7 (86)	54.3 (69)	44.1 (56)	11.8 (15)	1.6 (2)
Networking & Communications	54.3 (69)	44.1 (56)	16.5 (21)	3.2 (4)	0.00 (0)
Peripheral devices	62.2 (79)	30.7 (39)	29.9 (38)	11.8 (15)	1.6 (2)
Computing history	68.5 (87)	39.4 (50)	33.9 (43)	4.7 (6)	0.8 (1)
Memory types	66.1 (84)	44.9 (57)	0.8 (1)	0.00 (0)	0.00 (0)
Processors	20.5 (26)	10.2 (13)	1.6 (2)	0.00 (0)	0.00 (0)
Security & intellectual property	69.3 (88)	60.6 (77)	52.0 (66)	42.5 (54)	34.6 (44)
Operating systems	59.1 (75)	55.9 (71)	17.3 (22)	2.4 (3)	0.00 (0)

6 Extending to Postsecondary Level

The All of the examples and work described above were done in the context of high schools. Is there a place for level-oriented education in colleges and universities?

We think so. Consider the dilemma facing both students and instructors of introductory computing courses at post-secondary institutions. Students arrive with widely divergent backgrounds. Some have been constructing computers, using all manner of software, and even programming since grade school. Others are fairly adept at using computers for many kinds of applications, such as word processing, e-mail, and Web page development, but understand little of programming or the internal workings of a computer. Still others have almost no experience with computers.

Putting all of these students into the same introductory programming course on the way to a computer science degree causes all sorts of problems.

The result is that the most advanced students are not challenged and become bored with the course, whereas those at the other end are left gasping for air, feeling that the course is advancing far too quickly for them. The existing approach at our university for addressing this problem has been to introduce a new course since 2001, called Introduction to Computer Science which precedes the usual first programming course and is designed to

- give students an overview of computer science,
- provide students with all of the technical tools needed to be successful in the computer science curriculum, and
- provide a brief and gentle introduction to what programming involves.

Furthermore, there is already a course in the department, Computer Literacy, for non-majors that is even more elementary than this new course. So, we now have three courses that are appropriate for three different levels of entering freshmen. How should newcomers be assigned to the most appropriate course? We are all aware that many students arrive with inflated opinions of their understanding of computing, so if we leave it to the students to decide we will likely not be much better off than we are now. We also see students who underestimate their talents. What we need is an examination that does a good job of placing students in the appropriate course. Given that faculty have no time to oversee such an examination and that incoming students need to know in real time which course to enroll in, such an examination would need to be computer administered and graded. The approach presented in this paper can be adapted for this purpose.

As the first step, we identified the learning content and collected the discrete knowledge units that students are expected to learn in the introductory courses at postsecondary level based on Computing Curricula 2001. We classified the learning material into ten subareas by applying the approach similar to the case of high school.

We came up with 381 knowledge units which are about twice as many as that of high school. Based on the knowledge units, we developed questions per subarea considering the cognitive level. In order to get the reliability of them, we made Cronbach Alpha test using SPSS program based on the feedback information from graduate students on how much each question corresponds to the cognitive level and knowledge units. Then, we constructed the database using the MySQL on the web of the questions that the coefficient of Cronbach Alpha is over 0.6[12,13,14].

The table 2 represents the cognitive level and item difficulty using IRT for each question. The table represents the cognitive level and item difficulty using IRT for

Table 2. Analysis of Questions at Postsecondary Level

Subarea	Cognitive Level					
	1	2	3	4	5	6
Processor	578(41)	479(34)	324(23)	282(20)	170(12)	113(8)
Data storages	76.1(54)	74.7(53)	62.0(44)	57.8(41)	56.3(40)	35.2(25)
Operating System	64.8(46)	45.1(32)	45.1(32)	36.6(26)	22.5(16)	15.5(11)
Internet	74.7(53)	71.8(51)	46.5(33)	39.4(28)	25.4(18)	4.5(3)
Network &Comm.	42.3(30)	38.0(27)	33.8(24)	32.4(23)	19.7(14)	19.7(14)
Peripheral devices	56.3(40)	54.9(39)	28.2(20)	22.5(16)	14.1(0)	5.6(40)
Information	50.7(36)	64.8(46)	57.8(41)	23.9(17)	16.9(12)	33.8(24)
Programming	53.5(38)	42.3(30)	33.8(24)	31.0(22)	18.3(13)	3.8(3)
Application	43.7(31)	42.3(30)	33.8(24)	29.6(21)	5.2(4)	2.8(2)
Misc.	43.7(31)	42.3(30)	33.8(24)	29.6(21)	5.2(37)	2.8(2)

each question. It is possible to provide the 3 or 5 cognitive level per subarea for a quick test. Also, the multiple of the 6 cognitive level questions can be given about a specific subarea of interest to learners who want to take more detailed test. In our experiment, assuming that there is the 6 cognitive level per subarea, the totals of 60 questions for 60 minutes were given to students to measure them.

Also, we got the distribution of students by testing students during last two year. As a sample, the figure 1 shows the distribution of 71 learners tested this year.

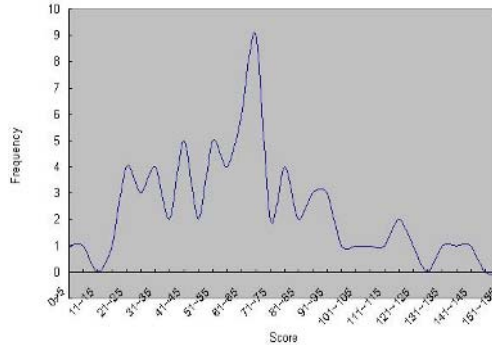


Fig. 2. Distribution of students at postsecondary level

The graph of Figure 2 indicates that the distribution is on a broad spectrum. The x-axis represents the weighted scores based on IRT.

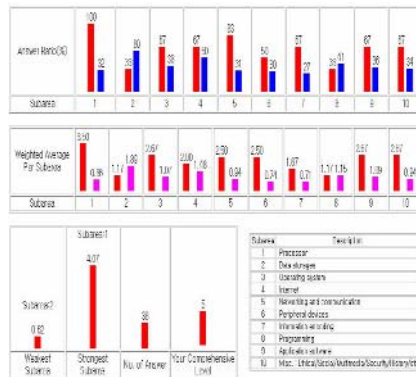


Fig. 3. Graphical results of diagnostic assessment

We also provide a graphical diagnostic assessment to learners who want to identify their level, as seen in Figure 3. The figure shows that a learner enables to identify his/her level of each subarea. From the results of the diagnostic assessment, the learner can study the specific subarea, which is not relatively competent. We implemented the diagnostic assessment system using PHP and MySQL on the web.

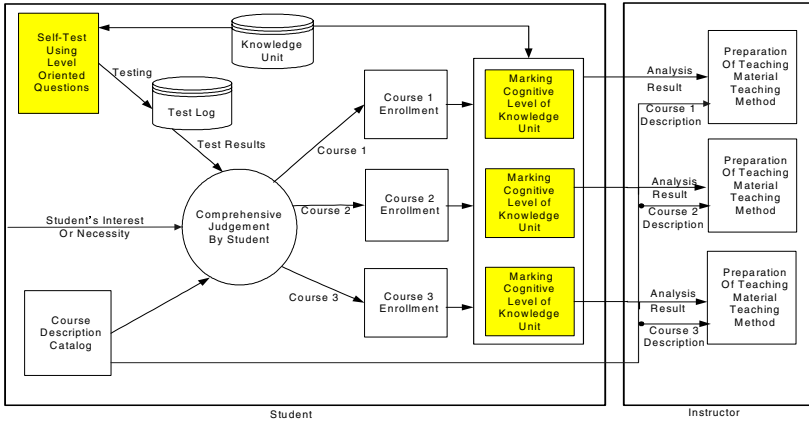


Fig. 4. Applying to postsecondary introductory courses

Each learner could get more detailed diagnostic result about a specific of interest subarea by answering more than the 6 questions per the subarea repeatedly.

Figure 4 represents how to apply our approach to postsecondary introductory courses. As you can see in the figure, the students who want to take one of three introductory courses mentioned above can measure their own backgrounds using the level-oriented questions before registering it. Also, instructors can get some information about the background of students.

Using the cognitive level analysis of knowledge units are covered in the course before giving the lecture to students. Based on this feedback information from students, teachers can understand what knowledge units (eventually topics including the related-knowledge units) require more time-consuming explanation and more sophisticated teaching materials. So, eventually, students can choose the course appropriate to them and instructors can prepare the teaching material and the teaching method considering the students' learning level.

Specially, it will be very helpful to entering freshmen who are almost ignorant of courses offered. The level-oriented questions and the question instrument for cognitive level analysis of knowledge units are provided in the web-based form. Also, the printed-out form can be available.

7 Conclusions

In the web-based e-learning, level-oriented education is very effective, because it can match instruction with the needs of students. We have presented here a method for grouping students into levels and identifying the knowledge each group needs to learn on the web using the item response theory (IRT) that can be computerized. Our method can be applied to solve the needs of both high school and introductory postsecondary students by constructing a discrete form about the knowledge to be learned. Thus, our method will increase learner's interest about lecture by enabling learner-centered education and eventually boost the learning achievement degree. In

addition, our approach could be used as a basic template in order to bring customized individualization learning through e-learning.

Acknowledgements

This study was partly supported by DCRC (Digital Contents Cooperative Research Center) and RIS (Regional Innovation System) Program, Cheju National University, Korea.

References

1. ACM/IEEE-CS Joint Curriculum Task Force, Computing curricula 2001, <http://www.computer.org/education/cc2001/final/index.htm>, 2001.
2. Bloom, B.S., et al, Taxonomy of Educational Objectives: Handbook I: Cognitive Domain, Longmans, Green and Company, 1956.
3. Boroni, C. M., et al, "Tying it All Together Creating Self-Contained, Animated Interactive, Web-Based Resources for Computer Science Education", Proc. of Thirtieth SIGCSE Technical Symposium on Computer Science Education, Vol. 31, 1999.
4. Lister, R., and Leaney. J., "Introductory Programming: Criterion-Referencing, and Bloom", Proc. of Thirty-Fourth SIGCSE Technical Symposium on Computer Science Education, Vol. 35, 2003.
5. Oliver, D., Dobeles, T., and Greber, M. "This Course Has A Bloom Rating Of 3.9", Proc. Of Sixth Australasian Computing Education Conference, Vol. 30, 2004.
6. Scott, T, "Bloom's Taxonomy Applied To Testing In Computer Science Classes", Proc. of the 12th Annual CCSC Rocky Mountain Conference, Vol. 19, 2003.
7. Task Force of the Pre-College Committee of the Education Board of the ACM, ACM Model High School Computer Science Curriculum, <http://www.acm.org/education/hscur/index.html>, 1997.
8. Wainer, H, Computerized Adaptive Testing: A Primer (second edition), Lea publisher, 2000.
9. Tim, F.M., Measuring Second Language Performance, Addison Wesley, Inc., 1996.
10. Sly, L. and Rennie, L.J., "Computer Managed Learning: It's Use in Formative as Well as Summative Assessment", Proc. of the 3rd Annual CAA Conference, 1999.
11. Gayo-Avello, D. and Fernández-Cuervo, H., "Online Self-Assessment as a Learning Method", Proc. of the 3rd IEEE International Conference on Advanced Learning Technologies, 2003.
12. HyeungJin Roh, "An Easy Guide to Multivariate Analysis Using Korean Spss 10.0", Hyungseul, 2003.
13. MaryAnne Atkinson, Christine Kydd, "Individual Characteristics Associated with World Wide Web Use: An Empirical Study of Playfulness and Motivation", The DATA BASE for Advances in Information Systems, Vol.28, No.2, 1997.
14. Rajeswari K. S. and R.N. Anantharaman, "Development of an Instrument to Measure Stress among Software Professionals: Factor Analytic Study", SIGMIS Conference, 2003.
15. Wesley W. Chu and Kuorong Chiang, Abstraction of High Level Concepts from Numerical Values in Databases, Proc. Of the AAAI Workshop on Knowledge Discovery in Databases, July, 1994.

Ontology-Based Edutainment System

Cheol Min Kim, Hye Sun Kim, and Seong Baeg Kim

Department of Computer Education, Cheju National University,
66 Jejudaehakno, Jeju, 690-756, Korea
cmkim@cheju.ac.kr, tonaa07@hotmail.com,
sbkim@cheju.ac.kr

Abstract. Recently the Semantic Web is emerging as a solution to problems in the existing Web. The outstanding features of the Semantic Web could contribute to establishing more effective e-learning systems than a conventional web-based e-learning system. However, studies on its applications to e-learning are insufficient. In this paper, we present a new edutainment e-learning system that uses the Semantic Web technology. We extract learning contents from middle school textbooks to generate our ontology. With the ontology, we are developing a learner assessment system, a learning guidance system, and an edutainment learning system. The learner assessment system assesses the current state of a learner's knowledge in the ontology. The learning guidance system categorizes the learners based on the results of the assessment system and dynamically generates a learning course to each learner. The edutainment learning system provides templates for making game-like items. We shall describe them respectively and state relations among them. Our system will be a good model of edutainment e-learning systems based on Semantic Web technologies.

1 Introduction

Information on the Web built in the hypertext-based HTML language requires some interpretation and determination of users in the process of selecting the needed information precisely when they search information. In other words, users ought to comb and check out web documents containing words and phrases that they type in and to distinguish web documents containing useful information from web documents without necessary information. Yet, because online information is vastly expanding out of control, searching is getting difficult. HTML, focusing on layout and display, falls short in expanding, integrating and sharing a variety of web documents. It is also difficult to automatically extract meaning out of HTML documents through certain programs or software agents.

Tim Berners-Lee said that the Semantic Web is an extension of the current web in which information is given well-defined meaning, better enabling computers and people to work in cooperation [1]. Thus the Semantic Web is to develop standards and technologies that help computers to more effectively and efficiently search, integrate, and understand information on the Web.

The basic need of a human being's living is the necessity of life-long education that is the need to consistently learn on a daily basis in order to lead a meaningful

social life. More precisely, the e-learning system enables the diversity of learning contents, the speeding up of acquiring knowledge, the maximization of associating knowledge with experience, working while learning and the minimization of education and training costs. Attention to the e-learning system is essentially transforming the educational environment. E-learning is being phased in all parts of education. It is especially getting a lot of attention from corporate education areas and being developed and used in the areas. This is because the web opens up more educational opportunities, has good accessibility to education transcending normal time and space limitations, reduces education costs, and improves the quality of education through autonomous interaction.

Despite the various merits of education through e-learning mentioned above, there is still a lot to be desired in terms of the overall design, delivery and application. Among these are the effective establishment of learning contents for e-learning, the reuse of established learning contents and the realization of intelligent searching. To that end, in our paper, we shall make a suggestion of a new edutainment e-learning system based on the Semantic Web for effective e-learning. In particular, we shall look into how to establish the Semantic Web in an effective manner on a computer textbook of middle school.

2 Theoretical Background

2.1 XML Schema

Representing learning contents is a significantly important skill. XML is of great usefulness in defining learning contents because data and representative information are separated. If some contents are defined in XML, a learner can get different representations from same contents at times.

Originally schema is not a term used only in XML. In computing, schema generally refers to “data definition” or “data description”. Schema in XML also carries the same meaning. It was suggested along with a DTD to define the structure of a document. However, because of DTD’s limitations it aroused the necessity for new rules to define the structure of an XML document.

XML schema is a standardized work initiated to make more efficient use of XML as well as to complement DTD’s limitations. It carries out jobs ranging from systematizing a document and putting information in hierarchical and systematic order to data type restrictions in usage areas to provide an effective way of searching data.

Representations in XML are still in many ways insufficient in creating the Semantic Web. For example, each individual could use different names to define tags even if they mean the same and utilize an XML document with various structures of the same contents.

2.2 RDF

RDF is a framework suggested to solve XML’s problems and to focus on semantics. The basis of RDF is metadata [2]. RDF is a foundation for processing; it provides interoperability between applications that exchange machine-understandable information on the web. RDF metadata can be used in a variety of application areas;

in resource discovery it is used to provide better search engine capabilities; in cataloging it is used for describing the content and content relations available at a particular web site page or digital library, by intelligent software agents that facilitate knowledge sharing and exchange; in content rating it is used in describing collections of pages that represent a single logical “document”; it is used for describing intellectual property rights of web pages, and it is used in many others. RDF with digital signatures will be a key to building the “Web of Trust” for electronic commerce, collaboration, and other applications [3].

The RDF model can solve problems XML has. For instance, it is easy to understand a document because there aren't as many ways to represent different structures as in XML. However, there exist some of the same problems in RDF as those in XML such as redundancies and ambiguities in tag names. In other words, different tags could mean in fact the same thing while same tags could have different meanings. Therefore this problem ought to be resolved with the ontology as in XML's case. In RDF, there exists RDF Schema similar to an ontology.

RDF schema is a language to define properties or to constrain the use of properties. Thus it can be correctly said that meaning in RDF is expressed through reference to a schema. RDF is expressed through the schema. For an easier understanding, it is helpful to associate schema with a dictionary. It first defines a term comprised of RDF statements and states specific meanings of terms. The ontology is similar to RDF schema on the whole but a more general and extended one.

2.3 Ontology

Ontology engineering is a technology, which derives, represents and stores semantic relations among concepts used in web documents. It is becoming an important essential technology in implementing the Semantic Web. Gruber said that an ontology is a formal, explicit specification of a shared conceptualization [4]. Simply put, it can be said an ontology is a dictionary made up of relations among words. It includes inference rules, which can show and extend domain-related terms in taxonomical hierarchy. An ontology has definitions of taxonomy and inference rules. Taxonomy defines classes of objects and a relationship between them. The ontology language is a language, which defines schema, syntactic structures, etc to represent an ontology. Now there are DAML+OIL, OWL, and Ontolingua in the ontology language. Of these, DAML+OIL, which was suggested as the standardized language by W3C, is a semantic markup language for web resources. It also is a frame-based ontology representation language extending RDF and RDF schema standards [5].

2.4 Authoring Tools for the Semantic Web

Tools to effectively set up an ontology have been developed. Of them, the most well known tools are as following.

2.4.1 Protégé 2000

The U.S. Stanford Medical Informatics developed Protégé 2000. It is the most commonly used authoring tools because of its outstanding editing functions. It consists of extensible plugins and is compatible with ezOWL plugins. There are such file formats as TEXT, RDF, JDBS supported in protégé. Protégé makes it easy to add

classes/subclasses or instances and manages an ontology in a prpj extension which is the project file format of the tool [12].

2.4.2 OntoEdit

The German ‘Ontoprise’ has developed the tool OntoEdit. It uses models of knowledge from applications to offer the ontology-engineering environment to create and handle these ontologies [13]. There are such file formats as F-Logic, DAML+OIL, XML supported in OntoEdit. With Excel files, It can only read them. The interface is not easy to use. It provides us with graphs connecting concepts and the corresponding instances.

2.4.3 OilEd

The development and implementation of OilEd was carried out by Sean Bechhofer of the University of Manchester and Gary Ng, formerly of the University of Manchester, now with Network Inference [14]. It provides a simple editor that demonstrated the use of, and stimulated interest in the OIL language. There are such file formats as RDF, DAML+OIL, SHIQ supported in OilEd. The interface is easy to use. However it is based significantly on math.

2.4.4 ezOWL

It was developed by the Korean Electronics and Telecommunications Research Institute in September, 2003 [15]. ezOwl is an ontology-based intelligent authoring tool enabling a computer to understand terms in web documents. Complex ontologies can be created and edited in a graphic diagram. It enables users to understand and produce contents although without the knowledge of the ontology. Also, It has high compatibility in supporting existing languages such as DAML+OIL and RDF/RDFS.

2.5 Related Work

Mikael et al.[6] explain effective learning scenarios using the Ontology. The paper is on various and comprehensive e-learning systems; a brief introduction of some of curiosity-arousing learning contents, search engines and advanced searching, learning with animation, multimedia, academic and detailed learning contents, and consulting and further learning through an individual portfolio and more. Cristina et al.[7] deal with PRIME CLIMB, a learning agent, which helps factorization. Also, they enable learners to be assessed and to gain knowledge effectively through various hints. Ljiljana et al.[8] make clear differences between existing learning methods and e-learning. They also state in detail the efficiency of e-learning methods based on the Semantic Web and proves that ontology technologies can be utilized as a basis for e-learning. Pythagoras et al.[9] suggest concrete learning methods through ontologies. They build an intelligent learning management system based on learning objects and provide each learner with an individualized learning process on the system.

3 Establishing an Ontology

One of the difficulties in building an ontology is to determine its domain. In this paper, the scope of a domain is limited to the contents in a middle school textbook.

Setting up an ontology in a computer textbook is currently underway and is planned to extend to other textbooks. In building the ontology, we are organizing information for differentiated learning and individualized learning. Differentiated education, which takes into account students of various learning abilities, is becoming popular. But in the case of information and computer areas which have a wide spectrum of the scope of learning contents and learners, specific studies on it are very meager.

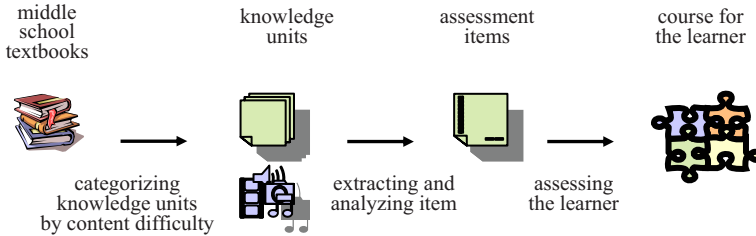


Fig. 1. Architecture of Generating Course for the Learner

As a way for differentiated and individualized education, we use an approach to turn continuous learning contents into discrete knowledge units. In addition, discrete knowledge units will be provided in a different fashion and a quantity depending on a learner's learning level and attention. For example, to a learner whose academic level is high, the contents in a text form with technical terminology are given. When a learner's academic level is low, the contents can be a text with explanations in plain and easy words. Additionally, when a learner is interested in a knowledge unit and is eager to learn more in detail, contents come in graphics and animations too. When a learner just wants to have a basic knowledge, contents will be offered mostly in the form of a text. For the purpose, our system has a mechanism for providing a learning course appropriate for the learner. Its architecture is shown in Figure 1.

To make it possible for a learner to learn according to their academic level, it is necessary not only to analyze content difficulty but also to carry out a precise assessment of a learner. Furthermore, it is needed to find out what a learner knows and does not know, in order to determine what learning contents a learner should be attentively educated on. To that end, we have developed items for a learner's assessment based on an analysis of learning content difficulty by knowledge unit. With the knowledge units examined above, items of each area have been developed reflecting the 6 steps of Bloom. For instance, difficult items have been developed with a majority of contents from knowledge units of high difficulty. On the contrary, easy items have been made reflecting mostly contents of low difficulty. Candidate learners for assessment are required to solve 6 items of different difficulty respectively from 10 specific areas. Thus, after all, learners get to solve a total of 60 items.

To improve the quality of evaluation tools, a test should consist of high quality items. To that end, it is necessary to examine whether each item is good or not. Basically, the quality of a test relies on the quality of its items. An item is the most basic unit of a test. Thus, if items of a test are not good, the whole quality of a test is

bound to be bad. So the examination of items should be done prior to the scrutiny of a test. It is called item analysis to examine the contribution that each item is making to the test. Item analysis is generally divided into difficulty of an item, item discrimination and an item response range. We have applied educational item analysis and analyzed them to scrutinize thoroughly developed items with the difficulty in consideration.

In building the ontology, one of the considerations is the fact that it is needed to keep and manage an index of knowledge in an effective way and to organize it for effective searching. Therefore, we implement frame-based ontology and a database system in a systematic fashion to magnify the effects of learning and make good use of them in the subsequent development of game-like items. Using frame-based ontology authoring tools, we built knowledge units of a computer textbook in middle school as illustrated in Figure 2. Through queries, it is possible to search words or vocabulary that is to be learnt. We also set up an ontology database which increases reuse by extracting or integrating various knowledge units. It is scheduled to develop CD/DVD titles for educational purposes with improvement to them.

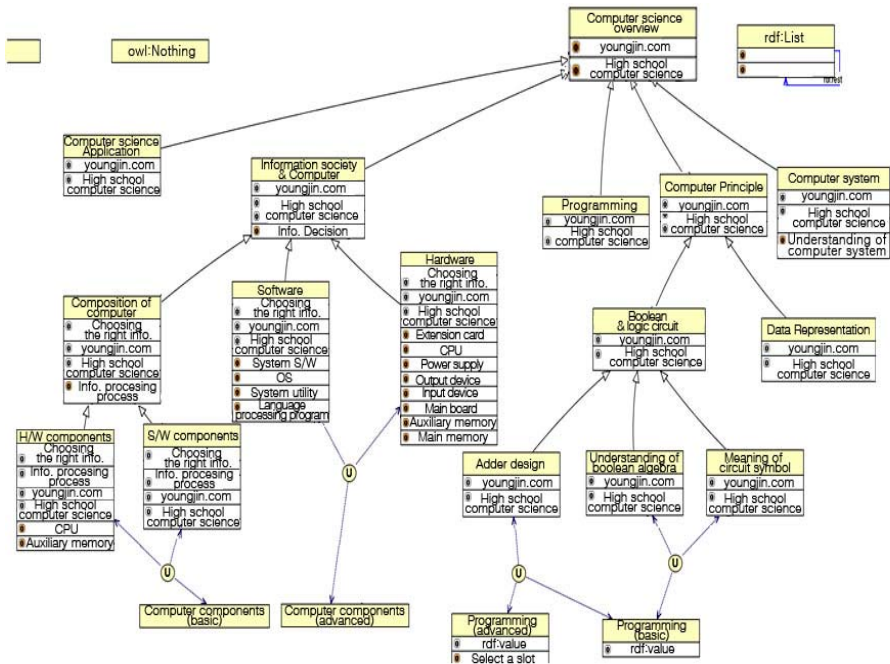


Fig. 2. An Ontology for a Middle School Textbook

4 Building Game-Like Items Based on the Ontology

There are few researches on educational games to enhance learning interest and learning effects. Despite outstanding merits of educational games, they are not well

developed and commonly utilized because of difficulties in development. However, it is drawing a lot of attention because it would be educationally very effective if games could be employed in education.

Thus we are developing quizzes and games in line with what is to be learnt. In particular, we develop a new type of game that can capture a learner’s attention by making use of multimedia effects such as animation. Further, it is expected to induce collaborative learning by introducing games and quizzes, which a group of learners solve together competing with other groups. Cross word puzzles or ‘Brain Survival Contest’ could be good examples and so fun that it is worth making educationally applied game-like items. Furthermore, we use Flash to exploit its display features and build the template for making instances of various types of quiz and game with XML[10] and ASP[11]. The game templates play a role of intermediate between instructor and learner in edutainment learning as illustrated in Figure 3.

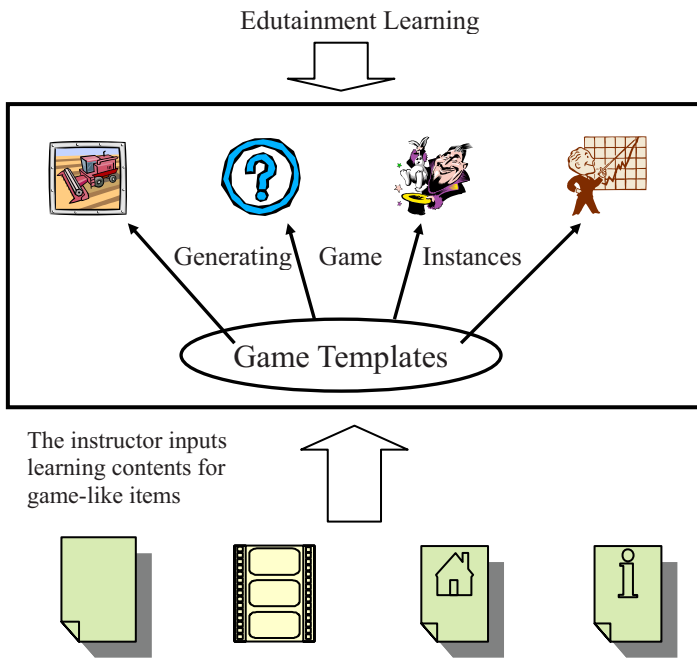


Fig. 3. Edutainment Teaching/learning using Game Templates

Until now, we have developed quizzes and games with a variety of styles as Figure 4. A teacher on manager mode can administer items for themselves which they think are necessary for a student to learn more and can change items easily into game-like items by using game types of their choice. In addition, there are attribute features such as hints and accumulation of points to stimulate learning interest and to have fun. These features are expected to increase a learner’s willingness to participate in learning and to help a learner stay concentrated. Through the process, a learner will acquire knowledge in a natural and systematic way.

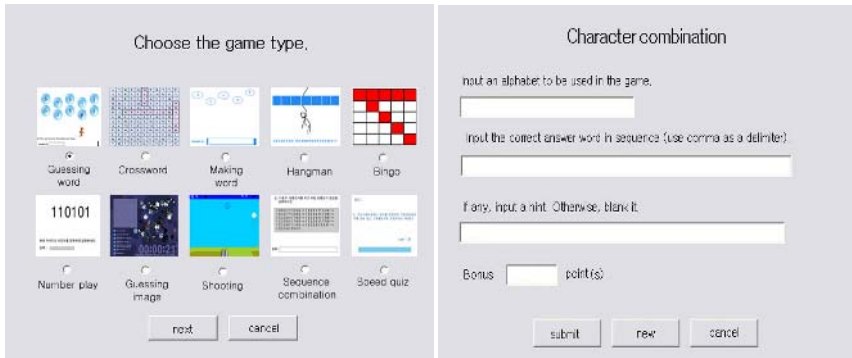


Fig. 4. Templates for Making Quiz and Game Instances

5 Building a Learning Guidance System Based on the Ontology

It needs to consider a lot of factors such as a learner's academic level, a learner's attention, and a learner's learning style to provide a learner with customized learning. In particular, an effectively built ontology shows relationships among knowledge, which is to be taught. Thus we offer each individual a customized learning guidance system. It utilizes correlations among knowledge in the ontology, information about a learner's academic level from a learner assessment, and a variety of other information. It finds out a proper learning order of precedence relationship among knowledge units to provide for a learner. Also, It gives a learner learning contents and various learning styles considering a learner's learning style and a learner's attention level etc. It would be beneficial to take the game-like items mentioned above into account in the learning guidance system to offer more interesting, effective customized learning.

6 The Whole Structure of the System

Figure 5 shows the whole structure of the ontology-based edutainment e-learning system. The very bottom of the picture is learning contents in a certain middle school textbook. It is also a domain of the ontology, which is to be built. The procedures of generating the ontology go like this; first, extract knowledge units from the textbook and then define relations among them and add attribute information such as information by academic level or information of before and after learning to assist in learning. During the procedures, we have made proper use of authoring tools, employed the logic language for inference rules and converted it in the form of XML Schema for use on the Web to facilitate the establishment of the ontology. Additionally, to boost efficiency in building the ontology on e-learning contents, it is advisable to provide a template or a plugin in existing ontology tools. Following this, it is needed to have a search engine for improved searching from the established ontology.

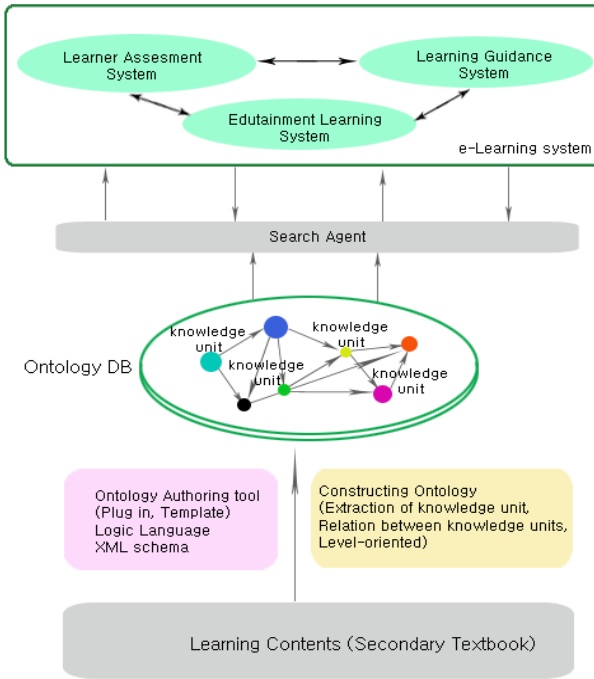


Fig. 5. The Whole Structure of the Edutainment e-Learning System

Our e-learning system that provides the learner with e-learning services based on the ontology includes three core subsystems; the learner assessment system, the edutainment learning system and the learning guidance system as illustrated in Figure 5. The learner assessment system generates assessment items by academic levels from the ontology and then diagnoses and assesses the learner with them. The edutainment learning system enables the instructor to produce game-like learning items and the learner to learn the knowledge with those items. The learning guidance system provides learning methods for each learner considering the correlation among knowledge units, the learner’s characteristics and academic level in a comprehensive manner. These subsystems altogether exchange needed information with one another through interaction.

7 Conclusion and Future Work

The existing e-learning contents can hardly be utilized once characteristics of the learner and the instructor change because it’s difficult to integrate, share and reuse them for a different content format. However, if ontology technology comes into use in e-learning, it is easy to share or reuse e-learning contents. In addition, it is possible to intelligently retrieve learning contents based on the ontology.

In the paper, we have made a suggestion of how to establish an ontology limiting the learning material to textbooks of middle school. Further, based on the ontology, we have proposed the three subsystems for learners and instructors; the learner

assessment system, the edutainment learning system and the learning guidance system. Especially we are developing the edutainment learning system with the templates for making instances of various types of quiz and game. The templates will enable the instructor to effectively employ the games in education and the learner to be provided with the entertaining learning environment proper to him.

We will build a more systematic ontology and implement the edutainment e-learning system with the ontology as a basis. Also, we have a plan to develop additional templates for instantiating quizzes and games and study on application of the e-learning system to learners.

Acknowledgements

This study was partly supported by DCRC (Digital Contents Cooperative Research Center), Cheju National University, Korea.

References

1. Berners-Lee, T., Hendler, J., and Lassila, O., "The Semantic Web", Scientific American, 2001.
2. Lassila, O., "Web metadata: a matter of semantics", IEEE Internet Computing, Vol. 2, No. 4, pp.30-37, 1998.
3. Lassila, O. and Ralph R. Swick, "Resource Description Framework (RDF) Model and Syntax Specification", W3C Proposed Recommendation, 1999.
4. Gruber, T., "A translation approach to portable ontologies", Knowledge Acquisition, Vol. 5, No. 2, pp.199-220, 1993.
5. McGuinness, D., Fikes, R., Hendler, J., and Stein, L., "DAML+OIL: an ontology language for the Semantic Web", IEEE Intelligent Systems, Vol. 17, No. 5, pp. 72-80, 2002.
6. Mikael N., Matthias P., and Ambjorn N., "Semantic Web Meta-data for e-Learning Some Architectural Guidelines", <http://www.aifb.uni-karlsruhe.de>.
7. Cristina C. and Xiaohong Z., "Building and Evaluating an Intelligent Pedagogical Agent to Improve the Effectiveness of an Educational Game", In Proceedings of the 2004 International Conference on Intelligent User Interfaces, 2004.
8. Ljiljana S., Steffen S., and Sudi S., "eLearning based on the Semantic Web", <http://kmr.nada.kth.se>.
9. Pythagoras K. and Demetrios S., "Adaptive Instructional Planning using Ontologies", The 4th IEEE International Conference on Advanced Learning Technologies, 2004.
10. Manny T., Jamie M. and Glen R., Flash Math Creativity, friendsofED Press, 2002.
11. Richard A., Components for ASP, WROX Press, 1999.
12. protégé-2000 project, <http://protege.stanford.edu>.
13. ONTOPRISE, <http://www.ontoprise.de>.
14. OilEd, <http://oiled.man.ac.uk>.
15. ezOWL, <http://iweb.etri.re.kr/ezowl>.

A Fast Video Encoding Algorithm by Skipping the Operations on Zero-Valued DCT Coefficients^{*}

Kook-Yeol Yoo

School of EECS, Yeungnam University, 214-1 Dae-Dong, Kyungsan-City,
Kyungpook 712-749, South Korea
kyoo@yu.ac.kr

Abstract. In this paper, we propose a computation-efficient DCT-based encoding algorithm for the standard video encoders. Most video coding standards consist of DCT and associated modules such as quantization, zigzag scan, VLC (Variable Length Coders). Commercial and standard video encoders implement the modules independently. In this paper, the relationship between the function modules is investigated and the unnecessary operations are removed. The simulation results show that the proposed method reduces the computation complexity of IDCT by 40 % compared with standard implementation.

1 Introduction

The digital videos in various forms, such as the digital TV, VoD in cellular phone, video clips for PDA, etc, become the part of daily life nowadays. With the rapid advance of the hardware and video compression technologies, the portable devices provide the digital videos in the format of MPEG-4 Simple Profile [1] and H.263 baseline codec [2]. Even the portable devices connected to the broadband wireless network will provide the bi-directional videophone-type application. As the display devices, such as PDA and cellular phone become portable, the most important thing for the multimedia service in the portable devices is how to effectively reduce the computational complexity due to the limitation of the battery power.

With the intensive research on the fast motion estimation algorithm, the portion of computational complexity of motion estimation in the video encoder is greatly reduced. More specifically the computational complexity used for the DCT (Discrete Cosine Transform) and IDCT (Inverse DCT) in the encoder occupies about 30.1% of the total complexity. This means that the optimization on the DCT encoding / decoding parts is highly necessary for computation-limited terminals [3, 4].

Most standard video encoders employ the hybrid MC-DCT (Motion Compensation – DCT) structure. For the DCT encoding part, the several function modules, such as DCT, quantization, zigzag scan, and VLC (Variable Length Coding), are connected in the cascaded forms. For the decoded images used as the reference images in the motion estimation and compensation, the IDCT and inverse quantization modules are necessary.

^{*} This research was supported by the MIC (Ministry of Information and Communication), Korea, under the ITRC (Information Technology Research Center) support program supervised by the IITA (Institute of Information Technology Assessment).

Conventionally, each function modules takes the output of the previous modules, processes independently, and produces the output for the input of the next modules. [5, 6].

In this paper, the relationships among the DCT encoding / decoding modules are thoroughly investigated. From the analysis, we found that the partial operations of each module can be skipped without the loss of quality or encoder-decoder mismatch problems, when the quantization process produces the zero-valued quantized coefficients. In other words, the zigzag scan, VLC, inverse quantization, and IDCT operations can be skipped for the zero-valued quantized coefficients. The simulation results show that the proposed algorithm greatly reduces the complexity for the VLC encoding, scanning, and inverse quantization. Especially the computational complexity for IDCT is reduced about 40%, which is great impact on the overall computation complexity of encoder.

This paper is organized as follows: Section 2 describes the basic structure of standard video codec which employs the hybrid MC-DCT. The proposed algorithm is explained in the Section 3. In Sections 4 and 5, the simulation results and conclusion are presented, respectively.

2 Basic Structure and Computation of Standard Video Encoders

In this section, we describe the hybrid MC-DCT encoding algorithm which is basic structure of ISO/IEC MPEG-4 Simple Profile (ISO/IEC 14496-2) and ITU-T Recommendation H.263.

2.1 Overview of the Basic Encoding Method

Fig. 1 depicts the basic structure of standard-compliant video encoders. The basic unit for the encoding is the Macroblock (16 pixels in lines x 16 lines for luminance block and two 8 pixels in lines x 8 lines chrominance block). The Macroblock is further divided into six 8x8 blocks, i.e., four luminance blocks and two chrominance blocks. The Macroblock is encoded in either INTRA coding mode or INTER coding mode.

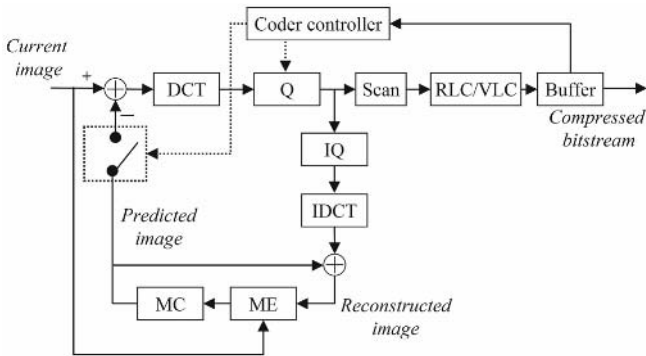


Fig. 1. Basic Structure of hybrid MC-DCT based video encoder

For the picture coding, the encoders operate in two kinds of modes, namely, INTRA and INTER picture coding modes. For the INTRA picture coding mode, all the Macroblocks are coded in INTRA coding mode. For INTER picture coding mode, the Macroblocks are coded either in INTRA coding mode or in INTER coding mode. For INTRA coding mode, the switch, indicated by the dotted-box in Fig. 1, is opened, so the only the Macroblock from the current image is encoded. For INTER coding mode, the switch is closed, so the difference Macroblock between the ones from the current and predicted images are encoded.

Each block from the Macroblock is processed by the series of function modules. The DCT transforms the pixel values or difference pixel values of block into DCT coefficients. The quantizer, which divides each DCT coefficients by quantization step size, converts them into the integer-valued quantized DCT coefficients. Since the energy of DCT coefficients are compacted into the low frequencies, most of the high frequency components are zero-valued after quantization. Especially, the quantized DCT coefficients for INTER coding mode are more likely to be zero-values, since the difference Macroblock has small energy by motion compensated prediction process. The quantized DCT coefficients are scanned to produce the one-dimensional coefficients sequence. The scanning pattern is depicted in Fig. 2. If all the quantized DCT coefficients of the block are zero-valued, the block is marked as non-coded block and no further processing is applied.

1	2	6	7	15	16	28	29
3	5	8	14	17	27	30	43
4	9	13	18	26	31	42	44
10	12	19	25	32	41	45	54
11	20	24	33	40	46	53	55
21	23	34	39	47	52	56	61
22	35	38	48	51	57	60	62
36	37	49	50	58	59	63	64

Fig. 2. Zigzag scanning pattern

Then the quantized DCT coefficients are encoded by RLC (Run-Length coding) coder and VLC encoder. The RLC of ISO/IEC MPEG-4 or ITU-T H.263 represents the scanned and quantized DCT coefficients in three-dimensional symbols, such as (EOB, RUN, LEVEL) where the LEVEL is the value of nonzero-valued quantized DCT coefficients, the RUN represents the number of zero-valued coefficients which precedes the LEVEL in the scanning order, and the EOB represents whether the current LEVEL is the last non-zero quantized DCT coefficients in the scanning order or not.

To produce the reconstructed images used for the motion compensation of the next image, the inverse operations is performed, such as IQ (inverse quantization), IScan (Inverse scanning), and IDCT (inverse DCT).

2.2 Redundant Computation Analysis

The VLC encoding for the given scanned 64 quantized DCT coefficients is performed as shown in Fig. 3. From the encoding algorithm of Fig. 3, the encoding procedure is complicated in finding out whether current coefficient is EOB or not. If the EOB location is known in advance, the loop repetition can be less than 64 and the comparison in Step 3 can be skipped.

Step 1: $i = R_p = L_p = 0$ and $L_C = QCOF[i]$, where i is the index for the scanned quantized DCT coefficients, and R_p and L_p are previous run and level, respectively. L_C is the current coefficients and $QCOF[i]$ is the i -th scanned quantized DCT coefficients.

Step 2: **If L_C is non-zero coefficient**, then go to Step 3. Otherwise, increments R_C and go to Step 4.

Step 3: **If L_p is non-zero valued**, then encodes the 3-D symbol of $(EOB = 0, R_p, L_p)$. Otherwise, $R_p = R_C$ and $L_p = L_C$.

Step 4: Increment i . **If i is larger than 63**, go to Step 5. Otherwise $L_C = QCOF[i]$ and go to Step 2.

Step 5: Encodes the symbol of $(EOB=1, R_p, L_p)$.

Fig. 3. The VLC encoding algorithm [4]

The reconstruction path in Fig. 1, i.e., IQ and IDCT can be also simplified if using the EOB location information. For the inverse quantization (IQ) process, the inverse quantization of quantized coefficients after EOB can be skipped.

(0,0)	(0,1)	(0,2)	(0,3)	(0,4)	(0,5)	(0,6)	(0,7)
(1,0)	(1,1)	(1,2)	(1,3)	(1,4)	(1,5)	(1,6)	(1,7)
(2,0)	(2,1)	(2,2)	(2,3)	(2,4)	(2,5)	(2,6)	(2,7)
(3,0)	(3,1)	(3,2)	(3,3)	(3,4)	(3,5)	(3,6)	(3,7)
(4,0)	(4,1)	(4,2)	(4,3)	(4,4)	(4,5)	(4,6)	(4,7)
(5,0)	(5,1)	(5,2)	(5,3)	(5,4)	(5,5)	(5,6)	(5,7)
(6,0)	(6,1)	(6,2)	(6,3)	(6,4)	(6,5)	(6,6)	(6,7)
(7,0)	(7,1)	(7,2)	(7,3)	(7,4)	(7,5)	(7,6)	(7,7)

Fig. 4. 2-D coordinate system for 8x8 block

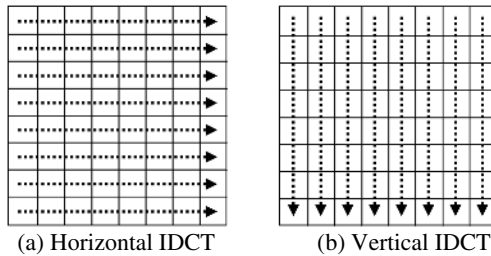


Fig. 5. Separable transformation of 2-D IDCT using 1-D IDCT

Both DCT and IDCT operations use the separable property of the transforms as shown in Fig. 5. Fig. 5 implicates that 2-D IDCT can be performed by using 16 8-points 1-D IDCT's. Let's assume that the shaded position in Fig. 4. represents the non-zero valued coefficient. Then the lower six 1-D IDCT transformations in the horizontal IDCT are not necessary to compute the 8x8 2-D IDCT transformation. In other words, the computational complexity in the IDCT operation can be reduced if the locations of non-zero valued coefficients are considered.

3 Proposed Fast Video Encoding Algorithm Using EOB Position

The proposed video encoding method is represented in Fig. 6. Basic idea of the proposed algorithm is that the zero-valued quantized DCT coefficients after EOB does not affect on the visual quality and coded bitstream as analyzed in the subsection 2-2. In the proposed algorithm, the EOB location is detected in the scanning module. This location information is used for the VLC, IQ, IScan, and IDCT modules. The detail proposed algorithms for each modules are described in the subsequent subsections.

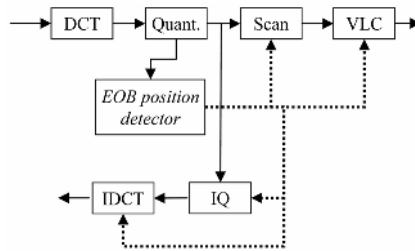


Fig. 6. Proposed fast video encoder using EOB position information

3.1 The EOB Detection Method in Quantization Module

During the quantization, the minimum rectangle, outside of which every quantized DCT coefficients are zero-valued, is detected for each 8x8 block. The detection algorithm is described in the Fig. 7. We call this rectangle 'minimum spanning rectangle of nonzero-valued quantized DCT coefficients' (MSR). The right and bottom position of MSR is represented by the point of (H_{MAX}, V_{MAX}) in Cartesian coordinate. We call this position MSR potion. The position relationship between scanning order and Cartesian coordinate, zigzag[.][.] is mapped by the figures 2 and 4. Based on the two figures, we can easily find the EOB position in scanning order corresponding to the MSR position, (H_{MAX}, V_{MAX}) . The EOB position will be denoted as I_{EOB} .

3.2 The VLC Encoding Method

The proposed VLC encoding method is described in the Fig. 8. If compared with the encoding method in Fig. 3, the number of the loop repetition is reduced from 64 to $I_{EOB}+1$, where the I_{EOB} is the location of the last nonzero-valued coefficients in the

```

HMAX = VMAX = IEOB = 0;
for ( i = 0; i < 8; i++) {
  for (j = 0; j < 8; j++) {
    QCOF2D[i][j] = Quantizer (COF2D[i][j], Qstep);
    if (QCOF2D[i][j] != 0) {
      if (i > HMAX) HMAX = i;
      if (j > VMAX) VMAX = j;
      if (IEOB < zigzag[i][j])
        IEOB = zigzag[i][j];
    }
  }
}

```

Fig. 7. Detection of the minimum spanning rectangle of nonzero-valued quantized DCT coefficients

Step 1: $i = R_C = 0$ and $L_C = QCOF[i]$, where i is the index for the scanned quantized DCT coefficients, and R_C and L_C are current run and level, respectively. And $QCOF[i]$ is the i -th scanned quantized DCT coefficients. I_{EOB} is the location of the last non-zero-valued coefficient in the scanning order.

*Step 2: **If $i = I_{EOB}$** , go to Step 5, otherwise go to Step 3.*

*Step 3: **If L_C is non-zero coefficient**, then encodes the 3-D symbol of ($EOB = 0, R_C, L_C$), otherwise, increments R_C .*

Step 4: Increment i and $L_C = QCOF[i]$ and go to Step 2.

Step 5: Encodes the symbol of ($EOB=1, R_C, L_C$).

Fig. 8. The proposed VLC encoding algorithm

scanning order. The reduction ratio is dependent on the input Macroblock statistics. Also the number of comparison operations (bold and underline marking in the figures) are reduced from three to two operations, and for assignment, reduction of two operations (bold marking in the figures).

3.3 The Inverse Quantization and Scanning Operations

The inverse quantization is normally performed for all the 64 coefficients. In the proposed algorithm, only the coefficients within the MSR are inverse quantized. The location of the coefficients is identified by the MSR position, (H_{MAX}, V_{MAX}). The inverse scanning is only performed for the de-quantized coefficients whose the indexes are less than I_{EOB} .

3.4 The IDCT Transformation

The definition of separable IDCT is given by the following equation:

$$f(x, y) = \frac{1}{4} \sum_{v=0}^7 C(v) \left\{ \sum_{u=0}^7 C(u) F(u, v) \cos \left[\pi(2x+1) \frac{u}{16} \right] \right\} \cos \left[\pi(2y+1) \frac{v}{16} \right] \quad (1)$$

with $u, v, x, y = 0, 1, \dots, 7$ and where (x, y) and (u, v) are coordinates in the spatial and the transform domains, respectively. $C(w)$ is $1/\sqrt{2}$ for $w = 0$, otherwise 1. Eq. (1) tells that for a given v , the horizontal 8-point IDCT is performed. After performing the eight horizontal IDCT's, the eight vertical 8-point IDCT's are conducted to get the final 2-D IDCT. In Fig. 5, this separable transformation method is depicted. If $F(u, v) = 0$ for $u > H_{MAX}$, then we don't need to perform the horizontal IDCT for the $u > H_{MAX}$. In summary, the $(7-H_{MAX})$ 8-point IDCT's can be skipped in the 2-D IDCT operation.

4 Simulation Results

To evaluate the proposed algorithm, we performed the simulation under the environment of the Table 1.

Table 1. Simulation environment

Item	Parameters
Video codec	ITU-T Rec. H.263
Format of test sequences	CIF (352x288, 10 or 30Hz)
Encoding bitrates	128kbps, 256kbs, 512kbps

In the Table 2, we summarize the computational complexity in encoding the 8x8 block for both proposed and conventional methods. The complexity of the proposed method is the function of the several parameters, such as I_{EOB} , H_{MAX} , and V_{MAX} . The parameter values depend on the image characteristics in the spatiotemporal domain and compression ratio. For instance, the image with the high spatial texture will have larger parameter values than the low textured image. Also the sequence with the non-translational motion or high speed motion larger than the search area will produce the larger parameter values. To evaluate the performance of the proposed algorithm, the video sequences with the different spatial and temporal characteristics are used in the comparison: 'Foreman' with high speed and complex (non-translational) motion and low spatial detail, 'Sign Irene' with low spatial detail and small moving area, and 'News' with medium spatiotemporal complexity.

The encoding bitrate is also important parameters in the performance. For the small encoding bitrate, the quantization step size will have larger value and the number of

Table 2. Computational complexity for each block

Function Module	Conventional method	Proposed method
No. of coeff in VLC encoding	64	$I_{EOB}+1$
No. of coeff. in inverse scanning	64	$I_{EOB}+1$
No. of coeff. in inverse quant.	64	$(H_{MAX} + 1) \times (V_{MAX} + 1)$
No. of IDCT	16	$\min\{H_{MAX} + 1, V_{MAX} + 1\} + 8$

zero-valued quantized coefficients will be increased. It means that the smaller bitrate will produce the smaller values of the I_{EOB} , H_{MAX} , and V_{MAX} .

In the Table 3, the reduction of computation complexity in percentage for 30Hz sequences is summarized for the cost function of Table 2. Also Table 4 corresponds to the 10Hz sequences. The absolute computation complexity can be affected by the skipped block, i.e., the block which do not have any non-zero valued. Since any encoding operation is not performed for the skipped block, we only measure the computational complexity for the non-skipped block. Also the portion of skipped block is showed in the Tables. For most cases, the proposed algorithm reduces about 80% for the VLC, scanning, and inverse quantization. For the IDCT, the computation complexity is reduced by 34 ~ 42%, compared with the conventional method. For the low bitrate, the reduction of computational complexity is higher than the one for the high bitrate, since the quantization step sizes for the low bitrate is higher than the other cases. For the 10Hz sequences, the number of bits assigned to each picture is larger by three times than the one for 30Hz. So the number of skipped block is reduced, compared with the 30Hz cases. Also the performance gain of proposed algorithm is slightly reduced since they produce smaller number of the non-zero valued coefficients.

Table 3. Summary of computational complexity of proposed algorithm; (%) reduction compared with conventional method for 30Hz sequences

Video Seq.	Bitrate (kbps)	Skipped Block (%)	Inv. VLC/ Scan	Inv. Quant.	IDCT
Foreman	128	87.93	61.29	31.42	42.94
	256	61.29	92.64	94.70	41.75
	512	31.42	87.97	91.36	40.13
News	128	78.46	91.92	94.36	41.63
	256	66.77	88.42	91.80	40.31
	512	55.23	83.47	87.73	38.38
Sign Irene	128	80.01	94.27	95.61	42.19
	256	69.60	89.70	92.08	40.38
	512	61.78	82.78	86.05	37.44

Table 4. Summary of computational complexity of proposed algorithm; (%) reduction compared with conventional method for 10Hz sequences

Video Seq.	Bitrate (kbps)	Skipped Block (%)	Inv. VLC/ Scan	Inv. Quant.	IDCT
Foreman	128	65.62	88.81	91.06	39.69
	256	57.76	81.13	84.14	36.38
	512	25.95	74.55	78.06	33.94
News	128	61.72	87.69	91.13	40.00
	256	49.53	82.31	86.58	37.81
	512	11.05	76.66	81.81	35.63
Sign Irene	128	52.92	92.36	94.39	41.56
	256	24.54	86.66	90.14	39.44
	512	2.48	75.55	81.22	35.31

In overall, the proposed algorithm greatly reduces the complexity for the VLC encoding, scanning, and inverse quantization. Especially, the computational complexity related to IDCT is reduced about 40%, which can be the great impact on the overall computation complexity of encoder.

5 Conclusion

In this paper, we investigate the relation of each encoding modules in the standard video encoders. Traditionally such modules are handled independently for both hardware and software implementations. From the analysis, if the location information of zero-valued quantized coefficients are effectively used, the most of computation can be skipped, especially IDCT which occupies the great portion of computational complexity in the encoding the video sequences. The simulation results show that the complexity for the IDCT process can be reduced by about 40% and the complexity for the other encoding modules can be greatly reduced. Based on the simulation results, we believe that the proposed method can be really powerful tool in the implementation of the visual communication system in the portable devices.

References

1. Information Technology - Coding of Audio-Visual Objects - Part 2: Visual, ISO/IEC 14496-2:2001, ISO/IEC/SC29/WG11 (2001)
2. Video Coding for Low Bitrate Communications, ITU-T Rec. H.263 (1998)
3. Richardson, I.E.G and Zhao, Y., "Adaptive algorithms for variable-complexity video coding," Proc. IEEE Int'l Conf. on Image Processing, vol. 1, (2001) 457-460
4. Kim, H.C. and Yoo, K.Y., "Complexity-scalable DCT-based video coding algorithm for computation-limited terminals," IEICE Trans. On Communications, vol. E88-B, No. 7, (2005) 2868-2871
5. UBC IPL, H.263 TMN encoder software implementation, available [online: <http://www.ee.ubc.ca/image>]
6. ACTS-MoMuSys, MPEG-4 VM encoder software implementation (ISO/IEC 14496-2), available [online: <http://www.chiariglione.org>]

Efficient Block Matching for Ray-Space Predictive Coding in Free-Viewpoint Television Systems

Gangyi Jiang^{1,3}, Feng Shao^{1,2}, Mei Yu^{1,3}, Ken Chen^{1,3}, and Tae-Young Choi⁴

¹ Faculty of Information Science and Engineering, Ningbo University,
Ningbo, 315211, China

² Department of Information and Electronics Eng., Zhejiang University,
Hangzhou, 310027, China

³ National Key Lab of Software New Technology, Nanjing University,
Nanjing, 210093, China

⁴ Division of Electronics Engineering, Ajou University, Suwon, 442-749, Korea

Abstract. Free viewpoint television (FTV) based on ray-space representation was adopted in the MPEG draft because the ray-space can generate an arbitrary viewpoint view without complicated analysis and rendering process. Ray-Space predictive coding is one of main techniques in ray-space based FTV systems, in which block matching and compensation plays a very important role to improve coding performance. However, the computational burden of block matching for ray-space coding is the problem to be solved. Ray-space representation of FTV is introduced and inter-slice correlations of ray-space data are analyzed. Then, a fast adaptive block matching algorithm for ray-space predictive coding is proposed to reduce the encoding complexity. Experimental results show that the proposed block matching method reduce the computational burden and speed up the coding process greatly.

1 Introduction

In recent years, image based rendering (IBR) techniques have been developed to generate novel views of an environment from a set of pre-acquired images^[1]. Ray-space representation is a novel IBR method to describe three-dimensional spatial information^[2,3]. Free viewpoint television (FTV) based on ray-space representation was adopted in the MPEG documents^[4] because the ray-space can generate an arbitrary viewpoint view without complicated analysis and rendering process. When a scene is captured using a dense array of synchronized cameras, the camera images are placed in a simple manner forming a ray space. The ray-space usually requires hundreds times of data than an ordinary 2D image, thus data compression in ray-space is one of key technologies in the ray-space based FTV systems.

It is indicated that at a particular time t_0 , ray-space can be described with a 3D function, and the 3D ray-space data $\{f(x, y, u)\}$ captured from real space is given in Fig.1. The 1th to 5th vertical sections in ray-space as shown in Fig.1 correspond to the five views in real space, and θ is the direction of a ray.

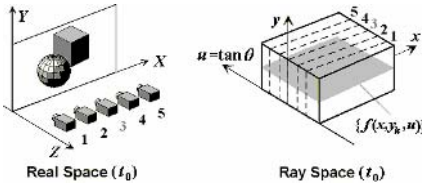


Fig. 1. 3D ray-space at time t_0

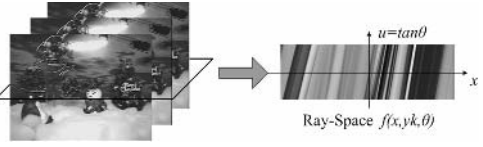


Fig. 2. An example of ray-space slice $\{f(x, y_k, u)\}$

In Fig.2, a ray-space section $\{f(x, y_k, u)\}$ is formed by horizontal segmentation in plane coordinate system. Obviously, ray distribution in ray-space is different from pixel distribution in 2D image. For a given $y=y_k$, a ray-space slice $S(y_k)=\{f(x, y_k, u)\}$ is formed by transforming data in multi-view images with respect to y_k . In fact, $\{f(x, y_k, u)\}$ corresponds to horizontal section with $y=y_k$ in ray-space. It looks like many overlapping or parallel rays with different luminances. Arbitrary view can be generated by simply reading and transforming the corresponding ray-space data. Because of enormous ray-space data, efficient ray-space coding scheme should be developed. Some methods of ray space coding, similar to 2D still image coding techniques, have been proposed, such as DCT transform^[5], vector quantization^[6], SPECK wavelet transform^[7]. Fujii et. al have discussed several ray-space coding schemes^[8]. However, the above schemes only utilized the techniques similar to 2D image compression, so that the compression performances are limited.

In this paper, inter-slice correlations of ray-space data are analyzed. Then, an efficient block matching algorithm for ray-space predictive coding is proposed. Experimental results show that the searching speed of block matching in ray-space data is improved greatly and the coding efficiency is also improved resultantly compared with 2D image-based ray-space data compression schemes.

2 Characteristic Analysis of Ray-Space Slice Sequence

The correlations between adjacent slices of ray-space are compared with the correlations between frames of “foreman” video sequence. The result is given in Fig.3, in which the correlation coefficient R is calculated by

$$R = \frac{1}{n-1} \sum_{i=1}^n \left[\frac{v_i - \bar{v}}{S_v} \right] \left[\frac{k_i - \bar{k}}{S_k} \right] \tag{1}$$

where $\{v_i|1 \leq i \leq n\}$ and $\{k_i|1 \leq i \leq n\}$ are the two adjacent slices (or frames), S_v and S_k are standard deviation of $\{v_i\}$ and $\{k_i\}$, and \bar{v} and \bar{k} are the mean of them, respectively. The mean correlation coefficient of ray-space slice is 0.985, while it is 0.976 for “foreman” sequence, a slightly lower than that of slices in ray-space. This explains why there exists large redundancy within slice sequence of ray-space alike video sequence. For foreground area, the inter-slice correlations are relatively smaller than for the background area, but the difference is insignificant. This phenomenon provides the basis for intra-slice and inter-slice compression with prediction technique.

In order to analyze characteristic of ray-space data, we analyzed distribution of matching vector of the full search, the statistic results are given in Fig.4(a). It is seen

that the matching vectors have significant center-biased characteristic and concentrates highly on the neighbor of (0,0). Then we analyzed the direction of matching vector without taking account of center point and vectors with horizontal or vertical directions. The results are shown in Fig.4(b). It is seen that there are two peaks around -110° and 63° , which means that the directions of matching vectors of many blocks lie around -110° and 63° , which are almost opposite in rectilinear direction. It should be noted that the rectilinear direction is associated with disparity between adjacent views.

Ray-space has strong inter-slice correlations, and the high coding efficiency will be obtained if inter-slice correlations prediction is utilized. We define error coefficient of block matching vector as follows

$$\lambda = (SAD_{\text{pred}} - SAD_{\text{best}}) / SAD_{\text{pred}} \quad (2)$$

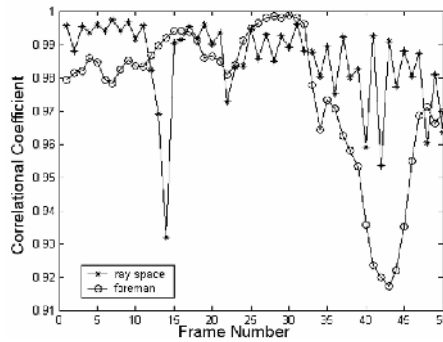


Fig. 3. Comparison between correlation coefficients of ray-space slices and correlation coefficients of “foreman” video sequence

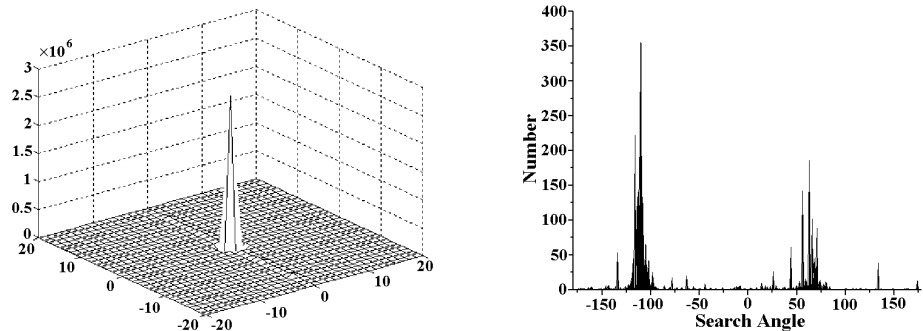


Fig. 4. (a) Statistic of matching vectors, (b) Directional distribution of matching vectors

Table 1. Statistic of parameter λ

Prediction method	0~0.10	0.10~0.20	0.30~0.40
Collocated block prediction	89.38%	1.57%	1.19%
Adjacent block prediction	95.27%	1.70%	0.84%

where, SAD_{pred} is the minimum SAD obtained by inter-block matching vector prediction, and SAD_{best} is the minimum SAD corresponding to the full search prediction. The error coefficient λ reflects matching degree between the best matching vector and the predictive matching vector. $\lambda=0$ means that the predicted matching vector happen to be the optimal matching vector within the searching window. Here, two inter-block prediction schemes are considered, one is collocated block prediction which predicts matching vector of current block from the vector of the block at the same location in previous slice, the other is adjacent prediction which predicts the matching vector of current block from adjacent blocks on the left, top, and top-right in current slice. Table 1 shows statistic of λ . It is seen that for most blocks the error between SAD_{pred} and SAD_{best} is slight, since about 89.38% of λ of collocated blocks or 95.27% of λ of adjacent blocks are less than 0.1, in other words, the current block is quite correlative with its adjacent blocks and the collocated block.

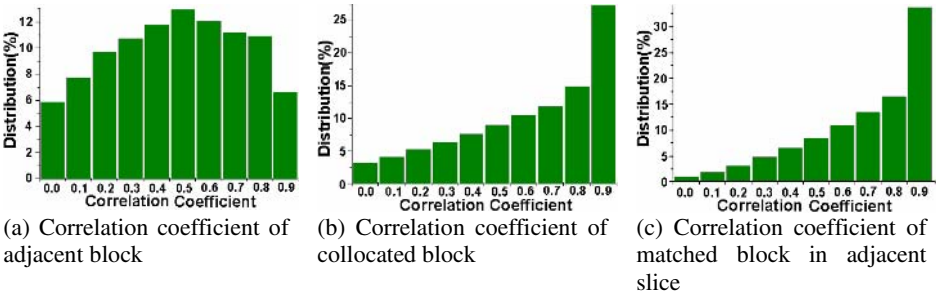


Fig. 5. Inter-block correlation coefficient distribution

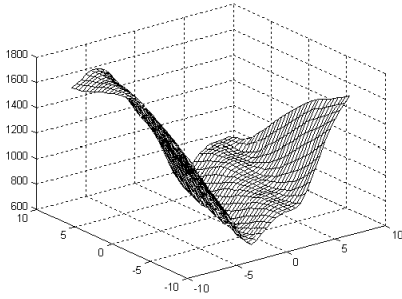


Fig. 6. Error Plane

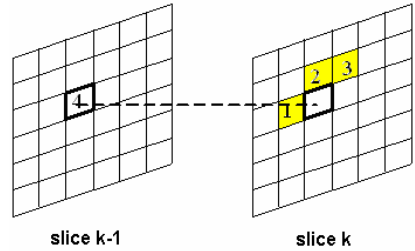


Fig. 7. Prediction of starting search point

Further, we analyzed the inter-block correlation coefficient. Let $\{X_{m,n}\}$ and $\{Y_{m,n}\}$ be luminance of two blocks with the size of $N \times N$, \bar{X} and \bar{Y} be the means of $\{X_{m,n}\}$ and $\{Y_{m,n}\}$, respectively, inter-block correlation coefficient R_B is defined as

$$R_B = \frac{\sum_{m=1}^N \sum_{n=1}^N (X_{m,n} - \bar{X})(Y_{m,n} - \bar{Y})}{\sqrt{\sum_{m=1}^N \sum_{n=1}^N (X_{m,n} - \bar{X})^2} \sqrt{\sum_{m=1}^N \sum_{n=1}^N (Y_{m,n} - \bar{Y})^2}} \quad (3)$$

Let R_1 , R_2 and R_3 be the block correlation coefficients which indicate the correlations between current block and its left, top, or top-right block respectively, and R_4 denote the block correlation coefficient corresponding to collocated block. We define the correlation coefficient of adjacent block $R=\{R_1, R_2, R_3\}$ and collocated correlation coefficient $R=R_4$. Additionally, R_5 corresponding to correlation coefficient of the matched block of current block in adjacent slice is also analyzed. Fig.5 gives the statistic of correlation coefficients of the adjacent blocks, the collocated block and the matched block. It is seen that adjacent block correlation in ray-space is very strong and the collocated block correlation is even greater.

3 Inter-slice Prediction Based Ray-Space Coding

In order to reduce computational burden on block matching, in some fast motion estimation algorithms, it is usually supposed that the matching error increases monotonously along with searching location far away from global best motion vector. But in some cases it is not satisfied and the search may fall in local optimization. Fig.6 gives an example of such situation. The figure is an error plane of an 8×8 block in "Xmas" sequence. It is clear that the plane has local optimizations.

If we can smooth the motion vector field, the local optimization problem will be easily solved. In this paper, we consider to perform starting search point prediction. The prediction utilizes inter-blocks correlation as shown in Fig7. From Fig.4(a), it is observed that for full searching, 44.8% of the matching vectors are (0,0), which indicates the best center-biased characteristic of ray-space. So we can determine a still block by a threshold Th_0 , that is, if SAD of current block with respect to zero matching vector is lower than Th_0 , it is regarded as a still block and skipped, so that the time-consuming searching is avoided. Here, an adaptive threshold Th_0 is defined by

$$Th_0 = \begin{cases} \text{median}(SAD_1, SAD_2, SAD_3), & \text{if reference frame is I frame} \\ \min\{\text{median}(SAD_1, SAD_2, SAD_3), SAD_4\}, & \text{if reference frame is P frame} \end{cases} \quad (6)$$

where SAD_1 , SAD_2 and SAD_3 are SAD values corresponding to the three adjacent blocks, and SAD_4 corresponds to the collocated block.

In this paper, we adopt the combination of gradient diamond search mode and rectilinear direction search mode. In the gradient diamond search, the search mode with step size 2 is called the large diamond search (LDS), while the search mode with step size 1 is called the small diamond search (SDS)^[9]. Based on ray-space characteristic analysis, ray-space matching vectors have significant rectilinear direction, commend to rectilinear direction strategy.

In some fast algorithms, SAD threshold has been used as the stop criteria to speed up the search. That is, the search process stops when the current minimum SAD of a block is less than a given threshold. But most of algorithms use a constant threshold, leading to inadaptability. Since there are strong correlations between current block and its adjacent blocks or collocated block, we use two adaptive thresholds $SAD_{\text{thr},1}$ and $SAD_{\text{thr},2}$, similar to threshold of early termination proposed in [10], defined by $SAD_{\text{thr}}=(1+\beta)SAD_{\text{predn}}$, where SAD_{predn} is the SAD of one of adjacent blocks or collocated block, and β is a modulated factor which will play a key role in keeping a trade-off between reconstructed quality and search speed. As in literature [10], β can be

chosen according to the distribution of NSD , which is defined to describe the property of SAD difference as $NSD=(SAD_{predn}-SAD_{best})/SAD_{predn}$

$$\beta_1 < \frac{Q_{step}}{M[0,0] \times 4} \times \left(\frac{B_{size}}{SAD_{predn}} \right)^2 - \alpha_1, \quad \beta_2 < \frac{Q_{step}}{M[0,0] \times 4} \times \left(\frac{B_{size}}{SAD_{predn}} \right)^2 - \alpha_2 \quad (7)$$

where Q_{step} is the quantization step, B_{size} is the current block size, the matrix $M[u,v]$ is deduced based on 4×4 DCT and can be found in [10]. In this paper, $P(NSD < \alpha_1) = 0.6$ and $P(NSD < \alpha_2) = 0.7$ are selected to determine β .

Additionally, multi-reference based ray-space coding is also simulated, and the results are tabulated in Table 2. As indicated in the table, the gain of utilizing multi-reference slices is insignificant in the improvement of the ray-space coding efficiency, on the contrary, multi-reference slices consumes much more encoding time. This may lead to the conclusion that in ray-space coding multi-reference slices offers no advantage or whatsoever.

Table 2. Results of multiple reference slices

Number of reference slices	PSNR(dB)	Total bits
1	34.24	1238312
2	34.27	1234264
3	34.29	1225984
4	34.30	1220608
5	34.31	1217456

According to the above analysis, this paper comes up with a fast adaptive block matching algorithm. Its main procedure is described as follows

Step 1: Let SAD_0 be the SAD of current block with respect to the zero matching vector $(0, 0)$, and $SAD_i (i=1, 2, 3, 4)$ correspond to the SAD of the three adjacent blocks and the collocated block.

If reference frame of current block is I frame, $SAD_{min} = \text{median}(SAD_1, SAD_2, SAD_3)$, if reference frame is P frame, $SAD_{min} = \min\{\text{median}(SAD_1, SAD_2, SAD_3), SAD_4\}$;

Step 2: Still block determination: If $SAD_0 < SAD_{min}$, then current block is considered as still block, so skip it to the next block.

Step 3: If $SAD_0 = SAD_{min}$, let the point indicated by zero matching vector as the search center, repeat SDS and modify the SAD_{min} until the best-matched point lies in the center of the diamond;

If $SAD_0 > SAD_{min}$, let the point indicated by the matching vector MV_{pred} with respect to SAD_{min} as the search center, and turn to Step 4;

Step 4: If the two components V_x and V_y of the matching vector MV_{pred} are larger or smaller than 0 simultaneously, and satisfy $V_x^2 + V_y^2 < T$ where T is a threshold, the point indicated by MV_{pred} is considered to be located within the rectilinear search region, so search the next point in the rectilinear direction indicated by V_y/V_x . If the SAD of the new point is the minimum SAD, moreover, satisfy $SAD_{min} < SAD_{thr-1}$, then turn to step 6, otherwise, if the second condition is not satisfied then turn to

step 5; If the SAD of the new point is not the minimum, then continue to search the next point in the rectilinear direction.

In other cases, that is, the point with respect to MV_{pred} is not within the rectilinear search region, then repeat LDS and modify the SAD_{min} until the best-matched point lies in the center of the diamond, and then turn to Step 5.

Note that if $SAD_{\text{min}} < SAD_{\text{thr}_1}$ at anytime during the searching, then turn to Step 6, or if $SAD_{\text{thr}_1} < SAD_{\text{min}} < SAD_{\text{thr}_2}$, then turn to Step 5;

Step 5: Do SDS once, and go to Step 6;

Step 6: Finish the searching process, and obtain the matching vector and the corresponding SAD_{min} of current block.

4 Experimental Results

In our experiments, two sets of grayscale multi-view images of real scene with the size of 640×480 , are used for the testing purposes, and the leftmost and rightmost image of the multi-view images are given in Fig.8. ‘‘Xmas’’ has 96 multi-view images, forming 480 slices with the size of 640×96 , and ‘‘Cup’’ has 144 multi-view images, forming 480 slices with the size of 640×144 .

From Eq.(7), it is seen that β is related to Q_{step} , $SAD_{\text{pred}}/B_{\text{size}}$ and α . When quantization step is larger, the quantization noise is also larger, and the larger β can speed up the searching without much loss in quality of reconstructed slices. On the other hand, $SAD_{\text{pred}}/B_{\text{size}}$ represents the energy of the residual signals. If $SAD_{\text{pred}}/B_{\text{size}}$ increase, it's very easy for motion search dropping into a local minimum. Therefore β is decreased in this case to keep the reconstructed image quality with the cost of speed. Table 3 gives the encoding results under different probabilities. It is seen that if $P(NSD < \alpha_1) = 0.8$ and $P(NSD < \alpha_2) = 0.9$ is selected, the quality of reconstructed images will be improved at the cost of decreasing in searching speed. In this paper, $P(NSD < \alpha_1) = 0.6$ and $P(NSD < \alpha_2) = 0.7$ are selected.

Table 4 gives the encoding results with respect to different thresholds Th_0 . From the table it is seen that if constant threshold is used, the lower threshold can achieve relatively higher PSNR as adaptive threshold as given in Eq.(6) does, but meanwhile the number of searching point is increased. High constant threshold reduces the number of searching point at the cost of decreasing in quality of reconstructed slices.

We compared two H.264 based ray-space compression methods, that is, intra-slice prediction method which only utilizes the intra-slice redundancies, and inter-slice prediction which uses both the inter and intra redundancies of ray-space slices. In the experiments, QP are 34, 36, 38 and 42, respectively. Compared with intra-slice prediction method, BDPSNR^[11] of Xmas and Cup of inter-slice prediction method are 2.46dB and 2.82dB, and BDBR^[11] of Xmas and Cup are -32.35% and -45.88%, respectively, which means that inter-slice prediction method achieves higher PSNR with lower bitrate in comparison with intra-slice prediction method. This implies that the correlations between adjacent slices are very strong and high compression efficiency can be obtained by using these correlations.

We also compared our fast adaptive block matching algorithm (FABMA) with full search (FS), novel three step search (NTSS), four step search (FSS), and block-based gradient descent search (BBGDS). The search range is 16. Table 5 lists the comparison between the above methods. The items contain check points that imply block

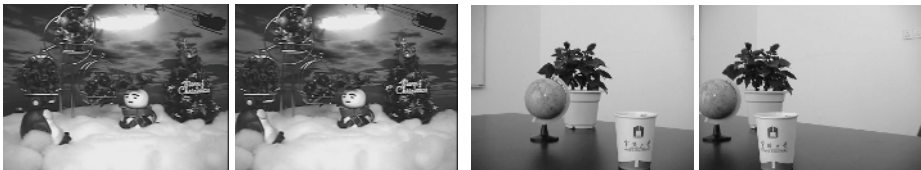
matching time, the speedup ratio, BDPSNR and BDBR, where FS is as the reference. The results demonstrate that FABMA can not only reach similar search accuracy as FS does, but also speed up the matching estimation largely. On the average, it runs 73% faster than BBGDS, 200% faster than FSS, and 500% faster than NTSS.

Table 3. Comparison of encoding results under different probability

Sequences	$P(NSD < \alpha_1), P(NSD < \alpha_2)$	PSNR	Total bits	Number of search points
Xmas	0.6, 0.7	37.13	1667768	4.7
	0.8, 0.9	37.13	1670296	12.5
Cup	0.6, 0.7	36.91	2576600	5.4
	0.8, 0.9	36.91	2572192	13.1

Table 4. Comparison of encoding results with different threshold Th_0

Sequences	Threshold selection	PSNR	Total bits	Number of search points
Xmas	Constant 100	37.13	1669968	8.4
	Constant 200	37.13	1669968	6.3
	Constant 300	37.04	1666984	5.0
	Adaptive	37.13	1667768	5.7
Cup	Constant 100	36.91	2577600	8.1
	Constant 200	36.90	2577600	5.9
	Constant 300	36.80	2566072	3.7
	Adaptive	36.91	2576600	5.4



(a) Leftmost and rightmost images of “Xmas” (b) Leftmost and rightmost images of “Cup”

Fig. 8. Test multi-view images for Ray-space compression

Table 5. Comparison of our algorithm and other block matching algorithms

Ray-space data	Algorithm	Check points	Speedup ratio	BDPSNR(dB)	BDBR(%)
Xmas	FS	1089	1.00	0	0
	BBGDS	9.9	110.00	-0.17	2.93
	FSS	17.1	63.68	-0.15	2.53
	NTSS	32.9	33.10	-0.12	2.02
	FABMA	5.7	191.05	-0.13	2.20
Cup	FS	1089	1.00	0	0
	BBGDS	9.4	115.85	-0.23	5.74
	FSS	17.3	62.94	-0.19	4.63
	NTSS	33.0	33.00	-0.14	3.48
	FAMBA	5.4	201.67	-0.18	4.53

This can be explained by following aspects. First, the smoother matching vector field obtained by matching vector prediction may avoid the searching falling in local optimization. Secondly, FABMA begins its search from the matching vector of one of the intra-slice or inter-slice adjacent blocks, which usually enable it to find an appropriate point earlier. Thirdly, adaptive still block determination can reduce unnecessary search, so search speed is accelerated. At last, the proposed adaptive stop criterion assures that the final point is good enough.

5 Conclusions

Ray-space representation is one of the main approaches to realizing FTV with complex scene. Because of enormous ray-space data, efficiency coding scheme must be developed. In inter-slice prediction based ray-space compression, the complexity of block matching is the most important factor to influence coding performance. In this paper, we propose a fast adaptive block matching algorithm using starting search point prediction, still block determination and search stop criteria strategies according to the characteristics of ray-space data, and give the corresponding ray-space compression scheme. Experimental results show that the search speed is improved significantly by the proposed method while the compression performance is maintained compared with full search scheme and some of the other fast block matching schemes.

Acknowledgment

This work was supported by the Natural Science Foundation of China (grant 60472100), the Natural Science Foundation of Zhejiang Province (grant RC01057, Y105577), the Ningbo Science and Technology Project of China (grant 2003A61001, 2004A610001, 2004A630002), and the Zhejiang Science and Technology Project of China (Grant 2004C31105).

References

1. Shum, H.Y., Kang, S.B., Chan, S.C.: Survey of Image-Based Representations and Compression Techniques, *IEEE Trans. on CSVT*, 13(2003), 1020-1037.
2. Tanimoto, M.: FTV (Free Viewpoint Television) Creating Ray-Based Image Engineering, *Int. Conf. on Image Processing 2005, II(2005)*, 25-28.
3. T. Fujii, M. Tanimoto, A Real-Time Ray-Space Acquisition System, *Proc. of SPIE-IS&T Electronic Imaging*, SPIE, 5291(2004), 179-187.
4. ISO/IEC JTC1/SC29/WG11 N5878, Report on 3DAV Exploration, Trondheim, Norway, (2003).
5. Fujii, T., Kimoto, T., Tanmoto, M.: Ray Space Coding Based on Arbitrary-Shaped DCT, *SPIE Electronic Imageing'98*, 3295 (1998), 258-268.
6. Kawaura, M., Ishigami, T., Fujii, T., et al.: Efficient Vector Quantization of Epipolar Plane Images of Ray Space by Dividing into Oblique Blocks, *Picture Coding Symposium*, (2001), 203-206.

7. Hayashi, Y., Fujii, T., Tanimoto, M.: Coding for Ray Space Based on SPECK, *Picture Coding Symposium*, (2003), 339-342.
8. Fujii, T., Kimoto, T., Tanimoto, M.: Free-Viewpoint TV System Based on Ray-Space Representation, *SPIE 2002 Three-Dimensional TV, Video, and Display*, 4864(2002), 175-189.
9. Lam, C., Po, L., Cheung, C.: A Novel Kite-Cross-Diamond Search Algorithm For Fast Block Matching Motion Estimation, *2004 International Symposium on Circuits and Systems*, Vancouver, Canada, 3(2004), 729-732.
10. Chen, Z. Zhou, P., He, Y.: Fast Motion Estimation for JVT, *The 7th Meeting: Pattaya II, Thailand*, (2003).
11. Bjontegaard, G.: Calculation of Average PSNR Differences between RD-curves, *VCEG-M33, 13th VCEG Meeting*, Austin, Texas, USA, (2001).

New Approach to Complexity Reduction of Intra Prediction in Advanced Multimedia Compression

Mei Yu^{1,2}, Gangyi Jiang^{1,3}, Shiping Li^{1,3}, Fucui Li^{1,2}, and Tae-young Choi⁴

¹ Faculty of Information Science and Engineering, Ningbo University,
Ningbo, 315211, China

² State Key Lab. for Novel Software Technology, Nanjing University,
Nanjing, 210093, China

³ Institute of Computer Technology, Graduate School of Chinese Academy of Sciences,
Beijing, 100871, China

⁴ Division of Electronics Engineering, Ajou University, Suwon, 442-749, Korea

Abstract. H.264 is the new multimedia compression standard developed by VCEG and MPEG. In order to maximize the compression performance, H.264 adopts RDO mode decision techniques at the cost of very remarkable computational complexity. To reduce encoder complexity associated with the intra-prediction mode selection, in this paper, a fast intra prediction mode selection scheme is proposed. It is based on three improvement parts, including improvement of the intra prediction algorithm structure, fast selection between intra 4×4 block mode and intra 16×16 block mode, and the fast 4×4 luma block mode selection based on the luma similarity between reference pixels. Experimental results show that the proposed scheme outperforms Pan's method, and compared with the test model JM8.6 provided by JVT, the proposed scheme reduces 83.10% coding time for intra frames and 50.94% coding time for all the frames while maintaining the PSNR and bit rate.

1 Introduction

H.264 is the new video compression standard developed by VCEG and MPEG. It is also called MPEG4 part 10 or AVC (Advanced Video Coding)^[1]. H.264 offers a significant performance improvement over previous video coding standards such as H.263++ and MPEG-4 at the expense of higher computational complexity^[2]. The enhanced intra prediction technique with the RDO (Rate Distortion Optimization) is one of the important factors that contribute to the success of H.264. However, the computational complexity of the H.264 encoder is dramatically increased by the optimization technique so that it is difficult to implement the RDO in real-time applications. Only a few attempts have been made to address this complexity bottleneck of the intra prediction mode selection. Pan et al. proposed a fast intra prediction mode selection algorithm (we called it Pan's scheme below) with the use of edge directional histogram^[3]. The algorithm can reduce the computational complexity effectively, so it has been adopted by JVT. Chang-sung Kim et al. proposed a two-step fast mode selection algorithm^[4]. The algorithm is effective, however, it doesn't

consider the fast selection between intra 4x4 block mode and intra 16x16 block mode, which can reduce the computational complexity significantly.

In this paper, we propose a fast intra prediction mode selection method with three improvement parts, including improvement of the intra prediction algorithm structure, fast selection between intra 4x4 block mode and intra 16x16 block mode, and the fast 4x4 luma block mode selection based on the luma similarity between reference pixels. The experimental results show that the proposed scheme is effective in reducing the encoding complexity of H.264.

2 Intra Prediction Technique in H.264

Previous multimedia compression standards, such as H.263 and MPEG4, exploit the spatial correlation inside macroblock in intra coding. H.264 exploits the spatial correlation between adjacent macroblocks/blocks for intra prediction. In H.264 intra prediction, the current macroblock/block is predicted by adjacent pixels in the upper and the left macroblocks/blocks that are previously encoded and reconstructed. H.264 offers a rich set of prediction patterns for intra prediction. For the luminance (luma) components, intra prediction may be used for each 4x4 sub-block or 16x16 macroblock. There are 9 prediction modes for 4x4 luma blocks and 4 prediction modes for 16x16 luma blocks. For the chrominance (chroma) components, there are 4 prediction modes that are applied to the two 8x8 chroma blocks (U and V). The resulting prediction mode for U and V components should be the same as luminance^[5].

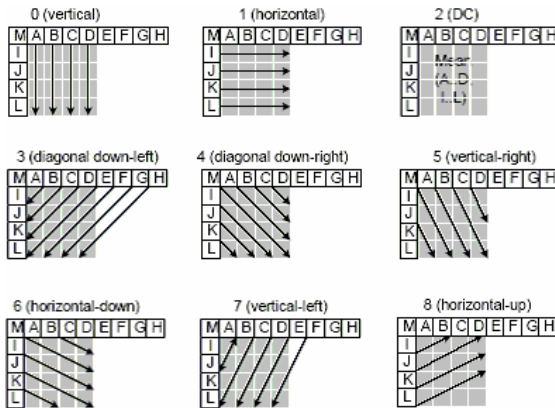


Fig. 1. Nine prediction modes of 4x4 luma block in H.264

Nine prediction modes for 4x4 luma blocks are illustrated in Fig.1, which includes the DC mode and eight directional modes, labeled 0 thru 8. The arrows in Fig.1 indicate the direction of prediction in each mode. For modes 3-8, the predicted samples are formed from a weighted average of the prediction samples A-M. For example, if mode 4 is selected, the top-right sample of the 4x4 block is predicted by: $\text{round}(B/4+C/2+D/4)$. As an alternative to the 4x4 luma modes described above, the

entire 16×16 luma component of a macroblock may be predicted. Four modes are available, including vertical, horizontal, DC and plane mode. The four prediction modes for each 8×8 chroma component of a macroblock are very similar to the 16×16 luma prediction modes. Note that if any of the 8×8 blocks of the luma component are coded in the intra mode, both chroma blocks for U and V are intra-coded using the same intra prediction mode.

To encode the prediction mode for each 4×4 block efficiently, the correlation between spatially adjacent blocks is exploited in H.264. For each current block, the encoder and decoder calculate the ‘most_probable_mode’, which is the minimum of the prediction modes of the left block and upper block. When the prediction mode for current 4×4 block is equal to ‘most_probable_mode’, the encoder sends a flag, which costs only one bit for the prediction mode.

3 Fast Mode Selection Method for Intra Prediction

In order to maximize the coding performance, H.264 adopts exhaustive RDO mode decision technique at the cost of a very high computational complexity. That is, the encoder has to encode the intra block using all the mode combinations and choose the one that gives the optimum RDO performance. According to the structure of intra prediction in H.264, the number of mode combinations for luma and chroma blocks in a macroblock is $M_8 \times (M_4 \times 16 + M_{16})$, where M_8 , M_4 and M_{16} represent the number of modes for 8×8 chroma blocks, 4×4 and 16×16 luma blocks, respectively. This means that, for a macroblock, it has to perform 592 different RDO calculations before a best RDO mode is determined. As a result, the computational complexity of the encoder is extremely high. Therefore, it is highly desirable to develop a fast mode selection algorithm for intra prediction.

3.1 Improvement of H.264’s Intra Prediction Algorithm Structure

In the test model JM8.6^[6] provided by JVT, all the combinations of luma and chroma blocks in a macroblock have to be checked with RDO calculation to determine the optimal modes. The RDO function for macroblock modes selection is as follows^[7]

$$J(s, c, MODE | QP, \lambda_m) = SSD(s, c, MODE | QP) + \lambda_m R(s, c, MODE | QP), \quad (1)$$

where $MODE$ indicates a mode out of the set of potential macroblock modes, QP is the macroblock quantizer, λ_m is the Lagrange multiplier for mode selection, $SSD(\cdot)$ means sum of the squared difference between s and c , and $R(\cdot)$ represents the number of bits associated with the chosen $MODE$ and QP .

In JM8.6, the best prediction mode of 8×8 chroma block is selected by the above macroblock modes selection. As the macroblock mode selection is based on the 4×4 luma block mode selection and 16×16 luma block mode selection, it results in huge computation load. Here, a new mode selection algorithm structure for 8×8 chroma block is proposed, and it chooses the best 8×8 chroma block prediction mode without the mode selection results of the macroblock’s luma component. That is, 8×8 chroma block mode selection can be independent from 4×4 luma block mode selection and

16×16 luma block mode selection. So the improved algorithm structure can reduce the computational complexity of intra prediction. The improved intra prediction structure is described as follows:

- a) Select the best chroma prediction mode from four prediction modes of 8×8 chroma block.
- b) Select the best 4×4 luma block prediction mode from the corresponding nine prediction modes, the best 16×16 luma block prediction mode from the four prediction modes.
- c) Do macroblock modes selection from the combination of the best luma block prediction modes (both 4×4 luma block and 16×16 luma block) and chroma block prediction mode, and calculate the macroblock RDO cost for each combination.
- d) Finally, choose the luma and chroma block prediction mode corresponding to the minimum macroblock RDO cost.

3.2 Fast Selection between Intra 4×4 Block Mode and Intra 16×16 Block Mode

In JM8.6, full search algorithm is used to select the block mode between intra 4×4 block mode and intra 16×16 block mode. This algorithm can achieve the optimal block mode by using the RDO mode decision technique, however, it is computationally expensive. Intuitively speaking, 16×16 luma block mode fits the macroblock with simple texture, especially the flat area, 4×4 luma block mode, on the other hand, fits the macroblock with complex texture. Thus, if we can find a feature representing the texture complexity, early termination can be performed to the selection between 4×4 luma block mode and 16×16 luma block mode.

Luma histogram is one of the effective features in measuring the macroblock texture complexity. Analyse the luma histograms of the number of nonzero coefficients of the common test sequences, it is found that blocks using 16×16 luma

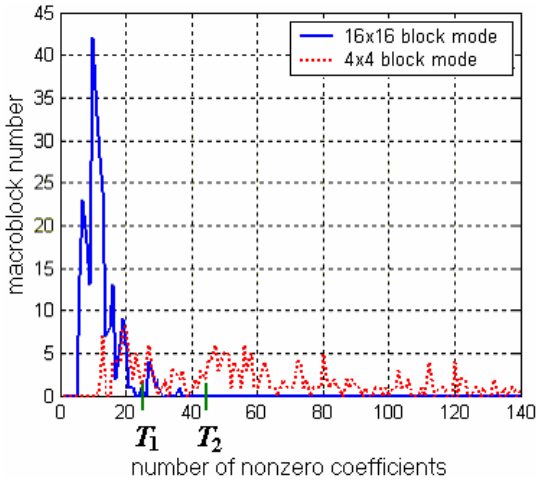


Fig. 2. Distribution of nonzero coefficient number of two block modes

block mode usually has fewer nonzero coefficients than blocks using 4×4 luma block mode. Fig.2 shows the histogram of the number of nonzero coefficients with respect to the two luma block modes of the sequence Claire.

In order to make a use of the number of nonzero coefficients for mode selection, two thresholds T_1 and T_2 are set, and $T_1 < T_2$. The early termination rule is as below, if the number of nonzero coefficients is smaller than T_1 , 16×16 luma block mode is used; if the number of nonzero coefficient is bigger than T_2 , 4×4 luma block mode is used; otherwise, the original full search method is used. Since most of macroblocks need computing the RDO cost only for one block mode, the computational load is reduced.

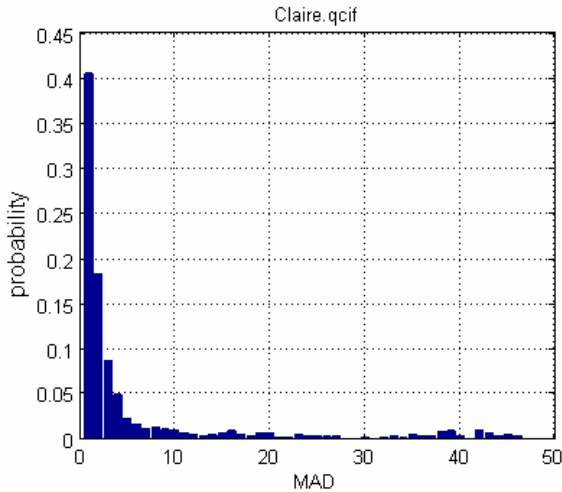


Fig. 3. Histogram of reference pixels' MAD of 4×4 luma blocks in Claire sequence

3.3 Fast 4×4 Luma Block Mode Selection Based on Reference Pixel Similarity

From Fig.1, each 4×4 luma block has 13 reference pixels, distributed in the left and upper blocks. Experimental analysis shows that the luma value of these 13 reference pixels is similar in most cases. Fig.3 gives the statistical results of similarity between 13 reference pixels of 4×4 luma blocks, in which MAD (mean of the absolute difference) between the reference pixels is used to describe the similarity of the reference pixels. Smaller the MAD is, more similar the reference pixels are. The figure indicates that most of 4×4 luma blocks have small MAD values. It is clear that the prediction results of the 9 prediction modes will be similar if the luma value of the reference pixels is quite similar with each other. Therefore, a good fast mode selection scheme for intra prediction can be proposed. That is, if the reference pixels' MAD value of a 4×4 luma block is smaller than a threshold T_3 , 'most_proable_mode' is directly chosen for the 4×4 luma block. Thus, the exhausted searching is avoided.

3.4 Proposed Fast Intra Prediction Mode Selection

In the above sections, three schemes to reduce complexity of intra mode selection is proposed, i.e. improvement of the intra prediction algorithm structure, fast selection between intra 4×4 block mode and intra 16×16 block mode, and the fast 4×4 luma block mode selection algorithm based on the luma similarity between reference pixels. These three algorithms emphasize particularly on different aspects to reduce the encoding complexity. Therefore, the combination of them is supposed to be more effective in reducing the intra prediction complexity. The new scheme is described as follows:

- a) Firstly, the structure of algorithm of intra prediction is changed according to the illustration in section 3.1.
- b) Secondly, before encoding a frame, the number of nonzero coefficients of each macroblock is computed, as so to make a selection between 16×16 luma block mode and 4×4 luma block mode early according to the proposed scheme in section 3.2.
- c) If 4×4 luma block mode is selected, the reference pixels' MAD value is calculated to decide whether the `most_probable_mode` should be chosen directly as mentioned in section 3.3 or the normal RDO is performed.

4 Experimental Results and Analyses

The mode decision schemes as described in section 3 have been integrated with the H.264 JM8.6^[6] for performance evaluation. It is compared with the RDO mode decision of H.264 in terms of the computational cost, PSNR and bit-rate for test

Table 1. The proposed scheme and Pan's scheme compared with JM8.6 in terms of computational cost *TS* (%)

Sequences	Schemes	QP=28		QP=32		QP=36		QP=40	
		ALL_I	ALL	ALL_I	ALL	ALL_I	ALL	ALL_I	ALL
Container (QCIF)	Pan	62.26	41.16	61.98	39.20	61.78	37.57	61.51	36.47
	Proposed	82.44	54.00	83.28	52.66	83.43	51.04	83.47	50.01
Foreman (QCIF)	Pan	62.37	40.21	61.89	38.34	61.90	36.87	61.67	35.62
	Proposed	77.65	50.13	78.13	48.60	77.70	46.48	76.03	44.33
Claire (QCIF)	Pan	62.05	38.44	62.19	37.73	61.72	37.23	61.18	36.58
	Proposed	89.08	55.18	89.55	54.74	89.97	54.26	89.53	53.20
Miss_am (QCIF)	Pan	59.16	34.69	59.37	34.64	59.37	35.02	59.44	34.59
	Proposed	88.02	51.62	88.48	51.84	88.85	51.52	88.62	51.68
Foreman (CIF)	Pan	62.99	39.64	62.68	38.34	62.39	37.39	62.40	36.89
	Proposed	81.48	51.05	80.42	48.98	80.51	47.97	80.05	46.94
Paris (CIF)	Pan	63.43	44.02	63.01	41.96	62.50	40.15	62.10	38.75
	Proposed	80.36	55.63	79.87	53.29	78.64	50.88	79.24	49.28
Mthr_dot (CIF)	Pan	63.51	39.52	64.12	38.76	62.74	37.55	62.33	37.14
	Proposed	83.56	52.11	83.06	50.54	82.88	49.50	82.53	48.85

Table 2. The proposed scheme and Pan’s scheme compared with JM8.6 in terms of bit rate and PSNR

Sequences	ALL_I				ALL			
	BDBR (%)		BDPSNR (dB)		BDBR (%)		BDPSNR (dB)	
	Pan	Proposed	Pan	Proposed	Pan	Proposed	Pan	Proposed
Container (QCIF)	3.71	2.00	-0.25	-0.13	3.56	1.92	-0.23	-0.13
Foreman (QCIF)	3.50	0.86	-0.21	-0.05	3.05	0.63	-0.18	-0.04
Claire (QCIF)	5.82	2.40	-0.46	-0.19	5.29	2.00	-0.40	-0.16
Miss_am(QCIF)	5.49	2.15	-0.33	-0.13	5.00	1.98	-0.29	-0.11
Foreman (CIF)	2.92	1.27	-0.15	-0.07	2.34	0.92	-0.11	-0.05
Paris (CIF)	2.87	0.32	-0.21	-0.02	2.67	0.27	-0.18	-0.02
Mthr_dotr (CIF)	3.93	1.59	-0.20	-0.08	3.43	1.41	-0.17	-0.07

Table 3. The proposed scheme compared with Pan’s scheme

Sequences	BDBR(%)		BDPSNR(dB)		TS(%)	
	ALL_I	ALL	ALL_I	ALL	ALL_I	ALL
Container (QCIF)	-1.65	-1.58	0.11	0.11	55.81	21.71
Foreman (QCIF)	-2.54	-2.34	0.16	0.14	40.53	15.46
Claire (QCIF)	-3.23	-3.12	0.25	0.24	72.61	26.96
Miss_am(QCIF)	-3.17	-2.88	0.20	0.18	71.70	25.94
Foreman (CIF)	-1.60	-1.39	0.08	0.07	48.15	17.23
Paris (CIF)	-2.49	-2.34	0.19	0.16	45.03	18.80
Mthr_dotr (CIF)	-2.25	-1.95	0.12	0.10	53.86	19.44

sequences recommended in [8]. Our proposed scheme and Pan’s scheme^[3] are implemented and compared. The parameter configure file is based on JVT main profile with reference frame number set to 1 and GOP structure set to IPPP. The system platform is the Intel Pentium IV Processor of speed 1.7GHz, 256MB DDR RAM and Microsoft Windows2000 professional. Seven test sequences are selected from the recommended sequences, including 4 QCIF sequences and 3 CIF sequences. For each sequence, 150 frames are encoded.

The comparison between our proposed scheme, Pan scheme and JM8.6 are given in Tables 1-3 by varying *QP* as 28, 32, 36 or 40. The thresholds *T*₁ and *T*₂ in section 3.2 are adopted as constants associated with the *QP*. In the experiments, *T*₁=25, while *T*₂=45, 56, 70, 83, with respect to *QP*=28, 32, 36 and 40, respectively. Another threshold *T*₃ in section 3.3 is 4. In the tables, “ALL_I” and “ALL” correspond to the results of all the I-frames and the entire sequence, respectively.

Table 1 shows the comparison results in terms of computational cost, where *TS* is used as the measurement. *TS* indicate the average time saving in encoding process, which is given as below

$$TS = \frac{Time[reference] - Time[evaluated]}{Time[reference]} \times 100 \quad [\%], \tag{2}$$

where *Time[reference]* and *Time[evaluated]* mean respectively the encoding times of reference scheme and the scheme to be evaluated. In Table 1, the reference scheme is

JM8.6. It is shown that, compared with JM8.6, Pan's scheme reduces about 61.93% and 38.02% computational costs of the I-frame and the entire sequence on average. The computational cost can be further reduced by our proposed scheme. This is supported by the fact that the average cost reduction for the I-frame is 83.10%, and 50.94% for the entire sequence.

Table 2 shows the comparison results in terms of BDBR and BDPSNR^[9] in which JM8.6 is used as the reference. Table 3 gives the comparison between the proposed scheme and Pan's scheme in which Pan's scheme is as the reference directly. It is seen that, the proposed scheme outperforms Pan's scheme, because the encoding time is further reduced while the PSNR and bit rate are better than that of Pan's scheme. As compared with JM8.6, the proposed scheme reduces the encoding time significantly at the cost of slightly increasing in the output bit rate and decreasing in the quality of decoded images.

5 Conclusions

In this paper, we propose a fast intra prediction mode selection algorithm based on three schemes to reduce complexity of intra mode selection, that is, improvement of the intra prediction algorithm structure, fast selection between intra 4×4 block mode and intra 16×16 block mode, and the fast 4×4 luma block mode selection algorithm based on the reference pixels' luma similarity. It is demonstrated by experimental results that, compare with JM8.6, the proposed scheme reduces the encoding complexity significantly while increases bit rate slightly and maintains the average PSNR, and is more effective than Pan's fast method of intra prediction mode selection.

Acknowledgment

This work was supported by the Natural Science Foundation of China (grant 60472100), the Natural Science Foundation of Zhejiang Province (grant RC01057, Y105577), the Ningbo Science and Technology Project of China (grant 2003A61001, 2004A610001, 2004A630002), and the Zhejiang Science and Technology Project of China (Grant 2004C31105).

References

1. ITU-T Rec. H.264 | ISO/IEC 11496-10 AVC. Document JVT-G050. 7th Meeting: Pattaya, Thailand. (2003).
2. Topiwala, P., Sullivan, G., Joch, A., Kossentini, F.: Performance Evaluation of H.26L, TML 8 vs. H.263++ and MPEG-4. Santa Barbara (CA; USA), (2001).
3. Pan, F., Lin, X., Susanto, R., Lim, K.P., et.al.: Fast Mode Decision for Intra Prediction, in ISO/IEC JTC1/SC29/WG11 and ITU-T SG16 Q.6, JVT 7th Meeting, Pattaya II, Thailand, (2003).
4. Kim, C., Li, Q., Kuo, C.C.J.: Fast Intra-prediction model selection for H.264 codec, SPIE International Symposium ITCOM 2003, Orlando, Florida, (2003).

5. T. Wiegand, GJ. Sullivan, et. al. Overview of the H.264/AVC Video Coding Standard, IEEE Trans. Circuits Syst. Video Technol., 13 (2003), 560-576
6. ITU-T Rec. H.264 | ISO/IEC 11496-10 AVC. JM8.6. (2004).
7. Takagi, K., Takishima, Y., Nakajima, Y.: A study on rate distortion optimization scheme for JVT coder, Proc. SPIE Visual Communications and Image Processing 2003, 5150 (2003), 914-923.
8. JVT Test Model Ad Hoc Group, Evaluation Sheet for Motion Estimation, ISO/IEC JTC1/SC29/WG11 and ITU-T SG16 Q.6, Draft version 4, (2003).
9. Bjontegaard, G.: Calculation of Average PSNR Differences between RD-curves, VCEG-M33, 13th VCEG Meeting, Austin, Texas, USA, (2001).

Reduction of Mode Decision Complexity in H.264/AVC Using Adaptive Selection of Reference Frame and Intra Prediction Mode*

Woongho Lee, Jungho Lee, Ik-hwan Cho, and Dongseok Jeong

Multimedia Lab., Inha University, 253 Yonghyun-Dong, Nam-Gu Incheon, Korea
{llee, jungho, ikhwan}@inhaian.net, dsjeong@inha.ac.kr

Abstract. Rate-constrained coding is one of the many coding-efficiency oriented tools of H.264/AVC, however, the mode decision process of Rate Distortion Optimization (RDO), is characterized by high computational complexity. Many fast mode decision algorithms have been proposed to reduce the computational complexity of mode decision. In this paper, two algorithms are proposed for reduction of mode decision in H.264/AVC, fast reference frame selection and selective intra prediction mode decision. Fast reference frame selection is efficient for inter prediction, and selective intra prediction mode decision can effectively reduce excessive calculation load of intra prediction mode decision. The simulation results demonstrated that the proposed two methods applied together could reduce the encoding time of the overall sequences by an average of 44.63%, without any noticeable degradation in coding efficiency.

1 Introduction

H.264/Advanced Video Coding (AVC) is the coding-efficiency video standard, containing many different features compared with the prevalent standards such as H.263 and MPEG-2/4, including the 4x4 block-based integer transform, variable block size motion compensation, intra coding in the P slice, multiple references for motion estimation, 1/4 pixel resolution motion vector estimation and so on. [1], [2]. Among these features, intra prediction coding is one of the main features, which provide H.264 with its high coding efficiency compared with other video coding standards. The advantages of intra prediction coding are detailed in [3], in which it was reported that this method outperforms the JPEG2000 and MPEG-4 standards and demonstrates an improvement in the PSNR of approximately 3-4 dB at the same bit rate. In H.264/AVC, intra prediction is adopted in not only I-slice, but also P-slice, and a decision criterion for the final block mode of target block is the RDO technique, driving encoder complexity high.

Recently, there has been growing interest in reducing the computational complexity of mode decision [4], [5], [6]. To accomplish this goal, selective intra mode

* This work is supported by INHA UNIVERSITY Research Grant.

decision was proposed, utilizing the spatial and temporal correlation of the blocks for the intra mode decision in the P-frame, thereby affording a reported reduction of approximately 72% in the Rate Distortion cost (RDcost) and an encoding time saving of approximately 30% [4]. F. Pan et al. proposed a fast mode decision algorithm that allows preprocessing of the block edge field in the intra prediction mode, thereby reducing the number of directional modes for calculation, and decreasing the RDcost. In spite of an increase in the bit rate of approximately 5%, the encoding time of the I-slice was reduced by approximately 55-65% [5]. In [6], spatial homogeneity of a MB is decided based on the MB's edge intensity, and temporal stationary is decided by the difference of the current MB. The experimental results demonstrate that the fast inter mode decision algorithm is able to reduce the encoding time by an average of 30%.

In this paper, preset fast reference frame selection algorithm and selective intra prediction mode decision algorithms are used, in order to reduce the complexity of mode decision. In Sections 2, 3, the proposed algorithms are explained and experiments were conducted with reference software, performance results are verified in Section 4. Performance results of the proposed algorithms demonstrated that encoding time could be reduced in the overall test videos.

2 Fast Reference Frame Selection

The conventional mode decision process is separated into two stages. The first stage is the inter prediction mode decision, that removes temporal redundancy, and second stage is the intra prediction mode, that reduces the spatial redundancy. For inter prediction, multiple reference frames for motion estimation used in H.264 is useful for the video with the repeated motions, however, the level of motion estimation calculation is proportional to the number of the reference frame. Motion estimation is executed with variable block size, and then each mode may occur on one of multiple reference frames.

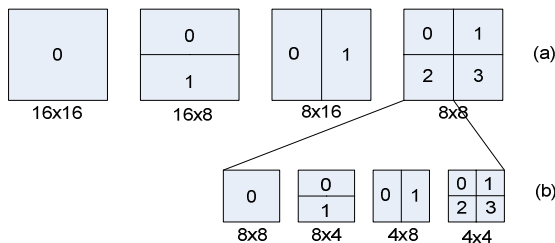


Fig. 1. MB partition and Sub-MB partition a) MB partition : mode 1(16×16), mode 2(16×8), mode 3(8×16), b) Sub-MB partition : mode 4(8×8), mode 5(8×4), mode 6(4×8), mode 7(4×4)

The luminance of each MB can be partitioned in four ways, as presented in Fig. 1 (a), and compensated either as one 16×16, two 8×16 or four 8×8 partitions. Furthermore, each of four 8×8 within each MB can be split in four ways, as

presented in Fig. 1 (b) either as one 8×8 sub-MB partition, two 8×4 sub-MB partitions, two 4×8 sub-MB partitions or four 4×4 sub-MB partitions.

In general, the MB partition size is appropriate for homogeneous block or motionless blocks and the sub-MB partition size may be efficient for non-homogeneous blocks. After motion estimation for each MB partition mode, if all MB partition modes occur in the same reference frame, the probability that the sub-MB partition mode can occur on the same reference frame of MB partitions is high. Therefore, it is assumed, that if the reference frame for the MB partition modes is identical, motion estimation for the sub-MB partition can be skipped for other reference frames, and processed on just one recommended reference frame used for the MB partition. Otherwise motion estimation for the sub-MB partition may be executed on all reference frames.

The proposed fast reference frame selection is processed in the following way.

First, check skip mode conditions, if skip mode conditions are satisfied, mode decision process is terminated.

Step 1: execute motion estimation of all reference frames for MB partitions: mode 1, mode 2, mode 3 and obtain the best reference frame for each mode.

Step 2: check the best reference frame of each MB partition mode (denoted as $best_ref_{mode}$).

If $best_ref_{mode_1} = best_ref_{mode_2} = best_ref_{mode=3}$, go to step 3

Else go to step 4

Step 3: recommended reference is set by $best_ref_{mode_1}$ and execute motion estimation of the recommend reference frame for sub-MB partitions: mode 4, mode 5, mode 6, mode 7 and go to step 5

Step 4: execute motion estimation of all reference frames for sub-MB partitions

Step 5: determine the best inter mode

3 Selective Intra Prediction Mode

After inter prediction, if the current MB is encoded by an intra mode, before deblocking, a prediction block is constructed by previously coded and reconstructed neighbor MBs. This predicted block is subtracted from the current MB and this difference is encoded. For luminance, the prediction block can be partitioned into 4×4 blocks (denoted as I4MB) or 16×16 block (denoted as I16MB). In general, a homogeneous MB can be encoded by I16MB, while a non-homogeneous MB can be encoded by I4MB.

In relation to the inter mode decision process, if the best inter mode occurs in MB partitions, the I4MB decision process can be skipped, only calculating the I16MB decision process. If the best inter mode occurs in the sub-MB partitions, the current MB can be assumed as non-homogeneous then the I16MB can be skipped, only processing the I4MB decision.

The proposed selective intra prediction mode algorithm is the following.

Step 1: Check inter mode and categorize best inter mode into Mode Group (MG)

Category 1: best inter mode \in MB partitions : MG1 {mode 1, mode 2, mode 3}

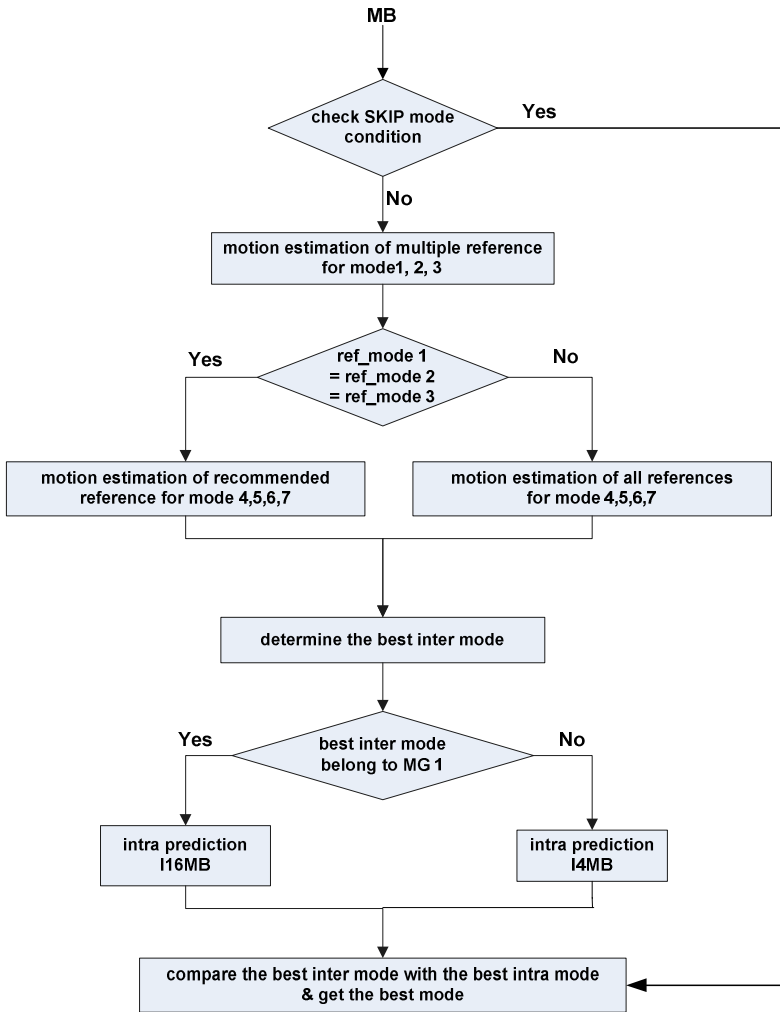


Fig. 2. Flowchart of proposed mode decision algorithm

Category 2: best inter mode \in Sub-MB partitions : MG2{ mode 4, mode 5, mode 6, mode 7 }

Step 2: If the best inter mode belongs to category 1, process I16MB intra mode decision

Step 3: If the best inter mode belongs to category 2, process I4MB intra mode decision

Step 4: Compare the RDcost of the best inter mode with the RDcost of the selected intra mode, and obtain the optimal mode with the least RDcost.

Fig. 2 presents the flowchart of proposed fast reference selection and proposed selective intra mode decision.

4 Experiments and Performances

Proposed fast reference frame selection and selective intra prediction mode decision algorithm were implemented on JM 10.1 reference software from [7]. Encoding options are as follows.

- 1) # of reference frames = 5,
- 2) Fast search motion estimation
- 3) Context-Based Adaptive Length Coding (CAVLC)
- 4) Rate Distortion Optimization (RDO)
- 5) GOP structure = IPPP
- 6) QP=24, 28, 32, 36, 40

A group of experiments were conducted on the recommended video sequences with variable size and frame, as described in Table 1.

Table 1. Test video sequences

Size	Video	Frames	Size	Video	Frames
QCIF (176×144)	container	200	CIF (352×288)	foreman	200
	carphone	150		football	150
	coastguard	100		crew	100

Five algorithms were conducted, as shown below:

Algo_A: JM original

Algo_B: JM with early termination and selective intra mode coding

Algo_C: JM with proposed selective intra mode coding algorithm

Algo_D: JM with proposed fast reference frame selection algorithm

Algo_E : JM with Algo_C + Algo_D

Algorithm B is one of the JM 10.1 encoding options. That algorithm proposed by [4] can be used for fast mode decision.

The comparison results were produced by defined subjective criteria as below:

- 1) PSNR difference

$$\Delta PSNR = PSNR_{proposed} - PSNR_{reference} \quad [\text{dB}] \quad (1)$$

- 2) Bit-rate difference

$$Ratio_Bits = \frac{(Bits_{proposed} - Bits_{reference})}{Bits_{reference}} \times 100 \quad [\%] \quad (2)$$

- 3) Difference of encoding time

$$Ratio_EncodingTime = \frac{EncodingTime_{proposed} - EncodingTime_{reference}}{EncodingTime_{reference}} \times 100 \quad [\%] \quad (3)$$

In equation (1), (2), (3), the PSNR of reference, Bits of reference and EncodingTime of reference are produced by using Algo_A.

In general, the fast algorithm produces side effects such as PSNR loss and bitrate increase. Comparing with JM original, PSNR value is dropped in Algo_C, Algo_D and Algo_E. Minus of value means the value decrease. PSNR differences are tabulated in Table 2. There is no PSNR change of Algo_B (JM with early termination and selective intra mode coding).

Table 2. PSNR difference of each test video

Video	$\Delta PSNR$ [dB]			
	Algo_B	Algo_C	Algo_D	Algo_E
container	0.000	-0.0024	-0.0025	0.0024
carphone	0.000	0.0112	-0.0572	-0.0560
coastguard	0.000	-0.0084	-0.0606	-0.0564
foreman	0.000	-0.0184	-0.0524	-0.0662
football	0.000	-0.0878	-0.0432	-0.1658
crew	0.000	-0.0248	-0.0418	-0.0758

However, in Algo_C and Algo_D, each PSNR value decreased by 0.0217 and 0.047 dB on average and PSNR drop was observed by 0.069 dB on average in Algo_E. In spite of 0.069 dB PSNR drop in Algo_E, overall PSNR loss of each algorithm is insignificant. In the proposed algorithms, PSNR difference of Algo_C is less than that of Algo_D. The selective intra mode decision of proposed algorithms has contributed less to the overall algorithm than fast reference frame selection, because the probability of intra mode occurrence in the P slice is low.

Table 3. Bit-rate difference ratio of each test video

Video	Ratio_Bits [%]			
	Algo_B	Algo_C	Algo_D	Algo_E
container	0.00	0.00	0.92	1.05
carphone	0.00	0.22	1.06	1.08
coastguard	0.00	0.06	1.31	1.44
foreman	0.00	0.47	1.37	1.87
football	0.00	1.72	-0.74	1.26
crew	0.00	1.30	-0.72	0.61

In Table 3, the bitrate of Algo_C increased slightly by 0.63% on average, and that of Algo_D also increased by an average of 0.53%. The bitrate increase of Algo_E is an average of 1.22%. The bitrate increase of the proposed algorithms is slight.

The Rate Distortion (RD) curve in Fig. 3 explains the image degradation caused by a reduction in mode decision complexity. The RD curves of algorithms in Fig. 3 (a)

QCIF container demonstrate that image degradations of all algorithms are not noticeable compared with the JM original. The RD curves of algorithms in CIF foreman demonstrate the RD curves of Algo_B and Algo_C overlap, and slightly lower RD curves of Algo_E are obtained, because degradations of Algo_D might propagate into Algo_E.

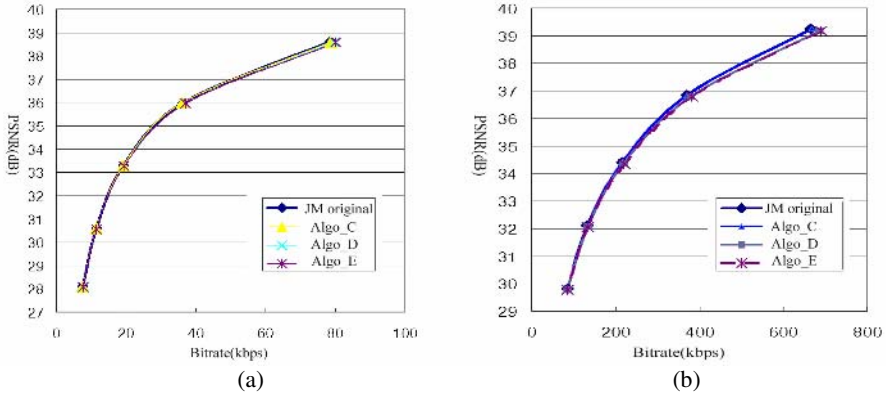


Fig. 3. RD curve of the test video sequences: (a) RD curve of QCIF container, (b) RD curve of CIF foreman

Table 4 demonstrates that the difference ratio of encoding time in each algorithm of variable test videos and Fig. 4 represents average saved encoding time of each algorithm. There is no image degradation of Algo_B but the difference of encoding time in Algo_B is less than 0.12% on average. Saved encoding time is not appropriate for the general fast algorithm. The encoding time of Algo_C is saved by an average of 23.03%, and that of Algo_D is saved by an average of 19.03%. Algo_C can reduce the overall complexity of encoder more than Algo_D, because the calculation portion of selective intra mode decision is bigger than that of Algo_D.

Especially in test videos with big motions such as football and crew, Algo_D affects the saving of overall encoding time.

Table 4. Difference ratio of encoding time in each algorithm

Format	Video	Ratio_EncodingTime [%]			
		Algo_B	Algo_C	Algo_D	Algo_E
QCIF	container	0.04	-30.47	-17.56	-50.09
	carphone	-0.34	-25.46	-16.22	-44.22
	coastguard	-0.13	-20.79	-21.83	-46.09
CIF	foreman	-0.21	-23.32	-17.95	-43.69
	football	0.03	-18.28	-20.60	-41.55
	crew	-0.08	-19.87	-20.02	-42.10

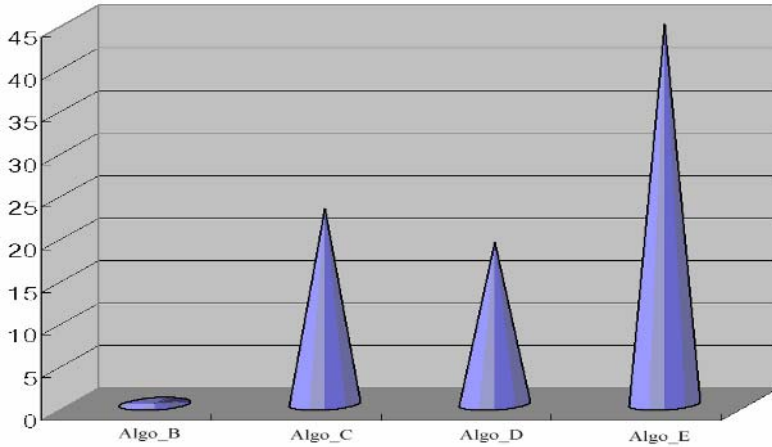


Fig. 4. Saved encoding time of each algorithm

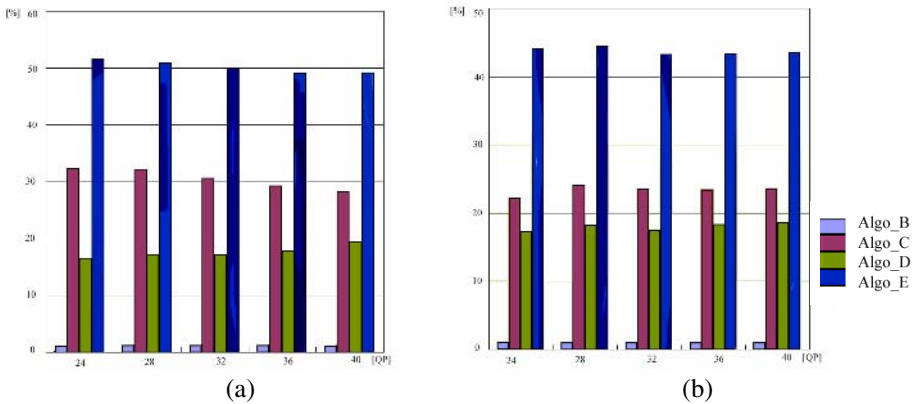


Fig. 5. Saved encoding time of test video sequences with variable quantization: (a) saved encoding time of QCIF container, and (b) saved encoding time of CIF foreman

Algo_E is combined with Algo_C and Algo_D, therefore, the encoding time of Algo_E is also saved by the saved encoding time of Algo_C plus the saved encoding time of Algo_D, with an average of 44.63%.

Fig. 5 presents the saved encoding time of each algorithm with variable quantization. Encoding times are saved almost equally in both the low bitrate and high bitrate.

5 Conclusions

The H.264/AVC overperforms other video coding standards such as H.263, MPEG-2, 4 in terms of coding efficiency and image quality. The mode decision process is one

of the features making it successful, and complex. The proposed algorithms deal with the most intensive computational part of the encoder.

The first proposed algorithm is fast reference frame selection, so that one of the multiple reference frames for sub-MB partitions inter mode can be selected after MB partition inter mode decision. The second proposed fast algorithm is selective intra mode decision, so that intra mode size such as I16MB or I4MB can be selected depending on the size of the best inter mode.

Each proposed algorithm can reduce the encoding time by an average of 23% and 19%, respectively. Furthermore, combining the algorithm with fast reference frame selection and selective intra mode decision can dramatically reduce the encoding time by an average of approximately 45%, with image degradations of proposed algorithms not being noticeable.

References

1. Wiegand, T., Sullivan, G.J., Bjntegaard, G., Luthra, A.: Overview of the H.264/AVC video coding standard, *IEEE Transactions on Circuits and Systems for Video Technology*, Vol. 13(7), (2003) 560 – 576
2. Ostermann, J., Bormans, J., List, P., Marpe, D., Narroschke, M., Pereira, F. Stockhammer, T., Wedi, T.: Video coding with H.264/AVC: tools, performance, and complexity, *IEEE Circuits and Systems Magazine*, Vol. 4(1), (2004) 7–28
3. Helbag T.: Performance comparison: H.26L intra coding vs. JPEG2000. Joint Video Team of ISO/IEC MPEG and ITU-T VCEG, Austria, July (2002)
4. Byeungwoo Jeon, Jeyun Lee: Fast mode decision for H.264, *JVT-J033*, (2003)
5. F. Pan, X. Lin, R. Susanto, K. P. Lim, Z. G. Li, G. N. Feng, D. J. Wu, and S. Wu: Fast Mode Decision for Intra Prediction, *G013*, (2003)
6. Wu, D., Pan, F., Lim, K.P., Wu, S., Li, Z.G., Lin, X., Rahardja, S., Ko, C.C.: Fast intermode decision in H.264/AVC video coding, *IEEE Transactions on Circuits and Systems for Video Technology*, Vol.15 (7), (2005) 953- 958
7. JVT Reference Software Version 10.1: <http://iphome.hhi.de/suehring/tml/>

3D Visualization for Tele-medical Diagnosis

Sun K. Yoo^{1,3}, Jaehong Key^{2,4}, and Kuiwon Choi⁴

¹ Dept. of Medical Engineering, Yonsei Univ. College of Medicine, 134 Shinchon-dong
Seodaemun-ku, Seoul Korea
sunkyoo@yumc.yonsei.ac.kr

² Human Identification Research Center, Yonsei University, Seoul Korea
jason1004@kist.re.kr

³ Center for Emergency Medical Informatics, College of Medicine Yonsei University,
Correspondence, Seoul Korea

⁴ Biomedical Research Center, Korea Institute of Science and Technology, Seoul Korea
choi@kist.re.kr

Abstract. It is widely accepted that 3D visualization of medical images helps in patient diagnosis. To visualize 3D images requires large computation loads. Therefore fast 3D visualization requires an expensive volume rendering board. Some web-based streaming techniques were suggested to construct high quality 3D visualizations even though only using a personal computer without a volume rendering board. These techniques could share the volume rendering board and diagnose 3D images together. To make a web-based 3D visualization system, the issues of time delay depending on limited network bandwidths need to be resolved. This delay directly influences the image quality. Through this study, we evaluated optimized streaming conditions to visualize and control the 3D medical image which has a high quality on the web. To construct this system, we primarily used three tools which included a VolumePro1000 board, WMV9 (Windows Media Video 9 codec) and TCP-IP based socket functions. The VolumePro1000 board could calculate quickly heavy matrixes of 3D images using Phong's shading and shear-warp factorization. WMV9 was able to efficiently compress live images and to apply image streaming techniques. TCP-IP based socket functions transmitted messages to control the 3D images. We developed a 3D visualization system and tested image qualities and transmission conditions of different compression rates for variable network conditions. It was very advantageous that the WMV9 encoding could be decoded automatically in many platforms (desktop, PDA, notebook, as long as the platform had Windows Media Player. We expect the 3D visualization system to be utilized in various biomedical fields such as IIGS (Interactive Image Guided Surgery), CAD (Computer Aided Diagnosis) and Tele-medicine technologies.

Keywords: 3D visualization, web, streaming, volume rendering.

1 Introduction

The development of image modalities makes it possible to visualize 3D images of anatomical structures and functional properties. The representative image modality devices include CT (Computerized Tomography), MRI (Magnetic Resonance

Imaging), PET (Positron Emission Tomography) and ultrasound, among others. Medical diagnosis using 3D volume rendering techniques remains an important issue.

Three-dimensional medical images have huge data sizes and require complex matrix calculations, so a high performance computer system was necessary. In CT images, there are 100 million voxels which have 512^3 sizes, therefore requiring the installation of an expensive volume rendering board and SDK (Software Development Tool Kit). While it is possible to construct 3D images without a rendering board, the process is slow and results in low quality images. Recently, to overcome these problems, some trials have been using web-based techniques in order to expand a computer's ability through access to a volume rendering board. To support 3D medical images in telemedicine, many studies have been reviewed. Carlos Dafonte et al. suggested a method visualizing the corresponding organ or object in a 3D virtual model of the patient using an OpenGL library [1]. Hiroyuki Sato et al. presented an interactive 3D presentation for medical images on the network using VRML 2.0 for remote medical service [2].

Web based 3D systems could make it possible for users to handle 3D images generated from high performance computers so that many users could share the resulting images from this system. However, when many users use this system, time lag could occur due to limited network bandwidth. Therefore, many researchers have suggested various compression techniques to overcome this problem using MPEG, JPEG, etc. In this study, we used the WMV9 codec and evaluated the most optimized 3D visualization through image streaming. The WMV9 codec is not only easy to use but also effective in data compression.

2 Method and Materials

2.1 System Configuration

Experimental objects were typical computers without volume rendering boards. These computers have 2.0-GHz Pentium 4 processors and 512 Mbytes of RAM (random access memory). A computer which has a volume rendering board is able to reconstruct high quality 3D medical images in real time. In this study, a computer with a 3.2-GHz Pentium 4 processor, 512 Mbytes of RAM, a 128-Mbyte 3D graphic card (GeForce FX 5700, nVIDIA, California, USA) with an AGP (accelerated graphics port) interface and real-time volume rendering board (VolumePro1000, TeraRecon, Massachusetts, USA) with a PCI interface was used. The operating system was Microsoft Windows XP.

2.2 Volume Rendering Techniques for 3D Visualization

To construct 3D images from 2D slice images, we needed five essential procedures [3]. First, we calculated the gradient of input data. This work determined the boundary between different objects through measuring the degree of change in 3D images. Second, we made samples through interpolation because voxels didn't align along a virtual ray when it passed through a set of voxels. Third, we classified the samples according to different degrees of opacity. In addition, a shading process was included. A virtual ray's position was determined such that the ray shaded objects.

Lastly, a final pixel was composed of many samples along the ray (Fig. 1). The volume rendering technique is different from the surface rendering technique. Surface rendering utilizes wire-frame models, where each polygon is placed on the models. These methods have many limitations when visualizing the inside of an object.

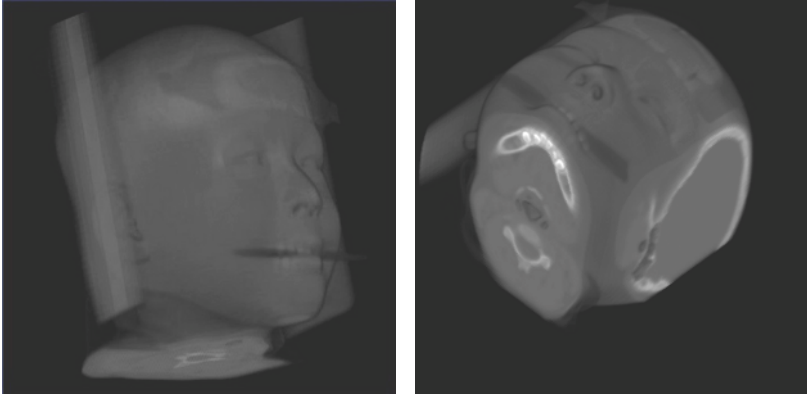


Fig. 1. 3D visualization using a VolumePro1000 board

The shading technique allocates shaded color to input data with consideration of light effects, and this method translates into perceived volume for users. To represent volume, the VolumePro1000 board supports Phong's illumination models [4]. Illumination models primarily incorporate three factors. First, the ambient reflection considers that entire light has the same reflection rates as the object's surface. Next, it is the diffuse reflection that considers the projecting angle of a ray. Finally, the specular reflection is the angle between one's eyes and the ray which is reflected from the objects.

Ray casting was attempted to produce 3D volume rendering. However, it couldn't access the data as a storage process because the random oriented ray exceeded the 3D volume. So a re-sampling process which calculates sample points that passed through a ray required a massive calculation. Shear-warp factorization decreases the time required to calculate the re-sampling process.

It is in the shear process that the 3D volume image composed of 2D slices (which are perpendicular to the ray) is sheared. Sheared slices do over operation along stored scan-line orders. This result makes 2D slices into a distorted 3D volume image. A final 3D volume image is completed by the warping process of an intermediate image [5].

The VolumePro1000 board with a 64-bit PCI interface rapidly produces real time 3D medical images. The VolumePro1000 board renders 256^3 (8- or 12-bit voxels) with tri-linear interpolation at a rate of 30 frames per second based on sheared warp transformation with Phong shading [6]. Also, functions provided by the VolumePro1000 SDK were used for real-time user interaction, including an opacity lookup table, a 3D cursor, and cropping utilities. The functions were programmed in Visual C++ 6.0 with VLI (Volume Library Interface, TeraRecon) [7-8] and OpenGL (Fig. 2).

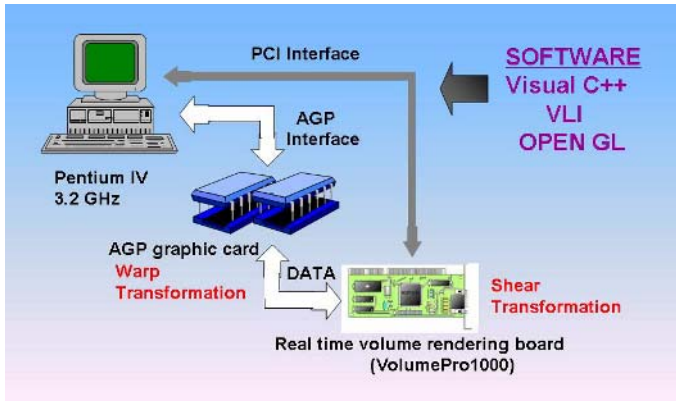


Fig. 2. System configuration of shear-warp factorization

2.3 Image Streaming Techniques Using WMV9

The image streaming technique demands broad network bandwidth when 3D volume images are transmitted. Therefore, an effective transmission technique is necessary to stream huge data on the web. In this study, we suggested the use of WMV9 (Windows Media Video 9 codec). The WMV9 codec was used as the solution of problems associated with high-bit transmission rates. The codec could decode automatically in Windows Media Player without installing a specific decoder, so that any platform devices could play the contents if equipped with Windows Media Player. To do these operations, there were a few procedures to follow. First, Window Media Encoder captured the 3D images on the server computer. Second, captured 3D images were encoded by the WMV9 codec. CBR (Constant Bit Rate) encoding, the efficient method for screen capturing and streaming scenario, was used. Finally, the encoded result video was streamed on the web. For high quality 3D image visualization, this study applied various compression bit rates to the LAN environment [9]. In addition, we needed to determine the buffer sizes which depend upon image quality and loading time. The WMV9 codec consists of three elements which are the encoder buffer, server buffer and player buffer (Fig. 3). The encoder buffer directly affects compression rates and the server buffer is dependent on loading time of play. The player buffer controls natural streaming images. If we establish big buffer, delay time to load images is inevitable, and if we set up tiny buffer, content quality might be

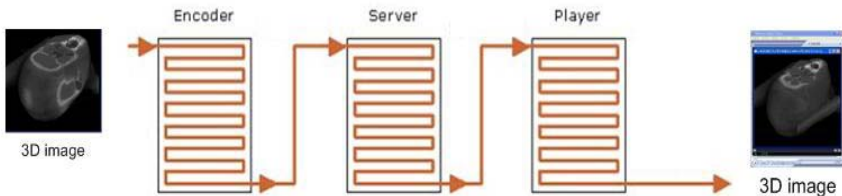


Fig. 3. Structure of image streaming scenario

diminished. First of all, we considered that the most important element for imaging was to play naturally, so we minimized the buffering time to load images to be one second [10]. In the LAN environment, however, network conditions were changed continuously so we applied various compression rates.

2.4 Web-Based 3D Medical Images Transmission and Manipulation

Figure 3 explains the system architecture. First, we defined a server that had a VolumePro1000 board. The server is able to render 3D images in real-time and these 3D images are streamed to clients after compression. Next, a master thin client system had a manipulative function over the server so that it could use the server computer's capabilities. For example, it is able to rotate 3D images, crop these images to see 2D slices, and control opacity to observe internal materials within 3D images. Finally, thin clients only had Windows Media Player so that they could only view 3D images. Of course, if the server grants a thin client authority of control, the thin client becomes a master thin client and can manipulate the server.

To communicate between server and client, we used a TCP (Transmission Control Protocol) based socket function [11]. The socket transmits messages to control the server and if message transmission fails, the message is tried again automatically.

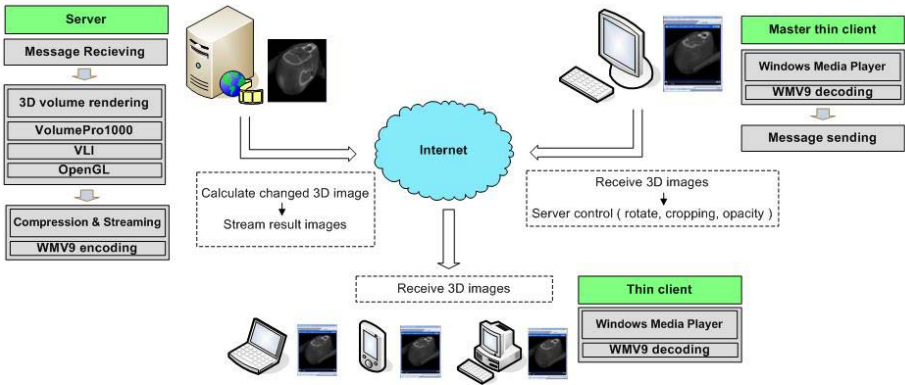


Fig. 3. System architecture

4 Results

We experimented with a LAN (Local Area Network), which is the representative network system in South Korea. In this study, the transmission rate was measured between Yonsei University and Severance Hospital (distance: about 1 km). We first measured the average download speed over seven days. The maximum speed measured was 38.3 Mbps, minimum speed was 4.78 Mbps and the mean value was 30.16 Mbps (Fig. 4). In Figure 4, the x-axis represents the day of measurement, the y-axis the average download speed for each day, and the green bold line the average speed for seven days.

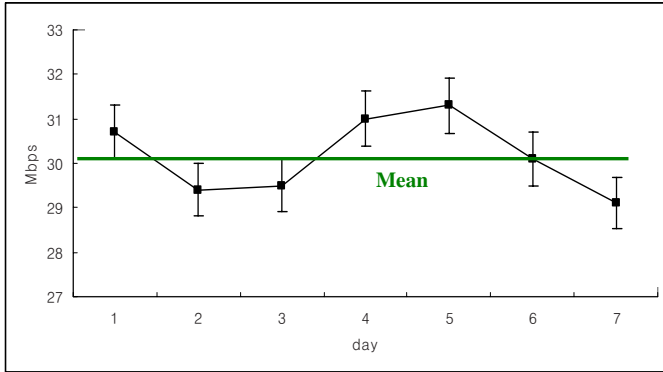


Fig. 4. Average download speed for 7 days

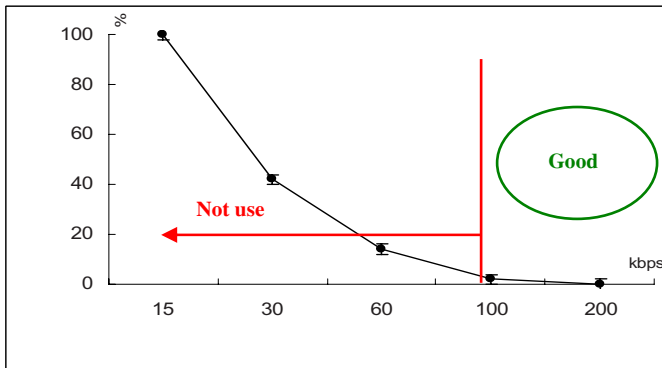


Fig. 5. Frame dropped rate on different encoding rates

Second, we measured WMV9 codec compression ability (Fig. 5). We tested the dropped frame rate on different compression bit rates. In Figure 5, the x-axis represents compression bit rates and the y-axis dropped frame rates. The occurrence of a high dropped frame rate may possibly cause a major problem even though any compression rate performs a very high speed interaction with the server. We measured about a 100% dropped rate on 15 kbps and below, and close to a 0% dropped rate on 100 kbps and beyond. We concluded that 100 kbps and below of compression bit rate could not be used in this study.

Third, we measured the delay time of 3D images (Fig. 6). In Figure 6, the x-axis represents different compression bit rates and the y-axis is delay time. Two types of delay can be seen, which are interactive delay and loading delay. Interactive delay refers to the waiting time of thin clients to see resulting images when the master thin client controlled the 3D images. For example, the master thin client uses a cropping function to see a 2D image through a 3D image. The server computer rapidly calculates the changed value using a VolumePro1000 board and streams the cropped result images. Finally all thin clients are able to see the result images. This requires a few seconds. Loading time refers to the initial waiting time for all thin clients

including the master thin client to see the 3D images when clients connect to the server computer.

There are many elements that cause delays. We only assumed three elements to affect delay: compression bit rates, network condition, and client number. But, we could not control the network condition because the LAN was not a private network environment for our research. Therefore, we applied a client number from one to four and various compression bit rates. As a result, we were able to determine that four clients were not affected by delay and conclude that a reasonable rate of compression would be between 100 kbps and 400 kbps. Even though 60 kbps and below are faster than others, image quality was poor at these compression rates. We only considered 100 kbps and beyond, regardless of whether loading time was fast or not.

Finally, we measured loading time when applying different image sizes. In this measurement, we fixed the value of compression bit rate at 200 kbps. The server computer made 512x512 sizes in real time. In Figure 7, the x-axis represents image sizes and y-axis is the loading delay. In the case of loading delay, images larger than 800x600 required more than 14 seconds and these images had low resolution from

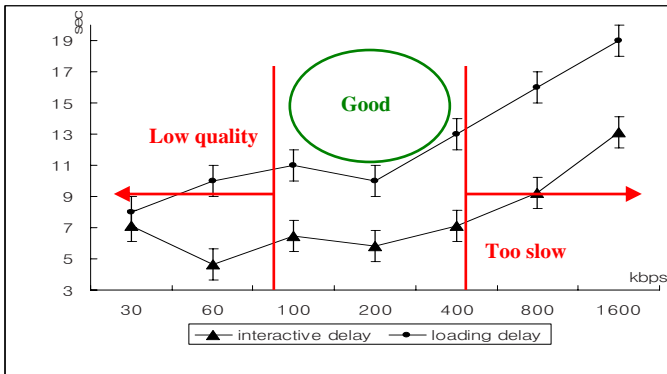


Fig. 6. Delay time on different encoding rates

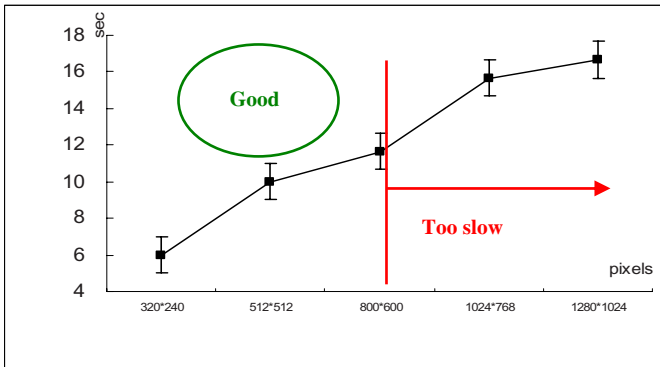


Fig. 7. Delay time on different image sizes

expansion. Therefore, we proved that 800x600 and smaller images were reasonable. In the case of 320x240 images, the images appeared somewhat limited in their diagnostic value when compared with the original images, but did, however, have a fast loading time.

5 Conclusion and Discussion

Through this study, we attempted to visualize and control the 3D medical image which has a high quality on the web. We implemented a 3D visualization system on a LAN environment and evaluated delay time and image qualities along with different compression rates and image sizes for variable network conditions.

We could conclude that reasonable compression bit rates and proper image sizes yield a short delay. This system has an important implication in terms of expanding a high performance system through the web without expensive hardware and software.

PACS (picture archiving communication system) system primarily supports 2D slice images. Present technique could make 3D images from 2D slice images, so the database of 3D images could be connected with the PACS system. Therefore, our web-based 3D visualization techniques could contribute to expand the PACS system's database of 3D images on the web. This means that a physician in a local hospital without a PACS system would be able to diagnose patients using 3D medical images.

In a future study, this system will support various functions of the 3D image processing on the remote site. Compression technologies will be developed to adaptively control the compression bit rates and image sizes for changed network conditions.

Acknowledgement. This study was supported by a grant from the Korea Health 21 R & D Project, Ministry of Health & Welfare, Republic of Korea (02-PJ3-PG6-EV08-0001).

References

- [1] Carlos Dafonte, Angel Gomez, Bernardino Arcay, Alfonso Castro, Javier Pereira: 3D Visualization Module in a Telemedicine Project: 15th IEEE Symposium on Computer-Based Medical Systems, (2002) 193
- [2] Hiroyuki Sato, Masaharu Shimanuki, Takao Akatsuka: Interactive 3-D presentation of medical images on network using VRML 2.0: 20th Annual International Conference of the IEEE, Vol. 3, (1998) 1246-1249
- [3] Barthold Lichtenbelt, Randy Crane, and Shaz Naqvi: Introduction To Volume rendering: Prentice Hall, (1998)
- [4] Philippe Lacroute, Marc Levoy: Fast Volume Rendering Using a Shear-Warp Factorization of the Viewing Transformation: Computer Graphics Proc. SIGGRAPH, (1994) 451-457
- [5] Philippe G.Lacrote: Fast Volume Rendering Using A Shear-Warp Factorization of The Viewing Transformation, Technical Report CSL-TR-95-678: Computer Systems Laboratory, Department of Electrical Engineering and Computer Science, Stanford University, September (1995)

- [6] Yoo SK, Wang G, Rubinstein JT, Skinner MW, Vannier MW: Tree-dimensional modeling and visualization of the cochlea on the internet: IEEE Trans Inf Technol Biomed, 4(2), (2000) 144-51
- [7] VolumeProTM 1000 Programmer's Guide: TeraRecon, Inc. MA, (2001)
- [8] Voxel File Formate Specification: TeraRecon, Inc. <http://www.terarecon.com> , MA, (2001)
- [9] Seth McEvoy: Windows Media Platform: Redmond, WA, Microsoft Press, (2003)
- [10] Window Media Encoder 9 Series: Microsoft Inc. <http://www.microsoft.com>
- [11] Kim SU: Windows Network Programming: Hanbit Media, Inc. Seoul, (2004)

Content Based Image Retrieval Based on a Nonlinear Similarity Model*

Guang-Ho Cha

Department of Computer Engineering, Seoul National University of Technology,
138 Gongreung-gil, Nowon-gu, Seoul 139-743, South Korea
ghcha@snut.ac.kr

Abstract. In this paper, we propose a new nonlinear paradigm to clustering, indexing and searching for content-based image retrieval (CBIR). The scheme is designed for *approximate searches* and all the work is performed in a transformed *feature space*. We first (1) map the input space into a feature space via a nonlinear map, (2) compute the top eigenvectors in that feature space, and (3) capture cluster structure based on the eigenvectors. We (4) describe each cluster with a *minimal hypersphere* containing all objects in the cluster, (5) derive the similarity measure for each cluster individually and (6) construct a *bitmap index* for each cluster. Finally we (7) model the similarity query as a *hyper-rectangular range query* and search the clusters near the query point. Our preliminary experimental results for our new framework demonstrate considerable effectiveness and efficiency in CBIR.

1 Introduction

CBIR has become a very active research area because both of the increasing amount of visual data available through the Internet. CBIR supports image searches based on perceptual features such as color, texture, and shape extracted from the media data. When a user poses a query represented by such features, a CBIR system returns a sorted list of relevant objects based on their *similarity* to the query object.

Similarity search is inherently expensive, especially in high dimensions. The prohibitive nature of exact similarity search has led to the interest in *approximate similarity search* that returns objects approximately similar to the query object. In this paper, we present a new approximate similarity search paradigm to clustering, indexing and searching for CBIR. All our work is conducted in a transformed feature space in order to make the best use of the nonlinear features of the dataset.

In our scheme, the dataset is first mapped to a feature space via a nonlinear kernel and then it is partitioned into similar clusters in the feature space. For clustering, we apply the kernel based method such as [5] because it has demonstrated good performance in a feature space.

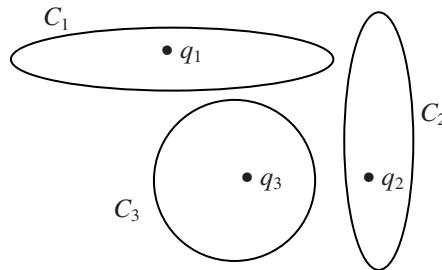
* This work was supported by grant No. B1220-0501-0233 from the University Fundamental Research Program of the Ministry of Information & Communication in Republic of Korea.

Table 1. PCA vs. kernel PCA

<i>original dim = 256</i>	PCA			Kernel PCA		
	precision	AVRR/IAVRR	tau	precision	AVRR/IAVRR	tau
<i>dim = 164</i>	0.62	3.45	0.42	0.74	3.04	0.71
<i>dim = 113</i>	0.59	3.65	0.37	0.68	3.16	0.63
<i>dim = 77</i>	0.53	3.70	0.38	0.65	3.24	0.64

To improve performance, we perform dimensionality reduction on the transformed feature space using the principal component analysis (PCA). The performance of PCA conducted on the feature space is usually better than that on the original data space. Table 1 shows our experimental result of k -nearest neighbor (NN) queries performed with 13,724 256-color images. The original dimensionality of images is 256 and the reduced dimensionalities are 164, 113, and 77. Kernel PCA is the PCA performed on the feature space. Precision [9] measures the ability to reject useless items. The ratio of AVRR to IAVRR [2] reflects the positions in which the set of relevant items appear in the retrieval sequence ordered by some similarity measure. It approaches to 1 as the relevant objects retrieved are near the top. Tau [7] gives a measure of the difference in ranking between the out of order sequence and the in order sequence. It ranges from -1, which represents complete disagreement, through 0, to +1, complete agreement. The performance of kernel PCA is better than that of traditional PCA with respect to all three performance parameters. In terms of precision and AVRR/IAVRR, kernel PCA is 10% – 20% better than PCA. With respect to tau, kernel PCA is better than PCA more than 50%.

We need to define the similarity measure locally. Let us consider Fig. 1. There are 3 clusters C_1 , C_2 , and C_3 with different shape boundaries. For query q_1 , the vertical coordinate is more relevant because a slight move along that axis may change the cluster label, while for query q_2 , the horizontal coordinate is more crucial to determine the cluster it belongs to. For query q_3 , however, both coordinates are equally important. This implies that distance computation does not vary with equal strength in all directions in the space emanating from the input query. Capturing such information is

**Fig. 1.** Feature relevance varies with query locations

of great importance to the result of the similarity search. Therefore, in our work, the similarity (or distance) measures are constructed on each cluster individually.

For efficient similarity search we construct an index for each cluster. To answer a query, clusters that are near the query point are searched.

The contributions made by this paper are as follows:

- We investigate *as a whole* the issues related with CBIR, i.e., similarity model, clustering, indexing, searching, and similarity measure, and study how they can be effectively combined in a feature space.
- We show that the performance of CBIR is improved by performing all work in a *feature space* instead of the original data space.
- We propose a new similarity measure for effective CBIR.
- We improve the search performance by *locally* applying the similarity measure.
- We present a new *indexing method* for efficient approximate similarity search.

2 Nonlinear Similarity Model

We establish a *nonlinear* similarity model to simulate human perception for similarity evaluation between images. In a *linear* model, the degree of similarity between two images is linearly proportional to the magnitude of their distances. In comparison, the assumption for nonlinear approach is that the same portions of the distances do not always give the same degrees of similarity when judged by humans [13]. The visual section of the human brain uses a nonlinear processing system for tasks such as pattern recognition and classification [3]. In other words, the linear model is not competent for the nonlinear nature of human perception and cannot cope with the complex decision boundary. We therefore propose to use a nonlinear criterion in performing similarity comparison.

To establish a nonlinear similarity model, we adopt a *Gaussian* function as a basic similarity model:

$$G(x_i, x_j) = \exp(-d(x_i, x_j)^2 / \sigma^2) \quad (1)$$

The activity of function G is to perform a Gaussian transformation of the distance $d(x_i, x_j)$, which describes the degree of similarity between x_i and x_j . The scaling parameter σ controls how rapidly the similarity $G(x_i, x_j)$ falls off with the distance between x_i and x_j . We can allow different σ 's for each feature dimension, corresponding to length scales in Gaussian processes. If a feature is highly relevant, the value of σ should be small to allow higher sensitivity to any change of the distance d . In contrast, a large value of σ is assigned to the non-relevant features so that the corresponding component can be disregarded when determining its similarity. The choice of σ according to this criterion will be discussed in Section 4. We utilize this property to simulate the human perception.

3 Clustering

In order to minimize the number of disk accesses in similarity searches, similar data need to be well partitioned into clusters. We use a simplified version of the kernel

based clustering algorithm such as the spectral clustering [5]. The spectral clustering has demonstrated good performance in a high-dimensional feature space.

Kernel based method works by mapping data to a high dimensional feature space implicitly defined by the choice of the kernel function. We start with a Gaussian kernel $G(x_i, x_j) = \exp(-d(x_i, x_j)^2/\sigma^2)$ defined by Eq. (1) according to our similarity model. The clustering algorithm is as follows:

Given a set of points $X = \{x_1, x_2, \dots, x_m\}$ in R^n that we want to cluster into K subsets,

1. Form the similarity matrix $G \in R^{m \times m}$ defined by $G_{ij} = G(x_i, x_j)$ if $i \neq j$, and $G_{ii} = 0$.
2. Find K largest eigenvectors v_1, v_2, \dots, v_K from G , and form the matrix $V = [v_1, v_2, \dots, v_K] \in R^{m \times K}$ by stacking the eigenvectors in columns.
3. Treating each row of V as a point in R^K , cluster them in to K clusters via K -means clustering algorithm [4].
4. Finally, assign the original point x_i to cluster j if and only if row i of the matrix V was assigned to cluster j .

The effect of applying K -means algorithm in a Gaussian feature space instead of applying directly to the original data is that the natural clusters do not correspond to convex regions and the K -means algorithm do not find satisfactory clustering. But once we map the points to R^K , they may form tight clusters from which the clustering algorithm obtains good clustering.

4 Local Similarity Measure

The choice of a distance measure is crucial in the result of similarity search. As shown in Fig. 1, we need to define the distance measure individually depending on spatial locations since the feature relevance varies with query locations.

In our work, we find top eigenvectors in each cluster by applying PCA to the feature space. The size of an eigenvalue λ corresponding to an eigenvector v of the similarity matrix G equals the amount of variance in the direction of v . Therefore, we can effectively assign the normalized Euclidean distance d_m to each cluster C_m with dimensionality n as follows:

$$d_m(x, y)^2 = \sum_{i=1}^n \left(\frac{x_i - y_i}{r_i} \right)^2, \quad r_i = \frac{|\lambda_i|}{\sum_{j=1}^n |\lambda_j|} \tag{2}$$

As a result, the scaling parameter σ in the Gaussian function of Eq. (1) is determined by r_i in each dimension i . Therefore, the similarity value between two objects x and y in cluster m is defined by $\exp(-d_m(x, y)^2)$.

5 Cluster Description

Since the shape of clusters in a feature space can be arbitrary as shown in Fig. 1, we need to have a technique to represent clusters for indexing. We describe the boundary of a cluster in our feature space based on the support vector domain description

(SVDD) technique of Tax and Duin [12]. SVDD was originally developed to detect outliers. As a by-product of the algorithm one can compute a set of contours which enclose the data points. In our work, we use these contours as the cluster boundary.

In the feature space transformed via Gaussian kernel $\exp(-d(x, y)^2/\sigma^2)$, we search for the *minimal sphere* enclosing n data points $\{x_i, i = 1, \dots, n\}$. The sphere is described by the constraints for the sphere with center a and radius R :

$$\|x_i - a\|^2 \leq R^2 + \xi_i, \text{ slack variable } \xi_i \geq 0 \tag{3}$$

To solve this problem the following Lagrangian is introduced:

$$L = R^2 + C \sum_i \xi_i - \sum_i \alpha_i \{R^2 + \xi_i - (x_i^2 - 2ax + a^2)\} - \sum_i \gamma_i \xi_i \tag{4}$$

where Lagrange multipliers $\alpha_i \geq 0$ and $\gamma_i \geq 0$. Setting the partial derivatives to 0 leads to

$$\sum_i \alpha_i = 1, \quad a = \frac{\sum_i \alpha_i x_i}{\sum_i \alpha_i} = \sum_i \alpha_i x_i, \quad \alpha_i = C - \gamma_i \tag{5}$$

Eq. (5) states that the center a is described by a linear combination of data objects, with weight factors α_i which are obtained by optimizing the following Eq. (6).

$$L = \sum_i \alpha_i (x_i \cdot x_i) - \sum_{i,j} \alpha_i \alpha_j (x_i \cdot x_j) \tag{6}$$

with constraints $0 \leq \alpha_i \leq C, \sum \alpha_i = 1$. Only for a small set of objects the equality in Eq. (3) is satisfied: these are the objects which are on the boundary of the sphere itself. For those objects, the coefficients α_i will be non-zero and are called the *support objects*. Only these objects are needed in the description of the sphere. The radius R of the sphere can be obtained by calculating the distance from the center of the sphere a to one of the support objects on the boundary with a weight smaller than C :

$$R^2 = x_k \cdot x_k - 2 \sum_i \alpha_i (x_i \cdot x_k) + \sum_{i,j} \alpha_i \alpha_j (x_i \cdot x_j) \tag{7}$$

for any $x_k \in$ (a set of support objects).

The scale parameter σ of the Gaussian kernel controls the tightness of the sphere. The smaller σ is, the tighter the sphere becomes. We maintain the center and radius of the sphere as the descriptor for each cluster.

6 Similarity Query Model

In order to efficiently apply our indexing method to high-dimensional similarity queries, we model the similarity query as a *hyper-rectangular range query* with the query point x_q as a center of the hyper-rectangle and the diameter $2R_i$ of a cluster C_i as the search range on each dimension when the query point x_q is within the cluster C_i . When the query point x_q does not reside on a certain cluster, we search the cluster C_i closest to the query point x_q .

In addition to the performance issue, the transformation to the range search implies limiting the similarity boundary to a certain extent. For k -nearest neighbor (k -NN) query, an answer should be returned even when there are no similar objects nearby. Fig. 2 illustrates this transformation is meaningful. Points d and e are the fourth and fifth nearest neighbors to the query point x . According to the ranking-based measure, d and e are considered fairly good neighbors, although d and e are not of interest. The transformation to the range query from k -NN query has an effect of restricting the search space to a certain range, for example, from R_1 to R_2 in Fig. 2. If we can determine the range for the query appropriately, we can reduce the search effort considerably.

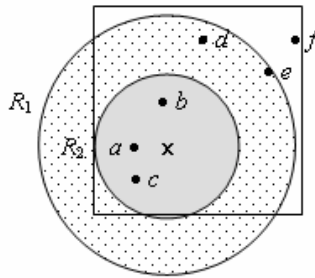


Fig. 2. Problem of ranking-based measures

7 Similarity Indexing

In order to perform the range query efficiently, we first discretize the data in each cluster into a set of intervals. Specifically, we divide each dimension into L *equi-depth* intervals such that each interval contains a fraction $1/L$ of the total number of objects in a cluster. This classification has an effect of similarity thresholding on each dimension. In other words, the two points classified into the same interval are defined to be similar within the interval. After the data is classified into L intervals on each dimension, for the j th interval I_{ij} on dimension i , we create a *bitmap* b_{ij} . The bitmap b_{ij} contains the binary information that says which objects are lying on the interval I_{ij} . Each bitmap has as many bits as the number of objects in a cluster. The p th bit of the bitmap for the j th interval I_{ij} on dimension i is set to 1 if the object numbered p resides on the interval I_{ij} , otherwise it is set to 0. For each dimension, the objects in the intervals that overlap the query range are regarded as the similar ones to the query object.

The key reasons to use bitmap indexing are two-fold: (1) it can treat each dimension independently and (2) it efficiently performs the bitwise AND/OR operations. Due to the great efficiency of bitwise operations for logical AND/OR, it finds k nearest neighbors far faster than a linear scan. Moreover, bitmap indices are much more compact than traditional tree-based indices and generally quite small compared to the database size. In a bitmap, a single bit represents an object, whereas objects are typically at least tens to hundreds of bytes long in a database.

7.1 Index Creation

We create an bitmap index for each cluster as follows:

- (1) For each dimension i , $1 \leq i \leq n$, we classify the data into a set of L intervals. Let us denote the j th interval for dimension i by I_{ij} .
- (2) For the interval I_{ij} , we create a bitmap b_{ij} and its lower and upper bounds $[l_{ij}, u_{ij}]$. The p th bit of the bitmap b_{ij} has the value 1 if the object numbered p lie on the interval I_{ij} .
- (3) For the objects lying on the interval I_{ij} , along with the bitmap b_{ij} , we keep the actual coordinates for the dimension i in those objects.
- (4) The bitmap index is simply an array of those bitmaps along with a list of actual coordinates and lower and upper bounds $[l_{ij}, u_{ij}]$'s for each interval I_{ij} .

7.2 Similarity Search

Given a query object, similarity search is performed in two steps. First, we find the clusters where the object resides, and then look up in the bitmaps for the clusters. The search takes the form of different actions depending on whether or not the clusters are found. The query point may reside on multiple clusters because cluster boundaries may overlap.

- If the clusters are found, we obtain the bitmap indices corresponding to the clusters, and then find k nearest neighbors using them.
- If the clusters are not found, we find some clusters closest to the query object by comparing the centers of clusters with the query object. We obtain the bitmap indices for the clusters and read them into memory.

When a user poses a k -NN query with feature vector $q = \{q_1, q_2, \dots, q_n\}$ and k , The search algorithm in a single bitmap index is as follows:

- (1) We transform the k -NN query with point $q = \{q_1, q_2, \dots, q_n\}$ into a rectangular range query Q whose center is q and rectangular search volume is $(2R)^n$, where R is the radius of the cluster associated with q .
- (2) For the range query Q and each dimension i , get the set S_i of bitmaps whose intervals overlap the rectangular search volume of Q .
- (3) For each set S_i ,
 - Create a bitmap b_i and set the all bits of b_i to 0.
 - $b_i = b_i$ OR (the bitmaps in S_i)
- (4) Create a bitmap b and set the all bits of b to 1.
- (5) for $1 \leq i \leq n$, do
 - $b = b$ AND b_i .
- (6) Obtain the set S of objects associated with the set bits in b .
- (7) For the objects in S , compute their distance values d_m and return the k objects in increasing order of d_m .

When we search multiple clusters for a query, for the candidates returned from the bitmap indices, we compute the normalized distance for each cluster and get the final k nearest objects.

8 Performance Experiments

It is difficult to directly compare our similarity search paradigm with some other competitors because many new techniques are included in our CBIR scheme. In other words, for a thorough performance evaluation of our scheme, the following comparison needs to be performed with respect to efficiency and effectiveness: kernel method (feature space) vs. non-kernel method (data space), spectral (feature space) clustering vs. non-spectral (data space) clustering, indexing method with clustering vs. indexing method without clustering, bitmap indexing vs. other indexing methods, local similarity measure vs. global similarity measure, etc.

In our preliminary experimental evaluation, we only assessed our scheme individually in view of kernel method (feature space) vs. non-kernel method (data space), indexing method with clustering vs. indexing method without clustering, and bitmap indexing vs. other indexing methods.

For our experiments, we used two real image datasets. The first dataset consists of 13,724 images from our video database and COIL(Columbia Object Image Library)-100 image dataset. To obtain feature vectors, we used MPEG-7 256-dimensional color structure descriptor. In the experiments, 100 k -NN queries were executed and their results were averaged. The second dataset is the MNIST database that contains 28×28 120,000 handwritten digit images. The MNIST database is the currently used classifier benchmark in the AT&T and Bell Labs and many methods have been tested with this database. The feature of each image is represented by a 784-dimensional vector. In our experiments, we use only the first 6,000 images from the MNIST database and perform a similarity search to return the k most similar images for the given query images.

Figs. 3 and 4 show the results of 100-NN queries on the MNIST dataset. The top-left two images are the query images. Fig. 3 shows the most similar 100 images by our similarity measure, and Fig. 4 shows the top 100 images by the Euclidean distance measure. As we can see, the result of Fig. 3 is closer to human perception than that of Fig. 4.

In terms of *precision*, the method employing both the kernel technique and the local similarity measure achieve 10 – 50% higher precision than the method using non-kernel methods and the global similarity measure.

The bitmap indexing method achieved speedups of several ten times over the linear scan that is usually used as a performance yardstick in high-dimensional indexing. Fig. 5 shows the total number of disk accesses actually performed to find k NNs in the first dataset with 13,724 images. In these experiments, 4-KB pages are used. The number of disk accesses performed by our bitmap index is far smaller than those of the VA-file [14] and the linear scan. The performance improvement of the bitmap

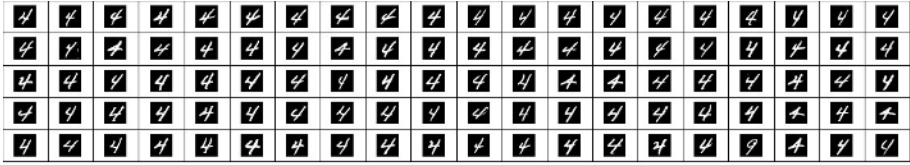


Fig. 3. Top 100 images by our similarity measure, where the top-left 2 images are the query images

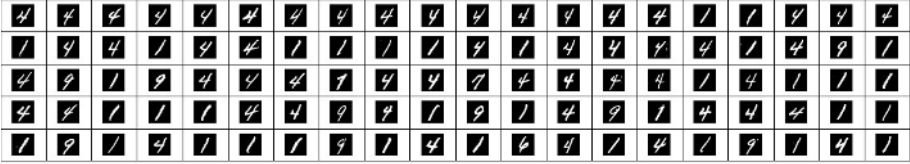


Fig. 4. Top 100 images computed by Euclidean similarity measure

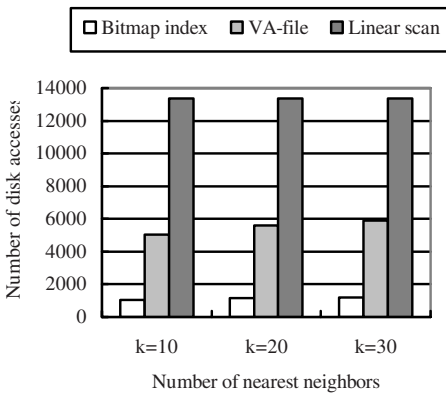


Fig. 5. Disk access experiments

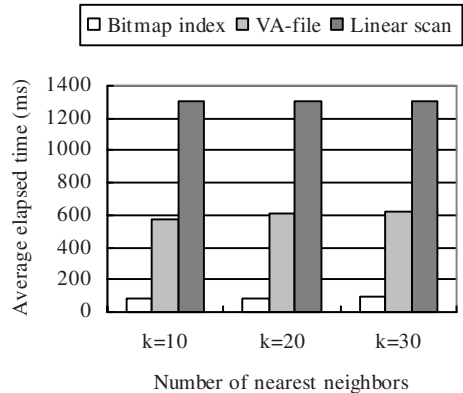


Fig. 6. Time experiments

index comes from the specialized bitmap indexing technique. Fig. 6 shows that the bitmap index achieves a remarkable speed-up over both of the VA-file and the linear scan. These observations demonstrate the efficiency of our bitmap index.

9 Conclusions

In this paper, we proposed a novel approximate similarity search paradigm in CBIR. This approach improves the efficiency of CBIR by employing the kernel method, spectral clustering, and bitmap indexing. It also improves the search effectiveness by adopting the kernel trick and the localized similarity measure. We believe that our scheme is an attractive approach to support approximate similarity search efficiently and effectively. More thorough performance evaluation is in the midst of our work.

References

1. G.-H. Cha, "Kernel Principal Component Analysis for Content Based Image Retrieval," *Proc. PAKDD 2005, LNAI 3518* (2005) 844-849.
2. C. Faloutsos et al., "Efficient and Effective Querying by Image Content," *Journal of Intelligent Information Systems*, Vol. 3 (1994) 231-262
3. S. Haykin, *Neural Networks: A Comprehensive Foundation*, NY: Maxmillan, 1994.
4. J. MacQueen, "Some methods for classification and analysis of multivariate observations," *Proc. 5th Berkeley Symp. Math. Statist. Prob.*, (1967) 1:281-297.
5. A.Y. Ng, M. J. Jordan, and Y. Weiss, "On spectral clustering: analysis and an algorithm," *NIPS* (2001)
6. P.E. O'Neil and D. Quass, "Improved Query Performance with Variant Indexes," *Proc. ACM SIGMOD* (1997) 38-49.
7. J. Payne, L. Hepplewhite, and T J stoneham, Texture, Hhuman perception and Information Retrieval Measures, *Proc. of ACM SIGIR 2000 Workshop* (2000)
8. J. Peng and D.R. Heisterkamp, "Kernel indexing for Relevance Feedback Image Retrieval," *Proc. of IEEE ICIP* (2003) 733-736
9. G. Salton and M.J. McGill, *Introduction to Modern Information Retrieval*, McGraw-Hill, New York (1983)
10. B. Schölkopf et al., Comparing Support Vector Machines with Gaussian Kernels to Radial Basis Function Classifiers, *IEEE Trans. on Signal Processing*, Vol. 45 (1997) 2758-2765
11. B. Schölkopf, A. Smola, and K. Müller, Nonlinear Component Analysis as a Kernel Eigenvalue Problem, *Neural Computation*, Vol. 10 (1998) 1299-1319
12. D.M.J. Tax and R.P.W. Duin, "Support vector domain description," *Pattern Recognition Letters*, Vol. 20 (1999) 1191-1199.
13. R.L.De Valois and K.K.De Valois, *Spatial Vision*, Oxford Science Publications (1988).
14. R. Weber, H.-J. Schek, and S. Blott, "A Quantitative Analysis and Performance Study for Similarity-Search Methods in High-Dimensional Spaces," *Proc. VLDB Conf.* (1998) 194-205.

Simple and Powerful Interactive E-Learning System Using VXML: Design and Implementation of Web and PSTN Linked Efficient Learning System

Jeong-Hoon Shin¹ and Kwang-Seok Hong²

¹ School of Computer and Information Communications Engineering,
Catholic University of Daegu, 330 Geumnak 1-ri, Hayang-eup, Gyeongsan-si,
Gyeongsangbuk-do, 712-702 Korea

only4you@chol.com
http://only4you.or.kr

² School of Information and Communication Engineering, Sungkyunkwan University,
300 Chunchun Dong, Jangan-gu, Suwon, Kyungki-do, 440-746 Korea

kshong@skku.ac.kr
http://hci.skku.ac.kr

Abstract. E-learning is increasingly being integrated into organizations and universities as a new means of learning and supporting learners. Even it has many advantages to support learners using multimedia systems, but it still has many weaknesses. A representative weakness using e-learning system is it needs specific extra equipments (like computers, monitors and keyboards and so on) and learners are requested unmoving status in the courses of lessons. But, nowadays most people make busy living. To say another word, learners have not enough time to hold unmoving status during their lessons. For this reason, in this paper we implement a novel architecture of e-learning system using VXML linked with PSTN (Public Switched Telephony Network). Our newly proposed system supports telephone-based learning as well as computer-based learning. Learners can choose their learning tools by the existing state of things at each time. Learners can choose computers as a learning tool when they are in the house, on the other case, learners can choose their telephones as a learning tool on the street. To verify performance of the implemented e-learning system, we conducted learning efficiency test after implementation.

1 Introduction

E-learning systems are in use today in many organizations (universities, schools and corporations). Traditional e-learning systems provide a content repository for course materials as well as facilities for learners tracking and management. But, nevertheless these advantages, there also are weaknesses in using traditional e-learning systems. Representative problems using traditional e-learning system is that learners are requested to have specific equipment and to hold their status unmoving during their lessons. And the other important problem in using traditional e-learning system is difficult to use. It is not easy things for the learner who is not familiar with the computer system to use traditional e-learning system. Learners are requested to learn how to use in some training courses.

To solve these problems, we propose novel architecture of e-learning system linked with PSTN. Our proposed system has several advantages. First, learners can fit their learning tools to their environments at that time. If he is at home, he can use his computers as a learning tool. He can operate e-learning system with keyboards, mouse, and monitors. And, if he is outside, then he can choose his mobile phone as a learning tool. He can operate learning system using voices through PSTN, and voice response from the e-learning system will help his learning. This method saves time and troubles. He can use time to spare at any places if he wants. Second advantage of our system is using VXML linked with PSTN. This architecture enables us to use common learner's database through PSTN and Web. Another advantage of our proposed system could be found in the resource reuse point of view. Whether the learners use computer or telephone as learning equipment, we can provide the same database for the lessons. In other words, though we provide two usable methods to the learners through PSTN and Web, there's no need to implement two different databases. Moreover, our proposed system can use formerly constructed databases for traditional services like Web. For this reason, we can reduce the expenses for constructing e-learning systems.

In this paper, we implement simple and powerful Web based e-learning system, which linked with PSTN. And the, we analyze strong points and weak points of implemented e-learning system comparing with traditional e-learning system. After that, to verify efficiency of implemented e-learning system, we conducted efficiency test.

2 Related Works

Definition of traditional e-learning system comes from the question that what is an e-learning system? There are plethora terms and acronyms for the system. If we sum up these terms and acronyms, definition of e-learning system could be brought to a conclusion. That is to say, traditional e-learning system is a comprehensive software package or system that supports courses that depend on the WWW for some combination of delivery, testing, simulation, discussion or other significant aspect. E-learning system is not only in vogue as a teaching device for students but also widely used within corporate organizations for training professionals.

Traditional e-learning systems could be classified into two groups. One group is learning system group using WWW and the other group is learning system using PSTN. The former case, most of e-learning systems provide lessons which are disseminated in the form of text, video, audio and animations. These kinds of information are delivered to the learners through WWW. In this group (using WWW), e-learning systems could be classified into four groups by system architecture - information databases, online supports, asynchronous training and linked training. Fig 1 shows general configuration of traditional e-learning systems using WWW.

Strong point of these kinds of e-learning systems is high learning efficiency. Due to using WWW and computers, e-learning systems in these groups could provide multimedia contents which help learners to gain a better understanding. Weak point of these kinds of e-learning systems is restricted condition by the time and by the situations. These weaknesses result from using specific equipments like computers, monitors and so on.

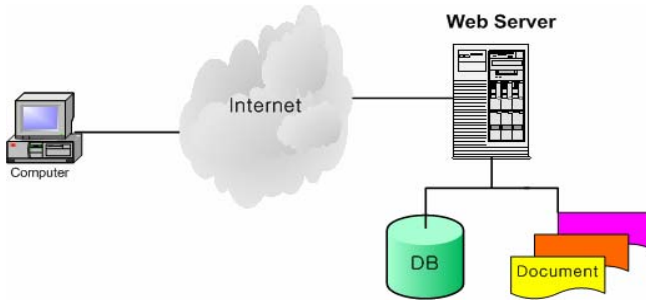


Fig. 1. General configuration of traditional e-learning system using WWW

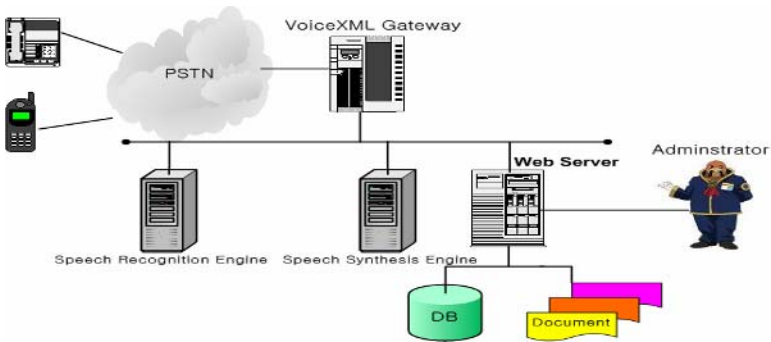


Fig. 2. General configuration of traditional e-learning system using PSTN

The latter case, e-learning systems adopt CTI (Computer Telephony Integration) technology or VXML (Voice Extensible Markup Language) service. These kinds of e-learning systems use voice through PSTN. Fig 2 shows general configuration of traditional e-learning system using PSTN. In this figure, the system adopts VXML service.

Strong point of these kinds of e-learning system is less restricted by the time and by the situations. Learners can use e-learning systems at any time, at any place using their spare time. Learners don't have to possess a specific equipment to join e-learning system except their mobile phone or wired phone. Weak point of these kinds of e-learning system is poor learning efficiency compared with the e-learning systems using WWW. Because these kinds of e-learning systems use PSTN and mobile phone, e-learning systems could not provide multimedia contents except using voice only to the learners. This restriction causes somewhat poor learning efficiency. For these reasons, we propose a novel architecture of e-learning system in the following chapter.

3 Implementation of e-Learning System with Complex Concepts

As shown in chapter 2, both kinds of e-learning system groups have strength and weakness. In this chapter, we propose novel architecture of e-learning system with

complex concepts. Newly proposed system in this paper adopts advantages of both groups. We linked WWW based e-learning system with the e-learning system using PSTN. As a result, learners can choose their learning method according to circumstances. In some case learners can choose their mobile phone as a learning tool, and in most cases learners can choose their computer as a learning tool. In both cases, learners could be served with the same contents and the same teaching schedules.

Our newly proposed system uses the same user DB and contents DB at the user interface module. Thus, choosing a learning tool for the e-learning system has no effect on individual learning schedules. That is to say, our system consists of two different user interfaces, but each user interface uses the same user DB and the same contents DB. Consequently, we can manage the learner's curriculum easily. Fig 3 shows basic configuration of newly proposed e-learning system.

Learners can use newly proposed e-learning system after registration process. During the registration process, new user DB and curriculum DB for the new learner are created on the web server.

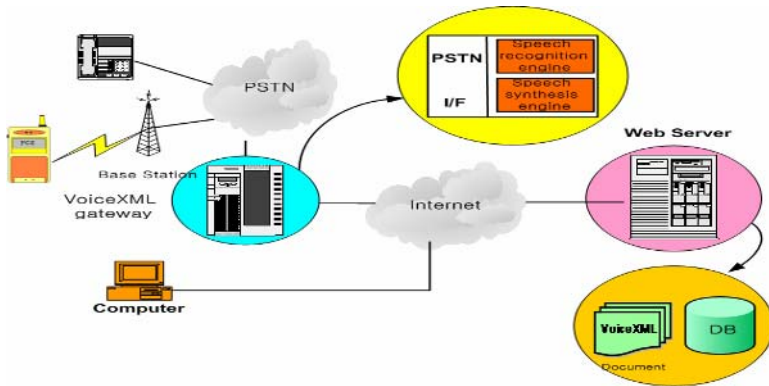


Fig. 3. Basic configuration of newly proposed e-learning system

3.1 System Configuration

On the WWW server, we use Windows 2000 professional software for operating system, and IIS (Internet Information Server) 5.0 software was installed additionally. To build login process for each learner, we also used ASP (Active Server Page). And Microsoft Access was used for managing user information DB on the web server. To construct computer-telephony network interface, we used Intel Dialogic 41JCT/LS board. And we also used HUVoice 1.0 of Korea Telecom for VXML service, which consists of VXML interpreter, speech recognizer and synthesizer

3.2 Service Flows

Figure 4 shows whole service flows of proposed e-learning system. The proposed system could be classified into four large modules, that is to say, membership

registration module, membership authentication module, curriculum management module, and the counselor connection module.

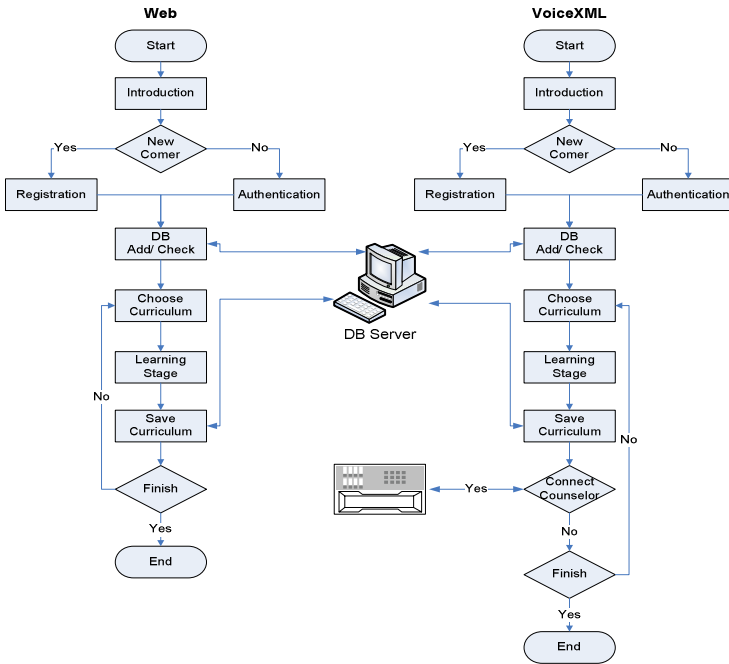


Fig. 4. Service flows for the newly proposed e-learning system

3.3 Menus for the Learning Stage

Figure 5 shows menus for the learning stage. The same menus are provided to the different kind of user interfaces. Summary explains learning contents of each sections, vocabulary of special study explains unfamiliar vocabularies and vocabularies which need more detailed explanation. Also, our system provides O/X test and descriptive questions to valuate the learner’s learning results.

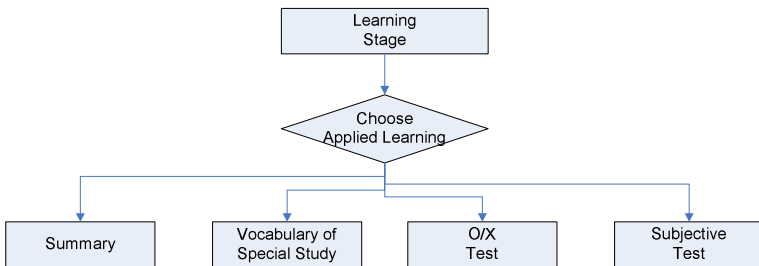


Fig. 5. Menus for the learning system

3.4 Member Registration and Authentication

Figure 6 shows the flows for the new comer registration and authentication process. User ID and password are repeatedly inputted using text or voice. After completion of new comer registration process, each user id, password and name are registered in the user DB. Also, user ID is automatically registered in the grammar file of VoiceXML for user certification.

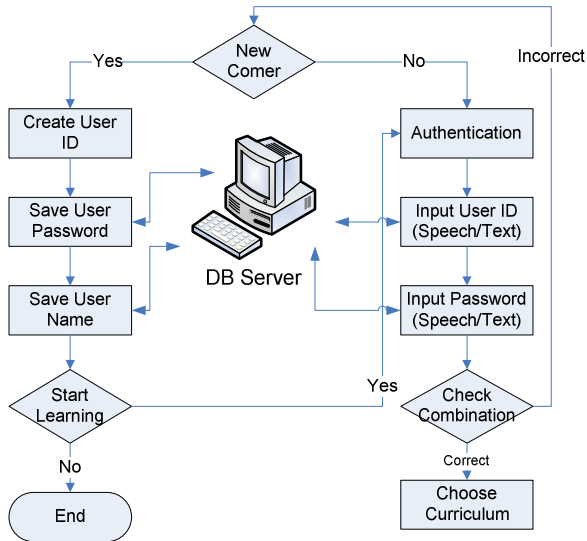


Fig. 6. Flows for the new comer registration and authentication process

3.5 Curriculum Management Module

Learning stage is composed of summary, vocabulary of special study, O/X test and subjective test. Each stage, several tests are conducted to check learner's results after a course of study. In the proposed learning system, there are two kinds of DB for a person. That is to say, the answer DB and score DB. Learner's accomplishments are evaluated through O/X test, subjective tests. Figure 7 shows the flows for curriculum management module for each learner, scores and accomplishment history are putted on the record.

3.6 Q & A Module

We implemented Q&A bulletin board for the Web interface and counselor connection function for the telephony network interface. Users are able to connect to counselor through telephony network to complement restriction of on-line learning.

Figure 8 shows flows for the connecting counselor and managing individual progress. Individual learning progress is recorded for user convenience before closing learning sessions. For these reasons, if the user connects to the proposed learning system again, then the user could progress further learning schedule.

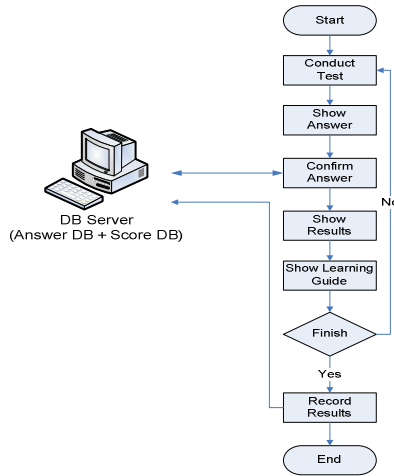


Fig. 7. Flows for managing learner's accomplishment degree

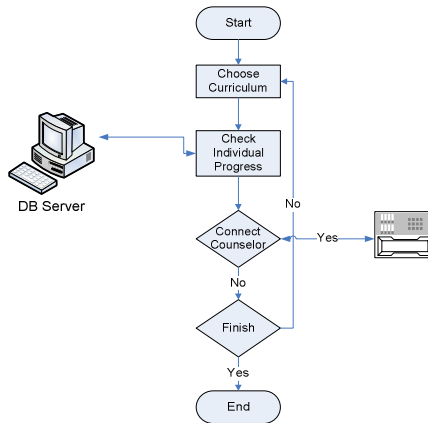


Fig. 8. Flows for connecting counselor

4 Performance Evaluation of Learning System

To verify the performance of proposed learning system, we have conducted performance evaluation. In this chapter, we compared the proposed learning system with other kinds of learning systems. Namely, learning system which is on the basis of Web and learning system which is on the basis of VoiceXML.

Ten subjects were selected for this performance evaluation and finished their learning courses with several kinds of learning systems. Time required means the time for finishing 10 chapters and results are recorded on the learner's score DB.

Table 1 shows learning efficiency and accomplishment degree for 10 subjects. We evaluated learning efficiency using time to finish 10 chapters and accomplishment degree using test scores.

According to Table 1, the proposed learning system, Web and VoiceXML linked learning system, is superior to any other kinds of learning systems from all angles.

Table 1. Performance evaluation for the proposed learning system

Learner	Web		VoiceXML		Web + VoiceXML	
	Time Required	Result (Points)	Time Required	Result (Points)	Time Required	Result (Points)
1	7days	80	5 days	70	4 days	90
2	6.5 days	90	5 days	70	3 days	100
3	10 days	80	8.5 days	80	7.5 days	90
4	9 days	90	7.5 days	80	7 days	90
5	7.5 days	70	6.5 days	50	5 days	80
6	5.5 days	80	5 days	80	4 days	90
7	6 days	60	4.5 days	50	3.5 days	70
8	7 days	70	5.5 days	70	4 days	80
9	8.5 days	80	7 days	80	6 days	90
10	7 days	90	6 days	70	4.5 days	100
Average	7.4 days	79	6 days	70	4.8 days	88

Table 2. MOS valuation table

Quality	Very Poor	Poor	Fair	Good	Excellent
Rating	1	2	3	4	5

Table 3. MOS valuation for satisfaction degree

Learner	Web	VoiceXML	Web + VoiceXML
1	4.0	3.6	4.2
2	4.2	3.7	4.3
3	3.9	3.6	4.1
4	4.3	3.8	4.2
5	4.2	3.9	4.1
6	3.7	3.7	4.2
7	3.7	3.9	4.3
8	4.0	3.8	4.3
9	3.9	4	4.2
10	3.8	3.9	4.2
Average	3.97	3.79	4.21

Table 2 shows MOS valuation table. Using this MOS valuation table, we have conducted subjective satisfaction degree.

Table 3 shows the results of MOS valuation for satisfaction degree. As shown table 3, learning system based on Web linked VoiceXML system is superior to any other systems. These results are caused by using advantages of Web and VoiceXML at the same time.

5 Conclusions

Speech is the most familiar communication methods for human. Recently, there is a tendency to integrate computer technology and telephony network technology. In this paper, we have noticed this kind of tendency and proposed an efficient learning system using Web and PSTN.

Our learning system uses newly proposed architecture, Web and VoiceXML linked architecture, and provide effective learning environment. For these reasons, proposed learning system has many advantages of Web and VoiceXML at a time. Because of using Web based learning contents, a lot of learners could study using proposed system at the same time, effective multimedia data could be used, and so on. And the more, proposed learning system uses learning contents based on VoiceXML, learners who do not have computers, blinded people could study also. And the learners could study at anytime, at anyplace using their spare time.

Acknowledgement

This research was supported by the Ministry of Information and Communication, Korea under the Information Technology Research Center support program supervised by the Institute of Information Technology Assessment, IITA-2005-(C1090-0501-0019) and Catholic University of Daegu.

References

1. W3C, "Voice Extensible Markup Language VoiceXML"(Version1.0), <http://www.w3.org/TR/voicexml>, 2000.
2. Danielsen, P.J, "The promise of a voice-enabled Web," *Computer*,33,8 ,Pages:104 106, 2000.
3. Kwang-Seok Hong, "VXML technology for voice interface", *Korean Society For Internet Information*, Vol.2, No.1, 2001.
4. In-Sook Lee, gi-Hyeng Hong, " VoiceXML Learning Evaluation System based on Wire.Wireless Telephone Speech", *Korea Multimedia Society Vol.005, No.004*, pages.59-70, 2001.
5. Quiane Ruiz, J.A.; Manjarrez Sanchez, J.R, "Design of a VoiceXML gateway," *Computer Science*, 2003. ENC 2003. Proceedings of the Fourth Mexican International Conference on, 49 53, 8-12 Sept. 2003.
6. Sup-Hyeng Park, "VoiceXML: For Construction of Voice Web Application", *Hanbit Media*, 2001.

7. Holcomb, L.B.; Brown, S.W.; King, F.B. "Examining self-efficacy and self-regulation levels across gender in business distance education courses," *Computers in Education*, 2002. Proceedings. International Conference on,, Pages.1463 - 1464, 2002.
8. Simonson, M," Distance education: trends and redefinition," *Frontiers in Education Conference*, 1996. FIE '96. 26th Annual Conference., Proceedings of,ume: 2., Pages: 549 552, 1996.
9. Harris, D.A, "Online distance education in the United States," *Communications Magazine*, IEEE,37,3 , 91, 1999 .
10. Garvin, J.; Alsheimer, E.; Bradshaw, Z.; Anselmo, P, "Simplified Authoring for Instructors using Distance Education (SAIDE),"*Information Technology: Coding and Computing [Computers and Communications]*, 2003. Proceedings. ITCC 2003. International Conference on, 47, 2003.

A Web-Based Tool for Entity-Relationship Modeling

Ferran Prados, Imma Boada, Josep Soler, and Jordi Poch

Departament Informàtica i Matemàtica Aplicada,
Universitat de Girona, Spain

{ferran.prados, imma.boada, josep.soler, jordi.poch}@ima.udg.es

Abstract. A web-based tool developed to automatically correct conceptual database schema is presented. This tool has been integrated into a more general e-learning platform and is used to reinforce teaching and learning on introductory database courses. This platform assigns to each student a set of database problems selected from a common repository. The student has to design a entity-relationship schema and enter it into the system through a user friendly interface specifically designed for it. The correction tool corrects the design and shows detected errors giving advice of how to solve them. The student has the chance to send a new solution. These steps can be repeated as many times as required until a correct solution is obtained.

1 Introduction

A database is a collection of related data representing some aspect of the real world. The importance of databases in many different fields (scientific, industrial, commercial, . . .) has lead database design courses to be essential in any Computer Science degree curriculum. Database design is the process of generating a model of a database, using a data model to specify the data types, structures and constrains for the data to be stored in the database. The definition of a database involves four different steps. First, the analysis design to provide understanding on the application domain. Second, the conceptual design to give a high level description of the database and the requirements that data must satisfy. Third, the logical design to obtain a high level schema that could be implementable on a database management system. Finally, the physical design to represent the internal data storage details.

Crucial to define a correct database design is the creation of the conceptual model. Among the different methods that have been proposed to design it, the Entity-Relationship (ER) model, proposed by Chen [2], has become the most popular. This model considers the world as a set of entities and the relationships between them. Currently, the ER modeling has become an standard in the majority of database design courses. To introduce it to the students, traditional teaching presents ER modeling concepts in a classroom environment and then, exercises are proposed to students to acquire expertise. Although concepts are not difficult to learn, practice is not as easy as it could be. There are two main

drawbacks that make difficult this practical process. On the one hand, there is not any strategy for deriving the ER model from a database problem. On the other hand, for a given problem it can be more than one correct ER model. Consequently, to success on the learning process, student require continuous supervision which, in current teaching university environments, is almost impossible. Undoubtedly, a good strategy to carry out this support are web-based tools.

Despite the great variety of web-based problem-solving environments that have been proposed in the last years, few of them support ER modeling. Motivated by this limitation and the difficulties we detected when teaching database design, we decided to develop a new web-based tool.

The web-based tool we propose is being used in different introductory database courses of our University. It is composed of two main modules: a student interface and a correction module. The student interface is a friendly interface that displays the problem to be solved and provides a set of tools to design the ER-schema in a working area. Once the student solution has been entered, it is send to the correction module which automatically corrects it and gives feedback to the student. This module compares the student solution with the correct solutions of the problem stored in the database of the system. The result of the correction is automatically communicated to the student. The tool for ER modeling has been conceived as a support for the teacher not as a substitute. For this reason, it has been integrated in a more general e-learning platform that supports continuous assessment. This platform stores student solutions in its database and provides teachers the information and the functions required to perform the continuous assessment [6, 8].

The paper has been structured as follows. In Section 2, different database design environments are briefly reviewed. In Section 3 the proposed ER designing environment is described. In Section 4 the integration of the proposed ER tool in a more general e-learning framework is presented. Experimental results are collected in Section 5. Finally, in Section 6 conclusions and future work are given.

2 Related Work

Over the last decade several attempts to develop a ER problem-solving web environment have been made. Some of them are briefly described in this section.

Hall et al. [5] propose the ERM-VLE, a text based virtual learning environment for ER modeling. Student model a database for a given problem by navigating the virtual world and manipulating objects. The virtual world consists of different types of rooms such as entity creation rooms and relationship creation rooms. The solution of each problem is embedded in the virtual world. If the student attempts to establish an association that does not comply with the system's solution, the system intervenes and informs the student that the association is not allowed. Main drawback of the method is that once student is used to design with this environment he has difficulties on modeling outside it. Constantino et al. [3] propose COLER, a coached collaborative learning environment for entity-relationship modeling. Students begin by constructing

individual entity-relationship diagrams expressing their solution to a database problem, and then work in small groups to agree upon a group solution. The system assumes that the combined solution agreed by all the members of the group is correct. COLER is not capable of evaluating the solution, its purpose is to help students to develop collaborative and critical thinking skills. Suraweewa et al. [9] propose KERMIT, a knowledge-based entity-relationship modeling intelligent tutor. KERMIT uses constraint-based modeling to model the domain knowledge and generate student models. Students construct ER schemas that satisfy a given set of requirements. The system contains an ideal solution for each of its problems and it assists students during problem solving. Student' solutions are evaluated by using the system domain knowledge represented as a set of constraints.

For our purposes, our interest is not only on ER-modeling but also on the continuous assessment of database design students. For this reason we decided to develop a tool that can be integrated in the e-learning platform we are developing. This platform [6] aims to improve both teaching and learning at the technical/engineering degrees at Girona Polytechnic University.

3 The ER-Modeling Tool

To describe the ER-modeling tool we are going to present the main modules that compose it: the student interface module and the ER-correction module. The student interface contains the problem that has to be solved, the different functions required to design the ER-schema and a channel to communicate students with the system in order to obtain feedback of the proposed solution. The ER-correction module automatically corrects a solution proposed by the student for an specific problem. In this section, a detailed description of both modules is given.

3.1 Student Interface

Student interact with the ER-modeling tool via its user interface. This is the first window that appears when the student enters into the system and selects a database problem. In Figure 1 a general overview of this interface is given. In this window we have considered the ER-schema designed for the database of a company, this problem can be found in [4]. Observe that this window has five main components: the problem descriptor area (see Figure 1(a)), the ER-designing tools, divided in two different areas (see Figure 1(b) and (c)), the zoom utility (see Figure 1(d)), the working area (see Figure 1(e)) and the feedback area (see Figure 1(f)). Let us consider each one of these components in detail.

Problem Descriptor Area. The problem descriptor area is the space where the system displays the database problem that has been assigned to the student (see Figure 1(a)). The problem descriptor is given as a set of requirements for a real life application. A constraint of our approach is that attributes of the database have to appear in the problem descriptor with an specific name and

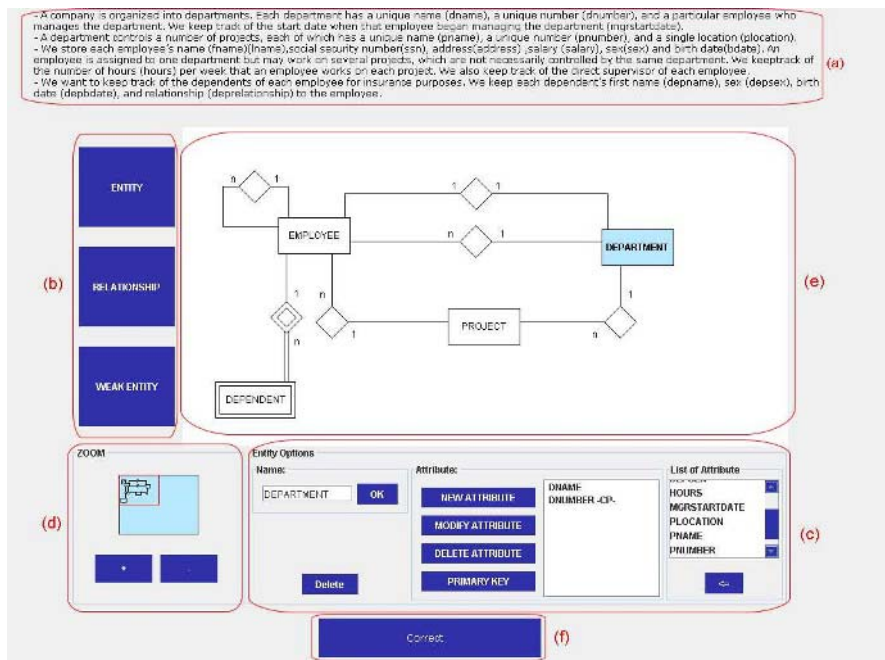


Fig. 1. Student interface. (a) Problem descriptor area. (b) ER-Objects that can be used to design the ER-schema. (c) Objects features related with the selected ER-object. (d) Zoom utility. (e) Working area. (f) Feedback area.

in brackets. This restriction has been imposed because it is the key of our ER-schema correction strategy, as it will be seen in Section 4. At first sight it could seem that we are giving a lot of information to the student and hence the effort it has to be made to design the solution is minimal. We can ensure that this is not true. It has to be taken into account that currently the tool is used in introductory database courses. Even though, the identification of attributes is an important skill to be acquired, for students of these courses we consider more important the capability to properly group attributes in the correct entities or attach to the corresponding relationships.

ER-designing Tools. To create the diagram the student uses the two different areas that constitute the ER-designing tools region (see Figure 1(b) and (c)). The first area (see Figure 1(b)) contains the ER-objects that can be used to draw the diagram. These objects are represented as buttons: the regular entity, the weak entity and the relationship. Each time one of these buttons is pressed the entity or the relationship is drawn on the working area as a rectangle or as a diamond, respectively. The second area is specifically designed for the drawn object and displays the attributes and the main features that can be attached to it (see Figure 1(c)). Whenever a new object is created, either an entity or a relationship, the user has to name it. This name is introduced in a text box.

The user also enters the attributes that have to be attached to the object. These attributes are selected from a list box which contains all the possible attributes that have appeared in the problem descriptor. In case of entities there is an additional dialog where the attribute key is entered. If the entity is weak it asks for the partial key and the regular entity of which depends. In case of relationships the user selects from the working area the related entities. Then, the user enters the relationship cardinality which will be also represented in the diagram. Only binary relations are allowed.

Working Area. The working area is the window space where student design the ER-schema (see Figure 1(e)). Since the dimension of the ER-diagram can be larger than this area, we have integrated a zoom button (see Figure 1(d)) that determines the part of the diagram it has to be displayed on the working area. All actions performed with the ER-modeling tools have an effect on the working area. For example, pressing the entity button a rectangle is drawn and pressing the relationship button a diamond with two lines connecting the two entities previously selected.

Feedback Area. The goal of the feedback area is to provide a student-system communication channel. This communication is established through the *Correct button* (see Figure 1(f)). Each time the student press this button the system automatically corrects the current ER-design and displays messages with the result of the correction. In case of a non-correct solution these messages give information and some advice of how to solve the error.

3.2 Correction Module

The correction module carries out the correction of the student proposed ER-schema. To describe the developed strategy the following parameters have to be taken into account. First, how the system stores the correct solution of a problem. Second, how the student solution is stored in the system. Third, how the student solution is corrected and the results of the correction are communicated to the student.

System Solution. It has to be considered that it can be more than one correct solution for the same database problem. Therefore the system has been designed to maintain more than one correct solution for a problem. Each solution is registered in the system database as a list where each entry represents an entity object or a relationship. For each regular entity we store its name, the key attribute and the set of attributes it has attached. For each weak entity we record its name, the partial key, its attributes and the regular entity of which depends. For each relationship we record its name, the two entities that relate and the attributes it has attached. An example of the internal representation of a system solution is given below. This example corresponds to the ER-schema of the problem illustrated in Figure 1.

```
*** <ENTITY,KEY ATTRIBUTES,(ATTRIBUTES)>
<DEPARTMENT,dnumber,(dname)>
<EMPLOYEE,ssn,(fname,lname,bdate,address,salary,sex)>
<PROJECT,pnumber,(pname,plocation)>
*** <WEAK_ENTITY,PARTIAL KEY,(ATTRIBUTES),REGULAR_ENTITY>
<DEPENDENT,depname,(depsex,depbdate,deprelationship), EMPLOYEE>
*** <RELATIONSHIP,ENTITIES,CARDINALITY,(ATTRIBUTES)>
<WORKS_ON,EMPLOYEE & PROJECT,N:M,(hours)>
<WORKS_FOR,EMPLOYEE & DEPARTMENT,N:1>
<MANAGES,EMPLOYEE & DEPARTMENT,1:1,(mgrstartdate)>
<CONTROLS,DEPARTMENT & PROJECT,1:N>
<SUPERVISION,EMPLOYEE & EMPLOYEE,1:N>
```

Student Solution. The student solutions are stored in the same way as the system solution. Thus, for each solution entered by the student the system maintains a list. When a student adds a new object in the working area the system adds information about it into the list. This list contains information of the entities and the relationships. For each entity the name assigned to the entity, the primary key and the set of attributes attached to it. In case of weak entities the name, the partial key, the regular entity of which depends and the attributes. For each relationship it maintains information of the two related entities, the cardinality and also the attributes.

Correction and Feedback. The correction strategy is based on a comparison. In a schematic way, the student's solution, entered via student interface, is compared with the possible correct solutions of the problem stored in the database of the system. If any one of the correct solutions coincide with the one of the student, the solution is considered incorrect. In this case the feedback module, taking into account the detected error, sends a message to the student giving information about this error. Student can correct the error and send a new solution. This process can be repeated until the student solution is correct.

The key of the correction process is on the name of the attributes. Note that the only restriction it has been imposed to design the solution is that only attributes marked in brackets in the problem descriptor can be used. There is not any restriction on the names of the entities nor the relationships. Entities are corrected by considering the identifier attribute and the set of attributes attached to it. Relationships are evaluated in terms of the entities they relate, the attributes they have associated and its cardinality.

The correction strategy is composed of different levels of comparison. The first level of comparison checks if there is a solution in the database of the system with the same number of entries of the students one. In case that more than one coincident solution exists, all of them can be evaluated in the next step of the process. When the student solution and one system solution are equal sized, the second level of comparison starts, otherwise an error message appears on the screen. In the second level, solution entries are compared. This level looks for entries with the same attributes. Since the names of the entities and relationships are not relevant, we consider two entities equal when they have the

same attribute key and the same set of attributes. Two weak entities are equal if they have the same partial key, the same attributes and they depend of the same regular entity. Finally, two relationships are equal if they relate the same entities, they have the same attributes and the same cardinality. The second level of comparison succeeds when all the entries are equal (i.e. there is a complete matching).

The differences between the correct solution and the student solution determines the message it has to be send. We have classified the different types of errors that can be found and we have assigned a message to each one of them. The feedback module maintains this set of possible messages and according to the type of error detected by the correction module it automatically selects the message to be sent.

4 Integration in a More General Environment

With the ER-tool presented in the previous section we reach our first objective. The next objective is the integration of this tool in the e-learning platform we are developing [7]. This platform improves both teaching and learning at the technical/engineering degrees of our university. The integration process has been straightforward since our e-learning framework is modular enough to integrate new typologies of problems with minimal modifications. To give an idea of how this process has been carried out we present an overview of the platform and its main components.

4.1 Our e-Learning Platform

The main modules that compose our e-learning platform are represented in Figure 2. These modules are:

- The repository of problems which maintains the problems entered by teachers in the system. It allows teachers to share a set of material.
- The work-book generation module which generates a personalized work book for each student. A work book is composed of exercises grouped into topics. The exercises are selected from the repository following the teacher indications. Problems can be added to the work-book at any time.
- The correction module which provides an environment to correct on-line a solution designed for a given problem. This module has an specific component for each typology of problems supported by the platform [1, 7, 8].
- The system database which stores all the student's work. Periodically the teacher selects a set of problems related to each topic from the repository. From these exercises the system automatically generates an exercise book that is different for each student. Students have to solve the problems, using the correction environment, and send the solutions to the system before a fixed deadline. All these solutions are stored in the system database.
- The continuous assessment module which collects from the data base quantitative data about student work such as number of errors, types of errors,

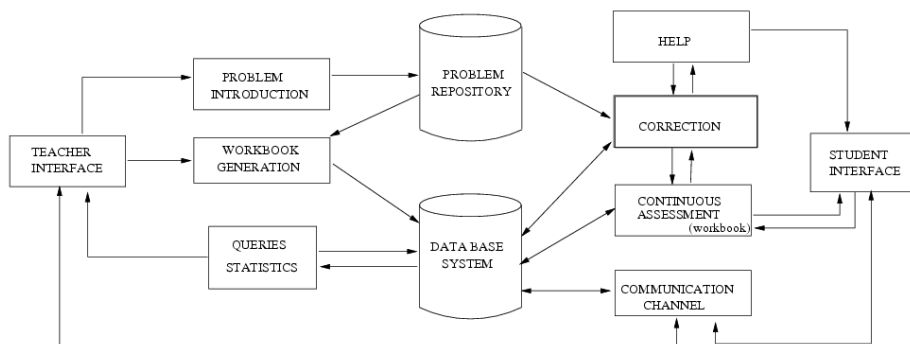


Fig. 2. Main modules of our e-learning platform

time taken to complete the problem, etc. The students' progress through their personal exercise book provides the basis for the continuous assessment of their skills and gives valuable information about their difficulties. On the other hand, this information can be used to guide the student through those topics which present a greater difficulty for them.

- The help module which supports help exercises. The help module according to the mistakes made by student activates the different levels of help.
- The communication channel which establishes a virtual communication channel between the teacher of a group and all the students that compose this group. This channel can be used by the teacher as a virtual tutoring system.

The system supports different type of users: students, teachers and administrator. Interface windows are specifically designed for each role.

To integrate the ER-tool in this environment modifications on the correction module, student and teacher interfaces and continuous assessment modules have been performed.

5 Experimental Results

Currently, the proposed ER tool is being used in two groups of 100 and 150 students, respectively. It is used as reinforcement in teaching and learning of introductory database courses. From the teacher's first impressions, we can remark that the environment is easy to use. It does not require any installation, only an internet connection. More importantly, it provides gains with respect to the classical teaching methodology in the sense that it offers a system for the continuous assessment of the student's progress, makes personalized attention to the student easier and assesses the degree of participation of the students. The students' impressions have also been positive especially the fact that to access the system they only need an internet connection. During the different sessions students were asked to comment on the problems they faced while using the system. The responses were very positive. The students feel motivated to solve the proposed problems. The possibility to correct a problem in real time encourages them to work until a correct solution is found.

6 Conclusions and Future Work

In this paper we have presented a web-based tool developed to assist students learning ER-modeling. The tool has been integrated in a more general e-learning platform that supports continuous assessment. The proposed environment is used in different courses of our university with very promising results.

Our future work will be centered on the definition of new modules to support the correction of SQL sentences and database normalization. Our idea is to integrate these modules with the ER-tool proposed in this paper and the relational correction module we proposed in [7], in order to support the main topics of a database course.

References

1. I.Boada, F.Prados, J.Soler and J.Poch. A teaching/learning support tool for introductory programming courses. Proceedings IEEE International Conference on Information Technology based higher Education and Training 2004, ITHET pp.604-609.
2. P.Chen. The Entity-Relationship model. Towards a Unified View of Data. ACM Transactions on Database Systems 1(1),pp.9-36.
3. M. Constantino-Gonzalez, D.D. Suthers. A coached collaborative learning environment for entity-relationship modeling. In G.Gauthier, C.Frasson and K.Vanlehn (Eds.) Intelligent Tutoring Systems (pp.324-333) Berlin. Springer 2000.
4. R.Elmasri and B. Navathe. Fundamentals of DataBase Systems. 3rd edition. Addison-Wesley, 2000.
5. L.Hall and A. Gordon. A Virtual learning Enviroment for Entity-Relationship Modeling. SIGCSE Bulletin, 30(1), 345-353, 1998.
6. F.Prados, I.Boada. J.Soler and J.Poch. Automatic generation and correction of technical exercices. International Conference on Engineering and Computer Education, ICECE, Madrid, 2005.
7. F.Prados, I.Boada. J.Soler and J.Poch. An Automatic correction tool for relational database schemas. Proceedings of IEEE International Conference on Information Technology based higher Education and Training, ITHET 2005, S3C, 9-14 .
8. J.Soler, J.Poch, E.Barrabés, D.Juher and J.Ripoll. A tool for the continuous assessment and improvement of the student's skills in a mathematics course. Technologies de l'information et de la Communication dans les Enseignements d'Ingieurs et dans l'Industrie. Proceedings of the Symposium. TICE 2002, pp-105-110.
9. P.Suraweera and A. Mitrovic. An Intelligent Tutoring System for Entity-Relationship Modeling. Int. J. Artificial Intelligence in Education, vol. 14, no. 3-4, 2004, 375-417.

Reusable Learning Objects (RLOs) for Computer Science Students

Birim Balci¹ and Mustafa Murat Inceoglu²

¹ Maltepe Univ., Dept. of Computer Eng., Marmara Egitim Köyü 34857 Istanbul, Turkey
birimb@maltepe.edu.tr

² Ege Univ. Dept. of Computer Eng., Bornova 35100 Izmir, Turkey
mustafa.inceoglu@ege.edu.tr

Abstract. The purpose of this study is to introduce an instructional technology known as the “learning object”. After a review of the literature, the designing steps of a learning object (LO) are tried to explain. As a learning object standard a few details are given about SCORM-Content Aggregation Model and common metadata elements. At the end, a case study about designing of a learning object with the subject of “Congestion Control in Computer Networks” is tried to give. The content is prepared in English and it contains 13 pictures within 22 .htm and 3 .exe files. The basic principles of the network congestion and the designed congestion control algorithms are given in the htm pages. Simulators are used to show the working way of the related algorithms step by step. The LO design is made with an open source program RELOAD Editor, according to the ADL SCORM package. The designed LO has been tested on computer engineering students and positive feedbacks are received.

1 Introduction

Learning Objects (LOs) are defined as “any entity, digital or non-digital, which can be used, re-used or referenced during technology supported learning” by IEEE-LTSC-LOM [1]. A LO can be a lesson or a part of a lesson like a simple jpeg, audio or text file, multimedia content, video, tutorials, simulations, case studies, digital pictures, animations, persons, organizations or events referenced during technology supported learning or web pages that includes text, image and media. Each piece of LO must have explanations for the representation which inform LMS about how the student moves ahead between LOs [2]. Each LO must have a metadata, the definitions about the LO that enables content developers to search and to reach related LO [3]. LOs’ advantages can be listed as flexibility, customization, interoperability, accessibility, adaptability, easy updating searching and content management by metadata, reusability, reshaping the education according the students’ knowledge and ability. By using LOs, educators can use modular and reusable pieces instead of developing a new lesson. Moreover, students can take information as they are needed and they can reach the information in a fast way [4].

2 Types of LOs

There are five types of RLOs [3]: fundamental, combined-closed, combined-open, generative-presentation and generative-instructional. An individual digital resource not combined with any other is called a *fundamental* RLO. If digital resources combined at design time by the LO's creator, it is called *Combined-closed* RLO (eg. a video clip). A larger number of digital resources combined by a computer in real-time when a request for the object is made, is called a *combined-open* RLO. A web page with components like images, video clips, text, and other media exist in reusable format and are combined into a learning object at request-time. *Generative-presentation* RLOs that can be used over and over again in similar contexts, can be defined as a logic and structure for combining or generating and combining lower-level LOs (fundamental and combined-closed types). The *Generative-instructional* type LO is a logic and structure for combining LOs except combined-open type and evaluating student interactions with those combinations, created to support the instantiation of abstract instructional strategies (such as "remember and perform a series of steps"). In this study, the created LO is for educational design. It is not only a combined-closed but also a generative-presentation type LO.

3 Components of a LO

LOs generally have no absolute time limit. But it is recommended to be a few minutes to 30 minutes [4]. As shown in Fig1, a combination of 7 ± 2 RLO (Reusable Information Object), an *overview*, a *summary* and an *assessment* instrument is called a RLO [5]. Information objects (IOs) like jpeg, movie or an html page, only have the information that will be transferred. Their length and time are limited. According to the Cisco model [6], by adding an overview, a summary and an assessment instrument to the IOs, they have an educational meaning and called RLO. Independent RLOs are combined to generate RLOs. LOs have data and a metadata. If an office picture is a LO then the picture itself is data. The information like description of the picture, time it is taken, the office it belongs is the metadata of it.

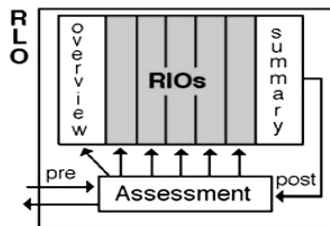


Fig. 1. RLO architecture

4 SCORM as a Learning Object Standard

The goal of the SCORM (Sharable Content Object Reference Model) [7] is to reproduce the computer and web-based learning reusable content as “educational objects”. The most important organizations work on specifications related to e-learning are AICC [8], ARIADNE [9], IEEE LTSC [10] and IMS [11]. SCORM defines a *Content Aggregation Model-CAM* [12], a *Run-Time Environment-RTE* and a *Sequencing and Navigation-SN* for LOs. RTE which is communicated the LMS with the content is the environment that shows the presentation of the content and how to store the student’s information [7]. SN covers the essential LMS responsibilities for sequencing content objects during run-time and allowing SCOs (Sharable Content Objects) to indicate navigation requests. SN book defines how the IMS Simple Sequencing (SS) Specification is applied and is extended in a SCORM environment [13]. In this paper we will mostly study about SCORM CAM model.

CAM specifies the preparation and packing of the content. It has 3 parts. Content Model, Meta-data and Content Packaging. CAM has three components called *Assets* (the simplest data files that transfer the educational content to the web), *SCOs* (combination of assets) and *Content Aggregations*. Content Aggregation Meta-data is applied to manifest file. By SCO meta-data, the content can be reused and shared. And asset meta-data gives descriptive information about the assets independent from the usage in the content. *Content packages (CP)* define the structure that describes the using order of the resources. *Manifest file* of the CP includes the metadata about the package, content structure organization, references to the resources. To transport the CP to a LMS, lesson is zipped to a **PIF** (Package Interchange File) file. Archive format must be PKZip v2.04g [12].

5 Elements of Metadata

The information (descriptions of the courses) imported to LMS is only in the metadata [12]. LOs include 69 metadata labels categorized in 9 topics that includes different *data elements*. For a table of the mandatory and optional data elements for SCORM content aggregation, SCO and assets references [2, 14] can be seen. Data elements:

1. *General*: General information about LO. Identifier, title, description.
2. *Lifecycle*: Past and present situation of the resource and people affect the resource. Which edition, status, publisher, editor, creator etc.
3. *Meta-metadata*: Information about the metadata.
4. *Technical*: Technical requirements. Format, size, URL, browser, OS
5. *Educational*: Pedagogical and educational characteristics. Type, audience, time...
6. *Rights*: Usage rights of the resource. Required payment, copyrights
7. *Relation*: The relations between the resource and the other related resources.
8. *Annotation*: Comments on the resource’s educational use, information about creation time and creators (optional).
9. *Classification*: Describes the reason for this classification (optional for assets).

6 A Simple LO Example

In this study, the created LO is for educational design. It is a combined-closed type LO because more than one digital resource combined at design time by the creator. The content consists largely of images and text, so a *website* model [15] is used as the format. Due to the fact that it can be used over and over again in similar contexts, it can also be defined as a generative-presentation type LO. The subject of the LO is “Congestion Control in Computer Networks”. It includes 13 pictures within 22 .htm files and 3 simulators in English. Due to the fact that it is difficult to make a network design in the laboratories at schools, simulators designed by Delphi programming language are used to show the working way of the explained algorithms step by step.

6.1 Content of the LO

The topics in the LO content package is given in the order as: An introduction, Definition of congestion, Reasons of congestion, Effects of congestion, Area and Level of congestion control algorithms, Avoidance, Traffic Control, Types of congestion, Congestion control approaches, Classification of algorithm with subtopics Open and Closed loop congestion control algorithm, List of algorithms, Leaky Bucket Algorithm (LBA), Definitions from the working steps of LBA, Simulator of LBA, Choke Packet Algorithm (CPA), Working rules of CPA, Advantages of CPA, Definitions from the working steps of CPA, Simulator of CPA, Hop-by-Hop Packet Algorithm, Advantages, Definitions from the working steps, Simulator of the algorithm, Quiz and Resources.

6.2 The Program and the Standard Used to Prepare Content Package

There are many programs for content packaging like RELOAD [16], Moodle [17], Claroline [18], dotLRN [19], Learnwise v2 and Learnwise Olympus [20], Teknical's Virtual Campus, Atutor. In this study RELOAD Editor, an open source program, is used to design the LO depending on the ADL SCORM package. In the organization all items are given in a hierarchical order as seen in the Fig.2. The *left pane* includes the imported resources. The *Attribute pane* includes a section with context sensitive information on the currently selected element as a table of values and boxes for editing attributes. The *Manifest pane* on the right presents the structure of the LO Content Package with a manifest containing Metadata, Organizations and Resources.

SCORM metadata can be kept in a file external to the content package. Here, LO metadata is kept in a file in the content package but as seen in Fig.2 items' metadata have external SCORM elements and are held as an external XML file. SCORM has extra 5 optimal elements for items to interact with LMS, and LMS can use these to define a set of rules to control learners' progression through content to be defined [16]. These are: *prerequisites* which defines any other item learner must have to complete before allowed to access the current item, *maxtimeallowed* which is the time that a LMS would permit access to the item for, *timelimitaction* which is the action specified if the “max time allowed” is exceeded, *datafromlms* that allows initialization data to be sent from the LMS to the item on launch and *masterscore* is a normalized score

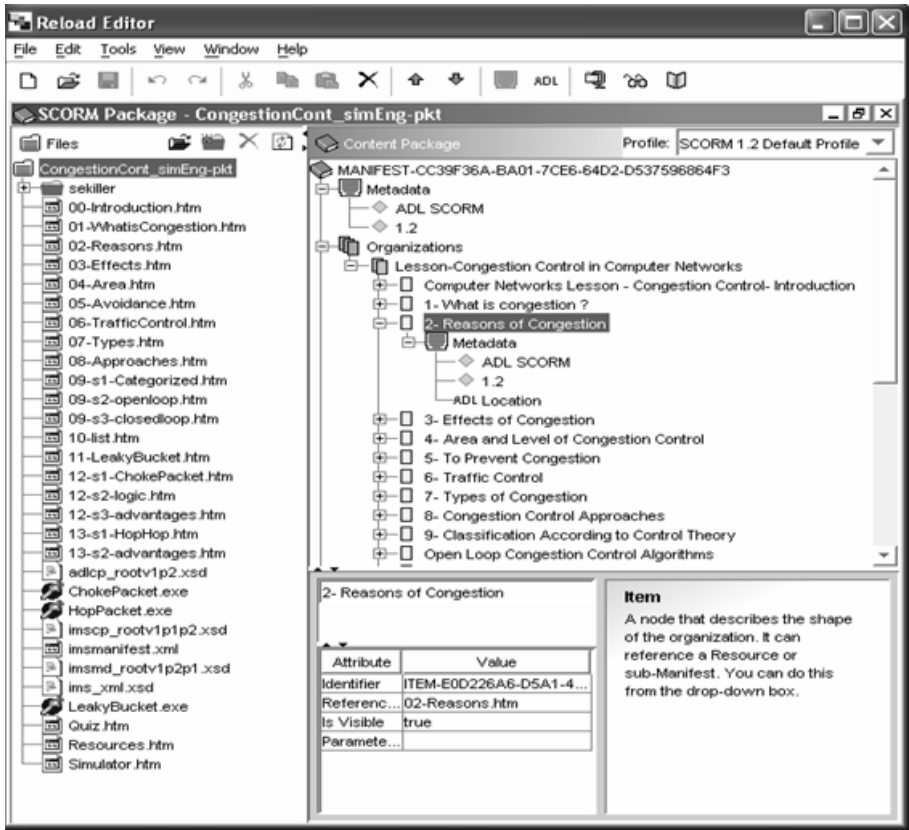


Fig. 2. RELOAD Editor and Structure of the content package

(between 0 and 100) which must be achieved to indicate satisfactory completion of an item. Normally content packages are imported into LMSs or repositories. But to utilize the content without an LMS or a repository, Reload Editor Content Package Preview (Fig.3) can be used. By this way content can be seen as it is in the browser.

6.3 Simulated Congestion Control Algorithms in the LO

Leaky bucket, Choke packet and Hop-by-hop packet algorithms [21,22] were simulated [21] in English by using Delphi programming language. Working rules are changing according to the algorithm. It is possible for the learners to run, pause, stop and download the simulators. They were designed as easy as possible having the purpose of education. The rules about taking and sending the packets of the routers were determined suitable to the real working rules of them. For each algorithm, a similar network model with 6 routers is chosen (Fig.4). To make more understandable, the traffic flow is chosen on the way of the routers A, B, C, and D from source to destination for each algorithm. Each simulator has detailed information about the decided working rules and value analyzes tables from the help menu on the interface.

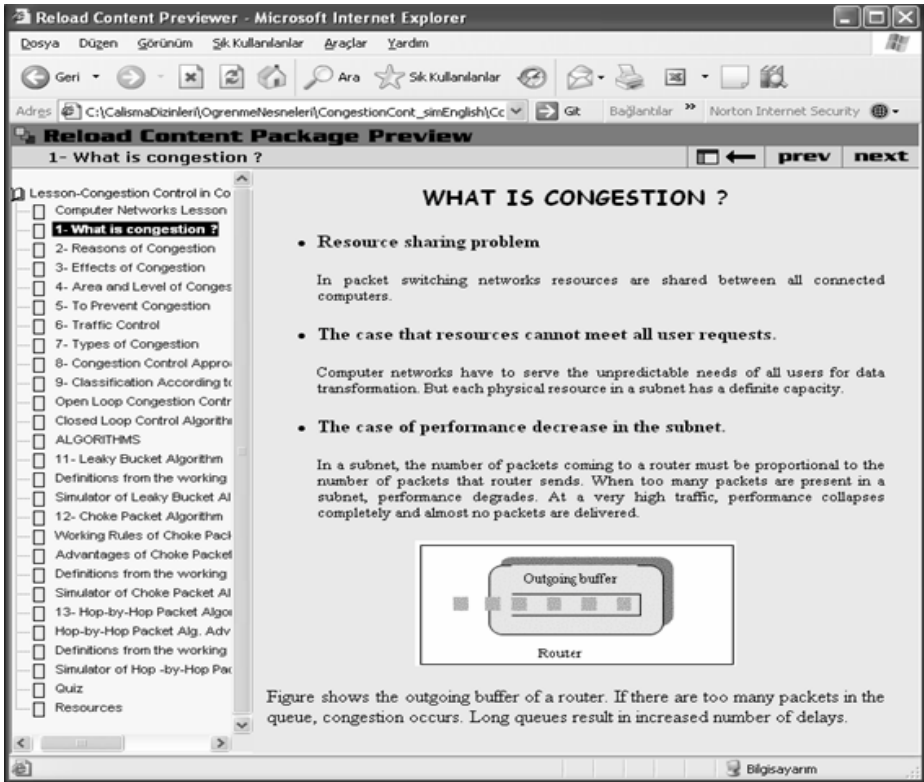


Fig. 3. Preview of the content package

Leaky Bucket Algorithm’s Simulator: In the designed LO, this simulator’s interface (Fig.4) has a table, which includes the generated packet number, the number of the packet, which is sent, time interval of each node and the number of packets that will be discarded. Interface also has 3 buttons to close, restart and to show next step of the simulation. If the "Continual" checkbox is checked the "step-by-step" mode is ignored. B and C send all the packets in their buffers to the next nodes while D sends a random number of packets from its buffer to an imaginary node.

Choke Packet Algorithm’s Simulator: The interface of the simulator (Fig.5) includes a table which shows generated packet number at node A, the speed mode of the node, the valid time of this speed mode (for how many packets) and the packet sending speed of node D. Also there are three buttons to start, Pause and Stop the simulation. Node B sends a choke packet to node A to inform about the risk of congestion at node B. Choke packets have the same colour with the node they are sent. After taking the it, node A will do a speed adjustment by decreasing its speed and the new values will be seen in the table. It is hard for a node to know how much it will to reduce the traffic. It depends on the traffic that is send, the capacity of the congested

area and the percentage of the congestion that the host causes. After taking the choke packet, the waiting time that the host will ignore the other incoming choke packets is not certain. Because of these reasons the working rules of the simulator are chosen like this: Buffer areas are for 10 packets. The threshold value is chosen as the %60 of the buffer area. Simulation works for 50 packets.

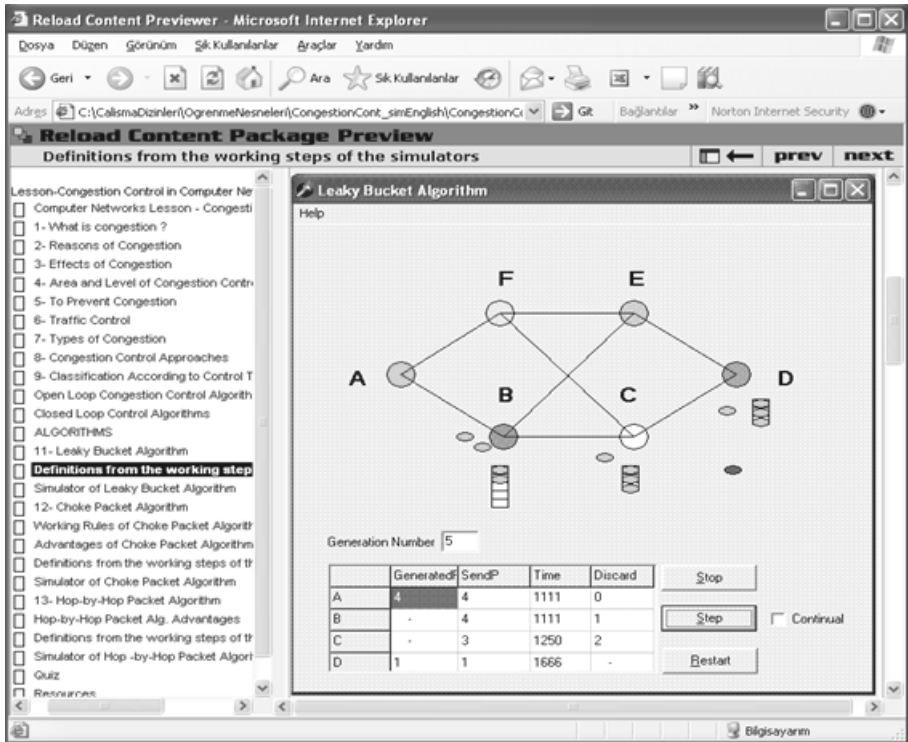


Fig. 4. Definition page of the LBA Simulator of LO

Hop-by-Hop Packet Algorithm: At high speeds or long distance, sending a choke packet to a source does not work well because the reaction is so slow. This algorithm is an alternative approach to CPA. The interface of the simulator includes a table that includes the speed mode of each node, the speed situation, and the number of active packet that this speed is valid. The defined working rules of the simulator are the same with the rules of the choke packet simulator except the changing speeds of sending packets of node B and C. The normal speeds of the nodes A, B, C are defined as 1000, 1500, 2000 ms respectively. They are increased or decreased according to the incoming choke packets. The changes in speeds are valid during 4 packets for the first choke packet, and 2 packets for the second one. Speed of D is selected randomly [21].

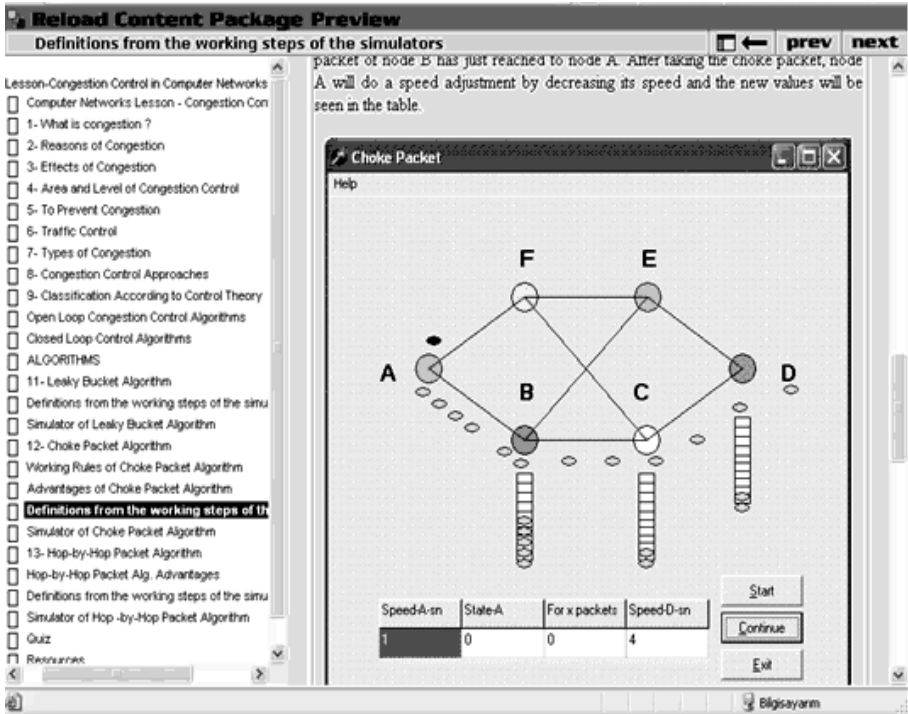


Fig. 5. Definition page of the Hop-by-Hop packet Algorithm’s Simulator of LO

6.4 Test Results of the LO

The designed LO has been tested on 20 forth-year (8th semester) computer-engineering students at *Data Communication and Computer Network* course (on May 2004) and positive feedbacks are received from students who use this system. The users of LO gave a score between one and five to each of four questions, with one being the lowest, and five being the highest. The average of score was 4.25. Table1 shows the results of the questionnaire. According to question (1), LO is so easy to use. In terms of computer networks learning, question (2) shows that LO is quite useful for it.

Table1. The results of questionnaires

Question No	Question	Average	St. Dev.
1	Do you think learning object easy to use?	4.1	0.56
2	Do you think learning object useful for congestion control algorithms learning?	4.0	0.41
3	Do you think learning object interesting?	4.5	0.31
4	Do you want to keep using this system?	4.4	0.51

The questions (3) and (4) show the users were very interested in this system, and that they would like to keep using it.

7 Conclusion

A new instructional technology, LO, and content package preparing standard SCORM are introduced in this study and a case study about LO design is made. While preparing LOs it is important to use the language and terms properly, to use sharable information, to give the content in an order, to have an introduction and a conclusion sections if it is possible, some elements like keywords and index must be used. As a LO subject, "Congestion Control in Computer Networks" is chosen. The content package and metadata design is made with an open source program RELOAD Editor, according to the ADL SCORM package. LO metadata is kept in the content package as an XML file. For each item in the content, a metadata is defined and it contains external SCORM elements to interact with LMS. Each item's metadata is kept as an external XML files in an ftp area. The designed LO can be used in many environments. It has been tested on computer engineering students as a part of *Data Communication and Computer Network* course and positive feedbacks are received about the subjects like difficultness, usefulness and so on. LO can be easily reorganized according to the different requirements. This property saves time for both content creators and students. By metadata it is easy and fast to make the content current and content management becomes simple. In developing a new course, LOs can be used in different ways (e.g. to support the lecturer at the class, to explain the applications at the laboratories, to support the learning of the student by himself etc.). For engineering education area, it is better to prepare LOs as html pages if the content includes many pictures and text. It is important to have a database of assets and SCOs for reuse. It may be better to use simulations, to facilitate the learning of the interactive content, applications, experiment.

The new LO will be designed for 'Discrete Mathematics' course and will be supported mobile devices [23].

References

1. LOM, 1484.12.1 IEEE Standard for Learning Object Metadata. (2002).
2. Robson, R.: Learning Object Tutorial, Eduworks (2000). (accessed February 2005. Online at <http://www.eduworks.com/LOTT/tutorial/index.html>).
3. Wiley, David. A.: Connecting learning objects to instructional design theory: A definition, a metaphor, and a taxonomy. In: D. Wiley (Ed.) *The Instructional Use of Learning Objects* (2000). (accessed December 2004. Online at <http://reusability.org/read/>).
4. Shepherd, C.: Objects of Interest 2004. (accessed December 2004. Online at [http:// www.fastrak-consulting.co.uk/tactix/features/objects/objects.htm](http://www.fastrak-consulting.co.uk/tactix/features/objects/objects.htm))
5. Barron T: Learning object approach is making inroads, *Learning Circuits* (2002). Online at <http://www.learningcircuits.org/2002/may2002/barron.html>
6. CISCO: Reusable Learning Object Strategy: Definition, Creation Process and Guidelines for Building (2003). (Online at http://www.cisco.com/warp/public/10/wwtraining/elearning/implement/rlo_strategy_v3-1.pdf)

7. ADL: SCORM 2004 2nd Edition Overview (2003). (accessed December 2004. Online at: <http://www.adlnet.org/>).
8. AICC-Aviation Industry CBT Committee. (Online at: <http://www.aicc.org/>)
9. ARIADNE- Alliance of Remote Instructional Authoring and Distribution networks for Europe. (Online at <http://www.ariadne-eu.org/>)
10. IEEE LTSC - Institute of Electrical and Electronics Engineers Learning Technology Standards Committee. (Online at <http://ltsc.ieee.org/>)
11. IMS (Instructional Management Systems) Global Learning Consortium, Inc. (Online at <http://www.imsglobal.org/>)
12. The SCORM Content Aggregation Model. (accessed December 2005. Online at http://www.adlnet.org/ADLDOCS/Document/SCORM_1.2_CAM.pdf)
13. Advanced Distributed Learning: SCORM Sequencing and Navigation Ver 1.3.1. (July 2004). (Online at <http://www.adl.org>)
14. UK Learning Object Metadata Core. Draft 0.2, May 2004). (accessed December 2005. online at http://www.cetis.ac.uk/profiles/uklomcore/uklomcore_vap2_may04.doc)
15. Smith, R.C.: Guidelines for Authors of Learning Objects. New Media Consortium.(May 2004). (Online at <http://www.nmc.org/guidelines/NMC%20LO%20Guidelines.pdf>)
16. RELOAD Editor Introductory Manual. RELOAD-Reusable eLearning Object Authoring & Delivery. (2004) (accessed Jan 2005. Online at <http://www.reload.ac.uk/interop.html>)
17. Moodle (Content Packaging Program). (accessed February 2005. Online at <http://moodle.org/>)
18. Claroline. (accessed February 2005. Online at <http://www.claroline.net/>)
19. dotLRN, Open Source Learning Environment. (accessed February 2005. Online at: <http://www.dotlrn.org/>)
20. Learnwise v2 and Learnwise Olympus. (accessed February 2005. Online at <http://www.learnwise.com/>)
21. Balci B.: Bilgisayar Ağlarında Tıkanıklık Kontrol Algoritmaları İcin Simulatör. MSc Thesis. Marmara University, Fen Bilimleri Enstitüsü , İstanbul, Turkey. (2001) (Simulator For Congestion Control Algorithms In The Computer Networks)
22. Tanenbaum, A.S.: Computer Networks. Prentice-Hall, 4th Ed.; United States of America, (2003) 384-410
23. Inceoglu, M.M.: A Discrete Mathematics Package for Computer Science and Engineering Students. Lecture Notes in Computer Science, **3482** (2005) 538-546

WebQuest Markup Language (WQML) for Sharable Inquiry-Based Learning

Sebastian Fleissner¹, Yuen-Yan Chan¹, Tsz Hon Yuen¹, and Victor Ng²

¹Department of Information Engineering,
The Chinese University of Hong Kong,
Shatin, Hong Kong
{sfleiss4, yychan, thyuen4}@ie.cuhk.edu.hk

²ETI Consulting Limited,
The University of Hong Kong,
Pokfulam, Hong Kong
vng@etic.com.hk

Abstract. WebQuest is a model for constructivist inquiry-based learning in which the information used by learners is collected from the Web. A WebQuest exists in form of a Web site that contains a defined set of componential Web pages. In this paper, we specify the WebQuest Markup Language (WQML) for WebQuest construction. WQML enables WebQuests to be implemented as sharable courseware objects and thus to be interoperable with most learning management systems (LMS).

1 Introduction

Alongside the evolution of educational technology, the mainstream perspective in teaching and learning has also been migrating. Starting from behaviorism in the 50s, to cognitivism in 70s and 80s, we are now in the era of constructivist teaching and learning. Nowadays, with the emergence of Internet and Web technology, the education field is experiencing a paradigm shift from the traditional teacher-centered model to the collaborative learner-centered model in which the teacher becomes a facilitator. Inquiry-based learning, a student-centered instructional approach focused on questioning, critical thinking, and problem solving [1], is a popular pedagogy under the constructivist context. As an old adage goes: *Tell me and I forget, show me and I remember, involve me and I understand*. Students learn the best when they are the center of the own learning. Inquiry-based learning enhances students' acquisition of new knowledge by actually involving them in the learning process and having them to seek resolutions to questions and issues.

WebQuest is a model for Web-enabled inquiry-based learning. It was proposed by Dodge in 1995 [9]. Nowadays, WebQuest is widely adopted around the world as an effective constructivist pedagogy. Its popularity is proven by the return of more than 1.5 millions of hits by querying the term *webquest* in major search engines. In fact, a vast amount of research (such as [8, 13, 15]) has demonstrated that WebQuest is an effective approach for inquiry-based learning,

scaffolding, and collaborative learning. WebQuest exists in form of a Web site that composed of a defined set of componential Web pages. Despite the regular WebQuest structure, WebQuest implementations are proprietary and there is no standardized WebQuest format at present.

Having a universal and comprehensive agreement on the format of the electronic learning materials enables such materials to be *sharable* and *reusable*. In fact, this is the main purpose of learning objects [10]. A *learning object* is the smallest chunk of content that can stand by itself as a meaningful unit of learning. It is a collection of digital materials coupled with a clear and measurable learning objective designed to support a learning process. Organizations developing standards for learning objects include the Advanced Distributed Learning Initiative (ADL) [11], the Instructional Management System Global Consortium (IMS) [6], the Learning Technology Standards Committee of the Institute for Electrical and Electronic Engineers (IEEE/LTCS) [5], and the Aviation Industry CBT Committee (AICC) [4]. For example, ADL defines the Sharable Content Object Reference Model (SCORM) [16] for reusable and interoperable learning objects. Standardized learning objects greatly facilitate their manipulations over Learning Management Systems (LMS) and Learning Content Management Systems (LCMS).

1.1 Our Contribution

In this paper, we propose the WebQuest Markup Language (WQML), an XML specification for the WebQuest learning objects as defined in [3]. We specify the WQML syntax and the DTD. We also describe how to generate a WebQuest from a WQML description.

1.2 Paper Organization

The rest of the paper is organized as follows. Section 2 provides an overview of WebQuest and detailed its constituent components, and also briefly reviews inquiry-based learning, information literacy. Section 3 provides the WQML syntax and its corresponding DTD. Section 4 describes how a WebQuest is generated from the WQML data, and briefly discusses on the interoperability of WQML and common e-Learning standards. The paper is concluded in Section 5.

2 Background

2.1 Inquiry-Based Learning

Inquiry is defined as *a seeking for truth, information, or knowledge* That is, seeking information by questioning [7]. Since the stage of infants, human beings begin to make sense of the world by inquiring. Such process begins with information and data gathering through the application of the senses of seeing, hearing, touching, tasting, and smelling. Through the process of inquiry, individuals construct their perspectives of the natural and human-designed worlds.

Inquiry creates a motivation to *need or want to know*. It is no longer equivalent to the seeking of a right answer, rather, it is to seek an appropriate resolutions to questions and issues. It also emphasizes on the development of inquiry skills and an inquiring attitudes. Only in this way individuals are enable to continue the quest for knowledge throughout life.

According to various research results, inquiry learning can be applied to any disciplines. Individuals need a lot of perspectives in the course of viewing the world, while disciplines should interrelate with each another. Here, inquiry-based learning applies a specific set of ground rules to ensure the integrity of the various disciplines and their corresponding world views.

However, traditional education is not working in a favourable way of inquiry. Students are not encouraged to raise questions. They are learnt to listen and memorize standard, fixed answers. Fortunately this paradigm has been shifting over recent years. With the advocating of constructivism, inquiry-based learning is also gaining its importance in various education levels.

2.2 Information Literacy

Effective generation of knowledge from information and data is a desirable outcome of inquiry-based learning. This lead to the promotion of information literacy. Information literacy is often confused with computer literacy. Rather, information literacy is the best to be described as *the ability to locate, evaluate, and use information to become independent life-long learners*[14]. It stresses the basic concepts of how information is organized, the formats it comes in, and the structures used by different disciplines to record and transmit information. Information literacy greatly facilitate inquiry-based learning.

Information literacy also encompasses computer literacy. Nowadays most information is available in digital formats, a computer-literate person can operate networked computers to access to information. Computers are also used as a tool to search, locate and identify, gather, and manipulate information and raw data. In other words, computers and Internet enhances inquiry-based learning.

2.3 WebQuest

WebQuest is a model for inquiry-based learning in which some or all of the information that learners interact with comes from resources on the Internet. It provides an authentic, technology-rich environment for problem-solving, information processing, and collaboration [17]. A WebQuest can be as short as a single class period (short-term WebQuests) or as long as a month-long unit (long-term WebQuests) and usually involves collaborative work, with group members taking on specific roles or perspectives. Well-designed WebQuests promote instructional practices by integrating research-supported theories with effective use of Internet resources, open-ended questions, and authentic tasks that motivate students. In fact, a number of pieces of research has demonstrated that WebQuest is an effective approach for inquiry-based learning [8, 12, 13, 15]. Figure 1 illustrates a WebQuest on cryptography.

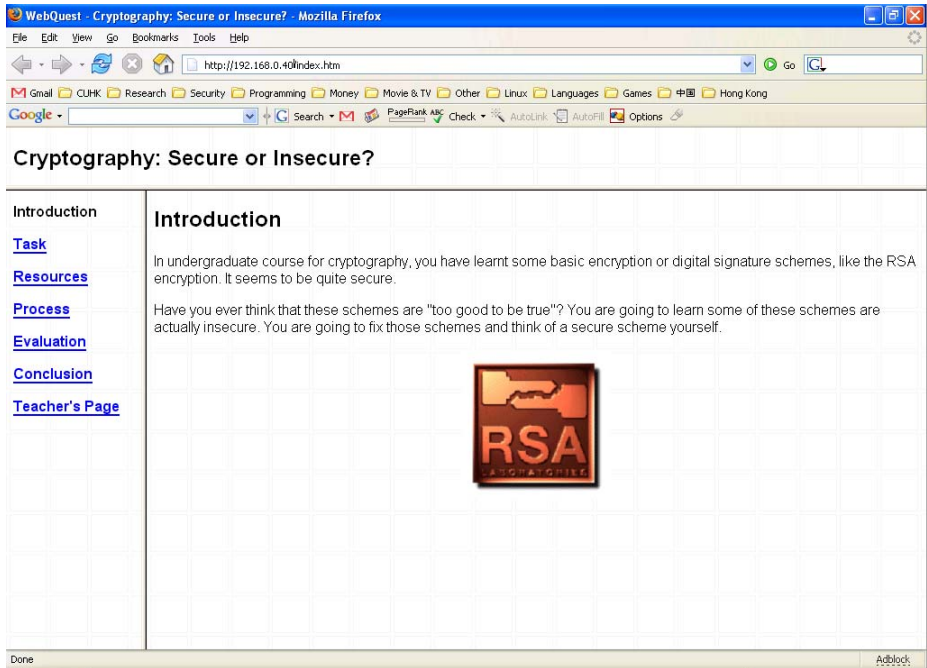


Fig. 1. A WebQuest Sample

2.4 WebQuests Components

A WebQuest *should* contain the following 6 components [9]:

1. *Introduction*. Sets the stage and provides some background information.
2. *Task*. Specifies a duty or an assignment which is doable and interesting.
3. *Resource*. Contains a collection (or the pointer) of information sources necessary to complete the task.
4. *Process*. Gives a description of the procedures that the learners should go through in accomplishing the task. The process is usually broken out into clearly described steps.
5. *Evaluation*. Include an assessment rubric which describes to the learners how their performance will be evaluated.
6. *Conclusion*. Brings closure to the quest and encourages reflections.

An optional *teacher page* that includes information to help other teachers implement the Webquest is also recommended.

3 WebQuest Markup Language

The WebQuest Markup Language (WQML) is a XML-based language for describing the contents of a WebQuest. In order to allow for a compact language

specification, WQML does not specify how the WebQuest is presented to the user in a web browser. Layout and color schemes to be applied to a specific WebQuest are described by XSL style sheets. The separation of content and style is generally desirable, because it allows for reusable content and flexible content presentations. We call the file containing the WQML description of a WebQuest a *WQML document*. Since we aim to support non-alphabetical languages, such as Chinese and Japanese, all WQML documents and XSL style sheets are required to be encoded in UTF-8.

3.1 WQML Elements

The WebQuest Markup Language consists of the 18 elements shown in Table 1. Details on each element along with DTD definitions are provided in the following subsections.

Table 1. WQML Elements

Element	Description
1. WebQuest	Root element. Contains 1 <i>Student</i> and optionally 1 <i>Teacher</i> element.
2. Student	Student page. Contains a sequence of elements 4 - 9.
3. Teacher	Teacher page. Contains a sequence of elements 4 - 9.
4. Introduction	Introduction component. Contains 1 or more <i>Section</i> elements.
5. Task	Task component. Contains 1 or more <i>Section</i> elements.
6. Resources	Resources component. Contains 1 or more <i>Section</i> elements.
7. Process	Process component. Contains 1 or more <i>Section</i> elements.
8. Evaluation	Element describing the evaluation component. Child element: <i>Section</i>
9. Conclusion	Conclusion component. Contains 1 or more <i>Section</i> elements.
10. Credits	Credits component. Contains 1 or more <i>Section</i> elements.
11. Section	A paragraph. Combination of text, <i>Object</i> , <i>Link</i> , <i>List</i> , <i>Table</i> elements.
12. Object	An image, sound, or video object.
13. Link	A hyperlink.
14. List	A list containing 1 or more <i>Item</i> elements.
15. Item	The contents of a list item.
16. Table	A table. Contains 1 or more <i>Row</i> elements.
17. Row	Table row. Contains 1 or more <i>Cell</i> elements.
18. Cell	Table cell.

The <WebQuest> Element. The *WebQuest* element is the root element of the WQML document. It has two required attributes for specifying the WebQuest's name and author. Child elements are one *Student* element and optionally one *Teacher* element. Specification and usage of <WebQuest> is given below:

Specification:

```
<!ELEMENT WebQuest (Student, Teacher*)>
```



```
<!ATTLIST WebQuest
  name CDATA #REQUIRED
  authors CDATA #REQUIRED
>
```

Usage:

```
<WebQuest name="Cryptography: Secure or Insecure?"
  authors="Tsz Hon Yuen">
...
</WebQuest>
```

The <Student> Element. The student's page is the main part of a WebQuest, and it is described by the <Student> element. The details of student's page are specified by child-elements corresponding to the 6 required components of a WebQuest. Apart from <Introduction>, <Task>, <Resources>, <Process>, <Evaluation>, <Conclusion>, WQML supplies the <Credits> and <Teacher> elements, which allow specification of two optional components stating credits and sharing teacher's implementation experience. DTD specification and usage of <Student> are given below:

Specification:

```
<!ELEMENT Student (Introduction, Task, Resources, Process,
  Evaluation, Conclusion, Credits*, Teacher*)>
<!ELEMENT Introduction (Section)+>
<!ELEMENT Task (Section)+>
<!ELEMENT Resources (Section)+>
<!ELEMENT Process (Section)+>
<!ELEMENT Evaluation (Section)+>
<!ELEMENT Conclusion (Section)+>
<!ELEMENT Credits (Section)+>
```

Usage:

```
<WebQuest name="Cryptography: Secure or Insecure?"
  authors="Tsz Hon Yuen">
  <Student>
    <Introduction>...</Introduction>
    <Task>...</Task>
    <Resources>...</Resources>
    <Process>...</Process>
    <Evaluation>...</Evaluation>
    <Conclusion>...</Conclusion>
  </Student>
</WebQuest>
```

The <Section> Element. The six elements describing the key WebQuest components (Introduction, Task, Resources, Process, Evaluation, and Conclusion) have the same structure. Each of the component elements contains one or more

sections described by the `<Section>` element, which has an optional `title` attribute. Apart from text, `<Section>` can contain `<Object>`, `<Link>`, `<List>`, and `<Table>` elements for defining multimedia objects, hyperlinks, lists, and tables respectively. Specification and usage of `<Section>` are given below:

Specification:

```
<!ELEMENT Section (Object, Link, List, Table)>
<!ATTLIST Section
  title #OPTIONAL
>
```

Usage: `<Section title="Introduction Page"> ... </Section>`

The `<Object>`, `<Link>`, `<List>`, and `<Table>` Elements. These four elements are used structure the contents a section. The `<Object>` element is used to embed images, videos, or sound into the WebQuest.

Specification:

```
<!ELEMENT Object (#PCDATA)>
<!ATTLIST Object
  type (image | audio | movie) #REQUIRED
  uri CDATA #REQUIRED
  width CDATA #IMPLIED
  height CDATA #IMPLIED
>
```

Usage: `<Object type="image" uri="intro.jpg">[Image]</Object>`

The `<Link>` element and its required attribute `uri` are used to point to resources on the World Wide Web.

Specification:

```
<!ELEMENT Link EMPTY>
<!ATTLIST Link
  uri CDATA #REQUIRED
>
```

Usage: `<Link uri="www.cuhk.edu.hk">CUHK</Link>`

`<List>` and `<Table>` tags are used for simple content formatting. The items of a list are specified by `<Item>` tags.

Specification:

```
<!ELEMENT List (Item)+>
<!ATTLIST List
  title CDATA #IMPLIED
>
<!ELEMENT Item (#PCDATA)>
```

Usage:

```
<List>
  <Item> Air production</Item>
  <Item> Water and food supplies</Item>
</List>
```

Tables, which are meant to be used for formatting the evaluation component of a WebQuest, are specified and constructed as follows:

Specification:

```
<!ELEMENT Table (Row)+>
<!ELEMENT Row (Cell)+>
<!ELEMENT Cell (#PCDATA | Object | Link | List)*>
```

Usage:

```
<Table>
  <Row>
    <Cell>Cell 1 in Row 1</Cell>
    <Cell>Cell 2 in Row 1</Cell>
  </Row>
  <Row>
    <Cell>Cell 1 in Row 2</Cell>
    <Cell>Cell 2 in Row 2</Cell>
  </Row>
</Table>
```

4 Deployment and Interparability of WQML

4.1 Deployment

WQML documents are transformed into HTML WebQuests by applying a XSL style sheets. As indicated in figure 2, we propose to deploy WQML documents and style sheets in a web server capable of performing the transformation dynamically, such as Apache's Cocoon. XSL style sheets are independent from the WebQuest's content and teachers can design a catalogue of different styles. Due to the dynamic transformation, students can select and change the style of WebQuests while they are using them.

The technical flow for this scenario is as follows. Students request a WebQuest through a Web browser. Upon receiving the request, the WebQuest hosting web server (WebQuest Server) identifies the corresponding WQML document and selects a default style sheet. Both WQML document and style sheet are passed to the XSLT processor to generate the HTML version of the WebQuest.

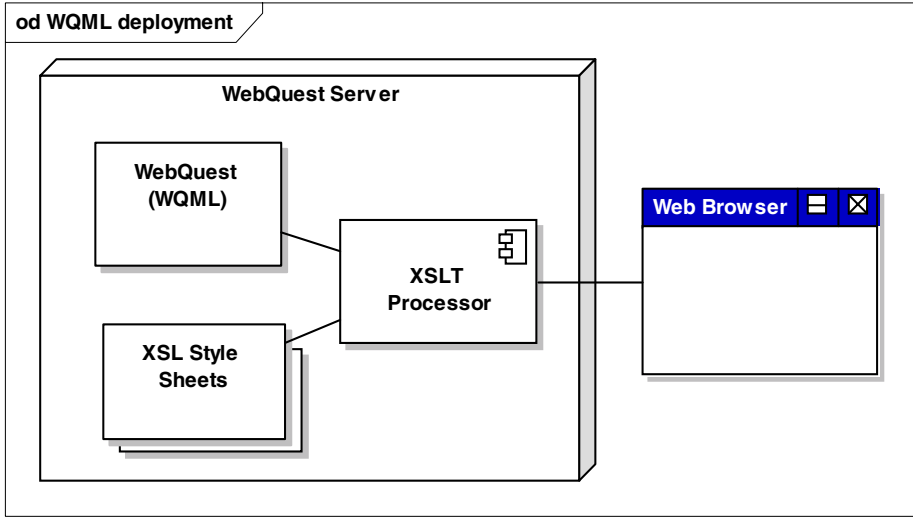


Fig. 2. WQML Deployment

4.2 Interoperability with LMS and LCMS

Since a WQML document is in pure XML format, it can be regarded as a *WebQuest object* which is basically a learning object. Being reusable units of instruction for teaching, WebQuest objects are interoperable in Learning Management Systems (LMS) as well as Learning Content Management Systems (LCMS) that conformed to learning object standards such as the Sharable Content Object Reference Model (SCORM) [16] and United Kingdom Learning Object Metadata Core (UK LOM Core) [2]. We encourage interested readers to a paper written by the second author of this paper [3] for further details.

5 Conclusion

In this paper, we have briefly reviewed WebQuest, a popular inquiry-based learning model with well-defined components. We also proposed the WebQuest Markup Language (WQML) as a structural XML-based language for describing the contents of a WebQuest. Implementation issues are also briefly discussed. These include the generation of WebQuest contents pages from a WQML document and its corresponding style sheets, and the integration of WebQuest objects into existing LMS and LCMS frameworks. We believe WQML can facilitate both development and usage of WebQuest, as it provides scaffolding effect to both the authoring and sharing of WebQuest contents.

Acknowledgements. Hong Kong Research Grant Council's Earmarked Grants 4232-03E and 4328-02E for sponsorship.

References

1. Bloom. *Inquiry: a Cross-Curricular Reader*. Prentice-Hall, Inc., Englewood Cliffs, NJ, 1993.
2. CETIS. *UK Learning Object Metadata Core*. The Centre for Educational Technology Interoperability Standards, May 2004.
3. Yuen-Yan Chan. Creating reusable webquest objects with webquest authoring engine. In *Fifth IEEE International Conference on Advanced Learning Technologies*, pages 282 – 284, July 2005.
4. Aviation Industry CBT Committee. <http://www.aicc.org/>.
5. IEEE Learning Technology Standards Committee. <http://ieeeltsc.org/>.
6. IMS Global Learning Consortium. <http://www.imsglobal.org/>.
7. Educational Broadcasting Corporation. <http://www.thirteen.org/edonline/>.
8. E.R. Delisio. Technology in the classroom: Webquest sends student back in time. *Education World*, July 2001.
9. B. Dodge. Some thoughts about webquests, Feb 1995.
10. S. Downes. Learning objects. Web Material., 2000.
11. Advanced Distributed Learning. <http://www.adlnet.org/>.
12. T. March. The learning power of webquests. *Educational Leadership*, 61(4):42 – 47, 2003.
13. C. Peterson, D.C. Caverly, and L. MacDonald. Developing academic literacy through webquests. *Journal of Developmental Education*, 26(3):38 – 39, 2001.
14. SACS. *Criteria for Accreditation. Library and Other Information Resources Services*. Commission on Colleges, Southern Association of Colleges and Schools, Dec 1996.
15. D. L. Spanfelner. Webquests, an interactive approach to the web. *Community and Junior College Libraries*, 9(4):23 – 28, 2000.
16. ADL Technical Team. *Sharable Content Object Reference Model (SCORM) 2004 2nd Edition Document Suite*. Advanced Distributed Learning Initiative, July 2004.
17. B. Teclehaimanot and A. Lamb. Reading, technology, and inquiry-based learning through literature-rich webquests. *Reading Online*, 7(4), 2004.

Practical Boolean Operations on Point-Sampled Models

Xujia Qin^{1,2}, Weihong Wang^{1,3}, and Qu Li¹

¹ College of Software Engineering, Zhejiang University of Technology, 310032 HangZhou
{qxj, wwh, liqu}@zjut.edu.cn

² State Key Lab of CAD&CG, Zhejiang University, 310027 Hanzhou

³ State key Lab. of Software Development Environment,
Beijing University of Aeronautics and Astronautics, 100083 Beijing

Abstract. Boolean operation is an important way in geometry modeling. This paper proposes a novel Boolean operations algorithm for point-sampled models based on implicit function transforming. In the algorithm, the point models are converted to implicit surfaces at first, and then Boolean operations for implicit surface are used to the point models. The simple forms of Boolean operations for implicit surfaces are presented. The method of RBF variational interpolation based on scattered points is used to convert the point models into implicit surfaces. Using this algorithm, complex point model can be constructed from several point models. This Boolean operations algorithm for point models is also suitable for Boolean operations for mesh models. It can implement the editing process of Cut-and-Paste for mesh models.

1 Introduction and Related Works

Boolean operation is an important way in geometry modeling. It is a main way to build a complex model from simple models, and it is widely used in computer-aided geometry design (CAGD) and computer graphics (CG). Traditional Boolean operation is mainly used in solid modeling to build an complex solid from primary solid [1](e.g. cube, column, cone, sphere, etc.). With the development of computer application, there are many ways to represent digital models, such as parametric surface, meshes, point models, etc. Models become more and more complex, and features on models such as on statuary artworks are more detailed. Using traditional modeling method to construct those complex models is a time-consuming work.

With the popularization of 3D data collecting equipments, e.g., laser scanner and high-resolution camera, sampled surfaces data of objects is often represented in the form of point-cloud. In CG and inverse engineering fields, surfaces or meshes of objects are often reconstructed by interpolation, approximation or polygonization of point-cloud data. In recent years, point based modeling and rendering techniques are well studied[2-8]. Most of these algorithms use discrete sampling points on surface as basic elements. Comparing to traditional surface based modeling; it has simpler topology and doesn't need to maintain complex topological information.

Traditional surface based Boolean operations are well developed after several years of study[9-11]. Boolean operations on model in the form of meshes require facet-to-facet and facet-to-line segment intersection so as to find points of intersection, use

meshes to reconstruct the intersection region and ensure its correct topology. When the two meshes performing Boolean operation are dense, the intersection testing would be very time-consuming. Another major problem of surface based Boolean operation is the stability of intersection testing[1,9]. When the two surfaces performing intersection operation are almost overlapped, Boolean operations on polyhedrons may fail. In order to avoid this kind of failure, complex extra processes are needed[12]. For Boolean operations on point models, Pauly et al combined unconstrained point-cloud and Moving Least Square(MLS) to approximate implicit surface, then build up the hybrid representation of solid model[6]. This method combines both the advantages of implicit surface and parametric surface, thus allowing massive deformation and Boolean operation on arbitrary shapes. Ohtake et al presented a new implicit shape representation method[7], he used multi-layer segmentation to construct surface model from large scale point-cloud data. He also used octree to divide the point-sampled model into several parts and use piecewise linear function to describe its local shapes. This method uses implicit function to approximate the surface of point model, thus implementing the point model construction and Boolean operations. Adams et al implemented Surfels representation based interactive Boolean operations[8]. These operations don't need to construct a continuous surface of the solid. But this method is only effective for uniformity sampled point model, and it is also noise sensitive.

In this paper, we present a new algorithm of Boolean operation on point-sampled models. The algorithm converts the point-sampled models to implicit surfaces firstly, and then uses Boolean operation of implicit surfaces to implement point-sampled model based Boolean operation. This algorithm can be used in cut-and-paste for constructing complex model from existing models, or reuse feature parts of models. The remaining sections of this paper are organized as follows. In sections 2, we introduce Boolean operations of implicit surfaces. Implicit surface constructing based on RBF interpolation and Boolean operations of point-sampled models are described in section 3. In section 4, we apply this method in the Boolean operations of general mesh models. Experimental results and conclusions are presented in section 5 and section 6.

2 Boolean Operations on Implicit Surface

In Euclid space R^3 , point set defined by inequation $f(x, y, z) \geq 0$ is a functional representation of geometry object. Surface (boundary of the object) defined by equation $f(x, y, z) = 0$ is an implicit surface. In solid defined by implicit function, let $p = (x, y, z)^T$, when $f(p) > 0$, and then p is inside the solid. When $f(p) = 0$, then p is on the boundary of the solid. And when $f(p) < 0$, then p is outside the solid.

Let $f_1 = 0$ and $f_2 = 0$ to define two implicit surface, f_3 is the result implicit surface by Boolean operation of f_1 and f_2 . Wyvill[13] presented a definition of implicit surface Boolean operation by means of limit form of functions fusion.

$$f_3 = (f_1^n + f_2^n)^{\frac{1}{n}} \tag{1}$$

Pasko proposed a general form of Boolean operations by functions fusion[14].

$$f_3 = (f_1 + f_2 + \alpha\sqrt{f_1^2 + f_2^2})(f_1^2 + f_2^2)^{\frac{1}{2}} \tag{2}$$

In equation (2), $\alpha \in [-1, 1]$, when $\alpha = -1$, the equation indicates intersection of f_1 and f_2 , and when $\alpha = 1$, indicates the union of f_1 and f_2 . Although the equation (2) presents a uniform mode of Boolean operations and functions fusion for implicit surfaces, it is inconvenient to implement. In order to decrease the computation cost and make it convenient to implement, we present following Boolean operations for implicit surfaces.

Union $f_3 = f_1 \cup f_2 = \max(f_1, f_2)$ (3)

Intersection $f_3 = f_1 \cap f_2 = \min(f_1, f_2)$ (4)

Subtract $f_3 = f_1 - f_2 = \min(f_1, -f_2)$ (5)

Figure 1 shows Boolean operation result of two spheres defined by implicit function.

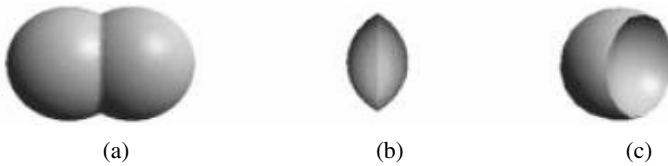


Fig. 1. Boolean operation results of two spheres defined by implicit function. (a)union; (b)intersection; and (c)subtract.

3 Implicit Surface Transforming and Boolean Operations on Point-Sampled Models

Transforming point model to implicit function representation, obviously it is a multi-variant scatter data interpolation problem. We use variational interpolation to obtain the implicit surface of the point model, the form is $f(p) = 0$. Considering that the interpolated surface is smooth, in CAGD, smooth property of surface can be evaluated by thin-plate energy function.

$$E = \int_{\Omega} [f_{xx}^2(x) + 2f_{xy}^2(x) + f_{yy}^2(x)] dx dy \tag{6}$$

Where f_{xx}, f_{xy}, f_{yy} are second partial derivatives of f , Ω is region of interpolate points. Because the energy E essentially is a square curvature evaluate of function f

in region Ω . When f is rumpled, the energy E is increasing. So, minimize the energy can make the surface f smooth.

The above energy function can be easily to extend to high dimension case. The equation's general solution form is linear combination of radial basis functions $\phi(p)$ and a linear term $Q(p)$. Its general expression is:

$$f(p) = \sum_{j=1}^n \lambda_j \phi(|p - p_j|) + Q(p) \tag{7}$$

where $Q(p)$ is a polynomial whose degree is less than a specified number, λ_j is a real-valued weight, $\phi(\bullet)$ is a radial basis, and $|\bullet|$ is a Euclid norm.

In order to solve the weights λ_j , we can convert to solve the following linear system:

$$\begin{bmatrix} \phi_{11} & \phi_{12} & \cdots & \phi_{1n} & x_1 & y_1 & z_1 & 1 \\ \phi_{21} & \phi_{22} & \cdots & \phi_{2n} & x_2 & y_2 & z_2 & 1 \\ \vdots & \vdots & \ddots & \vdots & \vdots & \vdots & \vdots & \vdots \\ \phi_{n1} & \phi_{n2} & \cdots & \phi_{nn} & x_n & y_n & z_n & 1 \\ x_1 & x_2 & \cdots & x_n & 0 & 0 & 0 & 0 \\ y_1 & y_2 & \cdots & y_n & 0 & 0 & 0 & 0 \\ z_1 & z_2 & \cdots & z_n & 0 & 0 & 0 & 0 \\ 1 & 1 & \cdots & 1 & 0 & 0 & 0 & 0 \end{bmatrix} \begin{bmatrix} \lambda_1 \\ \lambda_2 \\ \vdots \\ \lambda_n \\ c_0 \\ c_1 \\ c_2 \\ c_3 \end{bmatrix} = \begin{bmatrix} h_1 \\ h_2 \\ \vdots \\ h_n \\ 0 \\ 0 \\ 0 \\ 0 \end{bmatrix} \tag{8}$$

where $f(p_j) = h_j$, $\phi_{ij} = \phi(|p_i - p_j|)$, $Q(p) = c_0x + c_1y + c_2z + c_3$.

Equation (2) may be rewritten in matrix form as:

$$\begin{pmatrix} A & P \\ P^T & 0 \end{pmatrix} \begin{pmatrix} \lambda \\ c \end{pmatrix} = \begin{pmatrix} h \\ 0 \end{pmatrix} \tag{9}$$

where $A_{ij} = \phi(|p_i - p_j|)$, $P = \begin{bmatrix} x_1 & y_1 & z_1 & 1 \\ x_2 & y_2 & z_2 & 1 \\ \vdots & \vdots & \vdots & \vdots \\ x_n & y_n & z_n & 1 \end{bmatrix}$, $i, j = 1, 2, \dots, n$.

In linear system (8), the coefficient matrix is obviously real symmetric, and with proper selection of basis functions it can be made positive-definite. Thus, a solution always exists to the linear system[15].

Use the variational interpolation described above, we can construct a scalar distance field $f(p) = r$ from point-sampled model. This is a typical implicit surface form. When $r = 0$, $f(p) = r$ is the interpolated surface of the point model.

After obtaining the implicit surface of the point model, we can realize Boolean operations for point models by using the implicit surface Boolean operation method described in section 2. Those points in two point models that satisfy the equation $f_3(p) = 0$ are the points of Boolean operations result model. Figure 2 indicates the Boolean operation of two point models.

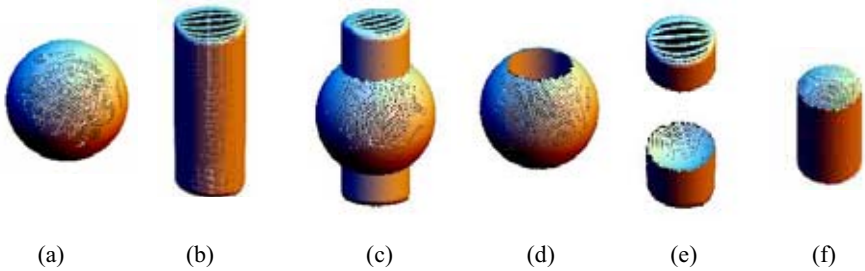


Fig. 2. Boolean operations on two point models. (a) sphere A; (b) column B; (c) $A \cup B$ (d) $A - B$; (e) $B - A$; (f) $A \cap B$.

4 Boolean Operations on Mesh Models

Nowadays, in computer graphics application field, mesh models are widely used. Direct Boolean operations with mesh models need a mass of intersection testing for facet-to-facet and facet-to-line segment. At the same time, in order to keep the correct topology of the mesh model, those new points created by intersection testing need polygonized (that is re-polygonized in fusion region of the two models). The stability of intersection testing is the main problem of Boolean operation for mesh models. The goal of our new algorithm is to avoid the complex and unstable intersection testing, as well as re-polygonizing for fusion region. So we implement the Boolean operation on mesh models by point transforming from the mesh models. After point models are transformed to implicit surfaces, the result of point model’s Boolean operation is also an implicit surface. We can obtain the mesh representation by polygonization from the result implicit surface.

When this method are used to carry out the Boolean operations for mesh models, if the mesh is dense, we can use the mesh models’ vertexes as the point model’s point set. If the mesh is sparse, it needs to be subdivided properly. In this paper, we use Loop method[16] to subdivide the mesh model. The precision of this mesh model Boolean operation method mainly depends on the denseness of the meshes and the sample precision when polygonizing the result implicit surface. Figure 3 shows that Boolean operation (union and subtract) of two mesh models (torus and Venus head).

With this method, we can implement the editing process of cut-and-paste for mesh models. That is to cut part of mesh from source model and paste it to target model[17].

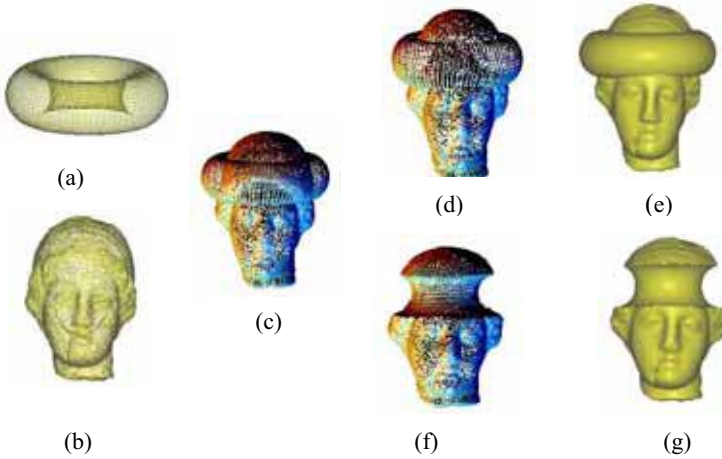


Fig. 3. Boolean operation on mesh models. (a) torus mesh; (b) Venus head mesh; (c) points representation of mesh models; (d) point mode after union operation; (e) mesh model of (d); (f) point mode after subtract operation; (g) mesh model of (f).

5 Experiment Results

We test our algorithm on PC with CPU of P4 2.4GHz and main memory of 512MB, and implement a point model Boolean operations system on the platform of VC++6.0. Figure 4 is the process of Boolean operations among three point models. Figure 4(a) , 4(b) and 4(e) are original models, figure 4(c) and 4(f) are models alignment before Boolean operation. Figure 4(g) is the result of the bunny subtracts the sphere, and then performs union with the man head. Because the Boolean operation result also has an implicit surface representation, we can polygonize the implicit surface to mesh model. Figure 4(h) is the mesh model of figure 4(g). Figure 5 is the mesh models of Venus head and bunny with the operations of union and subtraction. In this experiment we mainly test the time cost of transforming the point model to implicit surface with RBF interpolation, and the efficiency of implicit surface’s Boolean operation.

Table 1. Running time of Boolean operation on point models in figure 4

Model	number of point	RBF field constructing time	Boolean operation time
Bunny1	7012	1.178s	Bunny-Sphere
Sphere	4187	0.281s	0.640s
Bunny-Sphere	1728	0.176s	(Bunny-Sphere)U Man head
Man head	6743	0.889s	0.271s

Table 2. Running time of Boolean operation on point models in figure 5

Model	number of point	RBF field constructing time	Boolean operation time
Bunny2	35947	6.141s	(Union) 2.250s
Venus head	8266	1.203s	(Subtract) 2.203s

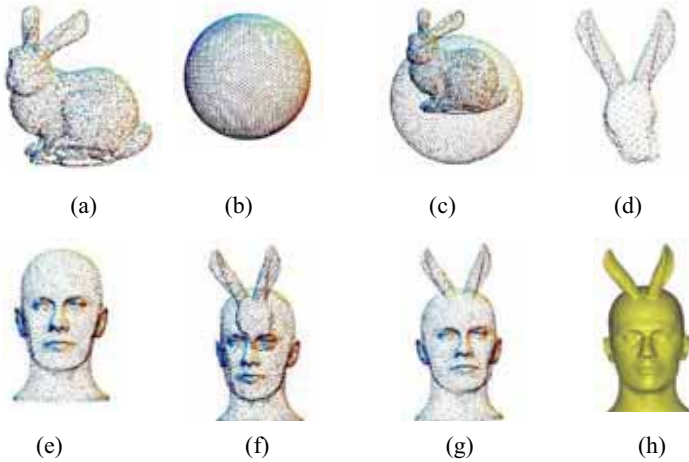


Fig. 4. Boolean operation on general mesh models. (a)bunny A; (b) sphere B; (c) mode alignment; (d) A-B; (e) man head ; (f) mode alignment ; (g) $(A-B) \cup C$; (h) mesh model.

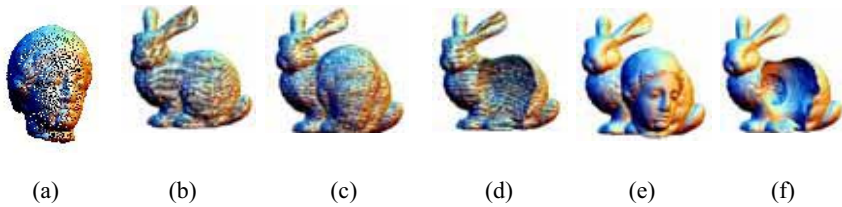


Fig. 5. Boolean operations on point models of Venus head and bunny. (a) Venus head; (b) bunny; (c) union of the two models; (d) subtract of the two models; (e) polygonization of (c); (f) polygonization of (d).

Table 1 and table 2 shows the running time of RBF distance fields constructing and Boolean operations in figure 4 and figure 5.

Figure 6 and figure 7 are results of Boolean operations on mesh models. Figure 6(a) and 6(b) are original models. Figure 6(c) and 6(d) are part of original models by cut editing. Figure 6(e) is the Boolean operation result of polygonization. In this way, we can cut part of mesh from one model and paste it on another model. Figure 7 shows an ox head fusion with horse head.

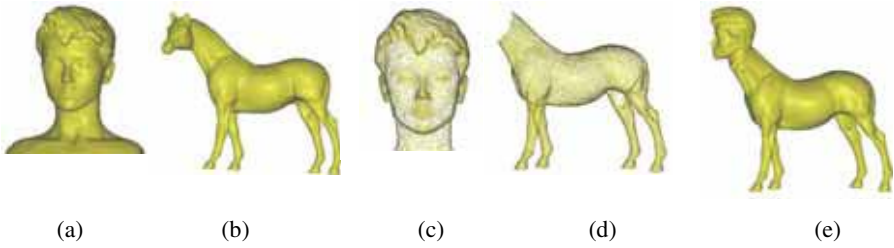


Fig. 6. Cut-and-paste editing for mesh models. (a) mesh model A; (b) mesh model B; (c)cutting part from model A; (d) cutting part from model B; (e) Cut-and-paste editing result.

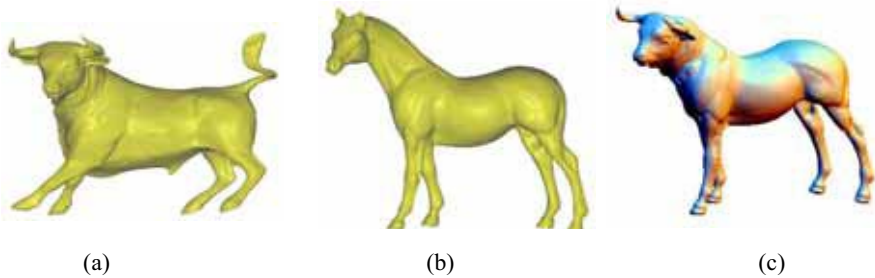


Fig. 7. Fusing the ox head with horse body. (a) ox model; (b) horse model; and (c) result model of fusion.

6 Conclusions

With the popularization of 3D digital data collecting equipments, such as 3D laser scanner, point set as the input data for geometry modeling or directly as a representation of object is widely used. Researchers have done much work on point based modeling and rendering, and now point model become an important representation form for geometry model. This paper presents a new Boolean operation algorithm for point-sampled models. The algorithm transforms the point model to implicit surface firstly, and then implements Boolean operations on implicit surfaces. The algorithm can also be used on general mesh models. For mesh models, we convert them to point models firstly, then use the point model Boolean operations algorithm, and finally polygonize the operation result to obtain the final mesh model. By this way, it can implement the editing process of cut-and-paste for mesh models. It can construct an complex model from existed models.

Acknowledgements

This research was supported by the National Nature Science Foundation of China under Grant No. 60473024, Zhejiang provincial Nature Science Foundation of China under Grant No. Y104341, and Opening Research Fund of State Key Laboratory of CAD&CG, Zhejiang University.

References

1. Mantyla M.: An introduction to solid modeling. Rockville, Maryland, USA: Computer Science Press (1988)
2. Rusinkiewicz S, Levoy M.: Qsplat: A multi-resolution point rendering system of large meshes. In: Computer Graphics Proceedings, Annual Conference Series, ACM SIGGRAPH, New Orleans, Louisiana, (2000) 343-352
3. Pauly M, Gross M, Zurich E.: Spectral processing of pointsampled geometry. In: Computer Graphics Proceedings, Annual Conference Series, ACM SIGGRAPH, Los Angeles, California, (2001) 379-390
4. Zwicker M, Pauly M, Knoll O, et al.: Pointshop 3D: An interactive system for point-based surface editing. In: Computer Graphics Proceedings, Annual Conference Series, ACM SIGGRAPH, San Antonio, Texas, (2002) 322-329
5. Alexa M, Behr J, et al.: Computing and rendering point set surfaces. IEEE Transactions on Visualization and Computer Graphics, Vol. 9(1): (2003)3-15
6. Pauly M, Keiser R, Kobbelt P L, et al.: Shape modeling with point-sampled geometry. In: Computer Graphics Proceedings, Annual Conference Series, ACM SIGGRAPH, San Diego, California, (2003) 641-650
7. Ohtake Y, Belyaev A, Alexa M, et al.: Multi-level partition of unity implicits. In: Computer Graphics Proceedings, Annual Conference Series, ACM SIG GRAPH, San Diego, California, (2003) 463-470
8. Adams B, Dutre P. Interactive Boolean operations on surfelbounded solids. In: Computer Graphics Proceedings, Annual Conference Series, ACM SIGGRAPH, San Diego, California, (2003) 26-31
9. Hoffmann M C. Geometric and Solid Modeling: An Introduction. San Francisco: Morgan Kaufmann Publishers Inc. (1989)
10. Kristjansson D, Biermann H, Zorin D.: Approximate Boolean operations on free-form solids. In: Computer Graphics Proceedings, Annual Conference Series, ACM SIGGRAPH, Los Angeles, California, (2001)185-194
11. Museth K, Breen D, Whitaker R, et al. Level set surface editing operators. ACM Transactions on Graphics, Vol.21 (3): (2002)330-338
12. Hoffmann M C. Hopcroft E J. Robust set operations on polyhydral solids. IEEE Computer Graphics and Applications, 1989,9(6):50-59
13. Wyvill B, Gallin E, and Guy A.: Extending the CSG tree: warping,blending and Boolean operations in an implicit surface modeling system. Computer Graphics Forum, Vol.18(2): (1999)149-158
14. Pasko A, Adzhiev V, Sourin A, and Savchenko V.: Function Representation in Geometric Modeling: Concepts, Implementation and Applications. The Visual Computer, Vol.11(8): (1995)429-446
15. Morse BS, Yoo TS, Rheingans P. et al.: Interpolating Implicit Surfaces From Scattered Surface Data Using Compactly Supported Radial Basis Functions. In Proceedings of Shape Modeling Conference, Genova, Italy, May (2001) 89-98
16. Loop C.: Smooth subdivision surfaces based on triangles. USA: Department of Mathematics, University of Utah (1987)
17. Biermann H, Martin I, Bernardini F, Zorin D.: Cut-and-Paste editing of multiresolution surfaces. ACM Transactions on Graphics, Vol.21(3): (2002)330-338

Dynamic Brush Stroke Generation for an Impressionist Effect

Youngsup Park and Kyunghyun Yoon

Computer Graphics Lab., CS&E, Chung-Ang University,
221, HukSeok-Dong, DongJak-Gu, Seoul, Korea
aupres98@hanmail.net, khyoon@cau.ac.kr

Abstract. We propose dynamic brush stroke generation for an impressionist effect of source images, using reference data. Colors used are formed by actual palette colors from artists. To create the palette, we have referred mostly to colors used in Van Gogh's works and determined the color of brush strokes by transferring it to the most similar one, through comparing colors used in source images and the palette colors. Also, by referring to the edge orientation of source images, we have applied a brush stroke direction that surrounds the edges. The sizes were determined depending on the different sizes of the objects from wide to narrow brushes. Finally, we applied spline curve and line shapes. The brush strokes created in such method, were applied separately according to its segmented images, and composed after rendering.

1 Introduction

Painters all have their own styles that they express through the color, orientation, shape and size of their brush strokes. The color and orientation of the brush strokes are largely dependent on the artist's motives. For example, Van Gogh had his own palette of colors, used curved rather than straight lines, superimposed action on to a calm subject, and expressed the effect of intense, bright colors using the contrast of complementary colors. In this paper, we will analyze the unique characteristics of Van Gogh's works, and use their analysis to propose a method of generating dynamic brush strokes based on the foundation of the analysis.

Most painterly rendering algorithms utilize simple brush strokes of the same shape and size. For this reason, the final images guess a machine-like implement, when compared with an artist's brushwork. We aim to improve computer based painterly rendering by using Van Gogh's palette colors, brush stroke orientation that follows the edges in the image, various sizes of brush, and long curved strokes.

2 Related Work

Litwinowicz[6] pioneered painterly rendering, by creating brush stroke that possesses both line and texture, and a direction determined by the orientation of features in the input image. He also varied the effect by adding random noise to the parameters of each brush strokes, and introduced a brush stroke clipping method that accommodates

edges within the image. However, because colors were taken from the input images and the brush strokes were straight, effects conveyed in the original pieces remained exclusive.

Hertzmann[5] proposed a method, to articulate brush strokes based on the geometry of the input image. This system creates brush strokes that follow spline curves that follow the grain of the image. The picture is built up from many layers, with identical brush strokes in each. A painterly sequence of wide to narrow brushes is used on each layer. However, this method is still unable to express the texture of the brush strokes shown in actual art works, and demonstrates a blurring effect that results from combining brush strokes with different properties. We have also used reference data in determining rendering parameters. Colors are determined by referring to Van Gogh’s palette colors using the color transfer method. The orientation of the brush strokes is determined by referring to edge orientation. Brush strokes of diverse sizes are created, and objects are expressed by segmented area clipping rather than by applying a separate clipping method to each brush stroke.

3 Dynamic Brush Stroke Generation

The creation of adaptive brush strokes based on reference data requires two steps. First the reference artwork is entered to establish palette colors used. Second, the brush stroke parameters such as color, orientation, size and shape are found. The color of a brush stroke is determined by selecting a pair of similar colors, one from the source images and one from the palette, and then applying the color transfer algorithm.

The brush stroke orientation is a spline curve that follows the orientation of image edges within a specified range of a pixel perimeter. The brush size is reduced as rendering progresses. We also employed the Deng and Manjunath method [1] to segment the source image. Figure 1 is a flowchart that summarizes our algorithm.

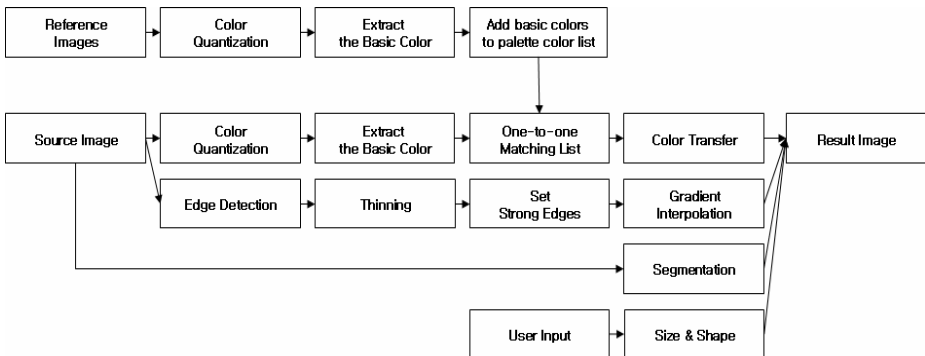


Fig. 1. System Flow

3.1 Color

An artist’s use of color is largely dependent on their motives and each individual has their own unique palette. We have analyzed the range of colors used by well-known

artists (concentrating mainly on Van Gogh, who used a lot of contrast) and we have also generated palette colors based on color theories. By color transfer between a palette reconstructed in this way, and the colors are the input image, we hope to express something of the style of a particular artist.

3.1.1 Palette Color Generation

There is no way of knowing the precise palette colors Van Gogh used: we can only attempt to reconstruct them from his work. Our method for doing this can be divided into three steps. First, we input the reference image. Second is process color quantization using Deng et al's method [2], which preserves image quality while reducing the number of colors. The results of quantization may be assumed to be representative colors and in the final stage of our algorithm, they are added into the palette. If several works are used as references, this may result in similar colors on the palette, which is then regenerated by calculating the average of two colors when the distance between them is lower than a threshold T .

3.1.2 Color Matching

The color matching is the one-to-one matching method between the color list of source image and the palette color list generated by reference images. The color matching method proposed by this paper consist of two steps and is used the mean and standard value of palette color list. First, calculate the stochastic values of the source image using the color quantization [2]. Second, selects the similar color between one color of source palette color list and the palette color list of reference images. The method compared and selected the similar color is selected when the distance between two colors is lower than a threshold T_{mean} and T_{standard} . This method is similar to Photo-mosaics method [9] that selects one photo in one grid.

3.1.3 Color Transfer

Color transfer, as proposed by Reinhard[3, 4], uses the $\ell\alpha\beta$ color space, in which there is usually little or no correlation between each channel. The α axis represents a chromatic yellow-blue channel, the β axis represents a chromatic red-green channel, and the γ axis represents an achromatic channel. We calculate statistical data for each axis in the $\ell\alpha\beta$ color space, is then used for color transfer between a set of representative colors in the source image and a set of representative colors from the reference images.

Color transfer is a one-to-one pixel matching that uses a linear map to match the means and variances in the $\ell\alpha\beta$ space using Equation 1[3, 4]:

$$X_{\text{target}} = \frac{\sigma_{\text{reference}}}{\sigma_{\text{source}}} (X_{\text{source}} - M_{\text{source}}) + M_{\text{reference}}, \quad (1)$$

where M_{source} and $M_{\text{reference}}$ are the mean of each axis, and σ_{source} and $\sigma_{\text{reference}}$ are the standard deviations of each channel.

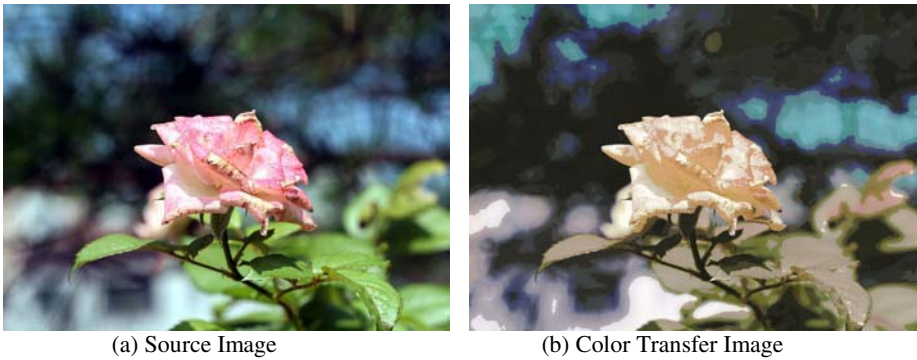


Fig. 2. The source image and the same image recolored using the color palette

Colors largely depend on the subjective motivations of the painters, and each painter has his own palette of distinctive colors. The Impressionists in particular were influenced by the flat form of the Japanese color prints. Considering this, this paper has attempted the method of flatizing the range of luminosity from 256 levels to 12 levels and the method of quantizing the colors [1, 2]. The painterly rendering in particular is handled by the units of random areas where the brush strokes are made, not by the pixel units, and thus, it is unnecessary to apply every color that forms an image of a source.

3.2 Direction

Painters usually draw a picture of an object following the edge line of that object. Litwinowicz[6] proposed a local gradient interpolation. This method determines the directions of the brush strokes by interpolating the gradients of the surrounding pixels in case of a pixel with a gradient located in a certain area with a magnitude near 0. Because this method applies the interpolation to the area where the direction of the strokes is not certain, the direction of the brush strokes does not comply with the direction of the edges. In order to resolve this problem, this paper set strong edges that determine the direction, and made the direction of the surrounding pixels correspond to the direction set by the edges. This is similar to the Hays method[7], but while Hays[7] used the gradient interpolation of the whole area, this paper used the local gradient interpolation.

There are three steps to finding strong edges: first, calculating the magnitudes of the gradients of pixels on the edges using thinned images; second, organize the calculated sizes of the gradients in a descending order; third, choose the biggest gradient as a strong edge and remove the surrounding edges only when their difference from the strong edge in direction is smaller than a fixed threshold. Many strong edges can be found by repeating this process.

The local gradient interpolation method using the strong edges calculated the weight of the distances between the edges that are within R radius, which is N times the shortest distance with the location of P as a point of reference. The gradients in pixels were calculated by adding the gradients and weights of the strong edges on the radius R and dividing the number. Variable N is an experimental number, and the values between 1.5 and 2.5 were given to it.

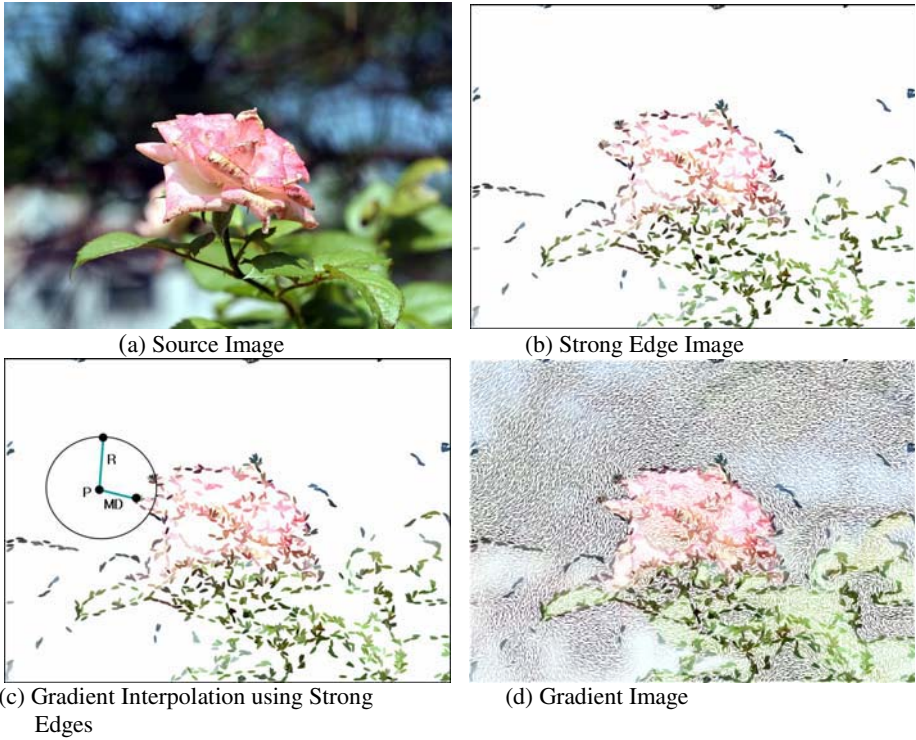


Fig. 3. Strong Edge Image and Gradient Interpolation Image



Fig. 4. Source Image and Result Image rendered in the impressionist effect of Van Gogh

$$Weight(i) = \left(\frac{MinDistance}{Distance(i)} \right)^b, i = 1, \dots, M \tag{2}$$

Equation (2) is a gradient interpolation function in order to calculate the weighted gradient value at each pixel (x, y) . The parameter *MinDistance* is the shortest distance from



(a) Source Image

(b) Result Image

Fig. 5. Source Image and Result Image using 120 palette colors from a 34 reference images

Point P to the strong edges on the radius R and is expressed as MD . The distance is the length between Point P and the strong edges on the radius R . M is the number of the strong edges on the radius R and b is a constant. Figure 3(c) explains Point P , MD and Radius R . This method is a variation of the method of interpolation used in morphing

[8]. Figure 3 shows the strong edges created and the interpolated gradient images using the method suggested in this paper.

3.3 Size and Shape

Brush strokes have sizes of 4 to 32 pixels depending on the area of their application. The divided areas are painted using big brushes first, and then smaller brushes. The brush strokes are expressed in spline curves as well as the linear lines as a result of the application of the edge clipping. The control points of the spline curves are chosen in reference to the gradient interpolation of each pixel, and expanded upward and downward or left and right with the spline curve as a line of reference that follows the minimum of 2 and the maximum of 10 control points along the gradient from the starting point.

4 Results

Figure 4 is an image rendered in the impressionist effect of Van Gogh using our algorithm. The color table of the brush stroke in Figure 4(b) is determined using palette colors from 75 palette colors generated by using 10 pictures of still life. Figure 5 are an images resulting from determining the 120 color of palette list generated by using 34 pictures of landscape. Also, the dynamic element that is dependent on the subjective motives of the artist is expressed, as the brush stroke follow the edges.

5 Conclusion and Future Work

We have proposed dynamic brush stroke generation method that produces painterly images. Brush stroke colors are derived from the palettes of well-known artists. Local gradients are supplemented by gradients interpolated from local edges.

The brush strokes in a real painting are determined by palette colors, varying orientation, shape, size, texture, grazing effect, mixed colors and other characteristics. To convey these effects, analyzing and simulating the hydro-mechanical characteristics of actual paints would be necessary.

Acknowledgement

This work was supported in part by MIC & IITA through IT Leading R&D Support Project.

References

1. Deng Y., B.S.Manjunath, Color image segmentation, CVPR'99, (1999) 2446-2451
2. Deng Y., Kenney C., M.S. Moore, B.S. Manjunath, Peer group filtering and perceptual color image quantization, ISCAS'99, (1999) 21-24

3. D.L. Ruderman, T.W. Cronin, C.C. Chiao, Statistics of cone response to natural images: implications for virtual coding, *Journal of Optical Soc. Of America*, Vol. 15, Number 8, (1998) 2036-2045
4. E. Euinhard, M. Ashikhmin, B. Gooch, P. Shirley, Color transfer between images, *IEEE CG&A*, Vol. 21, Number 5, (2001) 34-41
5. Hertzmann A., Painterly rendering with curved brush strokes of multiples sizes, *SIGGRAPH'98*, (1998) 453-460
6. Litwinowicz P., Processing images and video for an impressionist effect, *SIGGRAPH'97*, (1997) 407-414
7. Hays J., Essa I, Image and video based painterly animation, *NPAR2004*, (2004) 113-120
8. Beier T, Neely S, Feature based image metamorphosis, *SIGGRAPH'92*, (1992) 35-42
9. Silvers, R and Hawley, M. *Photomosaics*, New York:Henry Holt, 1997

Image-Based 3D Face Modeling from Stereo Images

Kyongpil Min and Junchul Chun

Department of Computer Science, Kyonggi University,
Yui-Dong Suwon, Korea
{cabbi, jcchun}@kyonggi.ac.kr
<http://giplab.kyonggi.ac.kr>

Abstract. This paper presents an automatic and novel method to generate a realistic 3D face model from stereo images. Typically, an image-based 3D face modeling system is in need of human intervention in facial feature extraction stage. To remove this human intervention, we propose HT(Hue-Tint) skin color model for facial feature extraction. Based on the proposed chrominance model, we can detect facial region and extract facial feature positions. Subsequently, the facial features are adjusted by using edge information of the detected facial region along with the proportions of the face. Moreover, the proposed facial extraction method can effectively eliminate the epipolar constraints caused by using stereo vision approach. In order to produce a realistic 3D face model, we adopt RBF(Radial-Based Function) to deform the generic face model according to the detected facial feature points from stereo images. For deformation locality parameter of RBF is critical since it can have significant impact on the quality of deformation. Thus, we propose new parameter decision rule that is applicable to scattered data interpolation. It makes clusters of feature points to detect points under the influence of each width parameter. From the experiments, we can show the proposed approach efficiently detects facial feature points and produces a realistic 3D face model.

1 Introduction

The requirements of a realistic and feasibly animated facial model have been increased because facial modeling has been an important field of diverse application areas such as virtual character animation for entertainment, 3D avatars in the internet, 3D teleconferencing, and face recognition. Face modeling technique is divided two categories by this information acquisition method. One is the method of using 3D scanning system and the other is acquisition method from 2D digital images. The basic idea is to take multiple simultaneous photographs of a face, each from a different point of view. Parke [1] improves a simple photogrametric method that uses orthogonal views of the face. Pighin et al. [2] have used an approach for creating photo-realistic textured 3D facial models from photographs of a human subject, and for creating smooth transitions of different facial expressions by morphing these different models. V. Blanz [3] proposes an approach that uses only a single photograph and a database of several hundred facial data and R. Enciso et al. [4] uses an approach that is based on computer vision techniques in which different pairs of stereo images are used to

create precise geometry. But these approaches require physical markers on the face, extensive human intervention because of correspondence or the need for a huge database of human faces.

In this paper we propose an automated 3D face modeling system from two frontal color face images. Figure 1 shows the block diagram of the proposed system. The system consists of three major phases: facial feature extraction process, 3D data acquisition process and face modeling process. In facial feature extraction phase, candidate skin region is determined by using HT color model. We verify candidate face region using feature's relational position information and apply Sobel edge detection method to candidate blocks of facial feature. These blocks are made by using the proportions of the face. In 3D data acquisition phase, we use stereo vision techniques to recover 3D scene from multiple images. In face modeling phase, we utilize scattered data interpolation with Gaussian RBF for 3D reconstruction of input face image. The performance of the interpolation depends critically on the choice of width parameter in Gaussian function. We can make more realistic face model, as we apply clustering method to parameter decision rule.

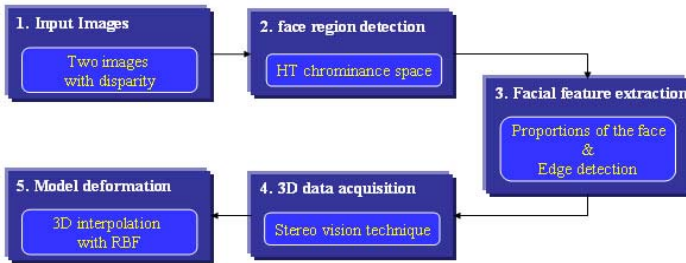


Fig. 1. Overview of the 3D Face Modeling Process

The rest of the paper is organized as follows. Section 2 explains the face and facial feature extraction method. Section 3 describes 3D information acquisition method from extracted feature points using stereo vision techniques. In section 4, we discuss scattered data interpolation with Gaussian RBF and width parameter decision rule. Face modeling results using proposed approach are provided in section 5. Conclusion is given in Section 6.

2 Face and Facial Feature Extraction

Face detection method can be broadly classified into feature-based methods and image-based methods. The feature-based methods make explicit use of face knowledge and follow the classical detection methodology in which low-level features such as color, edge, and are derived prior to knowledge-based analysis. In this paper, we use a new chrominance space for face detection and utilize the proportions of face and edge detection method for facial feature extraction.

2.1 Face Detection

Color information is efficient for identifying skin region. In computer vision, since every chrominance spaces have different properties, chrominance space selection is a very important factor for face detection. We use Hue-Tint chrominance space for face detection. Hue-Tint chrominance distribution is denser and easier to be represented by modeling method than other chrominance distribution[5]. And we calculate amount of the intersection between the normalized skin and non-skin histogram to evaluate the degree of overlap between the skin and non-skin distribution.

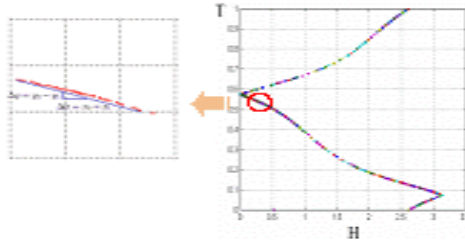


Fig. 2. Skin color distribution region in HT chrominance space[5]

Figure 2 shows that the shape of H-T distribution always looks like a straight line although distribution scatters longer than combinations of other components. We set up two points using the maximum and minimum values of H and T components. The skin chrominance distribution is modeled by a linear function defined as

$$f(h) = \frac{T_{min} - T_{max}}{H_{max} - H_{min}} (h - H_{min}) + T_{max}, \quad H_{min} \leq h \leq H_{max} \tag{1}$$

where h denote the H chrominance value of a pixel with coordinates (i, j) , the T_{min} , H_{min} are minimum values of T and H components, the T_{max} , H_{max} represent the maximum values of T and H components. To detect skin region, a decision rule is defined as follow:

$$d(x, y) = |f(x) - c(x, y)| \tag{2}$$

where $c(x, y)$ represents the measured values of the chrominance $(H(i, j), T(i, j))$ of a pixel with coordinates (i, j) in an image. If the equation (2) is less than threshold λ_s , then we consider $c(x, y)$ as a skin candidate pixel. Threshold value is obtained by comparison of every pixel over the skin samples with $f(c)$.

2.2 Facial Feature Extraction

We can detect face candidate region by HT chrominance space. Mouth and eyes region can be detected easily by relative positions of the holes in candidate facial region. But it is difficult to detect feature area without a distinct intensity variation, such as nose, jaw, cheek, and chin. So we apply the proportions of the face and edge detection method to exact facial feature extraction.

For facial feature analysis, we divide human face in the middle horizontally and can get two areas that include eyes and mouth respectively. The positions of eyes and mouth are determined by searching for minima in the topographic relief. We compute the mean value of every row and then search for minima in x-direction at the minima in the resulting y-relief. The eyes and mouse positions can be acquired respectively if significant minima in x-direction are detected.

The standard proportions of the human face can be used to determine its proper feature position and find their orientation. We can calculate these standard proportions on the basis of mouth and eyes positions. First, we create proper blocks that contain rough feature positions sufficiently by the proportions. Secondly, we apply 4×4 sobel edge detection method to a created block and make a histogram of detected edges in each blocks. Finally, by making an examination of variation positions in edge histogram we can extract facial feature positions.

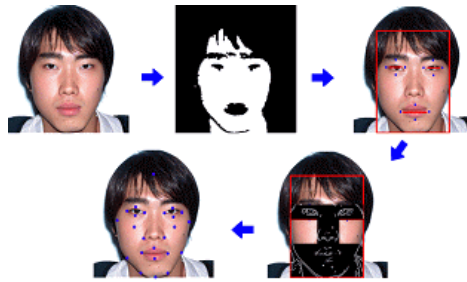


Fig. 3. The steps for facial feature positions extraction [5]

3 3D Information Acquisition

When 3D world coordinates is mapped on 2D image coordinates the depth information is lost. However, stereo vision technique can recover 3D scene from multiple images of the scene. Multiple cameras or one camera from different positions can give relative depth information. Thus, in this work, we use a single camera to acquire 3D information from two frontal face images.

3.1 Stereo Vision Techniques

In stereo vision[6], depth information is calculated by difference in locations and directions of two corresponding points which is called the disparity. In order to extract exact information about 3D coordinates of object, we must solve correspondence problem and reconstruction problem. The first one is to find corresponding matching points in stereo images and the second is to reconstruct 3D structure by interpolation method. Generally, human intervention is needed to find feature detection and the epipolar constraint is necessary to search entire image for every point in the other image to find corresponding points. Previously described facial feature extraction method using HT chrominance space and edge information can eliminate the epipolar

constraints and human intervention because the proposed method can extract feature point as corresponding points.

The coordinates of point P in the world coordinate system are given by (X_p, Y_p, Z_p) , whereas $(x_{left}, y_{left}), (x_{right}, y_{right})$ represent the coordinates of projections of P in image planes $Image_{left}, Image_{right}$, respectively. The (X_p, Y_p, Z_p) can be defined as

$$\begin{aligned}
 X_p &= \frac{(x_{left}y_{right} + y_{left}x_{right})\sin(\alpha) + (y_{right} - y_{left})f \cos(\alpha)}{(x_{left}y_{right} - y_{left}x_{right})\sin(\alpha) + (y_{right} + y_{left})f \cos(\alpha)} \cdot \frac{B}{2}, \\
 Y_p &= \frac{y_{left}y_{right}d}{(x_{left}y_{right} - y_{left}x_{right})\sin(\alpha) + (y_{right} + y_{left})f \cos(\alpha)} \\
 Z_p &= \frac{(f \sin(\alpha) - x_{right} \cos(\alpha)) \cdot y_{left}d}{(x_{left}y_{right} - y_{left}x_{right})\sin(\alpha) + (y_{right} + y_{left})f \cos(\alpha)} \\
 &= \frac{(f \sin(\alpha) - x_{left} \cos(\alpha)) \cdot y_{right}d}{(x_{left}y_{right} - y_{left}x_{right})\sin(\alpha) + (y_{right} + y_{left})f \cos(\alpha)}
 \end{aligned} \tag{3}$$

Where B represents the distance of projection centers in cameras, α denotes the degree of camera rotation, and f represent focal length. In this paper, we locate camera position in parallel. From equation, we have

$$X_p = B \cdot \frac{(x_{right} + x_{left})/2}{x_{right} - x_{left}}, \quad Y_p = B \cdot \frac{(y_{right} + y_{left})/2}{x_{right} - x_{left}}, \quad Z_p = B \cdot \frac{f}{x_{right} - x_{left}} \tag{4}$$

If the base line and focal length are known, Z can be calculated. The 3D information of facial feature points can be calculated by this method, but the other points is not. This problem is so-called to reconstruction problem. In order to solve this, we use interpolation technique to get 3D coordinates of these points. In the next chapter, we propose a suitable interpolation technique for a face modeling.

4 Face Model Generation

In order to generate specific face model, the generic face model is fitted to extracted geometric information from specific face images. We can make use of various deformation methods such as scattered data interpolation, anthropometry techniques, and projection onto the cylindrical coordinates incorporated with a positive Laplacian field function. In this research, we have used scattered data interpolation[7].

4.1 Scattered Data Interpolation with RBF

We have to consider two fitting process; the one fits estimated feature points in generic model to corresponding feature points and the other modify non-feature points in generic model using interpolation technique. Scattered data interpolation refers to the problem of fitting a smooth surface through a scattered or non-uniform distribution of data points. The advantage of using scattered data interpolation methods for fitting process is that they need fewer feature points than other method and guarantee

a smooth spatial deformation from corresponding feature points pair[8]. We have considered the problem of scattered data interpolation as follow:

Given

$$(p_i, q_i) \in \mathfrak{R}^3 \times \mathfrak{R}^3, \quad i = 1, \dots, N \quad (5)$$

find a continuous function $f: \mathfrak{R}^3 \rightarrow \mathfrak{R}^3$

$$f(p_i) = q_i, \quad i = 1, \dots, N \quad (6)$$

The points (p_i, q_i) are corresponding feature points pair and the points in \mathfrak{R}^3 are denoted either by \vec{x} , or $\vec{x} = (x, y, z)$. The class of solution to the scattered data problems is classified into five categories based on the form of the solutions: polynomial or piecewise continuous polynomial parametric solutions, algebraic solutions, radial basis function methods, Shepard's methods, and subdivision.

Radial basis functions, abbreviated RBF, is to define the interpolation function as a linear combination of radially symmetric basis functions, each centered on a particular feature point. In general, a RBF is a smooth, continuous function which interpolates the given data and provides at least C^1 [8]. A RBF is capable of closely interpolate smooth hyper-surface such as human facial structures. A scattered data interpolation methods based on RBF has the advantage as follows. First, the deformation process does not require equal number of nodes in the target meshes since missing points are interpolated. Second, mathematical support ensures that a deformed mesh approaches the target mesh, if appropriate correspondences are selected[7].

A RBF generally consist of two functions. Given N corresponding feature point pairs, they can be described by the following equation, where $\vec{x} = (x, y, z)$;

$$f_k(\vec{x}) = P_{mk}(\vec{x}) + \sum_{i=1}^N A_{ik} \Phi(\|\vec{x} - \vec{x}_i\|), \quad k = 1, 2, 3 \quad (7)$$

A_{Nk} is the weight associated with the N th RBF, centered at \vec{x}_i . $P_{mk}(\vec{x})$ is a polynomial of degree m , or is not present. Φ is a radial function, $\|\cdot\|$ denotes the Euclidean norm, such that:

$$\|\vec{x} - \vec{x}_i\| = [(x - x_i)^2 + (y - y_i)^2 + (z - z_i)^2]^{\frac{1}{2}} \quad (8)$$

It is necessary to decide a proper basis function, weight, centers, and width parameter for interpolation. The nonlinear basis function Φ can be formed using a number of different functions: multiquadric, inverse multiquadric, gaussian, thin-plate spline, shifted-LOG, cauchy function. The choice of a basis function is determined by the dimension of the interpolation problem, the interpolation conditions, and the desired properties of the interpolation[8]. Gaussian function can exist without polynomial precision and be used to deform a complex structure like a face. And gaussian is localized in a neighborhood near the center in comparison to other functions which have a global response. So we use gaussian function as a basis function. The basis function for the Gaussian is given by:

$$\Phi(\|\bar{x} - \bar{x}_i\|) = e^{-(\bar{x} - \bar{x}_i)^2 / \sigma} \tag{9}$$

In our research, since we consider feature points as center, we only decide weights and width parameter. Since we know 3D coordinates of feature points \bar{x} and vertices positions \bar{y} in generic face model corresponding to feature points, we can calculate weights by solving the following equations:

$$f_k(\bar{x}_i) = \bar{x}_i - \bar{y}_i$$

$$f_k(\bar{x}_i) = \sum_{j=1}^N A_{ik} \Phi(\|\bar{x}_i - \bar{x}_j\|), \quad k = 1, 2, 3 \tag{10}$$

4.2 Width Parameter Decision Rule

The range of influence of the basis function can be controlled by regulation a parameter σ of the RBF. σ is called the width or locality parameter. This parameter gives more weight value to near feature points and less weight value to far feature points. If the value of width parameter increases, they induce a smooth and more global interpolation. In our research, because basis function must be localized, we select a proper small parameter but it is as large as that represents the range of influence of the basis function sufficiently. A few selection method of width parameter is introduced [8, 9]. But currently used selection methods decide the width parameter by an experiment and applied it to the face model globally. Thus, when we set the same parameter values at different points it induces inaccuracy interpolation result because vertices of generic face model are scattered. Different parameter values at different points also been used to improve the accuracy of interpolation.

In this paper, we propose new parameter decision rule that is applicable to scattered data interpolation such as generic face model. We make clusters of feature points to detect points under the influence of each width parameter. We use the mahalanobis distance between feature points and furthest points from feature points in each clusters as width parameters.

$$\sigma_i = \max_i ([(\bar{x}_k - \bar{x}_i)' S^{-1} (\bar{x}_k - \bar{x}_i)]^{\frac{1}{2}}) \tag{11}$$

\bar{x}_k is points in k th cluster and S is the covariance matrix. Figure 4 shows a classification results by 25 feature points.

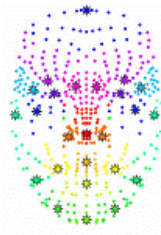


Fig. 4. Facial feature positions extraction Steps

In order to verify efficiency of interpolation by the proposed method, we make a comparison between our method and current state of art method. For test the average distance between feature points and the distribution of feature points are used for comparison. Since Gaussian functions present in the 2D are easily extendible into 3D, we can verify these efficiency by 2D graph. We set 100 points randomly and 5 feature points in these points arbitrarily. We measure position transformation of points except feature points according as feature points are moved. Figure 5 shows RBF interpolation results by each width parameter decision rule. A dotted line is a desired shape and a solid line is transformed from a straight baseline by interpolation.

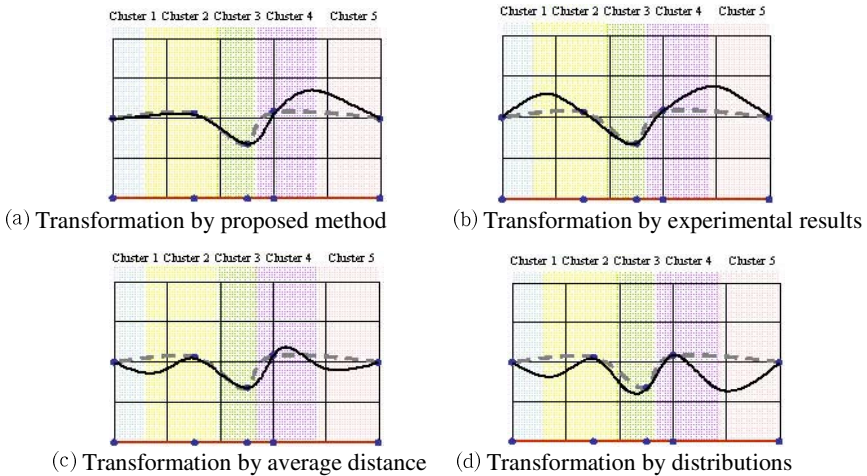


Fig. 5. RBF interpolation results using various width parameter decision rules

In figure 5, we can find difference of transformed line from desired line between fourth and fifth feature points according to every used decision rule. But we can find that transformed line by our proposed method is the more similar to desired line in other region within feature points than other decision rules.

5 Experimental Results

We have developed an automatic face modeling systems. It is programmed in C++/OpenGL/MFC and runs on a PC with 1.7GHz Pentium4 processors, 1GB RAM. Figure 6 shows face modeling steps by the proposed method. In our research, since we don't detect neck region in face detection stage, we eliminate neck from Waters's generic face model.

We can deform the specific person's face model in accord with various facial expressions. Figure 7 shows a smiling, disgusted, and angry face model.

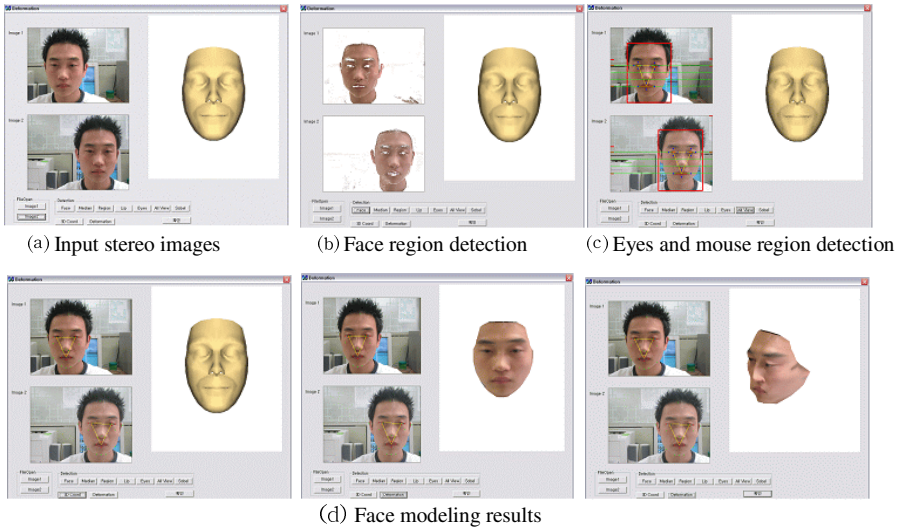


Fig. 6. Face modeling steps by the proposed method

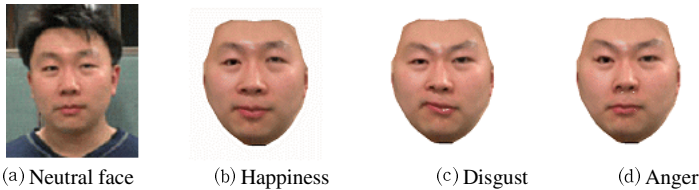


Fig. 7. Expressions synthesized on the face model

6 Concluding Remarks

In this paper, we have introduced an automatic 3D face modeling technique from stereo images. Our proposed method is based on stereo vision techniques. Stereo vision techniques have two problems: correspondence problem and reconstruction problem. Generally, the epipolar constraints and human intervention is necessary to solve a correspondence problem. In order to solve this problem, we use face and facial detection method based on a nonparametric skin color model. For facial feature extraction, HT chrominance space is applied to detect face region and we use the proportions of the face and edge detection method to detect facial feature position. In this process, we can effectively eliminate human intervention. We utilize scattered data interpolation with RBF to solve reconstruction problem. In this stage, it is necessary to decide a proper basis function, weight, centers, and width parameter for interpolation. Therefore, we use Gaussian function as basis function and propose a new width parameter decision rule, which makes clusters of feature points to detect

points under the influence of each width parameter. From experiments, we can prove that the proposed method is suitable to generate a realistic 3D human face model from 2D images.

References

1. F. I. Parke: *A parametric model for human faces*. PhD thesis, University of Utah, salt Lake City, UT, (1974).
2. F. Pighin, J. Hecker, D. Lischinski, R. Szeliski, and D. H. Salesin: Synthesizing realistic facial expressions from photographs. *In Computer Graphics SIGGRAPH'98 Proceedings*. (1998) 231-242.
3. Volker Blanz, Thomas Vetter: A morphable model for the synthesis of 3D faces. *In Computer Graphics, SIGGRAPH'99 Conference Proceedings*. (1999) 187-194.
4. R. Enciso, J. Li, D. Fidaleo, T. Y. Kim, J. Y. Noh and U. Neumann: Synthesis of 3D faces. *Proc. Int. Workshop on Digital and Computational Video*. (1999)
5. Kyongpil Min, Junchul Chun, Goorack Park: A Nonparametric Skin Color Model for Face Detection from Color Images. LNCS 3320. (2004) 115-119.
6. S. T. Barnard and M. A. Fischler: Computational Stereo. *ACM Computing Surveys (CSUR) Volume 14 Issue 4*. (1982) 553-572.
7. Noh, J., Neumann, U: A survey of facial modeling and animation techniques. *Tech. rep., USC 99-705*. (1998).
8. Wirth, M.A: A Nonrigid Approach to Medical Image Registration: Matching Images of the Breast. Ph.D. Thesis. RMIT University Melbourne Australia. (2000)
9. T. Lyche, L. Schumaker: Scattered Data Interpolation in Three or More Variables. *Mathematical Methods in Computer Aided Geometric Design*. Academic Press. (1989) 1-33.

Perception-Guided Simplification for Real Time Navigation of Very Large-Scale Terrain Environments*

Sheng Li^{1,2}, JunFeng Ji^{2,4}, XueHui Liu², GuoPing Wang¹, and EnHua Wu^{2,3}

¹ School of Electronics Engineering and Computer Science, Peking University, China
{lisheng, wgp}@graphics.pku.edu.cn

² State Key Lab. of Computer Science, Institute of Software, CAS, China
{jjf, lxx, weh}@ios.ac.cn

³ Dept. of Computer and Information Science, University of Macau, Macao, China

⁴ State Information Center of China, Beijing, China

Abstract. Interactive navigation over very large-scale terrain environments is a highly challenging topic since the model involved often contains huge amount of geometries and textures, even exceeds the capacity of system memory. In this paper, we put forward a high-performance technique for real-time walkthrough in very large-scale terrain environments. By the technique, perception-guided simplification is adopted through application of a new error metric-*Constrained Normal Cone* in the preprocessing stage. Both silhouette-preserving and shading-preserving criteria are satisfied in our navigation system. Furthermore, the pre-extracted *Potential Silhouette* from each block can be used to construct the incremental horizon at run time for delicate visibility testing. The consequent visibility information then can prevent the unnecessary data from loading into the main memory, so that the workload of out-of-core data paging and the number of triangles rendered are substantially reduced, and the frame rates are highly increased. Experiment results show the high performance of our novel approach.

1 Introduction

Ranging from drive simulation to 3D games, real-time rendering of large-scale terrain environment are widely used in a number of applications. However, the huge amount of primitive geometric data as well as the high precision texture often exceeds the real-time processing capability of the computer system. Two kinds of speedup method are usually discussed in virtual reality. One solution is to use the continuous level of detail (LOD) to simplify the complexity of the whole scene while maintaining the fidelity of the image to a certain extent [2, 4, 6, 11, 15]. The LOD technique can yield exponential reductions of polygons necessary to be rendered in each frame. Another solution is visibility culling technique, including frustum culling, backface culling and especially occlusion culling [10, 13, 17, 19]. During the course of terrain

* This research work is supported by National Key Project of Fundamental Research (973 Project No. 2004CB719403, 2002CB312102), NSFC (60573151, 60473105).

walkthrough, the viewpoint is generally close to the ground and the view direction is nearly kept on horizon, since the terrain has long depth of field, special culling algorithm is indispensable to accelerate rendering.

Both LOD and occlusion culling take CPU as the core engine to undertake most of the working load, so the speedup is obtained at the expense of extra CPU processing. Recently with the dramatic development of graphic processing units (GPU), the CPU-bound graphics pipeline shifts to high-speed GPU-centered framework with special graphics processing capability. The improvement on hardware results in the exploitation of new GPU-oriented terrain rendering algorithm [8, 9, 18]. In addition, along with the increase of details and expand of the terrain surface, a very large-scale scene generally contains massive data, often unable to be loaded in the RAM memory once-off. So to develop an efficient schedule algorithm for out-of-core data exchanging between RAM and external storage becomes more and more urgent.

In this paper we propose a high-performance real-time rendering technique for the navigation of out-of-core terrain environments. It may efficiently combine view-independent simplification with dynamic continuous block level of detail selection, which uses smooth vertex morphing between different levels of block to avoid popping artifacts. Using the importance of perception as the guide for simplification, a scheme of so-called *Constrained Normal Cone (CNC)* is proposed as a new error metric to decimate trivial triangles for each block in the preprocessing stage, thus the resultant mesh will have the silhouette-preserving and shading-preserving property. Compared with traditional simplification based on geometric error metric, the mesh generated by our method is more suitable to human perception in walkthrough system under the same simplification ratio. In our method, *Potential Silhouette (PS)* is extracted during the course of off-line mesh generation as a by-product, and it is ingeniously used to generate incremental horizon at run-time. As incremental horizon can provide the visibility information of the whole scene in advance, the invisible blocks won't be paged in and will not be rendered consequently, thus the interactive navigation process is greatly accelerated. Our technique makes the efficient use of CPU, GPU and I/O with high triangles throughput. Furthermore, incremental horizon can help accelerating the generation of real-time shadow for out-of-core outdoor terrain during navigation. Our method can not only be applied to PC platform but also be easily integrated into visualization system on C/S network infrastructure.

2 Related Work

Large-scale terrain visualization has been a research focus in recent years. Lots of continuous LOD (CLOD) algorithms have been developed to reduce the number of triangles. Quadtree structure is the most popular multi-resolution representation for terrain surface among them. It can generate hierarchical model easily and has the advantage of compact storage since connectivity and vertex positions are implicit in the regular grid. Classical quadtree-based algorithm [2, 11, 15] and semi-similar bintree-based algorithm [4] were used to generate view-dependent CLOD of the terrain scene. Regarding to the works, vertex error and block error computation based on screen space for simplification [11], smooth geomorphing between different LOD [2] and nicely generation of triangle strip of model surface [15] are discussed in detail.

Another important class algorithm of LOD organization is based on the construction of triangular-irregular-net (TIN) in different style [6]. It shows higher efficiency in approximating geometry surfaces than those based on regular hierarchical structure. But since more complicated data structure with more storage are required when building hierarchical representation, few large-scale terrain visualization systems use this scheme. Moreover, pyramidal structure texture is hard to be tiled on TIN surface.

The disadvantage of the CLOD is it is very costly to perform view-dependent LOD selection and triangulation. In order to decrease the CPU's workload on these tasks at run-time, a major bottleneck in the work, batched LOD strategy was put forward [9]. Batched LOD algorithm operates on clusters of triangles called batched triangles instead of manipulating single triangle directly, and the LOD selection is performed for each cluster of triangles. Cignoni et al provided the BDAM technique [1], in which TIN-structured triangle cluster is constructed off-line and the terrain rendering is the combination of a tiled quadtree for texture and a pair of bintrees of small triangular patched for geometry. Losasso et al harnessed the power of GPU, and proposed the geometry clipmaps techniques [8], which caches the terrain using video memory in a set of nested regular grids centered about the viewer. GPU-oriented batched LOD approach can be easily integrated with out-of-core data paging algorithm. Lindstrom put forward an efficient vertex storage scheme to optimize the data layout with good memory locality to improve memory coherency for data access [12].

Visibility determination is often used to accelerate terrain walkthrough. Cohen-Or et al made a good survey on visibility technique [3] for general virtual environment. To 2.5D terrain model, Stewart constructed a visibility structure of each block with fine-to-coarse resolution in turn for run-time culling [17]. Precomputation of voxel-tile visibility table for terrain was also used to facilitate occlusion culling in real-time terrain visualization [19]. The common weakness of the visibility culling algorithms mentioned above lies in that they all need to carry on a great deal of preprocessing, and the visibility information may take up lot of disk space for storage. Although dynamic horizon generation method for terrain works almost without any preprocessing [13] and feature-based cascading occlusion culling algorithm [10] do reduce the preprocessing, they do not provide support of out-of-core terrain data paging and the function of acceleration is merely restricted in reducing the number of triangles feeding to the rendering pipeline. So how to organize the visibility information and control the data paging in very large-scale terrain scene still need further investigation.

3 Framework Overview

The whole process of our navigation system is composed of two parts: off-line preprocessing stage and run-time rendering stage (see Fig. 1).

- Off-line stage

Through perception-guided simplification, the mesh generator converts the initial DEM data into hierarchical meshes. *CNC* is computed as the error metric for simplification, and the meshes are triangulated into triangle strips. At the same time, *PS* is constructed by sampling feature vertices during the course of triangulation. The whole hierarchical model is organized into a static quadtree with each node representing a portion of square area. Each quadtree node data is stored on the external storage with

linear index. Normal map of the scene can be obtained to enhance the realism of rendering while navigating.

- Run-time stage

Terrain visualization runs in multi-thread mode. The primary thread takes charge of the incremental horizon generation from *PS*, and then performs culling and LOD selection, finally activates the quadtree nodes and feeds the resultant meshes to the GPU. The slave thread is an I/O thread responsible for the geometry and texture paging from external storage. It accepts the uploading requests from the primary controlled by LOD and visibility information. Rendering process can be in different mode (texture, shading or shadow) according to user’s instructions.

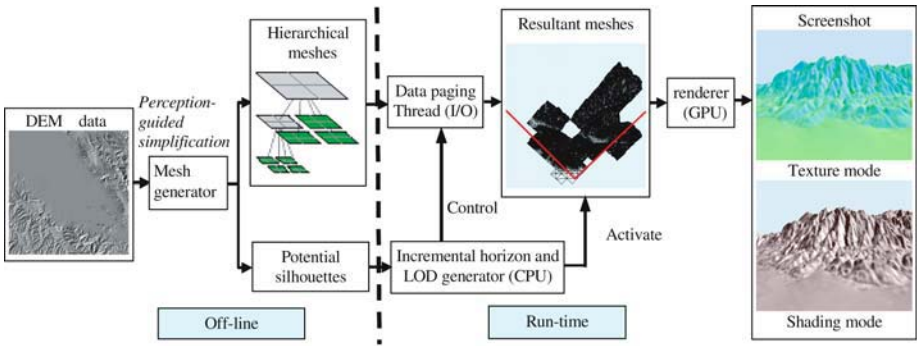


Fig. 1. High-performance terrain navigation system architecture

4 Perception-Guided Simplification

Hierarchical terrain structure is represented by a static quadtree in the similar form to that in [18]. Triangular mesh of a block is organized in triangles strip, and can be rendered simply by an OpenGL call. The level of node selection is determined by the view parameter at run-time navigation.

4.1 Constrained Normal Cone as Error Metric

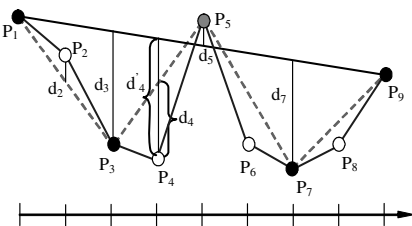


Fig. 2. 2D analogy to geometric error calculation of each vertex

simplified. Although the traditional error computation scheme can make the error of

Geometric error is generally used as error metric in previous simplification algorithm. But this kind of error computation can not reflect the shape of the model surface and its variation properly. As showed in Fig.2, vertical geometric error d_5 of vertex P_5 is determined by vertices P_1 and P_9 with a very small value. In fact, P_5 has high height difference with its left and right neighbors: P_4 and P_6 . A large error value ought to be assigned to P_5 to prevent it from being

P_5 as the maximum d'_4 finally by error transitivity, it is not scientific rigorously for model simplification after all. A good simplification algorithm should have high visual fidelity. The most important measure of fidelity is not geometric but perceptual [14]. Silhouette tends to be more perceptible than interior detail because it outlines the shape of a model or a scene (see Fig. 3). Furthermore, distortion in the silhouette is apt to mislead perception of the object in 3D space. In terrain visualization system, the mountains are continuous unceasingly and shelter from each other, fine silhouette detail seems to be the most valuable to the viewer. The importance of silhouette could be showed in Fig.3. In traditional CLOD algorithm, the popping artifact is more apparent at the silhouette region than others.

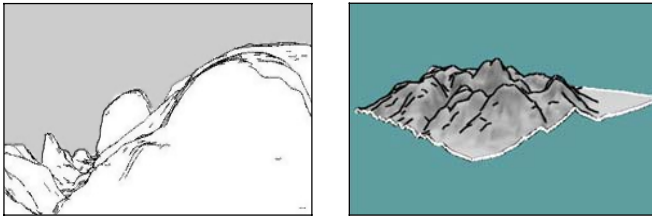


Fig. 3. The importance of silhouette to perception for terrain environments

In order to overcome the deficiency of traditional geometric-based simplification scheme, we propose a new perception-guided simplification by using *CNC* as a new error metric. It is a true local error representation and can maintain the silhouette detail.

Normal cone is an efficient method for silhouette testing

$\vec{n}_{NW}, S_{NE}, S_{SW}, S_{SE}$ with its normal $n_{NW}, n_{NE}, n_{SW}, n_{SE}$ respectively. $n_v = [n_{vx}, n_{vy}, n_{vz}]$ is the cone axis with cone semiangle θ . The cone axis and cone semiangle of each vertex V is computed by the following formula [16] :

$$\begin{cases} n_{vx} = \frac{1}{2} \left(\max_i n_{ix} + \min_i n_{ix} \right) \\ n_{vy} = \frac{1}{2} \left(\max_i n_{iy} + \min_i n_{iy} \right) \\ n_{vz} = \frac{1}{2} \left(\max_i n_{iz} + \min_i n_{iz} \right) \end{cases} \quad \begin{aligned} \cos(\theta) &= \min_i (n_i \cdot \bar{n}_v) \\ \bar{n}_v &\text{ is unit vector of } n_v \end{aligned} \quad (1)$$

where n_i represents $n_{NW}, n_{NE}, n_{SW}, n_{SE}$ in turn. Concave surface has no tendency to become silhouette through observation, therefore constraint on normal cone computation is necessary.

$$(n_{NW}, n_{NE}, n_z) > 0 \text{ and } (n_{SW}, n_{SE}, n_z) > 0 \Rightarrow \theta = 0 ;$$

$$(n_{NW}, n_{SW}, n_x) > 0 \text{ and } (n_{NE}, n_{SE}, n_x) > 0 \Rightarrow \theta = 0 ;$$

where n_x and n_z are the vectors of Z axis and X axis respectively (The terrain surface is defined on (x,z) domain). After cone semiangle of each vertex is computed, the error should have transitivity between relative vertices according to vertex dependency in the hierarchical structure. The error of each vertex is computed as follows: $e_v = \max\{\theta, \max_{v_i \in D_v}\{e_{v_i}\}\}$, where D_v is a set composed of all the descendents of

V. This error definition guarantees the monotonicity between son and father nodes. The error bound δ of each level of terrain block is defined as the following:

$$\begin{cases} \delta(0) = \max \theta, \delta(d) = \min \theta \\ \delta(i) = f(i, \max \theta, \min \theta) (0 < i < d) \end{cases} \quad (2)$$

Where $\max \theta$ represents the error bound for the largest block with coarsest resolution while $\min \theta$ for the block with the finest resolution; d is the depth of quadtree and f is a monotonically decreasing function of i . Using *CNC*, the simplified surface has feature of silhouette preserving. In comparison with traditional geometric-based simplification, mesh generated by our approach has more silhouette detail and is more suitable to terrain navigation. The pictures in Fig.4 are snapshots from the navigation, where (a) and (b) render with totally 25275 and 24677 triangles respectively. It is obvious that the image generated by our approach has fewer artifacts. The image quality improves a lot than before. For diffuse illumination the shading variation is proportional to cone semiangle. In general the simplified surface will exhibit more shading artifacts for larger cone semiangle. As cone semiangle could be defined as the error to conduct simplification, the vertex has high semiangle value will be decimated after those with low value. So the resultant shading artifact will be very small. It means that our simplification based on *CNC* satisfies the shading-preserving criteria.

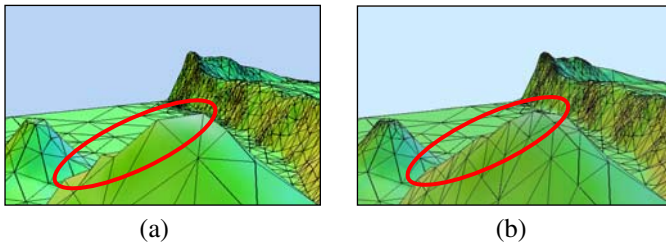


Fig. 4. (a) Geometric error based simplification (b) *CNC* based simplification

4.2 Potential Silhouette

Computation of *CNC* for each vertex can also be used to construct the *PS* of a terrain block in the preprocessing. *PS* is a polyline structure that can outline a portion of a terrain scene, it will play very important role for visibility determination in visualization stage. For any given viewpoint, the perspective of *PS* approximate the contour generated with perspective of real 3D scene. Extraction of *PS* includes double sampling. The first sampling process is a by-product of triangle strip generation of the block along with traversal of all the vertices. Each sampled vertex has a priority

value: $Priority_{(x,z)} \propto height_{(x,z)} \cdot \theta_{(x,z)}$, where $height_{(x,z)}$ is elevation value and $\theta_{(x,z)}$ is the cone semiangle of vertex. The vertex is added to priority set once its priority value exceeds the user-defined threshold. After sorting these vertices in the priority set according to x , we use linear optimization algorithm to perform second sampling from the priority set. A fixed number of vertices are extracted in x sequence that can be seen as a polyline representing the PS in x direction. Similarly, we can extract the PS in z direction. Two polylines constitute PS to approximate the profile of the terrain within a block. The silhouette is fusion of the exterior outline formed by perspective projection of two polylines while navigating. The PS within a terrain block is stored as the summary information for each block.

5 Incremental Horizon and Out-of-Core Paging

Horizon is the boundary between sky and terrain in 3D space. Any scene beyond and below the horizon is definitely invisible and will be culled out. The PS structure extracted in preprocessing stage provides us a good solution to get the horizon. In fact, terrain environment is not a true 3D but 2.5D model, so the silhouette can actually build the occlusion horizon of a terrain scene. After the preprocessing, bounding box, PS and block neighbours relation etc. are stored as summary information for each block. At run time, we can render the PS of each active node in front-to-back order to track the accurate horizon, therefore detect the self-occlusion in the scene within the view frustum. The whole testing and update process contains two steps:

- Top-most edges of the bounding box are perspective projected onto the screen space with scan-conversion, its projection heights are tested against the corresponding value stored in the 2D horizon. If the projection heights are higher than the horizon value at any point, the scene within the block is visible; otherwise the block is occluded and labeled as invisible.
- The PS of visible terrain block should be projected to update the horizon in the following. The elder value in the height array (2D horizon) should be replaced by a new one instead whenever the projected value is greater than the height in current array. The PS nicely extracted previously makes the horizon generation at very high precision. Hence it is guaranteed that the visibility testing is efficient.

The incremental horizon generation and occlusion culling function are as showed in Fig. 5. The images at the lower row represent different phase of traversal, where the blank regions are those being culled as occluded. The upper row illustrates the generation process of incremental horizon during the traversal, where the green curves represent the current horizon values used to cull the scene behind.

Data paging of very-large scale terrain is controlled by two key factors: valid view, level of block detail. The valid view denotes which blocks cover the visible scene to the current viewpoint. If the geometric data and texture data to be rendered are not resident in the system memory, they should be requested to be uploaded from external storage. During walkthrough, if a block belongs to the valid view but the geometric data not resident in the memory, an upload request then will be sent to the geometry request queue along with the movement of viewpoint, which will be processed by slave thread - I/O thread. Those lying in the view-frustum but occluded corresponding to the nodes and their parents and ancestors will not be added to the request queue,

although the correlative geometric data have not been in the system memory. Because the data uploaded each time are batched geometric data, the schedule will be at coarse granularity level and thus save much system overheads. Since communication between primary thread and slave I/O thread is required to cooperate with each other, mutex is used to synchronize the two threads. In our system implementation, some redundant block are necessary to resident in the system memory so that they can cover a bit larger area of valid view, such configuration can prevent frequent paging caused by fast movement of viewpoint despite of more memory overhead.

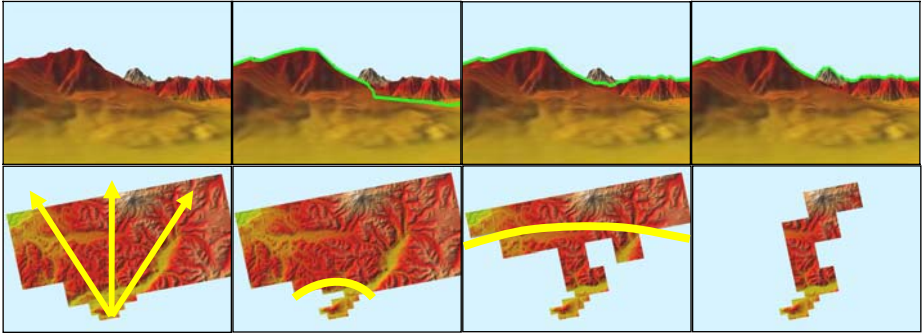


Fig. 5. The generation and update process of incremental horizon

6 Experiments and Analysis

Two models as listed in table 1 are tested. The program is running on a PC with P4 2.5G Hz CPU and a GeForce4 graphics card with a system memory of 512M. We design the experiment under two different modes: walkthrough under predefined course or walkthrough with freedom by user interaction. We sample 38575 frames and 39136 frames from course navigation of Puget Sound and Wenatchee respectively. Besides, 10000 frames are sampled for each in free walkthrough mode.

Table 2. first gives the statistics on geometric data exchange during course navigation. The comparison is between enabling incremental horizon state (IH on, our algorithm) and disabling incremental horizon (IH off, others). Both the number of data read from external storage and the number of data released from system memory in our algorithm are less than others. The reduction ratio seems not very high because we expand the resident area covered by valid view to maintain more terrain block in the memory, even then our algorithm consumes less system memory. The improvement of our approach is evident seen from Fig. 6. Three approaches including Lloyd [13], Ulrich [18] and our approach are adopted to test their performance. In the course of navigation, we obtain as much as 2~3 times frame rates in comparison with algorithm in [18]. Although similar horizon technique is used in algorithm [13], we improve about 50% of the performance. Since the *PS* is used to approximate horizon with more precision to perform occlusion culling and control out-of-core data paging efficiently, it is logical to archive much higher frame rates by our method.

Table 3 is the statistics data collected from the navigation, where the average frame rates and average number of triangles per frame are listed. It can be seen the speedup obtained by our approach is very obvious for very large-scale terrain. Our approach shows more privileges on speedup of those environments with many occluders.

Visibility information is essential to any shadow generation algorithm. Although Govindaraju proposed a new umbra shadow approach [5] using cross culling to reduce geometry complexity of large virtual environments, it is restricted by the complex multi-CPU&GPU architecture that has no generality. Incremental horizon technique mentioned above makes quick computation of Potential Visible Sets (PVS_E and PVS_L) available, and then a two-pass rendering by shadow map can generate the hard shadow in real time. Meanwhile, the perception-guided simplification induces smooth boundary of shadow with high fidelity and less aliasing artifact.

Table 1. Terrain models for experiments

Models	Dimension	File size(M)	Real Tri.s	Deg. Tri.s	Tree Depth
Puget Sound	8193	563.8	71842336	38301810	8
Wenatchee	8193	257.9	32667175	17498037	7

Table 2. Data exchange statistics during pre-defined course navigation

	Puget Sound		Wenatchee	
	IH on	IH off	IH on	IH off
Data uploaded	398.9M	455.6M	71.2M	82.9M
Data unloaded	381.8M	421.8M	58.0M	66.5M

Table 3. Statistics on terrain navigation with different approach

Model \ Approach	Our approach		[18]		[13]	
	Frames	Triangles	Frames	Triangles	Frames	Triangles
Puget Sound	80.7	479.5 K	31.3	1559.0 K	52.8	770.2K
Wenatchee	169.6	121.5 K	73.1	845.7 K	116.0	277.8K

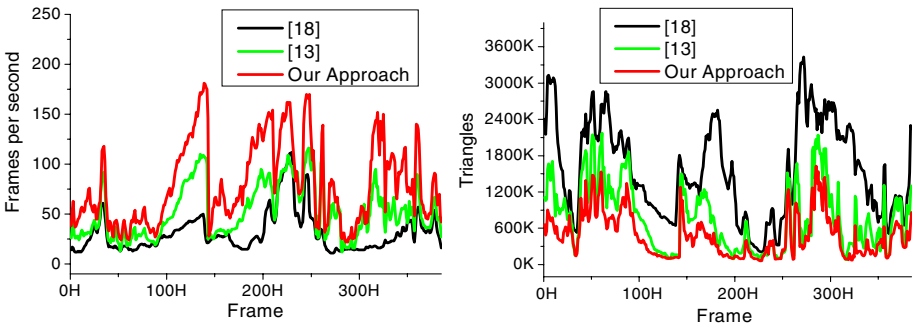


Fig. 6. Frame rates and rendering complexity in Puget Sound according to pre-defined course

7 Conclusion

We propose a new speedup technique for out-of-core terrain navigation. It makes real-time rendering of very large-scale terrain environments possible. Within the high-performance visualization framework, CPU, GPU and I/O work corporately to perform inactive navigation. The perception-guided simplification is more suitable to walkthrough of terrain scene, where most of the portions on terrain surface are occluded by mountains on either side. In the future, we will focus on more realistic rendering of complex outdoor environment, which will take sun lighting and atmosphere scattering etc. into account. How to reduce the rendering complexity of the scene and make use of the feature of new graphics card still need further exploration in computer graphics and terrain visualization.

References

1. P. Cignoni, F. Ganovelli, et al. BDAM – Batched Dynamic Adaptive Meshes for High Performance Terrain Visualization. *Computer Graphics Forum*, vol. 22(3), pp. 505-514, 2003.
2. D. Cline and P. Egbert. Terrain Decimation through Quadtree Morphing. *IEEE Trans. on Visualization and Computer Graphics*, vol. 7 (1), pp. 62-69, 2001.
3. D. Cohen-Or, Y. Chrysanthou, et al. Visibility: Problems, Techniques, and Applications. Course #30 SIGGRAPH 2001, August 2001.
4. M. Duchaineau, M. Wolinsky, et al. ROAMing terrain: real-time optimally adapting meshes. *IEEE Visualization97 Proceedings*, pp.81-88, October 1997.
5. K. Govindaraju, Brandon Lloyd, et al. Interactive shadow generation in complex environments. *ACM Transaction on Graphics*, 22(3), pp. 501 - 510, July 2003
6. H. Hoppe. Smooth view-dependent level-of-detail control and its application to terrain rendering. *IEEE Visualization'98*, pp. 35-42, Oct. 1998.
7. D. Johnson, and E. Cohen. Spatialized Normal Cone Hierarchies, *Proceedings of ACM Symposium on Interactive 3D Graphics*. pp. 129–134, March, 2001.
8. F. Losasso, H. Hoppe. Geometry clipmaps: Terrain rendering using nested regular grids, *ACM SIGGRAPH 2004* , 769-776, 2004
9. J. Levenberg. Fast view-dependent level-of-detail rendering using cached geometry. *IEEE Visualization 2002*, pp. 259-266, 2002.
10. S. Li, X. Liu, E. Wu. Feature-based visibility-driven CLOD for terrain. *Pacific Graphics'2003*, IEEE Computer Society Press, pp.313-322, Canmore, Canada, 2003.
11. P. Lindstrom, David Koller, et al. Real-time, continuous level of detail rendering of height fields. *Proceedings of SIGGRAPH'96*, August 1996. pp. 109-118, 1996.
12. P. Lindstrom, Valerio Pascucci. Visualization of large terrains made easy. *IEEE Visualization'2001 Proceedings*, pp. 363-370, October 2001.
13. B. Lloyd, P. Egbert. Horizon Occlusion Culling for Real-time Rendering of Hierarchical Terrains. *Proc. of IEEE Visualization2002*, pp.403-410, Boston, Oct. 2002.
14. P. Luebke, B. Hallen. Perceptually-Driven Simplification for Interactive Rendering, *Proceedings of the 12th Eurographics Workshop on Rendering Techniques*, pp.223-234, June 25-27, 2001.
15. R. Pajarola. Large scale Terrain Visualization Using the Restricted Quadtree Triangulation. *Proc. of IEEE Visualization '98*, pp. 19-26, 1998.
16. L. Shirman and S. Abi-Ezzie. The cone of normals technique for fast processing of curved patches. In *Eurographics'93 Conference Proceedings*, Vol. 12, pp. 261-272, 1993.

17. J. Stewart. Hierarchical visibility in terrains. Eurographics Rendering Workshop, pp. 217-228, June 1997.
18. T. Ulrich. Rendering Massive Terrains using Chunked Level of Detail Control. In Course Notes of ACM SIGGRAPH 2002, volume Course 35, 2002.
19. B. Zaugg and P. Egbert. Voxel Column Culling: Occlusion Culling for Large Terrain Models. *VisSym 2001-Eurographics/IEEE Symposium on Visualization*, pp. 85-93, May 2001.

3D Building Reconstruction from LIDAR Data

Yuan Luo¹ and Marina L. Gavrilova²

¹ Department of Computer Science, University of Calgary, Calgary, AB, Canada
yluo@cpsc.ucalgary.ca

² Department of Computer Science, University of Calgary, Calgary, AB, Canada
marina@cpsc.ucalgary.ca

Abstract. As a fast data acquisition technique, Light Detection and Ranging (LIDAR) can be widely used in many applications, such as visualization, GIS and mobile communication. Since manual surface reconstruction is very costly and time consuming, the development of automated algorithms is of great importance. In this paper a fully automated technique to extract urban building models from LIDAR data is presented. First, LIDAR points are re-sampled into regular grids with the optimal pixel size. After filling holes in the range image, Delaunay Triangulation is utilized to generate 3D triangle meshes. Building height mask is then applied to extract building roof points. Finally, a geometric primitive-based fitting approach is adopted to verify and refine the reconstructed models. The algorithm is tested on two buildings from a locally acquired LIDAR data set. The results indicate that our approach is suitable for automatically producing urban building models from LIDAR data.

1 Introduction

Accurate 3D surface models in urban areas are essential for a variety of applications, such as: urban planning, environment monitoring, geo-information systems, traffic managements, utility services, and military operations. In most of these cases, the models of buildings, terrain features, and vegetations are the primary features of interest. A European Organization for Experimental Photogrammetric Research survey on city models showed that 95 percent of participants were most interested in 3D building data [1]. Urban areas are rapidly changing mainly due to human activities in construction, destruction, or extension of topographic elements such as buildings and roads. This mandates the availability of fast data acquisition technique and automatic method for detecting and extracting 3D topographic objects from the data.

Airborne laser scanning is a new technology in which several sensors are integrated to obtain 3D coordinates of points on the earth. It makes use of precise GPS instruments to determine the position of the sensor, inertial navigation system (INS) to determine the attitude of the sensor, and narrow laser beams to determine the range between the sensor and the target points. Figure1 shows the LIDAR system components. The system is an active system, so the data can be gathered during the day and night. LIDAR data is dense, with high accuracy, but one still needs to extract higher-level features from it.

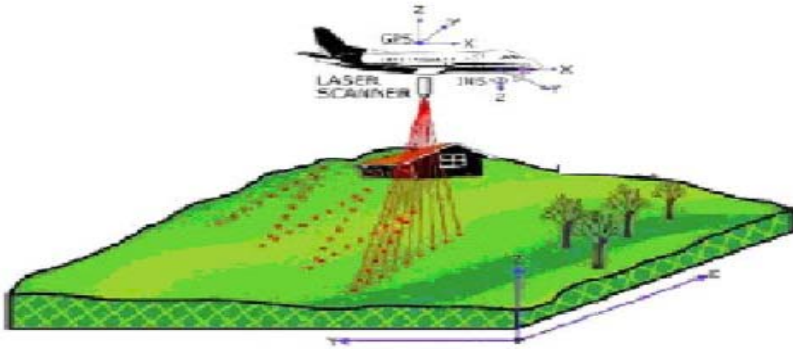


Fig. 1. LIDAR System Components (from reference [11])

In this paper, we present a fully automated system that can extract urban building models from LIDAR data. The system is tested on two buildings from locally acquired LIDAR data sets. The test results indicate that our system is suitable for automatically producing building models from LIDAR point clouds without other auxiliary information such as aerial images. The rest of this paper is organized as follows: Section 2 describes some related literatures. We present the whole system framework in Section 3. Detail description of each processing step is extended in the following subsections. Experimental results are given in Section 4. Finally, Section 5 draws some concluding remarks and includes proposal for future work.

2 Related Work

Over years, a number of researchers have appeared to address the urban building extraction problem from photogrammetry or from laser sensing data [2, 3]. Although one pair of images, using photogrammetry, is adequate to find the 3D position of two corresponding and visible image features; it is not sufficient to extract the entire building data due to the hidden parts. Building extraction can be done using multiple images to avoid this deficiency. On the other hand, buildings can also be extracted directly from digital surface models (DSM) as those produced by LIDAR.

LIDAR has received a growing amount of attention in research and commercial use in the recent years [4]. For example: Elaksher etc. [5] proposed a system for the reconstruction of planar rooftop building wire-frames from LIDAR data. Tse and Gold [6] presented two different methods for building reconstruction using LIDAR data. The first is a traditional method using filtered LIDAR data and combining cadastral building boundaries data. The second uses the Voronoi Diagram to trace building outlines and applies the CAD-type Euler Operators to create a TIN model. These two methods can extrude buildings on the terrain, however in general they are not suitable for reconstructing the roof structures. In [7], the authors describe a strategy for automatic building extraction from aerial imagery and digital elevation models. Building regions are extracted coarsely from DEM and then some filters are applied to the selected regions based on their shape, size and content to enhance the detectability of the buildings. Further recognition is achieved based on the image features. Buildings are then reconstructed from the listed features. However, this algorithm requires

additional information from aerial images to reconstruct building models. Morgan and Tempeli [8] present the technique to produce DEM from laser data. Prior knowledge about the buildings and terrain is needed for both their detection and extraction processes. Other similar methods ([9, 10]) either require reference points from users, or additional texture information from other image sources.

3 System Description

The block diagram shown in Fig.2 depicts the prototype of our modeling system. Three stages constitute the system. The first stage *Data Preprocessing* includes three steps: re-sampling, hole-filling and tessellation. At the very beginning, we resample LIDAR point clouds into regular grid cells to produce a range image suitable for tessellation. After filling the noise holes, Delaunay Triangulation (DT) is utilized to get the 3D triangle mesh model. Here, Quick Hull algorithm is used to calculate DT through Convex Hull. At the second stage - *Model Classification*, all the LIDAR points belonging to the building roof are extracted. A building mask based on height threshold is used for this purpose. Finally, a geometric primitive-based fitting approach is adopted to verify and refine the reconstructed model in the last stage - *Model Refinement*. Detail description of each stage will be given in the following subsections.

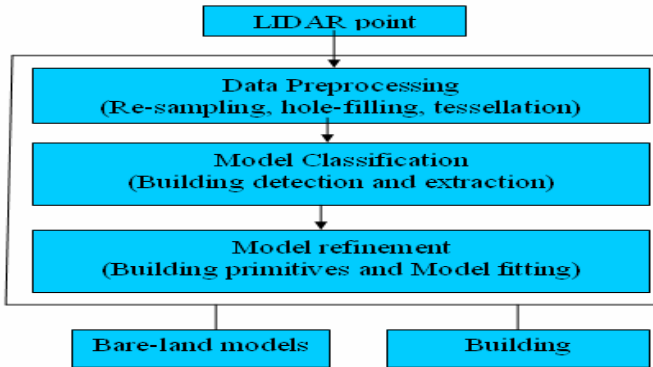


Fig. 2. A flowchart of the proposed building reconstruction system

3.1 Data Preprocessing

Prior to any analysis or segmentation of the laser data, processing of the laser point data should be performed. In order to acquire a height field for point clouds, we first project and re-sample LIDAR points onto regular grids. The best result of re-sampling is that each pixel/cell contains one and only one laser point. More points in a cell will increase the information loss since the cell at the end, after interpolation, will get only one value. On the other hand, if the pixel size is too small and the number of pixels that contain no laser points becomes large, the redundancy increases as well as the storage requirements. Considering laser points which are not highly irregular, the optimal re-sampling pixel size is equal to the minimum density of the LIDAR points: having n

points distributed as grid in a unit horizontal area, the linear spacing between each two points in a row or column is $1/\sqrt{n}$ meters.

Due to laser occlusions and the nature of the material being scanned, there are lots of holes in the height field. To remove those holes, hole-filling operation is performed directly by interpolating the height values in the height field. There are many interpolation methods, see [12] for a discussion. To preserve the edge information, an adaptive weighting distance-based interpolation approach is applied. The interpolation weights are determined by an inverse function of the distance between the neighbor points and the point to be interpolated. The window size of interpolation is adaptive to the LIDAR point density to ensure sufficient points for filling the holes.

The last step of *Data Preprocessing* is tessellation. Usually, triangular meshes are used as the primitive for representation and rendering because they are easily converted to other geometric representation; many level-of-detail techniques use triangular meshes; photometric information is easily added with texture projects, and graphic hardware supports fast rendering of triangular meshes. For triangulation algorithms, the closest-neighbor triangulation and Delaunay triangulation are the two most popular methods. Delaunay triangulation appears to be superior to preserve the topology and connectivity information of the original data. We implement Quick Hull algorithm ([13]) to compute the convex hull and Bowyer-Watson Algorithm ([14], [15]) for DT both in 2D and 3D. In 2D case, points are structured to shape triangles within 2D convex hull of the data. Only two sets of coordinates, namely, X and Y, are used for this purpose and the spatial relationships among points are limited to their projected distance to the X-Y plane. Constructing the 3D Delaunay tessellation on the laser data produces tetrahedrons that have laser points as their vertices within 3D convex hull. Comparing the results of 2D and 3D Delaunay, we can note that the topology of buildings is preserved better by using 2D Delaunay triangulation approach. Experimental results are shown in Section 4.

3.2 Model Classification

In our system, the original LIDAR model is segmented into two components: buildings and bare-land. The building subset is a collection of the building models represented through the parametric forms, while the bare-land subset is the reconstructed 3D mesh model with the buildings removed.

The differences in the elevations are used to select the candidate building points, because the objects, either vegetation or buildings, should have the height above a certain value. So, by applying a height threshold to the reconstructed 3D mesh data, we can create an approximate building mask. The mask is applied to filter all the mesh points, and only those marked points are extracted as building points. The algorithm detailed below:

- (1) *Project all preprocessed LIDAR points onto X-Y plane;*
- (2) *Form a 2D gray-level image, with each grid gray-scale indicated by its elevation;*
- (3) *Choose an appropriate height threshold (with a height of 5.0 meters or more above the surrounding terrain in our experiments) to binarize the gray-scale image.*

A classification example is shown in Fig.3. The white square in (c) is the building roof, a fraction of points belongs to the building model, while the points in the black area belong to surrounding terrain areas (the bare-land model).

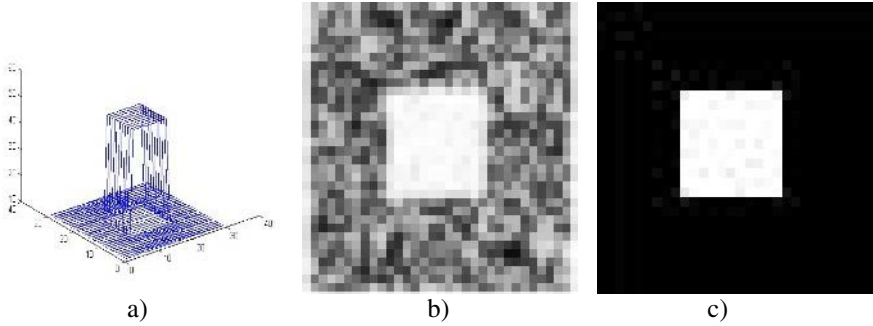


Fig. 3. One of the results of model classification: a) Preprocessed LIDAR point clouds that contain one flat-roof building; b) Projection result of (a), with points elevation as its gray-scale; c) Binarization result of (b)

3.3 Model Refinement

After all building points are extracted, a geometric primitive-based approach is adopted to verify and refine the reconstructed models. We divide a complex building into several basic building primitives and model them using a parametric representation. The parametric model describes the primitive by a small but fixed set of variable parameters. The number of parameters needed to be specified depends on the properties of each primitive and the knowledge assumed for model fitting. For example, a generic plane in 3D space can be represented as:

$$Z=aX+bY+c \tag{1}$$

where a, b represent two slopes in the X and Y directions and the parameter c is an offset parameter. For fitting strategies, the simplest and also the most effective one – the least-square fitting, is chosen. The method of least squares assumes that the best-fit curve of a given type is the curve that has minimal sum of the deviations squared (least square error) from a given set of data. For example, if we want n points to be fitted into the plane equation (1), i.e. the sum of least square error should be minimal. According to the Extremum Principle, we get three linear equations for a, b, c as follows:

$$\begin{aligned} \left(\sum_{k=1}^n X_k^2\right)a + \left(\sum_{k=1}^n X_k Y_k\right)b + \left(\sum_{k=1}^n X_k\right)c &= \sum_{k=1}^n Z_k X_k \\ \left(\sum_{k=1}^n X_k Y_k\right)a + \left(\sum_{k=1}^n Y_k^2\right)b + \left(\sum_{k=1}^n Y_k\right)c &= \sum_{k=1}^n Z_k Y_k \\ \left(\sum_{k=1}^n X_k\right)a + \left(\sum_{k=1}^n Y_k\right)b + nc &= \sum_{k=1}^n Z_k \end{aligned} \tag{2}$$

Solving this linear system, the best estimation for a, b, c is achieved. The adjusted plane parameters are then used to refine the LIDAR DSM points.

The following summarizes the two most commonly used building primitives, including their mathematical parametric representations, and examples of building fitting.

3.3.1 Plane Primitive

The flat-roof is a typical roof type of man-made buildings, which can be modeled using the plane-primitive group. Once the roof borders have been extracted (Fig.3.(c)), we parameterize them using least-square fitting (Equation (1)). The plane parameters are checked to find if any plane has small slope values, i.e. the values of the parameters a and b are negligibly different from zero. In this case, the plane is assumed horizontal. The mathematical description of the process is shown in Equation (3):

$$Z_{n \times 1} - aX_{n \times 1} - bY_{n \times 1} - c = 0$$

$$a=0 \text{ AND } b=0$$
(3)

where n is the number of points in the region.

3.3.2 Slope Primitive

The slope-roof is another typical roof type. Comparing the flat-roof building, the depth fitting for sloped surface is more complicated. The ridge line is detected to divide the roof into two planes, so that the least-square fitting also works for this case. As pictures shown in Fig.4, we depict Z coordinates of all building roof points. If it's a flat-roof building, all points' elevations are limited to a small range, like Fig.4.(a); if it is a slope-roof building, there is a peak which is also the position of roof ridge line, like Fig.4.(b).

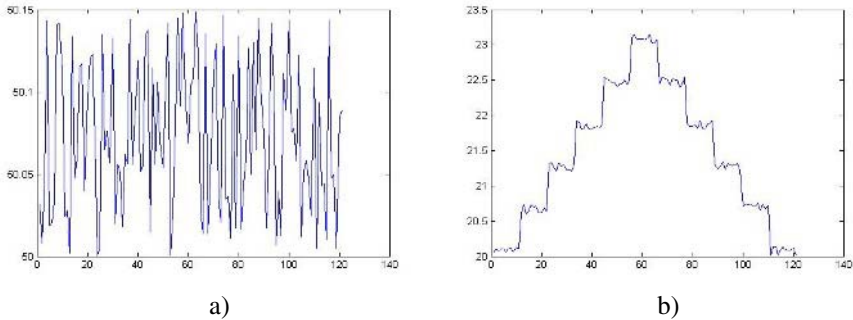


Fig. 4. Signature Graph of Building Points' Elevation: a) the result for flat-roof building; b) the result for slope-roof building

We observe that most of real buildings usually have two symmetric slopes. To facilitate this structure, each two adjacent planes are checked to find if they satisfy a slope symmetry condition, as one would expect in a conventional gabled roof. The complete mathematical description that is used to find the parameters of two symmetric planes is shown in Equation (4):

$$\begin{aligned}
 Z_{nx1} - a_i X_{nx1} - b_i Y_{nx1} - c_i &= 0 \\
 Z_{mx1} - a_j X_{mx1} - b_j Y_{mx1} - c_j &= 0 \\
 a_i + a_j = 0 \quad \text{OR} \quad b_i + b_j &= 0
 \end{aligned}
 \tag{4}$$

where n is the number of points in region (i), m is the number of points in region (j). Experimental results are shown in Section 4.

4 Experimental Analysis

Two datasets are acquired from the Department of Geomatics Engineering, courtesy of Prof. Ayman Habib, University of Calgary and our system is tested on these two LIDAR data sets. One dataset contains a flat-roof building with 900 LIDAR points; the other contains a garbled-roof building with the same amount of points. First, the point density of these two data sets is computed in order to get the optimal pixel size for re-sampling. The point density of 1st dataset is 0.971453, and the 2nd one is 0.971066. After re-sampling the points onto regular grids and filling the holes in the range image, we could directly plot the scattered points in 3D (Fig.5).

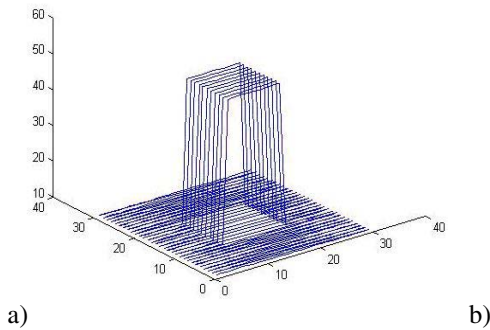


Fig. 5. 3D visualization of preprocessed LIDAR point clouds: a) The visualization result for the 1st dataset; b) The visualization result for the 2nd dataset

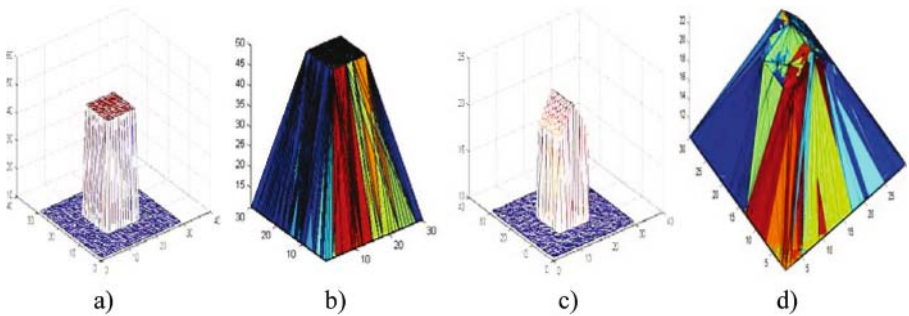


Fig. 6. Visualization Results of DT: a) The result of 2D DT on the 1st data set; b) The result of 3D DT on the 1st data set; c) The result of 2D DT on the 2nd data set; d) The result of 3D DT on the 2nd data set

Both 2D and 3D DT are implemented as tessellation methods for reconstructed models.

Obviously, the topology of buildings is preserved better by 2D Delaunay. In addition, the time to compute 2D DT is much less than that of 3D. That's why 2D DT is chosen to get the DSM of LIDAR points in this paper.

The model classification results on 1st dataset are shown in Fig.3. The segmentation result on the 2nd dataset is shown in Fig.7. The extraction results of plane-roof and slope-roof buildings are almost the same. That's why we have to detect the ridge line of slope-roof buildings, so that we can differentiate these two kinds of buildings.

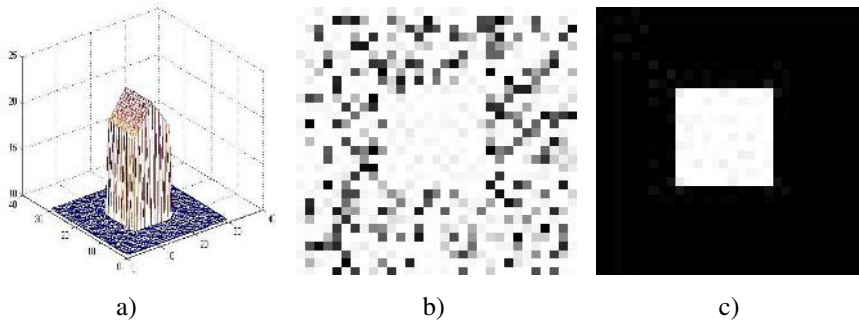


Fig. 7. Results of model classification on the 2nd dataset: (a) DTM of the 2nd dataset using 2D Delaunay triangulation b) Projection result of (a), with points' elevation as its gray-scale; c) Binarization result of (b)

Finally, as the results of the geometric fitting approach, the Bare-Land models and Building Models are shown in Fig.8.

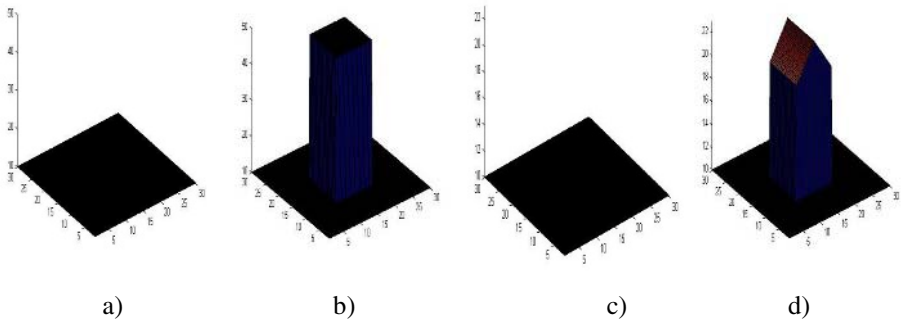


Fig. 8. Results of geometric primitive-based fitting: a) Bare-land model of 1st data set; b) Reconstructed flat-roof building model; c) Bare-land model of 2nd data set; d) Reconstructed garble-roof building model.

5 Conclusion and Future Work

In this paper a fully automated technique to extract urban building models from LIDAR data is presented. The system is tested on two buildings from locally acquired LIDAR data sets. The test results show that our system is suitable for automatically producing building models from LIDAR point clouds without other auxiliary information.

Future work includes modeling a range of complex buildings with irregular shapes by combining appropriate geometry primitives and fitting strategies. Also, in order to get high quality visualization result, some additional property data such as color or texture can be imported from other image sources.

References

1. W. Forstner, 3D-City Models: Automatic and Semiautomatic Acquisition Methods, *In Proc. Photogrammetric Week*, 1999, pp.291-303
2. J.Hu, S.You and U. Neuman, Approaches to Large-Scale Urban Modeling, *Journal of IEEE Computer Graphics & Applications*, November/December, 2003, pp.62-69
3. N.Shiode, 3D Urban Models: Recent Developments in the Digital Modeling of Urban Environments in Three-Dimensions, *GeoJournal*, vol.52, no.3, 2001, pp.263-269
4. J. Dash, E. Steinle, R. Singh, and H. Bahr, Automatic building extraction from laser scanning data: an input tool for disaster management, *Advances in Space Research*, vol.33, pp.317-322
5. A.F.Elaksher and J.S.Bethel, Building Extraction Using LIDAR Data, *In Proc. ASPRS-ACSM Annual Conference and FIG XXII Congress*, 2002, pp.22-26
6. R.O.C. Tse, M.Dakowicz, C.M.Gold, and D.B.Kidner, Building Reconstruction Using LIDAR Data, *In Proc. 4th ISPRS Workshop on Dynamic & Multi-dimensional GIS*, 2005, pp.156-161
7. M. Seresht and A. Azizi, Automatic Building Recognition from Digital Aerial Images, *In Proc. 19th ISPRS Congress*, Book 3B, 2000, pp.792-798
8. M. Michael and K. Tempeli, Automatic Building Extraction from Airborne Laser Scanning Data, *In Proc. 19th ISPRS Congress*, Book 3B, 2000, pp.616-623
9. S. You, J. Hu, U. Neumann, and P. Fox, Urban Site Modeling from LIDAR, *Springer-Verlag Berlin Lecture Notes in Computer Science*, Vol.2669, 2003, pp.579-588
10. J. Jiang, Y. Ming, Z. Zhang, J. Zhang, Point-based 3D Surface Representation from LIDAR Point Clouds, *In Proc. 4th ISPRS Workshop on Dynamic & Multi-dimensional GIS*, 2005, pp.63-67,
11. R. Michael, Development of a Bare Ground DEM and Canopy Layer in NW Forestlands Using High Performance LIDAR, *In Proc. 23rd ESRI international user conference*, 2003, pp.135-147
12. H.Ledoux, C.Gold, Interpolation as A Tool for the Modeling of 3D Geoscientific Datasets, *In Proc. 4th ISPRS Workshop on Dynamic & Multi-dimensional GIS*, 2005, pp.79-84,
13. C.B.Barber, D.P. Dobkin, and H.T. Huhdanpaa, The Quickhull Algorithm for Convex Hulls, *ACM Transactions on Mathematical Software*, vol. 22, no. 4, 1996, pp. 469-483
14. A. Bowyer, Computing Dirichlet tessellations, *The Computer Journal*, vol.24, 1981, pp.162-166
15. D.F. Watson, Computing the n-dimensional Delaunay tessellation with application to Voronoi polytopes, *The Computer Journal*, vol.24, 1981, pp.167-172

Efficient Computation of Elliptic Gabriel Graph

Changhee Lee¹, Donguk Kim¹, Hayong Shin², and Deok-Soo Kim¹

¹ Dept. of Industrial Engineering, Hanyang University, Seoul, Korea

² Dept. of Industrial Engineering, KAIST, Daejeon, Korea

Abstract. Searching neighboring points around a point in a point set has been important for various applications and there have been extensive studies such as the minimum spanning tree, relative neighborhood graph, Delaunay triangulation, Gabriel graph, and so on.

Observing the fact that the previous approaches of neighbor search may possibly sample severely biased neighbors in a set of unevenly distributed points, an elliptic Gabriel graph has recently been proposed. By extending the influence region from a circle to an ellipse, the elliptic Gabriel graph generalizes the ordinary Gabriel graph. Hence, the skewness in the sampled neighbors is rather reduced.

In this paper, we present a simple observation which allows to compute the correct elliptic Gabriel graph efficiently by reducing the search space.

1 Introduction

Given a set of points in an arbitrary dimensional space \mathbb{R}^d , locating the neighbors of each point in the set in a certain measure of distance is an important problem for various applications. When the case of two or three dimensions, the problem is of interest for various applications in CAD, CAM, CAE, and computational geometry.

In particular, this problem is becoming more important as the technology to collect point clouds improves. In these days, the laser scanning of 3D objects is popular. The applications of this problem are many. One immediate application is to compute normal vectors of each point [10, 9]. For example, estimating a normal vector for each point on a polyhedral model requires to find the appropriate neighbors from which the normal vector can be defined.

There are several previous studies regarding on this issue. The δ -neighbor approach selects all the points within a fixed distance δ from each point in the set [2], and the result is provided as a graph. On the other hand, k -nearest neighbor finds k number of points nearest from each point in the set [1]. By combining both the δ -neighbor and k -nearest neighbor approaches into a single framework, the $k\delta$ -neighbor approach is devised [2].

While these approaches are quite simple in their concepts as well as the algorithms, the previous approaches, however, suffer from the fact that the selected neighbors may be seriously biased especially when the input points are distributed unevenly. To compromise this defect, [6] recently proposed the concept of elliptic Gabriel graph.

One the other hand, the ordinary Voronoi diagram $VD(P)$ of the point set P provides a convenient computational construct to search through the topology among the points. The dual of $VD(P)$ is known as the Delaunay triangulation $DT(P)$ and is a complex.

2 Gabriel Graph

While the theory presented in this paper works in an arbitrary dimension, we consider our discussions primarily in \mathbb{R}^2 and \mathbb{R}^3 considering the main applications in CAD and CAGD.

Let $P = \{p_1, \dots, p_n\}$ be a set of points $p_i \in \mathbb{R}^2$. Suppose that we have two points $p = (-d, 0)$ and $q = (d, 0)$. Let a region $I^{GG}(p, q)$ be an open disc defined as follows.

$$I^{GG}(p, q) = \{(x, y) | x^2 + y^2 < d^2\} \tag{1}$$

where d is a half of the Euclidean distance between the two points p and q . In other words, $d = \text{Dist}(p, q)/2$. If $I^{GG}(p, q) \cap P = \emptyset$, then we assign an edge $e_{p,q}^{GG}$ between p and q . Applying this assignment of edges for all possible pairwise points in P yields a Gabriel graph $GG(P)$. The circular region $I^{GG}(p, q)$ is then called an **influence region** between the two points p and q for the Gabriel graph, and is an open ball with \overline{pq} as its diameter. Hence, a Gabriel graph $GG(P)$ is represented as $GG(P) = (V^{GG}, E^{GG})$ where $V^{GG} = P$ and $E^{GG} = \{e_1^{GG}, e_2^{GG}, \dots\}$. In addition, the Voronoi diagram and the Delaunay triangulation for the point set P are also denoted by $VD(P) = (V^V, E^V, F^V)$ and $DT(P) = (V^D, E^D, F^D)$ where the elements are appropriately defined.

It is known that the Gabriel graph $GG(P)$ of a point set P in the plane is the subgraph of the Delaunay triangulation $DT(P)$ of the point set P [4, 8]. It can be easily shown that each edge $e_{p,q}^{GG}$ in $GG(P)$ intersects with the Voronoi edge $e_{p,q}^V$ defined by the two points p and q in the Voronoi diagram $VD(P)$ [3, 5]. Note that the two edges $e_{p,q}^D$ and $e_{p,q}^V$ are dual to each other. Hence, in the planar case, $GG(P)$ can be easily computed from $VD(P)$ in $O(m)$ time in the worst case where m is the number of Voronoi edges in $VD(P)$.

3 Elliptic Gabriel Graph

Given a point set P , an elliptic Gabriel graph $EGG(P)$ is the generalization of the Gabriel graph $GG(P)$ in the sense that the influence region is extended from a circle to an ellipse. For the two points p and q as before, let an influence region $I^{EGG}(p, q)$ is now extended to an open elliptic region defined as the following.

$$I^{EGG}(p, q) = \{(x, y) | x^2 + (\frac{y}{\alpha})^2 < d^2\} \tag{2}$$

where d is again the half of the Euclidean distance between p and q . Let E be the boundary curve of the elliptic influence region $I^{EGG}(p, q)$. In other words, $E = \partial I^{EGG}(p, q)$. The parameter α is a shape descriptor which is given as

the aspect ratio of the ellipse as shown in Fig.1. When $\alpha < 1$, the major and the minor axes of the ellipse are placed on X-axis and Y-axis, respectively(The region (a) in Fig.1). In this case, the lengths of the major and minor axes in the influence region $I^{EGG}(p, q)$ are d and αd , respectively.

If $\alpha = 1$, then the influence region reduces to a circle with \overline{pq} as a diameter(The region (b) in Fig.1). When $\alpha > 1$, the ellipse is elongated in the Y-axis direction so that the major axis is now placed on Y-axis(The region (c) in Fig.1). Hence, the major and minor axes are switched and their lengths in the influence region are αd and d , respectively.

Consider the two intersection points between the ellipse E and the major axis. We call these intersection points **extreme points**. Hence, the two given points p and q are also extreme points if $\alpha < 1$.

Let an elliptic Gabriel graph $EGG(P)$ be represented by sets of vertices and edges as follows: $EGG(P) = (V_{EGG}, E_{EGG})$. Note that $V_{EGG} = P$. Then, an edge $e_{p,q}^{EGG}$ is defined in $EGG(P)$ iff the influence region $I^{EGG}(p, q)$ does not contain any other point $r \in P$.

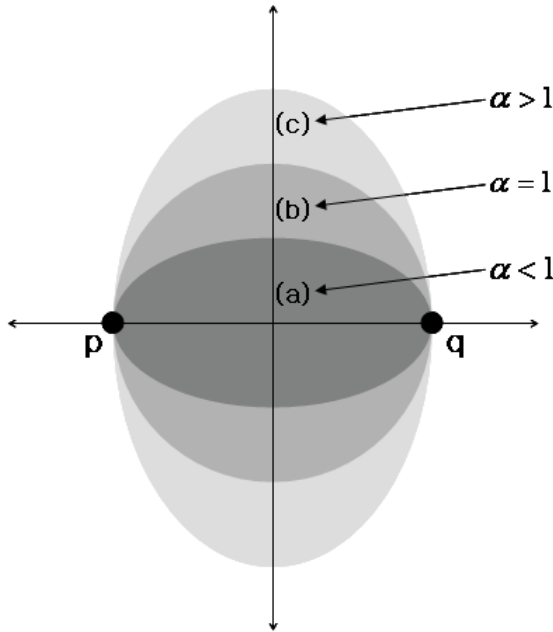


Fig. 1. Influence region of GG and EGG

The following relationships between $EGG(P)$ and $DT(P)$ are known [6].

- If $\alpha > 1$, $EGG(P) \subseteq DT(P)$.
- If $\alpha = 1$, $EGG(P) = GG(P) \subseteq DT(P)$
- If $\alpha < 1$, $EGG(P)$ is neither a super-graph nor a sub-graph of $DT(P)$.

3.1 Previous Algorithm for Computing EGG

Since $EGG(P)$ can be useful for many applications, the efficient and correct computation of $EGG(P)$ for a given point set P is important. In the previous research, $EGG(P)$ was computed as follows [6].

When $\alpha \geq 1$, $DT(P)$ was first computed and then some non-valid Delaunay edges are filtered out from the edges of $DT(P)$ by testing whether an edge between two points p and q intersects with the Voronoi edge defined by p and q . Hence, it can be always corrected computed in $O(m)$ time in the worst case where m is the number of Voronoi edges in $VD(P)$.

When $\alpha < 1$, they first located the neighboring points within the distance of δ from a given point p and called them δ -neighbors of p . Then, all the δ -neighbors are tested for the validity of edges in EGG. Suppose that there are k points in the δ -set. To determine edges connected to a point $p \in \delta$ -set, each point $q \neq p \in \delta$ -set is picked to compute an elliptic influence region $I_{p,q}^{EGG}$. Then, the point that have smaller distance from point p in the δ -set have inclusion test.(Because the point that far from point p is never included the test from near to point p .) Hence, it takes $O(k^2)$ for k points in δ -set in the worst case and therefore it takes $O(k^2n)$ for the construction of $EGG(P)$ for the δ -set.

Hence, to reduce the computation time, the smaller value of δ is preferred. However, the quality of solution deteriorates rapidly as the value of δ gets reduced. Basically, this approach is an approximation to the solution.

4 Search Space Reduction

Suppose that a point $p \in P$ is located at the origin and another point $q = (d, 0) \in P$ is located as shown in Fig.2(a). Let E be an ellipse passing through p and q with the given shape parameter α where $0 \leq \alpha < 1$. Assume that p is one of the two extreme points of the ellipse E , and the other extreme point is denoted by x . We call p a **fixed extreme point** and x a **free extreme point**. Then, the trajectory $r(\theta)$ of the free extreme point x for a given value of α is defined as the following polar form [7].

$$r(\theta) = d \cos \theta + \frac{d}{\alpha^2} \tan \theta \sin \theta. \tag{3}$$

In Fig.2(a), there are two instances of such an ellipse and two corresponding free extreme points x' and x'' . Let $T(p, q)$ be a subset of the space such as follows.

$$T(p, q) = \{(r, \theta) \mid r > d \cos \theta + \frac{d}{\alpha^2} \tan \theta \sin \theta, -\frac{\pi}{2} < \theta < \frac{\pi}{2}\}. \tag{4}$$

Then, $T(p, q)$ lies to the right side of the curve $r(\theta)$ in Fig.2(a) and therefore the following lemma holds.

Lemma 1. *Let E be an ellipse passing through two points $p, r \in P$ as its extreme points and has the aspect ratio α . Then, E always contains $q \in P$ iff $r \subseteq T(p, q)$.*

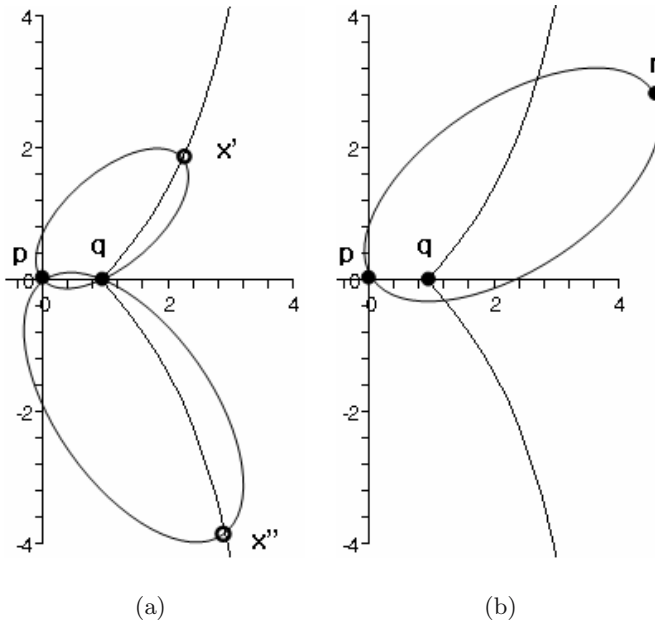


Fig. 2. The trajectory $r(\theta)$ of the free extreme point

Proof. This lemma can be easily verified by referring to Fig.2(b).

Suppose that an edge exists between the two points p and q in $EGG(P)$. Due to the above lemma, it can be then immediately observed that any point $r \in P$ can be ignored from the possibility of defining an edge with p in EGG if $r \in T(p, q)$.

Hence, if we know that an edge $e_{p,q}^{EGG}$ is an edge of $EGG(P)$, any point $r \in T(p, q)$ can be ignored since r does not define an edge with p . Hence, the region $T(p, q)$ stands for a *trash region*. This observation reduces the search time.

4.1 Conservative Approximation of Search Space

Solving the point location problem where the boundary is determined by the above equation is rather computationally expensive since it involves trigonometric functions. Hence, we make the following observation to simplify the computation. Note that the asymptotic line of Equation(3) is given as

$$x = \frac{d}{\alpha^2}. \tag{5}$$

Definition 1. Let $\tilde{T}(p, q)$ be the approximation of $T(p, q)$ defined as the following.

$$\tilde{T}(p, q) = \{(x, y) \mid x > \frac{d}{\alpha^2}\} \tag{6}$$

Fig.3 shows different situations of $\tilde{T}(p, q)$ depending on α for two given points $p = (0, 0)$ and $q = (1, 0)$. The shaded region in Fig.3(a) is the true $T(p, q)$ when $\alpha = 0.7$ and is bounded by a curve $r(\theta)$. The $\tilde{T}(p, q)$ is in this case is the subset of $T(p, q)$ which is to the right of the asymptotic line as shown in a broken line. When $\alpha = 1$ as shown in Fig.3(b), $T(p, q)$ and $\tilde{T}(p, q)$ coincide exactly. On the other hand, when $\alpha > 1$ as shown in Fig.3(c), note that the asymptotic line is located to the left of the boundary curve of $T(p, q)$, and $T(p, q) \subseteq \tilde{T}(p, q)$. Hence, the next lemma immediately follows.

Lemma 2. $\tilde{T} \subset T$ iff $\alpha < 1$, $\tilde{T} = T$ iff $\alpha = 1$, and $T \subset \tilde{T}$ if $\alpha > 1$.

Then, the following corollary immediately gives an effective and efficient search space reduction without any missing solution.

Corollary 1. Suppose that there is an edge $e_{p,q}^{EGG}$ between p and q in $EGG(P)$. When $\alpha < 1$, a point $r \in P$ does not define an edge with p if $r \subseteq \tilde{T}(p, q)$.

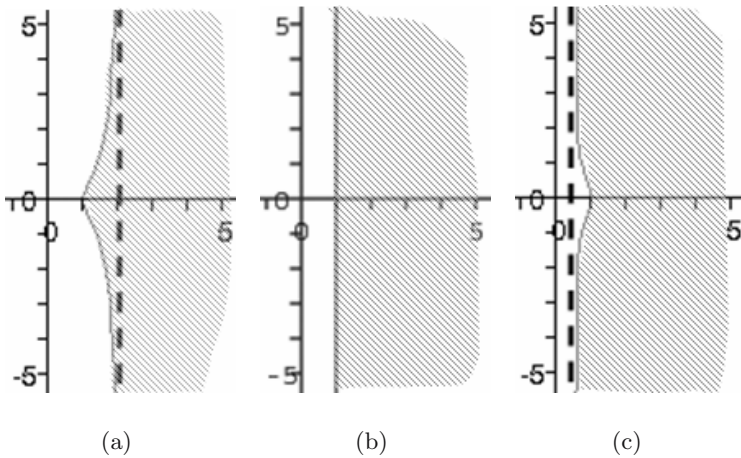


Fig. 3. Shading regions are the trash region. Solid lines are the curves of Equation(3), and dotted lines are the corresponding asymptotic lines(3). (a) $\alpha = 0.7$, (b) $\alpha = 1.0$, (c) $\alpha = 1.3$.

4.2 Reduced Search Space for Candidate Neighbors

Using the previous corollary, we can efficiently reduce the search space for getting the correct EGG. In this section, we will present a simple algorithm for finding the edges incident to a given point $p \in P$ in $EGG(P)$.

Suppose that we have a Delaunay triangulation $DT(P)$ of the point set P . Let $Q = \{q_1, q_2, \dots, q_m\}$, $Q \subseteq P$ where $q_i \in Q$ has a Delaunay edge with a point $p \in P$. Suppose that the points $q_i \in Q$ is ordered in the non-decreasing order of its distance from p . In other words, $Dist(p, q_i) \leq Dist(p, q_j)$ if $i < j$.

Then, it is guaranteed that p and q_1 has an edge in EGG when $\alpha \leq 1$. Suppose that we apply a transformation \mathcal{T} to the point set P so that $\mathcal{T}(p)$ is located at the origin and $\mathcal{T}(q_1)$ lies on the positive side on the X -axis. Then, the transformed point $\mathcal{T}(p)$ has its associated spaces of $T(\mathcal{T}(p), \mathcal{T}(q_1))$ and $\tilde{T}(\mathcal{T}(p), \mathcal{T}(q_1))$ with respect to $\mathcal{T}(q_1)$.

Let $T(\mathcal{T}(p), \mathcal{T}(q_1))^C$ be the complementary space of $T(\mathcal{T}(p), \mathcal{T}(q_1))$. In addition, let $\mathcal{T}^{-1}(T(\mathcal{T}(p), \mathcal{T}(q_1))^C)$ denote the complementary space after applying the inverse of \mathcal{T} to the system and denote it by $\mathcal{T}^{-1}(T(p, q_1))^C$ to avoid the abuse of symbols. Similar definitions are also made for $\tilde{T}(\mathcal{T}(p), \mathcal{T}(q_1))^C$ and $\mathcal{T}^{-1}(\tilde{T}(p, q_1))^C$.

Then, due to the theorem, the point $r \in P$ does not define an edge with p iff $r \in \mathcal{T}^{-1}(T(p, q_1))^C$. Hence, we collect to test only such points r in the valid space.

Hence, the neighboring points which may define incident edges with p in $EGG(P)$ always lie in the following region. Let $S(p)$ be a subspace defined as

$$S(p) = \bigcap_{q_i \in Q} \mathcal{T}^{-1}(T(p, q_i))^C \tag{7}$$

In addition, let $C = P \cap S(p)$. If a point c defines an edge $e_{p,c}^{EGG}$ with p , then $c \in C$. Hence, C is the set of candidates for the neighbors of p in $EGG(P)$. $S(p)$ may not be closed at all depending on the value of α . For example, $S(p)$ is the whole space if $\alpha = 0$.

However, the boundary of the region $S(p)$ consists of curves in trigonometric functions and therefore we replace the region by a conservative approximation as follows so that we do not miss any solution while achieving the computational efficiency.

$$\tilde{S}(p) = \bigcap_{q_i \in Q} \mathcal{T}^{-1}(\tilde{T}(p, q_i))^C \tag{8}$$

Note that $\tilde{S}(p)$ in the above equation is a convex set since $\mathcal{T}^{-1}(\tilde{T}(p, q_i))^C$ is a half-space. We want to also note that $\tilde{S}(p)$ is always a closed convex polyhedral set unless p is a vertex on the boundary of the convex hull of P . Note $S(p) \subseteq \tilde{S}(p)$ if $\alpha \leq 1$.

We want to note here that it is better to trim-off the more search space as early as possible for the computational efficiency. This is why we sort the set Q according to the distance of $q_i \in Q$ from p . Hence, the intersection operation is applied according to the order of distances.

4.3 Test of Edge Validity

Given $C = \{c_1, c_2, \dots, c_m\}$ of candidate neighbors from p , it is necessary to test whether $c_i \in C$ indeed defines a valid edge e_{p,c_i}^{EGG} in $EGG(P)$. Hence, the validity test runs for each candidates in the set C . To achieve the computational efficiency, we use the topology of the Delaunay triangulation $DT(P)$.

For a point $c_i \in C$, we define the ellipse E which is the boundary of the influence region between the two points p and c_i . Then, the validity check is exactly the inclusion test of other points $y \in P - \{p, c_i\}$ to test if $y \in E$ or not.

Note that we are given with $DT(P)$, or equivalently $VD(P)$. Given a triangle t in $DT(P)$, three vertices which define three triangles neighboring to t can be located in $O(1)$ time in the worst case. Therefore, given a vertex p in $DT(P)$, locating all k neighboring vertices which have Delaunay edges with the vertex p can be located in $O(k)$ time in the worst case.

Hence, given a point p , the triangles incident to p is first located. Among k triangles, the one which intersects the line segment $\overline{pc_i}$ is located and its vertices are tested for the inclusion in E . If any one of its vertices is included by E , the test is terminated since the point c_i cannot define an edge with p . If not, the search proceeds to the next triangles neighboring to this triangle. It is well known that this search can be done in the expected time of \sqrt{m} for n given points, even though the worst case time complexity is $O(m)$, where m is the number of elements in C . Note that testing if a point c_i is inside of an ellipse E can be done in $O(1)$ time in the worst case.

5 Conclusion

Given a set of points in an arbitrary dimensional space \mathbb{R}^d , locating the neighbors of each point in the set in a certain measure of distance is an important problem for various applications. In particular, this problem is becoming more important as the technology to collect point clouds improves.

Since the previous approaches of neighbor search may possibly sample severely biased neighbors in a set of unevenly distributed points, an elliptic Gabriel graph has recently been proposed. However, the currently known algorithm takes $O(n^3)$ time in the worst case to compute a correct $EGG(P)$ for n points. To improve the efficiency, the quality of solution was sacrificed.

In this paper, we proposed a scheme to reduce the search effort for the correct solution as much as possible while any of the correct solution is not missing. The algorithm is based on a simple observation that the region that need not be considered for the solution can be immediately identified once two points are chosen to be tested for an edge. While the proposed algorithm still has the worst case time complexity of $O(n^3)$, the expected time complexity is significantly improved while keeping the correct solution. As the value α gets smaller, the computational gain gets increased. The detailed analysis for the expected time complexity is an issue for the future study.

Acknowledgement

This research was supported by Creative Research Initiative from the Ministry of Science and Technology, Korea.

References

1. S. Arya, D. Mount, N. Netanyahu, R. Silverman, and A. Wu. An optimal algorithm for approximate nearest neighbor searching in fixed dimensions. *Journal of the ACM*, 45:891–923, 1998.
2. M. Berg, M. Kreveld, M. Overmars, and O. Schwarzkopf. *Computational Geometry - Algorithms and Applications*. Springer, 2000.
3. J. Jaromczyk and G. Toussaint. Relative neighborhood graphs and their relatives. In *Proceedings of the IEEE*, volume 80, pages 1502–1517, 1992.
4. D. W. Matula and R. R. Sokal. Properties of Gabriel graphs relevant to geographic variation research and the clustering of point in the plane. *Geographical Analysis*, 12(3):205–222, 7 1980.
5. A. Okabe, B. Boots, K. Sugihara, and S. N. Chiu. *Spatial Tessellations: Concepts and Applications of Voronoi Diagrams*. John Wiley & Sons, Chichester, 2nd edition, 1999.
6. J. C. Park, H. Shin, and K. Choi. Elliptic gabriel graph for finding neighbors in a point set. In *Proceedings of the Society of CAD/CAM Engineers Conference*, volume (in printing), 2006.
7. D. F. Rogers and J. A. Adams. *Mathematical elements for computer graphics*. McGraw-Hill, 2nd edition, 1989.
8. R. B. Urquhart. Some properties of the planar Euclidean relative neighbourhood graph. *Pattern Recognition Letters*, 1(5,6):317–322, 7 1983.
9. M. Zwicker, M. Pauly, O. Knoll, and M. Gross. Pointshop 3d: An interactive system for point-based surface editing. In *Proceedings of the SIGGRAPH 2002*, 2002.
10. M. Zwicker, H. Pfister, J. Baar, and M. Gross. Surface splatting. In *Proceedings of the SIGGRAPH 2001*, 2001.

Systematic Sampling in Image-Synthesis

Mateu Sbert, Jaume Rigau, Miquel Feixas, and Laszlo Neumann

Institut d'Informàtica i Aplicacions, Universitat de Girona, Spain

{mateu.sbert, jaume.rigau, miquel.feixas, laszlo.neumann}@udg.es

Abstract. In this paper we investigate systematic sampling in the image-synthesis context. Systematic sampling has been widely used in stereology to improve the efficiency of different probes in experimental design. These designs are theoretically based on estimators of 1-dimensional and 2-dimensional integrals. For the particular case of the characteristic function, the variance of these estimators has been shown to be asymptotically $N^{-3/2}$, which improves on the $O(N^{-1})$ behaviour of independent estimators using uniform sampling. Thus, when no a priori knowledge of the integrand function is available, like in several image synthesis techniques, systematic sampling efficiently reduces the computational cost.

1 Introduction

Systematic sampling [9, 10, 16] is a classical Monte Carlo technique that has been used for years in some fields, notably in stereology [3, 4, 15, 1]. In systematic sampling a uniform grid is translated by a random offset giving the sampling points to probe the target function obtaining thus a primary estimator (see Fig. 1a). Averaging values obtained with successive random offsets results in the corresponding secondary estimator. Because of being based in regular sampling, systematic sampling can provide cheaper samples than with independent random uniform sampling. This can be appealing nowadays in computer graphics, where powerful graphics cards are well suited for sampling on a regular grid.

In recent years, techniques similar to systematic sampling have appeared in computer graphics, i.e. z-buffer, ray-tracing, and also in the Monte Carlo field [7, 8], totally unaware of the systematic sampling heritage. The purpose of this paper is to remind the basics of systematic sampling and to study its applicability to ray-tracing, the most used computer graphics technique to generate realistic images. Although systematic sampling has not been applied explicitly in ray-tracing, related techniques can be tracked down in global illumination as *interleaved sampling* [7]. The use of systematic sampling in other computer graphics areas will be also explored.

This paper is organized in the following way. In section 2 the basics of systematic sampling are reviewed. In section 3 the potential use for ray-tracing is explored, studying the area sampling estimator and the so called force matrix [17, 18]. Results are given in section 4, and other applications are presented in section 5. Finally we present our conclusions.

2 Systematic Sampling

We follow here Cruz-Orive’s work [3] in the presentation of the Monte Carlo systematic estimator. Consider the integral

$$Q = \int_D f(x)dx. \tag{1}$$

Partition R^n into a denumerable set of bounded domains or tiles $\{\mathcal{J}_k, k\}$, k integer, so that any tile can be brought to coincide with a given tile $\{\mathcal{J}_0\}$ by a translation $-\tau_k$ which leaves the partition invariant. Take a uniform random point z in $\{\mathcal{J}_0\}$ (see Fig.1). The following is an unbiased estimator :

$$\widehat{Q} = v \sum_k f(z + \tau_k), \tag{2}$$

where v is the volume of a tile and k runs over all integers. Effectively, since $\{\mathcal{J}_k, k\}$ cover R^n without overlapping, we have

$$Q = \sum_k \int_{\mathcal{J}_k} f(x)dx \tag{3}$$

$$E(\widehat{Q}) = v \sum_k E f(z + \tau_k) = v \sum_k \int_{\mathcal{J}_0} f(z + \tau_k) \frac{dz}{v} = \sum_k \int_{\mathcal{J}_k} f(x)dx. \tag{4}$$

The variance of this estimator has been studied using the *covariogram* [3]:

$$Var(\widehat{Q}) = V \sum_k g(\tau_k) - \int_{R^n} g(h)dh \tag{5}$$

$$g(h) = \int_{R^n} f(x)f(x + h)dx, \tag{6}$$

where g is the covariogram of f .

3 Systematic Sampling for Image Synthesis

There are some widely used techniques in computer graphics like the simple z-buffer method, the radiosity method and different versions of ray-tracing. We have selected for our study the ray-tracing technique which is used mainly in global illumination. This technique traces rays from the observer through the pixels of a screen plane and gets the colour of the hit point in the scene (see Fig.1b).

In ray-tracing we deal with the integral over a pixel

$$L = \int \int_{S(P)} L(x, y)f(x, y)dx dy, \tag{7}$$

where $L(x, y)$ is the radiance coming to the eye through point (x, y) in the support region S of pixel P and $f(x, y)$ is a filtering function, integrating to 1. This integral is

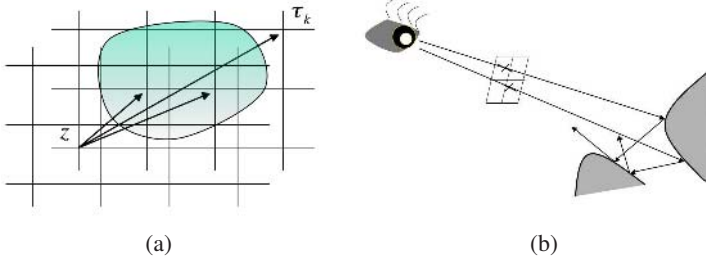


Fig. 1. (a) Systematic sampling. (b) In ray-tracing rays are traced from the observer through the pixels in the screen plane to get the radiance (computed recursively) from the hit point in the scene.

usually solved with Monte Carlo integration, selecting random points in S . A commonly used filtering function is the characteristic function of pixel P (box filter), and thus the integral to be solved is

$$L = \frac{1}{A_P} \int \int_P L(x, y) dx dy, \quad (8)$$

where A_P is the pixel area.

We want to evaluate here the efficiency of solving (7, 8) by using *systematic sampling* (see Fig. 1a) in front of uniform random sampling. First we will discuss this issue in a theoretical way, by studying the relative efficiency with respect to the hit-miss area estimator. This estimator has already been used in the ray-tracing context in the discussion of the efficiency of some supersampling estimators [5].

Although systematic sampling has not been applied explicitly in ray-tracing, related techniques can be tracked down in global illumination [7, 8]. In *interleaved sampling* [7] the screen plane is filled with tiles of a basic cell of irregularly distributed samples, usually generated with quasi-Monte Carlo and covering more than one pixel. Thus, although the net result is a systematic sampling grid covering the screen plane, it is not used to solve the pixel integral (7).

3.1 Evaluation of the Area Integral Using Systematic Sampling

Consider the integral

$$A = \int \int I_R(x, y) dx dy, \quad (9)$$

where I_R is the indicator function of the region R with area A and contour length B . We know from [3] that the variance of the hit-miss systematic sampling estimator, \widehat{A}^s , for (9) is asymptotically given by ¹

$$\text{Var}(\widehat{A}^s) = kBu^3, \quad (10)$$

¹ Isotropic rotation with respect to the grid is assumed.

where $k = 0.072$ and u is the length of the edge of the basic square cell. Let us consider now that the region R is included in a square region with area A_T . Thus, we only need to test $N = A_T/u^2$ points in this region. Expression (10) can be rewritten into

$$Var(\widehat{A}^s) = kBA_T^{\frac{3}{2}}N^{-\frac{3}{2}} \tag{11}$$

which explicits the assymptotic behaviour of the variance.

3.2 Relative Efficiency of Systematic Against Independent Sampling

The independent sample estimator, \widehat{A}^i , has variance

$$Var(\widehat{A}^i) = \frac{(A_T)^2p(1-p)}{N}, \tag{12}$$

where $p = \frac{A}{A_T}$. Using the relationship $N^2 = A_T^2/u^4$, we obtain

$$Var(\widehat{A}^i) = Nu^4p(1-p). \tag{13}$$

From (13), (11), and $u = \sqrt{A_T}/\sqrt{N}$, the relative efficiency of the systematic estimator with respect to the one based on independent random samples is given by

$$\frac{\sqrt{N}\sqrt{A_T}p(1-p)}{kB}. \tag{14}$$

Suppose now that we write in (14) $B = k'\sqrt{A}$, where k' depends on the form of the region (for instance, for a square, $k' = 4$). After simplifying we obtain:

$$\frac{\sqrt{N}\sqrt{p}(1-p)}{kk'}. \tag{15}$$

Maximum relative efficiency can be obtained by optimizing expression (15). The value obtained is $p = 1/3$. For small p expression (15) is approximated by

$$\frac{\sqrt{N}\sqrt{p}}{kk'}. \tag{16}$$

Equating to 1 we obtain that, for small p , systematic sampling is more efficient when

$$p \geq \frac{(kk')^2}{N}. \tag{17}$$

For p near 1, expression (15) is approximated by

$$\frac{\sqrt{N}(1-p)}{kk'}. \tag{18}$$

Equating to 1 we obtain that, for p near 1, systematic sampling is more efficient when

$$p \leq 1 - \frac{kk'}{\sqrt{N}}. \tag{19}$$

As an example, consider the square case ($k' = 4$). As $k = 0.0724$, from (17) and (19) we obtain that systematic sampling will be better whenever

$$\frac{0.0838}{N} \leq p \leq 1 - \frac{0.2896}{\sqrt{N}}. \tag{20}$$

For $N = 20$, (20) becomes $0.0042 \leq p \leq 0.9352$.

3.3 Force Matrix

Although the variance of the systematic sampling primary estimator for area sampling is $O(N^{-3/2})$, by using M successive offsets (this is, the secondary estimator) we approach progressively the usual convergence $O(M^{-1})$. Sometimes it is unavoidable to use several offsets to avoid the aliasing effects of using a single offset (this is, a single systematic grid). One possible escape way is the use of the so called force matrix [17, 18]. Instead of using all the sampling points in the grid, a highly uniform distributed subset of the grid points is preselected. Force matrix will be generated with successive point insertion by minimizing a given repulsion force function $f(r) = e^{-\left(\frac{r}{s}\right)^p}$, where r is the distance between already selected points in the grid and s and p are appropriate parameters. We can regulate on demand the sparseness of the selected points (see Fig.2). In the limiting case the force matrix reverts to the full systematic grid. Force matrix was first applied to obtain a dithering threshold matrix.

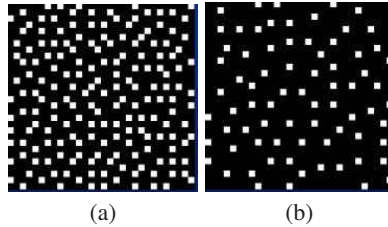


Fig. 2. Force matrix with different parameters

4 Results

4.1 Area Sampling

In Fig.3 we compare the efficiency of systematic and stratified sampling against independent sampling. The graphs show the average of hundred runs, each with 16, 64, 100 and 400 samples, respectively. Following [6] the variance of stratified sampling with one sample per stratus (also called jittered sampling [19] in computer graphics) is of the order $O(N^{-1-\frac{2}{n}})$, where n is the dimension. In our case, $n = 2$, the variance is of order $O(N^{-2})$, and thus it should be better than systematic sampling, which is $O(N^{-\frac{3}{2}})$ (11). The results in Fig.3, confirming the asymptotical behaviour, show however that for the samples considered, N till 400, systematic sampling is better. Observe also in the graph

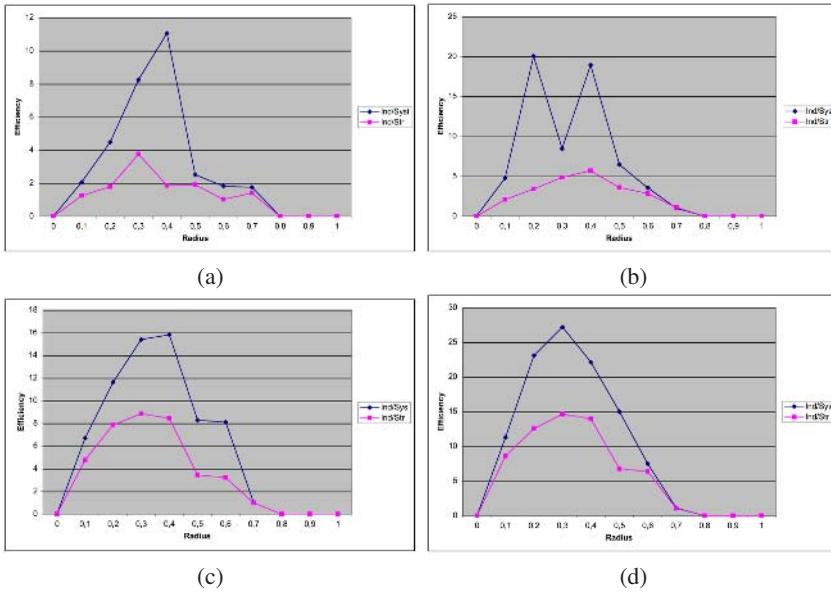


Fig. 3. Comparison of the efficiency (on y axis) of systematic and stratified sampling versus independent sampling to obtain the area of a circle centered in a unit square and with growing radius (in x axis) for 16, 64, 100 and 400 samples, from left to right and top to down respectively

in Fig.3 corresponding to 64 samples the peaks in the efficiency. This behaviour is characteristic of systematic sampling, and it is due to the *coupling*, for these radius values, of the the exact value of the area with the systematic sampling estimator. Barabesi in [2] compares systematic sampling against stratified (and randomized quasi-Monte Carlo) for the evaluation of the Horvitz-Thompson estimator, obtaining also a better behaviour for systematic sampling.

4.2 Ray-Tracing

A drawback for the use of systematic sampling in ray-tracing can be the visually unpleasant aliasing and other visual artifacts due to the regularity of sampling. One possible solution is the use of just a subset of sampling points, as the one provided by the force matrix. This will keep the convergence rate at the cost of using just a subset of all the potential sampling points. Another solution is the use of a secondary estimator, this is, averaging the results of several offsets, at the cost of lowering the convergence rate.

In Fig.4 and 5, we compare images obtained with interleaved sampling, force matrix, stratified sampling (one sample per stratus), systematic sampling with one offset and systematic sampling with several random offsets. From both images we conclude:

- Aliasing due to regular sampling can be observed in systematic sampling with one offset, this is, the primary estimator. See Fig.4d and 5d.
- Aliasing disappears in both force matrix (Fig.5a) and systematic sampling secondary estimator (Fig.4c and 5c). In addition, error decreases.

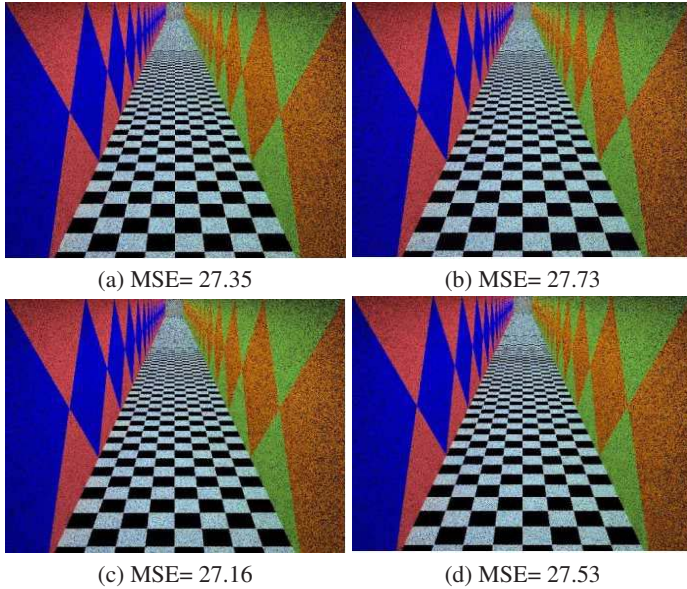


Fig. 4. From left to right and top to down, comparison of images obtained with interleaved sampling (16 samples per pixel, grid cell equal to four pixels, Halton sequences), stratified sampling (16 samples per pixel, one sample per stratus), systematic sampling (4 randomly shifted offsets with 4 samples per pixel each) and systematic sampling (one random offset with 16 samples per pixel), respectively. Mean square errors (MSE) are given.

- Force matrix appears as the better sampling scheme for the 256 samples case and systematic with 4 offsets for the 16 sampling case.
- Systematic sampling has a better behaviour than stratified sampling for low number of samples (compare errors in Fig.4c,d and 5c,d against Fig.4b and 5b).

Additional results comparing primary and secondary systematic estimators are given in Table 1 with mean square errors for different systematic sampling configurations and images with a total of 16 and 256 samples per pixel, respectively. This is, the first row of both tables gives the error for the primary estimator, and the other rows for secondary estimators. In each case the best way to sample N^2 points has been to use N offsets with N points each.

Table 1. Mean square errors for different systematic sampling configurations and images with a total of (a) 16 and (b) 256 samples per pixel, respectively. The left column indicates the number of offsets times the number of samples per pixel.

1 x 16	30.76	27.53
4 x 4	30.29	27.16

(a)

1 x 256	5.25	8.82	5.55
4 x 64	5.31	8.51	5.61
16 x 16	5.20	8.34	5.50

(b)

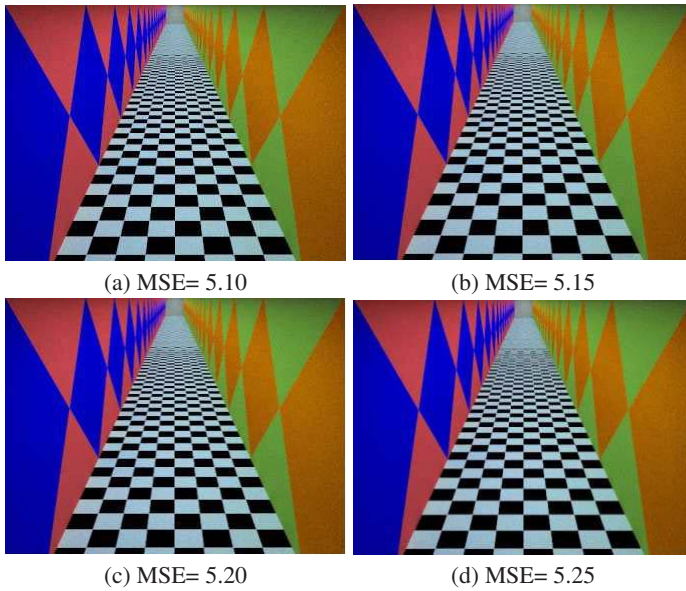


Fig. 5. From left to right and top to down, comparison of images obtained with force matrix (256 samples per pixel), stratified sampling (256 samples per pixel, one sample per stratus), systematic sampling (16 randomly shifted offsets with 16 samples per pixel each) and systematic sampling (one random offset with 256 samples per pixel), respectively. Mean square errors (MSE) are given.

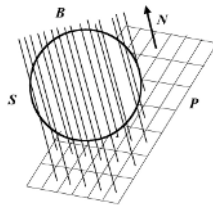


Fig. 6. A bundle of equidistant parallel lines. S is the sphere that wraps the scene, B is the bundle of lines, P is the projection plane orthogonal to S and N is the normal to P .

5 Other Applications

Systematic sampling has been used in the computation of bundles of parallel lines for their use in radiosity [14, 13]. Uniformly distributed random lines covering an sphere are substituted by bundles of equidistant parallel lines generated orthogonal to a random tangent plane to the sphere. The origin of the lines has also been randomly shifted (see Fig.6) . We can apply also systematic sampling when sampling directions on a sphere or hemisphere. We have applied it to sample cosine distributed directions to obtain the *obscurances* [11, 12] of the point on the scene seen from the eye. In Fig.7 we can compare pure Monte Carlo sampling against systematic sampling, and we can appreciate the important noise reduction.

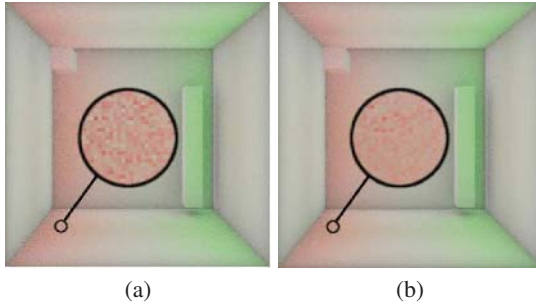


Fig. 7. On the left, obscurances computation with pure random sampling. On the right, with systematic hemispheric sampling.

6 Conclusions and Future Work

Systematic sampling is a classical Monte Carlo technique that has been successfully used in several fields, in particular in the stereology field. It joins the benefits of regular sampling and Monte Carlo sampling, obtaining a higher convergence rate than plain Monte Carlo. Systematic sampling can provide also cheaper samples than with independent uniform sampling. This can be appealing nowadays in computer graphics, where powerful graphics cards are well suited to regular sampling. A drawback however for its use in computer graphics and specifically in ray-tracing can be the visually unpleasant aliasing effects due to regular sampling. One possible solution is the use of just a subset of sampling points, as the one provided by the force matrix. This will keep the convergence rate at the cost of using just a subset of all the potential sampling points. Another possible solution is the use of a secondary estimator, this is, averaging the results of several offsets, at the cost of lowering the convergence rate. We have found surprisingly that the best compromise to sample N^2 points is to use N offsets with N points each. Both force matrix and secondary estimator alternatives have given good results, and new efficient and robust techniques in image synthesis. Further research is needed to clarify which alternative is better and to study the theoretical background of the empirically very efficient force matrix.

Other uses of systematic sampling in computer graphics have been illustrated. Bundles of parallel lines, with cheap cost thanks to the use of hardware and projection algorithms, have been used in radiosity and global illumination. Sampling systematically the hemisphere has resulted in a much more reduced noise in the computation of obscurances. Further applications of the new techniques, i.e. in computing direct illumination, will be explored. Experiments demonstrate that the introduced methods can substitute advantageously stratified sampling when the number of strata is not very high, according to the results of our study of the estimator for area sampling.

Acknowledgements

This project has been funded in part with grant number TIN2004-07451-C03-01 of the Spanish Government and IST-2-004363 (GameTools: Advanced Tools for Developing

Highly Realistic Computer Games) from the VIth European Framework. We are thankful to David Figuls for providing the tests in Fig.3 and to Alex Mendez for the images in Fig.7.

References

1. A. Baddeley and E.B. Vedel Jensen, *Stereology for Statisticians*, Chapman & Hall/CRC, 2005
2. Lucio Barabesi, A Monte Carlo integration approach to Horvitz-Thompson estimation in replicated environment designs, *METRON – International Journal of Statistics*, 2003, vol. LXI, n.3, pp-355–374
3. L.M. Cruz-Orive, On the precision of systematic sampling: a review of Matheron’s transitive methods, *Journal of Microscopy*, Vol. 153, Pt3, March 1989, pp. 315-333
4. L.M. Cruz-Orive, Systematic sampling in stereology, *Bull. Intern. Statist. Instit. Proceedings 49th Session, Florence, 1993*, **55**, 451–468.
5. W. Purgathofer, A statistical method for adaptive stochastic sampling. *Computers & Graphics*, 11(2):157–162, 1987.
6. I.M. Sobol, *Monte Carlo numerical methods*, Ed. Science, Moscou, 1973 (in russian).
7. A.Keller and W.Heidrich, *Interleaved Sampling*, Eurographics Workshop on Rendering 2001.
8. T.Kollig and A.Keller, *Efficient Multidimensional Sampling*, *Computer Graphics Forum*, Vol. 21 (2002), No. 3, pp. 557-563.
9. P.R. Krishnaiah and C.R. Rao, *Handbook of statistics*, Vol.6, Elsevier, Amsterdam, 1988
10. W.G. Cochran, *Sampling Techniques*, John Wiley and sons, New York 1997
11. A. Iones, A. Krupkin, M. Sbert and S. Zhukov, *Fast realistic lighting for video games*, *IEEE Computer Graphics & Applications*, 2003
12. A. Mendez and M. Sbert, *Comparing Hemisphere Sampling Techniques for Obscurance Computation*, 3IA’2004, Limoges, France, 2004.
13. M. Sbert, *The Use of Global Random Directions to Compute Radiosity*. *Global Monte Carlo Techniques*, PhD dissertation, Universitat Politècnica de Catalunya, 1997
14. L. Szirmay-Kalos, *Photorealistic Image Synthesis Using Ray-bundles*, D.Sc. dissertation, Hungarian Academy of Sciences, 2000
15. X. Gual–Arnaú and L.M. Cruz-Orive, *Systematic sampling on the circle and the sphere*, *Advances in Applied Probability (SGSA)* 32, 628–647, 2000
16. D. Stoyan, W.S. Kendall, and J. Mecke, *Stochastic Geometry and its Applications*, Wiley, Chichester, 1987
17. W. Purgathofer, R.F. Tobler, M. Geiler, *Forced Random Dithering: Improved Threshold Matrices for Ordered Dithering*, In *Proceedings of the First IEEE International Conference on Image Processing*, Austin, Texas, 1994.
18. W. Purgathofer, R.F. Tobler, M. Geiler, *Improved Threshold Matrices for Ordered Dithering*, *Graphics Gems V*, Academic Press, 1995.
19. Peter Shirley, *Discrepancy as a Quality Measure for Sample Distributions*. *Proceedings of Eurographics ’91*.

History-Based Selective Boolean Operations for Feature-Based Multi-resolution Modeling

Sang Hun Lee¹, Kunwoo Lee², and Sungchan Kim²

¹ School of Mechanical and Automotive Engineering, Kookmin University,
Seoul, 136-702, Korea
shlee@kookmin.ac.kr

² School of Mechanical and Aerospace Engineering, Seoul National University,
Seoul, 151-744, Korea
kunwoo@snu.ac.kr, sungchan@cad.snu.ac.kr

Abstract. The feature-based multi-resolution models of a solid represent an object at different levels of detail (LOD), particularly in the unit of feature, according to a certain LOD criterion. The need of feature-based multi-resolution modeling is currently increasing for various engineering tasks, such as analysis, network-based collaborative design, virtual prototyping and manufacturing. To provide feature-based multi-resolution models, it is essential to generate a valid and unique solid model at each LOD after feature rearrangement. To meet this requirement, we propose the *history-based selective Boolean operations* that satisfy the commutative law between union and subtraction by considering the history of the Boolean operations for the features. Owing to the commutative properties, the feature-based multi-resolution modeling technique based on these operations guarantees the same resulting shape as the original, and provides a unique and reasonable shape at each intermediate LOD after arbitrary feature rearrangement.

1 Introduction

Three-dimensional (3D) computer aided design (CAD) systems based on feature-based solid modeling techniques are widespread and commonly used for product design. However, when part models associated with features are used in various downstream applications, simplified models with various level of detail (LOD) are frequently more desirable than the full details of the parts. In particular, there is increasing need in engineering tasks for feature-based multi-resolution representations of a solid model, which represents an object using multiple LODs in the unit of feature, such as in analysis [1, 6], network-based collaborative design [5], and virtual prototyping and manufacturing [4].

To respond to this need, several researchers have examined feature-based multi-resolution modeling techniques. Choi et al. [2] studied multi-resolution representation of a B-rep part model. In their approach, the lowest resolution model was formed by uniting all of the additive features, and then higher resolution models were generated by applying the subtractive features successively in descending order of volume. This

method has the advantage in that it can be implemented in current commercial 3D CAD systems by virtue of sharing the same data structure. However, this method has several limitations. First, it requires a large volume of computation time to obtain an LOD model, as Choi et al. used conventional Boolean operations. (Here, an *LOD model* denotes a solid model at a specific LOD). Second, the method of Choi et al. cannot provide adequate LOD models for an arbitrary feature rearrangement, regardless of the feature type, which is additive or subtractive.

To reduce the computation time for the extraction of LOD models, Lee [7] and Lee, et al. [5] introduced the nonmanifold topological model of a cellular structure as the topological framework for a multi-resolution model. In this method, all the features are initially merged into a non-manifold cellular model, and then, if the LOD is given, the topological entities comprising the LOD model are selected and displayed. In particular, Lee et al. [5] addressed the incremental transmission of solid models for engineering tasks through a network in order to share the model at an adequate LOD. Kim, et al. [3] introduced a feature extraction method and proposed three operators to build multi-resolution models. Three operators include wrap-around, smooth-out, and thinning operators. However, it is not clear their proposed set of multi-resolution features and extraction operators are complete to perform multi-resolution modeling.

Recently, Lee [7] introduced the concept of an *effective volume of a feature* to provide valid solids for an arbitrary rearrangement of features, regardless of the feature type. The effective volume of a feature was defined as the actual volume of the feature in the rearranged feature tree when used as a tool body for the Boolean operation. When arranged in order of feature creation, the effective volume of each feature was defined as the entire volume of the feature. However, the effective volume of a feature can be reduced to a fraction of the original volume after feature rearrangement. Lee described a method to identify the effective volume and provided a mathematical proof of the method's correctness. By introducing the concept of an effective volume, an arbitrary rearrangement of features becomes possible, and arbitrary LOD criteria may be selected to suit various applications. However, the effective volume may be defined differently according to the order of relocation of the features. If the order is not selected properly, then some intermediate LOD models may have unacceptable shapes. (This problem is addressed in Section 2 in this paper in more detail). Therefore, a method to guarantee a reasonable and unique shape for each intermediate LOD needs to be developed.

To solve the feature rearrangement problem completely, we propose using history-based selective Boolean (HBS-Boolean) operations, and applying them to feature-based multi-resolution modeling. Since union and subtraction are commutative in HBS-Boolean operations, our approach guarantees the same result for an arbitrary rearrangement of features, and unique and reasonable shapes for each LOD. Since the HBS-Boolean operations are independent from the topological framework, they can be implemented using conventional solid data structures as well as nonmanifold data structures.

The remainder of the paper is organized as follows. Section 2 defines the problem. Section 3 introduces a definition of the union and subtraction operations of the HBS-Boolean operations, and describes their properties. Section 4 describes the implementation of HBS-Boolean operations, and discusses a case study, and some conclusions and future work are given in Section 5.

2 Problem Definition

Let F , P , and \otimes denote a feature, the primitive of a feature, and the \cup or $-$ Boolean operation of a feature, respectively. If X is one of F , P , or \otimes , then X^i denotes the i -th X in the initial feature creation order, while X_j denotes the j -th X in the current rearranged order. Since P is defined as a point set over the R^3 space in this work, it includes the solid and the 3D nonmanifold topological model.

If M_n denotes the resulting model of $n+1$ features, then it is created by applying n Boolean operations between the $n+1$ primitives of the features, $M_n = \prod_{k=0}^n \otimes^k P^k$, where $\otimes^0 P^0 = \phi \otimes^0 P^0$. However, if the features are rearranged, then the resulting shape, denoted by $M'_n (= \prod_{\ell=0}^n \otimes_{\ell} P_{\ell})$, is generally different from the original shape because union and subtraction Boolean operations are not commutative with each other. To apply feature-based multi-resolution modeling to a wide range of application areas, even though the features are rearranged arbitrarily regardless of whether the feature is additive or subtractive, the resulting shape must be the same as the original shape, and the models at the intermediate LODs must have a reasonable shape. This problem is denoted as the feature rearrangement problem.

To solve this problem, we introduced the concept of an effective volume of a feature [7]. The region influenced by a Boolean operation is altered when the order of application of the operations is changed. Thus, to obtain the same resultant shape regardless of feature rearrangement, it is necessary to exclude some feature volumes from the original shape. This adapted volume is called the effective volume of a feature, or, alternatively, the effective feature volume. The effective volumes of all the features in M_n are described by Eq. (1) when a feature, F_i , is relocated to the m -th place.

$$M_n = \left(\prod_{k=0, k \neq i}^j \otimes_k P_k \right) \otimes_i \left(P_i - \sum_{\ell=0}^{j-i} \psi(\otimes_i, \otimes_{i+\ell}) P_{i+\ell} \right) \left(\prod_{k=j+1}^n \otimes_k P_k \right), \quad i < j \tag{1}$$

where

$$\psi(a, b) = \begin{cases} 1 & \text{if } a \neq b \\ 0 & \text{otherwise} \end{cases}.$$

For an arbitrary feature rearrangement, the feature relocation operation using Eq. (1) guarantees the same resulting shape as the original. However, the intermediate LOD models are altered, depending on the order of the feature relocation operations. Moreover, there is no criterion to decide which is the most reasonable shape among the various options.

Let us investigate this problem using the example model shown in Fig. 1. This model has been created by applying four features, as illustrated in Fig. 1.

Let us rearrange the features in the order: $F^0 \rightarrow F^2 \rightarrow F^1 \rightarrow F^3$, and calculate the effective volumes of the rearranged features using Eq. (1). If the features are moved in

the manner shown in Figs. 2(a) and 3(a), then the resulting LOD models are shown in Figs. 2(b) and 3(b), respectively. Although the resulting shapes of the two cases are similar, the intermediate LOD models of the two cases are different. The LOD models in Fig. 2 appear unreasonable, while those in Fig. 3 appear reasonable. In the case of Fig. 2, the excessive part of the feature effective volume is removed, as on applying F^2 and F^1 , part of the volume, P^3 , is subtracted unnecessarily in advance.

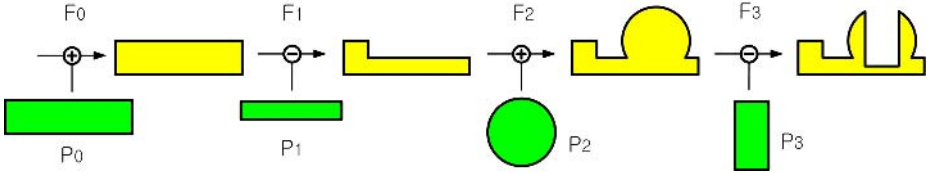


Fig. 1. An example of feature-based solid modeling: (a) the part model and its form features, and (b) the feature modeling tree

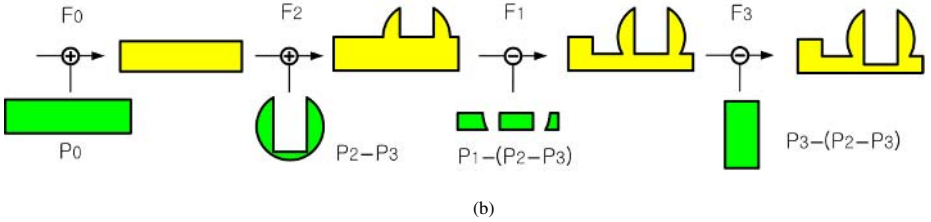
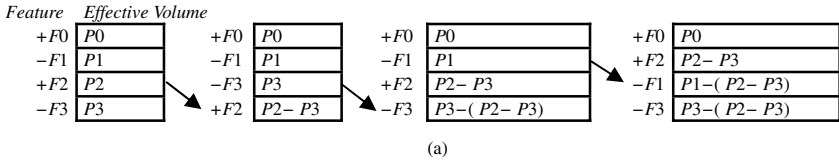


Fig. 2. A feature relocation process and the result for the feature rearrangement: $F^0 \rightarrow F^2 \rightarrow F^1 \rightarrow F^3$. (a) The series of feature relocations, and (b) the LOD models resulting from the feature relocation process in shown in 2(a).

As shown in Figs. 2 and 3, the intermediate LOD models may alter, depending on the order of the feature relocation operations. The reason for this, is that at each operation, the effective volume of the moved feature is calculated using the current definition of the effective volume. Therefore, to form intermediate LOD models with an acceptable shape using the operation based on Eq. (1), this order must be selected carefully. Moreover, there is no criterion that can be used to decide which is the most reasonable shape for an LOD model among the various options. Therefore, it is crucial to devise a method that guarantees a reasonable and unique shape for each intermediate LOD model independent of the order of the feature relocation operations.

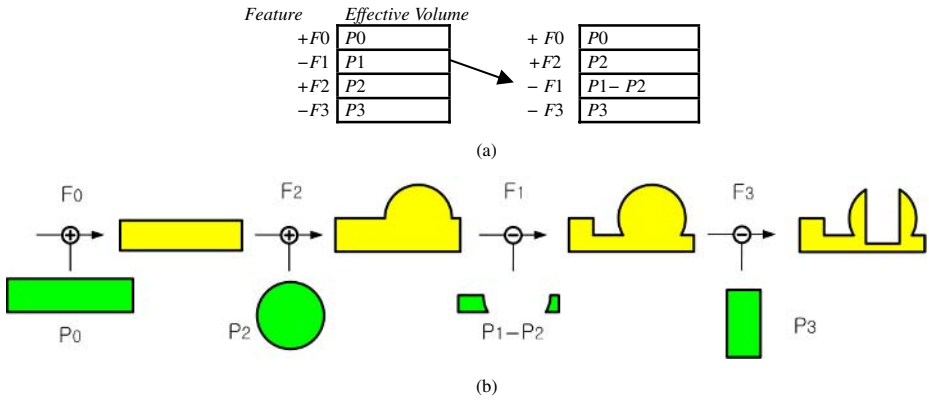


Fig. 3. Another feature relocation process and the result for the feature rearrangement: $F^0 \rightarrow F^2 \rightarrow F^1 \rightarrow F^3$. (a) The series of feature relocations, and (b) the LOD models resulting from the feature relocation process in shown in 3(a).

3 History-Based Selective Boolean Operations

To meet this requirement, we proposed *history-based Boolean (HBS-Boolean) operations* that obey commutative laws for union, subtraction, and intersection operations. By virtue of the commutative property of the union and subtraction operations, for an arbitrary feature rearrangement, these operations guarantee the same resulting shape as the original, and also a unique and acceptable shape at each intermediate LOD independent of the order of the feature movements. Although HBS-Boolean operations include intersection, we defined and will discuss only union and subtraction in this work because in general, feature-based modeling is implemented using only union and subtraction operations.

3.1 Definition

When the order of the Boolean operations is changed, the resulting shape may be different from the original. This phenomenon is due to the following reasons: (1) mixed union and subtraction operations do not obey the commutative law, and (2) Boolean operations are always applied to the entire shape, and thus, the region affected by each Boolean operation in the initial creation order is different from the affected region in the rearranged order.

In the HBS-Boolean operation, the volume of each feature is refined considering the above reasons to provide the same resulting shape, as well as a reasonable and unique shape at each intermediate LOD. The refinement is conducted by excluding the overlapping volume of the feature that satisfy the following conditions from the volume of each feature:

- To be located at the post-position in the initial creation order, but at the pre-position in the rearranged order, and
- To be of a different feature type, which is additive or subtractive.

The definition of the HBS-Boolean operations can be formalized from the refinement method above. Let F_j^i denote a feature that is applied at the i -th place in the original order, but is now located at the j -th place in the rearranged order. If $\hat{\otimes}$ denotes an HBS-Boolean operation, then the corresponding HBS-Boolean operation of F_j^i is $\hat{\otimes}_j^i P^i$. If Z_j^i denotes the refined volume of F_j^i , then the HBS-Boolean operation $\hat{\otimes}_j^i P^i$ can be represented by Eq. (2)

HBS-Boolean Operation:
$$\hat{\otimes}_j^i P^i = \otimes^i Z_j^i, \tag{2}$$

where

$$Z_j^i = P^i - \sum_{\ell=0}^{j-1} \varphi(j, \ell) \gamma(i, k(\ell)) P_\ell^{k(\ell)}, \tag{3}$$

and where $\varphi(i, j) = \begin{cases} 1 & \text{if } \otimes_i \neq \otimes_j \\ 0 & \text{otherwise} \end{cases}$, $\gamma(i, j) = \begin{cases} 1 & \text{if } i < j \\ 0 & \text{otherwise} \end{cases}$, and $k(\ell)$ is the initial location (in the original order) of the current ℓ -th feature (in the rearranged order).

3.2 Properties

The HBS-Boolean operations have the following properties:

- The resulting shape of the rearranged HBS-Boolean operations is the same as the original.
- The shape of each intermediate LOD model is determined uniquely and independently of the order of the feature relocation operations.
- Different types of HBS-Boolean operations obey the commutative law.
- The result of the HBS-Boolean operations is the same as that of the feature rearrangement algorithm that relocates the features in turn from the least significant feature in proportion to the feature significance.

Since the first four properties can be derived by the final property, we will investigate the final property first, and then prove the other properties using it.

3.2.1 Interpretation Using the Feature Rearrangement Algorithm

According to the feature rearrangement method of Algorithm 1 in Ref. [7], the least significant feature is selected first, and moved to the n -th place. Next, the second least significant feature is selected, and moved to the $n-1$ -th place. This is repeated until the most significant feature is located at the 0-th place. Whenever each feature is moved to its new place, the new effective volume is redefined using Eq. (1). Let us follow this algorithm.

Let $P_j^{(k)}$ denotes the feature primitive that is located at the j -th position in the k -th step. In the m -th step, let us assume that the m -th selected feature is located at an

arbitrary y -th place, ($0 \leq y \leq n-m+1$), in the step- $(m-1)$ order, and its primitive is P^i . If the feature is moved to the $n-m+1$ -th place, then its effective volume becomes

$$\begin{aligned}
 Z_{n-m+1}^i &= P_y^i - \sum_{\ell=y+1}^{n-m+1} \varphi^{(m-1)}(y, \ell) P_\ell^{(m-1)} = P_{n-m+1}^i - \sum_{\ell=y}^{n-m} \varphi^{(m)}(y, \ell) P_\ell^{(m)} \\
 &= P_{n-m+1}^i - \sum_{\ell=0}^{n-m} \varphi(n-m+1, \ell) \gamma(i, k(\ell)) P_\ell^{k(\ell)}
 \end{aligned} \tag{4}$$

When this process is repeated from Step I to Step n , all the effective volumes of the rearranged features are eventually determined. It should be noted that in Step m , P^i is moved to the j -th place in the step- $(m-1)$ order. Then j becomes. If $m=n-j+1$ and $P_j^i = P^i$ are applied to Eq. (4), then the result is the same $j=n-m+1$ as obtained using Eq. (3). This means that the result of the HBS-Boolean operations is always the same as that of Algorithm 1.

Figure 4 shows the result of the HBS-Boolean operations when the features are moved following the feature relocation sequence of Fig. 2(a). This example shows that HBS-Boolean operations guarantee the same resulting shape as the original, and provide a reasonable shape at the intermediate LODs independent of the order of the feature relocation operations.

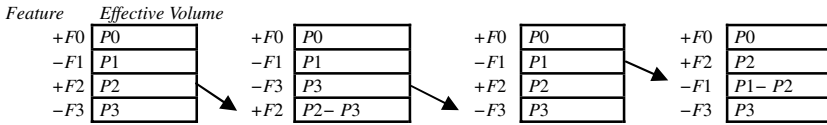


Fig. 4. The feature relocation process and the result using the HBS-Boolean operations for the feature rearrangement: $F^0 \rightarrow F^2 \rightarrow F^1 \rightarrow F^3$

3.2.2 Commutative Law

To prove the commutative laws of mixed union and subtraction HBS-Boolean operations, it is necessary to investigate a case of exchanging the j -th operation $\hat{\otimes}_j P_j$ and the $j+1$ -th operation $\hat{\otimes}_{j+1} P_{j+1}$. Let us assume that the original positions of F_j and F_{j+1} are an arbitrary x and y , respectively. Then, the model M_{j+1} at $\text{LOD} = j+1$ is represented by the following formula

$$M_{j+1} = M_{j-1} \hat{\otimes}_j^x P^x \hat{\otimes}_{j+1}^y P^y \tag{5}$$

On the other hand, if M'_{j+1} denotes the model after the exchange of the j -th and the $j+1$ -th operations, then it can be represented as follows

$$M'_{j+1} = M_{j-1} \hat{\otimes}_j^y P^y \hat{\otimes}_{j+1}^x P^x \tag{6}$$

To prove that the HBS-Boolean operations satisfy the commutative law, it is necessary to show that Eq. (5) is equal to Eq. (6), i.e. $M_{j+1} = M'_{j+1}$.

According to the algorithm described in Section 3.2.1, M_{j+1} can be represented by

$M_{j+1} = \prod_{i=0}^{j+1} \otimes_i^{(n-j-1)(n-j-1)} P_i$. Let us assume that in Step $n-j-1$ the locations of P^x and P^y are an arbitrary s and t , respectively. If P^y and P^x are moved to the $j+1$ -th and j -th place in turn, then M_{j+1} can be represented as follows

$$\begin{aligned}
 M_{j+1} &= \left(\prod_{i=0, i \neq t}^j \otimes_i^{(n-j-1)(n-j-1)} P_i \right) \otimes^y Z_{j+1}^y \\
 &= \left(\prod_{i=0, i \neq s, i \neq t}^j \otimes_i^{(n-j-1)(n-j-1)} P_i \right) \otimes^x Z_j^x \otimes^y Z_{j+1}^y \\
 &= \left(\prod_{i=0}^{j-1} \otimes_i^{(n-j+1)(n-j+1)} P_i \right) \otimes^x Z_j^x \otimes^y Z_{j+1}^y \\
 &= M_{j-1} \otimes^x Z_j^x \otimes^y Z_{j+1}^y \\
 &= M_{j-1} \hat{\otimes}_j^x P^x \hat{\otimes}_{j+1}^y P^y.
 \end{aligned} \tag{7}$$

Next, let us apply the relocation operation in a different order. If P^x and P^y are moved to the $j+1$ -th and j -th place in turn, then M_{j+1} can be represented as follows.

$$\begin{aligned}
 M_{j+1} &= \left(\prod_{i=0, i \neq s}^j \otimes_i^{(n-j-1)(n-j-1)} P_i \right) \otimes^x Z_{j+1}^x \\
 &= \left(\prod_{i=0, i \neq s, i \neq t}^j \otimes_i^{(n-j-1)(n-j-1)} P_i \right) \otimes^y Z_j^y \otimes^x Z_{j+1}^x \\
 &= \left(\prod_{i=0}^{j-1} \otimes_i^{(n-j+1)(n-j+1)} P_i \right) \otimes^y Z_j^y \otimes^x Z_{j+1}^x \\
 &= M_{j-1} \otimes^y Z_j^y \otimes^x Z_{j+1}^x \\
 &= M_{j-1} \hat{\otimes}_j^y P^y \hat{\otimes}_{j+1}^x P^x.
 \end{aligned} \tag{8}$$

From Eqs. (6), (7) and (8), the relationship $M_{j+1} = M'_{j+1}$ is established, regardless of the operation type. Therefore, the HBS-Boolean operations satisfy the commutative law for union and subtraction.

4 Implementation

The HBS-Boolean operation was implemented in a feature-based nonmanifold modeling system that was developed based on the Partial Entity Structure. The data

structures proposed in Ref. [7], such as multi-resolution features and the merged set, were also used to facilitate the implementation. The Boolean operations were implemented using the merge-and-select algorithm. For a case study, the well-known ANC-101 test part was chosen. Figure 5 shows the modeling process of the ANC-101 part composed of 8 steps. Figure 6 shows the result of the example where the features were rearranged in the order specified by the authors.

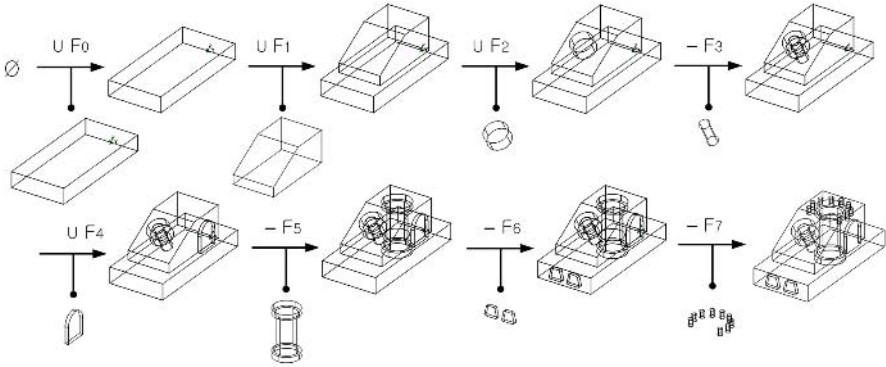


Fig. 5. Feature-based modeling process for the CAM-I ANC-101 test part

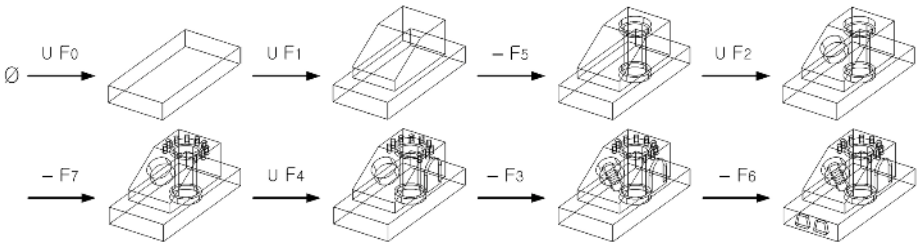


Fig. 6. Multi-resolution models where the features are rearranged in descending order of volume, regardless of the feature type

5 Conclusions

We have proposed HBS-Boolean operations for feature-based multi-resolution modeling, which satisfy the commutative laws for union and subtraction. Because union and subtraction are commutative, then for an arbitrary rearrangement of features, these operations guarantee the same result as the original part shape, and provide reasonable and unique shapes at each intermediate LOD independent of the order of the feature relocation operations. The HBS-Boolean operations were implemented based on a nonmanifold boundary representation and the merge-and-select algorithm. This approach allows for fast extraction of multi-resolution models for given LODs. Although a nonmanifold representation was adopted in this work, as the HBS-Boolean operations are independent from the topological frameworks, they can be

implemented using conventional solid data structures, as well as nonmanifold data structures. More applications of the HBS-Boolean operations should be investigated in the future.

Acknowledgement

This work is financially supported by the Ministry of Education and Human Resources Development(MOE), the Ministry of Commerce, Industry and Energy(MOCIE) and the Ministry of Labor(MOLAB) through the fostering project of the Lab of Excellency.

Reference

1. Belaziz, M., Bouras, A., Brun, J. M.: Morphological analysis for product design. *Computer-Aided Design*. 21 (2000) 377-388
2. Choi, D. H., Kim, T. W., Lee K.: Multiresolutional representation of b-rep model using feature conversion. *Transactions of the Society of CAD/CAM Engineer*. 7 (2002) 121-130
3. Kim, S., Lee, K., Hong, T., Kim, M., Jung, M., Song, Y.: An integrated approach to realize multi-resolution of B-rep model. *Proc. of the 10-th ACM Symposium on Solid Modeling and Applications* (2005) 153-162
4. Koo, S., Lee, K.: Wrap-around operation to make multi-resolution model of part and assembly. *Computers & Graphics* 26 (2002) 687-700.
5. Lee, J. Y., Lee, J.-H., Kim, H., Kim, H. S.: A cellular topology-based approach to generating progressive solid models from feature-centric models. *Computer-Aided Design* 36 (2004) 217-229
6. Lee, S. H.: A CAD-CAE integration approach using feature-based multi-resolution and multi-abstraction modeling techniques. *Computer-Aided Design* 37 (2005) 941-955
7. Lee, S. H.: Feature-Based Multiresolution Modeling of Solids. *ACM Transactions on Graphics* 24 (2005)1417-1441

Path Finding Method for Various Applications

Jaesung Song¹, Manseung Seo¹, and Masahiko Onosato²

¹ Tongmyong University, Busan 608-711, Korea
{jssong, sms}@tu.ac.kr

² Hokkaido University, Sapporo, Hokkaido, 060-0808, Japan
onosato@ssi.ist.hokudai.ac.jp

Abstract. Increasing the robustness and flexibility of the tool path finding method may broaden the application fields of pocket machining. We aim to develop a path finding method for various applications. Through an integration of the entire tool path finding process, the method becomes not merely optimal to generate an efficient path but also robust enough to be applied to any system with any configuration. The flexibility of the devised method enables us to broaden the application fields of pocketing to fields such as prototype printed circuit board manufacturing. The devised method is applied to generate a clearing path for prototype printed circuit boards. The results verify that the method is concise and simple, but robust and flexible enough to achieve the optimal path in any configuration.

1 Introduction

Conventionally in pocket machining, the contour-parallel tool path is most widely used for large-scale material removals. Many researches on contour-parallel cutting have been performed [1], [2], [3]. Various methods for generating tool paths have been developed [4], [5]. To produce a tool path without tool-retraction satisfying the Guyder's guidelines [6], several methods have been developed but those are not flexible enough to handle every kind of pocket configuration. The limitations on existing approaches are found in the literature. Bridges connecting a pocket and islands are inserted to form a boundary [2]. The particular sub-path is merged into the corresponding path to treat specific occasions such as nested offset loops [5].

Recently, Seo et al.[7] proposed a systematic approach on contour-parallel tool path generation in order to achieve all of the goals in the three categories simultaneously. In their approach, the contour-parallel tool path generation from offsetting to path linking was totally integrated hierarchically on classified levels being engaged by the devised process flow. Through their work, problems finding proper offset curves, preventing uncut regions and producing a tool path without tool-retraction were resolved sequentially.

In the present study, we aim to develop a path finding method for various applications. By increasing the robustness and flexibility of the path finding method, the application fields of pocketing can be easily broadened. The fields

may be enumerated as laser cutting, wire electrical discharge machining and prototype Printed Circuit Board (PCB) manufacturing. The PCBs are essential for products associated with mechatronics. Especially during the development period, highly customized prototype PCBs are required.

Nowadays, a prototype PCB is manufactured by either the printing or cutting method. For large quantities or mass production, the printing method may be better. For small quantities of customized manufacturing, cutting is proper. Therefore PCB layering, especially for highly customized prototypes, may be the right place to apply pocket machining, even though the features are more complicated than pockets.

To attain our aim, the tool path finding process is reconsidered in conjunction with the work of Seo et al.[7]. By the systematic integration of the entire tool path finding process, the method becomes not merely optimal to generate the efficient path but also robust and flexible enough to be applied to any system with any configuration.

To verify the proposed method, a prototype system is implemented and the system is examined with actual pocket machining. The results show that the proposed path finding method is proper and reliable. Moreover, the robustness and flexibility of the devised method enables us to broaden the application fields of pocketing. The devised method is applied to generate a clearing path for prototype PCBs upon cutting. The results verify that the devised method is concise and simple, but robust and flexible enough to achieve the optimal path in any configuration, even for PCBs.

2 Concepts

To integrate the complicated path generation process, we adopt some concepts defined by Seo et al.[7]. The Offset Loop Entity (OLE) was devised to be the unique object of every generation procedure. Throughout the entire path generation process in the OLE approach, each generation procedure was conserved upon various pocketing conditions.

The concepts for path finding used in this work is shown in Fig.1. The OLE is defined as the sequential linkage of the offset curves. The Path link Entity (PE) is defined as the element linking all validated OLEs. The Tool Path Entity (TPE) is defined as the entire path composed of all validated OLEs and all PEs. The cutting boundaries are shown as bold solid lines. Thin solid lines and thin dotted lines represent the OLEs and PEs, respectively. Consequently, all thin lines belong to the TPE.

3 OLE Generation

We focus our attention more on path finding. Thus, the offset curve generation procedures are briefly discussed based on the Offset-loop Dissection Method (ODM) by Seo et al.[7]. The ODM and extended ODM were proposed based on the OLE concept that enables the method to be implemented easily into

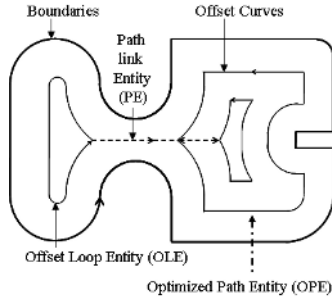


Fig.1. Concepts for path finding

the system at any condition, regardless of the number of offsets, the number of intersections, the number of islands, and even the number of uncut regions.

To avoid complication, we assume that all cutting boundaries are constructed with lines and circular arcs, even though some consider these as free-formed curves. Then the conventional expression for offset curves becomes $C_i(t) + d \cdot N_i(t)$, where, $C_i(t)$ is the cutting boundary, d is the offset distance, and $N_i(t)$ is the unit normal vector with offsetting direction. By connecting all offset curves in the sequence of creation, the inborn OLE is constructed.

In pocket machining, there is a strong possibility of the inborn OLE being formed into an open loop having local and global self-intersections. The local OLE reconstruction is performed sequentially through the OLE creation from offset curves. This is done by inserting additive offset curves or removing local self-intersections between two adjacent offset curves. The global OLE reconstruction is completed by two consequent procedures; detection of an OLE intersection, and dissection of the OLEs at the intersection and then reconnection of the dissected OLEs. A detailed description of the global OLE reconstruction procedure can be found at Seo et al.[7].

The OLE obtained by the global OLE reconstruction may still not be an appropriate OLE as an offset curve for cutting. The characteristics of the OLE, *i.e.*, closeness and orientation, need to be examined to confirm the validity of the OLE. The closeness of the OLE reflects the possibility of a continuous cutting path. Thus a valid OLE must be completely closed. The orientation of the OLE determines cutting directions, inwards or outwards of the cutting boundary. Fixing the orientation of the cutting boundary to be counterclockwise, the counterclockwise OLEs are selected as valid OLEs. Then, the valid OLEs are kept to play the role of offset curves for the path finding process.

4 Path Finding Method

In the present study, the path finding problem results in a variant of the searching problem but is more sophisticated. To attain both robustness and flexibility, a method that generally but accurately finds a path upon preceding constraints is proposed. The details of the path finding process are discussed through an illustrated example of pocketing.

In pocket machining fields, the efficient path is known as the path with minimal slotting, no over-milling, and no tool-retraction[5],[6]. In order to find the most efficient path with robustness and flexibility, a path finding method based on the OLE/PE concepts and the data structure accumulated throughout the OLE generation process is devised. The devised path finding method is so simple that the determination of the path linking sequence is accomplished by two searches; 1) the Breadth First Search (BFS)[8] on the OLE Generation History (OGH) graph and 2) the Depth First Search (DFS)[8] on the Tool Path (TP) tree. Even so, the method is robust and flexible enough to generate a path with minimized slotting/over-milling and no tool-retraction under any kind of geometry or configuration.

4.1 OGH Graph

The OGH graph is constructed, by connecting valid OLEs during the OLE generation process. An illustrated example of the OLE map generated by ODM [7] for a pocket with three islands is shown in Fig.2. The OGH graph corresponding to the OLE map is shown in Fig.3.

By means of the OGH graph, the OLE is stored in a linked list data structure such that the lineage of the OLE is expressed as a tree data structure. The information about the relationships among OLEs through the successive offsetting is contained in the OGH graph. The OLE itself is represented as a node and the birth of an OLE is expressed using branches like a family tree. The arrows in Fig.3 are used just for the representation of offsetting levels. The OGH graph itself is a graph without directions.

In this specific example, 25 valid OLEs are connected with 26 branches in the sequence of generation throughout the offsetting. However, anyone looking at the OGH graph could find that the minimal number of branches needed to connect 25 OLEs is 24. Over-milling is unavoidable if all 26 branches in Fig.3 are selected as the linking tool path segments for 25 OLEs. Thus, the modification of the OGH graph is inevitable to discard the redundant branches responsible for over-milling.

4.2 TP Tree

An OLE where the cutting starts is selected by considering technological constraints, such as tool-retraction and/or cutting strategy. From the selected starting OLE, a BFS on the undirected OGH graph is performed. Then, the TP tree is constructed upon the BFS result by linking all OLEs with a minimal number of PEs instead of excessive branches. The TP tree corresponding to the OGH graph is shown in Fig.4. The relational information about the OLEs/PEs with linking sequences and the geometric information on the OLEs upon creation are contained in the TP tree.

In this specific example, OLE_{24} is selected as a starting OLE to present outward cutting with minimized slotting. The TP tree shows that the reduction of over-milling is accomplished by the BFS search. By linking all OLEs with the minimal number of PEs in Fig.4, two redundant branches (b_{11} , b_{12}) from Fig.3

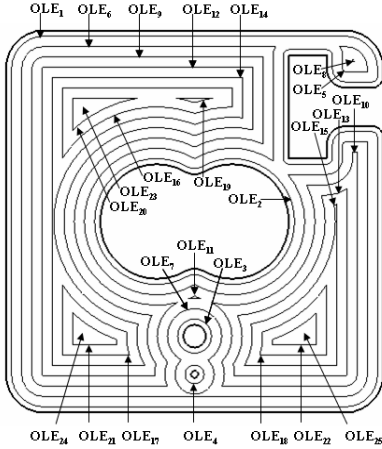


Fig. 2. OLE map by ODM

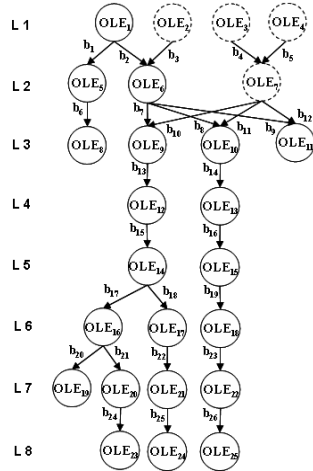


Fig. 3. OGH graph

are discarded. However, it is still not possible to start on the actual cutting relying only upon the information contained in the TP tree, even though the TP tree contains the logical link information on PEs upon OLEs. Therefore, the geometric information, *i.e.*, physical link information, on the PEs such as its position and entry/exit point must be determined.

4.3 PE Placement

An OLE where the cutting ends is selected by considering technological constraints and by accounting the number of PEs to the starting OLE. The one-way path from the starting OLE to the ending OLE is set. The PEs in the one-way path are placed onto the OLE map with the location of an entry/exit point on the OLE. Then, the OLEs/PEs on the one-way path are marked on the TP tree. The rest of PEs in breadth of the marked path are placed onto the OLE map with the location of an entry/exit point on the OLE, forming the shortest line segment upon upper PE position.

As the result of the PE placement on the OLE map, the physical link information is set. However, the parental OLE having two or more successive OLEs in the TP tree appears with multiple entry/exit points on it. The consideration on the visiting precedence of multiple entry/exit points existing on a single OLE is left for the next step.

In this specific example, OLE₁ is selected as an ending OLE to present outward cutting. The PEs (PE₂₅, PE₂₂, PE₁₈, PE₁₅, PE₁₃, PE₇, PE₂) in the one-way path are placed onto the OLE map with a bold lined arrow as shown in Fig.5. The OLEs (OLE₂₄, OLE₂₁, OLE₁₇, OLE₁₄, OLE₁₂, OLE₉, OLE₆, OLE₁)and

the PEs in the one-way path are marked on the TP tree to be searched last. Then, the rest of PEs in breadth of the marked path are placed onto the OLE map with the thin lines marking the location of an entry/exit point as shown in Fig.5.

The possibility of over-milling is not negligible, since the parental OLEs having two or more successive OLEs showed up with multiple entry/exit points on them shown as OLE_{14} , OLE_{16} , OLE_9 , OLE_7 , OLE_6 in Fig.4 and Fig.5. Therefore, the visiting precedence of multiple entry/exit points should be determined properly.

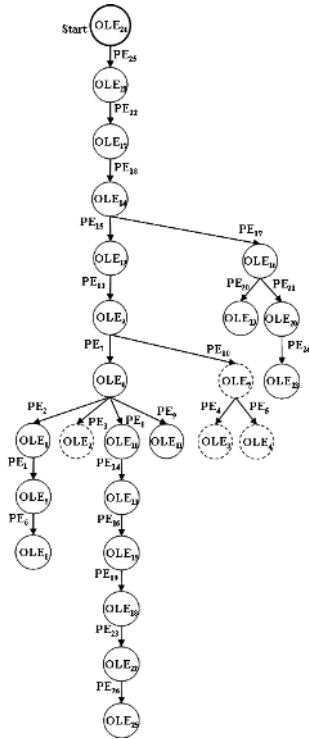


Fig. 4. TP tree upon BFS result

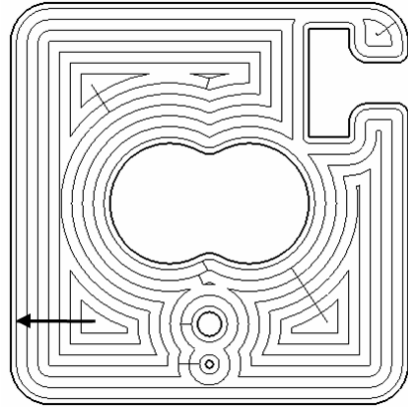


Fig. 5. OLE map with PE placement

4.4 Visiting Precedence

The OLEs/PEs on the marked path are placed on the rightmost of the TP tree to be searched last. The OLEs/PEs in breadth of the marked path are reordered, by comparing the travel distance of the tool upon parental OLE orientation, to confirm visiting precedence.

In this specific example, the bold lined marked path $OLE_{24} \rightarrow OLE_{21} \rightarrow OLE_{17} \rightarrow OLE_{14} \rightarrow OLE_{12} \rightarrow OLE_9 \rightarrow OLE_6 \rightarrow OLE_1$ is shown on the rightmost side of the TP tree being planned to be searched last as shown in Fig.6.

To prevent over-milling, the breadth order $OLE_2 \rightarrow OLE_{10} \rightarrow OLE_{11}$ in Fig.6 is changed to $OLE_{10} \rightarrow OLE_2 \rightarrow OLE_{11}$ in Fig.7 considering the counterclockwise orientation of the parental OLE (OLE_6).

4.5 Path Determination

The DFS is performed on the arranged TP tree to find the shortest path. To avoid tool-retractions, the marked one-way path is searched last. The shortest path upon the DFS result is written down and saved as the TPE with minimal slotting, no over-milling, and no tool-retraction.

In this specific example, the logical link information on the OLEs/PEs in the shortest tool path obtained by the DFS is shown in Fig.7 along with their physical link information engraved on the OLE map shown in Fig.4.3. Fig.5. The shortest path from the starting OLE (OLE_{24}) to the ending OLE(OLE_1) is represented by the TP tree with the precedence of visiting, from the top to the bottom, from the left to the right, and upon the unidirectional or bi-directional arrows. The result verifies the simplicity and excellence of the devised method in treating nested offset loops.

4.6 Path Efficiency

In use of the devised method, the selection of a starting point or an ending point of cutting is not restricted at all. Regardless of the starting/ending point, the method generates the shortest path from the starting point to the ending point. By being able to freely select a starting point or an ending point of cutting, the technological constraints upon cutting may be more easily satisfied.

On the other hand, the selection of starting and ending points is crucial for the minimization of over-milling and/or the reduction of the travel distance of the tool. The proposed method enables the efficient selection of starting and ending points feasible.

By taking a glance at the OGH graph, anyone can easily notice that where the starting/ending point should be to minimize over-milling. Looking at the OGH graph shown in Fig.3 for this specific example, any one can tell that the combinatorial selection of starting and ending OLEs among (OLE_{23} , OLE_{24} , OLE_{25}) would be the best.

Upon the selection of the starting/ending point, the total length of the most efficient path planned by the devised method, L may be written as:

$$L = \sum_{i=1}^n l_i + d(2n - m - 1) \tag{1}$$

where, n is the total number of OLEs, l_i is the length of i -th OLE, d is the fixed offset distance, and m is the number of OLEs on the marked one way path in TP tree, *i.e.* on the straight line in OLE map from a starting OLE to an ending OLE. By increasing m in equation (1), the total distance for tool to travel, L , is reduced. Thus, we may say that the devised method optimizes the path to be the most efficient one upon the selection of the starting/ending point accordant to technological constraints in cutting.

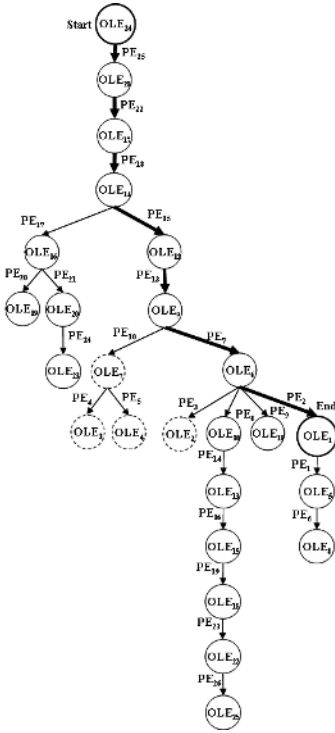


Fig. 6. Arranged TP tree

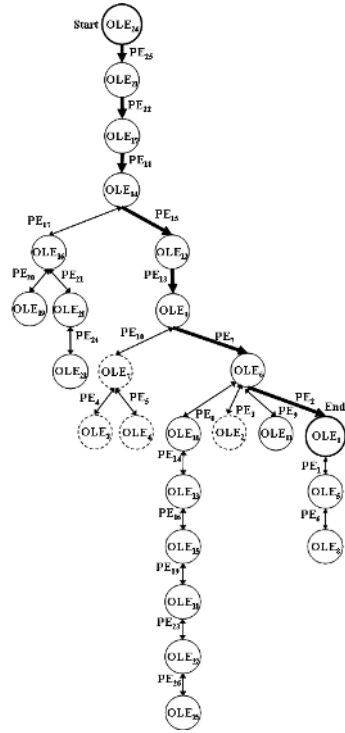


Fig. 7. The shortest path

4.7 Algorithm

The algorithm upon the proposed path finding method may be summarized as:

- Step 1 Generation of the OGH graph from the OLE map.
 - 1-1 Connect valid OLEs in the sequence of generation.
- Step 2 Construction of the TP tree.
 - 2-1 perform a BFS on the undirected OGH graph.
 - 2-2 Link OLEs by inserting PEs upon the BFS result.
- Step 3 Placement of PEs onto the OLE map.
 - 3-1 Select an ending OLE considering the number of needed PEs.
 - 3-2 Locate PEs in one-way path from starting OLE to ending OLE.
 - 3-3 Locate PEs in breadth upon upper PE position.
- Step 4 Confirmation of precedence.
 - 4-1 Allocate the marked path on the rightmost to be searched last.
 - 4-2 Reorder OLEs in breadth of the marked path upon parental OLEs.
- Step 5 Determination of the shortest path.
 - 5-1 perform a DFS through every OLE on the arranged TP tree.
 - 5-2 Confirm the shortest path as the TPE upon the DFS result.

The devised algorithm generates a tool path free from over-milling and tool-retraction, even with minimal slotting. Moreover, the algorithm is robust enough to generate a tool path under any kind of offset loop configuration including a nested one.

5 Implementation

In order to verify the robustness of the proposed path finding method, a prototype system is implemented using C language and OpenGL graphic library. Then, the system is examined with actual machining for pockets with multiple islands and even for uncut free pockets, on an IBM RS6000 140/43P.

The screen image of the uncut free tool path obtained from the implemented system is shown in Fig.8. The photograph of an actually machined wax part with the path created by the devised algorithm on the mini-milling machine, Modella 50, is shown in Fig.9. The results show that the proposed method is robust enough to generate an uncut free, over-milling free and tool-retraction free tool path for any kind of pocket.

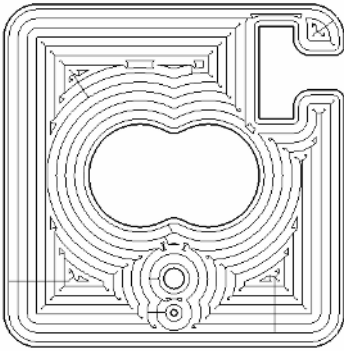


Fig. 8. Uncut free path

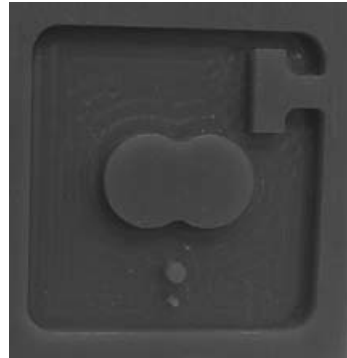


Fig. 9. Machined result

6 Application to PCBs

To ensure the flexibility of the devised path finding method and to broaden the fields where the method may apply, the clearing path is generated for the fabrication of a prototype PCB by the cutting method.

An illustrated example of a prototype PCB is shown in Fig.10. The screen image of the clearing path for a prototype PCB generated by the implemented system upon the devised method is shown in Fig.11. The result verifies that the devised method is robust and flexible enough to achieve the optimal tool path for any system under any configuration without trouble treating specific occasions.

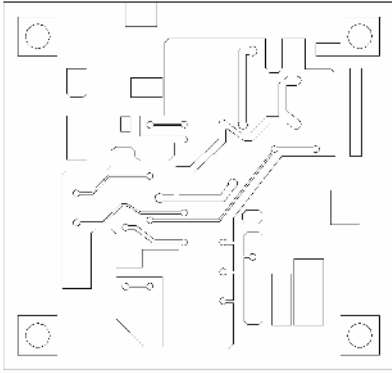


Fig. 10. PCB CAD data

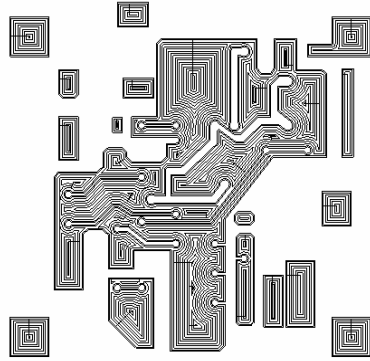


Fig. 11. Optimized path for PCB

7 Conclusions

To broaden the application fields of pocketing, a path finding method with robustness and flexibility is proposed. The devised method enables the proper selection of starting/ending points for the minimization of over-milling. Also, the method optimizes the path to be the most efficient one upon the selection of the starting/ending point in accordant to technological constraints in cutting.

The prominent features of the method are: *Simplicity*, the entire path finding process is systematically integrated in continuation from the offsetting procedure. *Flexibility*, every path finding procedure deals only with the OLE, which enables the algorithm to be applicable to any system. *Robustness*, each path finding step is devised based upon the geometry and the logical data structure. The method fulfills the optimal path generation upon any technological requirement with no burden treating specific occasions.

References

1. Held, M., Lukacs G., Andor, L.: Pocket machining base on contour-parallel tool paths generation by means of proximity maps. *Computer Aided Design* **26** (1994) 189–203
2. Hatna, A., Grieve, R.J., Broomhead, P.: Automatic CNC milling of pockets: geometric and technological issues. *Computer Integrated Manufacturing Systems* **11** (1998) 309–330
3. Kim, D.S.: Polygon offsetting using a Voronoi diagram and two stacks. *Computer Aided Design* **30** (1998) 1069–1076
4. Shan, Y., Wang S., Tong S.: Uneven offset of NC tool path generation for free-form pocket machining. *Computers in Industry* **43** (2000) 97–103
5. Park, S., Chung, Y., Choi, B.: Contour-parallel offset machining without tool-retractions. *Computer Aided Design* **35** (2003) 35–45
6. Guyder, M.: Automating the optimization of 2.5 axis milling. *Computer Industry* **15** (1990) 163–168

7. Seo, M, Kim, H., Onosato, M.: Systematic approach to contour-parallel tool path generation of 2.5-D pocket with islands. *Computer-Aided Design and Applications* **2** (2005) 213–222
8. Horowitz, E., Sahni, S., Anderson-Freed S.: *Fundamentals of data structures in C*. Computer Science PRESS, W. H. Freeman and Company (1993)

Natural-Textured Mesh Stream Modeling from Depth Image-Based Representation

Seung Man Kim, Jeung Chul Park, and Kwan H. Lee

Gwangju Institute of Science and Technology (GIST),
Intelligent Design and Graphics laboratory, Department of Mechatronics,
1 Oryong-dong, Buk-gu, Gwangju, 500-712, Korea
{sman, jucpark}@gist.ac.kr, lee@kyebek.gist.ac.kr
<http://kyebek.gist.ac.kr>

Abstract. This paper presents modeling techniques to generate natural-textured 3D mesh stream from depth image-based representation (DIBR). Although DIBR is a useful representation for expressing 2.5D information of dynamic real objects, its usage is limited to point-based applications. In order to generate smooth and textured 3D mesh models, depth images are captured using active depth sensors, and they are processed with segmentation, noise filtering, and adaptive sampling technique based on the depth variation. 3D meshes are reconstructed by constrained Delaunay triangulation and smoothed with the 3D Gaussian filter. Each mesh model is parameterized for texture mapping of a corresponding color image. Proposed procedures are automated to generate 3D mesh stream from hundreds of image sequence without user interventions. Final output is a natural-textured mesh model per frame, which can be used for arbitrary view synthesis in virtual reality or broadcasting applications.

1 Introduction

As realistic digital broadcasting is rapidly emerging, generation of 3D contents becomes important. 2D stream media, however, are still the conventional video- and audio-based contents in the broadcast industry. But end-users want realistic media contents, such as three-dimensional and multi-modal media. To realize more realistic multi-modal interactions, dynamic objects in the real scene should be modeled as accurate 3D meshes [1]. Geometric 3D models satisfy the demands of multi-modal interactions, but it is difficult to reconstruct a 3D mesh from 2D video data. In the E.U.-funded MetaVision project, they composed 3D CG objects into the real scene using a depth map of video sequences to support optical interactions. They estimated a sequence of 2.5D depth maps using the multi-baseline stereo approach [2], but they did not focus on the reconstruction of an explicit geometry from the depth map. In another E.U.-funded ORIGAMI project, on the other hand, they generated complete 3D models of dynamic scenes using the shape-from-silhouette approach [3]. They established the optical interactions such as occlusions, shadows, and reflections by using the render

functionality of the animation package. The experiment, however, was performed using the studio-based system that equipped with six calibrated cameras in fixed locations.

Recently, many research activities have been performed on 3D scene modeling from multiple 2D images or depth images. Image-based modeling (IBM) is a popular technique that refers to the reconstruction of 3D geometric models using 2D images [4][5]. However, image-based reconstruction of arbitrary shapes is a hard problem and a few techniques have been developed for reconstructing approximate models only. Space carving computes the 3D shape of an arbitrary scene from multiple photographs taken at arbitrary-view points [6]. Non-linear optimization algorithm is proposed to reconstruct 3D textured models of architectural elements from photographs [7]. This approach reconstructs an approximate parameterized model composed by simple 3D primitives from a set of calibrated photographs. The shape-from-silhouettes technique [8][9] requires camera calibration to obtain the camera parameters. After the intersection of the bounding volumes of each silhouette is computed, the 3D model is generated from the remaining convex hull in the form of a voxel representation. The techniques from multiple views have been proven to be sufficiently fast, scaleable, and robust for 3D reconstruction in real time. But, These are restricted to special environments equipped with multiple camera sensors. There is also the shape-from-one-silhouette technique that can generate an approximated 3D reconstruction using a polynomial function of the distance to a single 2D silhouette [10]. But the resulting 3D model from a single silhouette is inaccurate since volume expansion is assumed to reach the maximum level at the center of human images. Also, they need a special environment, like a blue screen in a virtual studio, because the actor needs to be segmented using the chroma-keying techniques. Image-based approaches can potentially reduce the labor-intensive task generally required for modeling detail geometric structures. Besides image-based techniques, the object-based active techniques are more accurate and robust [11][12]. Many active systems use lasers or structured light, but few systems are able to capture a moving 3D scene at video frame rate.

With the development of 3D depth sensors such as the *ZCamTM* depth camera [13], per-pixel depth information can be captured from dynamic real objects in real time. But real depth images usually contain quantization errors and optical noise, due to the reflectivity or color variation of the objects. For example, for the flat, black-and-white object that we capture by the depth camera, the white part shows a high depth value, while the black part, although the object is planar, shows a relatively low depth value. Reflectance properties and environmental lighting conditions also cause optical noise, which produce improper artifacts for rendering, or other interactions.

In this paper, we present a depth image-based modeling method of a dynamic real object, which is view-based 3D modeling processes offline for the recorded real-time contents. First, we segment the foreground object and apply the median-filtering technique to reduce noise. Then, we adaptively sample feature points using 1st gradient analysis, since depth variation greatly affects

the quality of a reconstructed surface. We triangulate the feature points using the Delaunay triangulation technique. Since initial 3D meshes still contain local noise that produce jagged surfaces, we apply Gaussian smoothing to enhance the smoothness of the surface. Finally, we map the texture image onto the refined 3D meshes, where the texture image is taken from the color frame captured together with the depth image.

2 Preprocessing of Depth Video

2.1 Depth Video Acquisition and Noise Filtering

Depth video consists of object appearance and geometry information as a form of two streams: color stream and depth stream. Simulated depth video is easily obtained using rendering of the animated object from each frame in offline rendering packages (e.g. Discreet 3DS MAX or Alias Maya), where depth image is saved using Z-buffer. The resulting data is a set of synchronized color and depth stream so called DIBR (Depth-image based representation)[14]. However, it is difficult to acquire real depth video from real scenes since it should be captured and processed in real time. To obtain the depth stream of dynamic real actors, we used a depth video camera that produces both RGB color and depth signals in real time. This camera captures the depth value for each pixel of dynamic actors in the field of view (FOV) so that it generates a depth image of an actor by scaling the real distances up to 256 levels. This modality makes it possible to record dynamic real actors at video frame rate.

We set the capturing range to cover the movement of dynamic objects. For this reason, the other ranges, except for the containing objects, have no depth value that is, the gray value of pixels in other ranges is zero. Since only interesting objects have depth values for their pixels, we can easily segment them using the thresholding histogram. Raw depth images contain noise, such as the isolated lines or pixels as shown in Fig. 1(a). If noise would be directly used to construct the 3D surface, jagged surfaces are generated as the right image of Fig. 1(a). We therefore apply median filtering to remove noise while preserving spatial resolution. Fig. 1(b) shows the median-filtered depth image with a 5x5 filter window. But 3D mesh shape still contains local shapes because the filtering operation is performed on local neighborhoods of pixels. Although the depth

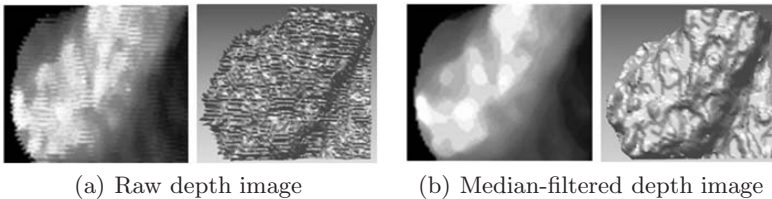


Fig. 1. Noise reduction by median filtering

image is smoothly enhanced through median filtering, 3D mesh surface lacks global smoothness.

2.2 Adaptive Point Sampling

If all pixels were used to build a 3D model, many superfluous triangles would be generated. For example, if the size of the depth image is M by N, the number of triangles would be almost 2MN if regular triangles were generated. Considering the surface quality and limited system resource, a small number of meaningful pixels should be extracted from the depth image. We define meaningful pixels as feature points located in the region where the gray values of the depth change greatly. That is, the feature points are adaptively extracted based on the magnitude of the 1st gradients. Adaptive sampling algorithm produces dense points in the region of high depth variation. The Sobel operator is applied to a median-filtered depth image to compute the magnitude of the 1st gradient g . The ideal sampling function eq.(1), which is a 2D finite array of Dirac delta functions situated on a rectangular grid with, spacing $\Delta x, \Delta y$, is used in this paper [15].

$$comb(x, y; \Delta x, \Delta y) \cong \sum_{n=0}^{H-1} \sum_{m=0}^{W-1} \delta(x - m\Delta x, y - n\Delta y) \tag{1}$$

Where, H and W are height and width of the depth image, respectively. The sampled image u_s is computed using the eq.(2):

$$u_s(x, y) = u(x, y)comb(x, y; \Delta x, \Delta y) \tag{2}$$

We determine the spacing based on the magnitude of the 1st gradients and the pixel location using the following rules. g_{th} is a threshold value of 1st gradients. The spacings are determined by the rounded sampling spacing sp that is defined by one percent of bigger one between height and width of the object. The spacing values are adjusted depending on the size of the object. Additionally, uniform sampling is conducted greatly by triple of sp not to generate big holes inside region of low depth variation. Silhouette points are detected by computing the

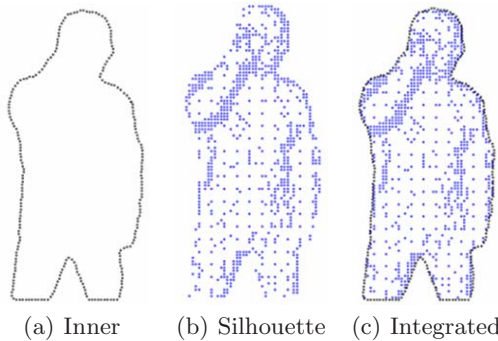


Fig. 2. Extracted feature points by an adaptive sampling scheme

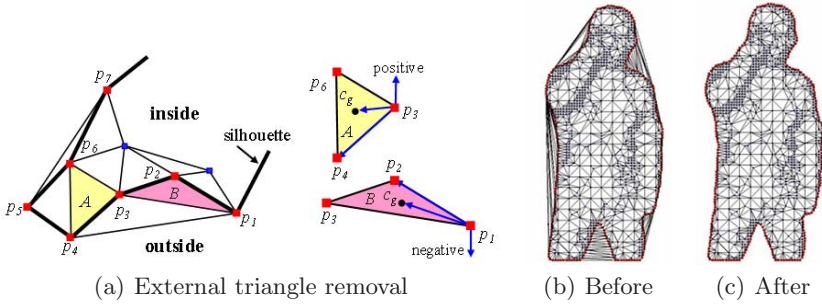


Fig. 3. Constrained Delaunay triangulation in 2D domain

second-order derivative at each pixel in the thresholded binary image. After silhouette points are extracted by setting the spacing to one, they are rearranged in nearest order, smoothed and down-sampled. Fig. 2 shows extracted feature points.

3 Triangulation and 3D Projection

3.1 Constrained Delaunay Triangulation

To generate 2D triangular mesh from feature points, the constrained Delaunay triangulation (CDT) is utilized [16]. The silhouette contour is used as the constraints for CDT. A Delaunay triangulation method produces fast and robust triangulation, but the output mesh normally contains external triangles outside the object. The output of triangulation becomes the convex hull of meshes as shown in Fig. 3(b). Those are unnecessary triangles that should be removed for an accurate shape modeling. Since output meshes are triangulated by the CDT algorithm, external triangles can be removed using the pre-computed silhouette contour points. External triangles are recognized with the cross product by distinguishing the internal and external of the object. In Fig. 3(a), each p_i indicates ordered silhouette points and c_g is the center of gravity (COG) of the triangle. The cross product of two vectors $p_i c_g$ and $p_i p_{i+1}$ is calculated and its direction is used as a criterion for the internal and external distinction. For instance, the internal triangle A is maintained since it has a positive direction, while the external triangle B with a negative direction is removed. Fig. 3(c) shows the refined mesh models.

3.2 Projection of 2D Mesh onto 3D Domain

To reconstruct a 3D surface, vertices of 2D mesh are projected onto 3D domain using camera parameters. We assume that the depth camera is the frontal pinhole camera model as shown in Fig. 4(a). The image of a 3D point P is the image point p at the intersection of the ray going through the optical center o , and the image plane at a distance f in front of the optical center. In the pinhole camera model, if a 3D point has coordinates $P = [X, Y, Z]^T$ relative to a reference frame

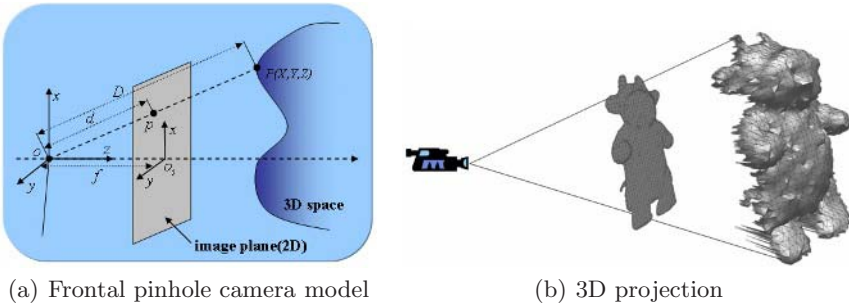


Fig. 4. 3D projection of 2D mesh onto 3D domain

centered at the optical center o , with the optical axis as its z -axis, the coordinate of P and its image $p = [x, y, f]^T$ are related by the ideal perspective projection in Eq. (3), where f is the focal length. Fig. 4(b) shows a projected 3D mesh model from 2D mesh. Although depth image is filtered and adaptively sampled, the projected 3D mesh still contains local shape noise.

$$x = f \frac{X}{Z}, y = f \frac{Y}{Z} \rightarrow X = x \frac{Z}{f}, Y = y \frac{Z}{f} \tag{3}$$

4 Mesh Smoothing and Texture Mapping

4.1 Gaussian Smoothing for 3D Mesh

To generate a smooth surface, the silhouette smoothing is firstly performed. And then a 3D Gaussian smoothing technique is applied for discrete mesh structures while silhouette shapes are kept during smoothing to prevent shape shrinkages. Gaussian smoothing is generally based on membrane energy minimization, and is the most popular smoothing method because of its linear computation and storage. For a parametric surface $S : P = P(u, v)$, the membrane energy functional is defined by Eq.(4) [17].

$$E_m(S) = \frac{1}{2} \oint (P_u^2 + P_v^2) dS. \tag{4}$$

In minimizing the membrane energy functional, its derivatives correspond to the Laplacian operator $L(P)$ of Eq. (5).

$$L(P) = P_{uu} + P_{vv}. \tag{5}$$

For a discrete mesh, the Laplacian $L(P_i)$ at vertex p_i can be linearly approximated using Eq.(6). Where p_j is a j^{th} neighboring vertex of vertex p_i , and n_i is the valence of p_i .

$$L(P_i) = \frac{1}{n_i} \sum_{i=0}^{n_i-1} (p_j - p_i) \tag{6}$$

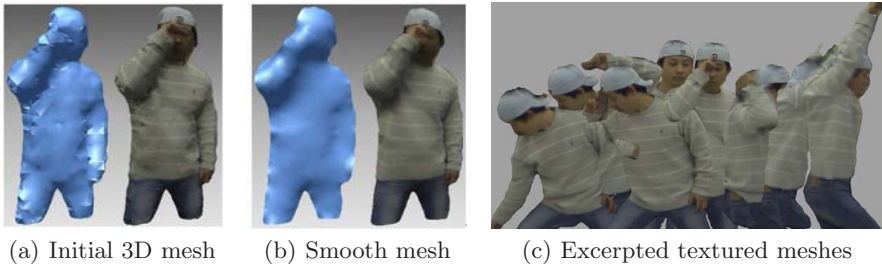


Fig. 5. Mesh smoothing and texturing

4.2 Texture Mapping

After 3D mesh models are smoothed as shown in Fig. 5(a) and Fig. 5(b), texture coordinates are computed by normalizing X and Y coordinates of vertices with the size of depth image. The color frame, which is corresponding to the depth image, is used as the texture source. The textured mesh stream is saved as Wavefront *OBJ* file format at each frame. All textured models consist of three files which represent geometry, material, and texture source. Fig. 5(c) shows some of textured mesh models after smoothing and texturing.

5 Evaluation and Application

5.1 Quality Evaluation and Computation Time

Fig. 6(a) shows a visual comparison between a uniform triangulation and the proposed method. The result of the proposed method is much smoother and has a smaller number of vertices and triangles as shown in fig. 6(b). The shape is not shrunk since the silhouette contour is fixed during a Gaussian smoothing. When the mesh is stored as *OBJ* file format, the mesh size is compressed almost to 2.3 percent compared with the original mesh 100 depth images are chosen from

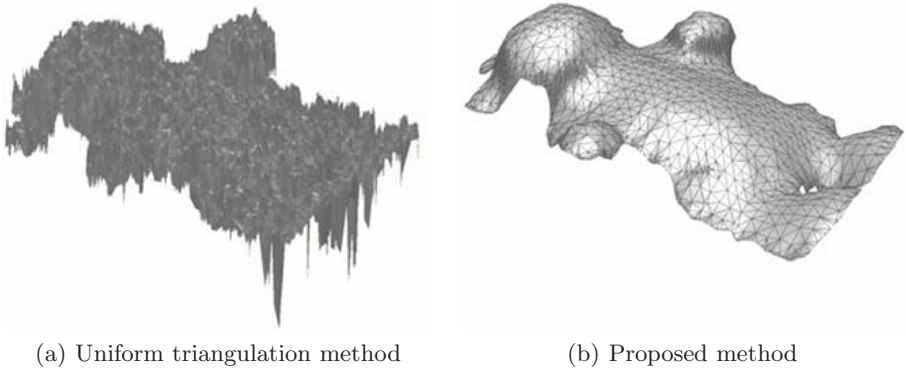


Fig. 6. Comparison of visual shape quality

a depth video to evaluate the computation time of the proposed algorithms. Testing system consists of a Pentium 4 PC running Windows XP, Intel CPU 3.4 GHz and 2GB memory. All images have a SD (standard definition) resolution which is 720 pixels in width and 486 pixels in height. Table 1 shows the computation time for each procedure. Total computation time is 221.923 seconds for generating 100 textured mesh models from 100 depth frames. On the average, a series of proposed procedures take roughly 2.22 seconds to generate a textured mesh model from one depth image.

Table 1. Reconstruction time

Modeling Procedures	100 depth images	one image
Median filtering	54.516	0.545
Adaptive sampling	51.266	0.513
Triangulation	71.044	0.710
Smoothing and texturing	45.097	0.451
Total time(sec.)	221.923	2.219

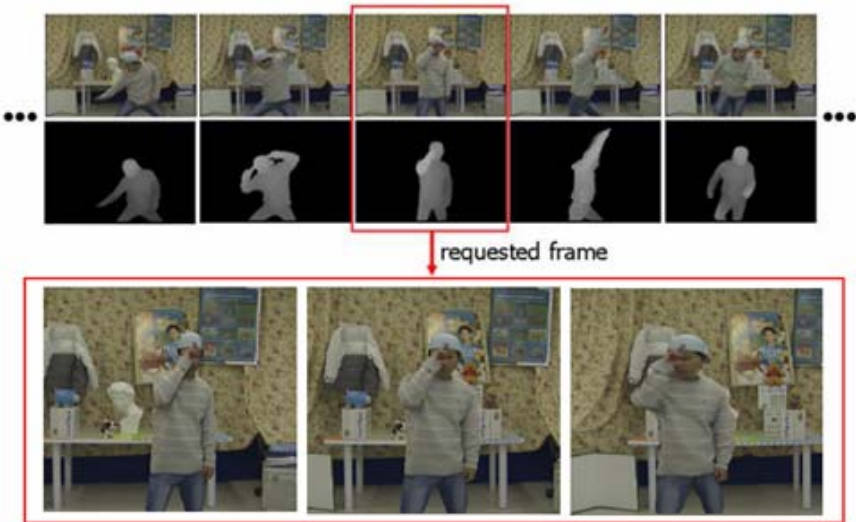


Fig. 7. Clients touch real actor using haptic interaction device

5.2 Arbitrary View Synthesis

In broadcasting applications, when viewers want to see different views at a specific frame, the virtual camera moves around the actor. Since we already have a 3D textured model, the server, such as the broadcasting station, can render an arbitrary view, which viewers are requesting for, and can send it to them. Fig. 7 shows a conceptual example of arbitrary view synthesis. The viewers can interactively choose a specific frame in video sequence to see different views of the actor.

6 Conclusion

We have presented the modeling algorithm to produce natural-textured 3D model at each frame, although it is difficult to reconstruct a 3D mesh model of dynamic real objects in video sequence. Unlike the existing depth image-based modeling, which produces only images with depth, we reconstructed an explicit 3D geometry that is smooth and textured. Our contribution is the reconstruction of a smooth 3D surface model from one depth image using adaptive sampling, triangulation and smoothing methods. The proposed algorithm enhances the mesh smoothness and decreases the number of meshes while preserving global shapes. Our second contribution is the automation of modeling procedures in a matter of seconds per frame. The usability of the proposed method is verified by applying experimental results to the arbitrary view synthesis.

Acknowledgements

This research was supported by RBRC funded by the Ministry of Information and Communication and ICRC funded by the Ministry of Science and Technology. We thank ETRI for letting us use their equipment where we captured depth video.

References

1. Smolic, A., Mueller, K., Merkle, P., Rein, T., Eisert, P., Wiegand, T.: Free Viewpoint Video Extraction, Representation, Coding, and Rendering. ICIP 2004, IEEE International Conference on Image Processing, Singapore, October 24-27. (2004)
2. Thomas, G. A., Grau, O.: 3D Image Sequence Acquisition for TV and Film Production. in Conference Proc. of 1st Symp. on 3D Data Processing Visualization Transmission. (2002)
3. Bazzoni, G., Bianchi, E., Grau, O., et al.: The Origami Project: Advanced Tools and Techniques for High-end Mixing and Interaction between Real and Virtual Content. in Conference Proc. of 1st Symp. on Data Processing Visualization Transmission. (2002)
4. Remondino, F., Roditakis, A.: 3D Reconstruction of human skeleton from single images or monocular video sequences. 25th Pattern Recognition Symposium. LNCS. DAGM03. (2003) 100-107
5. Matsuyama, T., Wu, X., Takai, T., Nobuhara, S.: Real-Time 3D Shape Reconstruction, Dynamic 3D Mesh Deformation, and High Fidelity Visualization for 3D Video. International Journal on Computer Vision and Image Understanding. Vol.96. No.3. (2004) 393-434
6. Kiriakos, K., Seitz, S. M.: A Theory of Shape by Space Carving. International Journal of Computer Vision, 38(3). (2000) 199 - 218
7. Debevec, P., Tayler, C., Malik, J.: Modeling and Rendering Architecture from Photographs: A Hybrid Geometry- and Image-based Approach. Proceedings of SIGGRAPH 96 proceeding. (1996) 11-20
8. Niem, W.: Robust and Fast Modelling of 3D Natural Objects from Multiple Views. SPIE Proceedings, vol. 2182. (1994) 388-397
9. Carranza, J., Theobalt, C., Magnor, M. A., Seidel, H.P.: Free-viewpoint video of human actors. ACM Transactions on Graphics, vol. 22, no. 3. (2003) 569-577

10. Grau, O., Price, M., Thomas, G. A.: Use of 3d techniques for virtual production. in Proc. of SPIE, Conference Proc. of Videometrics and Optical Methods for 3D Shape Measurement, vol. 4309. (2001)
11. Allen, B., Curless, B., Popovic, Z.: The space of human body shapes: reconstruction and parameterization from range scans. *ACM Transactions on Graphics*. 22(3). (2003) 587-594
12. Moccozet, L., Dellas, F., Magnenat-Thalmann, N., Biasotti, S., Mortara, M., Falci-dieno, B., Min, P., Veltkamp, R.: Animatable Human Body Model Reconstruction from 3D Scan Data using Templates. Proc. CapTech Workshop on Modelling and Motion Capture Techniques for Virtual Environments. (2004)
13. <http://www.3dvsystems.com>
14. Ignatenko, A., Konushin, A.: A Framework for Depth Image-Based Modeling and Rendering. Proc. Graphicon2003. (2003) 169-172
15. Jain, A.K.: *Fundamentals of Digital Image Processing*. Prentice-Hall, Inc. (1989)
16. Domiter, V.: Constrained Delaunay triangulation using plane subdivision. Proceedings of the 8th Central european seminar on computer graphics. Budmerice. April 19-21. (2004) 105-110
17. Eck, M., DeRose, T., Duchamp, T., Hoppe, H., Lounsbery, M., Stuetzle, W.: Multiresolution Analysis of Arbitrary Meshes. SIGGRAPH 95 proceeding. (1995) 173-182

Workload Characterization in Multiplayer Online Games*

Pedro Morillo², Juan Manuel Orduña¹, and Marcos Fernández²

¹ Universidad de Valencia, Departamento de Informática,
Avda. Vicent Andrés Estellés, s/n
46100 - Burjassot (Valencia), Spain
Juan.Orduna@uv.es

² Universidad de Valencia, Instituto de Robótica,
Polígono de la Coma s/n
46980 - Paterna (Valencia), Spain

Abstract. In recent years, distributed virtual environments (DVEs) have become a major trend in distributed applications, mainly due to the enormous popularity of multiplayer online games in the entertainment industry. Although the workload generated by avatars in a DVE system has already been characterized, the special features of multiplayer online games make these applications to require a particular workload characterization.

This paper presents the workload characterization of multiplayer online games. This characterization is based on real traces, and it shows that the movement patterns of avatars used to develop optimization techniques for DVE systems can be extrapolated to First Person Shooting networked games. However, the workload that each avatar adds to the game server is higher than the one proposed in the literature.

1 Introduction

The enormous popularity that multiplayer online games have acquired nowadays has allowed a huge expansion of Distributed Virtual Environments (DVEs). These highly interactive systems simulate a 3-D virtual world where multiple users share the same scenario. Each user is represented in the shared virtual environment by an entity called *avatar*, whose state is controlled by the user through the client computer. The system renders the images of the virtual world that each user would see if he was located at that point in the virtual environment. Hundreds and even thousands of client computers can be simultaneously connected to the DVE system through different networks, and even through the Internet. Although DVE systems are currently used in many different applications such as civil and military distributed training [1], collaborative design [2] or e-learning [3], the most extended example of DVE systems are commercial, multiplayer online game (MOG) environments [4, 5, 6, 7].

* This paper is supported by the Spanish MEC under grant TIC2003-08154-C06-04.

Different architectures have been proposed in order to efficiently support multiplayer online games: centralized-server architectures [5, 7], networked server architectures [8, 9] and peer-to-peer architectures [10, 11]. Figure 1 shows an example of each one of these architectures. In this example, the virtual world is two-dimensional and avatars are represented as dots. The area of interest (AOI) of a given avatar is represented as a circumference.

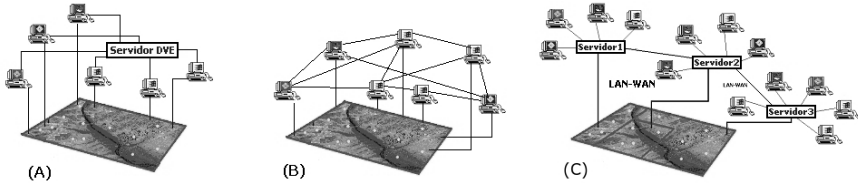


Fig. 1. Different architectures for DVE systems: a) Centralized b) Peer-to-peer c) Networked-server

Regardless of the system architecture, some key issues add complexity to the design of an efficient and scalable DVE system. Some of the following ones have become nowadays an open research topic:

- View Consistency: This problem has been already defined in other computer science fields such as database management [12]. In DVE systems, this problem consists of ensuring that all avatars sharing a virtual space with common objects have the same local vision of them [13, 14, 15]. Some proposals have been made to provide consistency [16, 17, 11].
- Message Traffic Reduction: Keeping a low amount of messages allows DVE systems to efficiently scale with the number of avatars in the system. Traditionally, techniques like dead-reckoning described in [8] offered some level of independence to the avatars. With network support, broadcast or multicast solutions [18, 11] decrease the number of messages used to keep a consistent state of the system.
- Partitioning scheme: In networked-server architectures, the problem of efficiently distributing the workload (avatars) among different servers in the system determines the throughput and the quality of service (QoS) provided to users [19, 20].

A common feature in all these research topics is the need of characterizing the user behavior, in order to determine the workload generated to the DVE system (both in terms of computational and communication requirements). This characterization must be performed in two aspects:

- High-level abstraction of the application. This item determines, for example, the user behavior in networked games, in terms of mobility and user actions. In this sense, several models have been proposed [21, 22].

- Low-level measurements of system workload. These measurements determines the workload generated by each user (avatar) to the system, in terms of computational and communication requirements. Typical examples of this kind of measurements are number of messages generated per second, average number of neighbor avatars inside the AOI of a given avatar, average movement rate of avatars, etc. Some characterization of these aspects have been already proposed [23, 24].

Nevertheless, multiplayer online games (which are the most popular real-time applications, making up around half the top 25 types of non traditional traffic for some Internet links [25]) have special requirements, due to their real-time characteristics [26]. Despite the video game market is currently divided in more than ten types of sub genres (fighting games, role-playing games, simulation games, etc.) [27], first person shooter games (FPS) have focused the attention of the research community. The reason for such interest is due to the fact that FPS games impose the most restrictive requirements on both network traffic and QoS, because of their fast-paced nature [21]. In FPS games, the game is visualized in a first person perspective by users, who are located in a 3D virtual scene (called map) holding a gun or similar weapon [27].

Therefore, both a high-level and a low-level workload characterization are required to determine the actual workload that users in these system generate. This characterization is essential to develop efficient optimization techniques for these systems and also to design methods for providing Quality of Service. Last years several proposals have been made about characterizing the high-level abstraction of networked games [26, 21, 22]. These studies have shown that multiplayer online games have distinctive features in terms of the effects of latency on users and user behavior. Nevertheless, to our knowledge no proposal has been still made about low-level workload characterization in networked games.

The purpose of this paper is to perform a low-level characterization of networked games, starting from real traffic obtained from real games. The characterization study shows that, unlike the case of high-level workload, the low-level workload generated in networked games do not significantly differ from the workload generated in other DVE systems. Therefore, the workload models used in optimization and QoS techniques can also be applied to multiplayer online games.

The rest of the paper is organized as follows: section 2 describes the characterization setup for obtaining real traces from real networked games. Next, section 3 shows the characterization study performed on the obtained traces. Finally, section 4 shows some conclusions and future work to be done.

2 Characterization Setup

Unreal Tournament (UT) is a popular first-person action game from Epic Games [5]. In recent years, this multiplayer game has become an important testbed for performance evaluation in fields like DVE systems [28], Human Computer Interaction (HCI) [29] and autonomous agents systems [30]. We have used a special

version of this multiplayer game, called UT Game of the Year (GOTY), to obtain real traces of a networked game. The low-level analysis of such traces allows the workload characterization of networked games. The considered version of the multiplayer game not only includes an improved graphical engine and a important set of game modes (DeathMatch, Capture-The-Flag, Domination), but it also allows control avatars by using a high level language called UnrealScript. From the system architecture's point of view [8], Unreal Tournament is based on a client/server model, where a single monolithic server of the game performs constant game updates, denoted as server ticks. In each server tick, server sequentially computes the current state of the simulation and sends game state information to each client. This technique is known as *Frequent State Regeneration (FSR)* [8], and data packets contain information about the position, speed and even the model of each avatar.

Despite Unreal Tournament includes different game modes, we have selected the opposite modes (called "DeathMatch" (DM) and "Capture-The-Flag" (CTF)) in terms of both interactivity and behavior of users. In DM mode, the purpose of the game consists of killing as many opponents as possible whilst avoiding being killed. In this mode, players are independent and spend the simulation time moving and jumping around the virtual scene to kill the rest of players by shooting or strafing them. However, in CTF mode both the goal and the user behavior are completely different. In this case, players are organized in two different teams (red and blue) which are represented by a flag. The flags of the teams are located in two different zones of the scene called bases. The purpose of the game consists of those players belonging to the same team to collaboratively finding the enemy base and carry enemy flag to the team base. Unlike other mode games, DM and CTF mode games are strongly recommended when the number of players in UT is high (UT dedicated servers support games of up to 16 players).

A UT Lan Party was organized at our laboratories in early September 2005. In this experiment, a selected set of students of our university were invited to play in a session of two hours of duration. The 16 players were playing UT-GOTY version 4.3.6. on a dedicated server. The hardware platforms used as computer clients as well as the server were PC's with Pentium IV processor running at 1.7 GHz, 256 Mbytes of RAM and NVidia MX-400 graphic cards. All of them have installed Windows Xp and shared a 10 Mbps Ethernet as the interconnection network. Unlike other older FPS games as Quake [31], it was not necessary to patch or modify the source code of the game server in order to obtain the traces of played games in our experiments. In this case, we used UnrealScript to define custom monitors inside of the game map. Once the monitored maps were loaded in the current game, they forced UT engine to write the position of all the simulation clients in each server tick. In order to define comfortable maps for the UT Lan Party, where 16 players can comfortably enjoy the game, the largest four maps were properly monitored. These maps correspond to maps called "DM-Deck16" and "DM-Shrapnel" for "DeathMatch" game mode, and "CTF-Darji16" and "CTF-HallOfGiants" for "Capture-The-Flag" game mode.

All of them are well-known in the UT player community and can be found in any of the existing commercial version of this popular multiplayer game.

We have obtained five different trace files of UT game played by 16 players. Three of them correspond to three DM mode games, and we have denoted them as DTH1A, DTH1B and DTH2A. DTH1A and DTH1B traces correspond to two traces of the game played with the same map (Deck16). The idea is to check if the results show significant changes in different instances of the same game. The other two trace files correspond to CFT mode-games, and we have denoted them as FLAG1 and FLAG2. The simulation times required for obtaining each trace file were 2,25 minutes for DTH1A, 4 minutes for DTH1B, 5 minutes for DTH2A, 4 minutes for FLAG1 and 16 minutes for FLAG2.

3 Workload Characterization

The first stage in the characterization study is to check if the movement patterns followed by avatars correspond to those used in the literature [19, 24, 32, 33]. We have depicted the successive locations of each of the avatars in the environment at every simulation time, according to the traces. Figure 2 graphically shows the results obtained for two of the traces. Although the other three are not shown here for the sake of shortness, they are very similar. Figures 2 A) and B) respectively show the location of avatars in trail mode (the lines represent the locations visited by each avatar) for one of the DM traces and one of the CTF trace files. Figure 2 C) is a snapshot of the location of avatars in a given instant for the same CTF trace file. Using this tool to visually check the movement patterns, we can conclude that all of the traces show a random movement pattern. In terms of workload, this pattern is equivalent to CCP [24] movement pattern.

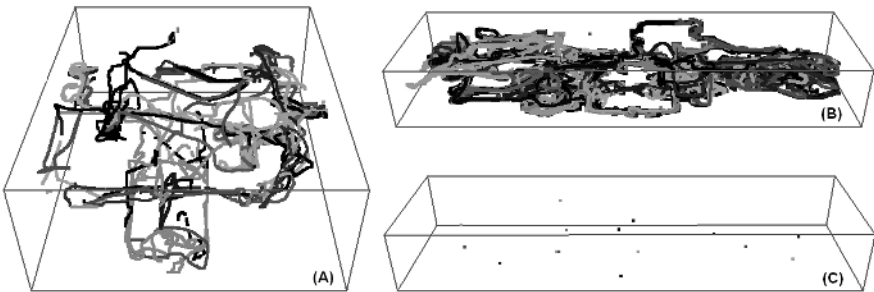


Fig. 2. Locations of avatars in different traces: A) DM mode of DTH1A trace file B) DM mode of FLAG2 trace file C) CFT mode of FLAG2 trace file

The next step in our analysis has been the detailed study of the timestamps and locations of avatars. A previous experiment was performed (before obtaining the file traces) in order to empirically measuring the vision range (the AOI size) of avatars. In this experiment (performed in a diaphanous map), we progressively moved away two close avatars while measuring the distance to each other, until

they could not see each other. Such distance was measured as 100 m. in the virtual world. It must be noticed that although two avatars cannot see each other at a given moment (due to the map geometry, including walls, corridors and/or corners) avatars must exactly know the location of all the neighbor avatars in their AOI, since they can become visible at any moment. Therefore, using 100m. as the AOI, we analyzed the obtained trace files. Although we have analyzed the values in the trace files for each of the avatars, in this paper we will only show the average and the standard deviation values obtained for the sixteen avatars, due to space limitations.

Table 1 shows the analysis of DTH trace files. This table shows in the first row the average values obtained for the sixteen avatars, while it shows the standard deviation in the next row. The average number of avatars in the AOI of each avatars were 15 in all of the DTH traces. That is, the AOI of avatars in UT reaches the whole virtual world for these maps. The most-left column shows the number of events generated in each trace (number of packets sent by each avatars). The the next column shows the number of useful events (notice that avatars send a packet at each server ticks, even though they remain stopped and have no change to report about) to compute movement rates and speeds. The column labeled with "Dist" shows the linear distance (in meters) traversed by the avatars during the game. Next, column labeled with "Speed" shows the average movement rate of avatars (in kilometers/hour) during the game. Finally, the column labeled with "Ev/sec" shows the rate of useful packets per second sent by avatars (that is, the communication workload).

Table 1. Empirical results for DTH traces

	DTH1A				
	Events	Useful Ev.	Dist.	Speed	Ev/sec
<i>Average</i>	4330	1295	382	10	10
<i>Std. Dev.</i>	167	779	181	5	6
	DTH1B				
	Events	Useful Ev.	Dist.	Speed	Ev/sec
<i>Average</i>	10721	2732	749	12	12
<i>Std. Dev.</i>	548	1285	273	4	6
	DTH2A				
	Events	Useful Ev.	Dist.	Speed	Ev/sec
<i>Average</i>	11373	4354	893	12	16
<i>Std. Dev.</i>	2937	2291	336	4	8

The results show in table 1 show that only around one third of the events are useful (that is, they include information about a new location of the avatar). This result indicates that avatars remains stopped most of the simulation time, as indicated in the DVE literature [34]. Another important result is that the useful event rate generated by avatars is no lower than 10 events per second in any case. These rates are higher than the ones of assumed as typical in previous studies focused on DVEs. This movement rate was assumed as 2 movements/second [35],

5 events/second [18, 36], or 10 events/second in the case of games [37]. If useless events are considered (as FSR scheme [8] does), then the event rate is even higher. This is the reason for games using FSR scheme [8] to limit the number of players to 16.

Table 2 shows the analysis of FLAG trace files. The average AOI of avatars in FLAG1 and FLAG2 trace files are 10 and 11, respectively. That is, these maps are bigger than DTH maps, allowing some avatars to remain most of the time out of the AOI of other avatars. Although in this version of the game the percentage of useful events are similar to the percentages shown in table 1, the rate of useful events per second significantly increases, showing that avatars move more often in this game mode. These results indicate that avatars in FPSs show higher movement rates than in typical DVEs, and therefore they generate a higher workload [23].

Additionally, we have measured the distances among the avatars during the simulations, in order to monitor how clustered they are in the virtual world and how these clusters vary during the simulations. Figures 3 and 4 show this measurements in a graphical way. This figures show on the x-axis the normalized simulation time (since each trace files contains different simulation times, this magnitude must be normalized in order to compare the different trace files). On the y-axis, these figures show the average value of the average distances from each avatars to all of its neighbors.

Table 2. Empirical results for FLAG traces

	FLAG1				
	Events	Useful Ev.	Dist.	Speed	Ev/sec
<i>Average</i>	11961	4782	710	10	18
<i>Std. Dev.</i>	4291	2559	340	5	10
	FLAG2				
	Events	Useful Ev.	Dist.	Speed	Ev/sec
<i>Average</i>	34575	23968	4028	15	25
<i>Std. Dev.</i>	1820	6527	825	3	7

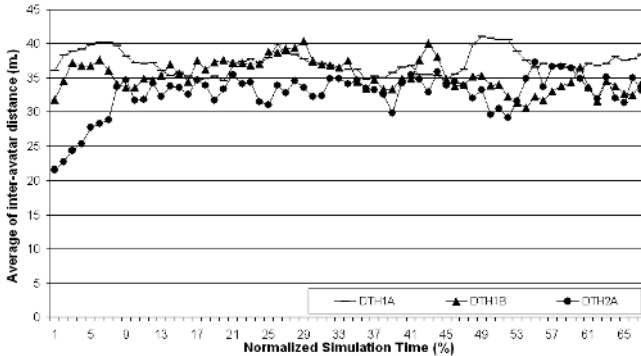


Fig. 3. Average inter-avatar distance for DTH file traces

Both figures show that the average inter-avatar distance do not significantly increase as the simulation time grows. That is, avatars do not tend to head for certain points in the virtual world, as HPN [33] or HPA [32] movement patterns assume. Instead, the inter-avatar distance keeps a flat slope during the simulation. Therefore, the number of neighbors inside the AOI of avatars remains practically constant. Since the same behavior can be seen in both figures, we can conclude that the most adequate movement pattern for FPS games is CCP [24], since this pattern generates a constant workload during all the simulation. The existence of some peaks in the plots suggests that although HPN pattern could appear during certain periods, avatars do not follow HPA pattern at all.

When comparing the two figures, we can see that the only difference between figure 3 and figure 4 is the different levels of inter-avatar distances. This difference is due to the nature of the different game modes. However, all of the plots in each figure show a flat slope.

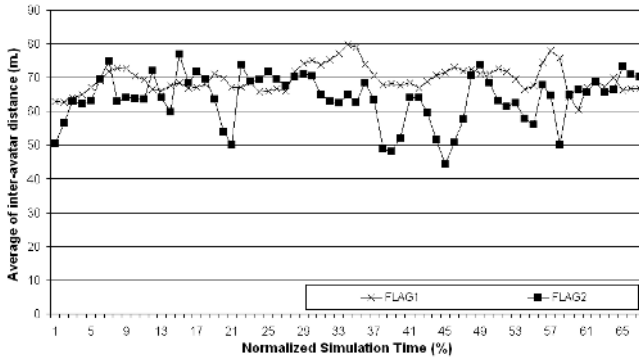


Fig. 4. Average inter-avatar distance for FLAG file traces

4 Conclusions

In this paper, we have proposed the workload characterization of multiplayer networked games by obtaining real traces and analyzing the low-level measurements of system workload. In order to analyze the obtained traces, we have performed both a visual and an statistical analysis.

The results show that the movement patterns followed by avatars are very similar (in terms of system workload) to some of the movement patterns proposed in the literature for DVE systems. However, due to the fast-paced nature of FPS games, the movement rate of avatars are higher than the movement rates proposed for DVE systems. Therefore, we can conclude that the workload generated by multiplayer networked games follow some movement patterns already proposed, but moving faster than other DVE applications.

References

1. Miller, D., Thorpe, J.: Simnet: The advent of simulator networking. *IEEE TPDS* **13** (2002)
2. Salles, J., Galli, R., et al., A.C.A.: mworld: A multiuser 3d virtual environment. *IEEE Computer Graphics* **17**(2) (1997)
3. Bouras, C., Fotakis, D., Philopoulos, A.: A distributed virtual learning centre in cyberspace. In: Proc. of Int. Conf. on Virtual Systems and Multimedia (VSMM'98). (1998)
4. (Everquest: <http://everquest.station.sony.com/>)
5. (Unreal Tournament: <http://www.unrealtournament.com/>)
6. (Lineage: <http://www.lineage.com>)
7. (Quake: <http://www.idsoftware.com/games/quake/quake/>)
8. Singhal, S., Zyda, M.: *Networked Virtual Environments*. ACM Press (1999)
9. Lui, J.C., Chan, M.: An efficient partitioning algorithm for distributed virtual environment systems. *IEEE Trans. Parallel and Distributed Systems* **13** (2002)
10. Mooney, S., Games, B.: *Battlezone: Official Strategy Guide*. BradyGame Publisher (1998)
11. Gautier, L., Diot, C.: Design and evaluation of mimaze, a multi-player game on the internet. In: *Proceedings of IEEE Multimedia Systems Conference*. (1998)
12. Bernstein, P.A., V.Hadzilacos, N.Goodman: *Concurrency, Control and Recovery in Database Systems*. Addison Wesley-Longman (1997)
13. Zhou, S., Cai, W., Lee, B., Turner, S.J.: Time-space consistency in large-scale distributed virtual environments. *ACM Transactions on Modeling and Computer Simulation* **14**(1) (2004) 31–47
14. Fujimoto, R.M., Weatherly, R.: Time management in the dod high level architecture. In: *Proceedings tenth Workshop on Parallel and Distributed Simulation*. (1996) 60–67
15. Roberts, D., Wolff, R.: Controlling consistency within collaborative virtual environments. In: *Proceedings of IEEE Symposium on Distributed Simulation and Real-Time Applications (DSRT'04)*. (2004) 46–52
16. Kawahara, Y., Aoyama, T., Morikawa, H.: A peer-to-peer message exchange scheme for large scale networked virtual environments. *Telecommunication Systems* **25**(3) (2004) 353–370
17. Hu, S.Y., Liao, G.M.: Scalable peer-to-peer networked virtual environment. In: *Proceedings ACM SIGCOMM 2004 workshops on NetGames '04*. (2004) 129–133
18. Knutsson, B., Lu, H., Xu, W., Hopkins, B.: Peer-to-peer support for massively multiplayer games. In: *Proceedings of IEEE InfoCom'04*. (2004)
19. Morillo, P., Orduña, J.M., Fernández, M., Duato, J.: Improving the performance of distributed virtual environment systems. *IEEE Transactions on Parallel and Distributed Systems* **16**(7) (2005) 637–649
20. Morillo, P., Orduña, J.M., Fernández, M., Duato, J.: A method for providing qos in distributed virtual environments. In: *Euromicro Conf. on Parallel, Distributed and Network-based Processing (PDP'05)*, IEEE Computer Society (2005)
21. Tan, S.A., Lau, W., Loh, A.: Networked game mobility model for first-person-shooter games. In: *Proceedings of the 2nd workshop on Network and system support for games (NetGames'05)*. (2005)
22. Henderson, T., Bhatti, S.: Modelling user behaviour in networked games. In: *MULTIMEDIA '01: Proceedings of the ninth ACM international conference on Multimedia*, New York, NY, USA, ACM Press (2001) 212–220

23. Morillo, P., Orduña, J.M., Fernández, M., Duato, J.: On the characterization of avatars in distributed virtual worlds. In: EUROGRAPHICS' 2003 Workshops, The Eurographics Association (2003) 215–220
24. Beatrice, N., Antonio, S., Rynson, L., Frederick, L.: A multiserver architecture for distributed virtual walkthrough. In: Proceedings of ACM VRST'02. (2002) 163–170
25. McCreary, S., Claffy, K.: Trends in wide area ip traffic patterns - a view from ames internet exchange. In: Proceedings of ITC Specialist Seminar, Cooperative Association for Internet Data Analysis - CAIDA (2000)
26. N. Sheldon, a.E.G., Borg, S., Claypool, M., Agu, E.: The effect of latency on user performance in warcraft iii. In: Proc. of 2nd workshop on Network and system support for games (NetGames'03), ACM Press New York, NY, USA (2003) 3–14
27. Wolf, M., Perron, B.: The Video Game Theory Reader. Routledge Publisher (2003)
28. Wray, R.: Thinking on its feet: Using soar to model combatants in urban environments. In: 22nd North American Soar Workshop Proceedings. (2002)
29. Beigbeder, T., Coughlan, R., Lusher, C., Plunkett, J., Agu, E., Claypool, M.: The effects of loss and latency on user performance in unreal tournament. In: Proc. of ACM Network and System Support for Games Workshop (NetGames). (2004)
30. Lozano, M., Cavazza, M., Meada, S., Charles, F.: Search based planning for character animation. In: 2nd International Conference on Application and Development of Computer Games. (2003)
31. Steed, A., Angus, C.: Supporting scalable peer to peer virtual environments using frontier sets. In: Proc. of IEEE Virtual Reality, IEEE Computer Society (2005)
32. Greenhalgh, F.C.: Analysing movement and world transitions in virtual reality teleconferencing. In: Proceedings of 5th European Conference on Computer Supported Cooperative Work (ECSCW'97). (1997)
33. Matijasevic, M., Valavanis, K.P., Gracanin, D., Lovrek, I.: Application of a multi-user distributed virtual environment framework to mobile robot teleoperation over the internet. *Machine Intelligence & Robotic Control* **1**(1) (1999) 11–26
34. Greenhalgh, C.: Understanding the Network Requirements of Collaborative Virtual Environments. In: Collaborative Virtual Environments. Springer-Verlag (2001)
35. Min, P., Funkhouser, T.: Priority-driven acoustic modeling for virtual environments. *Computer Graphics Forum* **19**(3) (2000)
36. Anthes, C., Haffegge, A., Heinzlreiter, P., Volkert, J.: A scalable network architecture for closely coupled collaboration. *Computing and Informatics* **21**(1) (2005) 31–51
37. Dickey, C.G., Lo, V., Zappala, D.: Using n-trees for scalable event ordering in peer-to-peer games. In: Proc. of Intntl. workshop on Network and operating systems support for digital audio and video (NOSSDAV'05), ACM Press (2005) 87–92

Delaunay-Based Polygon Morphing Across a Change in Topology

Xiaqing Wu and John K. Johnstone*

CIS Department, University of Alabama at Birmingham, Birmingham, AL USA 35294-1170
{wux, jj}@cis.uab.edu

Abstract. We present a new object-based algorithm for morphing between two shapes with an arbitrary number of polygons and arbitrarily different topology. Many solutions have been proposed for morphing between two polygons. However, there has been little attention to morphing between different numbers of polygons, across a change in topology. A modified conforming Delaunay triangulation is used to build the vertex correspondence. Polygon evolution is used to smooth the morph. The morph requires no user interaction, avoids self-intersection, uses dynamic vertex correspondence, and follows nonlinear vertex paths.

1 Introduction and Motivation

Polygon morphing conventionally models the change of shape between a single polygon A and another polygon B . An interesting generalization of this problem is the development of a morph between two arbitrary groups of polygons and a morph between shapes of different topology (Figures 1). This problem has been cited as a major challenge for next-generation morphing algorithms [1].

In the morphing literature, many successful algorithms have been developed, but most present algorithms can only morph between similar objects that share the same topology: that is, they are designed as 1-to-1 morphing methods. Some recent methods have been developed for morphing between different topologies, but they are either image-based, require user interaction, or expensive. A straightforward object-based method that requires no user interaction is still needed. One of the main barriers to the development of a morph between two groups of polygons is the difficulty of building a vertex correspondence. In traditional object-based morphing algorithms [7, 8, 12], the morphing procedure is decomposed into a vertex correspondence problem (how to build a vertex-to-vertex map between the source and target shapes) and a vertex path problem (how to move each vertex towards its partner). When the source and target shapes have a different topology (for example, morphing between two groups of polygons or morphing an X shape to an O shape as in Figure 1), it is particularly difficult to set up a reasonable correspondence between the vertices in the source and target shapes.

In this paper, we describe a new object-based approach to morphing across a change in topology. The input is two groups of polygons A and B , each with one or more

* The work of both authors was partially supported by the National Science Foundation under grant CCR-0203586.

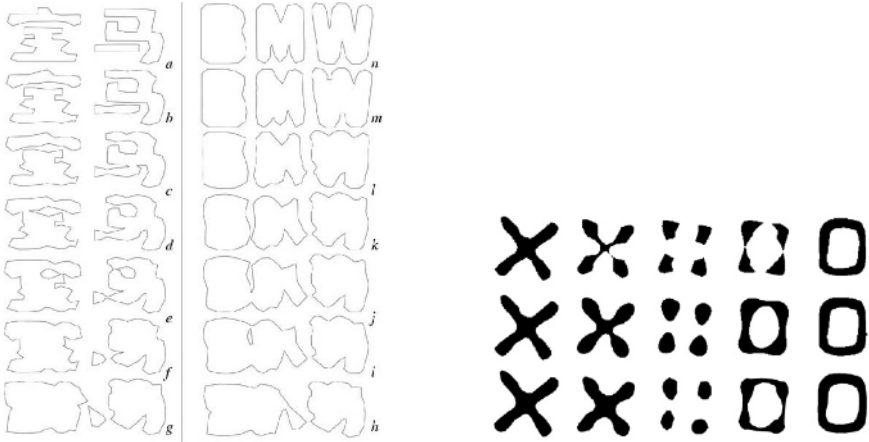


Fig. 1. Left: many-to-many morphing between BMW and its Chinese translation. Right: three techniques for morphing across a change in topology. 1st row: Cohen-Or's method; 2nd row: Turk's method; 3rd row: our method.

polygons (Figures 1a and 1n). The output is a series of intermediate polygons changing from the source group to the target group (Figure 1). We build a vertex-to-vertex correspondence directly (in contrast to other indirect methods), by transforming the correspondence problem into a triangulation problem. The first step of the algorithm is to build a good triangulation of the source and target polygons. We develop a new variant of the Delaunay triangulation for this purpose in Section 3. Section 4 defines a vertex correspondence from certain edges of this triangulation, and shows how to move each vertex towards its partner. Section 5 presents several enhancements to this algorithm, including the addition of an evolution component to the morph. Experimental results are presented in Section 6 and we conclude in Section 7. The paper starts with a review of previous methods for morphing and triangulation in the next section.

2 Related Work

2.1 Object-Space Morphing

There has been much research on morphing between two simple polygons (e.g., [1, 8, 12, 13]). Since we cannot consider this entire literature, we mention some papers that share ideas with our algorithm. Sederberg and Greenwood [12] morph between two polygons by treating the source polygon as if it was made from metal wire that must be deformed into the destination polygon, using the least work. To find this least work solution, they adapt an algorithm of Fuchs, Kedem and Uselton for computing an optimal triangulation between contours. In the method presented in this paper, we also build a special triangulation to generate vertex correspondence.

Goldstein and Gotsman [8] evolve the source and destination polygons down to their centroids, and then use an interpolation between the evolution frameworks to define the vertex paths of the morph. Evolution is a method that can be applied to morphing a

single polygon to a convex polygon (and eventually to a point). This evolution-based method cannot be extended directly to the more general case of this paper. However, we shall also use polygon evolution in our algorithm (Section 5.2) because it is a nice tool to control the smoothness of the intermediate shape during the morph.

There are a few existing morphing algorithms that can deal with multiple objects of different topology. These are the object-based method of DeCarlo and Gallier [5], the image-based method of Cohen-Or et. al. [4], and the implicit-function method of Turk and O'Brien [15]. They use various approaches to avoid the direct construction of a vertex correspondence in solving the morphing problem.

DeCarlo and Gallier [5] morph between surfaces of different topology. This method requires considerable user interaction, such as the definition of control meshes on the surfaces, correspondences between these meshes, and times when the topology should change, which has the advantage of strong user control but also its disadvantages.

The method of Cohen-Or et al. [4] uses distance field interpolation. The main advantage of their algorithm is that it can deal with very general representations of graphics objects and no correspondence between geometric primitives (e.g., vertices, edges, and faces) needs to be established. A disadvantage is that a discrete grid representation of an input image is necessary, leading to image-based characteristics. Like other image-based algorithms, the quality of the morph will largely depend on the resolution of the sample or the grid. This method involves some user interaction. It does not necessarily preserve the simplicity of each polygon.

The technique developed by Turk and O'Brien [15] reduces morphing to interpolation, translating the temporal dimension into an extra spatial dimension. It can be applied to morphing between different topologies. Their method involves sophisticated but expensive interpolation by implicit surfaces. Since their morph does not generate a vertex correspondence, and will generate all of the intermediate shapes in one step, it is difficult to add interactive control during the morphing procedure.

This survey of existing morphing algorithms reveals that an automatic, straightforward, correspondence-based method for morphing between two groups of polygons in object space is still needed.

3 The Edge Delaunay Triangulation

Our construction of a vertex correspondence depends on the construction of a triangulation. We certainly need a Delaunay triangulation so that closest vertex pairs will always be mapped to each other.¹ The Delaunay triangulation is not enough, though, because its edges may cross the polygonal boundary. If we use these edges to define a vertex correspondence, then the morph will generate self-intersections, a definite problem for a morph. We need a triangulation that honours the polygonal edges. The constrained [3] and conforming [14] Delaunay triangulations are natural candidates, but unfortunately the constrained Delaunay triangulation is not a true Delaunay triangulation, and the conforming Delaunay triangulation introduces Steiner points that need not lie on the

¹ In a point set, a point and its nearest neighbor will always define an edge of the Delaunay triangulation of the point set [11].

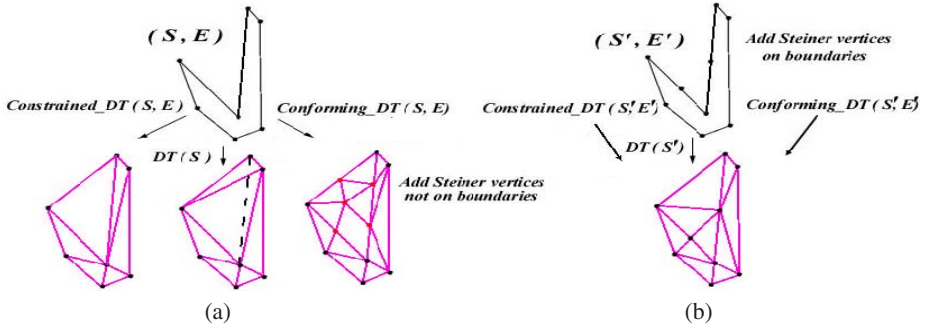


Fig. 2. (a) The Delaunay triangulation, constrained Delaunay triangulation, and a possible conforming Delaunay triangulation of a polygon. (b) The edge Delaunay triangulation, a special type of conforming Delaunay triangulation.

polygon’s boundary. We cannot introduce new Steiner points inside or outside the input shape, because we want to use the triangulation to build a correspondence between *boundary* vertices of the polygon. We need a Delaunay triangulation of a polygon that conforms to all of the polygon edges, and has Steiner vertices only on the boundary of the polygon. We name such a triangulation the edge Delaunay triangulation.

Definition 1. An **edge Delaunay triangulation** (or **EDT**, for short) of a polygon P is a conforming Delaunay triangulation of P with the added constraint that all the Steiner points lie on the boundaries. Equivalently, an EDT is the Delaunay triangulation of a resampled polygon P' of P that conforms to P .

Figure 2 shows the relationship between the Delaunay, constrained Delaunay, conforming Delaunay, and edge Delaunay triangulations. In other work [16, 17], we present an algorithm to build the EDT and discuss its advantages over other triangulations. We do not have the space to review this material here. With an incremental algorithm for Delaunay triangulation [10], it is simple to update the EDT of the polygons in the morphing algorithm as required in the next section.

4 An algorithm for Morphing Across a Change in Topology

The edge Delaunay triangulation is used to generate a vertex correspondence for a morph between the source and target shapes. Vertex correspondences are defined by certain edges of the triangulation, called correspondence edges. An edge of the EDT is a *correspondence edge* if it lies in the union of A and B but not in the intersection of A and B . The reasoning is as follows. To morph a source shape into a target shape, the differences between these shapes must be eliminated and the intersections extended. This motivates removing the geometric XOR of A and B : $A \cup B - A \cap B$. Pulling the two vertices of a correspondence edge together promotes the removal of the XOR region. The vertices adjacent to a vertex V through correspondence edges are called the *correspondence partners* of V .

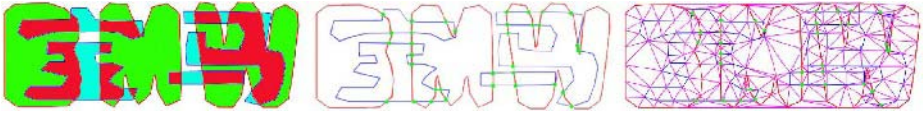


Fig. 3. Constructing the EDT of the input polygons. Left: overlap the source and target shapes. Middle: add the intersection points. Right: generate the EDT (German in red, Chinese in blue, EDT in magenta).

We now present the basic morphing algorithm. Enhancements will be introduced in Section 5. Let A be the set of source polygons and B the set of target polygons. Without loss of generality, we assume that the source and target polygons overlap (Figure 3). If they do not overlap properly, they are forced to overlap through an affine transformation (rotation, translation, and/or scaling) in a preprocessing step. This is done manually at present, but the success of the algorithm does not depend critically on the choice of overlap. The assumption of overlap factors out the lesser issue of rigid and scaling transformation from the more fundamental issue of morphing across a change in topology. Any affine transformation that is applied to the whole shape to force overlap can be easily incorporated into the morphing sequence as a postprocessing step.

During morphing, a vertex is 'frozen' to its correspondence partner when it is within a predefined small distance. When a vertex is frozen to another, the two vertices are identified and neither moves anymore.

1. $t = 0$ (t counts the frames in the morph)
2. While some vertices in A and B remain unfrozen,
 - a) Build the EDT of A and B plus intersections (Figure 3).
All intersection points of an edge in G_1 and an edge in G_2 are added as vertices,² and then an EDT of the input polygons in A and B is built. The intersection vertices are immediately frozen, since they are shared by the source and target polygons.
 - b) Use the correspondence edges of the EDT to set up a vertex correspondence.
 - c) Move each vertex a step towards the average of its correspondence partners (Figure 1b-m). The step vector Δv of the vertex p is:

$$\Delta v = \frac{\delta}{n} \sum_{i=1}^n \frac{p_i - p}{\|p_i - p\|} \quad (1)$$

where $\{p_1, \dots, p_n\}$ are the partners of p and δ is the length of a small step.

- d) For all pairs of polygon vertices p and q that are closer than a predefined threshold,³
 - 1) If p and q belong to different groups, freeze them.
 - 2) If p and q belong to the same group but to different polygons, combine the two polygons into one polygon at vertices p and q .

² Here we assume all edges are open segments. Other special cases will be discussed in detail later (Section 5.1).

³ Note that it is simple to compute close pairs from the EDT, since all the vertices close to p are adjacent to p in the triangulation.

- 3) If p and q belong to the same group and to the same polygon, split the polygon into two polygons at vertices p and q . If either of the new polygons is degenerate (that is, it has less than three vertices or an area less than a threshold), delete it.
- e) t^{th} frame of the morph = the new source polygons;
 $(N - t)^{th}$ frame of the morph = the new target polygons (where N is the number of animation frames, determined at the end of the morph).
 Note that to generate m frames of the morph, only $m/2$ steps are needed.
- f) Increment t .

The use of an edge Delaunay triangulation to define vertex correspondence defines morphs of good quality. Since the edge Delaunay triangulation is a conforming Delaunay triangulation, its edges do not intersect the polygonal boundary, which guarantees that no invisible vertices are partners, and self-intersection is avoided during the morph. Since the edge Delaunay triangulation is a Delaunay triangulation, closest vertices will always be partners. Finally, because all Steiner points are on the boundary of the polygons, and it is known that the Voronoi vertices of a polygon approximate its medial axis, the dual graph of the triangulation will be an approximation of the medial axis of the difference between the source and target shapes, and the vertex correspondence will tend to move vertices towards the medial axis.

5 Enhancements to the Algorithm

5.1 Handling Ties

Care must be taken when a vertex in one polygon group falls on a vertex or line segment in the other group. This event is called a *tie*: a vertex-to-vertex (V-V) tie when a vertex falls on another vertex, and a vertex-to-line (V-L) tie when a vertex falls on an open line segment. V-L ties can be reduced to V-V ties, if we subdivide the line segment of a V-L tie by adding the vertex. We can simply freeze the intersection of two open line segments, but special operations need to be carried out to handle V-V ties.

We may classify V-V ties into two types according to the local property of the vertices. Suppose vertex a is from group A , vertex b from group B , and $a = b$. An ϵ - neighborhood of vertex a is the set of all points within ϵ of a (this is an open set). We define the open sets α and β as the intersection of this ϵ - neighborhood and the interior of A and B , respectively (Figure 4a). We classify V-V ties into free and frozen ties through the relationship of α and β :

- a) A V-V tie is *free* (Figure 4b) if $\alpha \cap \beta = \emptyset, \forall \epsilon > 0$
- b) A V-V tie is *frozen* (Figure 5a) if $\alpha \cap \beta \neq \emptyset, \forall \epsilon > 0$

Since α and β have no intersection in a free tie, a and b will move in different directions. Therefore, we will set them free instead of freezing them. The tie will be removed in the next step of the morph.

For a frozen tie, on the other hand, the associated vertex will be frozen during the morph. The situation is similar to the intersection between two open line segments (Section 4), because the portion defined by $\alpha \cap \beta$ needs to grow in order to remove

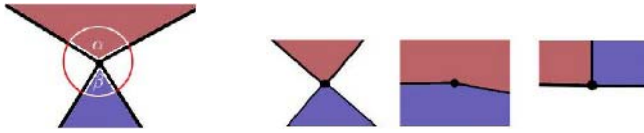


Fig. 4. (left image) Open sets α and β (group A, pink; group B, blue); (3 right images) Free V-V ties (group A, pink; group B, blue)



Fig. 5. (left 3 images) Frozen V-V ties (group A, pink; group B, blue; $A \cap B$, purple); (right image) Unwanted lock formed by frozen ties (Group A, purple; group B, blue)

$\alpha \cup \beta - \alpha \cap \beta$. However, extra care must be taken with frozen ties because these ties might generate an unwanted lock in the morph. For example, in Figure 5b, vertices a_0, a_1, a_2, a_3 in group A and b_0, b_1, b_2, b_3 in group B form four frozen ties. The rectangle defined by $a_0 \dots a_3$ needs to be zipped up, but the four vertices of this rectangle are frozen. We can remove such locks by adding a few vertices, as follows. For any polygon edge $\overline{a_i a_j}$ in group A, if a_i frozen-ties with b_m and a_j frozen-ties with b_n in group B, where $\overline{b_m b_n}$ is a polygon edge in B, we add the mid-point of $\overline{a_i a_j}$.

In the implementation, the order of tie-handling operations is important. These operations have to be carried out as follows:

- a) Add the intersections of the polygons' edges (as open line segments) to the vertex set. Mark these new vertices as frozen vertices.
- b) Add the vertices in V-L ties and transform these V-L ties into V-V ties.
- c) Mark all the V-V ties as free or frozen. Freeze all the vertices in frozen ties.
- d) Check and add the mid-point between two frozen ties if necessary.

5.2 Incorporating Locality Through Evolution

The fact that a vertex is not an independent point, but a vertex on a polygon, suggests that the motion of a vertex during a morph should be affected not only by its correspondence partners but also by its neighbors on the polygon. Polygon evolution [8] is a natural candidate for adding the effect of neighbors. The major advantage of adding evolution is that it smooths out the morph. During each step of the morph, a vertex moves in the direction of a vector that is a weighted blending of the vectors to its correspondence partners and a vector defined by polygonal evolution (see (3) below).

Curve evolution is a technique for changing the shape of a single curve, developed from work of Witkin on signals and Mokhatarian on curves. In the traditional form of curve evolution, a planar curve $C(t)$ moves according to

$$\partial C(t)/\partial t = \kappa(t)N(t) \tag{2}$$

where $\kappa(t)$ and $N(t)$ are the curvature and inward-pointing normal at $C(t)$, respectively. That is, each point of the curve evolves in the direction of the normal at a rate proportional to the curvature. Under this evolution, the curve converges to a simple convex curve [9] and then a point [6]. Concave parts of the curve are pushed out, since their curvature is negative, while convex parts are pulled in. From the physical point of view, curve evolution is like a two-dimensional analogue of surface tension, because it tries to minimize the perimeter of the curve.

Polygonal evolution is the discrete analogue of curve evolution, using a polygonal curvature and normal [2]. Bruckstein et. al. [2] believe from experimentation that the polygonal version of (2) always converges to a polygonal ellipse, but do not offer a proof.

Evolution is added to the morph as follows. When the step vector is computed in the third step of the algorithm, the following equation should replace (1):

$$\Delta v = (1 - e)\left(\frac{\delta}{n}\right) \sum_{i=1}^n \frac{p_i - p}{\|p_i - p\|} + e(k) \frac{c - p}{\|c - p\|} \tag{3}$$

where k is the polygonal curvature of the vertex and c is the center of the circumcircle of p and its two neighboring vertices. $e \in [0, 1)$ is a user-chosen evolution factor. e should never be chosen to be 1, since an evolution-only solution will not morph successfully. The larger the evolution factor e , the more the neighbors of a vertex will affect its motion in the morph, and the smoother the intermediate shape.

The mixed algorithm using (3) is no slower than the correspondence-only algorithm using (1), and often much faster. The evolution factor slows down the morphing speed of convex parts, but accelerates the morphing speed of concave parts. Another major advantage of evolution is an improvement of the speed of EDT computation. Since evolution can help prevent the generation of very sharp angles in the morph, the number of new points that need to be added to make the Delaunay triangulation conforming is reduced, and the generation of the EDT is sped up.

From a certain perspective, correspondence and evolution are different solutions of the same problem. However, to morph a polygon to disappear, correspondence tends to match all the boundaries of the shape and zip them up close to the medial axis of the shape; while evolution tends to shrink the shape by pushing all of the convex corners of the shape inward while pushing concave corners outward: the shape evolves to convex first, then to a polygonal circle, and finally to a point. If only correspondence is used, facing parallel features are pulled together quickly; but corner points move slowly and sharp angles get sharper, which may force many new samples to set up a valid EDT. If only evolution is used, on the other hand, sharp corner vertices move quickly, but flat parts of the polygon move slowly. In addition, evolution speed can decrease greatly as the polygon shrinks, and very close vertices can move apart.

Therefore, a method combining evolution and correspondence works best, as it benefits from the advantages of both techniques. Adding polygon evolution to correspondence can remove sharp angles in the morph and keep the intermediate shapes smooth, without a reduction in morphing speed.

6 Experimental Results

The algorithms of this paper have been implemented in C++. We implemented an incremental Delaunay triangulation using the quadedge data structure. More details of the algorithms can be found in [16]. Figures 1 and 6 show morphing for special visual effect generation. Figure 1 (right side) compares the image-based method [4], the implicit function method [15], and our approach to morphing between shapes of different topology. The topology of the intermediate shapes generated by our morphing method agrees closely with the results of the other two methods. We have also used the morphing algorithm in contour reconstruction.

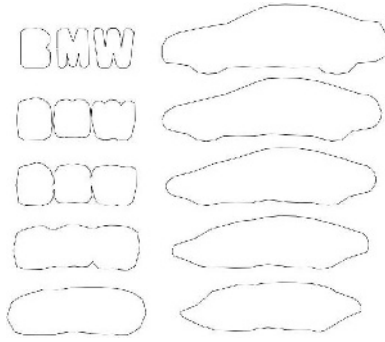


Fig. 6. Transforming three characters into a car

7 Conclusions

We have presented a new morphing algorithm that is able to morph from one group of polygons to another, regardless of how many polygons each group contains or how different their topology is. The algorithm solves the vertex correspondence problem using a modified Delaunay triangulation. This triangulation is independently interesting as it defines a conforming Delaunay triangulation with no interior Steiner points. The solution to the vertex path problem is guided by the correspondence from the triangulation, while the smoothness is controlled by polygonal evolution. The algorithm also works well for traditional 1-to-1 morphing. An important advantage of building and using the vertex correspondence directly is that the user can easily add interactive control during the morph. For example, the user might change the location of vertices in the intermediate shape to create the desired morphing effect.

The algorithm is fully automatic (unless interactive control is desired). It can be applied in many fields, such as animation, shape design, and contour reconstruction. The algorithm is able to set up a correspondence between vertices in the source and target polygons without invisible correspondence, and the resulting morph has no self-intersection. Polygon vertices follow nonlinear paths, and the smoothness of the intermediate shapes can be controlled by a user-supplied evolution factor. The algorithm is object-based and is therefore not limited by image resolution. Morphing algorithms

with all of these features have not been developed before. Future work includes the extension of these algorithms to polyhedra and surfaces.

References

1. Alexa, M., D. Cohen-Or and V. Koltun (2001) Object-space morphing. Tutorial notes, Shape Modeling International 2001.
2. Bruckstein, A., G. Sapiro and D. Shaked (1995) Evolutions of planar polygons. *International Journal of Pattern Recognition and Artificial Intelligence*, 9(6), 991–1014.
3. Chew, L. P. (1987) Constrained Delaunay triangulations. Proceedings of the third annual symposium on Computational geometry, June 08-10, 215–222.
4. Cohen-Or, D., D. Levin and A. Solomovici (1998) Three-dimensional distance field metamorphosis. *ACM Transactions on Graphics* 17(2), 116–141.
5. DeCarlo, D. and J. Gallier (1996) Topological Evolution of Surfaces. *Graphics Interface '96*, 194–203.
6. Gage, M. and R. Hamilton (1986) The heat equation shrinking convex plane curves. *J. Differential Geometry* 23, 69–96.
7. Gomes, J., L. Darsa, B. Costa and L. Velho (1998) Warping and morphing of graphical objects. Morgan Kaufmann Publishers, Inc.
8. Goldstein, E. and C. Gotsman (1995) Polygon morphing using a multiresolution representation. *Graphics Interface '95*, 247–254.
9. Grayson, M. (1987) The heat equation shrinks embedded plane curves to round points. *J. Differential Geometry* 26, 285–314.
10. Guibas, L. J., Knuth, D., and Sharir, M. (1992) Randomized incremental construction of Delaunay and Voronoi diagrams. *Algorithmica*, 7, 381–413.
11. Preparata, F. and M. Shamos (1988) *Computational Geometry: An Introduction*. Springer-Verlag (New York).
12. Sederberg, T. and E. Greenwood (1992) A physically based approach to 2-D shape blending. *SIGGRAPH '92*, 25–34.
13. Shapira, M., A. Rappoport (1995) Shape blending using the star-skeleton representation. *IEEE Computer Graphics and Applications*. March, 1995, 44–50.
14. Shewchuk, J. R. (2002) Delaunay Refinement Algorithms for Triangular Mesh Generation. *Computational Geometry: Theory and Applications* 22, 21–74.
15. Turk, G. and J. O'Brien (1999) Shape transformation using variational implicit functions. *SIGGRAPH '99*, 335–342.
16. Wu, X. (2003) Morphing many polygons across a change in topology. Ph.D. Thesis, Department of Computer and Information Sciences, University of Alabama at Birmingham.
17. Wu, X. and J. Johnstone (2006) A Visibility-Based Polygonal Decomposition. Manuscript under preparation.

Jittering Reduction in Marker-Based Augmented Reality Systems

Monica Rubio¹, Arturo Quintana¹, Hebert Pérez-Rosés¹, Ricardo Quirós²,
and Emilio Camahort³

¹ Universidad de Oriente. Patricio Lumumba S/N,
90500 Santiago de Cuba, Cuba

{mrubio, quintana, hebert}@csd.uo.edu.cu

² Universitat Jaume I. Av. Sos Baynat S/N,
12071 Castellón, Spain
quiros@lsi.uji.es

³ Universidad Politécnica de Valencia. Camino de Vera S/N,
46022 Valencia, Spain
camahort@dsic.upv.es

Abstract. Augmented Reality systems have recently become widely used. This is due to the new open source libraries that have emerged for fast application development. In this paper we address one of the most relevant problems in this type of systems, oscillation in the camera pose estimates. We study the oscillation of a system developed using the ARToolkit library. We apply both average and Kalman filters to stabilize the estimates. Using filter substantially reduces oscillation, thus improving the system's usability.

1 Augmented Reality Systems

Augmented Reality (AR) systems are an evolution of the concept of Virtual Environment (VE). In AR systems the environment is the real world which is enhanced with virtual elements. The similarity of AR and VE systems implies that their associated problems are nearly the same. Both AR and VE systems are made of three main sub-systems [1]:

- Scene generator (*graphics system*).
- Rendering devices (*rendering system*).
- Tracking and sensing (*tracking system*).

The scene generator synthesizes the virtual images at the right location using the information provided by the tracking system. The rendering system combines the image of the real world with the virtual elements. It then displays an enhanced image to the user.

Scene generation and rendering are not the main problems of the design of effective AR systems. VEs have more restrictive requirements because of the need to render the entire virtual world in the most realistic way. In AR the virtual images complement the real world. Therefore, we need to render only a few virtual objects. These objects do not necessarily have to be realistic, as long as the requirements of the application are met.

The tracking system obtains the viewing parameters (position and orientation) in the real world. This subsystem has *registration problems* – problems with the correspondence between the real and the computed viewing parameters –. Registration problems are more important in AR systems than in EVs. In an EV the user only sees virtual objects. So, registration errors produce conflicts that can induce confusion and disorderly movements. In an AR system the conflict is visual, because the user can compare the virtual and real worlds [1].

Most of current research in AR focuses on the registration problem, the most important one when building an effective AR system [2][3]. The tracking system is primarily responsible for the registration accuracy. In the following section we survey tracking systems commonly used in AR applications.

1.1 Tracking Systems

The most common AR tracking systems use either *hardware sensors* or *computer vision techniques*. There are also *hybrid approaches* that combine both techniques to improve registration. These systems are more complex and expensive, but they produce better results.

A traditional approach to tracking the viewer is the use of hardware sensors to estimate the viewing parameters. Commercial sensors come in different types: mechanical, optical and ultrasound sensors. They have been widely used in VE interaction and have been adopted by indoor AR applications. Even though these sensors are very accurate, they require a complex infrastructure and a substantial investment. This prevents their use in certain applications, especially in the outdoors.

Registration solely based on hardware sensors can be compared to an open-loop controller [4]. The system has no information to relate the real world to the virtual world. So it is difficult to obtain an accurate registration. In video based systems we can use image processing or computer vision techniques to improve registration. Computer vision techniques can be applied to tracking in two ways: (i) registration can be improved using reference points in the environment (*marker based tracking*), and (ii) pattern matching techniques can be used for registration [5][3]. The second approach, although promising, does not currently allow the development of effective AR systems.

Marker based tracking systems add a set of reference objects to the environment. These objects are commonly called *markers* or *fiducials*. The position and features of the different markers are known. This allows estimation of the real-world viewing parameters using an inverse projection transform. The main marker-based systems in the



Fig. 1. Marker types. TRIP, Colored Rings, Cybercode, ARToolkit.

literature are the *TRIP* system (*Target Recognition using Image Processing*) [6], *multiresolution colored rings* [7], the *CyberCode* system [8] and the *ARToolkit* library [9]. Fig.1 shows example markers used by these systems.

The most popular marker based tracking system is the *ARToolkit* library of Kato and Billinghamurst [9]. *ARToolkit* is an open source library that supports the development of AR applications with a marker based tracking system. The advantages of *ARToolkit* are: (i) it is open source, (ii) it uses simple low-cost technology, (iii) it runs in real time, (iv) it supports mobile devices like phones and PDAs, and (v) it produces results accurate enough for most applications.

One of the main limitations of the library is its inaccurate pose estimations. This produces a noticeable jittering, even when the camera and the markers are still. Nevertheless *ARToolkit* is an ideal tool for easy development of AR systems without demanding accuracy requirements. This fact is supported by the large number of applications developed using the library [10] [11], and by the celebration of conferences specifically devoted to it (*First & Second IEEE International Augmented Reality Toolkit Workshops, ART'02 & ART'03*).

2 Jittering in AR Systems

Our research work is part of a larger project called *VIRTAINER* [12]. *VIRTAINER* develops and implements acceleration techniques for rendering ordered stacked objects. Such techniques can be applied to industrial process monitoring and virtual environment navigation. One of the goals of the project is an *AR prototype system* to remotely access information related to containers in a maritime terminal [13].

On order to develop our tracking system we run some tests with vision based techniques. We implemented a low-cost tracking system using a TabletPC, USB webcams and the *ARToolkit* library [14]. The tests showed the limitations of using *ARToolkit* as our tracking system. The main limitation was the poor accuracy of the pose estimations. This produces a noticeable jittering, even when the camera and the markers are still. This problem occurs because *ARToolkit* processes the video sequence frame by frame. This effect in our prototype can be seen in a video located at the address <http://graficos.uji.es/TSCG06>.

The goal of our research is to reduce jittering by using filters that take into account the history of pose estimates. To achieve this goal we address the following issues:

- We design techniques for pose extraction given the estimates of *ARToolkit*. We also analyze different pose representations.
- We characterize jittering for different spatial relations between the camera and the marker.
- We propose filters for pose estimates and study their effect on jittering.

The rest of this section is devoted to analysing pose extraction techniques and characterizing the jittering. In the following section we present the filters applied to the tracking system to reduce jittering.

2.1 Pose Extraction

ARToolkit's tracking system runs frame by frame. For each frame the markers visible in the image are detected. Then the marker with highest confidence is selected and a transformation is returned. The transformation maps the camera coordinate system to the coordinate system of the marker selected. That transformation is stored as a 4x4 matrix M_T and returned to the application for processing (see Fig. 2).

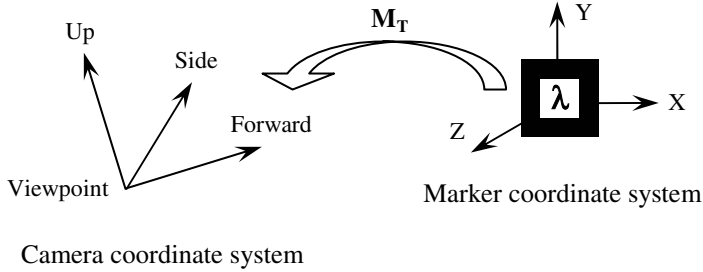


Fig. 2. Relationship between the coordinate systems of the camera and the marker. M_T matrix.

Given matrix M_T current AR systems use it as the OpenGL modelview matrix to render the virtual objects. That way the objects are rendered using a synthetic camera that has been registered with the real camera. Direct application of filters to matrix M_T has the disadvantage that it can produce non-orthogonal matrices. So, to apply filters to the pose estimates we need to use an alternative representation for the pose.

First, we consider directly extracting the camera coordinate system from matrix M_T . Note that M_T is a coordinate system transformation, and its first three rows contain the director vectors Forward, Up and Side. The fourth column is related to the viewing position. These relationships between M_T and the camera coordinate system are illustrated in the following equation:

$$M_T = \begin{bmatrix} S_x & S_y & S_z & T_x \\ U_x & U_y & U_z & T_y \\ F_x & F_y & F_z & T_z \\ - & - & - & - \end{bmatrix} \quad (1)$$

To guarantee an orthogonal pose we use a representation made of the viewpoint and the Forward and Up vectors. After applying the filters we compute Side as the cross product of Forward and Up. Then we re-compute Up as the cross product of Forward and Side. This technique is also used by the `gluLookAt` call of the GLU library. The first representation we consider for the pose has the following parameters:

$$\mathbf{P}_1 = \{T_x, T_y, T_z, F_x, F_y, F_z, U_x, U_y, U_z\} \quad (2)$$

Two alternative representations replace the Forward and Up vectors by three Euler angles or a quaternion. Both options support representing an orientation in 3D space. This allows conversion between them and the director vectors. To perform these conversions we use the algorithms by Shoemake published in the Graphics Gems [15].

Due to the large number of possible combinations of Euler angles, we selected the two most common combinations: XYZs (*yaw, pitch y roll*) used in computer graphics and navigation, and XYXr used in mechanics, where turns are made around a rotating system. These alternative representations have the following parameters:

$$\begin{aligned}
 \mathbf{P}_2 &= \{T_x, T_y, T_z, \theta_1, \theta_2, \theta_3\} \\
 \mathbf{P}_3 &= \{T_x, T_y, T_z, s, v_x, v_y, v_z\}
 \end{aligned}
 \tag{3}$$

2.2 Jittering Characterization

To characterize ARToolkit’s jittering under static conditions we run tests representing the pose as a local coordinate system (\mathbf{P}_1). Given the transformation matrix we extract the viewpoint (T_x, T_y, T_z), the Up vector (U_x, U_y, U_z) and the Forward vector (F_x, F_y, F_z). We analyze each of these parameters separately. For the viewpoint position the jittering amplitude is defined by the distance between two estimated positions in consecutive frames. For the orientation (Up and Forward vectors) the jittering amplitude is defined by the angle between two estimated vectors in consecutive frames.

We run multiple tests to measure the jittering under different spatial relations between the camera and the marker. On one side we consider the relative distance between them expressed as the percentage of the image covered by the marker. For each distance there are three possible angular relations per coordinate axis between the marker and the camera. We place the marker facing the camera (0°) or tilted 45° and 65° with respect to the X and Y axes. Altogether we have 9 different angular relations. Fig. 3 shows some of the relations used.

Combining 9 angular and 2 distance relations requires running 18 tests. Table 1 show average, maximum and standard deviation numbers for the jittering amplitude for both camera position and Up and Forward vectors. For brevity, we only show a



Fig. 3. Different camera-marker relations (setups) used in our tests

Table 1. Jittering amplitude measurements for different camera-marker relations

Spatial relation	Up			Forward			Position		
	Med	Max	σ	Med	Max	σ	Med	Max	σ
12% / 0^0 / 0^0	.0244	.0970	.0183	.0333	.1128	.0199	1.437	7.928	1.231
12% / 45^0 / 45^0	.0021	.0076	.0012	.0024	.0076	.0012	.7180	2.821	.4827
12% / 65^0 / 65^0	.0009	.0029	.0004	.0011	.0034	.0005	.2450	.9129	.1516
25% / 0^0 / 0^0	.0034	.0155	.0023	.0037	.0155	.0023	.2093	.8082	.1342
25% / 45^0 / 45^0	.0010	.0037	.0005	.0012	.0034	.0006	.1899	.7461	.1318
25% / 65^0 / 65^0	.0003	.0013	.0002	.0004	.0015	.0002	.0531	.2154	.0315

few of the combinations we tested. Results for all combinations can be found at the address <http://graficos.uji.es/TSCG06>.

Table 1 shows that jittering amplitude is reduced for all parameters when: (i) the size of the marker in the image increases or (ii) the magnitude of the angles increases. With this characterization of jittering we select one of the combinations with the worst jittering (12% / 0° / 0°). With this combination we test the filters we implement for our tracking system.

3 Filtering the Pose Estimate

To stabilize the pose estimated by ARToolkit we have to add to our system filters that take into account the recent history of estimates. A filter commonly used to stabilize noisy signals is the *average filter*. We use it to average the estimates of the last 6 and 12 frames.

Alternatively, other authors propose the use of the *Kalman filter*. The Kalman filter is a predictive recursive filter designed to estimate the state of dynamic systems [16]. The filter algorithm predicts the new state given a previous estimate and applying a correction term proportional to the prediction error. This way the error is statistically minimized. We use the implementation of the Kalman filter contained in Intel's *OpenCV* library [17]. This implementation provides a data structure and the functions needed to make predictions and to correct the state with the measurements.

3.1 Experimental Results

We have tested the application of average and Kalman filters to the position and orientation estimates provided by ARToolkit. For the orientation we consider the three possible representations (\mathbf{P}_1 , \mathbf{P}_2 , \mathbf{P}_3). To effectively compare the filters we always end up converting all other pose representations to a local coordinate system (\mathbf{P}_1 representation). This way all the results of our filter tests can be presented as the change of the viewpoint and the Up and Forward vectors between two consecutive frames. Experiments were run with a 1000-frame video.

Now we show graphically the original jittering and the jittering after applying the three filters: *6-frame average*, *12-frame average* and *Kalman*. Each of the following plots shows a subset of the experiment (80 consecutive frames) for each of the pose parameters: viewpoint, Up vector and Forward vector. There are four sets of plots, one for each possible orientation representation. Fig. 4 shows the results obtained for a local origin viewpoint and for director vectors (\mathbf{P}_1 representation) extracted from the matrix estimated by ARToolkit.

In the plots we observe that for the Up and Forward vectors the best filter is the 12-frame average, followed by the 6-frame average and Kalman. For the viewpoint, however, the Kalman filter behaves better. Its average variation is in the interval 10^{-2} - 10^{-3} . The results obtained with the other two representations, \mathbf{P}_2 and \mathbf{P}_3 are similar. In any case, the best results for the orientation are obtained with the 12-frame average filter. All the plots we generated with our tests can be found at the address <http://graficos.uji.es/TSCG06>.

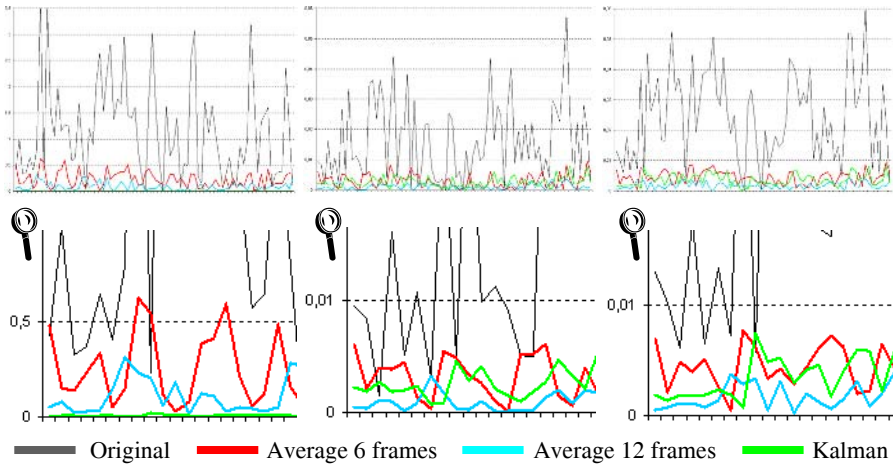


Fig. 4. Results of applying the different filters implemented to reduce jittering. Left, viewpoint, center, Up vector, right, Forward vector, and bottom, zoomed-in version of the top row plots.

In addition to the plots, we compared the different pose representations. For each filter we plotted the jittering amplitude for the different representations. For the average filters, the representation did not make a difference. When using the Kalman filter there are differences. Since orientation stabilizes better with average filters, we do not find these differences relevant. All the plots with the comparisons between representations can be found at the address <http://graficos.uji.es/TSCG06>.

4 Conclusions

In this paper we present methods to reduce jittering in marker based AR systems. We have defined three different pose representations: local coordinate system, Euler angles and quaternions. We have implemented average and Kalman filters and we have applied them to the pose estimated by ARToolkit. We have run tests and our results show that all filters reduce jittering.

Recall that all the running times of the filters are acceptable. The system runs in real time whether filters are used or not. We conclude that the best filter configuration is a Kalman filter for the viewpoint and an average filter for the orientation represented as a local coordinate system. We use this configuration in our AR system. A video showing our system running with and without filters can be found at the address <http://graficos.uji.es/TSCG06>.

Acknowledgments

This work was partially supported by grants TIC2002-4166-C03 and TIN2005-08863-C03 of the Spanish Ministry of Science and Education and by a STREP project IST-004363 of the 6th Framework Program of the European Union.

References

1. Azuma, R. T.: A Survey of Augmented Reality. *Presence: Teleoperators and Virtual Environments* 6, 4 (1997) 355–385
2. Auer, T.: *Hybrid Tracking for Augmented Reality*. Graz University of Technology (2000)
3. Comport, A., Marchand, E., Chaumette, F.: Robust and real-time image-based tracking for markerless augmented reality. Technical report, 4847, INRIA (2003)
4. Bajura, M., Ulrich, N.: Dynamic Registration Correction in Video-Based Augmented Reality Systems. *IEEE Computer Graphics and Applications* 15, 5 (1995) 52–60
5. Behringer, R.: Improving Registration Precision through Visual Horizon Silhouette Matching. *IEEE International Workshop on Augmented Reality* (1998) 225–232
6. López de Ipiña, D., Mendonça, P. R. S., Hopper, A.: TRIP: a Low-Cost Vision-Based Location System for Ubiquitous Computing. *Personal and Ubiquitous Computing* 6, 3 (2002) 206–219
7. Cho, Y., Lee, J., Neumann, U.: Multi-ring Color Fiducial Systems and An Intensity-Invariant Detection Method for Scalable Fiducial Tracking Augmented Reality. *IEEE International Workshop on Augmented Reality* (1998)
8. Rekimoto, J., Ayatsuka, Y.: CyberCode: Designing Augmented Reality Environments with Visual Tags. *Proceedings of DARE 2000 on Designing augmented reality environments* (2000) 1–10
9. Kato, H., Billinghurst, M., Poupyrev, I.: *ARToolkit Version 2.33 Manual* (2000)
10. Billinghurst, M., Kato, H., Poupyrev, I.: The Magic-Book. Moving Seamlessly between Reality and Virtuality. *IEEE Computer Graphics and Applications*, 21, 3 (2001) 2–4
11. Prince, S., Cheok, A. D., Farbiz, F., Williamson, T., Johnson, N., Billinghurst, M., Kato, H.: 3D Live: Real Time Captured Content for Mixed Reality. *International Symposium on Mixed and Augmented Reality* (2002) 7–13
12. Escrivá, M., Martí, M., Sánchez, J. M., Camahort, E., Lluch, J., Vivó, R.: Virtainer: Graphical Simulation of Container Storage Yard with Dynamic Portal Rendering. *Proceedings of the Ninth International Conference on Information Visualisation* (2005) 773–778,
13. Rubio, M., Quirós, R., Pulido, E.: Annotation of Features in Outdoor Augmented Reality Environments. *7th Conference on Geographic Information Science* (2004) 243–250
14. Rubio, M., Quirós, R., Pulido, E., Huerta, J., Camahort, E.: Wide Area Marker Based Tracking. *Intl. Conf. on Visualization, Imaging & Image Processing* (2005) 655–659
15. Shoemake, K.: Euler angle conversion. *Graphics gems IV*, Academic Press (1994) 222–229
16. Welch, G., Bishop, G.: *An Introduction to the Kalman Filter*. SIGGRAPH 2001 Course 8. ACM Press (2001)
17. *Open Source Computer Vision Library Reference Manual*. © Intel (1999–2001)

A Bias-Variance-Complexity Trade-Off Framework for Complex System Modeling

Lean Yu^{1,2}, Kin Keung Lai^{2,3}, Shouyang Wang^{1,3}, and Wei Huang⁴

¹ Institute of Systems Science, Academy of Mathematics and Systems Science,
Chinese Academy of Sciences, Beijing 100080, China
{yulean, sywang}@amss.ac.cn

² Department of Management Sciences, City University of Hong Kong,
Tat Chee Avenue, Kowloon, Hong Kong
{msyulean, mskklai}@cityu.edu.hk

³ College of Business Administration, Hunan University, Changsha 410082, China

⁴ School of Management, Huazhong University of Science and Technology,
1037 Luoyu Road, Wuhan 430074, China

Abstract. This study proposes a new complex system modeling approach by extending a bias-variance trade-off into a bias-variance-complexity trade-off framework. In the framework, the computational complexity is introduced for system modeling. For testing purposes, complex financial system data are used for modeling. Empirical results obtained reveal that this novel approach performs well in complex system modeling and can improve the performance of complex systems by way of model ensemble within the framework.

1 Introduction

In the last few decades, system modeling and optimization – an important aspect of complex systems – has proved to be one of the hardest tasks in studying complex systems. The topic has, as a result, received increased attention, especially due to its difficulties and wide applications. Two key problems are (i) how to select an appropriate model class from various model classes (i.e., modeling) and (ii) how to make the final model closer to specific complex systems; in other words how to improve final model performance based on the given data (i.e., optimization or improvement).

In order to solve these problems, a bias-variance-complexity trade-off framework is proposed. The theoretical background of our framework is provided by the bias-variance-noise decomposition of the generalization error and introduction of complexity (see below). We argue that the introduction of complexity into the framework can lead to an appropriate model class selection, and an ensemble of the selected model class can lead to performance improvement of the final complex systems model under the proposed framework. Our procedures and methods are described in Section 3. In Section 4 an example from the financial complex system domain is presented for further explanation. Some concluding remarks are drawn in Section 5.

2 The Bias-Variance-Complexity Trade-Off Framework

This section mainly describes the theoretical background of the proposed framework. It has two parts: bias-variance-noise decomposition and bias-variance-complexity trade-off.

2.1 Bias-Variance-Noise Decomposition

Assume that there is a true function $y=f(x)+\varepsilon$, where ε is normally distributed with zero mean and standard deviation σ . Given a set of training sets $D: \{(x_i, y_i)\}$, we fit the unknown function $h(x) = w \cdot x + \xi$ to the data by minimizing the squared error $\sum [y_i-h(x_i)]^2$. Now, given a new data point x^* with the observed value $y^* = f(x^*) + \varepsilon$, we would like to understand the expected error $E[(y^* - h(x^*))^2]$. We then decompose this formula into “bias”, “variance” and “noise” in the following:

$$\begin{aligned}
 E[(h(x^*) - y^*)^2] &= E[(h(x^*))^2 - 2h(x^*)y^* + (y^*)^2] \\
 &= E[(h(x^*))^2] - 2E[h(x^*)]E(y^*) + E[(y^*)^2] \quad (\because E(Z - \bar{Z})^2 = E(Z^2) - \bar{Z}^2) \\
 &= E[(h(x^*) - \bar{h}(x^*))^2] + (\bar{h}(x^*))^2 - 2\bar{h}(x^*)f(x^*) + E[(y^* - f(x^*))^2] + (f(x^*))^2 \\
 &= E[(h(x^*) - \bar{h}(x^*))^2] + E[(y^* - f(x^*))^2] + (\bar{h}(x^*) - f(x^*))^2 \tag{1} \\
 &= \text{Var}(h(x^*)) + E(\varepsilon^2) + \text{Bias}^2(h(x^*)) \\
 &= \text{Bias}^2(h(x^*)) + \text{Var}(h(x^*)) + \sigma^2
 \end{aligned}$$

From Equation (1), the expected error consists of three components: bias, variance and noise. The loss of the bias is from the difference between average prediction and optimal prediction, and is mainly caused by the learning algorithm. The variance originates from the difference between any prediction and the average prediction, and is often caused by using different training sets. The noise is very small and comes from the difference between optimal prediction and true function. Usually, the noise is hard to reduce, as in practice the inherent noise is often unknown. Thus the expected error is roughly equal to the sum of the squared bias and variance, as seen in Equation (2) below.

$$\text{Expected error } E[(h(x^*) - y^*)^2] = \text{bias}^2(h(x^*)) + \text{variance}(h(x^*)). \tag{2}$$

2.2 The Bias-Variance-Complexity Trade-Off Framework

According to [1], bias decreases as model complexity (i.e., the number of parameters) increases, whereas variance increases with model complexity, i.e., the more complex the model, the higher the variance. On the other hand, if the model is too simple, the bias will increase. There is a close relation among bias, variance and complexity, as is illustrated in Fig 1.

From Fig. 1, we can see that there is a trade-off relationship among bias, variance and complexity. Through this trade-off, the optimal complexity can be found. Also, bias and variance are optimal because the sum of two parts can attain the minimum in the total error curve.

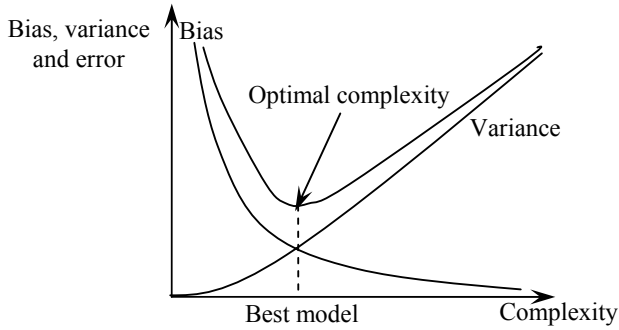


Fig. 1. The relationship among bias, variance and complexity

The bias-variance-complexity trade-off provides a conceptual framework for modeling complex systems, i.e., for determining a good model for complex systems. The detailed discussions are presented in the next section.

3 Complex System Modeling Under the Proposed Framework

In this section, we mainly discuss the two important modeling problems for complex systems – model selection and model improvement and optimization – under the proposed framework.

3.1 The Model Selection Under the Proposed Framework

As previously stated, the bias-variance-complexity trade-off provides a conceptual framework for determining a good model for complex systems. However, we need to obtain a practical criterion for determining a good model by optimizing the three components under the proposed framework. It should be noted that the ultimate goal of model selection under the proposed framework is to choose a good model which will perform the best on future testing data, i.e., a good generalization.

As earlier revealed, if the model is too complex for the amount of training data, it learns (or memorizes) parts of noise as well as problems in the underlying structure, resulting in “overfitting” or high variance as well as low bias. The selected model will perform badly in the testing data (or have a weak generalization). Inversely, if the model is not complex enough, it cannot capture the underlying structure in the data, no matter how much data it is given; this leads to “underfitting” or high bias. The selected model will also perform very badly (or have a poor generalization). In addition, the parsimony principle or Okham’s razor [2] shows that “from all models describing the process with the same level of accuracy, the simplest is the best”. This implies that we may find a good model selection criterion through a rational trade-off among bias, variance and complexity.

Based on the above descriptions and the proposed framework, it is possible to find a good model by minimizing the following selection criterion:

$$\text{Model selection criterion} = f(\text{bias, variance, complexity}). \quad (3)$$

From Equation (3), we see that the model selection criterion is actually a multi-objective optimization problem, i.e., minimizing the bias and variance for a given or appropriate complexity.

The aim of selection is for the model to perform good generalization of new observations or unknown data. However, as [3] pointed out, model generalization is often defined as the prediction risk. With the help of this concept and Equation (3), we suppose that $x \in \mathbf{R}^m$ is random sampled according to a distribution $p(x)$, the expected output for x is $y = f(x) + \varepsilon$ and the prediction output is $h(x)$. We can then formulate a concrete model selection criterion in the following:

$$\text{Model selection criterion} = \varphi(d/n) \int p(x) [f(x) - h(x)]^2 dx \tag{4}$$

where φ is a monotonically increasing function of the ratio of model complexity (i.e., the number of parameters or degrees of freedom) d and the training sample size n [4]. The function φ is often called the penalization factor because it inflates the average residual sum of squares for increasingly complex models. Several forms of φ have been proposed in the statistical literature, such as final prediction error (FPE) [5] and Schwartz' criterion (SC) [6]:

$$\text{FPE: } \varphi(q) = (1 + q)(1 - q)^{-1} \tag{5}$$

$$\text{SC: } \varphi(q, n) = 1 + 0.5 \cdot (\log n) \cdot q \cdot (1 - q)^{-1} \tag{6}$$

where q denotes the ratio of model complexity and training sample size. In this study we used FPE as the penalization factor of complexity.

In addition, in view of the results of [3], the model selection criterion can be approximated by the expected performance on a finite test set.

$$\text{Model selection criterion} = \varphi(d/n) E[(f(x) - h(x))^2]. \tag{7}$$

With Equations (1), (2) and (5), the final model selection criterion can be written as

$$\text{Selection criterion} = [(n + d)/(n - d)] \cdot [\bar{h}(x) - f(x)]^2 + E[(h(x) - \bar{h}(x))^2]. \tag{8}$$

As can be seen from Equation (8), the bias, variance and complexity are all taken into account in the model selection process. Through the trade-off of bias, variance and complexity, as shown in Fig. 1, we can find an appropriate model class from various model classes for specific complex systems. In practice, the generic judgment rule is known as “the smaller the selection criterion value the better the model”.

3.2 The Model Improvement Under the Proposed Framework

Although a good model can be selected using the model selection criterion described above, the model does not necessarily give a good generalization because of the difficulties of complex system modeling. In order for a complex system to perform well, it is necessary to improve and optimize the selected model from the previous phase. In this study, model ensemble is used.

Model ensemble is a subject of active research. It makes possible an increase in generalization performance by combining several individual models trained on the same tasks. The ensemble approach has been justified both theoretically [7] and empirically [8]. Generally, the creation of an ensemble is divided into two steps, the first being the judicious creation of the individual ensemble members and the second their appropriate combination to produce the ensemble output. The widely-used ensemble model includes bagging [9] and boosting [10]. In this study, we propose a new approach to building an ensemble model for complex systems based on the proposed bias-variance-complex trade-off framework.

Our proposed approach is based on the observation that the generalization error of an ensemble model can be improved if the predictors on which averaging is done disagree and if their fluctuations are uncorrelated [11]. We now consider the case of an ensemble model $\hat{h}(\mathbf{x})$ consisting of M individual models, $\hat{h}_1(\mathbf{x}), \dots, \hat{h}_M(\mathbf{x})$; the ensemble model is represented as

$$\hat{h}(\mathbf{x}) = \sum_{i=1}^M w_i \hat{h}_i(\mathbf{x}) \tag{9}$$

where the weights may sum to one, i.e., $\sum_{i=1}^M w_i = 1$. Given the testing data $D_{test} = \{(x_1, y_1), \dots, (x_N, y_N)\}$, then and the ensemble mean squared error is defined as:

$$\text{Ensemble mean squared error} = (1/NM) \sum_{i=1}^N \sum_{j=1}^M (y_i - \hat{h}_j(\mathbf{x}_i))^2 \tag{10}$$

By introducing the average model $\bar{h}(\mathbf{x}_i) = (1/M) \sum_{j=1}^M h_j(\mathbf{x}_i)$ the mean squared error can be decomposed into bias and variance in terms of Equations (1) and (2):

$$\text{Bias}^2 = (1/N) \sum_{i=1}^N (y_i - \bar{h}(\mathbf{x}_i))^2 \tag{11}$$

$$\text{Variance} = (1/NM) \sum_{i=1}^N \sum_{j=1}^M (\bar{h}(\mathbf{x}_i) - \hat{h}_j(\mathbf{x}_i))^2 . \tag{12}$$

We can examine the effects of bias and variance from Equations (11) and (12). The bias terms depends on the target distribution (y), while the variance term does not. A more elaborate formulation would further decompose the bias term into true bias and noise (see Equation (1)), but as in practice the inherent noise is often unknown, the current definition is used here. The variance terms of the ensemble could be decomposed in the following way:

$$\begin{aligned} \text{Var}(\hat{h}(\mathbf{x})) &= E[(\hat{h}(\mathbf{x}) - \bar{h}(\mathbf{x}))^2] = E[(\hat{h}(\mathbf{x}) - E(\hat{h}(\mathbf{x})))^2] \\ &= E[(\sum_{i=1}^M w_i h_i(\mathbf{x}))^2] - (E[\sum_{i=1}^M w_i h_i(\mathbf{x})])^2 \\ &= \sum_{i=1}^M w_i^2 (E[h_i^2(\mathbf{x})] - E^2[h_i(\mathbf{x})]) + 2 \sum_{(i < j)} w_i w_j (E[h_i(x) \cdot h_j(x)] - E[h_i(x)]E[h_j(x)]) \end{aligned} \tag{13}$$

where the expectation is taken with respect to D . The first sum in Equation (13) marks the lower limit of the ensemble variance and is the weighted mean of the variance of ensemble members. The second sum contains the cross terms of the ensemble members and disappears if the models are completely uncorrelated [11]. Thus, we focus on the second part so as to lower the variance.

Through observing Equations (11) and (13), we can find several ways to reduce the expected error by ensemble under the bias-variance-complexity trade-off framework: (i) increase the number of individual models with the given data as much as possible to lower bias; (ii) build some independent models for lowering variance; and (iii) keep an appropriate computational complexity for ensemble. The final ensemble model can improve the performance of complex systems by rational trade-off processing based on the proposed framework.

3.3 The New Modeling Approach for Complex Systems Under This Framework

Based on the previous two subsections, a novel modeling approach for complex systems is proposed. This approach consists of two phases, model selection and model improvement, or five steps. The procedure is as follows.

A. Model selection phase

- 1) Given a data set of complex system D , a disjoint training set D_{train} and D_{test} is first created. The former is used to build a model and the latter to test the model.
- 2) Because we do not know the patterns of complex systems due to their difficulties, different types of models (or model classes) are used to try to capture the characteristics of complex systems.
- 3) With the D_{train} , different model classes can be built. In terms of the D_{test} and corresponding model selection criterion mentioned in the Section 3.1, an appropriate model class can be selected. Generally, the selected model class can capture more useful patterns than can other candidate model classes, and so will have low bias in a sense.

B. Model improvement phase

- 4) As Section 3.2 showed, model ensemble can improve the model performance of a complex system. From Equation (11), we know that the improvement in the bias is very limited. Inversely, the improvement space in the variance is large (Equations (12) and (13)) only if the individual models are independent or completely uncorrelated [11]. The simplest method for creating diverse ensemble members is to train each model using randomly initialized conditions, such as different model architectures and

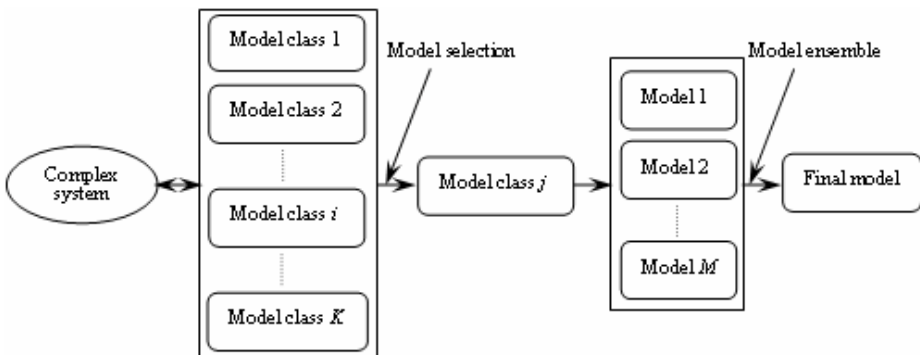


Fig. 2. The basic process of the proposed approach

different training subsets [12]. So in this step, we create a large number of ensemble members with different initialized conditions.

5) The different ensemble members obtained from the previous step are synthesized into the final model for a complex system.

The basic process is illustrated in Figure 2. For further interpretation, an example from the financial domain is presented in the following section.

4 The Empirical Study

In this section, foreign exchange rate modeling and forecasting is used as an illustrative example of our proposed approach. Two widely traded exchange rates the US dollar/euro (USD/EUR) and the US dollar/Japanese yen (USD/JPY) are chosen. We take daily data (source: DataStream) from 1 January 2000 until 31 October 2004 as entire data sets (partial data sets excluding holidays). For space reasons, the original data are not listed in this study but can be viewed on the website. For convenience, we take daily data from 1 January 2000 to 31 October 2003 as the training data set (D_{train}), and daily data from 1 November 2003 to 31 October 2004 as the testing set (D_{test}); these are used to evaluate the model performance. In this study, four model classes, linear polynomial model (LPM), K-Nearest-Neighbor (KNN) model, logit regression model (LRM), and feed-forward neural network (FNN) model, are selected as candidate model classes. We generated 100 training sets $\{D_i (i = 1, 2, \dots, 100)\}$ of fixed size N with the use of D_{train} to train different model classes. We let $\bar{h}(x) = (1/100) \sum_{i=1}^{100} h(x, D_i)$ denote the average of these model classes. We then verify our approach with the following procedures.

A. Model class selection phase

Based on the above descriptions and model selection criterion, the results of four model classes are reported below.

As can be seen from Table 1, we know that the best model class is the feed-forward neural network model in terms of the proposed model selection criterion for two exchange rates. With regard to complexity (here referring to model parameters), the effect of penalty has been taken into consideration by the selection criterion value.

Table 1. Simulation results of model selection for two exchange rates *

Exchange	Classes	Bias ²	Variance	Complexity	Criterion value
USD/EUR	LPM	0.065413	0.053815	10	0.129164
	KNN	0.058445	0.081252	14	0.156271
	LRM	0.075854	0.078639	12	0.171241
	FNN	0.032587	0.054014	30	0.110219
USD/JPY	LPM	0.184577	0.084758	14	0.301290
	KNN	0.223143	0.105472	13	0.364666
	LRM	0.254876	0.085347	8	0.351490
	FNN	0.128114	0.094756	37	0.300299

* Criterion value = (Bias² + Variance) × penalization factor of complexity.

In addition, we also see that the bias of the FNN model is the lowest of the four model classes, as earlier revealed. According to the proposed model selection criterion, we select the FNN model as an agent for exchange-rate modeling. However, we also note that the variance of the FNN model is relatively large in the four model classes, implying that there is room for improvement in the FNN model. In the sequel, model improvement is performed.

B. Model improvement phase

In this phase, we use model ensemble technique to improve the performance of the model selected in the previous phase. As Equation (13) shows, the variance will be reduced if the models are uncorrelated. That is, model diversity can reduce model error variance. In the case of neural network ensembles, the networks can have different architecture, different training algorithms or different training subsets, and different initialized weights or random weights [12–13]. In our study, we use these diverse methods to create different ensemble members. In order to have fair competition, the estimation of bias and variance is calculated for every ensemble with different complexity (here referring to the number of ensemble members). Simulation results are presented in the Table 2.

Table 2. Simulation results of different ensemble models for two exchange rates *

Exchange	Type	Complexity	Bias ²	Variance	Expected error
USD/EUR	Benchmark	1	0.032587	0.054014	0.086601
	Ensemble1	50	0.032225	0.050257	0.082482
	Ensemble2	100	0.032126	0.048253	0.080379
	Ensemble3	150	0.032158	0.048878	0.081036
	Ensemble4	200	0.032254	0.048854	0.081108
	Ensemble5	250	0.032545	0.048832	0.081377
USD/JPY	Benchmark	1	0.128114	0.094756	0.222870
	Ensemble1	50	0.127453	0.090015	0.217468
	Ensemble2	100	0.126587	0.089547	0.216134
	Ensemble3	150	0.127098	0.084854	0.211952
	Ensemble4	200	0.127805	0.087055	0.214860
	Ensemble5	250	0.127987	0.089811	0.217798

* Expected error = (Bias² + Variance).

From Table 2, we see that (a) the ensemble model with 100 members performs the best for USD/EUR, while for USD/JPY, the ensemble model with 150 members performs the best. The main reason is that the fluctuation of the Japanese yen is more complex than that of the euro; (b) compared to the benchmark model (i.e., single model), all the ensemble models lower the bias and variance, but bias reduction is less than variance reduction, implying that the ensemble can effectively reduce the variance; (c) of all the ensemble models, the most complex one does not necessarily give the best performance, as revealed by experiments, implying that an ensemble model should have an appropriate complexity (be neither too complex nor too simple); (d) all the ensemble models perform better by observing the expected error, implying that

the ensemble technique is an effective complex system modeling technique for improving modeling performance.

5 Conclusions

In this study we propose a novel complex system modeling approach based on the bias-variance-complexity trade-off framework. This approach consists of two phases: model selection and model improvement. In the first phase, we select an appropriate model class as modeling agent in terms of bias-variance-complexity trade-off. In the second phase, we improve complex system model performance by ensemble, based on the framework. Experimental results demonstrate that the proposed approach is effective.

Acknowledgements

This work is partially supported by National Natural Science Foundation of China (NSFC No. 70221001); Chinese Academy of Sciences; Key Research Institute of Humanities and Social Sciences in Hubei Province-Research Center of Modern Information Management and Strategic Research Grant of City University of Hong Kong (SRG No. 7001677).

References

1. Geman, S., Bienenstock, E., Doursat, R.: Neural networks and the bias/variance dilemma. *Neural Computation* 4 (1992) 1–58
2. Myung, I. J., Pitt, M. A.: Applying Okham's razor in modeling cognition: A Bayesian approach. *Psychonomic Bulletin & Review* 4 (1996) 79–95
3. Moody, J.: Prediction risk and architecture selection for neural networks. In: Cherkassky, V., Friedman, J. H., Wechsler, H. (eds.): *From Statistics to Neural Networks: Theory and Pattern Recognition Applications*. NATO ASI Series F, Springer-Verlag, 1994
4. Hardle, W., Hall, P., Marron, J. S.: How far are automatically chosen regression smoothing parameters from their optimum? *Journal of the American Statistical Association* 83 (1988) 86–95
5. Akaike, H.: Statistical predictor information. *Annals of the Institute of Statistical Mathematics* 22 (1970) 203–217
6. Shwartz, G.: Estimating the dimension of a model. *Annals of Statistics* 6 (1978) 461–464
7. Hansen, L. K., Salamon, P.: Neural network ensembles. *IEEE Transactions on Pattern Analysis and Machine Intelligence* 12 (1990) 993–1001
8. Opitz, D., Maclin, R.: Popular ensemble methods: An empirical study. *Journal of Artificial Intelligence Research* 11 (1999) 169–198
9. Breiman, L.: Bagging predictors. *Machine Learning* 24 (1996) 123–140
10. Freund, Y., Schapire, R. E.: Experiments with a new boosting algorithm. *Machine Learning: Proceedings of the 13th International Conference* (1996) 148–156
11. Krogh, A., Sollich, P.: Statistical mechanics of ensemble learning. *Physical Review E* 55 (1997) 811–825

12. Perrone, M. P., Cooper, L. N.: When neural networks disagree: Ensemble methods for hybrid neural networks. In: Mammone, R. J. (ed.): *Neural Networks for Speech and Image Processing*. Chapman-Hall (1993) 126–142
13. Krogh, A., Vedelsby, J.: Neural network ensembles, cross validation, and active learning. In: Tesauro, G., Touretzky, D., Leen, D. (eds.): *Advances in Neural Information Processing Systems*. MIT Press (1995) 231–238

A Neural Network Strategy for 3D Surface Registration

Heng Liu^{1,2}, Jingqi Yan¹, and David Zhang³

¹ Institute of Image Processing and Pattern Recognition, Min Hang District,
Shanghai Jiao Tong Univeristy, Shanghai, 200240, P.R. China
{hengliu, jqyan}@sjtu.edu.cn

² Southwest University of Science and Technology, Mianyang, 621000, P.R. China

³ Department of Computing, The Hong Kong Polytechnic University,
Hong Kong, P.R. China

csdzhang@comp.polyu.edu.hk

Abstract. 3D surface registration is commonly used in shape analysis, surface representation, and medical image aided surgery. This technique is extremely computationally expensive and sometimes will lead to bad result configured with unstructured mass data for its' iterative searching procedure and ill-suited distance function. In this paper, we propose a novel neural network strategy for surface registration. Before that, a typical preprocessing procedure-mesh PCA is used for coordinate direction normalization. The results and comparisons show such neural network method is a promising approach for 3D shape matching.

1 Introduction

Neural networks are able to extract latent rules from large amounts of chaotic, noisy data, making them especially suitable for processing 3D point clouds and triangle meshes so as to obtain geometrical 3D characteristics. So far, there are some approaches [1] [2] [3] using neural network for surface reconstruction and representation. And in computer vision field, works in [4] [5] [6] use neural network for stereo correspondence and motion estimation. However, few works are directly related to surface registration using neural network.

Surface registration or matching has turned out to be an essential step in 3D object recognition and representation. ICP [7] is a typical way for 3D surface matching. Although ICP is a numerical algorithm, due to the original data noises, blindness of large iterative searching and ill-suited distance function, ICP always cost extremely computation in unstructured data cases. Some methods are proposed to improve ICP [8] [9]. However, for rules of vertex corresponding cannot be expressed clearly, a good initial position guess and a suitable distance definition are not easily acquired for ICP performance improving.

For the same 3D models will have different representation if using different coordinate frames, coordinate direction normalization will be finished first. A classical preprocessing procedure-mesh PCA [10] is used for such task. Based on this, neural network are used to deal with 3D data to acquire finer registration effect. In this study, the whole surface registration flow is shown in Fig.1.

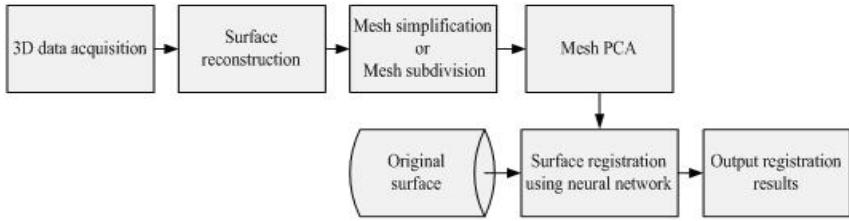


Fig. 1. A Proposed 3D surface registration flow

The remainder of the paper is organized as follows: Section 2 describes 3D data acquisition and mesh PCA procedure. In following Section 3, neural network mesh registration is provided in detail. Section 4 gives some experimental results and comparisons. Section 5 concludes and gives a further discusses.

2 3D Data Acquisition and Mesh PCA

There are two key steps in 3D data acquisition. Firstly, 3D vertices should be extracted from models. 3D models come from image based reconstruction or range scan. Data is obtained from 3D VRML file (.wrl file). 3D object in .wrl file is represented using vertices and triangular meshes. The entire vertices x, y, z and the vertex indices of triangular faces are extracted from .wrl file for Mesh PCA and surface registration processing.

The second step is trying to keep two different models holding the basic same sampling precision. Usually, models sampling precision is very different. For surface registration, we should keep models sampling precision basically equaling. There are two ways to finish such tasks: subdividing [11] the low precision surface to align the complex one; reducing [12] complex surface to align the low one. Thus we can keep the volumes of vertices coming from different models holding similar size. This is necessary step for insuring neural network convergence. In the following discussion, we assume that vertices have been extracted easily and the models hold the same sampling precision.

Mesh PCA [10] uses Principal Component Analysis (PCA) principles to analysis surface vertices data and extract principal directions of three largest spreads of the vertices distribution. Mesh PCA transformation will change the original coordinate system axes to new ones while the geometry shape of 3D model will not alter. So, if we adjust their three principal axes to three specific directions, we can furthest keep 3D models represented by using a unified coordinate frame. The covariance matrix C used as PCA caused matrix can be defined as following:

$$C = \frac{1}{\sum w_k} \sum_{k=1}^N w_k \left(\vec{v}_k - \vec{m} \right) \cdot \left(\vec{v}_k - \vec{m} \right)^T \tag{1}$$

where \vec{v}_k is a vertex of a mesh and k is the vertex index; \vec{m} is centroid of mesh. w_k is weight coefficient; N is the number of vertices. Eq. (1) solved by K-L

transformation [13], the normalized eigenvectors of the covariance matrix can be regarded as a coordinate transformation matrix $H(\in \mathbb{R}^{3 \times 3})$ for coordinate direction normalization.

Two reconstructed ear models and such models corresponding results by using mesh PCA for coordinate direction normalization are shown in Fig.2.

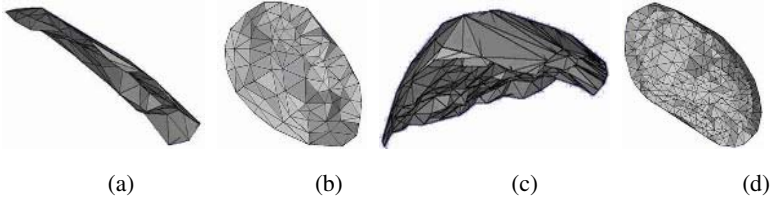


Fig. 2. Meshes PCA coordinate direction normalization. (a) (c) Original models; (b) (d) coordinate direction normalization models using mesh PCA transformation.

3 Neural Network Surface Registration

Assuming two surface A and B have been processed by mesh PCA, surface registration is the procedure that looks for the rotation matrix $R(\in \mathbb{R}^{3 \times 3})$, translation vector $T(\in \mathbb{R}^{3 \times 1})$, and scale coefficient $s(\in \mathbb{R})$, to make Error function E to get to a minimal value. This can be defined as:

$$\text{Min } E = \text{Dist}(A, R(s \cdot B) + T) \tag{2}$$

where $\text{Dist}(\cdot, \cdot)$ is a certain form distance function. Although Geodesic distance [14] [15] is more accurate than Euclidean distance when measuring vertices in meshes, we use Euclidean distance in neural surface registration for its easy representation. For neural network has powerful learning ability, we can apply neural network for such function approximation task.

Let $P_k(x, y, z)$ and $P_k'(x', y', z')$ are two vertices in two surfaces, $P_{ek}'(x', y', z')$ is corresponding vertex to vertex $P_k'(x', y', z')$ according to estimated rigid transformation. Eq. (2) can be expressed further as (k is the vertex index):

$$\text{Min } E = \sum_k (P_k - P_{ek}')^2 \tag{3}$$

$$P_{ek}' = s \cdot R P_k' + T \tag{4}$$

3.1 Neural Network Structure

For s in Eq. (4) is a scale value, let $\mathbf{R}' = s \cdot \mathbf{R}$, then we can rewrite Eq. (4) as:

$$\mathbf{P}'_{ek} = \mathbf{R}' \mathbf{P}'_k + \mathbf{T} \tag{5}$$

or equivalently

$$\mathbf{P}'_{ek}^{(H)} = \mathbf{M} \mathbf{P}'_k^{(H)} \tag{6}$$

where \mathbf{M} is the homogenous registration matrix:

$$\mathbf{M} = \begin{bmatrix} \mathbf{R}' & \mathbf{T} \\ 0 & 1 \end{bmatrix} \tag{7}$$

or equivalently

$$\mathbf{M} = \begin{bmatrix} \mathbf{W}_1 \\ \mathbf{W}_2 \\ \mathbf{W}_3 \\ \mathbf{W}_4 \end{bmatrix} = \begin{bmatrix} w_{11} & w_{12} & w_{13} & w_{13} \\ w_{21} & w_{22} & w_{23} & w_{24} \\ w_{31} & w_{32} & w_{33} & w_{34} \\ 0 & 0 & 0 & 1 \end{bmatrix} \tag{8}$$

and $\mathbf{P}'_k^{(H)} = \begin{bmatrix} \mathbf{P}'_k \\ 1 \end{bmatrix}$ is the corresponding homogeneous 3-D point.

If we take surface vertices coordinate as inputs, inspired by works in [4][5][6], we can construct a three-layer neural network (shown in Fig.3) based on the concept of least mean squared (LMS) error performance learning rule as Eq.(3).

From Eq. (8), we can deduce:

$$\mathbf{M} \mathbf{P}'_k^{(H)} = [\mathbf{W}_1 \ \mathbf{W}_2 \ \mathbf{W}_3 \ \mathbf{W}_4]^T \begin{bmatrix} \mathbf{P}'_k \\ 1 \end{bmatrix} = [\mathbf{W}_1 \cdot \mathbf{P}'_{kx}, \mathbf{W}_2 \cdot \mathbf{P}'_{ky}, \mathbf{W}_3 \cdot \mathbf{P}'_{kz}, \mathbf{W}_4] \tag{9}$$

Thus, Eq. (3) is equivalent to the following equations:

$$\text{Min} \sum_k (\mathbf{P}_{ki} - \mathbf{W}_i \cdot \mathbf{P}'_{ki})^2 \tag{10}$$

where k is the vertex index and $i \in (x, y, z)$.

At the other hand, if assuming x_{ij} represent s the sense and strength of the connection between neuron j of layer 1 and neuron of i of layer 2. A 4×4 weight matrix $\mathbf{X} = [\mathbf{X}_1, \mathbf{X}_2, \mathbf{X}_3, \mathbf{X}_4]^T$ can be constructed between layer1 and layer 2, where

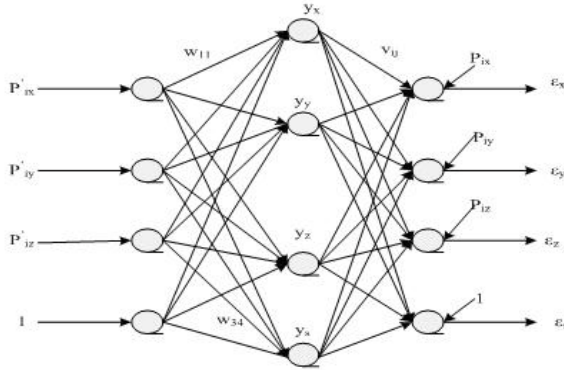


Fig. 3. Three layer network for determining the registration parameters

$$\begin{aligned}
 X_1 &= [x_{11}, x_{12}, x_{13}, x_{14}] \\
 X_2 &= [x_{21}, x_{22}, x_{23}, x_{24}] \\
 X_3 &= [x_{31}, x_{32}, x_{33}, x_{34}] \\
 X_4 &= [x_{41}, x_{42}, x_{43}, x_{44}]
 \end{aligned}$$

Let $y_i = [y_{ix} \ y_{iy} \ y_{iz} \ y_{is}]$ denote the actual outputs of layer 2. Then we can obtain

$$y_i = [X_1 \cdot P'_{ix} \ X_2 \cdot P'_{iy} \ X_3 \cdot P'_{iz} \ X_4 \cdot 1] \tag{11}$$

From Eq. (11) and Eq. (9) (in the two equations, k and i have the same meaning: vertex indices), we can deduce the relationship between the weight vector X and the unknown registration parameter matrix W as that:

$$X_i = W_i, W = [W_1, W_2, W_3, W_4] = [X_1, X_2, X_3, X_4] = X \tag{12}$$

Therefore matrix W can be computed through the process of performance learning as depicted in Fig.3. Then when neural network training converges, the optimal registration parameters can be acquired.

3.2 Neural Learning

Assume the weight vector matrix V between layer 2 and layer 3 is defined as

$$V = [V_1, V_2, V_3, V_4]^T \tag{13}$$

where $V_i = [v_{i1}, v_{i2}, v_{i3}, v_{i4}]$, $i \in (1,2,3,4)$ and v_{ij} denotes the sense and strength of the connection between neuron j of layer 2 and neuron i of layer 3. Let the weight

$$\text{matrix } V \text{ be a negative unit matrix, } v_{ij} = \begin{cases} -1 & \text{if } i = j \\ 0 & \text{otherwise} \end{cases}.$$

Let $P_i = [P_{ix}, P_{iy}, P_{iz}, P_{is}]^T$ (i is the vertex indices) denote the ideal outputs of layer 2(original mesh point coordinate value).The error \mathcal{E} , and the output of layer 3 can be obtained as follows

$$\mathcal{E}_i = [\mathcal{E}_{ix}, \mathcal{E}_{iy}, \mathcal{E}_{iz}, \mathcal{E}_{is}] = [P_{ix} - W_1 \cdot P'_{ix}, P_{iy} - W_2 \cdot P'_{iy}, P_{iz} - W_3 \cdot P'_{iz}, 0] \tag{14}$$

Using LMS algorithm, the estimated gradients can be gotten:

$$\lambda_{ij} = \frac{\partial \mathcal{E}_{ij}^2}{\partial W_i} = -2\mathcal{E}_{ij} P'_i \tag{15}$$

If we take Sigmoid function as activation function of neural unit, and use gradient descending algorithm to update the new weights: $W_{\text{new}} = W_{\text{old}} - \mu \lambda_{ij}$.Weight vector W_i can be acquired from following

$$W_i^{n+1} = W_i^n + 2\mu \mathcal{E}_{ij}^n \dot{P}_i \tag{16}$$

where μ the learning rate and n is the number of iterations. For homogenous weight coefficient, it keeps the constant: $W_4^n = W_4^{n+1} = [0,0,0,1]$.Weights matrix V between layer 2 and layer3 do not need to change in learning process.

In practical case, due to the meshes principal axis has been found by mesh PCA before using neural network, the procedure of neural network training converges very fast. Once neural network converges, the registration parameters will be gotten from the weight matrix W .

4 Experiments and Discussions

As we have stated above, any surface data should be preprocessed using PCA to acquire axis transformation matrix H for coordinate direction normalization. Then we use neural network to find finer registration matrix W . That is to say, an original vertex P_i should be take transformation $P'_i = W \cdot HP_i$. If we use triangular faces data besides, we need to keep normal vectors take same transformation to keep the faces direction right.

We take synthetic and range scanner surface data to test our methods. The results are shown in Fig.4. and Fig.5.

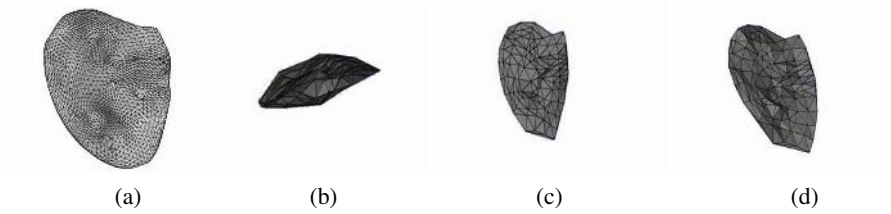


Fig. 4. Synthetic ear 3D surface registration. (a) The original synthetic surface. (b) Reconstructed low precision surface. (c) Mesh registration using neural network. Time consuming: $t < 10$ seconds. (d) Mesh registration using ICP. Time consuming $t = 40$ seconds.

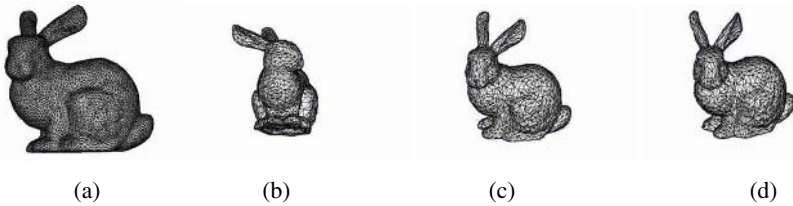


Fig. 5. Habit range data surface registration. (a) The original range surface. (b) Corresponding reconstructed low precision surface. (c) Mesh registration using neural network Time: $t = 27$ seconds. (d) Mesh registration using ICP. Time: $t = 121$ seconds.

We take learning rate μ is 0.01 and largest iteration number is 3000. For all the test data available, the network converges very fast. The iteration number is always under 200, and the computation time is within half a minute.

From the Figures, we see, compared with ICP, our method obvious get good results and low computation complexity. Using the same LMS rule, the error rate for neural network registration is under 3%, whereas for ICP the error rate can rise to 6%. In addition, ICP can not process scale problem in meshes registration procedure while our methods can do this easily. Further comparison with improved ICP need more materials to evaluate. Our methods use statistics analysis and learning algorithm, so we can get a fast and accurate registration results.

Using such neural network, the weight vector matrix V between layer 2 and layer 3 are defined as a minus identity matrix. This means, we use Euclidean distance to measure points. If we define different weight value of V , we will get different distance form for registration.

In surface registration procedure, we found mesh PCA pre-processing also have important effect on the last registration results. And our discussion is based on assumption that the two modes have been re-sampled with similar sampling precision and vertices are acquired after mesh filtering. If there are much too noise in vertices

or models precision are very different, then surface registration results are uncertainty. We should try to perfect pre-processing procedure to overcome such problems.

5 Conclusion

Due to powerful statistics analysis ability of neural network, mass unstructured 3D data are suitable for using neural network to manage. In this paper, we propose a novel neural network strategy for accurate surface registration. Experiments show our approaches are more efficient than the traditional ICP method. Further work on neural network surface registration will seek to reduce model precision dependency and to use the geodesic distance represented by neural networks to measure the vertex distance.

Acknowledgement

We would like to thank for Computer Vision Research Laboratory of the University of Notre Dame and the Stanford Computer Graphics Laboratory for providing their range scan data.

References

1. M Hoffmann, L Varady: Free-Form Modeling Surfaces for Scattered Data by Neural Networks. *Journal of Geometry and Graphics*, 1(1998)1-6
2. J Barhark, A Fishcher: Adaptive Reconstruction of Freeform Objects With 3D SOM Neural Networks Grids. *Conference proceedings in Pacific Graphics*, (2001)97-105
3. Lim Wen Peng, Siti Mariyam Shamsuddin: 3D Object Reconstruction and Representation Using Neural Networks. *Proceedings GRAPHITE 2004*, (2004)139-147
4. M.Nasser Nasrabadi, Y Chang Choo: Hopfield Network for Stereo Vision Correspondence. *IEEE Transactions On eural Networks*, 3(1) (1992)5-13
5. Dimitrios Tzouvaras, Nikiforos Ploskas, Michael G.Strintzis: Rigid 3-D Motion Estimation Using Neural Networks and Initially Estimated 2-D Motion Data. *IEEE Transactions On Circuits and Systems For video Technology*, 10(1) (2000)158-165
6. Ting Chen, Wei-Chung Lin, Chin-Tu chen: Artificial Neural Networks for 3-D Motion Analysis-Part I: Rigid Motion. *IEEE Transactions On Neural Networks*, 6(6) (1995)1386-1393
7. P. Besl, N. McKay: A Method for Registration of 3-D Shapes. *IEEE Trans. on Pattern Analysis and Machine Intelligence*, 14 (1992)
8. J. Feldmar, G. Malandain, J. Declerck, N. Ayache: Extension of the ICP Algorithm to Nonrigid Intensity-Based Registration of 3D Volumes. *Computer Vision and Image Understanding*, 66 (1997) 193-206
9. S. Rusinkiewicz, M. Levoy: Efficient Variants of the ICP Algorithm. *Proceedings of 3rd International Conference on 3D Digital Imaging and Modeling*, (2001) 145-152
10. D.V. Vranic, D. Saupe, J. Richter. Tools For 3D Object Retrieval: Karhunen-Loeve Transform and Spherical harmonics. In *Proceedings of IEEE 2001 Workshop Multimedia Signal Processing*, (2001) 293-298

11. Peter Schroder. Subdivision as a Fundamental Building Block of Digital Geometry Processing Algorithms. *Journal of Computational and Applied Mathematics*, 149(1)207-219
12. M. Garland and Y. Zhou. Quadric-based Simplification in any Dimension. *Transactions on Graphics*, 24(2) (2005)271-292
13. Andrew R.Webb. *Statistics Pattern Recognition*, second ed., Wiley, 2002
14. M.Sameh Yamany, A.Aly Farag: Surface Signatures: an Orientation Independent Free-Form Surface Representation Scheme for the Purpose of Objects Registration and Matching. *IEEE Transactions on Pattern Analysis and Machine Intelligence*, 24(8) (2002)1105-1120
15. Yiyong Sun, Joonki Paik, Andreas Koschan, David L.Page, Mongi A.Abidi: Point Fingerprint: A New 3-D Object Representation Scheme. *IEEE Transactions On System, Man, And Cybernetics-Part B: Cybernetics*, 33(4) (2003)712-717

Parallel Hierarchical Methods for Complex Systems Optimization

Ewa Niewiadomska-Szynkiewicz^{1,2}

¹ Institute of Control and Computation Engineering, Warsaw University of Technology, Nowowiejska 15/19, 00-665 Warsaw, Poland

ens@ia.pw.edu.pl

<http://www.ia.pw.edu.pl>

² Research and Academic Computer Network (NASK), Wawozowa 18, 02-796 Warsaw, Poland

<http://www.nask.pl>

Abstract. The paper is concerned with computational research for large scale systems. The focus is on the hierarchical optimization methods that can be successfully applied to large scale optimization problems. A key issue is the possibility of solving several less dimension problems instead of one global high dimension task. Particular emphasis is laid on coarse granularity parallel implementation and its effectiveness. The paper discusses the usage of price coordination for real-life systems optimization. The results of numerical experiments performed for mean-variance portfolio selection using cluster of computers are presented and discussed.

1 Introduction

The optimization methods discussed in this paper are addressed within the framework of systems that can be partitioned into smaller, which mathematical models represent the viewpoints of different decision makers or focus on one or more of the various aspects of the system. The general idea of hierarchical methods with coordination can be found in numerous algorithms, methods and structures being considered within the area of complex systems. In this paper we focus on the techniques associated with solving an optimization problems where the coordination is introduced after problem decomposition in order to modify in an iterative way the set of smaller problems, until their individual solutions provide jointly for a solution of the initial overall problem. The discussion of hierarchical approach can be found in the classic book by Mesarovic et al. [8].

The application of coordination schemes to the complex systems constitutes at the first level a finite number of simpler local optimization problems and at the second level – coordinator problem. It can be observed that introduction of hierarchical computational methods involves the possibility of parallel computations – usually of coarse granularity. The numerical techniques with iterative coordination such as the Price Method – known also as the Interaction Balance Method or the Direct Method, were developed in the beginning of 1970's and successfully used in modelling and optimization of large scale industrial systems

[1], [10], resource allocation [2], computer networks [3], [5], [11] and social systems [6]. The detailed description of methods and important issues of hierarchical computations can be found in [1], [2], [4].

2 Large Scale Systems Optimization

Consider the system consisting of N subsystems connected through the direct interconnections or common resources. The problem is to minimize a performance measure $f : \mathbb{R}^n \rightarrow \mathbb{R}^1$ w.r.t. the decision variables $x \in X$, $X \subset \mathbb{R}^n$. We can divide a vector of decision variables x into vectors u and v , $x = [u, v] = [u_1, \dots, u_N, v]$, where u_i , $i = 1, \dots, N$ denotes local decision variables of the i -th unit and v common interactions – variables that can not be decomposed. In the case of directly connected subsystems common interactions can be described by the equations $v_i = \sum_{j=1}^N H_{ij} y_j$, $i = 1, \dots, N$, where H_{ij} is the matrix with the elements from the set $\{0, 1\}$, y_j denotes vector of outputs from the j -th subsystem, $y_j = r_j(u_j, v_j)$, v_j is a subvector of v . The connection through the common resources can be described as $\sum_{i=1}^N z_i(u_i, v) \leq c$ or $\sum_{i=1}^N q_i(u_i, v) = s$, where c and s denote common resources. Taking into account the subsystems interconnections H , the common resources and local constraints ($g_i(u_i, v) \leq 0$, $h_i(u_i, v) = 0$, $i = 1, \dots, N$) we can formulate the optimization problem

$$\min_{(u,v) \in UV} [f(u, v) = \Psi(f_1(u_1, v), \dots, f_N(u_N, v))] \quad (1)$$

$UV = \{(u, v) : g_i(u_i, v) \leq 0, h_i(u_i, v) = 0, i = 1, \dots, N, \sum_{i=1}^N z_i(u_i, v) \leq c, \sum_{i=1}^N q_i(u_i, v) = s, u_i \in \mathbb{R}^{n_{u_i}}, v \in \mathbb{R}^{n_v}\}$. We assume that Ψ is strictly monotone, i.e. strictly order preserving.

The optimization problem (1) can be decomposed into N smaller tasks (local optimization problems LPi) and one coordinator problem CP. Hierarchical optimization methods can be applied to solve it, but under several conditions: for each LPi problem the solution is unique, and the solution of CP problem exists. The discussion of applicability and coordinability, which establishes required relationship between the original problem (1) and the hierarchical approach is presented in [1], [8] in details.

3 Optimization with Price Coordination

Different coordination strategies are discussed in [1]. In this paper we will focus on the algorithm with price coordination – the Price Method (PM) and its parallel implementation.

Consider the complex optimization problem (1) with an additional property; namely the performance function in (1) is a sum, i.e., $\Psi(f_1(u_1, v), \dots, f_N(u_N, v)) = \sum_{i=1}^N f_i(u_i, v)$. To decompose the optimization problem (1) into N smaller tasks instead of one vector v we can introduce N vectors v_1, \dots, v_N , where $v_1 = v_2 = \dots = v_N = v$. It results the additional constraints for variables v ,

$\sum_{i=1}^N A_{ji}v_i = 0, j = 1, \dots, m$, where m denotes number of subsystems interconnections and A matrix with elements from the set $\{-1, 0, 1\}$. Finally we obtain N local optimization problems with decision variables $[u_i, v_i], i = 1, \dots, N$. The admissible set for i -th local problem is: $UV_i = \{(u_i, v_i) : g_i(u_i, v_i) \leq 0, h_i(u_i, v_i) = 0, u_i \in \mathbb{R}^{n_{u_i}}, v_i \in \mathbb{R}^{n_{v_i}}\}$. Taking into account interactions between subsystems and constraints for common resources c and s we obtain the admissible set for the whole considered optimization problem $UV = \{(u_i, v_i) : (u_i, v_i) \in UV_i, i = 1, \dots, N, \sum_{i=1}^N z_i(u_i, v_i) \leq c, \sum_{i=1}^N q_i(u_i, v_i) = s, \sum_{i=1}^N A_{ji}v_i = 0, j = 1, \dots, m\}$. We can formulate the Lagrangian

$$\begin{aligned}
 L(u, v, \lambda, \mu) &= \sum_{i=1}^N f_i(u_i, v_i) + \sum_{j=1}^m \mu_j^T \left(\sum_{i=1}^N A_{ji}v_i \right) \\
 &+ \mu_{m+1}^T \left(\sum_{i=1}^N q_i(u_i, v_i) - s \right) + \lambda^T \left(\sum_{i=1}^N z_i(u_i, v_i) - c \right) \\
 &= \sum_{i=1}^N \left(f_i(u_i, v_i) + \sum_{j=1}^m \mu_j^T A_{ji}v_i + \mu_{m+1}^T q_i(u_i, v_i) + \lambda^T z_i(u_i, v_i) \right) - \mu_{m+1}^T s - \lambda^T c
 \end{aligned} \tag{2}$$

where $\mu_1, \mu_2, \dots, \mu_{m+1}$ and $\lambda \geq 0$ denote collection of Lagrange multipliers (prices) – dual variables associated with, respectively the constraints resulting subsystems interactions and common resources.

Assuming that the saddle point of function (2) in UV set exists we can formulate N local and one coordinator optimization problems:

LPi: $i = 1, \dots, N$, for given μ and λ , find minimum w.r.t. u_i and v_i of the local performance index

$$\min_{(u_i, v_i) \in UV_i} \left[L_i(u_i, v_i, \lambda, \mu) = f_i(u_i, v_i) + \sum_{j=1}^m \mu_j^T A_{ji}v_i + \mu_{m+1}^T q_i(u_i, v_i) + \lambda^T z_i(u_i, v_i) \right] \tag{3}$$

CP: for the results of LPi find maximum w.r.t. μ and λ , of the coordinator performance index

$$\max_{\lambda \geq 0, \mu} \left[\varphi(\lambda, \mu) = \sum_{i=1}^N L_i(\hat{u}_i(\lambda, \mu), \hat{v}_i(\lambda, \mu), \lambda, \mu) - \mu_{m+1}^T s - \lambda^T c \right] \tag{4}$$

The solution of the whole optimization problem is the saddle point $(\hat{u}, \hat{v}, \hat{\lambda}, \hat{\mu})$; $L(\hat{u}, \hat{v}, \lambda, \mu) \leq L(\hat{u}, \hat{v}, \hat{\lambda}, \hat{\mu}) \leq L(y, v, \hat{\lambda}, \hat{\mu})$. It is easy to solve the coordinator problem in PM. A solution vector is searched for as a point maximizing the concave dual function, defined in an easy way by local unconstrained problems solution. To solve those problems gradient methods can be applied. We can calculate gradients:

$$\nabla_{\mu_j} \varphi(\lambda, \mu) = \left[\sum_{i=1}^N A_{ji} \hat{v}_i(\lambda, \mu) \right]^T, \quad j = 1, \dots, m \tag{5}$$

$$\nabla_{\mu_{m+1}}\varphi(\lambda, \mu) = \left[\sum_{i=1}^N q_i(\hat{v}_i(\lambda, \mu), \hat{u}_i(\lambda, \mu)) - s \right]^T \tag{6}$$

$$\nabla_{\lambda}\varphi(\lambda, \mu) = \left[\sum_{i=1}^N z_i(\hat{v}_i(\lambda, \mu), \hat{u}_i(\lambda, \mu)) - c \right]^T \tag{7}$$

4 Parallel Price Coordination

The introduction of a hierarchical computational method allows to develop parallel computational tasks in a situation when such tasks do not naturally arise from an initial problem definition. We can distribute all local calculation processes and coordinator process over the processors. The algorithm may be implemented either on multiprocessor machine or cluster of computers. Let k denotes the iteration number, parallel version of PM algorithm is as follows:

LPi: $i = 1, \dots, N$

$$(u_i^{(k+1)}, v_i^{(k+1)}) = \arg \min_{(u_i, v_i) \in UV_i^{(k)}} L_i(u_i, v_i, \lambda^{(k)}, \mu^{(k)})$$

CP: the following algorithm can be applied

$$\mu_j^{(k+1)} = \mu_j^{(k)} + \tau_{\mu_j}^{(k+1)} d_{\mu_j}^{(k+1)}, \quad j = 1, \dots, m$$

$$\mu_{m+1}^{(k+1)} = \mu_{m+1}^{(k)} + \tau_{\mu_{m+1}}^{(k+1)} d_{\mu_{m+1}}^{(k+1)}, \quad \lambda^{(k+1)} = \lambda^{(k)} + \tau_{\lambda}^{(k+1)} d_{\lambda}^{(k+1)}$$

where τ_{μ_j} , $\tau_{\mu_{m+1}}$ i τ_{λ} denote positive step coefficients, $d_{\mu_j}^{(k+1)}$, $d_{\mu_{m+1}}^{(k+1)}$ i $d_{\lambda}^{(k+1)}$ gradients calculated w.r.t. (5), (6) and (7) for $v_i^{(k+1)}$ and $u_i^{(k+1)}$.

Coordinator starts calculations after obtaining LPi results $\hat{u}_i(\lambda^{(k)}, \mu^{(k)}) = u_i^{(k+1)}$ and $\hat{v}_i(\lambda^{(k)}, \mu^{(k)}) = v_i^{(k+1)}$, $i = 1, \dots, N$. Next, LPi are solved for new vector of multipliers $\lambda^{(k+1)}$ and $\mu^{(k+1)}$, etc. The local tasks can be solved in parallel. The parallel version allows to decrease the time of calculations from $t^{(k)} = \sum_{i=1}^N t_i^{(k)} + t_c^{(k)}$ to $t^{(k)} = \max_{i=1, \dots, N} t_i^{(k)} + t_c^{(k)}$, where $t_i^{(k)}$ and $t_c^{(k)}$ denote the time periods required to solve LPi and CP tasks in every iteration of the algorithm. The coordinator task is very simple, $t_c^{(k)} \ll t_i^{(k)}$, so whole calculation time $T \approx \sum_{k=1}^K \max_{i=1, \dots, N} t_i^{(k)}$, where K denotes the number of iterations to convergence to the optimal solution.

5 Practical Examples

Let us consider the applications of PM to solve the optimization problems formulated for exemplary interconnected system and system with common resources.

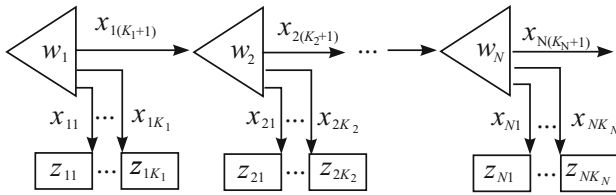


Fig. 1. System of water reservoirs

5.1 Water Management System

Consider the water system consisting of N reservoirs, as presented in Fig. 1. The basic objectives of the decision process include: drinking water supply to neighboring towns, industry and agriculture requirements, navigation and protection of hydrogenic habitats. We assume that i -th reservoir supply water to K_i users. Assume: w – the capacity of the reservoir, x – outflow from the reservoir ($\dim(x_i) = K_i + 1$), z – user requirements, p – required levels of flows, α and β – weighting factors (different users have different importance). We can formulate the optimization problem

$$\min_{x \in X} \left[f(x) = \sum_{i=1}^N \left(\alpha_i \sum_{k=1}^{K_i} (z_{ik} - x_{ik})^2 + \beta_i (p_i - x_{i(K_i+1)})^2 \right) \right] \tag{8}$$

where $X = \{x : \sum_{k=1}^{K_i} x_{ik} + x_{i(K_i+1)} - x_{(i-1)(K_{i-1}+1)} - w_i \leq 0, x_{ik} \geq 0, k = 1, \dots, K_i + 1, i = 1, \dots, N\}$.

We will divide a vector x into vectors u and v , $x = [u, v] = [u_1, \dots, u_N, v]$, where $u_i = [u_{i1}, \dots, u_{iK_i}] = [x_{i1}, \dots, x_{iK_i}]$ denotes the outflows to the users from the i -th reservoir. The flows from one reservoir to the next one are common interactions, $v = [x_{1(K_1+1)}, \dots, x_{N(K_N+1)}]$. Instead of one vector v we will introduce N vectors v_1, \dots, v_N , where $v_1 = v_2 = \dots = v_N = v$. According to (2) we can formulate the Lagrangian and after its decomposition we obtain local and coordinator tasks:

LPi:

$$\min_{(u_i, v_i) \in UV_i} \left[L_i(u_i, v_i, \mu) = \alpha_i \sum_{k=1}^{K_i} (z_{ik} - u_{ik})^2 + \beta_i (p_i - x_{i(K_i+1)})^2 - \mu_{i-1} v_{i(i-1)} + \mu_i v_{ii} \right]$$

$$UV_i = \{(u_i, v_i) : \sum_{k=1}^{K_i} u_{ik} + v_{ii} - v_{i(i-1)} - w_i \leq 0, u_{ik} \geq 0, v_{i(i-1)} \geq 0, v_{ii} \geq 0\}.$$

CP:

$$\max_{\mu} \left[\varphi(\mu) = \sum_{i=1}^N L_i(\hat{u}_i, \hat{v}_i, \mu) \right].$$

5.2 Portfolio Selection

The optimization technique with problem decomposition and price coordination was applied to calculate the optimal portfolio over a certain period of time. The

L risky assets were considered. The single-period mean-variance approach developed by Markowitz [7] was applied. Denote by x_l a share of the capital invested in asset l , $x \in \mathbb{R}^n$, by $r \in \mathbb{R}^n$ the random vector of asset returns. Two basic rates are defined: reward of a portfolio that is the mean of its return $S(x) := E(r^T x)$ and variance of returns (the measure of risk), $R(x) := E[(r^T x - E(r^T x))^2] = x^T \Sigma x$, where Σ denotes a covariance matrix. According to Markowitz formulation we obtain a mean-variance optimization quadratic problem – maximization of expected value and minimization of variance of profit, [12].

$$\max_{x \in \mathbb{R}^n} [f(x) = \gamma S(x) + \delta R(x)], \quad \sum_{l=1}^L x_l = 1 \tag{9}$$

Denote γ and δ tradeoff parameters, r_l return of the l -th asset, s_l standard deviation of the l -th asset returns, ρ_{lk} correlation coefficient of return for the l -th and the k -th assets. After approximations we can calculate $S(x) = \sum_{l=1}^L x_l r_l$ and $R(x) = \sum_{l=1}^L x_l^2 s_l^2 + 2 \sum_{l=1}^{L-1} \sum_{k=l+1}^L x_l x_k s_l s_k \rho_{lk}$.

All model parameters (r , s , ρ) can be adjusted based on historical data. Considering historical data containing T trading sessions we can estimate $r_l = (\sum_{t=1}^T r_{l,t})/T$, where $r_{l,t}$ is the return of the l -th asset in the t -th session calculated as follows: $r_{l,t} = [(p_{l,t} - p_{l,t-1}) + d_{l,t}]/p_{l,t-1}$, $p_{l,t}$ and $d_{l,t}$ denote price and dividend of the l -th asset in the t -th period. Similarly we can estimate the standard deviation of the l -th asset returns $s_l = [(\sum_{t=1}^T (r_{l,t} - r_l)^2)/(T - 1)]^{1/2}$ and the l -th and j -th assets correlation coefficient $\rho_{lj} = \frac{\sum_{t=1}^T (r_{l,t} - r_l)(r_{j,t} - r_j)}{(T-1)s_l s_j}$.

Optimization Problem Formulation. The risk $R(x)$ depends on all assets correlations, so $f(x)$ does not have additive property. To apply the Price Method to solve (9) we have to impose the additional constrains to decompose the problem. Consider all assets partitioning into N groups, each consisting of M assets, $x = [u_1, \dots, u_N]$, $u_i = [u_{i1}, \dots, u_{iM}]$, $i = 1, \dots, N$. Define the Lagrangian

$$L(u, \lambda) = \sum_{i=1}^N \left[\gamma \sum_{m=1}^M u_{im} r_{im} + \delta \left(\sum_{m=1}^M u_{im}^2 s_{im}^2 + 2 \sum_{m=1}^{M-1} \sum_{j=m+1}^M u_{im} u_{ij} s_{im} s_{ij} \rho_{imj} \right) - \lambda \sum_{m=1}^M u_{im} \right] + \lambda - \Theta$$

where $\Theta = \sum_{i=1}^{N-1} \sum_{k=i+1}^N \sum_{m=1}^M \sum_{j=1}^M u_{im} u_{kj} s_{im} s_{kj} \rho_{imkj}$ describes the correlation between different groups of assets (ρ_{imkj} denotes the correlation coefficient of return for the m -th asset from group i and the j -th asset from group k).

The Lagrangian can be easily decomposed in the case when $\Theta \approx 0$, that involve correlation-independent groups of assets. So, the key issue is the appropriate assets partitioning. In the case of proposed suboptimal technique N local problems LP $_i$ with performance measures (9) defined for M stocks each are formulated. The correlations between assets belonging to different groups are removed from the considerations (we assume very small correlation coefficients of

return for assets from different groups $\rho_{i_m k_j} \approx 0, l \neq k$). The objective of the coordinator is to guarantee the fulfillment of the global constraint for the budget.

LPi: $i = 1, \dots, N$, for given λ find maximum of the local performance index

$$\max_{u_i} \left[L_l(u_i, \lambda) = \gamma S(u_i) + \beta R(u_i) - \lambda \sum_{m=1}^M u_{im} \right] \tag{10}$$

where $u_{i_m \min} \leq u_{im} \leq u_{i_m \max}, m = 1, \dots, M$.

CP: for the results of LPi find minimum of the coordinator performance index

$$\min_{\lambda} \left[\varphi(\lambda) = \sum_{i=1}^N L_i(\hat{u}_i, \lambda) + \lambda \right] \tag{11}$$

Numerical Results. The task was to generate the optimal stationary investing policy for stocks from the Warsaw Stock Exchange, using data from period 1995-2002. The historical data gathered from WWW pages of brokerage houses were divided into two groups. The first group was used as a source of data for the optimization algorithm to adjust the model parameters. The second group was used to test a quality of obtained investing policies. Calculations were carried out on one computer and a cluster of computers. Numerical experiments were performed for four performance functions $f(x)$ in (9), describing different preferences of the investor: *A:* $f(x) = -0.5R(x)$ (risk minimization); *B:* $f(x) = 0.005S(x) - 0.5R(x)$ (risk minimization and profit maximization); *C:* $f(x) = 0.01S(x) - 0.5R(x)$ (risk minimization and profit maximization, risk less important than in *B*); *D:* $f(x) = 0.05S(x) - 0.5R(x)$ (risk minimization and profit maximization, risk less important than in *C*).

Two approaches to the given optimization problem solution were compared: *variant 1:* the whole problem (9) was solved w.r.t. all considered assets (approach without problem decomposition), and *variant 2:* all stocks of the considered companies were partitioned into N groups, each consisting of M companies, and PM was applied to calculate the optimal portfolio. The optimization results for different variants of the performance measure $f(x)$ are collected in Table 1. It can be observed that if we focus on risk minimization then our portfolio consists of many companies; else if we focus on profit maximization then our portfolio consists of only a few, the most profitable companies. Applying PM to calculate an investing strategy results less companies in computed portfolio than in the case without decomposition (*variant 1*). A quality of obtained investing policies were tested on historical data containing trading sessions from two years period 1998–2000, Fig. 2 presents the results of simulations of the policies calculated for model *B* and two variants of optimization. The curves represent the rates of return for variants 1 and 2. In the case of PM method (*variant 2*) two approaches to the optimization problem decomposition were considered: 2(a) random fixing of the companies to the local tasks LPi, 2(b) the companies dividing w.r.t. their size and capital. The available simulation results indicate that we would have achieved the advantage if we had done investments with respect to the policy

Table 1. The number of companies in the calculated portfolios; different models and optimization techniques

Optimization method	A	B	C	D
variant 1	59	55-56	21-22	3
variant 2	59	15-22	13-15	2-3

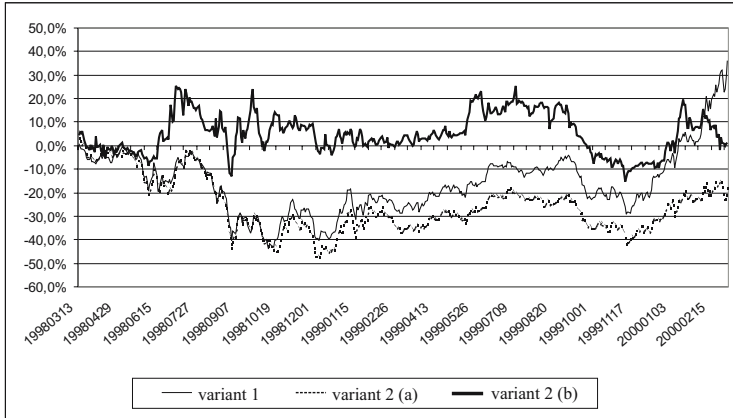


Fig. 2. Simulation results – different decomposition methods

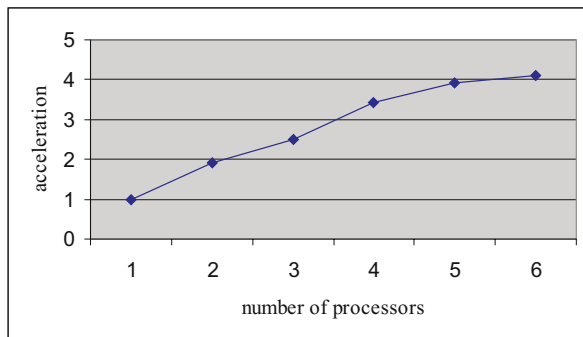
obtained with the help of PM algorithm. The key issue is adequate decomposition of the original problem (9). The worst results were obtained for random generation of the local problems, the best for decomposition w.r.t companies size and capital. The conclusion to be drawn is that the optimal portfolio is very sensitive to model and data accuracy. Due to high level of uncertainty, the estimation of all model parameters, is often not satisfactory. The inaccuracy may especially occur in correlation coefficients of weakly-correlated assets estimation. So, in some cases we obtain better results after removing inaccurate data from the calculations.

Next the simulation of the investor operation was performed using data from period 01.01.2002–31.08.2002. The investing strategy was changed in the beginning of each month. It was assumed that every month the budget equal 100 000 PLZ was invested in stocks. The results are given in Table 2. The values collected in the adequate columns present: *portfolio* – result of investing 100 000 PLZ in the end of the considered month, *commission* – fee paid for buying and selling stocks, *profit* – monthly profit from the portfolio.

Parallel Price Method Results. The application of the Price Method to portfolio optimization involves the possibility of parallel computations. The efficiency of parallel synchronous version of PM was tested. All stocks of 120 companies were partitioned into six groups (local problems LP1, . . . , LP6). The numerical experiments were carried out on the cluster of six machines with the help of

Table 2. Results of simulation

<i>month</i>	<i>portfolio</i>	<i>commission</i>	<i>profit</i>
January	110490	490	10490
February	95428	622	-4572
March	102079	531	2079
April	104209	471	4209
May	104178	382	4178
June	93351	539	-6649
July	96762	456	-3236
August	101306	424	1306
SUM		3915	7805

**Fig. 3.** Calculations acceleration: parallel PM w.r.t. sequential PM

the MPI (*Message Passing Interface* [9]). The results presented in Fig. 3 show that the number of processors influences the computation time. In the case of parallel synchronous version of PM this time strongly depends on the dimension of the largest local problem. The acceleration factor $S(n, p) = T(n, 1)/T(n, p)$, where n denotes the size of the problem, p number of processors, $T(n, p)$ time of calculations performed when p processors are available and the efficiency factor $\eta(n, p) = 1/(1 + h(n, p)/w(n))$, where $h(n, p)$ denotes transmission time, $w(n)$ calculation time, for the considered optimization problem and six processors were equal: $S = 4, 12$, $\eta = 0.65$. The results show the effectiveness of a parallel implementation even for small optimization problem. The efficiency factor should increase for the problem with higher dimension and time consuming calculations.

6 Conclusion

In this paper the optimization problem for large scale systems was defined and a hierarchical method – Price Method – was proposed to solve it. It was pointed that the introduction of a hierarchical techniques allows to develop parallel computational tasks – usually of coarse granularity – in a situation when such tasks do not naturally arise from the initial problem formulation. The presented case

study shows that in some cases it is profitable to simplify the initial model and apply methods with decomposition and coordination to solve it.

Acknowledgments. The author would like to thank Marcin Włodarczyk and Grzegorz Urbanowicz for assistance in preparing computational results.

References

1. Findeisen, W., Bailey, F.N., Brdys, M., Malinowski, K., Wozniak, A.: Control and Coordination in Hierarchical Systems. J.Wiley, London, (1980).
2. Haimes, Y., Li, D.: Hierarchical Multiobjective Analysis for Large-scale Systems: Review and Current Status. *Automatica*, **24**(1) (1988) 53–69
3. Low, S., Lapsley, D.E.: Optimization Flow Control, I: Basic Algorithm and Convergence. *IEEE/ACM Transaction on Networking* **7**(6) (1999) 861–874
4. Karbowski, A.: Modernization of the Direct Method of Hierarchical Optimizations, 10th IFAC/IFORS/IMACS/IFIP Symposium on Large Scale Systems: Theory and Applications, Osaka, Japan, **2** (2004) 458–463
5. Malinowski, K.: Optimization Network Flow Control and Price Coordination with Feedback: Proposal of a New Distributed Algorithm. *Computer Communications* **25** (2002) 1028–1036
6. Mayne, D.Q.: Decentralized Control of Large-Scale Systems. *Directions in Large-Scale Systems* (Ho, Y.C. and S.K. Mitter eds.). Plenum, New York (1976)
7. Markowitz, H.M.: *Portfolio Selection – Efficient Diversification of Investments*. Yale University Press, New Haven (1959)
8. Mesarovic, M.D., Macko, D., Takahara, Y.: *Theory of Hierarchical, Multilevel Systems*. Academic Press. New York (1970).
9. Message Passing Interface Forum, <http://www.mpi-forum.org/docs/>.
10. Roberts, P.D., Lin, J.: Potential for Hierarchical Optimising Control in the Process Industry. *Procc. of European Control Conference ECC* (1991) 213–217
11. Srikant, R.: *The Mathematics of Internet Congestion Control*, Birkhauser (2004).
12. Steinbach, M.C.: Markowitz Revisited: Mean-Variance Models in Financial Portfolio Analysis. *SIAM Review* **43**(1) (2001) 31–85

Numerical Modelling of Coastal Currents

Lale Balas, Asu İnan, and İpek Yıldız

Gazi University, Faculty of Engineering and Architecture, Civil Engineering Department,
06570 Maltepe, Ankara, Turkey
lalebal@gazi.edu.tr, asuinan@gazi.edu.tr,
iyildiz@gazi.edu.tr

Abstract. A numerical model has been developed for the simulation of transformations of traveling coastal waves and wave induced coastal currents. The model is applicable to varying bottom topographies and has two components, a wave propagation model and a wave driven current model. Wave propagation model is based on nonlinear parabolic mild slope equation and could simulate wave shoaling, refraction, diffraction and breaking. Different wave approach angles can be investigated on the same computational grid. Wave driven current model is based on vertically averaged non-linear shallow water equations. In the solution method, partial differential equations are replaced by a set of finite difference equations on a space staggered grid. Model has been applied to Obaköy coastal waters located at the Mediterranean coast of Turkey where there exist current measurements.

1 Introduction

Accurate numerical modeling of wave propagation from the deep ocean to a shoreline and precise prediction of wave induced coastal currents are quite important in the nearshore area. Berkhoff [1] solved the wave propagation from deep water to shallow water under combined refraction and diffraction effect with an elliptical equation, called as mild slope equation and valid for a bottom topography that has a mild slope. Mild slope equation includes combined refraction, diffraction, shoaling and reflection effects. Radder [2] recommended parabolic approach to overcome complexity in the solution of elliptical mild slope equation. Parabolic equation is applicable to the short waves over irregular bathymetries in large coastal areas. Kirby and Dalrymple [3] solved parabolic equation for the combined refraction-diffraction of Stokes waves on mildly varying topography. Ebersole [4], developed an alternative equation that expresses the propagation of linear waves over mild sloping bathymetry. This equation includes both refraction or diffraction effects, but not the reflection phenomena. Chamberlain and Porter [5] solved modified mild slope equation for the not evanescent modes. Massel [6], developed a modified mild slope equation including higher order bottom effect terms as wells as evanescent modes. Suh et al. [7] derived two equivalent time dependent wave equation for the

propagation of water waves on rapidly varying bottom topography. Recently, the researchers have concentrated on the improvement of unified phase resolving models describing transient fully nonlinear wave propagation from deep water to shallow water over a large area [8][9]. Wave propagation model developed in this study, is based on nonlinear parabolic mild slope equation and could simulate wave shoaling, refraction, diffraction and breaking. The spatially variable radiation stress gradients determined from developed wave propagation model serve as surface stress forcing in nearshore current model. In wave driven current model vertically averaged nonlinear shallow water equations that include nonlinear convective accelerations, lateral mixing and bottom friction, have been solved. Possibility of using finer resolutions in regions where the spatial gradients of the variables are sharp, is an advantage of the combined model. Only one computational domain is enough to simulate the transformation of waves from different directions with different approach angles. Therefore computationally, the numerical model is quite efficient for simulating wave propagation and wave induced circulation over large coastal areas subjected to varying wave conditions.

2 Theory

A combined numerical model is developed for the simulation of wave transformations and wave induced nearshore current, that is applicable to irregular bottom topographies. In the wave propagation model, the parabolic Schrödinger equation that describes the propagation of weakly nonlinear Stokes waves over slow but arbitrarily varying depths [3] given in Eqn(1) is used.

$$2ikCC_g A_x + 2k(k - k_0)(CC_g)A + i(kCC_g)_x A + (CC_g A_y)_y - k(C C_g)K'|A|^2 A = 0 \tag{1}$$

where, A: wave amplitude; C: wave celerity; C_g: group velocity; k: wave number calculated by the dispersion relation; k₀: initial wave number at deep water. The relationship between wave number and phase function is given below [4].

$$|\nabla s|^2 = k^2 + \frac{1}{H} \left[\frac{\partial^2 H}{\partial x^2} + \frac{\partial^2 H}{\partial y^2} + \frac{1}{CC_g} \left(\frac{\partial H}{\partial x} \frac{\partial CC_g}{\partial x} + \frac{\partial H}{\partial y} \frac{\partial CC_g}{\partial y} \right) \right] \tag{2}$$

where, s: scalar phase function of the wave; ∇: horizontal gradient operator; H: wave height. Equations (1) and (2) are used to solve the propagation of traveling waves from deep water to shallow water in a prespecified direction over a slowly arbitrary bottom topography under combined refraction-diffraction effects. The wave induced circulation model is based on vertically averaged nonlinear shallow water equations of constant density flows.

$$\frac{\partial u}{\partial t} + u \frac{\partial u}{\partial x} + v \frac{\partial u}{\partial y} = -g \frac{\partial \eta}{\partial x} + v \left(\frac{\partial^2 u}{\partial x^2} + \frac{\partial^2 u}{\partial y^2} \right) - \frac{gu|u|}{CZ^2H} \left(\frac{\partial S_{xx}}{\partial x} + \frac{\partial S_{xy}}{\partial y} \right) \frac{1}{\rho H} \tag{3}$$

$$\frac{\partial v}{\partial t} + u \frac{\partial v}{\partial x} + v \frac{\partial v}{\partial y} = -g \frac{\partial \eta}{\partial y} + v \left(\frac{\partial^2 v}{\partial x^2} + \frac{\partial^2 v}{\partial y^2} \right) - \frac{g v |v|}{CZ^2 H} \left(\frac{\partial S_{yx}}{\partial x} + \frac{\partial S_{yy}}{\partial y} \right) \frac{1}{\rho H} \tag{4}$$

$$\frac{\partial \eta}{\partial t} + \frac{\partial(Hu)}{\partial x} + \frac{\partial(Hv)}{\partial y} = 0 \tag{5}$$

where, u and v: depth averaged current velocity components in x and y directions respectively; g: gravity acceleration; H=h+η total water depth; h: still water depth; η: water surface elevation; v: turbulent eddy viscosity coefficient; CZ: Chezy friction coefficient; S_{xx} and S_{yy}: normal radiation stress components acting on the plane perpendicular to x and y directions respectively. Radiation stresses are computed from;

$$S_{xx} = E(2n-1/2-n\sin^2\theta); S_{yy} = E(n-1/2+n\sin^2\theta); S_{xy} = S_{yx} = E n \sin\theta \cos\theta \tag{6}$$

in which, θ: wave direction; E=ρgH²/8 wave energy, ρ: water density, H: wave height and n=C_g/C.

3 Combined Numerical Model

In the wave propagation model, MacCormack method is applied. Eqn. (1) is solved by Point Gauss Seidel iteration method. MacCormack method is a multilevel method. Firstly, forward finite difference approximations are used to obtain the predictor and then backward finite difference approximations are applied to the governing equation to find the corrector.

Predictor:

$$A_{i,j}^* \left[\begin{aligned} & \frac{ik_{i,j}R_{i,j}}{\Delta x} + k_{i,j}(k_{i,j}-k_0)R_{i,j} + ik_{i,j}C_{i,j} \left(\frac{C_{gi+1,j}-C_{gi,j}}{\Delta x} \right) + ik_{i,j}C_{gi,j} \\ & \left(\frac{C_{i+1,j}-C_{i,j}}{\Delta x} \right) + iR_{i,j} \left(\frac{k_{i+1,j}-k_{i,j}}{\Delta x} \right) - 2 \frac{R_{i,j}}{\Delta y^2} C_{i,j} \left(\frac{C_{gi,j+1}-C_{gi,j}}{\Delta y^2} \right) \\ & C_{gi,j} \left(\frac{C_{i,j+1}-C_{i,j}}{\Delta y^2} \right) - k_{i,j}^4 C_{i,j}^2 D_{i,j} |A_{i,j}^k|^2 \end{aligned} \right] = RP \tag{7}$$

$$RP = A_{i,j-1}^{k+1} \left(\frac{R_{i,j}}{\Delta y^2} \right) + A_{i+1,j}^k \left(\frac{ik_{i,j}R_{i,j}}{\Delta x} \right) + A_{i,j+1}^k \left(\begin{aligned} & \frac{R_{i,j}}{\Delta y^2} C_{i,j} \left(\frac{C_{gi,j+1}-C_{gi,j}}{\Delta y^2} \right) \\ & - C_{gi,j} \left(\frac{C_{i,j+1}-C_{i,j}}{\Delta y^2} \right) \end{aligned} \right) \tag{8}$$

Corrector:

$$A_{i,j}^{k+1} \left[\begin{aligned} & \frac{ik_{i,j}R_{i,j} + k_{i,j}(k_{i,j} - k_0)R_{i,j} + ik_{i,j}C_{i,j} \left(\frac{C_{gi,j} - C_{gi-1,j}}{\Delta x} \right) +}{\Delta x} \\ & ik_{i,j}C_{gi,j} \left(\frac{C_{i,j} - C_{i-1,j}}{\Delta x} \right) + iR_{i,j} \left(\frac{k_{i,j} - k_{i-1,j}}{\Delta x} \right) - 2 \frac{R_{i,j}}{\Delta y^2} + \\ & C_{i,j} \left(\frac{C_{gi,j} - C_{gi,j-1}}{\Delta y^2} \right) + C_{gi,j} \left(\frac{C_{i,j} - C_{i,j-1}}{\Delta y^2} \right) - k_{i,j}^4 C_{i,j}^2 D_{i,j} \left(A_{i,j}^{k+1/2} \right)^2 \end{aligned} \right] = RC \quad (9)$$

$$RC = A_{i-1,j}^{k+1} \left(\frac{ik_{i,j}R_{i,j}}{\Delta x} \right) + A_{i,j+1}^k \left(-\frac{R_{i,j}}{\Delta y^2} \right) + A_{i,j-1}^{k+1} \left[-\frac{R_{i,j}}{\Delta y^2} + C_{i,j}C_{gb} + C_{gi,j}C_b \right] \quad (10)$$

$$R_{i,j} = C_{i,j}C_{gi,j}; A_{i,j}^{k+1/2} = \frac{1}{2} (A_{i,j}^k + A_{i,j}^{*k}); C_{gb} = \frac{C_{gi,j} - C_{gi,j-1}}{\Delta y^2}; C_b = \frac{C_{i,j} - C_{i,j-1}}{\Delta y^2} \quad (11)$$

This method gives more realistic results than the other methods since it assures static stability. Point Gauss Seidel Iteration provides to reach the convergence more rapidly because the current variables of dependent variable are used to compute the neighboring points as soon as they are available.

A space staggered numerical grid has been used as shown in Figure 1.

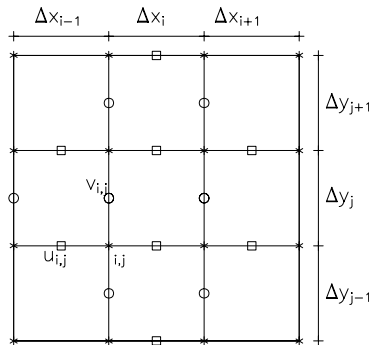


Fig. 1. Computational space staggered grid

System of nonlinear equations are solved by the adaptive step size controlled Runge-Kutta Fehlberg Method with respect to time. It requires six function evaluations per step, but it provides an automatic error estimate. The following numerical

algorithm has been applied in the solution [10] based on unequal mesh size for the space staggered numerical scheme shown in Figure 1.

$$\frac{\partial \eta}{\partial t} = \frac{-u_{i,j} H_{i,j}^u \left(\frac{3\Delta x_i + \Delta x_{i+1}}{2} \right) + u_{i+1,j} H_{i+1,j}^u \left(\Delta x_i + \frac{\Delta x_{i+1} - \Delta x_{i-1}}{2} \right)}{\frac{\Delta x_i + \Delta x_{i-1}}{2} \left(\Delta x_i + \frac{\Delta x_{i-1} + \Delta x_{i+1}}{2} \right) + \frac{\Delta x_i + \Delta x_{i-1}}{2} \frac{\Delta x_i + \Delta x_{i+1}}{2}} + \frac{u_{i+2,j} H_{i+2,j}^u \left(\frac{\Delta x_{i-1} - \Delta x_i}{2} \right) - v_{i,j-1} H_{i,j-1}^v \left(\frac{3\Delta y_j + \Delta y_{j+1}}{2} \right)}{\frac{\Delta x_i + \Delta x_{i+1}}{2} \left(\Delta x_i + \frac{\Delta x_{i+1} + \Delta x_{i-1}}{2} \right) + \frac{\Delta y_j + \Delta y_{j-1}}{2} \left(\Delta y_j + \frac{\Delta y_{j-1} + \Delta y_{j+1}}{2} \right)} \quad (12)$$

$$+ \frac{v_{i,j} H_{i,j}^v \left(\Delta y_j + \frac{\Delta y_{j+1} - \Delta y_{j-1}}{2} \right) - v_{i,j+1} H_{i,j+1}^v \left(\frac{\Delta y_{j-1} - \Delta y_j}{2} \right)}{\frac{\Delta y_j + \Delta y_{j-1}}{2} \frac{\Delta y_j + \Delta y_{j+1}}{2} + \frac{\Delta y_j + \Delta y_{j+1}}{2} \left(\Delta y_j + \frac{\Delta y_{j+1} + \Delta y_{j-1}}{2} \right)}$$

$$\frac{\partial u}{\partial t} = -u_a \frac{(\Delta x_{i-1} + \Delta x_i)(u_{i,j} - u_{i-1,j})}{(\Delta x_{i-1} + \Delta x_{i-2})(\Delta x_{i-1} + \frac{\Delta x_i + \Delta x_{i-2}}{2})} - u_d \frac{(\Delta x_{i-1} + \Delta x_{i-2})(u_{i+1,j} - u_{i,j})}{(\Delta x_{i-1} + \Delta x_i)(\Delta x_{i-1} + \frac{\Delta x_i + \Delta x_{i-2}}{2})} + \dots - v_a \frac{\Delta y_j (u_{i,j} - u_{i,j-1})}{\Delta y_{j-1} (\Delta y_j + \Delta y_{j-1})} - v_d \frac{\Delta y_{j-1} (u_{i,j+1} - u_{i,j})}{\Delta y_j (\Delta y_j + \Delta y_{j-1})} + \frac{g(\eta_{i,j} - \eta_{i-1,j})}{\Delta x_{i-1}} + \frac{g u_{i,j} |u_{i,j}|^2}{C^2 H_{i,j}^u} + \dots - v \left[\frac{2}{\left(\frac{u_{i-1,j}}{\frac{(\Delta x_{i-2} + \Delta x_{i-1})}{2} \left(\Delta x_{i-1} + \frac{(\Delta x_{i-2} + \Delta x_i)}{2} \right)} + \frac{u_{i,j}}{\frac{(\Delta x_{i-1} + \Delta x_i)}{2} \left(\Delta x_{i-1} + \frac{\Delta x_{i-2}}{2} \right)} \right)} + \frac{u_{i+1,j}}{\frac{(\Delta x_{i-1} + \Delta x_i)}{2} \left(\Delta x_{i-1} + \frac{(\Delta x_i + \Delta x_{i-2})}{2} \right)} \right] + \dots - v \left[\frac{2}{\left(\frac{u_{i,j-1}}{\Delta y_{j-1} (\Delta y_j + \Delta y_{j-1})} + \frac{u_{i,j}}{\Delta y_{j-1} \Delta y_j} + \frac{u_{i,j+1}}{\Delta y_j (\Delta y_j + \Delta y_{j-1})} \right)} \right] + \dots - 1 \left[\frac{1}{2} \left(\frac{\Delta y_{j-1} (S_{xy})_{i,j} - (S_{xy})_{i,j-1}}{\Delta y_{j-1} (\Delta y_j + \Delta y_{j-1})} + \frac{\Delta y_j (S_{xy})_{i,j+1} - (S_{xy})_{i,j}}{\Delta y_{j-1} (S_{xy})_{i-1,j+1} - (S_{xy})_{i-1,j}} \right) + \frac{\Delta y_j (\Delta y_j + \Delta y_{j-1})}{\Delta y_{j-1} (\Delta y_j + \Delta y_{j-1})} \right] + \frac{(S_{xx})_{i,j} - (S_{xx})_{i-1,j}}{\Delta x_{i-1}}$$

$$\begin{aligned}
 \frac{\partial v}{\partial t} = & -u_a \frac{\Delta x_i (v_{i,j} - v_{i-1,j})}{\Delta x_{i-1} (\Delta x_i + \Delta x_{i-1})} - u_d \frac{\Delta x_{i-1} (v_{i+1,j} - v_{i,j})}{\Delta x_i (\Delta x_i + \Delta x_{i-1})} \frac{g(\eta_{i,j+1} - \eta_{i,j})}{\Delta y_j} \frac{g v_{i,j} |v_{i,j}|}{C^2 H_{i,j}^v} \\
 & - v_a \frac{(\Delta y_j + \Delta y_{j+1})(v_{i,j} - v_{i,j-1})}{(\Delta y_j + \Delta y_{j-1})(\Delta y_j + \frac{\Delta y_{j+1} + \Delta y_{j-1}}{2})} - v_d \frac{(\Delta y_j + \Delta y_{j-1})(v_{i,j+1} - v_{i,j})}{(\Delta y_j + \Delta y_{j+1})(\Delta y_j + \frac{\Delta y_{j+1} + \Delta y_{j-1}}{2})} \\
 & - v \left[2 \left(\frac{v_{i-1,j}}{\Delta x_{i-1} (\Delta x_i + \Delta x_{i-1})} \frac{v_{i,j}}{\Delta x_{i-1} \Delta x_i} + \frac{v_{i+1,j}}{\Delta x_i (\Delta x_i + \Delta x_{i-1})} \right) + \right. \\
 & \left. 2 \left(\frac{v_{i,j-1}}{\frac{(\Delta y_{j-1} + \Delta y_j)}{2} \left(\Delta y_j + \frac{(\Delta y_{j-1} + \Delta y_{j+1})}{2} \right)} + \frac{v_{i,j}}{\frac{(\Delta y_j + \Delta y_{j+1}) (\Delta y_j + \Delta y_{j-1})}{2}} + \right. \right. \\
 & \left. \left. \frac{v_{i,j+1}}{\frac{(\Delta y_j + \Delta y_{j+1}) \left(\Delta y_j + \frac{(\Delta y_{j+1} + \Delta y_{j-1})}{2} \right)}{2}} \right) \right] \\
 & - \frac{1}{\rho H_{i,j}^v} \left[\frac{1}{2} \left(\frac{\Delta x_i ((S_{yx})_{i,j} - (S_{yx})_{i-1,j})}{\Delta x_{i-1} (\Delta x_i + \Delta x_{i-1})} + \frac{\Delta x_{i-1} ((S_{yx})_{i+1,j} - (S_{yx})_{i,j})}{\Delta x_i (\Delta x_i + \Delta x_{i-1})} \right) + \right. \\
 & \left. \frac{1}{2} \left(\frac{\Delta x_i ((S_{yx})_{i,j+1} - (S_{yx})_{i-1,j+1})}{\Delta x_{i-1} (\Delta x_i + \Delta x_{i-1})} + \frac{\Delta x_{i-1} ((S_{yx})_{i+1,j+1} - (S_{yx})_{i,j+1})}{\Delta x_i (\Delta x_i + \Delta x_{i-1})} \right) + \right. \\
 & \left. \frac{(S_{yy})_{i,j+1} - (S_{yy})_{i,j}}{\Delta y_j} \right]
 \end{aligned} \tag{14}$$

where,

$$u_{i,j}^v = \frac{u_{i,j} + u_{i,j+1}}{2} + \frac{\Delta x_{i-1} \left(\frac{u_{i+1,j} + u_{i+1,j+1}}{2} \frac{u_{i,j} + u_{i,j+1}}{2} \right)}{\frac{\Delta x_{i-1}}{2} + \frac{\Delta x_i}{2}}; H_{i,j}^v = \frac{H_{i,j} + H_{i,j+1}}{2} \tag{15}$$

$$v_{i,j}^u = \frac{v_{i,j-1} + v_{i-1,j-1}}{2} + \frac{\Delta y_{j-1} \left(\frac{v_{i,j} + v_{i-1,j}}{2} \frac{v_{i-1,j-1} + v_{i,j-1}}{2} \right)}{\frac{\Delta y_{j-1}}{2} + \frac{\Delta y_j}{2}}; H_{i,j}^u = \frac{H_{i,j} + H_{i-1,j}}{2} \tag{16}$$

$$u_a = \frac{u_{i,j} + |u_{i,j}|}{2}; v_a = \frac{v_{i,j} + |v_{i,j}|}{2}; u_d = \frac{u_{i,j} - |u_{i,j}|}{2}; v_d = \frac{v_{i,j} - |v_{i,j}|}{2} \tag{17}$$

Model uses a no flow boundary condition at the shoreline. A uniform flux type boundary condition is applied at the lateral boundaries. The flux at the adjoining interior grid has been equated to the flux at a lateral boundary grid. A radiation type boundary condition is used at the offshore boundary. Model can handle also the effects of non-overtopping structures such as jetties, breakwaters and groins, considering the diffraction and reflection in the wave model.

4 Combined Model Applications

Model has been applied to coastal waters of Obaköy village located at the Mediterranean Sea coast of Turkey. The bathymetry for the area is shown in Fig.2. For the area, wave transformations from the dominant wave directions, which are in the range of SSW and SE directions, are simulated.

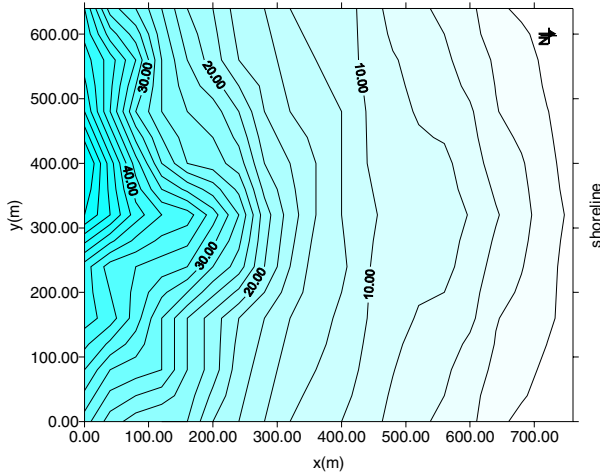


Fig. 2. Water depths (m.) of Obaköy

The deep water wave parameters are used to specify the offshore boundary conditions. Deep water parameters are selected as, wave period $T=5$ s., wave height $H=3.5$ m [11]. Predicted wave height distributions for waves approaching with an approach angle of $\theta=45^\circ$ (from SE) and of $\theta=-22.5^\circ$ (from SSW), are presented in Fig.3a and Fig.3b, respectively.

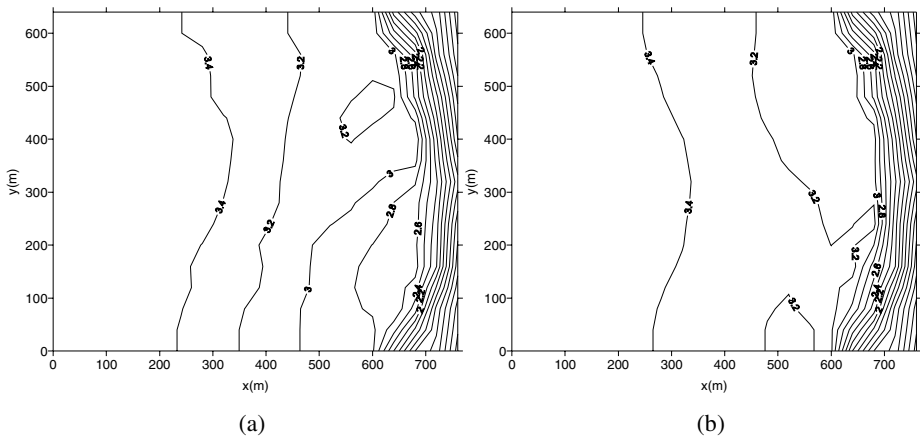


Fig. 3. Predicted wave height (meters) distributions for waves approaching with an approach angle of a) $\theta=45^\circ$ (from SE), b) $\theta=-22.5^\circ$ (from SSW)

Corresponding predicted wave induced circulations are given in Fig.4.

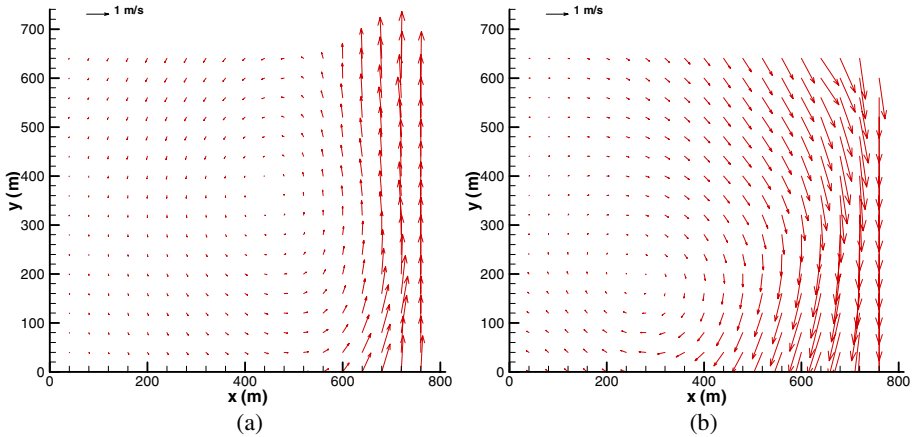


Fig. 4. Predicted wave induced circulations for waves approaching with an approach angle of a) $\theta = 45^\circ$ (from SE), b) $\theta = -22.5^\circ$ (from SSW)

Model predictions were compared with laboratory measurements for waves approaching from SE with a wave period of $T=5$ s. and wave height of $H=3.5$ m. Measurements were taken on a mesh with a grid size of 160×160 m. Comparisons of wave induced currents are given in Table (1).

Table 1. Comparison of measured and predicted wave induced currents

X , Y (m)	V (m/s)		E (%)	X , Y (m)	V (m/s)		E (%)
	Meas- ured	Pre- dicted			Meas- ured	Pre- dicted	
40,40	0,054	0,050	7,7	40,360	0,022	0,031	37,9
200,40	0,106	0,129	21,0	200,360	0,095	0,115	21,6
360,40	0,237	0,199	16,3	360,360	0,089	0,114	27,0
520,40	0,262	0,259	1,4	520,360	0,110	0,101	8,7
680,40	1,614	1,314	18,5	680,360	1,189	1,098	7,7
40,200	0,036	0,038	5,0	40,520	0,051	0,040	20,9
200,200	0,081	0,110	36,9	200,520	0,112	0,157	40,4
360,200	0,125	0,169	35,2	360,520	0,063	0,162	156,9
520,200	0,175	0,157	9,8	520,520	0,411	0,107	74,0
680,200	1,560	1,147	26,5	680,520	1,103	1,359	23,2

Model provides reasonable estimations for the area. Waves converge on the shoal, conveyance of energy onto shoal results in the decrease of wave heights. Inclusion of a turbulence model will improve the predictions.

5 Conclusions

A combined numerical model that simulates wave transformations and wave induced nearshore currents is presented. Model is applicable to irregular bottom topographies. Combined model has two components, a wave propagation model that is based on nonlinear parabolic mild slope equation and could simulate wave shoaling, refraction, diffraction and breaking. Wave driven circulation model solves vertically averaged non-linear shallow water equations. Model application to a real coastal water body, Obaköy, has been shown. Combined model can be successfully applied to complex bathymetries. Possibility of using finer resolutions in regions where the spatial gradients of the variables are sharp is an advantage of the model. Therefore computationally, the numerical model is quite efficient for simulating wave propagation and wave induced circulation over large coastal areas subjected to varying wave conditions. Only one computational domain is enough to simulate the transformation of waves from different directions with different approach angles.

References

1. Berkhoff, J.C.W.: Computation of Combined Refraction-Diffraction. Proceedings of 13th International Conference on Coastal Engineering, ASCE, Vol. 1 (1972) 472-490.
2. Radder, A.C.: On the Parabolic Equation Method for Water-Wave Propagation. Journal of Fluid Mechanics, Vol.95 (1979) 159-176.
3. Kirby, J.T., Dalrymple, R. A.: Verification of a parabolic equation for propagation of weakly- nonlinear waves. Coastal Engineering, Vol. 8 (1984) 219-232.
4. Ebersole, B. A.: Refraction-Diffraction Model for Linear Water Waves. Journal of Waterway, Port, Coastal and Ocean Engineering, Vol.111 (1985) 6-19.
5. Chamberlain, P.G., Porter, D.: The Modified Mild-Slope Equation, Journal of Fluid Mechanics, Vol. 291 (1995) 393-407.
6. Massel, S.R.: Extended refraction- diffraction equation for surface waves, Coastal Engineering, Vol. 23 (1993) 227-242.
7. Suh, K.D., Lee, C., Park, W.S.: Time- dependent equations for wave propagation on rapidly varying topography, Coastal Engineering, Vol.32 (1997) 91-117.
8. Maa, J.P.- Y., Hsu, T.-W., Lee, D.-Y.: The RIDE Model: an enhanced computer program for wave transformation, Ocean Engineering, Vol.29 (2002)1441-1458.
9. Hsu, T.W., Wen C.C.: On radiation boundary conditions and wave transformation across the surf zone, China Ocean Engineering, Vol. 15 (2001) 395-406.
10. Kowalik,Z., Murty, T.S.: Numerical Modeling of Ocean Dynamics. Advanced Series on Ocean Engineering, Vol.5, World Scientific,New Jersey (1993).
11. 11.Yıldız, İ., İnan,A.,Balas,L.: An Efficient Numerical Scheme to Simulate Wave Induced Circulation. In:Ozhan,E. (ed) Proceedings of the Seventh International Conference on the Mediterranean Coastal Environment, MEDCOAST'05, Vol.3.(2005) 1215-1224.

A Novel Model for Bacterial Foraging in Varying Environments

W.J. Tang¹, Q.H. Wu^{1,*}, and J.R. Saunders²

¹ Department of Electrical Engineering and Electronics
qhwu@liv.ac.uk

² School of Biological Sciences,
The University of Liverpool, Liverpool L69 3GJ, UK

Abstract. This paper presents the study of modelling bacterial foraging behaviours in varying environments. The purpose of the study is to investigate a novel biologically inspired methodology for complex system modelling and computation, particularly for optimisation of complex dynamic systems, although this paper is mainly concerned with a novel modelling methodology. Our study focuses on the use of individual-based modelling (IbM) method to simulate the activities of bacteria and the evolution of bacterial colonies. For this study, an architecture and a mathematical framework are designed to model bacterial foraging patterns. Under this architecture, the interactions between the environment and bacteria are investigated. A bacterial chemotaxis algorithm is derived in the framework and simulation studies are undertaken to evaluate this algorithm. The simulation results show that the proposed algorithm can reflect the bacterial behaviours and population evolution in varying environments, and also explore its potential for optimisation of dynamic systems.

1 Introduction

Evolutionary Algorithms (EAs), in particular, Genetic Algorithms (GAs), Evolutionary Programming (EP), Evolutionary Strategy (ES), have been well studied and applied for various optimisation problems [1][2][3]. These algorithms stemmed from very basic description of biological systems and were derived with a simple understanding of genetic evolution. However, they have shown the capabilities in solving optimisation problems of complex systems. Some ideas to improve the performance of these algorithms have been taken from the viewpoint of mathematics, such as the analysis of GA search performance in the Markov Chain domain [4]. It has been understood that the future advance of EAs should be stimulated by the further knowledge transfer from the biological systems to evolutionary computation. To this end, we have undertaken the preliminary studies of modelling biological systems [5][6], particularly, in the area of individual-based modelling (IbM) [7], which includes the development of models at levels of individuals and population respectively.

* Corresponding author.

However, our previous study has been only concerned with an invariant environment of biological systems. Hence, as the lack of understanding of biological foraging behaviours, our previous work did not fully explored the interactions between bacteria and environment. To advance the subject in this area, we have investigated a more biologically-plausible model. Since bacterial foraging behaviours, especially bacterial chemotaxis were thoroughly investigated recently [8], the model is based on the fundamental understandings of chemotaxis, which includes the basic activities of *run* and *tumble*. The evolvement of bacterial colony and the change of cell population are described in this model as well. In this paper, we present the results of our recent study, which includes: 1) An architecture that comprises environment, cells and their interaction; 2) A generic mathematical framework in which a novel algorithm is developed to describe the biological foraging behaviours; 3) The simulation study which has been undertaken to evaluate our model. The simulation results are presented in this paper to illustrate that our model can be used to describe the bacterial evolution in the varying environment from a biologically-realistic viewpoint, and also the potential of the new algorithm being used for optimisation of complex dynamic systems. This paper is organized as follows: Section 2 introduces the architecture and mathematical framework of our model. The simulation results are presented in Section 3, followed by the conclusion in Section 4.

2 Architecture and Mathematical Framework

In this section, a Varying Environment Bacterial Modelling (VEBAM) method is proposed, which aims to simulate the bacterial colony formation and evolution in a varying environment, while the foraging behaviour of each individual is modelled in detail. The architecture is shown in Fig. 1.

In this model, there are two fundamental elements: the environment and cells which are a set of bacteria. Both of them are synchronized at the beginning of each bacterial foraging step. In each step, cells move within the environment, consuming the nutrient and avoiding the toxin. After each step, a decision making system determines direction and velocity of the following step. At the synchronization stage, the status and positions of cells will be updated, so will the nutrient distribution of the environment.

2.1 Environment

The model is set in an artificial environment for bacterial movements, which is defined as

$$Env\langle\sigma, \beta\rangle$$

where σ indicates the nutrient distribution and β represents the characteristic of boundary in the environment.

This environment is covered by nutrient and toxin. The former provides the energy required by bacteria to survive, while the latter decreases the capability of bacteria's activities. The environment is segmented equally into small niches

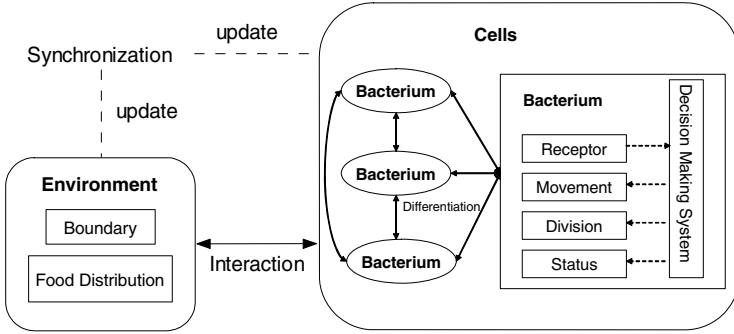


Fig. 1. VEBAM architecture

as a discrete grid, covering a 2-dimensional grid of $M \times N$ grid units. Thus the Env contains $M \times N$ equally divided units, which can be represented as:

$$Env = \{Env_{ij}^t | i = 1, 2, \dots, M; j = 1, 2, \dots, N; t = 1, 2, \dots, \infty\}$$

where Env_{ij}^t presents the nutrient or toxin level in the niche of (i, j) and a positive value of Env_{ij}^t indicates nutrient while negative ones represent toxin; i and j are indices of each dimensions along the coordinates; t denotes the time instant of the step of the model. When $t = 0$, the environment is initiated by a specified function. The interactions between the environment and cells are updated during the computation process, in which cells are moving to obtain energy. After each step of cells' movements, the nutrient distribution is modified in some grid units, a map can be expressed as Env_{ij}^{t+1} . The environment evolves in a longer time scale in which multiple cells exist in a shared space.

2.2 Cells

The cells are defined to consist of a collection of bacteria, which is represented as:

$$B = \{B_l^t | l = 1, 2, \dots, P; t = 1, 2, \dots, T\}$$

where

$$B_l^t = \langle p_l^t, \varepsilon_l^t, \varphi_l^t, \lambda_l^t, \tau_l^t, \delta_l^t, \phi_l^t \rangle$$

denotes an individual bacterium or cell; P denotes the maximum population in the foraging process; T is the final time of the process; B_l^t has its own position p_l^t , energy ε_l^t , status φ_l^t which could be active or inactive, and an action τ_l^t which depends on a probability λ_l^t to indicate whether the cell is running or tumbling at time t . If it is tumbling, the cell moves with an orientation ϕ_l^t as an angle formed by the flagella axis. For the activity of *run*, orientation ϕ_l^t is the same with ϕ_l^{t-1} . δ_l^t is the length of run, which is set to be a constant.

These properties of cells change with the interaction between the environment and cells. The cells consume their energy to move, meanwhile they are rewarded by nutrient proportionally according to the environmental conditions which are distributed immediately around the cells. If the available nutrient for a cell is less

than a preset amount, the cell gets all the available nutrient, and the nutrient is modified to zero on that specific unit. For each cell, if its energy falls below a critical level, its status becomes inactive. In this case, the cell is motionless. While the energy of a cell is higher than a certain level, it splits into two daughters, and each of them becomes a new cell in the environment.

2.3 Synchronization and Interaction

The synchronization unit is responsible for stepping the model in time scale. It keeps a global clock, which synchronizes the updating of both the environment and the cells. The updating of the environment includes the modification of the nutrient distribution, while the updating of cells consists of relocating the cells according to their positions and initialization of the newly created cells.

Once the action of synchronization and interaction has taken place, all bacteria are informed of their new properties, e.g. energy and positions, etc. They are then free to begin the next iteration. Their foraging process continues until all cells are inactive or the nutrient in the environment has been consumed completely. At this point it is known for certain that the computation has been terminated. Since different individuals typically evolve on very different dynamical timescales, the computation time varies, which depends on the calculation complexity at different phases of population development.

2.4 Bacterial Chemotaxis

Bacteria swim by rotating whip-like flagella driven by a reversible motor embedded in the cell wall. When all flagella rotate counterclockwise, they form a compact, helically propelling the cell along a helical trajectory. When the flagella rotate clockwise, they all pull on the bacterium in different directions, which causes the bacteria to tumble.

Chemotaxis is based on the suppression of tumbles in cells that happen by chance to be moving up the gradient. Bacteria make decision according to their ambient environment. The motion of *E.coli* can be described in terms of run intervals during which the cell swims approximately in a straight line interspersed with tumbles during which the organism undergoes a random reorientation. For *E. coli*, the *run* and *tumble* intervals are exponentially distributed with means of approximately 1s and 0.1s respectively in isotropic medium. Chemotactic bacteria sense temporal changes in concentration levels of chemical attractants and repellents. The direction of rotation depends upon chemoattractant concentration levels at the cell site over a time interval of up to 4s. If the concentration level of an attractant is increasing, a bacterium responds by reducing its tumbling probability. Thus the duration of run is longer when bacteria are swimming up a chemoattractant gradient [9]. Based on these activities, VEBAM uses a probability based decision making system to determine the direction of movements, and we describe this process as follows.

$$\lambda_l^t = \begin{cases} A_1, & : \text{ if } Env_{ij}^t \geq Env_{ij}^{t*} \\ A_0, & : \text{ if } Env_{ij}^t < Env_{ij}^{t*} \end{cases}$$

where λ_t^t is a probability of run, Λ_1 and Λ_0 assign λ_t^t with two different values respectively according to the change of environment, and $0 < \Lambda_0 < \Lambda_1 < 1$. This equation implies that a better environment leads to a higher probability of *run*. Considering the bacterial chemoattractant concentration, over a period of time, the past 3 values of environment, e.g. Env_{ij}^{t-3} , Env_{ij}^{t-2} and Env_{ij}^{t-1} , are adopted to obtain an average measure of the past environment, which is denoted by Env_{ij}^{t*} , where t^* indicates the time instant in associated with the average value of the changed environment. Bacteria compare their receptor occupancies between that occurred at t^* and t , i.e., let $d = Env_{ij}^t - Env_{ij}^{t*}$, if $d > 0$, the cell will reduce the rate of tumble to Λ_0 , otherwise, it remains to be Λ_1 . It should be mentioned that $\Lambda_1 + \Lambda_0 = 1$ and this equation is for making a decision of whether next action of the bacterium is *tumble* or *run*.

The tumbling angle of *E. coli* is randomly generated in a non-uniformly distributed most likely with small angles. Berg and Brown found that the mean tumbling angle of wild type *E. coli* to be about 68° with a standard deviation of 36° approximately [10]. In this case, we randomly choose tumbling angles by the following equation:

$$\theta = 2 \arcsin(2\mu)$$

where μ is a random number, $\mu \in [-0.5, 0.5]$. The angle for the next step is the previous angle plus θ . Theoretically, it could be any angle between $-\pi$ and π , as shown in Fig. 2.

2.5 Population Growth

The population in VEBAM has adjustable growth and reproduction rates that can be determined as the doubling growth [11]. The reproduction rates change dynamically according to the environment variation. In rich nutrient areas, a cell takes a shorter time to obtain enough energy for reproduction. In the simulation study, cells move in direct response to the surrounding substrate field. They consume a fixed amount of energy per time period. For simplicity we shall ignore

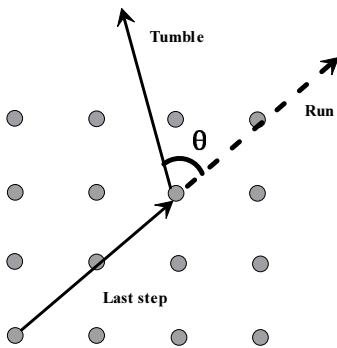


Fig. 2. Bacterial foraging patterns

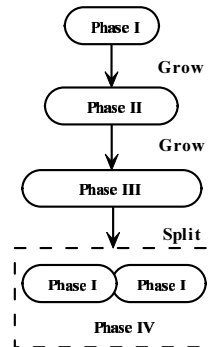


Fig. 3. Division process of a cell

the effect of lower energy consuming when their energy level is low. Instead, we assume that the consumption is fixed per unit time period. Meanwhile, a cell obtains energy from the environment if there is energy available, depending on the definition of environment. The mass of it grows as long as it obtains energy from the environment. When its energy exceeds a preset threshold, it divides into two daughters, each of them gets randomized initiated energy, as shown in Fig. 3. At anytime during its lifetime, if a cell could not get enough energy to remain active, it will die.

3 Simulation Studies

3.1 Initialization

VEBAM is set in a multi-modal environment. The nutrient distribution of the environment at $t = 0$ is set by the function $f(x, y)$ as follows [12]:

$$\begin{aligned}
 f(x, y) = & 5 \exp^{-0.1((x-15)^2+(y-20)^2)} - 2 \exp^{-0.08((x-20)^2+(y-15)^2)} \\
 & + 3 \exp^{-0.08((x-25)^2+(y-10)^2)} + 2 \exp^{-0.1((x-10)^2+(y-10)^2)} \\
 & - 2 \exp^{-0.5((x-5)^2+(y-10)^2)} - 4 \exp^{-0.1((x-15)^2+(y-5)^2)} \\
 & - 2 \exp^{-0.5((x-8)^2+(y-25)^2)} - 2 \exp^{-0.5((x-21)^2+(y-25)^2)} \\
 & + 2 \exp^{-0.5((x-25)^2+(y-16)^2)} + 2 \exp^{-0.5((x-5)^2+(y-14)^2)}
 \end{aligned}$$

It is normalised as $\bar{f}(x, y) = f(x, y)/f_{\max}$, where $f_{\max} = \max(f(x, y))$; $x, y \in [0, 30]$, with an incremental value of 0.1 respectively and this environment is divided into 300×300 grids.

The bacteria are initially located in a distribution generated by a Quasi-random sequence, which has been shown to assist the reduction of generations needed in GAs effectively [13]. The initial population is 100. They spread over the environment, having randomly allocated energy levels, and ready to tumble at the first step of computation.

3.2 Single Bacterial Behaviour

Figs. 4–7 illustrate the trajectories of bacteria in two separate experiments. The thresholds, A_1 and A_0 , introduced for a cell to split and become active, are set to 0.8 and 0.2, respectively. The swim length is set to 5 grid unites per step. The energy gained and the energy consumed by each cell per step are denoted by a and b respectively. Figs. 4 and 5 show the behaviours of cells 4 and 18, where $a = 0.2$ and $b = 0.1$, respectively. Figs. 6 and 7 concern cells 8 and 14, where $a = 0.02$ and $b = 0.01$ are adopted.

Fig. 4 shows that even when swimming down a gradient, the cell still run for a few steps before tumbling. This feature could be considered as a turbulence, which enables the capability of cell to avoid getting trap into the local minima. Fig. 5 describes the interaction of the cell with the periodical boundary. A pure random walk could be observed in Fig. 6, from which it can be seen that before

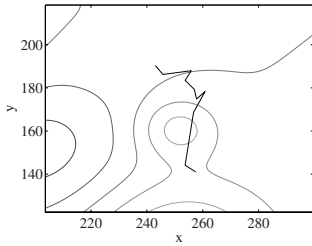


Fig. 4. Cell 4 ($a = 0.2, b = 0.1$)

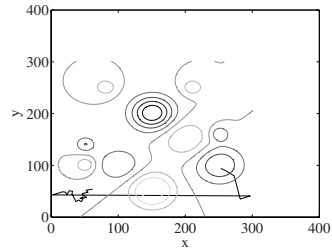


Fig. 5. Cell 18 ($a = 0.2, b = 0.1$)

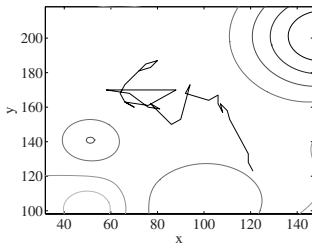


Fig. 6. Cell 8 ($a = 0.02, b = 0.01$)

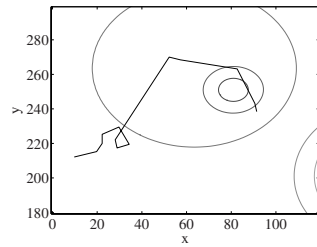


Fig. 7. Cell 14 ($a = 0.02, b = 0.01$)

a cell detects a gradient change, it chooses an action at the next step randomly according to the ambient environment. Meanwhile, Fig. 7 indicates that the cell takes a probability-based run and tumble strategy to approach the nutrient, and the probability of tumble is suppressed over this period.

3.3 Population Evolution

The population evolution of VEBAM has been simulated and it is illustrated in Fig. 8. The evolution process proceeds 100 steps, featuring the swarming of the cells to the highlighted areas where the nutrient level is high. The green dots and purple ones indicate the bacteria which are active and ready to divide, respectively. Fig. 8 also illustrates that bacteria have the trend to approach the nutrient, tracing the changes of nutrient distribution. If they could not consume enough nutrient in their ambient environment, they will be eliminated gradually and the survivors will search the space until they discover another nutrient concentration.

Fig. 9 describes the total population in the evolution process of 100 steps and the population of the inactive cells respectively. The result shown in Fig. 9 is consistent with the theoretical understanding of biological systems. The change of available nutrient is shown in Fig. 10. It was calculated using the following equation:

$$Nutrient = \sum_{i=1}^{300} \sum_{j=1}^{300} f(x_i, y_j)$$

where $x_i, y_j \in [0, 30]$, and $f(x_i, y_j) \geq 0$.

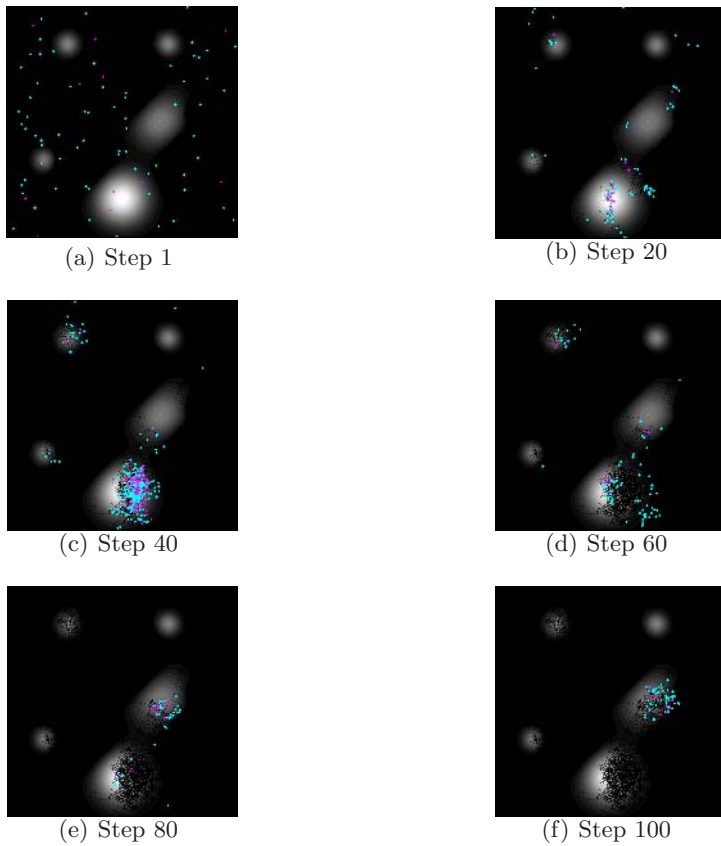


Fig. 8. Simulation results in 100 steps

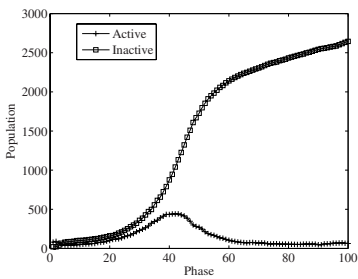


Fig. 9. Population variation

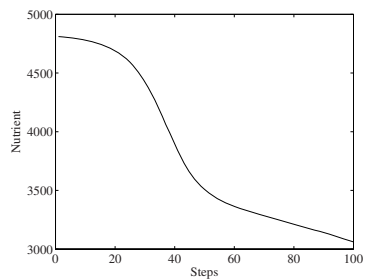


Fig. 10. Nutrient variation

3.4 Discussion

The VEBAM has been proposed to represent the survival and reproduction of bacteria from a viewpoint of underlying biological mechanisms. However, since it is inspired from the bacterial foraging patterns, it follows the basic biological

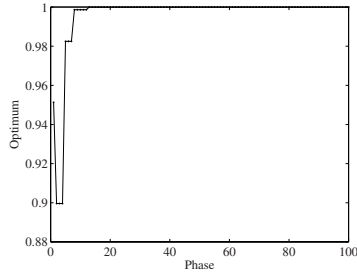


Fig. 11. Optimum found in each step

rules by which each cell attempts to obtain as much energy as possible in its lifetime. These cells are able to deal with unexpected events such as sudden changes of complex ambient environment or shortage of nutrient caused by a large population. Therefore, inspired by these rules, VEBAM provides a possible solution to complex global optimisation problems, especially in an adaptable framework to trace the changes in a varying environment.

By an appropriate observation of the population development and environmental energy variation in the bacterial foraging process, it is possible to discover the energy distribution and able to find the global optimum of the environment which is represented by an objective function. In this simulation study, VEBAM deems the position of the divided bacterium, which has the highest nutrient concentration in the initial environment, as the global optimum, providing a solution to a static optimisation problem. The optimum found in the simulation study above is shown in Fig. 11, which illustrates that the optimum found has reached the global optimum from step 12. Furthermore, for a dynamic optimisation problem, e.g. the objective function is time-variant, the most active bacteria are able to trace the varying nutrient concentration which represents the possible varying optima. With the trajectory of each cell traceable and the observation of varying nutrient, a new algorithm could be derived from VEBAM and it would be capable to handle dynamic optimisation problems, which cannot be solved currently by conventional optimisation algorithms. However, to this end, further work is required.

4 Conclusion

The paper has presented a novel architecture and mathematical framework leading to a biologically-inspired method for modelling bacterial foraging behaviours in varying environments. The details of individual foraging behaviours and colony evolution process have been described. The chemotaxis algorithm developed, as a kernel of IbM, from the novel model has been evaluated in a simulation study which includes modelling a group of bacteria in an evolution process. The simulation results show that the bacteria move close to nutrient, avoiding toxin by chemotaxis. It leads to the gathering of bacteria concentrat-

ing on the nutrient-rich areas, which could be represented by local optima and the global optimum in function optimisation. The phenomena of this evolution process have been discussed in detail. Although none of optimisation techniques are directly presented in this paper, the ideas and the model presented provide a base for developing novel evolutionary algorithms for solving more complex dynamic optimisation problems. To achieve this, our further study is in process.

References

1. Michalewicz, Z.: Genetic Algorithms + Data Structures = Evolution Programs. Springer - Verlag, Second, Extended Edition (1994)
2. Fogel, D.B.: Evolutionary Computation. IEEE Press (1995)
3. Back, T.: Evolutionary Algorithms in Theory and Practice. Evolutionary Algorithms in Theory and Practice. Oxford University Press (1996)
4. Cao, Y.J., Wu, Q.H.: Optimisation of control parameters in genetic algorithms: A stochastic approach. International Journal of Systems Science **30** (1999) 551–559
5. Gregory, R., Paton, R.C., Saunders, J.R., Wu, Q.H.: Parallelising a model of bacterial interaction and evolution. BioSystems **76** (2004) 121–131
6. Paton, R., Gregory, R., Vlachos, C., Wu, Q.H.: Evolvable social agents for bacterial systems modeling. IEEE Tran. on Nanobioscience **3** (2004) 208–216
7. Vlachos, C., Paton, R.C., Saunders, J.R., Wu, Q.H.: Rule-Based Bacterial Modelling - Part I: Model Development. BioSystems (to appear)
8. Bray, D.: Bacterial chemotaxis and the question of gain. PNAS **99** (1995) 7–9
9. Ben-Jacob, E., Shochet, O., Tenenbaum, A., et al.: Generic Modeling of Cooperative Growth Patterns in Bacterial Colonies. Nature **368** (1994) 46–49
10. Berg, H.C., Brown, D.A.: Chemotaxis in *Escherichia coli* analyzed by three-dimensional tracking. Nature **239** (1972) 500–504
11. Cooper, S.: What is the bacterial growth law during the division cycle? J. Bacteriol **170** (1988) 5001–5005
12. Passino, K.M.: Biomimicry of bacterial foraging. IEEE Control Systems Magazine, (2000) 52–67
13. Cao, Y.J., Wu, Q.H.: Study of Initial Population in Evolutionary Programming. Proceedings of the European Control Conference **368** (1997) 1–4

Stochastic Modeling of Cytoplasmic Reactions in Complex Biological Systems

Preetam Ghosh¹, Samik Ghosh¹, Kalyan Basu¹,
Sajal Das¹, and Simon Daefler²

¹ Dept. of Computer Science and Engineering, The University of Texas at Arlington

² Division of Infectious Diseases, Mount Sinai School of Medicine
{ghosh, sghosh, basu, das}@cse.uta.edu, simon.daefler@mssm.edu

Abstract. The use of “in silico” stochastic event based modeling can identify the dynamic interactions of different processes in a complex biological system. This requires the computation of the time taken by different events in the system based on their biological functions. One such important event is the reactions between the molecules inside the cytoplasm of a cell. We present a mathematical formulation for the estimation of the reaction time between two molecules within a cell based on the system state. We derive expressions for the average and second moment of the time for reaction to be used by our stochastic event-based simulation. Unlike rate equations, the proposed model does not require the assumption of concentration stability for multiple molecule reactions.

1 Introduction

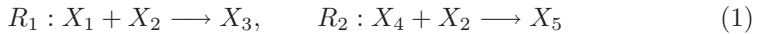
Today, a comprehensive modeling framework integrating molecular and genetic data is required for a quantitative understanding of physiology and behavior of biological processes at multiple scales. There exist mathematical models in mathematical physiology [11] and computational cell biology [2]. Although such models (e.g., the Hodgkins-Huxley equation) work very well for specific problem domains (e.g. cell membrane current and conductance), they rarely address an entire biological system. Alongside, researchers from diverse disciplines have developed models to capture the dynamics of biological processes [1][3]. These spatio-temporal models can be classified into: (a) quantum mechanics (b) molecular dynamics (c) mesoscale dynamics and (d) cellular/organ-level stochastic simulation. The first two models are limited in scope, as they cannot handle the complexity of an entire cell. The last two models have focused on a narrow range of biological components such as the wave model [1] for ventricular fibrillation in human heart, neural network signaling model [3] to control the onset of sleep in human, or simulation frameworks like E-Cell [5] and Virtual Cell [4] for biological processes. Mesoscale dynamics deal with rate equation based kinetic models and uses continuous time deterministic techniques. This model solves complex differential equations corresponding to chemical reactions. Since a biological system involves a very large number of such differential equations, the mesoscale model is not suitable for complete cell modeling. Stochastic simulation models are also

based on rate equations (e.g. Gillespie technique [6], Kitano's Cell Designer [10], BioSpice [9] and Cell Illustrator [8]). Due to the large number of protein complexes in a cell, these models lead to combinatorial explosion in the number of reactions, thus making them unmanageable for complex metabolic and signaling pathway problems.

Our goal is to design a discrete-event [7] driven paradigm for modeling a composite biological system by combining the state variables in the spatio-temporal domain as *events*, and determine the immediate dynamics between the events by using statistical analysis or simulation methods [12]. The key notion is that the dynamics of cell behavior is captured by discrete time (possibly a random variable) and space state variables, where an *event* is a combined process of a large number of micro-level state transitions between a set of state variables accomplished within event execution time. Identifying the biological discrete events based on system knowledge, the set of resources involved and calculating the time taken to complete an event (which is termed in system modeling as the *holding time* of the discrete event) are key challenges in this approach. In this paper, we use a collision theory based approach to estimate the average holding time of reactions taking place inside the cytoplasm of the cell.

2 Reaction Model

Consider the elementary reaction pair:



To model these reactions analytically in the time domain, we consider two different models for the arrivals of X_1 and X_4 types of molecules in the system which, we assume, contains a fixed number n_2 of X_2 molecules. Our goal is to derive expressions for the *average time* required for chemical reactions which is used by the discrete event scheme.

2.1 Model 1: Reactant Molecules Enter the System One at a Time

The molecules of X_1 and X_4 enter the system one at a time to start the reactions. From the principles of collision theory for hard spheres, we model each reactant molecule as a rigid sphere with radii r_1, r_2, r_3, r_4, r_5 respectively for molecules of type X_1, X_2, X_3, X_4, X_5 . We define our coordinate system such that molecule X_2 is stationary with respect to molecule X_1 , so that X_1 moves towards molecule X_2 with a relative velocity U_{12} . If the center of an X_2 molecule comes within a distance of the 'collision radius' (denoted by $r_{12} = r_1 + r_2$) from the center of the X_1 molecule, they will collide. In time Δt , the X_1 molecule sweeps out a collision volume ΔV such that the probability of collision (p_c) is given by:

$$p_c = \Delta V \cdot n_2 / V = \frac{n_2 \pi r_{12}^2 U_{12} \Delta t}{V} \quad (2)$$

where V denotes the cell volume (ideally V is the volume of the cytoplasm which can be approximated by the entire cell volume). To complete the reaction, the

molecules have to bind to each other. We assume that the colliding molecules must have free energy E_{Act} or greater to provide the binding energy. The overall probability, p , for reaction given that a collision occurred is given by:

$$p = \frac{n_2 r_{12}^2 \Delta t}{V} \sqrt{\frac{8\pi k_B T}{m_{12}}} e^{-\frac{E_{Act}}{k_b T}}$$

where k_b = Boltzmann’s constant = $1.381 \times 10^{-23} m^2/s^2/K/molecule$, T is the absolute temperature at which the reaction occurs and $m_{12} = \frac{m_1 m_2}{m_1 + m_2}$ = the reduced mass, m_1 = mass (in gm) of molecular species X_1 and m_2 = mass (in gm) of molecular species X_2 . The detailed derivations can be found in [13]. Next we compute the average time taken to complete the reaction with this probability. Let $\Delta t = \tau$ = an infinitely small time step. The molecules try to react through repeated collisions. We can interpret p as the probability of a successful reaction in time τ . Thus *average time of reaction* R_1 , T_{avg1}^{DE} , and the corresponding second moment, $T_{2ndmoment1}^{DE}$, can be formalized by Theorem 1.

Theorem 1. *The average and the second moment of reaction times of type R_1 for one molecule of X_1 reacting with n_2 molecules of X_2 is given by:*

$$T_{avg1}^{DE} = \frac{\tau}{p}, \quad T_{2ndmoment1}^{DE} = \frac{(2 - p)\tau^2}{p^2}$$

Note that the computation of T_{avg1}^{DE} and $T_{2ndmoment1}^{DE}$ assume that no other reaction (having the same reactant) is overlapping with R_1 . If reaction R_2 overlaps with R_1 the average time estimate (of R_1) should increase as R_2 will reduce the number of X_2 molecules available for reaction R_1 . The discrete event approach *serializes* such overlapping reactions and hence our estimates of T_{avg1}^{DE} and $T_{2ndmoment1}^{DE}$ is independent of the effect of R_2 .

2.2 Model 2: Reactant Molecules Enter the Cell in Fixed Size Batches

Now, we assume that the X_1 molecules arrive in batches of size b_1 and X_4 molecules arrive in batches of size b_4 in the system. We will analytically model the average time for reaction R_1 for only the discrete event case, $T_{avg1}^{batch/DE}$ (i.e. assuming no overlap between reactions involving shared reactants). Fig 1 depicts the scenario. Let, p_k^{ij} denote the probability of the j^{th} reaction (we can have a total of b_1 reactions in a batch size of b_1) of type R_i at the k^{th} collision. Thus, the probability of the *first reaction of type R_1* between one X_1 molecule and an X_2 molecule resulting from the first collision, p_1^{11} , is given by:

$$p_1^{11} = \frac{b_1 n_2 r_{12}^2 \tau}{V} \sqrt{\frac{8\pi k_B T}{m_{12}}} e^{-\frac{E_{A12}}{k_b T}}$$

The numerator on the right hand side of the above equation gets multiplied by b_1 to sum up the probability of reaction for all the b_1 molecules that arrived

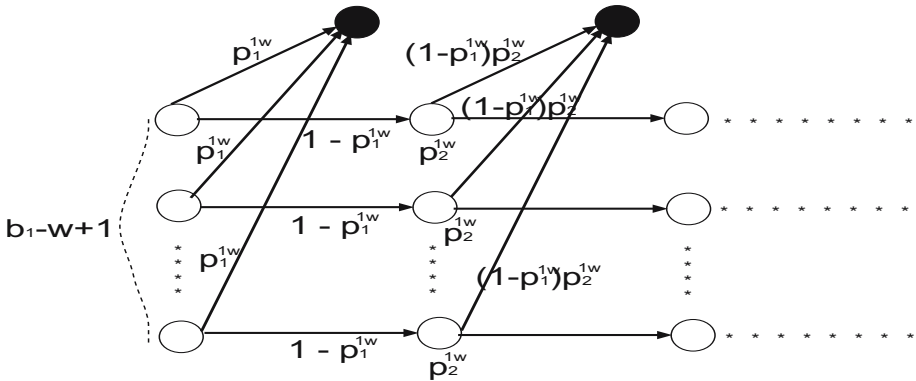


Fig. 1. State diagram for w^{th} reaction of type R_1 in a batch of size b_1

in a single batch. The black circles in Fig 1 signify the reaction R_1 occurring from the first collision, second collision and so on. Hence, probability of the first reaction of type R_1 from the i^{th} collision ($2 \leq i \leq \infty$), is given by:

$$p_i^{11} = p_1^{11}$$

Also, the probabilities of the w^{th} reaction of type R_1 from the first collision is given by:

$$p_1^{1w} = \frac{(b_1 - w + 1)(n_2 - w + 1)r_{12}^2\tau}{V} \sqrt{\frac{8\pi k_B T}{m_{12}}} e^{-\frac{E_{A12}}{k_b T}}$$

Similarly, the probabilities of the w^{th} reaction of type R_1 from the i^{th} collision, p_i^{1w} , is given by:

$$p_i^{1w} = p_1^{1w}$$

The average time to complete one reaction of type R_1 , $T_{avg1}^{batch/DE}$, and corresponding second moment, $T_{2ndmoment1}^{batch/DE}$, in the discrete event model is given by the following theorem:

Theorem 2. *The average and second moment to complete a reaction of type R_1 in a batch of size b_1 molecules of X_1 and n_2 molecules of type X_2 in the discrete event model is given by:*

$$T_{avg1}^{batch/DE} = \frac{\sum_{k=1}^{b_1} [\sum_{i=1}^{\infty} (p_i^{1k} i\tau \prod_{j=1}^{i-1} (1 - p_j^{1k}))]}{b_1} = \frac{\sum_{k=1}^{b_1} [\sum_{i=1}^{\infty} (p_1^{1k} (1 - p_1^{1k})^{i-1} i\tau)]}{b_1}$$

$$T_{2ndmoment1}^{batch/DE} = \frac{\sum_{k=1}^{b_1} [\sum_{i=1}^{\infty} (p_i^{1k} (i\tau)^2 \prod_{j=1}^{i-1} (1 - p_j^{1k}))]}{b_1} = \frac{\sum_{k=1}^{b_1} [\sum_{i=1}^{\infty} (p_1^{1k} (i\tau)^2 (1 - p_1^{1k})^{i-1})]}{b_1}$$

Proof. The time taken for the k^{th} reaction in the batch is computed by adding up the contributions from all the i collisions, (where $1 \leq i \leq \infty$) as follows:

$$\sum_{i=1}^{\infty} (p_i^{1k} i\tau \prod_{j=1}^{i-1} (1 - p_j^{1k})) \tag{3}$$

The average time of any reaction in the batch is then computed straightforwardly by adding up the times for all the possible b_1 reactions and taking the mean (i.e., dividing by b_1). The second moment can also be calculated in a similar fashion.

The batch model is required when number of reactions increase significantly in the system triggering a large number of discrete reaction events in the stochastic simulation. In such scenarios, we can club b_1 such reactions (of type R_1) together as a single event using the batch model thereby reducing the system complexity.

2.3 Probability of Collision Calculation for Large τ

The probability of collision, p_c , as calculated in Eqn 2 will change if τ increases sufficiently. This is because the number of collisions of one molecule of X_1 (under Model 1) with molecules of X_2 in the area ΔV is given by $n_2 \frac{\Delta V}{V}$, where $\Delta V = \pi r_{12}^2 U_{12} \tau$ and n_2 is the number of X_2 molecules. We can compute the estimated number of collisions of the X_1 molecule with a molecule of X_2 (Est_{col}) for a successful reaction as follows:

$$Est_{col} = p_c \cdot 1 + p_c^2 \cdot 2 + p_c^3 \cdot 3 + \dots = \frac{p_c}{(1 - p_c)^2} = n_2 \left(\frac{\Delta V}{V} \right)$$

Solving for p_c from the above quadratic equation and noting that $p_c \leq 1$, we get:

$$p_c = \frac{1 + 2n_2 \frac{\Delta V}{V} - \sqrt{1 + 4n_2 \frac{\Delta V}{V}}}{2n_2 \frac{\Delta V}{V}} \quad (4)$$

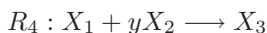
The probability of reaction, p , can be computed from this new estimate of p_c using the method outlined in [13].

For batch arrivals (Model 2), the estimated number of collisions should be added up for the b_1 molecules of X_1 arriving in a single batch. Thus,

$$Est_{coll}^{batch} = b_1 n_2 \frac{\Delta V}{V} = \frac{p_c}{(1 - p_c)^2} \implies p_c^{batch} = \frac{1 + 2b_1 n_2 \frac{\Delta V}{V} - \sqrt{1 + 4b_1 n_2 \frac{\Delta V}{V}}}{2b_1 n_2 \frac{\Delta V}{V}}$$

2.4 Generalization for Other Types of Reactions

We have considered simple reactions of type R_1 for the analysis of our discrete event based chemical reactions. The analysis become a little cumbersome for reactants having more than one molecules participating in the reaction. Nevertheless, such situations can also be modeled with our scheme. Note that, in such cases, only the p_c computation changes. Let us consider the following reaction:



Hence, the probability of collision, p_c for Model 1, and p_c^{batch} for Model 2 can be written as:

$$p_c = \binom{n_2}{y} \frac{\Delta V}{V}, \quad p_c^{batch} = b_1 \binom{n_2}{y} \frac{\Delta V}{V}$$

If more than one X_1 molecule is involved in the reaction, then we can only consider batch arrivals of Model 2. Thus for reaction R_5 :



3 Numerical Results

In this section, we first show the comparisons of our stochastic models with existing rate based equation models. Next we illustrate the effect of τ and number of X_2 molecules in the system on the reaction time.

Comparison with existing rate based equation model. The rate based model for reactions is a well studied topic. In [14], the authors apply a collision theory based approach to estimate the rate of reaction R_1 per unit time and per unit volume at absolute temperature T (denoted by $\tilde{k}(T)$) as:

$$\tilde{k}(T) = n_1 n_2 r_{12}^2 \sqrt{\frac{8\pi k_B T}{m_{12}}} e^{-\frac{E_{act}}{k_B T}} \tag{5}$$

Our estimate of T_{avg1}^{DE} can also be written as:

$$T_{avg1}^{DE} = \frac{V}{n_2 r_{12}^2 \sqrt{\frac{8\pi k_B T}{m_{12}}} e^{-\frac{E_{act}}{k_B T}}}; \tag{6}$$

Note that, if we compute T_{avg1}^{DE} per unit volume (denoted by $T_{avg1}^{DE/volume}$), we will have $T_{avg1}^{DE/volume} = \frac{1}{k(T)}$ (we have $n_1 = 1$ as 1 molecule of X_1 enters the cell). This illustrates the validity of our model with the existing rate based model. In particular, we can conclude that the inverse of the reaction rate estimation gives the time required for one reaction of type R_1 in the rate based model which is *exactly equal* to the average time for reaction R_1 by a single molecule of type X_1 estimated from our stochastic model. However, the rate based model can only return a *constant* time for completion of reaction R_1 . But such reactions in the cytoplasm are essentially chaotic and should be considered a *stochastic* process, thereby outlining the importance of our stochastic model.

To generate the numerical results, we consider the glycolysis reaction:



The corresponding parameters are shown in Table I in [13].

Fig 2 plots the cumulative distribution function for the time of reaction R_1 from Model 1 and also that from rate based equations. The time for reaction follows an exponential distribution with mean 0.003422 secs and variance 0.0000113 (note that the standard deviation is nearly equal to the mean). The rate based model however gives a constant reaction time of 0.003422 secs. Similar trends

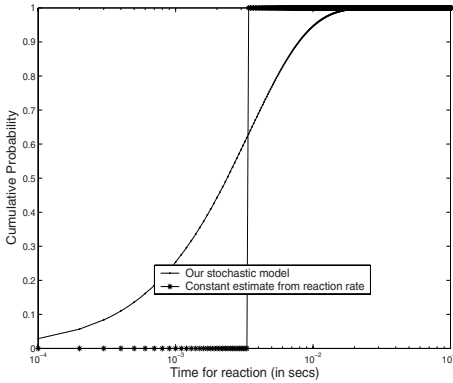


Fig. 2. Comparison of the CDF of our stochastic model (Model 1) and rate based equation model

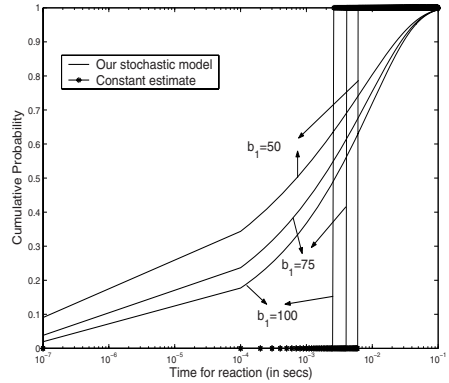


Fig. 3. Comparison of the CDF of our stochastic model (Model 2) and rate based equation model with 1200 ATP molecules

are seen for the batch model (Model 2) in Fig 4. In this case, the standard deviation is larger than the mean and hence it is not appropriate to assume any distribution that is based on a single moment (e.g., the exponential distribution). By appropriate Chi-square test, it is possible to fit the mean and variance (for the batch model) to a standard distribution like the Gamma distribution. We consider 3 instances of batch sizes $b_1 = 50, 75, 100$ respectively. The average time for reaction decreases as the batch size increases (because larger the batch size, more is the probability of the individual reactions in the batch which effectively decreases the average time for any one reaction). The reaction time from the rate based model however remains constant in all 3 cases (which is calculated by substituting $n_1 = b_1$ in Eq 5). We observe that the constant time for a reaction in the rate-based model is slightly *lower* than the corresponding average time of reaction in the batch model. This is because, the effect of reduction in probability of reaction for the later reactions in the batch is not considered in the rate based model.

Fig 3 however shows an interesting characteristic for the CDF of Model 2. We consider only 1200 ATP molecules in the system such that the reduction in probability due to the initial set of reactions in the batch of size b_1 is more pronounced. Note that this reduction in probability is because more ATP molecules are being used up by these initial set of reactions. As a result, the time taken for the later reactions in b_1 is more resulting in an overall increase in average reaction time of any reaction in the batch. Hence, the average time estimates increase as the batch size decrease. However, for the rate-based equation model, the time for a reaction in a batch of size b_1 is still constant. For different batch sizes, the reaction time for the rate-based equation model decreases with increase in batch size as normal. However, we observe that the reaction time estimates from rate-based equations are significantly less than that from our batch model

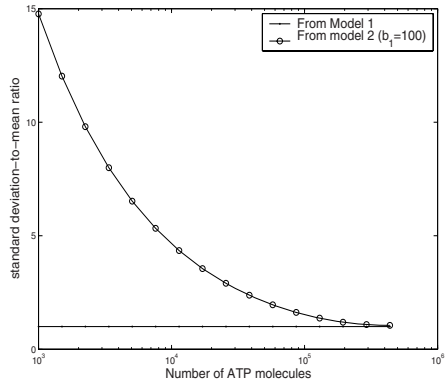
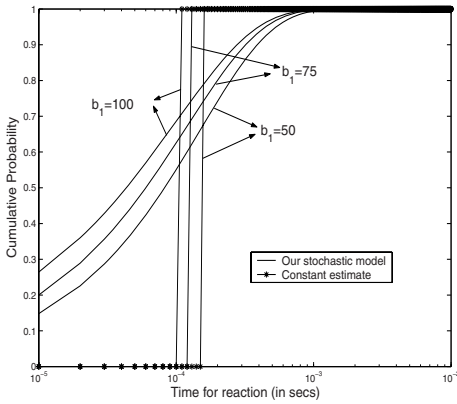


Fig. 4. Comparison of the CDF of our stochastic model (Model 2) and rate based equation model with 120000 ATP molecules

Fig. 5. Dependence of the standard deviation to mean ratio on number of ATP molecules

as the former does not consider the reduction in probabilities for each reaction in the batch. These effects however, fades off with more number of ATP molecules in the system (typically greater than 1500) for a batch size of 100. The above results indicate the limitations of the current rate based estimates for molecular reactions where we can have a large number of receptors that allows the molecules to arrive in batches.

Fig 5 plots the standard deviation to mean ratio i.e., $\frac{\sqrt{T_{2nd\,moment1}^{DE} - (T_{avg1}^{DE})^2}}{T_{avg1}^{DE}}$

(for Model 1) and $\frac{\sqrt{T_{2nd\,moment1}^{batch/DE} - (T_{avg1}^{batch/DE})^2}}{T_{avg1}^{batch/DE}}$ (for Model 2). We find that for Model 1, the ratio remains constant at 1 for appreciable number of ATP molecules in the system. This corroborates our assumption that the reaction time follows an exponential distribution for most cases. With further increase in the number of ATP molecules, however, it starts to decrease resulting in a constant reaction time where the rate equation-based model can be applied. Thus, for less number of ATP molecules in the system, our stochastic model gives a better estimate of the reaction time and becomes deterministic (i.e. constant) with further increase in ATP molecules. The curve for the batch model, however shows that the ratio is consistently greater than 1 for acceptable estimates of ATP molecules in the cell. This is why we model the reaction time for Model 2 using a Gamma distribution. However, as before, further increase in number of ATP molecules will bring down the ratio to less than 1 and again make the reaction time constant (as given by the rate-based model).

Dependence of the reaction time of our stochastic model on τ . Figs 6-7 plot the performance of our stochastic reaction models. The graphs are generated considering the following reaction pair:



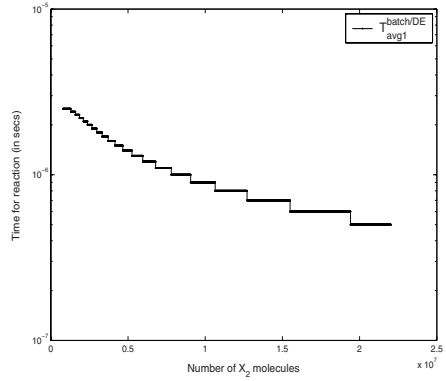
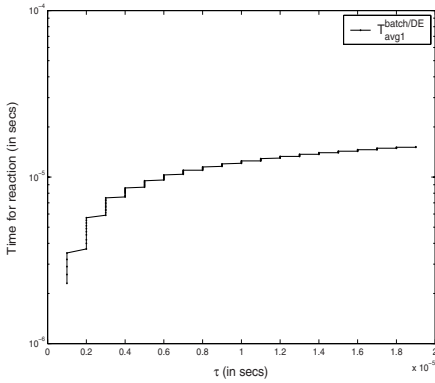


Fig. 6. Reaction time versus τ for Model 2 **Fig. 7.** Reaction time versus Number of Molecules of X_2 for Model 2

The corresponding parameters are depicted in Table II in [13]. Note that from our conventions in the previous section, the H molecules are the X_2 type molecules in R_1 and R_2 . The reaction time estimates are made *per unit volume*.

In Fig 6, we show the average time for reactions of type R_1 occurring in a single batch of size 100. We can observe that the average time increases with τ as more time is required for every single collision of the reactant molecules resulting in increased average reaction time. However, the average time becomes constant with $\tau \simeq 10^{-5}$. It should be noted that the batch model requires lower time for reaction than Model 1 because we have calculated the average of the times required to complete all the b_1 reactions corresponding to the b_1 molecules arriving in the batch which intuitively should need less time than a single reaction as in Model 1 as the probability of a single reaction in the batch increases.

Dependence of the reaction time on the number of X_2 molecules. Fig 7 plots the average time for reaction against the number of X_2 molecules in the system for Model 2. We find that the average time reduces with increasing number of molecules for obvious reasons. Here also, we observe that average time of reaction for Model 2 is slightly lower than that for Model 1. This is because, in the batch model, the effect of increase in time taken for the reaction of the last few molecules of a single batch because of reduction in the number X_2 molecules is overridden by the increase in probability of each reaction in the batch resulting in an overall lower average time for reaction than Model 1.

4 Conclusion

We have proposed a model to compute the reaction time for cytoplasmic molecular reaction as a stochastic variable that appropriately reflects the biological environment. The model can accept single molecules at a time or a batch of molecules as we normally encounter in the molecular diffusions inside a cell. The

current rate equations provide a deterministic estimate of reaction time and can not capture the dynamics of the reactions if the molecules arrive in batches. This random reaction time estimate is used in our “in silico” simulation that captures the dynamics of biological systems at multiple scales. The modeling technique presented in this paper allows to transform the modeling of biological reactions in the stochastic domain to make it applicable for discrete event simulation of biological process. At present all modeling techniques for a biological process is in continuous time domain thereby reducing the computational flexibility and scalability considerably. Also the estimate of the distribution of reaction time removes the unrealistic assumption of stability of reaction environment that is in violation of the biological environment in a cell. The average reaction time estimated from this method (for the single molecule model) is exactly same as the reaction rate estimates. The proposed batch molecule model will significantly reduce the computational complexity when large number of molecules enter a system in a very short time as seen in many biological cases. We have also outlined a method to estimate the reaction time for more complex reactions (e.g. different pathway processes) required for biological system simulation. The stochastic nature of the reaction time modeled in this paper is however not currently measured in biological experiments except the first moment.

References

1. Making Sense of Complexity *Summary of the Workshop on Dynamical Modeling of Complex Biomedical Systems*, (2002).
2. C. Fall, E. Marland, J Wagner and J. Tyson. Computational Cell Biology. *Interdisciplinary Applied Mathematics.*, Vol 20, 2002.
3. Drew Endy and Roger Brent. Modeling cellular behavior. *Nature.*, v 409, Jan. 2001.
4. L. Loew. The Virtual Cell Project. *'In Silico' Simulation of Biological Processes (Novartis Foundation Symposium No. 247)*., Wiley, Chichester, 207- 221, 2002.
5. M. Tomita et.al. The E-CELL Project: Towards Integrative Simulation of Cellular Processes. *New Generation Computing.*, (2000) 18(1): 1-12.
6. M. Rathinam, L. Petzold, D. Gillespie. Stiffness in Stochastic Chemically Reacting Systems: The Implicit Tau-Leaping Method. *Journal of Chemical Physics.*, 119 (24), 12784-12794, 2003.
7. Das, S. Sarkar, F.; Basu, K.; Madhavapeddy, S. Parallel Discrete Event Simulation in Star Networks with Applications to Telecommunications. *International Workshop on Modeling, Analysis and Simulation of Computer and Telecommunication Systems*, January, 1995, Durham, NC, USA.
8. Cell Illustrator, www.fqspl.com.pl/life-science/cellillustrator/ci.htm
9. BioSpice: open-source biology, <http://biospice.lbl.gov/home.html>
10. CellDesigner: A modeling tool of biochemical networks, <http://celldesigner.org/>
11. James Keener and James Sneyd. Mathematical Physiology. *Springer.*, 1 edition (October 1, 1998) ISBN: 0387983813.
12. S. Ghosh, K. Basu, S. Das and S. Daefler. iSimBioSys: A Discrete Event Simulation Platform for 'in silico' Study of Biological Systems *Proceedings of IEEE 39th Annual Simulation Symposium*, April 2 - 6, 2006, Huntsville, AL.

13. P. Ghosh, S. Ghosh, K. Basu, S. Das and S. Daefer. An Analytical Model to Estimate the time taken for Cytoplasmic Reactions for Stochastic Simulation of Complex Biological Systems. *Proceedings of the 2nd IEEE Granular Computing Conference*, May 10-12, 2006, Atlanta, USA.
14. H.S. Fogler and M.N. Gurmen. Elements of Chemical Reaction Engineering. Chapter 3.1, Equation 13, online at <http://www.engin.umich.edu/cre/03chap/html/collision/>.

Modelling of Complex Cryptographic Systems in Terms of Simple Cellular Automata *

Amparo Fúster-Sabater¹, Pino Caballero-Gil²,
and Maria Eugenia Pazo-Robles¹

¹ Instituto de Física Aplicada, C.S.I.C.,
Serrano 144, 28006 Madrid, Spain
amparo@iec.csic.es

² DEIOC, University of La Laguna,
38271 La Laguna, Tenerife, Spain
pcaballe@ull.es

Abstract. In this work, it is shown that binary sequences generated by a class of linear cellular automata equal the output sequences of nonlinear sequence generators. Emphasis is on cryptographic characteristics of such sequences (period, linear complexity or number of different output sequences). These simple linear automata easily model complex nonlinear generators with application in secret key cryptography.

Keywords: Linear cellular automata, nonlinear sequence generator, cryptography.

1 Introduction

Transmission of sensitive information between two interested parties needs several security requirements (confidentiality, integrity, non repudiation, authentication etc.) that can be satisfied by means of design, assessment and implementation of cryptographic algorithms and security protocols. Confidentiality makes use of an encryption function currently called *cipher* that converts the *plaintext* into the *ciphertext*. Ciphers are usually divided into two large classes: stream ciphers and block-ciphers. Stream ciphers are very fast (in fact, the fastest among the encryption procedures) so they are implemented in many technological applications e.g. algorithms A5 in GSM communications [6] or the encryption system E0 used in the Bluetooth specifications [1]. Stream ciphers try to imitate the ultimate one-time pad cipher and are supposed to be good pseudorandom generators capable of stretching a short secret seed (the secret key) into a long sequence (keystream) of seemingly random bits. This keystream is then XORed with the plaintext in order to obtain the ciphertext.

Most keystream generators are based on Linear Feedback Shift Registers (LFSRs) [4] whose output sequences are combined in a nonlinear way. Such is the

* Work supported by Ministerio de Educación y Ciencia (Spain) Projects SEG2004-02418 and SEG2004-04352-C04-03.

case of many popular sequence generators [8]: combinational generators, nonlinear filters, clock-controlled generators, multi-speed generators etc. All these structures produce keystreams with high linear complexity, long period and good statistical properties.

On the other hand, bit sequences generated by one-dimensional binary Cellular Automata (CA) with three site neighborhood and linear transition rules [2] have been found to generate exactly the same sequences as those of the LFSRs. Nevertheless, in contrast with such sequences, the bit sequences generated by adjacent cells in CA are not correlated. In this sense, linear CA are superior to common LFSRs. Moreover in [10], it is proved that linear CA are isomorphic to conventional LFSRs. Thus, the latter structures may be simply substituted by the former ones in order to accomplish the same goal: generation of keystreams with cryptographic application. Nevertheless, the main advantage of these CA is that multiple generators designed in terms of LFSRs as nonlinear structures preserve the linearity when they are expressed under the form of CA. More precisely, in this work it is shown that wide classes of LFSR-based nonlinear generators, Clock-Controlled generators, Cascade-Clock-Controlled generators, Shrinking generator or the generators producing Kasami sequences, GMW sequences, No sequences, Klapper sequences (see [5]), can be modelled in terms of linear CA.

All the sequences mentioned above are included in the class of *interleaved sequences* [5], that is pseudorandom sequences satisfying a common property: each sequence can be decomposed into a collection of shifts of an unique PN-sequence and zero sequences. This kind of sequences can be obtained from linear multiplicative polynomial CA. That is to say, CA made out of a basic structure concatenated a number of times. Moreover, the basic structure is a linear automaton based on rules 90 and 150, see [2]. Therefore the goal of this work is double:

- To analyze linear multiplicative polynomial CA with emphasis on the cryptographic parameters of their generated sequences (period, linear complexity, characteristic polynomial, number of different output sequences etc.).
- To model the above nonlinear LFSR-based generators in terms of linear multiplicative polynomial CA.

Once the generators have been linearized, all the theoretical background on linear CA found in the literature can be applied to their analysis and/or crypt-analysis.

2 Fundamentals and Basic Notation

CA are discrete dynamic systems characterized by a simple structure but a complex behavior, see [11], [12], [9]. They are built up by individual elements, called cells, related among them in many varied ways. CA are characterized by several parameters which determine their behavior e.g. the number of states per cell, the *transition rule* under which the cellular automaton evolves to the

next state, the number of neighbor cells which are included in the rule, the dimension, and the geometric structure. If the transition rule is *linear*, so is the cellular automaton. Note that different cells may follow different transition rules, making the cellular automaton *hybrid*. Our attention is concentrated on one-dimensional binary hybrid linear CA with three site neighborhood and rules 90 and 150. Both rules can be defined as follows:

$$\begin{array}{ll}
 \text{Rule 90} & \text{Rule 150} \\
 x_{n+1}^k = x_n^{k-1} + x_n^{k+1} & x_{n+1}^k = x_n^{k-1} + x_n^k + x_n^{k+1}
 \end{array}$$

Indeed, x_{n+1}^k the content of the k -th cell at time $n + 1$ depends on the content of either two different cells (rule 90) or three different cells (rule 150) at time n , for $(k = 1, \dots, L)$ where L is the length of the automaton. Next, some important definitions are introduced.

Definition 1. *A Multiplicative Polynomial Cellular Automaton is defined as a cellular automaton whose characteristic polynomial is of the form $P_M(X) = (P(X))^p$ where p is a positive integer. If $P(X)$ is a primitive polynomial, then the automaton is called a Primitive Multiplicative Polynomial Cellular Automaton.*

A widely accepted measure of the unpredictability of a sequence is its *linear complexity* [7] that can be defined as follows:

Definition 2. *The linear complexity of a sequence is the shorter linear recursion satisfied by such a sequence.*

For a binary sequence $\{x_n\}$, the linear recurrence relationship that specifies its n -th element can be written:

$$x_n + \sum_{i=1}^r c_i x_{n-i} = 0, \quad n \geq r \tag{1}$$

where the sequence elements (x_n) as well as the coefficients (c_i) belong to $GF(2)$. The linear recursion can be expressed as a linear difference equation:

$$(E^r + \sum_{i=1}^r c_i E^{r-i}) x_n = 0, \quad n \geq 0 \tag{2}$$

where E is the shifting operator that operates on x_n , i.e. $E x_n = x_{n+1}$. The characteristic polynomial of the difference equation (2) is:

$$P(X) = X^r + \sum_{i=1}^r c_i X^{r-i}. \tag{3}$$

Let $P(X)$ be a primitive polynomial of degree r and $\alpha \in GF(2^r)$ one of its roots. In this case [7],

$$\alpha, \alpha^2, \alpha^{2^2}, \dots, \alpha^{2^{(r-1)}} \tag{4}$$

are the r roots of such a polynomial. If $P_M(X) = (P(X))^p$, then the roots of $P_M(X)$ will be the same as those of $P(X)$ but with multiplicity p . Consequently, all the binary sequences generated by a primitive multiplicative polynomial cellular automaton will satisfy the linear difference equation:

$$(E^r + \sum_{i=1}^r c_i E^{r-i})^p x_n = 0, \quad n \geq 0. \tag{5}$$

Our analysis focuses on all the possible solutions $\{x_n\}$ of this equation. For a particular sequence generated at the k -th cell, the notation will be $\{x_n^k\}$.

3 Structural Properties of Multiplicative Polynomial CA

In this section, the characteristics of the sequences obtained from this kind of CA are considered in terms of their cryptographic parameters (period, linear complexity and number of different sequences).

3.1 Period of the Generated Sequences

The solutions of the equation (5) are linear combinations of $p \cdot r$ solutions of the form:

$$x_n = \sum_{i=0}^{p-1} \binom{n}{i} \sum_{j=0}^{r-1} A_i^{2^j} \alpha^{2^j n}, \tag{6}$$

where $S_n^i = \sum_{j=0}^{r-1} A_i^{2^j} \alpha^{2^j n}$ represents the n -th element of a PN-sequence [7] of period $2^r - 1$ where $A_i \in GF(2^r)$. Thus, the binary sequence $\{x_n\}$ can be written as the sum of p times the same PN-sequence weighted by a binomial coefficient

$$\{x_n\} = \sum_{i=0}^{p-1} \binom{n}{i} \{S_n^i\}. \tag{7}$$

In addition, each binomial coefficient defines a succession of binary values with a constant period p_i . Therefore, the sequence $\{x_n\}$ is the sum of p sequences of distinct periods $T_i = p_i \cdot (2^r - 1)$ and the period of the total sequence will be:

$$T = \max\{T_i \mid (i = 0, \dots, p - 1) / A_i \neq 0\}. \tag{8}$$

It can be noticed that the period of the different sequences $\{x_n\}$ generated by a multiplicative polynomial cellular automaton depends on the choice of the coefficients A_i in the equation (6). All the sequence generated at the same state cycle have the same period. Nevertheless, the same automaton can produce sequences with distinct periods depending on the state cycle considered.

3.2 Linear Complexity of the Generated Sequences

According to [7], the linear complexity of a sequence equals the number and multiplicity of characteristic polynomial roots that appears in the linear recurrence relationship. Therefore, coming back to the equation (6) the linear complexity of $\{x_n\}$ can be computed. In fact, we have r roots each of them with multiplicity p . Thus, if i_{max} is the greatest value of i ($i = 0, \dots, p - 1$) for which $A_i \neq 0$, then the linear complexity LC of the sequence $\{x_n\}$ will be:

$$LC = (i_{max} + 1) \cdot r . \tag{9}$$

It can be noticed that the linear complexity of the different sequences $\{x_n\}$ generated by a multiplicative polynomial cellular automaton depends on the choice of the coefficients A_i in (6). All the sequence generated at the same state cycle have the same linear complexity. Nevertheless, the same automaton can produce sequences with distinct linear complexities depending on the state cycle considered.

3.3 The Number of Different Generated Sequences

In order to count the number of different sequences $\{x_n\}$ generated, the choice of the coefficients A_i in the equation (6) must be considered. Different situations can take place:

- If $A_i = 0 \ \forall i$, then all the cells of the cellular automaton will generate the identically null sequence.
- If $A_0 \neq 0$ and $A_i = 0 \ \forall i > 0$, then all the cells of the cellular automaton will generate a unique PN-sequence $\{S_n^0\}$ of period $T_0 = 2^r - 1$ and characteristic polynomial $P(X)$.
- If $A_0 \in GF(2^r)$, $A_1 \neq 0$ and $A_i = 0 \ \forall i > 1$, then there will be $2^r \cdot (2^r - 1)$ possible choices of (A_0, A_1) . According to subsection (3.1), the period of these sequences will be $T_1 = p_1 \cdot (2^r - 1)$. Thus, the number of different sequences for these values of A_i is:

$$N_1 = \frac{2^r \cdot (2^r - 1)}{p_1 \cdot (2^r - 1)} = 2^{r-1} . \tag{10}$$

- In general, if $A_0, A_1, \dots, A_{i-1} \in GF(2^r)$, $A_i \neq 0$ and $A_j = 0 \ \forall j > i$, then there will be $2^{(i \cdot r)} \cdot (2^r - 1)$ possible choices of (A_0, A_1, \dots, A_i) . According to subsection (3.1), the period of these sequences will be $T_i = p_i \cdot (2^r - 1)$. Thus, the number of different sequences for these values of A_i is:

$$N_i = \frac{2^{(i \cdot r)} \cdot (2^r - 1)}{T_i} = \frac{2^{(i \cdot r)}}{p_i} . \tag{11}$$

The total number of different sequences obtained from a multiplicative polynomial cellular automaton (excluded the null sequence) will be:

$$N_{total} = \sum_{i=0}^{p-1} N_i . \tag{12}$$

3.4 A Practical Example

Let us see a simple example illustrating the previous subsections. Consider a primitive multiplicative polynomial cellular automaton of length $L = 20$, configuration rules $(150, 90, 90, 90, 150, 150, 90, 90, 90, 90, 90, 90, 90, 150, 150, 90, 90, 90, 150)$ and characteristic polynomial $P_M(X) = (P(X))^p$ with $P(X) = X^5 + X^4 + X^2 + X + 1$, $p = 4$, $r = 5$. Different choices of A_i (not all null) are considered separately.

1. If $A_0 \neq 0$ and $A_i = 0 \ \forall i > 0$, then the cellular automaton will produce $N_0 = 1$ sequences, that is a unique PN-sequence of period $T_0 = 31$, linear complexity $LC_0 = 5$ and characteristic polynomial $P(X)$. In addition, the automaton cycles through doubly symmetric states of the form:

$$(a_0, a_1, a_2, a_3, a_4, a_4, a_3, a_2, a_1, a_0, a_0, a_1, a_2, a_3, a_4, a_4, a_3, a_2, a_1, a_0)$$

with $a_i \in GF(2)$. Fig.(1.Left) illustrates the formation of the output sequences (binary sequences read vertically) and the succession of states (binary configurations of 20 bits read horizontally) for the previous cellular automaton of length $L = 20$ cells and initial state $(1, 1, 0, 0, 1, 1, 0, 0, 1, 1, 1, 1, 0, 0, 1, 1, 0, 0, 1, 1)$. In fact, diamonds represent 1's and blanks represent 0's. The 31 doubly symmetric states are concentrated into the same cycle.

2. If $A_0 \in GF(2^5)$, $A_1 \neq 0$ and $A_i = 0 \ \forall i > 1$, then the cellular automaton will produce $N_1 = 16$ different sequences of period $T_1 = 62$, linear complexity $LC_1 = 10$ and characteristic polynomial $(P(X))^2$. Moreover, the automaton cycles through symmetric states of the form:

$$(a_0, a_1, a_2, a_3, a_4, a_5, a_6, a_7, a_8, a_9, a_9, a_8, a_7, a_6, a_5, a_4, a_3, a_2, a_1, a_0)$$

with $a_i \in GF(2)$. Fig.(1.Right) illustrates the formation of the output sequences and the succession of states for the previous cellular automaton of length $L = 20$ cells and initial state $(0, 0, 0, 0, 0, 0, 0, 0, 0, 1, 1, 0, 0, 0, 0, 0, 0, 0, 0, 0)$. In fact, there are $2^{10} - 32 = 992$ symmetric states distributed in 16 cycles of 62 states.

3. If $A_0, A_1 \in GF(2^5)$, $A_2 \neq 0$ and $A_i = 0 \ \forall i > 2$, then the cellular automaton will produce $N_2 = 256$ different sequences of period $T_2 = 124$, linear complexity $LC_2 = 15$ and characteristic polynomial $(P(X))^3$. Moreover, the automaton cycles through several repetitive states of the form:

$$(a_0, a_1, a_2, a_3, a_4, a_5, a_6, a_7, a_8, a_9, a_0, a_1, a_2, a_3, a_4, a_5, a_6, a_7, a_8, a_9)$$

with $a_i \in GF(2)$.

4. If $A_0, A_1, A_2 \in GF(2^5)$, $A_3 \neq 0$, then the cellular automaton will produce $N_3 = 8192$ different sequences of period $T_3 = 124$, linear complexity $LC_3 = 20$ and characteristic polynomial $(P(X))^4$. In addition, the automaton cycles through the states not included in the previous cycles.

From a cryptographic point of view, maximum period and linear complexity are required.

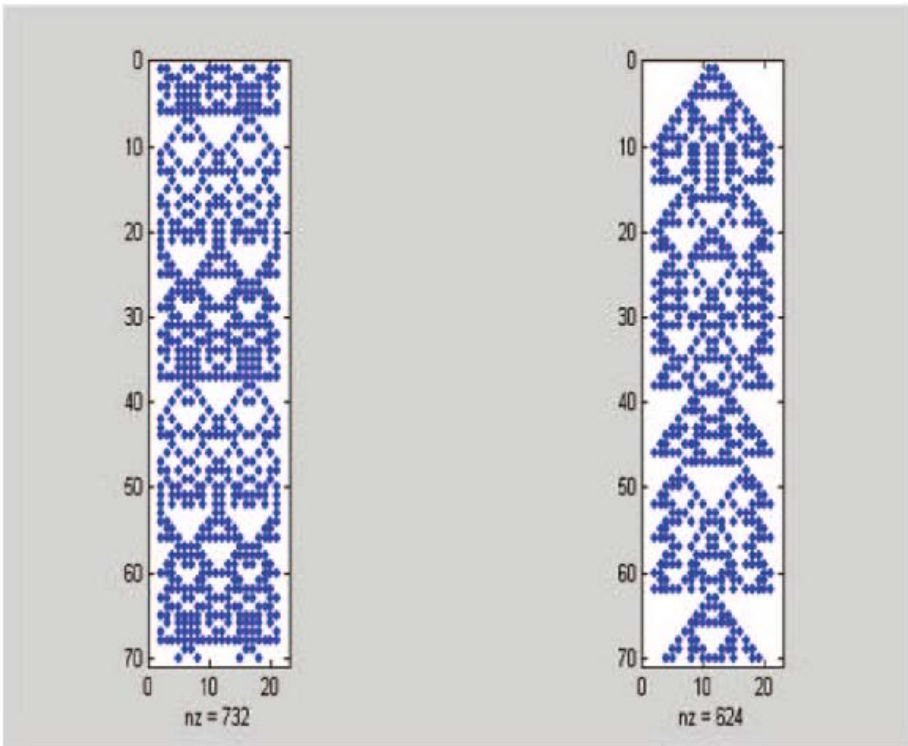


Fig. 1. Cellular automaton of configuration $(150, 90, 90, 90, 150, 150, 90, 90, 90, 90, 90, 90, 90, 90, 150, 150, 90, 90, 90, 150)$ Left: Initial state = $(1, 1, 0, 0, 1, 1, 0, 0, 1, 1, 1, 1, 0, 0, 1, 1, 0, 0, 1, 1)$ Right: Initial state = $(0, 0, 0, 0, 0, 0, 0, 0, 0, 1, 1, 0, 0, 0, 0, 0, 0, 0, 0, 0)$

4 Linear Modelling by Concatenation of Primitive CA

In the previous section, structural properties of the sequences obtained from multiplicative polynomial cellular automata have been considered. Now the particular form of these automata is analyzed. In order to simplify the notation, CA we are dealing with can be represented by means of binary strings with the following codification: 0 = rule 90 and 1 = rule 150. Since the characteristic polynomial of these automata is $P_M(X) = (P(X))^p$, it seems quite natural to construct a multiplicative polynomial cellular automaton by concatenating p times the basic automaton (or its reverse version). In this way, the construction of a linear model based on CA is carried out by the following algorithm:

Input: The parameters of a nonlinear keystream generator.

- *Step 1:* Determine the irreducible factor $P(X)$ of the characteristic polynomial of each interleaved sequence.
- *Step 2:* Compute the pair of basic CA whose characteristic polynomial is the irreducible factor $P(X)$.

- *Step 3:* For each one of these basic CA, construct by successive concatenations the longer cellular automaton able to generate the original interleaved sequence.

Output: Two linear CA producing the corresponding keystream sequence.

The shrinking generator [3] is a typical example of cryptographic generator with characteristic polynomial $P_M(X)$. The characteristics of this generator can be summarized as follows: The generator is made of two LFSRs, SR1 and SR2, with lengths $L_j (j = 1, 2)$ and feedback polynomials $P_j(X) (j = 1, 2)$, respectively. The decimation rule is: the bit produced by SR2 is discarded if the corresponding bit of SR1 equals 0. The decimated sequence is just the output sequence of the generator. The generator characteristic polynomial is of the form $P_M(X) = (P(X))^p$, $P(X)$ being a primitive polynomial of degree $r = L_2$ and $2^{(L_1-2)} < p \leq 2^{(L_1-1)}$. Moreover, $P(X)$ is the characteristic polynomial of the cyclotomic coset E in $GF(2^{L_2})$ with $E = 2^0 + 2^1 + \dots + 2^{L_1-1}$, see ([4]).

The output sequence will be a solution of a linear difference equation corresponding to primitive multiplicative polynomial CA. Consequently, the shrinking generator can be expressed in terms of a lineal model based on CA. A simple example illustrates the modelling procedure.

Input: A shrinking generator characterized by two LFSRs of lengths $L_1 = 3$, $L_2 = 5$ respectively and characteristic polynomial $P_2(X) = X^5 + X^4 + X^2 + X + 1$. Now, $p = 2^{L_1-1} = 4$ and $r = L_2 = 5$.

Step 1: $P(X)$ the irreducible factor of the generator characteristic polynomial is:

$$P(X) = X^5 + X^2 + 1 .$$

Step 2: The pair of basic CA whose characteristic polynomial is $P(X)$ are:

$$\begin{matrix} 0 & 1 & 1 & 1 & 1 \\ & 1 & 1 & 1 & 0 \end{matrix}$$

Step 3: Computation of the required pair of CA by successive concatenations.

For the first automaton:

$$\begin{matrix} 0 & 1 & 1 & 1 & 1 \\ 0 & 1 & 1 & 1 & 0 & 0 & 1 & 1 & 1 & 1 & 0 \\ 0 & 1 & 1 & 1 & 0 & 0 & 1 & 1 & 1 & 1 & 1 & 1 & 1 & 1 & 0 & 0 & 1 & 1 & 1 & 0 \end{matrix} \text{ (final automaton)}$$

For the second automaton:

$$\begin{matrix} 1 & 1 & 1 & 1 & 0 \\ 1 & 1 & 1 & 1 & 1 & 1 & 1 & 1 & 1 & 1 \\ 1 & 1 & 1 & 1 & 1 & 1 & 1 & 1 & 0 & 0 & 1 & 1 & 1 & 1 & 1 & 1 & 1 & 1 & 1 \end{matrix} \text{ (final automaton)}$$

For each automaton, the procedure in *Step 3* has been carried out $L_1 - 1$ times. In fact, each basic automaton with complementations has been concatenated $p = 2^{L_1-1}$ times.

Output: Two binary strings codifying the required CA.

In this way, we have obtained a pair of linear CA able to produce, among other sequences, the shrunken sequence corresponding to the given shrinking generator. Analogous procedure applies for any of the keystream generators mentioned in section 1.

5 Conclusions

In this work, structural properties of the primitive multiplicative polynomial CA have been analyzed. It is shown that wide classes of LFSR-based sequence generators with cryptographic application can be described in terms of CA-based structures. In this way, sequence generators conceived and designed as complex nonlinear models can be written in terms of simple linear models. The algorithm to convert a given LFSR-based generator into a CA-based model is very simple and can be applied to generators in a range of practical interest. The linearity of these cellular models can be advantageously used in the analysis and/or cryptanalysis of such keystream generators.

References

1. Bluetooth, *Specifications of the Bluetooth system*, Version 1.1, February 2001, available at <http://www.bluetooth.com/>
2. K. Cattell *et al.* Synthesis of One-Dimensional Linear Hybrid Cellular Automata, *IEEE Trans. Computers-Aided Design*, Vol. 15, No. 3, pp. 325-335, 1996.
3. D. Coppersmith, H. Krawczyk and Y. Mansour, The Shrinking Generator. *Proc. of CRYPTO'93. Lecture Notes in Computer Science*, Springer Verlag, Vol. 773, pp. 22-39, 1994.
4. S.W. Golomb, *Shift Register-Sequences*, Aegean Park Press, Laguna Hill, 1982.
5. G. Gong, Theory and Applications of q-ary Interleaved Sequences, *IEEE Trans. on Information Theory*, Vol. 41, No. 2, pp. 400-411, 1995.
6. GSM, *Global Systems for Mobile Communications*, available at <http://cryptome.org/gsm-a512.htm>
7. E.L. Key, An Analysis of the Structure and Complexity of Nonlinear Binary Sequence Generators, *IEEE Trans. Informat. Theory*, Vol. 22, No. 6, pp. 732-736, 1976.
8. Rueppel, R.A.: Stream Ciphers, in Gustavus J. Simmons, Editor, *Contemporary Cryptology, The Science of Information*. IEEE Press (1992) 65-134
9. M. Serra *et al.* The Analysis of One-dimensional Linear Cellular Automata and Their Aliasing Properties, *IEEE Trans. on Computer-Aided Design*, Vol. 9, No. 7, pp. 767-778, 1990.
10. X. Sun *et al.* The Concatenation and Partitioning of Linear Finite State Machines, *Int. J. Electronics*. Vol. 78, pp. 809-839, 1995
11. Wolfram, S.: Cellular Automata as Models of Complexity. *Nature*. **311** (1984) 419
12. Wolfram, S.: Cryptography with Cellular Automata. In: *CRYPTO'85. Lecture Notes in Computer Science*, Springer Verlag, New York. **218** (1994) 22-39

Modeling Supply Chain Complexity Using a Distributed Multi-objective Genetic Algorithm

Khalid Al-Mutawah, Vincent Lee, and Yen Cheung

Clayton School of Information Technology, Clayton Campus, Monash University,
Wellington Road, Clayton,
Melbourne, Victoria 3800, Australia
{Khalid.Al.Mutawah, Vincent.Lee,
Yen.Ping.Cheung}@infotech.monash.edu.au

Abstract. The aim of this paper is to use a Distributed Multi-objective Genetic Algorithm (DMOGA) to model and solve a three Sub-chains model within the supply chain (SC) problem for optimality. It is widely accepted that all SC problems are characterized by decisions that can be conflicting by nature, distributed, and constrained. Modeling these complex problems using multiples objectives, constrained satisfaction, and distribution algorithms gives the decision maker a set of optimal or near-optimal solutions from which to choose. This paper discusses some literature in SC optimization, proposes the use of the DMOGA to solve for optimality in SC optimization problems, and provides the implementation of the DMOGA to a simulated hypothetical SC problem having three Sub-chains. It is then followed by a discussion on the algorithm's performance based on simulation results.

1 Introduction and Research Motivation

There is a need for a variety of business strategies than what were adopted in the past in order to ensure competitiveness continuity in the present global marketplace. This need is a consequence to the continuous changes in today's dynamic market environment that has consequently grown to cope with the fluctuations in today's market. One way to face these challenges is to use a collaborative strategy where many organizations cooperate to achieve their objectives. Supply chain (SC) management is a strategy through where such integration can be achieved. A SC network commences when customers order a quantity of certain products. Then the raw material is procured from suppliers, transformed into completed goods by a manufacturer, and then delivered to the retailers or end customers [1].

From the previous definition it is obvious that there are many interdependent entities in a SC that collaborate to running the entire SC network. On the other hand, these entities try to maximize their own objectives and satisfy their own constraints. Therefore, many of their objectives and constraints will be conflicting. Consequently, this conflict impairs modeling the SC using the traditional optimization techniques (e.g. linear programming, and mixed integer programming). This is because the dynamic interplay between stochastic demands, inventory control, and delivery schedule [2-4] in a SC has implied that standalone traditional optimization techniques

are inadequate [5]. Therefore, other evolutionary techniques could to be implemented to cope with the nature of SC problems.

The Genetic Algorithm (GA) is one of a family of heuristic evolutionary optimization techniques, including simulated annealing, tabu search, and evolutionary strategies. The GA has been very reliable when combined with other techniques to solve complex problems. Though, the GA has been applied by many researchers to solve SC problems, these GAs were implemented as centralized GAs. For instance, the batches delivery on the supply chain has been optimized using GA approach in [6]. Truong and Azadivar [5] evolve GAs, mixed integer programming methods, and simulation techniques in a hybrid optimization technique to optimize the supply chain configuration. Other people expanded the capability of the GA and simulation techniques to include the supply chain Multi-objective problem by using *Pareto Optimal* [7]. This approach searches the space to obtain a set of non-dominated solutions to generate a Pareto optimal frontier.

The state-of-art of this research is to convert the centralized GA into a Distributed Multi-objective GA (DMOGA). The assumed hypothesis states that this new modified GA has a positive correlation with the SC optimization problem by the means that all organizational units that participate on a single SC network are Distributed by nature, constrained, and self-interested. Therefore, this paper particularly deals with the modeling and optimization of a three stage SC using our proposed GAs. The following sections provide an effective description and a mathematical formulation for the SC optimization problem. A description for the proposed approach is provided. A hypothetical scenario is presented and simulation results are given for validation of our approach. This is followed by a detailed discussion of obtained results.

2 Formulation of Supply Chain Optimization Problem

The three Sub-chains within a SC that used in this study are suppliers, manufacturers and retailers. Essentially this domain includes at least four major decisions i) Customer stochastic demands, ii) Procurement scheduling, iii) Production scheduling, and iv) Allocation of resources.

2.1 Problem Description

The main objective of the SC is to maximize the profitability of all organizational entities that participate to build the SC network. This, however, can only be achieved if all entities have the willingness to optimize the supply chain as a whole. In the real-world, however, several objectives are often conflicting with each other. Thus, the SC problem should be considered as a Multi-objective Optimization Problem (MOP) [7]. On the other hand, there are often constraints that violate the optimal solutions, thus the supply chain constraints must be satisfied, which formulates a Constraint Satisfaction Problem (CSP) [8]. Another aspect to consider is the notion that the supply chain problem is logically and sometimes physically distributed. Therefore, the supply chain problem needs Distributed Problem-Solving techniques. All these three SC definitions together define the SC problem as a Distributed Constraint Satisfaction Multi-objective Optimization (DCSMO) problem.

2.2 Mathematical Modeling of the Three Sub-chains Within a SC

Based on our literature review of some SC models [2] we have realized the complexity of solving the problem using one unified model. Therefore, we decompose the problem into four models such that each model represents a SC organizational entity. *Table 1* and *Table 2* show the parameters and decision variables for these models respectively.

Table 1. Set of Parameters

Parameter	Definition
S	set of all supplier partners $s \in (1,2,3,\dots,S)$
M	set of all manufacturers partners $m \in (1,2,3,\dots,M)$
R	set of all Retailers partners $r \in (1,2,3,\dots,R)$
C	set of all Customers $c \in (1,2,3,\dots,C)$
E	set of all raw material elements $e \in (1,2,3,\dots,E)$
CS_s	capacity of supplier s
CS_m	capacity of manufacturer m
a_{sr}^e	unit sell price of material e by supplier s to retailer r
b_{mr}^p	unit production price of product p by manufacturer m to retailer r
c_{mr}^p	unit sell price of product p by retailer r to customer c
d_s^e	total cost of manufacturing material e for supplier s
f_m^p	total cost of manufacturing product p for manufacturer m
g_r^p	total cost of acquiring product p for retailer r
h_{sm}^e	arrival date of raw material e from supplier s to manufacturer m
i_{mr}^p	arrival date of product p from manufacturer m to retailer r
j_{rc}^p	arrival date of product p from retailer r to customer c

Table 2. Set of Decision Variables

Decision Variable	Definition
x_{sr}^e	amount of raw material e produce by supplier s to retailer r
y_{mr}^p	amount of product p produced at manufacturer m to retailer r
z_{rc}^p	amount of product p delivered by retailer r to customer c

Supplier Model. The supplier model is responsible to resolve the procurement scheduling problem where retailers compete with each other to acquire adequate supplies from some suppliers in the global market. The objective of the supplier model, however, is maximizing the suppliers' utility ($U_{supplier}$) that can be achieved by maximizing the suppliers' net profit. The objective function is the following:

$$f_{supplier} = \text{Max} \left(\sum_{r=1}^R \sum_{s=1}^S a_{sr}^e \cdot x_{sr}^e - \sum_{r=1}^R \sum_{s=1}^S d_s^e \cdot x_{sr}^e \right) \forall s \in S, \forall r \in R. \quad (1)$$

Subject to the following constraints:

$$\sum_{r=1}^R \sum_{s=1}^S x_{sr}^e \leq CS_s \quad \forall s \in S, \forall r \in R \tag{2}$$

$$h_{sm}^e < CustomerOrderDueDate \quad \forall s \in S. \tag{3}$$

Manufacturer Model. The manufacturer model handles the production scheduling problem. The objective of this model is to maximize the utility of manufacturers, ($U_{\text{manufacturer}}$). The objective function is the following:

$$f_{\text{manuf.}} = \text{Max} \left(\sum_{r=1}^R \sum_{m=1}^M b_{mr}^p \cdot y_{mr}^p - \sum_{r=1}^R \sum_{m=1}^M f_m^p \cdot y_{mr}^p \right) \quad \forall m \in M, \forall r \in R \tag{4}$$

Subject to the following constraints:

$$\sum_{r=1}^R \sum_{m=1}^M y_{mr}^p \leq CS_m \quad \forall m \in M, \forall r \in R \tag{5}$$

$$i_{mr}^p < CustomerOrderDueDate \quad \forall m \in M. \tag{6}$$

Retailer Model. The retailer model controls the stochastic customers' demands and the delivery scheduling problems. The objective of this model is to maximize the utility of retailer (U_{retailer}). The objective function is the following:

$$f_{\text{retailer}} = \text{Max} \left(\sum_{c=1}^C \sum_{r=1}^R c_{rc}^p \cdot z_{rc}^p - \sum_{c=1}^C \sum_{r=1}^R g_r^p \cdot z_{rc}^p \right) \quad \forall c \in C, \forall r \in R \tag{7}$$

Subject to the following constraints:

$$j_{rc}^p < CustomerOrderDueDate \quad \forall r \in R. \tag{8}$$

Broker Model. The Broker model is designed to manage the allocation of resources problem amongst all aforementioned models (i.e. suppliers, manufacturers, and retailers). For example, raw materials ought to be allocated for production processes, while finished products must be allocated to retailers or customers.

So if we assumed that each model represents its optimum solutions in a set of tuples where all these solutions maximize its own utility and does not contradict its own constraints,

- $t_i(a_s, d_s, x_s, h_s) \quad \forall s \in S,$ i is the index of the optimum solution for suppliers s
- $t_j(b_m, f_m, y_m, i_m) \quad \forall m \in M,$ j is the index of the optimum solution for manufacturer m
- $t_k(c_r, g_r, z_r, j_r) \quad \forall r \in R,$ k is the index of the optimum solution for retailer r

Then given that the objective function of the Broker model is to maximize the entire supply chain network, the SC possible configuration is a set of tuples (t_i, t_j, t_k). This set, however, includes all optimum and non-optimum configurations; therefore we perform selection based on a set of criteria. These criteria are defined according to the following constraints:

$$\sum_{c=1}^C \left[\sum_{s=1}^S h_{sc} + \sum_{m=1}^M i_{mc} + \sum_r^R g_{rc} \right] \leq CustomerOrderDueDate \quad \forall c \in C \tag{9}$$

$$\sum_{c=1}^C \left[\sum_{s=1}^S a_{sc} + \sum_{m=1}^M b_{mc} + \sum_r^R c_{rc} \right] \leq CustomerOrderBidprice \quad \forall c \in C \tag{10}$$

$$\sum_{s=1}^S x_s = \sum_{m=1}^M y_m = \sum_{r=1}^R z_r \geq CustomerOrderQuantity \quad \forall c \in C \tag{11}$$

Therefore the Optimal configuration for the supply chain network is defined as

$$Z = \text{Max} (t_i, t_j, t_k) \tag{12}$$

3 The Proposed Distributed Multi-objective GA

A distributed Multi-objective GA provides an alternative means of parallel processing. Using several subpopulations allow information to be exploited in slightly better way [9]. Therefore, we break down the total population of the entire supply chain’s decisions into four subpopulations. Each of which execute a traditional GA to generate a set of optimal solutions. These subpopulations then can swap the strings by the mean of *migration* operator. This migration allows subpopulations to share information across the entire supply chain network. Therefore, we assumed that there are four different islands where each island carries its own subpopulation (suppliers, manufacturers’ plants, customers, matchmakers). The migration, however, is permitted only for the optimal set of populations that is discovered by running the local GA on each individual island. The proposed subpopulation approach will allow us to further reduce the set of available solutions and in such a case will consequently decrease the computation time to find the optimal configuration for the entire supply chain network.

3.1 The Procedure of the Distributed GA Optimization

The backbone schema of the new approach implement the basic framework of GAs from [10-12]. Modification steps are applied then to convert the traditional GA into distributed GA to solve the DCSMO SC optimization problem. This distributed approach allows subpopulations to run in parallel as threads and to distribute the process of computing optimal solutions. The procedure of the Distributed approach consists of the following steps:

Step 1. Setting: Define the Population size, Crossover rate, Mutation rate, number of generations, and constraints for all Supplier_GA, Manufacturer_GA, and Retailer_GA.

Step 2. Initialization: Generate an initial population N randomly for each of the three local GA.

- Step 3. Evaluation:** obtain fitness values of all new chromosomes by evaluating the suppliers, manufacturers, and customers models objective functions and the constraints (see section 2.3) respectively.
- Step 4. Selection:** apply selection operator N times to create a mating pool using a biased roulette wheel that has a slot sized the proportion to its fitness [12].
- Step 5. Crossover:** apply crossover operator to create a new offspring on pairs of mating pool according to crossover rate.
- Step 6. Mutation:** apply mutation operator to create a new offspring on individual of mating pool according to mutation rate.
- Step 7. Iteration:** repeat step 3 until reaching the maximum number of generations.
- Step 8. Migration:** allow population's migration from suppliers, manufacturers, and customers islands to matchmaker's islands, such that only optimal chromosomes can migrate.
- Step 9. Matchmaker Initialization:** generate an initial population for Matchmaker_GA using the migrated populations (suppliers, manufacturers, customers).
- Step 10.** Apply the same steps 3-7 to the Matchmaker_GA until reaching the maximum generation number.

3.2 Chromosome Representation

Each model is represented by strings of integers and real numbers that are associated with a stage on the supply chain configuration. A stage on the supply chain has more than one decision. Thus, each decision is represented by a group of genes on a chromosome called segment. Each gene within a segment corresponds to a variable's value on the mathematical model such as price and quantity. See the supplier's example in Fig. 1.

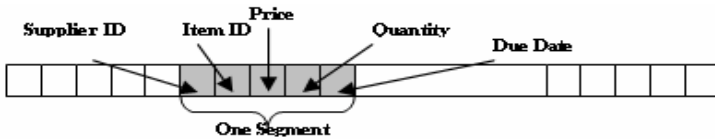


Fig. 1. Supplier's Chromosome Presentation

3.3 Crossover Operator

The crossover operator makes macro structural changes. A segment with a group of genes representing a single decision is switched in order to produce a new supply chain's configuration instead of swapping individual gene (see Fig. 2).

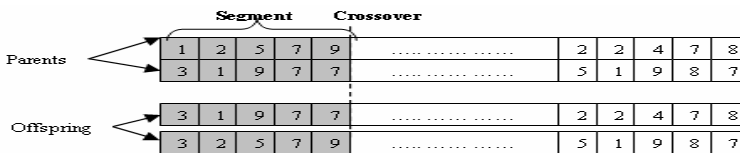


Fig. 2. Crossover Operator

3.4 Mutation Operator

One parent selected and a random segment of the entire chromosome is changed.(see Fig. 3).

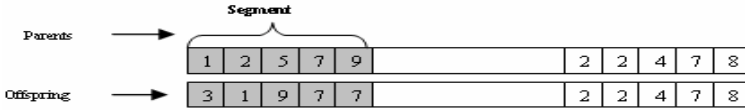


Fig. 3. Mutation Operator

4 Implementation and Results

In this section the DMOGA is implemented to measure the performance of the proposed approach. The implementation carried out is based on the mathematical formulations on section 2.3. Therefore, the total cost (TC), and revenue (RV) for the entire supply chain are defined as the following:

$$TC=[(\text{Part Cost } X x_{sr}^e)+(\text{Production Cost } X y_{mr}^p)+(\text{Delivery Cost } X z_{rc}^p)] \tag{13}$$

$$RV= \text{Customer Reserved Price } X \text{ Customer Ordered Quantity} \tag{14}$$

4.1 Parameters Settings

For this paper, the GA parameters are set according to some previous works obtained from the literature [7, 12]. Therefore, the population size is defined to be 100, the crossover probability is set to 0.7 and mutation rate is kept small (i.e. value of 0.01) because it causes little change to the chromosome.

4.2 Scenario Description

We constructed a simple SC model consisting of three stages. The model has suppliers each of which produces five different components. These components are used by manufacturers to produce three different products. There are three retailer centres; each has a group of customers who have different requirements to satisfy. Parts are in limited supply; there are limited capacities for suppliers and manufacturers, and time is highly tightened. We need to find out the best combination of products, parts, and customers that maximizes profit of all partners and increase the utility for the entire supply chain network.

The simulation is implemented using the **Premium Solver Optimizer**¹ tool and Microsoft Excel spreadsheet software. To confirm the effectiveness of the proposed approach, three different sizes of the test problems are used in the computational experiments. We used the same data for all tests, and for each test we used six

¹ <http://www.solver.com>

different generations. Each generation executed five times to assure the reliability of results the size of test problems are given Table 3. While the other parameters are randomly generated (e.g. capacity, fixed cost, sell price, delivery date, and demands). The aim of supplier, manufacturer, and customer models is to find the optimal $(x_{sr}^e, y_{mr}^p, z_{rc}^p)$ values respectively.

Table 3. The Size of Test Problems

Problem	Generation Size	<i>S</i>	<i>M</i>	<i>C</i>	<i>E</i>	<i>R</i>
P1	50-300	1	1	3	2	1
P2	100-600	3	2	6	4	3
P3	500-3000	5	3	9	5	3

Note: refer to section 2.2 for abbreviations definition

4.3 Results

DMOGA gave good results and provided for Near-optimal solutions which the decision maker can use in making his/her analysis to achieve the organization’s objectives. We summarize the results of our experiments in Table 4 . In this table, the figures show the convergence behavior of the Supplier_GA, Manufacturer_GA, and Retailer_GA average fitness value over different generations through all three test problems experiments. Furthermore, Table 5 shows the convergence of Matchmaker_GA average fitness value. In this table, the figures indicate the objectives of Matchmaker_GA to increase the revenue and reduce the total cost of the entire SC by making the proper match. All these results indicate that there is a positive correlation between the DMOGA and DCSMO supply chain optimization problem.

Table 4. Net Profit for the three SC Sub-chains

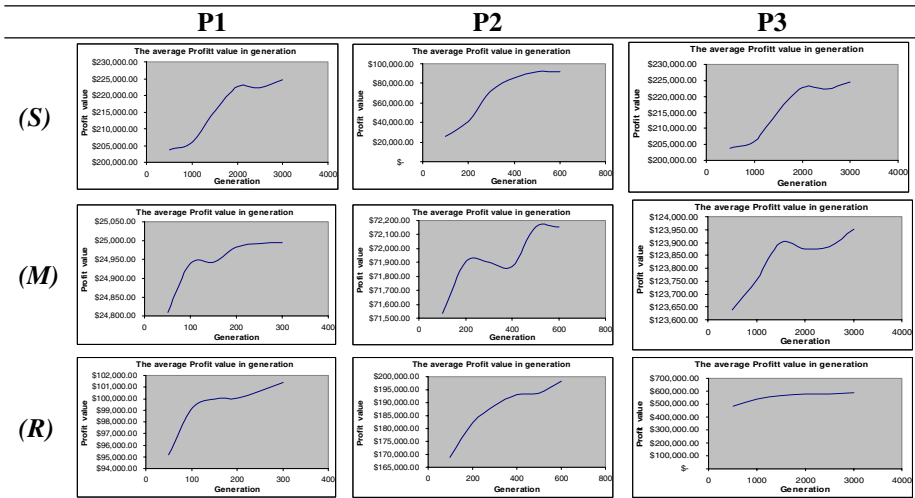
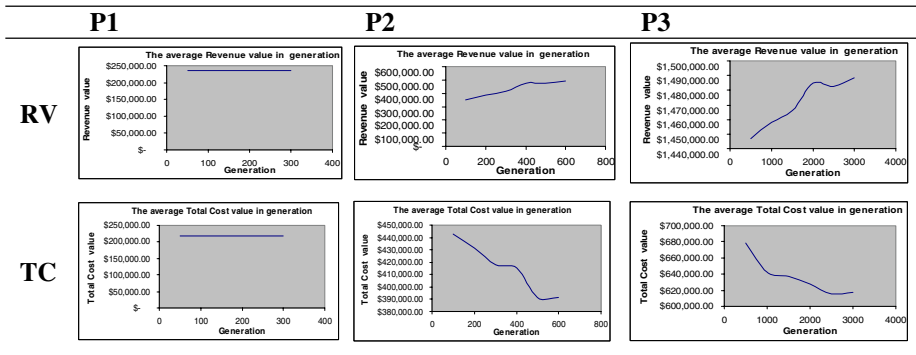


Table 5. Revenue and Total Cost Value for Matchmaker (Broker)



5 Conclusion and Future Works

In this paper we have introduced a novel approach called Distributed Multi-objective Genetic Algorithm (DMOGA) to find optimal or Near-Optimal solution for the DCSMO supply chain optimization problem. The proposed approach utilizes the subpopulation approach, which is known to be an efficient way to represent disturbed problems using GAs. We have performed several experiments by using the proposed approach, and subsequently the results show a positive correlation between our approach and the SC optimization problem. These test results show that the distributed approach is more efficient compared to the standard optimization approaches because real-world supply chain applications is distributed in nature. Therefore, adopting a distributed approach provides an improved computational performance. The novel work in this research is essentially ongoing work. Future research initiatives include, implement and integrate an autonomous or semi-autonomous agents that represent supply chain’s models, implement a profile for each agent that improves the demand forecasting and learning process to increase the agent’s gain, and experimenting with more variables.

References

1. Terry P. Harrison, Hau L. Lee, and J. J. Neale, *The Practice of Supply Chain Management*: Kluwer Academic Publishing, 2003.
2. S. Chopra and P. Meindl, *Supply Chain Management: Strategy, Planning, and Operations*: Prentice Hall College, 2001.
3. M. A. Cohen and H. L. Lee, "Resource Deployment Analysis of Global Manufacturing and Distribution Networks," *International Journal of Manufacturing and Operations Management*, vol. 2, pp. 81-104, 1989.
4. Robert B. Handfield and Ernest L. Nichols, *Introduction to Supply Chain Management*: Prentice Hall, Upper Saddle River, New Jersey 07458, 1999.
5. T. H. Truong and F. Azadivar, "Simulation based optimization for supply chain configuration design," presented at the Winter Simulation Conference, Piscataway, NJ, 2003.

6. I. Elmahi, S. Merzouk, O. Grunder, and A. El Moudni, "A Genetic Algorithm Approach for the Batches Delivery Optimization in a Supply Chain: case of multiple vehicle," presented at The 2004 IEEE International Conference on Networking, Sensing and Control (ICNSC'04), Taiwan, 2004.
7. J. A. Joines, D. Gupta, M. A. Gokce, R. E. King, and K. M.G., "Supply Chain Multi-Objective Simulation Optimization," presented at the 2002 Winter Simulation Conference, 2002.
8. J. M. Swaminathan, "Quantitative Analysis of Emerging Practices in Supply Chains." Pittsburg, PA: Carnegie Mellon University, 1996.
9. D. Whitley, "A Genetic Algorithm Tutorial," *Statistics and Computing*, vol. 4, pp. 65-85, 1994.
10. L. Davis, *Handbook on Genetic Algorithms*. New York: Van Nostrand Reinhold, 1991.
11. M. Mitchell, *An Introduction to Genetic Algorithms*. Cambridge, Massachusetts: MIT Press, 1996.
12. D. E. Goldberg, *Genetic Algorithms in Search, Optimization, and Machine Learning*. Reading, MA: Addison-Wesley, 1989.

Different Responses of Two Types of Class II Neurons for Fluctuated Inputs

Ryosuke Hosaka^{1,4}, Yutaka Sakai², Tohru Ikeguchi¹, and Shuji Yoshizawa³

¹ Graduate school of Science and Engineering, Saitama University,
255 Shimo-Ohkubo Saitama 338-8570, Japan

² Faculty of Engineering, Tamagawa University, Tokyo 194-8610, Japan

³ Tamagawa University Research Institute, Tokyo 194-8610, Japan
hosaka@nls.ics.saitama-u.ac.jp

Abstract. We investigated the statistical characteristics of spike sequences of two types of Class II neurons, neurons with subcritical or supercritical Hopf bifurcations, with uncorrelated fluctuation inputs by two statistical coefficients; coefficient of variation and skewness coefficient. We used the Morris-Lecar model and the Hindmarsh-Rose model as neuron models. As a result, even if the models belong to the same class, the interspike interval statistics exhibit different characteristics. We also discovered that the origin of the differences comes from a precise bifurcation structure, and the differences also affect the relationship on variation of input and variation of output. The results indicate that we have to introduce at least three classes by its bifurcation types to classify the neurons.

1 Introduction

The brain is composed of many neurons. In mammalian cortex, great number of neurons are regularly spiking neurons, which emit spikes “regularly.” The rests are intrinsically bursting neurons, chattering neurons, fast spiking neurons, low-threshold spiking neurons, and late spiking neurons [1, 3, 2]. The first four types of these neurons are excitatory neurons, and the rest two are inhibitory neurons.

Aside from above anatomical classification, neurons can be classified into two categories based on its firing frequency in response to constant inputs. Figure 1 shows schematic representation of firing frequency characteristics, when the injected constant inputs are ramped up slowly. The Class I neurons start to fire with a low frequency through a critical point of firing. In contrast, the Class II neurons start to fire with a high frequency that remains relatively constant even though the magnitude of the injected current increases. By this classification, regularly spiking neurons are included in the Class I neurons, and the fast spiking neurons are classified into the Class II neurons [14]. In some simulations, the regularly spiking neurons are used for excitatory neurons, and the fast spiking neurons are used of inhibitory neurons [6].

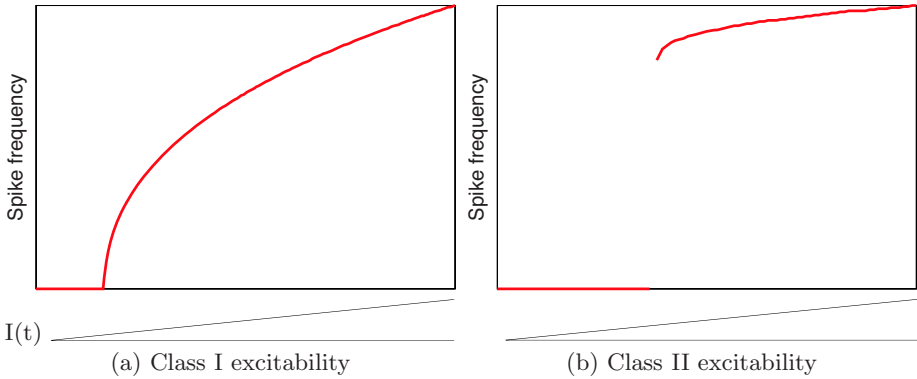


Fig. 1. Firing frequency of Class I and Class II neurons. Lower lines indicate a strength of input.

Different neuron models exhibit their own excitability because the models have different bifurcations of resting and spiking states [9]. The Class I excitability occurs when a neuron has a saddle-node bifurcation. The Class II excitability occurs when a neuron has a Hopf bifurcation.

However, the Hopf bifurcation can be classified into two sub-categories: a subcritical Hopf bifurcation and a supercritical Hopf bifurcation. Thus, we could raise a very important issue: which bifurcation should be involved for Class II neurons to reproduce neural responses from neurobiological points of view. Although responses of these two bifurcations to constant inputs are well known [4, 13], responses to more neurobiologically realistic inputs remain unclear.

It is generally difficult to observe input currents for a neuron of a behaving animal. However, if we can assume that the incoming inputs are independent each other and the change of the membrane potential caused by incoming inputs is small enough relatively to a spiking threshold, total sum of the inputs can be approximated by uncorrelated fluctuations [16].

In this paper, we compare responses of two neurons in responses to uncorrelated fluctuations: the first one has the subcritical Hopf bifurcation and the second one has the supercritical Hopf bifurcation.

Several literatures on nonlinear dynamical systems reveal a criterion to decide whether a bifurcation is the subcritical or the supercritical [4, 13]. According to the criterion, the bifurcation type of the original Morris-Lecar (ML) model is the subcritical [8]. Therefore, we used the ML model for a neuron model of the subcritical Hopf bifurcation. As a neuron model of the supercritical Hopf bifurcation, we used the Hindmarsh-Rose (HR) model modifying its parameter [5]. Then, we evaluated the responses of the ML model and the HR model by two dimensionless measures, a coefficient of variation (CV) and a skewness coefficient (SK), and compared them on a CV-SK plane.

2 Methods

2.1 Uncorrelated Inputs

In this paper, we used the uncorrelated continuous fluctuation expressed by Eq.(1) as an approximation of inputs.

$$I(t) = \mu + \sigma\xi(t), \quad (1)$$

where $\xi(t)$ is white Gaussian noise with zero mean and unit variance per unit time. The parameters μ and σ control mean and variance of $I(t)$. In the following simulations, these parameters were varied in the whole parameter space as far as the mean firing rates exist in a biologically feasible range.

2.2 Class II Neurons

The Morris-Lecar (ML) model

The ML model is described as follows,

$$\begin{cases} \dot{v} = -I_i(v, w) + 15 + I(t), & (2) \\ \dot{w} = \frac{w_\infty(v) - w}{\tau(v)}, & (3) \end{cases}$$

$$I_i(v, w) = \overline{G_{Ca}} m_\infty(v)(v - E_{Ca}) + \overline{G_K} w(v - E_K) + G_m(v - v_r), \quad (4)$$

$$m_\infty(v) = 0.5(1 + \tanh \frac{v+1}{15}), \quad (5)$$

$$w_\infty(v) = 0.5(1 + \tanh \frac{v}{30}), \quad (6)$$

$$\tau(v) = \frac{5}{\cosh v/60}, \quad (7)$$

where v is an absolute membrane potential, $I(t)$ is an injected input of Eq.(1), w is an activation variable for potassium, $\overline{G_{Ca}} = 1.1$, $\overline{G_K} = 2.0$, $G_m = 0.5$, $E_{Ca} = 100$, $E_K = -70$ and $v_r = -50$. With these parameters, the ML model yields the subcritical Hopf bifurcation.

The Hindmarsh-Rose (HR) model

The HR model is described by,

$$\begin{cases} \dot{v} = 3v^2 - v^3 - w + I(t), & (8) \\ \tau\dot{w} = 3v(v+h) - w, & (9) \end{cases}$$

where v is a membrane potential, $I(t)$ is an injected input of Eq.(1), τ is a temporal constant of the system ($\tau = 10$), w is a recovery variable, and h is a

parameter to decide the class of the model. The HR model belongs to the Class I with $h = 0$, while it belongs to the Class II with $h > 0$. In this paper, we set h to 1 for the Class II HR model, and then the HR model exhibits the supercritical Hopf bifurcation.

2.3 Higher Order ISI Statistics

We used two statistical coefficients, CV and SK, to evaluate the statistical characteristics of output spike sequences,

$$CV = \sqrt{\frac{(T - \bar{T})^2}{\bar{T}}}, \tag{10}$$

$$SK = \frac{(T - \bar{T})^3}{\sqrt{(T - \bar{T})^2}}, \tag{11}$$

where T_i is the i -th interspike interval (ISI), determined by the series of spike timings $\{\dots, t_i, t_{i+1}, \dots\}$ as $T_i \equiv t_{i+1} - t_i$, \bar{T}_i represents an averaging operation over the number of intervals, such that $\bar{T}_i \equiv 1/n \sum_{i=1}^n T_i$. The coefficient CV is a dimensionless measure of the ISI variation, and the coefficient SK is a dimensionless measure of the asymmetry in the ISI distribution. Regardless of the firing rate, spike event series generated by a Poisson process always gives $(CV, SK) = (1, 2)$.

In the following, we directly compare the coefficients CV and SK for the models, because these are dimensionless quantities. By contrast, we cannot compare the mean ISI or \bar{T} directly between the models, because \bar{T} is not dimensionless. However, the ratio of \bar{T} to the temporal scale of the dynamics can be directly compared between the different models. The time constants for the models depend on the state in the state space because of the nonlinearity of the models. However, with the parameter values used in this paper, the time constant of w, τ , is an upper limit on the slower time scale. Therefore, we regard τ as the time scale of the models. Hence, we compare the values of (CV, SK) between the models using a fixed \bar{T}/τ . For the ML model, we treat a numerator of $\tau(v)$, 5, as the time constant of the model. We estimated $(\bar{T}/\tau, CV, SK)$ from finite ISI sequences consisting of 10,000 ISIs obtained by numerical simulations.

3 Amplitude of Membrane Potentials in Response to Constant Inputs

Before we stimulate neurons by the fluctuated inputs, let us confirm differences on amplitudes of membrane potentials of the neurons receiving constant inputs. Figure 2 shows maximum and minimum of membrane potentials of the ML and the HR models.

As an input increases, an equilibrium of a neuron with the subcritical Hopf bifurcation loses its stability and a large amplitude oscillation is generated (black lines in Fig.2(a)). As an input decreases, the large amplitude oscillation suddenly disappears and an equilibrium becomes stable (grey lines in Fig.2(a)). However,

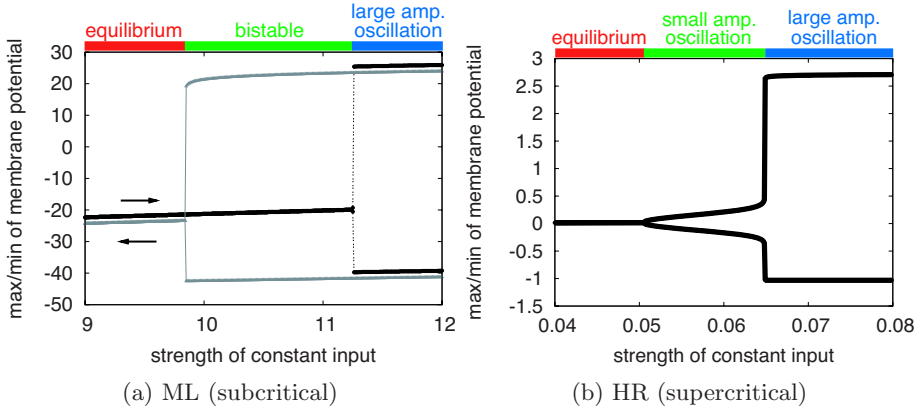


Fig. 2. Maximum and minimum of membrane potentials when the neuron models receive increasing (black lines) or decreasing (grey line) constant inputs. Although the real bifurcation curves are overlapped, we plot the potential with decreasing inputs (indicated by grey lines) beneath the black lines to show the hysteresis structure.

the transition points depend on direction of the input variation. With an increasing input, the equilibrium of the ML model loses its stability when the input is about 11.3. With a decreasing input, the limit cycle loses its stability when the input is about 9.8. Therefore, the period between the inputs of 9.8 and 11.3, a stable equilibrium and an oscillation coexist.

In contrast, a neuron with the supercritical Hopf bifurcation does not show such coexistence. For both of increasing and decreasing inputs, the amplitudes trace the same lines. In addition, there is one more difference. As an input increases, an equilibrium does not jump to a large amplitude oscillation. Instead, neurons with the supercritical Hopf bifurcation exhibit a continuous increase from a small amplitude oscillation to large one (Fig.2(b)).

4 Responses of Neurons in Response to Fluctuated Inputs

We calculated the statistical quantities ($\bar{T}/\tau, CV, SK$) as functions of the input parameters (μ, σ). These input parameters were swept, and the corresponding set of values ($\bar{T}/\tau, CV, SK$) were obtained. These values are plotted in the CV-SK plane as contour plots of \bar{T}/τ in Fig.3. Figures 3(a) and 3(b) display the structure of the ISI statistics in the CV-SK planes for the ML model and the HR model, respectively.

For most spiking data of cortical neurons, the condition $\bar{T} > \tau$ is satisfied. Decay time constants of cortical neurons have been estimated to be less than 20 ms [7, 15], and mean firing rates are no more than approximately 50 Hz. Moreover, the evaluation of (CV,SK) for $\bar{T} < 4\tau$ was unstable in the present simulation, because the models have an effective refractory period. Therefore, we compared ISI statistics whose condition \bar{T}/τ are 4, 5, 6, 10, and 40.

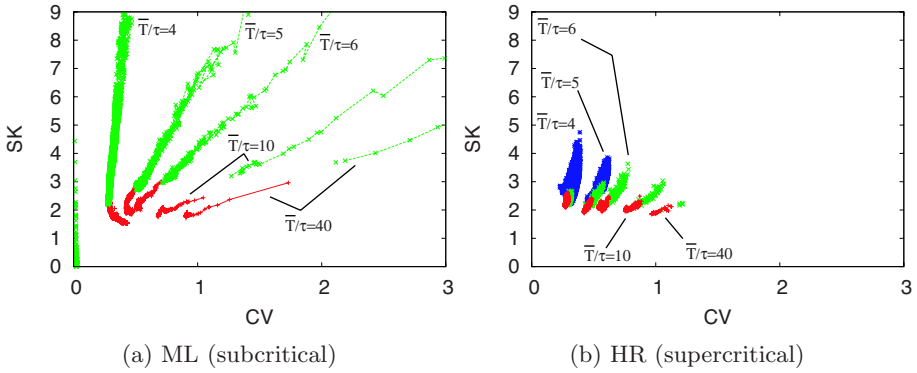


Fig. 3. Structures of the ISI statistical values (\bar{T}/τ , CV, SK) for (a) the ML and (b) the HR models in the CV-SK plane. The points correspond to data for which \bar{T} is within $\pm 1\%$ of the value satisfying $\bar{T}/\tau=4, 5, 6, 10, \text{ and } 40$, respectively.

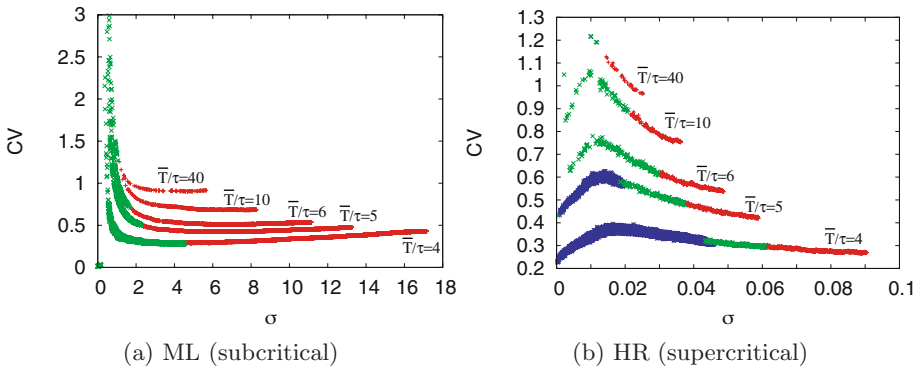


Fig. 4. Relationships between variation of input (σ) and variation of output (CV) for the ML and the HR models

The statistical measures (CV, SK) for the ML model are widely distributed on the CV-SK plane (Fig.3(a)). In the HR model, the corresponding (CV,SK) region is quite smaller than that in the ML model (Fig.3(b)).

The color of each point on Figs.3(a) and (b) indicates a mean value of the input, μ . The color on the top of Figs.2(a) and (b) corresponds to the value of μ : Red points on Figs.3(a) and (b) are obtained with μ which are in the equilibrium region on Figs.2(a) and (b), Green points are obtained with μ which are in either the bistable region for the ML model or the small amplitude oscillation region for the HR model, Blue points are obtained with μ which are in the large amplitude oscillation region. The color tells us that large values of CV and SK are realized by the inputs whose mean values exist in the bistable region, because the points on the right-upper region of the CV-SK plane are colored by green. The result indicates that the bistability is necessary for the large values of the statistics.

Next, we focus on the relationships between the variation of inputs and the variation of output. If a neuron model is a simple integrator, for example a leaky integrate-and-fire neuron, the variation of output spike sequences is proportional to the variation of inputs [11]. With such a model, large values of CV are realized by large values of input variations σ .

Figures 4 (a) and (b) show the relationships between σ (variance of the input) and CV (variance of output) of the ML and HR models. The color of points indicates the condition of μ as same as Fig.3. As shown, the ML model shows an inverse proportional relationship (Fig.4(a)). When σ is large, the value of CV is small. As σ becomes smaller, the value of CV exponentially increases. In the latter case, the mean values of inputs exist in the bistable region (the green region in Fig.2). The HR model shows neither the proportional nor the inverse proportional relationships (Fig.4(b)). When σ is large, the value of CV is small as in the case of the ML model. However, the value of CV does not monotonically increase as σ decreases. Therefore, the HR model cannot show large values of CV regardless of the parameter values (μ, σ) of the fluctuated inputs.

5 Discussions

The two types of the Class II neurons show differences on the reproducibility of the large values of CV and SK. Such large values of CV and SK are observed on cortical neurons [12]. If we can assume that the cortical neurons are Class II neurons and the receiving inputs have no correlation each other, neurons with the subcritical Hopf bifurcation are suitable models for cortical Class II neurons. However, the Leaky integrate-and-fire neuron with an assumption of temporally correlated inputs can account for the spiking characteristics of the cortical neurons, while the Leaky integrate-and-fire neuron with uncorrelated inputs cannot account for [10]. If we can observe temporal correlations in the fluctuating inputs, neurons with the supercritical Hopf bifurcation cannot be rejected. The HR model may generate large values of CV and SK with temporally correlated inputs. Therefore, confirming the reproducibility of neurons with supercritical Hopf bifurcation in response to temporally correlated fluctuation is an important future work.

6 Conclusions

We compared two types of Class II neurons, neuron models with the subcritical and the supercritical Hopf bifurcations, on the statistical coefficients of interspike intervals with fluctuated inputs. The two models show a significant difference on a variation of spike sequences.

The ML model generates large values of statistics, CV and SK, in response to the uncorrelated fluctuations. In contrast, the HR model cannot generate. The ML model realize the large values with the fluctuated inputs whose mean value makes the model on the bistable condition. The bistability is not shown

in models of the supercritical Hopf bifurcation. Therefore, the existence of the bistability is a key of the differences.

In conventional studies, the class of neurons is mainly discussed from the difference of the firing frequency on input constant currents, and the precise bifurcation structure is not considered. Our results indicate that it is necessary to classify neuron models with fluctuated inputs by different points of view; (1) the precise bifurcation structure of the neuron model and (2) the relationship of input-output variation the precise bifurcation structure generates. On the bases of these points, we have to introduce at least three classes by its bifurcation types to classify neurons.

The research of Y.S. was partially supported by Grant-in-Aids for Scientific Research on Priority Areas (Advanced Brain Science Project) from MEXT (No.14016002). The research of T.I. was partially supported by Grant-in-Aids for Scientific Research (B) from JSPS (No.16300072).

References

1. B. W. Connors and M. J. Gutnick. Intrinsic firing patterns of diverse neocortical neurons. *Trends in Neuroscience*, 13:99–104, 1990.
2. J. R. Gibson, M. Belerlein, and B. W. Connors. Two networks of electrically coupled inhibitory neurons in neocortex. *Nature*, 402:75–79, 1999.
3. C. M. Gray and C. A. McCormick. Chattering cells: superficial pyramidal neurons contributing to the generation of synchronous oscillations in the visual cortex. *Science*, 274:109–113, 1996.
4. J. Guckenheimer and D. Holmes. *Nonlinear Oscillations, Dynamical Systems, and Bifurcations of Vector Fields*. Springer-Verlag, New York, 1983.
5. J. L. Hindmarsh and R. M. Rose. A model of the nerve impulse using two first-order differential equations. *Nature*, 296:162–164, 1982.
6. E. M. Izhikevich. Simple model of spiking neurons. *IEEE Transactions on Neural Networks*, 14:1569–1572, 2003.
7. T. Kaneko, Y. Kang, and N. Mizuno. Glutaminase-positive and glutaminase-negative pyramidal cells in layer VI of the primary motor and somatosensory cortices: A combined analysis by intracellular staining and immunocytochemistry in the rat. *The Journal of Neuroscience*, 15:8362–8377, 1995.
8. C. Morris and H. Lecar. Voltage oscillations in the barnacle giant muscle fiber. *Biophysical Journal*, 193:193–213, 1981.
9. J. Rinzel and B. B. Ermentrout. Analysis of neural excitability and oscillations. In C. Kock and I. Segev, editors, *Methods in Neuronal Modeling*. MIT Press, 1989.
10. Y. Sakai, S. Funahashi, and S. Shinomoto. Temporally correlated inputs to leaky integrate-and-fire models can reproduce spiking statistics of cortical neurons. *Neural Networks*, 12:1181–1190, 1999.
11. Y. Sakai, M. Yamada, and S. Yoshizawa. Strange responses of the Hodgkin-Huxley model to highly fluctuated inputs. *Proceedings of International Joint Conference on Neural Networks*, page 1275, 2002.
12. S. Shinomoto, Y. Sakai, and S. Funahashi. The Ornstein-Uhlenbeck process does not reproduce spiking statistics of neurons in prefrontal cortex. *Neural Computation*, 11:935–951, 1999.

13. S. T. Strogatz. *Nonlinear Dynamics And Chaos*. Westview Press, Cambridge, 2000.
14. T. Tateno, A. Harsch, and H. P. C. Robinson. Threshold firing frequency-current relationships of neurons in rat somatosensory cortex: type 1 and type 2 dynamics. *Journal of neurophysiology*, 92:2283–2294, 2004.
15. A. M. Thomson and J. Deuchars. Synaptic interactions in neocortical local circuits: Dual intracellular recordings in vitro. *Cerebral Cortex*, 7:510–522, 1997.
16. H. C. Tuckwell. *Introduction to theoretical neurobiology*. Cambridge University Press, 1988.

Branching Method for Computation of Probability of Given Data Stream Transmission

Mikhail Y. Murzin and Alexey S. Rodionov

Institute of Computational Mathematics and Mathematical Geophysics,
Siberian Division of the Russian Academy of Science,
Novosibirsk, Russia +383-3326949
mrz@ngs.ru, alrod@sscc.ru

Abstract. Methods for network reliability and reliability polynomials computation are presented. Networks with absolutely reliable edges and unreliable nodes are considered. Tasks for reliability computation using such quality of service criteria as ability to transmit given data stream with time restrictions and without them are considered and corresponding algorithms are developed.

1 Introduction

Network reliability is one of the most important characteristics of any network. Random graphs are usually used for unreliable networks modeling. Mostly the case of absolutely reliable vertices and unreliable edges is considered while the case of unreliable nodes is also of great interest. As a reliability index the probability of some subset of nodes being connected is commonly used [1, 2, 3]. We think that more interesting index is the probability of whether some work can be completed in given time. As a “work” we can consider transferring of given amount of data between given pair of nodes or making a given number of connections, etc.

For structural optimization of a network with respect to a reliability the *reliability polynomials* are usually used. This polynomial shows dependency of a reliability index on reliabilities of a graph components in the case when all edges and all nodes are equally reliable. The case of reliability polynomials for probabilistic connectivity is discussed, for example, in [4, 6, 5, 7, 8, 9]. Networks with equally reliable nodes and absolutely reliable edges are studied in the current paper. We use an ability to transmit given data stream as a reliability index. Data stream transmission is considered in two cases: 1) in a given time and 2) without any time restrictions. The branching method discussed in [10] and based on well-known Moore-Shannon algorithm (see [11]) is used. The computation approach developed in [12] for polynomials is used. This approach in its program realization is based on a class framework presented in the same paper.

The rest of the paper is organized as follows: in section 2 we present some results which are used for further considerations. Section 3 contains the discussion

about the computation of a probability of given data stream transmission. In section 4 we present results of experiments that shows efficiency of our approach.

2 Preliminaries and Tools

As it have been stated above we consider a probability of successful transmission of the given data stream between 2 given nodes as the reliability index of a graph. Reliability polynomial (presence polynomial) for a separate node looks like $P(p) = p$, where p is the reliability of the node. The reliability polynomial of a given graph shows the dependence between nodes' and graph's reliabilities.

Let us denote:

$G(n, m, p, w)$ – non-oriented graph with m edges and n nodes, node's reliability p and edge capacity w ;

p_i – reliability of the vertex v_i ;

pol_i – presence polynomial of the node v_i ;

$S(G, s, t)$ – maximal possible data stream which can be transmitted from the node s to the node t if all elements of the graph G are reliable;

$S(G, s, t, T)$ – maximal possible data stream which can be transmitted from the node s to the node t in a given time T if all elements of the graph G are reliable;

$R(G, s, t, d)$ – probability of successful transmission of data stream d from node s to node t ;

$R_T(G, s, t, d)$ – probability of successful transmission of data stream d from node s to node t in a given time T ;

$Pol(G, s, t, d, p)$ – reliability polynomial for $R(G, s, t, d)$;

$Pol_T(G, s, t, d, T, p)$ – reliability polynomial for $R_T(G, s, t, d)$;

For the maximum data stream problem we use the well-known Ford-Fulkerson algorithm [13]. When it's necessary to compute how much time it will take, the well-known Deixtra's algorithm is used.

Obvious but inefficient way for calculating $R(G, s, t, d)$ is the complete enumeration of all subgraphs of G that includes nodes s and t (let \mathcal{G}_{st} be the set of such subgraphs):

$$R(G, s, t, d) = \sum_{H \in \mathcal{G}_{st}} P(H) \cdot I(H) \quad (1)$$

where $P(H)$ is a probability of H being the random realization of G and $I(H)$ is the indicator function:

$$I(H) = \begin{cases} 1, & \text{if } S(H, s, t) \geq d; \\ 0, & \text{otherwise.} \end{cases} \quad (2)$$

As a basis for new algorithms the factoring (branching) method is used. It is commonly used in the case of unreliable edges (first mentioned in [11]):

$$R(G) = p_{ij}R(G^*(e_{ij})) + (1 - p_{ij})R(G \setminus \{e_{ij}\}), \quad (3)$$

where $G^*(e_{ij})$ and $G \setminus \{e_{ij}\}$ are graphs obtained by contracting an edge e_{ij} with a reliability p_{ij} or deleting it. This formula is used for computation of k -terminal probabilistic connectivity but it can be used for probability computation of every known index of reliability, data stream transmission including.

This formula was modified in [10] for the task of probabilistic connectivity in the case of absolutely reliable edges and nodes with equal reliability. It can be represented in the following way:

$$R(G) = p_i R(G^*(v_i)) + (1 - p_i) R(G \setminus \{v_i\}), \tag{4}$$

where $G^*(v_i)$ is obtained by replacing the unreliable node v_i by absolutely reliable node and $G \setminus \{v_i\}$ is obtained by deleting it with all incident edges. We use p_i instead of p because it can be equal to 1 also (in this case the second item is zero). Naturally, we never make branching by such node. Note that the unreliable node with maximal number of incident edges is preferred to be chosen as a key node for branching. In this case more edges are deleted with a node and time of computation reduces. The branching process continues while all nodes become reliable.

The factoring method can be used for reliability polynomials computation also [9, 12], data structures and basic operations with polynomials for better programming are presented in [12]. For our task the factoring method gives the following equation:

$$Pol(G, d, s, t, p) = pol_i \cdot Pol(G^*(v_i)) + (1 - pol_i) \cdot Pol(G \setminus \{v_i\}), \tag{5}$$

where $G^*(v_i)$ is obtained by replacing the node v_i with absolutely reliable node with presence polynomial $pol_i = 1$ and $G \setminus \{v_i\}$ is obtained by deleting it with all incident edges. This formula should be applied to both of obtained graphs until graph is definitely unreliable or definitely reliable.

3 Probability of Given Data Stream Transmission

3.1 No Time Limitations

Let us consider a graph with absolutely reliable edges with known capacity and nodes with equal reliability. It is necessary to transmit the given data stream from one given node s to another node t . If only graph structure is considered then the algorithm given in [13] can be used for computing the maximal possible data flow. In our model there are unreliable nodes and if any of them fails all edges incident to it fail also and so can't be used for data transmission. Let us suppose that nodes s and t are reliable because if they are not there can't be transmitted any data stream between them. For computation of the probability of successful data transmission we use Eqn. (4) recursively until reaching one of the following cases:

1. $G(n, m, p, w)$ is unable to transmit given data stream even if all unreliable nodes present;
2. $G(n, m, p, w)$ has no unreliable nodes.

In the first case reliability of $G(n, m, p, w)$ is equal to 0. In the second case if d is less than $S(G, s, t)$ then reliability of G is equal to 1, otherwise to 0.

Thus the algorithm for computing the probability of transferring a given amount of data between given pair of nodes s and t in a graph $G(n, m, p, w)$ can be written as follows:

1. Calculate $S(G, s, t)$. If $S(G, s, t) < d$ then return 0. Exit.
2. Select the unreliable node v_i with maximal number of incident edges as a key element. If there are no unreliable nodes then return 1. Exit.
3. Calculate $R_1(G^*, s, t, d)$ and $R_2(G \setminus \{v_i\}, s, t, d)$ using current algorithm, where $G^*(v_i)$ is obtained by replacing the node v_i with absolutely reliable node and $G \setminus \{v_i\}$ is obtained by deleting it with all incident edges.
4. Calculate the reliability using Eqn. (4) and return the result.

Reliability Polynomial Coefficients. Reliability polynomials can be used for graph analysis and structural optimization with respect to given reliability index. They can be used for graph comparison from point of view of their reliability, for optimization of existing networks, for optimal addition of new elements, etc. Applying to current model the computation algorithm for calculating the reliability polynomial coefficients can be obtained in the similar way. The only difference is in using Eqn. (5) instead of Eqn. (4). Data structures for polynomials representation and basic necessary operations with polynomials were presented in [10].

3.2 Data Stream Transmission with Limited Time

In some cases time restrictions for data transmission are very important and they should be taken into account. In this case our algorithm should be modified. First of all the transmission time (edge length) must be defined for each edge in the input graph. Secondly, during the computing of $S(G, s, t, T)$ only pathes with length less than T should be taken into account. Thus, modified algorithm can be written as follows:

1. Calculate $S(G, s, t, T)$ using only ways shorter than T . If $S(G, s, t, T) < d$ return 0. Exit.
2. Select one unreliable node v_i with maximal number of incident edges as a key element. If there are no unreliable nodes then return 1. Exit.
3. Calculate $R_1(G^*, s, t, d, T)$ and $R_2(G \setminus \{v_i\}, s, t, d, T)$ using current algorithm, where $G^*(v_i)$ is obtained by replacing the node v_i with absolutely reliable node and $G \setminus \{v_i\}$ is obtained by deleting the key node it with all incident edges.
4. Calculate the reliability using the formula 4 and return the result.

Reliability Polynomial Coefficients. As in the previous model without time restrictions, polynomials can be computed using Eqn. (5) instead of Eqn. (4) by means of sufficient data structures and operations (see [10]).

4 Using Graph Particularities for Reduction of Task Dimension

It is possible to reduce a graph dimension before and during the calculation process thus significantly speeding up it.

4.1 Removing Dangling Nodes

If a graph has any dangling nodes except s and t then they can be removed without changing the result because no part of a flow between s and t goes through them.

4.2 Chain Reduction

If graph G has a simple chain $C_{xy} = e_{xi_1}, e_{i_1i_2}, \dots, e_{i_{k-1}y}$ connecting some nodes x and y thus that $s, t \notin \{1, \dots, k-1\}$ then all its inner nodes i_1, i_2, \dots, i_{k-1} can be replaced by one node with a presence polynomial $pol = \prod_{i=1}^{k-1} pol_i$. For keeping the capacity of a chain that now is reduced to two edges at least one of these edges ought have a capacity equal to minimum capacity of $\{e_{xi_1}, e_{i_1i_2}, \dots, e_{i_{k-1}y}\}$. For definiteness we assign this capacity to both new edges. If all inner nodes of a chain are absolutely reliable then we can connect x and y directly and assign a minimum capacity of chain's edges to the edge e_{xy} .

4.3 Cutnodes and Bridges

It is obvious that if a graph G consists of two graphs G_1 and G_2 that unite through some cutnode x or bridge e_{xy} and both s and t belongs to G_1 or G_2 then it is enough consider this subgraph only because all the flow between s and t goes through edges of this subgraph.

4.4 Disconnected Graphs

If during the branching process we obtain a disconnected graph after node removing and both s and t belongs to the same component of connectivity then further only this component needs consideration.

5 Case Studies

We use several graphs with rectangular lattice shape as testing examples. All edges have equal capacity 20 units. As a reliability index the ability to transmit 40-units stream from one corner to the opposite corner is used. Results are given

in the following table. The dimension of the lattice, computational time for reliability numeric value ($T1$), and computational time for reliability polynomial coefficients ($T2$) are presented for each example.

Dimension	T1	T2
4×4	0.13 sec.	0.153 sec.
4×5	1.16 sec.	1.3 sec.
5×5	25 sec.	27.5 sec.
5×6	8 min. 52 sec.	9 min. 09 sec.

Another test is an example of one more possible application for given algorithms. There are 24 terminals which should be connected in the way to form a lattice graph with maximal reliability (dimensions 4×6 , 3×8 and 2×12 are possible). Links' capacity is 20 units. We have computed the reliability polynomials for 40-units packets transmission from one lattice's corner to the opposite corner. The corresponding polynomials are

$$\begin{aligned}
 Pol_1(p) &= p^{22} + 4p^{21} - 13p^{20} - 5p^{19} + 23p^{18} - 33p^{17} + 111p^{16} - & (6) \\
 &\quad 130p^{15} + 21p^{14} + 16p^{13} + 6p^{12} \\
 Pol_2(p) &= -8p^{21} + 22p^{20} - 6p^{19} - 7p^{18} - 22p^{17} + 16p^{16} + 6p^{15} \\
 Pol_3(p) &= p^{22}
 \end{aligned}$$

Their graphics are shown in Fig.1.

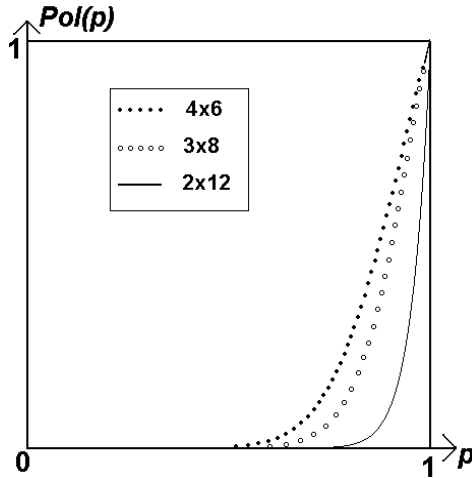


Fig. 1. Polynomials for lattices with different dimensions

From this picture it's obvious that the best shape for lattice graph with 24 nodes to provide maximal reliability is 4×6 for any node reliability.

6 Conclusion

In this paper we have considered such important network characteristics as probability of given data stream transmission without time restrictions and in a given time. The algorithms have been presented for computing a numeric value of target characteristics and polynomials for them. These researches allow to evaluate quality of service which can be provided by the network. Further researches can be done considering networks with both unreliable nodes and edges and variable data stream value. An interesting application of our approach is strict calculation of an expected value of a flow through an unreliable network. Another task that we deal with now is the calculation of an expected value of a number of disconnected pairs of nodes in an unreliable network and our approach proves to be efficient again.

References

1. Shooman, A.M.: Algorithms for Network Reliability and Connection Availability Analysis. Electro/95 Int. Professional Program Proc. (1995) 309–333
2. Palmer C.R., Siganos G., Faloutsos M., Faloutsos C., and Gibbons P.: The connectivity and faulttolerance of the Internet topology. Workshop on Network-Related Data Management (NRDM-2001), <http://www.research.att.com/divesh/papers/cjfgs98-ir.ps>.
3. Rodionova, O.K., Rodionov, A.S., and Choo, H.: Network Probabilistic Connectivity: Exact Calculation with Use of Chains. ICCSA-2004, Springer LNCS. **3046** (2004) 315–324
4. Ayanoglu E. and Cpih-Lin: A Method of Computing the Coefficients of the Network Reliability Polynomial. GLOBECOM '89, IEEE, vol.1 (1989) 331–337
5. Page L.B. and Perry J.E.: Reliability Polynomials and Link Importance in Networks. IEEE Transactions on Reliability. **43**, Issue 1 (1994) 51–58
6. A.K. Kelmans, “Crossing Properties of Graph Reliability Functions,” *Journal of Graph Theory*, Vol. 35, Issue 9, pp. 206–221, 2000.
7. Colbourn C.J., Harms D.D., and Myrvold W.J.: Reliability Polynomials can Cross Twice. Journal of the Franklin Institute **300**, Issue 3 (1993) 627–633
8. Camarda P.: Bounds Evaluation of Coefficients in the Reliability Polynomial. Microelectronics and Reliability. **30**, Issue 2 (1990) 1699–1110, 1990.
9. Rodionova O.K., Rodionov A.S., and Choo H.: Network Probabilistic Connectivity: Reliability Polynomial. ISPC Communication-2004. Proc. Of the 8th Int. Conf. “Problems of Operation of Information Networks”, Vol. 1, (2004) 321–327
10. Murzin M.Y.: Calculation of the reliability polynomial coefficients for an undirected graph. Proceedings of Young Scientists Conference, Institute of Computational Mathematics and Mathematical Geophysics, Novosibirsk (2004) 141–147 (in Russian)
11. Moore E.F., Shannon C.E.: Reliable Circuits Using Less Reliable Relays. J. Franclin Inst., **262**, n. 4b (1956) 191–208
12. Murzin M.Y.: Computation of reliability and reliability polynomial coefficients for telecommunication networks with reliable links and unreliable nodes. 8th International Conference “Problems of Operation of Information Networks”, Vol.2 (2004) 213–216. (in Russian)
13. Ford L.R. and Fulkerson D.R.: Flows in Networks. Princeton Pres, Princeton, (1962)

An Agent-Based Approach to Immune Modelling

Dimitri Perrin, Heather J. Ruskin, John Burns, and Martin Crane

Dublin City University, School of Computing, Dublin 9, Ireland
dperrin@computing.dcu.ie

Abstract. This study focuses on trying to understand why the range of experience with respect to HIV infection is so diverse, especially as regards to the latency period. The challenge is to determine what assumptions can be made about the nature of the experience of antigenic invasion and diversity that can be modelled, tested and argued plausibly. To investigate this, an agent-based approach is used to extract high-level behaviour which cannot be described analytically from the set of interaction rules at the cellular level. A prototype model encompasses local variation in baseline properties contributing to the individual disease experience and is included in a network which mimics the chain of lymphatic nodes. Dealing with massively multi-agent systems requires major computational efforts. However, parallelisation methods are a natural consequence and advantage of the multi-agent approach. These are implemented using the MPI library.

Keywords: HIV, immune response, complex system, agent-based, parallelisation methods.

1 Introduction

The objective of this study is to understand why the range of experience with respect to HIV infection is so diverse. In particular, the work aims to address questions relating to variation in length in individual latency period. This may be very long (for relatively low success of antipathetic mutation) in one individual, compared to another with much higher mutation levels.

The indications are that the observed variation lies in the priming and initial level of fitness of the immune response of the individual, together with the various factors influencing this [1]. If such “priming patterns” can be recognised, or even predicted, then in the long term we may have a way of “typing” an individual and targeting intervention appropriately. Unfortunately, understanding how the immune system is primed by experience of antigenic invasion and diversity is non-trivial [1]. The challenge is to determine what assumptions can be made about the nature of the experience, can be modelled, tested against clinical data and hence argued plausibly. The aim is to understand how the cell interactions lead to the observed endpoints.

The immune response is dynamic and includes growth and replenishment of cells and in-built adaptability, through mutation of its defences to meet new threats. It also includes aspects of cell mobility, which may be captured, by means

of defining movement and affinity of cell-types in a defined spatial framework. In particular, this will enable study of variation in viral load and the way in which host response may lead to degradation of protection.

To investigate these questions, an “agent-based” approach is chosen, as a means of inferring high-level behaviour from a small set of interaction rules at the cellular level. Such behaviour cannot be extracted analytically from the set of rules [1], but emerges as a result of stochastic events, which play an important part in the immune response [2].

The initial model consists of functional units, called agents, with designated properties which mimic the operation of a single lymph node. This test-case prototype, however, includes all known interactions contributing to cell-mediated immunity and the local evolution of the virions. The antibody-mediated response has not been considered initially, because the cell-mediated arm plays a dominant role in repelling attack. The agents implemented represent Th (helper, or CD4) and Tc (cytotoxic, or CD8) lymphocytes, Antigen Presenting Cells, and virions. The computational structure of the numerical experiments is based on inheritance from a common C++ class designed to deal with features such as the mobility and then each class includes specific attributes and methods to implement specific properties of each cell type. The lymph node itself is modelled as a matrix, in which each element represents the physical neighbourhood of a cell type, (in terms of its agent neighbours). The frequency with which an infected cell will produce a new virion is used as the simulation time-step. At each time step, agents can move from one matrix element to another, and interact with the other agents present in their physical neighbourhood (i.e. with cell types in the same neighbourhood).

Current development is focused on increasing the number of lymph nodes, which involves millions of agents, requiring major computational effort and parallelisation methods. These are, however, a natural consequence and advantage of the multi-agent approach [3]. The aim is to extend the size and complexity of the systems modelled to something approaching realism.

2 A Complex Biological Mechanism

2.1 The Immune Response Against a Viral Attack

Immunity can be defined as all mechanisms which allow the body recognition of that which belongs to its system and consequently tolerate it, and recognise what does not and fight to eradicate it. The immune system is complex and involves various types of cells. When a foreign element is recognised, it can be dealt with in two different ways: the immune response can be non-specific or specific. A non-specific response is based upon the fact that the foreign element does not show, at its surface, the antigens characterising the cells belonging to the body. This is the response that has to be diminished when transplants are carried out. In contrast, the specific response is based on the accurate recognition of foreign antigens. This response can be cell-mediated or antibody-mediated. The second one, also known as humoral response, is carried out by B lymphocytes

and mainly targeted at bacterial attacks. We present here a few details about the cell-mediated response, targeted more specifically at viral attacks and taking place in lymphatic nodes. More details about the immune system can be found in specialised journals and immunology courses, such as [4].

The effector cell, in the cell-mediated response, is the Tc lymphocyte. However, it cannot act on its own, needing a chain reaction to achieve activation. The first step is carried out by Antigen Presenting Cells which recognise foreign biological entities and start presenting these antigens at their surface. It will then encounter Th lymphocytes. If a Th cell encounters an APC presenting an antigen, which it has been specifically designed to recognise, it activates itself. The Th cells main function is then to coordinate the immune response by activating specific Tc cells.

2.2 The HIV Expansion Strategy

HIV virions use the Th cells described above as hosts to multiply themselves, as detailed in [5]. The gp120 glycoprotein of the virion envelope first attaches itself to the CD4 receptor, characteristic of these immune cells. Then the virion fuses with the lymphocyte using gp41 and the viral RNA is freed into the cell. The viral reverse transcriptase copies the RNA into DNA and integrates it into the cellular DNA. To be successful, this integration has to take place in activated cells. More details about this process can be found in [6]. An important aspect is the high rate of mutation: there is on average a transcription error every 10.000 nucleotides. Since the HIV genome contains about 10.000 nucleotides, this means there is on average a single difference between two “brother virions”. All these mutants of course have various fates. On the one hand, most of them will result, for instance, in the suppression of an enzyme, and will be unsuccessful. On the other hand, a mutation can be successful and, for instance, modify the envelope glycoprotein, thus allowing the new virion to temporarily escape from the immune system.

The macroscopic evolution of the disease is divided into three phases. The first one corresponds to the typical immune response against a viral attack. The production of lymphocytes specific to the viral strains is launched, and within a few weeks, all the original strains are eradicated. The mutation rate here becomes critical. It has allowed the appearance of new strains, which have not been detected by the organism yet, and can therefore develop freely. As soon as a strain becomes too intrusive, its detection probability increases and it is eradicated. During this second phase, there are no symptoms. This is known as the latency period, and can last up to ten years. The immune system is heavily loaded, and the destruction of each strain also implies the destruction of the infected cell. A time comes when the immune system cannot cope with the ever increasing number of strains or remain viable, given a strong decrease of the number of the Th cells. During this last phase, known as AIDS (acquired immunodeficiency syndrome), the whole immune system is diminished and opportunistic diseases start appearing, leading to the death of the patient.

3 Simple Rules to Control the Agents

3.1 The Agent-Based Approach

There is no unique definition of what an agent is. However, Wooldridge and Jennings proposed in [7] a definition which is widely accepted and specifies characteristics that an agent must have. An agent has to be autonomous: it can act without any intervention and has some control over its actions and its internal state. It has a social behaviour: it can interact with other agents thanks to a specific language. It can also react: the agent has the ability to scan part of its environment and change its behaviour to take advantage of it. The agent is proactive: it not only reacts to its environment but also acts and takes initiatives so as to satisfy goals. Building on this definition an agent-based model is a model in which the key abstraction elements are agents.

Obviously, each agent has only a limited knowledge of the world in which it evolves, and communication between agents is therefore an important aspect of this approach. This communication is sometimes referred to as linguistic actions, as opposed to non-linguistic actions which are modifications of the environment. Interaction between agents is not limited to communication: they have to share their environment. This implies that agents' actions have to be coordinated. Of course coordination does not mean cooperation: a good competitor maximizes his advantage by coordinating his actions according to the others' decisions. It also does not imply reciprocity of action: a car driver can go past another and coordinate this safely without the second driver knowing it. The key factor when choosing a coordination strategy is the size of the agent population. If every agent can interact with every other one, the number of interaction pairs increases quadratically with the population size. If interaction can occur between several agents instead of pairs, the coordination overhead increases exponentially and can easily exceed the computing facilities [8]. Developing a coordination strategy is therefore both essential and difficult. In many cases, managing to avoid conflicts and blocks is itself an important achievement. This gives us the opportunity to put the emphasis on the main drawback of this approach: it is highly resource-consuming. However, the approach also provides a solution as it is often combined with parallel methods. We develop this idea later on (section 4.2).

This approach being generic, it has been used in various fields. It has for instance been used for aerial traffic planning [9], vehicle monitoring [10] and even to manage chirurgical intensive care units [11]. It has also been extensively used in Natural Sciences, as it provides a very intuitive way to model systems: biological entities are implemented as agents, and interactions between them are dealt with through linguistic and non-linguistic actions among the agent population. In particular, the immune system itself is a discrete system in which the individual behaviour of every cell adds to create to high-level behaviour of the whole system. A simple set of local rules can therefore provide an accurate model of this complex system. This is the approach we have chosen to take.

As we have seen earlier, most of the immune response against HIV is taking place in the lymphatic nodes. The world we model need only be a network of

such nodes. The communication inside the network will be discussed later (section 4.1). Each node is implemented as a matrix. Each element of the matrix correspond to a physical neighbourhood. All the interactions between the agents therefore happen inside this local element and there is no need to consider surrounding matrix elements as would be done if using Moore or Von Neumann neighbourhoods [12].

3.2 The Implemented Features

There are several platforms supporting generic agent-based environments, such as Swarm [13]. However, due to the high number of agents we plan to simulate, we think it is more efficient to have an approach fully dedicated to this particular environment, and therefore optimized. Because of the very detailed knowledge of the cell interactions, we are using a bottom-up approach: we first specify in detail the individual parts of the system (here, the agents), we then link them together to form layer components (here, the lymphatic node), which are in turn linked until a complete system is formed (here, the lymphatic network).

As noted earlier, this study focuses on the cell-mediated response. Thus, we first need to implement three types of cells, corresponding in the code to three types of agents: Th and Tc lymphocytes, and Antigen Presenting Cells (APC). Of course, we also need a fourth type of agent to model the virions. Each type is implemented into the code using a specific C++ class.

Interestingly, even if all four types of cells have totally different roles, they have a common feature that we want to take into account, i.e. their mobility. This is implemented by another class. This class is then inherited by the four types described above. It also implements other basic properties such as the age of the agents and allow us to have the four agent classes contain only specific features; an advantage of object-oriented programming.

An agent coding a virion only has one specific attribute in the model, its viral strain. In order to prevent the code from allocating too much memory for each agent, the viral strain is only coded as an integer which links to the corresponding strain in an array containing all the useful properties of the strain (e.g. lymphocytes which recognize it, immunogenicity, etc.). The agent has a short-term and partial knowledge of its environment. It is partial in the sense that it only knows whether there are Th cells in its physical neighbourhood (i.e. the matrix element). It is short-term in the sense that it has no memory of the evolution of the number of lymphocytes. This knowledge is the only piece of information it needs, since its unique objective is to infect a Th cell. Therefore, the typical behaviour of a virion in the model can be given as the following triptych, repeated until a lymphocyte is infected: the agent moves, scans its environment looking for a Th cell, and if possible infects the immune cell.

A Th agent has three specific attributes in the model: an integer coding its surface antigens, another integer coding its “activation state” and a third integer coding its “infection state”. Once again, it has no memory of its environment and the only part it knows of it is reduced to the presence, or not, of Tc agents. If the agent is neither activated nor infected, both integers coding the states are

set to zero, and the agent's objective is only to be ready to answer an attack. There is therefore no particular action, apart from moving. The objective of an activated agent is to activate Tc cells. Its "activation state" is set to the value coding the viral strains which activated it, so that it can communicate on the threat. If the agent is infected, it produces new virions belonging to the strain coded in its "infected state", or to a new one if there is a mutation.

A Tc agent has four specific attributes: its surface antigens, its "activation state", its "expansion state" and its "memory state", all implemented as integers. The Tc agents also have a short-term and partial view of their environment: each looks only for agents having the antigens corresponding to the strain which activated it, and destroys them. When activated, an agent multiplies itself during an expansion phase, corresponding to a non-zero "expansion state". After an immune response, a small amount of the Tc agents will become memory cells: their "memory state" will keep track of the strain they fought, the reactivation will be easier, and if reactivated, the expansion phase will be more productive.

An APC agent only has one specific attribute, its "presenting state", coded as an integer. As long as the agent is not presenting any antigen at its surface, the integer stays at zero, and the agent's behaviour is focused on moving and looking for "foreign" entities in its physical neighbourhood, in order to get antigens to present. Then, the "presenting state" codes the strain corresponding to the antigens, and the agents starts looking for Th agents in order to activate them, if they are geared recognise this particular antigen.

Another aspect of the implementation chosen is the allocation of the agents. Memory allocations are among the slowest operations on a computer, and here, we have a model in which thousands of agents are created and destroyed every iteration. Dynamic allocations would make the program too slow. The approach we have chosen is to have, in each matrix element, a static allocation of the maximum number of agents we want to implement. Then, an agent moving from an element to another is coded as the transfer of its attributes from one static memory slot to another. Every agent being small and with few attributes, this gives satisfying results.

3.3 How to Deal with Stochastic Events?

In this model, most methods and functions have to include random number generation. This is due to the fact that many aspects of the real-life system involve stochastic events. More details can be found in [2], but here are a few examples. First, an aspect we have to deal with is the process by which new lymphocytes are created. A lymphocyte can only recognize a specific set of antigens so, to protect itself against any attack, the body has to generate thousands of "variations" between lymphocytes. This has to be implemented using random numbers. Likewise, we noted that one of the most decisive features of the virions is their high mutation rate, and this implies another use of random numbers. Finally, there is no sensible way to deal with mobility unless we include stochasticity.

Stochastic events are essential to this work and a reliable random number generator is needed. A full-scale model will involve millions of agents in very

long simulations. Therefore, the generator also has to be very efficient. As parallel aspects are involved, it would also be a plus for the generator to include such features. There are many generators available, and good ones can also be designed explicitly (see e.g. [14]). However, due to our model requirements, what is needed here is a top-quality parallel generator, and we chose to use the Scalable Parallel Random Number Generators library (SPRNG) [15]. This library incorporates recent, state-of-the-art, developments in the mathematics and computer science of parallel pseudorandom number generation. It is an efficient library with an existing, active, user base, ensuring high standards. It allows the streams to be also absolutely reproduced, for computational verification, independent of the number of processors used in the computation and of the loading produced by sharing of the parallel computer. Using it, we can be confident we will produce statistically significant results at a very low computing cost.

4 Interactions Between the Lymphatic Nodes

4.1 Sharing Knowledge and Transferring Agents

The immune system is organised so that every lymphatic node is a small defence unit in which the immune response is taking place. There is no need for the response to take place in every node, which is why we built our model as a network of independent matrices (putting the emphasis on the local model of the node). The only physical exchange between lymphatic nodes happens through the recirculation and the mobility of cells which go from one node to another. Each node in the model therefore needs an entry point and an exit point. If, when moving inside the node, an agent reaches the exit point, it is removed from the node and put into a transfer list. The list is dealt with at the end of the iteration. In the meantime, other agents move, interactions take place, as time passes. This accounts for the time it takes the agent in real-life to commute between two nodes. The way in which agents are transferred between the nodes mimics the transfer between matrix elements: we consider only attributes, rather than the agent itself. Thus, an entry in the transfer list contains the type of the agent, its attributes, and its destination. At the end of the iteration, all lists are put together and the moving agents are transferred to the entry point of their destination node.

The other aspect of the communication between our nodes is inherent to our implementation. Since we decided not to put all the strain properties into each agent, we need a way to code them somewhere and make them available to all the agents, wherever they are in the model. These are important properties, and must not be neglected. For instance we need to know, for each strain, which lymphocytes will recognise it for sure and which lymphocytes might recognise it. One characteristic is that when a lymphocyte from the second category recognises the strain, it moves from the second into the first. This is critical to the realism of the model, since it allows us to introduce some adaptability and emergent behaviour. One answer could have been to create a linked list containing the strains active in the current simulation. The obvious advantage is to limit the

size allocated to the strains to what is actually needed. However, it has one major drawback which makes it pointless in our case, namely that the high mutation rate means a large number of strains, increasing as the simulation continues. The bigger the list, the longer it will take to get the properties for a particular strain and since this list has to be accessed thousands of times in every iteration, this process would slow the whole program down. We therefore decided to have an array of strains. This array is large (i.e. tens of thousands of strains) and represents potential strains for the simulation to be implemented. Considering that a strain in the array can account for various strains in real life (if they differ on properties we do not code explicitly), we are confident this should give us enough diversity.

4.2 Parallelisation Efforts

When the program is running at full scale, each node contains hundreds of thousands of agents. In real life, a human body contains about a thousand lymphatic nodes. Matching this value is a long-term objective and may not be achievable, but even with fifty nodes, we would have to deal with millions of agents. The time-step of the program is about fifty seconds, so about six million iterations are needed for a 10-year simulation. Running such a program on a single computer would take months, and not even have enough memory might be available to initialize all the matrices. If we also consider the fact that we have to run several simulations to statistically assess the role of each parameter such as the mutation rate, a parallel approach makes even more sense.

The approach we develop here is to mimic the immune system, in the sense that each lymphatic node will be computed by a different computer (also called node) on a cluster. As the lymphatic nodes are mainly independent from each other, this is the best way to take advantage of the parallel option. Moreover, the local model is already known to run on a single computer so approximate expectations on performances are known also. This type of spatial parallelisation has been studied in [16] for Monte-Carlo simulations. The main disadvantage in that study is the communication overload. Here, most of the communication taking place on the cluster is the transfer of agents from one node to another. Using the list process described above, this is kept to a minimum. This parallel approach is implemented using the Message-Passing Interface (MPI) [17, 18]. It is under validation on a cluster composed of a Dell PowerEdge 1750 acting as the master node and sixteen of these machines acting as slaves. More important clusters will also be used for full-scale runs.

The most difficult part here is to deal with the updates of the array containing the strain. On the one hand, if we keep only one array (on the main node of the cluster) it would lead to excessive communication: each agent would have to ask for the viral strain properties at each iteration. On the other hand, having an array linked to every node would impose a process to make sure that at every instant all arrays contain the same information, for all the strains. Using MPI advanced features, this can be done through “collective communication”.

This approach provides an intuitive way to combine the parallel computing features with a process which mimics the immune system. The transfer of the agents is currently being optimized. This will allow us to then run full-scale simulations. Our objective is to first reproduce the three-phase evolution of the disease and then alter the parameters (mobility, viral load) to study how they affect the latency period length.

5 Conclusion

The objective of this study is to understand why the range of experience with respect to HIV infection is so diverse, addressing in particular questions relating to variation in length in individual latency period. To investigate these questions, an “agent-based” approach is chosen, as a means of inferring high-level behaviour from a small set of interaction rules at the cellular level as well as including stochastic events.

The model developed mimic the immune system, as it is organised as a network of matrices, each of them corresponding to a lymphatic node. Matrix elements can host several agents, of four different types, accounting for virions, Th and Tc lymphocytes, and Antigen Presenting Cells. Thus, it is possible to model the HIV spreading strategy and the cell-mediated immune response.

Because the system we study is so complex, millions of agents are needed, and it is not possible to run the model on a single computer. Therefore, parallel methods are implemented. Using MPI, every lymphatic node is allocated to a different computer on a cluster, and “collective communication” is used to share knowledge common to all nodes.

This parallel implementation is currently being tested and the first results should be available in the coming months.

Acknowledgements

The authors would like to thank the Irish Research Council for Science, Engineering and Technology for the funding made available through the Embark Initiative.

References

1. Burns, J.: Emergent networks in immune system shape space. PhD thesis, Dublin City University, School of Computing, 2005.
2. Germain, R.N.: The Art of the Probable: System Control in the Adaptive Immune System. *Science* 239 **5528** (2001) 240–245.
3. Jennings, N., Sycara, K., Wooldridge, M.: A roadmap of agent research and development. *Autonomous agents and multi-agents systems* 1 **1** (1998) 7–38.
4. Lemahieu, J.C.: Le systeme immunitaire. Immunology courses [French] (available online at <http://anne.decoستر.free.fr/immuno/orgcelri/orgcelmo.htm>), last access on December 14th, 2005.

5. Klatzmann, D., Champagne, E., Chamaret, S., Gruest, J., Guetard, D., Hercend, T., Gluckman, J.C., Montagnier, L.: T-lymphocyte T4 molecule behaves as the receptor for human retrovirus LAV. *Nature* 312 **5596** (1984) 767–768.
6. Decoster, A., Lemahieu, J.C.: Les retrovirus. *Immunology courses* [French] (available online at <http://anne.decoster.free.fr/d1viro/vretrov0.html>), last access on December 14th, 2005.
7. Wooldridge, M., Jennings, N.: Intelligent agents: Theory and practice. *The Knowledge Engineering Review* 2 **10** (1995) 115–152.
8. Durfee, E.H.: Scaling up agent coordination strategies. *Computer* 34 **7** (2001) 39–46.
9. Cammarata, S., McArthur, D., Steeb, R.: Strategies of cooperation in distributed problem solving. *proceedings of the Eighth International Joint Conference on Artificial Intelligence (IJCAI-83)*, Karlsruhe, Germany (1983).
10. Durfee, E.H.: *Coordination of distributed problem solvers*. Kluwer Academic Publishers (1998).
11. Hayes-Roth, B., Hewett, M., Washington, R., Hewett, R., Seiver, A.: Distributing intelligence within an individual. *Distributed Artificial Intelligence Volume II*, L. Gasser and M. Huhns (editors), Pitman Publishing and Morgan Kaufmann (1989) 385–412.
12. Kari, J.: Theory of cellular automata: A survey. *Theoretical Computer Science* 334 **2005** (2005) 3–35.
13. Minar, N., Burkhart, R., Langton, C., Askenazi, M.: The Swarm simulation system: A toolkit for building multi-agent simulations. Working Paper 96-06-042, Santa Fe Institute (1996).
14. Press, W.H., Vetterling, W.T., Teukolsky, S.A., Flannery, B.P.: *Numerical Recipes in C++: the art of scientific computing*. Cambridge University Press (2002).
15. Srinivasan, A., Mascagni, M., Ceperley, D.: Testing parallel random number generators. *Parallel Computing* 29 **2003** (2003) 69–94.
16. Hecquet, D., Ruskin, H.J., Crane, M.: Optimisation and parallelisation strategies for Monte Carlo simulation of HIV infection. Submitted to *Computers in Biology and Medicine* (2005).
17. Gropp, W., Lusk, E., Skjellum, A.: *Using MPI: Portable Parallel Programming With the Message-Passing Interface*, second edition. MIT Press (1999).
18. Gropp, W., Lusk, E., Skjellum, A.: *Using MPI-2: Advanced Features of the Message Passing Interface*. MIT Press (1999).

Comparison of Homogeneous and Heterogeneous Motorised Traffic at Signalised and Two-Way Stop Control Single Lane Intersection

Puspita Deo and Heather J. Ruskin

School of Computing, Dublin City University, Dublin, Dublin 9, Ireland
{dpuspita, hruskin}@computing.dcu.ie

Abstract. Results of a microscopic model of mixed motorised traffic consisting of short vehicles, (e.g. cars), and long vehicles, (taken to be double the length of the short vehicles), for an urban two-way single lane intersection are presented here. We model the intersection using both signalised and un-signalised stop control rules. The model allows for the detection of bottleneck activity in both homogenous and heterogeneous traffic conditions, and was validated by means of field data collected in Dublin, Ireland. The validated model was used to study the impact of inclusion of long vehicles on traffic performance in an urban environment. Traffic mix is, however, taken to be dominated by short vehicles overall, in argument with observed live data collected.

1 Introduction

Homogeneous traffic flow has attracted much attention, not only for exclusively single lane roads but also for more complex configurations [1]. We focus here however on factor that contributes to heterogeneous traffic flow inability for a single lane. A major issue is clearly that of bottlenecks. Bottleneck conditions are crucial for single lane flow when right turning (RT) and long vehicle (LV) proportions increase. The focus of the research community on homogeneous, ignores many important features of real heterogeneous traffic and it is clear that more experimental work on heterogeneity is needed.

Heterogeneous motorised traffic flow characteristics for single lane roads are essential to understanding urban traffic problems. Such models would be of significant help to traffic planners, in making key decisions. Simulation modelling is an increasingly popular and effective tool for analysing a wide variety of dynamic problems, which are not amenable to study by other means [2] and there are many examples of their use in modelling traffic.

Unfortunately, the literature shows that limited studies only have concentrated on heterogeneous traffic movements for single-lane situations in Western European countries. Yet many European cities have a wide range of road capacity within the city environment and rely on single lane connection to major arterial routes. Different heterogeneous urban traffic models have already been reported in some cases, these include:

A stochastic traffic-flow simulation model [3] for urban highways looked specifically at collection and extraction of headway data. The model is also capable of simulating traffic movements at curbside bus stops and bus bays; microscopic simulation model [2] of mixed motorised and no motorised traffic over an urban arterial mid block section, the passenger car unit (PCU) technique [4] for estimating the influence of heavy vehicles to modify the gap acceptance parameters for drivers of heavy vehicles and drivers who accept a gap just ahead of a heavy vehicle; first-order second moment method [5] used to estimate the saturation flow and the delay caused to traffic at signalised intersections under heterogeneous traffic conditions; a model for depicting road traffic behaviour (MORTAB) [6] under mixed traffic conditions and heterogeneous traffic flow on roads where vehicles move without lane discipline [7]. These have in most cases, discussed validation of the proposed model and their outcomes, these studies, though intended for simulating heterogeneous flows are moving of vehicles on any available part of road space without lane discipline.

In multi class traffic flow models, the focus is mainly on using macroscopic conditions for highway multi class flows [8]. Vehicle interactions, such as over taking and lane changing are also taken into account.

In comparing the homogeneous original LWR model (i.e. Lighthill, Whitham, and Richards macroscopic first-order continuum model) to a heterogeneous version [9]. The authors divided the heterogeneous traffic population into homogeneous classes, so that the original LWR model describes vehicles of each particular class if and only if the road is free of other vehicles. This permits deviation of a fundamental diagram for each class separately. The characteristic properties of each class is described by its fundamental diagram.

The impact, of mixed traffic conditions on delay due to vehicle interaction, persons and vehicle stopping rules at a signalised intersection are described in [10]. The author's note that the most important limitation, inherent to all analytical delay models for signalised intersections, is their inability to predict delay for traffic conditions that are different from those assumed in the models. In particular, because they were designed to evaluate flow patterns from a macroscopic point of view, (that is, by considering only hourly flows and average traffic behaviour), these models cannot be used to analyse the delay incurred by individual vehicles.

The paper presented here, describes the development of a traffic-flow model using a two component cellular automata for urban single-lane intersection with heterogeneous motorised traffic. The advantages of cellular automata models are that they are computationally simple and flexible and can encapsulate the complexity of real world traffic behaviour through detailed specification. Such models are capable of producing clear physical patterns that are similar to those we see in everyday life. Where as mathematical models have a closed form solution, which describes properties of the traffic flow in general. The model attempts to simulate the presence of both short and long vehicle interaction at the urban intersection and the impact of this mix on intersection performance. This is constructed based on previous work on homogeneous flows at an intersection [11], which was designed to describe stochastic interaction between individual vehicles and independent of headway distribution.

2 Two Component Cellular Automata Model

The model proposed in this article simulates single lane two-way signalised and un-signalised intersections. For the cellular automaton (CA) model, the road is considered as divided into cells of length 7.5m. Each cell is occupied by one particle per cell corresponding to a standard car of length less then or equal to 7.5metres. Long vehicles (LV) are taken for simplicity, to be double the length of a standard car, i.e. two cells are considered occupied by one LV. In our model a car is thus a short vehicle (SV) of length 1 and a LV is of length 2. Both the SV and LV will move exactly one cell in one time step if the cell in front is vacant. The state of each cell at the next time step is determined from the state of the cell itself and of its nearest neighbouring cell in the direction of movement at the current time.

2.1 Vehicle Manoeuvre at a Two-Way Stop (TWSC) Control Intersection

A two component one-dimensional Cellular automata is used to simulate the interaction between the vehicles, in which a vehicle will move only one cell in a given time step. Minor-road vehicles will move on to the junction only when the required numbers of empty cells are available. In the CA model described, the states of all cells update simultaneously. Figure 1 represents the current situation for available spaces and, to follow through on the movement, we consider the situation at the next time-step. We assume that all driver behaviour is rational and that, for our CA model, the space required in terms of different number of vacant cells in the opposing directions of flow road for SV and LV is an extension of that specified in [11] for rational and conservative driver checks.

Fig. 1 indicates the conditions for RT vehicle (SV or LV) driver to enter the intersection from a minor road. A SV and LV need to check 8 and 11 marked cells respectively. Marked cells are denoted as 0, L, nR, sR. A "0" means that the cell needs to be

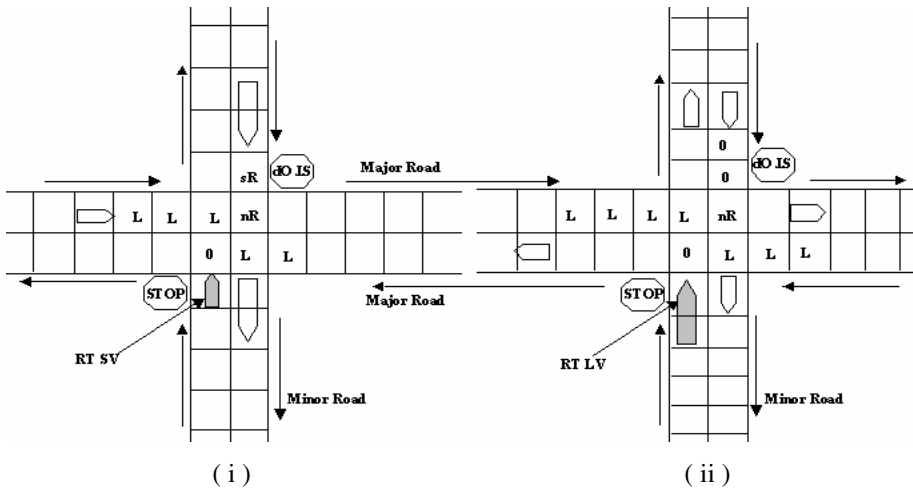


Fig. 1. A right turning vehicle from minor road TWSC Intersection (i) SV (ii) LV

vacant,” L” means that the cell needs to be either vacant or occupied by vehicle that will turn left, “nR” means that the cell must not be occupied by right-turning vehicle, “sR” means the cell needs to be either occupied by a right turning short vehicle or vacant.

A vehicle from the opposing minor road at a two way stop control intersection (TWSC), which intends to move straight-ahead or turn left (LT), has priority over a RT vehicle from the given minor-road according to rule of the road. However, priorities between minor-road vehicles might not be distinct [12]. They indicated that drivers were observer to enter the intersection on a first come, first-served basis.

The movement of the RT SV and LV vehicle from a minor road does not need to consider opposing vehicles if one of the conditions is met: (a) for SV vehicle first cell in the opposing minor road is vacant and for LV two cells opposing minor road should be vacant, (b) RT vehicle is the first vehicle in the opposing minor-road, (c) The first vehicle in the opposing minor-road arrives at a stop-line in less than stop time delay time.

2.2 Right Turning Vehicle Manoeuvre at a Traffic Light Controlled (TLC) Intersection

In Fig. 2 show the requirements in terms of cells free for a right turning vehicle from both the major and minor road at a controlled intersection are shown. If a designated cell is not vacant, than the entering vehicle has to wait before manoeuvring. An SV vehicle needs one time step to crossing a given cell, while LV needs two time steps.

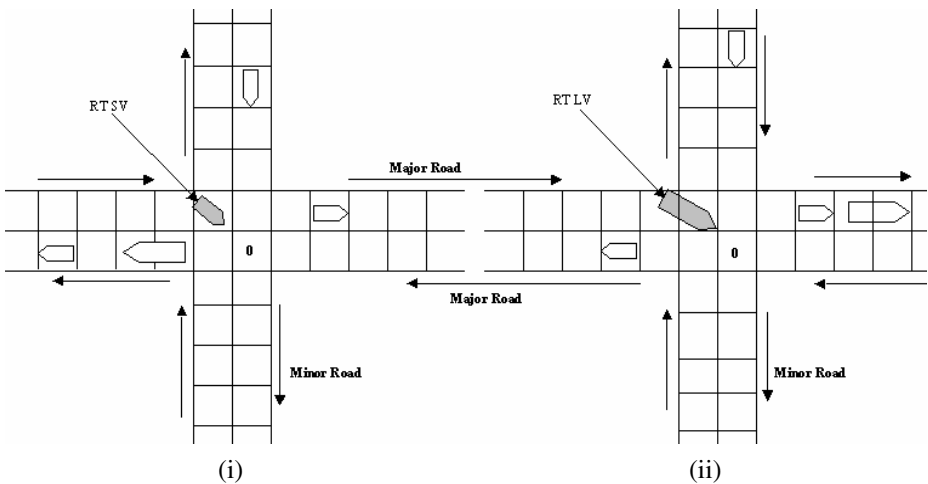


Fig. 2. A right turning (RT) vehicle from major road (i) SV (ii) LV

2.3 Control Rule: Signalised and TWSC Intersection

In the signalised intersection, the traffic flow is controlled by a set of traffic lights, which are operated in a fixed cycle manner, (constant period of time T). A cycle is

divided into three phases; green, yellow and red, all with fixed periods which sum to T. In our model we consider two main stages for control. In Stage-1, the traffic light is green for major roads and simultaneously red for minor roads. At the second part, the lights change colour to yellow for the major roads and simultaneously change to red for minor roads. In the stage-2 the same cycle is repeated in reverse, i.e. minor roads become green and yellow and major roads become red. In the case of a TWSC intersection, a minor road vehicle has to wait for 2-time steps to prior entering the intersection in before checking available of the space.

3 Real Traffic Data of the Local Intersection

Dublin City Council collects detailed traffic in a variety of ways. A particular forms is local single lane two-way intersection (Single as that for Rathgar Road/ Frankfort Avenue used here). The checks on data are collected manually over a 10-hour period at 15-minute intervals. In this instance, the weather is recorded as fair. The composition of traffic and turning percentage at the study location is shown in Tables 1 and 2.

Table 1. Turning Percentage (%) and flow (Total vehicles in10 hours)

Characteristic	(Road-1)*		(Road-2)*		(Road-3)*		(Road-4)*	
	Flow	%	Flow	%	Flow	%	Flow	%
Left turning traffic	532	10	387	16	140	3	481	23
Straight through traffic	4160	85	1569	65	4427	90	1526	71
Right turning traffic	245	5	472	19	374	7	131	6
Totals for 10 hours	4937	100	2428	100	4941	100	2138	100
Averages per hour	494		243		494		214	

* Road-1 and Road-3 are major roads and Road-2 and Road-4 are minor roads.

Table 2. Traffic Composition (Total vehicles in10 hours)

Vehicle Types	(Road-1)		(Road-2)		(Road-3)		(Road-4)	
	Flow	%	Flow	%	Flow	%	Flow	%
Short vehicle (Car)	4703	95	2391	98	4678	95	2111	99
Long vehicle (bus or lorry)	234	5	31	2	263	5	27	1
Total for 10 hours	4937	100	2428	100	4941	100	2138	100
Averages per hour	494		243		494		214	

4 Result from Computer Simulations

Our simulations were carried out for 36000 seconds, equivalent to 10 hours for a all length of each entrance road=100 cells. For turning rate and traffic composition, the real traffic data (references Section 3) is used to specify initial values, unless other wise specified. This is a baseline, we would be expected to vary, the baseline values in a sensibility analysis to determine how robust this model is to different assumptions and values.

Table 3. Comparison: Overall Throughput of Homogeneous and Heterogeneous Traffic (TWSC and TLC Intersections)

AR(1,2,3&4)		Throughput (vph)		
		SV	SV+LV	LV
0.05	TLC	866	871	52
	TWSC	863	872	415
0.1	TLC	1593	1481	17
	TWSC	1568	998	99
0.15	TLC	2303	1221	10
	TWSC	1773	747	95
0.2	TLC	3020	807	5
	TWSC	1859	664	61
0.25	TLC	3559	424	5
	TWSC	1944	339	18
0.3	TLC	4039	343	5
	TWSC	2147	250	17
0.35	TLC	4330	248	4
	TWSC	2293	175	13
0.4	TLC	4683	139	4
	TWSC	2429	121	12

Table 3 show results for a series of simulations with arrival rates of four roads equal ($AR_1=AR_2=AR_3=AR_4$) and which varied from 0.05 to 0.4 (equivalent to 180 vph to 1440 vph). For turning rate and traffic composition for all approaches Table 1 and 2 values were used. We found that throughput of homogeneous traffic (i.e. 100 percent passenger cars or a SVs in our model) increases linearly as arrival rate of all approaches increase simultaneously. It is also clear that the throughput of 100 percent SV in TLC intersection is higher than that of TWSC intersection. In this case arrival rates were not high enough to produce the saturation but were designed to assess impact of vehicle mix on the flow.

In the case of heterogeneous traffic (i.e. SV+LV), when the arrival rate of all approaches increases throughput increases up to certain extent and then minimal at $AR=0.2$ both in TWSC and TLC intersection. The throughput of the heterogeneous traffic in TLC intersection is higher again than that of the TWSC intersection.

When the traffic is 100 per cent long vehicles the throughput obtained in TLC intersection is nearly zero as compare with the 100 percent short vehicle traffic. In the case of TWSC intersection throughput increases up to maximum at $AR=0.05$ then falls to minimal throughput at $AR=0.2$. Homogeneous long vehicle traffic clearly does better at a TWSC intersection, but in reality no city traffic is 100 per cent long vehicles. Clearly, while conditions are extreme and therefore artificial in these test. Our model can be used to predict the impact of traffic mix on intersection performance.

4.1 Comparison of Entry Capacity of the Major Road: (TLC and TWSC Intersections)

Right-turning vehicles from a major road where RT, ST and LT vehicles share road space, can block ST and LT vehicles behind and in the same road in single lane

found. RT rates (RTR) of the major roads thus have great impact on major-road capacity. In order to examine this for road entry, we varied right turning rate (RTR) of the roads from 0.01 to 0.1. Arrival rate was fixed at $AR_1=AR_2=AR_3=AR_4=0.15$, (equivalent to 540 vph) for this test case.

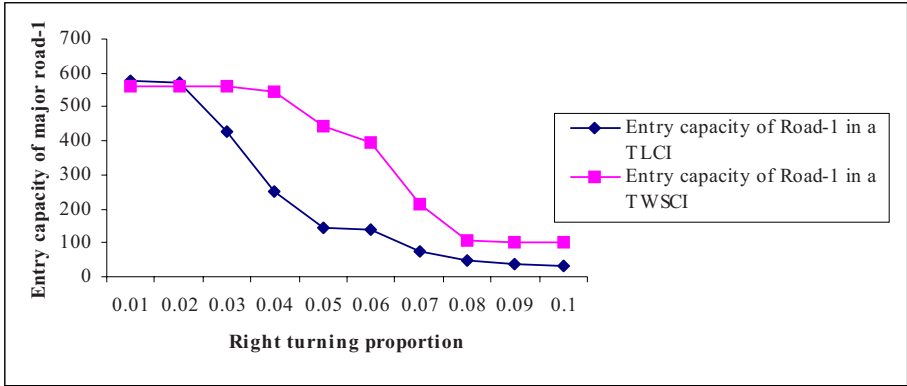


Fig. 3. Entry Capacity of major road1 Vs Right turning rate

Fig. 3 shows, unsurprisingly, that the entry capacity of the major road intersection declines with RTR increase. We conclude that the capacity for mix traffic of the major road declines when the percentage of RTR increases for both TLC and TWSC intersections. TLC entry capacity curve is lower than that for the TWSC intersection, since the TWSC intersection free flow traffic.

4. 2 Proportion of Vehicles at a TLC Intersection

Table 4 illustrates effects of different SV: LV proportions on overall throughputs. In each scenario, the turning rates of all approaches are based on the field data (Table 1). The arrival rate of the two major roads and minor roads are taken to be equal and vary from 0.05 to 0.25 (equivalent to 180 vph to 900 vph). It is found that the throughput of the intersection increases when the traffic is homogeneous (100 percent SV) even if

Table 4. Overall Throughput for different SV: LV mix. All arrival rates (AR) taken to be the same for all roads.

AR _(1,2,3,4)	SV: LV					
	1:0	0.9:0.1	0.8:0.2	0.7:0.3	0.6:0.4	0.5:0.5
0.05	8657	1675	1260	875	767	691
0.1	16021	3274	931	746	668	482
0.15	23911	1242	716	472	377	464
0.2	30362	1152	503	300	250	186
0.25	35697	940	406	191	119	99

the arrival rate is increased. In contrast the heterogeneous traffic throughput decreases with increased arrival rates and proportion of LV in the traffic mix.

4.3 Model Validation

Our model has been validated, by simulating heterogeneous traffic on a single lane road using field data collected by Dublin City Council (ref. Tables 1 and 2). The model was run 50 runs of ten hours and the average result is presented in Tables 5 and 6. The data on Tables 5 and 6 were used and the graph obtained is presented in Fig. 4 and Fig. 5.

Table 5. Comparison of real data of Table1 with simulated Data

Road Number	Turning Rate								
	LTR			STR			RTR		
	*Obs	*Sim	% Error	*Obs	*Sim	% Error	*Obs	*Sim	% Error
Road-1	532	500	-6.01	4160	4243	+1.99	245	251	+2.53
Road-2	387	403	+4.13	1569	1626	+3.63	472	474	+0.42
Road-3	140	156	+11.42	4427	4662	+5.30	374	171	-54.27
Road-4	481	515	+7.06	1526	1593	+4.39	131	50	-61.83

* Obs= Observed and *Sim=Simulated data.

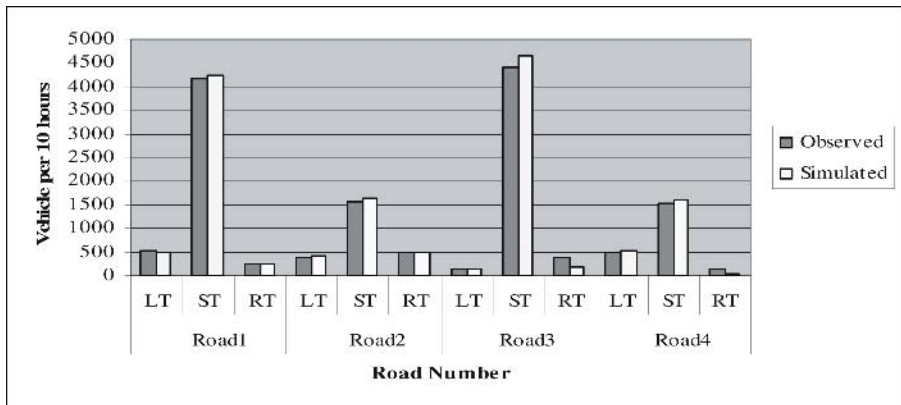


Fig. 4. Model validation (Comparison of Observed and simulated turning data)

It can be shown in Fig. 4 that the simulated data of different turning rates match corresponding observed values well except for the right turning rate (RTR) of roads 3 and 4. The reason is that, in our model we have 2 flow cycle phases i.e., in the first phase roads 1 and 3 have a green light and roads 2 and 4 become red. In the second phase, the lights change colour and movement is allowed for road-2 and road-4 sequentially. So, road-1 and road-2 right turning traffic always takes higher priority than road-2 and road-4 traffic.

Table 6. Comparison of real data of Table2 with simulated Data

Road Number	Traffic composition					
	SV			LV		
	*Obs	*Sim	% Error	*Obs	*Sim	% Error
Road-1	4703	4777	+1.57	234	217	-7.26
Road-2	2391	2456	+2.71	31	47	+51.61
Road-3	4678	4771	+1.98	263	218	-17.11
Road-4	2111	2137	+1.23	27	20	-25.9

* Obs= Observed and * Sim=Simulated data.

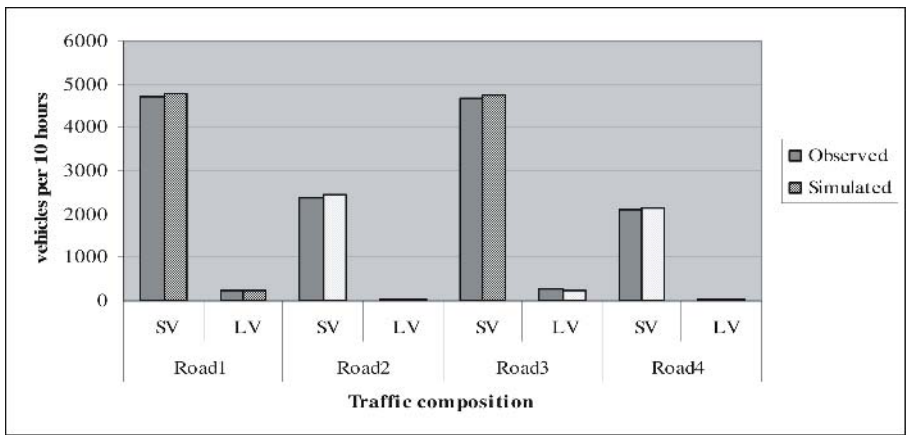


Fig. 5. Model validation (Comparison of Observed and simulated turning data)

As shown in Fig. 5 and Table 6 the simulated value of long vehicle and short vehicle traffic is in reasonable agreement with real traffic data except for road-2 and road-4 long vehicle traffic. Possible reason may be that result is averaged over 50 runs but the real data was collected in just one 10 hour period.

5 Conclusions

In this paper, we have described a prototype two component cellular automata model which attempts to simulate traffic flow at a TWSC and TLC intersection for both homogeneous and heterogeneous traffic in a single lane two-way road. These studies have shown that the throughput and entry capacity of mixed traffic depends on the arrival rate and right turning rates of vehicles, as well as proportion of LV. For exclusively single lane homogeneous traffic 100 percent SV actually leads to better than found for heterogeneous traffic flow. Turning rates and traffic composition have been validated using field data collected by Dublin City Council (1997). The simulation

result show reasonable agreement is found between observed and simulated values, particularly for low proportion of LV.

We developed novel methodology for modelling motorised heterogeneous traffic flow using two-component cellular automata. It has been found that the method of treating vehicles as two different lengths enables replication of the field conditions of mixed traffic flow. Comparison with work of others: we look at heterogeneity for urban traffic features, such as intersection, controlled and uncontrolled and compares with empirical data, as highlighted in the paper, Sections 2.1, 2.2, 2.3 and 4.4. Although limited to date in terms of vehicle type to our knowledge, only linear traffic for a variety of vehicle types has been presented to date [2,3,7] or controlled intersection for a range of vehicle types [5]. Methods used in these examples are not based on detailed consideration of vehicle manoeuvres using cellular automata.

The present CA model has also been used to investigate traffic conditions of both homogeneous (100 percent SV and 100 percent LV) and heterogeneous traffic (SV+LV) flow at urban intersections. It is clear that investigations of the nature and impact of long vehicles in exclusively single lane traffic are vital to understanding urban flows. The change in proportion of such traffic has *strong impact* on these shared roads, which are bottlenecks and dictate feeder traffic flow to larger arterial routes. Future work will examine alternative mixes and saturation factors. Further potential development can thus incorporate the effects of other motorised and non-motorised vehicles (i.e. trucks, cycles respectively) for similar or alternative roadway geometry.

References

1. Daganzo C.F.: Remarks on Traffic Flow Modelling and its Applications, (available on <http://www.ce.berkeley.edu/~daganzo/PAPER.PDF>) [accessed on December 1, 2005]
2. Arasan, V.T, Koshy, R.Z.: Modelling Heterogeneous Traffic flow on Urban Roads, Proceedings of National Conference on Transportation Systems, IIT Delhi (2002), 394-404
3. Koshy, R.Z., Arasan, V.T.: Modelling Stochasticity of Heterogeneous Traffic, Proceedings of the Fourth International Symposium on Uncertainty Modelling and Analysis, ISUMA(2003), IEEE Computer Society
4. Troutbeck, R. J.: Effect of Heavy Vehicles at Australian Traffic Circles and Unsignalised Intersections, Transportation Research Record 1398 (1993), 54-60
5. Arasan, V.T, Jagadeesh, K.: Effect of Heterogeneity of Traffic on Delay at Signalised Intersections, Journal of Transportation Engineering (1995), 397-404
6. Ramanayya, T. V.: Highway Capacity under mixed traffic conditions, Traffic Engineering and control (1988), 284-287
7. Arsan, V. T. and Koshy, R. Z. "Methodology for Modelling Highly Heterogeneous Traffic Flow" Journal of Transportation Engineering (2005), Vol. 131, No. 7, July 1, 544-551
8. Hoogendoon S.P. and Bovy, P.H.L.: Continuum modelling of Multiclass traffic flow, Transportation Research part B (2000), 34, 123-146
9. Logghe, S.: Dynamic Modelling of Heterogeneous Vehicular Traffic", Ph.D. thesis (2003), Katholi University Leuven, Kasteelpark Arenberg 40, B [http:// www.kuleuven.ac.be/traffic/](http://www.kuleuven.ac.be/traffic/)

10. Youn-Soo, K.: Delay, Stop and Queue Estimation for Uniform and Random Traffic Arrivals at Fixed-Time Signalised Intersections”, PhD thesis (2000), Civil Engineering, Virginia Tech, Virginia, USA.
11. Wang, R., Ruskin, H.J: Modelling Traffic Flow at an Urban Unsignalised Intersection, ICCS (2002), LNCS 2329, 381-390.
12. Tian, Z., Troutbeck, R., Kyte, M., Bilon, W., Vandehey, M., Kittelson, W.: Ribinson, B.M. A further investigation on critical gap and follow-up time, Transportation Research Circular **E-C108**: 4th International Symposium on Highway Capacity (2000), 397-408

A New Algorithm for Complex Stochastic Boolean Systems*

Luis González

University of Las Palmas de Gran Canaria,
Department of Mathematics, Research Institute IUSIANI,
35017 Las Palmas de Gran Canaria, Spain
luisglez@dma.ulpgc.es
<http://www.dma.ulpgc.es/profesores/personal/lgs/>

Abstract. Many different complex systems depend on a large number n of mutually independent random Boolean variables. For these systems, each one of the 2^n possible situations is described by its corresponding binary n -tuple, (u_1, \dots, u_n) , of 0s and 1s, and it has its own occurrence probability $\Pr \{(u_1, \dots, u_n)\}$. In this context, this paper provides a simple algorithm for rapidly generating all the binary n -tuples of 0s and 1s whose occurrence probabilities are always greater than or equal to (less than or equal to) the occurrence probability $\Pr \{(u_1, \dots, u_n)\}$ of an arbitrary fixed binary n -tuple $(u_1, \dots, u_n) \in \{0, 1\}^n$. The results can be applied to many stochastic Boolean phenomena related to any scientific, technical or social area. All required previous results are described in detail, so that the presentation is self-contained.

1 Introduction

The study of complex systems is at present one of the most relevant research areas in Computer Science. In this paper, we focus our attention on the complex stochastic Boolean systems, that is, those complex systems which depend on a certain number n of independent random Boolean variables. These systems can appear in any knowledge area, since the assumption “independent random Boolean variables” is satisfied very often in practice (see, e.g., [6]).

Using the statistical terminology, a stochastic Boolean system can be modeled by the n -dimensional Bernoulli distribution. As is well known (see, e.g., [8]), this distribution consists on n random variables x_1, \dots, x_n , which only take two possible values, 0 or 1, with probabilities

$$\Pr \{x_i = 1\} = p_i, \quad \Pr \{x_i = 0\} = 1 - p_i \quad (1 \leq i \leq n).$$

In the following, we assume that the marginal Bernoulli variables x_1, \dots, x_n are mutually independent, so that the probability of occurrence of each binary n -tuple, $u = (u_1, \dots, u_n) \in \{0, 1\}^n$, can be computed as the product

* Partially supported by MEC (Spain) and FEDER. Grant contract: CGL2004-06171-C03-02/CLI.

$$\Pr \{(u_1, \dots, u_n)\} = \prod_{i=1}^n \Pr \{x_i = u_i\} = \prod_{i=1}^n p_i^{u_i} (1 - p_i)^{1-u_i}, \quad (1)$$

that is, $\Pr \{(u_1, \dots, u_n)\}$ is the product of factors p_i if $u_i = 1$, $1-p_i$ if $u_i = 0$. Throughout this paper, the binary n -tuples (u_1, \dots, u_n) of 0s and 1s will be also called binary strings, and the parameters p_1, \dots, p_n of the n -dimensional Bernoulli distribution will be also called basic probabilities.

One of the most relevant questions in the analysis of stochastic Boolean systems consists on ordering the binary strings (u_1, \dots, u_n) by their occurrence probabilities. Of course, the theoretical and practical interest of this question is obvious. For instance, in [1, 4] the authors justify the convenience of using binary n -tuples with occurrence probabilities as large as possible, in order to solve, with a low computational cost, some classical problems in Reliability Theory and Risk Analysis.

In this context, the main goal of this paper is to answer the following question: *Given a certain binary n -tuple $(u_1, \dots, u_n) \in \{0, 1\}^n$, how can we determine the binary n -tuples $(v_1, \dots, v_n) \in \{0, 1\}^n$ whose occurrence probabilities are always greater than or equal to (less than or equal to) $\Pr \{(u_1, \dots, u_n)\}$? A simple algorithm will provide the answer to this question.*

However, this is not a simple question because one thinks that the answer always depends on the basic probabilities or parameters p_1, \dots, p_n , as the following simple example shows.

Example 1. For $n = 4$ and $u = (0, 1, 1, 0)$, $v = (1, 0, 0, 0)$, using (1) we have

$$p_1 = 0.1, p_2 = 0.2, p_3 = 0.3, p_4 = 0.4 : \Pr \{v\} = 0.0336 > \Pr \{u\} = 0.0324,$$

$$p_1 = 0.2, p_2 = 0.3, p_3 = 0.4, p_4 = 0.5 : \Pr \{v\} = 0.042 < \Pr \{u\} = 0.048,$$

so that, depending on the parameters p_i , $\Pr \{v\}$ may be greater than or less than $\Pr \{u\}$.

Consequently, to answer the proposed question it seems necessary to compute a priori all the binary n -tuple probabilities (using formula (1)), and then we can know which of them are greater than or less than $\Pr \{(u_1, \dots, u_n)\}$. But, obviously, this procedure is not feasible due to its exponential complexity: There are 2^n binary n -tuples and, in practice, n use to be very large.

To avoid this obstacle, in [3, 4] the authors have established a simple criterion (the so called *intrinsic order criterion*) that allows us to compare the occurrence probabilities of two given binary strings without computing them, just looking at the positions of their 0s and 1s (see [1, 2] for other theoretical aspects and applications of the intrinsic order criterion).

All the propositions about the intrinsic order established in our previous works [1, 2, 3, 4], as well as the new results we state here, require certain assumptions on the parameters p_i of the n -dimensional Bernoulli distribution. However, it is important to emphasize here that, although these hypothesis are essential for the theoretical model, they are not restrictive for practical applications, as we shall justify in the next section.

This paper has been organized as follows. In order to make this work self-contained, in Sect. 2 we describe all the required background. In Sect. 3, we present our new, unpublished results, which can be summarized in a simple algorithm for answering to the above proposed question. Finally, in Sect. 4, we present some practical applications of our theoretical results.

2 Background in Intrinsic Order

2.1 Notation and Definitions

Definition 1. Let $u = (u_1, \dots, u_n) \in \{0, 1\}^n$.

- The (Hamming) weight of u is the number of “1” bits in u , i.e.,

$$w_H(u_1, \dots, u_n) := \sum_{i=1}^n u_i.$$

- Any binary n -tuple u of weight $m > 0$, whose 1s are placed at the positions $i_1 < \dots < i_m$, will be denoted by the vector of positions of its 1s, i.e.,

$$u := [i_1, \dots, i_m]_n \text{ means that } u_i = 1 \text{ iff } i \in \{i_1, \dots, i_m\}.$$

Definition 2. Let $u = (u_1, \dots, u_n), v = (v_1, \dots, v_n) \in \{0, 1\}^n$.

- The lexicographic order “ \leq_{lex} ” on $\{0, 1\}^n$ is the usual truth-table order between the binary n -tuples, with the convention that $0 < 1$, i.e.,

$$u <_{lex} v \text{ iff the left – most components s.t. } u_i \neq v_i, \text{ are } u_i = 0, v_i = 1.$$

- The decimal numbering or representation of u will be denoted by

$$u_{(10)} := \sum_{i=1}^n 2^{n-i} u_i,$$

so that $u \leq_{lex} v$ iff $u_{(10)} \leq v_{(10)}$.

Definition 3. Let $u = (u_1, \dots, u_n) \in \{0, 1\}^n$ and $S \subseteq \{0, 1\}^n$.

- The complementary n -tuple of u is the n -tuple obtained by changing all its 0s by 1s and all its 1s by 0s, i.e.,

$$(u_1, \dots, u_n)^c := (1 - u_1, \dots, 1 - u_n).$$

- The complementary set of S is the set of the complementary n -tuples of all the n -tuples of S , i.e.,

$$S^c := \{u^c / u \in S\}.$$

Remark 1. In the following, we shall denote any binary n -tuple, indistinctly, by its binary representation, by its decimal representation, or by the vector of positions of its 1s, i.e.,

$$(u_1, \dots, u_n) \equiv u_{(10)} \equiv [i_1, \dots, i_m]_n.$$

For instance, note that the sum of two any complementary n -tuples is always

$$u + u^c = (1, \dots, 1) \equiv 2^n - 1 \equiv [1, \dots, n]_n, \text{ for all } u \in \{0, 1\}^n.$$

Example 2. For $n = 6$ and $u = (1, 0, 1, 1, 1, 0)$ we have

$$w_H(u) = 4, u = [1, 3, 4, 5]_6, u_{(10)} = 46, u^c = (0, 1, 0, 0, 0, 1), u^c <_{lex} u.$$

2.2 The Intrinsic Order Theorem

Now, we present the basic proposition of our model [3, 4], which provides us with a simple criterion to compare the occurrence probabilities of two given binary strings $u, v \in \{0, 1\}^n$ without computing them.

Theorem 1 (The intrinsic order theorem). *Let x_1, \dots, x_n be n mutually independent Bernoulli variables, with parameters $p_i = \Pr\{x_i = 1\}$ ($1 \leq i \leq n$) satisfying:*

$$0 < p_1 \leq \dots \leq p_n \leq \frac{1}{2}. \tag{2}$$

Then, the probability of the n -tuple $(u_1, \dots, u_n) \in \{0, 1\}^n$ is intrinsically greater than or equal to the probability of the n -tuple $(v_1, \dots, v_n) \in \{0, 1\}^n$ (that is, for all set of parameters $\{p_i\}_{i=1}^n$ s.t. (2)) if, and only if, the matrix

$$M_v^u := \begin{pmatrix} u_1 & \dots & u_n \\ v_1 & \dots & v_n \end{pmatrix}$$

either has no $\binom{1}{0}$ columns, or for each $\binom{1}{0}$ column there exists (at least) one corresponding preceding $\binom{0}{1}$ column.

Remark 2. In the following, we assume that the parameters p_i always satisfy condition (2). Note that this hypothesis is not restrictive for practical applications because, if for some $i : p_i > \frac{1}{2}$, then we only need to consider the variable $\bar{x}_i = 1 - x_i$, instead of x_i . Next, we order the n Bernoulli variables by increasing order of their probabilities.

Remark 3. The $\binom{0}{1}$ column preceding to each $\binom{1}{0}$ column is not required to be necessarily placed at the immediately previous position, but just at previous position.

Remark 4. The term *corresponding*, used in Theorem 1, has the following meaning: For each two $\binom{1}{0}$ columns in matrix M_v^u , there must exist (at least) two

different $\binom{0}{1}$ columns preceding to each other. In other words: For each $\binom{1}{0}$ column in matrix M_v^u , the number of preceding $\binom{0}{1}$ columns must be strictly greater than the number of preceding $\binom{1}{0}$ columns.

The condition “ M_v^u has no $\binom{1}{0}$ columns, or for each $\binom{1}{0}$ column there exists (at least) one *corresponding* preceding $\binom{0}{1}$ column”, stated by Theorem 1, is called the *Intrinsic Order Criterion* (IOC), because it is independent of the basic probabilities p_i and it depends only on the relative positions of the 0s and 1s in the binary n -tuples u, v . Theorem 1 naturally leads to the following partial order relation on the set $\{0, 1\}^n$. The so called intrinsic order, will be denoted by “ \succeq ”, and we shall write $u \succeq v$ ($u \preceq v$) to indicate that u is intrinsically greater (less) than or equal to v .

Definition 4. For all $u, v \in \{0, 1\}^n$

$u \succeq v$ iff $\Pr\{u\} \geq \Pr\{v\}$ for all set $\{p_i\}_{i=1}^n$ s.t. (2) iff M_v^u satisfies IOC.

Example 3. $(0, 0, 1, 1) \succeq (1, 1, 0, 0)$ because matrix

$$\begin{pmatrix} 0 & 0 & 1 & 1 \\ 1 & 1 & 0 & 0 \end{pmatrix}$$

satisfies IOC (Remark 3). Then

$$\Pr\{(0, 0, 1, 1)\} \geq \Pr\{(1, 1, 0, 0)\}, \text{ for all } 0 < p_1 \leq p_2 \leq p_3 \leq p_4 \leq \frac{1}{2}.$$

Example 4. $(0, 1, 1, 0) \not\succeq (1, 0, 0, 0)$ and $(1, 0, 0, 0) \not\succeq (0, 1, 1, 0)$ because

$$\text{neither } \begin{pmatrix} 0 & 1 & 1 & 0 \\ 1 & 0 & 0 & 0 \end{pmatrix}, \text{ nor } \begin{pmatrix} 1 & 0 & 0 & 0 \\ 0 & 1 & 1 & 0 \end{pmatrix}$$

satisfies IOC (Remark 4). Then, the ordering between the occurrence probabilities $\Pr\{(0, 1, 1, 0)\}$ and $\Pr\{(1, 0, 0, 0)\}$ depend on the basic probabilities p_i , as Example 1 has shown.

Example 5. For all $(u_1, \dots, u_n) \in \{0, 1\}^n$

$$0 \equiv (0, \dots, 0) \succeq (u_1, \dots, u_n) \succeq (1, \dots, 1) \equiv 2^n - 1,$$

because the matrices

$$\begin{pmatrix} 0 & \dots & 0 \\ u_1 & \dots & u_n \end{pmatrix} \text{ and } \begin{pmatrix} u_1 & \dots & u_n \\ 1 & \dots & 1 \end{pmatrix}$$

satisfy IOC, since they have no $\binom{1}{0}$ columns. Then, for all $u \in \{0, 1\}^n$

$$\Pr\{(0, \dots, 0)\} \geq \Pr\{u\} \geq \Pr\{(1, \dots, 1)\}, \text{ for all } 0 < p_1 \leq \dots \leq p_n \leq \frac{1}{2}.$$

The simple matrix description IOC of the intrinsic order (Theorem 1) allows us to derive many necessary and/or sufficient conditions for intrinsic order [2]. Anyway, for the purpose of this paper the following two necessary conditions are enough (see [2, 4] for the proof).

Corollary 1. For all $u, v \in \{0, 1\}^n$

$$u \succeq v \Rightarrow u_{(10)} \leq v_{(10)} \text{ and } w_H(u) \leq w_H(v).$$

2.3 The Intrinsic Order Graph

Since the intrinsic order (Definition 4) is a partial order relation on the set $\{0, 1\}^n$, we can represent, as usual, the partially ordered set $(\{0, 1\}^n, \succeq)$ by the classical Hasse diagram (see, e.g., [7] for more details about partially ordered sets and Hasse diagrams). This is a directed graph in which every pair (u, v) of vertices connected either by an edge ($u \rightarrow v$), or by a path (sequence of consecutive edges $u \rightarrow \dots \rightarrow v$) means that $u \succeq v$. On the contrary, each pair (u, v) of nonconnected vertices means that its elements are incomparable by intrinsic order, i.e., $u \not\succeq v$ and $u \not\preceq v$.

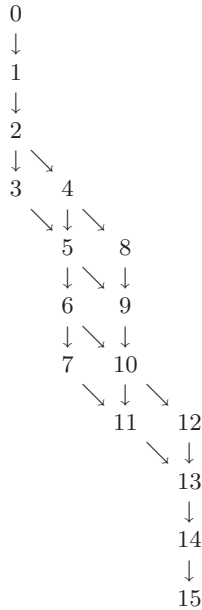


Fig. 1. The intrinsic order graph for $n = 4$

In Fig. 1 we present the Hasse diagram of $(\{0, 1\}^4, \succeq)$. All the binary 4-tuples are denoted by their decimal numbering (Definition 2, Remark 1), and this simple graph can be constructed by direct application of IOC. For instance, looking at Fig. 1 we can confirm that $3 \equiv (0, 0, 1, 1) \succeq (1, 1, 0, 0) \equiv 12$ (Example 3), while $6 \equiv (0, 1, 1, 0)$ and $8 \equiv (1, 0, 0, 0)$ are incomparable by intrinsic order (Example 4). See [2] for more properties of the intrinsic order graph.

3 The Algorithm

Let $u \in \{0, 1\}^n$ be an arbitrary, fixed binary n -tuple, and let us denote

$$S^u := \{v \in \{0, 1\}^n / u \succeq v\} = \{v \in \{0, 1\}^n / \Pr(u) \geq \Pr(v), \forall p_i \text{ s.t. (2)}\},$$

$$S_u := \{v \in \{0, 1\}^n / u \preceq v\} = \{v \in \{0, 1\}^n / \Pr(u) \leq \Pr(v), \forall p_i \text{ s.t. (2)}\}.$$

With this notation, the central question of this work, that is: *How can we identify the binary n -tuples $v \in \{0, 1\}^n$ whose occurrence probabilities are always greater than or equal to (less than or equal to) $\Pr\{u\}$?*, can be reformulated in a more precise and simple way. Now the question is: *How can we characterize, in an efficient way, the sets S^u and S_u ?* That is, the term “always” in the initial formulation of our question has the precise meaning of “intrinsically”, because the hypothesis (2) is not restrictive (Remark 2).

First, we focus our attention onto the set S^u . At the end of this section we shall see that if we can characterize the set S^u , then the characterization of the set S_u will be obvious via complementary n -tuples (Definition 3).

With respect to the set S^u , we begin noting that, according to Corollary 1, we have

$$u \succeq v \Rightarrow u_{(10)} \leq v_{(10)} \Leftrightarrow u \leq_{lex} v, \text{ i.e.,}$$

$$\forall u \in \{0, 1\}^n : S^u = \{v \in \{0, 1\}^n / u \succeq v\} \subseteq \{v \in \{0, 1\}^n / u_{(10)} \leq v_{(10)}\}, \quad (3)$$

that is, the set S^u of binary n -tuples intrinsically less than or equal to u is included in the set of binary n -tuples whose decimal numbering are greater than or equal to the decimal numbering of u . Sometimes, the equality holds in the inclusion (3). This happens, for instance, for the two following special cases

$$u = (0, \dots, 0) \equiv 0, \quad u = (1, \dots, 1) \equiv 2^n - 1,$$

for which

$$S^0 = \{0, 1\}^n = \{v \in \{0, 1\}^n / 0 \leq v_{(10)}\}, \quad (4)$$

$$S^{2^n-1} = \{2^n - 1\} = \{v \in \{0, 1\}^n / 2^n - 1 \leq v_{(10)}\}, \quad (5)$$

since $(0, \dots, 0) \equiv 0$ and $(1, \dots, 1) \equiv 2^n - 1$ are the maximum and minimum elements, respectively, of the partially ordered set $(\{0, 1\}^n, \preceq)$, as shown in Example 5 and as illustrated in Fig. 1.

Now, we establish our main result in the next theorem. This theorem provides us with a simple algorithm for rapidly generating all the binary strings belonging to the set S^u , for all $u \in \{0, 1\}^n$. The binary n -tuples generated by the algorithm are represented by the vectors of positions of their “1” bits. The extreme cases $u = 0$, $u = 2^n - 1$ are not considered in the algorithm, since they have already been solved (equations (4) and (5), respectively).

Theorem 2 (The algorithm). *Let $u \in \{0,1\}^n$, $u \neq 0, 2^n - 1$, with weight $w_H(u) = m$ ($0 < m < n$). Let $u = [i_1, \dots, i_m]_n$ be the vector of positions of 1s of u . Then S^u is the set of binary n -tuples $v = [j_1, \dots, j_t]_n$ of weight t ($m \leq t \leq n$) generated by the following algorithm:*

```

(i) Step 1 (Generation of the  $n$ -tuples of weight  $t = m$ ) :
    For  $j_1 = 1$  to  $i_1$  Do:
        For  $j_2 = j_1 + 1$  to  $i_2$  Do:
            .....
                For  $j_m = j_{m-1} + 1$  to  $i_m$  Do:
                    Write  $v := [j_1, \dots, j_m]_n$ 
                EndDo
            .....
        EndDo
    EndDo
EndDo

(ii) Steps  $2, \dots, n-m+1$  (Generation of the  $n$ -tuples of weight  $t = m + 1, \dots, n$ ) :
    For  $t = m + 1$  to  $n$  Do:
        For all  $n$ -tuple  $[j_1, \dots, j_{t-1}]_n$  with weight  $t-1$  (generated by the previous
        step  $t-m$ ) s.t.  $j_{t-1} < n$ , Do:
            For  $j_t = j_{t-1} + 1$  to  $n$  Do:
                Write  $v := [j_1, \dots, j_{t-1}, j_t]_n$ 
            EndDo
        EndDo
    EndDo
EndDo
    
```

Proof. From Corollary 1 we get

$$v \in S^u \Leftrightarrow u \succeq v \Rightarrow m = w_H(u) \leq w_H(v) = t,$$

and since the maximum weight of a binary n -tuple v is n , we get

$$m \leq w_H(v) = t \leq n,$$

and that is why the algorithm described by Theorem 2 consists on $n - m + 1$ steps, $1, 2, \dots, n - m + 1$, which respectively correspond to the $n - m + 1$ possible weights, $m, m + 1, \dots, n$, of the generated n -tuples $v \in S^u$.

Now, note that the matrix description IOC (Theorem 1) of the intrinsic order (expressed in terms of the binary representations of u, v) can be reformulated (in terms of the vectors of positions of the “1” bits of u, v) as follows:

$$u = [i_1, \dots, i_m]_n \succeq [j_1, \dots, j_t]_n = v$$

if, and only if, v contains at least one “1” bit among the positions 1 and i_1 , at least two “1” bits among the positions 1 and i_2, \dots , at least $m - 1$ “1” bits among the positions 1 and i_{m-1} , and at least m “1” bits among the positions 1 and i_m . We distinguish the following two cases:

(i) Generation of the n -tuples $v = [j_1, \dots, j_m]_n \in S^u$, that is, those n -tuples v with weight m , such that $u \succeq v$. Since these n -tuples have exactly m “1” bits

then, according to the above positional description of IOC, they are characterized by the conditions: v contains at least one “1” bit among the positions 1 and i_1 , at least two “1” bits among the positions 1 and i_2, \dots , at least $m - 1$ “1” bits among the positions 1 and i_{m-1} , exactly m “1” bits among the positions 1 and i_m , and it has no “1” bits among the positions i_{m+1} and n . But, obviously, these conditions are equivalent to the ones described by the step 1 of the algorithm.

(ii) Generation of the n -tuples $v = [j_1, \dots, j_t]_n \in S^u$ ($m < t \leq n$), that is, those n -tuples v with weight t greater than m , such that $u \succeq v$. For each fixed weight $t = m + 1, \dots, n$, all the n -tuples $v_t = [j_1, \dots, j_{t-1}, j_t]_n \in S^u$, of weight t , can be generated by replacing one “0” bit by one “1” bit at any of the positions $j_{t-1} + 1, \dots, n$ of any n -tuple $v_{t-1} = [j_1, \dots, j_{t-1}]_n \in S^u$, of weight $t - 1$, such that $j_{t-1} < n$. This happens because the substitution of 0s by 1s in any n -tuple v such that $u \succeq v$ does not avoid the IOC condition. In particular:

$$\begin{aligned} v_{t-1} \in S^u &\Leftrightarrow u \succeq v_{t-1} \Leftrightarrow M_{v_{t-1}}^u \text{ satisfies IOC} \\ &\Leftrightarrow M_{v_t}^u \text{ satisfies IOC} \Leftrightarrow u \succeq v_t \Leftrightarrow v_t \in S^u. \end{aligned}$$

Since this procedure obviously generates all the n -tuples $v_t \in S^u$ with weight $t = m + 1, \dots, n$, without repetitions (from the n -tuples $v_{t-1} \in S^u$ with weight $t - 1$ such that $j_{t-1} < n$), and it is equivalent to the procedure described by the steps $2, \dots, n - m + 1$ of the algorithm, the proof is concluded. \square

The characterization of the set S_u follows immediately from the characterization of the set S^u (stated by Theorem 2), as the following theorem shows.

Theorem 3. For all $u \in \{0, 1\}^n$: $S_u = (S^{u^c})^c$.

Proof. The $\binom{0}{0}, \binom{1}{1}, \binom{0}{1}$ and $\binom{1}{0}$ columns in matrix M_u^v respectively become $\binom{1}{1}, \binom{0}{0}, \binom{0}{0}$ and $\binom{1}{0}$ columns in matrix $M_{v^c}^{u^c}$. Therefore, M_u^v satisfies IOC if, and only if, $M_{v^c}^{u^c}$ satisfies IOC. Consequently, we get

$$\begin{aligned} v \in S_u &\Leftrightarrow u \preceq v \Leftrightarrow M_u^v \text{ satisfies IOC} \Leftrightarrow M_{v^c}^{u^c} \text{ satisfies IOC} \\ &\Leftrightarrow u^c \succeq v^c \Leftrightarrow v^c \in S^{u^c} \Leftrightarrow v \in (S^{u^c})^c, \end{aligned}$$

as was to be shown. \square

Remark 5. Obviously: $\{v \in \{0, 1\}^n / u \not\preceq v, u \not\preceq v\} = \{0, 1\}^n - (S^u \cup S_u)$.

Example 6. Let $n = 4$ and $u = (0, 1, 1, 0) \equiv 6$. Then

$$m = w_H(u) = 2 \text{ and } u = [i_1, i_2]_4 = [2, 3]_4.$$

On one hand, using Theorem 2 we get

$$\begin{aligned} S^6 &= \left\{ v \in \{0, 1\}^4 / 6 \succeq v \right\} \\ &= \{[1, 2]_4, [1, 3]_4, [2, 3]_4\} \cup \{[1, 2, 3]_4, [1, 2, 4]_4, [1, 3, 4]_4, [2, 3, 4]_4\} \cup \{[1, 2, 3, 4]_4\} \end{aligned}$$

$$= \{12, 10, 6, 14, 13, 11, 7, 15\} = \{6, 7, 10, 11, 12, 13, 14, 15\}.$$

On the other hand, using Theorems 3 and 2 we get

$$\begin{aligned} S_6 &= \{v \in \{0, 1\}^4 / 6 \preceq v\} = (S^{6^c})^c = (S^9)^c \\ &= (\{[1, 2]_4, [1, 3]_4, [1, 4]_4\} \cup \{[1, 2, 3]_4, [1, 2, 4]_4, [1, 3, 4]_4\} \cup \{[1, 2, 3, 4]_4\})^c \\ &= \{12, 10, 9, 14, 13, 11, 15\}^c = \{3, 5, 6, 1, 2, 4, 0\} = \{0, 1, 2, 3, 4, 5, 6\}. \end{aligned}$$

Finally, the 4-tuples incomparable by intrinsic order with $u = 6$ are

$$\{v \in \{0, 1\}^4 / 6 \not\preceq v, 6 \not\preceq v\} = \{0, 1\}^4 - (S^6 \cup S_6) = \{8, 9\},$$

and Fig.1 illustrates the sets S^6, S_6 and $\{0, 1\}^4 - (S^6 \cup S_6)$.

4 Applications

Our approach can be applied to real complex stochastic Boolean systems as follows. (i) Redefine the n original Boolean variables x_i of the system so that all their probabilities p_i are less than or equal to 0.5. For this purpose, call: $y_i = x_i$ if $p_i \leq 0.5$, and $y_i = 1 - x_i$ if $p_i > 0.5$. Next, order the Boolean variables y_i by increasing order of their probabilities. In this way we assure condition (2), according to Remark 2, that is, denoting by z_i the new ordered variables we get: $0 < p_1 \leq \dots \leq p_n \leq 0.5, p_i = \Pr\{z_i = 1\} (1 \leq i \leq n)$. (ii) For each given n -tuple $u = (z_1, \dots, z_n)$, represent u by the vector of positions of its 1s (Definition 1) and then apply Theorems 2 and 3 to obtain the sets S^u, S_u and $\{0, 1\}^n - (S^u \cup S_u)$, as illustrated by Example 6. The main advantages are: (a) We do not need to compute the binary n -tuple probabilities $\Pr\{v\}$ (not even $\Pr\{u\}$ need to be evaluated!). (b) Our method drastically reduces the high computational cost of sorting algorithms usually employed for the same task, from ordering 2^n binary n -tuples to ordering n Boolean variables. (c) Our approach is unified, valid for all stochastic Boolean systems depending on n independent Boolean variables.

Among the many different application areas where stochastic Boolean systems appear, we can mention, for instance [5]: Artificial Intelligence; Behavioral and Social Sciences; Biological Processes; Chemical Industry; Cybernetics; Economics and Cost Analysis; Environment Pollution; Financial Systems; Fuzzy Logic; Geosciences; Meteorology and Climatology; Nuclear Physics; Operations Research; Reliability Theory; Risk Analysis; Robotics; Traffic Flow, etc. Furthermore, the results may be also applied in Fault Tree Analysis for evaluating stochastic Boolean functions [4, 6] and, in particular, for estimating the unavailability of many different technical systems [5, 6].

References

1. González, L.: A new method for ordering binary states probabilities in Reliability and Risk Analysis. *Lect. Notes Comput. Sc.* **2329**(1) (2002) 137-146
2. González, L.: N-tuples of 0s and 1s: Necessary and sufficient conditions for intrinsic order. *Lect. Notes Comput. Sc.* **2667**(1) (2003) 937-946
3. González, L., Galván, B., García, D.: Sobre el análisis computacional de funciones Booleanas estocásticas de muchas variables. In: González, L., Sendra, J.R. (eds.): *Proc. Primer Encuentro de Álgebra Computacional y Aplicaciones (EACA-95)*. Santander (1995) 45-55
4. González, L., García, D., Galván, B.J.: An intrinsic order criterion to evaluate large, complex fault trees. *IEEE Trans. Reliability* **53**(3) (2004) 297-305
5. National Aeronautics and Space Administration: *Fault Tree Analysis: A Bibliography*. Technical report NASA/SP-2000-6111 (2000)
6. Schneeweiss, W.G.: *Boolean Functions with Engineering Applications and Computer Programs*. Springer-Verlag, Berlin Heidelberg New York (1989)
7. Stanley, R.P.: *Enumerative Combinatorics. Volume 1*. Cambridge University Press, Cambridge (1997)
8. Stuart, A., Ord, J.K.: *Kendall's Advanced Theory of Statistics. Volume 1: Distribution Theory*. Oxford University Press, New York (1998)

Theoretical Steps Towards Modelling Resilience in Complex Systems

Cathy Hawes¹ and Chris Reed²

¹ Scottish Crop Research Institute, Invergowrie, Dundee, DD2 5DA
chawes@scri.ac.uk

² Department of Applied Computing, University of Dundee, Dundee, Scotland, DD1 4HN
chris.reed@computing.dundee.ac.uk

Abstract. This paper reports on theoretical work aimed at providing a harmonious set of tools for tackling the thorny problem of resilience in complex systems. Specifically, key features of resilience are laid out, and the ramifications on necessary theoretical and implementational machinery are analysed. These ramifications constitute a problem definition that, to the authors' knowledge, no extant system is sufficiently sophisticated to meet. It is, however, possible to identify existing components that can be combined to provide the necessary expressivity. In particular, theoretical ecology has individual based modelling approaches that are consonant with artificial intelligence techniques in multi-agent systems, and in philosophical logic, channel theory provides a mechanism for modelling both system energy and system information flow. The paper demonstrates that it is possible to integrate these components into a coherent theoretical framework, laying a foundation for implementation and testing.

1 Overview

Resilience is a property of complex systems that is widely used in describing such systems in both ecological theory and computational practice. In ecology, however, the term is used to refer to a wide variety of different phenomena, and in computer science it is often used either as a synonym of robustness or fault tolerance. In neither domain is resilience consistently or universally defined, and it is often employed simply to appeal to a reader's intuitions. The intuitions to which it appeals concern the ability of a large, complex system to recover from disturbance, to withstand external perturbation, to evolve, and to adapt. It seems, therefore, to be describing a set of properties that are essential measures of the health of a system, and therefore to be relevant not only in academic theory but also in public and political arenas.

Though there are many models of system change and resilience in ecology, and many applications of computational techniques to ecological systems, there are few that unite the two disciplines, placing ecological interactions at the heart of new computational algorithms.

The project of which this work forms a part aims to take ecological approaches to system function, and individual-based modelling in particular, as a starting point for

development of a massively scaled multi-agent system that uses inter-agent communication to model the flow of energy through the system. The close analogy between energy flow and information flow is employed to build a bridge between ecological and computational theory, and to provide a basis for a domain-independent definition of resilience (generalising conclusions of, e.g. [1]). The system implementation and resilience analysis protocol will first be validated by comparison with existing ecological data, before then being applied to new problems of larger, more complex ecosystems, and thence to similar problems of large scale distributed and Grid computing. In this way, we aim to develop a practical theory of resilience which can be reused in the design of artificial complex systems in eScience and e-commerce domains.

2 Motivation

There are a wide variety of platforms designed for modelling of complex systems using discrete events and, often, employing multi-agent systems as an enabling technology. One of the most mature is the Swarm platform [2] that aims to provide a generic platform for simulation, though other more recent developments extend and specialise these techniques to social simulation [3] and ecology [4]. These systems aim to provide an environment in which domain experts (e.g. sociologists or ecologists) can construct simulation models rapidly and easily. This inevitably has an impact upon the expressiveness of the languages they provide. In particular, previous approaches have omitted some or all of the following features:

- An explicit dynamic environment
- Agentive models (by which individuals might maintain partial, local, representations of their environment)
- Spatial extent (with individuals occupying different – and changing – volumes in the environment)
- Proactive behaviour (in which individuals' activities are not determined solely by Markovian reactive rules)
- Information flow (by which the transfer of energy, artefacts or data between individuals can be modelled)
- Dynamic topology (whereby the agents with which another can communicate change over time)

Bordini et al. [3] use ELMS to model the environment, but have no mechanism for capturing spatial extent; Swarm agents can model consumption, but act only reactively in a (primarily) static environment [4]; DSDEVs [5] can handle dynamic topology, but models only simple reactions, and so on. In order to explore the emergent character of resilience in both ecological and other complex systems, every one of these features is indispensable, and will be integrated into a single framework here. The resulting sophistication of the model as a whole is likely to limit its use to teams involving not only domain specialists but also computer scientists, but will allow those teams to probe fundamental questions of the properties of complex systems that previous approaches have simply not supported.

3 Foundation

The work builds upon three key notions: (i) using agents in a multi-agent system to model individuals in an ecosystem; (ii) modelling energy flow as information flow; (iii) supporting the primary ecological interactions (trophic, competitive, sexual and mutualistic) between system components in a common modelling framework.

Using agents for individual based modelling. Individual based modelling (IBM) is becoming established as a novel way of exploring ecosystem structure and function [6]. Multi agent systems (MAS) offer a computational platform upon which to construct decentralised distributed processing software [7]. Here, agents are used to embody the processing and characteristics corresponding to an individual. The paradigm of multi-agent system development offers a convenient computational metaphor for exploring individual behaviour and, in particular, the relationships between individuals.

Modelling energy flow as information flow. Energy flow is a powerful fundamental mechanism in describing ecosystem function [8]. Recent advances in multi-agent systems focus on semantically rich models of information flow to enhance robustness, fault tolerance and openness [9]. We can employ a mapping between these two to harness the developments in the latter to produce models of the former with greater explanatory power.

Complex interactions as inter-agent communication. Encounters between individuals in an ecosystem can be of four main types: (i) interactions involving energy flow (trophic); (ii) competition for resources (competitive); (iii) reproduction (sexual); and (iv) synergistic collaboration (mutualistic). Under different terminology, competitive and mutualistic interactions have formed the focus of much work in multi-agent systems, with the game theoretic approach often focusing on the former [10] and the distributed AI approach focusing on the latter [7]. Many recent systems have brought together the cooperative and competitive facets in fecund new research, with the Trading Agent Competition a now well-established example [11]. Building on these foundations, the two remaining classes of interaction are also directly implementable using the same principles. Trophic exchange can be modelled through a negotiation over energy flow; the semantics of that communication are then not denotational in the usual Tarskian sense, but rather directly operational in the fabric of the environment in which the agents operate. Sexual interaction is modelled similarly except that rather than negotiating over the flow of energy, agents instead negotiate of the exchange of genetic material.

4 Framework

The environment is structured as a set of contiguous, spatially explicit 3D cells characterised by a number of fixed and variable properties (including size, location and topography amongst the former and temperature and radiation amongst the latter). These cells can be managed by a class of “environment” agents to simplify

implementation (though could be implemented as part of the structure of the environment itself given recent models of agent environments [3]).

Individual organisms within an environment are modelled by agents, but by itself, this is not sufficient for capturing spatial identity (i.e. location) and spatial extent (i.e. size). To model such spatial characteristics, agents are responsible for *projecting* the appropriate properties of the individual they represent into the physical, perceivable environment. Specifically, an agent that represents an individual that is located within an environment cell must communicate the appropriate properties of the individual to that cell, and similarly if the individual has spatial extent across multiple cells, then its properties must be communicated to all those cells. The properties that must be projected into the environment include chemical, physical and chromatic facets. So, for example, an agent representing an oil seed rape individual might project glucosinolates amongst its chemical properties, waxy surface amongst its physical properties and 80% reflected light in the 510nm band amongst its chromatic properties. An agent representing an aphid might similarly project honeydew and 60% reflected light in the 490nm band. Though the approach could be extended to handle a more detailed account of the three classes of properties, or indeed a richer range of properties, this level of abstraction suffices for exploring a range of interesting phenomena in high detail.

Agents interact with the environment and each other through a simple perceive-interpret-act cycle. Perception is straightforwardly characterisable as information flow, which in this model is implemented through communication, and in this case, communication with the environment (agents). Interpretation is the integration and interpretation of percepts with existing knowledge, a process entirely internal to individual agents, and one which concludes with the determination of appropriate action (including null actions). Finally, an agent's action is executed through the appropriate communication with either the environment (agents), other agents representing individuals, or both.

Agent communication is typically marshalled in traditional multi-agent systems through lookup services of one sort or another (JADE for example uses JINI [12]). Without further restrictions, any one agent in the system might communicate with any other. Here, agent communication is marshalled through a combination of the environment and an agent's own capabilities. So the possibility of communication between two individuals depends upon their spatial proximity and their innate communication capabilities.

The outcome of an initial, information-gathering communication between two agents will depend on the interpretation of that information and can take one of four forms: competitive, mutualistic, trophic or sexual.

Competition in ecosystems occurs through interference (direct, physical interaction) or exploitation (indirect, via utilisation of a shared resource). If a caterpillar consumes a leaf, there is no phloem for an aphid to consume; the caterpillar has exploited the resource to the detriment of the aphid, resulting in the indirect, exploitation type of competition. Such exploitation does not need to be modelled explicitly as this interaction operates solely through a change in resource availability handled by the extant modelling machinery. Interference competition, in contrast, involves a direct, aggressive encounter in which one individual threatens another (in territorial disputes, for example). This type of competition demands explicit handling

in the model, through negotiation between individual agents based on perceived ownership and defence capabilities. Limitation of resources and subsequent dispute over those resources (whether explicit as interference, or implicit as exploitation) has been a fundamental part of the dynamics that drive scenarios tackled by agent systems. From early competitive tendering models such as CNET [13], through rich academic environments such as TAC [11], to commercial marketplace and auction protocol design [10], the ways in which resource limitation can drive sophisticated agent dialogue are well known. Rather less common are mechanisms by which agents can specifically employ the techniques of interference competition in making threats to disadvantage competitors (see, e.g. [14]). In those models the felicitous performance of a threat is dependent upon social relationships between agents, here they are dependent upon the ecological counterparts to those relationships.

Mutualism is handled in a similar way to interference competition, but rather than an aggressive encounter, negotiation is used to the benefit of both partners. Models of cooperative problem solving (such as [7]) explore many aspects of mutualism, but all are characterised by a strong focus on the reasoning capabilities of the individuals, and the communication structures by which they reach joint plans. This focus on information exchange and representation forms a cornerstone of the approach proposed here.

Trophic interactions concern the identification of one individual as food by another. In the model, they occur where the agent *perceives* the projection of another agent in the same environment cell, *interprets* this projection as an appropriately available food resource, and *acts* by requesting an amount of that resource from the perceived agent. An agent's food requirement and degree of specialism is defined in the set of internal properties of that agent.

Sexual interactions are not usually modelled (see [15] for a rare example) because they result in an open system in which agents can come into existence (and usually also terminate). Agent creation on-the-fly is also rarely tackled in academic work for the more prosaic reason that it is seldom an important or technically challenging part of a system. It is included here both for completeness and to support future extensions in adaptation.

Finally, all forms of interaction (competitive, mutualistic, trophic, sexual between individuals, and projective and perceptive between individuals and the environment) are mediated through *device constraints*. An individual without a device sensitive to light cannot detect chromatic percepts; an individual with a dermis-puncturing device may be able to consume sap, etc. Device constraints can be expressed as agent-relativised infomorphisms in Channel Theory [16]. In essence, an agent A might implement an infomorphism between a physical, environmental relation \mathbb{F}_{phys} that maps states of the world onto vectors of values representing the environment in that state, and its own perceptual relation $\mathbb{F}_{A-Percepts}$ corresponding to how the agent perceives that state of the world (and thereby its own internal representation of the state). This approach allows the model to capture the intuition that the information is “there”, regardless of whether or not a particular agent is able to perceive and internalise it. A key technical novelty of this work is that consumption is modelled in exactly the same way, leading to parsimony and simplicity in implementation: the same agent A maintains a second infomorphism, $\mathbb{F}_{A-Consumes}$, from what exists in the environment to what it (decides to) consume.

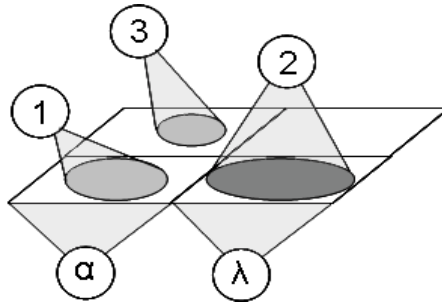


Fig. 1. Model schematic

To illustrate how these components fit together, a simple scenario involving perception and trophic interaction is presented (illustrated in Figure 1). At the first step, individual agent 1 (I_1) requests from environment agent α (E_α) a list of the properties associated with that part of the environment:

- (1) $I_1 \rightarrow E_\alpha$: perception-request “What properties are in this locale?”
- (2) $E_\alpha \rightarrow I_1$: $s_1 \varepsilon_{phys} < (I_1, \{...\}) > \Rightarrow_{f1}$
 $s_1' \varepsilon_{I1-Percepts} < \text{empty} >$ “None other than yours.”
- (3) I_1 Interpretation: no resources available, internal food store sub-optimal, current plan is foraging. The appropriate action is to move.
- (4) $I_1 \rightarrow E_\alpha$: remove-projection “Delete my properties from your locale.”
- (5) $I_1 \rightarrow E_\lambda$: add-projection($I_1, \{...\}$) “Add my properties to your locale.”
- (6) $I_1 \rightarrow E_\lambda$: perception-request “What properties are in this locale?”
- (7) $E_\lambda \rightarrow I_1$: $s_2 \varepsilon_{phys} < (I_1, \{...\}), (I_2, \{...\}) > \Rightarrow_{f2}$
- (8) $s_2' \varepsilon_{I1-Percepts} < (I_2, \{\text{glu, waxy, green}\}) >$
 “There is an individual projecting glucosinolates, waxy surface, 80% reflection at 510nm”
- (9) I_1 Interpretation: I_2 projection matches food profile. Appropriate action is to eat.
- (10) $I_1 \rightarrow I_2$: $s_3 \varepsilon_{I1-Energy} < (+I_2, \{1\text{ml-of-sap}\}) > \Rightarrow_{f3}$
 $s_3' \varepsilon_{I2-Energy} < (-I_1, \{...\}) >$ Transfer energy by consuming sap.

The agent communication language is simple, comprising a few key primitives (such as *perception-request*), and the ability to exchange logical structures instantiating channel theoretic classifications, for example, that a given state is of a type with a given vector of variables. State types are described by a vector of individual / property-set pairs, in which property sets are arbitrarily complex descriptions of individuals (as trivial as a statement of the individual's volume, or as complex as a description of its chemical make-up). Communication is summarised by the application of an infomorphism (marked \Rightarrow_f) implemented in the recipient agent.

At step (1) I_1 initiates a perception event, the response to which at (2) is the description of the state of the environment managed by environment agent α . The physical classification of this state (by ε_{phys}) is one which includes only I_1 ; in I_1 's own classification (reached by the infomorphism $f1$), this is a state with no individuals present (that is, it ignores the part of the environment occupied by itself). At (3), its own local logic responds (in this case reactively, but including reference to the current intentional state) producing an appropriate action. After moving, its perception at (7)

identifies another individual I_2 characterised by a set of percepts that at (8) it associates with food. At (9) it performs an energy transfer (that is it consumes some of I_2). It formulates its “request” according to its own local logic (that is, according to its own consumption device constraints), but for I_2 the request may have a different interpretation, built from the infomorphism f_3 .

In this way, the energy flow in the ecosystem is modelled by the exchange of information between the two agents, with the formal similarity between steps (7) and (9) emphasising the similar treatment of energy flow and perceptual data flow. Though the consumed agent (I_2) is compelled by the semantics of the interaction to release some energy package, the nature of that package is determined by three things: (i) the consumption device by which it has been requested; (ii) I_2 's own status; and (iii) I_2 's own predefined tailored response. In particular, this final component allows for modelling responses in which *permanent* defences are employed (such as a plant maintaining levels of chemical defences in its phloem, or waxes on its leaf surface). *Induced* defences, in which a response is produced dynamically, can also be accounted for through I_2 's internal processing in its immediate and subsequent interpretation phases.

The individuals and the infomorphisms that they embody represent packages of functional traits. System level properties emerge from the combination of these traits represented by the individuals and the interactions between them. Maintaining the functioning of complex systems has been shown to be dependent upon their diversity and productivity [17], and this gives a basis for exploring explicit definitions of system resilience.

5 Towards Resilience

Resilience is the ability of a system to return to a stable state following perturbation, and can be viewed in two distinct ways: Engineering Resilience has been defined as the rate at which a system returns to a global equilibrium following perturbation [18]; Ecological Resilience is the amount of disturbance required to change from one steady or cyclic state to another [19]. The former focuses on maintaining efficient system function and predictability, and tends to assume a single, constant, global steady state. The latter focuses on maintaining the existence of function, and is more concerned with the factors that drive instabilities that cause the system to flip between multiple stable states [1]. A third approach, used in economic theory, is based on the engineering approach, but adapted to allow for multiple stable states through path dependency and other mechanisms [20].

The degree to which any complex system is resilient by these definitions depends to a large extent on the characteristics of the components of that system with respect to a given process or function. In ecological systems, resilience (frequently thought of in terms of the temporal stability of a process such as productivity) is thought to increase with functional diversity [21] and is affected by the strength of the interaction between different species in the system [22]. Ecological theory attempts to explain these patterns through a variety of models: “species richness-diversity” draws

a linear relation between species richness and ecological function [23]; “idiosyncratic theory” proposes that stability depends on merely the identity of species present [24]; “functional redundancy” is based on the principle that compensating complementarity between species allows functions to be maintained in the face of species extinctions [25]; and finally the “keystone species hypothesis” extends the functional redundancy ideas to include differentiation in the strength of species functional roles in the community [26]. Theoretical frameworks have also been proposed that attempt to unify and simplify these models by combining their different elements or embedding them in gradients of the functional overlap between species or the degree of variation between them [27]. These theoretical models are based on the concept of species populations as the basic functional unit, and therefore fail to capture the complexity or importance of the interactions amongst individual organisms in the system. Here we attempt to overcome this subjective classification of organisms into potentially artificial groupings by modelling individual behaviour at the level that organisms interact with each other in real systems. Interaction strengths, overlap in ecological function and differentiation between individuals therefore emerge as a property of the simulated system rather than being imposed as a fixed or required feature. This allows the relative importance of functional overlap, interaction strength and diversity in determining system resilience to be tested directly. At the same time, it is possible to avoid oversimplifying the functional representation of individuals by eschewing traditional reactive models [4] in favour of autonomous proactive software entities (in the style of [7]) supporting goal-directed and coordinated behaviour.

Resilience can be measured in terms of change in a system level property and function following perturbation. Perturbation can be simulated as addition, removal or alteration of one or more system components (mirroring catastrophic ecological invasion, extinction or mutation processes). The system component is a class of individuals with similar trait packages that perform a particular function in the system (i.e. a set of individuals with the same resource requirement, method of acquiring that resource, and strength of interaction with other individuals in the system). The impact of addition, removal or modification of this system component on resilience will be measured through responses of system properties and processes. The system property is trait diversity (the number and frequency of each trait represented by the individuals in the system), and the change in trait diversity (over sufficient generations to allow the detection of stable or cyclically stable states). The system processes are energy capture efficiency (ECE) and change in ECE and, its related measure, total system productivity (SP) and change in SP. ECE is the proportion of energy entering the system that is captured by each individual and converted to new biomass. SP is the resulting cumulated biomass across all individuals in the system. The combination of traits represented by the individuals in the system and the interactions between them that result in enhanced system resilience can then be objectively evaluated. This framework therefore allows the exploration of the properties of a generic complex system whose emergent behaviour is dependent upon the diversity of functional traits of surviving or successful individual agents and the number, type and strength of the interactions between them.

6 Concluding Remarks

Our aim here has been twofold: first, to identify an omission in current research on properties of complex systems, and on resilience in particular; and second, to lay the groundwork upon which formal theories and then subsequently implemented systems might be developed. The preliminary framework sketched here has a number of important advantages not only for complex systems research, but also specifically for the two contributing fields harnessed here, namely, ecosystem theory and multi-agent systems. In particular, from an ecological modelling perspective, this framework provides the ability to integrate a wide range of interaction types and offers a generic approach that can handle individual behaviour with out the need to hard-wire specific behaviours or trophic structures. For multi-agent systems, it provides a mechanism by which to apply the techniques of information exchange which are increasing well understood in new modelling scenarios involving energy or artefact exchange. More broadly though, the approach offers avenues to developing domain-independent definitions of system resilience that hold the potential to provide new ways of exploring the dynamic, emergent character of complex systems.

References

1. Gunderson, L., Holling, C.S., Pritchard, L., Peterson, G.D.: Resilience. In: Mooney, H.A., Canadell, J.G. (eds.): SCOPE The Earth system: biological and ecological dimensions of global environmental change. Encyclopedia of Global Environmental Change (2002) 530-531
2. Daniels, M.: Integrating Simulation Technologies with Swarm. In: Working Notes of the Workshop on Agent Simulation: Applications, Models and Tools. University of Chicago (1999)
3. Bordini, R.H., da Rocha Costa, A.C., Hubner, J.F., Moreira, A.F., Okuyama, F.Y., Vieira, R.: MAS-SOC: A Social Simulation Platform based on Agent-Oriented Programming. *Journal of Artificial Societies and Social Simulation* 8 (3) (2005) <http://jasss.soc.surrey.ac.uk/8/3/7.html>
4. Langton, C.: The Swarm Simulation System and Individual Based Modelling. Santa Fe Institute Working Paper (1996)
5. Duboz, R., Cambier, C.: Small world properties in a DSDEVS model of ecosystem. In: Proceedings of the Open International Conference on Modeling and Simulation (OICMS-2005), (2005) 65-71
6. Breckling, B., Muller, F., Reuter, H., Holker, F., Franzle, O.: Emergent properties in individual-based ecological models – introducing case studies in an ecosystem research context. *Ecological Modelling* 186 (2005) 376-388
7. Jennings, N.R.: On Agent-Based Software Engineering. *Artificial Intelligence* 117 (2) (2000) 277-296
8. Schulze, E. D.: Flux control at the ecosystem level. *TREE* 10 (1995) 40-43
9. Foundation for Intelligent Physical Agents, ACL Spec (2002) www.fipa.org
10. Sandholm, T.: Agents in Electronic Commerce: Component Technologies for Automated Negotiation and Coalition Formation. *Autonomous Agents and Multi Agent Systems* 3 (1) (2000) 73-96
11. TAC: Trading Agent Competition (2005) home at www.sics.se/tac

12. JADE home at jade.tilab.com
13. Smith, R.G.: The contract net protocol: high level communication and control in a distributed problem solver. *IEEE Transactions on Computers* 29 (1980) 1104-1113
14. Sycara, K.: Persuasive Argumentation in Negotiation. *Theory and Decision* 28 (3) (1990) 203-242
15. Dumont, B., Hill, D.R.C.: Spatially explicit models of group foraging by herbivores: what can agent-based models offer? *Animal Research* 53 (2004) 419-428
16. Barwise, J., Seligman, J.: *Information Flow: The Logic of Distributed Systems*. CUP (1997)
17. Bolnick, D.I., Svanback, R., Fordyce, J.A., Yang, L.H., Davis, J.M., Hulsey, C.D., Forister, M.L.: The ecology of individuals: incidence and implications of individual specialization. *Am. Nat* 161 (2003) 1-28
18. Holling, C.S.: Engineering resilience versus ecological resilience. In: Schulze, E.D. (ed.): *Engineering within ecological constraints*. National Academy Press, Washington DC (1973) 31-43
19. Pimm, S.L.: *The balance of nature*. University of Chicago Press, Chicago (1984)
20. Clark, N., Juma, C.: *Long-run economics: an evolutionary approach to economics growth*. Pinter, London (1987)
21. Tilman, D., Wedin, D., Knops, J.: Productivity and sustainability influenced by biodiversity in grassland ecosystems. *Nature* 379 (1996) 718-720
22. Root, R.B.: Organization of a plant-arthropod association in simple and diverse habitats: the fauna of collards. *Ecological Monographs* 43 (1973) 95-117
23. MacArthur, R.H.: Fluctuations of animal populations and a measure of community stability. *Ecology* 36 (1955) 533-6
24. Lawton, J.H.: What do species do in ecosystems? *Oikos* 71 (1994) 367-74
25. Ehrlich, P.R., Ehrlich, A.H.: *Extinction: the causes and consequences of the disappearance of species*. New York: Random House (1981)
26. Walker, B.: Biological diversity and ecological redundancy. *Conservation Biology* 9 (1992) 747-752
27. Peterson, G., Allen, C.R., Holling, C.S.: Ecological resilience, biodiversity and scale. *Ecosystems* 1 (1998) 6-18

Collaborative Multidiscipline/Multiscale Analysis, Modeling, Simulation and Integration in Complex Systems: System Biology

Thomas J. Wheeler

University of Maine, Computer Science Dept
wheeler@umcs.maine.edu

Abstract. Analysis, Modeling and Integration of Complex Systems are difficult. Collaboration among dissimilar disciplines is difficult. But, integrated interdisciplinary collaboration is essential in making sense of complex systems. This creates a dilemma with complex systems at the end of one horn and interdisciplinary collaboration at the other. There is another wrinkle, combining the conceptual spaces at the ends of the horns makes each much more difficult.

Rather than trying to pass between the horns of this dilemma, we weave a semantic unification space between them. This does more than ironing out the wrinkle; the threads of common image schemas, cognitive metaphors and conceptual interfaces form a mesh between the organizations of each problem, making the combined problem easier than either is separately. This paper presents a naturally valid, both discipline specific and discipline integrating, framework and a new foundational semantic mechanism for making multidisciplinary sense of complex systems

1 Introduction

This paper reports on an exploration of a new way of making integrated multidisciplinary and multiscale sense of complex systems. It uses insights from Software Engineering, which studies analysis, modeling and integration of complex software systems to address physical, chemical and biological analogs of integration via coupling of “Abstract Interfaces” in these areas. It also uses insights of a Cognitive Science group which studies analysis, modeling and integration of percepts and concepts via grounded, embodied “Image Schema, (abstract spatial) Metaphors and Conceptual Blends” to understand mental models. We developed an external representation and mechanism of this semantics for multidiscipline, multiscale collaborative analysis, modeling and integration in System Biology.

The paper focuses on a number of major problems which show up in complex systems research areas. Complex systems are composed of large numbers of subsystems, functioning in different modes, spanning many levels of scale. Smaller subsystems compose and interact to create larger subsystems. Subsystems interact in various ways, which can make different sense from different perspectives. Thus, integrated multiscale interdisciplinary collaboration is essential in making sense of complex systems.

Background

Our work is a software engineering analysis, modeling and integration effort aimed at complex systems. It takes a multifaceted approach. The facets are: *scale*, focusing on levels which are understood with different thought patterns; *subsystems*, usually interacting across multiple levels; *semantics*, introducing a “function follows from form” imaginative semantics; and *integration* based on interfaces of subsystems being based on aspects of their form affording activity they participate in.

We use Cognitive Science’s embodied[1,2] form-affordance semantics: “Ecological Perception” [3,4,5] and “Image Schemas,”[3,6] conceptual metaphors[7] and conceptual blends[8] Conception.

This research needs to be grounded in a complex system problem and whose approach needs multidisciplinary collaboration; we chose “System Biology.” Our start was noting Biologists and other scientists, using informal, “natural” illustrations and imaginative descriptions while working out a concept. They collaborate via imaginative explanations and depictions, informally, at meetings and in journals.

A meta-principle in software engineering is “make informal, implicit issues explicit.” To make this possible, we note that software engineering theory research has, since its beginnings, been driven by insights from the well of human cognition issues. Software engineering is about how people’s minds create superior software.

To enable “making it explicit,” we reach deeper into the well of practical cognitive understanding to address the next level of problem, multidiscipline collaboration on complex systems. In this well is the “complex systems understanding” layer, where the nascent “system biology” approach currently is. Looking in further with our imaginative semantics, metaphorical “glasses”, we see a mapping of “natural” description onto valid, sharable, insightful, natural semantics.

Outline of Paper

After discussing related research, we begin by providing a grounded, empirically validated overview of embodied, imaginative semantics. Imaginative semantics attaches meaning to images based on “form affords function.” Objects are afforded activity with other objects, by the interaction of parts of each object’s form. To enable use of this semantics we developed the (few) foundational image schema for systems: surface, path (and movement), container, (or context) and structure. These foundational schemas, for example “path”, have extensive imaginative semantics already *entrenched* in our “embodied minds.” We finish this section with a methodology and architecture for using them and infrastructure for computer assisted collaboration, on whole subsystems and interaction of subsystems.

We then discuss physical Abstract Interfaces of subsystems, both conceptual and computer simulated and how they handle scalability. We follow that with an in depth example of its use in System Biology, grounding the explanation with an enlightening envisioning of blends in action. This applies system thought patterns to “system biology” and the computer infrastructure for supporting it. Engineering fields have long used this approach to their domain’s models, learning previously unknown concerns from enlightening disasters. Biology and medicine are in a somewhat similar situation, but without the blueprint.

We end with some concluding comments addressing how this work fits into the evolution to integrated lexical (ontological) and imaginative semantics based system biology.

2 Related Research

From the system biology perspective: This project relates to James Collins' integration of synthetic & systems biology[9], but concentrating on the physical modeling aspect his work needs. This project provides a concrete proposal for David Harel's general approach to comprehensive and realistic system biology modeling[10]. It is most similar to Norm Patton's[11], informatics work on conceptual models of eukaryotic genome sequence data and genome organization. While he used a general purpose graphical formalism, UML, for models, we use a unified general purpose and domain specific imagistic semantics, allowing integrating domain expert's insights into the general purpose representation.

The curated ontology based work at Jackson Labs [12] addresses the same concerns that we do, based on curated lexical semantics. Ontologies[13] do not overtly provide a conceptual representation of models but rather provide structural framework of the conceptual terms used in the domain. Ontologies rely on an annotation framework for adding prose, semistructured text, numeric information and informal depictions. Image schema semantics provides conceptual models with structural and functional "entailments." Imagistic Semantic annotation of ontologies would add valid sharable models facilitating collaborative work [14].

From the software engineering integration perspective: This work is related to the software integration work, based on XML and Ontologies[15], semi-structured data integration [16] and mediators[17], but differs significantly in that their core they are based on lexical, "two world" external reference semantics, while imaginative semantics has "single-internal-world" reference semantics.

It is related to work in spatial science [18, 19, 20] but with abstraction from concrete domains and using imagistic simulation rather than formal, logic based simulations. It is also similar to visual recognition work [21], differing in that we use image schema simulation synchronized by perception. It is also similar to collaboration support work in computer supported cooperative work, e.g. [22], but that community concentrates on collaboration tools.

Our essential concept of "Physical Abstract Interfaces" is similar, but more general than Jensen's [23, 24] work on efficient equivalent expression for molecular contexts.

The closest computer assisted system understanding research is "f-struct, x-schema" work at Berkeley [25] whose work is based on denotational static semantics, and Petri nets with operational (computer program) dynamic semantics. Our work addresses conceptual and computer simulation semantics, based on coupling of affordances causing activity in classical and quantum physics.

3 Embodied Semantics

Grounding introduction: Embodied perception

Our research investigates system conceptualization and design within the situated activity [26] thought pattern, using environmental perception, situated image schemas and metaphor conception. Experientially entrenched awareness of valid, repeatedly

noticed similarities in external objects, events and activities, allows abstracting them into perceptual and conceptual image schemas.

Environmental perception produces, by a predictive filter, imagistic simulation of a meaningful perceptual environment [3]. Perception from the surface reflectivity of our environment’s veneer synchronizes embodied mental simulation of our environment. Figure 1 illustrates experiential grounding; the illustration becomes a meaningful environment *in your perceptual facility*. It produces an ambient sensory array *to your embodied vision*.

The perceptive array senses *actual shapes and properties of surfaces* that are naturally valid [4, 5]. Shade is not brightness; it does not change with change in ambient illumination. Nonuniform reflected illumination from the snow is validly seen as change in surface orientation to ambient illumination or as shadow, not change in snow color. The cognitive aspect of your embodied mind works on this.

Grounding our cognition [3] are the substances and arrangement in our static schemas envisioned in dynamic instances in an imaginative, dynamic model. The shape of the rock is seen through the snow. The dynamics of our conceptual model is also induced in you. Stepping on the snow covered rock will ruin my picture, but it will support you.

Edwin Land [4] and Semir Zeki[5], a micro-neurobiologist, showed that vision perceives objects in the real world as valid¹ representation of actual invariant surface reflectances, extracted from differential illumination.

Conception: Grounding, image schemas and metaphors

Basic image schemas, metaphors, affordances & fundamental composites become entrenched in the embodied mind in early infancy, with entrenched image schemas and metaphors being the raw material for future making sense. Even before an infant can see (~11 days old), (s)he has had a lifetime’s experience in various environments.

The validity of the (context, image, affordance, metaphor, blend) schema conceptualization paradigm is grounded. Environmental perception and imaginative cognition are jointly created by predictive filter, imagistic simulations of a meaningful perceptual environment. Imaginative embodied mental models, the whole body makes sense of its whole environment in natural perceptual and conceptual valid¹ models.

Image Schema models have affordances, [3, 27] parts which afford interactions with affordances of other objects. Objects’ semantics: structure, behavior and interactions, emerge by imaginative simulation of interactions of their, metaphorically interpreted, foundational image schema instances in their local environments. Working memory,



Grounding Image of an Artificial(3D) Perceptual Experience, Causing a Conceptual Envisioning *in Your Mind* of a Rock Partially Snow Covered. The Rock’s Shape is Obtained From the Reflectance Properties of the Surfaces, Especially the Surface of the Snow that the Rock’s Surface is Supporting.
 “ Spring in Maine ”

Fig. 1.

¹ Automatically “effectively” valid, i.e. valid with respect to all imaginable aspects, both evolutionary and individual.

using this imaginative simulation facility creates understanding on the fly of effects and entailments of interactions of these complementary affordances. Interaction of complementary affordances on inter-acting objects causes all semantics.

Foundational image schemas

We conceive, as well as perceive, metaphorically from Foundational Image Schemas, making sense of concepts and collaborating with others doing the same. Foundational Schemas are small in number and anchor the semantics in any domain.

Any environment is metaphorically projected from foundational schemas. It is made up of “*Surfaces*,”² organized by other foundational image schemas. “*Paths*” have a source, a trajectory and a goal. It affords “*movement*”, “*mapping*”, and “*structuring*”. Bounded, adjoining or folded surface(s) is a “*container*.” Viewed from outside, it affords containment and in(to)/out(of). Viewed from inside, it is a *context*.

The number of image schemas and the number of affordances of any instance are unlimited. Image schemas are related like subclasses, but the relation is on affordances, not categorization, and is direct to the fundamental image schemas, transitive closure is naturally automatic.

Form-Affordance Semantics

In embodied, image schema semantics, objects are thought about in terms of their “*surfaces*”, those surface areas which afford an interaction/activity, affordances, are a natural way of representing an interface of that object. In figure 5, the left cylinder has on its bottom surface a wide arrow, naturally representing “am able to rotate about my axis.” The supporting surface’s complementary wide arc represents “am able to support rotation.”

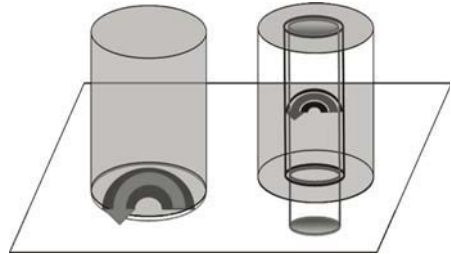


Fig. 2.

Complementary affordances need to have some similarities, rotational slipperiness, in this case, and some opposites, needs to be supported and supports. An abstract way of characterizing each of the complementary affordances in an interface, more easily seen in the right hand example where, if you focus on the inner surface of the outer cylinder you see it’s concave, has a negative curvature. You see the outer surface of the inner cylinder as convex, has a positive curvature. Affordances can be abstractly characterized as a positive affordance (curvature, charge, causing motion, supporting, etc.) or negative (curvature, charge, accepting motion, needing support etc.).

Valid Multi-discipline, Heterogeneous, Collaboration: Blends (and Metaphors)

Blends (figure 3) are a multiple image schema, metaphor mapping mechanism which integrates (object oriented) *generalization of extensional semantics* (top of diagram) and *image schema, metaphor imaginative semantics* (bottom of diagram). In a blend (at least two) domains/ disciplines, with its own core image schema and metaphor semantics, are set within their natural environments. In the figure, image schemas are rectangles, representing concepts, lines are conceptual metaphors, representing

² Quotes around the foundational names indicate that we are referring to both concrete and abstract instances.

relationships. Trapezoids are domains, with models (e.g. domain₁ & domain₂) enclosed in (container) lines, representing environments.

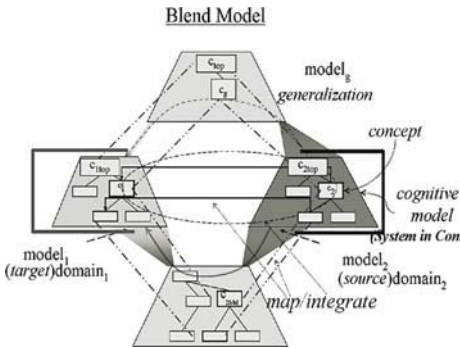


Fig. 3. Image Schema, Metaphor Blend

Analysis *posits* a semantic relationship, allowing lower level concepts to be interpreted, more weakly, in higher level classes.

In use, Blends are viewed through one of the domain models, acting as a “conceptual lens.” Viewing through generalization, the funnel shaped mapping (right) and the tube mapping (left), show generalizing (upward) losing semantics, which are not replaced by the downward mapping (automatic specialization does not take place).

On the other hand, the funnel shaped mappings down to the blend, on the right, and up from the blend, on the left, restores the full specialized semantics within the left model, via its (affordances) interaction with (the affordances of) the left’s context. In addition, with blends, combining generalized *logical inferences* (going over) with *imaginative entailments* (going under) is allowed and is often enlightening.

To illustrate the valid sharing of semantics and the compatibility of the discipline specific views of those shared semantics, consider the interaction of a Geologist and a

The actual “blend” is the trapezoid at the bottom of the diagram and is created (denoted by the domain model to blend, dot-dash lines) by *metaphorical mappings from the common structure of the domains being blended*. The blend’s concepts are mapped from each domain’s concepts which “make sense” to be blended³ The blend’s metaphor structure abstracts that of the domains.

The trapezoid at the top is the Object-Oriented class hierarchy. It hierarchically relates domain’s *extensional meanings*.

Environments Object and Conceptual Model built from same small number of Fundamental Image Schemas

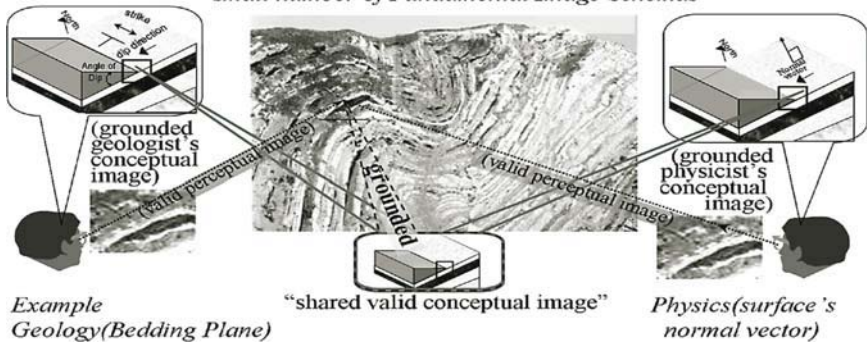


Fig. 4.

³ This will be explained, or more accurately illustrated, in the example(s) below.

Physicist with respect to the ledge they are both looking at (figure 4). Because of grounded effective validity of image schemas, at the conceptual as well as perceptual level, both metaphoric interpretations are effectively valid. The geologists “strike and dip” model and the physicists “normal vector” model are valid. They can collaborate based on the map in common, which is also valid.

4 Abstract Interfaces: The System Way of Thinking

The System Point of View

The perspective we take in providing conceptual and computational support for understanding, analyzing or developing complex systems is the system’s point of view. It takes synergistic structural, functional approach to system understanding and development, *function follows from form*; form is constructed and manipulated by function. They are indelibly intertwined in a hierarchy of scales, layers and subsystems, with tiny things interacting with their environments, and from these emerges the next level up form and function, etc. This point of view is in the structuralist culture [28], not the reductionist culture, and intermediate levels and subsystems have real existence. It concurrently unifies discipline specific and general systems thought patterns. It addresses a system’s interoperation via interfaces between the system and other objects within its context. Interfaces define the semantics of systems. Semantics of interfaces emerge [29] from inner subsystems and interaction.

External Semantics

Shared System Thinking is based on real function following from real form. Complementary affordances of component’s surfaces interact, creating the system. System’s affordances interact with environment’s affordances, creating functionality.⁴

The foundational schemas of the real world are just place, paths, surfaces, containers, motion and interaction. External models need to model affordances, which interact with other objects affording activity. External models activities and structure must emerge, by external imaginative simulation of (possibly) potential interactions.

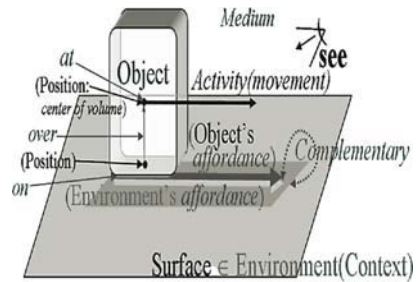


Fig. 5.

Objects in Contexts

An object in a local environment, its context, is what it is and does what it does, with objects in its that environment, when their affordances couple. Semantics is what happens when, possibly abstract, surfaces of one object, with of positive or negative valued affordances, “touch” a complementary pattern of oppositely polarity affordances.

⁴ The familiar aphorism form follows function is only fundamental evolutionarily i.e. Fish, sharks and dolphins have, evolved, analogous, hydrodynamic, overall shapes, a convergent evolution optimization.

A physical example was shown above.(figure 2) Slightly more abstract⁵ (figure 5) is the “touching” of the end of the seeing eye’s gaze to the reflecting surface of the object, affording the observation of the object. Abstract affordances exam- ples: in (the context of) a research (/design) review, a mentor’s (/manager’s) insightful question “seeing” a researcher’s idea, “leading to” progress via the researcher’s illuminating response, and the mentor’s “observation” of that progress.

Model’s Abstract Interfaces

An interface in systems is all of the assumptions about interactions with or activities of an object that can be made by any other object outside that object. When objects are perceived and thought about in terms of their “surfaces”, those surface areas which

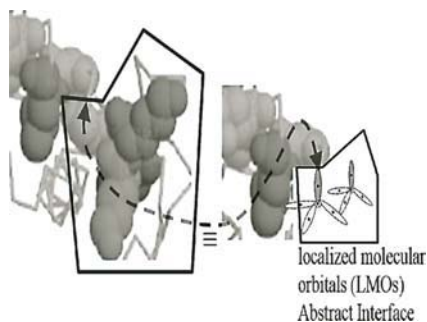


Fig. 6.

afford an interaction/activity, its affordances, are a natural way of repre- senting an interface of that object. Figure 6 illustrates a molecular interaction Abstract Interface: the use of localized “Molecular” Orbital Model, which is just four charge centers(for Carbon), the nucleus, and the center of each ellipsoidal electron orbital. This simplified model has been shown to be a valid model(<.1%) [23,24] for inter- actions of water and Lysine. Our strategy is to keep Abstract Interface Models as simple and valid as possible, growing $O(N\log M)$ in subsystems(N) or interactions(M).

5 System Biology: Life, Highly Complex Hierarchical Systems

System Biology works towards integrating the data and analyses of life’s multiple levels, components, and aspects. System biology approaches life as a system. It structures life into multiple levels and subsystems. When changing focus between levels/subsystems, thought patterns and organizing principles change to accommodate/integrate insights into/between disciplines. Interdisciplinarity and fostering and supporting collaboration are essential in system biology.

Semantics for system biology: Image, affordance, metaphor schema semantics

The central idea structuring our work is that embodied modeling is more natural, more productive and more insightful especially for collaboration, that current objectivist based modeling. The proximate contexts mutual interaction with objects/ systems in it, defines the semantics of both. The mutual affordance point of view facilitates envisioning character and functionality during collaboration.

The image schema based semantic lens provides a point of view and a context, within which to interpret a single, subsystem within a system biology hierarchy (figure 7).

⁵ The mental representation is, of course, inside people’s minds and thereby not representable, but there is considerable experimental evidence that figure 5 is an effectively valid model of “envisioning”, (seeing with your mind’s eye).

The fundamental and fundamental composite schemas are used to conceptual metaphorically make sense of concepts and collaborate. It also shows how “natural” depictions, both graphical and textual, provide imaginative semantics annotations of a system biology account of the protein creation, g-actin, through functioning creation, lengthening f-actin pushing out on the cell wall.

Figure 7 illustrates the conceptualization part of the system bioinformatics system consists of image schematic, affordance based envisioning of multi-level processes. It shows the DNA to function of g-actin/f-actin in its physical location in the cell’s hierarchy (labels 1..8). Scanning the path (upward open arrow), the process starts with the g-actin gene on the DNA (1), being transcribed to mRNA by correspondence. The mRNA moves (2), to the ribosome picking up a tRNA carrier, adding an amino acid to the growing amino acid sequence (aas) (3). The aas moves (4), while folding (5), into a g-actin, which moves (6), towards where the cell wall is being pushed (8), appending to the growing f-actin (7), fulfilling its function. Feedback (downward open arrow) from (8) back to (1) through the regulatory network, closes the loop.

Figure 8a illustrates some natural isomorphism mapped natural depictions which ground our envisioning of image schema system biology models.



Fig. 7.

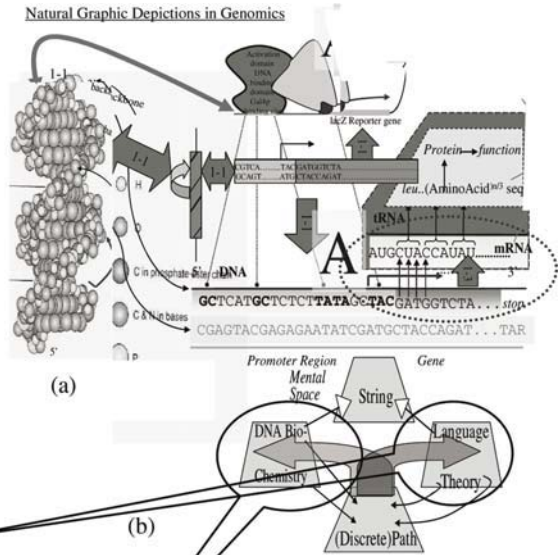


Fig. 8.

The “picture” of DNA is mapped to “wound ribbon” model and unwound to a ribbon model. This is mapped to a “CGAT” sequence which can be genomically processed, as depicted by the right flow (open arrow) in figure 8b.

At the top, the DNA “picture” is isomorphically mapped to a line to which imagistic or diagrammatic processing can be applied to envision spatial functions/activities, depicted by the left flow (open arrow) in the blend, figure 8b.

6 Conclusions

The power of image schema, affordance, metaphor, and blend semantics can be seen in the examples. Blends provide a conceptualization integration mechanism which appears to have an analogous power to humans “working memory”, keeping a small number of concepts and their gestalt in an integrated view at the same time. The power of the image schema, affordance, metaphor, blend mechanisms is because of the integration of these mechanisms. “Making sense” semantics readily transfers to supporting tools, greatly increasing collaboration’s valid productivity.

This form of mental and computer supported, simulation, literature reference annotations and semantic models of lexical semantics, is readily integrated, via mutual informal and formal annotations of providing a transition path from annotated lexical semantics to validly simulatable, envisionable and manipulable semantics.

References

1. Johnson, M.: *The Body In The Mind: Bodily Basis Of Meaning, Imagination, And Reason*, university of Chicago press, 1987.
2. Lakoff, G. and Johnson, M.: *Philosophy In The Flesh-The Embodied Mind And Its Challenge To Western Thought*, Basic Books,
3. Gibson, J.: *Ecological Visual Perception*:Lawrence Erlbaum Associates, Hillsdale,NJ1986
4. Land, E.:*The Retinex Theory Of Colour Vision*, Proc. R. Instn. G. B., 47: 23-58, 1974.
5. S. Zeki, *A Vision Of The Brain*, Blackwell Scientific Publications, 1993.
6. Mandler, J. M" *The Foundations of Mind: Origins of Conceptual Thought*", published by Oxford University Press, 2004
7. G. Lakoff and m. Johnson, *Metaphors We Live By*, University Of Chicago Press, 1980.
8. G. Fauconnier and M. Turner, *The Way We Think: Conceptual Blending And The Mind’s Hidden Complexities*, Basic Books, 2002
9. Collins, J.: *Integrating synthetic biology and systems biology ICSB 2005*
10. Harel, D.: *Comprehensive and realistic modeling of biological systems: what, how and why ICSB 2005*
11. N. Paton et.al. *Conceptual modelling of genomic information bioinformatics v16,no.6 2000*
12. Bult, C.: *Curated Ontologies and Semantic Integration*, BIBE 2000
13. Hill, D.: *An Introduction to the Gene Ontology*, GORECOMB 2005, Cambridge MA 2005
14. Wheeler, T.and Dolan,M.: "Support for Interdisciplinary Conceptual Model Blending" Intl. Conf. Intelligent User interfaces Oct. 2001
15. Philippi S, Kohler J.: *Using XML technology for the ontology-based semantic integration of life science databases. IEEE Trans Inf Technol Biomed. 2004 Jun;8(2)*

16. Davidson, S.: Bioklesli: A Digital Library For Biomedical Research Intl. J. Digit. Lib. 1(1, 1997)
17. Wiederhold, Gio: Mediators In The Architecture Of Future Information Systems; Published In IEEE Computer, March 1992 Bloom, M. Peterson, M. Nadel, L. Garrett, M. editors, language and space, mit press, 1996.
18. Frank, A.U., & Mark, D.M., (eds.). 1991. *Cognitive and Linguistic Aspects of Geographic Space*. Vol. 63, *NATO ASI Series D*, Dordrecht, The Netherlands, Kluwer Academic Publishers
19. Frank, A.U., & Mark, D.M., (eds.). 1991. *Cognitive and Linguistic Aspects of Geographic Space*. Vol. 63, *NATO ASI Series D*, Dordrecht, The Netherlands, Kluwer Academic Publishers
20. Worboys, M.F. and Duckham, M. (2004) *GIS: A Computing Perspective, Second Edition*, CRC Press, ISBN: 0415283752.
21. Bastian Leibe and Bernt Schiele Analyzing Appearance and Contour Based Methods for Object Categorization Proc. *IEEE Conference on Computer Vision and Pattern Recognition (CVPR'03)*, Madison, USA, June 2003.
22. Espinosa, J. A., Kraut, R.E., Slaughter, S. A., Lerch, J. F., Herbsleb, J. D., Mockus, A. Shared Mental Models, familiarity, and coordination: A multi-method study of distributed software teams (2002). International Conference in Information Systems, Barcelona, Spain
23. Jensen J. H. and Gordon, M. S. : J. Chem. Phys. **108**, 4772 ~1998.
24. Jensen, J. H. : J. Chem. Phys. **114**, 220~2001
25. D Bailey, J Feldman, S Narayanan, G Lakoff : Modeling embodied lexical development Proceedings of the 19th Cognitive Science Society Conference, 1997
26. Suchman, L.: Plans and Situated actions Cambridge University Press 1987
27. D. Norman, The Design Of Everyday Things, Penguin, 1986.
28. Piaget J.: Structuralism Harper 1970
29. Bar-yam, Y. A Mathematically Theory of Strong Emergence. Complexity Vol8, No6 2004 Wiley Press

On the Structuring of the Computational Chemistry Virtual Organization COMPCHEM

Antonio Laganà¹, Antonio Riganelli², and Osvaldo Gervasi³

¹ Department of Chemistry, University of Perugia, Via Elce di Sotto, 8,
06123 Perugia, Italy
lag@unipg.it

² Master-up s.r.l., Via Elce di Sotto, 8,
06123 Perugia, Italy
a.riganelli@tiscali.it

³ Department of Mathematics and Computer Science,
University of Perugia, Via Vanvitelli, 1,
06123 Perugia, Italy
osvaldo@unipg.it

Abstract. The first moves to structure the COMPCHEM Grid virtual organization of the computational chemistry community are discussed. A tool based on a credit system developed to guarantee its sustainability is presented.

1 Introduction

There is increasing pressure on computational chemists to develop new approaches to the a priori determination of complex molecular structures and processes in order to face the need for innovative products and procedures in several scientific and engineering fields. Appropriate answers to these requests of innovation can be provided only by carrying out a priori realistic simulations of productive processes. In order to assemble such simulators several computational resources and competences need to be gathered together and collaborate.

To the end of developing collaborative endeavours in science and technology various initiatives have been started in various places. One of the most effective cooperation oriented European initiative in this field is COST. In particular the Chemistry domain of COST [1] has implemented an Action (Action D23 [2], METACHEM: Metalaboratories for complex computational applications in chemistry) in which cooperative research and knowledge handling in chemistry is promoted through the funding of networks of Laboratories (called Metalaboratories). These Metalaboratories have been structured as virtual communities made of real Laboratories cooperating to achieve common goals in computational chemistry by sharing hardware, software and know-how. In METACHEM they have operated in the following areas: the calculation and fitting of the electronic energies of atomic and molecular aggregates using high level ab initio methods; the use of statistical, kinetics and dynamics means to study chemical processes; the handling and creation of molecular and chemical e-knowledge for research and education.

A key outcome of METACHEM has been the recommendation to the computational chemistry community to structure itself as a Virtual Organization (VO) [3]. Accordingly the COMPCHEM VO has been registered and its members have begun to operate on the production Grid of EGEE [4]. This paper illustrates the development of a Grid environment for the molecular science community in section 2, the assemblage of the molecular science simulator in section 3, the articulation of the organization in a sustainable fashion in section 4 and the formulation a credit system within the VO in section 5.

2 The Development of a Grid Environment for the Molecular Simulator

The first attempt to build a molecular simulator running distributed tasks in a cooperative fashion dates back to the mid '90s [5]. The goal of that embryonic simulator was the calculation of the properties of an atom diatom reactive system. The collaboration environment used for that purpose was particularly simple and involved only the Computer Centre and the Department of Chemistry of the University of Perugia. The specific focus of the simulator was the reproduction of some measured properties of atom diatom crossed beam experiments. For this reason further developments derived from that software were called SIMBEX (Simulator of Molecular Beam Experiments [6]). After the first implementation at the end of the '90s the development of SIMBEX occurred in the homonymous working group of the already mentioned COST Chemistry Action METACHEM. Though still confined to the calculation of classical trajectories for atom diatom systems, the sharing of the simulator among the members of a larger community prompted the request of improving the communication between the codes and the users (for both input and output not only at the beginning and the end of the application, but also during the intermediate steps) and to provide links with the calculation (either direct or indirect) of the potential energy surface [7, 8].

The key step forward on the Grid Enabling side was made within the Italian project GRID.IT [9] in which a fruitful collaboration with national top computer science laboratories was established to the end of designing effective gridization strategies and tools for scientific applications.

The first part of the work consisted in gathering a significant sample of computational chemistry laboratories active in the field. Such a sample (named CHEM-GRID.IT) is made of the following laboratories:

1. CNR-Mi (the Milano branch of the CNR Institute ISTM)
2. CNR-Pg (the Perugia branch of the CNR Institute ISTM)
3. CNR-Pd (the Padova branch of the CNR Institute ISTM)
4. ENEA-Rm (the ENEA laboratory at Casaccia)
5. INSTM-Ba (the branch of the National Institute INSTM at the Bari University)
6. INSTM-Bo (the branch of the National Institute INSTM at the Bologna University)

7. INSTM-Na (the branch of the National Institute INSTM at the Napoli University)
8. INSTM-Pg (the branch of the National Institute INSTM at the Perugia University)

The second part of the work consisted in assembling in CHEMGRID.IT a distributed platform made of the computers conferred by the partner laboratories specifically devoted to the Grid activity. This distributed platform of CHEMGRID.IT consists of:

- A front-end Intel Pentium 4 Hyper-Threading 3.06 GHz 512 Kb level 2 Cache; 1 GB PC2100 ECC DDR SDRAM; 80 GB Ultra ATA/100 7200 RPM; GNU/Linux Fedora Core 1; Globus Toolkit 3.2; This machine hosts also the CHEMGRID.IT web page (<http://www.chemgrid.unipg.it/>) and also the first CHEMGRID.IT application SUPSIM (<http://www.chemgrid.unipg.it:8080/>). The web page has been used widely to exchange all the CHEMGRID.IT related documents and tutorial. The same machine is devoted also to be the front-end to the Pg cluster incorporating the four nodes of CNR-Pg and the four nodes of INSTM-Pg. The whole grid is set-up by several Beowulf GNU/Linux cluster all based on Fedora Core 1 and Globus Toolkit 3.2 and using OpenPBS as the default batch queuing system.
- CNR-Mi: a cluster of 8 nodes (Intel Pentium III Coppermine 1.0 GHz, 1 GB RAM, 16GB SCSI Ultra 160 discs) interconnected via a Fast Ethernet switch.
- CNR-Pd: a cluster of 4 nodes (Intel Pentium IV 2.4 GHz, 512 MB RAM, 40 GB EIDE disc) interconnected via a Fast Ethernet switch.
- CNR-Pg: a cluster of 4 nodes (Intel Pentium IV Hyper-Threading 3.06 GHz, 1 GB PC2100 ECC DDR SDRAM, 80 GB disk Ultra ATA/100 7200 RPM) interconnected via a Gigabit Ethernet switch.
- ENEA-Rm: a cluster of 4 nodes (Intel Pentium IV 1.8 GHz, 512 MB RAM, 70 GB EIDE disc) interconnected via a Fast Ethernet switch.
- INSTM-Ba: a cluster of 3 nodes (double processor Intel Xeon 2,4 GHz, 2 GB DDR ECC Registered RAM, 40 GB 7200 rpm EIDE discs) plus 1 node (single processor Intel Xeon 2,4 GHz, FSB 533 MHz, 2 GB DDR ECC Registered RAM, 40 GB 7200 rpm EIDE disc) interconnected via a Fast Ethernet switch.
- INSTM-Bo: a cluster of 8 nodes (AMD Athlon K7 700 Mhz, 512 MB RAM, 26 GB EIDE disc) interconnected via a Fast Ethernet switch.
- INSTM-Na: a cluster of 4 nodes (AMD Athlon 1.0 GHz, 256 MB RAM, 20 GB EIDE disc) interconnected via a Fast Ethernet switch.
- INSTM-Pg: a cluster of 4 nodes (Intel Pentium IV Hyper-Threading 3.06 GHz, 1 GB PC2100 ECC DDR SDRAM, 80 GB disk Ultra ATA/100 7200 RPM) interconnected via a Gigabit Ethernet switch.

A great deal of work has been devoted to the analysis of the specific necessities of Grid computations in Chemistry. To this end some technological choices put forward by the other (computer science) laboratories working within the project

GRID.IT were analysed and whenever appropriate adopted. Among the others the following products have been considered: PHP, Java Servlet and Portlets, with the related container for the portal developing Assist (a coordination language being developed in Pisa [10]), mpich-g and P-Grade for the intensive distributed computing and GridBus as an alternative middleware.

This CHEMGRID.IT environment has been intensively used during the project life as a laboratory for designing and experimenting Grid middleware and software solutions for the molecular simulator to be eventually exported to the production environment.

3 The Assemblage of the Grid Enabled Molecular Simulator

The third part of the work consisted of actually gathering and implementing the software needed to assemble the Grid Enabled Molecular Simulator (GEMS). The main software gathered together were the following suites of codes:

1. ABCtraj: A classical trajectory program for atom diatom systems;
2. ADC: An electronic structure program to calculate single and multiple excitation electronic energies;
3. AMBER: A force field assembler for complex systems;
4. CPMD: A car-Parrinello program for complex systems;
5. CRYSTAL: An electronic structure program for solid state aggregates;
6. DL_POLY: A classical dynamics program for complex systems;
7. GAMESS-UK, GAMESS-US, GAUSSIAN and MOLPRO: Suites of programs for electronic structure calculations for isolated molecules;
8. QM/MM: A Molecular mechanics program for complex systems;
9. RWAVE_PR- A quantum mechanics program for atom-diatom systems (wave-packet method);
10. VENUS: A classical trajectory program for polyatomic systems.

The main characteristics of the programs more relevant to GEMS and to its immediate future evolution is given in the following Table.

Table 1. Main features of the suites of programs considered

APPLICATION	SEQ./PAR.	MEM.	DISK	CPU	LIBRARIES
DL_POLY	Seq/Par	10 MB	10 MB	3 h	FFT, BLAS
ABCtraj	Parallel	1 MB	1 MB	120 s	
VENUS	Parallel	1 MB	100 MB	1 week	
GAUSSIAN03	Seq/Par	64 MB	256 MB	90 s	Atlas (in G03)
MOLPRO	Sequential	80 MB	500 MB	120 s	Intel MKL 6.1
GAMESS-UK	Sequential	80 MB	500 MB	120 s	Lapack, Blas
GAMESS-US	Sequential	80 MB	500 MB	120 s	Lapack, Blas
ADC	Seq/Par	10 MB	500 MB	600 s	Intel MKL 6.1, Scalapack
RWAVE_PR	Sequential	.1-1 GB	1.5 MB	1-6 days	FFT, BLAS, Lapack

Each suite of programs has been implemented and maintained locally on the machines of the laboratory having either written the codes or paid related licence fees. Centralized activities were taken care by the Perugia laboratories. The coordination of the activities has shown to be extremely difficult for an experimental (non production) GRID like CHEMGRID.IT. This is due to the fact that no mechanism for enforcing or providing incentives for the Grid work could be adopted. A second difficulty evidenced by the project is that CHEMGRID.IT (as part of GRID.IT) being an experimental rather than a production project has not a sufficient mass to set de facto standards. As a result related choices were often in conflict with those made by EGEE which were dictated by a broader range of requirements (especially in terms of security) and therefore slower in adopting newer and more efficient versions of Grid middleware. This has sometimes created mismatches between the needs of computer science and application laboratories about the alignment to the choices of EGEE production Grid environment.

Therefore one of the main outcomes of GRID.IT has been the decision of keeping the CHEMGRID.IT environment for experimenting new Grid solutions in computational chemistry and molecular science and to implement the simulator on the production Grid of EGEE. For this purpose, starting from the molecular dynamics engine of SIMBEX the first demonstrator of GEMS (GEMS.0) was constructed. The Workflow Manager (WM) of GEMS.0 assumes the potential energy surface to be of the LEPS type and the value of its parameters (best fitting either theoretical or experimental information) to be stored in an ad hoc library. The WM deals also with the problem of guiding the user to select the parameters of the calculation (*e.g.* the system considered, the initial conditions chosen, the product properties to monitor, etc.) through a suitable graphical user interface (GUI) and to work out from the calculated quantities the desired observable properties to be rendered as a virtual signal on the corresponding virtual monitors.

The WM has also been designed in a way that makes it easy to upgrade GEMS.0 by inserting further choices. One of these possibilities is that of determining the parameters of the LEPS potential by fitting ab initio potential energy values either by taking them (if available) from the web or by calculating them afresh. For this purpose the FITTING [11] and the SUPSIM [12] procedures have already been developed. Another of these possibilities is to carry out atom diatom quantum scattering calculations (using for example the above mentioned RWAVE_PR code instead of the ABCtraj program of GEMS.0). Progress is also being made to include in the near future DL_POLY or similar suites of codes to deal with larger systems. As to the virtual monitors, in addition to those already implemented in GEMS.0 and showing internal energy distributions of the products (rotation and vibration) and translational energy and angular distributions as well the existing WM can be easily adapted to render other final or intermediate properties of the system.

The first field tests of GEMS.0 were presented in February 2005 at the first review workshop of EGEE [13] in the NA4 (Application Identification and

Support) session among the unfunded generic applications. For this purpose the GILDA [14] testbed environment and certificates were adopted and the demonstrator was run using the Genius portal [15]. The present version of GEMS.0 has shown to be a cpu bound application which takes dramatic advantage from Grid operating conditions and from the large amount of cpu cycles available on it.

4 The Sustainability of the Virtual Organization

Crucial to the growth of a virtual organization is its sustainability. For this purpose, first of all, COMPCHEM must offer to its members clear advantages for carrying out their computational campaigns (especially when they are so complex to not be feasible using other computing platforms). Only in this way the laboratories will take the burden of carrying out the extra duties necessary to work within a collaborative environment.

Therefore the entry level of the VO offers to the user the possibility of implementing a code at wish for personal use. This is a pre-membership situation and has a limited validity. It is useful for screening the laboratories on the real willingness to operate on a Grid platform. Already at this level, in fact, several competences necessary to restructure the code to run in a distributed way by exploiting the advantages of using a Grid platform need to be acquired. In return one gets the advantage of distributing the code on a much larger platform and an easier interaction with the codes of other users of the VO.

One becomes real member of COMPCHEM only after committing him/herself to open the code implemented on the Grid to a shared use by the other members of the VO. This implies the validation of a stable version of the code and the assemblage of all the necessary GUIs for use by other researchers. It also implies software maintenance services and user support. It may also imply the commitment to confer to the Grid additional hardware (especially for those suites of codes which need special devices) after a negotiation with the Management Committee (MC) of the VO about the relevance of such a commitment to the strategic choices of the virtual organization. Obviously, the conferring of both software and hardware to COMPCHEM will take place gradually due to the time needed to validate the software and to gridify the machines. A member will likely devote to VO related activities other unshared resources (e.g. for development work). To become member of the VO and acquire the status of "COMPCHEM stakeholder" a user should place a specific application to the MC. While the user status has a limited time validity (after which a user may become either a paying customer and/or a paid supplier of services) the status of member has no time limit (though its terms could be periodically revised). The status of COMPCHEM member may imply further levels of involvement. The stakeholder, in fact, should take care of maintaining the software and the local segment of Grid hardware (a particular attention is needed for the conferring of software, either commercial or not, with special constraints like the payment of fees since in this case commercial, legal and financial aspects are better dealt centrally). However,

apart from these more formal aspects a member of the VO should always harmonize the various local activities with the guidelines issued by the MC.

This means that the members of the VO are requested to be proactive in providing either their own work or attract financial resources specifically for the development of the VO. As to contributing by providing their own work this may be under the form of participation to the management of the Grid, to the development of WMs, etc.. As to attracting financial resources VO members should elaborate joint applications for funding, research projects and even develop within the VO commercial services. However, the most important contribution to the sustainability of COMPCHEM that is requested to the stakeholders is a high dynamisms in research and in the transfer of its outcomes into innovation and developments (R&D). This means that, ideally, all members of the VO should excell in basic and applied research and that a proper reward for that has to be given in the VO.

5 The CompChem Credit System

As discussed above, COMPCHEM is founded on the activities carried out on its behalf by its members. This mechanism, however, may become sustainable only if the VO rewards active members for the work done. For this purpose we have designed in a credit system. This means that stakeholders get credits for the activities carried out on behalf of COMPCHEM and can redeem them either by acquiring services from the VO or by trading credits for financial resources. Financial resources may become available to COMPCHEM as a result of services sold to paying customers or by participation of its members to projects.

Stakeholders can get credits from the VO also by conferring it further assets, by contributing to its management and even by procuring orders for commercial activities. However, the most important way of obtaining credits from COMPCHEM is that of carrying out R&D activities. R&D activities are, in fact, the most strategic asset of COMPCHEM because this is its key mission and the key mission of the stakeholders. This is due to the fact that COMPCHEM considers R&D as a resource in itself independently of its short term productivity (though not independently from its efficiency and efficacy). For this reason it is not only treated as a specially protected area of free circulation of ideas and innovation but it is financially supported regardless of the financial income (including projects) generated. Accordingly, out of the Services and Financial Resources (SFR) generated by the VO in the previous year a quota (say around 50 %) of what remains after covering the planned expenses for the current year will be devoted to support the R&D of the partner laboratories upon request to the MC. Contributions to R&D are evaluated on the basis of regular internal reports and articles in international scientific journals. In any case a peer review will be carried out and reports will have to include detailed description of successes, failures, failure recovery and retrieval of wrong data (together with the relevant motivations and rationalizations). Particular emphasis will be given to the stimulation and creation of new ideas as well as to innovation. This applies

also to the design and development of tools evaluating the cost of implementing and validating further research evolution that starts from the existing products.

The remaining part of the SFR will be distributed to the stakeholders (as a reward for their service activities) proportionally to the credits acquired. Services are classed as internal, external and special. The main regular internal service to be guaranteed by the member laboratories is the efficient functioning of all the (hardware and software) assets conferred to the virtual community. Are also considered internal services those duties undertaken by the partner laboratories within the realization of a project or a commercial service requested by a third body (and vehiculated either through the central management or through a member laboratory which will be assigned additional credits for that). Are instead considered external services those rendered directly by a member laboratory to a third party (with the request not being vehiculated through the central management of the virtual community though still using the common infrastructure). Among the internal services are also those addressed to the management of the infrastructures and activities of the virtual community, to the creation of new activities and to the running of existing ones including direct and indirect marketing. External services are agreed directly by a laboratory of the VO with the third party after a negotiation of the community services and costs with the central management. Special services are those related to the selling and maintaining of the virtual community services and products to third parties.

To the end of giving a quantitative basis and a fair criterion for the distribution of the SFR, we have worked out the algorithm given in eq. 1. The assignment of credits is straightforward for the conferring of machines and software. For them evaluation of usage and performances, historical series, statistical parameters are easily automated in a Grid environment. Also the accounting of any other possible service request and provision is in this way made objective. Additional implementations may provide an evaluation of the activation of synergistic activities, introduction of good practices, adoption of new procedures, development or acquisition of innovation, coordination for previously dispersed tasks, dissemination of new ideas, etc. which at present have no direct and unique correspondence with popular indicators like computing elapsed time, lines of code, pieces of hardware, etc..

Accordingly, the assignment of credits to the partner laboratories directly depends on the identification and quantification of the costs met, the usefulness of the services provided and of the income generated. These criteria are incorporated into the index \wp_l (called terms of exchange) that is defined as:

$$\wp_l = \alpha_T \sum_s w_s T_{sl} + \alpha_I \sum_i w_i I_{il} + \alpha_C \sum_k w_k C_{kl} \quad (1)$$

where l , s , i and k are the labels for laboratories, services, incomes and costs respectively, while T_{sl} , I_{il} and C_{kl} are the computing time associated with the service s provided by laboratory l , the income generated by the commercial activity or project i provided (for the related fraction) by laboratory l and the k costs met (or the value of the assets conferred) by laboratory l . The factors w_s ,

w_i and w_k are the weights given to the various terms of the sums while α_T , α_I and α_C are the normalization coefficients (taking into account also the different units used) of the services, income and costs components. Obviously some of the weights and normalization coefficients considered here heavily depend also on the strategies chosen by the MC of the VO. This is, indeed, the case of the normalization coefficients α which depend not only on the units used for time, incomes and costs but also on the policy chosen, for example, to enhance investments and productivity. The same is true for the weights w . For example, the value of certain services may vary from year to year. Extra credits from a specific budget may be assigned as an incentive to stimulate particularly valuable contributions (including the knowledge gained with failures, failure recovery and retrieval of lost information) typical of research activities). In this case the key means to be used to assess the achievement of the planned targets. A specific budget can also be assigned to dissemination and marketing aimed at making the VO and its activities known to other scientists.

6 Conclusions

The paper discusses the evolution of molecular simulators towards grid applications. In particular it has been analysed the constitution and the evolution of the virtual organization of Computational Chemistry and Molecular science. For this VO the levels of partnerships and the reorganization of the activities have been considered and an algorithm has been proposed to make it sustainable based on credit assignment. Extension of such an approach to mixed computational and experimental communities is also in the process of being systematically investigated.

Acknowledgments

This work has been financially supported by MIUR, ASI, CNR and COST in Chemistry (Action D23). Specific mention needs to be made to the project ASI-PQE2000, to the FIRB Grid.it project (RBNE01KNFP) on High performance Grid Platforms and Tools and to the MIUR CNR Strategic Project L 499/97-2000 on High performance Distributed Enabling Platforms.

References

1. The COST Chemistry web page (<http://www.unil.ch/cost/chem> and <http://costchemistry.epfl.ch/docs/actions.htm>)
2. Preparatory workshop "METACHEM", Brussels, November, 1999 and Action D23 of COST in Chemistry Memorandum of understanding (see <http://costchemistry.epfl.ch/docs/D23/d23-main.htm>).
3. D23 Final evaluation workshop, October 2005, ETH, zurich
4. Enabling Grids for E-Science in Europe (EGEE) <http://www.eu-egee.org>
5. Gervasi, O., Cicoria, D., Laganà, A., Baraglia, R.: Pixel, 10, 19 (1944)

6. Gervasi, O., Laganà, A.: Future Generation Computer Systems, 20(5), 703 (2004).
7. Laganà, A.: Towards a Grid Based universal molecular simulator in Theory of Chemical Reaction Dynamics, A. Laganà, G. Lendvay Eds. Kluwer (2004) p. 333.
8. Gervasi, O., Dittamo, C., Laganà, A.: A Grid Molecular Simulator for E-Science, Lecture Notes in Computer Science 3470, 16-22 (2005).
9. MIUR, Project RBNE01KNFP, High performance Grid Platforms and Tools (<http://www.grid.it>)
10. M. Vanneschi, The programming model of Assist, an environment of parallel and distributed portable applications, Parallel computing 28, 12 (2002)
11. Borgia, D.: SIMBEX: raccordo tra calcoli di dinamica e di struttura elettronica, Tesi di laurea, Università di Perugia (2005).
12. Storchi, L., Tarantelli, F., Laganà, A., Computing Molecular Energy Surfaces on a Grid, ICCSA 2006, Glasgow (2006).
13. First Egee Application Migration Report, 2005, EGEE-DNA4.3.1.523422-v4-7-13.doc; First Egee review workshop, (<http://agenda.cern.ch/fullAgenda.php?ida=a043803>) February 8-11, Geneva, 2005.
14. The Gilda portal (<https://gilda.ct.infn.it/>)
15. The Genius portal (<http://genius.ct.infn.it>)

Computing Molecular Energy Surfaces on a Grid

Loriano Storchi¹, Francesco Tarantelli^{1,2}, and Antonio Laganà¹

¹Department of Chemistry, University of Perugia,
via Elce di Sotto, 8, I-06123 Perugia, Italy
redo@thch.unipg.it, franc@thch.unipg.it, lag@unipg.it

²Istituto di Scienze e Tecnologie Molecolari, CNR,
via Elce di Sotto, 8, I-06123 Perugia, Italy
franc@thch.unipg.it

Abstract. SUPSIM is a web application, based on the Java Servlet technologies, to compute ab-initio potential energy surfaces of molecular systems for subsequent dynamical properties calculation. We describe the architecture of SUPSIM, its current implementation, and its possible future developments to tackle chemical systems of increasing complexity.

1 Introduction

As the complexity of a computational problem grows, it is crucial, in order to continue being able to solve it, to design a computational system flexible enough to grow comparably in complexity. Solutions can be worked out only by gathering together sufficient computing power and the appropriate know-how. This is, indeed, the case of the a-priori realistic simulation of a molecular process for which only the grid [1] can provide a computing platform suitable to make possible the needed cooperation among the various competences and laboratories involved.

The a-priori simulator proposed for the Molecular Science community, and the related Virtual Organization (VO) Compchem [2], is GEMS (Grid Enabled Molecular Simulator) that is derived from SIMBEX [3] (an a-priori simulation of crossed molecular beam experiments). The prototype version of GEMS has been implemented as a demo application [4] of the NA4 work-package of the EGEE project [5]. GEMS is articulated in four main steps (see Fig. 1): the calculation of the ab-initio values of the potential energy surface (PES), the fitting of the ab-initio points, the integration of the nuclei dynamics equations and the final statistical analysis and visualization of the results. The current version of GEMS (GEMS.0) assumes that the PES has already been generated by fitting a LEPS [6] functional form to the calculated ab-initio values, then GEMS.0 runs the necessary batches of trajectories by taking the value of the LEPS parameters from a library, and renders the properties of the process on some virtual monitors. To build the next, more general, version of GEMS two new computational modules have been created: SUPSIM and FITTING.

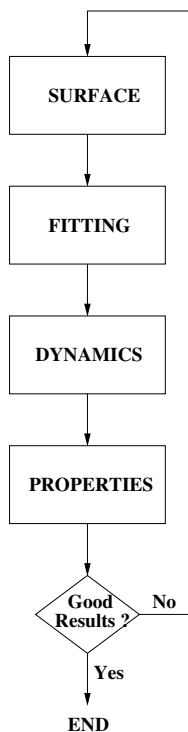


Fig. 1. A schematic diagram of the GEMS workflow. The first step (SURFACE) is the one to which SUPSIM corresponds. The other steps (FITTING, DYNAMICS and PROPERTIES) are devoted to the fitting of the potential energy values, the calculation of the dynamical properties and the statistical assembly of the observable quantities, respectively.

SUPSIM is the module devoted to the calculation of the potential energy surfaces using ab-initio methods. FITTING, instead, is the module that best fits the computed ab-initio points and stores the fitted values of the PES parameters (it can also build the related Fortran routine). The parameters (as well as the routine, conventionally called `Pesfunction`), are used for the subsequent dynamical calculations, carried out in the DYNAMICS module, for which either the Quasiclassical Trajectory or Quantum Mechanical approaches [7] are used. At the end, the last module PROPERTIES evaluates the observable properties of the system and of other relevant features of the chemical process by properly combining the calculated quantities.

The present paper is devoted to a description of SUPSIM. We illustrate the basic features of SUPSIM in section 2, give details of its design and implementation in section 3 and describe the communication frame in section 4. Further developments and the outlook are discussed in section 5.

2 What Is SUPSIM

SUPSIM is the module that will enable a GEMS user to submit the computation of a potential energy surface on a grid through a user friendly interface. At the present time SUPSIM has been deployed on the web with a test version reachable at the URL: <http://www.chemgrid.unipg.it:8080/>. Therefore, the present version of SUPSIM, that already displays some of the essential features of the complete product, is publicly available. Work is already in progress to insert SUPSIM in the GEMS workflow because its components have been already tailored for this purpose.

The PES calculation is articulated in three principal steps: parameters insertion, job submission, results retrieval. In the first step, the user is requested to specify the parameters of the calculation (such as, for example, the basis set and the theoretical method to be used, the electronic state parameters, the grid of nuclear positions where the electronic energy is to be computed, and so on). All the parameters can easily be specified via a simple HTML form. Then, the job for electronic energy computation can be submitted. Job submission can take place on an arbitrary grid. Once the necessary parameters are selected the user should choose a credential server, from where to retrieve a valid GLOBUS [8, 9] certificate, a suitable site where to run and a suitable quantum chemistry package to use. The present test version of SUPSIM runs on a local cluster of CHEMGRID (see section 5) and makes use of the ab-initio package MOLPRO [10]. The job is monitored using the standard GLOBUS [8] and OpenPBS [11] tools which notify the user about usage and the changes of state of the job.

At the end of the computation, all results can be collected from the hosts involved and inspected by the user to examine the key features of the computed surface, verify the suitability of the grid of points used, supplement, eliminate or recompute unconverged points, and generally take further action. At the end of this process, the computed PES values will be ready either to be used directly or to be fitted by the FITTING module. The computed PES values can also be graphically rendered or returned as an ASCII file.

3 SUPSIM Design and Implementation

SUPSIM is built using the Java Servlet technology [12] and runs in the Apache Tomcat Servlet container [13]. SUPSIM is actually divided in three different servlets:

- **SubCalc**. This servlet provides the user interface for job preparation and job submission. Actually this servlet builds the script used by the selected ab-initio program starting from the parameters specified by the user, and submits it for the computation.
- **ViewRes**. This servlet is devoted to monitor the progress of job execution and to retrieve, process and visualize the results.
- **CommErr**. This servlet is devoted to the management of the communication errors.

The first servlet, `SubCalc`, enables the user to specify the PES parameters and submit the job. In particular, the user specifies the parameters for the calculation using HTML forms. The present version of SUPSIM permits only the calculation of triatomic potential energy surfaces. The user must in general be able to select the basis set and the ab-initio method employed. At present, in order to provide a minimal qualitative description of the surface, use is made of the cc-pVDZ basis set [14] and of the valence CASSCF [14] level of theory. With a second HTML form it is possible to specify the parameters which determine the grid of nuclear geometries to be used for the calculation of the electronic energy. The nuclear positions can be specified either as internal coordinates or as bond-order [15] ones. Other parameters are concerned with the space/spin symmetry of the surface. This specification is related to the atoms constituting the system, so that, once the user has selected the molecular system, SUPSIM is able to build a list of all the possible symmetry and spin multiplicities. The user is then prompted for a list of selectable symmetries and spin multiplicities.

In general, the user should be able at this point (after obtaining a valid certificate) to select both the site or sites where to submit the calculation and the ab-initio programs to be used. He/she may be presented with a list of all the available ab-initio packages and prompted to select one. Otherwise, the grid interface will search the network for a list of sites offering the appropriate resource. At the moment the list of available sites and packages is not dynamic, but it is hard-written in an ASCII file.

After that, the servlet builds the script for the available quantum chemistry programs. `SubCalc` then generates a new thread that performs the job submission. As already mentioned, in the current version of SUPSIM the calculation is submitted on a local cluster of machines using the facilities offered by OpenPBS [11].

After submission, the user can obtain information on the status of the job by interrogating the second servlet, `ViewRes`. The first task of this servlet is, in fact, to retrieve the information on the job status. In the present implementation of SUPSIM this is achieved again by using OpenPBS services. The `ViewRes` servlet also provides the functionality to collect and display the results of the computation when this is completed. Two different display methods are available, a plain ASCII representation and a graphical rendering. If the user chooses the latter, the servlet builds and displays some images, presenting different views and sections of the surface along with the list of parameters used for the computation. All the images are built on the fly the first time that the user asks for the visualization. After this, the images are stored away to be retrieved on subsequent requests, until the computation is deleted. Similarly, the user can choose to visualize the PES values in ASCII format. The servlet then shows the contents of an ASCII file which contains some basic information on the calculation, such as the molecule, basis set and method used along with the calculated energies at each point of the chosen grid of geometries. Because all the data related to a single computation are stored in a separate directory, a user can retrieve, display and

use all the results of previous computations. In other words, a user has access to the history list of all her/his past computations, with the capability to manage it.

The third servlet, `CommErr`, is responsible for the proper handling of all communication errors. Communication is intended here as a transfer of information between SUPSIM and the other GEMS modules. When a PES calculation is completed, the data can be transmitted to subsequent GEMS modules, which in general reside somewhere else on the grid. This is in line with the fact that the overall application is designed to be an assembly of grid services implemented in various platforms, as is in the spirit of the Metalaboratories [16]. Because of the criticality of this function we devote the next section to a more detailed discussion of its implementation.

4 Communication

Communication between SUPSIM and GEMS takes place in two different phases. First, when it is required, GEMS asks SUPSIM to compute a certain set of PES values. This is achieved in GEMS by redirecting the user to the `SubCalc` URL. The second phase of the communication takes place in the reverse direction, from SUPSIM to GEMS. When the computation of the PES values is completed, SUPSIM transfers, upon user's request, the results to the `FITTING` module, and the user is then redirected to GEMS. More specifically (see Fig. 2), when the user logs into GEMS and indicates the chemical reaction to be simulated, it may happen that the necessary PES is already available in the user SUPSIM archive or somewhere else on the network. In this phase GEMS tries to locate the PES and, if it is available, it will simply retrieve it from the appropriate source. Otherwise, GEMS redirects the user to the `SubCalc` module of SUPSIM, to perform the electronic structure calculations. Some basic information on the computation, and in particular a unique identification number (ID), is transferred to SUPSIM. The ID number is stored by SUPSIM along with all other parameters of the computation and can be used, at any time, to identify the specific user

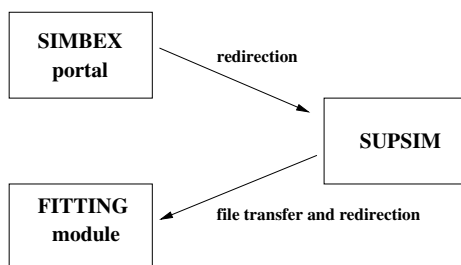


Fig. 2. A schematic representation of the GEMS communication process. The process takes place in two different phases: *a*) when it is required, GEMS asks SUPSIM to compute a certain set of PES values, *b*) when the computation is over, SUPSIM transfers the results to the `FITTING` module.

session. Once the job carrying out the calculation of the PES has been submitted, the information necessary to identify the user and the job for future use is recorded. The user can therefore logout and login again at some later time to resume work. In general, the user may also be e-mailed with information about the status of the job.

Once the PES calculation is finished and the user decides to continue with the dynamical simulation, SUPSIM transfers the PES values to GEMS. The file transfer takes place through a TCP communication and a simple protocol has been designed to allow this file transfer. The transaction can be summarized as follows:

- The client (SUPSIM) sends an *HELLO[id]* command, where *id* is the identification number related to the specific PES computation that *SubCalc* has received. The server checks if the *id* is valid and determines the user and the computation to which the files to be transmitted belong. If this phase is successful, the server send an *OK[id]*.
- After the first phase of communication is finished, the file transfer itself can be carried out. First of all the client sends a *FILE[nfile]* message to specify how many files there are to be transferred. If the server is able to receive them, an *OK[nfile]* message is sent back. Next, the server must be informed about the size of the incoming files. This is conventionally measured in units of transfer buffers, set at 4096 bytes. For each file to be transmitted, the client sends first the dimension with a *SET[dimfile]* message and waits for the return of an *OK[dimfile]* message from the server. Then the client starts sending the *dimfile* buffers of data one by one and, for each buffer it receives, the server responds with an *OK[n]* message, where *n* is the buffer counter.
- The TCP transaction is closed with an *ENDCOM[id]* message from the client followed by an *OKENDCOM[id]* from the server.

If the file transfer is successfully completed, the FITTING process can take control, otherwise the *CommErr* servlet will visualize the transaction error which has occurred. The use of a simple TCP connection rather than the GlobusFTP protocol [20] has historical reasons: originally, GEMS was built in a generic grid environment with no relationship with the Globus middleware. Switching to the GlobusFTP standard is a simple change that will be incorporated in the future versions of SUPSIM.

5 Developments and Future Work

In order to build an effectively grid-enabled version of SUPSIM, work will be undertaken to make it run as a testbed on CHEMGRID [17, 18] and on the EGEE production grid environment. This work will be articulated two steps. In the first step we shall enable *SubCalc* to submit the job using the GLOBUS environment [8] instead of the OpenPBS one. In the second step we shall modify *ViewRes* to enable it to retrieve job progress information and final results on the grid. We also envisage the possibility of having a more general and portable output format for the PES instead of a simple ASCII file.



Fig. 3. A map of the CHEMGRID sites

Depending on funding evolution SUPSIM will, as GEMS, develop along a double track. The first track is that of the production grid of EGEE. The second track is that of CHEMGRID, a project developed within GRID.IT [18]. CHEMGRID involves several Italian chemistry laboratories and is built using Globus toolkit 3.2 (see Fig. 3). Each site has, at present, a small Beowulf-type cluster [22] (see Tab. 1 for details), with a front-end which represents the public access point to the grid resources and two or more worker nodes. The request for a job is processed from the front end and is submitted to a worker node through the local resource management interface (OpenPBS, or LSF [19]).

Each site of the grid offers to the users the possibility of using various quantum chemistry packages. This will allow the SUPSIM users to choose a site and the ab-initio package best suited to his/her needs. The servlet will be shaped accordingly to build the script appropriate to the chosen ab-initio program and will submit the computation on the selected sites. At this point the other servlet, `ViewRes`, will be able to retrieve job processing information and the final results.

The retrieval of certificates will be implemented using a MyProxy server [21] (an on-line credential repository). A MyProxy server is already installed and usable for test and development on the front-end of the Perugia site, where also SUPSIM is currently installed.

Table 1. Characteristics of the Beowulf clusters involved in CHEMGRID

<i>Site location</i>	<i>CPU</i>	<i>Number of nodes</i>	<i>RAM</i>	<i>HD</i>
Perugia	Intel PIV HT 3.06 GHz	8	1024 MB	80 GB
Perugia	Intel PIV HT 2.08 GHz	1	1024 MB	80 GB
Bologna	AMD Athlon K7 1.2 GHz	4	512 MB	60 GB
Bologna	AMD Athlon K7 700 MHz	4	512 MB	26 GB
Padova	Intel PIV, 2.4 GHz	4	512 MB	40 GB
Napoli	AMD Athlon 1.0 GHz	4	256 MB	20 GB
Milano	Intel PIII Coppermine 1.0 GHz	8	1024 MB	16 GB
Bari	Intel Xeon HT 3.2 GHz	3	2048 MB	40 GB
ENEA	Intel PIV 1.8 GHz	4	512 MB	70 GB

Job submission and resource discovery/selection will be managed in the future by a grid service broker such as GridBus [23]. In such case it will be up to the grid broker to dynamically select a specific site or sites, starting from some basic information on the necessary resources, such as, for example the required ab-initio program, memory and disk space capabilities, machine architecture and so on.

An important point that will need attention is devising an appropriate and standardized format for the computed PES representation. This is an open problem that must be discussed in the general context of knowledge representation paradigms [24] and the specific representation of chemistry data. In recent years, the general problem of data representation and format has been widely discussed, especially with regard to the portability of data (see for example [25]). An appropriate solution for our purposes would be the adoption of an XML schema such as the CML [26], or QMCL [25], which is more suitable for quantum chemistry problems. Alternatively, the RDF [27, 28] format could be adopted. In this case, the PES could generally be made available and published on the WEB not only for a human, but also for an arbitrary software agent. It is clear that many of the ideas and tools exploited in the SUPSIM project can generally be used also for other complex quantum chemistry applications.

Acknowledgments

Financial support to this work has been provided by MIUR, ASI, CNR and COST in Chemistry (Action D23). Specific mention needs be made to the italian MIUR FIRB GRID.IT project (RBNE01KNFP) on High Performance Grid Platforms and Tools.

References

1. Foster, I. and Kesselman, C. Eds.: The Grid: Blueprint for a Future Computing Infrastructure, Morgan Kaufmann Publishers, USA (1999).
2. Gervasi, O., Dittamo, C., Laganà, A.: A Grid Molecular Simulator for e-Science, Lecture Notes in Computer Science, **3470**, (2005), 16-22.

3. Gervasi, O., Laganà, A.: SIMBEX: a portal for the a priori simulation of crossed beam experiments. *Future Generation Computer System*, **20(5)**, (2004), 703-716.
4. The EGEE (Enabling Grids for E-science in Europe) project: <http://public.eu-egee.org/>
5. Laganà, A., Gervasi, O.: GEMS: an EGEE application migration report. The First EGEE Assessment workshop, Geneva, 9-11 February 2005.
6. Polanyi, J.C., Schreiber, J.L.: *The Dynamics of Bimolecular Reactions*, Physical Chemistry-An Advanced Treatise, Volume VIA, Kinetics Gas Reactions, Eds., H. Eyring, W. Jost and D. Henderson (Academic Press, New York, 1974), Ch. 6, p. 383.
7. Laganà, A., Riganelli, A.: *Lecture Notes in Chemistry*, **75**, (2000).
8. The Globus Project: <http://www.globus.org/>.
9. Foster, I., Kesselman, C., Tsudik, G., Tuecke, S.: A Security Architecture for Computational Grids. *Proc. 5th ACM Conference on Computer and Communications Security Conference*, pp. 83-92, 1998.
10. Werner, H.-J., P. J. Knowles, P. J.: MOLPRO, a package of *ab-initio* programs version 2002.6. (<http://www.molpro.net/>).
11. OpenPBS home page: <http://www.openpbs.org/>.
12. Sun Java Servlet home page: <http://java.sun.com/products/servlet/>.
13. Apache Jakarta Tomcat home page: <http://jakarta.apache.org/tomcat/>.
14. Helgaker, T., Jørgensen, P., Olsen J.: *Molecular Electronic-Structure Theory*, Wiley, June 2002.
15. Laganà, A., Ferraro, G., Garcia, E., Gervasi O., Ottavi, A.: Potential energy representations in the bond order space, *Chem. Phys.*, **168**, (1992), 341.
16. Laganà, A.: Second Annual report of the activities of the workpackage 13 of GRID.IT (see ref. [18]) Annex: Structuring Chemistry Metalaboratories for Grid servicing.
17. The Chemgrid Project home page: <http://www.chemgrid.unipg.it/>.
18. GRID.IT: An Italian National Research Council Project on High Performance Grid Computing (RBNE01KNFP) (<http://www.grid.it>).
19. LSF (Load Sharing Facility): <http://www.platform.com/>.
20. GridFTP Protocol Specification (Global Grid Forum Recommendation GFD.20). W. Allcock, editor. March 2003.
21. Novotny, J., Tuecke, S., Welch, V.: An Online Credential Repository for the Grid: MyProxy. *Proceedings of the Tenth International Symposium on High Performance Distributed Computing (HPDC-10)*, IEEE Press, August 2001.
22. See e.g. <http://www.beowulf.org>.
23. Buyya, R., Venugopal, S.: The Gridbus Toolkit for Service Oriented Grid and Utility Computing: An Overview and Status Report, *Proceedings of the First IEEE International Workshop on Grid Economics and Business Models (GECON 2004, April 23, 2004, Seoul, Korea)*, 19-36pp, ISBN 0-7803-8525-X, IEEE Press, New Jersey, USA. (<http://www.gridbus.org/>).
24. Goble, C. A., Roure, D. De: The Grid: an application of the semantic web, *ACM SIGMOD Record*, **31**, (2002), 65-70.
25. Rossi, E., Emerson, A., Evangelisti, S.: Common Data Format for Program Sharing and Integration, *Lecture Notes in Computer Science*, **2658**, (2003), 316-323.
26. Murray-Rust, P., Rzepa, H. S., Wright, M.: Development of Chemical Markup Language (CML) as a System for Handling Complex Chemical Content, *New J. Chem.*, (2001), 618-634. (<http://www.xml-cml.org>).
27. Resource Description Framework: <http://www.w3.org/RDF/>.
28. The Semantic Web: <http://www.w3.org/2001/sw/>.

Electronic States in Three Dimensional Quantum Dot/Wetting Layer Structures

Marta Markiewicz and Heinrich Voss

Institute of Numerical Simulation,
Hamburg University of Technology,
D-21071 Hamburg, Germany
{m.markiewicz, voss}@tu-harburg.de

Abstract. Although self-assembled quantum dots are grown on wetting layers, most simulations exclude the wetting layer. The neglected effects on the electronic structure of a pyramidal InAs quantum dot embedded in a GaAs matrix are investigated based on the effective one electronic band Hamiltonian, the energy and position dependent electron effective mass approximation, and a finite height hard-wall 3D confinement potential. By comparing quantum dots with wetting layers and a dot without a wetting layer, we find that the presence of a wetting layer may effect the electronic structure essentially.

1 Introduction

Semiconductor nanostructures have attracted tremendous attention in the past few years because of their unique physical properties and their potential for applications in micro- and optoelectronic devices. In such nanostructures, the free carriers are confined to a small region of space by potential barriers, and if the size of this region is less than the electron wavelength, the electronic states become quantized at discrete energy levels. The ultimate limit of low dimensional structures is the quantum dot, in which the carriers are confined in all three directions.

Quantum dots can be produced today by the Stranski–Krastanov process which uses the relief of the elastic energy when two materials with a large lattice mismatch form an epitaxial structure. The deposited layer initially grows as a thin two dimensional (2D) wetting layer. As the deposited layer exceeds a critical thickness, the growth mode switches from 2D to 3D leading to the formation of a self-assembled quantum dot on top of the wetting layer.

Most simulations neglect the effect of wetting layers on the electronic structure of self-assembled quantum dots (cf. [5, 6, 8, 9, 10, 11, 19, 20] and the literature given therein). In this paper we report on numerical simulations investigating the effect of a wetting layer on the electronic structure of a pyramidal InAs quantum dot embedded in a GaAs matrix. We consider the one-band envelope-function formalism for electrons and holes assuming non-parabolicity for the electron's dispersion relation and an electron effective mass depending on the position and the energy level. Then the discretization of the Schrödinger equation results in a

sparse eigenvalue problem depending nonlinearly on the eigenparameter. Similar experiments are contained in [12, 13, 14, 15] where the authors assumed an axially symmetric quantum dot and an electron effective mass which does not depend on the energy level. These assumptions lead to linear eigenvalue problems of much smaller dimension.

Our paper is organized as follows. In Section 2 we state the rational eigenvalue problem which models the electronic behavior of a quantum dot (possibly including a wetting layer) assuming a position and energy dependent quasiparticle effective mass approximation. Discretization by a Galerkin method yields a sparse rational matrix eigenvalue problem which allows a minmax characterization of its eigenvalues. Section 3 describes the iterative projection methods introduced already in [20], and discusses the solution of the projected rational eigenproblems by safeguarded iteration. Numerical results are given in Section 4 demonstrating that the effect of the wetting layer on the electronic structure of a quantum dot is essential.

2 Position Dependent Effective Mass Model

We consider the problem to compute relevant energy states and corresponding wave functions of a three dimensional semiconductor quantum dot with or without a wetting layer. Let $\Omega_q \subset \mathbb{R}^3$ be a domain occupied by the quantum dot with the possible inclusion of a wetting layer, which is embedded in a bounded matrix Ω_m of different material. A typical example is an InAs pyramidal quantum dot grown on a wetting layer, which is embedded in a cuboid GaAs matrix (cf. Fig. 1).

We consider the one-band envelope-function formalism for electrons and holes in which the effective Hamiltonian is given by

$$\hat{H} = -\frac{\hbar^2}{2} \nabla \cdot \left(\frac{1}{m(\lambda, x)} \nabla \right) + V(x) \tag{1}$$

where \hbar is the reduced Planck constant, and ∇ denotes the spatial gradient.

Assuming non-parabolicity for the electron’s dispersion relation, the electron effective mass $m(\lambda, x)$ is constant on Ω_q and on the matrix Ω_m for every fixed energy level λ , and is taken as [1, 3]

$$\frac{1}{m_j(\lambda)} := \frac{1}{m(\lambda, x)} \Big|_{x \in \Omega_j} = \frac{P_j^2}{\hbar^2} \left(\frac{2}{\lambda + E_{g,j} - V_j} + \frac{1}{\lambda + E_{g,j} - V_j + \Delta_j} \right), \tag{2}$$

for $j \in \{m, q\}$, where the confinement potential $V_j := V|_{\Omega_j}$ is piecewise constant, and P_j , $E_{g,j}$ and Δ_j are the momentum matrix element, the band gap, and the spin-orbit splitting in the valence band for the quantum dot material ($j = q$) and the matrix ($j = m$), respectively.

To determine the relevant energy states and corresponding wave functions ψ we have to solve the governing Schrödinger equation

$$-\nabla \cdot \left(\frac{\hbar^2}{2m_j(\lambda)} \nabla \psi \right) + V(x)\psi = \lambda\psi, \quad x \in \Omega_q \cup \Omega_m. \tag{3}$$

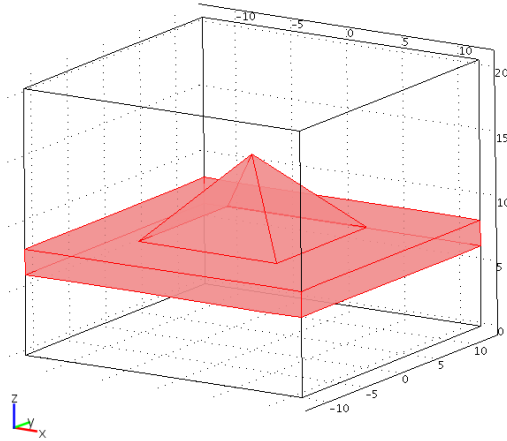


Fig. 1. Quantum dot with wetting layer

Since the wave function decays outside the quantum dot (and possibly the wetting layer) very rapidly, it is reasonable to assume homogeneous Dirichlet conditions $\psi = 0$ on the horizontal part $\partial\Omega_h$ of the outer boundary of Ω_m (cf. Fig. 1). Following [12] we impose Neumann boundary conditions $\frac{\partial\psi}{\partial n} = 0$ on the vertical part $\partial\Omega_v$ of the outer boundary of Ω_m , since far away from the quantum dot wave functions must approach asymptotically ordinary quantum well envelope functions where the wetting layer is the quantum well. On the interface between the quantum dot material and the matrix the Ben Daniel–Duke condition [7] holds

$$\frac{1}{m_q} \frac{\partial\psi}{\partial n_q} \Big|_{\partial\Omega_q} = \frac{1}{m_m} \frac{\partial\psi}{\partial n_m} \Big|_{\partial\Omega_m}, \quad x \in \partial\Omega_q \cap \partial\Omega_m. \tag{4}$$

Here n_q and n_m denote the outward unit normal on the boundary of Ω_q and Ω_m , respectively.

Let $\Omega := \bar{\Omega}_q \cup \Omega_m$ and $H := \{\psi \in H^1(\Omega) : \psi = 0 \text{ on } \partial\Omega_h\}$. Multiplying equation (3) by $\phi \in H$ and integrating by parts, one gets the variational form of the Schrödinger equation

$$\begin{aligned} a(\psi, \phi; \lambda) &:= \frac{\hbar^2}{2m_q(\lambda)} \int_{\Omega_q} \nabla\psi \cdot \nabla\phi \, dx + \frac{\hbar^2}{2m_m(\lambda)} \int_{\Omega_m} \nabla\psi \cdot \nabla\phi \, dx + V_q \int_{\Omega_q} \psi\phi \, dx \\ &+ V_m \int_{\Omega_m} \psi\phi \, dx = \lambda \int_{\Omega} \psi\phi \, dx =: \lambda b(\psi, \phi) \quad \text{for every } \phi \in H. \end{aligned} \tag{5}$$

In a similar way as in [20] it can be shown, that problem (5) has a countable set of positive eigenvalues $0 < \lambda_1 \leq \lambda_2 \leq \dots \rightarrow \infty$ of finite multiplicity which satisfy a minmax characterization. Namely, for fixed $\psi \neq 0$ the real equation

$$f(\lambda; \psi) := \lambda b(\psi, \psi) - a(\psi, \psi; \lambda) = 0 \tag{6}$$

has a unique positive solution $p(\psi)$. Hence, equation (6) defines a functional $p : H \rightarrow \mathbb{R}$ called Rayleigh functional (which generalizes the Rayleigh quotient for linear eigenproblems), and the k :th smallest eigenvalue of (5) satisfies

$$\lambda_k = \min_{\dim V=k} \max_{u \in V, u \neq 0} p(u). \tag{7}$$

Moreover, an eigenvalue $\tilde{\lambda}$ of (5) is the k :th smallest eigenvalue if and only if $\mu = 0$ is the k :th largest eigenvalue of the linear eigenvalue problem

$$\tilde{\lambda}b(\psi, \phi) - a(\psi, \phi; \tilde{\lambda}) = \mu b(\psi, \phi) \quad \text{for every } \phi \in H. \tag{8}$$

Discretizing the Schrödinger equation (3) with the boundary and interface conditions specified above by a Galerkin method (finite elements, e.g.) one gets a rational matrix eigenvalue problem

$$S(\lambda)x := \lambda Mx - \frac{1}{m_q(\lambda)}A_q x - \frac{1}{m_m(\lambda)}A_m x - Bx = 0 \tag{9}$$

where

$$A_j = \left(\int_{\Omega_j} \nabla \phi_k \cdot \nabla \phi_\ell \, dx \right)_{k,\ell}, \quad j \in \{q, m\}$$

$$M = \left(\int_{\Omega} \phi_k \phi_\ell \, dx \right)_{k,\ell} \quad \text{and} \quad B = \left(V_q \int_{\Omega_q} \phi_k \phi_\ell \, dx + V_m \int_{\Omega_m} \phi_k \phi_\ell \, dx \right)_{k,\ell}$$

and ϕ_i denotes a basis of the ansatz space.

A_q , A_m and B are symmetric and positive semi-definite, and M is positive definite, and for $\lambda \geq 0$ the matrix

$$\frac{\hbar^2}{2m_q(\lambda)}A_q + \frac{\hbar^2}{2m_m(\lambda)}A_m$$

is positive definite. Hence, the eigenvalues of the discretized problem (9) satisfy a minmax principle as well, and it follows from the minmax characterization (7) of the nonlinear Schrödinger equation that the k :th smallest eigenvalue of the discretized problem (9) is an upper bound of the corresponding eigenvalue of problem (3).

3 Solving the Discretized Problem

In this section we consider the problem to compute a few eigenvalues and corresponding eigenvectors at the lower end of the spectrum of the discretization (9) of the Schrödinger equation (3).

For linear sparse eigenproblems $S(\lambda) = \lambda B - A$ very efficient methods are iterative projection methods like the Lanczos, the Arnoldi, and the Jacobi–Davidson method, e.g., where approximations to the wanted eigenvalues and eigenvectors are obtained from projections of the eigenproblem to subspaces of small dimension which are expanded in the course of the algorithm.

Let $V \in \mathbb{R}^{n \times k}$ be an (orthonormal) basis of the current search space $\mathcal{V} \subset \mathbb{R}^n$, and assume that θ is an eigenvalue of the projected eigenvalue problem

$$V^T S(\lambda) V y = 0, \tag{10}$$

$y \in \mathbb{R}^k$ is a corresponding eigenvector, and denote by $x := V y$ the corresponding Ritz vector. To obtain an improved approximation it is reasonable to expand \mathcal{V} by a direction with a high approximation potential for the eigenvector wanted next.

There are two approaches in the literature for expanding the search space, both approximating inverse iteration: a Jacobi–Davidson type method [2] and the Arnoldi method [18] based on the residual inverse iteration. Here we restrict ourselves to the latter one.

Residual inverse iteration (introduced by Neumaier [16]) suggests the expansion

$$v = S(\sigma)^{-1} S(\theta) x, \tag{11}$$

of the search space \mathcal{V} , where σ is a fixed parameter close to the wanted eigenvalues.

For a linear eigenproblem $S(\lambda) = A - \lambda B$ this is exactly the Cayley transform with pole σ and zero θ , and since $(A - \sigma B)^{-1} (A - \theta B) = I + (\sigma - \theta) (A - \sigma B)^{-1} B$ and Krylov spaces are shift-invariant the resulting projection method expanding \mathcal{V} by v is nothing else but the shift-and-invert Arnoldi method.

If the linear system $S(\sigma)v = S(\theta)x$ is too expensive to solve for v we may choose as new direction $v = K^{-1} S(\theta)x$ with $K \approx S(\sigma)$, and for the linear problem we obtain an inexact Cayley transform or a preconditioned Arnoldi method. The resulting iterative projection method given in Algorithm 1. therefore is called nonlinear Arnoldi method, although no Krylov space is constructed and no Arnoldi recursion holds.

There are many details that have to be considered when implementing the nonlinear Arnoldi method concerning the choice of the initial basis, when and how to update the preconditioner, and how to restart the method. A detailed discussion is given in [18].

A crucial point in iterative projection methods for general nonlinear eigenvalue problems when approximating more than one eigenvalue is to inhibit the method from converging to the same eigenvalue repeatedly. For linear eigenvalue problems this is easy to do by using Schur forms or generalized Schur forms for the projected problem and then locking or purging certain eigenvectors. For nonlinear problems, however, such Schur forms do not exist and this presents one of the most difficult tasks in achieving good convergence.

For symmetric nonlinear eigenproblems satisfying a minmax characterization however, its eigenvalues can be computed safely one after the other. The minimum in (7) is attained by the invariant subspace of $S(\lambda_k)$ corresponding to the k :th largest eigenvalues, and the maximum by every eigenvector corresponding to the eigenvalue 0. This suggests the safeguarded iteration for computing the

Algorithm 1. Nonlinear Arnoldi Method

```

1: start with an initial pole  $\sigma$  and an initial orthonormal basis  $V$ ,  $V^T V = I$ 
2: determine preconditioner  $K \approx S(\sigma)$ ,  $\sigma$  close to first wanted eigenvalue
3:  $k=1$ 
4: while  $k \leq$  number of wanted eigenvalues do
5:   compute the  $k$ :th smallest eigenvalue  $\mu$  and corresponding normalized eigenvector  $y$  of the projected problem  $V^T S(\mu) V y = 0$ 
6:   determine Ritz vector  $u = V y$  and residual  $r = S(\mu) u$ 
7:   if  $\|r\| < \varepsilon$  then
8:     accept eigenvalue  $\lambda_k = \mu$ , and eigenvector  $x_k = u$ ,
9:     choose new pole  $\sigma$  and update preconditioner  $K \approx S(\sigma)$  if indicated
10:    restart if necessary
11:     $k = k + 1$ 
12:   end if
13:   solve  $K v = r$  for  $v$ 
14:    $v = v - V V^T v$ ,  $\tilde{v} = v / \|v\|$ ,  $V = [V, \tilde{v}]$ 
15:   reorthogonalize if necessary
16: end while

```

Algorithm 2. Safeguarded iteration

```

1: Start with an approximation  $\mu_1$  to the  $k$ -th smallest eigenvalue of  $P(\lambda) y = 0$ 
2: for  $\ell = 1, 2, \dots$  until convergence do
3:   determine an eigenvector  $u$  corresponding to the  $k$ :th largest eigenvalue of the matrix  $P(\mu_\ell)$ 
4:   evaluate  $\mu_{\ell+1} = p(u)$ , i.e. solve  $u^T P(\mu_{\ell+1}) u = 0$  for  $\mu_{\ell+1}$ 
5: end for

```

k :th smallest eigenvalue which reads as follows for the projected eigenproblem $P(\lambda)y := V^T S(\lambda) V y = 0$:

The safeguarded iteration has the following convergence properties [17]: It converges globally to the smallest eigenvalue λ_1 . The (local) convergence to simple eigenvalues is quadratic. If $P'(\lambda)$ is positive definite, and u in Step 3 of the last algorithm is replaced by an eigenvector of $P(\mu_\ell)u = \mu P'(\mu_\ell)u$ corresponding to the k :th largest eigenvalue, then the convergence is even cubic. Moreover, a variant exists which is globally convergent also for higher eigenvalues.

4 Numerical Experiments

We consider a pyramidal quantum dot with width 12.4 nm and height 6.2 nm embedded in a cuboid matrix of size 24.8 nm \times 24.8 nm \times 18.6 nm. We computed the band structure for the pure dot without a wetting layer, for the combined quantum dot and wetting layer structures (cf. Fig. 1) for two wetting layers of thickness 1 nm and 2 nm, respectively, and for the pure wetting layer.

In the calculations of the electron energy spectra for a narrow gap InAs quantum dot in a GaAs matrix we used the semiconductor band structure parameters for InAs as: $P_q = 0.8503$, $g_q = 0.42$, $\delta_q = 0.48$, and $V_q = 0$, and for GaAs we chose $P_m = 0.8878$, $g_m = 1.52$, $\delta_m = 0.34$, and $V_m = 0.77$ as in [9].

Using FEMLAB [4] we discretized the Schrödinger equation by the finite element method with quadratic Lagrangian elements on a tetrahedral grid. Since the envelope functions are mainly concentrated on the quantum dot (which occupies only less than 3 % of Ω) and the wetting layer, and since they decay very rapidly outside the quantum dot/wetting layer structure, we chose a non-uniform grid such that roughly half of the degrees of freedom are in the InAs structure and the remaining ones are in the GaAs matrix.

The arising rational eigenvalue problems were solved under MATLAB 7.0.4 on an Intel Pentium D processor with 4 GByte RAM and 3.2 GHz by the non-linear Arnoldi method, where the projected eigenproblems were solved by the safeguarded iteration. We started the method with a constant vector on $\overline{\Omega}_q \cup \Omega_m$ which is far away from an eigenvector, and we terminated the iteration for an eigenvalue, if the residual norm was less than 10^{-8} . Due to the symmetry of the problem there exist multiple eigenvalues (for instance the second eigenvalue in all cases). The Arnoldi method had no problems to detect these multiple eigenvalues with the right multiplicity.

Table 1. Electronic eigenstates

	pure QD	QD/WL 1 nm	QD/WL 2nm	pure WL 2 nm
dimension	183124	156479	152928	10903
CPU	297.8	251.2	235.0	46.4
λ_1	0.41621	0.35741	0.30864	0.45720
$\lambda_{2/3}$	0.59909	0.51472	0.43239	0.47149
λ_4	0.71802	0.60738	0.46590	0.48545
λ_5	0.72956	0.61991	0.47964	0.51246

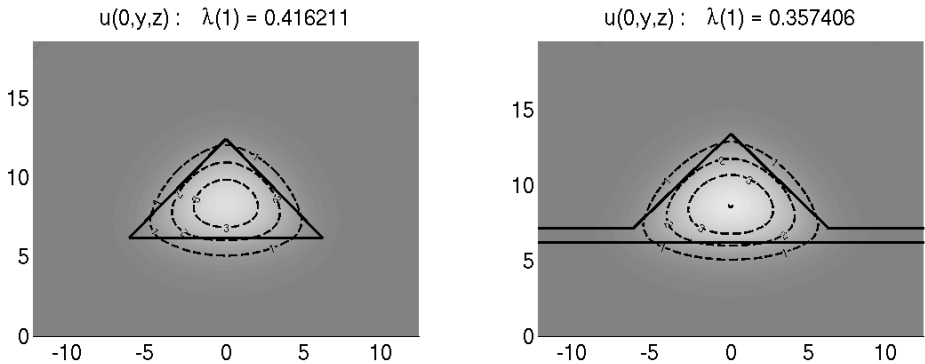


Fig. 2. Eigenvector of quantum dot without and with wetting layer

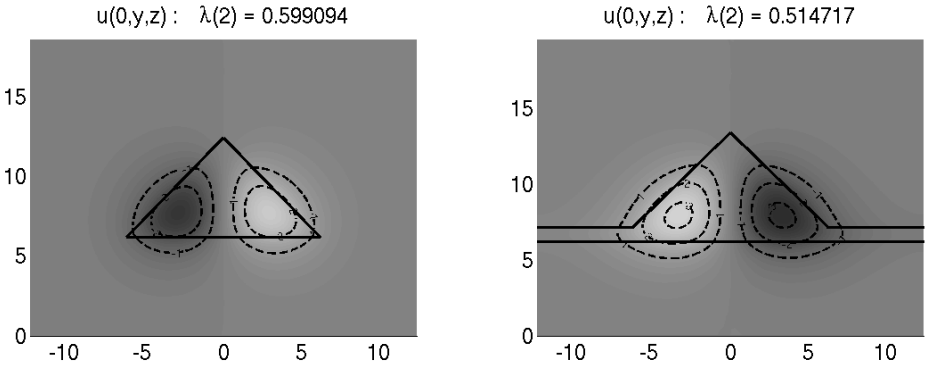


Fig. 3. Eigenvector of quantum dot without and with wetting layer

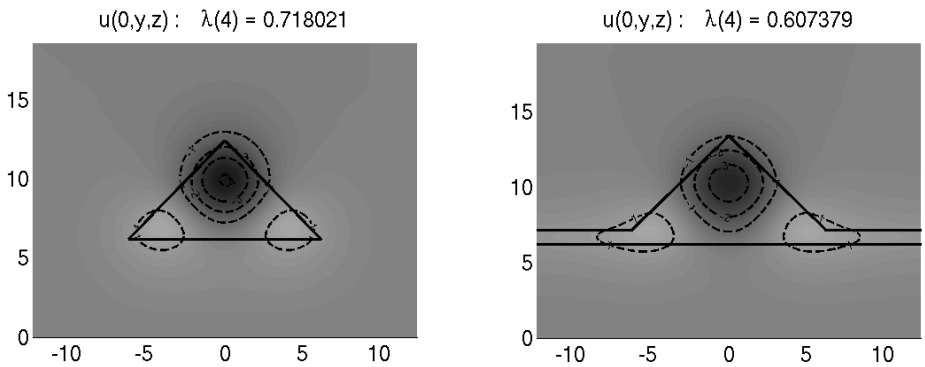


Fig. 4. Eigenvector of quantum dot without and with wetting layer

We first consider the pure quantum dot problem which has five energy eigenvalues smaller than the confinement potential $V_m = 0.77$ displayed in the second column of Tab. 1. The discretized problem has 183124 degrees of freedom, and it takes 297.8 seconds to solve it. The envelope functions ψ_j corresponding to these states are essentially confined to the quantum dot. Fig. 2 - 4. show on the left a cut $\{\psi_j(0, y, z) : (0, y, z) \in \overline{\Omega}\}$ through ψ_j for $j = 1, 2, 4$. ψ_3 is obtained from ψ_2 rotating it about the z -axis by 90 degrees, and ψ_5 is skew-symmetric with respect to the plain $\{0, y, z\} : y, z \in \mathbb{R}\}$ (and therefore its cut is identical to 0).

Next we added to the quantum dot a wetting layer of thickness 1 nm and 2 nm, respectively. In this case there are 18 and 31 eigenvalues smaller than V_m , respectively, most of them being approximate quantum well eigenstates corresponding to pure the wetting layer. The smallest 5 eigenvalues are shown in columns 3 and 4 in Tab. 1. They are substantially smaller than the corresponding ones of the pure quantum dot. For instance, the ground state is smaller by 14 and 26 percent, respectively.

The envelope functions ψ_1, ψ_2 and ψ_4 for the case of a wetting layer of thickness 1 nm are displayed in Fig. 2 - 4. on the right. While the ground state is

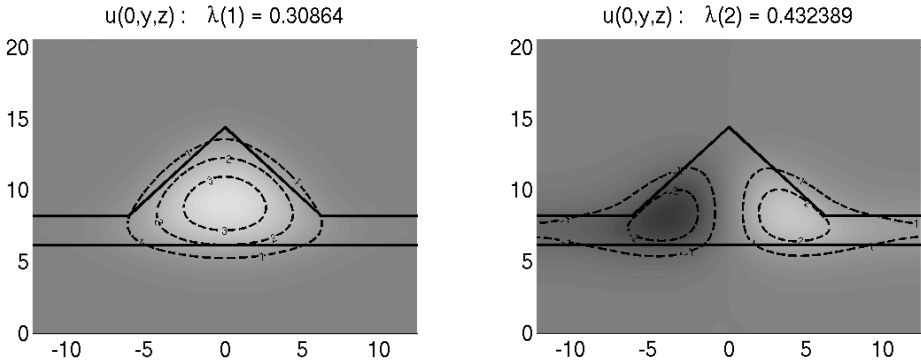


Fig. 5. Eigenvector of quantum dot with thick wetting layer

localized quite well to the quantum dot, this property gets lost for excited eigenstates. For the wetting layer of thickness 2 nm this is even more pronounced. The envelope functions ψ_1 and ψ_2 for this case are shown in Fig. 5.

References

1. G. Bastard. *Wave Mechanics Applied to Semiconductor Heterostructures*. Les editions de physique, Les Ulis Cedex, 1988.
2. T. Betcke and H. Voss. A Jacobi–Davidson–type projection method for nonlinear eigenvalue problems. *Future Generation Computer Systems*, 20(3):363 – 372, 2004.
3. S.L. Chuang. *Physics of Optoelectronic Devices*. John Wiley & Sons, New York, 1995.
4. FEMLAB, Version 3.1. COMSOL, Inc., Burlington, MA, USA, 2004.
5. I. Filikhin, E. Deyneka, G. Melikian, and B. Vlahovic. Electron states of semiconductor quantum ring with geometry and size variations. *Molecular Simulation*, 31:779 – 785, 2005.
6. I. Filikhin, E. Deyneka, and B. Vlahovic. Energy dependent effective mass model of InAs/GaAs quantum ring. *Model.Simul.Mater.Sci.Eng.*, 12:1121 – 1130, 2004.
7. P. Harrison. *Quantum Wells, Wires and Dots. Theoretical and Computational Physics*. John Wiley & Sons, Chicester, 2000.
8. T.-M. Hwang, W.-W. Lin, J.-L. Liu, and W. Wang. Jacobi–Davidson methods for cubic eigenvalue problems. *Numer.Lin.Alg.Appl.*, 12:605 – 624, 2005.
9. T.-M. Hwang, W.-W. Lin, W.-C. Wang, and W. Wang. Numerical simulation of three dimensional quantum dot. *J. Comput.Phys.*, 196:208 – 232, 2004.
10. Y. Li. Numerical calculation of electronic structure for three-dimensional nanoscale semiconductor quantum dots and rings. *J. Comput. Electronics*, 2:49 – 57, 2003.
11. Y. Li, O. Voskoboynikov, C.P. Lee, and S.M. Sze. Computer simulation of electron energy level for different shape InAs/GaAs semiconductor quantum dots. *Comput.Phys.Comm.*, 141:66 – 72, 2001.
12. R.V. Melnik and M. Willatzen. Modelling coupled motion of electrons in quantum dots with wetting layers. In *Proceedings of the 5th Internat.Conference on Modelling and Simulation of Microsystems, MSM 2002*, pages 506 – 509, Puerto Rico, USA, 2002.

13. R.V. Melnik and M. Willatzen. Bandstructures of conical quantum dots with wetting layers. *Nanotechnology*, 15:1 – 8, 2004.
14. R.V. Melnik and K.N. Zotsenko. Computations of coupled electronic states in quantum dot/wetting layer cylindrical structures. In P.M.A. Sloot, D. Abramson, A.V. Bogdanov, J.J. Dongarra, A.Y. Zomaya, and Y.E. Gorbachev, editors, *Computational Science – ICCS 2002, 3rd International Conference, Proceedings, Part III*, volume 2659 of *Lecture Notes in Computer Science*, pages 343–349, Berlin, 2003. Springer Verlag.
15. R.V. Melnik and K.N. Zotsenko. Finite element analysis of coupled electronic states in quantum dot nanostructures. *Modelling Simul. Mater. Sci. Eng.*, 12:465 – 477, 2004.
16. A. Neumaier. Residual inverse iteration for the nonlinear eigenvalue problem. *SIAM J. Numer. Anal.*, 22:914 – 923, 1985.
17. H. Voss. Initializing iterative projection methods for rational symmetric eigenproblems. In *Online Proceedings of the Dagstuhl Seminar Theoretical and Computational Aspects of Matrix Algorithms, Schloss Dagstuhl 2003*, <ftp://ftp.dagstuhl.de/pub/Proceedings/03/03421/03421.VoszHeinrich.Other.pdf>, 2003.
18. H. Voss. An Arnoldi method for nonlinear eigenvalue problems. *BIT Numerical Mathematics*, 44:387 – 401, 2004.
19. H. Voss. Electron energy level calculation for quantum dots. Technical Report 91, Institute of Numerical Simulation, Hamburg University of Technology, 2005. To appear in *Comput. Phys. Comm.*
20. H. Voss. A rational eigenvalue problem governing relevant energy states of a quantum dots. Technical Report 92, Institute of Numerical Simulation, Hamburg University of Technology, 2005. To appear in *J. Comput. Phys.*

A Web Based Application to Fit Potential Energy Functionals to *ab Initio* Values

Leonardo Arteconi¹, Antonio Laganà¹, and Leonardo Pacifici²

¹ Department of Chemistry, University of Perugia,
via Elce di Sotto, 8 06123 Perugia, Italy

² Department of Mathematics and Computer Science, University of Perugia,
via Vanvitelli, 1 06123 Perugia, Italy
{bodynet, lag, xleo}@dyn.unipg.it

Abstract. The implementation of a prototype Internet portal devoted to the fitting of *ab initio* potential energy values for three atom reactions is discussed. The application has been designed to run as a part of a Grid simulator of molecular processes.

1 Introduction

Molecular Simulators are always based on the construction of a suitable potential energy surface (PES) on which the dynamics of the intervening atoms and molecules takes place. If the system to be investigated is made of atoms and small molecules the usual way of building such a PES is by carrying out extended *ab initio* calculations and then fitting calculated potential energy values using a suitable functional form.

This paper focuses on the development and implementation of an Internet portal dealing with such a fitting by assuming that *ab initio* potential energy values are either already available on the web or can be computed on demand (using for example SUPSIM [1], a tool developed in our laboratory).

This internet portal, called FITTING, has therefore the goal of searching for the values of the PES parameters available on the web. In the case of the LEPS surface already built-in in the prototype version of the Grid Enabled Molecular Simulator (GEMS.0) [2] that has been already implemented as a demo within the NA4 work package of EGEE [3], this means a search for three pairs of diatomic Morse parameters and three Sato parameters. FITTING offers also the possibility of determining the Sato parameters or to construct an *ad hoc* PES (different from LEPS) as a fortran routine to be used for the new version of the simulator (GEMS.1) which is in the process of being implemented.

The basic idea of a simulator of molecular processes was developed in our laboratory in the second part of the Nineties [4] and led to the birth of SIMBEX (Simulation of Molecular Beam Experiments) [5].

SIMBEX simulates a priori fashion the elementary chemical processes occurring in a crossed beam apparatus [6] and estimates the characteristics of the measured signal.

More recently, the dynamics engine of SIMBEX has been implemented as the already mentioned GEMS.0 prototype which has then evolved into GEMS.1. The key novelty of GEMS.1 is concerned with both the extension of dynamical treatments to quantum methods and the development of the FITTING portal. In this paper the web environment in which FITTING operates (see section 2) and the structure in which it is articulated (see section 3) are illustrated.

2 The Web Environment

For the FITTING portal we have developed a web interface. This choice allows several advantages for a Grid use. These are namely: the independence from the user OS platform; the possibility of modifying and upgrading the software without a direct participation of the customer; the simplicity of the realization of the graphical interface; the ubiquitous use of the application.

For this purpose we have created a cross-browser site using only server-side technologies. Accordingly, the end-user can utilize the FITTING web GUI (Graphical User Interface) by making use only of a W3-Compliant web browser [8] as sketched in Fig. 1.

As shown in the figure the related Web Environment has been implemented using the following elements:

1. A dynamic web server, based on the Apache Web [9] server with the PHP4 module [10].
2. An RDBMS (MySQL [11] in our case) that handles the user data and supports the authentication phase.

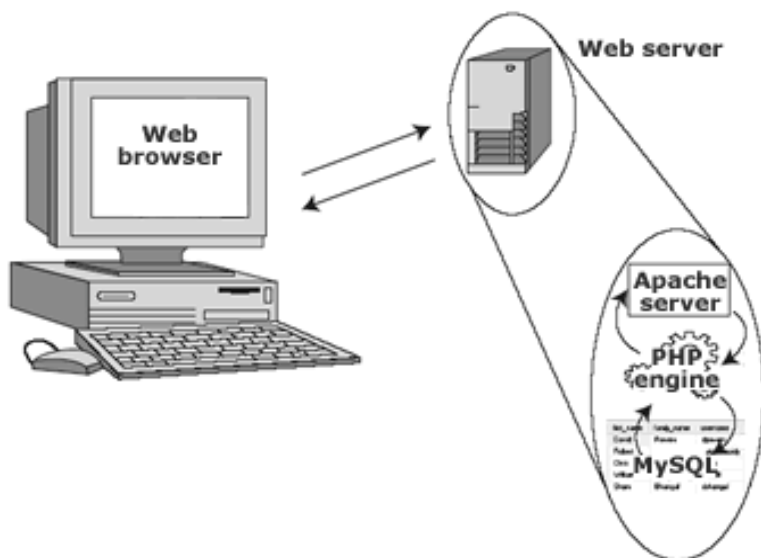


Fig. 1. Web environment

The Portal has been developed and tested using GPL Software and FreeSoftware. More specifically we used Apache Web Server 1.3.32 and MySQL 4.1.3 powered by FreeBSD 5.4.

3 The Internet Portal Architecture

Because of the complexity of the FITTING workflow, we produced a set of dynamically generated pages. These pages take care of managing the execution of the computational procedure by the Web server and help the user to define the input parameters of the fitting calculation through the Graphical User Interfaces. As schematized in Fig. 2 the user needs to register when first accessing the portal. After the verification of the identity, the user is assigned an account and the associated login and password. At this point the user can access the portal and use the fitting environment. Because of the multiuser environment in which we operate, multiple requests to the web server are dealt using the Session support (enabled in PHP by default).

In the next step, the user selects which atoms compose the triatomic system to consider and the fitting functional form to use (corresponding to the System configuration box of Fig. 2), using the GUI illustrated in Fig. 3 that shows the data for the $N+O_2$ reaction and the choice of the LEPS functional form (which is at the present the only working option).

For this purpose the server creates a dynamical web page which prompts the user to supply the name of the file of the *ab initio* data to use in the calculation. The same page allows him/her to insert the *ab initio* data in the web server (Upload File box in Fig. 2) using the GUI illustrated in Fig. 4 (in the figure the upload page of the data of the $N+O_2$ reaction is shown).

The page asks also for one to three (depending on the symmetry of the investigated system) files of diatomic *ab initio* data. These files specifies in the first record the number of *ab initio* points it contains. The *ab initio* data need to be arranged in a two column format (the first column contains the value of

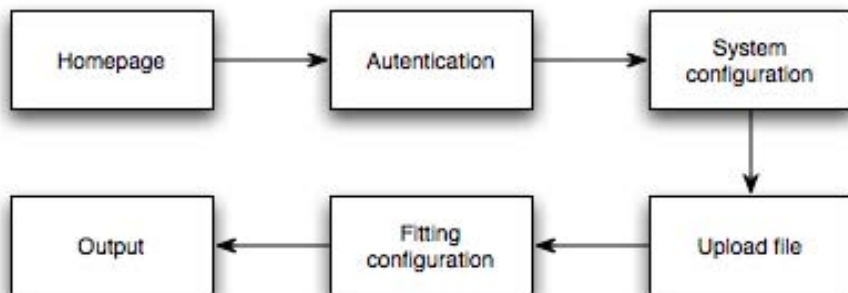
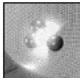


Fig. 2. Portal workflow



Register Documentation FAQ Info Contact

User info

You are logged as

Username: demo

Email: email@email.com

Account information: demo user account [\[Logout\]](#)

Job info

Job ID: 685308fab5ee7906416e8beb9f71177

System: none

Function: none

Diatomic file:

Triatomic file: [\[Clean Job\]](#)

Select system atoms:

Select the system:


Atom:

Select the functional form:

LEPS [\[about the LEPS method\]](#)

Bond Order [not implemented]

Fig. 3. Screenshot of System configuration site page



Register Documentation FAQ Info Contact

User info

You are logged as

Username: demo

Email: email@email.com

Account information: demo user account [\[Logout\]](#)

Job info

Job ID: 77d0526f0851124018dfcd95ee26743f

System: N-O-O

Function: LEPS

Diatomic file:

Triatomic file: [\[Clean Job\]](#)

Upload File

Diatomic file:

Select and upload file for the N-O molecule calculation of diatomic parameters [\[about the diatomic file format\]](#):

Select N-O file:

Select and upload file for the O-O molecule calculation of diatomic parameters [\[about the diatomic file format\]](#):

Select O-O file:

Triatomic file:


Upload the triatomic data file [\[about the triatomic file format\]](#):

Select triatomic file:

Fig. 4. Screenshot of System configuration site page

the internuclear distance while the second one the value of the related *ab initio* potential energy). The page prompts also the request for a file containing the *ab initio* triatomic data.

This file specifies also the number of *ab initio* point it contains. The *ab initio* data need to be arranged in a four column format (the first three columns contain the value of the three internuclear distances while the fourth one the value of



FITTING
on demand

Register [Documentation](#) [FAQ](#) [Info](#) [Contact](#)

User info

You are logged as

Username: demo

Email: email@email.com

Account information: demo user account [\[Logout\]](#)

Job info

Job ID: 685308fab5ee7906416e8bebb9f71177

System: N-O-O

Function: LEPS

Diatomic file: no_copy2.dat [\[view\]](#)
oo_copy2.dat [\[view\]](#)

Triatomic file: abinitio_copy2.dat [\[view\]](#) [\[plot\]](#) [\[Clean Job\]](#)


Complete the input file

Number of points:

	N-O	O-O	N-O
Dissociation energy:	6.54702245348742	5.09670939353612	6.54702245348742
Beta parameter:	3.35287832493631	3.96548003013965	3.95287832493631
Equilibrium distance:	1.12755930423737	1.19547808170319	1.12755930423737
Sato variable:	<input type="text" value="0"/>	<input type="text" value="0"/>	<input type="text" value="0"/>
ia:	<input type="text" value="1"/>	<input type="text" value="1"/>	<input type="text" value="1"/>

[Submit information](#)

Fig. 5. Screenshot of Fitting configuration site page



FITTING
on demand

Register [Documentation](#) [FAQ](#) [Info](#) [Contact](#)

User info

You are logged as

Username: demo

Email: email@email.com

Account information: demo user account [\[Logout\]](#)

Job info

Job ID: 77d0526f0851124018dfcd95ee26743f

System: N-O-O

Function: LEPS

Diatomic file: no.dat [\[view\]](#)
oo.dat [\[view\]](#)

Triatomic file: abinitio.dat [\[view\]](#) [\[Clean Job\]](#)

Output: LEPS Fortran Routine

```

c
c      N-O-O
c
c Dab = 6.547022d0      (eV)
c Dbc = 5.096707d0
c Dca = 6.547022d0
c
c betaAB,betaBC,betaAC = 3.352878d0 3.965534d0 3.352878d0      (A**-1)
c
c rAB, rBC, rCA =1.127559d0 1.195479d0 1.127559d0      (A)
c
c SAB, SBC, SAC = 0.11 0.35 0.11
c
c*****
C
C THE ROUTINE CALCULATES THE LEPS POTENTIAL FOR THE NOO SYSTEM
C
C      SUBROUTINE NOOLEPS (VR1,VR2,VR3,VLSAB,VLSBC,VLSAC,XU)
C
C      IMPLICIT REAL*8(A-H,O-Z)
C      IMPLICIT INTEGER*8(I-N)
C      data VLDAB,VLDBC,VLDAC /6.547022d0,5.096709d0,6.547022d0/
C      data VLBAB,VLBBC,VLBAC /3.352878d0,3.965548d0,3.352878d0/
C      data VLRRAB,VLRRBC,VLRRAC /1.127559d0,1.195478d0,1.127559d0/
C      data VLSAB,VLSBC,VLSAC /0.11,0.35,0.11
C
C
C      PLEAB= EXP (VLBAB*(VLRAB-VR1))
C      PLEBC= EXP (VLBBC*(VLRBC-VR2))
C      PLEAC= EXP (VLBAC*(VLRAC-VR3))
C
C      COULOMB AND EXCHANGE TERM
C      PLQAB= VLDAB*((.75+.25*VLSAB)*PLEAB**2- (.5+1.5*VLSAB)*PLEAB)
C      PLQBC= VLDBC*((.75+.25*VLSBC)*PLEBC**2- (.5+1.5*VLSBC)*PLEBC)
C      PLQAC= VLDAC*((.75+.25*VLSAC)*PLEAC**2- (.5+1.5*VLSAC)*PLEAC)
C      PLJAB= VLDAB*((.25+.75*VLSAB)*PLEAB**2- (1.5+.5*VLSAB)*PLEAB)
C      PLJBC= VLDAC*((.25+.75*VLSBC)*PLEBC**2- (1.5+.5*VLSBC)*PLEBC)
C      PLJAC= VLDAC*((.25+.75*VLSAC)*PLEAC**2- (1.5+.5*VLSAC)*PLEAC)
C      PLRSRT= SQRT (ABS ((PLJAB/(1.E0+VLSAB)-PLJBC/(1.+VLSBC))**2+
C      > (PLJBC/(1.+VLSBC)-PLJAC/(1.+VLSAC))**2+(PLJAC/(1.+VLSAC)-
C      > PLJAB/(1.+VLSAB))**2))
C***** THE POTENTIAL (THE ZERO IS AT TOTAL DISSOCIATION) *****
C      XU=PLQAB/(1.+VLSAB)+PLQBC/(1.+VLSBC)+PLQAC/(1.+VLSAC)-
C      *1.d0*PLRSRT*SQRT (.5E0)
C      close(5)
C      RETURN
C      END
                
```

Fig. 6. Screenshot of Output site page

the *ab initio* potential energy). The final section allows the user to configure the remaining input parameters. These parameters depend on the functional form chosen for the fitting.

As already mentioned for a LEPS the three parameters to be determined are the Sato parameters for which a default value of zero is assumed (see the GUI screenshot in Fig. 5 for the N+O₂ case considered).

As a result of the use of FITTING one has the values of the Morse diatomic parameters and the Sato parameters displayed by the GUI to be passed to GEMS. One has also the complete fortran routine for the potential (incorporating the above mentioned parameters, see GUI output in Fig 6).

4 Conclusion

We have described in this paper the portal FITTING, one of the key step forward from the GEMS.0 to the GEMS.1 version of the Grid Enabled Molecular Simulator implemented within EGEE. The FITTING portal bridges electronic structure to dynamical calculations by handling the delicate phase of representing in a proper functional form the potential energy values imported from Web or generated by SUPSIM. The paper discusses the articulation of the workflow by considering as a case study the popular LEPS PES and shows how the structure of the portal is already prepared to accept other functional forms for which also the related fortran routine has to be written for the dynamics section of GEMS. Future work will be concerned with the actual introduction of other fitting functional forms (eg: Bond Order) and the connection of FITTING with portals taking care of the calculation *ab initio* potential energy values.

Acknowledgments

Financial support from from MIUR (project RBNE01KNFP) and ASI (PQE2000) is acknowledged.

References

1. Storchi, L., Tarantelli, F., Laganà, A.: Computing Molecular Energy surfaces on a Grid ICCSA Glasgow 2006 (submitted)
2. Gervasi, O., Dittamo, C., Laganà, A. A Grid Molecular Simulator for E-Science, Lecture Notes in Computer Science **3470** (2005) 16 - 22
3. The Enabling Grids for E-science (EGEE) project (<http://public.eu-egee.org>)
4. Gervasi, O., Laganà, A., Cicoria, D., Baraglia, R.: Animazione e Calcolo Parallelo per lo Studio delle Reazioni Chimiche Elementari. Pixel **10** (1994) 19
5. Gervasi, O., Laganà, and Lobbiani, M.: Towards a GRID based portal for an a priori molecular simulation of chemical reactivity. Lecture Notes in Computer Science **2331** (2002) 956-965
6. Lee, Y.T.: Atomic and Molecular Beam Methods, ed. G. Scoles, Oxford University Press, New York **1** (1987)

7. Boyd, D., Jeffreys, P., Goodfellows, J., Steenman-Clark, L., Allan, P.: Ercim News, **45** (2001) 11
8. World Wide Web Consortium (<http://www.w3.org>)
9. The Apache Software Foundation (<http://www.apache.org>)
10. PHP: Hypertext Preprocessor (<http://www.php.net>)
11. Popular Open Source Database (<http://www.mysql.com>)

Dynamic Load-Balancing for the STEM-II Air Quality Model*

J. Carlos Mouriño¹, María J. Martín², Patricia González²,
and Ramón Doallo²

¹CESGA Supercomputing Center. Santiago de Compostela, Spain
jmourino@cesga.es

²Computer Architecture Group. Department of Electronics and Systems,
University of A Coruña, Spain

Abstract. The aim of this work is to improve load balance of the MPI parallel version of the STEM-II air quality model. Several dynamic data distributions are proposed and evaluated on different systems: homogeneous and dedicated, and heterogeneous and/or non-dedicated. Results prove that dynamic distribution strategies perform better than traditional static distributions. Although all the data distributions presented here have been developed to be used with the STEM-II air quality model, they are also very suitable for use in other parallel applications.

1 Introduction

High performance computing is essential for solving the highest demanding computational problems found in areas such as climate research, astrophysics, high energy physics, etc. In recent years the use of CPU-intensive complex simulations has increased significantly, and air quality simulations are not an exception. Traditionally, supercomputers have been used to solve these problems. More recently, with the emergence of cluster, heterogeneous systems with non-dedicated machines have begun to be used in the resolution of these simulations, with the aim of increasing the number of processors and decreasing the execution time while maintaining a low cost.

Load balance is already a problem in an homogeneous and dedicated system due to the possible load unbalance caused by the data distribution in the parallelization of the application. The problem increases in a heterogeneous or non-dedicated system due to its own load unbalance generated by the heterogeneity or the dynamic changes in the platform.

The application used in this work is the STEM-II model [3], an Eulerian air quality model which simulates transport, chemical transformations, emissions and deposition processes in an integrated framework. It is used to know in advance how the meteorological conditions, obtained from a meteorological prediction model [11], will affect the emissions of As Pontes Power Plant [1],

* This work has been supported by the Xunta de Galicia (Project PGIPIT04TIC105004PR).

sited in A Coruña, Spain. The speedup in the simulation process is important in order to make decisions about modifications in the industrial process. The final aim is fulfilling the European regulations concerning the emission of pollutants. As this model is computationally intensive, it has been parallelized using MPI for distributed memory machines and OpenMP for shared memory systems. Details about the parallelization and performance results on different platforms, including the Grid, can be found at [8, 9, 10]. The code was initially parallelized using a static load balance strategy that turns out to be quite inefficient for some input data.

There exists, in the literature, several research papers concerning the parallelization of air quality models, but most of them consider only static load balancing and therefore are not adequate for non-dedicated environments [13, 12, 5, 4]. In [7, 6] Elbern compares several static and dynamic load balancing strategies for the European air pollution dispersion model (EURAD), achieving better results with dynamic strategies.

In this paper a set of new dynamic distributions strategies are presented to achieve an optimum load balance and, therefore, a better performance of the simulation. The target architecture is a cluster of commodity machines. The structure of the paper is as follows. Section 2 describes the computational structure of the STEM-II model. Section 3 analyzes and evaluates the load balance problem. In Sections 4 and 5 different dynamic data distribution strategies are presented, for homogeneous and heterogeneous systems. The experimental results are shown in Section 6, comparing the dynamic distributions presented with two well-known static distributions, block and cyclic distributions. Finally, Section 8 concludes the paper.

2 The STEM-II Model

Air quality models can be mathematically described as time-dependent, 3D partial differential equations. The underlying equation used is the atmospheric-diffusion equation. The numerical solution of this equation consists of the integration of a system of coupled non-linear ordinary differential equations. STEM-II solves this system using a finite difference method [3].

A simplified pseudo-code of the STEM-II model is shown in Figure 1. The sequential program consists mainly of four nested loops, a temporal loop (`loop_t`) and a loop for each dimension of the simulated space (`loop_x`, `loop_y` and `loop_z`). In our experiments, each iteration of the temporal loop corresponds to a minute of real time. In addition, a fifth loop exists (`loop_trf1`), corresponding to the reaction time of the aqueous phase.

The basic modules and routines of the program are marked in the figure in bold lower case font. The main modules are: horizontal transport (`hor`), vertical transport and chemical reactions (`vert1q`) and I/O module. The model requires as input data the initial pollutant concentrations, topological data and meteorological data. The output consists of spatially and temporally gaseous and aqueous concentrations of each modeled specie, reaction rates, in and out fluxes, amount deposited and ionic concentrations of hydrometeor.

```

input1: Input time independent data
DO loop_t
  input2: Input time dependent data
  hor: Horizontal transport

  ——— Begin vertlq Module

  DO loop_x ( $n_x$  iterations)
    DO loop_y ( $n_y$  iterations)
      IF ( $\exists$  gas_phase and  $\exists$  aqueous_phase) THEN
        asmm: clouds model (includes loop_z)
        vertcl: vertical transport, gas phase (loop_z)
        DO loop_trfl
          vertcl: vert. transp., aqueous phase (loop_z)
          rxn: chemical reaction (includes loop_z)
        END DO
      ELSE
        vertcl: vertical transport, gas phase (loop_z)
        rxn: chemical reaction (includes loop_z)
      END IF
    END DO
  END DO

  ——— End vertlq Module

  output: print totals accumulated in the time
END DO

```

Fig. 1. Pseudocode of the STEM-II program

The most-time consuming module is **vertlq**. This module can be parallelized both in the **loop_x** and in the **loop_y**. In order to obtain a better exploitation of the memory hierarchy the outer loop has been parallelized [8].

3 Load Balance Problem

The simulation space of the parallelized STEM-II model is $60 \times 60 \text{ Km}^2$, reaching the height of 4200 m . This environment has been discretized in a 3D matrix, with an horizontal resolution of $1 \times 1 \text{ Km}^2$ and a vertical resolution of 300 m , thus this space is represented by a $61 \times 61 \times 15$ mesh.

Due to the physical and meteorological conditions, each point of the simulated environment has different computational load, and a load balance problem comes up in the parallelization of the model. The presence of rain is the main cause of this load unbalance.

Figure 2(a) shows the computational load of one iteration of the model in a given instant of time. Each point of the graph represents the sum of the FLOPs of all the points in the same vertical of a given coordinate. Dark areas correspond

to high computational load. Figure 2(b) shows the precipitation rate for this instant. The correlation between the presence of rain and the number of FLOPs can be clearly observed.

In the MPI parallel version of the STEM-II code the 3D simulation space is divided into 61 two-dimensional layers [8]. Each layer represents a section of the $60 \times 60 \times 4.2Km^3$ of the simulated space. Figure 3 shows the computational load for each one of the layers. Note that the most time consuming layers are consecutive in the simulation space.

A wide variety of load balancing algorithms can be proposed. Load balancing can be static or dynamic. Static methods involve deciding in advance the mapping of tasks to processors and leaving the balance unchanged for the duration of the execution. Static distributions do not guarantee an optimum load balance as the computational load of each layer depends on the meteorological conditions. New meteorological data are read for each hour of simulation, and 60 temporal iterations are executed with these data (60 iterations of `loop_t` in Figure 1), one for each minute of real time. Therefore, a good initial distribution could turn into a totally inefficient one along the time. A better solution is to use a

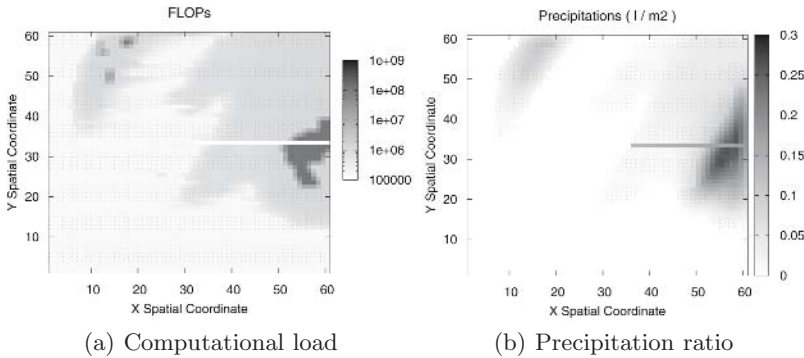


Fig. 2. Computational load of an iteration of the model and precipitation ratio into the simulation space (meteorological data of 2004 October 20th 7.00 am)

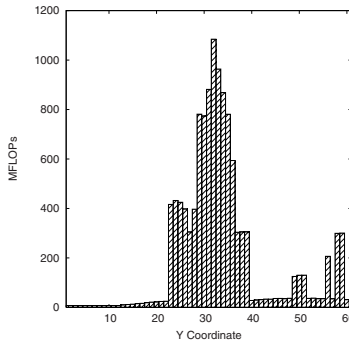


Fig. 3. Computational load associated to each layer (2004 October 20th 7.00 am)

dynamic strategy. Dynamic load balancing involves changing the allocation of tasks to the processors during the execution of the simulation. The following sections present different dynamic distributions. They have been designed as *ad-hoc* distributions for the problem at hand, however, they may be efficient in other similar simulation problems.

4 Dynamic Distributions for Homogeneous and Dedicated Systems

This section describes two new dynamic strategies for homogeneous and dedicated systems, the distribution by time and the distribution by prediction. The first one is based on the block static distribution. The second one makes use of the PPC tool [2], developed at the University of Santiago de Compostela, Spain.

4.1 Distribution by Time

Taking into account the easy implementation of the block distribution, but also its poor efficiency when the blocks have a fixed size, a new block distribution with variable block size is proposed. The new block size is calculated taking into account information from the run-time. Measuring the execution time of all the layers in the first iteration, when new meteorological data are read, a better balance for the remaining 59 iterations can be achieved. When the program starts, a classic block distribution is applied. After the first iteration, the computation time of each layer is measured and stored in an array of execution times. The length of this array is the number of layers, and the indexes are the layer's number. Once this vector is computed, a simple balance algorithm is applied to distribute the simulation space among the processors taking into account the time consumed by each layer. The idea of the algorithm is simple, instead of dividing the number of layers by the number of processors, the total execution time is divided by the number of processors, calculating how many layers must be executed on each processor.

We assume that all processors take the same time in processing the same layer. This distribution is almost optimum for this kind of system. It only needs an extra time for data redistribution, every time new data are read (each 60 iterations of `loop_t`).

4.2 Distribution by Prediction

It is known that the computational weight of each layer depends on meteorological conditions of the simulated environment, above all precipitation. Thus, the meteorological data could be analyzed in order to predict the execution time of the different layers of the simulation space. If the computational weight of each layer is known in advance with enough precision, the overhead associated to data redistribution would be eliminated.

Using the “Performance Prediction Tool (PPC)” [2] several parameters have been found to control the computational load of the program. These

parameters can be obtained directly from the meteorological data. The physical meaning of these parameters is related to the presence of water and humidity. An array of FLOPs by layer is built, and a similar balance algorithm to that used in previous distribution can be applied, using FLOPs instead of time. When new meteorological data are read the characterization parameters are recalculated.

With this new distribution, the load is balanced from the first iteration and data redistribution is not needed. The only existing overhead is due to the calculations of the characterization parameters and the FLOPs array, but this overhead is very small as we will show in the experimental results section.

5 Dynamic Distributions for Heterogeneous or Non-dedicated Systems

Previous distributions are not suitable for heterogeneous and/or non-dedicated systems, since they assume that the time needed to compute the same layer (or the same number of FLOPs) is the same in any of the processors. This section describes two new strategies for heterogeneous and/or non-dedicated systems, that takes into account that the computational power of every processor and its load could be different, and, moreover, that they could change dynamically during the computation.

5.1 Iterations Queue

In this approach each layer will be processed under request, i.e., the root processor will send the layers individually to the client nodes. When an specific node finishes, the root processor receives the computed layer and sends another one to the idle client.

There are two main disadvantages of this new distribution. First, not all the processors perform computations since the root only maintains the queue. Second, this distribution needs some extra communications for the synchronization between the root and the clients. Besides, all communications are point to point messages and only one layer is sent and processed every step, increasing the number of communications and decreasing data locality. This last issue can be changed, at the expense of balance, sending and processing more than one layer at a time. However, we have experimentally observed that the best speedup is obtained when the granularity of the queue is one layer, due to the fact that the most time consuming layers are consecutive in the simulation space.

5.2 Hybrid Distribution

Although the previous distribution is efficient, it has a serious drawback, the root CPU cycles are spent in layer management instead of being used for useful computations. The following distribution is also dynamic and solves this disadvantage.

The solution adopted in this case is to distribute the layers with an hybrid distribution, predicting FLOPs when new data are read and using the execution time

from the first iteration to calculate the *power factor* of each machine involved. Then, the FLOPs are distributed taking into account the calculated power factor.

The power factor of a machine j (W_j) is defined as:

$$W_j = \frac{FLOPS^l}{t_j^l} \quad , \quad j = 1, \dots, NP$$

where $FLOPS^l$ is the number of FLOPs of layer l , t_j^l is the execution time of layer l in machine j (being l the first layer assigned to node j in the first iteration), and NP is the number of processors. The power factor characterizes not only the computational power of each machine but also its load.

In order to calculate the number of FLOPs that each machine must execute, the *scaled power factor* (Ws_j) is defined:

$$Ws_j = \frac{W_j}{\sum_{i=1}^n W_i} \quad , \quad j = 1, \dots, NP$$

Note that the sum of scaled power factors is the unit ($\sum Ws_j = 1$).

The number of FLOPs that correspond to a machine j can be calculated by multiplying the total number of FLOPs by its scaled power factor.

$$FLOPS_j = \sum_{l=1}^{nl} FLOPS^l * Ws_j \quad , \quad j = 1, \dots, NP$$

Knowing the number of FLOPs that every node must execute in function to its power factor, a similar balance algorithm to that used in the previous section can be applied. This distribution has, as the distribution by time, an overhead due to data redistribution and the overhead associated to the prediction of FLOPs.

6 Experimental Results

In order to evaluate the different strategies developed, a simulation of a specific day with a significant load unbalance has been chosen (February 15, 2003). All the distributions have been executed in two different systems, an homogeneous and an heterogeneous one. The first one is a dedicated Beowulf cluster sited at CESGA (Supercomputing Center of Galicia). It consists of 8 Pentium III at 550 MHz interconnected by Myrinet. The heterogeneous system consist of four machines of our department interconnected by a Ethernet network and with different characteristics and load levels: a dual Pentium III at 933 GHz with 1 GB of memory, an Athlon 64 at 2.2 GHz with 1 GB of memory and two Pentium III at 800 GHz with 128 MB each. The load of these machines varies along the time, because each one is used by different users.

In order to compare different distributions, we define the balance factor as:

$$balance = \frac{\sum_{i=1}^{NP} t_i}{(NP) \times \max_{i=1}^{NP}(t_i)}$$

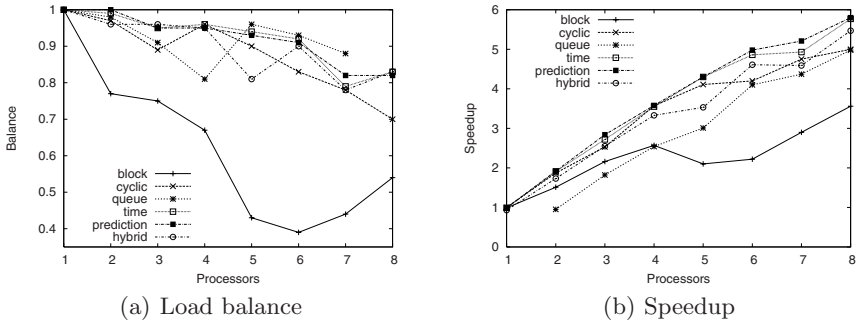


Fig. 4. Load balance and speedup on the homogeneous system

where NP is the total number of processors and t_i the computation time consumed by processor i . The balance factor is a measure of the load distribution among the processors. A balance factor equal to one means a perfect load distribution. The worse the load distribution, the lower the balance factor will be.

Figure 4(a) shows the balance factor on the homogeneous system for all the dynamic distributions proposed in this paper. Two well-known static distributions, block and cyclic, have been included for comparative purposes.

The block distribution presents the worst load balance, and the cyclic distribution get worse as the number of processors grows. There are not significant differences among the other distributions, and their load balance depends on the number of processors. Note the similar behavior of the three distributions: distribution by time, distribution by prediction and hybrid, which indicates the good results in the prediction of FLOPs obtained using PPC tool. It seems that the best load balance is achieved by the iterations queue distribution when increasing the number of processors. Remember that the root processors in this distribution does not do useful work (it only maintains the queue and communicates the data). For this reason there are no measurements for the iterations queue distribution using 8 processors, since only 7 processors execute the parallel part of the code. For this case, the balance factor is calculated as:

$$balance = \frac{\sum_{i=2}^{NP} t_i}{(NP - 1) \times \max_{i=2}^{NP}(t_i)}$$

where NP is the total number of processors and t_i the computation time consumed by processor i , being the root processor excluded from the calculation.

The speedup achieved with the different distributions is shown in Figure 4(b). The speedup has been calculated as the parallel execution time divided by the execution time of the sequential program. The block distribution obtains the worst results since the load balance is poor. The distribution by iterations queue, in spite of being the best balanced, does not obtain a satisfactory speedup, due to the idle (root) processor. The other distributions present a similar behavior, although the cyclic seems to be worse when the number of processors increases. The best results are obtained with the distribution by prediction.

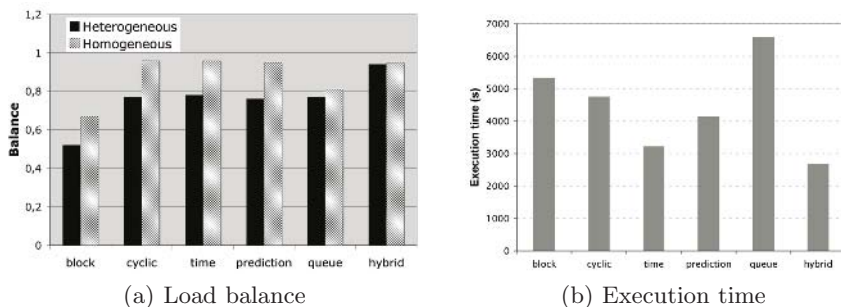


Fig. 5. Load balance and execution time on the heterogeneous system

The load balance achieved on the heterogeneous system is shown in Figure 5(a). The balance of the homogeneous system over four processors is also shown as a reference. Figure 5(b) shows the corresponding execution times. Note that all the distributions obtain poorer balance results than in the homogeneous system. The block distribution is again the worst distribution in terms of balance. The hybrid distribution, designed for these kinds of systems, clearly obtains the best load balance among the processors. There are no significant differences among the other four distributions, in terms of load balance. Figure 5(b) indicates that hybrid distribution achieves the best result in terms of execution time. Note also that the queue distribution obtains the worst execution time, since in this case only three of the four processors are performing computational work, as previously indicated in Section 5.1.

7 Conclusions

Traditional data distribution strategies are not adequate for the parallel MPI STEM-II model. Other data distributions are proposed in order to improve load balance of this specific application. The strategies have been designed keeping in mind two different kinds of systems: homogeneous and dedicated and heterogeneous and/or non-dedicated, both with an homogeneous LAN.

We can conclude that the *hybrid distribution* is the best strategy for heterogeneous environments with non-dedicated machines. With the help of this new distribution any machine can be added to the platform to carry out useful work. In the case of dedicated homogeneous clusters or supercomputers, the distribution by prediction has proved to be the most suitable.

References

1. C. Balseiro, M. Souto, E. Penabad, J. Souto, V. P. Muñuzuri. Development of a limited-area model for operational weather forecasting around a power plant: the need for specialized forecasts. *Journal of Applied Meteorology* 41 (9), pp. 919–939, 2002.

2. M. Boullón et al. Modeling execution time of selected computation and communication kernels on Grid. *LNCS* 3470, pp. 731–740, *Springer Verlag*, 2005.
3. G. Carmichael, L. Peters, R. Saylor. The STEM-II regional scale acid deposition and photochemical oxidant model - I. An overview of model development and applications. *Atmospheric Environment* 25A (10), pp. 2077-2105, 1991.
4. D. Dabdub and R. Manohar. Performance and portability of an air quality model. *Parallel Computing* 23 (14), pp. 2187–2200, 1997.
5. I. Dimov, K. Georgiev, J. Wasniewski and Z. Zlatev. Three-dimensional version of the Danish Eulerian Model. *LNCS* 1041, pp. 151–157, *Springer Verlag*, 1996
6. H. Elbern. On the load balancing problem of comprehensive atmospheric air quality models. *Journal System Analysis-Modelling-Simulation* 32, pp. 31–56, 1998.
7. H. Elbern. Parallelization and load balancing of a comprehensive atmospheric chemistry transport model. *Atmospheric Environment* 31, pp. 3561–3574, 1997.
8. M.J. Martín, D.E. Singh, J.C. Mouriño, F.F. Rivera, R. Doallo, and J.D. Bruguera. High Performance Air Pollution Modeling for a Power Plant Environment. *Parallel Computing* 29 (11–12), pp. 1763–1790, 2003.
9. M.J. Martín, M. Parada and R. Doallo. High Performance Air Pollution Simulation Using OpenMP, *The Journal of Supercomputing* 28, pp. 311-321, 2004.
10. J.C. Mouriño, M.J. Martín, P. González, M. Boullón, J.C. Cabaleiro, T.F. Pena, F.F. Rivera, and R. Doallo. A Grid-enable Air Quality Simulation. *LNCS* 2970, pp. 155–162, *Springer-Verlag*, 2004.
11. M. Niezgodka and B. Jakubiak. Numerical Weather Prediction System: Scientific and Operational Aspects. In *Proceedings of the III Symposium on Military Meteorology*, pp. 191–197, 1998.
12. T. Ostromsky and Z. Zlatev. Flexible Two-Level Parallel Implementations of a Large Air Pollution Model. *LNCS* 2542, pp. 545–554, *Springer Verlag*, 2003.
13. J. Subhlok, P. Steenkiste, J. Stichnoth, and P. Lieu. Airshed pollution modeling: A case study in application development in an HPF environment. In *12th International Parallel Processing Symposium* Orlando, FL, pp. 701–710, April 1998.

New Molecular Mechanism of Dextran Extension in Single Molecule AFM

Igor Neelov^{1,2}, David Adolf¹, and Tom McLeish¹

¹ IRC in Polymer Science and Technology,
University of Leeds, Leeds LS2 9JT, UK

² Institute of Macromolecular Compounds, RAS,
Bolshoi pr. 31, 199004, St.Petersburg, Russia,
i.neelov@leeds.ac.uk

Abstract. A dextran monomer and a 10mer under constant pulling speed or constant force were studied using the atomistic simulations. Molecular dynamics (MD) with the Amber94 and Amber-Glycam04 forcefields were performed. The main result of the present Amber-based MD simulations is that the experimental plateau of the force-extension dependence for dextran can be explained by a transition of the glucopyranose rings in the dextran monomers from a chair (4C_1) to an inverted chair (1C_4) conformation whereas chair to boat transitions occur at higher forces. MD simulation of a coarse-grained model of dextran consisting of two- or three-state monomers were performed to clarify the molecular mechanism of dextran extension.

1 Introduction

Polysaccharides are fundamental components of cells and have many potential applications. Polysaccharides are cations in the pharmaceutical industry and material science. Mechanical properties are important because they constitute cell walls in plants and bacteria and take part in cell interactions and adhesion. They also serve as a simple model for studies into the mechanical properties of protein concatemers. Dextran is an important representative of polysaccharides with 1-6 linkages (i.e. connecting C_1 and C_6 carbon atoms on neighbouring sugar monomers). The mechanical extension of dextran has been performed in single molecule AFM experiments by Rief et al¹ and by Marszalec et al². A key finding was the existence of a plateau in the force-extension dependence for dextran at forces near 700-1000pN. Additionally Rief et al performed molecular dynamic (MD) simulations of dextran 5mer extension at a constant pulling speed to obtain the force-extension curve. Rief et al attributed the plateau to a rotation around C_5 - C_6 bonds (i.e. to conformational transition of $O_5C_5C_6O_6$ angle) while Marszalec and Fernandes suggested the plateau occurs due to a forced chair-boat transition of the glucopyranose rings.

Recently, Lee et al³ presented results of a MD simulation of dextran extension at constant pulling speed. A CHARMM based force field elaborated by Kuttel et al⁴ was used. With this forcefield it was observed that the glucopyranose ring conformational

transition from the chair to the boat conformation is the main source of the plateau on the force-extension curve.

In our recent work⁵ Amber-based (Amber94 and Amber Glycam04) forcefields were used to study the extension of dextran and its monomer at different constant forces. In addition to Lee and Marszalec chair-boat transitions, a significant amount of forced transitions from the chair (⁴C₁) to inverted chair (¹C₄) conformation was found in the plateau region. In the present paper, the extension of dextran at constant pulling speed and at constant force is presented and compared with results for two types of coarse grained models of linear dextran consisting of three-state and two-state monomers correspondingly.

2 Models and Methods of Molecular Simulation

Amber⁶, CHARMM⁷ and some other forcefields and their modifications (Amber-Homans⁸ Amber-Glycam⁹, CHARMM-Parm22/SU01¹⁰) have been used for the simulations of mono saccharides.

A comparison of 20 different forcefields for monosaccharides was carried out recently¹¹. Surprisingly the best forcefield in this review was found to be the Amber-like forcefield (Amber94) which was not specially designed for carbohydrates.

In cited paper of Lee et al, it was shown that solvent has no significant effect on the force-extension behaviour of dextran. They also evaluated characteristic conformational transition times in dextran between 10⁻⁹ s and 10⁻⁶ s. The only way to achieve this interval of times in molecular dynamics simulation is to perform MD without an explicit solvent. These reasons explain the absence of water molecules in most of their and our simulations.

In this paper, the results of MD simulations of the extension of the dextran monomer and 10mer at constant pulling speed and by constant force are presented. The Amber94 and Amber-Glycam04 forcefields were used. One chain end was fixed. The second one was extended by constant force or restrained harmonically to another point which was moved with constant speed dx/dt ($dx/dt=0.1-0.00001\text{\AA}/ps$) along the X axis. The Verlet algorithm with a time step $\Delta t=1fs$ was used in all simulations. To achieve suitable local equilibration of dextran without explicit solvent molecules, the Andersen thermostat¹² was used.

In addition to simulation of model with full atomic details we performed the simulation of coarse-grained model of linear dextran polymer. Each dextran monomer was represented by one particle with effective mass equal to mass of all atoms of monomer. Neighboring particles were connected in linear chain by potential which has 2 or 3 minima (two-state monomers or three-state monomers, correspondingly). We use the same computer program to run the MD simulations with exactly the same parameters and conditions as for full atomic model. The goal is to understand how the shape of experimental force-extension curve for dextran will depend on parameters of potential (energies of minima) and on number of states (2 or 3) in monomer.

3 Results and Discussion

3.1 Extension of Dextran at Constant Pulling Speed

The extension of a dextran 10mer was simulated at constant pulling speeds 0.1- 0.0001 Å /ps. The pulling speed in single molecule AFM experiments is usually

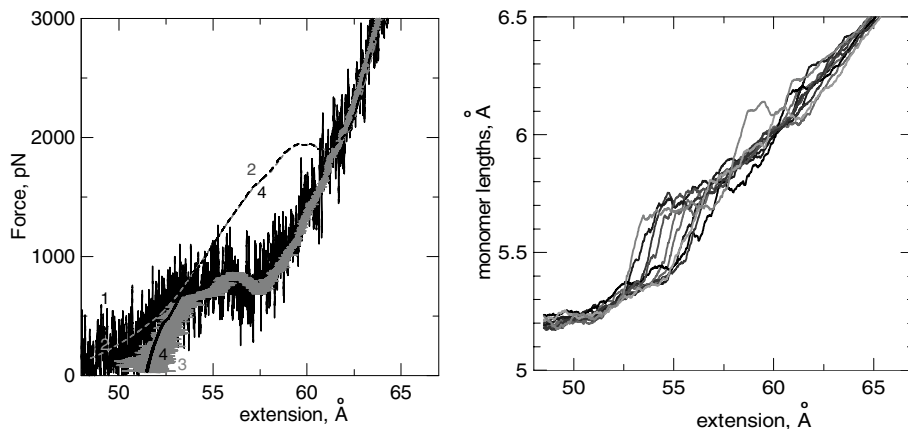


Fig. 1. a) Force-extension dependence for dextran 10mer extended at constant pulling speed 0.0001 Å /ps (solid lines 1 at T=300K, and 2 at T=0K), and force vs contour length (dashed lines 3 and 4, correspondingly), b) Monomer length for each monomer of the 10mer as function of extension at T=300K

several orders of magnitude lower so the most of results in this paper are presented for slowest speed used. Force-extension curve (i.e. force F acting on the pulled chain end as function of the extension) is presented in Fig.1a. There are rather strong thermal fluctuations of the force at room temperature. At small and high extensions the force depends linearly on extension and the ratio of the elasticity constants for these regions is nearly 1:3-4 which is in agreement with the experimental data. At the intermediate extensions (between 54 and 58 Å) there is a clear plateau on this curve. The value of the plateau force between 700-900pN is in agreement with the experimental plateau force (700-1000pN) for dextran. For zero temperature (gray dashed line in Fig.1a) a similar dependence at small and high extensions was obtained. But due to lack of thermal fluctuations the plateau region at zero temperature appears at higher extensions (59-60 Å) and at forces more than twice higher (near 2000pN).

It is necessary to take into account that the end-to-end distance of the 10mer is less than the sum of the monomer length (contour length) since the monomers are not perfectly orientated along the axis of extension. Thus the evaluation of monomer length from a normalized end-to-end distance leads to an underestimation of this value especially at small extensions. To find the real average monomer length we calculate the contour length of the chain and plot its dependence on force in Fig.1a both at T=300K (line 3) and at T=0K (line 4). At high distances the extension (lines 1 and 2) and the contour length (lines 3 and 4) dependencies for each temperature

coincide but at small distances dependencies on contour length drop abruptly at d near 52\AA (i.e. at average monomer length 5.2\AA) in comparison with force-extension curves. The plateau region ($55\text{-}58\text{\AA}$) for force-contour length dependence is also shorter and displaced to slightly higher distances than for force-extension curves.

To understand the molecular mechanisms of the dextran extension it is necessary to see the behaviour of monomers under extension. There are two ways of doing this. First, to see the extension behaviour of each monomer in the 10mer under extension. Second to perform an additional simulation of a single dextran monomer extension at constant pulling speed. We applied both these approaches. Fig.1b gives the dependence of length of each monomer (distance between O1-O6 atoms) in 10 mer as a function of the extension of chain as whole. It is easy to see that until $d=5.4\text{\AA}$ only small linear extension of the monomers occurs. In the interval $d=5.4\text{\AA} - 5.8\text{\AA}$, a step-like increase of monomer length occurs for almost all monomers. Subsequently, a second interval of step-like increases in monomer lengths can be seen at $d=6.0\text{-}6.3\text{\AA}$.

To understand the molecular mechanism of the dextran extension, we need to take into account that the monomer length can be increased by rotation around C5-C6 bond attached to monomer glucopyranose ring (the mechanism of dextran extension suggested by Ries et al) or by conformational transition of ring itself (for example due to chair-boat transitions suggested by Marszalec et al and observed in CHARMM based MD simulations by Lee et al).

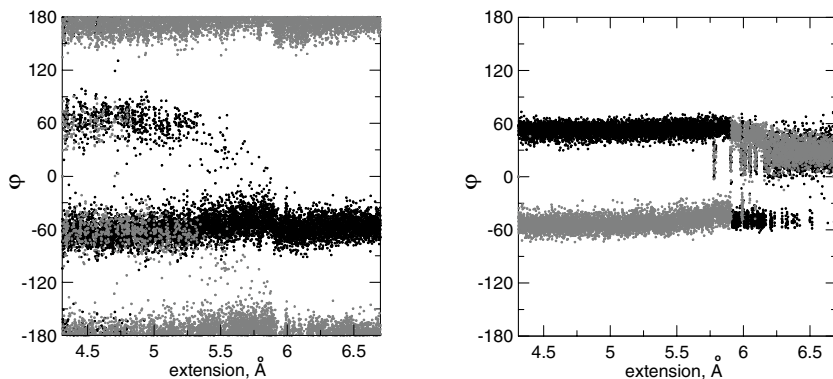


Fig. 2. Dihedral angles for a) rotation around C5C6 bond: O5C5C6O6 (grey) and C4C5C6O6 (black) for the monomer vs monomer extension, b) dihedral angles (C2C1O5C5 (grey), C2C3C4C5 (black) in glucopyranose ring vs monomer extension. Temperature $T=300\text{K}$

The orientation of the C5C6 bond is defined by the conformation of two dihedral angles O5C5C6O6 (grey) and C4C5C6O6 (black) (see Fig.2a). For not extended monomer the dominant conformations of C5C6 bonds should be g+t: g+ (gauche+, 60°) for the first angle and t (trans, 180°) for the second angle with small monomer length 4.5\AA and g-g+ with larger monomer length 5.2\AA (the third, tg-, conformation (with length equal 5.2\AA) is almost absent at this conditions). But we have got (in agreement with earlier simulation of Lee et al (2004) for dextran 10mer using CHARMMM forcefield) that already at small extension of the 10mer there is almost no “short” g+t conformation

of C5C6 bond (i.e. no grey points at $+60^\circ$ and no black points at 180° Fig.2a). After the extension of 10mer to 55-57 Å the transition from g-g+ ($-60^\circ, 60^\circ$) to tg- ($180^\circ, -60^\circ$) conformational state occur. But last transition do not change the length of the monomer and the 10mer because both g-g+ and tg- conformations have near the same monomer length. Thus the origin of plateau in force-extension dependence at room temperature is probably the transition of glucopyranose rings in dextran monomers.

To check the molecular structure of the glucopyranose rings (chairs, boats etc) we calculated the dihedral angles C2C1O5C5 (grey) and C2C3C4C5 (black) (Fig.2b) as function of normalized extension per monomer. If the first type of the angles is close to -60° , and the second is roughly $+60^\circ$ it corresponds to the chair (4C_1) conformation of glucopyranose ring which should be dominant in the absence of extension. If these angles have reverse signs ($+60^\circ, -60^\circ$) it corresponds to an inverted chair (1C_4) conformation. If both angles have the same sign (both positive or both negative) it gives boat-like states of the glucopyranose ring. At small extension (between 4.5 and 5.8 Å) all angles of the first type (grey points) fluctuate around -60° and angles of the second type (black points) - around 60° . It means that given monomer is initially in the unperturbed chair (4C_1) conformation which is most favorable in the absence of force. At distances near 5.8-5.9 Å the significant amount of the positive values of first type of dihedral angles and the negative values of second angle occur. It is easy to see that angles switch sign simultaneously and it means transition of the ring from chair (4C_1) to inverted chair (1C_4) occurs. Some amount of other conformations of ring also present here. Thus in the transition region there is coexistence of all three states (chair, inverted chair and boat). The boat state (both angles are positive) becomes dominant at the extensions of monomer greater than 6.2 Å.

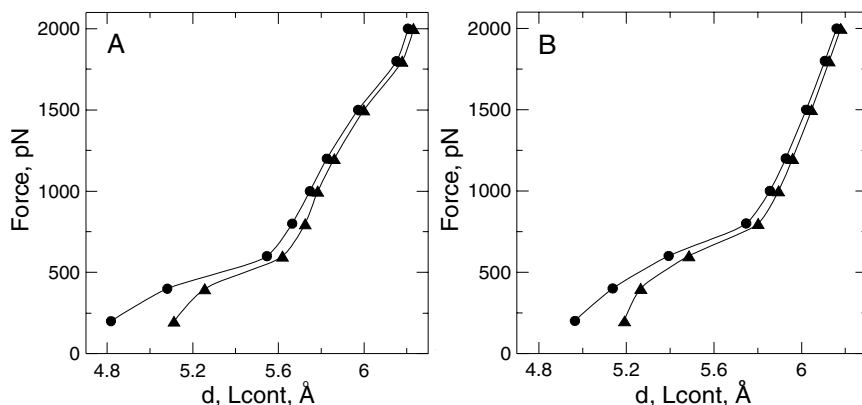


Fig. 3. Force-extension curve for dextran 10mer. Circles – Force vs normalized end-to-end distance, triangles – Force vs normalized contour length of chain. a) Amber94 and b) Amber-Glycam04 forcefields.

3.2 Extension of Dextran at Constant Force

The extension of a dextran monomer and a 10mer were simulated at a series of constant forces ranging from $F=200$ to 2000 pN. This interval of forces corresponds to the experimental interval used in single molecule dextran extension by AFM¹³.

Force-extension curves (i.e. extension force F vs the average end-to-end distance, d , at each given F for the 10mer) are shown for the Amber94 in Fig.3a and for Amber-GLYCAM04 forcefields in Fig.3b (circles). The end-to-end distance is normalized by the number of monomers in the chain to provide an easier comparison with experimental results. Amber94 and Amber-GLYCAM04 give qualitatively similar curves but the force dependence for the latter is shifted to slightly higher distances. There is a clear plateau on the force-extension curves for both forcefields. It is noted that the normalized end-to-end distance used in experimental papers on carbohydrates extension in AFM does not give the actual monomer length because monomers are not perfectly oriented along the direction of extension especially at small extension of dextran chain. To demonstrate the difference between normalized length per monomer and real monomer length the average 10mer contour length was calculated at several constant forces. The force as a function of normalized contour length (equal to the average length of one monomer) is shown in Fig.3a and Fig.3b as triangles. At high forces (when the orientation of the monomers is strong) the difference between the two curves is small. However, at small forces the difference can be large; for example it is 0.37 \AA at $F=200\text{pN}$ per monomer for the Amber94 forcefield and 0.32 \AA for the Amber-Glycam04 forcefield.

Fig.4a shows that in the case of Amber94 forcefield there exists a transition from a state with $d=5.6 \text{ \AA}$ to a second state with d near 5.9 \AA (at time near 500ps) and also rare transitions to a third short-living state with d near 6.1 \AA (at time near 9500ps). Similar transitions between three states (with length of monomer d near 5.6 , 5.9 and 6.1 \AA) can be seen at the same conditions for Amber-GLYCAM04 forcefield in Fig.4b.

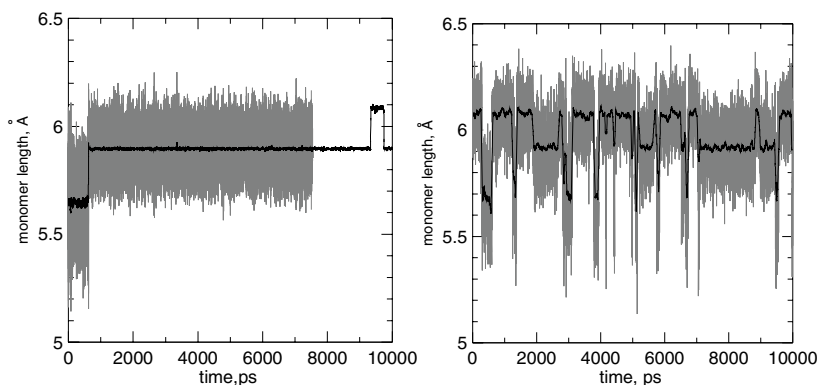


Fig. 4. The monomer length (distance between O1 and O6 atoms, grey) as function of time for a) Amber94 and b) Amber-Glycam04 forcefields at force $F=1000\text{pN}$. The black curve corresponds to data averaged over each 100 neighbouring points.

To determine the identity of these states, reference is made to the dihedral angles ($\phi_1=C2C1O5C5$, $\phi_2=C2C3C4C5$) inside of glucopyranose rings (not shown). At times less than 500ps in Fig.4a (with Amber94 forcefield), ϕ_1 is close to -60° , while ϕ_2 is roughly 60° . It means that glucopyranose ring is in 4C_1 state. At times near 500ps, they

interchange signs so that ϕ_1 is 60° and ϕ_2 is -60° i.e. transition to 1C_4 occurs. The state in Fig.4a at near 9500ps has positive ϕ_1 and ϕ_2 . This corresponds to a boat/twisted boat conformation.

Similar analysis for Fig.4b (with Amber-Glycam04 forcefield) gives almost the same result but in this case the transitions between states occur more frequently.

3.3 Extension of Coarse-Grained Model by Constant Force

To understand how the shape of experimental force-extension curve for dextran depends on actual number of conformational states of glycopyranose ring (2 or 3 state) we performed simulation of coarse grained model of dextran 10mer consisting of two- or three-state monomers (see part 2 of this manuscript). The potentials used in this paper are shown in Fig.5a for 3-state model and in Fig.5b for 2-state model. We used different energies of minima and potential barriers to understand how variation of these parameters will influence the force-extension curve.

For three-state model we use as positions of minima the 3 monomer lengths obtained in our simulation of dextran monomer and 10mer: $d_1=5.2 \text{ \AA}$, $d_2=5.9 \text{ \AA}$ and $d_3=6.2 \text{ \AA}$ (see above). For two state model we used two possible combination of this lengths: $d_1=5.2 \text{ \AA}$, $d_2=5.9 \text{ \AA}$ and $d_1=5.2 \text{ \AA}$, $d_2=6.2 \text{ \AA}$ which correspond to chair and inverted chair conformations or chair and boat conformations of glycopyranose ring, correspondingly. First value ($d_1=5.2 \text{ \AA}$) is not equal to 5.6 \AA as it follows from Fig.4 because 5.6 \AA is the value obtained at high force ($F=1000\text{pN}$) for elastically extended conformation. We have independent evaluation of $d_1=5.2 \text{ \AA}$ from normalized persistence length (equal to length of monomer) and DFT simulations.

The values of energy were evaluated from result of DFT calculations of Appel et al^{14,15}, our own DFT calculations and difference between energies of two states model¹⁶ which was used for fitting of experimental data for dextran. All of them give the difference of energy between first and second minima close to 8kcal/mol. In the case of DFT simulation this value corresponds to inverted chair conformation of glycopyranose ring. The difference between the energy of third and first state was taken equal 8 kcal/mol or 16 kcal/mol. First value is the result of our evaluation of energy of boat state from below while second one – from above. The energy barrier between first and second state E_{12} was taken equal to 12 kcal/mol (evaluation from below for cyclohexan). The values obtained by Donoghue et al¹⁶ for α -D-glucose (13-15kcal/mol) are also close to it. The value of energy for second barrier (E_{23} between second and third minima) is not so clear. Due to this reason we varied the second barrier between 12 and 20kcal/mol.

The force-extension curves for 10mers of coarse-grained model with different values of energy in minima (corresponding to potentials in Fig.5) are presented in Fig.6. Fig.6a gives force-extension curves for models consisting of 3-state monomers and Fig.6b – for 2-state monomers. It is interesting that for 3-state model the two plateau-like regions exist only for the case when energy E_3 is essentially larger than energy of second state E_2 (16kcal/mol and 8 kcal/mol, correspondingly) (see solid lines on Fig.5a and Fig.6a). When both energies are the same $E_2=E_3=8\text{kcal/mol}$ (dashed lines on Fig.5a and Fig.6a) there is only one long plateau-like region. In this case the curve for 3 state model is very similar to that for two state model (see Fig.5b and Fig.6b). Both curves for two-state model (solid line corresponding to energy of second

minimum $E_2=16$ kcal/mol and energy barrier between 1 and 2 state $E_{12}= 20$ Kcal/mol and dashed line for the case $E_2=8$ kcal/mol and $E_{12}= 12$ Kcal/mol) show the broad plateau-like region (see Fig.6b) in force-extension curve. We made simulation of three-state 10mer with intermediate values of energies $E_3=12$ kcal/mol and $E_{23}= 16$ Kcal/mol ($E_1=8$ kcal/mol and $E_{12}= 12$ Kcal/mol was as before) and obtain that for it also there is no second plateau and its behaviour is similar to that for two-state model.

This behaviour is similar to force-extension curves obtained from simulation of dextran 10mer with full atomic details (see Fig.3). In particular the force-extension curve in Fig.3a obtain with Amber94 forcefield gives two plateau-like regions while the curve obtained from simulation with Amber-Glycam04 forcefield (Fig.3b) gives only one plateau-like region. Because we found earlier that for both forcefields there

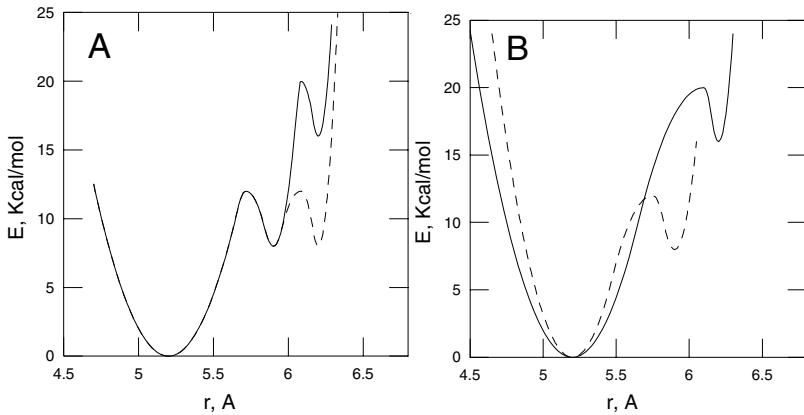


Fig. 5. Potential connecting neighboring beads into monomer in coarse-grained model of dextran 10mer for a) 3-state and b) 2-state models

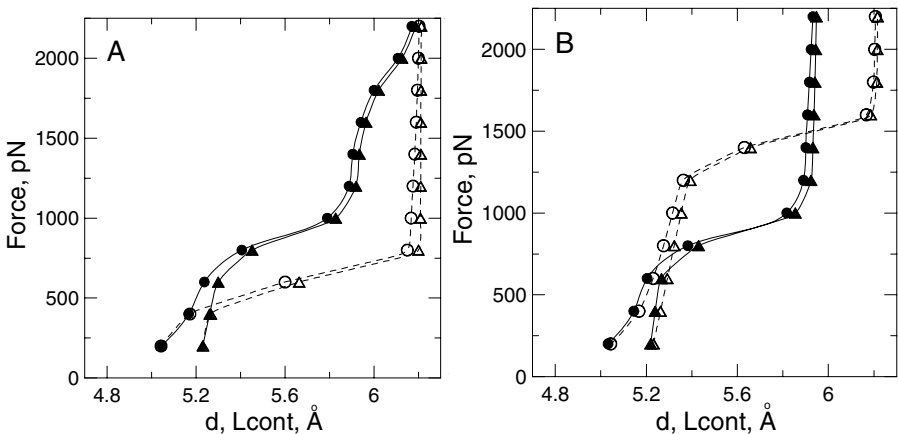


Fig. 6. Force-extension curve for 10mer of coarse-grained model. a) three-state model, b) two-state model

are all three states in transition region of forces (500-100pN) it probably means that energy difference between second and third states is different in these two forcefields. It also can explain why force-extension curves obtained in AFM do not give force-extension curves with two plateau-like regions even if three states really exist. The existence of 3rd intermediate state of dextran monomers under extension was demonstrated in recent experimental paper of Fernandes et al using new variance single dextran molecule AFM technique.¹⁷

4 Conclusion

The structure and dynamical properties of the dextran under extension with constant pulling speed were calculated using Amber-Glycam04 forcefield. The main result of the present Amber-based simulation is that the plateau on the force-extension dependence can be explained by a transition of the glucopyranose rings in dextran monomers from the chair (⁴C₁) to the inverted chair (¹C₄) at distances near 5.7-6.0Å, while most of the chair to boat transition occur at higher extension.

Our simulation of coarse-grained model of dextran 10mer under the constant extension force show how the shape of force-extension curve is changed by changing the values of energy and distances of stable states (chairs and boats) of dextran monomer. It also allows to understand why the three-state behaviour was not obtained in AFM experiment earlier.

Acknowledgment. This work was supported by grants EPSRC GR/S67388/01, EP/C528336/1 and INTAS 05-100004-7747.

References

1. Rief, M., F. Oesterhelt, B. Heymann, and H. E. Gaub.. Single molecule force spectroscopy on polysaccharides by atomic force microscopy. *Science* (1997) 275:1295-1297.
2. Marszalek, P. E., A. F. Oberhauser, Y. P. Pang, and J. M. Fernandez. 1998. Polysaccharide elasticity governed by chair-boat transitions of the glucopyranose ring. *Nature* 396: 661-664.
3. Lee, G., W. Nowak, J. Jaroniec, Q. M. Zhang, and P. E. Marszalek.. Molecular dynamics simulations of forced conformational transitions in 1,6-linked polysaccharides(2004).
4. Kuttel, M., J. W. Brady, and K. J. Naidoo.. Carbohydrate solution simulations: Producing a force field with experimentally consistent primary alcohol rotational frequencies and populations. *Journal of Computational Chemistry* (2002) 23, 1236-1243.
5. Neelov, I.M., D.B.Adolf, E.Paci, T.C.B.McLeish Biophys.J., Molecular dynamics simulation of dextran extension by constant force in single molecule AFM, in press(2006)..
6. Weiner, S. J., P. A. Kollman, D. T. Nguyen, and D. A. Case. An All Atom Force-Field for Simulations of Proteins and Nucleic-Acids. *Journal of Computational Chemistry* (1986), 7, 230.
7. MacKerell, A. D., D. Bashford, M. Bellott, R. L. Dunbrack, J. D. Evanseck, M. J. Field, S. Fischer, J. Gao, H. Guo, S. Ha, D. Joseph-McCarthy, L. Kuchnir, K. Kuczera, F. T. K. Lau, C. Mattos, S. Michnick, T. Ngo, D. T. Nguyen, B. Prodhom, W. E. Reiher, B. Roux, M. Schlenkrich, J. C. Smith, R. Stote, J. Straub, M. Watanabe, J. Wiorkiewicz-Kuczera, D. Yin, and M. Karplus. 1998. All-atom empirical potential for molecular modeling and dynamics studies of proteins. *Journal of Physical Chemistry B* (1998)102:3586-3616.

8. Homans, S. W.. A Molecular Mechanical Force-Field for the Conformational-Analysis of Oligosaccharides - Comparison of Theoretical and Crystal-Structures of Man-Alpha-1-3man-Beta-1-4glcnac. *Biochemistry* (1990) 29:9110-9118.
9. Woods, R. J., R. A. Dwek, C. J. Edge, and B. Fraserreid.. Molecular Mechanical and Molecular Dynamical Simulations of Glycoproteins and Oligosaccharides .1. Glycam-93 Parameter Development. *Journal of Physical Chemistry* (1995) 99:3832-3846.
10. Eklund, R. and G. Widmalm.. Molecular dynamics simulations of an oligosaccharide using a force field modified for carbohydrates. *Carbohydrate Research* (2003) 338:393-398.
11. Hemmingsen, L., D. E. Madsen, A. L. Esbensen, L. Olsen, and S. B. Engelsen.. Evaluation of carbohydrate molecular mechanical force fields by quantum mechanical calculations. *Carbohydrate Research* (2004) 339:937-948.
12. Andersen, H. C.. Molecular-Dynamics Simulations at Constant Pressure and-or Temperature. *Journal of Chemical Physics* (1980) 72:2384-2393.
13. Kawakami, M., K. Byrne, B. Khatri, T. C. B. McLeish, S. E. Radford, and D. A. Smith.. Viscoelastic properties of single polysaccharide molecules determined by analysis of thermally driven oscillations of an atomic force microscope cantilever. *Langmuir* (2004) 20:9299-9303.
14. Appell, M., G. Strati, J. L. Willett, and F. A. Momany. B3LYP/6-311++G** study of alpha- and beta-D-glucopyranose and 1,5-anhydro-D-glucitol: C-4(1) and C-1(4) chairs, B-3,B-O and B-3,B-0 boats, and skew-boat conformations. *Carbohydrate Research* (2004) 339:537-551.
15. Momany, F.A., Appell, M., Willett, J.L., Bosma W.B. 2005. B3LYP/6-311++G** geometry-optimization study of pentahydrates of alpha- and beta-d-glucopyranose, *Carbohydrate Research*, 340: 1638-1655
16. O'Donoghue P., Z.A.Luthey-Shulten. Barriers to Forced Transitions in Polysaccharides, *J.Physical Chemistry B* (2000) 104, 10398-10405
17. Walther K.A, J.Bruijic, H.Li, J.F.Fernandes Sub Angstrom conformational changes of single molecule captured by AFM variance analysis, *Biophysical J.* (2006), in press

Atom-Bond Additive Potentials for Benzene-Rare Gas Clusters

Margarita Alberti¹, Antonio Laganà*, Fernando Pirani²,
Massimiliano Porrini², and David Cappelletti³

¹On leave from: Departament de Química Física, CERQT,
Parc Científic, Universitat de Barcelona,
Martí i Franquès, 1. 08028 Barcelona, Spain

²Dipartimento di Chimica, Università di Perugia, 06123 Perugia, Italy

³Dipartimento di Ingegneria Civile ed Ambientale,
Università di Perugia, 06123 Perugia, Italy

Abstract. In the process of constructing a realistic *a priori* modeling of the solvation processes of the benzene molecule we have carried out a systematic comparison of the popular atom atom representation of the interaction with the recently proposed atom bond model for the series of benzene-rare gas systems. Calculated static and dynamic properties of this family of systems are discussed.

1 Introduction

In recent years interest for benzene containing clusters has significantly grown [1, 2, 3, 4, 5, 6, 7, 8, 9, 10]. This is motivated by the fact that this type of clusters play a key role in practical problems and applications such as biological systems (like, for example, cation molecular channels in membranes [11, 12, 13]). This makes it vital to develop proper methods for constructing the Potential Energy Surfaces (PES) of these systems. The construction of an accurate PES for these systems, however, is not an easy task. In fact, despite the clear non-covalent nature of the intermolecular interaction often involved in benzene containing systems and the availability of a relatively large body of electronic structure calculations [14, 15, 16], the accurate *ab initio* determination of the related PESs is quite difficult. In particular the strength of these interactions, in neutral systems, is often so weak to fall within the numerical error of the *ab initio* computational machineries presently available.

However, in some favorable cases, as those involving benzene-rare gas interactions, it has been possible to derive important features of the most stable structure (like the equilibrium distances, dissociation energies and force constants) referred to the configurations exhibiting the rare gas atom located along the sixfold axis of benzene. It has been possible also to figure out the characteristics of related collision complexes like the range and strength of the average interaction energy. Such a wealth of information, obtained from spectroscopic

* Corresponding author. lag@unipg.it

and scattering experiments, must be considered as complementary to the information obtained from *ab initio* methods. Moreover, the analysis of experimental data often provides a reasonable good estimate of the key parameters of empirical and semiempirical potential models. In this paper two different intermolecular potential models used to describe the interaction in the full benzene-rare gas family, are investigated. Their choice and their systematic study has been motivated by their extensibility to more complex systems and by the implications of their different formulation on same key features of the PES and, as a consequence of the dynamical properties of the system. The models of interest are based on a pairwise additive formulation of the PES which uses different two-body potential functionals: the atom-atom (AA) and the atom-bond (AB) ones. PESs-AA utilize the usual atom-atom model potential based on the atom-atom distance, whereas PESs-AB utilize the more recently proposed model potential based on the distance of the atom from the center of the considered bond. In the case of atom-bond PESs the potential parameters refer to the interaction of the atom with each bond of the molecule considered as a pseudo-diatomic molecule.

The study is based on a systematic investigation of Rg_n -benzene (with Rg being He, Ne, Ar, Kr, Xe and n being 1 and 2) clusters and considers both their static and dynamic properties. The paper is articulated as follows. In section 2 the key features of the AA and AB two body potentials for the pairs relevant to the systems under investigation are analyzed in detail. In section 3 the analysis and the comparison are extended to some static and dynamic properties of PES-AA and PES-AB.

2 A Comparison of the AA and AB Two Body Potentials

As already mentioned we first analyze the two body components of the pairwise additive functional representation used to describe the interaction of the *Rg-benzene* systems.

2.1 The Two Body PES-AA and PES-AB Potentials

The atom-atom contributions, relevant to the interactions considered in this paper, are the V_{Rg-X} ones ($X=C, H, Rg$ and $Rg=He, Ne, Ar, Kr, Xe$). The functional form most used to represent these two body terms, V_{Rg-X} , is the Lennard-Jones(12,6) atom-atom model potential:

$$V_{Rg-X}(r_{Rg-X}) = \epsilon_{Rg-X} \left[\left(\frac{r_{0Rg-X}}{r_{Rg-X}} \right)^{12} - 2 \left(\frac{r_{0Rg-X}}{r_{Rg-X}} \right)^6 \right] \quad (1)$$

where r_{Rg-X} represents the internuclear distance between Rg and X and ϵ and r_0 two arbitrary parameters usually referred to the dissociation energy and the distance at which the potential is minimum. The basic parameters for the present systems have been proposed in Ref [17].

The PES-AA potential energy functional gives, in general, a good description of the intermolecular interaction for several molecular aggregates. However, this

seems not to be the case for strongly anisotropic systems, like the benzene-rare gas clusters considered here, since, in this case, less stable geometries are poorly described by PES-AA and radial distribution functions of the electrons are expected not to be always spherically symmetric. Yet, these less stable geometries are of paramount importance for the rationalization of the isomerization processes. In fact, as the temperature of the system rises, they become increasingly more accessible opening so far alternative routes to isomerization. This is, for example, the case for the inter-conversion between stereo-isomers of van der Waals clusters occurring at low temperatures in supersonic expansions of gaseous jets and beams [18].

The alternative AB formulation of the interaction makes the parameters of the radial functional depend on the angle α that the radius r forms with the bond. The functional form adopted [19] to express these two body terms is an anisotropic modified Maitland-Smith function:

$$V(r, \alpha) = \varepsilon(\alpha) \left[\frac{6}{n(r, \alpha) - 6} \left(\frac{r_0(\alpha)}{r} \right)^{n(r, \alpha)} - \frac{n(r, \alpha)}{n(r, \alpha) - 6} \left(\frac{r_0(\alpha)}{r} \right)^6 \right] \quad (2)$$

where in our case r is the distance of the Rg atom from the geometric center of the considered C–C or C–H bond. This formulation of the atom bond potential removes part of the inadequacies of a pure Lennard-Jones model occurring both at long and short range [19].

The dependence of ε and r_0 on α is given, as usual for atom-diatom systems, by the following expressions:

$$\varepsilon(\alpha) = \varepsilon_{\perp} \sin^2(\alpha) + \varepsilon_{\parallel} \cos^2(\alpha) \quad (3)$$

$$r_0(\alpha) = r_{0\perp} \sin^2(\alpha) + r_{0\parallel} \cos^2(\alpha) \quad (4)$$

with ε_{\parallel} , $r_{0\parallel}$, ε_{\perp} and $r_{0\perp}$ representing, respectively, the well depth and location for both the parallel and the perpendicular approaches of the Rg atom to the diatom segment of the molecular frame and identified as a given bond.

In Eq. 2 it is also

$$n(r, \alpha) = 10 + 4 \left(\frac{r}{r_0(\alpha)} \right)^2. \quad (5)$$

For the systems considered here six Rg–CC and six Rg–CH independent pairs of atom-bond potentials are considered.

The atom bond formulation of the two body components of the interaction is, in general, believed to be more solidly grounded from the physical point of view than the corresponding atom-atom one. The model is based on the additivity of the bond polarizability tensor components and on the dependence of the intermolecular interaction on the polarizabilities of involved partners. This allows the model to take into better account some key features of the electronic structure of the molecular aggregates such as the charge distribution around each bond and incorporates some features of the three body interaction.

2.2 The Determination of the Parameters

The values of the PES-AA and PES-AB parameters used in this paper are given in Table 1. The PES-AA parameters have been taken from the Ref. [17], while the values of the PES-AB parameters have been derived using the procedure illustrated in Ref. [20], in which an initial estimate of ϵ_{\parallel} , $r_{0\parallel}$, ϵ_{\perp} and $r_{0\perp}$ parameters is worked out as described in Ref. [21]. Then the parameters are refined by optimizing the reproduction of the experimental binding energy and of the equilibrium intermolecular distances of the most stable geometry [19, 22]. Moreover the ϵ and r_0 values of the two body terms of Rg-CC and Rg-CH are forced to scale in the same way with the polarizability change between C-C and C-H bonds and along the rare gases family. The differences between initial estimates and final convergence values are of the same order of the uncertainty of the input parameters. They may be seen as a manifestation of the contribution of the higher order components of the MBE (Many Body Expansion) formulation of the interaction [23] that is particularly important for aromatic molecules. It is worth noting here that the value of the parameters related to the Ar atom have been further improved with respect to those given in Ref. [20].

The particularly simple pairwise additive analytical formulation adopted for both PES-AA and PES-AB has proven to be useful especially when extending the study to clusters containing more than one rare gas atoms. In the AB case the formulation of the Rg-Rg (atom-atom) interaction is formally identical to that of an atom bond term (as in Eq. 2) from which the dependence of ϵ and r_0 on α has been removed. The n exponent of the repulsive term of the potential depends only on r , according to the expression

$$n_{\text{Rg-Rg}}(r) = 10 + 4 \left(\frac{r}{r_0} \right)^2 \quad (6)$$

Table 1. PES-AA and PES-AB parameters. Distances in Å, energies in meV.

Rg	PES-AA			PES-AB				
	X	$r_{0\text{Rg-X}}$	$\epsilon_{\text{Rg-X}}$	atom-bond pair	$r_{0\perp}$	$r_{0\parallel}$	ϵ_{\perp}	ϵ_{\parallel}
He	He	2.970	0.891	He-CC	3.583	4.005	0.860	0.881
	C	3.335	1.611	He-CH	3.234	3.480	1.364	1.016
	H	2.950	1.178					
Ne	Ne	3.100	3.632	Ne-CC	3.629	4.015	1.706	1.862
	C	3.400	3.294	Ne-CH	3.316	3.549	2.544	1.960
	H	3.015	2.372					
Ar	Ar	3.760	12.214	Ar-CC	3.879	4.189	3.895	4.910
	C	3.730	6.183	Ar-CH	3.641	3.851	4.814	3.981
	H	3.345	4.162					
Kr	Kr	4.010	17.325	Kr-CC	3.997	4.284	4.824	6.365
	C	3.854	7.334	Kr-CH	3.782	3.987	5.667	4.781
	H	3.469	4.828					
Xe	Xe	4.360	24.291	Xe-CC	4.163	4.425	5.654	7.849
	C	4.030	8.551	Xe-CH	3.976	4.175	6.233	5.384
	H	3.645	5.469					

3 Static and Dynamic Properties of Benzene Rare Gas Clusters

To compare the suitability of PES-AA and PES-AB to formulate the interaction for the considered Rg_2 -benzene systems we carried out an analysis of their main static and dynamical properties.

3.1 The One Rg Atom Systems

The fixed angle one dimensional cuts of both PES-AA and PES-AB potentials are similar [20] when the Rg atom approaches the center of mass of benzene, perpendicularly to the molecular plane. Several differences are instead observed when the Rg atom approaches the benzene molecule along other directions. The largest differences occur for in-plane approaches in which PES-AB shows a substantially stronger interaction than PES-AA. These differences show up also in the spherical average of the interaction.

In order to more extensively analyze the behaviour of the system on the two PESs, we carried out some molecular dynamics calculations for Rg approaching the benzene molecule frozen at its equilibrium geometry using the DL_POLY program package [24]. For each set of initial conditions a preliminary simulation was run to equilibrate the temperature and the geometry of the system. Then, a longer simulation was started to follow in detail its evolution. The initial position of the Rg atom was taken from spectroscopic data (He from Ref. [25], Ne and Xe from Ref. [4] and Ar and Kr from Ref. [26]). The time step used for the integration of the classical equations of motion was 1.0 fs. Calculations performed on PES-AB show that the r.m.s. relative total energy fluctuations are of the order of 10^{-5} . This deviation is comparable with that obtained on PES-AA. The elapsed time of the simulation performed on PES-AB is about 30% larger than that required on PES-AA because of the more complex formulation of the atom bond functional.

The plots of total energy for the two surfaces have the same increasing trend with temperature though with different absolute values. Such a difference reflects in a semiquantitative way the different strength of the interaction for the two PESs. As a matter of fact, for the same amount of supplied heat, the system has an higher total energy (which is the summation of the kinetic energy and of the configuration energy) on PES-AB than on PES-AA. This means that on PES-AB the system has the possibility of reaching a larger number of allowed configurations. This effect will be discussed in greater detail when analyzing the isomerization processes for systems having more than one Rg atom.

3.2 The Two Rg Atom Systems

In order to test the suitability of both PES-AA and PES-AB to be extended to $n \neq 1$ Rg_n -benzene clusters we have carried out dynamical simulations for Rg_2 -benzene. As it has been already shown in the literature (both experimentally [3]

and theoretically [27]) Rg₂-benzene clusters exist in at least two different geometric configurations: the symmetric (1|1) isomer (having a sixfold symmetry with the two Rg atoms placed on the opposite sides of the benzene ring) and the asymmetric (2|0) one (having both Rg atoms on the same side of the benzene ring). The case of two Ar atoms has been already discussed in detail in Ref. [20]. Here the study is extended to the whole sequence of rare gas atoms. To this end the interaction between the two Rg atoms has been described using a Lennard-Jones (12,6) potential (see Eq. 1) whose parameters have been derived from scattering data of Ref. [28].

The existence of more than one isomer prompts also the question about their relative abundance. In the expansion of a supersonic jet (in which the clusters form) the isomer relative population at the end of the colliding process depends on the isomer ratio associated with the intermediate value of the temperature [27, 29]. To this end the same computational procedure adopted for the study of the dynamical behavior of the Rg-benzene cluster has been used. The simulations were run by starting from the global minimum associated with the most stable (1|1) isomer. Also in these simulations a time step of 1.0 fs was adopted and a short run of temperature equilibration was performed.

In the computational study the fraction of the time that the clusters spend wandering about the related equilibrium geometry has been taken as an index of the relative isomeric abundance. To investigate its variation as a function of temperature, several runs were performed by increasing T from 5.00 K to the dissociation temperature of one Rg atom in steps of 1.00 K.

Results obtained at the temperatures considered show that isomeric interconversions are quite likely to occur. This is shown in figures 1-5 in which the plots of the number of interconversions (central panel), the relative abundance of the (1|1) isomer (top panel) and the total energy (bottom panel) are plotted as a function of the temperature for each rare gas.

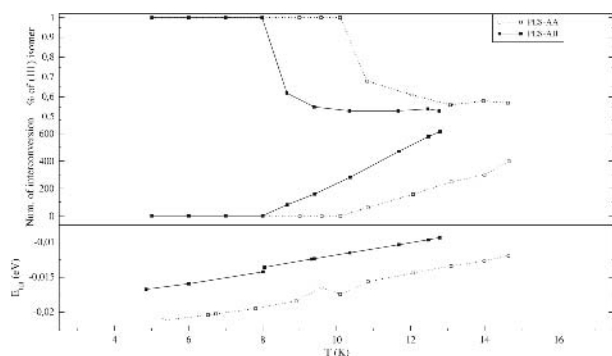


Fig. 1. Values of the fraction of the (1|1) He₂-benzene isomers (top panel), of the number of interconversions (central panel) and the total energy (bottom panel) plotted as a function of T

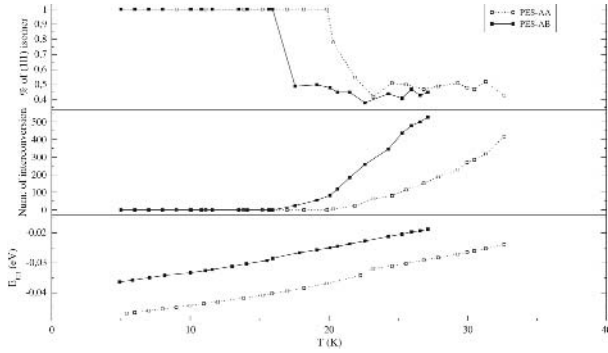


Fig. 2. As in Fig. 1 for Ne₂-benzene

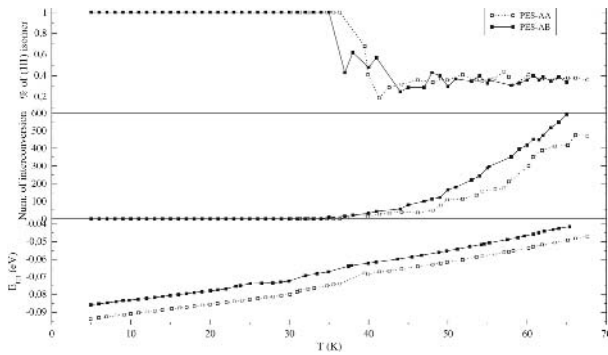


Fig. 3. As in Fig. 1 for Ar₂-benzene

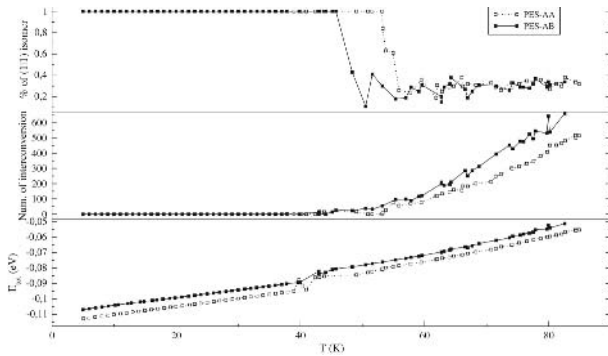


Fig. 4. As in Fig. 1 for Kr₂-benzene

A comparison of figures 1-5 shows that, for a given rare gas, the ratio of relative abundances tends to the same limiting value regardless the PES used. This value is 0.52 for helium, 0.45 for neon, 0.34 for argon, 0.30 for krypton and

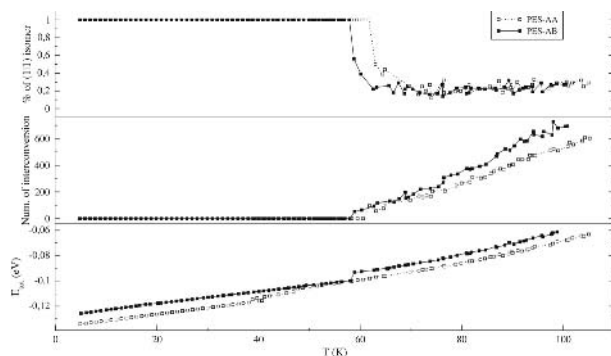


Fig. 5. As in Fig. 1 for Xe₂-benzene

finally 0.27 for xenon. The sequence of the limiting values is consistent with the ordering of the properties of the rare gases. This implies that the value of the isomeric abundance is limited to the polarizability and mass of the rare gas. On the contrary, the dependence of the number of interconversions on the temperature clearly reflects the type of the PES used. A clear fingerprint of the system being investigated is the value of the temperature at which the isomerization starts. This value is for PES-AB lower than for PES-AA. An interesting feature shown by the plots is the fact that the total energy has an inflection point (and sometimes also a switch between the PES-AB and PES-AA relative positions) at the temperature at which the isomerization process starts. This can be rationalized in terms of the fact that the heating provides one of two rare gas atoms with the possibility of forming the less stable isomer (2|0). In these conditions, during the simulation, the (2|0) isomer forms and contributes to the total energy with a positive term which is originated from the repulsive region of the Rg-Rg interaction. This situation occurs on PES-AB at temperature lower than for PES-AA and is associated to the height of its barrier.

4 Concluding Remarks

The paper presents a systematic study of the interaction of rare gas atoms with the benzene molecules in the prospect of better understanding solvation processes. To this end we have calculated the total energies, the number of interconversion and the isomeric relative abundance of the various Rg-benzene systems. The calculations indicate that the choice of the PES is crucial because it strongly influences the threshold isomerization temperature.

Acknowledgments

The research has been supported by MIUR, CNR and ASI.

References

1. Ondrechen M. J., Berkovitch-Yellin Z., Jortner J.: Model calculations of potential surfaces of van der Waals complexes containing large aromatic molecules. *J. Am. Chem. Soc.*, 103 (1981) 6586-6592.
2. Fried L. E., Mukamel S.: Structure, dynamics, and the electronic absorption of benzene argon clusters. *J. Chem. Phys.*, 96 (1991) 116-135.
3. Schmidt M., Le Calvè J., Mons M.: Structural transitions in benzene-argon clusters: size and temperature effects. *J. Chem. Phys.*, 98 (1993) 6102-6120.
4. Brupbacher Th., Makarewicz J., Bauder A.: Intermolecular dynamics of benzene rare-gas complexes as derived from microwave spectra. *J. Chem. Phys.*, 101 (1994) 9736-9746.
5. Hobza P., Bludsky O., Selzle H. L., Schalg E. W.: Ab initio calculations on the structure, vibrational frequencies, and valence excitation energies of the benzene-Ar and benzene-Ar₂ cluster. *Chem. Phys. Lett.*, 250 (1996) 402-408.
6. Lenzer T., Luther K.: Intermolecular potential effects in trajectory calculations of collisions between large highly excited molecules and noble gases. *J. Chem. Phys.*, 105 (1996) 10944-10953.
7. Dullweber A., Hodges M. P., Wales D. J.: Structure, dynamics, and thermodynamics of benzene-Ar_n clusters ($1 \leq n \leq B$ and $B = 19$). *J. Chem. Phys.* 106 (1997) 1530-1544.
8. Mons M., Courty A., Schmidt M., Le Calvè J., Piuze F., Dimicoli I.: New assignments in the UV spectroscopy of the small benzene-argon, clusters: The effects of a structure-selective vibrational predissociation. *J. Chem. Phys.*, 106 (1997) 1676-1686.
9. Bernshtein V., Oref I.: Dynamics and energy release in benzene-Ar cluster dissociation. *J. Chem. Phys.*, 112 (2000) 686-697.
10. Riganelli A., Memelli M., Laganà A.: Computational Science-ICCS 2002, PT III, Proceedings Lecture Notes in Computer Science 2331. Lecture Notes in Comp. Science, 2331 (2002) 926-931.
11. Kumpf R. A., Dougherty D. A.: A mechanism for ion selectivity in potassium channels. Computational studies of cation- π interactions. *Science*, 261 (1993) 1708-1710.
12. Dougherty D. A.: Cation- π interactions in chemistry and biology: A new view of benzene, Phe, Tyr, and Trp. *Science*, 271 (1996) 163-168.
13. Arteconi L., Laganà A.: A molecular dynamics study of ion permeability through molecular pores. Lecture Notes in Comp. Science, 3480 (2005) 1093-1100.
14. Hobza P., Selzle H., Schlag E. W.: Structure and properties of benzene-containing molecular clusters - Nonempirical ab-initio calculations and experiments. *Chem. Rev.*, 94 (1994) 1767-1785.
15. Kloppe W., Lüthi H. P., Brupbacher Th., Bauder A.: Ab-initio computations close to the one-particle basis-set limit on the weakly-bound van-der-Waals complexes benzene-neon and benzene-argon. *J. Chem. Phys.*, 101 (1994) 9747-9754.
16. Koch H., Fernández B., Makarewicz J.: Ground state benzene-argon intermolecular potential energy surface. *J. Chem. Phys.*, 111 (1999) 198-204.
17. Amos A. T., Frank Palmer T., Walters A., Burrows B. L.: Atom atom potential parameters for vanderWaals complexes of aromatics and rare-gas atoms. *Chem. Phys. Lett.*, 172 (1990) 503-508.
18. Boucher D. S., Bradke M. D., Darr J. P., Loomis R. A.: Preferential stabilization of different isomers of weakly bound complexes. *J. Phys. Chem. A*, 107 (2003) 6901-6904.

19. Pirani F., Albertí M., Castro A., Moix Teixidor M., Cappelletti D.: Atom-bond pairwise additive representation for intermolecular potential energy surfaces. *Chem. Phys. Lett.*, 394 (2004) 37-44.
20. Albertí M., Castro A., Laganà A., Pirani F., Porrini M., Cappelletti D.: Properties of an atom-bond additive representation of the interaction for benzene-argon clusters. *Chem. Phys. Lett.*, 392 (2004) 514-520.
21. Pirani F., Cappelletti D., Liuti G.: Range, strength and anisotropy of intermolecular forces in atom-molecule systems: an atom-bond pairwise additivity approach. *Chem. Phys. Lett.*, 350 (2001) 286-296.
22. Pirani F., Porrini M., Cavalli S., Bartolomei M., Cappelletti D.: Potential energy surfaces for the benzene-rare gas systems. *Chem. Phys. Lett.*, 367 (2003) 405-413.
23. Murrell J. N., Carter S., Farantos S. C., Huxley P., Varandas A. J. C.: *Molecular potential energy surfaces* (Wiley, New York, 1984).
24. http://www.dl.ac.uk/TCSC/Software/DL_POLY.
25. Beck S. M., Liverman M. G., Monts D. L., Smalley R. E., *J. Chem. Phys.*: Rotational analysis of the ${}^1B_{2u}(\pi\pi) \leftarrow {}^1A_{1g^*}, (6\frac{1}{0})$ band of benzene and helium-benzene van der Waals complexes in a supersonic jet. 70 (1979) 232-237.
26. Krause H., Neusser H. J.: Dissociation-energy of neutral and ionic benzene-noble gas dimers by pulsed-field threshold ionization spectroscopy. *J. Chem. Phys.*, 99 (1993) 6278-6286.
27. Vacek J., Konvicka K., Hobza P.: A molecular-dynamics study of the benzene- Ar_2 complex. Applications of the nonempirical ab-initio and empirical Lennard-Jones 6-12 potentials. *Chem. Phys. Lett.*, 220 (1994) 85-92.
28. Cambi R., Cappelletti D., Liuti G., Pirani F.: Generalized correlations in terms of polarizability for vanderWaals interaction potential parameter calculations. *J. Chem. Phys.*, 95 (1991) 1852-1861.
29. Vacek J., Hobza P.: A molecular-dynamics study of the benzene- Ar_n ($n = 3 - 5$) complex using the ab-initio intermolecular potential. *J. Phys. Chem.* 98 (1994) 11034-11039.

A Simplified Myoglobin Model for Molecular Dynamics Calculations

Federico Filomia and Noelia Faginas Lago

Department of Chemistry, University of Perugia, Perugia
{kikko, noelia}@dyn.unipg.it

Abstract. The Myoglobin active site has been investigated using Molecular dynamics means in order to model its behaviour as gas molecules carrier. The simulations carried out using the DL-poly package and the Dreiding force field were able to rationalize some of the observed properties of the system and well compared with DFT results.

1 Introduction

Myoglobin (MG) and Hemoglobin (HG) are proteins which contain the Heme group (a prosthetic group consisting of the Protoporphyrin ring and a central Iron atom) whose physiological importance is mainly related to their ability to bind molecular Oxygen selectively with respect to other gas molecules and to ensure their trasportation in living bodies. HG forms with O_2 a complex ($HG - O_2$). This complex acts as an effective Oxygen carrier to deliver O_2 to the muscles via the blood. Once in the vicinity of the muscle tissues the complex releases the O_2 molecule that is transferred to MG. MG provides its trasportation trough the muscles. The nature of the molecular processes involved in the binding of the gas molecule to MG and HG is very interesting because these globines can discriminate among gas molecules having similar structures like O_2 , NO and CO . In this paper we discuss first the modeling of the structure and then the dynamics of the process.

2 The Heme and the Force Field

As a first step to the rationalization of the properties of the Heme group we singled out and reproduced the structure of its basic components which are evidenced using red arrows and a dashed plane in Fig. 1. The structure of Fig. 1 was built by taking the geometrical information from a PDB (Protein Data Bank) file obtained from RSCB [1]. From this file we took only the HEM and the HIS coordinates related to the two Histidines marked as $E2$ and $F8$ in Fig. 1. The figure shows also that the Heme group is characterized by a Protoporphyrin IX of iron(II) lying centrally on the horizontal plane. In the shown arrangement of the Porphyrin the Iron atom is coordinated with four on plane Nitrogen atoms (N_p), with one Histidine ($F8$) Nitrogen atom (N_{his}) on the fifth position under

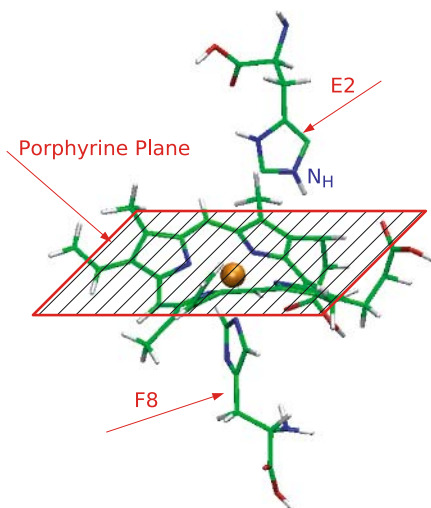


Fig. 1. A picture of the calculated structure of Heme with the Protoporphyrin evidenced by thick lines. (green spheres = C, blue spheres = N, red spheres = O, white spheres = H and orange spheres = Iron(II)).

the plane. The Heme group is surrounded by a large number of proteic residues which form a hydrophobic hole preventing water from entering. Each residue plays a specific role. In particular, the second Histidine (*E2*) residue placed over the Protoporphyrin plane has biological relevance. This residue provides steric impediment for gases other than Oxygen. The resulting reduction in strength of the bond tying Iron to *CO* or *NO* destabilizes the related complex. Recently it was found that the *E2* Histidine plays an even more important role because the Nitrogen marked as N_H in Fig. 1 and placed near the gas molecule is protonated and is capable to bind the hydrogen atom to the gas. The hydrogen bond is directional. As a result, the structure of the complex is twisted causing a partial destabilization [2] of the system. In absence of *E2*, Oxygen, Carbon monoxide and Nitrogen monoxide bind to the Iron with different angles: for Oxygen the angle is about 120° , for Nitrogen monoxide the angle is about 140° and for Carbon monoxide the angle is about 180° . The presence of N_H of the *E2* residue reduces all these angles to the limiting value of the Oxygen. This reduces also the stability of the complex and discriminates so far O_2 from *CO* and *NO*.

To reproduce such a behaviour we built a specific model having the following characteristics: the *E2* Histidine in MG is not bound to the peptide chain but it is bound to a spheric ensemble, made by a large number of fixed in space Van der Waals spheres to mimicking the effect of the surrounding residues (see Fig. 2).

These spheres interact only with the Heme system and do not reciprocally interact.

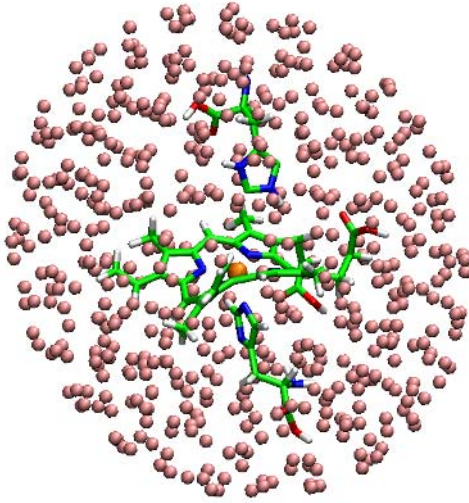


Fig. 2. In figure it can see the Van der Waals pink spheres, that are dummy atoms and are important to reproduce the interaction with the protein residues

The initial config file was obtained by extrapolating the coordinates of the pdb file of MG. To reproduce the entire system we made use the Dreiding force field[3]. Though this is not the most recent force field yet it is a very useful tool to describe organic and biological molecules. Atoms are classified by their hybridization states and masses. Accordingly, an sp^2 Carbon atom is considered equal to an sp^3 Carbon atom with the geometry of the chemical bonds being the only difference.

The energy potential is calculated as a sum of bonded and non-bonded energy contributions. Bonded contributions are formulated as stretching (E_s), bending (E_b) and torsion (E_t) terms:

$$E_{bond} = E_s + E_b + E_t \quad (1)$$

The non-bonded contributions are formulated as Van der Waals (E_{vdw}) and Coulomb (E_{Coul}) terms:

$$E_{non-bond} = E_{vdw} + E_{Coul} \quad (2)$$

The stretching contribution E_s for the diatom ij is formulated as Morse potentials:

$$E_s = E_0[(1 - e^{-k(r_{ij} - r_{e_{ij}})})^2 - 1] \quad (3)$$

where E_0 is the dissociation energy, $k=2.236 \text{ \AA}^{-1}$ is a constant, r_{ij} is the inter-nuclear distance, $r_{e_{ij}}$ is the equilibrium distance calculated as:

$$r_{e_{ij}} = r_i^0 + r_j^0 - 0.01 \quad (4)$$

Table 1. Values of r_e used in our calculation. N_R and C_R are the aromatic Nitrogen and Carbon atoms.

Bond type r_e (Å)	
Fe-N_R	1.925
C_R-N_R	1.340
C_R-C_R	1.390

with r_i^0 and r_j^0 being the atom radii of atoms i and j respectively. The values of r_0 are taken from the DL_poly database file Minidrei. Some r_e values obtained in this way and used in our calculation are given in Table 1.

Typical E_0 values of Dreiding for the Morse potentials used in our calculations are given in Table 2

Table 2. E_0 values used in the adopted force field

Bond type - E_0 (kcal/mol)	
single	70
double	140
triple	210
conjugated	105

The bending contributions E_b are formulated as harmonic potentials of the type:

$$E_b = \frac{1}{2}C(\cos \theta - \cos \theta^0)^2 \quad (5)$$

where C is defined as:

$$C = \frac{K_{ijl}}{(\sin \theta_j^0)^2} \quad (6)$$

with i, j and l being the three atoms forming the bending angle θ centered on j . In equation 5 and 6 θ^0 is the equilibrium value of θ and K_{ijl} is set equal to $100 \text{ kcal mol}^{-1} \text{ rad}^{-2}$. Values of θ^0 are listed in the already mentioned Minidrei file. The values of θ^0 more relevant to the present work are given in Table 3.

Table 3. N_R and C_R are aromatic Nitrogen and Carbon atoms. Other angles values are given in the Minidrei file.

atom θ^0 (degree)	
Fe	90
N_R	120
C_R	120

Torsional contribution E_t are formulated as cosine potentials:

$$E_t = A[1 + \cos(m\phi - \delta)] \quad (7)$$

where A is the barrier to rotation (always positive), m is the periodicity (an integer) and ϕ is the dihedral angle. The coulombic contributions E_{coul} are formulated as:

$$E_{Coul} = \frac{q_i q_j}{\epsilon r_{ij}} \quad (8)$$

where q_i e q_j are the respective charges of the atoms i e j , r_{ij} is the distance between the i and j atom and ϵ is the dielectric constant (usually $\epsilon = 1$). Coulombic interactions are not calculated for bound atoms because these are already incorporated into E_s and E_b . The Van der Waals contributions E_{vdw} are formulated as Lennard Jones (12-6) potential:

$$E_{vdw} = \left(\frac{A}{r^{12}} \right) - \left(\frac{B}{r^6} \right) \quad (9)$$

where A_{ij} and B_{ij} are defined as:

$$A_{ij} = [A_{ii}A_{jj}]^{1/2} \quad (10)$$

$$B_{ij} = [B_{ii}B_{jj}]^{1/2} \quad (11)$$

from the A_{ii} and B_{ii} values of the Lennard Jones parameters for homonuclear molecules.

3 The Gas Insertion and Dynamical Calculations

Our simulation is carried out in vacuo using an NVE ensemble (in the NVE ensemble we can control the total energy of the system) for 2×10^7 steps with a time step equal to 10^{-5} ps after thermalizing the system for 10^6 steps at 298 K. In Fig. 3 we plot the configuration energy defined as sum of $E_{bond} + E_{non-bond}$ (see equations 1 and 2). The figure shows that the thermalization leads to a stable geometry.

The corresponding plot for the temperature is given in Fig. 4. The mean temperature is 294.40 K. The thermalized sample is the starting point for the simulation. The simulation was performed by following the evolution in time of the structural features of both the pentacoordinated Iron (no gas inserted) and the esacoordinated one (gas inserted). The simulation shows that following the insertion of the gas molecule the Iron atom has a vertical displacement due to the rearrangement of its orbitals. This means that the pentacoordinated Iron (in absence of the ligand gas) places itself about 0.3 angstrom below the Protoporphyrin plane while the esacoordinated one places itself on the same plane. The two arrangements are sketched in Fig. 5.

The results obtained for the pentacoordinated iron is given on the left hand side of the figure and shows a good agreement with data obtained using the Car Parrinello (C.P.) DFT method [4].

These results are given in a more quantitative way in Table 4. The results of the esacoordinated Iron results are given in Table 5.

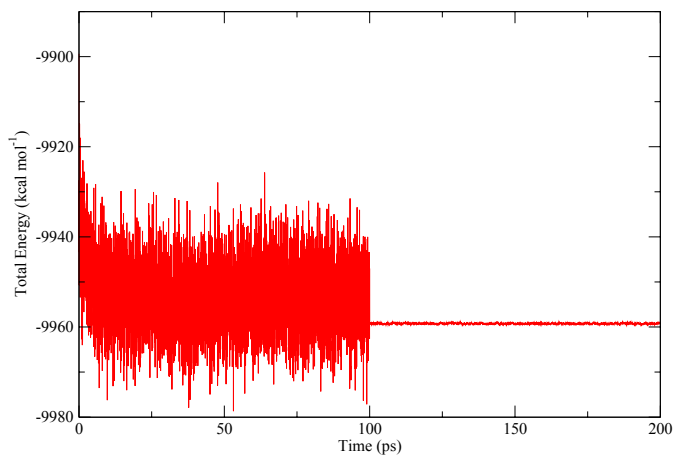


Fig. 3. Plot of the configuration energy given as a function of integration time

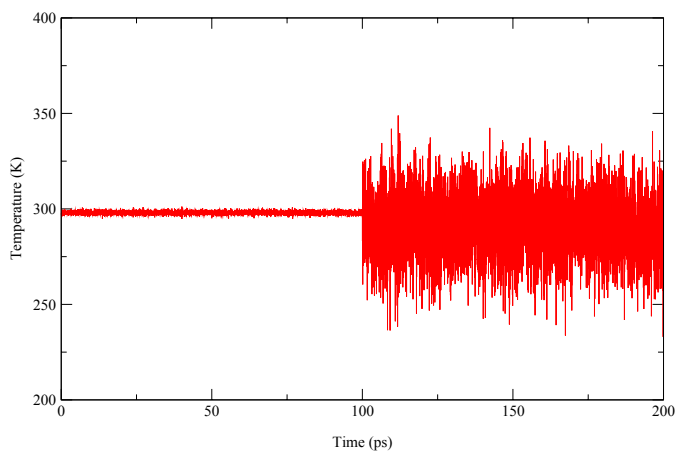


Fig. 4. Plot of the temperature given as a function of integration time

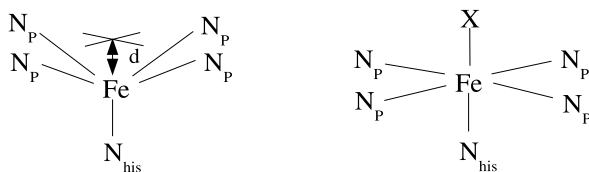


Fig. 5. Sketch of the Iron placement as a result of the simulation; N_p are the Nitrogen atoms of the Protoporphyrin plane, N_{his} is the Histidine Nitrogen atom and X is the ligand gas molecule; d is the distance of Iron(II) from the Porphyrin plane

Table 4. Distance of Iron from the reference Nitrogen atoms and Porphyrine plane

	Fe-N _p (Å)	Fe-N _{his} (Å)	d (Å)
C.P.	2.04	2.1	-0.33
dl_poly	2.05	2.04	-0.46

Table 5. Relevant internuclear distances for the system after adding the gas molecule

	Fe-O (Å)	O-O (Å)	Fe- \hat{O} -O	Fe-N _p (Å)	Fe-N _{his} (Å)	d (Å)
C.P.	1.77	1.30	121	1.99	1.99	-0.24
dl_poly	2.15	0.95	169	2.05	2.05	-0.03

4 Conclusions

In this paper, we report a preliminary result of a calculation performed for the Heme group. To the end of understanding the behaviour of the Heme group we built a model allowing us to study the dynamics of its active site MG, using a dynamical molecular software (DL-poly). The first part of the work has been devoted to the construction of the model and its force field. The second part has been devoted to the calculation of the effect of inserting a gas molecule in terms of distances of the bonds between the ligand and Iron and to a comparison with DFT results. The agreement was found to be good for both pentacoordinated and esacoordinated systems. These results indicate that when inserting the Oxygen molecule the system shapes itself in a clear bipyramidal geometry allowing the Iron to lie on the same plane of the Porphyrin.

Acknowledgments

Financial support from MIUR (project RBNE01KNFP) and ASI (PQE2000) is acknowledged.

References

1. (<http://www.rcsb.org/pdb/>)
2. Olson, J.S., Phillips, G.N.J.: Myoglobin discriminates between O(2), NO and CO by electrostatic interactions with the bound ligand. *JBIC* **2** (1997) 544–552
3. Stephen, L., Mayo, S.L., Olafson, B.D., Goddard III, W.A.: Dreiding: A generic force field for molecular simulations. *J. Phys. Chem.* **94** (1990) 8897–8909
4. Rovira, C., Ballone, P., Parrinello, M.: A density functional study of iron-porphyrin complexes. *Chem. Phys. Lett.* **271** (1997) 247–250

Parallel Calculation of Propane Bulk Properties

Alessandro Costantini, Antonio Laganà, and Fernando Pirani

Dipartimento di Chimica, Università di Perugia, Perugia, Italy
{alex, lag, pirani}@dyn.unipg.it

Abstract. The density of propane bulk system (in gas and liquid phase) have been estimated using molecular dynamics calculations. The effect of adopting two different force fields (OPLS/AMBER and Atom-Bond), varying the number of processors and increasing the numbers of molecules has been analysed.

1 Introduction

The increasing number of processors which can be used by a single calculation has allowed us to perform molecular based simulations for complex systems. As an example, we have now reached a stage in which it is possible, using molecular dynamics tools, to mimic the behaviour of condensed phase and to reproduce, using a priori approaches, the properties of bulk systems. In this paper we discuss the case of Propane in liquid and gas phase. Propane is an hydrocarbon commonly used as a fuel but also increasingly utilized as a refrigerating fluid inside common electrical appliances like air conditioners and fridges. For this reason we started an investigation aimed at constructing in an a priori fashion the state diagram of propane by using two different definitions of the force field. In particular we used both OPLS/AMBER all-atoms potential [1] and the more recently proposed atom-bond potential [2] [3]. The main difficulty of the task was the possibility of running calculations for a sufficiently large ensemble of molecules. For this reason we applied for an EPCC grant. Thanks to this grant we have been able to implement the DL_POLY [4] suite of code on the Blue Gene/L IBM cluster. The calculations were also performed on a XEON Intel node located at the School of Chemistry of the University of Edinburgh.

The paper is organized as follows: in section 2 and 3 the two formulations of the potential are discussed; in section 4 the results of the dynamical calculations are reported; in section 5 some conclusions are drawn.

2 The OPLS/AMBER Force Field

In the OPLS/AMBER force field [1] for organic molecules the nonbonded interactions are represented by a Coulomb plus a Lennard-Jones pair of terms as follows:

$$V_{OPLS} = \sum_i^{mol.a} \sum_j^{mol.b} \left[\frac{q_i q_j e^2}{r_{ij}} + 4\epsilon_{ij} \left(\frac{\sigma_{ij}^{12}}{r_{ij}^{12}} - \frac{\sigma_{ij}^6}{r_{ij}^6} \right) \right] f_{ij} \quad (1)$$

where q_i and q_j are the charges of atom i and j respectively, e is the charge of the electron, ϵ_{ij} , σ_{ij} and r_{ij} are the depth, the equilibrium and the actual distance respectively between atom i and j . In eq. 1 f_{ij} is always taken equal to 1 for all ij interactions. The same expression is used for intramolecular nonbonded interactions between all pairs of atoms separated by three or more bonds. The intermolecular interactions for angular (eq. 2) and torsional (eq. 3) motions are given as

$$V_{angle} = \sum_{angle} K_{\theta} (\theta - \theta_{eq})^2 \quad (2)$$

$$V_{dihedral} = \sum_i \frac{V_1^i}{2} [1 + \cos(\phi_i)] + \frac{V_2^i}{2} [1 + \cos(2\phi_i)] + \frac{V_3^i}{2} [1 + \cos(3\phi_i)] \quad (3)$$

where θ is the bending angle, the value of θ_{eq} is 109.5° while ϕ_i is the dihedral angle and V_1 , V_2 and V_3 are the coefficients of the Fourier series.

In the present system all the bonds have been considered constant and the total energy is taken as

$$V = V_{OPLS} + V_{angle} + V_{dihedral} \quad (4)$$

The values of the parameters used in the adopted OPLS/AMBER potential are shown in Tables 1 and 2 [1].

Table 1. Values of the parameters of the OPLS/AMBER bending and torsion potentials of the Propane system

Bending			
Group	θ_{eq} / °	K_{θ} / kcal mol ⁻¹	
H - C - H	109.5	35.00	
H - C - C	109.5	35.00	
C - C - C	109.5	40.00	

Torsion			
Group	V_1 /kcal mol ⁻¹	V_2 /kcal mol ⁻¹	V_3 /kcal mol ⁻¹
H - C - C - H	0.000	0.000	0.318
H - C - C - C	0.000	0.000	0.366

Table 2. Parameters for the OPLS/AMBER nonbonded potential of the Propane system

Atom	q/e^-	$\sigma/\text{Å}$	$\epsilon/\text{kcal mol}^{-1}$
C, RCH ₃	-0.180	3.500	0.066
C, R ₂ CH ₂	-0.120	3.500	0.066
H	0.060	2.500	0.030

3 The Atom-Bond Force Field

The atom-bond interaction [3] is formulated as

$$V = \sum_i \sum_j^{atom\ bond} V_{ij}(r_{ij}, \vartheta_{ij}) \quad (5)$$

where

$$V(r_{ij}, \vartheta_{ij}) = \epsilon_{ij}(\vartheta_{ij}) \left[\frac{m}{n_{ij}(r_{ij}, \vartheta_{ij}) - m} \left(\frac{r_{0ij}(\vartheta_{ij})}{r_{ij}} \right)^{n_{ij}(r_{ij}, \vartheta_{ij})} \right] - \left[\frac{n_{ij}(r_{ij}, \vartheta_{ij})}{n_{ij}(r_{ij}, \vartheta_{ij}) - m} \left(\frac{r_{0ij}(\vartheta_{ij})}{r_{ij}} \right)^m \right] \quad (6)$$

In the atom-bond formulation of the interaction the indices i and j have a different meaning from that of the atom-atom formulations. Accordingly the index i indicates the atom while the index j indicates the bond. Therefore, in eq. 5 and 6, r_{ij} is the distance between the atom i and the center of the bond j , ϑ_{ij} is the planar angle that r_{ij} forms with the j bond axis, r_{0ij} is the equilibrium value of r_{ij} and ϵ_{ij} is the value of the energy associated with the ij atom-bond interaction at r_{0ij} . In eq. 6 m is taken for any neutral-neutral system equal to 6 and $n_{ij}(r_{ij}, \vartheta_{ij})$ is calculated using the following equation:

$$n_{ij}(r_{ij}, \vartheta_{ij}) = \beta + 4.0 \left(\frac{r_{ij}}{r_{0ij}(\vartheta_{ij})} \right)^2 \quad (7)$$

with β being a constant parameter within a broad class of systems which characterizes the nature and the hardness of the interacting particles (in our case $\beta = 10$). The angular dependence of both $r_{0ij}(\vartheta_{ij})$ and $\epsilon_{ij}(\vartheta_{ij})$ is usually parametrized in terms of parallel (\parallel) and perpendicular (\perp) contributions as follows

$$\epsilon_{ij}(\vartheta_{ij}) = \epsilon_{\perp ij} \sin^2(\vartheta_{ij}) + \epsilon_{\parallel ij} \cos^2(\vartheta_{ij}) \quad (8)$$

$$r_{0ij}(\vartheta_{ij}) = r_{0\perp ij} \sin^2(\vartheta_{ij}) + r_{0\parallel ij} \cos^2(\vartheta_{ij}) \quad (9)$$

where $r_{0\perp ij}$, $r_{0\parallel ij}$, $\epsilon_{\perp ij}$ and $\epsilon_{\parallel ij}$ represent the well location and depth for perpendicular and parallel approaches respectively. The values of the atom-bond pairs of the Propane system worked out using the procedure to ref. [5] are shown in Table 3 (with the Propane bonds frozen at their equilibrium geometry).

Table 3. Parameters for the atom bond potential of the Propane system

Atom bond	$r_{0\perp ij}/\text{\AA}$	$r_{0\parallel ij}/\text{\AA}$	$\epsilon_{\perp ij}/\text{cm}^{-1}$	$\epsilon_{\parallel ij}/\text{cm}^{-1}$
C-C ... C	3.696	4.283	15.64	16.91
C-H ... C	3.663	3.873	24.69	20.48
C-C ... H	3.441	4.159	8.25	6.92
C-H ... H	3.410	3.634	12.54	9.74

4 Calculations and Results

The calculations were performed using the DL_POLY [4] software package on two different machines:

- one processor Intel XEON machine at the School of Chemistry, Edinburgh University;
- IBM Blue_Gene/L cluster (1064 nodes, 4.7 Tflops) at the Edinburgh Parallel Computer Center (EPCC), Edinburgh University.

All the calculations were carried out using the same statistical ensemble (npt) at two different temperatures (200 K and 288 K) in order to simulate both the liquid and the gas phase out of equilibrium. To obtain a preliminary indication on the suitability of the adopted potentials to describe the interaction of the system we have first performed our calculations on the XEON machine at an increasing number of Propane molecules. The results obtained are shown in Table 4.

As shown by the table, where results of calculations performed for simulations of 50 *ps* are given, the atom-bond formulation of the interaction seems not only to be, on the average, less efficient than the OPLS/AMBER one but it also seems to be less appropriate to reproduce the experimental density data reported

Table 4. Calculated properties of the Propane system

OPLS/AMBER						
Phase	Molecules	Temperature <i>/ K</i>	Pressure <i>/ bar</i>	Density <i>/ kg m⁻³</i>	Simulation time/ <i> ps</i>	Elapsed time/ <i> s</i>
liquid	8	200	25	680	50	583
gas	8	288	2.3	3.66	50	209
liquid	64	200	7.6	638	50	6304
gas	64	288	1.03	2.72	50	3772
Atom-Bond						
Phase	Molecules	Temperature <i>/ K</i>	Pressure <i>/ bar</i>	Density <i>/ kg m⁻³</i>	Simulation time/ <i> ps</i>	Elapsed time/ <i> s</i>
liquid	8	200	2.4	6.05	50	442
gas	8	288	2.7	2.91	50	455
liquid	64	200	1.3	33.9	50	31035
gas	64	288	1.05	5.29	50	36554

in the literature (respectively 582 Kg m^{-3} and 1.92 Kg m^{-3} for the liquid at $T = 230 \text{ K}$ and the gas at $T = 288 \text{ K}$ at $P = 1 \text{ atm}$) [6]. To improve the quality of the simulation we have increased the number of molecules of the system and carried out a new batch of calculations for 512 molecules using the OPLS/AMBER potential. To carry out related calculations we had to move to a larger platform and we implemented DL_POLY on the Blue_Gene/L machine. Results obtained by running DL_POLY in parallel on 32 and 128 nodes for 512 molecules are given in Table 5. The change of platform gave us also the possibility of doubling the simulation time for the gas phase calculations. A first important result shown in the table is that it has become easier to obtain a value of the pressure close to the atmospheric condition of the experiment. The other important point is that the calculated densities (apart from small fluctuations due to the different partitioning of the particles domain for machines not having the same number of processors) reasonably well reproduce measured values. However a rather disappointing result is the low speedup measured for parallel calculations. An increase, in fact, of the number of processors of a factor of 4 (from 32 to 128) leads to a reduction of the elapsed time of the calculations of only a factor 1/3.

Table 5. Elapsed time as a function of the used nodes by IBM Blue_Gene/L machine

		OPLS/AMBER potential					
Phase	Molecules	Nodes	Temperature / K	Pressure / bar	Density / $kg \text{ m}^{-3}$	Simulation time/ ps	Elapsed time/ s
liquid	512	32	200	1.27	573	50	12209
gas	512	32	288	1.01	2.69	100	15957
liquid	512	128	200	1.22	574	50	8532
gas	512	128	288	1.02	3.11	100	16490

5 Conclusion

We have studied the Propane system in both liquid and gas phase using two kinds of force fields (OPLS/AMBER and atom-bond) and two types of computing platforms (a one node Intel XEON and a Blue_Gene/L IBM cluster). In order to reproduce the properties of the system and to evaluate the performance of the parallel calculations we increased both the number of the molecules of the system and the number of computing nodes. We found that when the number of molecules increases, the calculated value of the density of the system gets closer to the data given in the literature especially when using the OPLS/AMBER formulation of the interaction. We also found that the computational effort to be spent for further improving the result by increasing the number of molecules is far too large since the gain in time obtained by increasing the number of computing nodes for parallel calculations is too poor with presently available platforms. Possible ways out of this problem that we have started to experiment are a different formulation of the interaction (atom block-wise), a different parallelization model for DL_POLY and the development of a grid based approach.

Acknowledgements

This work was carried out under the HPC-EUROPA project (RII3-CT-2003-506079), with the support of the European Community - Research Infrastructure Action under the FP6 Structuring the European Research Area Programme. Financial support from MIUR (project RBNE01KNFP) and ASI (PQE2000) is also acknowledged.

References

1. Jorgensen, W. L., Maxwell, D.S., Tirado-Rives, J.: *J. Am. Chem. Soc.* **118** (1996) 11225-11236
2. Alberti, M., Castro, A., Laganà, A., Pirani, F., Porrini, M., Cappelletti, D.: *Chem Phys. Lett.* **392** (2004) 514-520
3. Pirani, F., Alberti, M., Castro, A., Moix Teixidor, M., Cappelletti, D.: *Chem Phys. Lett.* **394** (2004) 37-44
4. Smith, W., Forester, T.R.: DL_POLY2: a general-purpose parallel molecular dynamics simulation package. *J. Mol. Graph.* **14** (3) (1996) 136-141
5. Pirani, F., Cappelletti, D., Liuti, G.: *Chem Phys. Lett.* **350** (2001) 286-296
6. Air liquid group website: <http://www.airliquide.com>

Ab-Initio Multi-reference Study of a Bistable Spiro Molecule

Wissam Helal, Benoît Bories, Stefano Evangelisti,
Thierry Leininger, and Daniel Maynaud

Laboratoire de Physique Quantique UMR 5626 du CNRS, IRSAMC,
Université Paul Sabatier,
118, Route de Narbonne, 31062 Toulouse, Cedex, France
`stefano.evangelisti@irsamc.ups-tlse.fr`

Abstract. CAS-SCF and MRCI calculations are presented, in order to investigate the electronic states involved in the intramolecular charge-transfer process of a bistable spiro cation. The potential energy curves of the ground and the first three excited states have been calculated, and a double well potential has been obtained for the ground state. The effect of dynamical correlation was found to be crucial for a quantitative description of this system. Our results also indicate the usefulness of a local-orbital description of bistable systems.

1 Introduction

Mixed-Valence compounds have been widely studied in recent times, particularly for their interest in molecular electronics [1]. Although many of the considered systems contain transition-metal atoms as mixed-valence centers [2], purely organic compounds have also been investigated theoretically [3]. Among these types of molecules, the spiro $\pi - \sigma - \pi$ system $C_{13}N_2H_{14}$ has been often studied as a model system [3]-[7], since its relatively small size, permits high-level *ab initio* investigations.

The geometry of the spiro molecule, which is the object of the present study, is shown in Figure 1. The system consists of two π moieties, placed on two orthogonal planes, and separated by a σ bridge. If an electron is extracted from this molecule, the resulting hole tends to localize either on the left or the right π system, inducing a deformation of the molecular geometry. Therefore two equivalent minima exist for the cation, and the ground state presents the double well curve which is typical for mixed-valence systems.

In this contribution, we present the results of Complete-Active-Space Self-Consistent-Field (CAS-SCF) and subsequent Multi-Reference Configuration-Interaction (MRCI) investigations on the spiro molecular cation of Figure 1. The ground-state geometry of this system shows two equivalent minima having C_{2v} symmetry, separated by a D_{2d} saddle point, at any level of calculation. It is shown that the contribution of the dynamical correlation is crucial in order to obtain quantitative results.

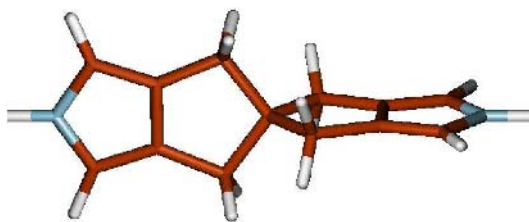


Fig. 1. The spiro molecular system

Spiro cation was studied in the C_{2v} point group (if the charge is localized on either one of the two aromatic moieties in the molecule), while a D_{2d} geometry was taken for the totally delocalized state [6]. More recent studies, suggested C_1 and C_2 point groups for the two situations, respectively [3]. However, according to these calculations, the difference from exact C_{2v} and D_{2d} symmetries are extremely small. Therefore, in view of the preliminary character of the present investigation, we decided to use the high symmetry groups in this study.

2 Computational Details

The principal axis of rotation, the C_2 axis, is the straight line connecting the two nitrogen atoms. B_1 , B_2 and two averaged states of A_2 symmetry (which will be designated as $A_2(1)$ and $A_2(2)$ in the present article) were calculated for the two geometries. No A_1 symmetry states were considered in this study since their energies are much higher than that for the other states. In all our CAS-SCF calculations, we were only interested in the π electrons of the cation, since these are the electrons engaged in the electron transfer process in conjugated systems.

Restricted Hartree Fock (RHF), CAS-SCF and Contracted MR-CI (C_MRCI) calculations were done using the MOLPRO computer code version 2002.6 [8] and MOLCAS code version 6.0 [9]. Both MOLPRO and MOLCAS codes can only treat abelian point groups. Therefore, since D_{2d} is a non-abelian group, D_{2d} symmetry orbitals calculations were performed using the C_{2v} symmetry generators.

Atomic Natural Orbitals (ANO) basis sets [10] were used in all calculations, by using different contraction levels: SZ ((1s) for H and (2s1p) for C and N), DZ ((2s) for H and (3s2p) for C and N), DZP ((2s1p) for H and (3s2p1d) for C and N) and TZP ((3s1p) for H and (4s3p1d) for C and N). Geometry optimization of the A_2 state for both C_{2v} and D_{2d} geometries were calculated for the cation at the RHF level, by using the TZP basis set.

The Born-Oppenheimer potential surfaces were obtained by calculating the corresponding states energies of each point on the reaction geometry coordinate, which in turn was obtained by mixing linearly the optimized coordinates of the two equilibrium C_{2v} geometries [6]:

$$Q(\xi) = \xi Q_B + (1 - \xi) Q_A \quad (1)$$

Table 1. Energy differences (KJ/mol) between the different states of the spiro cation, computed at (7/4) CAS-SCF level and by using different basis sets. For each method, the energy zero has been taken as the energy of the ground state $A_2(1)$ in the D_{2d} geometry.

CAS-SCF:	SZ	DZ	DZP	TZP
D_{2d}				
$A_2(1)$	0.000	0.000	0.000	0.000
$A_2(2)$	9.043	9.987	9.664	9.626
B_1	44.748	51.646	46.521	45.181
B_2	44.748	51.646	46.521	45.181
C_{2v}				
$A_2(1)$	-8.328	-5.640	-6.528	-6.753
$A_2(2)$	48.362	40.185	39.852	39.390
B_1	52.655	56.923	51.802	50.231
B_2	66.710	69.636	63.421	61.731

where $Q(\xi)$ is the nuclear configuration at any point on the reaction path, while Q_A and Q_B represent the nuclear coordinates of the two C_{2v} geometries. The mixing parameter ξ was varied from -1.00 to 2.00 in steps of 0.05 . In such a way, Q_A (the first C_{2v} minimum), corresponds to the point $\xi = 0.00$, where the positive charge is localized on one moiety of the molecule; Q_B (the second C_{2v} minimum) corresponds to the point $\xi = 1.00$, where the positive charge is localized on the second moiety; the D_{2d} geometry, being the average of the two C_{2v} geometries, is represented by the point $\xi = 0.50$ on the reaction coordinate. In order to test the quality of this averaged D_{2d} geometry, the corresponding state energies of the later were compared with those of the optimized D_{2d} geometry. The results show a very small difference between the averaged and the optimized D_{2d} geometries (see next section). For this reason, we believe that the geometry path obtained through equation (1) is very close to the optimal one.

The energy of the A_2 , B_1 and B_2 states of the potential surface were calculated, for different values of the parameter ξ , with a TZP basis using CAS-SCF method with 7 active electrons and 4 active space π orbitals (one b_1 , one b_2 and two a_2). Contracted MRCI(SD) were also performed using the same active space, with the $1s$ orbitals of the carbon and nitrogen atoms being frozen.

In order to assess the validity of a Contracted approach, uncontracted MRCI(SD) were also performed for the two key points on the reaction coordinate,

Table 2. Energy differences (KJ/mol) between the different states of the spiro cation, computed at Contracted MRCI (C_MRCI) and Uncontracted MRCI (MRCI) by using different basis sets. For each method, the energy zero has been taken as the energy of the ground state $A_2(1)$ in the D_{2d} geometry.

<i>C_MRCI:</i>	SZ	DZ	DZP	TZP	<i>MRCI:</i>	SZ	DZ
<i>D_{2d}</i>							
$A_2(1)$	0.000	0.000	0.000	0.000		0.000	0.000
$A_2(2)$	9.323	10.290	10.077	9.999		9.246	10.187
B_1	53.972	62.400	61.379	59.461		51.888	61.207
B_2	53.972	62.400	61.379	59.461		51.888	61.207
<i>C_{2v}</i>							
$A_2(1)$	-6.684	-4.669	-5.196	-5.580		-6.476	-4.410
$A_2(2)$	47.076	39.319	39.042	38.523		47.325	39.455
B_1	59.732	65.467	64.937	62.704		58.181	64.810
B_2	78.682	82.888	80.668	78.246		76.537	81.448

namely, the C_{2v} minimum ($\xi = 0.00$) and the D_{2d} saddle point ($\xi = 0.50$). This was done by using the Toulouse program CASDI [11], and for the two smallest basis sets only.

These two points, were also chosen to perform a CAS-SCF/TZP calculation, using the MOLPRO code, with a larger active space: we selected 10 active orbitals (three b_1 , three b_2 and four a_2), which can represent in principle the complete (valence) π system of this molecule. Local CAS-SCF/SZ calculation with 8 active space orbitals (two b_1 , two b_2 and four a_2) were done using CASDI code. The justification of the choice of the later active space is discussed in the next section.

3 Results and Conclusion

The energy differences (KJ/mol) between the different states, with 4 active orbitals computed by using different methods, are shown in Tables 1 and 2. For each type of calculation, the energy zero has been taken as the energy of the ground state $A_2(1)$ in the D_{2d} geometry.

In Table 3 the difference between the results of the D_{2d} geometry, obtained with the averaged and optimized geometries (at CAS-SCF TZP level), are reported. From a comparison with the corresponding results of Table 1, it is clear that the effect of replacing the optimized D_{2d} geometry by the averaged one is extremely small (about 0.8 KJ/mol at most).

Table 3. Energy differences (KJ/mol) between the states of the spiro cation, computed at the optimized and the averaged D_{2d} geometries, using TZP basis set

CAS-SCF		
	$D_{2d}(\text{opt})$	$D_{2d}(\text{opt}) - D_{2d}(\text{av})$
$A_2(1)$	-0.112	-0.112
$A_2(2)$	9.697	0.017
B_1	44.378	-0.803
B_2	44.378	-0.803

The reaction coordinates of the spiro cation calculated at the (7/4) CAS-SCF/TZP for the ground and the first three excited states are shown in Figure 2 (top). A smooth adiabatic two-well curve was obtained for the ground state, while a parabolic curve is obtained for the first excited state. These two lower states have an A_2 symmetry and correspond actually to the averaged two states of A_2 ($A_2(1)$ and $A_2(2)$). The second and third excited states are degenerate at the D_{2d} geometry and correspond to the B_1 and B_2 symmetries. In the electron transfer process, an electron is excited at any equilibrium C_{2v} geometry, from the ground to the first excited state. This transition is governed by Frank-Condon principle. After geometrical rearrangement to D_{2d} geometry the electron will make transition to the ground state followed by a geometrical relaxation to the other side of the molecule.

In Figure 2 (bottom), the reaction coordinates of the ground and first three excited states of the spiro cation calculated with MRCI(SD)/TZP are shown. The global behaviour of CAS-SCF and MRCI are similar, although the well depth is lower at MRCI level. On the other hand, the energy of the excited states of B symmetry tends to be higher at MRCI level.

It can be seen from Table 2 that the effect of dynamical correlation is very important in order to get quantitative results on this mixed-valence system. This is particularly true as far as the well depth is concerned, since its value is reduced by about 20% at C_MRCI level. A much smaller reduction is shown at uncontracted MRCI level. Energy differences between the two non-crossing states are considerably less affected by dynamical correlation.

In order to improve these results, we were interested in considering the whole π valence system of the molecular cation. The results obtained with the 10 active orbitals show a different physical content, since some of the π orbitals are replaced by orbitals having a σ character. This is a common problem with CAS-SCF algorithms based on canonical orbitals, and was one of the reasons that pushed our group to the development of the local CAS-SCF algorithm [12], [13].

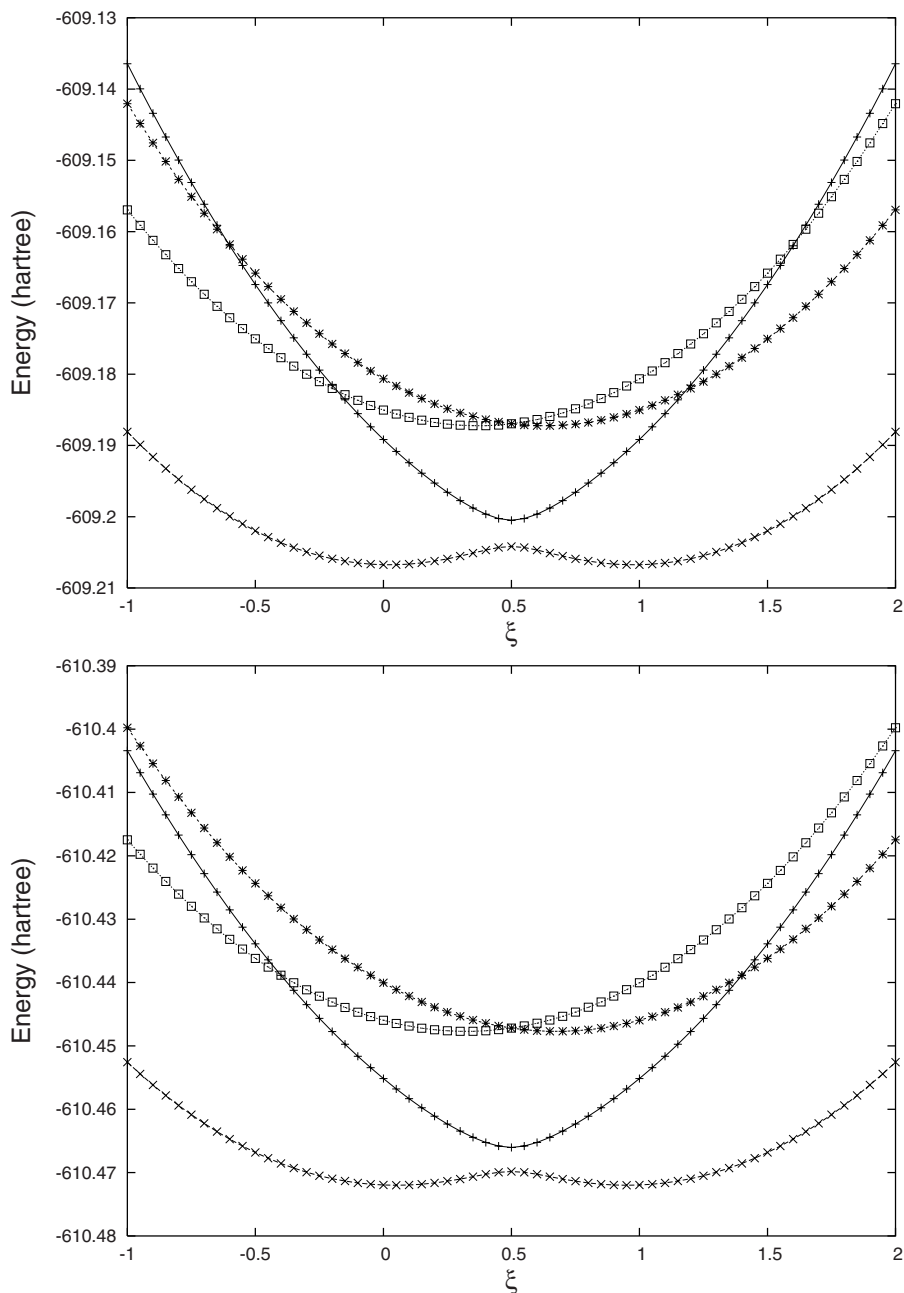


Fig. 2. Potential energy curves, in a.u., of the spiro cation for the ground and the first three excited states, as a function of the mixing parameter ξ : CAS-SCF/TZP (top), C_MRCI/TZP (bottom). (\times) $A_2(1)$, ($+$) $A_2(2)$, ($*$) B_1 , and (\square) B_2 .

Table 4. Energy differences (KJ/mol) between the different states of the spiro cation, computed at Localized (7/8) CAS-SCF using SZ basis set. For each method, the energy zero has been taken as the energy of the ground state $A_2(1)$ in the D_{2d} geometry.

<i>Localized CAS-SCF:</i>	SZ
<hr/>	
D_{2d}	
$A_2(1)$	0.000
$A_2(2)$	8.147
B_1	69.673
B_2	69.673
<hr/>	
C_{2v}	
$A_2(1)$	-4.011
$A_2(2)$	44.775
B_1	75.360
B_2	96.261
<hr/>	

This directed us to perform Local CAS-SCF calculation. We used an active space composed of $2b_1$, $2b_2$ and $4a_2$ orbitals. This corresponds to the π systems of the eight carbon atoms located on the external cycles. The C-N distance has a very small dependence on the geometry rearrangement described by the reaction coordinate $Q(\xi)$. This justifies the exclusion of the two nitrogen π orbitals (one b_1 and one b_2 orbitals) from the active space.

The energies of the different states of the two geometries for the 8 orbitals active space using local CAS-SCF are presented in table 4. With this active space, the depth of the two equivalent minima is strongly reduced, being 4.1 KJ/mol with the smallest basis set. This value should be compared with 8.3 KJ/mol, obtained with the 4 orbitals active space. The difference between the two A_2 states at D_{2d} is also reduced, but to a smaller extent: it passes from 9.0 KJ/mol with the (7/4) active space to 8.1 KJ/mol with the (7/8) space.

As a more general conclusion, it can be said that the use of large active space seems to be necessary for an accurate description of the small energy differences found in these types of molecules. However, the control of the nature of the active space is an extremely difficult task in canonical CAS-SCF, and the use of large active space is often problematic. For this reason, we believe that the use of local orbitals in a CAS-SCF context can be a very powerful tool for the treatment of mixed-valence systems.

References

1. Joachim, C., Gimzewski, J. K., Aviram, A.: Electronics using hybrid-molecular and mono-molecular devices. *Nature*. **408** (2000) 541–548
2. Launay, J.-P.: Long-distance intervalence electron transfer. *Chem. Soc. Rev.* **30** (2001) 386–397
3. Dehareng, D., Dive, G., Moradpour, A.: Ab Initio Study of Organic Mixed Valency. *Int. J. Quantum Chem.* **76** (2000) 552–573
4. Aviram, A., Ratner, M. A.: Molecular rectifiers. *Chem. Phys. Lett.* **29** (1974) 277–283
5. Aviram, A.: Molecules for Memory, Logic, and Amplification. *J. Am. Chem. Soc.* **110** (1988) 5687–5692
6. Farazdel, A., Dupuis, M., Clementi, E., Aviram, A.: Electric Field Induced Intramolecular Electron Transfer in Spiro π Electron Systems and Their Suitability as Molecular Electronic Devices. A Theoretical Study. *J. Am. Chem. Soc.* **112** (1990) 4206–4214
7. Sanz J. F., Calzado C. J., Marquez, A.: DFT *versus* CI Determination of the Electron-Transfer Matrix Element in some Case Examples. *Int. J. Quantum Chem.* **76** (2000) 458–463
8. R. D. Amos, A. Bernhardsson, A. Berning, P. Celani, D. L. Cooper, M. J. O. Deegan, A. J. Dobbyn, F. Eckert, C. Hampel, G. Hertzner, P. J. Knowels, T. Korona, R. Lindh, A. W Lloyd, S. J. McNicholas, F. R. Manby, W. Meyer, M. E. Mura, A. Nicklass, P. Palmieri, R. Pitzer, G. Raunhut, M. Schütz, U. Schumann, H. Stoll, A. J. Stone, R. Tarroni, Thorsteinsson, and H.-J. Werner. MOLPRO Version 2002.6
9. Andersson, K., Barysz, M., Bernhardsson, A., Blomberg, M. R. A., Carissan, Y., Cooper, D. L., Fulscher, M. P., Gagliardi, L., de Graaf, C., Hess, B. A., Hagberg, D., Karlstrom, G., Lindh, R., Malmqvist, P.-A., Nakajima, T., Neogrady P., Olsen, J., Raab, J., Roos, B. O., Ryde, U., Schimmelpfennig, B., Schutz, M., Seijo, L., Serrano-Andres, L., Siegbahn, P. E. M., Stalring, J., Thorsteinsson, T., Veryazov, V., Widmark, P.-O. MOLCAS Version 6.0, Lund University, Sweden, 2004
10. Widmark, P.-O., Malmqvist, P.-A., Roos, B.: Density matrix averaged atomic natural orbital (ANO) basis sets for correlated molecular wave functions. I. First row atoms. *Theoret. Chem. Acta.* **77** (1991) 291–306
11. Maynaud, D., Ben-Amor, N., Pitarch-Ruiz, J.: CASDI Program, University of Toulouse, Toulouse, France, 1999
12. Maynaud, D., Evangelisti, S., Guihéry, N., Calzado, C. J., Malrieu, J.-P.: Direct generation of local orbitals for multireference treatment and subsequent uses for the calculation of the correlation energy. *J. Chem. Phys.* **116** (2002) 10060–10068
13. Angeli, C., Evangelisti, S., Cimiraglia, R., Maynaud, D.: A novel perturbation-based complete active space-self-consistent-field algorithm: Application to the direct calculation of localized orbitals. *J. Chem. Phys.* **117** (2002) 10525–10533

On the Algorithm of Calculation of the Equilibrium Gas-Phase Concentration at the Particle Surface in the Kinetic Models of Aerosol Dynamics

Elena N. Stankova

Institute for High Performance Computing and Information Systems,
Politekhnicheckaya 29,
195251, St. Petersburg, Russia
lena@csa.ru

Abstract. The paper is dedicated to the description of the algorithm of calculation of the equilibrium gas-phase concentration at the surface of the aerosol particle – a parameter, which defines the rate of mass transport between the gas and aerosol phases in the kinetic models of atmospheric aerosol dynamics. Some problems concerning deducing of the surface equilibrium gas-phase concentrations from thermodynamic equilibrium aerosol models are discussed. It is shown that computational algorithm should be split in two steps; the sought quantity is defined on the second step, after ion concentration calculation.

1 Introduction

Aerosol dynamics simulation is a consistent part of air quality models, which provide a prediction of the spatial and temporal distributions of pollutant species resulting from emissions, advection, diffusion, dry deposition and chemical reaction. Traditionally the mass, composition, and size distribution of the volatile inorganics in atmospheric aerosol have been predicted assuming local thermodynamic equilibrium between the aerosol and gas phases. Nevertheless investigations show that under typical atmospheric conditions the volatile inorganics are not in equilibrium with the aerosol and both mass transfer and thermodynamic considerations determine their size distribution [1]. In [2] 3 different models to the treatment of mass transfer between the bulk gas phase and the surface of atmospheric particles were compared. It was shown that only in kinetic model, where mass transfer is simulated explicitly, chemical concentrations in the bulk gas phase and in the particles may or may not be in equilibrium. The rate of mass transport between the gas and aerosol phases in kinetic model is dependent upon the value of equilibrium gas-phase concentration at the surface of the aerosol particle, which in turn depends upon the particle size. Equilibrium gas-phase concentration can be deduced either with the help of Henry's law constant for gas/liquid equilibrium, or using thermodynamic equilibrium aerosol models [2]. However using both approaches in kinetic aerosol models is connected with some difficulties. In case of dissociation reactions (the most frequent in the atmosphere) we should use effective or pseudo Henry's constants [3] that depend

upon the hydrogen ion concentration, the value, which is a priori unknown, and have to be calculated from different considerations. The use of the equilibrium thermodynamic models in case of kinetic models also needs some special approach, connected with reformulation of system of chemical equations and input/output parameters. The paper is dedicated to the description of such an approach, connected with splitting the calculation of the chemical reactions in aqueous phase and equilibrium gas/aqueous phase reactions in two steps.

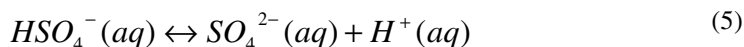
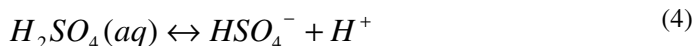
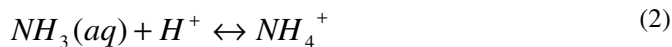
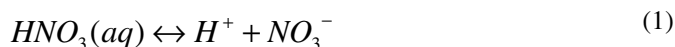
2 Model Description

Calculations of the interfacial mass transport is based upon the proportionality of the mass flow of species i to the term $(p_{i,\infty} - p_{i,s})$, where $p_{i,\infty}$, $p_{i,s}$ are the atmospheric partial pressure and the particle surface vapor pressure respectively. We assume that if aerosol particle consists of more than one phase, these phases are in thermodynamic equilibrium. It is considered that solid phases do not form until very low relative humidities are reached and therefore aerosol is completely aqueous.

Thermodynamic equilibrium chemical model PEQIONH (Pressure EQUilibrium and ION concentration calculation using Henry's law constants) was developed for prediction of equilibrium pressures of chemical components in case of kinetic approach, where chemical concentrations in the bulk gas phase and in the particles may or may not be in equilibrium.

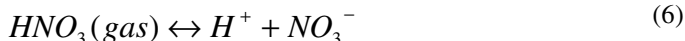
Unlike the other thermodynamic models, intended for calculation concentrations of each phase being in equilibrium with each other, and using total amount of chemical species in gas, liquid and solid phases as an input parameter, in case of kinetic approach we do not know a priori total concentration, but have to use aqueous concentrations of undissociated chemical species as a model input. This requires reformulation of the system of model equations. We have to withdraw mass balance equations and to add equations describing dissociation reactions in the liquid phase.

In the PEQIONH model algorithm of chemical equation calculation is split in two steps. At the first step the following set of equilibrium dissociation reactions in aqueous phase are considered:



where designation (*aq*) refers to unassociated values of aqueous chemical species. Taken values of $H_2SO_4(aq)$, $HNO_3(aq)$, $NH_3(aq)$ as an input, ionic concentrations in aqueous phase are calculated.

At the second step the following equilibrium gas/aqueous phase reactions are considered.



Using ionic concentrations obtained at the first calculation step and corresponding reaction constants (the Henry's law constants) the system of equations allows to obtain equilibrium values of ammonium and nitric acid vapor pressures ($NH_3(gas)$ and $HNO_3(gas)$) consequently.

Numerical solution of the system of equations (1)–(7) is based upon the 4 steps iterative algorithm proposed by Jacobson [4] with the only exception that all concentrations of gas, aqueous and ionic species were set in $mol/(m^3 \text{ air})$.

3 Model Sensitivity Studies

The model was used to simulate equilibrium concentrations of sulfate, nitrate, ammonia, aerosol liquid water content and saturation pressure values of ammonia and nitric acid under various input concentrations, which vary from a low value of 5 $\mu g/m^3$ up to 45–70 $\mu g/m^3$. Input conditions together with simulation results obtained by PEQION and for comparison by three other chemical equilibrium models KEQUIL [7], EQUIL [8] and MARS [6] are presented in Table 1.

Table 1. Aerosol-phase concentrations in $\mu g/m^3$ predicted by various equilibrium models at 298 K, RH = 0,9

N	TS	TN	TA	Ammonium				Nitrate			
				1	1	2	3	4	2	3	4
1	40	45	70	24,0	36,7	44,2	44,2	44,2	27,6	27,6	27,6
2	40	45	12	12,4	13,8	7,0	7,5	6,8	12,7	12,7	12,7
3	40	45	10	10,4	9,5	3,8	4,3	4,2	10,6	10,6	10,6
4	40	45	5	5,3	2,9	0,7	0,8	0,8	5,3	5,3	5,3
5	40	5	12	12,0	1,1	1,4	1,5	1,5	12,6	12,6	12,7
6	40	5	10	10,3	0,6	0,6	0,7	0,7	10,5	10,5	10,6
7	5	45	5	4,9	14,2	11,7	11,9	11,2	5,1	5,1	5,1
8	5	5	5	1,8	0,71	3,1	3,3	3,2	2,7	2,8	2,8

where 1,2,3,4 – model types: PEQIONH, KEQUIL, EQUIL and MARS consequently, RH – relative humidity value, TS, TN, TA – are total input sulfate, nitrate and ammonia concentrations in $\mu g/m^3$ consequently.

As it is evident from Table 1 PEQIONH model demonstrates very good agreement with the other equilibrium model results regarding ammonia and sulfur concentration and more or less satisfactory results in case of nitric concentrations. The largest differences between PEQIONH and other models appear while nitrate concentration simulation in case of small amount of the input ammonia and when the input total nitrate was relatively large or equal to the rest input parameters. That can be caused both by insufficient number of chemical equations used in PEQIONH model describing the interaction of the nitrates with the other chemical species and neglect of the solid phase presence.

The main purpose for model PEQIONH development was its incorporation into aerosol microphysical block for proper simulation of chemical composition of aerosol particles and gas/particle mass transfer processes in case of kinetic approach to the treatment of mass transfer between the bulk gas phase and the surface of atmospheric particles. PEQIONH model was used to calculate saturation vapor pressure of the chemical components at the surface of the particles and to calculate ion concentrations resulted from dissociation process.

To test coupled model (PEQIONH + microphysics) applicability it should be compared with the model, using the same kinetic approach Zhang [2]. The difficulty was that Zhang results were not provided with the data concerning temperature and relative humidity at which they were achieved. We had to vary corresponding parameters to find conditions where result coincidence might have take place. Corresponding results are given in table 2.

Table 2. Total ion and summary (ion + undissociated species) mass concentrations of chemical species in the aqueous phase. Comparison results obtained in PEQIONH + MICROPHYSICS and ZHANG models.

CS	Zhang	PEQIONH + MICROPHYSICS								
		T = 288K			T = 298K			T = 300K		
		RH	RH	RH	RH	RH	RH	RH	RH	RH
		90%	80%	50%	90%	80%	50%	90%	80%	50%
NO ₃ ⁻ HNO ₃	17,7	18,2 19,7	16,0 18,6	10,8 16,0	13,7 17,4	9,4 15,2	3,4 12,2	12,4 16,8	8,1 14,6	2,6 11,7
NH ₄ ⁺ NH ₃	11,2	12,1 20,1	11,2 19,8	9,2 19,1	10,5 19,5	9,0 18,9	6,7 18,1	10,1 19,3	8,6 18,7	6,4 18,0
SO ₄ ²⁻ + HSO ₄ ⁻ H ₂ SO ₄	20,0	19,6 20,0	19,6 20,0	19,6 20,0	19,6 20,0	19,6 20,0	19,6 20,0	19,6 20,0	19,6 20,0	19,6 20,0

CS – chemical species concentrations in µg/m³, T – temperature, RH – relative humidity, summary concentration values are in the second line of each cell.

As it is evident from Table 2, there is rather good agreement in ion concentrations of the condensable species obtained with the help of the two models in the following range of atmospheric conditions: temperature between 288K and 298K at RH = 90%, and RH between 80% and 90% at T = 288K.

Calculations, conducted with the help of PEQIONH + MICROPHYSICS model show that at all conditions ion concentrations are less than summary (ion + undissociated) concentrations. So it should be concluded that HNO_3 , NH_3 did not dissociate completely in aerosol particles, opposite to H_2SO_4 that presented practically fully in dissociated state.

4 Conclusions

Thermodynamic equilibrium chemical model PEQIONH was developed for prediction of equilibrium pressures of chemical components in case of kinetic approach to aerosol dynamics simulation, where chemical concentrations in the bulk gas phase and in the particles may or may not be in equilibrium. System of equilibrium chemical equations was reformulated to have aqueous concentrations of undissociated chemical species as a model input. Calculation of the chemical reactions in aqueous phase and equilibrium gas/aqueous phase reactions were split in two steps, the sought value of the equilibrium gas-phase concentration at the surface of the aerosol particle was defined on the second step, after ion concentration calculation. Comparison test studies showed good agreement of the results obtained by PEQIONH model with the results obtained by the other equilibrium models and with the models, using the same kinetic approach.

Acknowledgments

This work was fulfilled in the frame of the ISTC Project N 2834.

References

1. Wexler A.S. and Seinfeld J.H. Second generation inorganic aerosol model // *Atmospheric Environment*. 1991. Vol. 25A, P. 2731-2748.
2. Y. Zhang, C. Seigneur, J. H. Seinfeld, M. Z. Jacobson, and F. S. Binkowski. (1999). Simulation of Aerosol Dynamics: A Comparative Review of Algorithms Used in Air Quality Models. *Aerosol Science and Technology*. **31**, 487-514.
3. Warneck P. The Equilibrium Distribution of Atmospheric Gases Between the Two Phases of Liquid Water Clouds.
4. Jacobson, M.Z., *Fundamentals of Atmospheric Modeling*, Cambridge University Press, New York (1998)
5. Piskunov V.N., Zatevakhin M.A. Numerical modeling of aerosol particles formation dynamics at large fires. V MMFTM, May 24-28, 2004, Minsk ITMO NANB, **1**, 208-210 (in Russian).
6. Saxena, P., Hudischewsky, A.B., Seigneur, C., Seinfeld, J.H. (1986). A comparative study of equilibrium approaches to the chemical characterization of secondary aerosols. *Atmos. Environ.*, **20**, 1471-1483.
7. Bassett, M., Seinfeld, J. H. (1984). Atmospheric equilibrium model of sulfate and nitrate aerosols.-II. Particle size analysis. *Atmos. Environ.*, **18**, 1163-1170
8. Bassett, M., Seinfeld, J. H. (1983). Atmospheric equilibrium model of sulfate and nitrate aerosols. *Atmos. Environ.*, **17**, 2237-2252.

Study of the Passage of an H^+ Ion Along a Carbon Nanotube Using Quantum Wavepacket Dynamics

Dimitris Skouteris¹ and Antonio Laganá²

¹ Department of Mathematics and Computer Science, University of Perugia,
Via Vanvitelli, 1, I-06124 Perugia, Italy

`dimitris@dyn.unipg.it`

² Department of Chemistry, University of Perugia,
Via Elce di Sotto, 8, I-06123 Perugia, Italy

`lag@dyn.unipg.it`

Abstract. The passage of an H^+ ion along a carbon nanotube is studied using a time-dependent wavepacket method. The initial state of the problem can be completely specified in terms of the mean energy of the ion along the nanotube, its radial energy (which is necessarily quantised given the wall boundary condition) and its angular momentum along an axis parallel to the nanotube. Its time-dependent flux across two boundaries on the two ends of the nanotube is monitored and examined for various initial conditions. Such calculations can serve to model more complicated systems, such as the migration of ions along cellular membranes.

1 Introduction

It is well known that, apart from systems comprising three or four atoms at maximum, the exact quantum mechanical treatment of a dynamical system is prohibitive at present. This is particularly the case for systems of interest in biology, such as the passage of ions along semipermeable membranes, or in engineering, where semipermeable membranes are substituted by structures which can be modelled in a simplistic way, such as carbon nanotubes [1]. Additionally, carbon nanotubes are interesting in themselves because of their potential technological uses, for example to store hydrogen for use in fuel cells.

The best way of attacking this problem is, at present, through the use of classical mechanics (for example through a molecular dynamics scheme). The potential energy for such systems, arising from the electronic motion, is typically formulated in terms of tentative force fields [2]. As far as the actual nuclear dynamics is concerned, quantum mechanics enters only (at maximum) as a perturbation, for example when one wishes to include specific interference or tunnelling contributions to the dynamics.

Given the situation as it is, it would be interesting to confront standard dynamics results using classical mechanics with quantum mechanical ones. Not

only would the latter ones serve as a benchmark for various approximate treatments of quantum effects (such as the tunnelling mentioned above) but one can conceive of effects such as quasibound states arising from a temporary trapping of molecules in potential wells, which are difficult to account for classically.

The problem of hydrogen molecules confined in carbon nanotubes has been treated quantum mechanically by Lu et al. [3, 4]. These authors have tackled the problem of computing bound states of an H_2 molecule inside a C nanotube, treating rigorously all degrees of freedom of the molecule. Such studies are intimately connected with the use of C nanotubes as 'quantum sieves' to separate molecules similar in size [5, 6, 7, 8, 9].

In this paper, we are presenting a method to tackle molecules in carbon nanotubes in the continuous (as opposed to discrete) energy spectrum. The passage of an H^+ ion across a carbon nanotube is studied from a purely quantum mechanical view, utilising a time dependent wavepacket propagation algorithm. The algorithm is an adaptation of the RWAVEPR code written by us to study three-atom chemical reactions [10, 11] to the atom-in-nanotube problem. The coordinates of the ion are the only degrees of freedom treated quantum mechanically, while the nanotube itself is assumed rigid, without internal vibrations.

2 Theory

The formulation of the problem is in terms of a wavepacket being propagated in the interior of a carbon nanotube. Because of the inherent quasi-cylindrical symmetry of the problem, the wavefunction is expressed in cylindrical polar coordinates (r, θ, z) where z is the longitudinal distance (along the nanotube), r is the distance from the axis of the nanotube and θ is the azimuthal angle ranging from 0 to 2π . In these coordinates, the Hamiltonian for the system is :

$$\hat{H} = -\frac{\hbar^2}{2m} \left(\frac{\partial^2}{\partial z^2} + \frac{\partial^2}{\partial r^2} + \frac{1}{r} \frac{\partial}{\partial r} + \frac{1}{r^2} \frac{\partial^2}{\partial \theta^2} \right) + V(r, \theta, z) \quad (1)$$

which can be written in an alternative way, avoiding the first derivative term :

$$\hat{H} = -\frac{\hbar^2}{2m} \left(\frac{\partial^2}{\partial z^2} + r^{-1/2} \frac{\partial^2}{\partial r^2} r^{1/2} + \frac{1}{4r^2} + \frac{1}{r^2} \frac{\partial^2}{\partial \theta^2} \right) + V(r, \theta, z) \quad (2)$$

and, finally, using the substitution $\Psi = r^{1/2}\psi$ for the wavefunction, we get the Hamiltonian :

$$\hat{H} = -\frac{\hbar^2}{2m} \left(\frac{\partial^2}{\partial z^2} + \frac{\partial^2}{\partial r^2} + \frac{1}{4r^2} + \frac{1}{r^2} \frac{\partial^2}{\partial \theta^2} \right) + V(r, \theta, z) \quad (3)$$

(Notice that a negative, inverse-square 'centripetal' potential has been added as a result of the transformation).

The potential is a function of the three coordinates of the ion. In this work, it has been calculated simply as a sum of Lennard-Jones (6-12) contributions arising from atom-atom interactions between the H^+ ion and each of the C atoms of the nanotube within a certain threshold distance from the ion.

The mean position and energy of the wavepacket, as well as its angular momentum K around the central axis of the nanotube, are initially read from an input file, and subsequently the wavepacket is set up on a grid in the three cylindrical polar coordinates. The grid parameters have been suitably chosen to represent well the maximum energies and angular momenta of the wavepacket. The z-part of the wavepacket is normally a suitable Gaussian, whereas the radial-angular part is a product of a suitably scaled Bessel function of the r coordinate and an imaginary exponential dependent on the angle θ .

$$\phi(r, \theta, z) \propto \exp\left(-\frac{(z - z_0)^2}{2\sigma^2}\right) \times J_K(kr) \times \exp(iK\theta) \quad (4)$$

In this way, the transverse energy (radial and angular) is equal to

$$E_r = \frac{k^2 \hbar^2}{2m} \quad (5)$$

Here k is proportional to a zero of the J_K Bessel function, suitably chosen to give a transverse energy as close as possible to the one desired. After that, the wavepacket propagates in time, and the expectation value of the flux operator across two surfaces with constant z is monitored. These two surfaces correspond to the two ends of the nanotube. Suitable artificial potentials have been included (an imaginary one near the longitudinal ends of the nanotube and a real, high one near the radial end) to avoid unphysical behaviour of the wavepacket.

The flux operator has the form :

$$\hat{F} = \frac{i}{\hbar} [\hat{H}, \theta(z - z_0)] \quad (6)$$

where $\theta(z)$ is a Heaviside step function corresponding to the surface $z = z_0$. The expectation value of the flux operator corresponds to the temporal derivative of the fraction of the wavepacket that has already exited from the nanotube. Thus, its integral over time gives the total probability of exit from the particular part of the nanotube and the sum of the two probabilities (for the two sides) should give 1. This has been checked to ensure that no scaling errors occurred in the calculation.

3 Results and Discussion

The parameters used for the nanotube and the wavepacket are shown in Table 1. The nanotube used has been made rather wide on purpose, so that the potential is only felt as a minor perturbation by the H⁺ ion and thus the correspondence of its motion with that of classical mechanics is made more manifest. We present four figures here, each one presenting a different degree of freedom 'excited' and thus different kinds of effects. In all cases, the wavepacket exits completely through the face of the nanotube towards which it was originally directed. This is to be expected, given the large amount of longitudinal energy it has been given.

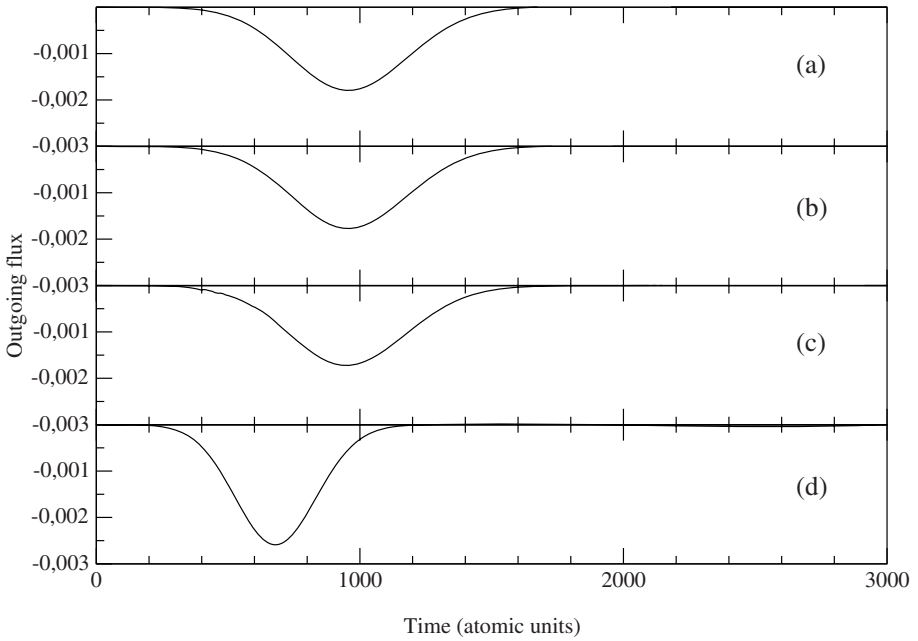


Fig. 1. Graphs of the outgoing flux of the wavepacket (negative) as a function of time. The four figures have the characteristics : (a) Zero radial energy, $K = 0$, Longitudinal energy 0.02 hartree, (b) Zero radial energy, $K = 5$, Longitudinal energy 0.02 hartree, (c) Radial energy 0.01 hartree, $K = 0$, Longitudinal energy 0.02 hartree, (d) Zero radial energy, $K = 0$, Longitudinal energy 0.04 hartree.

In Fig. 1a the wavepacket has no radial excitation. Classically, one would say it is moving purely parallel to the nanotube, but in fact it has a minor component of zero-point transverse motion. Moreover, it also has no angular momentum ($K = 0$). One sees a smooth pattern of exiting flux, of Gaussian shape, which mirrors the Gaussian distribution of the wavepacket. For the time scales involved here, the spreading of the wavepacket is still minor by the time it 'reaches the exit'. Notice that, because of the convention we use, the flux is a negative quantity.

In Fig. 1b the wavepacket is as in Fig. 1a, with 5 quanta of angular momentum added. It is seen that the curve is almost identical to that of Fig. 1a, but it is slightly broader. It is conceivable that the centrifugal barrier induced by the angular momentum pushes the wavepacket towards the walls of the nanotube, where it is more likely to interact with a C atom. Such collisions would be expected to both accelerate and decelerate the ion, and thus would cause a spreading of the corresponding exit flux. However, given the small value of the angular momentum, $K = 5$, it is not a large effect.

In Fig. 1c, an amount of radial energy of 0.01 hartree has been added (with zero angular momentum). Again, the flux curve is broadened, and this time the effect is much more noticeable. For the same reason, an increased radial energy is

Table 1. Grid and initial condition details for wavepacket calculations using cylindrical polar coordinates

Quantity	Value
Longitudinal coordinate (z) range/ a_0	0.1-12.8
Number of grid points in z ,	128
Radial coordinate (r) range/ a_0	0.1-12.8
Number of grid points in r	128
Number of angular grid points	32
Absorption region length/ a_0	1.5
Centre of initial wavepacket (z_0)/ a_0	6.0
Width of the wavepacket (δz)/ a_0	1.0
Initial mean longitudinal energy, E /hartree	0.02
Initial radial energy, E /hartree	0.0
Initial angular momentum, K /hartree	0
Position of analysis line, z_{an} / a_0	10.5

^a The parameters refer to the exact data for Fig. 1a. Any changes pertaining to the other Figures are explained in the text.

expected to broaden the flux curve as a result of an increased degree of interaction of the wavepacket with the walls of the nanotube. Moreover, at short times, one can notice minor peaks on the curve which are not present in the original one of Fig. 1a. It is almost certain that such features are of quantum mechanical origin, although their nature is still to be rationalised. They might represent minor, short-lived trappings of amplitude from the wavepacket in potential wells caused by the C atoms on the nanotube wall. We are currently trying to see how they differ with changing initial conditions and whether their exact cause can be elucidated.

Finally, in Fig. 1d, an extra amount of 0.02 hartree of longitudinal energy has been added to the wavepacket. As can be seen, the only effect of this is to shorten the time needed for the wavepacket to exit from the nanotube. This, of course, is in perfect accordance with what would be expected on the basis of classical mechanics.

4 Conclusions

A first, very preliminary study on the quantum effects of an H^+ ion moving across a C nanotube has been presented here. The study is purely quantum mechanical as far as the actual dynamics is concerned, and the results are in good correspondence with what would be observed on the grounds of classical mechanics. Moreover, it is seen that visible quantum effects can arise on radial excitation of the ion in the nanotube, and these are very probably connected with transient trappings of the ion in the pseudowells against the wall of the nanotube. More work is needed to be able to get a clear picture of the quantum mechanics of the problem.

Acknowledgements

Financial support from ASI, FISIR MIUR and the University of Perugia is acknowledged.

References

1. Arteconi, L., and Laganá, A.: A molecular dynamics study of ion permeability through molecular pores, *Lecture Notes - Computer Science* **3480**,(2005) 1093-1100.
2. Brooks, B.R., Bruccoleri, R.E., Olafson, B.D., States, D.J., Suaminathan, S., and Karplus, M.: CHARMM - A program for macromolecular energy, minimisation and dynamics calculations, *J. Comp. Chem.*, **4**, (1983) 187-217.
3. Lu, T., Goldfield, E.M., and Gray, S.K., *Journal of Theoretical and Computational Chemistry*, **2**, (2003) 621-626.
4. Lu, T., Goldfield, E.M., and Gray, S.K., *J. Phys. Chem. B*, **107**, (2003) 12989-12995.
5. Beenakker, J.J.M., Borman, V.D., and Krylov., S.Y., *Chem. Phys. Lett.*, **232**, (1995) 379-382.
6. Wang, Q.Y., Challa, S.R., Sholl, D.S., and Johnson, J.K., *Phys. Rev. Lett.*, **82**, (1999) 956-959.
7. Challa, S.R., Sholl, D.S., and Johnson, J.K., *Phys. Rev. B*, **63**, (2001) 245419-247200.
8. Challa, S.R., Sholl, D.S., and Johnson, J.K., *J. Chem. Phys.*, **116**, (2002) 814-824.
9. Hathorn, B.C., Sumpter, B.G., and Noid, D.W., *Phys. Rev. A.*, **64**, (2001) 22903.
10. Skouteris, D., Laganá, A., Capecchi, G., and Werner, H.-J., *Int. J. Quant. Chem.*, **96**, (2004) 562-567.
11. Skouteris, D., Laganá, A., Capecchi, G., and Werner, H.-J., *Int. J. Quant. Chem.*, **99**, (2004) 577-584.

Invariance Properties of Practical Test-Functions Used for Generating Asymmetrical Pulses

Stefan Pusca

Politehnica University, Department of Physics, Bucharest, Romania

Abstract. This paper presents a heuristic algorithm for generating asymmetrical practical test functions using MATLAB procedures. Based on the fact that differential equations can generate only functions similar to test functions (defined as practical test functions), the invariance general properties suitable for generating symmetrical pulses as related to the middle of the working interval are presented. Then some possibilities for obtaining asymmetrical pulses as related to this middle of the working interval using the derivative of such symmetrical pulse are studied, for certain differential equations corresponding to second order systems (with unity-step input and for an input represented by a gaussian pulse). Finally it is shown that we can obtain an oscillating system by joining such working intervals and restoring the initial null conditions for a second order system, in an adequate manner.

1 Introduction

Many times the analysis of signals on limited time intervals requires the use of adequate mathematical models able to generate alternating function. For obtaining sine functions are well-known undumped differential equations of second order, able to generate signals with a certain angular frequency. But for obtaining pulses limited on certain time intervals some specific models must be used. An alternative is represented by the use of test-functions, but ideal test functions can not be generated by a differential equation of evolution [1]. By the other side, a propagation phenomenon for an ideal test function can not be taken into consideration as in [2], because we are looking for causal pulses, generated in a rigorous manner by an equation of evolution. This implies the use of practical test-functions (functions which possess a limited number of derivatives equal to zero at the limits of the working interval and which can be solutions of a differential equations). So we must study invariance properties of such equations, so as the output to be represented by a function asymmetrical as related to the middle of the working period. If we consider as working interval the time interval $(-1, 1)$, then the middle of the interval would be the origin, and the condition for the output $f(t)$ to be asymmetrical corresponds to the condition

$$f(-t) = -f(t) \tag{1}$$

For obtaining such a function on the time interval $(-1, 1)$, we must begin by studying equations able to generate a symmetrical function g on this time interval [3] so as to find a method for translating some of their properties to

asymmetrical functions; finally we must use Runge-Kutta equations ([4]) for studying the properties of the mathematical models obtained. We are looking for controlled oscillations on a limited time interval (unlike unstable oscillations for second order difference systems [5]).

A first attempt would be the use of the signal which is integrated for sampling electronic or optoelectronics signals in a robust manner -using oscillating second order systems working on a period [6], the filtering possibilities of such systems (as low pass filters) being presented in [7]. This would lead to a sine or cosine function, with possibilities of joining together such working intervals for obtaining a controlled oscillation extended in time. Yet we are looking for general differential equations able to generate asymmetrical pulses of different shapes (not only sine or cosine functions). We can extend our analyze at wavelets corresponding to PDE [8] or to equations able to generate wavelets represented by solitary waves [9].

Both previously mentioned aspects can be joined together if we are looking for functions similar to test-functions having a shape similar to wavelets. As can be noticed studying [3], practical test-functions of second order possess a derivative with null initial and final values. Analyzing its mathematical expression on the whole working interval $(-1, 1)$, we can notice that this derivative is an asymmetrical function as related to the middle of the working interval (considered as origin), while the symmetry of g function implies that its slope is asymmetrical as related to the origin (the same modulus and opposite sign). So we must analyze the differential equations able to generate symmetrical functions g and to study the shape of their derivatives for different input functions.

2 Asymmetrical Pulses Obtained as Derivatives of Symmetrical Functions

As it is known, a *test-function* on $[a, b]$ is a C^∞ function on \mathbf{R} which is nonzero on (a, b) and zero elsewhere. For example, the bump-like function

$$\varphi_a(\tau) = \begin{cases} \exp\left(\frac{1}{\tau^2-1}\right) & \text{if } \tau \in (-1, 1) \\ 0 & \text{otherwise} \end{cases} \quad (2)$$

is a test-function on $[-1, 1]$.

By the other side, test-functions as the bump-like function

$$\varphi_b(\tau) = \begin{cases} \exp\left(\frac{0.1}{\tau^2-1}\right) & \text{if } \tau \in (-1, 1) \\ 0 & \text{otherwise} \end{cases} \quad (3)$$

are almost equal to a constant value for $2/3$ of the working period (similar to a step-function).

Such functions can not be generated by differential equations of evolution; however, we can use differential equations able to generate a practical test-function on $(-1, 1)$ (a C^n nonzero function on $(-1, 1)$ which satisfies the boundary conditions $f^{(k)}(a) = f^{(k)}(b) = 0$ for $k = 0, 1, \dots, n$ and can be a solution of an initial value problem on this interval).

The first and second derivatives of φ_a are

$$\varphi_a^{(1)}(\tau) = \frac{-2\tau}{(\tau^2 - 1)^2} \exp\left(\frac{1}{\tau^2 - 1}\right) \tag{4}$$

$$\varphi_a^{(2)}(\tau) = \frac{6\tau^4 - 2}{(\tau^2 - 1)^4} \exp\left(\frac{1}{\tau^2 - 1}\right) \tag{5}$$

and by simply dividing the function $\varphi_a(\tau)$ at $\varphi_a^{(1)}(\tau)$ we obtain

$$\varphi_a^{(1)} = \frac{-2\tau}{(\tau^2 - 1)^2} \varphi_a \tag{6}$$

Considering the corresponding differential equation

$$f^{(1)} = \frac{-2\tau}{(\tau^2 - 1)^2} f \tag{7}$$

with initial values considered at $\tau_0 = -0.99$ as

$$f_0 = \exp\left(\frac{1}{0.99^2 - 1}\right) \tag{8}$$

it results a function f symmetrical as related to the middle of the working interval. Its derivative, a saw-teeth asymmetrical pulse, is represented in figure 1.

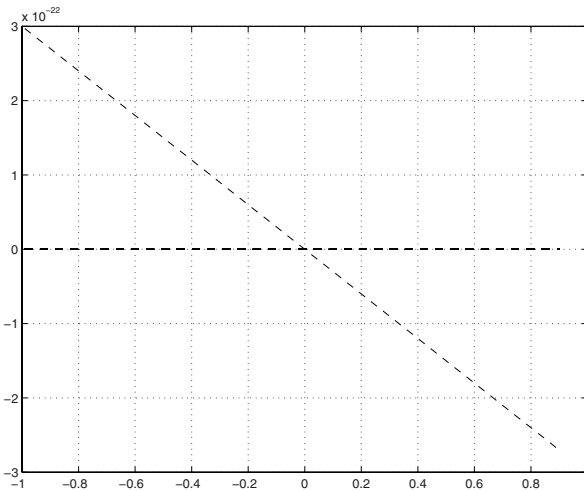


Fig. 1. Asymmetrical pulse for a first-order system

The same way the correspondence between $\varphi_a, \varphi_a^{(2)}$ results under the form

$$\varphi_a^{(2)} = \frac{6\tau^4 - 2}{(\tau^2 - 1)^4} \varphi_a \tag{9}$$

By considering the corresponding differential equation

$$f^{(2)} = \frac{6\tau^4 - 2}{(\tau^2 - 1)^4} f \tag{10}$$

with initial values considered at $\tau_0 = -0.99$ as

$$f_0 = \exp\left(\frac{1}{0.99^2 - 1}\right) \tag{11}$$

$$f_0^{(1)} = \left[2\frac{0.99}{(0.99^2 - 1)^2}\right] \exp\left(\frac{1}{0.99^2 - 1}\right) \tag{12}$$

it results also a function f symmetrical as related to the middle of the working interval. Its derivative, an asymmetrical pulse, is represented in figure 2.

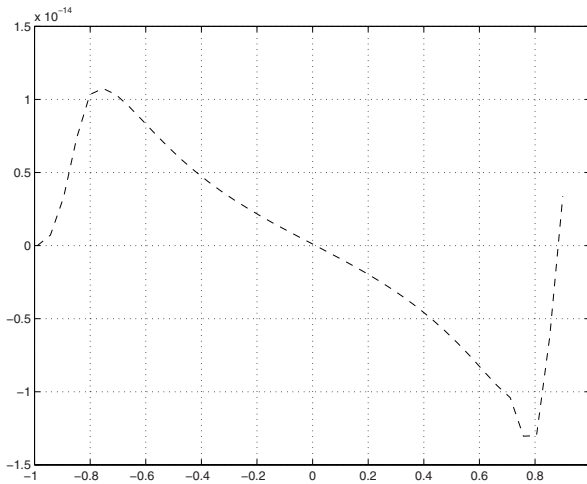


Fig. 2. Asymmetrical pulse for a second order system

In a similar way, for the function $\varphi_b(\tau)$ we obtain the correspondence

$$\varphi_b^{(2)} = \frac{0.6\tau^4 - 0.36\tau^2 - 0.2}{(\tau^2 - 1)^4} \varphi_b \tag{13}$$

By considering the corresponding differential equation

$$f^{(2)} = \frac{0.6\tau^4 - 0.36\tau^2 - 0.2}{(\tau^2 - 1)^4} f \tag{14}$$

with initial values considered at $\tau_0 = -0.99$ as

$$f_0 = \exp\left(\frac{0.1}{0.99^2 - 1}\right) \tag{15}$$

$$f_0^{(1)} = \left[0.2 \frac{0.99}{(0.99^2 - 1)^2} \right] \exp \left(\frac{0.1}{0.99^2 - 1} \right) \tag{16}$$

we obtain a function f symmetrical as related to the middle of the working interval. Its derivative, a sharp asymmetrical pulse, is represented in figure 3.

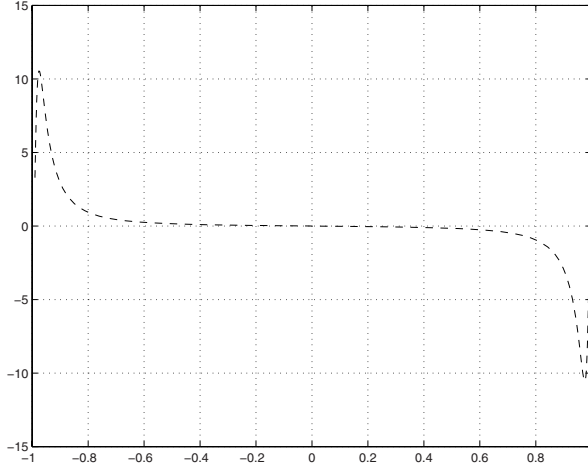


Fig. 3. Sharp pulses for a fast varying second order system

The shape of these outputs offers also the possibility of joining together such time intervals and the corresponding asymmetrical pulses so as to obtain a controlled oscillation. While at the beginning and the end of each working interval the state-variables of the differential system are approximately equal to zero it would be quite easy to adjust the final values of these variables for a working interval to the initial values of these variables for the next working interval; thus the cycle can continue in a controlled manner.

We must point the fact that an asymmetrical pulse represents in fact a test function for the derivative of an input signal; by multiplying an input signal with an asymmetrical pulse and by integrating the resulting function on the working interval, we obtain a result proportional to the slope of the input signal (as can be easily checked). Thus a possible application would be a faster estimation of acceleration by multiplying the input signal corresponding to velocity (a robust method which is faster than the method presented in [10], based on an estimation performed over two working periods). Another application can be represented by phase-detection; by multiplying the alternating input signal with an asymmetrical function and integrating the resulting function we obtain a result proportional to the amplitude of an input sine function (a more robust method than the one presented in [11], where the input function is processed by a nonlinear second order system).

Finally we must study the output generated by a second order differential equation able to generate an asymmetrical output for an input represented by a very short pulse, so as to check its stability at such kind of disturbances. For this, we consider the differential equation

$$f^{(2)} = \frac{0.6\tau^4 - 0.36\tau^2 - 0.2}{(\tau^2 - 1)^4} f + 0.1 \exp \left[-\frac{(\tau + 0.9)^2}{0.01^2} \right] \tag{17}$$

with initial null conditions (the external pulse being represented by a short gaussian pulse received at the moment of time $t_p = -0.9$). The derivative of the output is represented in figure 4.

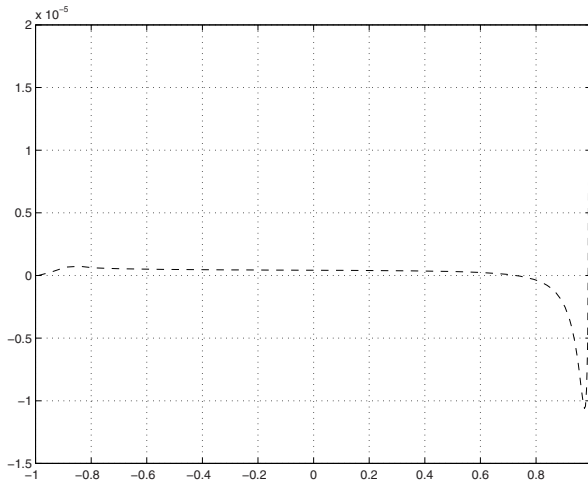


Fig. 4. Output derivative for a gaussian pulse input

It can be noticed that a major influence appears at the end of the working interval, after a time interval of about 1.8 units. Thus the final output pulse can be considered as an acausal pulse for an external observer studying the input and the output of the system on the time interval $(0, 1)$, for example.

Unlike aspects connected with acausal travelling waves as possible solutions of the wave equation presented in [12] (where are no sources inside a certain string beginning to move from initial null conditions), the acausal pulse generated by the previous equation appears with *almost* null conditions existing for the state variables of a unique system (a single point). The term *almost* null conditions implies the use of a multiscale analysis of phenomena [13]. The study must be completed by searching invariance properties for a good determination of inner structure of material [14], for a corresponding computer programm able to perform an accurate estimation of the corresponding parameters [15], taking also into consideration phenomena appearing for thin-walled materials subject to external pulses [16].

For rejecting the influence of such short gaussian pulses, we must use some low-pass filters for delaying the moment of time when such short pulses are received by the processing system with about 0.2 units, so as no effect upon the output to be noticed any more (the whole working interval is about 2 units).

3 Conclusions

This paper presents some methods for generating asymmetrical practical test functions using MATLAB procedures (based on Runge-Kutta equations). Based on the fact that differential equations can generate only functions similar to test functions (defined as practical test functions), the invariance general properties suitable for generating symmetrical pulses as related to the middle of the working interval are presented. Then some possibilities for obtaining asymmetrical pulses as related to this middle of this interval using the derivative of such symmetrical pulse are studied, for certain differential equations corresponding to second order systems. Finally it is shown that we can obtain an oscillating system by joining such working intervals and restoring the initial null conditions for a second order system, in an adequate manner. Possibilities of using such asymmetrical functions for analyzing Schroedinger equation (similar to [17]) will be studied in the future.

References

1. Toma, C. : An extension of the notion of observability at filtering and sampling devices, Proceedings of the International Symposium on Signals, Circuits and Systems Iasi SCS 2001, Romania 233–236
2. Toma, C.: The possibility of appearing acausal pulses as solutions of the wave equation, The Hyperion Scientific Journal **4** 1 (2004), 25–28
3. Toma, G. : Practical test-functions generated by computer algorithms, Lecture Notes Computer Science **3482** (2005), 576–585
4. Kulikov, G. : An advanced version of the local-global step-size control for Runge-Kutta methods applied to index 1 differential algebraic systems, Lecture Notes in Computer Science **3037** (2004), 565–569
5. Zhang, Zh., Ping, B., Dong, W. : Oscillation of unstable type second order nonlinear difference equation, Korean J. Computer and Appl. Math. **9** 1 (2002) 87–99
6. Toma, C.: The necessity for using oscillating systems for sampling optoelectronic signals, Bulgarian Journal of Physics **27**, Suppl. 2 (2000), 187–190
7. Toma, C.: Filtering possibilities based on oscillating systems for optoelectronic signals, SPIE Proceedings **4430** (2001), 842–845
8. Cattani, C.: Harmonic Wavelets towards Solution of Nonlinear PDE, Computers and Mathematics with Applications, 50 (2005), 1191–1210.
9. Rushchitsky, J.J., Cattani, C., Terletskaia, E.V.: Wavelet Analysis of the evolution of a solitary wave in a composite material, International Applied Mechanics, **40**, 3 (2004) 311–318
10. Sterian, A., Toma, C.: Filtering possibilities for processing optoelectronic current for acceleration measurements, SPIE Proceedings 4827 (2002), 403–408

11. Sterian, A., Toma, C.: Phase detection for vibration measurements based on test functions, SPIE Proceedings 5503 (2004), 164–168
12. Toma, C.: Equations with partial derivatives and differential equations used for simulating acausal pulses, International Conference Physics and Control Physcon 2003, 20-22 August, Sankt-Petersburg, Russia (2003), 1178–1183
13. Cattani, C.: Multiscale Analysis of Wave Propagation in Composite Materials, *Mathematical Modelling and Analysis*, **8** 4 (2003), 267–282
14. Paun, V.P.: A Model for the Accurate Determination of Crystalline Network Parameters, *Revue Roumaine de Chimie* **54** (4), Bucharest (2003), 335–336
15. Paun, V.P.: Computer programme for the determination of the crystalline network parameters, *Revue Roumaine de Chimie* **49** (1), Bucharest (2004), 85–92
16. Paun, V.P.: A creep collapse model for thin-walled Zircolay-4 tubes, *Revue Roumaine de Chimie* **48** (11), Bucharest (2003), 903–906
17. Cattani, C.: Harmonic Wavelet Solutions of the Schroedinger Equation, *International Journal of Fluid Mechanics Research* **5** (2003), 1–10

Simulating Superradiant Laser Pulses Using Partial Fraction Decomposition and Derivative Procedures

Theodora Toma¹, Stefan Pusca², and Cristian Morarescu³

¹ Nicolae Iorga College, Department of Mathematics, Bucharest, Romania

² Politehnica University, Department of Physics, Bucharest, Romania

³ Politehnica University, Department of Computers, Bucharest, Romania

Abstract. Some phenomena in physics (such as the phenomenon of photonic echo) appears for an external observer as non-causal pulses suddenly emerging from an active medium (prepared by some other optical pulses). Such a pulse is very hard to be simulated without using physical quantities corresponding to the internal state of a great number of atoms. Moreover, the high intensity of the photonic echo pulse is proportional to N^2 , where N represents the number of atoms involved in emission. An attempt of simulating such pulses without using a great number of variables consists in the use of test-functions, which can be put in correspondence with acausal pulses in physics. However, such an attempt can not explain the dependence on N^2 for the intensity. This study will show that this problem can be solved in a simple manner using principles of partial fraction decomposition and derivative procedures.

1 Introduction

Usually the procedures for detecting optical signals are based on an optoelectrical conversion. The optical signal which possess certain properties (amplitude, frequency, phase) is transformed into an electrical signal. This electric signal is then processed (usually by filtering) and a final pulse is generated when certain parameters are detected in this signal. However, such procedures possess two major disadvantages: a low speed (an optoelectrical conversion being necessary), and a low intensity of the final pulse (which shows that certain parameters were detected in the input signal), some amplifiers being necessary. So at high frequencies some other procedures, which do not require a conversion, must be used. Such a method consists in using the properties of the photonic echo generated by superradiance states in an active medium. First we suppose that the active medium receives a $\pi/2$ pulse (from the superradiance states point of view); if another optical signal which is a π pulse (from the superradiance states point of view) is received inside a certain time interval, a high intensity optical pulse will be generated inside the active medium. This high intensity pulse shows that the property of the second optical signal of being a π pulse has been detected; besides, it can directly command other transmitting, displaying or memory devices, without any optoelectrical conversion to be necessary.

Thus the final pulse (the photonic echo) shows that the received optical beam possess certain properties. If the received pulse is not a π pulse (that means a certain relation between light intensity, frequency and timelength is not valid) the high intensity pulse is not generated. If the received signal is also prepared, using a device which establish with a great accuracy a certain light intensity over a certain timelength (as presented in [1]), and the optoelectronic current is filtered in an adequate manner [2] than the high intensity pulse shows that the received signal possess a certain frequency. Yet such methods require a good mathematical model for the photonic echo generation, so as its dynamic to be taken into account for modeling interactions between the pulse and transmitting, displaying or memory devices.

2 Structure for Paralel Detecting Optical Signals

Mathematically, the property of the reference pulse of being a $\pi/2$ pulse is represented by the relation

$$\eta E_A \Delta t_A = \pi/2 \quad (1)$$

where E_A stands for the electric field of this signal A (generated by the laser generator R), Δt_A stands for its timelength and η represents a parameter depending on frequency. The condition the received optical pulse of being a π pulse is represented by the relation

$$\eta E_B \Delta t_B = \pi \quad (2)$$

where E_B stands for the electric field of this signal B (the signal received by the structure and processed by the device S), Δt_B stands for its timelength and η represents the same parameter depending on frequency.

If the above condition is fulfilled, a high intensity pulse C is generated inside the active medium at a time interval Δt_2 equal to the time interval Δt_1 between pulses A and B . If the received optical signals have constant frequency and timelength the generation of the high intensity pulse shows that the received pulse possess a certain intensity. If the received signals have constant intensities and timelength the generation of the high intensity pulse shows that the received pulse possess a certain frequency. However, a direct command of this high-intensity pulse upon other transmitting, displaying or memory devices (without any optic-electrical conversion) still requires an accurate study for its dynamics, so as any wrong actions of these devices (due to possible internal oscillations, for example) to be avoided.

3 Simulating the High Intensity of the Photonic Echo Pulse Using a Partial Fraction Decomposition

A major problem in simulating the high-intensity pulse (the photonic echo pulse) is represented by its power. Unlike amplified optical pulses, its power is proportional to N^2 where N represents the number of atoms involved in the emission of

high intensity light pulse. Using usual mathematical models based on instability [3] or bifurcations [4] we can not explain this dependence (it is well known that an ordinary pulse light possess an intensity proportional to N). Models based on equations with partial derivatives able to generate suddenly emerging pulses [5] or travelling waves obtained as solutions of the wave equation [6] can only simulate the photonic echo as suddenly emerging phenomenon on a certain length inside the active medium, without any connection with its intensity. Mathematical models based on wavelets analysis leading to nonlinear solutions of PDE [7] or an analysis of solitary waves in dispersive media [8] represents at first sight some interesting alternatives. However, they can not explain the generation of a high-intensity pulse at a time moment when no waves exist inside the active medium.

The main idea of this paper (established by the coauthor learning at Nicolae Iorga College) is to take into account a very simple similitude between coefficients appearing in case of partial fractal decomposition and the electric field intensity E depending on distance $a - b$ (in electrostatics). If we write the decomposition

$$\frac{1}{(x - a)(x - b)} = \left(\frac{1}{a - b}\right) \left(\frac{1}{x - a}\right) - \left(\frac{1}{a - b}\right) \left(\frac{1}{x - b}\right) \tag{3}$$

and compare the coefficient $1/(a - b)$ of each term with the electromagnetic field

$$E = \left(\frac{Q}{4\pi\epsilon}\right) \left(\frac{Q}{a - b}\right) \tag{4}$$

for the classical case in electrostatics when in a point situated in $x_d = b$ is received an electric field emitted by a body with Q charge, situated in a point $x_s = a$ (the unidimensional case) - without taking the sign into consideration - we can notice that coefficient $1/(a - b)$ is also the coefficient of $Q/(4\pi\epsilon)$. This suggests to consider such coefficients of $1/(x - a)$ as corresponding to certain physical quantities noticed in point $x = b$ and associated to a field emitted in the point $x = a$. It also involves that the whole system $S_{a,b}$ should be described as

$$S_{a,b} = \left(\frac{Q}{4\pi\epsilon}\right) \left(\frac{1}{(x - a)(x - b)}\right) \tag{5}$$

and it can be decomposed in phenomena taking place in point $x = a$ or $x = b$ by taking into consideration the coefficient of $1/(x - a)$ or $1/(x - b)$ from partial fraction decomposition. Mathematically, these coefficients c_a, c_b can be written as

$$c_a = \lim_{x \rightarrow a} (x - a)S_{a,b}, \quad c_b = \lim_{x \rightarrow b} (x - b)S_{a,b} \tag{6}$$

An important feature of partial fraction decomposition must be also noticed: when the two roots of the polynomial $(s - a)(s - b)$ (the symbolic mathematical expression for the whole system) are equal ($a = b$), the coefficient of $1/(x - a)$ vanishes; instead of this, a coefficient c_a of $1/(x - a)^2$ appears. Mathematically, this coefficient can be written as

$$c_a = \lim_{x \rightarrow a} (x - a)^2 \frac{1}{(x - a)^2} = \lim_{x \rightarrow a} (x - a)^2 S_{ab} \tag{7}$$

For the general situation when terms $1/(x - a)$, $1/(x - a)^2$... appear, expressions based on differentiation for obtaining the coefficients of these terms are known. This suggests next step in our analyze: the use of differentiation procedure for obtaining specific coefficients when some elements composing the system possess the same parameter a (corresponding to the root of the denominator polynomial). In the previous case (the electrostatic field) the parameter was represented by x-coordinates (the unidimensional case). Yet for the case we intend to analyze (the photonic echo) we are looking for mathematical quantities proportional to N and proportional to N^2 ; this step must be performed in a similar manner used for passing from coordinates representation to momentum representation in quantum theory, by the aid of Fourier transformation (the basic variables being changed) [9]. Taking into account the previous observations about differentiation procedures when many bodies with the same parameter interact, we can notice that the derivatives of different order for $f = x^N$ are directly proportional to $N, N(N - 1)$... according to:

$$\frac{df}{dx} = Nx^{N-1} \quad (8)$$

$$\frac{d^2f}{dx^2} = N(N - 1)x^{N-2} \quad (9)$$

For great values of N (a great number of atoms involved - the usual case), the coefficient $N(N - 1)$ is similar to the coefficient N^2 we are looking for, because

$$\lim_{N \rightarrow \infty} \frac{N^2}{N(N - 1)} = 1 \quad (10)$$

This derivative procedure can be considered as a result of an interaction between the ensemble of atoms involved and a certain wave trapped inside this ensemble, similar to the action of the material medium upon a received wave train [10] - the connection between this aspect and quantum theory being shown in [11]. Next step consists in searching for a mathematical expression which possess the derivative of first order (directly proportional to N), but which does not possess the derivative of second order (directly proportional to $N(N - 1)$), in case of non-coherent states of atoms (when the high intensity pulse is not emitted). The term *coherent states* implies the existence of a certain parameter which characterizes the whole ensemble of atoms). The term *coherent states* implies the existence of a certain parameter α which characterizes the whole ensemble of atoms, unlike the case of non-coherent states where each atom i is characterized by a distinct parameter a_i . These parameters must appear in a mathematical expression $E(x)$ having the general form

$$E(x) = \sum_i A_i(x - a_i) \quad (11)$$

(for non-coherent states) and the general form

$$E(x) = A(x - \alpha)^N \quad (12)$$

(for coherent states). But we must search for a more general expression for $E(x)$, so as the expression for the case of coherent states to correspond to a particular case of non-coherent states (when all parameters a_i are equal to a certain parameter α). But the sum of terms like $(x - a_i)$ can not be translated as a product $(x - \alpha)^N$ as can be easily checked. So we must extend our search at other functions f which possess the coefficient $N(N - 1)$ for the second derivative. This property is also fulfilled by functions having the form

$$f(x) = x^{-N} = \left(\frac{1}{x}\right)^N \tag{13}$$

According to this, the general expression $E(x)$ which corresponds to an ensemble of N atoms can be written as

$$E(x) = \sum_i A_i \left(\frac{1}{x - a_i}\right) \tag{14}$$

(for non-coherent states) and the general form

$$E(x) = A \left(\frac{1}{x - \alpha}\right)^N \tag{15}$$

(for coherent states). The main advantage of this form is that the expression corresponding to non-coherent states *can be translated* in the expression corresponding to coherent states using the principles of partial fraction decomposition. According to these, a polynomial fraction where the degree of the numerator polynomial is less than the degree of the denominator polynomial can be decomposed as

$$E(x) = \sum_{i=1 \rightarrow N} \frac{A_i}{x - a_i} \tag{16}$$

if the roots of the denominator polynomial a_i are different one to another, and can be decomposed as

$$E(x) = \sum_{k=1 \rightarrow N} A_k \left(\frac{1}{x - \alpha}\right)^k \tag{17}$$

in case of mutple roots. For modeling the high intensity pulse (emitted when the atoms involved are in coherent states) we must postulate that the numerator polynomial of $E(x)$ is equal to unity or to a certain constant, so as the expression $E(x)$ to be written as

$$E(x) = \left(\frac{1}{x - \alpha}\right)^N \tag{18}$$

Finally we should consider that the intensity of a low intensity pulse emitted by an ensemble of N atoms for non-coherent states corresponds to the sum of coefficients of first derivative of the general term

$$A_i(x - a_i)^{-1} \tag{19}$$

and thus it results that (for all A_i equal to a constant value A) the sum will be less or equal to NA . The same result appears for a low intensity pulse emitted by N atoms in a coherent state, while the coefficient of the first derivative of the expression

$$E(x) = A(x - \alpha)^{-N} \tag{20}$$

is NA , being directly proportional to N . We should also consider that the intensity of a high energy pulse emitted by an ensemble of N atoms in a coherent state corresponds to the coefficient of the second derivative of the term $(x - \alpha)^{-N}$, which means that it is directly proportional to $N(N - 1) \approx N^2$. For an ensemble of N atoms in non-coherent states, it results that the possible intensity of a high energy pulse would be represented by the sum of coefficients of second derivative for general terms $A_i(x - \alpha_i)^{-1}$, and thus it results that the intensity of a possible high energy pulse will be less or equal to $2NA$, being also directly proportional to N . Due to this reason, this possible high intensity pulse for non-coherent states can not be noticed as a distinct pulse (its intensity depends on N , like the intensity of the low intensity pulse, and an observer could notice their sum as a single pulse depending on N). On the contrary, for coherent states the low intensity pulse (directly proportional to N) would have a very low intensity, and an observer would notice only the high energy pulse (the photonic echo) which is directly proportional to N^2 .

The previous mathematical model justifying the dependence on N^2 for the intensity of the photonic echo must be improved by adding the variable t , so as a time dependence of this intensity according to experimental results to be obtained. This require the use of certain mathematical expressions of variable x as function of t (while x variable is the one taken into consideration in the previous derivative procedure). While photonic echo acts on a limited time interval, we wish to obtain a function $f(t)$ corresponding to test-function (in the ideal case) or a practical test-function (which can be generated by a differential equation of evolution) which should multiply the term proportional to N^2 . For this, the symbolic variable x must be replaced by a function of time $x = x(t)$ and the whole differentiation procedure must be represented by a time differentiation. This means

$$\frac{d^2}{dt^2} \left(\frac{1}{x(t) - \alpha} \right)^N = \dots + N(N - 1) \left(\frac{dx}{dt} \right)^2 \left(\frac{1}{x(t) - \alpha} \right)^{N-2} \tag{21}$$

(only the term proportional to $N(N - 1)$ being of interest for our case, how it was shown). This implies

$$N(N - 1) \left(\frac{dx}{dt} \right)^2 \left(\frac{1}{x(t) - \alpha} \right)^{N-2} = N(N - 1)f(t) \left(\frac{1}{x(t) - \alpha} \right)^{N-2} \tag{22}$$

($f(t)$ being a test function or a practical test function). Simplifying $N(N - 1)$ and $1/(x - \alpha)^{N-2}$ on both sides, it results

$$\left(\frac{dx}{dt} \right)^2 = f(t) \tag{23}$$

It results that the required function $x = x(t)$ should be computed as

$$x(t) = \int_0^t \int_0^\theta f(\tau) d\tau d\theta \quad (24)$$

For experimental cases when the photonic echo pulse intensity presents a time dependence $f(t)$ according to a gaussian function or to any damped function, the required function $x(t)$ should be computed in the same manner.

4 Conclusions

This study has presented simulations possibilities for optical pulses generated by the photonic echo; these possibilities are based on the use of partial fraction decomposition and on derivative procedures. It has been shown that the use of principles for partial fraction decomposition and a supplementary derivative procedure can explain the dependence of the photonic echo pulse on N^2 , where N represents the number of atoms involved in the light emission. The derivative procedure acts upon certain state variables describing the number of atoms involved in photonic-echo emission; the fact that the intensity of this high-energy pulse does not present significant fluctuations (despite the fact that usually derivative procedures generate significant noise) can be put in correspondence with robust derivative procedures performed on a finite time interval [12], [13]. Most probably, this analyze will continue by studying multiscale aspects similar to those presented in [14] as relayed to estimation of crystalline network parameters [15], using performant computer programmes able to use mathematical models in an optimum manner [16]. The spatial distribution of the N atoms involved (inside materials presenting isotropy, at the surface of a certain material medium or in thin-walled materials subject to external perturbations [17]) will probably lead to more accurate symbolic models (most probably matrices instead of a single polynomial ratio).

References

1. Toma, C., Sterian, P. : Theoretical control method available for fast variable optoelectronic phenomena , *Balkan Physics Letters Supplement* **5** (1997), 2059–2062
2. Toma, C. : An extension of the notion of observability at filtering and sampling devices, *Proceedings of the International Symposium on Signals, Circuits and Systems Iasi SCS 2001, Romania* 233–236
3. Carr, T.W., Bilings, L., Schwartz, I.B., Triandaf, I.: Bi-instability and the global role of unstable resonant orbits in a driven laser, *Physica D* **147** (2000) 59–82
4. Shilnikov, A., Nicolis, G., Nicolis, C. : Bifurcation and predictability analysis of a low-order atmospheric circulation model, *Int. J. Bifur. Chaos Appl. Sci. Engrg.* **5** (1995) 1701–1711
5. Toma, C.: Equations with partial derivatives and differential equations used for simulating acausal pulses, *International Conference Physics and Control Physcon 2003, 20-22 August, Sankt-Petersburg, Russia*, 1178–1183

6. Toma, C.: The possibility of appearing acausal pulses as solutions of the wave equation, *The Hyperion Scientific Journal* **4**, 1 (2004), 25–28
7. Cattani, C.: Harmonic Wavelets towards Solution of Nonlinear PDE, *Computers and Mathematics with Applications*, 50 (2005), 1191–1210.
8. Rushchitsky, J.J., Cattani, C., Terletskaia, E.V.: Wavelet Analysis of the evolution of a solitary wave in a composite material, *International Applied Mechanics*, **40**, 3 (2004) 311–318
9. Sterian, P., Toma, C.: Methods for presenting key concepts in physics for MS students by Photon-MD program, *Bulgarian Journal of Physics* **27**, No. 4 (2000), 27–30
10. Toma, C.: A connection between special relativity and quantum theory based on non-commutative properties and system - wave interaction, *Balkan Physics Letters Supplement* 5 (1997), 2509–2513
11. Toma, C.: The advantages of presenting special relativity using modern concepts, *Balkan Physics Letters Supplement* 5 (1997), 2334–2337
12. Sterian, A., Toma, C.: Filtering possibilities for processing optoelectronic current for acceleration measurements, *SPIE Proceedings* 4827 (2002), 403–408
13. Sterian, A., Toma, C.: Phase detection for vibration measurements based on test functions, *SPIE Proceedings* 5503 (2004), 164–168
14. Cattani, C.: Multiscale Analysis of Wave Propagation in Composite Materials, *Mathematical Modelling and Analysis*, **8**, 4 (2003), 267–282
15. Paun, V.P.: A Model for the Accurate Determination of Crystalline Network Parameters, *Revue Roumaine de Chimie* **54** (4), Bucharest (2003), 335–336
16. Paun, V.P.: Computer programme for the determination of the crystalline network parameters, *Revue Roumaine de Chimie* **49** (1), Bucharest (2004), 85–92
17. Paun, V.P.: A creep collapse model for thin-walled Zircolay-4 tubes, *Revue Roumaine de Chimie* **48** (11), Bucharest (2003), 903–906

Simulating Delayed Pulses in Organic Materials

Bogdan Lazar¹, Andreea Sterian¹, Stefan Pusca¹, Viorel Paun¹,
Cristian Toma², and Cristian Morarescu³

¹ Politehnica University, Department of Physics, Bucharest, Romania

² Titu Maiorescu University, Bucharest, Romania

³ Politehnica University, Department of Computers, Bucharest, Romania

Abstract. Fatty acids and cholesterol are important substances for the living matter, especially for the biological membrane [1]. Since the liquid crystal state of these substances can give information on some membrane mechanism [2], their answer to some external stimuli within the mesomorphism interval has been widely studied. The possibility of inducing a non-linearity in such systems could lead to a radical change of their dynamics. Interesting non-linear optical laser based answers were obtained in different thin film samples. We analyzed these effect answers and the measurement procedures. For simulating the generation of delayed pulses inside organic mixtures a mathematical model based on practical test-functions has been used. The input pulse (usually represented by an optical or electromagnetic pulse) generates a delayed pulse inside the material medium, and thus a modulated input pulse represented by a gaussian function modulated by a sine function has been used for simulation, with good results.

1 Introduction

Fatty acids and cholesterol are important substances for the living matter, especially for the biological membrane [1]. Since the liquid crystal state of these substances can give information on some membrane mechanism [2] we studied their answer to some external stimuli within the mesomorphism interval. It is known that the relative motion of molecules varies considerably in terms of membrane type, from highly mobile arrangements to rigid structures. Mixtures of cholesterol and fatty acids undergo a melting process by which molecules turn from a close-packed crystalline or a gel-type into a disordered liquid phase, via a liquid crystal phase.

The possibility of inducing a non-linearity in such systems could lead to a radical change of their dynamics. Interesting non-linear optical laser based answers were obtained in different thin film samples.

However, for simulating the generation of delayed pulses inside organic mixtures a mathematical model based on practical test-functions has been used. Aspects connected with gaussian pulses and sensitivity at detector vibrations were also studied, using Matlab simulations procedures, but an important aspect could not be explained: the important time difference between the time moment when an external optical or electromagnetic pulse is received and the time

moment when the organic material medium generates its answer (phenomenon appearing under certain circumstances). This time difference (also known as dead time in control engineering) is sometimes simulated by differential equations of higher order, but these kind of simulations lead to a dead time having the same order of magnitude as the response time. Such a simulation is not adequate for delayed pulse, where many times this so-called dead time is much greater than the response time (see the case when a fast alternating output is generated after a time interval much greater than the time period of the output oscillation). Due to this reason, some specific mathematical models for the organic material medium and for the input pulse must be found, so as to justify such a behaviour.

The input pulse (usually represented by an optical or electromagnetic pulse) generates a delayed pulse inside the material medium, and thus a modulated input pulse represented by a gaussian function modulated by a sine function has been used for simulation, with good results.

2 Aspects Connected with Signal Processing

Theoretically, the optical signal received by the photodetector generates an electronic signal; using a differential equation able to generate a practical test-function [3] having the form

$$f^{(2)} = \frac{0.6\tau^4 - 0.36\tau^2 - 0.2}{(\tau^2 - 1)^4} f + u(t), \quad (1)$$

where $u(t)$ represents the input signal (supposes to be constant) we can obtain a signal symmetrical as related to origin 0 (the previous differential equations works on time interval $(-1, 1)$ from initial null conditions). The property of symmetry previously mentioned is justified by invariance properties of this type [4]. However, even for $u(t) = 1$ (the most simple form of the input signal which is also symmetrical as related to time origin 0) the numerical simulations in Matlab presents an asymmetry of the output signal, justified by numerical errors (see fig. 1).

As a first conclusion, the shape of this output represents a certain response time due to numerical errors of the mathematical algorithms, not due to specific properties of the differential mathematical model. The same shape of the output can be noticed for an input represented by a gaussian pulse, beginning to act at the time moment $t_i = -0.9$ and having a width ten times smaller than the working period. In such a case the differential equation is represented by

$$f^{(2)} = \frac{0.6\tau^4 - 0.36\tau^2 - 0.2}{(\tau^2 - 1)^4} f + \exp - \frac{(\tau + 0.9)^2}{(0.01)^2} \quad (2)$$

and the corresponding output is represented in figure 2.

So we must extend our search for adequate mathematical models, and we shall try an input $u(t)$ represented by

$$u(t) = \exp \left(- \frac{(\tau + 0.9)^2}{(0.01)^2} \right) \sin 10^4 \tau \quad (3)$$

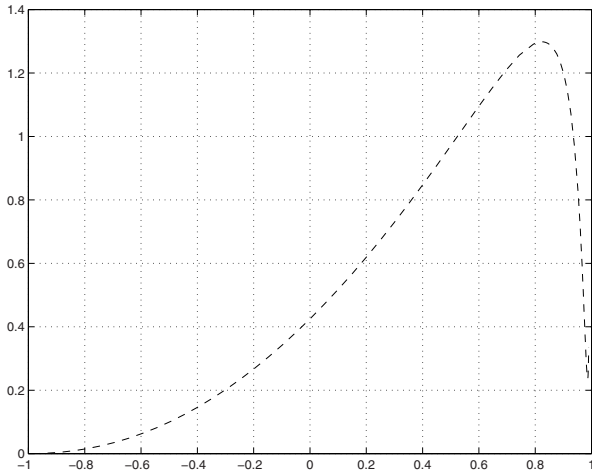


Fig. 1. Output asymmetry for unity-step input

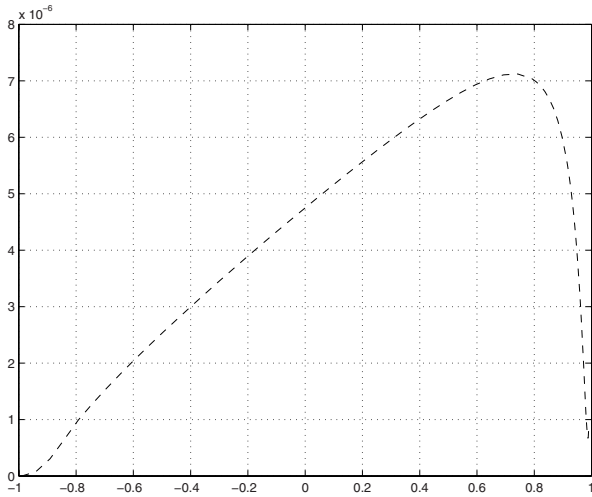


Fig. 2. Output of the system for a gaussian input

The corresponding output is represented in figure 3; it can be noticed that finally we have obtained an important delay time (dead time) for the output of the system, as related to the input pulse (represented in figure 4). Unlike aspects connected with propagation of acausal pulse [5], this model does not require a propagation phenomenon; it takes in consideration phenomena taking place in a certain area (all previous equations are differential equations, not equations with partial derivatives as the wave-equation).

For the case when the gaussian input is modulated by a cosine function - which means that

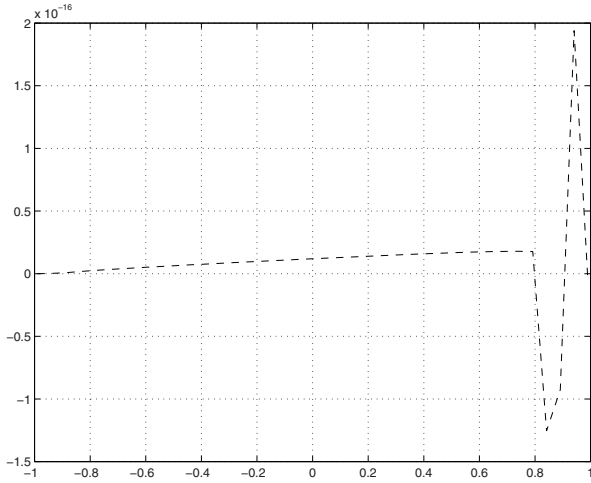


Fig. 3. Sine modulation

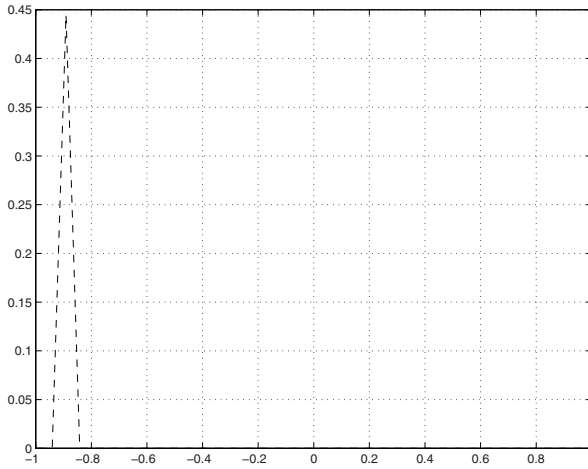


Fig. 4. Gaussian input modulated by sine function

$$u(t) = \exp\left(-\frac{(\tau + 0.9)^2}{(0.01)^2}\right) \cos 10^4 \tau \tag{4}$$

we obtain the output represented in figure 5. It can be noticed that in this case the output is represented by a slowly varying function, and no delay time appears (we can take into consideration just a certain response time, corresponding to the time interval where the slope of the output is constant). So a cosine modulation of a gaussian input is not suitable for simulating delayed pulse in the organic material medium.

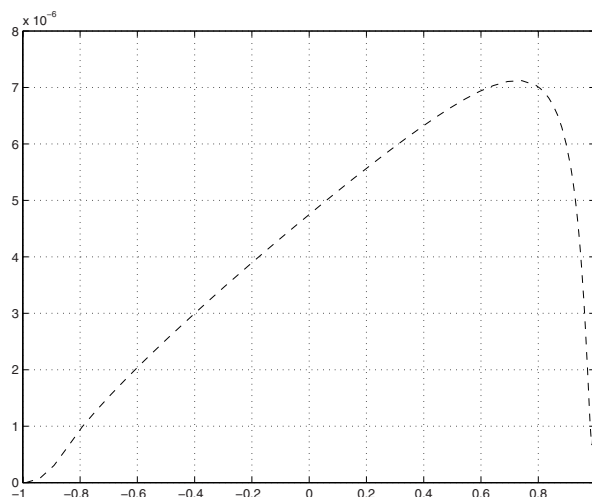


Fig. 5. Cosine modulation

We must point the fact that such delayed pulses generated by systems working on a limited time interval differ to wavelets resulting from PDE equations (see [6]) and to propagating wavelets through dispersive media [7], while the shape of the resulting output (the delayed pulse we have obtained) is not symmetrical as related to Ox axis (its mean value differs to zero). However, a multiscale analysis of such pulses (similar to [8]) will be performed by taking into account the ratio between the delay time and the response time.

3 Conclusions

This study has presented mathematical models for simulating the generation of delayed pulses inside organic mixtures. Aspects connected with gaussian pulses and sensitivity at detector vibrations were also studied, using Matlab simulations procedures, but best results were obtained using a modulated input pulse represented by a gaussian function modulated by a sine function. Thus the important time difference between the time moment when an external optical or electromagnetic pulse is received and the time moment when the organic material medium generates its answer (phenomenon appearing under certain circumstances) could be explained.

References

1. Guyton, A.C., Hall, J.E.: Textbook of Medical Physiology, 9th edn., Saunders, 1966
2. Brown, G.H., Wolken, J.J.: Liquid Crystals and Biological Structures, Academic Press, New York, 1979

3. Toma, C. : An extension of the notion of observability at filtering and sampling devices, Proceedings of the International Symposium on Signals, Circuits and Systems Iasi SCS 2001, Romania 233–236
4. Toma, G. : Practical test-functions generated by computer algorithms, Lecture Notes Computer Science **3482** (2005), 576–585
5. Toma, C.: The possibility of appearing acausal pulses as solutions of the wave equation, The Hyperion Scientific Journal **4**, 1 (2004), 25–28
6. Cattani, C.: Harmonic Wavelets towards Solution of Nonlinear PDE, Computers and Mathematics with Applications, **50** (2005), 1191–1210.
7. Rushchitsky, J.J., Cattani, C., Terletskaia, E.V.: Wavelet Analysis of the evolution of a solitary wave in a composite material, International Applied Mechanics, **40**, 3 (2004), 311–318
8. Cattani, C.: Multiscale Analysis of Wave Propagation in Composite Materials, Mathematical Modelling and Analysis, **8**, 4 (2003), 267–282

Wave Propagation of Shannon Wavelets*

Carlo Cattani

DiFARMA, Università di Salerno
Via Ponte Don Melillo, 84084 Fisciano (SA), Italy
ccattani@unisa.it

Abstract. The problem of the evolution of solitary profile having the form of a Shannon wavelet is considered as solution of a generalization of the Burger equation. Some nonlinear effects such as the breaking down of the wave into localized chaotic oscillations are shown.

Keywords: Solitary wave, evolution, Shannon functions.

1 Introduction

We consider the hyperbolic modification of the Burgers equation

$$\tau \frac{\partial^2 u}{\partial t^2} + \frac{\partial u}{\partial t} + \varepsilon u \frac{\partial u}{\partial x} - \sigma \frac{\partial^2 u}{\partial x^2} = 0 \quad (1)$$

where τ is the relaxation time, σ viscosity, $u = u(x, t)$ velocity, which is a generalization of many well known hyperbolic-parabolic type equations, as, for instance,

$$\varepsilon = \tau = 0 \quad \frac{\partial u}{\partial t} - \sigma \frac{\partial^2 u}{\partial x^2} = 0 \quad (\text{heat propagation})$$

$$\varepsilon = 0: \quad \tau \frac{\partial^2 u}{\partial t^2} + \frac{\partial u}{\partial t} - \sigma \frac{\partial^2 u}{\partial x^2} = 0 \quad (\text{Cattaneo-Vernotte})$$

$$\tau = 0: \quad \frac{\partial u}{\partial t} + \varepsilon u \frac{\partial u}{\partial x} - \sigma \frac{\partial^2 u}{\partial x^2} = 0 \quad (\text{nonlinear Burger})$$

Equation (1) is the simplest modification of the one-dimensional Navier-Stokes system and includes in the parabolic-type equation non-local effects [4] as it has been done by Cattaneo [2], Vernotte, Joseph in order to take into account memory effects.

* This work has been partially supported by Regione Campania, under contracts: "Modelli nonlineari di materiali compositi per applicazioni di nanotecnologia chimica-biomedica", LR 28/5/02 n. 5, Finanziamenti 2003, and by D.G.R. n. 2534, 30/12/04.

We will search the solution of (1) in the form [2,3]

$$u(x,t) = B F(z) \tag{2}$$

being $z = x - vt$, and it is assumed that the phase velocity $v = v(z)$ depends on z

$$v = v(z) \quad , \quad z = x - v(z)t \tag{3}$$

so that the evolution implies a nonlinear dependence on the phase velocity [4,5].
As initial profile

$$u(x,0) = B F(x) \tag{4}$$

where $F(x)$ is a given function, we take a solitary profile [2,3,5,6,7] having the form of a Shannon wavelet. This could be further developed as follows: once we can represent the evolution of a wavelet function we can easily generalize to any function that can be represented in the wavelet basis.

2 Method of Solution for the Propagation of a Solitary Wave

From equation (3) by a derivation we have

$$\begin{aligned} \frac{dz}{dx} &= \frac{1}{1+v't} \quad , \quad \frac{d^2z}{dx^2} = -\frac{v''t}{(1+v't)^3} \\ \frac{dz}{dt} &= -\frac{v}{1+v't} \quad , \quad \frac{d^2z}{dt^2} = \frac{2v'v - v''\frac{v^2}{1+v't}t}{(1+v't)^2} \end{aligned}$$

being $(\cdot)' \equiv \frac{d}{dz}(\cdot)$, $(\cdot)'' \equiv \frac{d^2}{dz^2}(\cdot)$, so that the derivatives of (2) are

$$\begin{aligned} \frac{\partial u}{\partial x} &= B F' \frac{dz}{dx} \quad , \quad \frac{\partial^2 u}{\partial x^2} = B F'' \left(\frac{dz}{dx}\right)^2 + B F' \frac{d^2z}{dx^2} \\ \frac{\partial u}{\partial t} &= B F' \frac{dz}{dt} \quad , \quad \frac{\partial^2 u}{\partial t^2} = B F'' \left(\frac{dz}{dt}\right)^2 + B F' \frac{d^2z}{dt^2} \end{aligned}$$

In order to simplify this model, it is assumed that during the evolution, from eq. (3), there results

$$t \frac{dv}{dz} \equiv 0 \quad , \quad v \frac{dv}{dz} \equiv 0 \quad , \quad \frac{d^2v}{dz^2} \equiv 0 \tag{5}$$

so that

$$\frac{dz}{dx} = 1 \quad , \quad \frac{d^2z}{dx^2} = 0$$

$$\frac{dz}{dt} = -v \quad , \quad \frac{d^2z}{dt^2} = 2v'v \quad .$$

With this hypothesis we have $\frac{\partial u}{\partial t} = -B F' v$, $\frac{\partial^2 u}{\partial t^2} = B F'' v^2 + B F' v' v$

and $\frac{\partial u}{\partial x} = B F'$, $\frac{\partial^2 u}{\partial x^2} = B F''$. Moreover, among all functions $F(z)$ we choose an eigenfunction, in the sense that

$$F' \equiv \frac{dF(z)}{dz} = f_1(z) F(z) \quad , \quad F'' \equiv \frac{d^2F(z)}{dz^2} = f_2(z) F(z) \quad (6)$$

with $F(z)$ given for all z , so that $f_1(z)$, $f_2(z)$ can be explicitly computed, being, in particular, $f_2(z) = f_1'(z) + f_1^2(z)$.

With these assumptions, when

$$F(z) \neq 0 \quad (7)$$

equation (1) gives

$$\tau(B F'' v^2 + B F' v' v) - B F' v + \varepsilon B^2 F F' - \sigma B F'' = 0$$

i.e.

$$\tau(f_2 v^2 + f_1 v' v) - f_1 v + \varepsilon B F f_1 - \sigma f_2 = 0$$

and, according to (5), the constraint

$$\tau f_2 v^2 - f_1 v + \varepsilon B f_1 F - \sigma f_2 = 0 \quad (8)$$

Thus we have for the phase velocity ,

$$v(z) = \begin{cases} \frac{1}{2\tau f_2(z)} \left[f_1(z) \pm \sqrt{f_1^2(z) - 4\varepsilon \tau B f_1(z) f_2(z) F(z) + 4\tau \sigma f_2^2(z)} \right] , & \tau \neq 0 \\ \varepsilon B F(z) - \sigma \frac{f_2(z)}{f_1(z)} , & \tau = 0 \end{cases} \quad (9)$$

or, by defining

$$g^2(z) = f_1^2(z) - 4\varepsilon \tau B f_1(z) f_2(z) F(z) + 4\tau \sigma f_2^2(z) =$$

$$= \left[f_1(z) - 2\sqrt{\tau \sigma} f_2(z) \right]^2 + 4\sqrt{\tau} f_1(z) f_2(z) \left[\sqrt{\sigma} - \varepsilon \sqrt{\tau} B F(z) \right]$$

it is

$$v(z) = \begin{cases} \frac{1}{2\tau f_2(z)} [f_1(z) \pm |g(z)|] & , \tau \neq 0 \\ \varepsilon B F(z) - \sigma \frac{f_2(z)}{f_1(z)} & , \tau = 0 \end{cases} \tag{10}$$

with

$$g(z) = \begin{cases} \sqrt{f_1^2(z) - 4\tau\varepsilon f_1(z) f_2(z) B F(z)} & , \tau \neq 0 \quad , \sigma = 0 \\ \sqrt{f_1^2(z) + 4\tau\sigma f_2^2(z)} & , \tau \neq 0 \quad , \varepsilon = 0 \\ f_1(z) & , \tau \neq 0 \quad , \varepsilon = \sigma = 0 \end{cases}$$

so that the speed of propagation is

$$v(z) = \begin{cases} \frac{1}{2\tau f_2(z)} [f_1(z) \pm \sqrt{f_1^2(z) - 4\varepsilon\tau B f_1(z) f_2(z) F(z) + 4\tau\sigma f_2^2(z)}] & , \tau \neq 0 \\ \frac{1}{2\tau f_2(z)} [f_1(z) \pm \sqrt{f_1^2(z) - 4\tau\varepsilon f_1(z) f_2(z) B F(z)}] & , \tau \neq 0 \quad , \sigma = 0 \\ \frac{1}{2\tau f_2(z)} [f_1(z) \pm \sqrt{f_1^2(z) + 4\tau\sigma f_2^2(z)}] & , \tau \neq 0 \quad , \varepsilon = 0 \\ \frac{f_1(z)}{\tau f_2(z)} & , \tau \neq 0 \quad , \varepsilon = \sigma = 0 \\ \varepsilon B F(z) - \sigma \frac{f_2(z)}{f_1(z)} & , \tau = 0 \end{cases}$$

or,

$$v(z) = \begin{cases} \frac{1}{2\tau} [k(z) \pm \sqrt{k^2(z) - 4\varepsilon\tau B k(z) F(z) + 4\tau\sigma}] & , \tau \neq 0 \\ \frac{1}{2\tau} [k(z) \pm \sqrt{k^2(z) - 4\tau\varepsilon B k(z) F(z)}] & , \tau \neq 0 \quad , \sigma = 0 \\ \frac{1}{2\tau} [k(z) \pm \sqrt{k^2(z) + 4\tau\sigma}] & , \tau \neq 0 \quad , \varepsilon = 0 \\ \frac{k(z)}{\tau} & , \tau \neq 0 \quad , \varepsilon = \sigma = 0 \\ \varepsilon B F(z) - \frac{\sigma}{k(z)} & , \tau = 0 \end{cases} \tag{11}$$

being

$$k(z) = \frac{f_1(z)}{f_2(z)} = \frac{F'(z)}{F''(z)} \tag{12}$$

In order to fulfill condition (5), by direct computation of the first derivative of (10), it is enough to assume (up to the first order on z), e.g.

1. when $\tau \neq 0$, either $\tau \gg 0$ or choose the function $F(z)$ such that $f_2(0) = f_2'(0) = 0$;
2. when $\tau = 0$, either $\varepsilon \ll 1, \sigma \ll 1$ or choose the function $F(z)$ such that $f_1(0) = 0$.

From equations (11), (2),(3) there follows the general solution

$$u(z) = \begin{cases} B F\left(x - \frac{1}{2\tau} \left[k(z) \pm \sqrt{k^2(z) - 4\varepsilon\tau B k(z) F(z) + 4\tau\sigma} \right] t\right) & , \tau \neq 0 \\ B F\left(x - \frac{1}{2\tau} \left[k(z) \pm \sqrt{k^2(z) - 4\tau\varepsilon B k(z) F(z)} \right] t\right) & , \tau \neq 0, \sigma = 0 \\ B F\left(x - \frac{1}{2\tau} \left[k(z) \pm \sqrt{k^2(z) + 4\tau\sigma} \right] t\right) & , \tau \neq 0, \varepsilon = 0 \\ B F\left(x - \frac{k(z)}{\tau} t\right) & , \tau \neq 0, \varepsilon = \sigma = 0 \\ B F\left(x - \left[\varepsilon B F(z) - \frac{\sigma}{k(z)} \right] t\right) & , \tau = 0 \end{cases} \tag{13}$$

with $z = x - v(z)t$. So that under the constraint (8), it is

1. $\tau \neq 0$

$$u(z) = B F\left(x - \frac{1}{2\tau} \left[k(x - v_0 t) \pm \sqrt{k^2(x - v_0 t) - 4\varepsilon\tau B k(x - v_0 t) F(x - v_0 t) + 4\tau\sigma} \right] t\right)$$

2. $\tau \neq 0, \sigma = 0$

$$u(z) = B F\left(x - \frac{1}{2\tau} \left[k(x - v_0 t) \pm \sqrt{k^2(x - v_0 t) - 4\tau\varepsilon B k(x - v_0 t) F(x - v_0 t)} \right] t\right)$$

3. $\tau \neq 0, \varepsilon = 0$

$$u(z) = B F\left(x - \frac{1}{2\tau} \left[k(x - v_0 t) \pm \sqrt{k^2(x - v_0 t) + 4\tau\sigma} \right] t\right)$$

4. $\tau \neq 0, \varepsilon = \sigma = 0$

$$u(z) = B F\left(x - \frac{1}{\tau} k(x - v_0 t) t\right)$$

5. $\tau = 0$

$$u(z) = B F\left(x - \left[\varepsilon B F(x - v_0 t) - \frac{\sigma}{k(x - v_0 t)} \right] t\right).$$

According to (7), the ikonal lines in the plane (x, t) , where singularities propagate, are given by $F(x - v(x - v_0 t)) = 0$.

In some particular case, equations (11) can be solved with respect to $B F(z)$. In fact, when $\epsilon \neq 0$, we immediately have from (2),(9),

$$u(x, t) = B F(z) = \begin{cases} \frac{1}{\epsilon} v(z) + \frac{\sigma}{\epsilon} \frac{f_2(z)}{f_1(z)} - \frac{\tau}{\epsilon} \frac{f_2(z)}{f_1(z)} [v(z)]^2, \\ \frac{1}{\epsilon} v(z) + \frac{\sigma}{\epsilon} \frac{f_2(z)}{f_1(z)} & , \tau = 0 \\ \frac{1}{\epsilon} v(z) - \frac{\tau}{\epsilon} \frac{f_2(z)}{f_1(z)} [v(z)]^2 & , \sigma = 0 \\ \frac{1}{\epsilon} v(z) & , \tau = \sigma = 0 \end{cases} \quad (14)$$

Giving the initial profile

$$u(x, 0) = B F(x) \quad (15)$$

under the constraint (6), the wave propagates according to (13)-(14), with phase velocity given by (9).

3 Evolution of a Solitary Profile in the Form of a Shannon Wavelet

Let us take as initial function the sinc function, or Shannon scaling function (see Fig. 1)

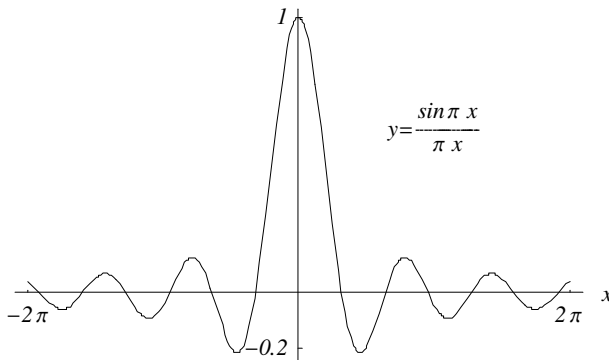


Fig. 1. Shannon wavelet

$$\varphi(x) = \frac{\sin \pi x}{\pi x}$$

so that $u(x, 0) = \frac{\sin \pi x}{\pi x}$ and $F(x) = \varphi(x) = \frac{\sin \pi x}{\pi x}$, $B = 1$. According to (6), it is

$$F'(x) = \frac{1}{x} \left(\cos \pi x - \frac{\sin \pi x}{\pi x} \right) \Rightarrow f_1(x) = -\frac{1}{x} + \frac{\pi}{\tan \pi x},$$

$$F''(x) = \frac{1}{\pi x^3} \left[(2 - \pi^2 x^2) \sin \pi x - 2 \pi x \cos \pi x \right] \Rightarrow f_2(x) = -\pi^2 + \frac{2}{x^2} - \frac{2 \pi}{x \tan \pi x}$$

from where

$$f_1(x - vt) = -\frac{1}{(x - vt)} + \frac{\pi}{\tan \pi(x - vt)},$$

$$f_2(x - vt) = -\pi^2 + \frac{2}{(x - vt)^2} - \frac{2 \pi}{(x - vt) \tan \pi(x - vt)},$$

$$k(x - vt) \equiv \frac{f_1(x - vt)}{f_2(x - vt)} = \frac{(x - vt) \left[-\pi(x - vt) + \tan \pi(x - vt) \right]}{2 \pi(x - vt) + \left[-2 + \pi^2(x - vt)^2 \right] \tan \pi(x - vt)}$$

The MacLaurin series expansion of $k(z)$, up to the 7th order, is

$$k(x - vt) = (x - vt) + \frac{\pi^2}{5}(x - vt)^3 + \frac{8 \pi^4}{175}(x - vt)^5 + \frac{83 \pi^6}{7875}(x - vt)^7 + O(x - vt)^8$$

When $\tau \neq 0, \sigma \neq 0, \varepsilon \neq 0$, the speed of propagation, according to (11), is

$$\begin{aligned} v(x, t) = & \frac{1}{2 \tau} \frac{(x - vt) \left[-\pi(x - vt) + \tan \pi(x - vt) \right]}{2 \pi(x - vt) + \left[-2 + \pi^2(x - vt)^2 \right] \tan \pi(x - vt)} \pm \\ & \pm \frac{1}{2 \tau} \left[\left(\frac{(x - vt) \left[-\pi(x - vt) + \tan \pi(x - vt) \right]}{2 \pi(x - vt) + \left[-2 + \pi^2(x - vt)^2 \right] \tan \pi(x - vt)} \right)^2 + 4 \tau \sigma \right. \\ & \left. - 4 \varepsilon \tau \frac{\sin \pi(x - vt) - \pi(x - vt) \cos \pi(x - vt)}{\pi \left(-2 + \pi^2(x - vt)^2 + 2 \pi(x - vt) \cot \pi(x - vt) \right)} \right]^{1/2} \end{aligned}$$

and the solution is

$$\begin{aligned}
 u(x,t) = & \pi^{-1} \left\{ x - \frac{1}{2\tau} \frac{(x-vt) [-\pi(x-vt) + \tan \pi(x-vt)]}{2\pi(x-vt) + [-2 + \pi^2(x-vt)^2] \tan \pi(x-vt)} t \pm \right. \\
 & \pm \frac{1}{2\tau} \left[\left(\frac{(x-vt) [-\pi(x-vt) + \tan \pi(x-vt)]}{2\pi(x-vt) + [-2 + \pi^2(x-vt)^2] \tan \pi(x-vt)} \right)^2 \right. \\
 & \left. \left. - 4\varepsilon\tau \frac{\sin \pi(x-vt) - \pi(x-vt) \cos \pi(x-vt)}{\pi(-2 + \pi^2(x-vt)^2 + 2\pi(x-vt) \cot \pi(x-vt))} + \right. \right. \\
 & \left. \left. + 4\tau\sigma \right]^{1/2} t \right\}^{-1} \sin \pi \left\{ x - \frac{1}{2\tau} \frac{(x-vt) [-\pi(x-vt) + \tan \pi(x-vt)]}{2\pi(x-vt) + [-2 + \pi^2(x-vt)^2] \tan \pi(x-vt)} t \pm \right. \\
 & \left. \pm \frac{1}{2\tau} \left[\left(\frac{(x-vt) [-\pi(x-vt) + \tan \pi(x-vt)]}{2\pi(x-vt) + [-2 + \pi^2(x-vt)^2] \tan \pi(x-vt)} \right)^2 \right. \right. \\
 & \left. \left. - 4\varepsilon\tau \frac{\sin \pi(x-vt) - \pi(x-vt) \cos \pi(x-vt)}{\pi(-2 + \pi^2(x-vt)^2 + 2\pi(x-vt) \cot \pi(x-vt))} + 4\tau\sigma \right]^{1/2} t \right\}
 \end{aligned}$$

If we restrict ourselves to the linear approximation it is (Fig. 2)

$$u(x-v_0t) = \frac{\sin \pi \left(x - \frac{1}{2\tau} \left[(x-v_0t) \pm \sqrt{(x-v_0t)^2 - 4\varepsilon\tau \sin(x-v_0t) + 4\tau\sigma} \right] t \right)}{\pi(x-v_0t)}$$

while up to the third order (see Fig. 3)

$$\begin{aligned}
 u(x-v_0t) = & \pi^{-1} \left(x - v_0t + \frac{\pi^2}{5}(x-v_0t)^3 \right)^{-1} \sin \pi \left(x - \frac{1}{2\tau} \left\{ \left(x - v_0t + \frac{\pi^2}{5}(x-v_0t)^3 \right) \pm \right. \right. \\
 & \left. \left. + \left[\left(x - v_0t + \frac{\pi^2}{5}(x-v_0t)^3 \right)^2 - 4\varepsilon\tau \sin \left(x - v_0t + \frac{\pi^2}{5}(x-v_0t)^3 \right) + 4\tau\sigma \right]^{1/2} \right\} t \right)
 \end{aligned}$$

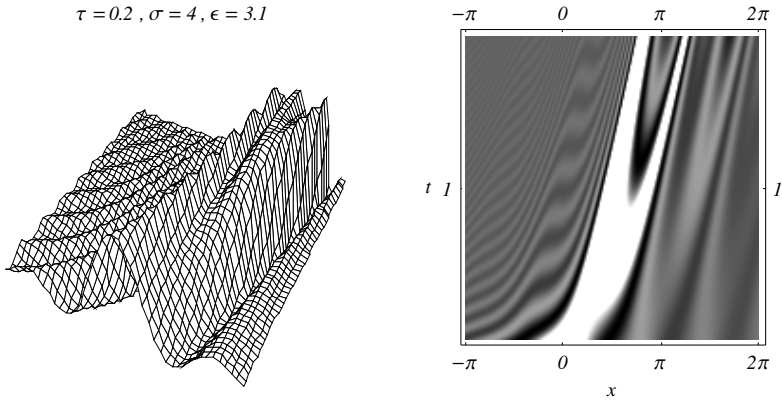


Fig. 2. Evolution of Shannon wavelet in linear approximation

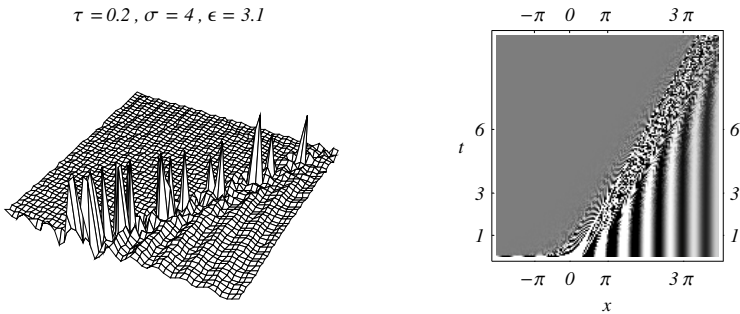


Fig. 3. Evolution of Shannon wavelet up to the third order approximation

References

1. Cattaneo C., "Sur une forme de l'équation de la chaleur éliminant le paradoxe d'une propagation instantanée" C.R.Acad. Sc. Paris, 1958. - 247. - P. 431-433.
2. Cattani C. "Multiscale Analysis of Wave Propagation in Composite Materials" Mathematical Modelling and Analysis, 2003. - 8, № 4. - P. 267-282.
3. Cattani C. "The wavelet based technique in the dispersive wave propagation", Int. Appl. Mech. - 2003.-39, № 4. - P. 493 - 501.
4. Hudson J.A. The excitation and propagation of elastic waves. - Cambridge: Cambridge University Press, 1980. - 226 pp.
5. Rushchitsky J.J., Cattani C., Terletska E.V. "Analysis of solitary wave evolution in a material with the microstructure using wavelet analysis", Int.Appl.Mech. - 2004. - 40, № 3. - P.197 - 202.
6. Sterian R., Toma C., "Simulating Laser Pulses by Practical Test Functions and Progressive Waves", International Conference on Computational Science and its Applications (ICCSA 2005), May 9-12, 2005 Singapore, O. Gervasi et al. (Eds.), Springer-Verlag Berlin Heidelberg (2005), 592-597.
7. Sterian A., Toma G., "Possibilities for obtaining the derivative of a received signal using computer-driven second order oscillators", International Conference on Computational Science and its Applications (ICCSA 2005), May 9-12, 2005 Singapore, O. Gervasi et al. (Eds.), Springer-Verlag Berlin Heidelberg (2005), 585-592.

Finite Element Analysis of the Thermoforming Manufacturing Process Using the Hyperelastic Mooney-Rivlin Model

Pierpaolo Carlone and Gaetano Salvatore Palazzo

University of Salerno, Department of Mechanical Engineering, Via Ponte Don Melillo 1,
84084 Fisciano (SA), Italy
pcarlone@unisa.it, gspalazzo@unisa.it

Abstract. Thermoforming is a manufacturing process widely used to produce thin thermoplastic parts. In this process a previously extruded thermoplastic sheet is clamped and then heated and formed into a mold cavity using a differential pressure. In this paper a finite element model of the thermoforming process of an ABS sheet is proposed and numerical results are compared to data from literature. Thermoplastic sheet is modelled according to the membrane formulation. An implicit time scheme has been adopted for the integration algorithm. Mechanical behaviour of the processing material is assumed as hyperelastic, according to the two parameters Mooney-Rivlin model. Mathematical formulation of the mechanical model is exposed. The proposed model allows to evaluate material thinning, stresses, strains and contact status between the processing material and the die.

1 Introduction

Thermoforming is a manufacturing process used to form polymeric sheet into complex three-dimensional shape. The temperature of a previously extruded thermoplastic sheet is raised far above the glass transition temperature of the specific resin system to deform the material to the desired shape using a differential pressure and a male or female die. Different kinds of the thermoforming process have been developed in the past years, such as vacuum forming, drape forming, inverse drape forming, drape forming reverse, blow forming with or without plug assistance, blow up reverse, vacuum reverse, blow up vacuum reverse, skin pack, blister ball packaging, and continuous cycling. The most common resins manufactured using the thermoforming process and their relative applications are:

- polyester (PET) for boxes and bottles;
- polymethyl methacrylate (PMMA) for building applications;
- polycarbonate (PC) for windows, helmets, glasses, and suitcases;
- polyethylene (PE) and polypropylene (PP) for industrial, automotive, and electrical applications;
- high-impact polystyrene (HIPS), polyacrylonitrile butadiene styrene (ABS), and polyvinyl chloride (PVC) for food packaging and other applications.

Nowadays the thermoplastic forming industry is mostly based on trial and error methods to design and develop new products. These procedures, however, result relatively time and money expensive.

Finite element analysis is considered as a good tool for product design and for the process set-up. However, to obtain a realistic simulation of process it is very important to evaluate accurate mechanical properties of the processing material, as well as to use opportune models to describe its mechanical behavior. In recent years several researchers have focused their attention on the numerical simulation of the thermoforming process. In [3], Stephenson *et al.* proposed a mechanical characterization and an experimental analysis of a styrene-butadiene copolymer with polystyrene for thermoforming applications. Different constitutive model for processing material modelling were investigated in [11] by Erchiqui *et al.*, in which a dynamic finite element procedure, based on membrane theory and Lagrangian formulation, is used to model thermoforming of an ABS thin sheet under the action of perfect gas flow. The influence of hyperelastic models (Ogden and Mooney-Rivlin) and viscoelastic models (Lodge and Christensen) assumption on thickness and stress distribution into the formed part was analyzed. In [4], a creep constitutive model was developed by McEvoy *et al.* for blow forming simulation of PET bottles using both solid and shell elements. Three dimensional solid elements and membrane (shell) elements were used in [7] by Nam *et al.* to model free inflation, vacuum forming and plug assisted forming. Constitutive laws based on the hyperelastic Mooney-Rivlin model were used and the influence of non-isothermal temperature distribution was investigated. A similar model, based on an explicit time integration scheme, was proposed by Marckmann *et al.* in [8]. The influence of temperature in the thermoforming process was numerically investigated also in [6] by Song *et al.*, who developed a FEM software combining rigid-visco-plastic equation for forming computation, Arrhenius and Williams equations for viscosity computation, and Galerkin FEM equation for temperature field. Temperature variations were neglected by Bourgin *et al.* [1]. In [2], Schmidt *et al.* proposed an axisymmetric numerical simulation based on a volumic approach, using an Update-Lagrangian finite element formulation and automatic remeshing technique. Industrial case studies were carried out by Wiesche [10] and by Gao *et al.* [5]. The implementation of automatic procedures for design optimization of thermoformed parts, based on parameterized geometry model in an interactive design environment was suggested in [12] by Unwin *et al.*, who performed experimental investigation on the deformation behavior of polystyrene sheet. In [9], Yu *et al.* developed a process optimization procedure based on fuzzy neural-Taguchi network with genetic algorithm, in which a back propagation Taguchi network was used to predict the relationship between design variables and process features and then a genetic algorithm was applied to optimize die design. In this paper a transient finite element model of the thermoforming process of an ABS sheet is proposed, according to the membrane formulation. An implicit time scheme has been adopted for the integration algorithm. Mechanical behavior of the processing material is

assumed as hyperelastic, according to the two parameters Mooney-Rivlin model. The proposed model allows to evaluate material thinning, stresses, strains and contact status between the processing material and the die. In Section 2 the mathematical formulation of the mechanical model is exposed; Section 3 deals with numerical modelling and results. Concluding remarks and future perspectives are discussed in Section 4.

2 On the Material Constitutive Model

Thermoplastic materials, heated far above their glass transition temperature, are considered as rubber-like materials, characterized by non-linear visco-elastic incompressible behavior. During the forming stage, related to pressure (or vacuum) application, plastic sheet is often modelled as a viscoelastic or as a hyperelastic material.

In this work hyperelastic behavior has been assumed. In this section a mathematical formulation of hyperelasticity, according to Mooney-Rivlin and Ogden models is given. Hyperelasticity refers to materials which can experience large elastic strain, with negligible volume variation (incompressibility). The constitutive behavior of hyperelastic materials are usually derived from the strain energy potentials.

A material is said to be hyperelastic if exists an elastic potential function W (or strain energy density function) which is a scalar function of one of the strain or deformation tensors, whose derivative with respect to a strain component determines the corresponding stress component. This can be expressed by the following:

$$S_{ij} = (\partial W / \partial E_{ij}) = 2 (\partial W / \partial C_{ij}), \quad (1)$$

where S_{ij} are the components of the second Piola-Kirchhoff stress tensor, W is the strain energy function per unit undeformed volume, E_{ij} are the components of the Lagrangian strain tensor, and C_{ij} are the components of the right Cauchy-Green deformation tensor. The Lagrangian strain may be expressed as follows:

$$E_{ij} = (1/2)(C_{ik} - \delta_{ij}), \quad (2)$$

where δ_{ij} is the Kronecker delta ($\delta_{ij} = 1, i = j; \delta_{ij} = 0, i \neq j$) and the deformation tensor C_{ij} is comprised of the products of the deformation gradients:

$$C_{ij} = F_{ik} F_{kj}, \quad (3)$$

where F_{ij} are the components of the second Piola-Kirchhoff stress tensor, X_i is the undeformed position of a point in direction i , $x_i = X_i + u_i$ is the deformed position of a point in direction i , and u_i is the displacement of a point in direction i . The eigenvalues (principal stretch ratios) of C_{ij} are λ_1^2, λ_2^2 , and λ_3^2 , and exist only if:

$$\det [C_{ij} - \lambda_p^2 \delta_{ij}] = 0, \quad (4)$$

which can be re-expressed as:

$$\lambda_p^6 - I_1 \lambda_p^4 + I_2 \lambda_p^2 - I_3 = 0, \quad (5)$$

where I_1 , I_2 , and I_3 are the invariants of C_{ij} :

$$\begin{aligned} I_1 &= \lambda_1^2 + \lambda_2^2 + \lambda_3^2, \\ I_2 &= \lambda_1^2 \lambda_2^2 + \lambda_2^2 \lambda_3^2 + \lambda_1^2 \lambda_3^2, \\ I_3 &= \lambda_1^2 \lambda_2^2 \lambda_3^2 = J^2 = (\det[\mathbf{F}_{ij}])^2, \end{aligned} \quad (6)$$

J is also the ratio of the deformed elastic volume over the undeformed volume of materials. According to the two parameters Mooney-Rivlin theory for isotropic materials, energy can be described as a function of the three Cauchy strain invariants, as follows:

$$W = c_{10}(I_1 - 3) + c_{01}(I_2 - 3) + (1/d)(J - 1)^2. \quad (7)$$

The form of the strain energy potential for the three parameters Mooney-Rivlin model writes:

$$W = c_{10}(I_1 - 3) + c_{01}(I_2 - 3) + c_{11}(I_1 - 3)(I_2 - 3) + (1/d)(J - 1)^2. \quad (8)$$

The form of the strain energy potential for the five parameters Mooney-Rivlin model writes:

$$W = c_{10}(I_1 - 3) + c_{01}(I_2 - 3) + c_{20}(I_1 - 3)^2 + c_{11}(I_1 - 3)(I_2 - 3) + c_{02}(I_1 - 3)^2 + (1/d)(J - 1)^2. \quad (9)$$

The form of the strain energy potential for the nine parameters Mooney-Rivlin model writes:

$$W = c_{10}(I_1 - 3) + c_{01}(I_2 - 3) + c_{20}(I_1 - 3)^2 + c_{11}(I_1 - 3)(I_2 - 3) + c_{02}(I_2 - 3)^2 + c_{30}(I_2 - 3)^3 + c_{21}(I_1 - 3)^2(I_2 - 3) + c_{12}(I_1 - 3)(I_2 - 3)^2 + c_{03}(I_2 - 3)^3 + (1/d)(J - 1)^2, \quad (10)$$

where c_{10} , c_{01} , c_{20} , c_{11} , c_{02} , c_{30} , c_{21} , c_{12} , c_{03} , and d are material constants. c_{10} , c_{01} , and d are related to the shear modulus (μ) and to the bulk modulus (K) according to the followings:

$$\mu = 2(c_{10} + c_{01}), \quad (11)$$

$$K = 2/d.$$

A different formulation for the strain energy function was provided by Ogden and it is based on the principal stretches from the left Cauchy strain tensor, as follows:

$$W = \sum_{i=1}^N ((\mu_i/\alpha_i) (\lambda_1^{\alpha_i} + \lambda_2^{\alpha_i} + \lambda_3^{\alpha_i} - 3)) + \sum_{k=1}^N (1/d_k)(J - 1)^{2k}, \quad (12)$$

where N , μ_i , α_i , and d_k are material constants.

The initial shear modulus is given by:

$$\mu = (1/2) \sum_{i=1}^N \alpha_i \mu_i. \quad (13)$$

The initial bulk modulus is:

$$K = 2/d_1. \quad (14)$$

3 Numerical Modelling and Results

To validate the hyperelastic Mooney-Rivlin assumption as constitutive law for the mechanical behavior of the processing material, the free inflation of a polymeric sheet has been modelled and then numerical results have been compared with data from literature. An ABS sheet, whose dimension are 25 mm, 35 mm, and 0.82 mm (width, length, and thickness, respectively) has been modelled using a membrane formulation. Gas flow was simulated using an uniformly distributed pressure, applied on the lower surface of the sheet; displacements of the sheet edges were constrained to simulate the clamping system. Process simulation has been performed in isothermal conditions, assuming material properties as constants. The proposed model, however, allows to take into account non-isothermal temperature distribution on the sheet, using different material properties for each zone at a certain temperature in a really simple way. Some results obtained from the proposed model are shown in Fig. 1-4. Fig. 5 and Fig. 6 show a comparison, based on the relative (final/initial) thickness, of the present model with data from literature (Ref. [7]). Small differences between numerical results and data from reference can be related to element formulation and applied boundary conditions. As expected the minimum value of the relative thickness was found at the top center of the sheet, which shows the maximum y-displacement (height direction), while wrinkling was evidenced by a certain increase in sheet thickness at the edge. In Fig. 3 and Fig. 4 the influence of applied pressure on sheet height and thickness is evidenced. As it can be seen, over a certain value of the applied pressure (3500-4000 Pa) sheet height at the top center suddenly increases; this can be explained taking into account that sheet resistance decreases with its thickness.

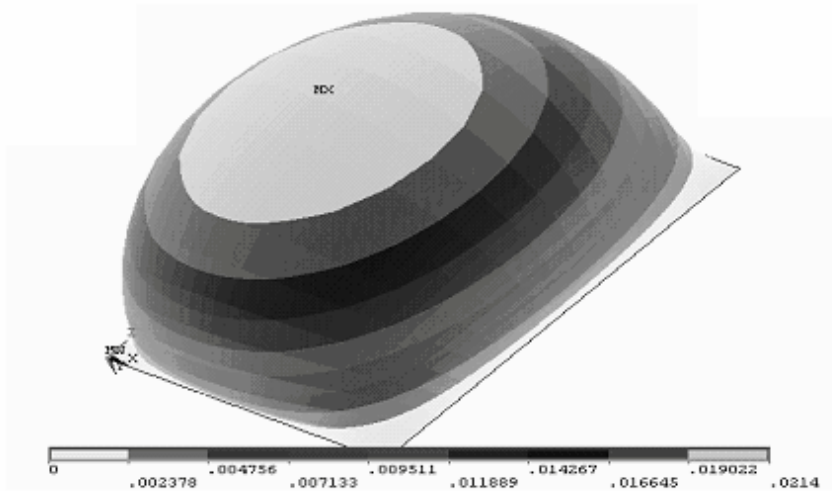


Fig. 1. Sheet y-displacement distribution at the end of the analysis

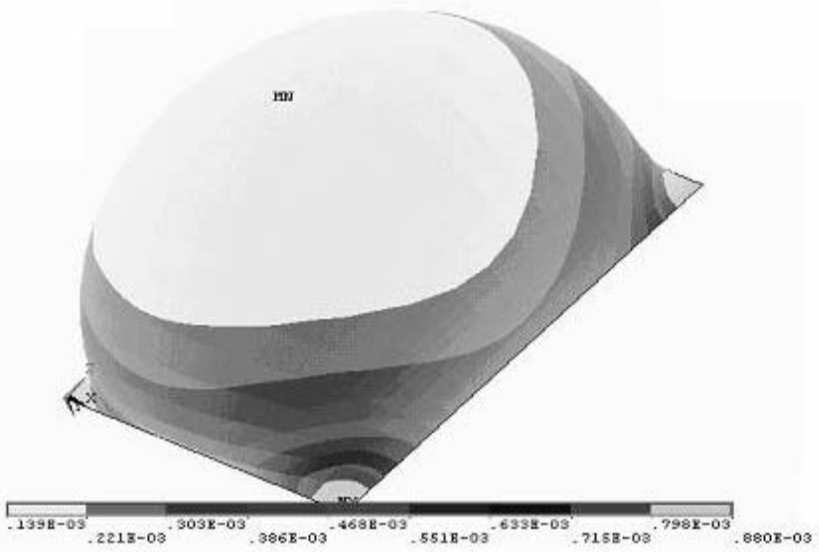


Fig. 2. Sheet thickness distribution the end of the analysis

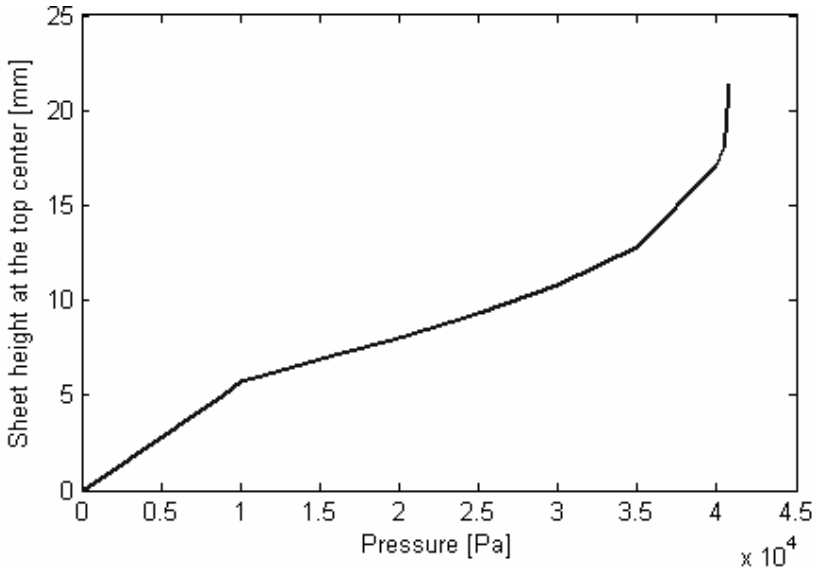


Fig. 3. Height at the top center of forming sheet versus applied pressure

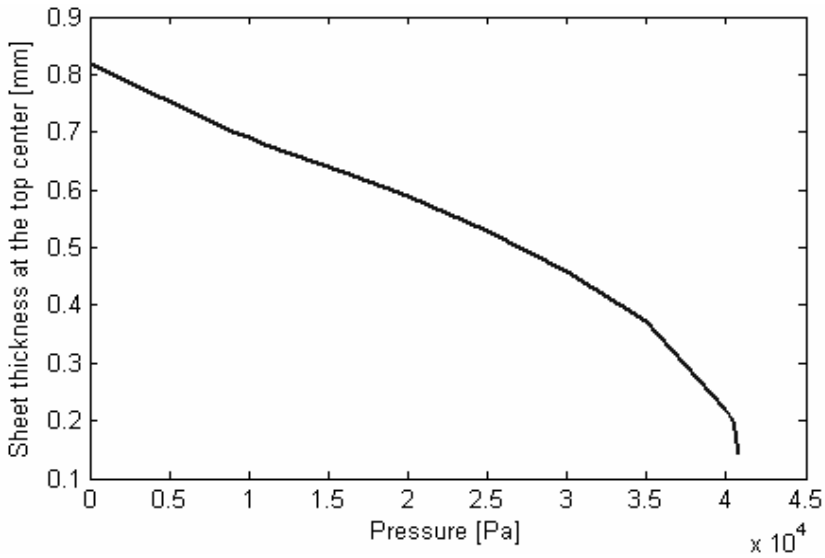


Fig. 4. Thickness at the top center of the sheet (minimum sheet thickness) versus applied pressure

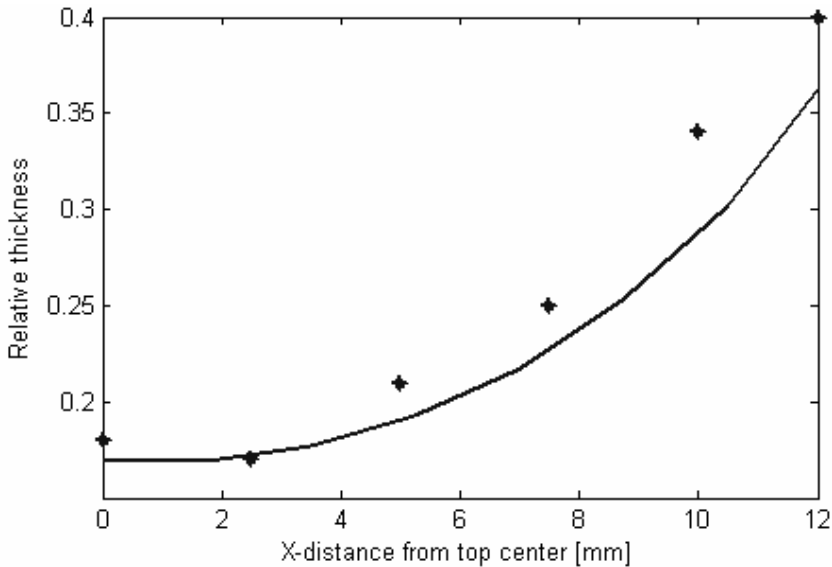


Fig. 5. Relative thickness versus x-distance from the top center of the sheet at the end of the process; continuous line represents the proposed model numerical results, points represent data from Ref. [7]

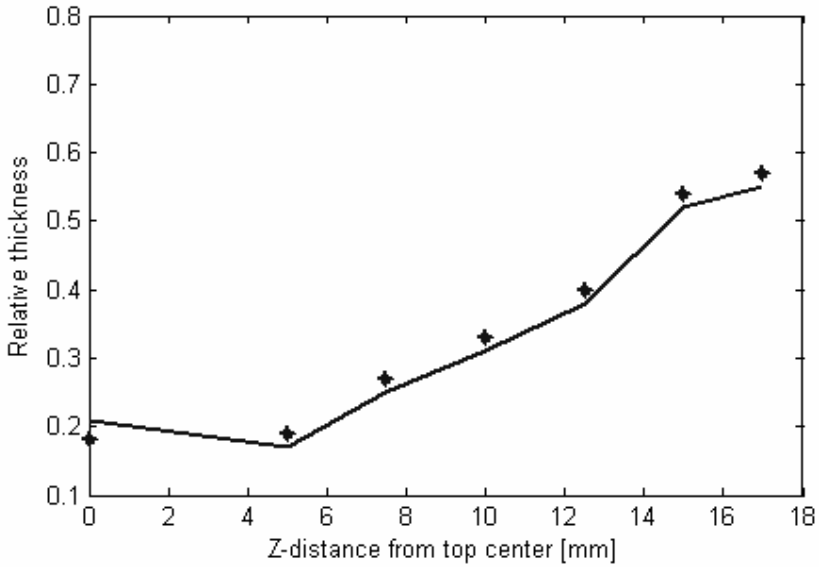


Fig. 6. Relative thickness versus z-distance from the top center of the sheet at the end of the process; continuous line represents the proposed model numerical results, points represent data from Ref. [7]

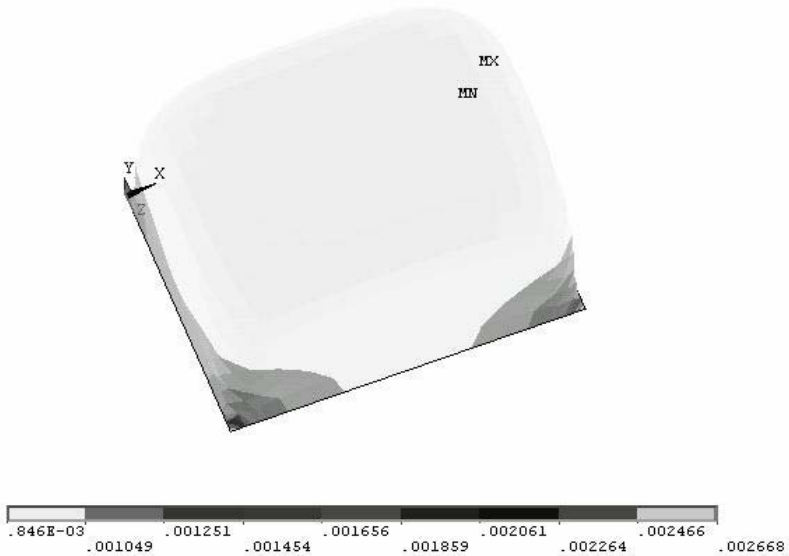


Fig. 7. Part thickness at the end of the analysis

In the following, the simulation of a rectangular box thermoforming is proposed using the above constitutive law. Die dimensions have been assumed as 520 mm, 400 mm, and 318 mm (length, width, and height, respectively); sheet thickness has been assumed as 3.2 mm. Contact between sheet and forming die has been modelled as a surface-to-surface rigid-to-flexible contact, assuming the die as the target surface and the forming sheet as a standard contact surface. Augmented Lagrange method has been adopted as contact algorithm and contact detection has been based on Gauss points. Fig. 7 shows part thickness at the end of the thermoforming process. As expected, the minimum value of the thickness is located at the upper part of the sheet, near box edges, which are the last zones of the die to be touched by the sheet, as evidenced in Fig. 8. This figure shows also that the simulated process leads to a non optimal part forming, however this is related to a not realist design of the die, whose corners are not filled as it happens in any real forming process.

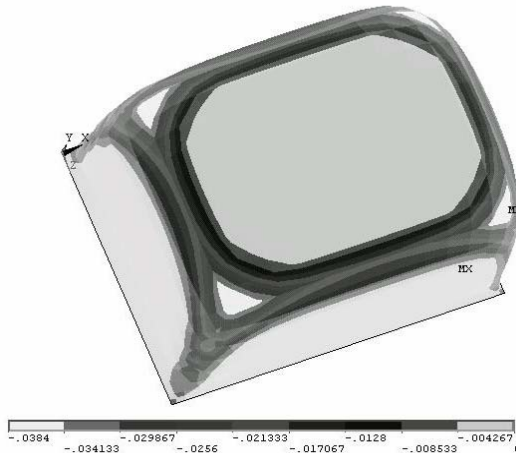


Fig. 8. Distance between die (target) and formed plastic sheet (contact)

4 Conclusions and Future Perspectives

In this paper a finite element model of the thermoforming manufacturing process has been proposed, assuming that the forming material obeys to a hyperelastic constitutive law, according to the two parameters Mooney-Rivlin model. The validity of the adopted mechanical behavior has been evidenced performing a simulation of a free forming of a rectangular sheet and comparing numerical results with data from literature. The simulation of a rectangular box thermoforming underlines model capabilities for process analysis and development. Further improvement of the proposed model are based, above all, on a better consideration of thermal aspects related to the process, in particular taking into account non uniform temperature distributions (due to the specific heating system) and, in some cases, temperature variations during the forming time. A coupled thermo-mechanical analysis, and then a

relatively more accurate modelling of the cooling stage, probably leads to better results about contact status. Material mechanical model can be improved using higher order formulation of the Mooney-Rivlin model. From a numerical point of view, the present model could be improved by the adoption of explicit scheme of time integration and adaptive meshing technique.

References

1. Bourgin, P., Cormeau, I., Saint-Matin, T.: A First Step Towards the Modelling of the Thermoforming of Plastic Sheets. In: *Journal of Materials Processing Technology*, Vol. 54 (1995) 1-11
2. Schmidt, F.M., Agassant, J.F., Bellet, M., Desoutter, L.: Viscoelastic Simulation of PET Stretch/Blow Molding Process. In: *Journal of Non-Newtonian Fluid Mechanics*, Vol. 64 (1996) 19-42
3. Stephenson, M.J., Ryan, M.E.: Experimental Study of the Thermoforming of a Blend of Styrene-Butadiene Copolymer with Polystyrene. In: *Polymer Engineering and Science*, Vol. 37, No. 2 (1997) 450-459
4. McEvoy, J.P., Armstrong, C.G., Crawford, R.J.: Simulation of the Stretch Blow Molding Process of PET Bottles. In: *Advances in Polymer Technology*, Vol. 17, No. 4 (1998) 339-352
5. Gao, D.M., Nguyen, K.T., Hetu, J.F., Laroche D., Garcia-Rejon, A.: Modeling of Industrial Polymer Processes: Injection Molding and Blow Molding. In: *Advanced Performance Materials*, Vol. 5 (1998) 43-64
6. Song, Y.H., Zhang, K.F., Wang, Z.R., Diao, F.X.: 3-D FEM Analysis of the Temperature Field and the Thermal Stress for Plastic Thermalforming. In: *Journal of Materials Processing Technology*, Vol. 97 (2000) 35-43
7. Nam G.J., Ahn, K.H., Lee, J.W.: Three-Dimensional Simulation of Thermoforming Process and Its Comparison With Experiments. In: *Polymer Engineering and Science*, Vol. 40, No.10 (2000) 2232-2240
8. Marckmann, G., Verron, E., Peseux, B., Finite Element Analysis of Blow Molding and Thermoforming Using a Dynamic Explicit Procedure. In: *Polymer Engineering and Science*, Vol. 41, No. 3 (2001) 426-439
9. Yu, J.C., Chen, X.X., Hung, T.R., Thibault F.: Extrusion of Extrusion Blow Molding Processes Using Soft Computing and Taguchi's Method. In: *Journal of Intelligent Manufacturing*, Vol. 15 (2004) 625-634
10. Wiesche, S., Industrial Thermoforming Simulation of Automotive Fuel Tanks. In: *Applied Thermal Engineering*, Vol. 24 (2004) 2391-2409
11. Erchiqui, F., Gakwaya, A., Rachik, M.: Dynamic Finite Element Analysis of Nonlinear Isotropic Hyperelastic and Viscoelastic Materials for Thermoforming Applications. In: *Polymer Engineering and Science*, Vol. 45 (2005) 125-134
12. Unwin, A.P., Ward, I.M., Ugail, H., Bloor, M.I.G., Wilson, M.J.: Optimal Design and Manufacture of Thin-Walled Polystyrene Structures. In: *Polymer Engineering and Science*, Vol. 45, (2005) 694-703

Analysis of Compatibility with Experimental Data of Fractal Descriptions of the Fracture Parameters

Dan Iordache¹, Stefan Pusca¹, Ghiocel Toma¹, Viorel Paun¹,
Andreea Sterian¹, and Cristian Morarescu²

¹ Politehnica University, Department of Physics, Bucharest, Romania

² Politehnica University, Department of Computers, Bucharest, Romania

Abstract. In order to check if the Fractal theory could be a useful tool for some quantitative descriptions of the fracture parameters, the present work studied different theoretical models (e.g. the Bazant's Size Effect Law (SEL) [1], the Modified Size Effect Law [2, 3] and the Carpinteri's MultiFractal Scaling Law (MFSL) [4] of the fracture parameters of concrete specimen, and the compatibility of some of the above studied theoretical models relative to the experimental data, using certain recent procedures to study the global and local compatibility. The fracture parameters can be considered as main quantities for computational procedures for modeling the fracture of a certain ensemble (a suddenly emerging phenomena). In the next phase, the thermoelastic generation of ultrasonic perturbations in semitransparent solids was analyzed (using computer simulation) so as to find similarities with material properties as fractal dimensions, when the heat source is a laser radiation. The algorithm, the numerical analysis has taken into account three main physical phenomena: the absorption of electromagnetic energy in substance with heat generation; thermal diffusion with electromagnetic energy based heat source and elastodynamic wave generation by thermoelastic expansion.

1 Introduction

The applications in Physics of the mathematical theory of the ideal fractals [5] need a good understanding of this concept, from the physical point of view. A first attempt in this direction was done recently by M. Rybaczuk and W. Zielinski [6], the presence of measurement errors being presented in [7]. In frame of their well-known paper [11], B.B. Mandelbrot and his collaborators claimed that the value of (the fractal dimension) D decreases smoothly with an increase of the impact energy and D is shown to be a measure of toughness in metals; moreover, Mandelbrot stated [12] that the frequent use of numbers by physicists is a mistake and it would be better if they could focus mainly on the study of plots. Taking into account that for high accuracy of the experimental data, the theoretical relations are not more compatible with these experimental data, even for high values of the correlation coefficient, and using the existence for concrete of several experimental data [3], [14] referring to the size dependence

of the fracture parameters, as well as of some (multi)fractal descriptions of these effects (see also [7], [8] and [9]), this work will start by presenting a numerical analysis of these existing experimental data, as well as of the compatibility of the multifractal and similitude expressions of the fracture parameters relative to the analyzed experimental results.

2 Experimental Data for the Size Dependence of Fracture Parameters of Some Concrete and Rock Specimen

The study of the compatibility of some theoretical relations relative to the analyzed experimental data needs the previous elimination of the rough errors. This was performed using the Chauvenet’s criterion [15], and eliminating the individual values whose absolute values of the reduced errors were larger than the Chauvenet’s threshold. The use of this procedure to the study of the numerical values of some fracture parameters [3], [14] pointed out that some individual values of the critical strain corresponding to some specimens of size equal to 20cm of dry and wet concrete [3], respectively are roughly erroneous. After the elimination of these individual values, the mean values were recalculated for the compatible individual values. The obtained results corresponding to the tensile strength $Ts(MPa)$, critical strain (deformation) $w(\mu m)$ and to the fracture energy $Gf(N/m)$ for specimens of different natures (materials) and sizes were synthesized in the following tables; they present the average values corresponding to some existing experimental data concerning the main fracture parameters of some concrete and rock specimens, respectively.

Table 1. Material: Concrete

Specimen size (cm)	Av. value $Ts(MPa)$	Av. value $w(\mu m)$	Av. value $Gf(N/m)$
2.5	4.7925	-	146.25
5.0	4.56	-	257.57
10.0	4.3543	-	236.25
20.0	3.80	-	158.0
40.0	3.7225	-	214.0

Because the studies [13], [14] point out a considerable curvature of the plots for certain logarithmic representations, some semiempirical expressions of the tensile strength and of the fracture energy have to be obtained (which differ to that of Bazant [5], [6] and to those of Carpinteri [7], [8]).

3 Obtained Results

The obtained results concerning the compatibility of the (multi)fractal (Carpinteri’s) expressions and of the classical elasticity theory (Bazant’s) expressions of the size-effects presented by the tensile strength Ts , the fracture energy Gf and

Table 2. Material: DRY Concrete

Specimen size (cm)	Av. value $T_s(MPa)$	Av. value $w(\mu m)$	Av. value $Gf(N/m)$
5.0	2.536	1.64	97.045
10.0	2.9725	5.20	125.70
20.0	2.750	9.833	124.243
40.0	2.298	14.78	125.22
80.0	2.0725	22.025	142.30
160.0	1.8575	44.40	141.10

Table 3. Material: WET Concrete

Specimen size (cm)	Av. value $T_s(MPa)$	Av. value $w(\mu m)$	Av. value $Gf(N/m)$
5.0	2.174	2.180	91.48
10.0	2.230	4.10	99.66
20.0	2.476	8.025	88.92
40.0	2.365	15.725	100.367

Table 4. Material: RED FELSER SAND-STONE

Specimen size (cm)	Av. value $T_s(MPa)$	Av. value $w(\mu m)$	Av. value $Gf(N/m)$
5.0	2.450	28.45	76.75
10.0	1.2167	44.167	111.333
20.0	1.010	69.20	93.80
40.0	0.960	156.80	135.067
80.0	1.300	263.70	143.350
160.0	1.200	434.70	81.80

by the critical strain w relative to the existing experimental data are synthesized in frame of next table. The analysis points out: a) the local incompatibility of the studied theoretical models with the experimental data (TM/ED) corresponding to the tensile strength of the Red Felser Sandstone for 3 or 4 sizes (from the 6 studied ones) of the studied specimens, the Carpinteri’s expression being though somewhat more accurate, b) the compatibility TM/ED for Dry Concrete specimens, the Bazant’s description being somewhat more accurate, c) the compatibility TM/ED for Wet Concrete, but with strange (negative) values of the characteristic lengths, d) the compatibility TM/ED for Gf , with somewhat better accuracy and physical meaning of the values of the characteristic lengths obtained by means of Carpinteri’s model for the Red Felser Sandstone and Dry Concrete specimens, e) the compatibility TM/ED for Gf , with somewhat equal accuracy of both studied models for the Wet Concrete, f) the compatibility TM/ED with somewhat better accuracy (excepting the van Vliet’s results for Dry Concrete) of Bazant’s type description of $w(b)$.

In this table Sp(Ref.) represents Specimen (with Reference written into brackets), Rs dm represents Range of sizes in dm (with Theoretical model written into brackets), Rfd represents Range of fractal dimensions, Rev I represents Ratio of

Table 5.

Sp(Ref.)	Rs dm (Th-m)	Rfd	Rev I	MPa	dm
(RFS) [3]	0.5...16 [7]-[9]	1.6747...1.9725	11.831	1.02726	9.31076
RFS [3]	0.5...16 [4]-[6]	1.99896...1.99997	31.941	1.15839	77082.17
(DryC) [3]	0.5...16 [7]-[9]	1.76495...1.98651	17.427	2.0753	4.43573
Dry C. [3]	0.5...16 [4]-[6]	1.71015...1.97934	14.0293	2.7873	116.005
(WetC) [3]	0.5...4 [7]-[9]	2.01381...2.13695	9.9172	2.43535	- 1.075
Wet C. [3]	0.5...4 [4]-[6]	2.01054...2.0989	9.3845	2.21002	242.225
Conc. [14]	0.25...4 [7]-[9]	1.78465...1.97743	9.5395	3.74006	1.8913
Conc. [14]	0.25...4 [4]-[6]	1.77875...1.9764	9.3627	4.77456	50.3977

extreme values of Increment, T_s (in MPa) represents tensile strength and L_{ch} (in dm) represents the characteristic length the characteristic lengths obtained by means of Carpinteri's model for the Red Felser Sandstone and Dry Concrete specimens.

The accomplished study allows the obtainment of the following conclusions: a) despite of its fruitful qualitative contribution (which allowed the derivation of Carpinteri's relations) of the Fractal Theory to the description of the size effects on fracture parameters, itself this theory cannot ensure always accurate results concerning the fracture parameters corresponding to specimens of different dimensions, b) it seems that the fractal character of fracture surfaces and the (classical) elasticity theory implications on the size-effects of fracture parameters represent cooperative processes, the most accurate descriptions implying (generally) contributions of both these factors.

4 Ultrasonic Waves, Generated by Heat Sources

Short ultrasonic pulses can be induced in solids using a range of techniques, most of them being direct contact procedures. In other words, the excitation device has to be placed directly onto the surface of a certain solid body. However, using laser energy based thermoelastic expansion of the substance [22], [23], the disadvantage of direct coupling is eliminated. In essence, a strong and short time volumic dilatation appears if a narrow and short duration beam of light, having high enough power density in its transversal section, hits a solid surface belonging to a semitransparent object. The laser energy, absorbed within the penetration depth is transformed in heat, which in its turn leads to an increase in the temperature of the irradiated portion of substance. The quick dilatation that follows is in fact the source of a high frequency elastic perturbation which propagates inside and onto the separation surface of the investigated object [24], [25].

The thermo - generation of ultrasound relies on an equation that makes the connection between the source time dependent thermal gradient and the generated elastodynamic field is needed. Secondly an equation that associate the thermal gradient with the laser generated heat distribution, $Q(r, t)$, inside the semitransparent object, is required. This connection is made by the thermal diffusion equation. The only unknown that remained to be expressed in a

mathematical form is $Q(r, t)$ which depends on the particular property of the radiated material. The heat distribution can be considered as having an exponential decay rate with the depth in substance, according to

$$Q(z, t) = F(z)G(t) = Q_0 \exp \left[-\eta^2 \left(z - \frac{h}{2} \right)^2 \right] \frac{t}{t_0} \exp \left(-\frac{t}{t_0} \right) \quad (1)$$

or can be represented as a test function - for example the bulk-like function

$$\varphi(\tau) = \begin{cases} \exp \left(\frac{1}{\tau^2 - 1} \right) & \text{if } \tau \in (-1, 1) \\ 0 & \text{otherwise} \end{cases} \quad (2)$$

or a practical test function. Unlike test functions, practical test functions can be represented as solutions of differential equations as

$$\varphi^{(2)} = \frac{6\tau^4 - 2}{(\tau^2 - 1)^4} \varphi \quad (3)$$

(generating a function similar to the bump-like function). Yet such practical test-functions possess only a finite number of continuous derivatives on the whole real axis.

Numerical simulations for an usual medium which receives a laser pulse with parameters: $t_0 = 10ns$, $Q_0 = 1x10^{15}W/m^3$ show a thermoelastically generated ultrasonic pulse traveling inside the structure with a speed less than $1cm/s$. This velocity corresponding to a certain axis can be put in correspondence with characteristics of material (characteristic length of fractal structure, for example, as was shown in previous paragraphs). However, such generalization procedures must fulfill certain requirements which are studied at this time moment by the working team:

- a) the possibility of establishing time relaxation constants for explaining propagation patterns of sound and ultrasound waves (or other type of vibrations) inside the structure
- b) the accuracy of measuring methods for propagation patterns inside materials (for selecting the proper theoretical model using measuring methods of higher accuracy)
- c) the possible implementation of specific computational architecture based on parallel computing, with many computing units (corresponding to a granular component of the material) connected in greater computing units (corresponding to medium size component of the material) and with the same type of connections implemented at a large scale, according to fractal laws.

5 Some Elements on the Physical Similitude and Fractals Theory

For a rigorous connection between propagation patterns and the structure of material, we must search for the relaxation time constants (for electromagnetic

or acoustic phenomena) as related to the fractal structure of the material. In order to do this, some elements of physical similitude and fractal theory must be taken into account.

Unlike the mathematical systems (geometrical figures, symmetry groups, polynomes, etc), whose elements are determined by a given (specific) number n_U of uniqueness parameters, the number U_i of uniqueness parameters corresponding to a physical state (or process) depends on the required accuracy, increasing with the accuracy level. If the physical dimension of a parameter specific to the studied state (or process) is:

$$[P] = \prod_{i=1}^{n_U} [U_i]^{\alpha_i} \tag{4}$$

then 2 states (or processes) S', S'' are named similar if the values of the parameters $[U_i], i = 1..n$ and P corresponding to these states fulfill the relation:

$$\frac{P'}{P''} = \prod_{i=1}^{n_U} \left(\frac{U'_i}{U''_i} \right)^{\alpha_i} . \tag{5}$$

Some of the uniqueness parameters could be similitude criteria, i.e. non dimensional parameters: $[s] = 1$, with equal values: $s' = s''$ in all similar states or processes. In the macroscopic Physics, the similitude indices α_i are integers or semi-integers, very seldom intervening other rational values. In order to explain the rather strange similitude indices intervening in the description of turbulent flows parameters, Kolmogorov proposed a hierarchical structure of vortices, the energy being injected firstly in the largest vortices and transferred in a cascade from the larger to the smaller vortices, up to the smallest ones, where the energy is dissipated. This hypothesis was strengthened by the contributions of Mandelbrot. Taking into account that (for samples of different sizes) it is difficult to have exactly equal values of all uniqueness parameters (excepting the sample size), in order to fulfill the classical relation:

$$C = L^D \tag{6}$$

(with a non-rational similitude index D , called the fractal dimension of the fractal theory), it results that the physical applications of the fractal theory correspond to the prevalence (dominance) of the size (length) uniqueness parameter. If for different size domains, the values of D belong to a set (discrete or continuous) of real numbers, the corresponding physical structure is called multi (poly)fractal. In the last years, there were published several identifications of multi (poly)fractal structures, as those corresponding to: the fracture surfaces of metals, (ii) fracture surfaces of concrete specimen, (iii) several parameters of disordered and porous media, aggregates, polymers and membranes , (iv) electrode surfaces (of fractal dimension. We have to underline that even some classical equations of the relaxation phenomena could reflect some fractal

structures. E.g., the well-known relations of Cole-Cole for dielectrics, and Mikami for magnetic materials,

$$\epsilon' = \frac{\epsilon_0 + \epsilon_\infty (i\omega\tau)^\beta}{1 + (i\omega\tau)^\beta}, \quad \chi' = \frac{\chi_0}{1 + (if/f_i)^\beta} \tag{7}$$

can be obtained starting from constitutive equations as:

$$D + \tau^\beta \frac{d^\beta D}{d\tau^\beta} = \epsilon_0 E + \epsilon_\infty \tau^\beta \frac{d^\beta E}{d\tau^\beta} \tag{8}$$

using fractional derivatives. In order to explain the appearance of both the frequency power laws and fractals, we will mention here also some theorems of the physical similitude: a) the number n_{is} of irreducible similitude numbers (criteria) corresponding to a state (or process) of a physical system is equal to the difference between the number n_U of independent uniqueness parameters and the number n_{aF} of the active fundamental physical quantities, and b) every physical law or relation can be expressed by means of some similitude numbers (criteria) and only by means of similitude criteria (Federman’s theorem).

The time constants corresponding to relaxation phenomena can be observed as time constants for transient phenomena when external pulses are applied or generated at the material surface; an accurate measurement can’t be achieved without using a great amount of energy received on a very short time interval, and ultrashort high-energy laser pulses are the best choice.

6 (Multi)Fractal Scaling and Frequency Power Laws

The fractal distribution of the main parameters (area, perimeter) of the slit islands (of steel, surrounded by nickel) of the fracture surfaces was pointed out for some steel specimen plated with electroless nickel. Assuming a similar fractal distribution of the grains of some ferrimagnetic materials, the effectively occupied (by grains) part of a volume $V = l^3$ being $V^* = l^{3-d}$ (where d is the corresponding fractal decrement), it results that the magnetic energy stored in a such material is:

$$W = \frac{B^2}{2\mu_{app}} V = \frac{B^2}{2\mu} V^* \tag{9}$$

resulting that:

$$\mu_{app} = \mu \frac{V}{V^*} = \mu l^d \Rightarrow \log \mu_{app} = \log \mu + d \log l \tag{10}$$

That is why we can compare the main parameters of the parabolic correlations:

$$\log P = c_0 + c_1 \log l + c_2 \log P^2 \tag{11}$$

corresponding to multifractal scalings of some microstructural parameters of certain alloys (steel) and of some ferrimagnetic materials, respectively. A study of the experimental results shows a multi-fractal grains size dependence of the apparent permeability of some Mn-Zn ferri-magnetic materials, somewhat similar to that reported for some steels.

Both the electromagnetic waves dispersion and the elastic waves propagation can be described by means of the 6 uniqueness parameters: specimen size D , microelements (grains, inclusions, cracks, pores, etc) size d , characteristic (wave phase, oscillations) velocity v and frequency f , the density ρ and the dynamic viscosity η of the medium. Because the above indicated phenomena have a dynamical character (with 3 active fundamental quantities), it results that the number of irreducible similitude criteria for the above processes is: $n_{is} = 6 - 3 = 3$. These irreducible similitude criteria can be chosen as: $D/d, fD/v, \rho dv/\eta$. From the Federman's theorem of the similitude theory, it results that any other physical parameter (similitude criterion) can be expressed as a function of (only) irreducible criteria:

$$P = f(D/d, fD/v, \rho dv/\eta) \quad (12)$$

According to Barenblatt's theorem, if f is a self-similar (and differentiable) function, so that $f(x_2/x_1) = f(x_2)/f(x_1)$, then $f(x) = x^{n_1}$, where $n_1 = f'_1$. From previous relations, it results for a such self-similar function:

$$P = \left(\frac{D}{d}\right)^{n_1} \left(\frac{fd}{v}\right)^{n_2} \left(\frac{\rho dv}{\eta}\right)^{n_3}, \quad \frac{P'}{P^n} = ct. \left(\frac{f'}{f^n}\right)^{n_3} \quad (13)$$

This explains the concomitant appearance of: (i) frequency power laws (of flicker noise, particularly): $P = f^{n_3}$, (ii) size effects relative to the microstructure elements sizes, (iii) size effects relative to the specimen dimensions. The concomitant presence of some frequency power laws and of the fractal scaling seems to indicate the appearance of some self-organized criticality states; it allows us to determine the fractal parameters of the material using also a set of measurements based on frequency power laws. This requires the use of continuous waves inside the material (instead of pulses) and a good intensity and frequency stabilization for the laser source.

7 Conclusions

This paper has presented an analysis of compatibility with experimental data of fractal descriptions of the fracture parameters for materials as concrete, wet concrete and red felsler sand-stone. The differences between predicted values according to certain theoretical models and experimental data were analyzed, being pointed out the fact that this aspect requires better theoretical and experimental methods. Then it was shown that major advances would be achieved if the fractal methods for spatial structure of materials would be replaced by four-dimensional fractal models able to predict also the propagation patterns of sound and ultrasound waves (or other type of vibrations) inside the structure.

By comparing the experimental patterns (an example being the heat generated ultrasound pulses in a semitransparent medium, differing to the rocks presented in first paragraph - electrical and optical insulating materials, and differing also to conductors where the small penetration depth, characteristic to conductors, acts as a singularity similar to a short impulse, leading to a very broad spectrum and to a great number of coefficients affecting the accuracy of numerical simulations) we can check the validity of theoretical models. For a better accuracy, specific computational architecture based on parallel computing (with many computing units - corresponding to a granular component of the material - connected in greater computing units corresponding to medium size component of the material and with the same type of connections implemented at large scale, according to fractal laws) should be implemented.

References

1. Bazant, Z. P.: Size effect in blunt fracture: Concrete, rock, metal, *Journal of Engineering Mechanics*, ASCE Journal of Engineering Mechanics, ASCE, **110** (1984), 518–535
2. Kim, J. K., Eo, S.H.: Size effect in concrete specimens with dissimilar initial cracks, *Magazine of Concrete Research*, **42** (1990), 233–238
3. Bazant, Z. P., Kazemi, M. T., Hasegawa, T. : Size effects in Brazilian split-cylinder tests: measurements and fracture analysis, *J. Mazers, ACI Materials Journal*, **88** (1991), 325–332
4. Carpinteri, A.: Fractal nature of material microstructure and size effects on apparent mechanical properties, *Mechanics of Materials*, **18** (1994), 89–101
5. B. B. Mandelbrot, *The Fractal Geometry of Nature*, W. H. Freeman, San Francisco, 1982
6. Rybaczuk, M., Zielinski, W. : The concept of fractal dimension, *Chaos, Solitons and Fractals*, **12**, (2001), 2517–2535 (part I) and 2537–2552 (part II)
7. M. R. A. van Vliet, Ph. D. Dissertation, Technical University of Delft, January 31, 2000
8. A. Carpinteri, F. Ferro, : Scaling behaviour and dual renormalization of experimental tensile softening responses, *Materials and Structures*, **31** (1998), 303–309
9. Carpinteri, A., Chiaia, B. : Size Effects on Concrete Fracture Energy: dimensional transition from Order to disorder, *Materials and Structures*, **29** (1996), 259–264
10. Iordache, D.: On the Compatibility of some Theoretical Models relative to the Experimental Data, *Proceedings of the 2nd Colloquium Mathematics in Engineering and Numerical Physics*, Bucharest **2** (2002), 169–176
11. Mandelbrot, B.B., Passoja, D.E., Paullay, A.J.: Fractal character of fracture surfaces of metals, *Nature*, **6** (1984), 721–722
12. Mandelbrot, B.B.: Opinions, *Fractals (Complex Geometry, Patterns, and Scaling in Nature and Society)*, 1(1), (1993), 117–123
13. Delsanto, P.P., Iordache, D., Pusca, St.: Study of the Correlations between different effective fractal dimensions used for fracture parameters descriptions, *First South-East European Symposium on Interdisciplinary approaches in fractal analysis*, Bucharest, May 7-10 (2003)
14. Carpinteri, A., Ferro, F.: Scaling behaviour and dual renormalization of experimental tensile softening responses, *Materials and Structures*, **31**, (1998), 303–309

15. Jnossy, L.: Theory and Practice of the Evaluation of Measurements, Oxford University Press, 1965
16. Gukhman, A.A.: Introduction to the Theory of Similarity, Academic Press, New York, 1965
17. Eadie, W.T., Drijard, D., James, F.E., Roos, M., Sadoulet, B.: Statistical Methods in Experimental Physics, North-Holland Publ. Company, Amsterdam-New York-Oxford, 1982
18. *** Handbook of Applicable Mathematics, chief editor Walter Ledermann, volume VI: Statistics, John Wiley & Sons, New York, 1984
19. John, P.W.M.: Statistical Methods in Engineering and Quality Assurance, John Wiley & Sons, New York, 1990
20. Levenberg, K.: A method for the solution of certain nonlinear problems in least squares, *Quart. Appl. Math.*, **2** (1944), 164–168
21. Marquardt, D.W.: An algorithm for the least-square estimation of non-linear parameters, *J. of Soc. Industr. Appl. Math.*, **11**, (1963), 431–441
22. Gaele, R., Pandora, P., Roland, O., Sophie, C., Christian, C.: Simultaneous Laser Generation and Laser Ultrasonic Detection of Mechanical Breakdown of a Coating – Substrate Interface, *Ultrasonics*, (2001)
23. Storkely, U.: GHz Ultrasound Wave Packets in Water Generated by an Er Laser, *J. Phys. D: Appl. Phys.*, (1998)
24. Kritsakorn, L., Wonsiri, P., Laurence, J.J.: Guided Lamb Wave Propagation in Composite Plate, *Journal of Engineering Mechanics*, (2002) 1337 – 1341
25. Andrea, F., Gottfried, L., Alexey, L., Peter, H.: Linear and Nonlinear Elastic Surface Waves; From Seismic Waves to Materials Science, *Analytical Sciences*, Vol. 17, (2001) 9 –12

Inner Potential of Generating Pulses as a Consequence of Recurrent Principles and Specific Computing Architecture

Cristian Morarescu

Department of Computer Science, Politehnica University, Bucharest, Romania

Abstract. This study presents the existence of inner potential of generating pulses in physics based on existence of recurrent formulation of fundamental physics principles. It is shown that basic principles in physics (like the principle of constant light in vacuum in any reference system and the uncertainty principle in quantum theory) make use in an implicit manner of terms which are defining also the conclusion. For example, the idea of constant light speed implies the use of a measuring method based on a clocks' synchronization performed using a supposed antecedent light signal transmitted and reflected towards the observer. In a similar manner, the uncertainty principle implies the existence of a measuring method for position or time correlated with a subsequent measurement for momentum or energy (measurements which also make use of position and time). For avoiding logic contradictions, it is shown that the most simple solution consists in defining the class of reference systems (large-scale elements which are not affected by propagation phenomena or interaction)) and the class of transient phenomena (small-scale bodies or waves which undergo an interaction). The inner potential of such a classification (based on different-scale elements) is also shown, together with a specific architecture.

1 Introduction

This study presents the existence of inner potential of generating pulses in physics based on existence of recurrent formulation of fundamental physics principles. It is shown that basic principles in physics (like the principle of constant light in vacuum in any reference system and the uncertainty principle in quantum theory) make use in an implicit manner of terms which are defining also the conclusion. For example, the idea of constant light speed implies the use of a measuring method based on a clocks' synchronization performed using a supposed antecedent light signal transmitted and reflected towards the observer. In a similar manner, the uncertainty principle implies the existence of a measuring method for position or time correlated with a subsequent measurement for momentum or energy (measurements which also make use of position and time). Yet a logic definition of a physics principle can not be based on the use of the same terms in both sides of it; like in the case of an algebraic calculus, the quantity to be determined must be finally placed in the opposite side of an

equality, as related to the already known quantities joined in a mathematical operation. More precisely, we can not define in a rigorous manner a certain term using the same term in the corresponding definition.

In case of the constant light speed principle (in vacuum), considered as

Definition 1. It exists a quantity *light speed in vacuum* noted as c , which is *constant* for any observer inside an inertial reference system

We can notice at first phase (**PHASE A**) that in an implicit manner the previous definition requires the existence of a measuring method for light speed in vacuum; any method for measuring a speed requires the use of time measurements (while $v = \Delta \mathbf{r} / \Delta t$). For our case (special relativity theory) the correspondence of time moments in different reference systems is based on a previous synchronization procedure implying an emission of light from an observer to another and a reflection of this light signal from the other observer to the first one; the reflection moment (considered as synchronization moment \equiv zero moment) is considered by the first observer to take place at the middle of the time interval between the initial emission of light and the return of it. But the previous definitions can be written under more compact forms

PHASE A

STEP 1

$$\left. \begin{aligned} LSpC &= Use(LW) \\ Use(LW) &= Use(SpMM) \end{aligned} \right\} \rightarrow LSpC = Use(SpMM) \quad (1)$$

(where LSPC represents the light speed constance principle, LW - a light wave, SpMM - speed measuring methods, and $f = Use(g)$ means that f makes use of g),

STEP 2

$$\left. \begin{aligned} SpMM &= Use(t) \\ Use(t) &= Use(t_0) \end{aligned} \right\} \rightarrow SpMM = Use(t_0) \quad (2)$$

(where t and t_0 represents time and the origin of time (the zero moment) respectively

STEP 3

$$\left. \begin{aligned} t_0 &= Use(SyncP) \\ Use(SyncP) &= Use(LW) \end{aligned} \right\} \rightarrow t_0 = Use(LW) \quad (3)$$

where *SyncP* denotes a synchronization procedure based on a previous light wave *LW*. The whole chain implies that the use of a wave light *LW* appears in the definition of the light speed constance principle (in vacuum) *LSpC* under an explicit form at **STEP 1**, and it appears also under an implicit form at **STEP 3**. From the formal logic point of view, this represents a contradiction. The problem is similar to aspects connected with terminological cycles [1], and a first attempt to solve it would be in taking into account the fact that **STEP 1**

and **STEP 3** corresponds to different time moments (the light wave considered at **STEP 3** corresponds to the zero moment of time, while the light wave whose speed is considered in light speed constance principle at **STEP 1** corresponds to a subsequent moment of time). This aspect is similar to computer instructions in programming language, where an instruction having the form

$$LW = f(LW) \quad (4)$$

means that at a certain step of the algorithm the previous value of variable LW_{old} is replaced by a new value LW_{new} established using a function f of the previous value (old value) of variable LW .

However, the use of such a set of different light waves (a light wave whose speed has to be measured and a previous pair of emitted-reflected light wave necessary for the synchronization procedure) implies the use of an extended time interval required by a light speed measurement as

$$T_m = [t_0, t_m] \quad (5)$$

where T_m is the time interval required by a light speed measurement at t_m time moment. But at next phase (**PHASE B**) we can notice that a speed corresponds to an almost instant moment of time, being defined as

PHASE B

STEP 1

$$v = \lim_{t \rightarrow t_m} \frac{\Delta \mathbf{r}}{\Delta t} = \frac{d\mathbf{r}}{dt} \quad (6)$$

This implies immediately that the time interval required by a speed measurement must be infinitely small

STEP 2

$$T_m = [t_m - \Delta t, t_m] \quad (7)$$

which implies that the corresponding length interval L_{T_m} is infinitely small

$$L_{T_m} \rightarrow 0 \quad (8)$$

But this is in contradiction with the previous consideration $T_m = [t_0, t_m]$ (the corresponding timelength

$$L_{T_m} = t_m - t_0 \gg 0 \quad (9)$$

can be much greater than zero. So the contradiction can be easily proved as

$$L_{TM} \rightarrow 0 \text{ and in the same time } L_{T_m} \gg 0 \quad (10)$$

From the intuitive point of view, this means that a light wave emitted in a certain reference system interacts in the most general case only on a limited time interval with another measuring reference system, the use of a previous procedure of emission-reflection for synchronization being impossible in practice. So the solution of such a contradiction (determined by implicit aspects of the terms used in definitions) must be found by taking into consideration other properties of physics entities involved in definition - see also [2].

2 Aspects Connected with Uncertainty Principle in Quantum Mechanics

If we study the uncertainty principle in quantum mechanics, we can notice quite similar aspects. According to this principle, a measurement performed with a greater accuracy upon space or time coordinates for a quantum particle must generate a greater error upon a subsequent measurement for momentum or energy, according to

$$\Delta x \Delta P_x \geq \frac{h}{4\pi} \tag{11}$$

or

$$\Delta t \Delta E \geq \frac{h}{4\pi} \tag{12}$$

But the existence of a measuring method for position or time is correlated with a subsequent measurement for momentum or energy (measurements which also make use of position and time); this can be written under the form

$$\left. \begin{aligned} (ST - M) = Use(ME - M) \\ Use(ME - M) = Use(ST - M) \end{aligned} \right\} \rightarrow (ST - M) = Use(ST - M) \tag{13}$$

(where ST-M represents the accuracy of a measuring Space or Time method and ME-M represents the accuracy of a subsequent Momentum or Energy Measurement method). It can be noticed that a term (a space-time measurements) is explained using (in an implicit manner) the same term at a subsequent moment of time. Without being a contradiction (like in the case of light speed constance principle), it still remains a recurrent definition. In the same manner presented for special relativity, we can take into consideration the different moments of time for space-time measurements. Yet the fact that (in an implicit manner) the principle requires the use of a measurement performed at a later time moment generates another logical problem: can a space-time measurement performed at a certain moment of time be influenced by previous space-time measurements performed upon the same quantum particle? When a space-time measurement belongs to the class of space-time coordinates measurement, and when it belongs to the class of momentum or energy measurements (performed in an indirect manner using also space-time measurements)? Under which circumstances a measurement can be considered as an initial action (in this case its accuracy

can be greater) or as a subsequent action (its accuracy having to be less than a certain value, according to Heisenberg relation)?. The time always appears in quantum mechanics, while two physical quantities can not be measured *exactly* at the same moment of time. Using formal logic, these aspects can be written as:

$$Ac(ST - M) \nearrow \Rightarrow Ac(ME - M) \searrow \Rightarrow Ac_{ind}(ST - M) \searrow \quad (14)$$

where $Ac(ST - M) \nearrow$ means a greater accuracy Ac for a space-time measurement, $Ac(ME - M) \searrow$ means a lower accuracy Ac for a momentum or energy measurement performed at a subsequent moment of time, and $Ac_{ind}(ST - M) \searrow$ means a corresponding lower accuracy Ac_{ind} for an indirect measuring method for momentum or energy based on a space or time measurement. So a space or time measurement ($ST - M$) performed at a certain time moment belongs to the class $Ac_{ind}(ST - M) \searrow$ (being a subsequent indirect method for measuring momentum or energy and having as a consequence a limited accuracy), or to the class $Ac(ST - M) \nearrow$ (being an initial direct method for measuring space or time and having a possible greater accuracy)? A rigorous classification according to certain patterns should be made - see also [3], taking into consideration similarities in fundamental physics laws [4]

3 Different-Scale System Properties Used for Explaining Implicit Generation of Pulses and Specific Computing Architecture

This problem suggests also a possible solution: if we continue our analysis of terms involved in measuring procedures, we can notice that both basic principles (light speed constance principle and uncertainty principle) use the term of measuring method. In an implicit manner the terms *reference system* (for special relativity theory) and *measuring system* (for quantum theory) appear. Yet a measuring system implies the fact that it is not affected by the measuring procedure (otherway the physical quantity having to be measured would possess different values, depending on this interaction). So a first conclusion appears: the measuring system must be defined at a much larger scale than the body or the wave which interacts with it. The different scale system properties must be taken into consideration from the very beginning, so as to put them into correspondence with:

- i) the class of reference systems, which are not affected by interaction (where wave trains similar to wavelets can appear [5]) and
- ii) the class of transient phenomena, which undergo specific interactions (such transient phenomena can be represented as solitary waves [6])

while estimations for the space coordinates for the source of the received wave-train, based on space relations [7] are not suitable for this purpose. As a further consequence, the constance light speed principle appears as a simple generation of another light wave (LW) when a received wave train arrives in the *material*

medium of the observer's reference system, and the uncertainty principle appears as a spread of a wave corresponding to a quantum particle by the measuring system, according to a kind of Fourier transformation performed on limited space and time intervals (the aperture and a certain working period). Due to these reasons, a specific architecture for computing such transformations requires the use of certain storage devices receiving informations as inputs (sampled in a robust manner as presented in [8] and performing well defined and robust transformations according to physics laws. Each device corresponds to a reference system (which can be considered also as measuring system), and the whole chain of such devices can be simulated by neuronal networks. Only a limited number of parameters are transformed by such a device - for example the space and time coordinates in relativity theory and Fourier distributions (as related the same spatial and temporal variables) in quantum theory, using mathematical equations with specific invariance properties -see also [9]. As has been already shown, the input of such devices corresponds to the class of transient phenomena (which are transformed) and the device performing the transformation corresponds to the class of reference systems (not affected by the input signal). Thus mathematical possibilities of generating acausal pulses as in [10] can be avoided if supplementary requirements as the invariance of quadridimensional interval when the received wave train is transformed are fulfilled (see also [11]).

4 Conclusions

This study presents the existence of inner potential of generating pulses in physics based on existence of recurrent formulation of fundamental physics principles. It is shown that basic principles in physics (like the principle of constant light in vacuum in any reference system and the uncertainty principle in quantum theory) make use in an implicit manner of terms which are defining also the conclusion. For example, the idea of constant light speed implies the use of a measuring method based on a clocks' synchronization performed using a supposed antecedent light signal transmitted and reflected towards the observer. In a similar manner, the uncertainty principle implies the existence of a measuring method for position or time is correlated with a subsequent measurement for momentum or energy (measurements which also make use of position and time). For avoiding logic contradictions, it is shown that the most simple solution consists in defining the class of reference systems (large-scale elements which are not affected by propagation phenomena or interaction)) and the class of transient phenomena (small-scale bodies or waves which undergo an interaction). The inner potential of such a classification (based on different-scale elements) is also shown. The multiscale analysis presented in this paper represents an extension of multiscale analysis of wave propagation through certain material media [12] to wave generation at interaction between a received wave-train and a material reference system [13]. Similarities with wavelets solutions of Schrodinger equation [14] will be studied in the future, for better connections with quantum theory.

References

1. Baader, F. : The instance problem and the most specific concept in the description logic w.r.t. terminological cycles with descriptive semantics, *Lecture Notes in Computer Science* **2821** (2003) 64–78
2. Toma, C.: A connection between special relativity and quantum theory based on non-commutative properties and system - wave interaction, *Balkan Physics Letters Supplement* 5 (1997), 2509–2513
3. Takeda, M., Inenaga, Sh., Bannai, H.: Discovering most classificatory patterns for very expressive pattern classes, *Lecture Notes in Computer Science* **2843** (2003) 486–493
4. Toma, C.: The advantages of presenting special relativity using modern concepts, *Balkan Physics Letters Supplement* 5 (1997), 2334–2337
5. Cattani, C.: Harmonic Wavelets towards Solution of Nonlinear PDE, *Computers and Mathematics with Applications*, 50 (2005), 1191–1210.
6. Rushchitsky, J.J., Cattani, C., Terletskaia, E.V.: Wavelet Analysis of the evolution of a solitary wave in a composite material, *International Applied Mechanics*, 40, 3 (2004), 311–318
7. Toma, C.: About some space relations of the electromagnetic interaction, *Revue Roumaine des Sciences Techniques, Serie Electrotechnique et Energetique*, **34**, 3 (1989), 431–435
8. Toma, C. : An extension of the notion of observability at filtering and sampling devices, *Proceedings of the International Symposium on Signals, Circuits and Systems Iasi SCS 2001, Romania* 233–236
9. Toma, G. : Practical test-functions generated by computer algorithms, *Lecture Notes Computer Science* **3482** (2005), 576–585
10. Toma, C.: The possibility of appearing acausal pulses as solutions of the wave equation, *The Hyperion Scientific Journal* 4 1 (2004), 25–28
11. Toma, C.: The use of the quadridimensional interval - the main possibility for improving the Lorentz formulae interpretation, *Proceedings of ECIT-97 Symposium - Pitesti (Romania)*, **2** (1997), 202–206
12. Cattani, C.: Multiscale Analysis of Wave Propagation in Composite Materials, *Mathematical Modelling and Analysis*, **8**, 4 (2003), 267–282
13. Sterian, P., Toma C.: Methods for presenting key concepts in physics for MS students by Photon-MD program, *Bulgarian Journal of Physics* **27** 4 (2000), 27–30
14. Cattani, C.: Harmonic Wavelet Solutions of the Schroedinger Equation, *International Journal of Fluid Mechanics Research* **5** (2003), 1–10

Phenomenological and State Coefficients in Viscoanelastic Medium of Order One (with Memory)

Vincenzo Ciancio, Francesco Farsaci, and Antonino Bartolotta

Department of Mathematics,
University of Messina,
Sicily, Italy
ciancio@unime.it
Institute for Chemical – Physics Processes,
C.N.R. section of Messina,
Sicily, Italy
farsaci@me.cnr.it

Abstract. The aim of this work is to indicate a method to measure experimentally some phenomenological and state coefficients, and so to verify some inequalities that follow from principle of entropy production.

In particular, we will consider the Kluitenberg-Ciancio model for a viscoanelastic medium of order one with memory and the relative rheological equation in which, neglecting cross effects between viscous and inelastic flow, four phenomenological and state coefficients appear.

Assuming an harmonic deformation as cause and the stress as effect we will compare the solution of the Kluitenberg-Ciancio's equation with a well known expression of the stress obtained, by experimental considerations in the linear response theory, as function of the frequency of deformation at a constant temperature. This comparison will be able to determine the phenomenological and state coefficients as function of frequency dependent quantities experimentally measurable.

This method will be applied to polymeric materials as Polyisobutylene.

1 Remarks on Kluitenberg-Ciancio Theory on Viscoanelastic Medium

It has been demonstrated that, for isotropic viscoanelastic medium of order one can be derived a differential equation in which phenomenological and state coefficients appear. For one-dimensional case and neglecting cross-effect between viscous and inelastic flow, has the form [1],[2]:

$$\frac{d\tau}{dt} + R_0^{(\tau)}\tau = R_0^{(\varepsilon)}\varepsilon + R_1^{(\varepsilon)}\frac{d\varepsilon}{dt} + R_2^{(\varepsilon)}\frac{d^2\varepsilon}{dt^2} \quad (1)$$

where τ is the stress and ε the shear deformation and

$$\begin{aligned} R_0^{(\tau)} &= a^{(1,1)}\eta_s^{(1,1)} & R_1^{(\varepsilon)} &= a^{(0,0)} + a^{(1,1)}\eta_s^{(1,1)}\eta_s^{(0,0)} \\ R_0^{(\varepsilon)} &= a^{(0,0)}(a^{(1,1)} - a^{(0,0)})\eta_s^{(1,1)} & R_2^{(\varepsilon)} &= \eta_s^{(0,0)} \end{aligned} \quad (2)$$

in which $a^{(0,0)}, a^{(1,1)}$ are state coefficients while $\eta_s^{(1,1)}, \eta_s^{(0,0)}$ are phenomenological coefficients related to the following physical phenomena

$$\begin{aligned} a^{(0,0)} &\Rightarrow \textit{elasticity} & \eta_s^{(1,1)} &\Rightarrow \textit{fluidity} \\ a^{(1,1)} &\Rightarrow \textit{inelasticity} & \eta_s^{(0,0)} &\Rightarrow \textit{viscosity} \end{aligned} \tag{3}$$

We purpose to relate phenomenological and state coefficients (3) to quantities which can be experimentally measured and then to verify the following inequalities, obtained by the principle of entropy production :

$$\begin{aligned} a^{(0,0)} > 0 & \quad \eta_s^{(1,1)} > 0 \\ a^{(1,1)} > 0 & \quad \eta_s^{(0,0)} > 0 \end{aligned} \tag{4}$$

2 Experimental Approach of Linear Response Theory (Single Relaxation Time)

In all that follow we assume that the temperature is constant.

Let a generic continuum medium be subject to one-dimensional harmonic shear deformation (extensive variable=cause) of the form [3]:

$$\varepsilon = \varepsilon_0 \sin \omega t \tag{5}$$

where ε_0 and $\omega = 2\pi\nu$ are respectively the amplitude and the angular frequency of the deformation. Of course the medium will oppose by a stress [4] (intensive variable=effect) of the form

$$\tau(t) = (\varepsilon_0 G_1) \sin \omega t + (\varepsilon_0 G_2) \cos \omega t \tag{6}$$

of amplitude $\tau_0 = \tau_0(\omega)$ and with a phase lag $\delta = \delta(\omega)$ where

$$G_1 = \frac{\tau_0(\omega)}{\varepsilon_0} \cos \delta(\omega) \quad G_2 = \frac{\tau_0(\omega)}{\varepsilon_0} \sin \delta(\omega) \tag{7}$$

The quantity $G_1(\omega)$ and $G_2(\omega)$ are called dynamic moduli and are related respectively to **non dissipative** phenomena and to **dissipative** ones [3],[4].

These are the quantities which will be experimentally measured and which we will show to be related to phenomenological and of state coefficients (3).

We assume (by experimental observations) that there exist two values ω_R and

ω_U , with $\omega_R < \omega < \omega_U$, such that [5]:

$$\begin{aligned} \delta(\omega) &= \delta_R \cong 0 & \text{for } \omega \leq \omega_R \\ \delta(\omega) &= \delta_U \cong 0 & \text{for } \omega \geq \omega_U \end{aligned} \tag{8}$$

$$\begin{aligned} G_1(\omega) &= G_{1R} \cong \text{const.} & \text{for } \omega \leq \omega_R \\ G_1(\omega) &= G_{1U} \cong \text{const.} & \text{for } \omega \geq \omega_U \end{aligned} \tag{9}$$

And consequently from (7):

$$\begin{aligned} G_2(\omega) &= G_{2R} \cong 0 & \text{for } \omega \leq \omega_R \\ G_2(\omega) &= G_{2U} \cong 0 & \text{for } \omega \geq \omega_U \end{aligned} \tag{10}$$

Moreover we assume that $\tau_0(\omega)$ as $G_1(\omega)$ are increasing continuous and derivable functions for $\omega_R < \omega < \omega_U$. From equations (7) it follows:

$$\begin{aligned} G_1(\omega_R) &= \frac{\tau_0(\omega_R)}{\epsilon_0} \cos \delta(\omega_R) = \frac{\tau_{0R}}{\epsilon_0} = G_{1R} ; \\ G_1(\omega_U) &= \frac{\tau_0(\omega_U)}{\epsilon_0} \cos \delta(\omega_U) = \frac{\tau_{0U}}{\epsilon_0} = G_{1U} \end{aligned} \tag{11}$$

where obviously result

$$G_{1R} < G_{1U} \tag{12}$$

G_{1R} represents the value assumed by $G_1(\omega)$ when the deformation is so slow that the medium remain near the mechanical equilibrium state (low frequency) [5]; while G_{1U} represent the value assumed by $G_1(\omega)$ when the deformation changes so rapidly that no relaxation has time to occur (high frequency) [5].

3 Viscoelastic Medium of Order One (with Memory)

Let an isotropic viscoelastic medium of order one be subject to one-dimensional harmonic shear deformation (extensive variable=cause) of the form (5). In such a way the equation (1) become

$$\frac{d\tau}{dt} + \frac{\tau}{\sigma} = \alpha \sin \omega t + \beta \cos \omega t \tag{13}$$

where

$$\begin{aligned} \alpha &= (R_0^{(\varepsilon)} - \omega^2 R_2^{(\varepsilon)}) \varepsilon_0 \\ \beta &= R_1^{(\varepsilon)} \varepsilon_0 \omega \\ \sigma &= \frac{1}{R_0^{(\tau)}} \end{aligned} \tag{14}$$

where σ is the relaxation time, experimentally measurable [5].

Our viewpoint is such that we consider \mathcal{E} (extensive variable) as cause and τ (intensive variable) as effect; this allows us to study relaxation phenomena.

The solution of (13) is

$$\tau(t) = \tau_0(\omega) \sin[\omega t + \delta(\omega)] \tag{15}$$

provided that

$$\begin{aligned} \tau_0(\omega) &= \sqrt{\frac{(\alpha^2 + \beta^2)\sigma^2}{1 + \omega^2\tau^2}} \\ \cos \delta(\omega) &= \frac{\alpha + \beta\omega\sigma}{\sqrt{(1 + \omega^2\sigma^2)(\alpha^2 + \beta^2)}} \\ \sin \delta(\omega) &= \frac{\beta - \alpha\omega\sigma}{\sqrt{(1 + \omega^2\sigma^2)(\alpha^2 + \beta^2)}} \end{aligned} \tag{16}$$

Since, equations (6) and (15) are two mathematical representations of the same phenomena, identifying these equations one has

$$\frac{\alpha\sigma + \beta\omega\sigma^2}{1 + \omega^2\sigma^2} = \varepsilon_0 G_1 \qquad \frac{\beta\sigma - \alpha\omega\sigma^2}{1 + \omega^2\sigma^2} = \varepsilon_0 G_2 \tag{17}$$

which together (14)_{1,2} become :

$$R_0^{(\varepsilon)} = \frac{R_2^{(\varepsilon)}\omega^2\sigma + G_1 - G_2\omega\sigma}{\tau} \qquad R_1^{(\varepsilon)} = \frac{G_2 + G_1\omega\sigma}{\omega\sigma} \tag{18}$$

Taking in account (2) and (14) it follows from (18)

$$\begin{aligned} a^{(0,0)}(a^{(1,1)} - a^{(0,0)})\eta_s^{(1,1)} &= \frac{\eta_s^{(0,0)}\omega^2\sigma + G_1 - G_2\omega\sigma}{\sigma} \\ a^{(0,0)} + a^{(1,1)}\eta_s^{(1,1)}\eta_s^{(0,0)} &= \frac{G_2 + G_1\omega\sigma}{\omega\sigma} \\ a^{(1,1)}\eta_s^{(1,1)} &= \frac{1}{\sigma} \end{aligned} \tag{19}$$

This is an algebraic system made by three equations with four unknown functions $a^{(0,0)}, a^{(1,1)}, \eta_s^{(1,1)}, \eta_s^{(0,0)}$; G_1, G_2 and σ can be experimentally measured. To complete the system (31) we need a fourth equation that can be derived observing that for sufficiently small ω from (1) and (11) it follows:

$$\tau_{0R} = G_{1R} \varepsilon_0 \quad R_0^{(\tau)} \tau = R_0^{(\varepsilon)} \varepsilon \tag{20}$$

In such conditions, taking in account equations (2), from equations (20) it follows:

$$G_{1R} = \frac{a^{(0,0)}(a^{(1,1)} - a^{(0,0)})}{a^{(1,1)}} \tag{21}$$

so we have obtained the fourth equation to add to the system (19).

The solution of such a system is:

$$\begin{aligned} a^{(0,0)}(\omega) &= \frac{G_1(1 + \omega^2 \sigma^2) - G_{1R}}{\omega^2 \sigma^2} \\ a^{(1,1)}(\omega) &= \frac{1}{\omega^2 \sigma^2} \left\{ \frac{[G_1(1 + \omega^2 \sigma^2) - G_{1R}]^2}{(G_1 - G_{1R})(1 + \omega^2 \sigma^2)} \right\} \\ \eta_s^{(1,1)}(\omega) &= \omega^2 \sigma \left\{ \frac{(G_1 - G_{1R})(1 + \omega^2 \sigma^2)}{[G_1(1 + \omega^2 \sigma^2) - G_{1R}]^2} \right\} \\ \eta_s^{(0,0)}(\omega) &= \frac{G_{1R} + G_2 \omega \sigma - G_1}{\omega^2 \sigma} \end{aligned} \tag{22}$$

So we have obtained the variables $a^{(0,0)}, a^{(1,1)}, \eta_s^{(1,1)}, \eta_s^{(0,0)}$ as function of the quantity experimentally determinable G_1, G_2 and σ .

The equations (22)_{1,2,3} satisfy the inequalities (4), while the equation (22)₄ is positive for those values of $G_1(\omega), G_2(\omega)$ and ω that satisfy the following inequality

$$G_{1R} + G_2 \omega \sigma - G_1 > 0 \tag{23}$$

We will observe that if dissipative phenomena are present (related to G_2) the inequalities (23) will not be verified as we can see in the application on Polyisobutylene shown in fig. 1.

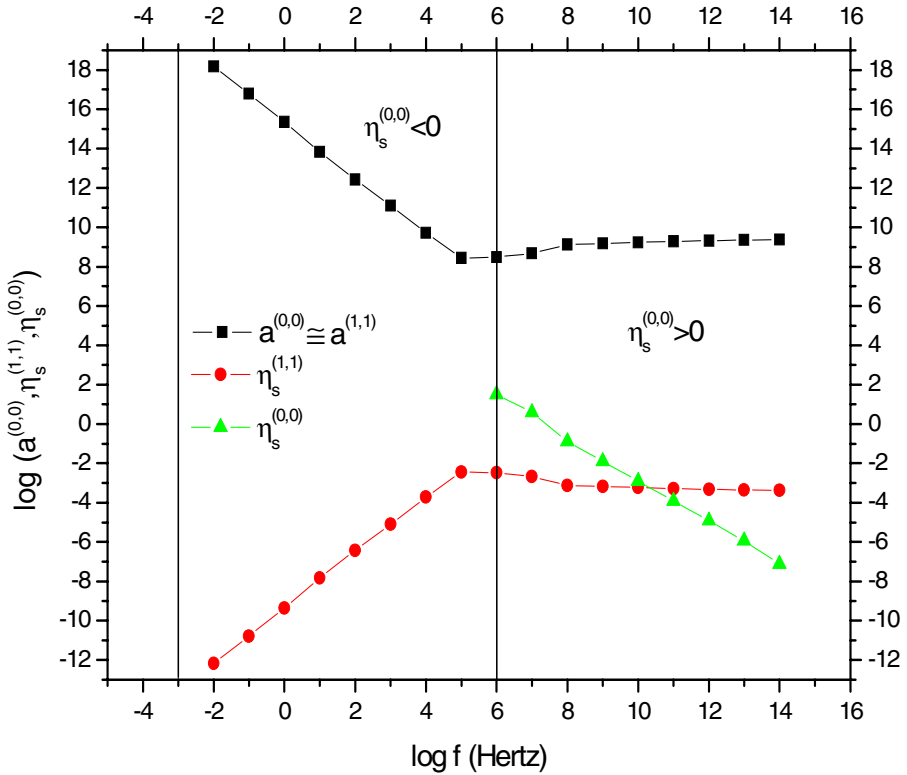


Fig. 1. Poly-isoButylene; M.w. = 106 g/mol; T₀ = 273 K (G_{IR} ≅ 10^{5.4}Pa; G_{IU} ≅ 10^{9.38} Pa; σ ≅ 10⁻⁶ s)

References

- [1] Kuitenberg G.A. and Ciancio V. 1978. On linear dynamical equation of state for isotropic media I. *Physica* 93 A: 273-286.
- [2] Ciancio V. and Kluitenberg G.A. 1979. On linear dynamical equation of state for isotropic media II. *Physica*, 99A: 592-600.
- [3] *Comprehensive polymer science* vol 2, chp.16, eds. Sir G. Allen, J.C. Bevington. Pergamon press, 1989.
- [4] Ward I.M., Hadley D.W., *An Introduction to the mechanical properties of solid polymers*, 1993. Wiley.
- [5] N.G. McCrum, B.E. Read, G.Williams, *Anelastic and Dielectric Effects in Polymeric Solids*, John Wiley&Sons, London-New York, Sydney, 1967.

Appendix A. Comments to Figure 1

In fig.1 $a^{(0,0)}, a^{(1,1)}, \eta_s^{(1,1)}, \eta_s^{(0,0)}, R_1^\varepsilon$ as function of the frequency at a fixed temperature $T_0=273$ K are plotted for a polymeric material as PolyIsobutylene. We know perfectly that this material has not a linear behaviour in all the range of frequency that we have chosen, but we can approximately deduce some qualitative information by curves plotted in fig.1. Obviously, from (20) and (21) it follows that $R_0^{(\varepsilon)}$ and $R_0^{(\tau)}$ will be constant for any value of the frequency.

- 1) The coefficients $a^{(0,0)}$ and $a^{(1,1)}$ differ not much and show the same trend; this means that the medium will not presents great memory effects. Moreover, observing $\eta_s^{(1,1)}$ we can see a reciprocal trend with respect to $a^{(1,1)}$, as predict by (19)₃.
- 2) Every curve, except $\eta_s^{(0,0)}$, present an almost constant trend for $\omega > 2\pi 10^9$; this mean that elastic and inelastic properties of the medium don't change in this range of frequencies. While the trend of $\eta_s^{(0,0)}$ (relate to dissipative phenomena) show a decreasing of viscous effects for $\omega > 2\pi 10^6$. The inequalities (4) are verified.
- 3) For $\omega < 2\pi 10^6$ we observe that $\eta_s^{(0,0)}$ shows negative values in contrast with inequalities (4); this mean that, in this range of frequencies, non linear effects are present (this is confirmed by the trend of G_1 and G_2 experimentally measured). Then, in such a region, our coefficients represent the mechanical behaviour of the medium in an approximate way.

Analysis of Singularities by Short Haar Wavelet Transform

Armando Ciancio¹ and Carlo Cattani²

¹ Dip. di Matematica , Univ. di Messina, c.da Papardo,
salita Sperone 31, I-98166 Messina, Italy
aciancio@unime.it

² DiFarma, Università di Salerno, Via Ponte Don Melillo, I-84084 Fisciano (SA)
ccattani@unisa.it

Abstract. Wavelets give significant information on the evolution of a time series. In particular, due to their localization properties the significant local changes in observed data (both in time and in frequency) can be easily detected by a limited set of their corresponding wavelet coefficients. Some examples will be given, in the following, showing the effectiveness of this method.

Keywords: Wavelets, Jumps, Haar, time series.

1 Introduction

Wavelets are one of the most significant tool for the analysis of signals, because of their good localization either in time such as Haar, Daubechies, Symlet, Coiflets, etc...[12, 11], or frequency (as harmonic, Shannon, Meyer). The first group of wavelets are useful when we want to decompose a signal into uncorrelated components, and, in particular, we want to single out localized sharp jumps (in time). The second group of wavelets, instead make possible to detect sharp jumps in frequency. However, it is possible to refine the Haar wavelet transform (by using th so-called short Haar wavelet transform [2, 3, 4, 5, 6, 8, 10]) in such way to improve the local analysis both in time and in frequency. Sharp changes can be detected by analysing the wavelet coefficients (in general), but more in particular by focussing only on a few of them [2, 10].

It is well known [13, 14, 15], that each time-series might be roughly represented by the composition of a sequence of high and low frequency “small” waves with a trend. These waves have bounded frequencies, and are localized according to the fact that what happen at a given time t , in general, has a negligible influence (correlation) with the other data at time $t' \gg t$. Due to these properties, the local properties of the time-series are well described by a reduced number of wavelet coefficients, i.e. one can choose a limited number of the basis (wavelet) functions to locally represent the time-series. As a consequence, the local analysis can be improved by slicing the time-series of length N into a set of small segments of length p ($= N/\sigma$) (at a fixed time intervals) and analysing each segment.

We propose a method (see also [2, 10]) based on the following steps:

1. The sequence of N data is sliced into σ short segments of p ($= N/\sigma$) data.
2. Each segment is transformed by using the discrete wavelet transform into the finite length p vector of the wavelet coefficients. So that locally the time-series is characterized by the wavelet coefficients restricted to the indexed segment.
3. The jumps (and anomalies) might be easily detected by the relations existing between the wavelet coefficients, i.e. according to the relations among the wavelet coefficients independently on the chosen wavelet basis.

In doing so only the first set of detail coefficients are considered for the analysis and moreover the computational complexity is strongly reduced. With some examples given in the following, we will see that jumps are strictly connected with detail coefficients.

2 Short Haar Discrete Wavelet Transform

Let $\mathbf{Y} \equiv \{Y_i\}$, ($i = 0, \dots, 2^M - 1$, $2^M = N < \infty$, $M \in \mathbb{N}$), be a real and square summable denoised (see e.g. [2, 3, 4, 8, 7]) time-series $\mathbf{Y} \in \mathbb{K}^N \subset \ell^2$ (where \mathbb{K} is a real field); $t_i = i/(2^M - 1)$, is the regular equispaced grid of *dyadic points* on the interval restricted, for convenience and without restriction, to $\Omega = [0, 1]$.

The *Haar scaling function* $\varphi(t)$ is the characteristic function on $[0, 1]$; its family of translated and dilated scaling functions is defined (in $[0, 1]$) as

$$\begin{cases} \varphi_k^n(t) \equiv 2^{n/2} \varphi(2^{n t} - k) , & (0 \leq n , 0 \leq k \leq 2^n - 1) , \\ \varphi(2^{n t} - k) = \begin{cases} 1 , & t \in \Omega_k^n \\ 0 , & t \notin \Omega_k^n . \end{cases} & \Omega_k^n \equiv \left[\frac{k}{2^n} , \frac{k+1}{2^n} \right) , \end{cases} \quad (2.1)$$

The *Haar wavelet* family $\{\psi_k^n(t)\}$ is the orthonormal basis for the $L^2([0, 1])$ functions [12]:

$$\begin{cases} \psi_k^n(t) \equiv 2^{n/2} \psi(2^{n t} - k) , & \|\psi_k^n(t)\|_{L^2} = 1 , \\ \psi_k^n(t) = \begin{cases} -2^{-n/2} , & t \in \left[\frac{k}{2^n} , \frac{k+1/2}{2^n} \right) , \\ 2^{-n/2} , & t \in \left[\frac{k+1/2}{2^n} , \frac{k+1}{2^n} \right) , \\ 0 , & \text{elsewhere .} \end{cases} & (0 \leq n , 0 \leq k \leq 2^n - 1) , \end{cases} \quad (2.2)$$

Although, without loss of generality, we restrict ourselves to $0 \leq n , 0 \leq k \leq 2^n - 1 \implies \Omega_k^n \subseteq [0, 1]$, for other integer values of k the family of the Haar scaling functions and wavelets are defined also outside $[0, 1]$ making possible to extend the following considerations to any interval of \mathbb{R} .

The wavelet transform (2.3) implies the computation of $N = 2^M$ wavelet coefficients, at the resolution M , with N basis functions $\psi_k^n(t)$ involved, and a computation complexity $\mathcal{O}(N^2)$. However, as shown in [2, 3, 4], if we consider only $p = 2^m \leq N$ basis functions the complexity reduces to $\mathcal{O}(pN)$. This corresponds to slicing the data with a fixed window, as it is usually done, for instance, in the local sine and cosine transforms or in the wavelet packet decomposition [1, 11]. With the short Haar transform it is possible both to reduce the number of basis functions and the computational complexity.

Algorithm 1. *Let the set $\mathbf{Y} = \{Y_i\}$ of N data, segmented into σ segments (in general) of different length, each segment \mathbf{Y}^s , $s = 0, \dots, \sigma - 1$ is made of $p_s = 2^{m_s}$, ($\sum_s p_s = N$), data:*

$$\mathbf{Y} = \{Y_i\}_{i=0, \dots, N-1} = \bigoplus_{s=0}^{\sigma-1} \{\mathbf{Y}^s\}, \quad \mathbf{Y}^s \equiv \{Y_{sp_s}, Y_{sp_s+1}, \dots, Y_{sp_s+p_s-1}\},$$

being, in general, $p_s \neq p_r$. The adapted discrete Haar wavelet transform of \mathbf{Y} is $\mathcal{W}^{p_s, \sigma} \mathbf{Y}$, being explicitly

$$\left\{ \begin{array}{l} \mathcal{W}^{p_s, \sigma} \equiv \bigoplus_{s=0}^{\sigma-1} \mathcal{W}_s^{p_s}, \quad \mathbf{Y} = \bigoplus_{s=0}^{\sigma-1} \mathbf{Y}^s, \\ \mathcal{W}^{p_s, \sigma} \mathbf{Y} = \left(\bigoplus_{s=0}^{\sigma-1} \mathcal{W}_s^{p_s} \right) \mathbf{Y} = \left(\bigoplus_{s=0}^{\sigma-1} \mathcal{W}_s^{p_s} \mathbf{Y}^s \right), \\ \mathcal{W}^{2^{m_s}} \mathbf{Y}^s = \left\{ \alpha_0^{0(s)}, \beta_0^{0(s)}, \beta_0^{1(s)}, \beta_1^{1(s)}, \dots, \beta_{2^{m_s}-1}^{m_s-1(s)} \right\}, \quad (2^{m_s} = p_s, \sum_{s=0}^{\sigma-1} p_s = N), \end{array} \right.$$

being $\mathcal{W}^N : \mathbb{K}^N \subset \ell^2 \rightarrow \mathbb{K}^N \subset \ell^2$ the discrete Haar wavelet transform which associates to a given finite energy vector \mathbf{Y} the finite energy vector of the wavelet coefficients $\{\alpha, \beta_k^n\}$:

$$\mathcal{W}^N \mathbf{Y} = \{\alpha, \beta_0^0, \dots, \beta_{2^M-1}^{M-1}\}, \quad \mathbf{Y} = \{Y_0, Y_1, \dots, Y_{N-1}\}, \quad (2^M = N). \tag{2.3}$$

In the following we will consider only the case, when $p_s = p = N/\sigma$, $s = 0, \dots, \sigma - 1$, ($\sigma > 1$) [2, 3, 4, 5, 6, 8, 7] so that the data slices have the same length. When $p_s = p = N$, $\sigma = 1$, the above coincides with the ordinary wavelet transform.

In general, for a vector of 2^M elements, $\mathbf{Y} = \{Y_i\}_{i=0, \dots, 2^M-1}$, the Haar wavelet transform is the vector $\mathcal{W}^{2^M} \mathbf{Y}$, while there are different short wavelet transforms that can be done with one of the following matrices, even if the resulting piecewise interpolation will be the same. There follows that, in order to transform the vector \mathbf{Y} , instead to use the $N \times N$ matrix \mathcal{W}^N up to the resolution $M = \log_2 N$, we can use the $N \times N$ matrix $\mathcal{W}^{p_s, \sigma}$, which is the direct sum of $p_s \times p_s$ matrices:

$$\mathcal{W}^{p_s, \sigma} = \bigoplus_{s=0}^{\sigma-1} \mathcal{W}_s^{p_s}.$$

For example the reduced wavelet transform $\mathcal{W}^{4,2}$, is:

$$\mathcal{W}^{4,2} = \mathcal{W}^4 \oplus \mathcal{W}^4 = \begin{pmatrix} \mathbf{W}^4 & \mathbf{0} \\ \mathbf{0} & \mathbf{W}^4 \end{pmatrix}$$

and explicitly

$$\mathcal{W}^{4,2} = \mathcal{W}^4 \oplus \mathcal{W}^4 = \begin{pmatrix} \frac{1}{2} & \frac{1}{2} & \frac{1}{2} & \frac{1}{2} & 0 & 0 & 0 & 0 \\ -\frac{1}{2} & -\frac{1}{2} & \frac{1}{2} & \frac{1}{2} & 0 & 0 & 0 & 0 \\ -\frac{1}{\sqrt{2}} & \frac{1}{\sqrt{2}} & 0 & 0 & 0 & 0 & 0 & 0 \\ 0 & 0 & -\frac{1}{\sqrt{2}} & \frac{1}{\sqrt{2}} & 0 & 0 & 0 & 0 \\ 0 & 0 & 0 & 0 & \frac{1}{2} & \frac{1}{2} & \frac{1}{2} & \frac{1}{2} \\ 0 & 0 & 0 & 0 & -\frac{1}{2} & -\frac{1}{2} & \frac{1}{2} & \frac{1}{2} \\ 0 & 0 & 0 & 0 & -\frac{1}{\sqrt{2}} & \frac{1}{\sqrt{2}} & 0 & 0 \\ 0 & 0 & 0 & 0 & 0 & 0 & -\frac{1}{\sqrt{2}} & \frac{1}{\sqrt{2}} \end{pmatrix} \tag{2.4}$$

More in general for σ segments of length 4, we have the 4σ order matrix

$$\mathcal{W}^{4,\sigma} = \mathcal{W}^4 \oplus \mathcal{W}^4 = \begin{pmatrix} \mathcal{W}^4 & & & \mathbf{0} \\ & \ddots & & \\ \mathbf{0} & & \ddots & \\ & & & \mathcal{W}^4 \end{pmatrix}$$

3 Wavelet Analysis of Jumps

Let us consider first a sharp jump in time-space and for this let us take the 4-length segment \mathbf{Y} where is located the jump X i.e.

$$|X| \gg |Y_0| \cong |Y_1| \cong |Y_2| , \tag{3.1}$$

We can have three different situation:

1. X is the third or fourth value of the sequence. Let it be

$$\mathbf{Y} = \{Y_0, Y_1, Y_2, X\} .$$

By explicitly computing the wavelet coefficients we have:

$$\begin{aligned} \alpha &= \frac{1}{4} (Y_0 + Y_1 + Y_2 + X) , \\ \beta_0^0 &= \frac{1}{2} (-Y_0 - Y_1 + Y_2 + X) , \\ \beta_0^1 &= \frac{1}{\sqrt{2}} (Y_1 - Y_0) , \\ \beta_1^1 &= \frac{1}{\sqrt{2}} (X - Y_2) , \end{aligned}$$

so that, according to (3.1),

$$|\alpha| \gg 0 , |\beta_0^0| \gg 0 , \beta_0^1 \cong 0 , |\beta_1^1| \gg 0$$

This condition holds, analogously if X is the third value of the sequence, i.e.

$$\mathbf{Y} = \{Y_0, Y_1, X, Y_2\} .$$

2. X is the first or second value of the sequence, like e.g.

$$\mathbf{Y} = \{Y_0, X, Y_1, Y_2\} .$$

In this case there results:

$$|\alpha| \gg 0 , |\beta_0^0| \gg 0 , |\beta_0^1| \gg 0 , \beta_1^1 \cong 0$$

Therefore we can conclude that if one of the detail coefficient β_k^1 , $k = 0, 1$ is very large and the other is very small than we can assume that there is a significant jump. More in general for a different scale analysis, by using the wavelet transform \mathcal{W}^N , ($N = 2^M$) we can say that the condition for the existence of a jump is that all the finest detail coefficients β_k^{M-1} are vanishing but one which is very large.

As a second case, let us consider a sharp jump in frequency-space and for this let us take the 4-length segment \mathbf{Y}^s with

$$\mathbf{Y}^s = \{0, \sin \frac{1}{3}\omega, \sin \frac{2}{3}\omega, \sin \omega\} ,$$

and the subsequent segment

$$\mathbf{Y}^{s+1} = \{0, \sin \frac{1}{3}\Omega, \sin \frac{2}{3}\Omega, \sin \Omega\} .$$

with different frequency. The corresponding wavelet coefficients are:

$$\begin{aligned} \alpha^{(s)} &= \frac{1}{4} \left(\sin \frac{1}{3}\omega + \sin \frac{2}{3}\omega + \sin \omega \right) , \\ \beta^{(s)0}_0 &= \frac{1}{2} \left(-\sin \frac{1}{3}\omega + \sin \frac{2}{3}\omega + \sin \omega \right) , \\ \beta^{(s)1}_0 &= \frac{1}{\sqrt{2}} \sin \frac{1}{3}\omega , \\ \beta^{(s)1}_1 &= \frac{1}{\sqrt{2}} \left(-\sin \frac{2}{3}\omega + \sin \omega \right) , \end{aligned}$$

and analogously for the slice $s + 1$ (where $\Omega \rightarrow \omega$). There follows that, the change in the frequency can be immediately detected by the ratio

$$\frac{\beta^{(s+1)1}_0}{\beta^{(s)1}_0} = \frac{\sin \frac{1}{3}\Omega}{\sin \frac{1}{3}\omega}$$

which is different from 1 in case of a frequency variation. Thus if the frequency is growing we have

$$\alpha^{(s+1)} > \alpha^{(s)} , \beta^{(s+1)0}_0 > \beta^{(s)0}_0 , \beta^{(s+1)1}_0 > \beta^{(s)1}_0 , \beta^{(s+1)1}_1 > \beta^{(s)1}_1 .$$

the contrary if the frequency is lowering (see Fig. 2).

4 Examples of Jump Detection by Wavelets

We consider in the following four one-dimensional examples of jumps and an example of a jump in a two dimensional array.

Example 1. Let us take, the sequence of numbers $\{1, 2, 3, 9, 10, 11, 12, 13\}$, the reduced wavelet transform gives as wavelet coefficients $\{1.5, 0.7071\}$, $\{6, 4.2426\}$, $\{10.5, 0.7071\}$, $\{12.5, 0.7071\}$. The first coefficient of each group reflects the average value (see e.g [2, 3, 4, 9]) while the second coefficient is proportional to the difference of each pair of values. Thus we can say that the second segment with the highest coefficient $\beta^0_0 = 4.2426$, shows the presence of a jump. Applying the short wavelet tranform $\mathcal{W}^{(2,4,2),3}$ we have the following coefficients $\{1.5, 0.7071\}$, $\{8.25, 4.5, 4.2426, 0.7071\}$, $\{12.5, 0.7071\}$. In this case both wavelet coefficients of the second slice, namely $\beta^0_0 = 4.5$, $\beta^1_0 = 4.2426$, represent the jump in correspondence on the third-fourth element of the initial sequence of numbers.

Example 2. Starting from the following function (see Figure 1):

$$y(t) = \begin{cases} t & , t \in (0, t^*] \\ t^* + t & , t \in (t^*, 1] \\ 0 & , \text{elsewhere} , \end{cases}$$

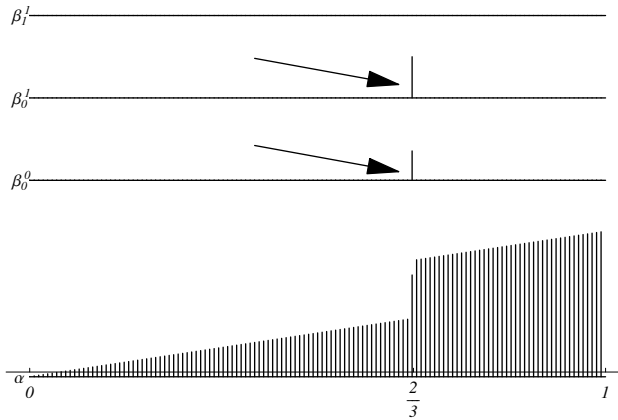


Fig. 1. Wavelet jump detection in time $t^* = 2/3$

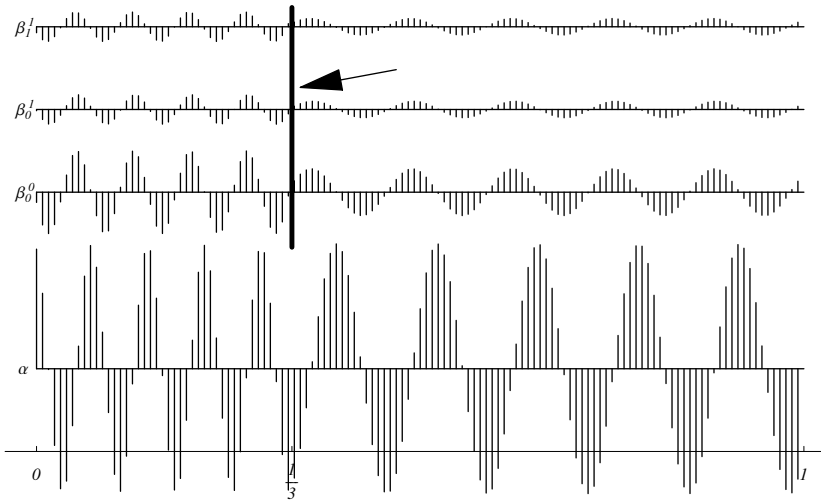


Fig. 2. Wavelet jump detection in frequency $t^* = 1/3$

let us discretize in equispaced dyadic points in order to construct a sequence \mathbf{Y} having a jump in correspondence of t^* . The data \mathbf{Y} are then defined by a sufficient fine dyadic discretization (512 points) of $y(t)$. By computing the wavelet coefficients it is easily (and exactly) shown in each coefficient where the jump occurs (see Figure 1, bottom left).

Example 3. Frequency sorting can be considered as the problem of detecting the point where there is a sharp change in frequency in the signal, or, equivalently a jump in the frequency.

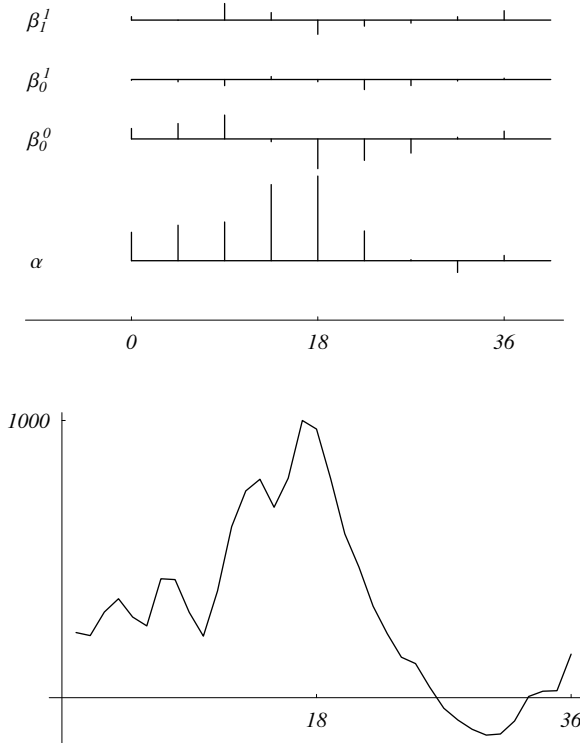


Fig. 3. Wavelet jump detection in a time series of experimental data

Let us consider the following function

$$y(t) = \begin{cases} S_1(t) & , t \in (0, t^*] \\ S_2(t) & , t \in (t^*, 1] \\ 0 & , \text{elsewhere} \end{cases}$$

being

$$S_1(t) = A_1 \cos \omega t \quad , \quad S_2(t) = A_2 \cos \omega t .$$

It is well known that the Fourier transform does not allow to single out the point t^* where there is a jump in the frequency. This point, instead can be easily detected by the above wavelet technique. Assuming $A_1 = A_2 = \sqrt{2}$, $\omega_1 = 27\pi$, $\omega_2 = 15.2\pi$ and discretize the function $y(t)$, in a sufficiently fine dyadic grid (512 points) of the interval $[0, 1]$, it is recovered (see Figure 2) the point $1/3$ where the frequency changes.

Example 4. In Figure 3 it is shown how sharp jumps can be detected in a time series of experimental data. Since they are, in general, uncorrelated there will be more frequent changes both in time-space and in frequency-space.

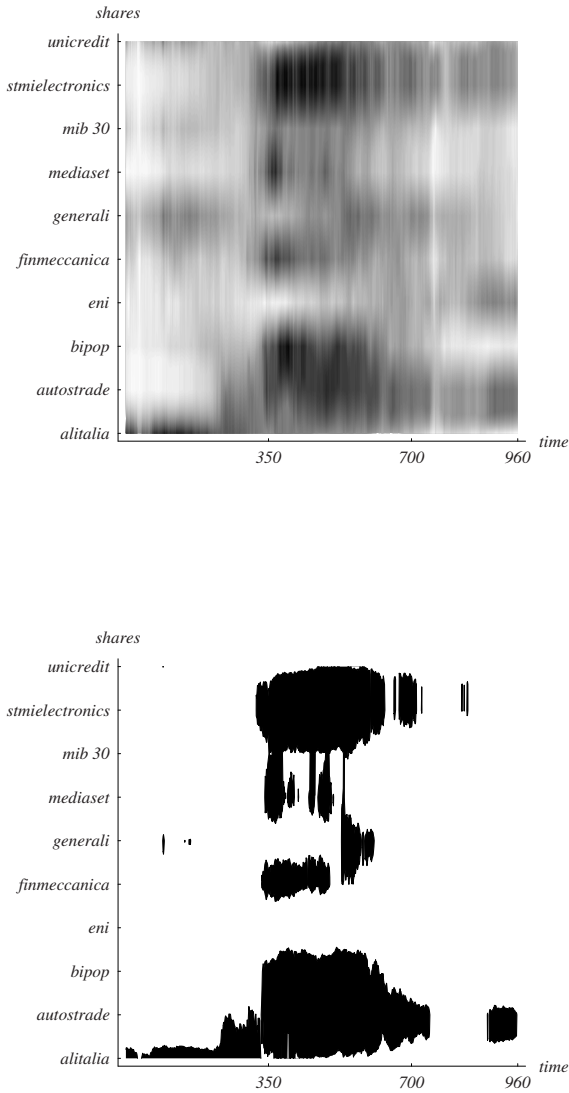


Fig. 4. Array of data (shares) focussing on the highest values (at the highest scale)

Example 5. As a last example, let us consider a 2-dimensional array of points obtained as a collection of 10 stock shares (alitalia, autostrade, bipop, eni, finmeccanica, generali, mediaset, mib 30, stmielectronics, uncredit) of the Italian Stock Market collected during the time interval 3/01/2000 until 3/01/2003, for a length of 960 data each. This array contains 9600 data. If we remove by a wavelet threshold the lowest values of the coefficients we obtain the representation of Fig. 4. From this figure we can focus on autostrade-data and represent

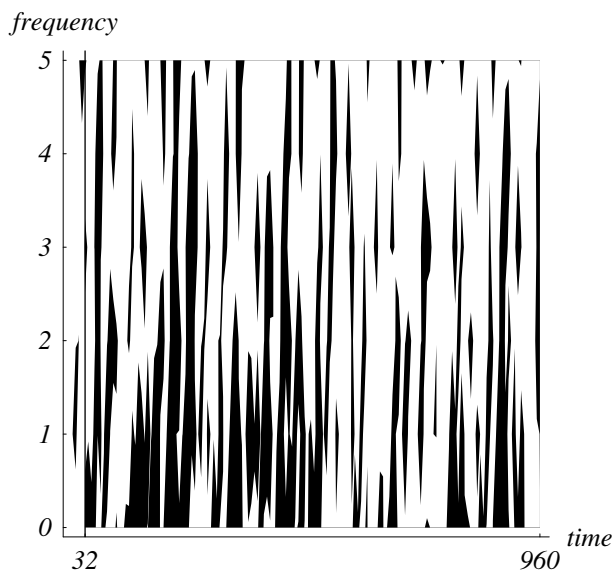


Fig. 5. Short wavelet transform (of 16-parameters) showing the highest values in frequency in corresponding of the jumps

its 16-parameters short wavelet transform (see Fig. 5), thus showing the highest values of wavelet coefficients (at the higher scales) in correspondence of jumps.

References

1. A. Auscher, G. Weiss and M.V. Wickerhauser, Local sine and cosine bases of Coifman and Meyer and the construction of smooth wavelets, *Wavelets: A tutorial in Theory and Applications*, C.K. Chui (ed.), Academic Press, San Diego, 237-256, (1992).
2. C. Cattani, "Haar Wavelet based Technique for Sharp Jumps Classification", 39, (2004) 255-279.
3. C. Cattani, "Wavelet Analysis of Nonlinear Dynamical Systems", Bulletin of Academy of Sciences of Moldova, Mathematics, (Buletinul Academiei de Stiinte a Republicii Moldova, Matematica), Nr. 1 (41), (2003), 58-69.
4. C. Cattani, "Wavelet Analysis of Dynamical Systems", Electronics and Communications, 17, (2002), 115-124.
5. C. Cattani, Reduced Haar Wavelet Spline Analysis, *Pharos*, 8 (1), 47-62 (2001).
6. C. Cattani, Haar Wavelet Spline, *Journal of Interdisciplinary Mathematics*, 4 (1), 35-47, (2001).
7. C. Cattani and A. Ciancio, "Wavelet estimate of time series", *Atti Accademia dei Pericolanti, Classe I, Scienze Fis. Mat. e Nat.*, vol. LXXIX (2001), 105-116.
8. C. Cattani and A. Ciancio, Spike Sorting by Wavelet Time Decomposition, *Rend. Seminario Matem. di Messina, Ser. II*, 8, 1-12, (2001).
9. C. Cattani and A. Ciancio, Energy wavelet analysis of time series, *Atti Accademia Peloritana dei Pericolanti, Classe I, Scienze Fis. Mat. e Nat.*, vol. LXXX, 67-77, (2002).

10. C.Cattani and A.Ciancio, "Jumps Detection by Adapted Haar Wavelet Time Decomposition", U.P.B. Scientific Bulletin of Politechnic University of Bucharest, Series A: Applied Mathematics and Physics vol 66, No 1-4 (2004) 13-22.
11. R.Coifman and Y.Meyer, Remarques sur l'analyse de Fourier á fenetre, *Comptes Rendus de l'Académie des Sciences de Paris*, **312**, 259-261, (1991).
12. I. Daubechies, *Ten lectures on wavelets*, CBMS-NSF Regional Conference Series in Applied Mathematics, SIAM, Philadelphia (1992).
13. E.Hulata, R.Segev and E.Ben-Jacob, A method for spike sorting and detection based on wavelet packets and Shannon's mutual information, *Journal of Neuroscience Methods*, **117**, 1-12, (2002).
14. D.B.Percival and A.T.Walden, *Wavelet Methods for Time Series Analysis*, Cambridge University Press, Cambridge, (2000).
15. O.A.Rosso, S.Blanco, J.Yordanova, V.Kolev, A.Figliola, M.Schürmann and E.Basar, Wavelet entropy: a new tool for analysis of short duration brain electrical signals, *Journal of Neuroscience Methods*, **105**, 65-75, (2000).

Spatial Aspects of Interaction Between High-Energy Pulses and Waves Considered as Suddenly Emerging Phenomena

Alexandru Toma¹, Stefan Pusca², and Cristian Morarescu³

¹ Marin Preda College, Department of Mathematics and Informatics, Bucharest, Romania

² Politehnica University, Department of Physics, Bucharest, Romania

³ Politehnica University, Department of Computers, Bucharest, Romania

Abstract. As it is known, practical test-functions are very useful for modeling suddenly emerging phenomena [1]. By this study we are trying to use some specific features of these functions for modeling aspects connected with interactions between electromagnetic pulses and material bodies for the relativistic case, when the material body moves with speed c as related to the reference system where this pulse was emitted. At the beginning the problem appearing for high-energy electromagnetic pulses interacting with very small particles is presented; in this case, the model considering the transformation of a received wave train by observer's material medium must be replaced, while the energy of a received high-energy pulse can be higher than the whole energy mc^2 of some small (elementary) particles. Thus it results that in this case the associated wave-train corresponding to the body should be transformed also by the received pulse (scaling aspects having to be taken into consideration). Then it is shown that integral properties of test functions can be used for modeling smooth transitions when the resulting force changes its sign.

1 Introduction

As it is known, basic concepts in physics connected with interaction are the wave and corpuscle concepts. In classical physics the corpuscle term describes the existence of certain bodies subjected to external forces or fields, and the wave concept describes the propagation of oscillations and fields. In quantum physics, these terms are closely interconnected, the wave train associated to a certain particle describes the probability of a quantum corpuscle (an electron or a photon) to appear; the results of certain measurements performed upon the quantum particle are described by the proper value of the operators corresponding to the physical quantity to be measured. Certain intuitive problems connected with measurement procedures on closed-loop trajectories in special relativity and non-commutative properties of operators in quantum physics [2] imply a more rigorous definition of measurement method and of the interaction phenomena, classified from the wave and from the corpuscular aspect of matter,

so as to avoid contradiction generated by terminological cycles [3]. Logic definition for the class of measuring methods based on the wave aspect of matter and for the class of measuring methods based on the corpuscular aspect of matter upon interaction phenomena, based on considerations about a possible memory of previous measurements (operators) in case of a sequence of received pulses were presented in [4], trying to obtain expressive pattern classes (similar to those presented in [5]).

2 Preliminaries

As it is known, the special relativity theory considers that the Lorentz formulae describe the transformation of the space-time coordinates corresponding to an event when the inertial reference system is changed. These formulae are considered to be valid at any moment of time after a certain synchronization moment (the zero moment) irrespective to the measuring method used. However, there are some problems connected to the use of mechanical measurements on closed-loop trajectories. For example, by considering that at the zero moment of time, in a medium with a gravitational field which can be neglected (the use of the galileean form of the tensor g_{ik} being allowed) two observers are beginning a movement from the same point of space, in opposite directions, on circular trajectories having a very great radius of curvature. After a certain time interval, the observers are meeting again in the same point of space.

For very great radii of curvature, the movements on very small time intervals can be considered as approximative inertial (as in the case of the transverse Doppler effect, where the time dilation phenomenon was noticed in the earth reference system which is approximative inertial on small time intervals). The Lorentz formulae can be applied on a small time interval $\Delta t(1)$ measured by one of the observers inside his reference system, and it results (using the Lorentz formula for time) that this interval corresponds to a time interval $\Delta t'(1) > \Delta t(1)$ in the reference system S_2 of the other observer, which moves with speed $v(1)$ as related to the reference system S_1 on this time interval. So the time dilation phenomenon appears. If each observer considers the end of this time interval ($\Delta t(1)$ or $\Delta t'(1)$) as a new zero moment (using a resynchronization procedure), the end of the second time interval $\Delta t(2)$ (with the new zero moment considered as origin) will correspond to a time moment $\Delta t'(2) > \Delta t(1)$ measured in the other reference system S_2 which moves with speed $v(2)$ as related to system S_1 on the time interval $\Delta t'(2)$ (with the new zero moment considered as origin). As related to the first zero moment (when the circular movement has started) the end of the second time interval appears at the time moment $t_2 = \Delta t(1) + \Delta t(2)$ for the observers situated in reference system S_1 , and at a time moment $t'(2) = \Delta t'(1) + \Delta t'(2) > \Delta t(1) + \Delta t(2)$ for the other observer. Thus a global time dilation for the time interval $\Delta t(1) + \Delta t(2)$ appears. The procedure can continue till the end of the whole circular movement (noted as T in system $S(1)$ and T' in system $S(2)$), and by joining together all these time intervals $\Delta t(i)$ we obtain that $T' > T$. But the whole procedure can be applied starting from another set of small time intervals $\Delta_n t'(i)$ considered in the reference system

S_2 which corresponds to a new set of time intervals $\Delta_n t(i)$ considered in the reference system S_2 (established using the same Lorentz relation) and finally it would result that the period of the circular movement T' measured in system S_2 corresponds to a period T greater than T' considered in reference system S_1 (see [4] for more details). Contradiction appearing in case of measurements based on mechanical or biological methods (as statement: a metallic plate is younger as another plate, so it has a greater mechanical resistance and can destroy the other, but in the same time it is older than the other, so it has a less mechanical resistance and can be destroyed by the other when the observers are meeting again). So the Lorentz transformation should be associated with a transformation of a certain wave train when it interacts with the observer's material medium, and this interpretation can be extended at wave-trains associated to particles in quantum physics [7].

Moreover, this aspect implies an intuitive interpretation for the dependence of the mass of a body inside a reference system. Thus, it was shown that for the case when the Lorentz transformation doesn't generate a pulse (for example when the relative speed between the material body and the wave is equal to c , the speed of light in vacuum), the mass m is equal to ∞ , which means that no interaction due to the received pulse exists. This manner the notion on infinite mass is connected with the absence of interaction) [8]. So $m = \infty$ for a body inside a reference system S shows that we can't act upon the material body using wave pulses emitted in system S ; however, changes in the movement of the body (considered in system S) due to other external forces seem to be allowed. The absence of interaction is connected also with absence of estimation for space coordinates of the wave source (the general case being presented in [9]). This aspect can be considered as a suddenly emerging phenomenon, while the interaction disappears when the relative speed v between the system which emits the wave and the system which receives it becomes equal to c . Most probably, a relative speed v greater than c would appear for the material body as a wave received from the opposite direction (the body would reach the emitted wave-train, and perhaps the resulting forces would change the sign).mits the wave and the system which receives it becomes equal to c .

However, some intuitive problems appear: each material body (corpuscle) being associated to a wave, when should we consider that a wave train associated to a body transforms a received wave train? At first view, the element performing the transformation should be a solid body and the element which undergoes the transformation should be a received wave corresponding to a certain field - otherway would appear other phenomena as mechanical collisions or intersections of wave trajectories without any generation of a new wave train. But the problem is more complex if a high energy pulse interacts with a single or with a small number of elementary (small) particles. In this case the total energy of the particles (according to relativistic expression $E = mc^2$) can be much smaller than the energy of the received pulse which interacts with them. For a correct analysis (according to previous considerations) the small (elementary) particles should be considered as associated wave trains interacting with a high-energy environment

(some scaling aspects [10] appearing). The high energy pulses would be much less affected by interaction, which means that it is the element performing the transformation; associated wave-train of the particles would be the much more affected by interaction, being the element which undergoes the transformation. In the most general case, the study of wave transformations according to Lorentz formulae in a certain environment must be performed in the reference systems where the total momentum is zero (by analogy with the study of collisions in the reference system associated to the center of mass).

3 Connections with Test Functions

For modeling phenomena connected with wave-train transformation in a certain environment, we could use the formalism of topological solitary waves with arbitrary charge [11] or of harmonic wavelets [12]. However, the disappearance of interaction when the relative speed v equals c implies the absence of certain state-variables at that very moment of time when $v = c$, when v pass from a value less than c to a value greater than c ; this is similar to aspects connected with integration of functions similar to test functions on a working interval [13] - a certain number of derivatives vanishing at the end of this interval. Specific features from modeling solitary waves in composite materials [14] could be useful, avoiding mathematical possibilities of generating acausal pulses [15] (the Lorentz transformation of a received wave-train does not generate any wave without a certain received wave to exist, and it acts instantly). Stochastic aspects of Schroedinger equation imply a probability of measuring a certain value for a physical quantity connected with an associated wave, not a probability of appearing different associated waves (see [16] for a wavelets analysis of Schroedinger equation).

From basic mathematics it is known that the product $\varphi(t)g(t)$ between a function $g(t)$ which belongs to C^∞ class and a test-function $\varphi(t)$ which differs to zero on (a, b) is also a test-function, because:

- a) it differs to zero only on the time interval (a, b) where $\varphi(t)$ differs to zero (if $\varphi(t)$ is null, then the product $\varphi(t)g(t)$ is also null)
- b) the function $\varphi(t)g(t)$ belongs to the C^∞ class of functions, while a derivative of a certain order k can be written as

$$(\varphi(t)g(t))^{(k)} = \sum_{p=0}^k C_k^p \varphi(t)^{(p)} g(t)^{(k-p)} \tag{1}$$

(a sum of terms represented by a product of two continuous functions).

Yet for practical cases (when phenomena must be represented by differential equations), the $\varphi(t)$ test functions must be replaced by a practical test functions $f(t) \in C^n$ on R (for a finite n - considered from now on as representing *the order* of the practical test function) having the following properties:

- a) f is nonzero on (a, b)
- b) f satisfies the boundary conditions $f^{(k)}(a) = f^{(k)}(b) = 0$ for $k = 0, 1, \dots, n$ and

c) f restricted to (a, b) is the solution of an initial value problem (i.e. an ordinary differential equation on (a, b) with initial conditions given at some point in this interval).

The generation of such practical test functions is based on the study of differential equations satisfied by the initial test functions, with the initial moment of time chosen at a time moment close to the $t = a$ moment of time (when the function begins to present non-zero values).

By using these properties of practical test-functions, we obtain the following important result for a product $f(t)g(t)$ between a function $g(t)$ which belongs to C^∞ class and a practical test-function of n order $f(t)$ which differs to zero on (a, b) :

General Property for Product : The product $g(t)f(t)$ between a function $g(t) \in C^\infty$ and a practical test function f of order n is represented by a practical test function of order n .

This is a consequence of the following two properties:

- a) the product $g(t)f(t)$ differs to zero only on the time interval (a, b) on which $f(t)$ differs to zero.
- b) the derivative of order k for the product $g(t)f(t)$ is represented by the sum

$$(f(t)g(t))^{(k)} = \sum_{p=0}^k C_k^p f(t)^{(p)} g(t)^{(k-p)} \quad (2)$$

which is a sum of terms representing products of two continuous functions for any $k \leq n$, (n being the order of the practical test-function f) - only for $k > n$ discontinuous functions can appear in the previous sum.

Now we shall begin the study of integral properties of practical test functions of certain order. For this, we note that the integral $\varphi(t)$ of a test function $\phi(t)$ (which differs to zero on (a, b) interval) is a constant function on the time intervals $(-\infty, a]$ and $[b, +\infty)$; it presents a certain variation on the (a, b) time interval, from a constant null value to a certain Δ quantity corresponding to the final constant value. Moreover, all derivatives of order $k \leq n + 1$ for the integral function $F(t)$ are equal to zero for $t = a$ and $t = b$ (this can be easily checked by taking into account that all derivatives of order p for $f(t)$ are equal to zero at these time moments, for $p \leq n$, and a derivative of order p for $f(t)$ corresponds to a derivative of order $p + 1$ for function $F(t)$, the integral function of $f(t)$). This suggests the possibility of using such integral functions for modeling smooth transitions from a certain state to another in different kind of applications, when almost all derivatives of a certain function are equal to zero at the initial moment of time. In our case the absence of interaction at the time moment t_{in} (when $v = c$), considered as initial moment of time, implies that all (or a great number) of derivatives of functions $x = x(t), y = y(t), z = z(t)$ (the space coordinates) are null for $t = t_{in}$ and present a certain variation at a time interval close to t_{in} (when v is no longer equal to c).

For modeling such a transition, we analyze the general case when a function f and a finite number of its derivatives $f^{(1)}, f^{(2)}, \dots, f^{(n)}$ present the variations from null values to values $\Delta, \Delta_1, \Delta_2, \dots, \Delta_n$ on the time interval $[-1, 1]$. We begin by looking for a function f_n which should be added to the null initial function so as to obtain a variation Δ_n for the derivative of n order. By multiplying the bump-like function

$$\varphi(\tau) = \begin{cases} \exp\left(\frac{1}{\tau^2-1}\right) & \text{if } \tau \in (-1, 1) \\ 0 & \text{otherwise} \end{cases} \tag{3}$$

(a test-function on $[-1, 1]$) with the variation Δ_n of the derivative of n order and by integrating this product $n + 1$ times we obtain:

- after the first integration: a constant value equal to Δ_n at the time moment $t = 1$ (while the integral of the bump-like test function on $[-1, 1]$ is equal to 1, and a null variation on $(1, +\infty)$).
- after the second integration (when we integrate the function obtained at previous step): a term equal to $\Delta_n(t - 1)$ and a term equal to a constant value c_{n1} (a constant of integration) on the time interval $(1, +\infty)$.
- ..-after the $n + 1$ integration: a term equal to $\Delta_n(t - 1)^n/n!$ and a sum of terms having the form $c_{ni}(t - 1)^i/i!$ for $i \in N, i < n$ (c_{ni} being constants of integration) on the time interval $(1, +\infty)$.

All previous constants of integration are determined by successive integration of the test function on $[-1, 1]$. The procedure continues by looking for the other functions f_{n-1}, f_{n-2}, \dots which must be added to the initial null function. However, we must take care to the fact that the function f_n previously obtained has non-zero variations $d_{n-1}, d_{n-2}, \dots, d_1$ for its derivatives of order $n - 1, n - 2, \dots, 1$ on the working interval and so we must subtract these values from the set $\Delta_{n-1}, \Delta_{n-2}, \dots, \Delta_1$ before passing to the next step.

Then we multiply the bump-like function with the corrected value $\Delta_{n-1} - d_{n-1}$ and by integrating this product n times we obtain in a similar manner a function with a term equal to $\Delta_n(t - 1)^{n-1}/(n - 1)!$ and a sum of terms having the form $c_{ni}(t - 1)^i/i!$ for $i \in N, i < n - 1$ (c_{ni} being constants of integration) on the time interval $(1, +\infty)$. It can be noticed that the result obtained after n integration possess the $n - 1$ order derivative equal to Δ_{n-1} , a smooth transition for this derivative from the initial null value being performed. So the second function which must be added to the initial null function is the integral of $n-1$ order for the bump-like function multiplied by this variation $\Delta_{n-1} - d_{n-1}$ (the function being noted as f_{n-1}). This function f_{n-1} has a null value for the derivative of n order, so the result obtained at first step is not affected. We must take care again to the fact that the function f_{n-1} previously obtained has non-zero variations $d_{n-1}^1, d_{n-2}^1, \dots, d_1^1$ for its derivatives of order $n - 1, n - 2, \dots, 1$ and so we must once again subtract these values from the previously corrected set $\Delta_{n-1} - d_{n-1}, \Delta_{n-2} - d_{n-2}, \dots, \Delta_1 - d_1$ before passing to the next step. Finally we obtain all functions f_{n+1}, f_n, \dots, f_1 which represent the terms of function f modeling the smooth transition from an initial null function to a function having

a certain set of variations for a finite number of its derivatives on a small time interval. The procedure can be also applied for functions possessing a finite number of derivatives within a certain time interval by time reversal (t being replaced with $-t$).

4 Conclusions

This study has used specific features of test functions and of practical test functions for modeling aspects connected with interactions between electromagnetic pulses and material bodies for the relativistic case, when the material body moves with speed c as related to the reference system where this pulse was emitted. At the beginning the problem appearing for high-energy electromagnetic pulses interacting with very small particles has been presented; in this case, the model considering the transformation of a received wave train by observer's material medium must be replaced, while the energy of a received high-energy pulse can be higher than the whole energy mc^2 of some small (elementary) particles. It is shown that in the most general case, the study of wave transformations according to Lorentz formulae in a certain environment must be performed in the reference systems where the total momentum is zero (by analogy with the study of collisions in the reference system associated to the center of mass). Thus it results that in this case the associated wave-train corresponding to the body should be transformed also by the received pulse (scaling aspects having to be taken into consideration). Then it is shown that integral properties of test functions can be used for modeling smooth transitions when the resulting force changes its sign.

References

1. Toma, G. : Practical test-functions generated by computer algorithms, Lecture Notes Computer Science **3482** (2005), 576–585
2. Toma, C.: The advantages of presenting special relativity using modern concepts, Balkan Physics Letters Supplement 5 (1997), 2334–2337
3. Baader, F. : The instance problem and the most specific concept in the description logic w.r.t. terminological cycles with descriptive semantics, Lecture Notes in Computer Science **2821** (2003) 64–78
4. Toma, C.: A connection between special relativity and quantum theory based on non-commutative properties and system - wave interaction, Balkan Physics Letters Supplement 5 (1997), 2509–2513
5. Takeda, M., Inenaga, Sh., Bannai, H.: Discovering most classificatory patterns for very expressive pattern classes, Lecture Notes in Computer Science **2843** (2003) 486–493
6. Toma, C.: The use of the cuadridimensional interval - the main possibility for improving the Lorentz formulae interpretation, Proceedings of ECIT-97 Symposium - Pitesti (Romania), **2** (1997), 202–206
7. Sterian, P., Toma C.: Methods for presenting key concepts in physics for MS students by Photon-MD program, Bulgarian Journal of Physics **27** 4 (2000), 27–30

8. Simeonidis, M., Pusca, St., Toma, G., Toma, A., Toma, Th.: Definition of wave-corpucle interaction suitable for simulating sequences of physical pulses, *Lecture Notes in Computer Science* **3482** (2005), 569–576
9. Toma, C.: About some space relations of the electromagnetic interaction, *Revue Roumaine des Sciences Techniques, Serie Electrotechnique et Energetique*, **34**, 3 (1989), 431–435
10. Cattani, C.: Multiscale Analysis of Wave Propagation in Composite Materials, *Mathematical Modelling and Analysis*, **8**, 4 (2003), 267–282
11. D’Avenia, P., Fortunato, D., Pisani, L. : Topological solitary waves with arbitrary charge and the electromagnetic field, *Differential Integral Equations* **16** (2003) 587–604
12. Cattani, C.: Harmonic Wavelets towards Solution of Nonlinear PDE, *Computers and Mathematics with Applications*, 50 (2005), 1191–1210
13. Toma, C. : An extension of the notion of observability at filtering and sampling devices, *Proceedings of the International Symposium on Signals, Circuits and Systems Iasi SCS 2001, Romania* 233–236
14. Rushchitsky, J.J., Cattani, C., Terletskaia, E.V.: Wavelet Analysis of the evolution of a solitary wave in a composite material, *International Applied Mechanics*, 40, 3 (2004), 311–318
15. Toma, C.: The possibility of appearing acausal pulses as solutions of the wave equation, *The Hyperion Scientific Journal* **4** 1 (2004), 25–28
16. Cattani, C.: Harmonic Wavelet Solutions of the Schroedinger Equation, *International Journal of Fluid Mechanics Research* **5** (2003), 1–10

Noise Level Estimation Using Haar Wavelet Packet Trees for Sensor Robust Outlier Detection

Paolo Mercorelli¹ and Alexander Frick²

¹ University of Applied Sciences Wolfsburg,
Dep. of Vehicles, Production and Process Engineering,
Robert-Koch-Platz 8-a., 38440 Wolfsburg, Germany
Tel.: +49-(0)5361-831615; Fax: +49-(0)5361-831602

p.mercorelli@fh-wolfsburg.de

² ABB Utilities GmbH UTD/PAT2 Kallstadter Strasse 1,
DE 68309 Mannheim, Germany

Phone: +49 621 381 4539; Fax: +49 621 381 2244

alexander.frick@de.abb.com

Abstract. The paper is related to the on-line noise variance estimation. In practical use, it is important to estimate the noise level from the data rather than to assume that the noise level is known. The paper presented a free thresholding method related to the on-line peak noise variance estimation even for signal with small S/N ratio. The basic idea is to characterize the noise like an *incoherent* part of the measured signal. This is performed through the wavelet tree by choosing the subspaces where the median value of the wavelet components has minimum. The paper provides to show nice general properties of the wavelet packets on which the proposed procedure is based. The developed algorithm is totally general even though is applied by using Haar wavelet packets and it is present in some industrial software platforms to detect sensor outliers. More, it is currently integrated in the inferential modeling platform of the Advanced Control and Simulation Solution Responsible Unit within ABB's industry division.

1 Introduction and Motivation

The recent appearance of explicit orthonormal bases based on multiresolution analyzes has exciting implication for non-parametric function estimation. In general, wavelet bases offer a degree of localization in time as well as in frequency. This aspect enables envelopment of simple estimate functions which respond to the discontinuity and the time-varying of the oscillations in real signals. As applications in the process industries rely more on large amounts of raw data, which directly originate either from a distributed control system (DCS) or historians, there is an increasing need for automated data preprocessing, e.g., cleaning of data. Soft sensing, data reconciliation, and parameter estimation are example applications that often require the existence of "clean data". In case of data reconciliation, the data cleaning has been done simultaneously. Noise probability

density estimation represents a fundamental step in monitoring and detection of wanted data in process malfunctions. It is well known, for instance, in most of the algorithms which detect Outlier as in [9] one needs to know the level of the noise. In thresholding method of denoising optimum threshold is obtained as a function of additive noise variance. In practical problem, the noise variance is unknown. The thresholding method removes the additive noise by eliminating the basis coefficients with small absolute value which tend to be attributed to noise. One of the first methods was proposed by Donoho and Johnstone in wavelet denoising [8]. In [10] another thresholding method is proposed. A new method of denoising is presented in [1]. It is based on comparison of an information theoretic criterion which is the "description length" of the data. The description length is calculated for different subspace of the basis and the method suggests to choose the noise variance and the subspace for which the description length of the data is minimum. In the work, based on [1], is shown that the denoising process can be done simultaneously. The approach presented in [1] and [2] is based on "minimum description length" and for that it seems not suitable for on-line detection because it needs relative long data. More, our approach is looking for a two steps denoising technique as motivated above. The proposed methodology is totally general and doesn't specify any class of model as well as any a priori knowledge either about the noise or about the signals. Moreover, the technique is also suitable for white noise as well as for colored noise thanks to the orthogonality of the discrete wavelet transform. To be more precise, the orthogonal wavelet transforms estimators in one domain into estimators in another domain, but with isometry of risk. The paper applies in the context of probability density estimation the wavelet transformations structured in wavelet packets. Wavelet functions are used as analyzing function structured in wavelet packets in order to choose the best function set which can estimate adaptively the noise in the data. In this sense the "best basis" representing the noise is selected according to a predefined criterion. One proposes an on-line technique which can be used in every champagne of measure. Any family of wavelets could be used, but here Haar wavelet packets are selected. In fact working on relative short sequence, the Haar functions fit the local time characteristic of the analyzed sequence very well. More, the Haar function is the easiest function to be implemented. The novelty consists of a new idea to define the incoherent part of a sequence and thanks to a proven property one uses few branches of the wavelet tree in order to estimate the variance-peak of the wanted sequence. The proposed algorithm is easy to be implemented and needs few mathematical calculations, therefore its industrial application appears to be suitable. The paper presented a free thresholding method particularly suitable for on-line variance noise estimation. After a short introduction of the wavelet packets through section 2, in section 3 a short introduction to the thresholding methods is provided. Section 4 shows the problem formulation and provides to prove a nice general property of the wavelet packets that the proposed procedure is based on. Section 5 is devoted to the description of the proposed procedure. Validation, simulation results and some conclusion remarks close the paper.

2 Background

The function $\psi_{(d,j,n)}(t) = \psi_j(2^d t - n)$ has support of size 2^{-d} of the Nyquist frequency. More, d is a scale parameter, j is a phase parameter and n is a time translation parameter. Here, the *pyramidal* packet is represented by the indices (d, j, n) , d is the level of the tree (scaling parameter), j is the frequency cell (oscillation parameter) and n the time cell (localization parameter). In order to understand better we will show an example of a set of Haar wavelet function which represents a part of a 'Haar wavelet packet tree', see Fig. 1. This figure shows a tree with two levels and at the level 1 just two Haar functions with $n = 1$ are considered. Basically the Haar basis has the two following properties:

- the $\psi_{(d,j,n)}^h(t)$ are orthonormal;
- any $\mathcal{L}^2(\mathfrak{R})$ function $f(t)$ can be approximated, up to arbitrarily small precision, by a finite linear combination of the $\psi_{(d,j,n)}^h(t)$.

In particular, to be more precise, the coefficients $w_{(d,j,n)}$ (the weight coefficients) are calculated as follows:

$$w_{(d,j,n)} = \int_I f(t)\psi_{(d,j,n)}^h(t)d(t).$$

For $j = 0$ it is possible to define the following coefficients:

$$w_{(d,0,n)} = \int_I f(t)\psi_{(d,0,n)}^h(t)d(t).$$

Where $f(t)$ is the wanted signal, I is the considered time interval and $\psi_{(d,0,n)}^h(t)$ is the well known *mother function*. To conclude

$$f(t) = \sum_n s_{(d,n)}\psi_{(d,0,n)}^h(t) + \sum_j \sum_n w_{(d,j,n)}\psi_{(d,j,n)}^h,$$

where $s_{(d,n)} = w_{(d,0,n)}$. It is shown that the independent parameters are just two and that the parameter d characterizes the *level of the tree*.

3 State of the Art

One of the first complete contributions in this area are [4], [6], [8] and [7]. A number of different methods for selecting appropriated threshold values for wavelet de-noising have been proposed. Recent literature, as in [11], in applied domain dedicates a big part of its contribution in order to indicate the importance of the good estimation of noise. This big variability generates difficulty and thus different and heuristic criteria. However the "true" signal tends to dominate the low-frequency, especially in chemical process where the dynamic of the systems is characterized by relative low frequency band. The traditional approach

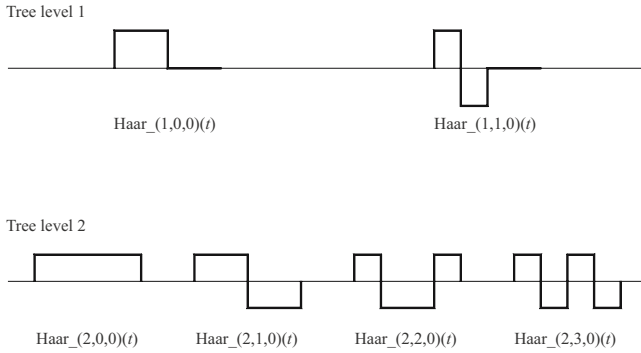


Fig. 1. A set of Haar functions

of filtering is to remove the high-frequency components above a "certain level" since they are associated with the noise. Small wavelet coefficients at high frequency area are usually expected to be mainly to noise components. The actual technique could be summarized in the following way:

- I. Apply the wavelet transform to a noisy signal and obtain the noise wavelet coefficients.
- II. Threshold those element in the wavelet coefficients which are believed to be attributed to noise.
- III. To reconstruct the noise, apply the inverse wavelet transform to the threshold wavelet coefficients.

In this approach the crucial point is the threshold step, in other words, that wavelet coefficients are believed to be attributed to the noise. In general, wavelet thresholding methods could be classified either on a soft or a hard threshold. The idea in soft threshold is that every coefficient has a level of noise. When speaking about wavelets, the above described methods are normally divided into two categories: global thresholding and level-depend thresholding. In particular, when a global thresholding is selected, it is globally applied to all wavelet coefficients above a certain frequency level. The level-depending threshold is a different threshold for the wavelet coefficient at level l . The latter technique is suitable when the noise is colored or/and correlated.

In [6] and in particular in 5.4 a practical estimation of the noise is given. The author indicates a derivation of the estimate from the finest scale of wavelet coefficients:

$$\hat{\sigma} = median\{|w_{(d,n,j)}| : d = 1, 0 < n \leq 2^{N_0-d}, 0 \leq j \leq 2^d - 1\}.$$

Here is the idea to use a robust estimator like the median in case of the fine scale, because the respectively wavelet coefficients contain a small portion of strong "signals" mixed with "noise".

4 Problem Statement

When the problem is to detect information from a signal about the level of the noise or in general about some other thing inside the analyzed signal, a procedure which can illuminate the difference between the signal and the wanted information is needed. An illuminating basis which can discriminate the wanted information from the signal is chosen. The basic idea is to estimate the peak noise density variance in wavelet packet tree with an adaptive method which looks for the best representation of the noise according to the following definitions.

Definition 1. *Given the oscillating part of the sequence $y(t)$ as follows*

$$y(t) - \sum_{n=0}^{2^{N_0-d}} s(d, n)\psi(d, n)(t) = \sum_{j=1}^{2^d-1} \sum_{n=0}^{2^{N_0-d}} w(d, j, n)\psi(d, j, n)(t),$$

where $s(d, n) = w_{(d,0,n)}$. Then the time-frequency map of the peak values in wavelet domain is a table of real values specified $\forall d \in \mathbf{N}$ and by the triplet (d, \hat{j}, n) as

$$w_{p_{(d,\hat{j},n)}} = \max_j (w_{(d,j,n)} \|\psi_{(d,j,n)}(t)\|). \quad \square$$

Definition 2. *Given an observed sequence*

$$y(t) = x(t) + e(t).$$

Let $e(t)$ be defined incoherent part of the sequence $y(t)$ at every level d of the packet tree as follows:

$$e(t) = \sum_n N_{(d,\hat{j},n)} \psi_{(d,\hat{j},n)}(t),$$

where $\psi_{(d,\hat{j},n)}(t)$ are the wavelet bases and $N_{(d,\hat{j},n)}$ their coefficients. The selected wavelets are characterized by (d, \hat{j}, n) indices such that:

$$\{(d, \hat{j}, n)\} = \arg\left(\min_j \left(\text{median}_n \{w_{p_{(d,j,n)}}\} \right) : \{0 < n \leq 2^{N_0-d}, 0 < j \leq 2^d - 1, \forall d \in \mathbf{N}\} \right) \quad (1)$$

where median_n is the median calculated on the elements which are localized with index n (time localized). The coefficients $w_{p_{(d,\hat{j},n)}}$ are the wavelet table coefficients of the sequence $y(t)$ as given in Def. 1. □

It is easy to see how the idea behind Def. 2 is to sort the basis which can illuminate the difference between the coherent and incoherent part of the sequence, where *incoherent* is the part of the signal that either has no information or its

information is *contradictory*. In fact, the procedure looks for the subspace characterized either from small component or from opposite components in wavelet domain.

Proposition 1. *Let $y(t)$ be a sequence and $w_{p_{(d,j,n)}}$ its corresponding wavelet sequence on different levels of the tree. At every level d and at every frequency cell j*

$$|\text{median}_n(w_{p_{(d,\hat{j},n)}})| \leq |\text{median}_n(w_{p_{(d+1,2\hat{j},n)}})| + |\text{median}_n(w_{p_{(d+1,2\hat{j}+1,n)}})|.$$

Then

$$|\text{median}_n(w_{p_{(d,\hat{j},n)}})| \leq |\text{median}_n(w_{p_{(d+m,2\hat{j},n)}})| + |\text{median}_n(w_{p_{(d+m,2\hat{j}+1,n)}})|.$$

$\forall m \geq 1$. □

Proof 1. *By observing that, from the orthogonality,*

$$\sum_{(d,j,n)} w_{(d,j,n)} \psi_{(d,j,n)} = \sum_{(d,j,n)} w_{(d+1,2j,n)} \psi_{(d+1,2j,n)} + \sum_{(d,j,n)} w_{(d+1,2j+1,n)} \psi_{(d+1,2j+1,n)}. \quad (2)$$

The functions $\psi_{(d,j,n)}$ are organized in packets and they are scaled functions, $\forall d, j$ and $\forall m \geq 1$,

$$\max(\psi_{(d,j,n)}) \leq \max(\psi_{(d+m,2j,n)}) + \max(\psi_{(d+m,2j+1,n)})$$

then

$$\max_j (w_{(d,j,n)} \psi_{(d,j,n)}) \leq \max_j (w_{(d+1,2j,n)} \psi_{(d+1,2j,n)}) + \max_j (w_{(d+1,2j+1,n)} \psi_{(d+1,2j+1,n)}). \quad (3)$$

From Def. 1, $\forall d$ and $\forall n \geq 1$, it follows:

$$w_{p_{(d,\hat{j},n)}} \leq w_{p_{(d+1,2\hat{j},n)}} + w_{p_{(d+1,2\hat{j}+1,n)}}.$$

Considering that the "median" is a monotonic function:

$$\text{median}_n(w_{p_{(d,\hat{j},n)}}) \leq \text{median}_n(w_{p_{(d+1,2\hat{j},n)}}) + \text{median}_n(w_{p_{(d+1,2\hat{j}+1,n)}}).$$

Thus

$$|\text{median}_n(w_{p_{(w,\hat{j},n)}})| \leq |\text{median}_n(w_{p_{(d+1,2\hat{j},n)}})| + |\text{median}_n(w_{p_{(d+1,2\hat{j}+1,n)}})|.$$

by proceeding $\forall m \geq 1$ the proposition is proven. □

Remark 1. *In other words the proposition says that, if the minimum of the median at the level d , according to Def. 1, is not more than the minimum of the median at the level $d + 1$ (one more in depth) then this is also not more than minimum of the median at the level $d + m$ (all the deeper), with d and m integer. \square*

The introduced definitions and proposition 1 allow to build an efficient procedure in order to estimate the level of the noise like an incoherent part of the signal. One can say that the incoherent part of a signal is the part which doesn't "match" the desired signal. It estimated the peak-to-peak noise variance considering the incoherent part of the signal defined above.

5 The Proposed Procedure

Given a sampled signal of length n .

- **Step 0:** Specify the length L as 8, 16, 32, or 64 (dyadic length) and set the end of shifting window $esw = \mathcal{L}$. Determine height of wavelet tree: $h = \log_2(\mathcal{L})$. Take the last data points with respect to the end of shifting window, "esw", of the sampled signal.
- **Step 1:** Construct the wavelet coefficient tree $W(d, j, n)$ for every $d, j > 1$ and for every n , related to the current shifting data window.
- **Step 2:** Build the wavelet coefficients corresponding to the incoherent part of the signal according to Def. 2. In particular for $d = 1$ (first level of the wavelet tree, this yields $j = 1$).
- **Step 3:**

Step 3a:) For all time-frequency intervals such that $j = 1, 2, \dots, 2^d - 1$ with $d > 1$, calculate the absolute of the median for the same time-frequency interval, that is, $Wmed(d, j) = abs(median_n(W(d, j, \forall n)))$.

Step 3b:) For every "wavelet father" $W(d, j)$ at the node (d, j) with $j > 0$ calculate its left child at the node $(d + 1, jLeft)$ and its right child $(d + 1, jRight)$. Then calculate the absolute of the medians and denote them as

$$WmedChildLeft = abs(median_n(Wmed(d, jLeft, \forall n)))$$

and

$$WmedChildRight = abs(median_n(Wmed(d, jRight, \forall n))).$$

While $(d < h)$

For $j \leq 2^d - 1$.

If $Wmed(d, j) \leq WmedChildLeft + WmedChildRight$, then denote

$Peak(\hat{d}, \hat{j}) = \inf_{d,j}(Wmed(d, j))$ and bound the tree of the children of this branch

else

End If

End j loop
End While-d loop

- **Step 4:** Sum up all of the $Peak(\hat{d}, \hat{j})$ of the different levels, that is,
 $Peak = sum_{(\hat{d}, \hat{j})}(Peak(\forall \hat{d}, \forall \hat{j}))$.

6 Discussion and Simulations

The proposed procedure is quite fast, the wavelet decomposition has the mathematical complexity of the calculations proportional to N, where N is the number of the samples, but the complexity of the calculation of the procedure is proportional to $N \log_2(N)$ as in [3] because of the dyadic structure of the wavelet tree. Anyhow, during the evaluation of the value on the tree, thanks to remark (1), the branch of the algorithm is very often bounded, this yields a fast procedure. The algorithm is tested in several ways. Signal with different dynamics are considered as well as different number of transients in superposition with white and colored noise. The algorithm is validated by using the known data.

The performances with the free software available in [5] are compared. In Fig. 2 an example is reported in which a known variance of the noise in superposition is simulated. Fig. 3 shows how the proposed technique estimates correctly the variance of the noise also for small S/N ratio. Fig. 4 shows how the old technique goes wrong for small and big S/N ratio (high variance).

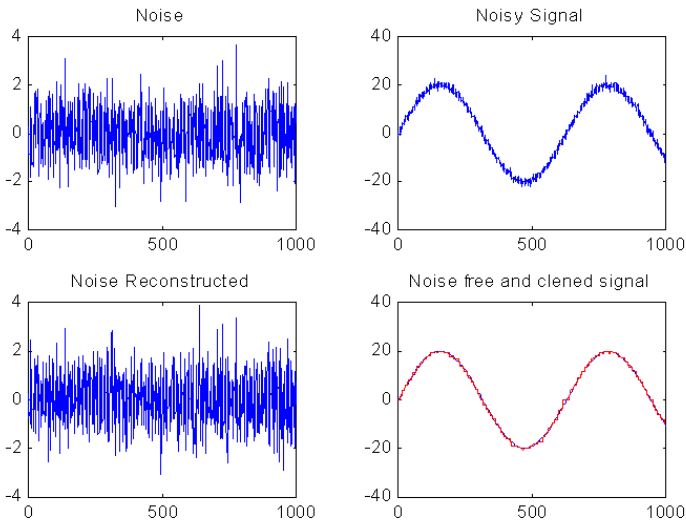


Fig. 2. Testing example $20\sin(n)+noise(n)$

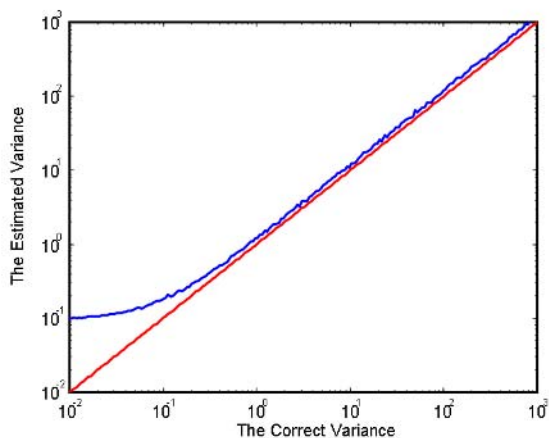


Fig. 3. Wavelets Algorithm: The estimated and true variance using the proposed algorithm

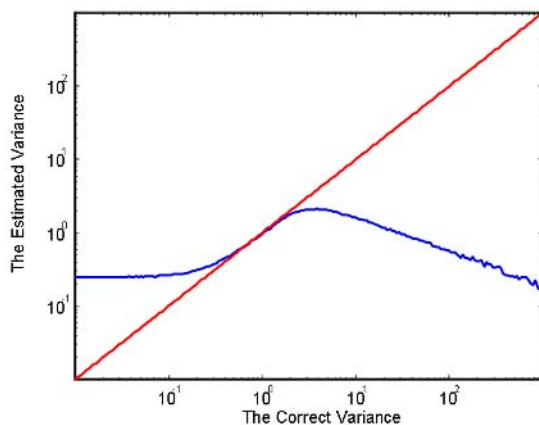


Fig. 4. WaveLab Algorithm: The estimated and true variance using a typical denoising algorithm

7 Conclusions

The paper applies in the context of probability density estimation through the wavelet transformations structured in wavelet packets. The goal is to obtain an on-line algorithm to estimate noise variance, to avoid classical thresholding techniques, and to be used in the two steps de-noise techniques. Real implementation and real applications are shown.

References

1. S. Beheshti and M. A. Dahleh. On denoising and signal representation. In *Proc. of the 10th Mediterranean Control Conference on Control and Automation*, 2002.
2. S. Beheshti and M. A. Dahleh. Noise variance and signal denoising. In *Proc. of IEEE International Conference on Acoustic, Speech, and Signal Processing (ICASSP)*, 2003.
3. R. R. Coifman and M. V. Wickerhauser. Entropy based algorithm for best basis selection. *IEEE Trans. Inform. Theory*, 32:712–718, 1992.
4. D. L. Donoho. Denoising and soft thresholding. *IEEE Transactions on Information Theory*, 41(3):613–627, 1995.
5. D. L. Donoho. www-stat.stanford.edu/~wavelab/. 1999.
6. D. L. Donoho and I. M. Johnstone. Adapting to unknown smoothness via wavelet shrinkage. *Journal of the American Statistical Association*, 90(432):1220–1224, 1994.
7. D. L. Donoho, I. M. Johnstone, G. Kerkyacharian, and D. Picard. Density estimation by wavelet thresholding. *Annals of Statistics*, 24(2):508–539, 1996.
8. D. L. Donoho and I.M. Johnstone. Ideal spatial adaptation by wavelet shrinkage. *Biometrika*, 81(3):425–455, 1994.
9. P. H. Menold, R. K. Pearson, and F. Allgöwer. Online outlier detection and removal. In *Proc. of Mediterranean Control Conference*, 1999.
10. J. Rissanen. Minimum description length denoising. *IEEE Trans. on Information Theory*, 46:2537–2543, 2000.
11. R. Shao, F. Jia, E. B. Martin, and A. J. Morris. Wavelets and non linear principal component analysis for process monitoring. *Control Engineering Practice*, 7:865–879, 1999.

A Theoretical Multiscale Analysis of Electrical Field for Fuel Cells Stack Structures

Carlo Cattani¹, Paolo Mercorelli², Francesco Villecco¹, and Klaus Harbusch²

¹ Department of Mechanical Engineering University of Salerno,
Via Ponte Don Melillo-Invariante 84084 Fisciano, SA, Italy
{fvillecco, ccattani}@unisa.it

² University of Applied Sciences Wolfsburg,
Dep. of Vehicles, Production and Process Engineering,
Robert-Koch-Platz 8-a., 38440 Wolfsburg, Germany
Tel.: +49-(0)5361-831615; Fax: +49-(0)5361-831602
{k.harbusch, p.mercorelli}@fh-wolfsburg.de

Abstract. Fuel cell stack systems are under intensive development for mobile and stationary power applications. In particular, Proton Exchange Membrane (PEM) Fuel Cells (also known as Polymer Electrolyte Membrane Fuel Cells) are currently in a more mature stage for ground vehicle applications. This paper proposes a theoretical innovative approach to the analysis of the electrochemical transient behavior (anode-cathode). The transient behavior due to the electrochemical dynamic may impact the behavior of the resulting load current. Boundary conditions influence the resulting electric field, the boundary condition are strongly depending of H_2 and O_2 physical parameters. Maxwell's equations are used in order to describe the model. Solutions through dyadic harmonic wavelets at different levels of resolution are presented. Wavelets approach, through their different space-time levels of resolution, can favorable describe the segmented space structure of the stack. In the meantime, transient dynamic inside of the stack can be adaptively studied. An outlook closes the paper.

1 Introduction and Motivation

Inside of a fuel cell an oxidant and a combustible provide a chemical reaction which produces, at the end of the process, electrical energy and water in vapor form. Basically the structure of the system has two electrodes, anode and cathode. A current from these two elements is present when chemical elements, as for instance Hydrogen and air, come to be put in contact. The velocity of this oxidation reaction depends on the load current connected with the cell. This yields that if the load current is strongly variable, or whether this one exceeds some values, a very high ion flux which produces an undesired acceleration of the chemical reaction arises. On the contrary, if the current is small or equal to zero, then the chemical reaction is not possible. The electrical current depends on the electrical load and it is the control variable of the chemical oxidant reaction, in practical application the flux of the combustible is regulated through the required current. In Fig. 1 the above explained working principle is depicted.

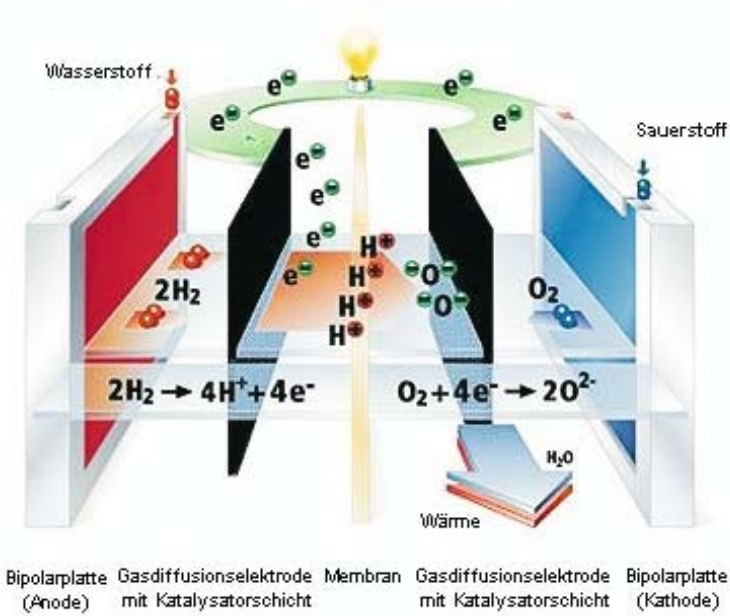


Fig. 1. Working principle of a fuel cell

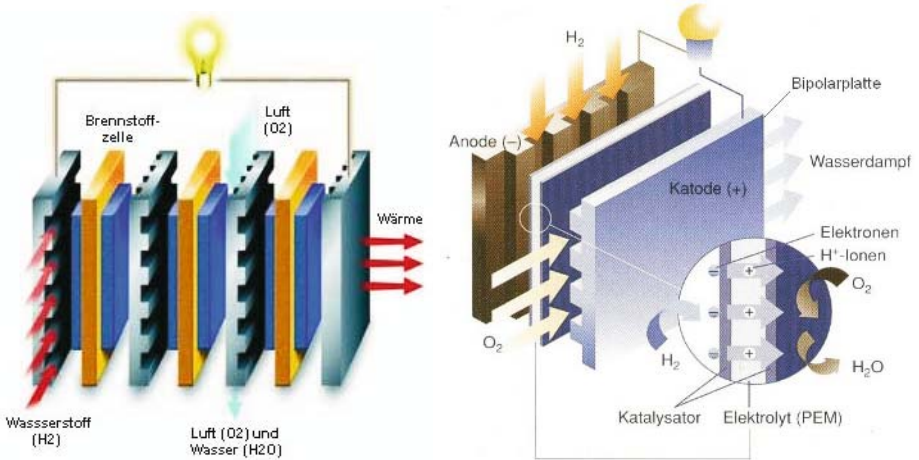


Fig. 2. Right: Structure of a fuel cell stack. Left: Detail.

The transient behavior due to the electrochemical dynamic may impact the behavior of the load current. Many publications treat the fuel cell model in steady-state way in order to choose operating points, [1, 9]. In this context it is important to start an analysis of the dynamic of the fuel cells. Wavelets approach is already used in industrial applications for similar approaches, where an analysis of a transient is required, see [8, 7].

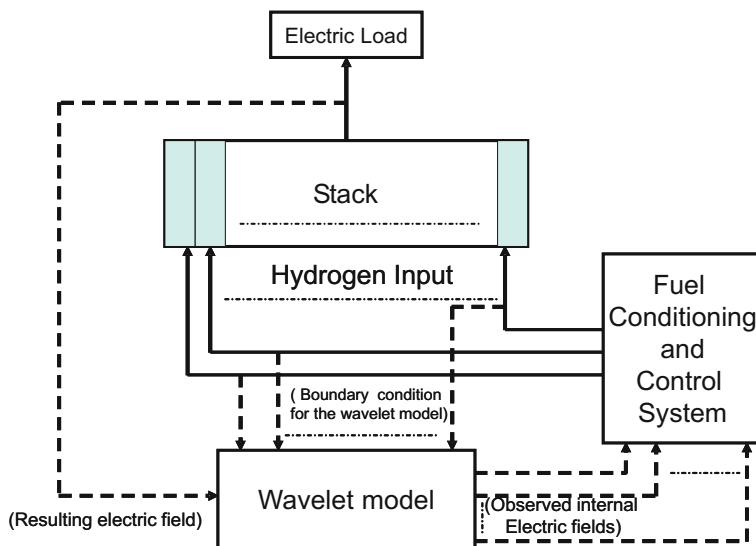


Fig. 3. Principle of a possible control scheme

According to the structure of fig. 2 it seems suitable a tool in which a *segmented approach* is possible. Wavelets tool offers through their level of resolution the possibility to implement algorithms in which a segmentation in space and time can be adapted to the model analysis. Fig. 2 shows how the system can be seen as a multi-input/multi-output system. Each fuel cell component gives its electric output field which can be seen as a series of uncorrelated components. Nevertheless the solutions have boundary conditions in a *cascade* structure. The boundary conditions can be seen as inputs of the considered system. These inputs depend on the temperature, pressure and other parameters of H_2 (anode) and of O_2 . A possible future development of the presented approach involves a detailed analysis of the boundary conditions in order to find some optimal operating point for some given load constraints. In particular possible control scheme can be conceived, fig. 3. The paper is organized as follows. Section 2 deals with the problem formulation. Section 3 presents the structure of the harmonic wavelets and the section 4 shows a possible solution. Conclusions and outlook close the paper.

2 Problem Formulation

Assuming a model with just one dimension, assuming the charge density $\rho(x, J)$ as a function of the current, as described above, the well known following Maxwell equation

$$\operatorname{div} \mathbf{E} = \nabla \mathbf{E} = \rho(x) \quad (1)$$

becomes

$$\frac{\partial E_x}{\partial x} = \rho(x, J). \quad (2)$$

If the a spacial one-dimensional model is considered, the Maxwell equation

$$\operatorname{rot} \mathbf{B} = \nabla \times \mathbf{B} = \mu \left(\mathbf{J} + \epsilon \frac{\partial \mathbf{E}}{\partial t} \right) \tag{3}$$

becomes

$$\mu \left(J + \epsilon \frac{\partial E_x}{\partial t} \right) = 0. \tag{4}$$

Problem 1. *If $\rho = b - aJ$ is a affine function of the current density, with $a = \text{constant} > 0$, $b = \text{constant} > 0$ and $\rho > 0$. Combining eq. (4) with (3) the following equation is obtained:*

$$\frac{\partial E_x}{\partial x} = \frac{a\epsilon}{\mu} \frac{\partial E_x}{\partial t} + b. \tag{5}$$

Find a solution in wavelet domain depending on the scale level of approximation.

In the following we will sketch a multiscale solution based on a series of harmonic wavelets (see e.g. [2, 3, 4, 5] and references therein). This choice is due to the localization property of harmonic wavelets in frequency domain, moreover they allow us to represent the solution in complex domain.

3 Periodic Harmonic Wavelets

Periodic harmonic wavelets are the complex valued functions [2, 4, 6, 10]

$$\Psi_k^n(x) \equiv 2^{-n/2} \Psi(2^n x - k) = 2^{-n/2} \sum_{s=2^n}^{2^{n+1}-1} e^{-2\pi i s(x-k/2^n)}, \tag{6}$$

with $n, k \in \mathbb{N} \cup 0$. They are defined in the interval $(-\infty, +\infty)$ with slow decay, but their Fourier transforms $\widehat{\Psi}_k^n(\omega)$ are disjoint rectangle functions:

$$\widehat{\Psi}_k^n(\omega) = \begin{cases} 1/(2^{n+1}\pi), & 2^{n+1}\pi < \omega < 2^{n+2}\pi \\ 0, & \text{elsewhere,} \end{cases}$$

with compact support at each frequency, thus having a good localization in frequency. More in general, we can consider harmonic wavelets based on the interval $[0, 2^{-m})$, with fixed $m \in \mathbb{N} \cup \{0\}$,

$$\Psi_k^n(x) \equiv 2^{-n/2} \sum_{s=2^n}^{2^{n+1}-1} e^{-2^{m+1}\pi i s(x-k/2^n)},$$

with period 2^{-m} and dyadic intervals $(k2^{-m}, (k+1)2^{-m})$, $k \in \mathbb{Z}$.

Harmonic wavelets have an exact analytical expression and are infinitely differentiable functions, so that from (6), the first and second derivatives are:

$$\begin{cases} \frac{d\Psi_k^n(x)}{dt} = -2^{-n/2+1} \sum_{s=2^n}^{2^{n+1}-1} i \pi s e^{-2\pi i s(x-k/2^n)} \\ \frac{d^2\Psi_k^n(x)}{dt^2} = -2^{-n/2+2} \sum_{s=2^n}^{2^{n+1}-1} \pi s^2 e^{-2\pi i s(x-k/2^n)} . \end{cases} \tag{7}$$

Harmonic wavelets form an orthogonal set of independent periodic functions locally concentrated at the values $k/2^n$, ($k, n \in \mathbb{Z}$), with unit period, i.e. based on the unit interval $[0, 1]$.

3.1 Connection Coefficients

Harmonic wavelets are periodic functions thus we restrict to the unit interval $[0, 1]$ and there we assume as scalar product

$$\langle f, g \rangle \equiv \int_{-\infty}^{\infty} f(x)\overline{g(x)}dx ,$$

where the bar stands for the complex conjugate.

From the definition (6) and the equations (7), it easily follows for the linear connection coefficients (see also [10]), applying the Plancherel-Fubini theorem

$$\begin{aligned} \gamma_{kh}^{nm} &\equiv \left\langle \frac{d}{dx}\Psi_k^n(x), \overline{\Psi_h^m(x)} \right\rangle \\ &= -2^{-(n+m)/2+1} \sum_{s=2^n}^{2^{n+1}-1} \sum_{r=2^m}^{2^{m+1}-1} i \pi s \int_{-\infty}^{\infty} e^{2\pi i [(r-s)x-(h/2^m-k/2^n)]} dx , \end{aligned}$$

so that the unvanishing components of the connection coefficients are those for which $n = m$.

There follows

$$\gamma_{kh}^{nm} = -2^{-(n+m)/2+1} \left[\sum_{s=2^n}^{2^{n+1}-1} \sum_{r=2^m}^{2^{m+1}-1} i \pi s e^{-2\pi i (h/2^m-k/2^n)} \delta_{rs} \right] \delta^{nm} ,$$

and explicitly,

$$\gamma_{kh}^{nm} = \begin{cases} -2^{1-n} \pi i \sum_{s,r=2^n}^{2^{n+1}-1} s e^{-2^{1-n}\pi i (h-k)} \delta_{rs} & , \quad n = m , \\ 0 & , \quad n \neq m . \end{cases} \tag{8}$$

In particular, taking into account that $k = 0, \dots, 2^n - 1$, $h = 0, \dots, 2^m - 1$, we have

$$\gamma_{00}^{00} = -2\pi i ,$$

and up to $n = m = 3$, the (first order) connection coefficients are the matrices

$$\gamma_{kh}^{11} = (5\pi) \begin{pmatrix} -i & i \\ i & -i \end{pmatrix},$$

$$\gamma_{kh}^{22} = (11\pi) \begin{pmatrix} -i & 1 & i & -1 \\ -1 & -i & 1 & i \\ i & -1 & -i & 1 \\ 1 & i & -1 & -i \end{pmatrix},$$

4 Periodic Harmonic Wavelet Solutions

We assume as a wavelet solution of equation (5) the following function depending on the (scale) level of approximation $N \leq \infty$

$$E_x(x, t) = \sum_{n=0}^{2^N-1} \sum_{k=0}^{2^n-1} \beta_k^n(t) \Psi_k^n(x), \tag{9}$$

with $\Psi_k^n(x)$ given by (6). Taking into account the orthogonality property of the harmonic wavelets with the corresponding conjugate functions, equation (5) becomes

$$\sum_{n,k} \beta_k^n(t) \frac{d}{dx} \Psi_k^n(x) = \frac{a\epsilon}{\mu} \sum_{n,k} \left[\frac{d}{dt} \beta_k^n(t) \right] \Psi_k^n(x) + b,$$

in the unknown functions $\beta_k^n(t)$ with $n = 0, \dots, 2^N - 1, k = 0, \dots, 2^n - 1$ and,

$\sum_{n,k} = \sum_{n=0}^{2^N-1} \sum_{k=0}^{2^n-1}$. So that according to the definition of the connection coefficients (8) and the orthonormality of wavelets it is

$$\sum_{n,k} \beta_k^n(t) \left[\frac{d}{dx} \Psi_k^n(x) \right] \Psi_h^m(x) = \frac{a\epsilon}{\mu} \sum_{n,k} \left[\frac{d}{dt} \beta_k^n(t) \right] \Psi_k^n(x) \Psi_h^m(x) + b \Psi_k^n(x) \Psi_h^m(x),$$

and

$$\sum_{n,k} \beta_k^n(t) \int_{-\infty}^{\infty} \left[\frac{d}{dx} \Psi_k^n(x) \right] \Psi_h^m(x) dx = \frac{a\epsilon}{\mu} \sum_{n,k} \frac{d}{dt} \beta_k^n(t) \left[\int_{-\infty}^{\infty} \Psi_k^n(x) \Psi_h^m(x) dx \right] + \int_{-\infty}^{\infty} b \Psi_k^n(x) \Psi_h^m(x) dx$$

from where

$$\sum_{n,k} \beta_k^n(t) \gamma_{kh}^{nm} = \frac{a\epsilon}{\mu} \left[\frac{d}{dt} \beta_h^m(t) \right] + b \delta_h^m. \tag{10}$$

4.1 Harmonic Wavelet Solution at the Level $N = 0$

At the lowest resolution level ($N = 0 \Rightarrow n = k = 0$), it is $\gamma_{00}^{00} = -2\pi i$ so that, we have, from (10), the following equation

$$\begin{aligned} \frac{d}{dt}\beta_0^0(t) &= \frac{\mu}{a\epsilon} [\beta_0^0(t)\gamma_{00}^{00} - b], \\ &= \frac{\mu}{a\epsilon} [-2\pi i\beta_0^0(t) - b], \end{aligned} \tag{11}$$

with a solution given by

$$\beta_0^0(t) = c_1 e^{-2\pi i\mu t/(a\epsilon)} + \frac{b}{2\pi i} \tag{12}$$

and since $\Psi_0^0(x) = e^{-2\pi i x}$, the periodic harmonic wavelet solution at the level $N = 0$ is

$$E_x(x, t) = c_1 e^{-2\pi i[x + \mu t/(a\epsilon)]} + \frac{b}{2\pi i} e^{-2\pi i x} . \tag{13}$$

5 Conclusion and Outlook

In this paper we have shown how to decompose a signal (the solution of differential system) which describes the evolution in time of the electric field inside a fuel cell, into series of uncorrelated components. Each component gives the content at a given scale of the electric field. Thus allowing us to connect the evolution with the scale content. Considering that the solutions have boundary conditions in a *cascade* structure. The boundary conditions can be seen as inputs of the considered system. A possible future development of the presented approach involves a detailed analysis of the boundary conditions in order to find some optimal operating point of H_2 and O_2 for some given load current constraints. In particular possible control scheme can be conceived, fig. 3. The control scheme consists of an internal electric field observer to control the multi hydrogen inputs.

References

1. J. C. Amphlett, R. M. Baumert, R.F. Mann, B. A. Peppley, and P. R. Roberge. Performance modelling of the ballard mark iv solid polymer electrolyte fuel cell. *Journal of Electrochemical society*, 142(1):9–15, 1995.
2. C. Cattani. Harmonic wavelet solutions of the schrödinger equation. *International Journal of Fluid Mechanics Research*, 5(1-10):ISSN 1064–2277, 2003.
3. C. Cattani. Harmonic wavelets towards solution of nonlinear pde. *Computers and Mathematics with Applications*, 50:1191–1210, 2003.
4. C. Cattani. The wavelet-based technique in dispersive wave propagation. *International Applied Mechanics*, 39(4):493–501, 2003.
5. C. Cattani and A.Ciancio. Wavelet analysis of linear transverse acoustic waves. LXXX:ISSN 1–20, 2002.

6. D.E.Newland. Harmonic wavelet analysis. A 443:203–225, 1993.
7. P. Mercorelli, M. Rode, and P. Terwiesch. System and methodology for dominant frequency detection by using a set of trigonometric wavelet functions. *Patent N 7759 in Patentamt ABB Corporate Research Mannheim. Code in the German Patent Office 10 25 89 21. 6*, 2001.
8. P. Mercorelli and P. Terwiesch. A black box identification in harmonic domain. *VDE European Transactions on Electrical Power*, 13(1):29–40, 2003.
9. T. E. Springer, T. A. Zawodzinski, and S. Gottesfeld. Polymer electrolyte fuel cell model. *Journal of Electrochemical society*, 138(8):2334–2342, 1991.
10. S.V.Muniandy and I.M.Moroz. Galerkin modelling of the burgers equation using harmonic wavelets. *Phys.Lett, A* 235:352–356, 1997.

Tangent-Linear Models by Augmented LL-Parsers

Uwe Naumann and Andre Vehreschild

Department of Computer Science, RWTH Aachen University,
52056 Aachen, Germany
naumann@stce.rwth-aachen.de,
vehreschild@sc.rwth-aachen.de

Abstract. We describe a novel method for the generation of tangent-linear code by augmentation of LL-parsers generated by the software tool ANTLR. The main advantage of this approach to source code augmentation is the missing requirement for an internal representation of the original program. We consider this work as the basis for further investigations into how far this technique can be extended in the context of more sophisticated transformations, for example, the automatic generation of adjoint codes. Our prototype tool AD_C_ANTLR currently accepts a subset of the ANSI C standard. We discuss its theoretical basis, and we present a case study to underline the elegance of the parser-based approach to source augmentation.

1 Motivation

What are tangent-linear models good for? Consider the elliptic partial differential equation

$$-\Delta y - \lambda e^y = 0 \tag{1}$$

on the unit square Ω where $y(x_1, x_2) = 0$ on $\partial\Omega$.¹ The Laplacian operator is defined as $\Delta \equiv \frac{\partial^2}{\partial x_1^2} + \frac{\partial^2}{\partial x_2^2}$. It can be solved using a centered finite difference scheme by approximating the first derivative with respect to x_1 and x_2 at the midpoints of the discretization intervals

$$a = \left(\frac{x_i^1 - x_{i-1}^1}{2}, x_j^2 \right), \quad b = \left(\frac{x_{i+1}^1 - x_i^1}{2}, x_j^2 \right),$$

$$c = \left(x_i^1, \frac{x_j^2 - x_{j-1}^2}{2} \right), \quad \text{and} \quad d = \left(x_i^1, \frac{x_{j+1}^2 - x_j^2}{2} \right)$$

as

$$\frac{\partial y}{\partial x_1}(a) \approx \frac{y_{i,j} - y_{i-1,j}}{h}, \quad \frac{\partial y}{\partial x_1}(b) \approx \frac{y_{i+1,j} - y_{i,j}}{h}$$

¹ Our intention is not to discuss state-of-the-art methods for solving this problem. We would rather like to give an intuitive example to motivate the need for tangent-linear models. Similar situations occur in the context of more sophisticated numerical methods.

and

$$\frac{\partial y}{\partial x_2}(c) \approx \frac{y_{i,j} - y_{i,j-1}}{h}, \quad \frac{\partial y}{\partial x_2}(d) \approx \frac{y_{i,j+1} - y_{i,j}}{h} .$$

We have chosen uniform step size h both in the x_1 and x_2 directions such that $1/h \in \mathbb{N}$. Similarly, the second derivatives with respect to x_1 and x_2 at (x_i^1, x_j^2) can be approximated as

$$\frac{\partial^2 y}{\partial x_1^2}(x_i^1, x_j^2) \approx \frac{1}{h} \left[\frac{y_{i+1,j} - y_{i,j}}{h} - \frac{y_{i,j} - y_{i-1,j}}{h} \right] = \frac{y_{i+1,j} - 2 \cdot y_{i,j} + y_{i-1,j}}{h^2}$$

and

$$\frac{\partial^2 y}{\partial x_2^2}(x_i^1, x_j^2) \approx \frac{1}{h} \left[\frac{y_{i,j+1} - y_{i,j}}{h} - \frac{y_{i,j} - y_{i,j-1}}{h} \right] = \frac{y_{i,j+1} - 2 \cdot y_{i,j} + y_{i,j-1}}{h^2} .$$

It follows that a numerical approximation to the solution of the partial differential equation can be computed by solving the discretized problem

$$f(y) = -\frac{y_{i+1,j} - 2 \cdot y_{i,j} + y_{i-1,j}}{h^2} - \frac{y_{i,j+1} - 2 \cdot y_{i,j} + y_{i,j-1}}{h^2} - \lambda e^{y_{i,j}} = 0 \quad (2)$$

for $i, j = 1, \dots, 1/h - 1$. Since the values of y on $\partial\Omega$ are known Eqn. (2) is a system of $(1/h - 1)^2$ nonlinear equations in the same number of unknowns. Given a good start estimate y^0 it can be solved by Newton’s method with quadratic convergence as follows:

$$\begin{aligned} \delta y^i &= -(f'(y^i))^{-1} \cdot f(y^i) \\ y^{i+1} &= y^i + \delta y^i \end{aligned}$$

for $i = 0, \dots$. At each step the algorithm requires the Jacobian f' of f at the current estimate y^i . Alternatively the Newton step can be obtained as the solution of the linear system

$$f'(y^i)\delta y^i = -f(y^i) \quad (3)$$

at each Newton iteration. Direct methods may be prohibitive due to the size of the problem. Iterative methods are likely to be more suitable. For example, iterative refinement computes the iterates as

$$\delta y^{i+1} = \delta y^i + B(f(y^i) - f'(y^i)\delta y^i) \quad (4)$$

for a suitable preconditioner B . Note that Eqn. (4) involves the computation of a Jacobian-vector product. This is done by a tangent-linear code that can be generated efficiently from a routine implementing f by the source transformation technique proposed in this paper. There is no need to form the whole Jacobian explicitly.

Tools for *automatic differentiation (AD)* [11] by source transformation such as ADIFOR2.0 [5], its successor ADIFOR3.0 [6], TAF [10], the commercial successor of TAMC [9] distributed by FastOpt GmbH, TAPENADE [14], the successor of Odyssee [8], ADiMat [4], and OpenAD [19] transform numerical simulation

programs into an abstract internal representation (annotated parse tree, symbol tables, control flow graphs, call graph). The transformation algorithms operate on this often very complex data structure to obtain the semantically modified code that computes derivatives of various kinds. The intermediate representation allows for a large number of static analyses to be performed with the objective to optimize the resulting transformed code. However, the development of a complete compiler front-end is a difficult and time-consuming task. Many AD-related code transformations can be integrated directly with the parser. Parser generators such as Bison [7] and ANTLR [17] provide a very convenient platform for this integration.

Our main intention is to investigate the level of complexity in terms of semantic transformations that can be realized by a single-pass compiler through augmentation of the parser. Initially we focus on LL(k)-parsers [1] for a subset of ANSI C that are generated by ANTLR. Similar, investigations are underway for LR(1)-parsers generated by Bison. In this paper we present a feasibility study for the parser-based generation of tangent-linear code. After a brief introduction to the underlying principles of AD in Sec. 2 we present algorithmic details of the augmented LL-parser in Sec. 3. In Sec. 4 we present our prototype tangent-linear model compiler `AD_CANTLR` followed by a case study in Sec. 5. Conclusions are drawn in Sec. 6 together with an outlook to the possible application of similar techniques in the context of adjoint codes.

2 Background: Automatic Differentiation

For a given implementation of a vector function $f : \mathbb{R}^n \rightarrow \mathbb{R}^m$ as a computer program² we use AD by source transformation to generate code for computing first derivatives of f . Therefore the computation of $\mathbf{y} = f(\mathbf{x})$ is expected to decompose into a sequence of elemental assignments

$$v_j = \varphi_j(v_i)_{i \prec j} \quad (5)$$

for $j = 1, \dots, p + m$ and $i \prec j$ if and only if v_i is an argument of φ_j . Eqn. (5) is referred to as the *code list* of f . We set $v_{i-n} = x_i$ for $i = 1, \dots, n$ and $v_{p+j} = y_j$ for $j = 1, \dots, m$. The v_k , $k = 1 - n, \dots, p + m$, are called *code list variables*. Forward mode AD transforms f into the tangent-linear model \hat{f} that computes a total (or directional) derivative $\dot{\mathbf{y}} = \hat{f}(\mathbf{x}, \dot{\mathbf{x}})$ as $\dot{\mathbf{y}} = f' \dot{\mathbf{x}}$. The $m \times n$ matrix $f' = f'(\mathbf{x})$ is the Jacobian of f with entries defined as $f'_{ji} = \frac{\partial y_j}{\partial x_i}$ for $i = 1, \dots, n$ and $j = 1, \dots, m$. This transformation is achieved by applying well-known differentiation rules to the elemental functions

$$\varphi_j \in \{+, -, *, /, \sin, \exp, \dots\}$$

followed by the application of the chain rule as

$$\dot{v}_j = \sum_{i \prec j} c_{ji} \dot{v}_i \quad (6)$$

² From now on we will use f to refer to this implementation as a computer program.

for $j = 1, \dots, m$ and total derivatives \dot{v}_k of the code list variables v_k , $k = 1 - n, \dots, p + m$. The elemental functions φ_j are assumed to be continuously differentiable in a neighborhood of the current argument. The corresponding local partial derivatives are denoted by $c_{ji} = \frac{\partial \varphi_j}{\partial v_i}$.

As a convenient alternative to source transformation, tools for the automatic differentiation of numerical programs can be implemented by operator overloading. Established representatives are ADOL-C [12], AD01 [18], and FADBAD [3].

3 Augmented LL-Parsing

We present an algorithm that augments scalar assignments syntactically defined by the context-free grammar $G = (N, T, S, P)$ with nonterminal symbols $N = \{ASGN, EXPR, EXPR_LIST\}$, terminal symbols $T = \{'=', '(, \varphi, ')', ', '\}$, where $\varphi \in \{\varphi_j, j = 1, \dots, p + 1\}$, start symbol $S = ASGN$, and production rules

$$P = \left\{ \begin{array}{l} ASGN := var \ '= ' \ EXPR \\ EXPR := var \\ EXPR := \varphi \ '(\ EXPR_LIST \)' \\ EXPR_LIST := EXPR \\ EXPR_LIST := EXPR \ ', ' \ EXPR_LIST \end{array} \right\} .$$

LL-parsers traverse the abstract syntax tree (ast) in depth-first order, making recursive calls to “matching” routines defined for each non-terminal and terminal symbol. For example, the simple assignment $y = x_1 * x_2$ is parsed as follows:

```

ASGN
  var(y)
  EXPR(*)
    EXPR_LIST
      EXPR
        var(x1)
      EXPR_LIST
        EXPR
          var(x2)

```

We associate post-order actions A , Φ , and V with $ASGN$, $EXPR$, and var , respectively. In order to relate the indexing to the code list in Eqn. (5) we set $\Phi \equiv \Phi(j)$ and $V \equiv V(j)$ in the following definition.

```

A :      CALL  $\Phi(p + 1)$ 
        EMIT( $\dot{y} = \dot{v}_{p+1}$ )
        EMIT( $y = v_{p+1}$ )

 $\Phi \equiv \Phi(j)$  : CALL  $\Phi(i)$ ,  $\forall i \prec j$ 
                P := POP( $(\{i : i \prec j\})$ )
                if ( $P = \emptyset$ ) then

```

```

    CALL  $V(v_j = x_k)$ 
  else
    EMIT( $\dot{v}_j = \sum_{k \in P} c_{jk} \cdot \dot{v}_k$ )
    EMIT( $v_j = \varphi_j(v_k)_{k \in P}$ )
    PUSH( $j$ )
  end if

```

```

 $V \equiv V(j)$  : if NEW( $x$ ) then
    EMIT( $v_j = x$ )
    PUSH( $j$ )
  else
    PUSH(ID( $x$ ))
  end if

```

Processing an assignment starts with processing its right-hand-side whose value is stored in v_{p+1} as in Eqn. (5). Hence, the required assignments of the value v_{p+1} and its directional derivative \dot{v}_{p+1} to the corresponding left-hand-side variables are generated by calling the EMIT function. Expressions are processed recursively. A stack is used to PUSH and POP the indexes of the respective code list variables. When matching a variable x the boolean function NEW is called to check if x has already been assigned to a code list variable. If so, then ID(x) returns the corresponding index. According to the assumption that $V = V(j)$ is called with the correct code list variable index we have implicitly ID(x) = j . However, the emission of the assignment $v_j = x$ is omitted in this case. The algorithm is illustrated with the help of a simple example in Fig. 1.

The augmentation can be performed irrespective of the flow of control. Hence, an existing parser can easily be extended to become a tangent-linear code generator.

4 Implementation

A first prototype has been implemented using ANTLR. The grammar of the prototype is based on the GNU C grammar provided by John Mitchell and Monty Zukowski provided on the website of ANTLR at www.antlr.org. The portion of the grammar implementing ANSI C was separated from code for building the AST, so that only the rules for recognizing C input remained. Support for the symbol table, scoping, and unparsing was dropped completely. The implementation language was changed from Java to C++. The full source of the current prototype can be downloaded from www.stce.rwth-aachen.de/research/antlr. Below we briefly explain the implementation of the actions associated with assignments, operators or function calls, and variable references.

All grammar rules handling expressions take a flag as argument that selectively activates the generation of tangent linear code. For example, the generation is switched off if indexes of arrays are computed, or when parsing the conditions in loops or in branch statements. A pair of identifiers is returned consisting of

```

[1] A :
[2]   .Φ :
[3]   . . Φ :
[4]   . . . V :
[4]   . . . . .EMIT( $\dot{v}_0 = \dot{x}_2$ )
[5]   . . . . .EMIT( $v_0 = x_2$ )
[6]   . . . . .PUSH(0)
[7]   . . Φ :
[8]   . . . Φ :
[9]   . . . . V :
[9]   . . . . .EMIT( $\dot{v}_{-1} = \dot{x}_1$ )
[10]  . . . . .EMIT( $v_{-1} = x_1$ )
[11]  . . . . .PUSH(-1)
[12]  . . . Φ :
[13]  . . . . Φ :
[14]  . . . . . V :
[14]  . . . . . . . . . . .PUSH(0)
[15]  . . . . .P := POP(1) = {0}
[16]  . . . . .EMIT( $\dot{v}_1 = -\sin(v_0) * \dot{v}_0$ )
[17]  . . . . .EMIT( $v_1 = \cos(v_0)$ )
[18]  . . . . .PUSH(1)
[19]  . . . P := POP(2) = {1, -1}
[20]  . . . .EMIT( $\dot{v}_2 = v_{-1} * \dot{v}_1 + v_1 * \dot{v}_{-1}$ )
[21]  . . . .EMIT( $v_2 = v_{-1} * v_1$ )
[22]  . . . .PUSH(2)
[23]  . . .P := POP(2) = {2, 0}
[24]  . . . .EMIT( $\dot{v}_3 = 1/v_2 * \dot{v}_0 - v_0/v_2^2 * \dot{v}_2$ )
[25]  . . . .EMIT( $v_3 = v_0/v_2$ )
[26]  . . . .PUSH(3)
[27]  . . .P := POP(1) = {3}
[28]  . . . .EMIT( $\dot{y} = \dot{v}_3$ )
[29]  . . . .EMIT( $y = v_3$ )

```

The following tangent-linear code is generated:

```

 $\dot{v}_0 = \dot{x}_2$ 
 $v_0 = x_2$ 
 $\dot{v}_{-1} = \dot{x}_1$ 
 $v_{-1} = x_1$ 
 $\dot{v}_1 = -\sin(v_0) * \dot{v}_0$ 
 $v_1 = \cos(v_0)$ 
 $\dot{v}_2 = v_{-1} * \dot{v}_1 + v_1 * \dot{v}_{-1}$ 
 $v_2 = v_{-1} * v_1$ 
 $\dot{v}_3 = 1/v_2 * \dot{v}_0 - v_0/v_2^2 * \dot{v}_2$ 
 $v_3 = v_0/v_2$ 
 $\dot{y} = \dot{v}_3$ 
 $y = v_3$ 

```

Fig. 1. Example: $y = x_2/(x_1 * \cos(x_2))$

the names of the variables that the result of the last computation and the value of the corresponding total derivative are assigned to, respectively.

Assignments are implemented as described in Sec. 3. Derivative code is generated only if the type of the variable on the left-hand side is `float` or `double`. The prototype stores the association of variables and their types in a simple map that is far from a full featured symbol-table.

The right-hand side of the assignment is known to return a pair of names of temporary variables. The output generated is the assignment of the temporary variable to the variable on the left-hand side. The C-compiler's copy propagation algorithm [2, 15] is set in charge of removing these obsolete assignments.

Multiplications and other operators and calls to intrinsic functions are treated by distinct grammar rules preserving priority. After such a rule is matched completely, two new temporary variables are allocated. The declaration of these variables is written to a second stream which is merged to the output stream when the current statement list is closed, i.e. when the associated closing curly bracket is parsed. The expressions to compute the derivative is usually written to the output stream first followed by the expression to compute the original expression. The order of the derivative and original computation is arbitrary. Only for the division operator and the exponential the order is exchanged to take advantage of the computed original result in the derivative expression.

Variables are looked up in the map of variables. A derivative variable is generated and its declaration is emitted depending on their type.

5 Case Study

We consider a very simple example that is similar to the one used in Sec. 3. The original input code is given as follows.

```
void f(double *x) {
    x[2]= x[1]/(x[0] * exp(x[1]));
}
```

It implements a scalar function $f : \mathbb{R}^2 \rightarrow \mathbb{R}^1$. AD_C_ANTLR produces the following tangent-linear code.

```
void f(double * x, double * g_x){
    double v_00;
    double g_v_00;
    double v_01;
    double g_v_01;
    double v_02;
    double g_v_02;
    v_00= exp(x[1]);
    g_v_00= g_x[1]* exp(x[1]);
    g_v_01= g_x[0]* v_00+ x[0]* g_v_00;
    v_01= x[0]* v_00;
```

```

v_02= x[1]/ v_01;
g_v_02= (g_x[1]- v_02* g_v_01)/ v_01;
g_x[2]= g_v_02;
x[2]= v_02;
;
}

```

The gradient $f' \in \mathbb{R}^2$ can be computed by two executions of the tangent-linear code initializing $g_x[0]=1$, $g_x[1]=0$ and $g_x[0]=0$, $g_x[1]=1$, respectively. These initializations are performed within the following driver routine.

```

#include <stdio.h>

void f(double * x, double * g_x);

int main(int argc, char **argv) {

    double x[]={2.0, 4.0, 0.0};
    double g_x[]={0,0,0};
    int j;

    for(j=0;j<2; ++j) {
        g_x[j]=1;
        f(x, g_x);
        printf("%f\n", g_x[2]);
        g_x[j]=0;
    }

    return 0;
}

```

Running the corresponding executable results in the following output

```

-0.018316
-0.027473

```

that is exactly equal to the gradient of $x[2]$ with respect to $x[0]$ and $x[1]$ at the point $(2.0, 4.0)$.

6 Conclusion and Outlook

An approach to the automatic generation of tangent-linear code was presented that does not rely on the construction of an intermediate representation of the original program. Special post-order traversal actions were associated with an LL(k)-parser generated by ANTLR to cover a subset of the ANSI C standard. The simplicity of the implementation is apparent from the freely available source code. Feasibility and correctness of this approach was illustrated by a case study.

An obvious disadvantage of the single-pass approach is the missing infrastructure for static data-flow analysis [13]. Nevertheless we believe that the parser-based source transformation represents a reasonable trade-off between efficiency and ease of implementation.

We are currently working on the extension of AD_CANTLR to the parser-based generation of adjoint code defined by $\bar{v}_j = \sum_{k:j \prec k} c_{kj} \bar{v}_k$ for $j = p, \dots, 1-n$. Adjoint code requires the reversal of the flow of control. The straight-forward approach is to augment the original code with statements to PUSH values of overwritten variables and indexes of basic blocks [16]. These values are POPed in the adjoint section of the code to achieve the control-flow reversal and to compute the local partial derivatives c_{kj} .

References

1. J. Ullman A. Aho. *The Theory of Parsing, Translation, and Compiling. Volume 1: Parsing*. Prentice Hall, 1972.
2. J. Ullman A. Aho. *The Theory of Parsing, Translation, and Compiling. Volume 2: Compiling*. Prentice Hall, 1972.
3. C. Bendtsen and O. Stauning. FADBAD, a flexible C++ package for automatic differentiation. Technical Report IMM-REP-1996-17, Department of Mathematical Modelling, Technical University of Denmark, Lyngby, Denmark, August 1996.
4. C. Bischof, M. Bücker, B. Lang, A. Rasch, and A. Vehreschild. Combining source transformation and operator overloading techniques to compute derivatives for MATLAB programs. In *Proceedings of the Second IEEE International Workshop on Source Code Analysis and Manipulation (SCAM 2002)*, pages 65–72, Los Alamitos, CA, USA, 2002. IEEE Computer Society.
5. C. Bischof, A. Carle, P. Khademi, and A. Maurer. The ADIFOR 2.0 system for Automatic Differentiation of Fortran 77 programs. *IEEE Comp. Sci. & Eng.*, 3(3):18–32, 1996.
6. A. Carle and M. Fagan. ADIFOR 3.0 overview. Technical Report CAAM-TR-00-02, Rice University, 2000.
7. C. Donnelly and R. Stallman. *The Bison Manual*. Free Software Foundation, 2003.
8. C. Faure and Y. Papegay. Odyssée User’s Guide. Version 1.7. Rapport technique RT-0224, INRIA, Sophia-Antipolis, France, September 1998.
9. R. Giering and T. Kaminski. Recipes for Adjoint Code Construction. *ACM Trans. Math. Software*, 24(4):437–474, 1998.
10. R. Giering and T. Kaminski. Applying TAF to generate efficient derivative code of Fortran 77-95 programs. In *Proceedings of GAMM 2002, Augsburg, Germany*, 2002.
11. A. Griewank. *Evaluating Derivatives. Principles and Techniques of Algorithmic Differentiation*. Number 19 in Frontiers in Applied Mathematics. SIAM, Philadelphia, 2000.
12. A. Griewank, D. Juedes, and J. Utke. ADOL-C, a package for the automatic differentiation of algorithms written in C/C++. *ACM Trans. Math. Software*, 22(2):131–167, 1996.
13. L. Hascoët, U. Naumann, and V. Pascual. TBR analysis in reverse-mode Automatic Differentiation. *Future Generation Computer Systems*, 21:1401–1417, 2005.
14. L. Hascoët and V. Pascual. Tapenade 2.1 user’s guide. Technical report 300, INRIA, 2004.
15. S. Muchnick. *Advanced Compiler Design and Implementation*. Morgan Kaufmann Publishers, San Francisco, 1997.
16. U. Naumann, J. Utke, A. Lyons, and M. Fagan. Control flow reversal for adjoint code generation. *Science of Computer Programming*, 2005. To appear.

17. T. Parr and R. Quong. Antlr: A predicated-ll(k)-parser generator. *Software Practice and Experience*, 7(25):789–810, 1995.
18. J. Pryce and J. Reid. ADO1, a Fortran 90 code for automatic differentiation. Technical Report RAL-TR-1998-057, Rutherford Appleton Laboratory, Chilton, Didcot, Oxfordshire, OX11 0QX, England, 1998.
19. C. Wunsch, C. Hill, P. Heimbach, U. Naumann, J. Utke, M. Fagan, and N. Tallent. Openad. Preprint ANL/MCS-P1230-0205, Argonne National Laboratory, Argonne, IL, February 2005.

GIS-T Web Services: A New Design Model for Developing GIS Customized ITS Application Systems

Xiaolin Lu

School of Information Technology, Zhejiang University of Finance & Economics,
Hangzhou 310012, China
luxiaolin@mail.hz.zj.cn

Abstract. The GIS-T web services can provide the hosted spatial data and GIS functionalities that can be accessed and integrated into the different customized ITS applications. This paper presents the system design for building the Web GIS based intelligent transportation application system with GIS-T web service technology. The GIS-T web services are designed to perform basic geo-processing tasks, such as address matching, map image display, and routing, without maintaining GIS tools or the associated geographical data. The system architecture is designed as a multi-layer framework that integrates the web services, Servlet/JSP functions and GIS APIs based on the J2EE infrastructure.

A prototype of a Web-GIS transportation planning system is designed and implemented with the proposed GIS-T web service platform. Through the GIS-T web service, the hosted spatial data and GIS functionalities that can also be accessed and integrated to other different ITS application systems. It has an important application prospect in the Web GIS based ITS development and application.

1 Introduction

The geographical information system for transportation (GIS-T) plays an important role in the intelligent transportation system (ITS). Generally ITS mainly includes the subsystems of the intelligent transportation control systems, the video supervisory systems, the electronic police systems, the 110/122 alarm systems, vehicle movement management systems, the street intersection control systems and the mass transportation systems [1,2,3]. In the process of design and development of all those ITS subsystems, the GIS is an absolutely necessarily function that needs to be integrated with all the subsystems.

While the traditional GIS software development method would be very difficult to meet the needs for all the subsystems of ITS with single GIS-T platform, the GIS web service technologies have provided a new efficient solution for all those ITS application systems [4,5,6]. The GIS web services are the software components that can provide the hosted spatial data and GIS functionalities that can be accessed and integrated to the different practical customized GIS-T applications. Developers can apply the GIS web services to perform geographical information processing and return the results to the customized ITS applications without maintaining the basic GIS system

or the geographical data. The web service technology is a very promising architecture for practical implementation of the Web-GIS based intelligent transportation application system.

Although many researches have been devoted to apply the web services technology to GIS system with different kinds of GIS Web Services [7,8], few studies have been reported on the design for building Web GIS based intelligent transportation application system with GIS web service technology. The purpose of this paper is to explore and investigate the service-oriented architecture for building a distributed and web service enabled Web-GIS based intelligent transportation application system. The GIS web service architecture, GIS functions, ITS system integrations, and some key technical problems are discussed in this paper.

2 Overview of Related Works

2.1 Web Services Oriented Architecture

Web Services are the software components that are well defined, self-contained, and does not depend on the context or state of other services [9]. Web services essentially use XML to create a robust connection. The web services architecture has three roles: a provider, a requestor, and a broker. The provider creates the web service and makes it available to clients who want to use it. A requestor is a client application that consumes the web service. The broker, such as a service registry, provides a way for the provider and the requestor of a web service to interact. The provider, requestor, and broker interact with each other through the operations of publish, find, and bind. A provider informs the broker about the existence of the web service by using the broker's publish interface to make the service accessible to clients. The information published describes the service and specifies where the service is located. The requestor consults the broker to locate a published web service. With the information it gained from the broker about the web service, the requestor is able to bind, or invoke, the web service. The following figure illustrates a basic service-oriented architecture.

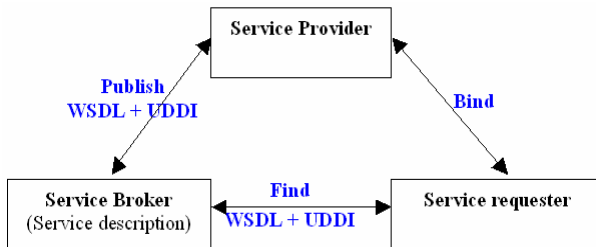


Fig. 1. Web services oriented architecture

The web services use SOAP (Simple Object Access Protocol), WSDL (Web Services Description Language), UDDI (Universal Description, Discovery and Integration), and WSIL (Web Services Inspection Language) to communicate. Web services are published on the UDDI registry. A WSDL document defines the target service so

the client knows what the service does. SOAP standardizes the way a Web service communicates with a client and allows programs written in different languages and on different platforms to communicate. SOAP works with standard Web protocols including XML, HTTP, and TCP/IP, as well as WSDL.

2.2 Open GIS Consortium Web Services (OWS)

OGC is an international industry consortium of more than 220 companies, government agencies and universities. In order to allow interoperability between server and client software from multiple vendors, the request and response must be standardized. By focusing standardization on the interface, the software developers, data custodians, and processing-service providers can work to their particular software components, while connecting with other systems for complementary services. Open GIS Consortium is developing specifications to standardize the message interfaces [10]. These include

- Web Map Service (WMS) for maps encoded as images;
- Web Feature Service (WFS) for geographic objects or vector data;
- Web Coverage Service (WCS) for continuous data;
- Sensor Collection Service (SCS) for live access to observations from sensors;
- Geography Markup Language (GML): XML components for encoding geographic objects for transport.

The OGC WMS specification offers a standard client-server interaction protocol that each map server implements as a common interface for accepting requests and returning responses [11]. The same client is able to access to all available OGC web map servers over the Internet. The client through the common interface accesses each map server. In a distributed OGC WMS, a WMS server can also run as a WMS client that requests capabilities and maps from other WMS servers.

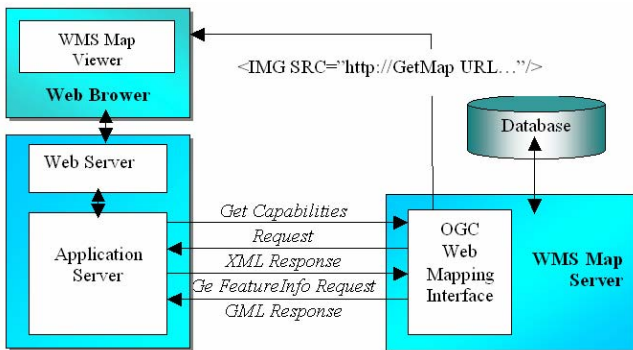


Fig. 2. The system structure of OGC WMS mapping application

A system structure of WMS mapping application is illustrated in Figure 2. The OGC web map server implements three functions: GetCapabilities, GetMap, and GetFeatureInfo. The GetCapabilities function provides the client with a map server's

service metadata, specifying its capabilities. The GetMap function specifies map request parameters that enable the client to request an image map. Finally, the GetFeatureInfo function allows the client to request more information about features at a specific location in the map.

The client application requests the information from the web map server. The map server retrieves from the database the appropriate layers of geo-feature data for the specified spatial domain and generates a map that can be viewed directly in a graphical web browser or other pictorial software. The client and web map server interact using Hypertext Transfer Protocol.

OGC WMS is an interoperable web mapping system. It provides common interfaces to connect with the client application and dynamically process geo-referenced data such as geographic maps and features coded using Geography Markup Language (GML) documents. The OGC Web Map Service specification defines a set of functions that clients may use to interact with WMS providers (servers). Any client making requests that conform to the specification can interact with any server that implements the WMS service. In effect, this creates an interoperable, distributed web mapping systems [12].

3 Web GIS Service Based ITS Application System

The GIS technologies used for the intelligent transportations system have been studied by many investigators in recent years. GIS mapping for the intelligent transportations system is an essential, efficient, and effective tools for planning and managing transportation information resources [1]. With the development of the Internet enable the GIS system, some authors have investigated the Web-based GIS applications for environmental analysis for planning and management. The Web, Java, and CORBA technologies were explored in implementing GIS-T systems. The researches on Web-Based GIS for transportation (Web-GIS-T) have attracted much attention [13-15].

As the technology of web services evolves, the web service becomes a main working pattern and a significant application model for next generation Internet application [16-20]. The Web GIS service based ITS application system is to provide a web GIS environment by the dynamic integrating GIS-T service components of vector and raster maps to customized ITS application system with geo-reference data and information. It supports the complex rendering, navigation and allows working with multiple layers, thematic maps, hyper linked features and attribute data. The fundamental GIS platform is based on the web service oriented architecture. The map features are stored on a SQL database according OGC SFS and WMS that can be used as raster maps source.

3.1 GIS-T Web Service Architecture Design

The GIS-T web services are used by a number of ITS application systems which include the intelligent transportation control systems, the video supervisory systems, the electronic police systems, the 110/122 alarm systems, vehicle movement management systems, the street intersection control systems and the mass transportation systems. A customized ITS application system, which need the geo-reference data and information, can be viewed directly in a graphical web browser or other pictorial software.

The ITS application system can be integrated with the GIS client and web map service by Hypertext Transfer Protocol. The GIS-T web service architecture includes the web service engine, ITS application clients and web service interface and data storages. The GIS-T web service system framework for ITS application system is illustrated in Figure 3.

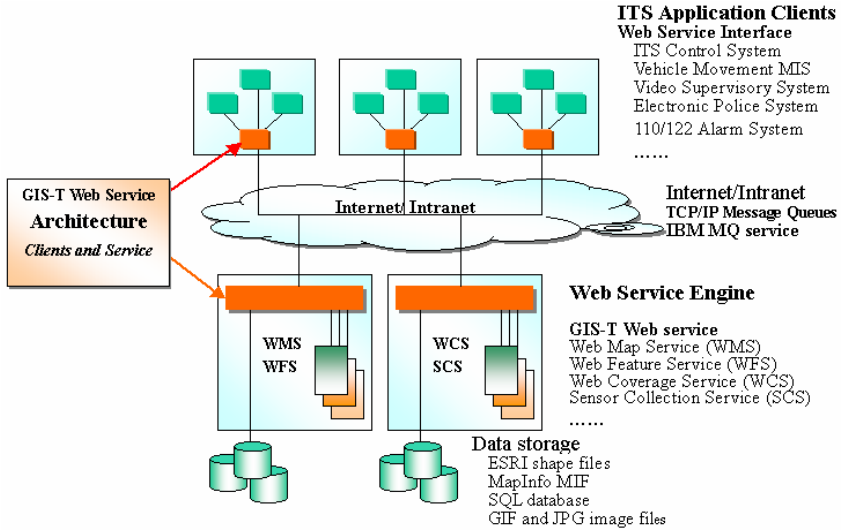


Fig. 3. The GIS-T Web service system framework for ITS application systems

3.2 GIS-T Web Services Design Principles

GIS-T Web Services are discoverable, self-describing software components. UDDI is an open standard with broad industry support standard. When an implemented GIS Web Service is exposed in any Web Services portal, it can be discovered in any Web Services portal. Once a GIS Web Service is discovered, the developer can begin using it immediately. All they need is the full URL path to the services WSDL. Each method, parameter, property, and return value of the service is described in a standard way, allowing modern development tools to immediately allow access to the exposed functionality.

GIS-T Web Services conceal complexity. Web Services embed its complex data processing within itself in server side. Client side application developer make use of Web Services through standard interface which described in Web Services WSDL, therefore the application developer don't need dealing with Web Services internal process.

The following principles are considered in the design for the service oriented distributed GIS-T platform. Web GIS platform should provide a variety of interfaces for integration and interoperability with customized ITS application system.

(1) **GIS-T Web Services:** Web GIS-T platform should support the standard enterprise application server technologies to build web services with embedded spatial

services, software components and APIs to easily embed spatial capabilities in customized ITS application system built using standard technologies and architectures.

(2) **Web Mapping Services (WMS):** WMS can display map layers for all the customized ITS application system and allow all the customized ITS application system to display map layers from Web GIS platform

(3) **OpenGIS Consortium Interoperability Services and Standards:** The Web GIS platform should be implemented with the OpenGIS interoperability standards:

(4) **Geography Markup Language (GML):** GML is a common XML-based file format for exchanging spatial information and attributes. The Web GIS platform should support the GML standards.

(5) **Common Database Environment:** Specifications on spatial entities and the space/time reference systems have been provided by the OpenGIS Consortium.

3.3 GIS Platform Architecture Design

The GIS-T platform architecture is designed as a multi-layer architecture that integrated the web service, Servlet/JSP functions and GIS APIs based on the framework of J2EE infrastructure. The GIS system can be accessed by lots of different computers in network with different kinds of operating system.

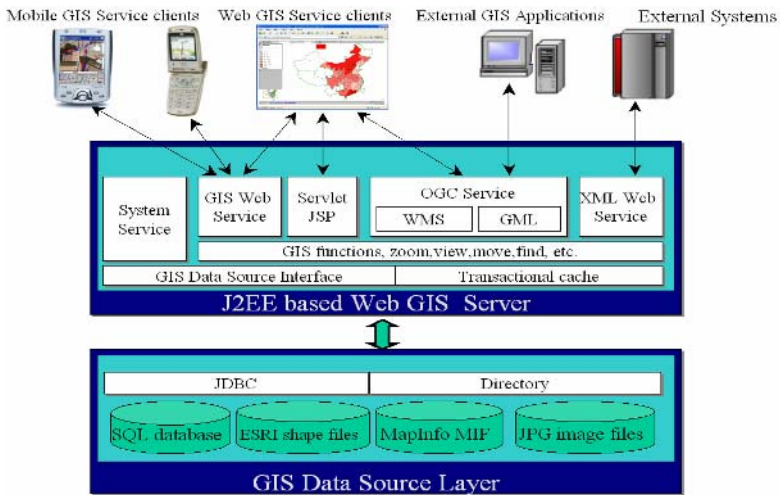


Fig. 4. Service oriented architecture for GIS-T Web Service platform

The figure 4 shows the service oriented architecture of GIS-T Web Service platform. It is a distributed, platform independent system architecture. The data are stored and managed with EJB. The distributed systems enable the databases and services in the same or different computers. The Web GIS platform Server architecture is consisted of three layers: User Interface Layer, Application Server Layer and Database Layer.

(1) **Application Server Layer:** In the application server layer, the GIS web services, Servlet/JSP interface, GCO services which include GML and WMS map

service, and basic system application service is deployed in the J2EE server container. The GIS function such as the zooming out and in, viewing, panning and finding will be designed as an function session bean that can be accessed by the GIS web service, Servlet/JSP and other Application interfaces. The application server layer is built as a J2EE application, with several EJB modules, to provide server-centric spatial functions to applications. Key components of the server that implemented as EJBs are: Web GIS services, Geo-spatial functions, such as the viewing, layer selection, editing, querying, and analysis Data Source Management. The J2EE based Web GIS server layer is shown in the figure 4.

(2) User Interface: Web GIS platform provides a number of user interface components: Web service client, GIS java Applet and any other web service enabled applications. The mobile and PDA that support the web service standards interface could get the map and geo-referenced data through the GIS web service interface. The web browser based clients could communicate with the Web GIS service through the GIS web service, Servlet/JSP and OGC service. The clients perform URL requests to Map Service and obtain maps rendered in a pictorial format such as GIF or JPEG. A GIS Java Applet is another user interface that can be used to retrieve and handle the vector and raster map using the map tools. Java applet enables spatial viewing, querying, and richer editing capabilities to be easily embedded in desktop and web applications.

(3) Database Layer: The GIS data are stored and managed with the distributed systems architecture that enables the GIS data, databases and services in the same or different computers. The GIS platform should support following GIS data format: Vector data and Raster data

- ESRI shape files: ESRI shape files can contain points, multipoint, poly-lines and polygons objects. The attribute data is stored in dBase.
- MapInfo MIF: MapInfo MIF is stored in pair with DBF file not with MID. MIF contains region, poly-line, multiple, line and point. All objects are the same type.
- SQL database: It can be any SQL server with JDBC driver.
- GIF and JPG image files.
- OpenGIS Web Map Service

4 System Implementation and Discussions

We have applied the GIS-T web service in constructing a Web-GIS based CSCW system for transportation planning. The system includes following basic principles:

(1) Information Sharing: The databases of GIS, transportation planning projects, and CSCW are the information center of the system. All the geo-referenced cooperating work and information sharing depend on the GIS-T web service.

(2) Human Computer Interaction Based on WEB-GIS: The Web-GIS is the basis graphical user interface of man-machine interface in the system. Based on GIS-T web service, interoperable information system obtains the geographical position simultaneity. The transportation relevant departments could use the GIS-T web service interface to work together. It provides the basic functions in coordination working environment.

(3) Transportation Planning Projects Broadcasting: In this system, every one participates in the activities to cooperate, broadcast the data of transportation planning through GIS-T web service.

(4) Transportation Planning Department, Traffic Department, Relevant Government Department, and Public Cooperation: The system can synchronize transportation planning department, traffic department, relevant government department, and public through the center databases. The GIS, transportation-planning project, and CSCW information can be shared and exchanged.

The figure 5 demonstrates the implementation of the system. The GIS-T Web service is used to show the GIS information in the transportation planning information system.

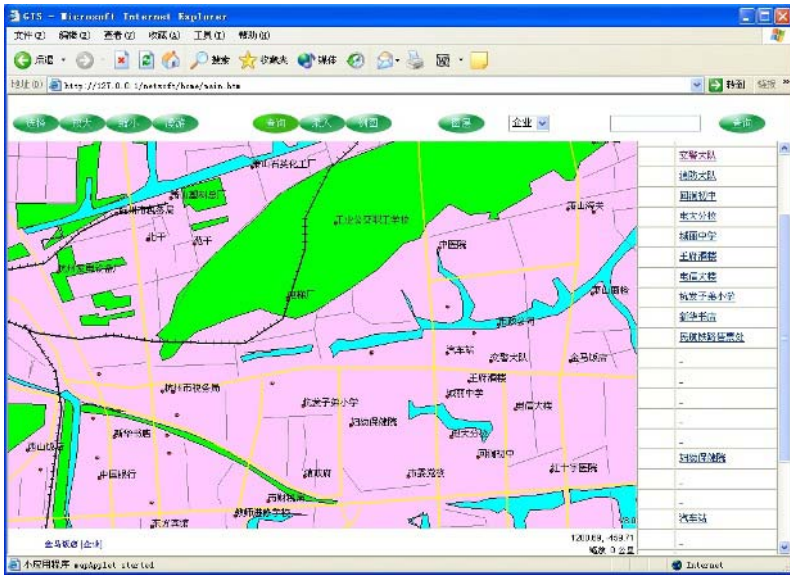


Fig. 5. GIS-T Web service for the transportation planning information system

The system can provide an efficient means for the transportation planning with following advantages. Firstly, the hosted spatial data and GIS functionalities that can be accessed and integrated to the different customized GIS-T applications to meet the practical need in the processes of transportation planning. Secondly, running on the Internet, the system is accessible from anywhere in the world. Web-GIS service technologies not only make the system broadly accessible through Internet and but also provide the precise geo-referenced data for public and transportation planning researchers.

Although we have implemented the prototype of the service oriented architecture of distributed GIS platform and adopted it into a Web-GIS based CSCW system for transportation planning, this study only focused on the system architecture design for the GIS-T platform. Since the requirement of the practical GIS applications in different application domain and field are quite complicated, a general GIS-T Web service

will be integrated into the different user customized application. Further work should be performed to establish the common GIS-T Web services that could be easily used and integrated in different ITS application systems.

5 Conclusions

This paper presented the system design for building a distributed Web-GIS based intelligent transportation application system with web service technology and service-oriented architecture. The GIS-T web services were designed to provide the hosted spatial data and GIS functionality to integrate the customized ITS applications to perform basic geo-processing tasks, such as address matching, map image display, and routing, without maintaining GIS tools or the associated geographical data.

We designed and implemented a prototype of a Web-GIS based CSCW system for transportation planning, which includes the GIS functions and the geo-referenced cooperating work and information sharing depend on the GIS-T web service. The transportation relevant departments could use the GIS-T web service interface to work together. It provides the basic functions in coordination working environment. Through GIS-T web service, the hosted spatial data and GIS functionalities that can be accessed and integrated to the different customized ITS applications.

The service-oriented architecture is a very promising architecture for practical implementation of the next generation GIS-T information systems. It has an important application prospect in the ITS development and application. Further work will be performed to establish the common GIS-T Web services that can be easily used and integrated in different ITS application systems.

References

1. Gui L., Li Y., Chen X.: Study and Development of WebGIS-T for Transportation. *Journal of Changsha Communications University (in Chinese)*, Vol.17 No.4, (2001) 18-22
2. Gil Nicholas T., Al Akhras Ahmad: Transportation Plan Information Management System. In: *Proc. of the Conference on Transportation, Land Use, and Air Quality*, (1998) 606 – 613
3. Li X., Tu S., He X., Ratcliff J. J.: Web-Based Distribution of GIS Metropolitan Maps. In: *Proc of Fifth International Conference on Information Visualization (IV'01) London, England*, (2001) 419-424
4. Shanzhen Y., Lizhu Z., Chunxiao X., Qilun L., Yong Z.: Semantic and Interoperable WebGIS. In: *Proc of International Conference on Web Information Systems Engineering (WISE'01)*, Vol.2, Kyoto, Japan, (2001) 42-48
5. Tu S., Maik F., Wu Y., Mahdi A., Normand E., Mahadevan V., Ratcliff J. J., Shaw K.: Design Strategies to Improve Performance of GIS Web Services. In: *Proc of the International Conference on Information Technology: Coding and Computing (ITCC'04)*, Volume 2, Las Vegas, Nevada, USA, (2004) 444-449
6. Jong W. K., Park S. S., Kim C. S., Lee Y.: The Efficient Web-Based Mobile GIS Service System through Reduction of Digital Map. In: Antonio Laganà, et al. Eds. *Computational Science and Its Applications - ICCSA 2004, International Conference*, Vol. I. Assisi, Italy, May 14-17, 2004, *Lecture Notes in Computer Science* 3043, Springer, (2004) 410-417

7. Domenico Cotroneo, Cristiano di Flora and Stefano Russo: An Enhanced Service Oriented Architecture for Developing Web-based Applications. *J. Web Eng.*, 1(2), (2003) 128-146
8. Ming-Hsiang Tsou: An Operational Metadata Framework for Searching, Indexing, and Retrieving Distributed Geographic Information Services on the Internet. In: Max J. Egenhofer, David M. Mark. Eds. *Geographic Information Science, Second International Conference, GIScience 2002*, Boulder, CO, USA, September 25-28, 2002. *Lecture Notes in Computer Science 2478*, Springer, (2002) 313-332
9. IBM: Web Services architecture overview. Available at <http://www-106.ibm.com/developerworks/webservices/library/w-ovr/>, (2003)
10. Open GIS Consortium Inc: OpenGIS Simple Feature Specification For SQL Version 1.1. Open GIS project document 99-049. (1999)
11. Open GIS Consortium Inc: Web Map Service Implementation Specification 1.1.0. Open GIS project document: OGC 01-047r2. (2001)
12. Cox S., Daisey P., Lake R., Portele C., Whiteside: A. Geography Markup Language (GML) Implementation Specification version 3.0.0: OpenGIS project document: OGC 02-023r4. Available at <http://www.opengis.org/techno/documents/02-023r4.pdf>. (2002)
13. Kingston R., Carver S., Evans A., Turton I.: Web-Based Public Participation Geographical Information Systems: An Aid To Local Environmental Decision-Making. *Computers, Environment and Urban Systems*, Vol. 24, No. 2, (2000) 109-125
14. Coddington P.D., Hawick K.A., James H.A.: Web-Based Access to Distributed High-Performance Geographic Information Systems for Decision Support. In: *Proc of Thirty-second Annual Hawaii International Conference on System Sciences*, Vol. 6 Maui, Hawaii, (1999) 6015- 6016
15. Lu X. Infrastructure for Intelligent Transportation Planning CSCW System based on WEB-GIS Technology. In: *Prof of 2004 World Congress on Intelligent Control and Automation (WCICA'04)*, Hangzhou, China, IEEE Press, (2004) 5297-5301
16. ESRI: An Overview of ArcWeb Services. Available at <http://www.esri.com/library/whitepapers/pdfs/arcweb-services.pdf>. July 2004.
17. Tang W., Selwood J.: *Connecting Our World: GIS Web Services*. ESRI Press, (2003)
18. Microsoft: MapPoint .NET Demos. Available at <http://demo.mappoint.net/>, (2003)
19. Lu X. An Investigation on Service-Oriented Architecture for Constructing Distributed Web GIS Application. In: *Proc of IEEE International Conference on Services Computing (SCC 2005)*, Vol. 1, Orlando, Florida, USA, IEEE Press, (2005) 191-197
20. Peter Baumann: Web-Enabled Raster GIS Services for Large Image and Map Databases. In: A. Min Tjoa, Roland Wagner. Eds. *12th International Workshop on Database and Expert Systems Applications (DEXA 2001)*, Munich, Germany, 3-7 September 2001. IEEE Computer Society, (2001) 870-874

An Algorithm on Extraction of Saline-Alkalized Land by Image Segmentation Based on ETM⁺ Image

Li Jianping, Zhang Bai, Zhang Shuqing, and Wang Zongming

Northeast Institute of Geography and Agriculture Ecology, C A S, 130012,
3195 Weishan Road, Changchun, China
lijianping@neigae.ac.cn

Abstract. Based on ETM⁺ remote sensing image, according to geographical distribution and spectral characteristics of saline-alkalized land, especially that of light, and moderate saline-alkalized land, an algorithm of semi-supervised multi-grade mean weighed seed region searching is presented. Experimental results indicate that the algorithm has high operation speed, high segmentation accuracy and certain fault tolerance, and also, to a great extent, over-segmentation problem can be perfectly solved. But because of mixed distribution of sand land and saline-alkalized land, they can not be effectively segmented by the algorithm.

1 Introduction

Remote sensing(RS) played a key role in dynamic monitoring of saline-alkalized land[1][2][3][4]. Based on remote sensing images, basically, approaches of extraction of saline-alkalized land are classified into manual visual interpretation and computer auto-classification. As far as manual visual interpretation is concerned, there are lots of drawbacks[5], such as low efficiency, time-consuming, inevitable omitting, etc. Computer auto-classification mainly depends on the statistical relation between characteristics of statistical values of remote sensing data and training samples, and because of the complexity of object distribution, if we only use single classification principle and ignore such various factors as spatial position, hue feature and so on, possibly, classification effects are unsatisfactory. So, in the paper, based on ETM⁺ image, an algorithm of semi-supervised multi-grade mean weighed seed region searching to extract saline-alkalized land is presented, this algorithm can fast accurately extract saline-alkalized land of large region, which provides scientific basis for preventing and controlling land salinization.

2 Spectral Characteristics of Saline-Alkalized Land

According to classification system of land use in China[6], saline-alkalized land includes three types, namely light saline-alkalized land, moderate saline-alkalized land, and heavy saline-alkalized land. Interpretation keys of saline-alkalized lands in pseudo color ETM⁺ image (bands 4,3,2) are shown as Table.1[7]. Seen from Table.1,

light white color of different levels denotes hues of various saline-alkalized lands in pseudo color ETM⁺ image, and hue of heavy saline-alkalized land is most outstanding, whereas red vegetations of various coverage degrees are distributed into light, and moderate saline-alkalized lands, so there are many mixed pixels in image, and hue is most indistinct. So extraction of light saline-alkalized land and moderate saline-alkalized land are rather difficult and also, it is the research key in the paper.

Table 1. Interpretation keys of various saline-alkalized lands

<i>Types of saline-alkalized land</i>	<i>Distribution</i>	<i>Spectral characteristic</i>	<i>Area percentage</i>
light saline-alkalized land	indistinct distribution and bad growing trends of vegetations or crops	light white color distributed into light red(vegetations)	less than 20%
Moderate saline-alkalized land	periphery of heavy saline-alkalized land, covered by some vegetations	white color distributed into light red(vegetations) or light grey(mixed pixels of thin grass or water)	20-50%
heavy saline-alkalized land	around bottomland lake, the places of low topography	light white color	more than 50%

3 Data Processing

3.1 Composing, Rectification and Enhancement of Image

Daan (44°57'~45°45'N, 123°08'~124°21'E), a city in western Jilin province of China, is a typical region of saline-alkalized land[8]. One Landsat ETM⁺ image of August, 2002 in the region is acquired as experimental data. Standard false color image composite of bands 4,3 and 2 is performed, followed by precise geometric rectification which ground control points were chose referencing to topographic map of 1:50000, then equal-area conical projection of the image based on two standard parallels is done. We use quadratic polynomial to accomplish geometric rectification, and resample is achieved by cubic convolution with matching error under one pixel to meet the demand of interpretation of saline-alkalized land. Finally, we spatially enhanced the image through contrast transform and histogram equalization.

3.2 Color Model Transform

In the field of digital image processing, various color models were proposed, like RGB,HSI,HSV,CIE,etc. But selecting most optimal color space is still one problem to color image segmentation[9].

The RGB color model is suitable for color display, but is not good for color analysis because of its high correlation among *R*,*G*,and *B* color components[10].In color image processing and analysis, the HSI model is widely used, *H*,*S*, and *I* denote hue, saturation, intensity, respectively. In the paper, the causes of choosing HSI model are as follows:1)*H* and *S* components are closely correlative with the color sense of eyes[11];2)Hue information and intensity information are distinctly differentiated in HSI model;3)By HSI model, computer program can easily process color information

after color sense of eyes are transformed into specific values. RGB model is firstly transformed into HSI model, the formulas are expressed as [12]:

$$I = \frac{1}{3}(R + G + B) \quad (1)$$

$$S = 1 - \frac{3}{R + G + B}[\min(R, G, B)] \quad (2)$$

$$H = \arccos \left\{ \frac{[(R - G) + (R - B)] / 2}{[(R - G)^2 + (R - B)(G - B)]^{1/2}} \right\} \quad (3)$$

4 Algorithm of Image Segmentation

Based on image segmentation, an algorithm of semi-supervised multi-grade mean weighed seed region searching is presented. The algorithm is described as: firstly, feature samples of various saline-alkalized lands are manually selected, weighed mean values of color components and mean values of color gradients of several sub-blocks of each type of saline-alkalized land are calculated, rules of selecting seeds are constructed, then image is searched by the scanning approach of raster image, the locations of pixels which satisfy the rules of seeds are recorded, and the spatially connected pixels are combined into one region, namely seed region, then weighed mean values of color components and mean values of color gradients of each seed region are calculated, growing rules of seed regions are established, and seed regions are taken as growing points for region growing, self-adaptive growing rules are automatically updated, finally, regions are merged according to the rules of region merging.

4.1 Samples of Saline-Alkalized Lands

Light, and moderate saline-alkalized lands are usually distributed together with vegetations and lakes, which are mixed pixels in image. In the paper, several sub-blocks of light, moderate, and heavy saline-alkalized land are manually selected from image, and by weighed mean values of color components and mean value of color gradients of selected sub-blocks of saline-alkalized lands, we can acquire prior color feature values and gradient values which are basis of selecting seeds.

Suppose n sub-blocks of certain type of saline-alkalized land are selected from image, and the size of each sub-block image is S_1, S_2, \dots, S_n , calculation methods of average values of color components and gradients are presented as the following.

4.1.1 Weighed Mean Color Components

In HSI color space, mean values of each color component of n sub-block images of certain type of saline-alkalized land are written as:

$$AH = \frac{1}{n} \left(\sum_{i=1}^{S_1} H_i + \sum_{i=1}^{S_2} H_i + \dots + \sum_{i=1}^{S_n} H_i \right) \quad (4)$$

$$AS = \frac{1}{n} \left(\sum_{i=1}^{S_1} S_i + \sum_{i=1}^{S_2} S_i + \dots + \sum_{i=1}^{S_n} S_i \right) \tag{5}$$

$$AI = \frac{1}{n} \left(\sum_{i=1}^{S_1} I_i + \sum_{i=1}^{S_2} I_i + \dots + \sum_{i=1}^{S_n} I_i \right) \tag{6}$$

Where AH, AS , and AI denote the mean values of H, S , and I components, respectively.

Different weighed coefficients are given to mean values of H, S , and I components, then linear equation is constructed, let

$$C = \alpha_1 AH + \alpha_2 AS + \alpha_3 AI \tag{7}$$

Where α_1, α_2 , and α_3 are weighed coefficients, and the values of α_1, α_2 , and α_3 are on the basis of the degree in which various color components influence image segmentation. In HSI color space, H and I components have a relatively great impact on segmentation of saline-alkalized land, so weighed coefficients of H and I components should be relatively larger.

4.1.2 Mean Gradients of Color Image

According the gradient formula of grey image, we defined gradient of color image in three-dimensional color space, the formula is expressed as:

$$\begin{aligned} grad(x, y) &= \left| f'_x \right| + \left| f'_y \right| \tag{8} \\ &= \left| w_1 \frac{\partial_{C_1} f(x, y)}{\partial x} + w_2 \frac{\partial_{C_2} f(x, y)}{\partial x} + w_3 \frac{\partial_{C_3} f(x, y)}{\partial x} \right| + \\ &\quad \left| w_1 \frac{\partial_{C_1} f(x, y)}{\partial y} + w_2 \frac{\partial_{C_2} f(x, y)}{\partial y} + w_3 \frac{\partial_{C_3} f(x, y)}{\partial y} \right| \end{aligned}$$

Where $f(x, y)$ is the function of color image in $C_1 C_2 C_3$ color space, $\frac{\partial_{C_1} f(x, y)}{\partial x}$ denotes X-axis gradient of C_1 component, other may be deduced by analogy. w_1, w_2 , and w_3 are weighed coefficients, their values are on the basis of the degree in which various color components influence image segmentation.

We select Sobel operator as gradient mask in X-axis and Y-axis, the operator is as follows:

$$\frac{\partial f(x, y)}{\partial x} = \begin{bmatrix} 1 & 2 & 1 \\ 0 & 0 & 0 \\ -1 & -2 & -1 \end{bmatrix} \quad \frac{\partial f(x, y)}{\partial y} = \begin{bmatrix} -1 & 0 & 1 \\ -2 & 0 & 2 \\ -1 & 0 & 1 \end{bmatrix} \tag{9}$$

By the above formulas, the gradients of pixels of sub-block image are calculated, and mean gradients of n sub-blocks of image are expressed as :

$$AG = \frac{1}{S_1 + S_2 + \dots + S_n} \left(\sum_{(i,j) \in S_1} grad(i,j) + \sum_{(i,j) \in S_2} grad(i,j) + \dots + \sum_{(i,j) \in S_n} grad(i,j) \right) \quad (10)$$

4.2 Region Growing

The essential concept of region growing is that starting from seed points or seed regions selected, the spatially connected pixels of similar character are clustered to form one integrated meaningful region according to certain growing rules. Because color distribution and spatial location of pixels are fully taken into account, compared with such methods as cluster, edge detection and so on, region growing approach is more suitable for color image segmentation[13][14].

4.2.1 Seed Points and Seed Regions

By raster scanning method, the image is searched to get seed points. Suppose through the above formulas, prior weighed mean values of color components of light, moderate, and heavy saline-alkalized land are $D_L, D_M,$ and D_H respectively, mean values of color gradients of light, moderate, and heavy saline-alkalized land are $G_L, G_M,$ and G_H respectively, and $p(x,y)$ is the pixel point which is currently searched, the weighed color component of the point is written as : $D_p = \alpha_1 H + \alpha_2 S + \alpha_3 I$, where $\alpha_1, \alpha_2,$ and α_3 are weighed coefficients, and gradient of the point is calculated according to formula(8), then rules of choosing seed points are as follows:

$$\left| D_p - D_i (i = L, M, H) \right| < T_D \quad (11)$$

$$\left| G_p - G_i (i = L, M, H) \right| < T_G \quad (12)$$

Where T_D and T_G are threshold values.

We laid a strong emphasis on the study of segmentation of light, and moderate saline-alkalized land, and they are usually distributed together with vegetations and water areas, so if seed points are selected according to the above rules, vegetations and water areas maybe are mistakenly selected as seed points, and good segmentation results will be not achieved if region growing begins with the mistaken seed points. So in the paper, region growing begins with not seed points, but seed regions derived from seed points. Formation of seed regions is described as: pre-segmentation image is searched, seed points which satisfy rules are selected and recorded, then the spatially connected seed points are merged into regions, the regions are seed regions.

4.2.2 Rules of Region Growing

The key of region growing approach is rules of region growing. In the paper, we construct two rules, namely color difference and gradient of color image. Let seed region is A , the size of A is S , certain connected pixel of A is $p(x,y)$.

4.2.2.1 Rule of Color Difference. The weighed variances of color components of A are as follows.

$$E_H = \frac{1}{S} \sum_{(i,j) \in S} H(i,j), E_S = \frac{1}{S} \sum_{(i,j) \in S} S(i,j), E_I = \frac{1}{S} \sum_{(i,j) \in S} I(i,j) \tag{13}$$

$$D_H = \frac{1}{S} \sum_{(i,j) \in S} (H(i,j) - E_H)^2,$$

$$D_S = \frac{1}{S} \sum_{(i,j) \in S} (S(i,j) - E_S)^2,$$

$$D_I = \frac{1}{S} \sum_{(i,j) \in S} (I(i,j) - E_I)^2 \tag{14}$$

$$\sigma_H = \sqrt{D_H}, \sigma_S = \sqrt{D_S}, \sigma_I = \sqrt{D_I} \tag{15}$$

$$C_A = \alpha_1 \sigma_H + \alpha_2 \sigma_S + \alpha_3 \sigma_I \tag{16}$$

Where $H(i, j)$, $S(i, j)$, and $I(i, j)$ are the values of H, S , and I components of the point (i, j) in A , respectively. E_H, E_S , and E_I are the mean values of H, S , and I components respectively, D_H, D_S , and D_I are variances of H, S , and I components respectively, σ_H, σ_S , and σ_I are standard deviations of H, S , and I components respectively, α_1, α_2 , and α_3 are weighed coefficients.

The weighed value of color components of $p(x, y)$ is C_p with $C_p = \alpha_1 H_p + \alpha_2 S_p + \alpha_3 I_p$, and if $|C_p - C_A| < T_C$, then $p(x, y)$ satisfies the rule of color difference, where T_C is threshold value with $T_C = \lambda C_A$, where λ is scale factor, the value of λ can be confirmed through experiments, usually, $0.15 < \lambda < 0.2$.

4.2.2.2 *Rule of Gradient of Color Image.* By formula (8), the gradient of $p(x, y)$ is

$$G_p, \text{ mean gradient of } A \text{ is } G_A \text{ with } G_A = \frac{1}{S} \sum_{(i,j) \in S} grad(i, j), \text{ and if } |G_p - G_A| < T_G,$$

then $p(x, y)$ satisfies the rule of gradient of color image, where T_G is threshold value with $T_G = \lambda G_A$.

On condition that $p(x, y)$ satisfies the above two rules, $p(x, y)$ can be merged into A to form a new region whose size is $S+1$, then the new region is regarded as seed region to continue region growing, edge pixels of saline-alkalized lands are recorded when region growing is finished. If any one of the following three conditions is satisfied, namely 1) $p(x, y)$ does not satisfy the above two rules; 2) $p(x, y)$ is recorded edge pixel; 3) $p(x, y)$ is pixel of another seed region, then $p(x, y)$ can not be merged into A , and the next pixel is judged with the same approach. After the current region growing is finished, the next seed region will be searched, and the above process is repeated till there are no seed regions. Edge cluster may be ignored because only saline-alkalized lands are segmented in the paper.

4.2.3 Segmentation of Water Areas

Usually, some large or small lakes are distributed into saline-alkalized lands, moreover, the lakes and saline-alkalized lands are mutually transformed under certain conditions, for instance, saline-alkalized lands are transformed into water areas when rainfall is heavy, and water areas are transformed into saline-alkalized lands when the weather is hot and drought, so in the paper, some season lakes under threshold value of area are regarded as saline-alkalized lands. By the above approach, water areas are segmented in ETM⁺ image, and water areas are merged into saline-alkalized lands on the basis of the following rules of region merging.

4.3 Region Merging

Usually, some small fragmentary regions maybe arise or homogeneous regions are segmented into several regions by region growing, thus in order to form a meaningful whole region, some small regions must be merged into large connected regions according to certain rules, which is region merging. In the paper, rules of region merging are as follows: 1)spatial relation of regions; 2)regional area; 3)color moments; 4)regional gradient.

Firstly, concept of color moment is introduced. Color moment means that any color distribution of images can be denoted through its moments. Color distribution information is mainly focused on low-order moments, so only by using first-order, second-order, and third-order moments of color, color distribution of images can be expressed. And first-order, second-order, and third-order moments represent the mean value, standard deviation and unsymmetrical cubic root of image or sub-image respectively, their formulas are expressed as:

$$e = \frac{1}{m \times n} \sum_{j=1}^n \sum_{i=1}^m p(i, j) \quad (17)$$

$$\sigma = \left[\frac{1}{m \times n} \sum_{j=1}^n \sum_{i=1}^m (p(i, j) - e)^2 \right]^{1/2} \quad (18)$$

$$s = \left[\frac{1}{m \times n} \sum_{j=1}^n \sum_{i=1}^m (p(i, j) - e)^3 \right]^{1/3} \quad (19)$$

Where e , σ , and s denote first-order, second-order, and third-order moments respectively, $m \times n$ is the size of image, $p(i, j)$ is the value of linear combination of H, S , and I components.

Detail rules of region merging are described as the following:

Suppose A and B are two different regions, their image areas(pixel number) are R_A and R_B respectively, and $R_A > R_B$.

If A and B are spatially connected or B is contained within A , then rule of region merging is satisfied(for short "rule 1", the following may be deduced by analogy), otherwise A and B can not be merged and stop judging;

If “rule 1” is satisfied and $area(B) < T$, where T is threshold value(pixel number), then “rule 2” is satisfied, thus A and B can be combined into one region.

If “rule 1” is satisfied and “rule 2” is not satisfied, then A and B can be merged into one region on condition that both “rule 3” and “rule 4” are satisfied.

“rule 3” is described as: first-order, second-order, and third-order moments of A and B are calculated by formula(17),(18),and (19), the results are $e_A, \sigma_A, s_A, e_B, \sigma_B,$ and s_B ,if $|e_A - e_B| < T_e, |\sigma_A - \sigma_B| < T_\sigma,$ and $|s_A - s_B| < T_s,$ then “rule 3” is satisfied, where $T_e, T_\sigma,$ and T_s are threshold values.

“rule 4” is as follows: gradients of each pixel of A and B are calculated by formula(8), then average gradients of each region can be get.

$$G_A = \frac{1}{R_A} \sum_{(i,j) \in R_A} grad(i, j), G_B = \frac{1}{R_B} \sum_{(i,j) \in R_B} grad(i, j)$$

Where $grad(i,j)$ is gradient value of pixel, G_A and G_B are average values of gradient of A and B respectively. If $|G_A - G_B| < T_G$, then “rule 4” is satisfied, where T_G is threshold value.

5 Experiments and Discussion

The above algorithm is achieved in VC++.NET 2003 development software. We select the ETM+ image of quite typical region in Daan city as experimental data, the size of the image acquired in August 30th,2002 is 921×643pixel(Figure.1). Through lots of experiments, light, moderate, and heavy saline-alkalized land are segmented and extracted respectively(Figure.2).

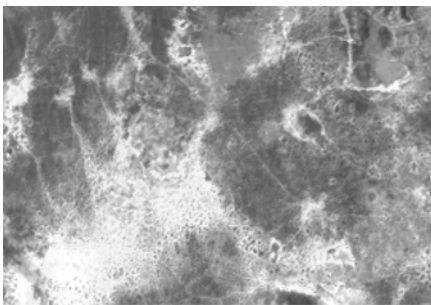


Fig. 1. Original image

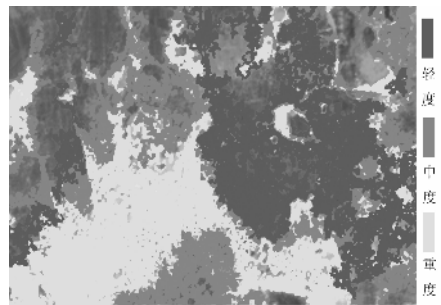


Fig. 2. Segmentation result

Considering geographical distribution and spectral characteristics of saline-alkalized lands, especially that of light saline-alkalized land, we manually select various saline-alkalized lands from image to get prior knowledge, then seed points are automatically selected, region growing is performed on the basis of seed regions derived from seed points, and threshold values are self-adaptively updated. Compared with common approaches of region growing and region merging, the approach of image

segmentation based on mean, variance, color gradient of sub-block can effectively control the deviation of more pixels and decrease the amount of small objects to control noise. According to the rules of region merging in the paper, over-segmented problem can be perfectly solved, and meaningful large regions are formed. Sub-image after segmentation is quite clear, and the differences of various types of saline-alkalized land are distinct, also, uncertainties of segmentation results are decreased.

In order to assess extraction accuracy of saline-alkalized lands, we randomly selected 350 samples, and the sample numbers of light, moderate, and heavy saline-alkalized lands are 150,100,100, respectively. By assessment tool of classification accuracy in ERADS IMAGINE8.4 software, together with the distribution map of saline-alkalized lands in Daan city from resources and environment academy of Jilin agriculture university, we assessed the extraction accuracy of saline-alkalized lands, results show that the extraction accuracy of light, moderate, and heavy saline-alkalized lands reach 82.34%,87.41%,93.77% respectively, and total accuracy is 87.84%. However by traditional MLC(Maximum Likelihood Classification) method, extraction accuracy of light, moderate, and heavy saline-alkalized lands are only 61.53%,64.32%,75.64% respectively, and total accuracy is 67.16%. Compared with some traditional classification methods of remote sensing image, the algorithm in the paper not only lay emphasis upon especial spectral characteristics of saline-alkalized lands but also stress spatial information of objects, and image segmentation is finished after image is searched once, hence extraction accuracy of the algorithm is high, and satisfactory results can be get, moreover, the algorithm has certain fault tolerance.

Although segmentation results are rather perfect by the method in the paper, there are some defects in detail, for instance, because of mixed distribution of sand lands and saline-alkalized lands, it is difficult to segment them by the algorithm, hence further research need be carried out.

References

1. Li Xiaoyan, Zhang Shuwen. Tempo-spatial dynamic and driving factors of saline-alkali land in Daan city of Jilin province. *Resources science*, Vol.27,Issue.3, (2005)92–97.
2. Pang Zhiguo, Li Jiren, Li Qusheng. Spatial variation of saline-alkalized land in western Jilin province and countermeasures for its prevention and treatment. *Remote sensing and land & resources*, Vol.6,Issue.1, (2004)57–61.
3. Dwivedi R S,Sreenivas K.Image transforms as a tool for the study of soil salinity and alkalinity dynamics.*International Journal of remote sensing*, Vol.19,Issue.4, (1998)605–619.
4. Wang D,Wilson C,Shannon M C.Interpretation of salinity and irrigation effects on soybean canopy reflectance in visible and near infrared spectrum domain.*International Journal of remote sensing*, Vol.23,Issue.5, (2002)811–824.
5. Zhou Bin, Yang Bailin. The research on land use change detection by using direct classification of stacked multitemporal TM images. *Journal of natural resources*, Vol.16,Issue.3, (2001)263–268.
6. Zou Yarong, Zhang Zengxiang,Zhou Quanbin,*et al.* Spatial pattern and its analysis of China's grassland change in recent ten years using remote sensing and GIS. *Journal of remote sensing*, Vol.7,Issue.5, (2003)428–433.

7. Chen Jianjun,Zhang Shuwen, Zhang Jing. Soil salinization detection with remote sensing and dynamic analysis in Daqing city. *Journal of arid land resources and environment*, Vol.17,Issue.4, (2003)101–107.
8. Pang Zhiguo,Lv Xianguo,Li Qusheng. Study on saline-alkalized land status appraising and developing countermeasures supported by 3S techniques.*Territory & natural resources study*, Vol.16,Issue.4, (2000)42–45.
9. Cheng H D,Jiang X H,Sun Y,*et al.* Color image segmentation:advances and prospects. *Pattern recognition*, Vol.34,Issue.12, (2001)2259–2281.
10. Frank Y.Shih,shouxian Cheng. Automatic seeded region growing for color image segmentation. *Image and vision computing*, Vol.23, Issue.10, (2005)877–866.
11. Liu Chong,Xia Zeyi. Sub-pixel edge detection method for SLM color microscopic images. *Chinese journal of mechanical engineering*, Vol.41,Issue.1, (2005)71–76.
12. Zhan Yujin(ed.).*Image processing and analysis*. Beijing: Tsinghua university press(2004).
13. Tremeau A,Nathalie Borel N.A region growing and merging algorithm to color segmentation.*Pattern recognition*, Vol.30,Issue.7, (1997)1191–1203.
14. Zhi Liu, Jie Yang, Ning Song Peng. Semi-automatic video object segmentation using seeded region merging and bidirectional projection.*Pattern recognition letters*, Vol.26,Issue.5, (2005) 653–662.

GIS Web Service Using Context Information in Mobile Environments*

Xun Li, Woochul Shin, Li Li, and Sang Bong Yoo

School of Computer Science, Inha University,
Incheon, Korea

Fax: 82-32-874-1435

{inhalgm, woochul, lizz}@dbsi.inha.ac.kr, syoo@inha.ac.kr

Abstract. Recently the computing environment has been moved to open architectures that include Web technologies. Web Service is one of import component of the new paradigm. This paper presents a design and implementation of GIS Web Service for mobile devices. As many mobile devices are equipped with GPS (Global Positioning System), it is required to handle the position information more effectively. We have extended the proxy program in the client device to actively send the context information to the server. Based on the context information the server determines the optimal service mode to a particular client. A working example of location-based GIS Web Service is also presented. By using Web Service standards and XML messages we can achieve the maximal interoperability for heterogeneous mobile devices.

1 Introduction

Recently, with the rapid development of the information systems and mobile communication technology, major computing power has now evolved from personal computer to being embedded in chips in many surrounding objects. In realizing this kind of ubiquitous computing environment, computers should automatically identify information and the environments of users in order to execute tasks more effectively.

The definition of context is not the same in various fields. In this paper we focus on the mobile terminals that are equipped with GPS (Global Positioning System) like PDAs. The information about user's location, moving direction, operating system, and screen size represents the context of mobile devices. The information obtained from a user can be classified into software, hardware and geographic information. For most standard client developers, programming to collect context information are not trivial because they include many system variables and GPS APIs. In this paper, we present a novel concept of active proxy, which not only helps the user to develop the client system efficiently but also collects the context information from mobile devices.

Most GIS systems are developed in some specific service environments; it is quite difficult to exchange information in different systems. For example PLIS (Productivity

* This work was supported (in part) by the Ministry of Information & Communications, Korea, under the Information Technology Research Center (ITRC) Support Program.

Layout Information System) and LMIS (Land Management Information System) and other systems use a specific database and development environment. Therefore, it is hard to directly exchange information each other. Being based on Web technologies, Web Service is promising technology for system integration. It is especially adequate for mobile environments because it employs simple XML messages. A Web Service interface and the message structure have been designed and implemented for location-based GIS service.

This paper is organized as follows. Section 2 discusses related work. Section 3 describes structure and handling of context-aware information for the location-based GIS Web Service. In Section 4, implementation of the Web Service is described. A working example of the Web Service is also presented. Section 6 concludes the paper and summarizes the contributions of this paper.

2 Related Work

Researches on context-awareness technologies have been emerged in the field of natural language processing. However, as the more devices are controlled by embedded computers, it is required to handle the context information more effectively [3, 5, 6, 7, 11].

Context Toolkit (CT) is developed by Georgia Tech to facilitate building context-aware applications with standard components, such as context widgets, context aggregators and context interpreters [1]. CT utilizes these three components to offer appropriate services, and uses necessary context information; however the systems are not widely used. University of Arizona research relating to context-awareness technology is accomplished in the RCSM project [2]. The university had designed a kind of a high-efficiency description language based context interface.

However, common characteristics of the researches in this field are they usually require a large number of sensors [12, 13]. The GIS Web Service presented in this paper, the sensor that users contain is only GPS. The application areas that we are targeting are location-based service to mobile devices such as PDA and mobile phones. Because there are various platforms for those mobile devices, it is important task to collect context information correctly and provide services suitable for users [4, 9].

In this paper the proposed standard Web Service technologies are used to realize the Active Proxy for Web Service [8, 10]. Using the Active Proxy, programmers are not required to consider OS system variables and hardware properties. The Active Proxy will be embedded in user's terminal and provide the context information to the server.

3 Modeling Context Information in Mobile Devices

3.1 Data Types including Context Information

Context Information in mobile devices comes from GPS and OS. Because we provide location-based service, the data from GPS are important. Standard GPS system provides the following location data.

- Universal Time
- Latitude ddmm.mm
- N or S (North or South)
- Longitude ddmm.mm
- E or W (East or West)
- GPS Quality Indicator
 - 0 - fix not available
 - 1 - GPS fix
 - 2 - Differential GPS fix
- Number of satellites in view2
- Antenna Altitude above/below mean-sea-level
- WGS-84 Geoidal separation, the difference between the WGS-84 earth ellipsoid and mean-sea-level
- Units of antenna altitude, meters
- Client speed
- Checksum

Other context data come from the operating system variables. The following variables are defined in Windows CE.

- public SIZE sizeScreenSize; // Screen Size
- public String szComputerName; // Computer Name
- public String szUserDomainName; // Domain Name
- public String szUserName; // User Name
- public String szLocalIP; // IP
- public String szOSType; // OS Type
- public OS_VERSION OsVersion; // OS Version
- public Int32 dwSystemLanguageID; // System Language
- public bool bCanPlaySound; // Sound Availability
- public Int32 dwMonitorCount; // Monitor count
- public Int32 dwMemorySize; // Memory Size
- public Int32 dwTickCount; // Running Time
- public DATE_TIME dtSystemTime; // System Time
- public Int32 dwNetworkSpeed; // Network Speed
- public String szProcessModel; // Process Model

The context data listed above will be collected by the Active Proxy automatically and sent to the Web Service Server.

3.2 Handling Context Information

The context information received from a user's terminal will be classified into two categories, i.e., software and hardware. The platform of the web service is based on XML. There are various kinds of operating systems in the market. There are large differences between Linux and Windows systems, in terms of naming objects, memory processing, and allocating hard disk space. Moreover, different versions of

operation systems from the same corporation have different services. This section outlines the handling of context information.

The server decides the size of the map to be displayed on the client's screen based on the size of the user's screen. For example, large maps are delivered to large monitors those are usually used for desktop computers. On the other hand, smaller maps are delivered to devices with small monitors such as PDAs to be more effective. Considering the security, the system should check the validity of users in terms of computer-name, user-location-name and user-name. The system also traces the location of the clients through their local IPs and provides proper services to them by considering the trajectories.

Directions of moving to a inquired destination can be informed by means of a voice information. The server check the client system if it equipped with a sound card or not. It also checks the network speed in order to determine the optimal voice quality and transmission time. The server also verifies the language of the client system by its system language ID. Proper voice messages should be delivered depending on the system language of the client.

Multiple monitors on the client enable the server to provide some additional services. For instance, if a client has two monitors; one shows a map of overall area and the other shows map zoomed up the target area searched by the users. The server also determines the computing capability of the client by means of the memory-size and CPU. If the memory-size is small or the processing speed of CPU is low, it will be difficult to transmit large information from server to client. The server should decrease image resolution automatically. The client's system time are used for determining the time difference between the server and the client.

4 Implementation of GIS Web Service

4.1 Development Environment

In this research, the overall systems are developed on Microsoft platforms. Detail information of the development environment is summarized in Table 1.

Table 1. Development Environment of GIS Web Service

Operating System	Microsoft Windows XP (SP2)
	Microsoft Windows CE.NET
Web Server	Microsoft IIS Server 5.1
Develop Framework	Microsoft .NET Framework 1.1
Develop Platform	Microsoft Visual Studio.NET 2003
Voice Generation	TTS Voiceware
GPS Interface	NMEA0183

The function of the Web Service server is to collect context information from the client and generate the information to be responded to the client. To be interoperable, it is required to use WSDL and SOAP to provide information to the client for development and service. The server is mainly divided into three parts: network interface,

user authentication service and DB interface module. The features of this Web Service can be summarized as follows:

- For the sake of internationalization, Unicode encoding is employed.
- Standard GPS interface is used.
- Client and server are synchronized.
- The maps are fitted to client's monitor automatically.
- Web Service standards, i.e., UDDI, WSDL, and SOAP are employed
- User and messages are authenticated before served.

4.2 Active Proxy for Client Development

In order to provide proper service, the server should collect the context information from clients. One approach would be define the variables for the required context information and make the users to provide their own information to the server. However, it is not trivial for average programmers to make programs to collect all the context information such as position, speed, OS type, screen size, memory size, network speed, so on. In this work we have extended the functionality of proxy to solve this problem.

A proxy exists in the form of window.dll on client device. The proxy has two main functions: one is to provide a web service interface; the other is to communicate with the server according to user's request. We have added one more function to the proxy, which is to collect context information of the client. The overall structure of Web Service system is depicted in Figure 1.

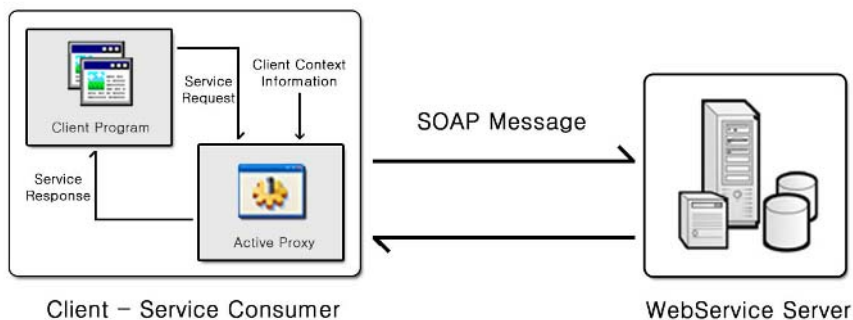


Fig. 1. Structure of GIS Web Service using active proxy library

The active proxy connects to the GIS Web Service and provides context data to the server. The client program can just refer the active proxy library and use the operations and types. A simple declaration of the web service object using dll library (it is named ISLAB.dll in this work) can be done as follows.

```

// declares an object for the GIS Web Service by ISLAB
private ISLABGIS.refGWS.ISLABGISWebService GisWebService;
// declares a service object by the GIS Web Service
private ISLABGIS.refGWS.GIS_SERVICE_DATA GisServiceData;
  
```



```
// declares an object of client information
private ISLABGIS.refGWS.CLIENT_INFO ClientInfo;
// declares an object of geographic data
private ISLABGIS.refGWS.CLIENT_GEOGRAPHY_DATA CGData;
```

Using these objects, the active proxy can directly call the Web Service operations. A simple example is shown below.

```
// sends the client's context information to server
GisWebService.GetClientInfo(ClientInfo);
// receives the response from server
GisServiceData = GisWebService.GISService(CGData);
```

The ISLAB.dll library includes the function to collect the context information of a client system as follows.

```
// collects the context information of client system
Public CLIENT_INFO GetClientInfo()
```

This method returns the context information that will be sent to the server. This library is compiled in a .NET CLI environment; therefore it cannot be used in other environments, such as a java and MFC. For such platforms, different versions of libraries need to be developed.

4.3 Web Service Interface Design

The overall structure of operations provided by the GIS Web Service is presented in Figure 2. First the system verifies system performance of client device and network status using the CheckSystemStatus() operation. It decides if the Web Service can be provided properly. It then waits a service request from the client. Receiving a request, the system checks the validity of user by UserAuthentication(). After user

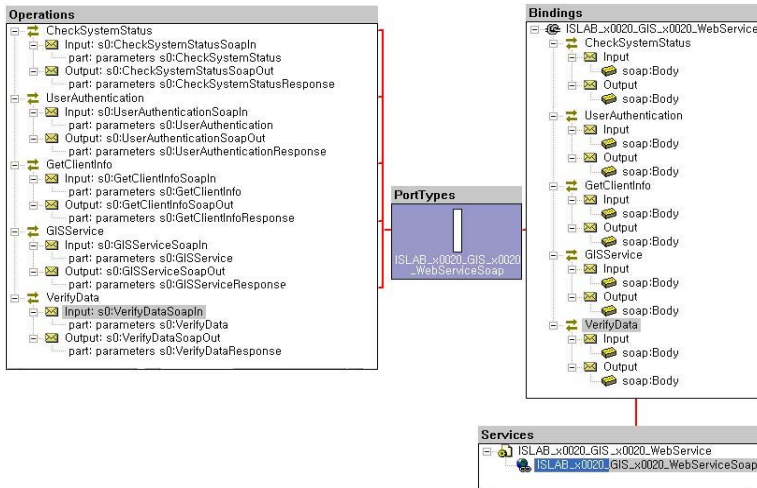


Fig. 2. Interface structure for GIS Web Service

authentication, the GetClientinfo() method receives context information of the client through the active proxy. The response to the client's request will be provided to the users via GISService() operation. The VerifyData() operation checks the integrity of service data.

4.4 A Working Example of Web Service

The procedure for users to use the Web Service is as follows.

1. Web application developer searches the Web Service that he/she want to use. Proper Web Services can be located using UDDI.
2. Download the WSDL files that describe the Web Services.
3. In a .NET environment, using the trace function of WSDL an active proxy can be created.
4. The active proxy collects context information of the client. Then it sends the value to the server using SOAP transmitted over HTTP.
5. The client and the server communicate each other according to the requests from the client.

When a client program connects the server, it will be requested to login to the system. If login succeeds, the server will begin to analyze the received context information as defined in the previous section. Some of the basic context information will be displayed on the client's monitor as shown in Figure 3.

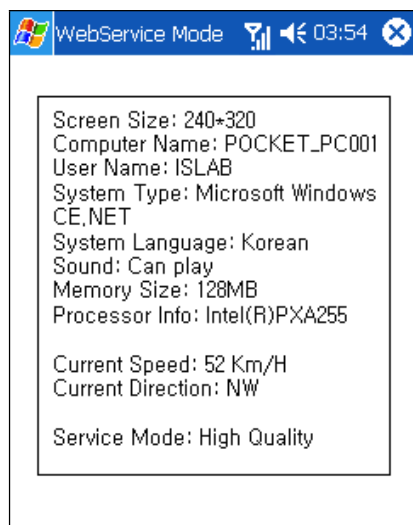


Fig. 3. Context information displayed on client's monitor

Using the "Path" menu, the user can search his/her destination. For example, when the user searches for the nearest university, the server will search it and respond the result to the user. For this query, a template written in XQuery language will be executed. The search result is shown in Figure 4. The blue arrow points the current

position of client and the red arrow points the destination. The path from the current position to the destination is drawn by black solid lines. When the server searches the shortest path, it considers the moving direction of the user. When the menu “Voice” is selected, the moving direction to the destination is guided until the client arrives the destination.

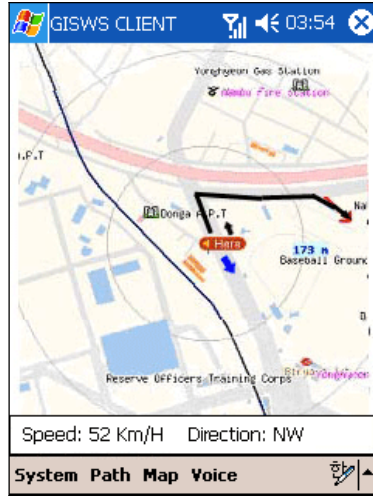


Fig. 4. A Map showing the path from the current position to destination

5 Conclusion

Location-based GIS service has been designed and implemented as a Web Service. Because many of mobile devices as PDA are equipped with GPS, the server can be informed the location of the clients more easily. In order to provide more appropriate service to each client, we need to analyze the context information from the client’s device. The context information of mobile devices can be classified into three categories, i.e., position information, S/W information, and H/W information. Most of the context information can be acquired from the GPS string and OS system variables. Microsoft proxy in client devices has been extended in order to actively send the context information to the server. Using the active proxy client program, developers have no burden of handling GPS string and system variables. A working example of Location-based GIS System is also presented. The contribution of this paper can be summarized as follows.

- The context model of mobile devices has been defined. It includes position information, S/W information, and H/W information.
- Microsoft proxy has been extended in order to actively send the context information to the server.

- Interface structure for Location-based GIS Web Service have been designed and implemented. Messages structures to be used in this service are also designed in XML.
- Message structures for in XML, which can improve the interoperability of the service.

Because the proposed system follows all the standard technologies of Web Service, in can interoperable most of mobile devices. The proposed system can be easily extended to almost all mobile and location-based systems such as POI systems, tracking systems, ubiquitous systems, and distributed control and management systems. Some user-friendly designed GUI tools could make the system more effective and the active proxy currently based on .Net environment needs to be extended to other platforms such as J2EE.

References

1. G. Abowd and E. Mynatt, "Charting Past, Present, and Future Research in Ubiquitous Computing," *ACM Transactions on Computer-Human Interaction*, Vol. 7, No. 1, pp 29-58, March 2000.
2. J. Altmann et al., "Context-awareness on mobile devices - the hydrogen approach," *Proceedings of the 36th Annual Hawaii International Conference on 6-9*, pp.10 Jan. 2003.
3. S. Berger, H. Schulzrinne, S. Sidiroglou, and X. Wu, "Ubiquitous Computing Using SIP," *NOSDAV'03*, PP.82-89, June 2003.
4. P. Brezillon, "Using context for supporting users efficiently," *Proceedings of the 36th Annual Hawaii International Conference on 6-9* pp.9 Jan. 2003.
5. R. Hall and H. Cervantes, "Gravity: Supporting Dynamically Available Services in Client-Side Applications," poster paper at *ESEC/FSE 2003*.
6. Jeffrey Hightower and Gaetano Borriello, "Location Systems for Ubiquitous Computing," *IEEE Computer*, Volume 34, Issue 8, pp.57-66, August 2001.
7. Eija Kaasinen, "User needs for location-aware mobile services," *Personal and Ubiquitous Computing*, Volume 7, Issue 1, pp. 70-79, May 2003.
8. F. Leymann, "Web Services: Distributed Applications without Limits - An Outline," *Procds. of Database Systems for Business, Technology and Web*, 2003.
9. Jian Li, Ruofeng Tong, MinTang, and Jinxiang Dong, "Web Service-based distributed feature library" *Computer Supported Cooperative Work in Design*, 2004. *Proceedings. The 8th International Conference on Volume 1*, pp. 753 – 758, May 2004.
10. M. Moschgath, J. Hahner, and R. Reinema, "Sm@rtLibrary - An Infrastructure for Ubiquitous Technologies and Applications," *Proceedings of Distributed Computing Systems Workshop 2001*, pp. 208-213, April 2001.
11. M. P. Papazoglou, "Web Services and Business Transactions," *World Wide Web Journal*, vol. 6, March 2003.
12. Tak-Goa Tsuei and Chin-Yang Sung, "Ubiquitous Information Services with JAIN Platform," *Mobile Networks and Applications*, Volume 8, Issue 6, pp. 655-662, December 2003.
13. J. Yang and M.P. Papazoglou, "Service Components for Managing the Life-Cycle of Service Compositions," *Information Systems*, Vol. 29, Issue 2, pp. 97-125, April 2004.

The System for Predicting the Traffic Flow with the Real-Time Traffic Information

Mi-Gyung Cho¹, Young Jung Yu², and SungSoo Kim³

¹ Department of Multimedia Engineering, Tongmyong University,
608-711, 535 Yongdang-dong, Nam-gu, Busan, Korea
mgcho@tit.ac.kr

² Division of Computer Engineering, Pusan University of Foreign Studies,
608-738, Wooam-dong, Nam-gu, Busan, Korea
yjyu@pufs.ac.kr

³ Digital Content Research Division,
Electronics and Telecommunication Research Institute,
305-700, 161 Gajeong-dong, Yuseong-gu, Daejeon, Korea
sungsoo@etri.re.kr

Abstract. One of the common services of telematics is the car navigation that finds the shortest path from source to target. Until now, some routing algorithms of the car navigation do not consider the real-time traffic information and use the static shortest path algorithm. In this paper, we proposed the method to predict the traffic flow in the future. This prediction combines two methods. The former is an accumulated speed pattern, which means the analysis results for all past speeds of each road by classifying the same day and the same time interval. The latter is the Kalman filter. We predicted the traffic flows of each segment by combining the two methods. By experiment, we showed our algorithm gave a better precise prediction than only an accumulated speed pattern that is used commonly. The result can be applied to the car navigation to support a dynamic shortest path. In addition, it can give users the travel information to avoid the traffic congestion areas.

Keywords: Telematics, Intelligent Transportation System, Dynamic Shortest Path, Real-time Traffic Information, Prediction of Traffic Flow.

1 Introduction

Telematics combines the wireless internet, GPS(Global Positioning System), various multi-media services and GIS(Geographical Information System) and so on to support the telecommunication services in a driving car[1]. Some of the most popular service are to find the shortest path from source to target, and location based services. An example of location based services would be finding the nearest gas station from a current position. Many navigation systems use static information such as a distance and a limited speed of each road. Sometimes, the result of these algorithms can not be the shortest path when the traffic congestion occurs at some intermediate segments. This results from not considering a real-time

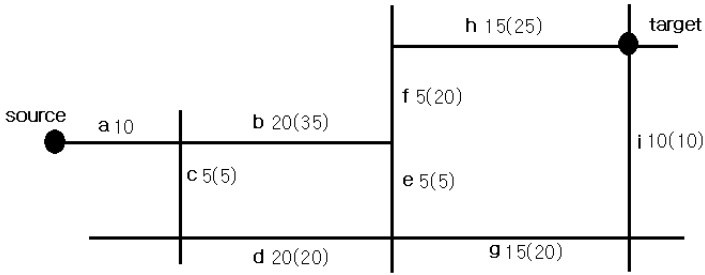


Fig. 1. Traveling time of each segment depending on the existence of traffic congestion

traffic information. If a user can predict traffic jams at some particular segments after a few minutes, he can find another path to avoid the congestion areas.

We suppose that a road network consists of lots of segment units as shown in Fig. 1. A segment means the region between the two crossroads. In Fig. 1, segments are represented as 'a', 'b', etc.. The times required for traveling through each segment 'a', 'b' and 'c' are 10, 20 and 5 minutes, respectively. This is the cost when we only consider the static information such as its limited speed and the length of each segment. The number of the parenthesis shows the time when a car arrives at the start of each segment. We guess that some segments have traffic jams in Fig. 1. For example, it usually requires five minutes to pass the segment 'f' but now it requires twenty minutes because of traffic congestion. The shortest path from source to target without the real-time traffic information is 'a', 'b', 'f' and 'h'. But when a dynamic traffic flow is considered, the shortest path changes to 'a', 'c', 'd', 'e', 'f' and 'h'.

Many efforts have been done to enhance the quality of telematics and to give users more precise traffic information by reflecting the real-time traffic information[1]. In this paper, we studied the method to predict the traffic flow in the future using the real-time traffic data. We want to predict whether a traffic congestion occurs or not when a car starts from the source and passes segment 'a' and then arrives at the intersection of segment 'b' and 'c'. Our system received the average speed of driving cars on each segment of the road network in every five minutes and predicted the speed of each segment from after five minutes to after three hours. This can answer two types of questions such as "What is the average speed of driving cars on the segment 'f' after fifty minutes?" and "Is there traffic jams at the segment 'f' after fifty minutes?".

Related works on the dynamic routing algorithm and the prediction of the duration of an automobile trip were released since 1998[2, 3, 4]. In addition, metropolitan cities have various ITS(Intelligent Transportation Systems) services using the real-time traffic information. According to Chon[2]'s research, a dynamic routing assignment resulted in reducing total moving times compared to a static routing algorithm. In order to predict the traffic jams by his method we have to know the routing information of all moving objects. However it is

impossible in the real situation. Handley[3] predicted the duration of an automobile trip using collected data from 116 sensors, updated periodically, at fixed locations. To calculate the trip duration he used the current traffic speed at all segments instead of the future traffic speed, at the location the car will arrive in which.

The method proposed in this paper does not need prerequisite conditions that the routing information of all moving objects should be given to predict traffic jams. We take the real-time speed of all segments of the road network in every five minutes to analyze current traffic flow. The novelty of our research is that we consider a speed of the particular segment in the future time.

The remainder of this paper is organized as follows. In Section 2, we explain the architecture of our system and the input data format used for real-time traffic data. In Section 3, we propose two methods for predicting the traffic flow in the future time. In Section 4, we show the experiment results to verify the precision of our prediction. We present our conclusion in Section 5.

2 The Overview of Prediction System and Real-Time Traffic Data

Our system received an average speed at each segment in every five minutes through the web. These data were from LBS team of Electronics and Telecommunication Research Institute in Korea[7]. They obtained these data from a company collecting the real-time traffic information. The results of our system are the predicted speed of all segments, the precision of the prediction, and whether the traffic jam exists or not. Fig. 2 shows the architecture of our traffic prediction system.

At the preprocessing step, we treated some segments which missed their average speeds. Generally, all segments had to get their average speeds at the real-time traffic information. But when we received these data, some segments had a value of -1 instead of their speeds. Therefore, we had to compute the speeds of these segments. We call these segments as missing segments. For our data, about 1% of all segments were the missing segment. Currently, some softwares have been developed to compute the speeds of missing segments.

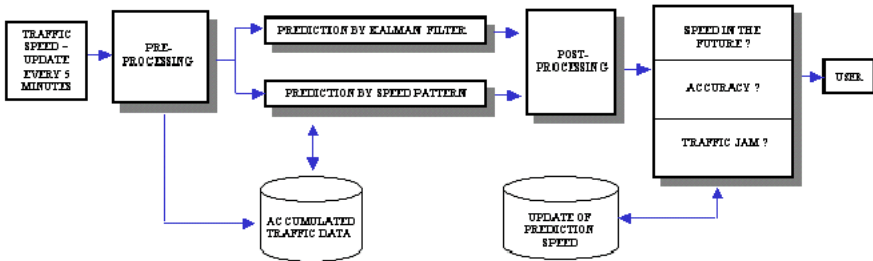


Fig. 2. The architecture of the prediction system

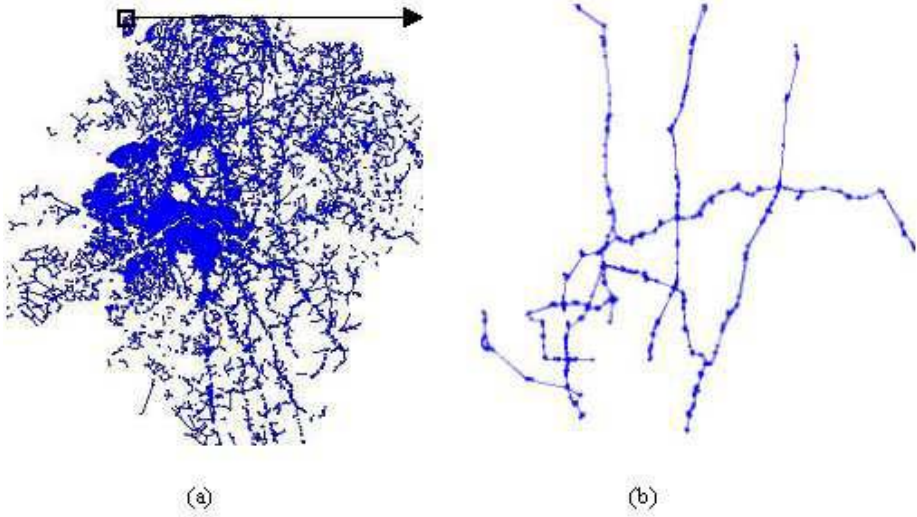


Fig. 3. The part of the road network of Seoul city

In this study, we computed the speeds of missing segments using the graph topology nearby these segments. A vertex of the road graph represents an intersection and an edge means an interval between two intersections. A road graph is the digraph because each segment has two directions. In order to compute the speed of missing segments we found incoming edges and outgoing edges of the node adjacent to a missing segment. And we computed an average speed of these incoming and outgoing edges as the speed of a missing segment. After the preprocessing step, all real-time data were stored in the accumulated database for later use of prediction.

We combined two methods to compute in the future speed: the accumulated speed pattern and the Kalman filter. We will explain these methods in detail in Section 3. Two speeds obtained by two methods proceeded at the post-processing step. We calculated the final speed at this step. The result was then stored and transferred through the web when a user wanted to know the prediction of a particular segment.

Fig. 3 shows the road network of Seoul city that was used for the real-time traffic data; the left one (a) means a map on a reduced scale of Seoul city and the right one (b) magnifies the area inside the rectangle. Seoul city has very complicated road network as shown in Fig. 3. The number of its vertices is more than ten thousands and it have more than fifteen thousand edges. The format of the real-time data is triples of $(time_sequence, link_id, speed)$. If the value of the first parameter is 200410231205, it means that the current time is 5 seconds, 12 minutes, 23th, October, 2004. All segments had their $link_id$ to identify each other. The speed that means the average speed of driving cars on each segment represented as km per hour.

3 Accumulated Speed Pattern and Kalman Filter

We used two methods for predicting the traffic speed in the future time. The first method is to use accumulated data of each segment stored in the database that resulted from the analysis of a usual traffic flow. The second method was to use the Kalman filter. We combined the two methods to compute the final speed.

3.1 Prediction by Accumulated Speed Pattern

An accumulated database maintained the information about accumulated speed pattern that resulted from the same day and time interval of the real-time data. This database had an average speed and a standard error of each segment for each day and time interval. We used seven days and divided a day by 48 time intervals considering each interval as 30 minutes. Therefore, each segment in the accumulated database had 336 average speeds and standard errors. This gave us usual traffic flows of each segment. We found that each segment had a similar speed pattern for the same day and time interval.

Fig. 4 shows an accumulated speed pattern of a segment located in downtown. We see a severe traffic jam from one o'clock to eight o'clock on Saturday afternoon. We guess this is because many cars were in downtown during the time interval. In the case of Sunday, the average speed of the entire time intervals was higher than the other days. This was the result of a segment located in downtown and some segments near a park might have a different speed pattern.

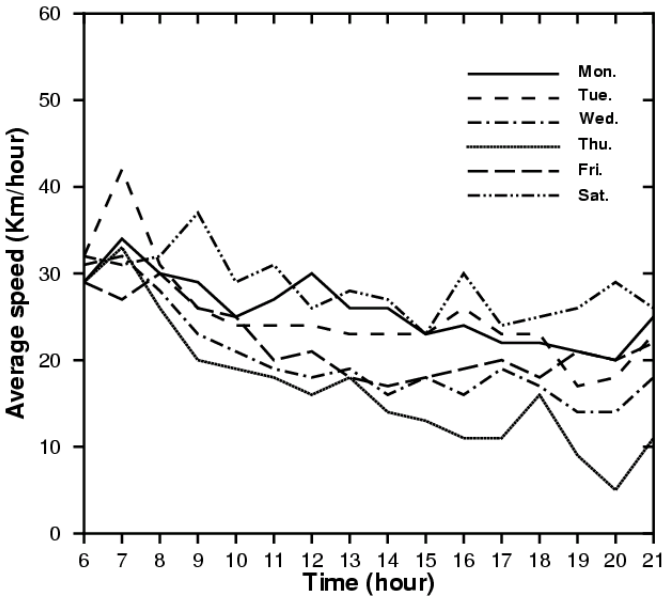


Fig. 4. An accumulated speed pattern of a segment located in downtown

Our system maintained the real-time data for an hour in server to check the current traffic flow at each segment. If the present speed pattern is similar to the corresponding speed pattern of the accumulated database because of no traffic jam, we could predict the speed by the accumulated speed pattern in the future time, from after five minutes to after three hours. To check whether the current traffic follows the usual flow or not, we used the average speed and the standard error stored in the accumulated database.

The following algorithm shows how to predict the speed by the accumulated speed pattern in the future time.

[Algorithm] Prediction by the accumulated speed pattern

1. Get $CV_{k-j}(L_i)(0 \leq i < N, 0 \leq j < 12)$ which is the current speeds of all segments in a hour.
2. Get $AV_{k-j}(L_i)(0 \leq i < N, 0 \leq j < 12)$ which means the corresponding speeds in the accumulated database.
3. Compute the function $f(CV_{k-j}(L_i))$.

$$f(CV_{k-j}(L_i)) = \begin{cases} -1 & \text{if } AV_{k-j}(L_i) - \sigma(AV_{k-j}(L_i)) \geq CV_{k-j}(L_i) \\ 1 & \text{if } AV_{k-j}(L_i) + \sigma(AV_{k-j}(L_i)) \leq CV_{k-j}(L_i) \\ 0 & \text{otherwise} \end{cases}$$

4. Predict the speed $PV_{k+p}(L_i), (1 \leq p \leq 68)$ of all segments.

$$PV_{k+p}(L_i) = AV_{k+p}(L_i) + \sum_{j=1}^{12} (f(CV_{k-j}(L_i)) * g(L_i))$$

$$g(L_i) = \alpha * \sqrt{\frac{\sum_{j=0}^{11} (CV_{k-j}(L_i) - AV_{k-j}(L_i))^2}{12}}$$

The function $CV_k(L_i)$ means the real-time speed of the segment L_i at the current time k , $CV_{k-1}(L_i)$ is the previous five minutes and $CV_{k-2}(L_i)$ is the previous ten minutes, respectively. In addition, $AV_k(L_i)$ is its corresponding speed in the accumulated database and its corresponding speed as the accumulated speed before five minutes is $AV_{k-1}(L_i)$. The value $\sigma(AV_k(L_i))$ means a standard error of the segment L_i obtained from the accumulated data. The speed $PV_{k+1}(L_i)$ means the predicted speed after five minutes and $PV_{k+68}(L_i)$ is that after three hours, respectively.

3.2 Prediction by the Kalman Filter

The Kalman filter proposed by Rudolf E. Kalman is a recursive solution to the discrete-data linear filtering problem[5, 6]. The Kalman filter is a set of mathematical equations that provides an efficient computational means to estimate the state of a process, in a way that minimizes the mean of the squared error. This

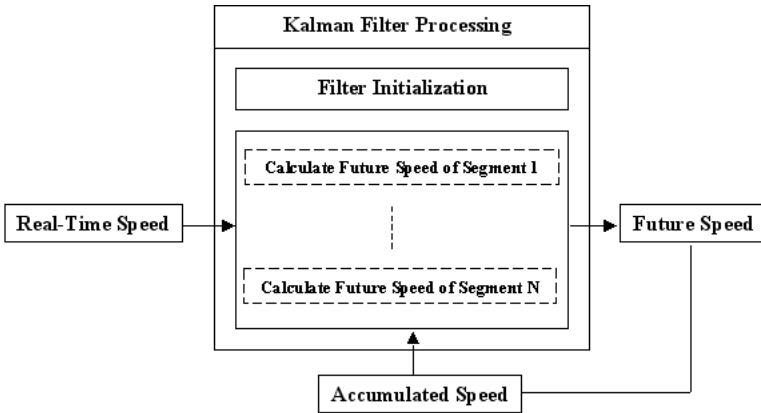


Fig. 5. The computational process for predicting the speed by the Kalman Filter

is mainly used to find out the signal from noises to predict the time-dependent change properly.

The Kalman filter tries to estimate the state $x \in R^n$ of a discrete-time controlled process that is governed by the linear stochastic difference equation $x_k = Ax_{k-1} + Bu_{k-1} + w_{k-1}$ with a measurement $z_v \in R^m$ that is $z_k = Hx_k + v_k$. The random variables w_k and v_k represent the process and measurement noise. The $n \times n$ matrix A relates the state at the previous time step $k - 1$ to the state at the current step k , in the absence of a driving function of process noise. The $n \times l$ matrix B relates the optional control input $u \in R^l$ to the state x . The $m \times n$ matrix H relates the state to the measurement z_k .

For applying the Kalman filter to our system, the state vector x_k becomes a vector that has the same number of segments N . The $N \times N$ matrix A means the spatial relationship of each segment. Fig. 5 shows the computational process by the Kalman filter used in this study. Each matrix is initialized as 2×1 or 2×2 because two real-time data both at the current time and before five minutes were used at the initialization process. In addition, the variation of the noise for the prediction and the measurement were initialized by ten and used continuously.

The number of segments of Seoul road network used in this study is more than 15,000. We want to predict the speed of each segment from after five minutes to after three hours. Because the real-time data were updated in every five minutes, we needed to compute the final result before inputting the next data. To do this we exclude the topological relationship of each segment and process each segment independently. It takes about ten seconds to be predicted using the Kalman filter.

3.3 Combine of Accumulated Speed Pattern and Kalman Filter

To compute the final speed with the results by two methods described in previous sections, the standard error of the speeds of each segment stored in the accumulated database was used. We checked that the real-time speeds $CV_{k-j}(L_i)$, $(0 \leq$

$i < N, 0 \leq j < 12$) for one hour were in the significant interval of its corresponding accumulated speed $AV_{k-j}(L_i)$, ($0 \leq i < N, 0 \leq j < 12$) by using equation 1.

$$AV_{k-1}(L_i) - \delta * \sigma(AV_{k-j}(L_i)) \leq CV_{k-j}(L_i) \leq AV_{k-1}(L_i) + \delta * \sigma(AV_{k-j}(L_i))$$

$$(1 \leq i \leq N, 0 \leq j < 12) \quad (1)$$

In the equation 1, δ is a constant value. If we want to check that it is within the significant interval with 95%, the value of δ will be 1.96.

If all of the current speeds $CV_{k-j}(L_i)$ for one hour are within the interval of equation 1, they means that the current traffic has the usual flow. Therefore they are recommended to follow the speed in the accumulated database. We computed the final prediction speed using equation 2.

$$PV_{k+j}(L_i) = \alpha * speedByPattern_{k+j}(L_i) + \beta * speedBykalman_{k+j}(L_i) \quad (2)$$

$$\beta = 1 - \alpha, \quad 1 \leq j \leq 68$$

In the above equation, α means the ratio that $CV_{k-j}(L_i)$ ($0 \leq j < 12$) is within the significant interval. And $speedBypattern_{k+j}(L_i)$ is the result of prediction by the accumulated speed pattern and $speedBykalman_{k+j}(L_i)$ is that of by the Kalman filter. The index j indicates the future time. When the value of j is 1, it means that the time is after five minutes and when 2, it means the time after ten minutes and so on.

4 Experimental Results

To verify the precision of our algorithm, we conducted the experiment using the real-time data of Seoul road network for one month, September, 2004. First of all, we produced the accumulated speed pattern using the first three weeks and predicted the speed in the future while inputting the fourth week data as the real-time data. And then we compared the results of the prediction with the real data. To measure the precision of the prediction, we defined the speed error $e_k(L_i)$ as follows.

$$e_{k+j}(L_i) = |PV_{k+j}(L_i) - RV_{k+j}(L_i)|, \quad 0 \leq i < N, \quad 1 \leq j \leq 68 \quad (3)$$

In equation 3, $RV_{k+j}(L_i)$ is the real speed of each segment L_i after $5 * j$ minutes from the current time. If the value of the speed error is 0, it means that the system predicts the future speed of the segment exactly. The smaller the speed error is, the better the prediction is.

Fig. 6 shows the results by our algorithm(pattern+kalman) and by only an accumulated speed pattern(pattern) that is used commonly when there is no real-time data. We experimented with some parts of Seoul road network. Our system predicted the future speed exactly for more than twenty four hundred of segments, whereas the accumulated speed pattern did for about fifteen hundred of segments.

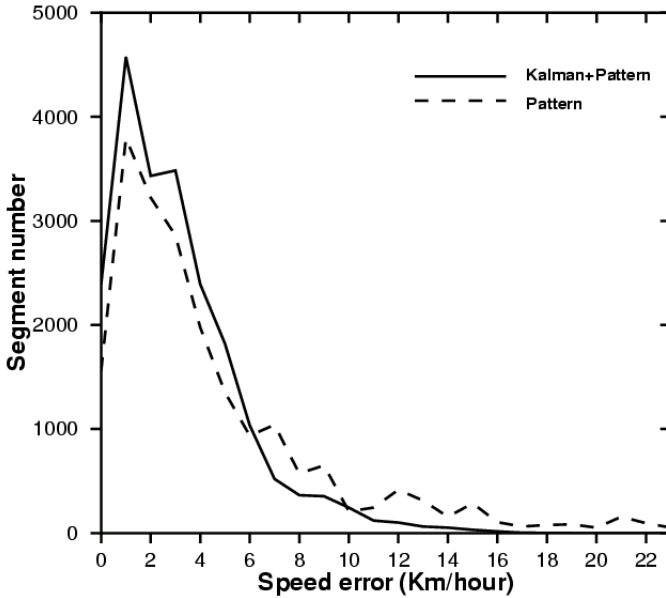


Fig. 6. The Comparison of the results of two methods

Totally, 91% of total prediction had a speed error less than 7 km/hour, and 98% had a speed error less than 10km/hour. But for using only accumulated speed pattern, 77% had a speed error less than 7km/hour. The ratio having less than 10km/hour was about 89%. This result implies that our algorithm predicted to be more precise than the other method. When the accumulated speed pattern is used alone, it could not reflect the current traffic information.

5 Conclusion

We proposed the method to predict the traffic flow in the future using the real-time traffic information. Our system can answer two types of questions such as “What is the average speed of driving cars on the segment f' after fifty minutes?” and “Is there the traffic jams at the segment f' after fifty minutes?”. The system received the real-time data of all segments in every five minutes and predicted the speed of driving cars on each segment from after five minutes to after three hours. The two methods, the Kalman filter and the accumulated speed pattern, were combined.

To verify the precision of the prediction, we defined the speed error which means the difference of the prediction speed and its real speed. The experimental result showed that our algorithm gives less speed errors than using the accumulated speed pattern alone. Our results can be applied to the car navigation to support a dynamic shortest path. In addition, they can give users the travel information to avoid the traffic congestion area.

References

1. Joonwan Kim, Trends of Services and Technology of Telematics, IITA IT Korea, 2004.
2. H. D. Chon, D. Agrawal and A. E. Abbadi, "FATES: Finding A Time dEpendent Shortest path," Proc. of the fourth International Conference on Mobile Data Management, pp. 165-180, 2003.
3. S. Handley, P. Langley and F. Rauscher, "Learning to Predict the Duration of an Automobile Trip," Proc. of the fourth International Conference on Knowledge Discovery and Data Mining, pp. 219-223, 1998.
4. D. Moriarty, S. Handley and P. Langley, "Learning Distributed Strategies for Traffic Control," Proc. of the fifth International Conference of the Society for Adaptive Behavior, pp. 437-446, 1998.
5. Kalman, R. E., "A New Approach to Linear Filtering and Prediction Problems," Transaction of the ASME Journal of Basic Engineering, pp.35-45, March, 1960.
6. Grewal, Mohinder S., and Angus P. Andrews, *Kalman Filtering : The theory and Practice*, Prentice Hall, 1993.
7. <http://www.etri.re.kr>

Versioning Based Spatial Record Management Technique for Non-blocking Search Operations of Moving Objects *

Ho Seok Kim¹, Hee Taek Kim², Myung Keun Kim¹,
Gyoung Bae Kim³, and Hae Young Bae¹

¹ Department of Computer Science and Information Engineering, Inha University
Yonghyun-dong, Nam-gu, Incheon, 402-751, Korea
{hskim, kimmkeun}@dblab.inha.ac.kr, hybae@inha.ac.kr

² GIS Engineering Research Institute, Korea Telecom Information Technology, 320 Korea
TechnoComplex Building, Korea University, Anam-dong, Seongbuk-gu, Seoul 136-713, Korea
htkim@ktit.com

³ Department of Computer Education, Seowon University, 231 Mochung-dong Heungduk-gu
Cheongju-si Chungbuk, 361-742, Korea
gbkim@seowon.ac.kr

Abstract. This paper proposes the multi-version based spatial record management technique for non-blocking search-operation for managing moving objects. The storage manager used for LBS should consider the efficient and concurrent control of searching and updating operations of moving objects. Traditionally, the In-place update method with lock is used for updating records in storage manager. But, this method cannot guarantee that each transaction conflicts on the same object. Unlike this, the multi-version concurrency control is a standard technique for avoiding conflicts between reads and writes of the same object. When multi-version technique is applied to spatial database systems, search and update-transactions can access different versions individually. But, the storage will be wasted as the version of whole spatial record is needed to be stored even if only the aspatial data is updated. In multi-version based spatial record management technique, each of aspatial data versions and spatial data versions are managed separately to improve concurrency and reduce the wastage of storage.

1 Introduction

The first-generation Location-Based Services (LBS) performed relatively trivial spatial search operation in order to determine the location of the nearest restaurants or other businesses by a user. The important observation which is particularly relevant to this paper is the data which is queried is static, while the reference point is moving.

The spatial search operation is principal operation mainly in existent spatial DBMS. But, the frequent update operation of spatial data such as tracking or real

* This research was supported by the MIC (Ministry of Information and Communication), Korea, under the ITRC (Information Technology Research Center) support program supervised by the IITA (Institute of Information Technology Assessment).

time position update of moving object happens in the spatial DBMS recently. The necessity of concurrency improvement between search and update operation in spatial DBMS is increasing.

Already, many techniques have studied to solve problem related with concurrency of transaction and to improve performance of DBMS. Among them, the multi-version algorithm is the algorithm that improves concurrency through minimizing conflict between search and update transaction[2, 5, 6, 8, 9].

The version means a copy of record which is created by update transaction at multi-version algorithm. Because there are several versions related to one record, search transaction and update transaction can use different version for accessing a record. After all, through accessing many versions about a record, it improves concurrency of transactions. Especially, it resolves the problem of search transaction waiting caused by update transaction[1, 3, 4].

But, if multi-version algorithm is applied to spatial database management system, because several versions are created about a spatial record, it is possible that search transaction and update transaction access different version individually. Therefore, it can improve concurrency among transactions. However, it wastes the storage to save whole versions that is created by update operation.

This paper has proposed the version based spatial record management technique which manages both aspatial data version and spatial data version separately. This technique can improve concurrency among transactions about spatial record, and reduce storage space to store spatial record version.

This paper is as following. Section 2 describes concurrency technique using existing multi-version algorithm. Section 3 describes the proposed data structure of spatial record management technique based on version and algorithm which manages aspatial and spatial record version. The last section, conclusion and future works.

2 Related Works

In multi-version algorithm, new version is created in case that update transaction modifies record, and search transaction reads stable version among versions. That is, multi-version algorithm improves concurrency of transaction because search transaction and update transaction access different version each other.

This Chapter describes multi-version technique with timestamp and 2PL(Two Phase Locking)[7, 10].

2.1 Multi-version Algorithm with Timestamp

The multi-version algorithm with timestamp is algorithm using timestamp for concurrency among transactions. Each transaction is assigned a unique timestamp which means time transaction begin. After retrieving stable version about record, search transaction compares with transaction's timestamp and version's timestamp and sets version's timestamp to newer timestamp between timestamps.

If the current version's search timestamp is newer than search transaction's timestamp or current version's update timestamp is newer than transaction's timestamp, update transaction is aborted. In case is not so, new version is created and new version's update timestamp is set current transaction's timestamp.

2.2 Multi-version Algorithm with 2PL

If any transaction gets exclusive lock on record R in database, the other transaction is limited to get shared lock on same record. By using version of record R, such conflict can be avoided. If a transaction T creates new version R' of record R, other transaction can't read or write on R' by using lock. But, search transaction can read record without conflict of lock by permitting new transaction to read record R. Therefore, it can remove the problem for search transaction to wait due to exclusive lock on record or update transaction to wait due to shared lock on record.

3 Version Based Spatial Record Management Technique

This Section describes the data structures of version based spatial record management technique and the algorithm that manage aspatial & spatial record version individually.

3.1 Data structures

Figure 3.1 describes aspatial data version and spatial data version of spatial record.



- pTxPrev : pointer to indicate previous version that is created by same transaction.
- pPrev : pointer to indicate previous version that is created in same record.
- pNext : pointer to indicate next version which is created in same record.
- pPair : pointer to indicate aspatial or spatial data
- pData : pointer to indicate data
- Timestamp : timestamp of version
- TxID : the Transaction ID that create version

Fig. 3.1. Structure of version

If version of spatial record is exist, each record slot of record page indicates aspatial data version. Figure 3.2 describes version management technique of aspatial data and spatial data.

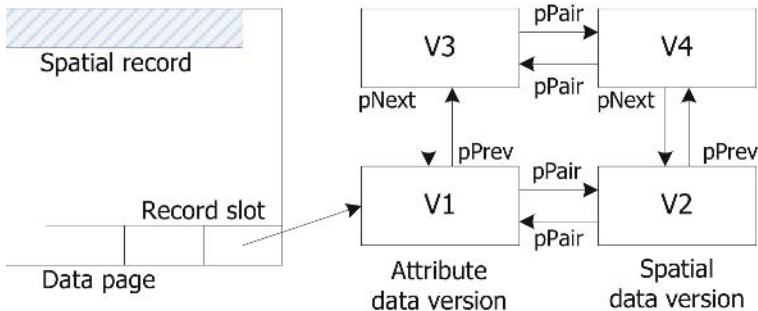


Fig. 3.2. Separate aspatial data version and spatial version

3.2 Spatial Record Version Management Algorithm

This section describes spatial version management algorithm.

3.2.1 Insertion Operation

Special record Insertion operation creates an empty data version and a data version that has the data to be inserted. And each version is connected by pointer. The empty version means there is no record or the record is deleted. The whole method are described in figure 3.3.

- 1) Create aspatial data version V1 and spatial data version V2 of spatial record to be inserted. Each version's timestamp get initial value ∞ . In this way all previous transaction can't read this created version.
- 2) Create empty aspatial data version V3 and spatial data version V4 with initial value $-\infty$. ($-\infty$ is smaller than any other timestamp that existed).
- 3) V3 and V4 are connected by pPair.
- 4) V3 and V4 indicate created version in insertion operation with pNext.
- 5) Created version in insertion operation indicates V3 and V4 with pPrev.
- 6) Aspatial data version V1 and V2 which is created by Insertion operation is linked by pPair each other.
- 7) Finally, the pointer which indicate record version in record slot points to aspatial data version V1 that is created recently.

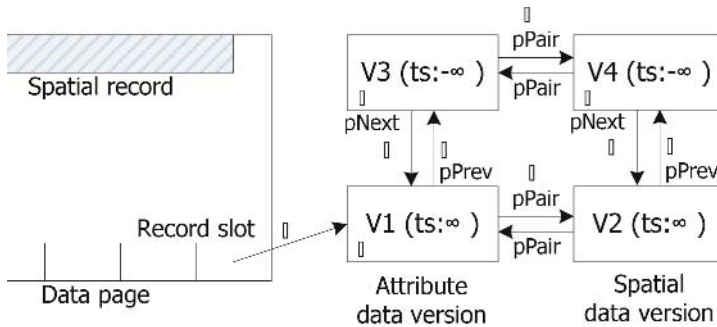


Fig. 3.3. Insertion Operation in Spatial Record

3.2.2 Update / Deletion Operation

Update operation of spatial record links previous record version to record version created newly. As follow Figure 3.4.

- 1) If updated data is aspatial data, create aspatial data version V1. Otherwise, create V2. Each version's timestamp has ∞ as initial value.
- 2) In case which spatial record to be updated is stable record, create spatial data version V3 that store aspatial data of data page and spatial data version V4 that store spatial data of data page. V3 and V4's timestamp is set $-\infty$. If there is version of spatial record, set version of aspatial data created recently to V3 and version of spatial data to V4. And go to step 4.

- 3) V3 links to V4 by pPair.
- 4) V3 and V4 indicate version that is created by update operation by pNext.
- 5) version that is created by update operation indicates aspatial data version and spatial data version which is created recently by pPrev.
- 6) Aspatial data version that is created by update operation indicates the recentest spatial data version by pPair, spatial data version indicates the recentest aspatial data version by pPair.
- 7) Finally, pointer which indicate record version in record slot link to aspatial data version which is created recently.

Deletion operation is same with update operation that updates spatial record by aspatial data version that has no data and spatial data version that has no data.

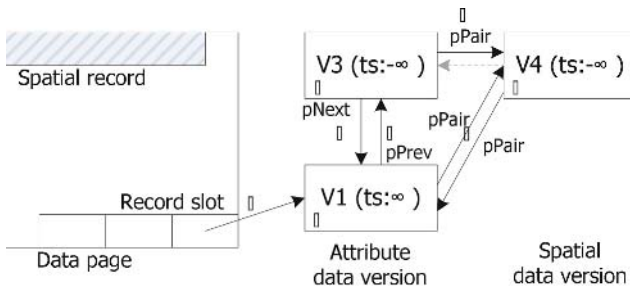


Fig. 3.4. In case update only spatial data part of spatial record

3.2.3 Search Operation

The search operation which retrieves spatial record compares timestamp of search operation and timestamp of version, selects suitable version. Whole method is as following.

- 1) In case that version of record to retrieve does not exist, retrieve spatial record in data page.
- 2) In case that version of record to retrieve exists, retrieve aspatial data version first. In case that current transaction has created aspatial data version to retrieve, after retrieving current version, retrieve spatial data version that pPair indicates. Also, in case that timestamp of aspatial data version is older than time stamp of retrieval transaction, after retrieving current version, retrieve spatial data version that pPair indicates. But, in case that current version does not fit with timestamp to read by oneself, retrieve previous version that pPrev indicates. After retrieving suitable aspatial data to own, retrieve spatial data that pPair indicates again.
- 3) Search method of spatial data version is the same in case of above aspatial data.

Figure 3.5 is example of spatial record retrieval operations of in case timestamp of retrieval transaction is 4. Aspatial data version of retrieval transaction retrieves version that time stamp is 3 and spatial data version that time-stamp is $-\infty$.

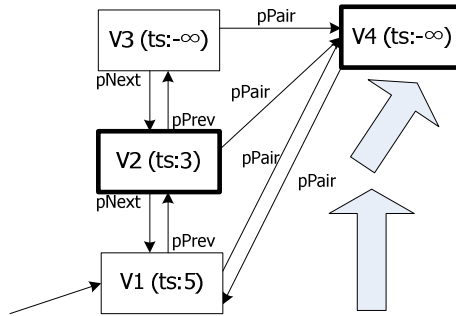


Fig. 3.5. Retrieval operation of in case timestamp of retrieval transaction is 4

3.2.4 Commit / Abort Operation

At the first, the increased timestamp is assigned to commit operation by the system. And the Commit operation changes timestamp of all versions that was created by update transaction. And besides, the Commit operation adds all versions which were created before the update transaction to garbage collector. In this paper, we don't explain about garbage collection algorithm.

In the case of abort transaction, all versions which were created by update transaction are changed to old versions that are before the transaction's occurrence. And all versions which were created by update transaction are deleted.

4 Conclusion and Future Work

The proposed technique manages several versions about one spatial record. So, search transaction and update transaction are able to use different versions. As a result, search transaction could conduct the operation without any interference of update transaction. And because the proposed technique creates and manages aspatial data version and spatial data version of spatial record separately, it could save only updated data version without saving large amount of entire spatial record version. As a result, the proposed technique doesn't waste space of spatial record version. For future work, we consider about the recovery algorithm in environment that attribute data version and spatial data version individually.

References

1. Baojing Lu, Qinghua Zou, William Perrizo : A Dual Copy Method for Transaction Separation with Multiversion Control for Read-only Transactions, ACM 2001
2. CHRISTOS H. PAPADIMITRIOU and PARIS C. KANELLAKIS : On Concurrency Control by Multiple Versions, ACM 1984
3. C. Mohan, Hamid Pirahesh, Raymond Lorie : Efficient and Flexible for Transient Versioning of Record to Avoid Locking by Read-Only Transactions, ACM SIGMOD 1992
4. D. Agrawal and V. Krishnaswamy : Using Multiversion Data for Non-interfering Execution of Write-only Transaction, ACM 1991

5. Divyakant Agrawal and Soumitra Sengupta : Modular Synchronization in Multiversion Database : Version Control and Concurrency Control, ACM 1989
6. MICHAEL J.CAREY and WALEED A. MUHANNA : The Performance of Multiversion Concurrency Control Algorithm, ACM 1986
7. Philip A. Bernstein, Nathan Goodman : Concurrency control algorithms for multiversion database systems, ACM 1982
8. P.Bohannon, D.Lieuwen, R.Rastogi, S.Seshadri, A.Silberschatz, S.Sudarshan : Logical and physical versioning in main memory databases, VLDB 1997
9. PHILP A. BERNSTEIN and NATHAN GOODMAN : Multiversion Concurrency Control - Theory and Algorithm, ACM 1983
10. SILBERSCHATZ. A. : A Multi-version concurrency control scheme with no rollbacks, ACM 1982.

A Wavelet Packets Watermarking Algorithm Based on Chaos Encryption

Jin Cong, Yan Jiang, Zhiguo Qu, and Zhongmei Zhang

Department of Computer Science,
Central China Normal University,
Wuhan 430079, P.R. China

{jincong, jiangyan, quzhiguo, zzhongm}@mail.ccnu.edu.cn

Abstract. In this paper, a wavelet packets watermarking algorithm based on chaos encryption for still digital images is presented. The watermarking is changed into bit sequence by modular arithmetic, at the same time, a random sequence is gotten by using a chaos map and deal with it also by modular arithmetic. After getting these two sequences, we do XOR arithmetic, then getting a new encrypted watermarking sequence. At the embedding stage, wavelet packets decomposition is used for original image, then embedding encrypted watermarking sequence into some frequency bands of original image by repeatedly embedding four times. At the extracting stage, wavelet packets decomposition for original image and watermarked image are used to inverse process. The experiment results demonstrated the new algorithm is robust for scaling, cropping, JPEG compression and noise attack.

1 Introduction

With the rapid growth of Internet and networks technique, multimedia data transforming and sharing is very common to everyone. Multimedia data is easily copied and modified so copyright protection gets more and more important. Digital watermarking^[1-3] has been proposed as technique for copyright protection of multimedia data. Digital watermarking invisibly embeds copyright information into multimedia data. Thus, digital watermarking has been used for copyright protection. We know that a watermarking algorithm requires invisibility and robustness, which conflict with each other.

In general, there are two domains of watermarking embedding-the spatial domain and the frequency domain. Several methods have been processed in frequency domain such as DCT, DFT, and DWT. Recently, DWT-based watermarking methods have been researched intensively, due to the fact that the current image compression is based on wavelet domain such as JPEG 2000.

In this paper, we introduced the wavelet packets that are better decomposition than wavelet. From spatial frequency aspect, the wavelet decomposition just decompose low frequency band recurrently, the wavelet packets decomposition decompose low frequency band and three high frequency bands at the same time. So wavelet packets decomposition allows us to choose bands more widely and better for embedding. In

previous work, Podilchuk *et al.*^[4] embedding watermark into low frequency bands. In [5], embedding watermarking into three high frequency bands. These two method focus on different requirements of watermarking, embedding watermarking into low frequency bands due to the robustness, another due to the invisibility. So selection of bands is a conflict problem. Wavelet packets decomposition can solve this problem for embedding watermarking.

2 The Watermarking Embedding Process

The wavelet-based algorithm^[6] had been analysis three kinds of method for embedding, *i.e.*, HVS model, constant energy, and simplified technique. Constant energy embedding is best robustness although lowest invisibility. In this paper, we choose α as a constant energy, where $\alpha=10$.

Before embedding, a very important process is focused, *i.e.*, chaos encryption of watermarking. The main processes are as follows

Using logistic map to generate a real value sequence $\{x_k : k=1, 2, \dots\}$, we choose a certain values as watermarking size, where logistic map is one of the simplest chaotic maps, described by

$$x_{k+1} = \mu \cdot x_k(1 - x_k). \quad (1)$$

where $\mu = 4$, the initial condition is 0.123. Moreover, all the orbits of the logistic map are dense in the range $[0, 1]$.

(2) A threshold T is redefined to get a binary logistic sequence $\{T(x_k) : k=1, 2, \dots\}$. If $x_k > T$ then $x_k=1$, else $x_k=0$.

(3) Because the watermarking is a binary image, we deal with it by modular arithmetic that can get a vector which length is the number of image pixels. Similarly deal the matrix generated by Equation 1 and (2) with the same process. Where the modular arithmetic can be do by the following process

a) Assume a key K ;

b) Assume A is the height of a matrix, and B is the width of a matrix. The matrix don't be scanned from $(1,1)$ but from (x, y) , where $x=(K) \bmod A$, $y=(K) \bmod B$.

Specifically, the scan process can be described as following. From a starting location (x, y) , the algorithm starts scanning the matrix from line x line by line downward to line A , back to line 1, line 1 till line $x-1$. For each line, the scan starts at column y , rightward to column B , back to column 1, column 1, till column $y-1$. So, the watermark sequence $W = \{w(i, j) | i=1,2,\dots,A; j=1,2,\dots,B\}$ can be obtained. W is rescanned into a one-dimensional vector $W = \{w(j) | j=1,2,\dots,A \times B\}$ still denoted W .

For embedding process, the original image is decomposed into three resolution levels using Daubechies-1. In each level, there are one compressed matrix and three detail matrixes. The Fig. 1 shows the decomposition into three resolution levels. Continually, we deal with the three detail matrixes of the level 3. The Fig. 2 shows some changes according Fig. 1.

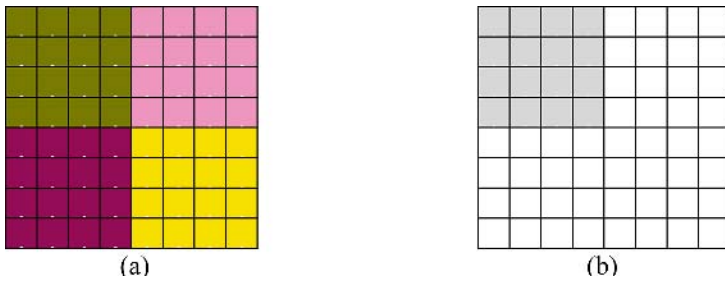


Fig. 1. (a) Decomposed into 3 resolution levels obtained by wavelet packets decomposition. (b) A new resolution levels decomposition figure modified by Fig. 1.

We denote I^{lk} is the l -th level matrix with the direction θ and k , where l is $\{0,1,2,3\}$, θ is $\{0,2\}$ and k is $\{1,2,3\}$. The watermark is embedded along the band in the Figure 3, modifying the wavelet packets coefficients of these matrices. The embedding method is given by Equation 2.

$$I'3^k = I3^k + \alpha \cdot w(i). \tag{2}$$

Where, $I3^{lk}$ is the original wavelet packets coefficients of θ -th and k -th matrix in level 3, $I'3^{lk}$ is the marked wavelet packets coefficients of θ -th and k -th matrix in level 3, α is a constant which controls the watermark embedding energy, and w is the watermarking sequence.

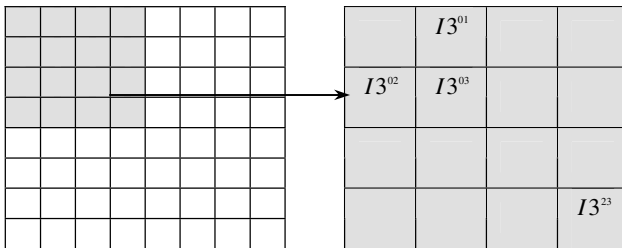


Fig. 2. The embedding bands

For every embedding band, we embedding the watermark repeatedly four times. For example, if we embedded a bit in (i, j) , then the same process will be done in $(i+1, j)$, $(i, j+1)$, $(i+1, j+1)$.

In the end, the watermarked images is obtained after recomposed the band with the same resolution levels.

3 The Watermarking Extraction Process

For watermarking recovery from watermarked image, the steps for watermarking extraction are as follows

- 1) Both the original images and the watermarked images are decomposed as the embedding stage.
- 2) Carry out a reverse process of the embedding Equation 3.

$$h(i) = (I'3^k - I3^k) / \alpha . \quad (3)$$

- 3) Getting a sequence v by more selection vote because we have embedded the watermarking repeatedly four times in the embedding the same stage. Threshold 0.5 is chosen as judging for more selection vote. After the inverse modular arithmetic to v , v' can be obtained.
- 4) Generated the same logistic sequence f with the embedding the same stage.
- 5) The watermarking sequence is extracted $w' = v' \oplus f$.

4 Experimental Results

The performance of the proposed algorithm is tested on various types of images. Here the results are presented for grayscale 8-bit *Lena* image of size 256×256. The watermarking is a binary image of size 32×32. Original image *Lena* and watermarking image are shown in Fig. 3(a) and (b) respectively. Watermarked *Lena* image and extracted watermarking image are shown in Fig. 3(c) and (d) respectively. The watermarked *Lena* image has PSNR=41.958.

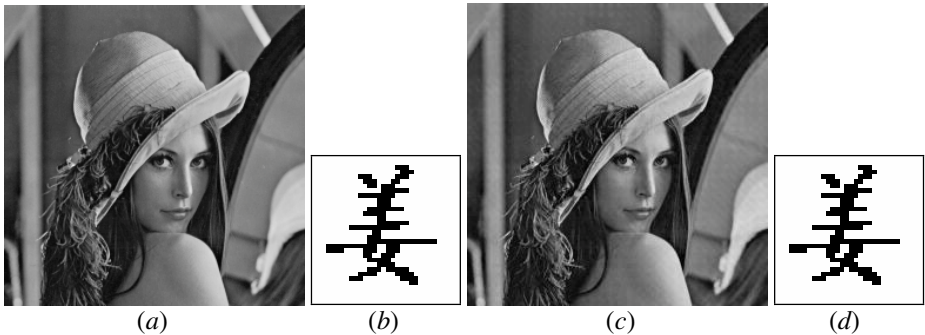


Fig. 3. (a) Original *Lena* image (b) Watermark image (c) Watermarked image (d) Extracted watermark image

To observe the robustness of the new algorithm, attacks were used to Fig. 3(c). The used attacks are JPEG compression, contamination by Gaussian noise, cropping, luminosity modification, geometrical distortions and scaling.

A. JPEG Compression

The quality factors of the JPEG compression are 90,80,60,50 to Fig. 3(c) respectively. The extracted watermarks are shown in the Fig. 4.

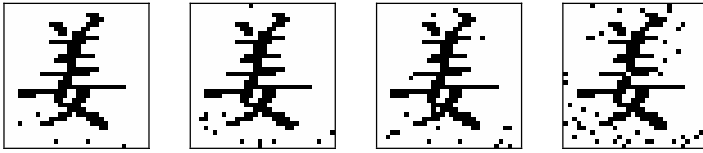


Fig. 4. Extracted watermarks after attacked by JPEG compression with quality factors of 90,80,60,50 respectively

B. Contamination by Gaussian Noise

Gaussian noise is added into Fig. 3(c), where Gaussian noises are zeros mean, with variance 0.002, 0.004, 0.006, 0.008, 0.01 respectively. The extracted watermarks are shown in Fig. 5.

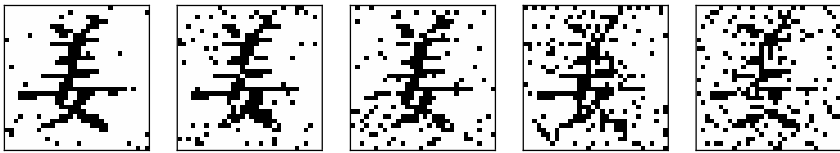


Fig. 5. Extracted watermarks after attacked by Gaussian noise with variance 0.002, 0.004, 0.006, 0.008, 0.01 respectively

C. Cropping

Fig. 3(c) is cropped a part, the results are shown in Fig. 6(a) and (c).

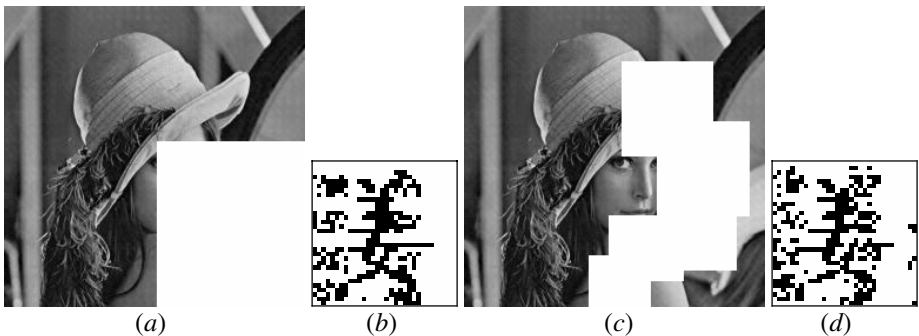


Fig. 6. (a) and (c) are the images after cropped , (b) and (d) are extracted watermarks

D. Luminosity Modification

Three types of brightness are applied to Fig. 3(c), the results are shown in Fig. 7.

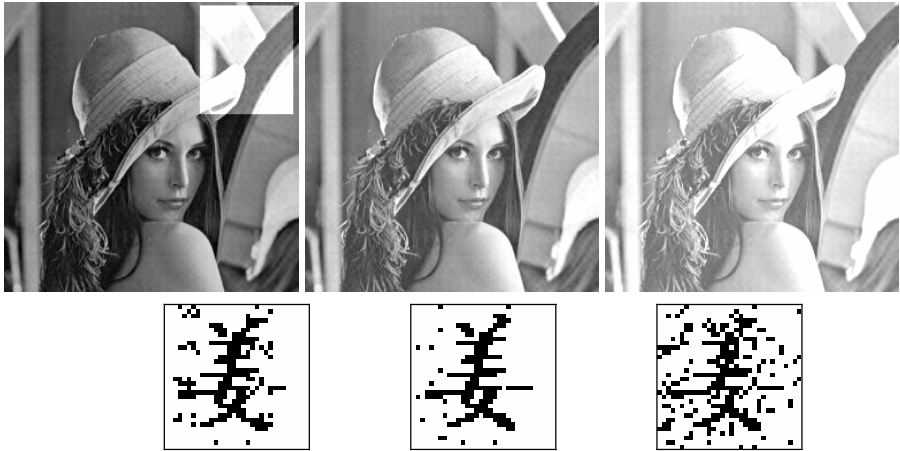


Fig. 7. Change brightness of Fig. 3(c) respectively and extracted watermarks

E. Geometrical Distortions

Two geometrical distortions were used to Fig. 3(c), the results are shown in Fig. 8(a) and (c).

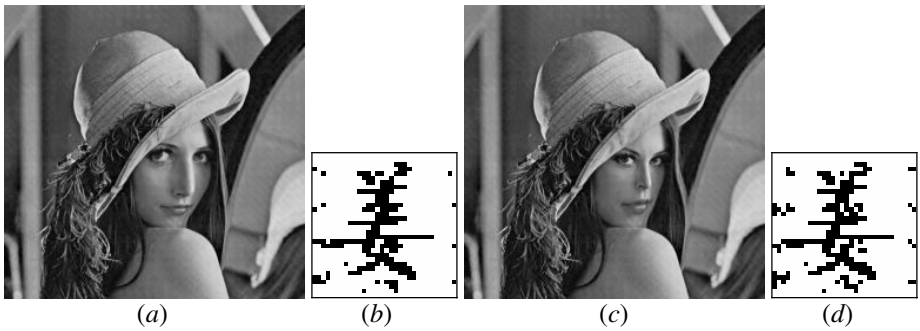


Fig. 8. (a) and (c) are the watermarked images after distorted, (b) and (d) are extracted watermarks

F. Scaling

Fig. 3(c) is scaled according to 80%, the results is shown in Fig. 9(a).

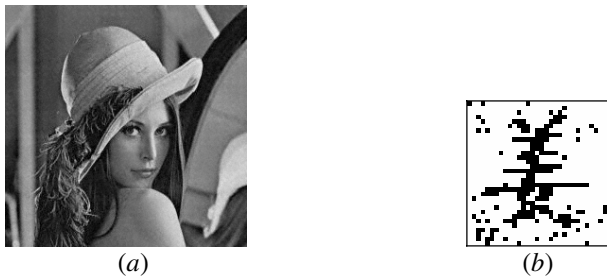


Fig. 9. (a) is the watermarked images after scaling of 80%. (b) is extracted watermarks.

G. Comparison with other methods

The proposed new algorithm was compared to the Podilchuk's method^[4], the results shown in Table 1. The proposed algorithm was found to be superior to Podilchuk's algorithm in PSNR.

Table 1. The PSNR of the proposed algorithm and Podilchuk's algorithm (dB)

Image	Algorithm	Proposed algorithm	Podilchuk's algorithm
	Baboon		34.621
Lena		41.958	39.54
Goldhill		38.906	37.51
Man		39.003	36.96

5 Conclusions

By the experimental results, proposed algorithm has the following properties:

1. *Robustness.* Under standard attacks, new algorithm is robust to various image processing and geometric distortions, such as JPEG compression, contamination by Gaussian noise, cropping, luminosity modification, geometrical distortions and scaling.

2. *Invisibility.* It is noted that there is almost no perceptual difference between Figure 4(a) and Figure 4(c). In practice, this is an essential property of the copyright protection.

By the experimental, we believe that wavelet packets can play an important role in the digital image watermark. Based on this idea, we use wavelet packets in proposed algorithm. This novel algorithm can be resistant to common image processing and simple geometric distortion attacks. Furthermore, watermark has also very good invisibility. It shows that proposed algorithm can apply in the copyright protection.

References

1. Lino Coria-Mendoza, Panos Nasiopoulos, Rabab Ward: A Robust Watermarking Scheme Based on Informed Coding and Informed Embedding. IEEE International Conference on Image Processing ICIP 2005. Genova, Italy, (2005)
2. Chang-Tsun Li: Reversible Watermarking Scheme with Image-independent Embedding Capacity. IEE Proceedings - Vision, Image, and Signal Processing, Vol.152, No.6: 779-786, (2005)
3. Ni J.Q., Zhang R.Y., Huang J.W. and Wang C.T.: A Robust Multi-bit Image Watermarking Algorithm Based on HMM in Wavelet Domain. Proceedings Of 4th International Workshop, IWDW 2005, Siena, Italy, Lecture Notes in Computer Science, Vol. 3710, Springer-Verlag, 110-123, (2005)

4. Podilchuk C. I. and Zeng W.: Image-Adaptive Watermarking Using Visual Models. *IEEE Journal on Selected Areas in Communications*, Vol.16, No.4: 525–539, (1998)
5. Paquet, A., Ward, R.K. and I. Pitas.: Wavelet Packets-based Digital Watermarking for Image Verification and Authentication. *Signal Processing, Special Issue on Security of Data Hiding Technologies*, Vol. 83, No. 10: 2117-2132, (2003)
6. Wang H.J.M., Su P.C., and Kuo C.C.J.: Wavelet-based Digital. Image Watermarking. *Optics Express*, Vol. 3, No. 12: 491- 496, (1998)

On a Face Recognition by the Modified Nonsingular Discriminant Analysis for a Ubiquitous Computing

Jin Ok Kim¹, Kwang Hoon Jung², and Chin Hyun Chung²

¹ Faculty of Multimedia, Daegu Haany University,
290, Yugok-dong, Gyeongsan-si, Gyeongsangbuk-do, 712-715, Korea
bit@dhu.ac.kr

² Department of Information and Control Engineering, Kwangwoon University, 447-1,
Wolgye-dong, Nowon-gu, Seoul, 139-701, Korea
chung@kw.ac.kr

Abstract. This paper presents an efficient face recognition by the modified nonsingular discriminant analysis for a ubiquitous computing. It is popular to extract discriminant features using Fisher linear discriminant analysis (LDA) for general face recognition. In this paper, we propose the modified nonsingular discriminant analysis in order to overcome the problem of small sample size and prone to be unrealizable due to the singularity of scatter matrices. The scatter matrix of transformed features is nonsingular. From the experiments on facial databases, we find that the modified nonsingular discriminant feature extraction achieves significant face recognition performance compared to other LDA-related methods for a limited range of sample sizes and class numbers. Also, recognition by the modified nonsingular discriminant analysis by using TMS320C6711 DSP Vision Board is set to highlight the advantages of our algorithm.

1 Introduction

The term biometric comes from the Greek words bios (life) and metrikos (measure). It is well known that humans intuitively use some body characteristics such as face, gait or voice to recognize each other. Since, today, a wide variety of applications require reliable verification schemes to confirm the identity of an individual, recognizing humans based on their body characteristics became more and more interesting in emerging technology applications. Traditionally, passwords and ID cards have been used to restrict access to secure systems but these methods can easily be breached and are unreliable. Biometric can not be borrowed, stolen, or forgotten, and forging one is practically impossible. This paper proposes the modified nonsingular discriminant feature [1] extraction for face recognition under different sample sizes and class numbers on the wavelet [2, 3, 4, 5, 6, 7, 8, 9] feature face images. The general concept is motivated from solving the singular [10] problem for scatter matrices for LDA [10, 11] procedure.

We transform the face data using the eigenvectors of scatter matrix [10, 11] corresponding to all nonzero eigenvalues. This step assures that the scatter matrix of transformed data is nonsingular and positive definite. Even if the original scatter matrix is nonsingular, this transformation is able to optimize the between-class scatter, which is beneficial for pattern recognition. At second step, the Fisher criterion using the modified nonsingular scatter matrices is maximized so as to improve the class discriminability. Also, we apply the LDA scheme to linearly transform the wavelet transformed face images to new feature space with higher separability and lower dimensionality. Using the modified nonsingular discriminant analysis, the recognition robustness is improved.

2 Linear Discriminant Analysis

Linear discriminant analysis easily handles the case where the within-class frequencies are un-equal and their performances has been examined on randomly generated test data. This method maximizes the ratio of between-class variance to the within-class variance in any particular data set thereby guaranteeing maximal separability.

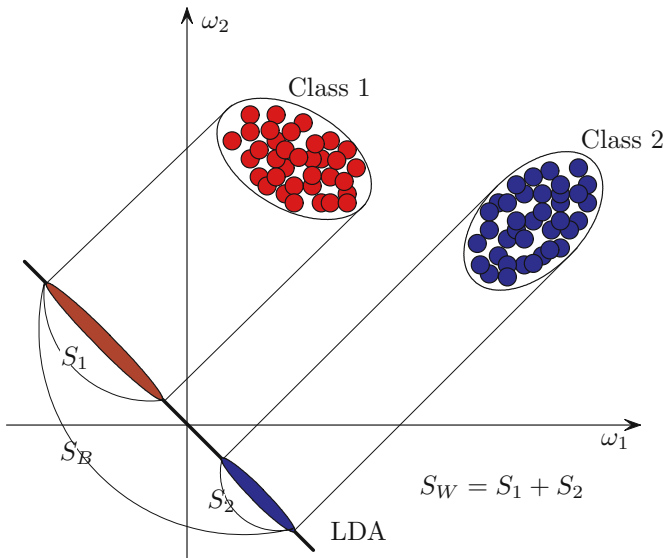


Fig. 1. Comparison of PCA and LDA

Let the between-class scatter matrix be defined as

$$S_b = \sum_{j=1}^c N_j (\mu_j - \mu)(\mu_j - \mu)^T \tag{1}$$

and the within-class scatter matrix be defined as

$$S_w = \sum_{j=1}^c \sum_{\mathbf{x}_k \in \mathbf{X}_i} (x_i^j - \mu_j)(x_i^j - \mu_j)^T \tag{2}$$

where the μ_i is the mean vector of class X_i , and N_i is the number of samples in class X_i . If S_W is nonsingular, the optimal projection W_{opt} is chosen as the matrix with orthogonal columns with maximizes the ratio of the determinant of the between-class scatter matrix of the projected samples, i.e.

$$W_{opt} = \frac{|S_B|}{|S_W|} = \frac{W^T S_b W}{W^T S_w W} \tag{3}$$

$$= [\mathbf{w}_1 \quad \mathbf{w}_2 \quad \dots \quad \mathbf{w}_m]$$

where $\{\mathbf{w}_i = 1, 2, \dots, m\}$ is the set of the generalized eigenvectors of S_B and S_W corresponding to the m largest generalized eigen values $\{\lambda_i | i = 1, 2, \dots, m\}$, i.e.

$$S_b W = \lambda S_w W, \quad i = 1, 2, \dots, m. \tag{4}$$

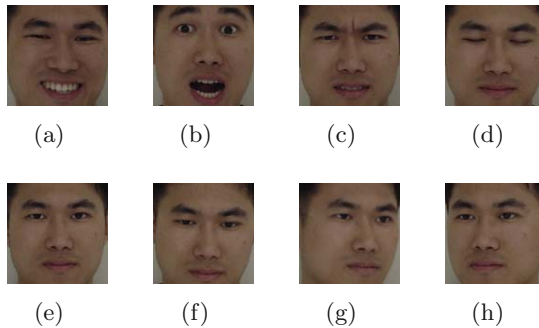


Fig. 2. Training samples of a person, $m = 8$ (a)Smile (b)Surprise (c)Scowl (d)Close eyes (e)Look front (f)Look bottom (g)Look right (h)Look left.

3 Modified Nonsingular Discriminant Analysis (NDA)

After extraction of waveletface, the original facial vector $\mathbf{x} \in \mathfrak{R}^n$ is transformed to the feature vector $\mathbf{y} \in \mathfrak{R}_m$ with $m < n$. To further reduce the feature dimensionality and enhance the class discriminability, we apply LDA to convert the feature vector \mathbf{y} into a new discriminant vector:

$$\mathbf{z} = W_{lda}^T \mathbf{y} \in \mathbf{R}^p, \quad p < m. \tag{5}$$

The linear transformation matrix W_{lda} aims to pull apart the centroid of different classes and reduce the degree of data scattering within the same class. The optimal transformation matrix $J(W_{lda})$ is estimated by maximizing the ratio of the determinants of between-class scatter matrix S_b and within-class scatter S_w

of the transformed samples, i.e., $(W^T S_b W)/(W^T S_w W)$. The matrix S_b and S_w are positive semi-definite matrices. Then, the columns of optimal transformation matrix $W_{lda} = \{\mathbf{w}_i\}$ correspond to the generalized eigenvectors for p leading eigenvalues in $S_b \mathbf{w}_i = \lambda_i S_w \mathbf{w}_i$. If S_w is nonsingular, this can be a conventional eigenvalue problems of $S_w^{-1} S_b$. In this paper, we concern the maximizing the Fisher criterion

$$J(W_{lda}) = \frac{W^T S_b W}{W^T S_w W}. \tag{6}$$

With this variant, the discriminant vectors are derived via maximizing $J(W_{lda})$ or correspondingly finding the eigenvectors of $S_w^{-1} S_b$.

However, in case of small sample size, i.e, the number of prototype samples smaller than the feature vector dimensionality, the scatter matrix is singular and the LDA has no solution to generalized eigen-equation. In real world, the training face images of each person are usually insufficient. When the number of training samples is small or the feature dimension is high, LDA will become unrealizable because of the property $rank(S_w) = \min(n, C \times (M - 1))$ and $rank(S_b) = \min(n, C - 1)$ where C is class numbers and M represents the sample numbers of each class. We are unable to realize the calculation for the eigenvectors of $S_w^{-1} S_b$. The nonsingular transformation of S_w aims to optimize the trace of within-class scatter matrix through

$$W_w = \arg \max_W (W^T S_w W). \tag{7}$$

The optimal solution W_w satisfies the diagonalization process $W_w^T S_w W_w = D_w$ with $n \times n$ diagonal matrix D_w . In case of singular S_w , there existing zero eigenvalues. We may construct a $n \times m$ nonsingular transformation matrix \widehat{W}_w consisted of m eigenvectors with nonzero eigenvalues of S_w . Applying the nonsingular transformation $\mathbf{y}_w = \widehat{W}_w^T \mathbf{x} \in \mathfrak{R}^m$, we can maximize the distance between the class mean $\overline{\mathbf{y}}^c$ and the total mean $\overline{\mathbf{y}}$. This discriminant process is significantly beneficial for pattern classification. The resulting within-class scatter matrix $\widehat{S}_w = \widehat{W}_w^T S_w \widehat{W}_w = \widehat{D}_w$ is a $m \times m$ diagonal and nonsingular matrix. Notably the transformed \widehat{S}_w is positive definite, nonsingular and invertible.

At the same time, the new between-class scatter matrix due to $\mathbf{y}_b = \widehat{W}_b^T \mathbf{x}$ is derived by $\widehat{S}_b = \widehat{W}_b^T S_b \widehat{W}_b$, which is diagonal. With the new \widehat{S}_b and nonsingular \widehat{S}_w , we may fulfill LDA for the transformed features \mathbf{y}_w . This resolves the small sample size problem of LDA. Besides, for the case of nonsingular S_w , it is easy to find that the conditions $m = n$, $\widehat{W}_w = W_w$ and $\widehat{D}_w = D_w = \widehat{S}_w$ hold.

After the original features $\mathbf{x} \in \mathfrak{R}^n$ are transformed to $\mathbf{y} \in \mathfrak{R}^m$, the second step of proposed nonsingular discriminant transform is to fulfill the standard LDA and transform \mathbf{y} to $\mathbf{z} \in \mathfrak{R}^p$, $p \leq m \leq n$ using the transformed within-class scatter and between-class matrices. Namely, we will estimate the transformation matrix \widehat{W}_d by maximizing the Fisher criterion where the new scatter matrixes \widehat{S}_w and \widehat{S}_b are considered

$$\widehat{W}_d = \arg \max_W \frac{W^T \widehat{S}_b W}{W^T \widehat{S}_w W}. \tag{8}$$

Algorithm 1. Modified Nonsingular Discriminant Analysis Algorithm

- (1) Estimate scatter matrixes S_b and S_w .
 - (2) **if** S_w is nonsingular, then
 - (3) Fisher criterion $J(W) = \frac{W^T S_b W}{W^T S_w W}$ by solving $S_b W = \lambda S_w W$.
 - (4) **else**
 - (5) S_w is singular, then
 - (6) Construct a nonsingular transformation matrix \widehat{W}_b and \widehat{W}_w for the nonsingular scatter matrix $\widehat{S}_w = \widehat{W}_w^T S_w \widehat{W}_w$ and $\widehat{S}_b = \widehat{W}_b^T S_b \widehat{W}_b$.
 - (7) Estimate the fisher criterion $\widehat{W}_d = \frac{W^T \widehat{S}_b W}{W^T \widehat{S}_w W}$ by solving $\widehat{S}_w^{-1} S_b$.
-

Similar to the general LDA procedure, the discriminant transformation matrix \widehat{W}_d is established using the eigenvectors of $\widehat{S}_w \widehat{S}_b^{-1}$. Because \widehat{S}_w is nonsingular after nonsingular transformation, \widehat{W}_d always exists.

4 Face Recognition by NDA

There are many possible techniques for classification of data. Principal Component Analysis (PCA) and Linear Discriminant Analysis (LDA) are two commonly used techniques for data classification and dimensionally reduction. Most Face recognition schemes can be divided into two different strategies.

The first method is based on the detection of facial features, whereas the second approach, each image pattern of dimension I by J can be considered as a vector x in a $N = IJ$ dimensional space. The three-level lowest frequency subimage with a matrix of $I/8 \times J/8$ is extracted as the feature vector \mathbf{y} , referred as waveletface. Generally, low frequency components represent the basic figure of an image, which is less sensitive to varying images. These components are the most informative subimages gearing with the highest discriminating power. Similar to eigenface, waveletface can be expressed by a form of linear transformation, $\mathbf{y} = \mathbf{W}_{wavelet}^T \mathbf{x}$, where $\mathbf{W}_{wavelet}$ is composed of impulse responses of low pass filter. But, different from eigenface [12, 13], the waveletface can be independently extracted without the effect of new enrolled users.

5 Experiments

As displayed in Table 1, we applied three-level wavelet decomposition and reduced the size of all images to 12×13 , i.e, $\mathbf{x} \in \mathfrak{R}^{156}$, before executing LDA related methods.

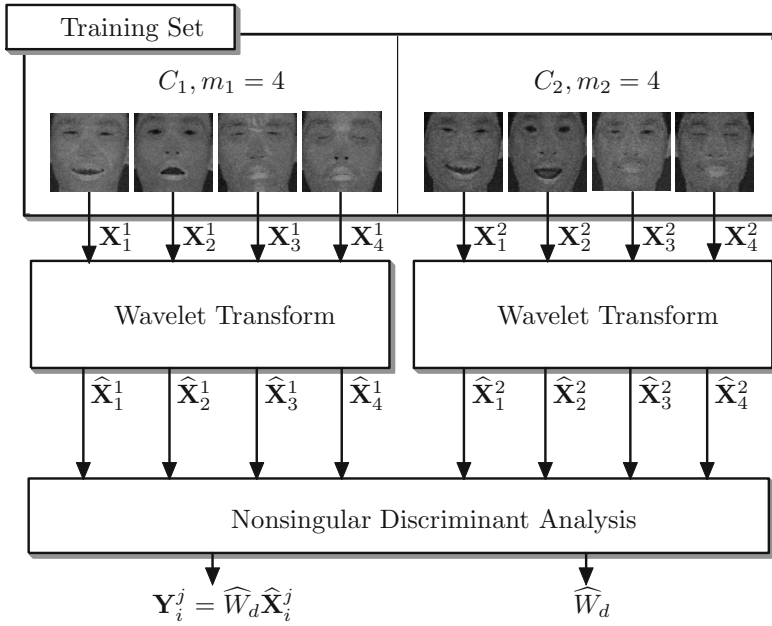


Fig. 3. Flow of training phase of recognition

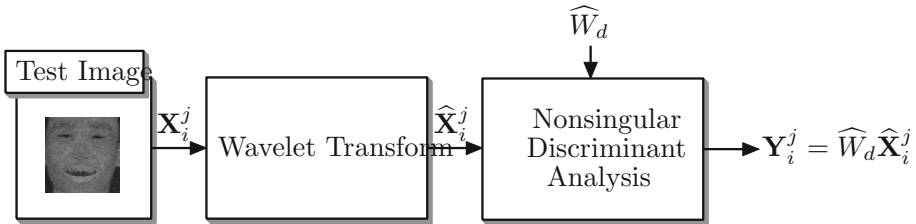
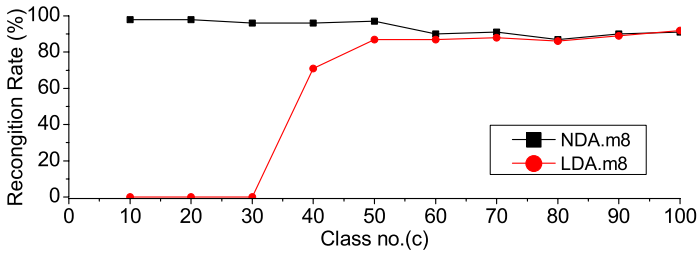
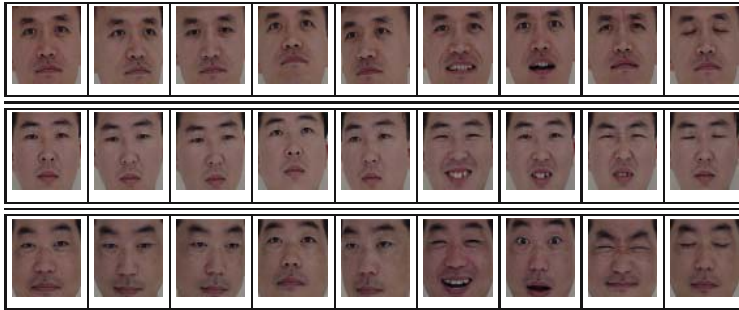


Fig. 4. Flow of test phase of recognition

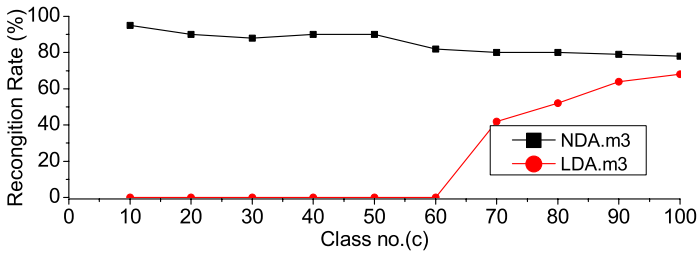
In this paper, the proposed MNDA (Modified Nonsingular Discriminant Analysis) was implemented for a face recognition. To observe the cases of singular and nonsingular scatter matrices, several class numbers C and training sample numbers per class M are chosen for face recognition.

For objective comparison, the dimension of the extracted features $\mathbf{z} \in \mathbb{R}^p$ is set to be $p = C - 1$ when using different methods. This dimension is considered because NDA is dealt with eigen-analysis of S_B having the property $rank(S_B) = \min(n, C - 1)$. Figure 5 displays the recognition rates of LDA and NDA when evaluating them using POSTECH databases. We can conclude that NDA is better than LDA for different C and M .

Table 1. Face recognition sample images ($c = 3, m = 8$)



(a)



(b)

Fig. 5. Comparison of recognition rates of LDA and NDW under different class numbers and training sample rates. (a) $c = 100, m = 8$ (b) $c = 100, m = 3$

Table 2. Comparison of the PCA plus LDA and wavelet plus NDA with various class and training sample size

Various Condition	PCA plus LDA		Wavelet plus NDA	
	$C = 30, m = 8$	$c = 30, m = 3$	$C = 30, m = 8$	$c = 30, m = 3$
Training Time	3min	5.2min	3.2min	4min
Recognition Time	8sec	8.4sec	7.7sec	8sec
Recognition Rate	0%	0%	98.3%	98.9%

6 Conclusion

We have presented a modified NDT facial feature extraction for face recognition under different categories and training data numbers. NDT aimed to transform the original features into the nonsingular or principal space of between-class scatter matrix. The singularity problem of scatter matrices is resolved so as to fulfill the optimization of Fisher criterion. This scheme was applicable for LDA procedures in cases of singular as well as nonsingular scatter matrices. Using NDT, the transformed within-class and between-class scatters were unchanged when S_b was nonsingular. The resulting Fisher class separability was increased as Fig. 5(a) and 5(b). Our proposed method recorded 98.9% recognition rate. This method was different from principal component analysis (PCA) plus LDA, which transformed the features using the eigenvectors of total scatter matrix. In the experiments, we evaluated the feature extraction algorithms on POSTECH face databases. It is found that NDT solves the small sample size problem. NDT is superior to LDA. Recognition performance of NDT is substantially higher than LDA for various conditions.

References

1. Liao, C.P., Chein, J.T.: Nonsingular discriminant feature extraction for face recognition. ICASSP 4 (2005) 957–960
2. Mallat, S.: A Wavelet Tour of Signal Processing. Volume 2. Academic Press, A Harcourt Science and Technology Company Sandiego USA (1998)
3. Burrus, C.S., Gopinath, R.A., Guo, H.: Introduction to Wavelets and Wavelet Transforms. Prentice Hall International, New Jersey (1998)
4. Rao, R.M., Bopardikar, A.S.: Wavelet Transforms Introduction to Theory and Applications. Addison Wesley, Massachusetts (1998)
5. Vetterli, M., Kovacevic, J.: Wavelets and Subband Coding. Prentice Hall, New Jersey (1995)
6. Prasad, L., Lyenger, S.S.: Wavelet Anaysis with Applications Image Processing. CRC Press, Boca Raton Boston London Newyork Washington, D.C. (1997)
7. Massopust, P.R.: Fractal Functions, Fractal Surfaces, and Wavelets. Academic Press, California (1994)

8. Akansu, A.N., Haddad, R.A.: Multiresolution Signal Decomposing, Transforms, Subband, and Wavelets. Academic Press, INC., Harcount Brace Javanovichm (1992)
9. Chan, A.K., Peng, C.: Wavelets for sensing Technologies. Arthech House, Inc., Boston (2003)
10. Duda, R.O., Hart, P.R., Stork, D.G.: Pattern Classification. John Wiley and Sons, LTD, New york, USA (2001)
11. Kim, J.S.: Real-time implementation of face recognition by the lda-based algorithm for a video surveillance system on DSP. Master's thesis, Kwangwoon University (February 2005)
12. Wang, X., Tang, X.: Dual-space linear discriminant analysis for face recognition. Proceeding of the 2004 IEEE Computer Society Conference on Computer Vision and Pattern Recognition (2004) 711–720
13. Lyons, M.Y., Budynek, J., Akamatsu, S.: Automatic classification of single facial images. IEEE Trans Pattern Analysis and Machine Intelligence **21** (1999) 1357–1362

Rapid Determination of Compound Rifampicin Tablets Using Near Infrared Spectroscopy with Artificial Neural Network

Weiliang Guo¹, Qingfan Meng¹, Jiahui Lu¹, Chaojun Jiang¹,
Yanchun Liang², and Lirong Teng^{1,*}

¹ College of Life Science, Jilin University, Changchun 130012, China

² College of Computer Science, Jilin University, Changchun 130012, China

Tel./Fax: +86-431-5168646

tenglr@jlu.edu.cn

Abstract. This paper has investigated the application of near infrared (NIR) spectroscopy with artificial neural network (ANN) for synchronous and rapid determination of rifampicin, isoniazid and pyrazinamide in compound rifampicin tablets. We have developed Back-Propagation (BP) Networks which adopted Levenberg-Marquardt training algorithm and Log-sigmoid transfer function basing on NIR spectra of samples and contents of rifampicin, isoniazid and pyrazinamide. The degree of approximation, a new evaluation criterion of the network was employed, which proved the accuracy of the predicted results. The BP Networks have been optimized by selecting suitable topologic structure parameters and the best numbers of training. Using these BP Networks for predicting the amounts of rifampicin, isoniazid and pyrazinamide in prediction set, the root mean square error of prediction (RMSEP) are 0.00668, 0.00508 and 0.00680. These results demonstrate that this method is feasible. This method is convenient, rapid, has no pretreatment and no pollution.

1 Introduction

Compound rifampicin tablets containing antituberculosis first-line drugs rifampicin (RMP), isoniazid (INH) and pyrazinamide (PZA) were used increasingly. Such tablets had high bactericidal activity, preventing treatment failure caused by the emergence of acquired resistance during chemotherapy and were highly effective for the treatment of patients with strains of tubercle bacilli initially resistant to INH or streptomycin. However, rather imprecise combination of these three drugs could reduce curative effect or lead to toxic reaction[1, 2]. Conventional quantitative analytical methods of compound rifampicin tablets, such as UV spectrophotometer, micellar electrokinetic capillary chromatography (MEKC), HPLC and thin layer chromatography (TLC) methods[3, 4, 5, 6, 7] usually required laborious pretreatment of samples and expensive chemical reagents. In this paper near infrared spectroscopy (NIR) technique was introduced, which

* Corresponding author.

was a rapid, synchronous determination of multi-ingredient and online measurement technique of the sample with no need for reagents or solvents[8]. In quantitative analysis, artificial neural networks (ANN) were more and more widely applied during the past several years. The better advantages of ANN were its anti-jamming, fault tolerance and robust nonlinear transfer ability[9]. In this paper the models has been developed by NIR with ANN for determination of contents of RMP, INH and PZA in compound rifampicin tablets. These models resulted in lower calibration errors and prediction errors. It demonstrated that this method was feasible. With its various advantages, it could be popularized in the in situ measurement and the on-line quality control for drug productions.

2 Experimental

2.1 Materials and Instrument

NIR spectra of compound rifampicin tablets in the 1200~2500 nm wavelength range were obtained using an UV-Vis-NIR spectrophotometer model UV-3150 (SHIMADZU Corporation, Japan), and the scan may go in 1 nm step increment with a 12 nm slit width. The measure was made with barium sulfate as background. Each sample was scanned three times with their average as NIR spectrum. ANN was compiled by MATLAB 7.0.

2.2 Preparation of Samples

Six different batch compound rifampicin tablets were purchased from North China Pharmaceutical Group Corporation. Three of them were used for calibration set, 2 of them were used for prediction set and 1 of them was used for validation set. The contents of RMP, INH and PZA in these compound rifampicin tablets were determined by using HPLC. Compound rifampicin stock standard powder was prepared by accurately weighing the amount of RMP, INH and PZA raw materials which were purchased from Zhejiang Jiangbei Pharmaceutical Co.,

Table 1. Calibration and validation results for quantification of samples in different wavelength ranges

Data set	Samples number	Component	Min content	Max content	Mean content
Calibration set	25	RMP	0.15007	0.24996	0.20510
		INH	0.10203	0.17982	0.14015
		PZA	0.36244	0.45964	0.41300
Prediction set	10	RMP	0.24479	0.15497	0.19831
		INH	0.17402	0.10008	0.13495
		PZA	0.45212	0.35986	0.40623
Prediction set	15	RMP	0.15497	0.24479	0.20090
		INH	0.10008	0.17402	0.13746
		PZA	0.35986	0.45212	0.40968

Ltd. and excipients including magnesium stearate, starch, microcrystalline cellulose and dextrin which were purchased from Chengdu Taishan Bomo Baoyi Co. Ltd. 44 different content standard powder were prepared totally, 22 of them were used for calibration set, 8 of them were used for prediction and 14 of them were used for validation set. Table 1 showed statistical contents of RMP, INH and PZA in calibration set, prediction set and validation set.

3 Results and Discussion

3.1 NIR Spectra

NIR spectra of RMP, INH and PZA raw materials and excipients including magnesium stearate, starch, microcrystalline cellulose and dextrin were recorded over the wavelength range 1200~2500 nm (Fig. 1). These spectra were serious overlapping and quite complicated. Traditional linear algorithms can not parse easily, while ANN was applied to develop a model for determination of RMP, INH and PZA in compound rifampicin tablets in the paper.

3.2 Data Processing

We have developed BP networks based on NIR spectra and the contents of RMP, INH and PZA in compound rifampicin tablets. These BP Networks included three layers, namely, input layer, hidden layer and output layer. The initial weights and biases of each layer were obtained based on Nguyen-Widrow rule. Suitable training algorithm seriously affects the capability of the BP Network. Levenberg-Marquardt training algorithm were applied, which had advantages of having quick speed of convergence and training stability[10] to train the weights and biases of each layer. As the data of input layer and output layer ranged from 0 to 1, we have adopted Log-sigmoid transfer function between input layer and hidden layer, linear transfer function between hidden layer and output layer. The present criterion of optimization was to make the error of the calibration set

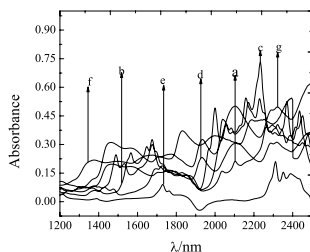


Fig. 1. NIR spectra of raw material and excipients (a) Rifampicin (b) Isoniazid (c) Pyrazinamide (d) Starch (e) Magnesium stearate (f) Microcrystalline cellulose (g) Dextrin

the smallest; however, it was very easy to choose an overfitting model. The error of the prediction set was not the smallest. This was also another optimization method by which the model giving the smallest error of validation set is chosen, while the situation of the training set was ignored. It was very possible that the error of the validation set was the smallest while that the error of the prediction set was large. This kind of network was unsteady when it was used to predict an unknown sample. These unsteady factors were usually due to the number of training[11]. In order to avoid these two kinds of situations, a new evaluation criterion of network, the degree of approximation was employed. The definition of this criterion was given by Eqs. (1) and (2):

$$e_a = \left(\frac{n_c}{n}\right)e_c + \left(\frac{n_v}{n}\right)e_v + |e_c - e_v| \quad (1)$$

where e_a was the error of the approximation, e_c , e_v were the root mean square errors of calibration set and validation set, n_c , n_v were the sample numbers of calibration set and validation set, n was the whole number of known samples, n_c/n , n_v/n were the weights contributed to the error of approximation (e_a) by calibration set and validation set:

$$D_a = \frac{c}{e_a} \quad (2)$$

where D_a was the degree of approximation, and c a constant number by which D_a was adjusted to get a good chart (In this paper c was 0.0002). It was obviously that the smaller e_a was or the larger D_a was the more the models of ANN approach the real nature of the data. Therefore, the effect of both calibration set and validation set were considered in this evaluation criterion. The predictive ability of calibration set, validation set and prediction set were compared in terms of root mean square error (RMSE), defined as:

$$RMSE = \sqrt{\frac{\sum_{i=1}^n (C_{NIR_i} - C_{REF_i})^2}{n}} \quad (3)$$

where n was the number of the samples, and C_{NIR} and C_{REF} the sample contents provided by NIR method and the state drug standard method, respectively. The RMSE of calibration set, validation set and prediction set were named RMSEC, RMSEV and RMSEP.

3.3 Selection of Number of Input Nodes

The different number of input nodes, namely, the different interval of wavelength was changed in order to sieve the data. Fig. 2 showed the effect of the different number of input nodes. It can be seen, the network for determination of RMP had highest degree of approximation, when the number of the input nodes was 10. Both the best numbers of the input nodes in the networks for determination of INH and PZA were 22.

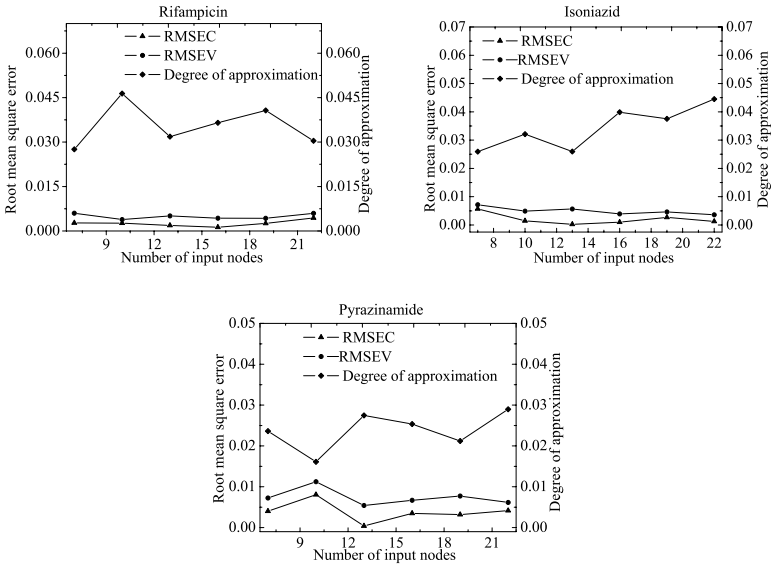


Fig. 2. Effect of different number of input nodes

3.4 Selection of Number of Hidden Nodes

The number of hidden nodes had great effect on the predictive result. Fig. 3 showed the effect of different number of hidden nodes. As can be seen, both

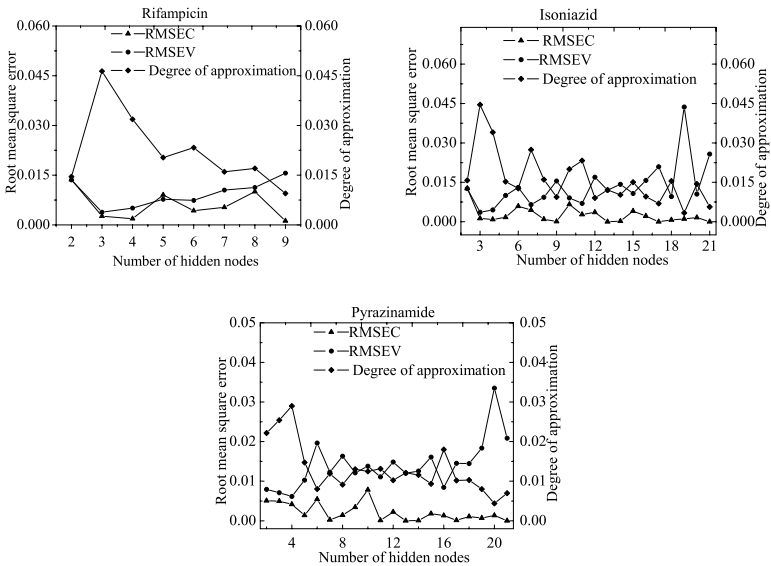


Fig. 3. Effect of different number of hidden nodes

networks for determination of RMP and INH had the highest degree of approximation, when the numbers of hidden nodes were 3, while the network for determination of PZA had highest degree of approximation, when the number of the hidden nodes was 4.

3.5 Selection of Number of Training

Number of training was very important for determinability of network models. The selection of number of training was made by RMSEC curve, RMSEV curve and degree of approximation curve as shown in Fig. 4. With number of training increasing, the RMSEC curve reduced obviously. RMSEV curve reduced obviously at first. When it reached a smallest values, it began to increase. But degree of approximation curve just reversed. It was obvious that network for determination RMP had the highest degree of approximation and the smallest RMSEV when the number of training was 150. Both the best numbers of training in the networks for determination of INH and PZA were 40.

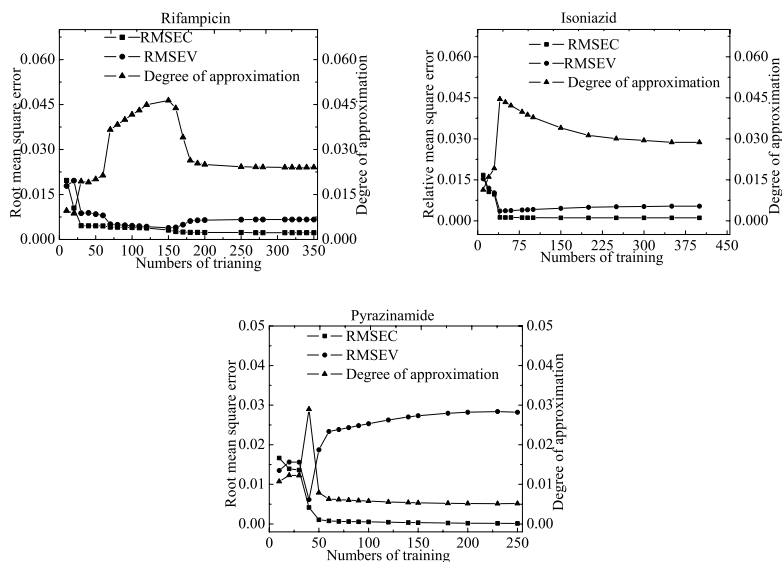


Fig. 4. Effect of different number of training

3.6 The Capability of the Optimum Networks

From foregoing work, we have obtained the optimum networks for determination RMP, INH and PZA in compound rifampicin tablets. Their topologic structures (input nodes-hidden nodes) were 10-3, 22-3 and 22-4 and their best numbers of training were 150, 40 and 40. Fig. 5 showed the correlation between NIR predicted values and actual values. The referent values and the predicted values fitted well.

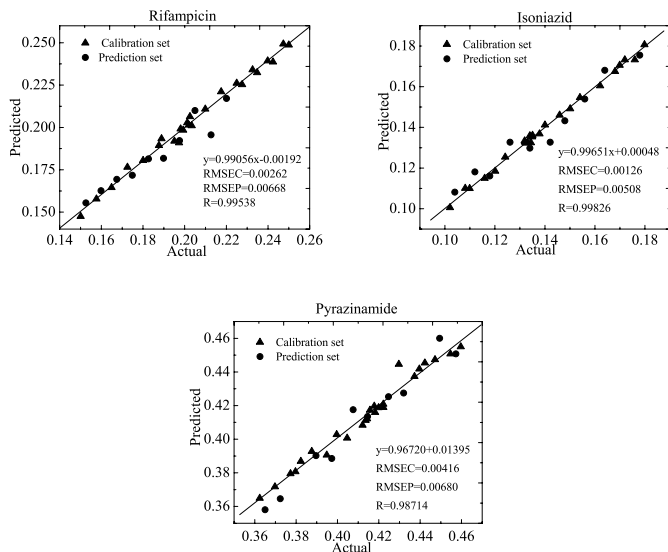


Fig. 5. Correlation between NIR predicted values and actual values

4 Conclusions

In this paper, we have studied the application of ANN in quantitative analysis using NIR spectroscopy. The contents of RMP, INH and PZA in compound rifampicin tablets have been determined simultaneously with this method. By selecting better topologic structure parameters of networks and best numbers of training, optimum networks have obtained. Using these optimum networks for predicting the contents of RMP, INH and PZA in prediction set, satisfactory results have been obtained. The method was a rapid, non-destructive, cost-efficient and easily automatable method for quantitative determination of compound rifampicin tablets. It can be generalized to on-line and real-time quality control in pharmacy.

References

1. Gurumurrthy, P., Ramachandran, G., Vijayalakshmi, S., Hemanth-Kumar, A.K. (ed.): Bioavailability of rifampicin, isoniazid and pyrazinamide in a triple drug formulation: comparison of plasma and urine kinetics. *Int. J. Tuberc. Lung. Dis.* **3** (1999) 119–125
2. Vij, J.C., Govil, A., Jain, N.K., Nath, T., Srivastava, D.K. Gulati, R., Triloki N.: Bioavailability of rifampicin, isoniazid and pyrazinamide in patients with intestinal tuberculosis with malabsorption. *Indian Journal of Tuberculosis.* **42** (1995) 211
3. Espinosa-Mansilla, A., Acedo-Valenzuela, M.I., Munoz, de, la, Pena, A., Salinas, Lopez, F., Canada, Canada, F.: Comparative study of partial least squares and a modification of hybrid linear analysis calibration in the simultaneous spectrophotometric determination of rifampicin, pyrazinamide and isoniazid. *Anal. Chim. Acta.* **427** (2001) 129–136

4. Acedo-Valenzuela, M.I., Espinosa-Mansilla, A., Munoz, de, la, Pena, A., Canada, Canada, F.: Determination of antitubercular drugs by micellar electrokinetic capillary chromatography (MEKC). *Anal. Bioanal. Chem.* **374** (2002) 432–437
5. Calleri, E., Lorenzi, E.D., Furlanetto, S., Massolini, G., Caccialanza, G.: Validation of a RPLC method for the simultaneous determination of isoniazid, pyrazinamide and rifampicin in a pharmaceutical formulation. *J. Pharm. Biomed. Anal.* **19** (2002) 1089–1096
6. Smith, P.J., Van-Dyk, J., Fredericks, A.: Determination of rifampicin, isoniazid and pyrazinamide by high performance liquid chromatography after their simultaneous extraction from plasma. *Int. J. Tuberc. Lung. Dis.* **3** (1999) 325–328
7. Argekar, A.P., Kunjir, S.S., Purandare, K.S.: Simultaneous determination of rifampicin, isoniazid and pyrazinamid by high performance thin layer chromatography. *J. Pharm. Biomed. Anal.* **4** (1996) 1645–1650
8. Nikolich, K., Sergides, C., Pittas, A.: The application of Near Infrared Reflectance Spectroscopy(NIRS) for the quantitative analysis of hydrocortisone in primary materials. *J. Serb. Chem. Soc.* **2846** (2001) 189–198
9. Blanco, M., Villarroya, I.: NIR spectroscopy: A rapid-response analytical tool. *Trends. Analyt. Chem.* **21** (2002) 240–250
10. Marquardt, D.: An Algorithm for Least Squares Estimation of Nonlinear Parameters. *J. Soc. Ind. Appl. Math.* **11** (1963) 431–441
11. Ying, D., Ying, S., Yu-Qiu, R., Yu-Lin, R.: Artificial neural network for simultaneous determination of two components of compound paracetamol and diphenhydramine hydrochloride powder on NIR spectroscopy. *Anal. Chim. Acta.* **528** (2005) 55–61

An Efficient Search Algorithm for High-Dimensional Indexing Using Cell Based MBR

Bo-Hyun Wang and Byung-Wook Lee

College of Software, Kyungwon University,
Bokjeong-Dong, Sujung-Gu, Seongnam-Si,
Gyeonggi-do, South Korea 461-701
bhwang99@hanmail.net, leebw@kyungwon.ac.kr

Abstract. Among the many issues in high dimensional index structures using Minimum Bounding Rectangle(MBR), the reduction of fan-out and increase of overlapping area are the key factors in reduction of search speed. It is known that the usage of only minimum and maximum distance in MBR's pruning process lowers the accuracy of search. In this paper, we present an index structure using cell based MBR in which fan-out gets increased and overlapping is avoided, and a search algorithm which reflects the distribution status of data in MBR to the search. The proposed index structure produces MBR as Vector Approximation-file(VA-file)'s cell units and produces child-MBR by dividing cells. The search algorithm raises the search accuracy by executing pruning using centroid of values included in MBR other than the minimum and maximum distance of cell based MBR and query vector in the k-nn query concerned. Through experiment, we find that the proposed search algorithm has improved its search speed and its accuracy in comparison with existing algorithm.

1 Introduction

As image data has increased its importance and the necessity of quick search have become important, many researches have been done for a search algorithm to raise the accuracy and an index structure using the high dimensional features vector which can raise the search speed.

The previously proposed index structures can be divided into methods using vector area fragmentation, using approximation and a method combining these two. The typical index structures using vector area fragmentation are R^* -tree, SR-tree, etc and a typical method using approximation is VA-file [1][3][4][5]. An example of a method using these two is A-tree [1]. R^* -tree divides the vector space into MBR and SR tree is a technique which indexes by combining bounding sphere and the MBR [3]. R^* -tree has disadvantage in that the fan-out of the node reduces as dimension increases and that the search speed gets slower than the speed of searching high dimensional data in sequence. Also, there's a disadvantage of having to include unrelated data into one of the nodes or search several paths in tree because of overlapping area. Although the A-tree [1] which indexes using VBR instead of MBR by applying a relative approximation concept has an advantage in that the fan-out gets increased in comparison with

R^* -tree or SR-tree, it still includes the problem concerning overlapping area and uses only minimum and maximum distance in VBR's pruning process. The VA-file [5] is a technique which approximates vector spaces into cell having a fixed size. It has a disadvantage in that the performance gets reduced when the data is crowded at a specific cell.

This paper proposes index structure where the approximation technique of VA-file and the clustering technique using MBR are combined and a search algorithm which reflects the distribution status of data to the search. The proposed index structure produces MBR including similar data in cell units of VA-file and produces child-MBR by dividing cells to increase fan-out. The produced MBR based on VA-file's cell does not cause overlapping. Also, by executing pruning using centroid of the data included in MBR other than the minimum and maximum distance of MBR and the query vector toward the k-nn query, it increases the accuracy of search.

The structure of this paper is as follows. Chapter 2 describes related researches. Chapter 3 describes index structure and search algorithm which is being proposed. Chapter 4 describes the contents related to evaluation and the conclusion is made in Chapter 5.

2 Related Work

The previously proposed indexing structures are divided into the clustering technique where the vector domain is indexed by dividing it into MBR or bounding sphere, the approximation technique of dividing vector domain evenly and approximating it into representative value and a technique where these two are combined. There are R^* -tree and SR-tree as typical techniques of clustering, VA-file for the typical approximation technique and A-tree is the typical technique for the combined technique.

R^* -tree [3] is a technique which fragments vector domain into MBR and indexes them into tree structures. Although it is similar to R-tree, it fragments while considering the size of MBR as well as the overlapping area while fragmenting the node. But if the dimension increases, the fan-out gets increased and the search speed gets considerably reduced as the height of tree gets taller. Although it has reduced the overlapping area in comparison with R-tree, it still includes problems concerning the overlapping area.

The SR-tree [4] indexes the area where MBR and bounding sphere are intersected. The center of bounding sphere is the center of vectors that are included and by fragmenting the vector area into a bounding sphere, the performance gets better than R^* -tree with the search of nearest neighbor vector at similar distance. But it has a disadvantage of increased overlapping area because the bounding sphere takes more area than MBR. To solve this problem, an intersecting domain of MBR and bounding sphere is used. But there's a disadvantage in that as SR-tree increases its dimension similar to the case of R^* -tree, the node's fan-out gets reduced and tree's height gets taller so that the search speed gets slower than searching high dimensional data in sequence.

The VA-file [5] divides each dimension of vector into 2^b and express divided domain into b bit. The intersecting part of fragmented area in each dimension is called a

cell and if d is a dimension, one cell is expressed as $d*b$ bit. As the VA-file expresses high dimensional vectors into $d*b$ bit of cells in which vector is included, it approximates the vector into one value. While the VA-file is effective when feature vectors are evenly distributed on the vector space, it had disadvantage in that the performance gets reduced when vectors are crowded at a specific cell.

The A-tree [1] is an index technique where approximation technique of VA-file and MBR of R^* -tree are applied. After dividing data space into MBR, it produces a VBR of relatively approximate rectangle with parent MBR as standard for child-MBR. The VBR gets expressed with a relative approximate value for the parent MBR and one node includes information on parent MBR and VBR. Because approximate value of MBR gets stored in a node, the fan-out gets increased in comparison with R^* -tree or SR-tree. But there's a disadvantage of overhead calling for VBR during index creation and update is required and the overlapping area getting increased as VBR gets bigger than the actual MBR. Also, in k-nn searching, it doesn't reflect data distribution status of VBR by using only minimum and maximum distance to VBR.

In this paper, I want to increase fan-out by producing MBR based on VA-file's cell and reduce overhead as well as solve the problem of overlapping toward VBR in A-tree. Also, I propose search algorithm using centroid value of vectors at pruning process to reflect distribution status of data included in cell based MBR to the search.

3 High Dimensional Index Structure Using Cell Based MBR and Search Algorithm

In this chapter, the proposed high dimensional index structure and search algorithm are described.

3.1 Overview

The outline of proposed index structure is as follows.

First, the MBR in cell unit is configured. In order to increase fan-out of the tree node, the MBR is configured in VA-file's cell units. The figure 1 shows the cluster using cell based MBR. The overlapping area is avoided by producing a cell based MBR.

Second, the disadvantage of cell based MBR is that the effectiveness of search gets reduced when feature vectors are crowded in a cell. In order to solve this problem, the cell which becomes the foundation for child node MBR gets produced by dividing the cell which becomes the foundation for the parent node MBR. The dividing formula is like the formula (1). In formula (1), the range of I is between 1 and dimension D , $P_C(i)$ is the length in i dimension of cell and $C_C(i)$ is the length of a fragmented cell in i dimension. The figure 1's dotted rectangle represents a cell-based MBR composed of fragmented cells.

$$C_C(i) = P_C(i)/2 \quad (1)$$

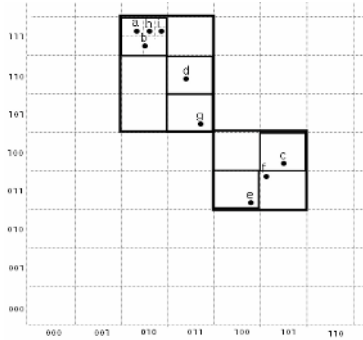


Fig. 1. Cell based MBR

Third, while performing k-nn search using the proposed index structure, the centroid value of feature vectors included in the cell based MBR is used other than the minimum and maximum distance between MBR and query vector during the pruning process to determine candidate cell based MBR. This is to solve the problem of search error created by the range of minimum and maximum distance from the query vector getting longer while using the cell based MBR rather than the existing MBR. The formula for getting the centroid value is like the formula (2). In formula (2), the range of i is between 1 and dimension D and FV is a feature vector included in a cell based MBR. n is the number of feature vectors included in a cell based MBR and C_FV is the center vector of n number of feature vectors.

$$C_FV(i) = \frac{\sum_{k=1}^n FV_k(i)}{n} \tag{2}$$

3.2 Index Structure

The high dimensional index structure proposed in this paper is like the figure 2. The figure 2 expresses feature vectors of figure 1 as index structures. The tree is composed of highest node, non-leaf node, leaf node and data node.

The following is explanation of each node.

① Highest node : Composed of cell based MBR’s information which includes all feature vectors included in child-nodes and a pointer to the child-node.

② non-leaf node : Composed of centroid value in all feature vectors included in the child node, a pointer to the child node and the MBR information toward the cell to be fragmented based on the cell of parent node. The non-leaf node can be an MBR composed of many cells, can be an MBR composed of one cell or an MBR produced by a cell getting fragmented. If an MBR is produced by a cell getting fragmented, the cell based MBR is one of four part of parent MBR and expresses as four bits.

③ Leaf node : Composed of MBR’s information including data from the data node, a pointer to the data node and the centroid value of data existing at the data

node. The MBR stored at the leaf node can also be one cell, composed of many cells or made by fragmented cell. If an MBR is produced by a cell getting fragmented, the cell based MBR is one of four part of parent MBR and expresses as four bits.

④ Data node : This is a node where the actual feature vector gets stored.

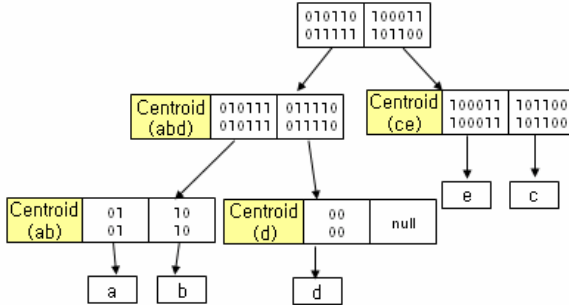


Fig. 2. Index structure using cell based MBR

3.3 Search Algorithm

Table 1 is an algorithm to search k number of nearest neighbor vector data. One queue and two lists are used for the search algorithm. A node searched from the root is stored at the queue. At the KnnData List, the k number of feature vectors gets stored. The cell based MBR stored in leaf node gets stored at the KnnCell. Step 1 is a function of reading the node from the tree and storing it to the Queue.

Step 2~3 is a step to refresh two lists. Steps 4~25 are pruning process and k-nn data search phase toward each cell based MBR. At steps 5~11, when the data read from the queue is a data node, it gets the values of distance between the query vector and feature vectors within the data node and if the distance is shorter compared to the data in the KnnData list's k th data, it gets stored in the k th location of the list. Arrange the list after storing. Step 12 is the pruning phase of queue and the nodes stored in the queue are pruned if minimum distance between node stored in queue and query vector is larger than data stored in the k th location in KnnData list.

From step 14, if the data read from the queue is not a data node, the minimum and maximum distance from MBR to query vector is calculated in order to determine whether to search or not search each cell based MBR stored in node.

If distance from KnnData list's k th location's stored feature vector to the query vector and KnnCell list's k th location's stored distance is larger than minimum distance from MBR to the query vector, the child node pointed by the cell based MBR is included in the first search candidates.

If the node including current MBR is a leaf node and max distance from the cell based MBR to the query vector is shorter than KnnCell list's k th distance and the centroid value of current searching node is shorter than the centroid value of node including MBR stored in k th location of KnnCell list, the values of current searching MBR is stored in k th location of KnnCell list. And KnnCell is sorted. Explanation to now is the contents of step 17~22.

Step 19 is the step using centroid proposed in this paper. It is not because the maximum distance between the cell based MBR included in the leaf node and query vector is short that the data in the MBR is close to Query. For the more accuracy search, the centroid value of the data which reflects the data distribution is used.

Table 1. Search algorithm

```

SearchKnnData(querydata, k)
1. InsertIntoQueue(a pointer to the root, 0);
2. for i = 1 to k   KnnData[i] = (node : dummy, dist : ∞);
3. for i = 1 to k   KnnCell[i] = (centroid : ∞, dist : ∞);
4. while emptyQueue() = false do {
5.   N = GetNodeFromQueue();
6.   if (N is a data node )
7.     for each entry ∈ N {
8.       if DIST(query, entry.vector) ≤ KnnData[k].dist {
9.         KnnData[k].node = entry.oid;
10.        KnnData[k].dist = DIST(query, entry.vector);
11.        sort KnnData by dist;
12.        pruneQueue(KnnData[k].dist); }
13.    }
14.  else // N is an index node
15.    for each entry ∈ N do {
16.      MBR = decode(N.MBRbasedCell);
17.      if (MINDIST(query, MBR) ≤ KnnData[k].dist) &&
18.         MINDIST(query, MBR) ≤ KnnCell[k].dist {
19.        enqueue(entry.ptr, MINDIST(query, MBR));
20.        if N is a leaf node && MAXDIST(query, MBR) ≤ KnnCell[k].dist
21.           && CentroidOfNode ≤ KnnCell[k].centroid {
22.          KnnCell[k].dist = MAXDIST(query, MBR);
23.          KnnCell[k].centroid = CentroidOfNode ;
24.          sort KnnCell(dist, centroid);
25.          pruneQueue(KnnCell[k].dist); } }
26.    } /*end for */
27.  } /* end while */
28. output(KnnData); // output the result

```

4 Performance Evaluation

In order to prove effectiveness of search algorithm proposed in this paper, the accuracy and speed of the search has been compared with A-tree. We compared the search speed as we was changing the dimension from 4th to 64th toward 1000 data after setting k to 20 for the k-nn. For the k-nn query, when k was 10, 20, 30, I measured the accuracy of the search with 1000, 2000, 3000, 4000, 5000, 6000 number of 16th dimension's data as candidate. For experiment data, the set of real number data with [0,1] range having equal and unequal distribution by using random number generator are used.

Figure 3 is a graph comparing the search speed of A-tree and proposed tree according to the increase of dimension. Although the speed is similar until the 28th dimension, we can see that there is rapid increase in the speed of A-tree when it gets higher than 28th dimension. We could know the difference of overheads get sharply increased as the dimension increases, and as the overhead used for changing VBR into the specific vector value is bigger than that for changing the cell based MBR into the specific vector axis.

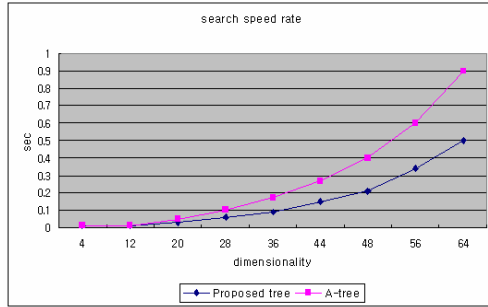


Fig. 3. search speed rate

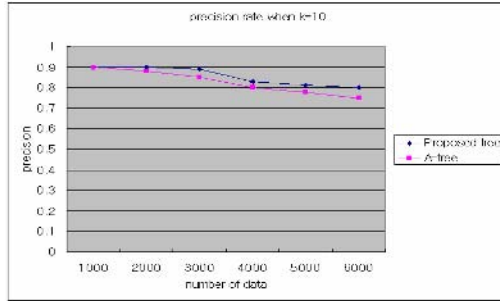


Fig. 4. precision rate when k=10

Figure 4, 5 and 6 describe the search accuracy in comparison with A-tree for 16-dimensional vector data at the points that k value is 10, 20 and 30 each.

In figure 4, there is only slight difference between that of A-tree and proposed search algorithm when k value is 10. When the number of data is 1000, there is almost same in accuracy of two search algorithm. From 2000 there is slightly difference in accuracy. We can find that as the number of data increases, the proposed algorithm get higher than that of A-tree.

Figure 5 show that the accuracy of two algorithm when k is 20 is higher than when k value is 10 for values of x-axis. This fact shows that as k value increases, the accuracy is improved because the more data are returned and the probability including related data is higher. The difference between two search algorithm get wider than figure 4.

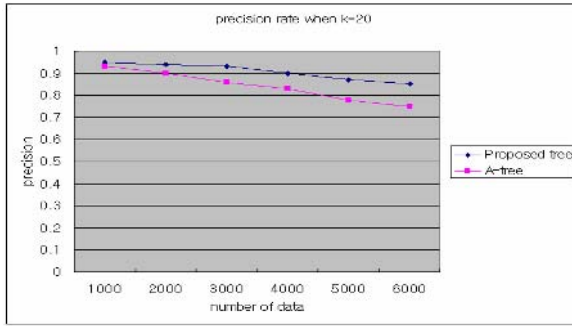


Fig. 5. precision rate when k=20

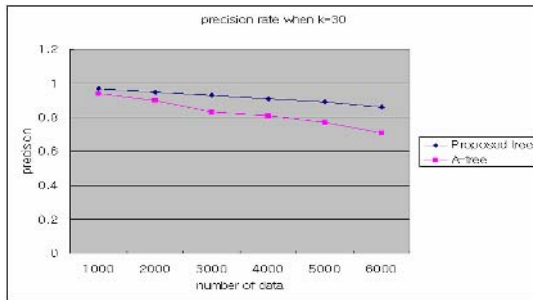


Fig. 6. precision rate when k=30

Figure 6 also shows that the difference between two search algorithm get wider than that of figure 4 and figure 5.

We can find the accuracy of search algorithm in A-tree and proposed tree get improved as the k value increases, and as the number of data increases, the accuracy get lowered. However, the accuracy of proposed tree is higher than that of A-tree on all the three of graphs, and as k value increases, the difference between two trees get wider. Thus we can find that as k value increases, the proposed search algorithm is more effective than that of A-tree.

5 Conclusion

The index technique proposed in this paper indexes using cell based MBR. Also, in order to solve the ineffective index creation in case the crowded data within the MBR occurs, the MBR is composed in fragmented cell units by fragmenting cells. Using of cell based MBR doesn't occur overlapping area and increase fan-out of node.

For the accuracy of search using cell based MBR, the search algorithm which executes the pruning phase using not only the minimum and maximum distances between the query vector and MBR, but the distance between the centroid values of data within the MBR and the query vectors is proposed. Through experiment, we found

out that the proposed search algorithm has improved its search speed and its accuracy compared to A-tree.

But we can show the decrease of accuracy according to the increase of the number of data in both A-tree and the algorithm proposed in this paper. The improving of search algorithm so as not to decrease the accuracy of search although the number of data is increased remains as problems to be solved.

Acknowledgement

This work is supported by Technical Development project of Growth Engines of Gyeonggi-do.

References

1. Yasushi Sakurai., Masatoshi Yoshikawa., Shunsuke Uemura., Hruhiko Kojima.: "The A-tree: An Index Structure for High Dimensional Spaces Using Relative Approximation," Proceedings on the 26th VLDB Conference, Egypt, 2000, pp.516-526
2. Yasushi Sakurai., Masatoshi Yoshikawa., Shunsuke Uemura., Hruhiko Kojima.: "The A-tree: An Index Structure for High-Dimensional Spaces Using Relative Approximation," Technical report, Nara Institute of Science and Technology, 2000, pp.1-22
3. Beckmann N., Kriegel H.-P., Schneider R., SeegerB.: "The R*-tree: An Efficient and Robust Access Method for Points and Rectangles," Proceedings on ACM SIGMOD International Conference on Management of Data, Atlantic City, NJ, 1990, pp.322-331
4. N. Katayama., S. Satoh.: "The SR-tree: An index structure for high-dimensional nearest neighbor queries," Proceedings on the ACM SIGMOD International Conference on Management of Data, Volume 26, Issue 2, Tucson, Arizona USA, 1997, pp.369-380
5. Weber R., Schek HJ., Blott S.: "A quantitative analysis and performance study for similarity-search methods in highdimensional spaces," Proceedings on the 24th VLDB Conference, New York City, 1998, pp.194-205
6. D. A. White., R. Jain.: "Similarity Indexing with the SS-tree," Proceedings Of the 12th International Conference on Data Engineering, New Orleans, USA, 1996, pp.516-523
7. N. Roussopoulos., S. Kelley., F. Vincent.: "Nearest Neighbor Queries," Proceedings ACM SIGMOD, San Jose, USA, 1995, pp.71-79
8. Stefan Berchtold., Keim D. A., Kriegel H.-P.: "The X-tree: An Index Structure for High-Dimensional Data", Proceedings on the 22nd VLDB Conference , Bombay, 1996, pp. 28-39
9. Lin K., Jagadish H. V., Faloutsos C.: "The TV-tree : An Index Structure for High-Dimensional Data," VLDB Journal, Vol. 3, Issue 4, 1994, pp.517-542
10. Stefan Berchtold., Christia Bohm., Hans-Peter Kriegel.: "The Pyramid-Technique : Towards Breaking the Curse of Dimensionality," ACM SIGMOD, Vol. 27, Issue 2, Seattle, 1998, pp.142-153

Bimanual Hand Tracking

Hye-Jin Kim, Keun-Chang Kwak, and Jaeyeon Lee

Human Robot Interaction Research Team,
Intelligent Robot Research Division, ETRI,
161 Gajeong-Dong, Yuseong-Gu, Daejeon 305-350, Korea
{marisan, kwak, leeejy}@etri.re.kr

Abstract. This paper proposes a novel real-time hand tracking algorithm in the presence of occlusion. For this purpose, we construct a limb model and maintain the model obtained from ARKLT methods with respect to second-order auto-regression model and Kanade-Lucas-Tomasi(KLT) features, respectively. Furthermore, this method do not require to categorize types of superimposed hand motion based on directivity obtained by the slope's direction of KLT regression. Thus, we can develop a method of hand tracking for gesture and activity recognition techniques frequently used in conjunction with Human-Robot Interaction (HRI) components.

1 Introduction

Robot and human interaction has received a significant amount of attention in the robot vision research community in the past decades. This has been motivated by the desire of understanding human gesture/motion tracking and recognition.

If you solve tracking problems under the circumstance of fast movement, occlusion, and illumination, then you need to complicate calculation, and hence the computational complex prevents to work in real time. For example, particle filter is an useful algorithm to track objects, even under occlusion and nonrigid motion difference. However, particle filter needs to enough samples to support reliability of the potential candidates of the target. There have done many works in hand tracking. To track hands in real time, Shan [1] made particle filter faster by reducing sample size according to mean shift. On the other hand, Kolsch[2] designed a fast tracking algorithm that combined Kanade-Lucas-Tomasi(KLT) flocks and k-nearest neighborhood.

Some papers concentrated on the particular properties of hands and their features. Non-rigidity of the hand causes difficulties to track because of non-linear dynamics of the articulation. Fei and Reid[3] dealt with deformation of the hand by constructing two models according to non-rigid motion from rigid motion. HLAC(Higher-Order Local Auto-Correlation) features of Ishihara[4] achieved efficient information over time domain by Auto-Regressive model.

The size of interesting objects is another critical factor for tracking because if its size is too small or changes too fast, object tracking becomes very challenging problem. François[5] dealt with blobs varying their resolution, hence made it possible to track the object with various size in the image sequence. Both hands

tracking is simultaneously different from one hand tracking since features such as shape, color etc. between both hands is almost the same each other. Shamaie[6] built the model of the movements of bimanual limbs. However, the model needs large enough time to compute distance transform in the image. McAllister[7] solved the both hands tracking by employing contour distance transform and 2D geometric model.

In this paper, we propose a new 2D both hands tracking algorithm based on the articulated structure of human body in real time. This method is efficient enough to perform in real time due to the limb model tracking. The model enables to deal with the deformation of hands and nonrigid motion because of the articulate structure of the arm for both hands. The model can be tracked by a linear line obtained from the regression of KLT features in order to represent the target information. Unlike Shamaie and McAllister, the proposed algorithm outperforms previous method in occlusion handling of both hands. For instance, some methods require to restrict occlusion cases because similar features prevent a hand to differentiate from another. However, this method track superimposed hands correctly by virtue of its prediction of the moving direction.

In the next section, we will elaborate our proposed algorithm step by step. In the section 2 A-B, we will illustrate key algorithms to build our model. In 2.3, we give brief explanation about how to segment and extract hands from the background. The section 2.4 is dedicated to the dynamic model and the algorithms for occlusion detection and tracking. Some experimental results are presented in the section 3. Our contribution in hand tracking and conclusion are presented at the end of paper.

2 Articulate Hand Motion Tracking Method

2.1 Building the Auto-regression Model

Auto-regression model is one of dynamical mode that is a statistical framework for motion tracking. Through accumulated motion sequences, dynamical model obtains the information to predict motion in the next frame. Second-order auto-regression model is a special Markov process model with gaussian priors $\mathbf{X} \sim N(\bar{\mathbf{X}}, \bar{P})$ the dynamical model.

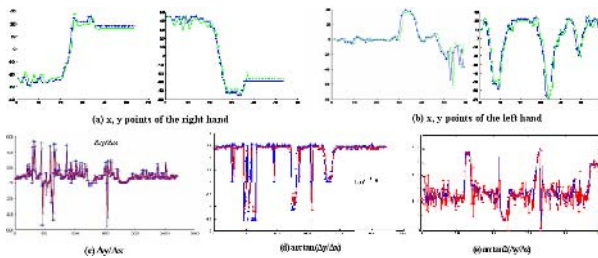


Fig. 1. Learning and prediction accuracy using auto-regressive second-order model. Blue line stands for the original data and green and red lines are predicted data by AR2 model.

$$p(\mathbf{X}(t_k)|\mathbf{X}(t_{k-1})) \propto \exp\left\{-\frac{1}{2} \| B^{-1}(\mathbf{X}(t_k) - A\mathbf{X}(t_{k-1}) - \mathbf{D}) \|^2\right\} \quad (1)$$

Also the Markov process can be expressed in a generative form:

$$\mathbf{X}(t_k) - \bar{\mathbf{X}} = A_2(\mathbf{X}(t_{k-2}) - \bar{\mathbf{X}} + A_1(\mathbf{X}(t_{k-1}) - \bar{\mathbf{X}}) + B_0 w_k \quad (2)$$

where A_2 , A_1 and B_0 are all $N_X \times N_X$ AR coefficients. We set the order of auto-regression model as 2 because it can handle motions with different velocity and noisy direction [8]. AR2 coefficients were learned from the manually marked ground truth data. Training data consist of 100 samples and test data 53 samples with 7 dimension with respect to x and y point of 2D hand, elbow and shoulder points, and a slope between an elbow and an hand. The AR2 model predicts most points well except for the gradients. Fig.1(a) is the image of test samples (above row). Fig.1(b) shows how to estimate the slope. We attempt to extract the slope in several ways: (1) $\Delta y/\Delta x$ (2) $\theta_1 = \tan^{-1}(\Delta y/\Delta x)$ (3) $\theta_2 = \tan_2^{-1}(\Delta y/\Delta x)$. The period of θ_1 ranges from $-\pi/2$ to $\pi/2$ and that of θ_2 ranges $-\pi$ to π . We emphasize on the gradient factor because it gives useful clues that a predicted hand belongs to which side when both predicted hands are crossed each other.

2.2 KLT Features and Linear Regression

KLT features, named after Kanade, Lucas and Tomasi, provides steepest density gradients along the x and y directions(see [9]). The features are corner points with the largest eigenvalues. The size of each feature represents the amount of context knowledge and depends on two factors: quality level of a corner' intensity and minimum distance between corner points.

To match the image I and J, the current and the next image, we minimize the error function ε by the following equation:

$$\varepsilon = \int \int_W [J(\mathbf{x} + d) - I(\mathbf{x})] dx \quad (3)$$

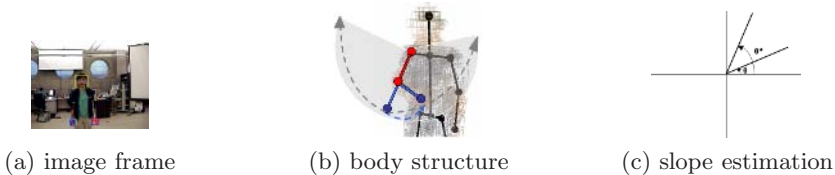


Fig. 2. We define a body structure consists of both hands, shoulders and elbows. The elbow points, green cross marks in (a), represent the base point of the arm's slope. In the first frame, the elbow points are assumed by the ratio of the length between a shoulder and an elbow and the length between the elbow and a hand. For the slope estimation, the difference between slope($\theta^* - \theta$)is considered to predict the next change of the slope.

where W is the given feature window and $w(\mathbf{x})$ is a weighting function. Minimizing Eq.(3), you find the A and d corresponding to the affine motion field and the translation of the feature window's center, respectively. The largest eigenvalue of A estimates feature quality. In the presented system, KLT features calculate their density gradient on the skin and motion image when the object has motion, or on the skin image if there is no object to move. By adjusting the feature size in the skin image or in the skin-motion image, KLT features can be spread out over the whole image plane. Therefore, we filtered KLT features using mean and variance constraint. That is, we removed all KLT features of which variances are more than 2.5 times the overall variance. Linear regression is applied to the filtered KLT features in order to get the slope and find the end point of each hand. Here, we note that the end point extraction needs a reference point because the slope and y-axis intercept need to fit the exact tracking position by removing noisy data and abstract the structural information of the arm by linear regression. This bias will be adjusted and removed by the reference point. As you can see in Fig.2, we construct the arm model for reflecting articulate motion of hands in tracking issue. There are three points for each arm: the shoulder, elbow and hand points. We take each elbow point into the reference point instead of the shoulder point because if you set the shoulder point up as the reference point, then you may lose the elbow point and cannot figure out the status of arms : stretched out , curved and so on. Fig. 2(c) shows the elbow and hand points and the line between them and the slope of the line illustrating in Fig. 2(c) gives the directional information when the occlusion of both hands or arms is detected. Therefore, we know which hand is the right hand and which one is the left when one hand, completely or partially, covers the other hand. In short, the regression of KLT features gives you the position of the hands and the direction to move.

2.3 Hand Detection and Pre-processing

Skin-colour and motion cues are adopted for pre-processing the image. Motion cues are obtained from differentiating the current frame with the previous frame. Skin-colour segmentation requires the following four steps.

1. construct skin-colour database with about one million size samples on RGB plan.
2. generate non-skin colour database.
3. train the skin-colour pixel and non-skin colour pixel after transforming RGB spaces into YUV spaces.
4. obtain the U-V image sequence along the Y plan.
5. create the representative U-V lookup table of skin-colour at the mean point of Y.
6. find skin-colour pixels in an input image using the U-V lookup table.

The forth and fifth steps are essential steps to achieve real-time skin colour segmentation. In the third step, skin-colour detection scheme needs $256 \times 256 \times 256$ comparison per a pixel on the YUV space. However, it is revealed that the trained U-V ranges did not have much difference on Y-spaces. Therefore, U-V values are chosen at the average point of Y as the skin-colour lookup table.

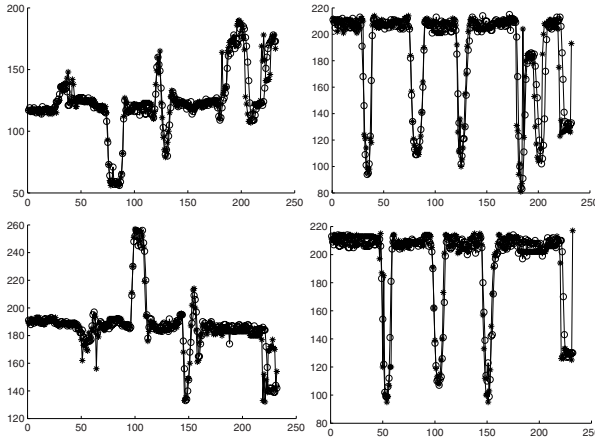


Fig. 3. 'x-' line: original data, 'o-' line: tracked data. Left side plots: x-axis movement, Right side plots:y-axis movement. Tracking results of the right(upper row) and left (lower row) hand.

Finally, the interesting target the motion of skin-coloured regions, the input image is processed by the logical AND operator between the color probability image and the difference image.

2.4 A Dynamic Model for Occlusion Detection and Tracking

In this section, detecting occlusion and tracking is dealt with for both hands at once as shown in Fig.4.

For tracking hands in an image, the limb model is useful to predict future movement of each hand and catch occlusion. Tracking is divided by two parts:crossed motion and uncrossed motion. Hand occlusion in the next frame can be detected by the following factors: (1)the size of superimposed region between predicted areas of both hands should be large enough; (2) the product of two slopes from left and right hands should be non-positive; (3) the amount of slope changes from one frame to a consecutive frame should be beyond threshold. If these three conditions are all satisfied, it is the alarm that two hands are crossed each other.

Detection and Tracking issues highly depend on characteristic of targets. Therefore, it is hard to find targets such as both hands with similar color and similar shape. This fact invokes the need of special features that can decide whether a hand belongs to left or right one. The proposed method uses directivity of hands because the limb structure of human body enables to restrict discriminative movement for each hand. Directivity can be obtained by KLT features and its regression result as already shown in 2.2. When predictive both hands are occluded each other, KLT features are collected when they are close enough to the predicted linear line from the previous frame. Closeness is calculated by the following eq.(4). Where a line equation $ax + b - y = 0$ and a point (x_0, y_0) are given, the distance d is obtained by

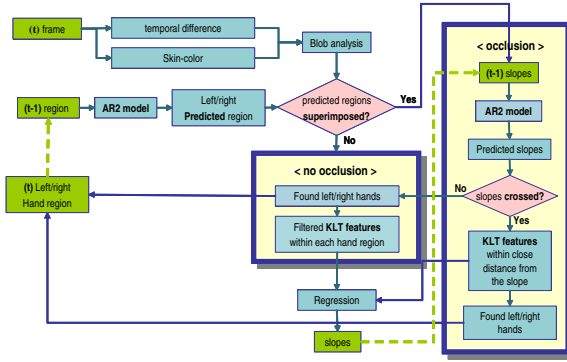


Fig. 4. Overview of fast 2D both hands tracking with articulate motion prediction

$$d = \frac{|ax_0 + b - y_0|}{\sqrt{a^2 + b^2}} \tag{4}$$

The close KLT feature to the predicted line is highly possible a candidate of the target feature in the current frame. Therefore, The filtered KLTs are regressed in order to find the proper end point of the hand.

On the other hand, this method analyzes blobs on the skin and motion image since blobs segments generic features without domain-dependent information. Difficulties that use blobs are the change of size and the velocity of a object corresponding to a blob. Such changes can be serious under the Ubiquitous Robotic Companion(URC) circumstance where image transmission is usually much slower than other mediums such as USB camera because of server-robot transmission system. Fast movement and sudden magnification/reduction of a target leads to lose the target information, preventing from tracking. In the proposed method, the AR2 dynamic model is used for eliminate such risk because second-order of auto-regression can enlarge/abridge the search range of the target according to the status of the target movement. Moreover, the 2nd-order dynamic model gives the alarm of the occlusion. It is a cue of occlusion that each predictive region of both hands coincides with the same place. Based on this cue, tracking system selects occlusion process as shown in Fig.4.

3 Experimental Results

Fig.1(a) and (b) are the image of test samples (above row). We attempt to extract the slope in several ways: (1) $\Delta y/\Delta x$ (2) $\theta_1 = \tan^{-1}(\Delta y/\Delta x)$ (3) $\theta_2 = \tan_2^{-1}(\Delta y/\Delta x)$. The period of θ_1 ranges from $-\pi/2$ to $\pi/2$ and that of θ_2 ranges $-\pi$ to π . We emphasize on the gradient factor because it gives useful clues that a predicted hand belongs to which side when both predicted hands are crossed each other. Fig.1(a) and (b) represented how well the learned AR2 parameters predicted x-/y- coordinates of both hands. Specially in Fig.1(b), predicted points were well tracked even if fast movement - the rapid change at x or



Fig. 5. Both hands are crossed each other

Table 1. Tracking accuracy

side	left	right
hand(x-axis)	94.39±0.62	94.84±0.56
hand(y-axis)	93.01± 1.96	91.32± 1.75
elbow(x-axis)	99.09±0.68	99.78±0.30
elbow(y-axis)	99.77±0.33	99.57±0.61

y coordinate axis of the hand occur. On the other hand, Fig.1(c)-(e) showed that the gradient was hard to make an pre-estimation. Although various approaches such as tangent and arc tangent were taken to calculate gradients, it is revealed that the gradient was very sensitive to the difference of the x coordination, Δx between (t-1) frame and (t) frame. For example, negligible Δx much less than 1 could cause remarkable change of its gradient but such difference in an image can be considered as roughly no change. In other words, although the hand stayed little motion along the x-axis in an image changes, robot considered it big hand movement while human-beings can ignore such changes. Therefore, the effort to reduce the effect of Δx was made by transforming the gradient $\Delta y/\Delta x$ into $\theta_1 = \arctan(\Delta y/\Delta x)$, or $\theta_2 = \arctan 2(\Delta y/\Delta x)$. However, some parts still failed to get correct prediction because tangent and arc tangent is a trigonometrical function having own period. That is, prediction could not but be failed at the extreme point of its period, $\theta_1 : -\pi/2$ and $\pi/2$ and $\theta_2 : -\pi$ and π , as shown in Fig.1(c)-(e). Despite of such restrictions of the slope prediction, the gradient information can provide the key clue that a hand belongs to left or right one. To adopt benefits of slope, tracking process was decomposed into two processes(see Fig.4). One is for the uncrossed hand tracking. Here, the slope information is kept in until the next frame. This process used x- and y- coordinates of both hands and confirmed the tracking result. Another handles the hand occlusion. That is, if the occlusion is detected by the AR2 model, then the previous slope for each hand is prepared for finding the correct hand position.

For the bimanual tracking, it is hard to figure out whether both hands are crossed each other as well as which hand is a left or right one because both hands'properties are almost the same. Our method propose a good feature to discriminate two hands: directivity. The well-known law of inertia can tell that

a hand belongs to a right or left hand because moving object suddenly do not change its direction. The directivity can be obtained from the slope. Fig.4 shows that the slope gives a cue whether both hands are superimposed. According to this information, we can track both hands simultaneously as shown in Fig.5.

In order to measure the performance of the algorithm, 900 experiments were performed on many different hand shapes. The result of the experiments is listed in Table 1. Fig.3 shows a part of our experimental results. We performed the experiment using multimodal hand gesture database such as drawing 'O' and 'X', pointing left and right and so on. In Fig.3, the movement velocity along y-axis is higher than x-axis direction. Despite the velocity difference, our proposed algorithm adaptively found correct hand position whether its velocity is fast or slow.

Another important issue in tracking is that an algorithm can be simulated under the real time system. Wever, a robot for cheap practical use, has limited computing power, can transport a image through the internet only in 6.5 frames per a second on average without additional image processing. Furthermore, the target - a hand - was often found out of detectable range because of slow image transportation. Under this circumstance we achieved real-time tracking in 4.5 frames per a second.

4 Conclusion

Our ARKLT methods is very useful for tracking and gesture recognition. As mentioned before, the ARKLT methods consists of three points for each hand: the shoulder, elbow and hand. Since the model reflects the articulated motion of the human body which is restrained by the each limb's degree of freedom. That is, the possible region for hand movement is restricted in the elongated region of the shoulder and elbow movement. Therefore, the proposed method can devise effective prediction method, which enables to pre-detect crossing hands based on the body structure. In addition, the proposed method applies the KLT features and their regression line so that the body structure can effectively be fitted into the target. Also, the well-fitted KLT line can provide the exact point of a hand, meanwhile most tracking methods provide the broad region of the target. When it comes to practical uses such as gesture recognition, the find location of the target improves to draw accurate outcome, for example, gesture recognition.

References

- [1] C. Shan et al., "Real time hand tracking by combining particle filtering and mean shift," *IEEE International Conference on Automatic Face and Gesture Recognition*, 2004.
- [2] M. Kolsch and M. Turk, "Real time hand tracking by combining particle filtering and mean shift," *IEEE International Conference on Automatic Face and Gesture Recognition*, 2004.

- [3] H. Fei and I. Reid, "Probabilistic tracking and recognition of non-rigid hand motion," *IEEE International Workshop on Analysis and Modeling of Faces and Gestures*, 2003.
- [4] T. Ishihara and N. Otsu, "Gesture recognition using auto-regressive coefficients of higher-order local auto-correlation features," *Proceedings of IEEE International Conference on Automatic Face and Gesture Recognition*, 2004.
- [5] A. Franc¸ois, "Real-time multi-resolution blob tracking," *IRIS Technical Report*, 2004.
- [6] A. Shamaie and A. Sutherland, "A dynamic model for real-time tracking of hands in bimanual movements," *Gesture Workshop*, 2003.
- [7] S. J. McKenna G. McAllister and I. W. Ricketts, "Hand tracking for behavior understanding," *Image and Vision Computing*, vol. 20, pp. 827–840, 2002.
- [8] A. Blake and M. Isard, , " *Active Contours*, 2000.
- [9] J. Shi and C. Tomasi, "Good feature to track," *Proc. IEEE Conference on Computer Vision and Pattern Recognition*, 1994.

On a Feature Extraction by LMCUH Algorithm for a Ubiquitous Computing

Jin Ok Kim¹, Jun Yeong Jang², and Chin Hyun Chung²

¹Faculty of Multimedia, Daegu Haany University,
290, Yugok-dong, Gyeongsan-si, Gyeongsangbuk-do, 712-715, Korea
bit@dhu.ac.kr

²Department of Information and Control Engineering, Kwangwoon University,
447-1, Wolgye-dong, Nowon-gu, Seoul, 139-701, Korea
chung@kw.ac.kr

Abstract. This paper proposes an algorithm to detect human faces under various environments. In the first step, information on three color spaces of various features is used to determine histogram of color in the first frame of an image. The histogram obtained by interpolation after combining three color of the image is used as an input of LMCUH network. In the second step, the neural network of Levenberg - Marquadt training algorithm minimizes the error. Next, we find the face in test image by using the trained sets. This method is especially suited for various scales, rotations, lighting levels, or occlusions of the target image. Experimental results show that two - dimensional images of a face can be effectively implemented by using artificial neural network training under various environments. Thus, we can detect the face effectively and this can inevitably lead to the Ubiquitous Computing Environment.

1 Introduction

Face detection is an important and fundamental problem in computer vision [1]. More friendly and effective methods regarding human activity are in constant development to free users from manual interaction [2]. Gesture recognition, robot interaction, multimedia, face detection and recognition, hand detection, teleconference and many other applications can be based on skin detection to restrict the complexity of further processing [3]. Size, quality and cost of image acquisition are also very important. Because, the rapid growing needs for such systems and commercial applications are now available [2, 4]. Among this, the purpose of skin segmentation is for better interaction of human and computer. And many methods have been studied for better effectiveness. The one among them is neural network. In this paper, we present neural network based systems for detecting human faces in color images[5]. The problems of object detection and object recognition are closely related. An object recognition system can be made of a set of object detectors. Similarly, an object detector can be made of an object recognition system. Object detection is the problem of determining whether or not a sub - window of an image belongs to the set of images of an object of

interest [6]. Thus, anything that increases the complexity of the decision boundary for the set of images of the object will increase the difficulty of the problem and possibly increase the number of errors the detector will make [6]. For this reason, there are specifically many situation in the problem of face detection. These situations are variation of in image plane, pose variation, lighting and texture variation etc.. Generally, there are two basic face detection techniques: content - based methods and color - based methods[5]. Most content - based methods were developed for grayscale images and are very complex and expensive computationally. Also, this methods are disadvantaged to find rotated face or partially obscured face. On the other hand, color - based methods are very efficient and the methods handle color images in a more straightforward manner than the content - based methods. This methods are calculate histograms of the color values and then develop a chroma chart to identify the probability that a particular range of pixel values represent human flesh[5]. Color histograms are the global distribution of colors, but do not tell how the colors are arranged to form shapes and features[5]. However, this methods have several disadvantages. In particular, there are information loss due to quantization. Despite these drawbacks, this methods are very popular due to simplicity and ease of computation.

2 Skin Color Classification Models

The most popular algorithm to face localization is the use of color information. In this paper, we use a algorithm based on skin color classification in RGB, YCbCr and YIQ color models[7]. This algorithm has taken the combination of the three results to find the skin region and then from the skin region facial features have been extracted to get the face from the skin region.

2.1 The RGB Color Space

In the RGB model, each color appears in its primary spectral components of red, green, and blue. This model is based on a cartesian coordinate system. The color subspace of interest is the cube shown in Fig. 1, in which RGB values are at three corners[8]. In this model, the gray scale (points of equal RGB values) extends from black to white along the line joining these two points. The different colors in this model are points on or inside the cube, and are defined by vectors extending from the origin. And all values of R, G, and B are assumed to be in the range $[0,1]$.

2.2 The YCbCr Color Space

YCbCr color space has been defined in response to increasing demands for digital algorithms in handling video information, and has since become a widely used model in a digital video[7]. In this format, luminance information is stored as a single component (Y), and chrominance information is stored as two color - difference components (Cb and Cr). Cb represents the difference between the

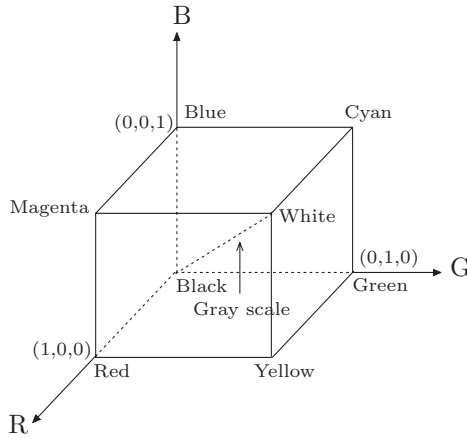


Fig. 1. Schematic of the RGB color cube

blue component and a reference value. C_r represents the difference between the red component and a reference value[9]. The transformation from the standard RGB space to the YcbCr space is given by the equations below:

$$\begin{aligned}
 Y &= 0.299R + 0.587G + 0.114B \\
 Cb &= -0.16874R - 0.33126G + 0.5B \\
 Cr &= 0.5R - 0.41869G - 0.08131B
 \end{aligned}
 \tag{1}$$

2.3 The YIQ Color Space

This model was designed to separate chrominance from luminance. This was a requirement in the early days of color television when black and white sets still were expected to pick up and display what were originally color pictures. The Y - channel contains luminance information (sufficient for black and white television sets) while the I and Q channels (in - phase and in - quadrature) carried the color information. A color television set would take these three channels, Y, I, and Q, and map the information back to R, G, and B levels for display on a screen. The transformation from the standard RGB space to the YIQ space is given by the equations below:

$$\begin{aligned}
 Y &= 0.299R + 0.587G + 0.114B \\
 I &= 0.596R - 0.275G - 0.321B \\
 Q &= 0.212R - 0.523G + 0.311B
 \end{aligned}
 \tag{2}$$

3 A Feature of Skin Color

Skin color has been long used for recognition and segmentation[10] and recently has been successfully used face locating and tracking[11, 12, 13, 14]. However,

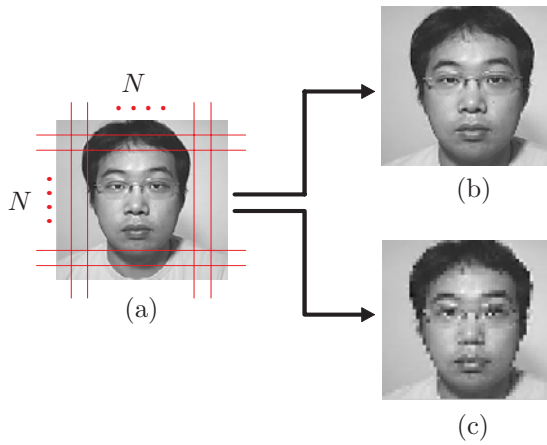


Fig. 2. (a) Y element of converting YCbCr colors from original color image. (b) When $N = 100$ grid points, interpolated image. (c) When $N = 50$ grid points, interpolated image.

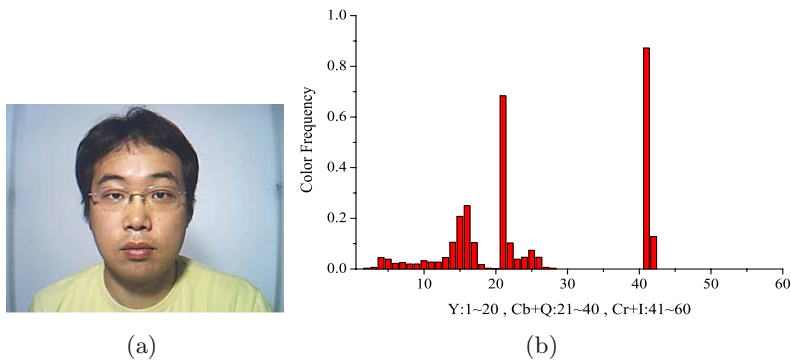


Fig. 3. (a) Original color image. (b) Histogram of combined color models.

color is not a physical phenomenon and is related to the spectral characteristics of electro - magnetic radiation in the visible wavelengths striking the retina[15]. Using skin color of human faces has some problems. Priority, the color representation of a face obtained by a camera is influenced by many factors such as ambient light, object movement, etc.[16]. Also, different cameras produce significantly different color values even for the same person under the same lighting condition[16]. In this paper, this drawbacks are complemented by using interpolation and histograms of the colors (RGB, YCbCr, YIQ).

3.1 Nearest Neighbor Interpolation

Interpolation (sometimes called resampling) is an imaging method to increase (or decrease) the number of pixels in a digital image. Interpolation is used to produce

a larger image than the sensor captured or to create digital zoom. We uses the nearest neighbor interpolation for zooming. Nearest neighbor interpolation is the simplest method and basically makes the pixels bigger. The Zooming requires two steps: the creation of new pixel locations, and the assignment of color levels to those new locations[8]. Conceptually, one of the easiest ways to visualize zooming is laying an imaginary zooming grid over the original image. The spacing in the grid would be less than one pixel because we are fitting it over a smaller image. In order to perform color level assignment for any point in the overlay, we look for the closest pixel in the original image and assign its color level to the new pixel in the grid. When we are done with all points in the overlay grid, we simply expand it to the original specified size to obtain the zoomed image. This method of color level assignment is called nearest neighbor interpolation. For example, if you enlarge 200%, one pixel will be enlarged to a 2×2 area of 4 pixels with the same color as the original pixel.

We tried to feed the color image itself into the network as our input vector. However, even a small color image contains thousands of pixels and it would be unreasonable to feed such a large input vector into the network. So we interpolated the image by selecting N evenly - spaced grid points on the image.

3.2 Histograms of Combined Color Models

On the basis of experiment, we could more well show face region in image with Cr component of YCbCr color model and the I component of YIQ color model. Therefore, we can combine Cr and I component and union Cb and Q component since YCbCr and YIQ components are transformed by interpolated RGB components. And we can represent histogram by using the this information and common Y component of YCbCr and YIQ. These data are used to input of neural network by this algorithm. We classified the combined color values of each pixel in the image in relative frequency histograms, where each component of the combined color space was represented by optional N bins.

4 Levenberg - Marquadt Algorithm of Color Union Histogram (LMCUH)

4.1 Neural Network

Our face verification method is based on multi layer perceptrons (MLP). The input of the MLP is a feature vector corresponding to the face image with its skin color. The output of the MLP is either 1 (if the input corresponds to a client) or -1 (if the input corresponds to an impostor)[17]. The MLP is trained using both client images and impostor images, often taken to be the images corresponding to other available clients.

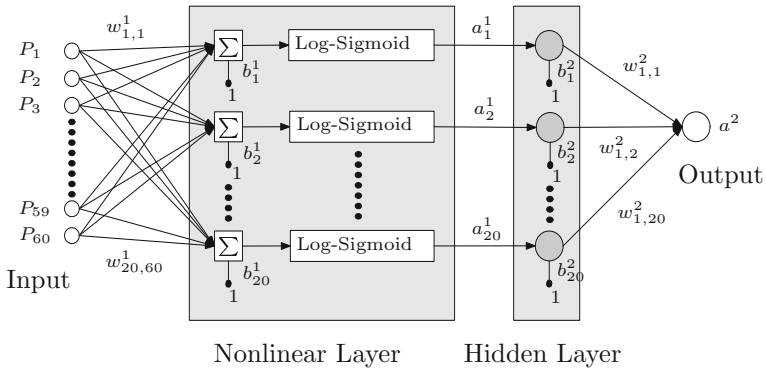


Fig. 4. A graphical representation of the computational structure of an MLP network with one hidden layer of nonlinear neurons

4.2 Steepest Descent Method

When we update our guess of the optimum (minimum) point using Eq. 3, we would like to have the function decrease at each iteration. In other words,

$$F(\mathbf{x}_{k+1}) < F(\mathbf{x}_k) \tag{3}$$

$$\mathbf{x}_{k+1} = \mathbf{x}_k + \alpha_k \mathbf{g}_k \tag{4}$$

$$F(\mathbf{x}_{k+1}) = F(\mathbf{x}_k + \Delta \mathbf{x}_k) \approx F(\mathbf{x}_k) + \mathbf{g}_k^T \Delta \mathbf{x}_k \tag{5}$$

Equation 4 is $\mathbf{g}_k^T \Delta \mathbf{x}_k = \alpha_k \mathbf{g}_k^T \mathbf{p}_k < 0$ by Eq. 3. And we will select an α_k that is small, but greater than zero. This implies $\mathbf{g}_k^T \mathbf{p}_k < 0$. Any vector \mathbf{p}_k that satisfies this equation is called a descent direction. If the inner product between the gradient and the direction vector is orthogonal, these vectors are $\mathbf{p}_k = -\mathbf{g}_k$. Using this in the iteration of Eq. 4 produces the method of steepest descent:

$$\mathbf{x}_{k+1} = \mathbf{x}_k - \alpha_k \mathbf{g}_k \tag{6}$$

4.3 Newton's Method

The derivation of the steepest descent algorithm was based on the first - order Taylor series expansion. When we update our guess of the optimum (minimum) point[18], use the steepest descent. Newton's method is based on the second - order Taylor series:

$$F(\mathbf{x}_{k+1}) = F(\mathbf{x}_k + \Delta \mathbf{x}_k) \approx F(\mathbf{x}_k) + \mathbf{g}_k^T \Delta \mathbf{x}_k + \frac{1}{2} \Delta \mathbf{g}_k^T \mathbf{A}_k \Delta \mathbf{x}_k \tag{7}$$

Newton’s method is then defined:

$$\mathbf{x}_{k+1} = \mathbf{x}_k - \mathbf{A}_k^{-1} \mathbf{g}_k \tag{8}$$

where \mathbf{x}_{k+1} is new input, \mathbf{x}_k is old input, \mathbf{A}_k is $\nabla^2 F(\mathbf{x})$ (Hessian matrices). And \mathbf{g}_k is $\nabla F(\mathbf{x})$ (gradient). This method finds the minimum of a quadratic function. Because Newton’s method is designed to approximate a function as quadratic and then locate the stationary point of the quadratic approximation (stable state)[18]. However, if the function $F(\mathbf{x})$ is not quadratic, then Newton’s method will not generally converge in one step. At this time, Newton’s method converges quickly in many applications because analytic functions can be accurately approximated by quadratic functions in a small neighborhood of a strong minimum.

4.4 Levenberg - Marquadt Algorithm

The Levenberg - Marquadt algorithm is a non - linear regression algorithm that uses least squares minimization to obtain parameter estimates of a nonlinear function. The Levenberg - Marquadt algorithm is a variation of Newton’s method that was designed for minimizing functions that are sums of squares of other nonlinear functions[18]. This is very well suited where the performance index is the mean squared error. The mean squared error is performed in environment of multilayer network training. If each target occurs with equal probability, the mean squared error is proportional to the sum of squared errors over the targets (Q) in the training set[18].

$$F(\mathbf{x}) = \sum_{q=1}^Q (\mathbf{t}_q - \mathbf{a}_q)^T (\mathbf{t}_q - \mathbf{a}_q) = \sum_{q=1}^Q \mathbf{e}_q^T \mathbf{e}_q = \sum_{q=1}^Q \sum_{j=1}^{S^M} (\mathbf{e}_{j,q})^2 = \sum_{i=1}^N (\mathbf{v}_i)^2 \tag{9}$$

where $\mathbf{e}_{j,q}$ is the j th element of the error for the q th input/target pair. $N(Q \times S^M)$ is the parameter vector about weight and bias. The key step of this algorithm is the Jacobian Calculation. If we then substitute Jacobian matrix ($\mathbf{J}(\mathbf{x})$) into Eq. 9. The gradient can be written in matrix form:

$$\nabla F(\mathbf{x}) = \mathbf{g}_k = 2\mathbf{J}^T(\mathbf{x})\mathbf{v}(\mathbf{x}) \tag{10}$$

Also, the Hessian matrix can be expressed in matrix form:

$$\nabla^2 F(\mathbf{x}) = \mathbf{A}_k = 2\mathbf{J}^T(\mathbf{x})\mathbf{J}(\mathbf{x}) + 2\mathbf{S}(\mathbf{x}) \tag{11}$$

where $\mathbf{S}(\mathbf{x}) = \sum_{i=1}^N v_i(\mathbf{x})\nabla^2 v_i(\mathbf{x})$. If we assume that $\mathbf{S}(\mathbf{x})$ is small, we can approximate the Hessian matrix as

$$\nabla^2 F(\mathbf{x}) = \mathbf{A}_k \cong 2\mathbf{J}^T(\mathbf{x})\mathbf{J}(\mathbf{x}) \tag{12}$$

As mentioned above, the iterations of the Levenberg - Marquadt algorithm of Color Union Histogram (LMCUH) can be summarized as follows:

Algorithm 1. LMCUH Algorithm

Input: p (vector values of combined color image)

Output: a (identified faces)

LMCUH_ALGORITHM(p)

- (1) Set histogram data by interpolation and combination of the color models.
 - (2) **Weight initialization:** Set random weights by input and output neuron, w .
 - (3) Present all inputs to the network and compute the corresponding network outputs and the errors $\mathbf{e}_q = \mathbf{t}_q - \mathbf{a}_q^M$. Compute the sum of squared errors over all inputs, $F(\mathbf{x})$, using Eq. 9.
 - (4) Compute the Jacobian matrix. Calculate the sensitivities with the recurrence relations .
 - (5) Solve to obtain $\Delta \mathbf{x}_k$.
 - (6) **Weight training:** Recompute the sum of squared errors using $\mathbf{x}_k + \Delta x_k$.
 - (7) **if** $\mathbf{x}_{k+1} < \mathbf{e}_q$
 - (8) Divide μ by ϑ
 - (9) **return** Step 3.
 - (10) **else**
 - (11) Multiply μ by ϑ go to Step 6 and repeat the process.
-

5 Experimental Result

We experimented with the color images of 400×400 size for training and the the color images of various size. We make use of the face images and the non - face images of 20 units (image index) respectively as the training images. As we mentioned in the previous chapters, vector values of combined color image

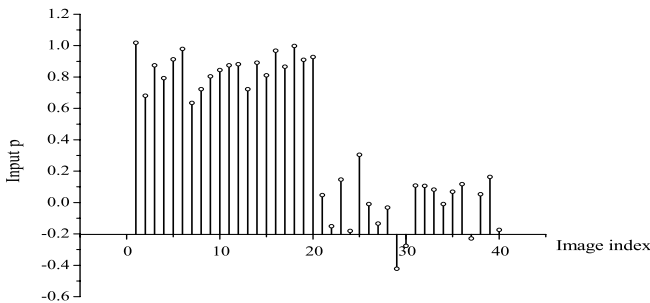


Fig. 5. Network outputs for training set after 200 iterations of LMCUH algorithm

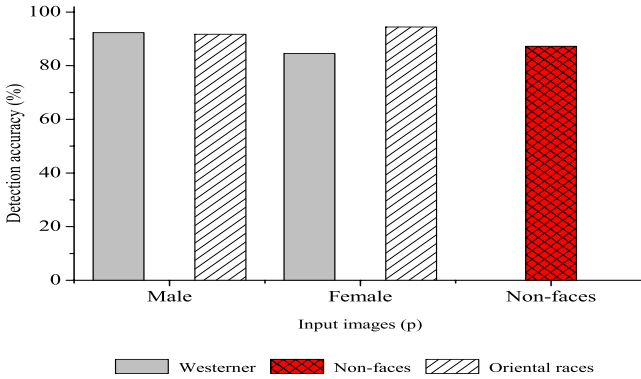


Fig. 6. Detection accuracy by using LMCUH

can acquire the identified faces by using LMCUH algorithm. In experiment, we use that two hundred iterations of the LMCUH algorithm scheme took approximately five minute on a window platform. In fig.5, image index is the face images from 1 to 20 and the non - face images from 21 to 40. The face images are used eight westerner (male: 6, female: 2) and twelve oriental races (male: 6, female: 6). And the non - face Input p is vector values of input image. The images containing faces will result in outputs $p > 0.5$ while the non - face images will result in outputs $p < 0.5$.

For testing, we use the other input images of 50 westerner, oriental race respectively. The westerner and the oriental race images are classified as 50 female and male each. In addition, we make an experiment on the input images of 50 non - faces.

6 Conclusion

By the experiment, histogram approach of the three color models was the most successful in correctly identifying human faces. We made the best use of the combination information of the color models. It could conform that this method can use more effective than the information of one color model. And the iteration value of LMCUH training is very important. However, this could be a week point of the neural network. But, ideal weights can use very effectively for the testing of various images by these methods. The testing time also appears to be a remarkable fruit. Thus, we can detect the face effectively and this can inevitably lead to the Ubiquitous Computing Environment.

Acknowledgements. The present Research has been conducted by the Research Grant of Kwangwoon University in 2006.

References

1. Yang, M.H., Kriegman, D.J., Ahuja, N.: Detecting faces in images: a survey. *IEEE Transactions on Pattern Analysis and Machine Intelligence* **24** (2002) 34–58
2. Vezhnevets, V., Sazonov, V., Andreeva, A.: A survey on pixel-based skin color detection techniques. *GraphiCon, Moscow, Russia* (2003)
3. Yow, K.C., Cipolla, R.: Feature-based human face detection. *Image and Vision computing* **15** (1997) 713–735
4. Hsu, R.L., Mottaleb, M.A.: Face detection in color images. *IEEE Pattern Analysis and Machine Intelligence* **24** (2002) 696–706
5. Wittman, T.: *Face Detection and Neural Networks*. report, University of Minnesota (2001)
6. Rowley, H.A.: *Neural Network-Based Face Detection*. Phd thesis, MIT AI Lab (1999)
7. Singh, S.K., Chauhan, D.S., Vatsa, M., Singh, R.: A robust skin color based face detection algorithm. *Tamkang Journal of Science and Engineering* **6** (2003) 227–234
8. Conazlez, R.C., Woods, R.E.: *Digital Image Processing*. Second edn. Prentice Hall, Inc., New Jersey (2002)
9. *Mathworks: Image Processing Toolbox Users' Guide*. The MathWorks, Inc., Natick, MA (2002)
10. Swain, M.J., Ballard, D.H.: Color indexing. *International Journal of Computer Vision* **7** (1991) 11–32
11. Hunke, M., Waibel, A.: Face locating and tracking for human-computer interaction. *Proc. Twenty-Eight Asilomar Conference on Signals, Systems Computers, CA, USA* (1994)
12. Chang, T.C., Huang, T.S., Novak, C.: Facial feature extraction from color images. *Proc. the 12th IAPR International Conference on Pattern & Recognition* **2** (1994) 39–43
13. Yang, J., Waibel, A.: A real-time face tracker. *Proceedings of the Third IEEE Workshop on Applications of Computer Vision (Sarasota, Florida)* (1996) 142–147
14. Yang, J., Waibel, A.: Tracking human faces in real-time. Technical report cmu-cs-95-210, Carnegie Mellon University (1995)
15. Wyszecki, G., Stiles, W.S.: *Color Science: Concepts and Methods, Quantitative Data and Formulae*. Second edn. John Wiley & Sons, New York (1982)
16. Yang, J., Lu, W., Waibel, A.: Skin-color modeling and adaptation. *Proceedings of Asian Conference on Computer Vision (ACCV'98)* **2** (1998) 687–694
17. Marcel, S., Bengio, S.: Improving face verification using skin color information. Technical Report 44, Dalle Molle Institute for Perceptual Artificial Intelligence - IDIAP (2001)
18. Hagan, M.T., Demuth, H.B., Beale, M.: *Neural Network Design*. PWS publishing company, Voston, MA 02116 (1995)

Autoregressive Models of Speech Signal Variability in the Speech Commands Statistical Distinction

Victor Krasheninnikov¹, Andrey Armer¹,
Natalia Krasheninnikova²,
Valery Derevyankin³, Victor Kozhevnikov³, and Nikolay Makarov³

¹ Ulyanovsk State Technical University, 32 Severny Venets St.,
432027 Ulyanovsk, Russia

a.armer@ulstu.ru

² Ulyanovsk State University, 42 Leo Tolstoy St., 432970 Ulyanovsk, Russia

kiv@simcom.ru

³ Ulyanovsk Instrument Manufacturing Design Bureau,
10a Krymov St., 432001 Ulyanovsk, Russia

ukbplkv@mv.ru

Abstract. In the task of speech commands (SC) statistical distinction the SC variability models application considerably simplifies both the likelihood ratio construction procedure, and the likelihood ratio expression itself, reducing it to well-known criterion χ -square. Computer modeling allows us to use SC variability models at SC distinction decision rule synthesis.

1 Introduction

Many tasks of pattern recognition are based on theses of decision theory. According to the decision theory, the task of speech commands (SC) recognition from a limited dictionary can be considered as a multi-alternative decision where it is necessary to choose one of $m + 1$ alternatives. Besides the decision that a recognizing command belongs to one of the command classes from the dictionary corresponds to m alternatives, and the decision that it belongs to neither of these classes corresponds to $(m + 1)$ -th alternative. Pronouncing varieties of each command from the dictionary can be considered as classes of commands (at announcer dependent recognition every SC is pronounced by the same announcer). Formally the task whether a recognizing SC belongs to a certain class is a two-alternative decision on, whether a recognizing command is a pronunciation variant of a certain SC from the dictionary or not. When standard SC from the dictionary are set as readout of sound pressure upon a microphone membrane, and classes of their pronunciation variants are not determined, decision on belonging of a recognizing SC to the class of standard SC variants is accepted in partial a priori uncertainty conditions. In this case it is impossible to use the Bayesian classical method of decision rule synthesis. In such a situation it is necessary to use one of the statistical decisions synthesis methods in a

priori uncertainty conditions. However under the circumstances the decision rule synthesis procedure can demand significant computing expense. Besides a great number of pronunciation variants of recognizing and standard SC are necessary in order to make a decision. This paper suggests using computer modeling of SC pronunciation variants, which allow essential simplification of decision rules synthesis in the task of SC recognition. Besides the given approach makes it possible to use a significantly smaller number of actual SC pronunciations at decision-making.

2 Decision Rule Synthesis at SC Distinction

In a most common case if a priori information concerning statistical description of recognizing SC is absent the task of definition of a recognizing command belonging to a class of some standard command pronunciation is represented as a task of two objects X and Y distinction (a standard SC and a recognizing SC) on observable set of their attributes $z = \{x, y\}$, where x is an observable set of object X attributes, y - of object Y attributes. Objects X and Y can be either identical, thus condition parameter $\lambda = 1$, or X and Y are somewhat different then the condition parameter $\lambda = 2$. Taking into consideration observation data z it is necessary to find out, what condition takes place, i.e. to accept one of two possible decisions: u_1 - objects are identical, u_2 - objects differ. Thus it is considered, that a priori probabilities of conditions $p(\lambda = 1) = P_1$ and $p(\lambda = 2) = P_2 = 1 - P_1$ and distributions of attributes z probabilities (likelihood function) are completely unknown. In conditions of a priori uncertainty the given task can be solved as it contains some a priori information that statistical properties of sets x and y can be either different or identical [1].

Let all observable attributes of objects X and Y have only discrete values. Then it is possible to number these values using common numbering from 1 up to N and without loss of generality to replace all set of attributes by one-dimensional variable with possible integer values from 1 up to N . The entire statistical description of this set would consist in the task of probability distribution of these values, i.e. probabilities $p_i, i = 1, \dots, N$. Moreover if objects X and Y differ ($\lambda = 2$) these probabilities for sets x and y will have different values:

$$p_{1i} \geq 0; p_{2i} \geq 0; \sum_{i=1}^N p_{1i} = 1; \sum_{i=1}^N p_{2i} = 1. \quad (1)$$

If objects are identical, these values are also identical:

$$p_{1i} = p_{2i} = p_i \geq 0; \sum_{i=1}^N p_i = 1. \quad (2)$$

Let observation data sets x and y of the first and second objects be represented as n_1 and n_2 multiple recurrences of these objects attributes observation. Let us

designate through n_{1i} and n_{2i} the number of times when for the first and the second object correspondingly i -th value of attributes was observed. Thus

$$\sum_{i=1}^N n_{1i} = n_1; \sum_{i=1}^N n_{2i} = n_2. \tag{3}$$

The totalities of observation data x and y can be described by totalities of numbers $\{n_{1i}\}$ and $\{n_{2i}\}$ values, i.e.

$$x = \{n_{11}, n_{12}, \dots, n_{1N}\}; y = \{n_{21}, n_{22}, \dots, n_{2N}\}; z = \{x, y\}. \tag{4}$$

If the probabilities p_{1i}, p_{2i} are known, the totalities $\{n_{1i}\}$ and $\{n_{2i}\}$ are described by multinomial distributions of the following kind:

$$P(z|\lambda = 2) = n_1!n_2! \prod_{i=1}^N \frac{p_{1i}^{n_{1i}}}{n_{1i}!} \prod_{i=1}^N \frac{p_{2i}^{n_{2i}}}{n_{2i}!},$$

$$P(z|\lambda = 1) = n_1!n_2! \prod_{i=1}^N \frac{p_i^{n_{1i}}}{n_{1i}!} \prod_{i=1}^N \frac{p_i^{n_{2i}}}{n_{2i}!}. \tag{5}$$

At the least a priori uncertainty case the probabilities $p_i, p_{1i}, p_{2i}, i = 1, \dots, N$ and also a priori probabilities of conditions P_1 and P_2 are unknown, and in order to solve the problem it is necessary to find the least preferable probabilities measures determined on the set of these unknown values. The totality of these probability measures includes: $\mu_0(P_1, P_2)$ - for a priori probability conditions which is determined on value set P_1 and P_2 provided that $P_1 + P_2 = 1$; $\mu_1(p_1, p_2, \dots, p_N)$ for probabilities of attribute values if objects are identical (this measure is determined on the value set p_1, \dots, p_N limited by conditions (2)); $\mu_2(p_{11}, p_{12}, \dots, p_{1N}, p_{21}, p_{22}, \dots, p_{2N})$ for probabilities of attribute values if objects differ (this measure is determined on the value set p_{11}, \dots, p_{2N} limited by conditions (1)). In order to find all indicated measures the search of least preferable ones is used. According to [1] likelihood ratio for objects X and Y distinction using loss function is

$$g(u, \lambda) = g(u = j, \lambda = i) = 1 - \delta_{ij}, \tag{6}$$

where δ_{ji} is Kroneker symbol, and j can be 1 or 2, taking into account

$$P_1 = P_2 = \frac{1}{2} \tag{7}$$

will be

$$A_{12}(z) = \frac{P_1(z)}{P_2(z)} = \frac{(n_1 + N - 1)!(n_2 + N - 1)!}{(N - 1)!(n_1 + n_2 + N - 1)!} \prod_{i=1}^N \frac{(n_{1i} + n_{2i})!}{n_{1i}!n_{2i}!}. \tag{8}$$

Comparing (8) to threshold C it gives a final form of a decision-making rule on objects X and Y identity. Changing loss function or setting a priori probability conditions P_1 and P_2 which are different from (7), it is only the size

of a threshold C in $A_{12}(z) \geq C$ decision-making u_1 rule that changes. The $(n_{11}, \dots, n_{1N}, n_{21}, \dots, n_{2N})$ sufficient statistics kind from (8) thus remains invariable. Thus, the decision rule will have the following structure:

$$u(z) = \begin{cases} u_1 & \text{at } A_{12}(z) \geq C, \\ u_2 & \text{at } A_{12}(z) < C. \end{cases} \quad (9)$$

3 SS Variability Models Used for Decision Rule Synthesis Simplification

The main difficulty in decision-making (9) rule finding is obtaining of n_1 and n_2 multiple recurrences of distinguishing objects attributes observation. Formally it means the necessity of realizing objects experience recurrence, or multiple recurrence of object parameter randomization. In particular, finding a decision-making rule (9) on belonging of a recognizing command to a class of pronouncing variants of a certain SC from the dictionary it is necessary to have its n_1 pronunciations and n_2 pronunciations of a standard SC from the dictionary. If it is possible to keep many variants of each SC pronunciation in the library, though it is connected with some difficulties concerning pronunciation obtaining and also with necessity to increase resources for its storage, then multiple SC recurrence at recognition is unacceptable. The possibility to obtain n -multiple recurrences of each SC pronunciation proceeding from smaller number of actual SC pronunciation by some announcer will essentially simplify a decision-making task on recognizing SC belonging to some class of pronunciation variants of some standard SC from the dictionary. In such a case the application of SS mathematical models [2, 3, 4, 5, 6, 7, 8] is likely to be useful. However many SS models do not take into account speech change which are characteristic for different pronunciations of one and the same speech unit. In order to obtain n_1 and n_2 multiple recurrences of SC observation it is necessary to take into account SC variability at modeling. The use of SS variability models considered in [9, 10, 11] gives such an opportunity. As the given SS variability models make it possible to obtain a great number of SS pronunciation variants from one actual pronunciation, they considerably simplify finding of decision-making rule (9) on recognizing command belonging to a certain SC class. Modern computers make possible the use of variability models at SC recognition. Thus together with simplification of decision-making procedure computers in this case relieve a person of necessity repeatedly to pronounce SC in order to increase SC recognizing commands.

Let's consider, for example, a model which allows us to obtain initial SC pronouncing variants along a trajectory on the image generated by two-dimensional Habibi model [12]:

$$x_{11} = \sigma\xi_{11}, \quad x_{1j} = \rho x_{1,j-1} + \sigma\sqrt{1-\rho^2}\xi_{1j}, \quad (10)$$

$$x_{i1} = r x_{i-1,1} + \sigma\sqrt{1-r^2}\xi_{i1}, \quad (11)$$

$$x_{ij} = r x_{i-1,j} + \rho x_{i,j-1} - r\rho x_{i-1,j-1} + \sigma\sqrt{(1-r^2)(1-\rho^2)}\xi_{ij}, \quad (12)$$

where r is a correlation coefficient between neighboring rows; ρ is a correlation coefficient between neighboring elements within a row; σ^2 is the variance on an outcome process; ξ_{ij} are independent Gaussian standard random variables. Process x_{ij} obtained with (10)-(12) is set on a rectangular lattice the size of which is $M \times K (i = 1..M, j = 1..K)$. Model (10)-(12) produces two-dimensional stationary Markov random field (image). In order to obtain SC command-variations let us consider SC pronounced by an announcer and consisting of M discrete readings as an initial SC. Let it be the first lattice row in the model (10)-(12). Each next row is formed with the help of autoregression (11) making an image. Then SC variants are simulated in the following way [11]. Let the trajectory coordinate g , which determines the image column number, be generated by an autoregression process

$$g_1 = 1, \quad g_n = g_{n-1} + \kappa \zeta_n \quad (n = 1..W), \tag{13}$$

which operates time distortions of modeled commands-variations, and coordinate h which determines row number producing by the process

$$h_1 = 1, \quad h_n = h_{n-1} + \gamma \psi_n \quad (n = 1..W), \tag{14}$$

which operates intensity of common command-variation distortions (where ζ_m and ψ_n are independent random variables, κ and γ are constant coefficients). Obtained according to [11] W elements \hat{x}_{gh}^n (Fig. 1), will be determined as:

$$\begin{aligned} \hat{x}_{gh}^n = & \frac{(c - dr)[(a - b\rho)x_{[g]-1,[h]-1} + (b - a\rho)x_{[g],[h]-1}]}{(1 - r^2)(1 - \rho^2)} + \\ & + \frac{(cr - d)[(b\rho - a)x_{[g]-1,[h]} + (a\rho - b)x_{[g],[h]}]}{(1 - r^2)(1 - \rho^2)}, \\ a = r^{\langle h \rangle}, & b = r^{\langle 1-h \rangle}, c = \rho^{\langle g \rangle}, d = \rho^{\langle 1-g \rangle}, n = 1..W, \end{aligned} \tag{15}$$

where $\langle \bullet \rangle$ is fractional part of a number and $\langle \bullet \rangle$ is its integral part. The signal obtained with the help of (15) along the trajectory (13)-(14) on the image generated by the initial SC produces variant of the very SC. Using this model let us create at first a set of variants of one SC pronunciation, let it be a recognizing SC, then let us create a set of pronunciation of some standard SC. Using SC actual pronouncing readouts as the first line of two-dimensional Habibi model let us create with the help of (10)-(15) $n_1 - 1$ variants of recognizing SC and $n_2 - 1$ variants of standard SC. The obtained pronunciations together with the initial ones form n_1 - and n_2 - multiple recurrences of recognizing SC attribute observations which can be used for statistical decision-making rule (9) construction. It is necessary to note that a great number of SC variants can be obtained with the help of the model (10)-(15). It makes possible to increase values n_1 and n_2 , which simplify construction of decision-making rule (9). If values n_{1i}, n_{2i} are large enough it is possible to simplify likelihood ratio expression (8). Supposing that possible distinctions between recognizing commands may be not so significant (the most difficult for the correct decision case), it is possible to present

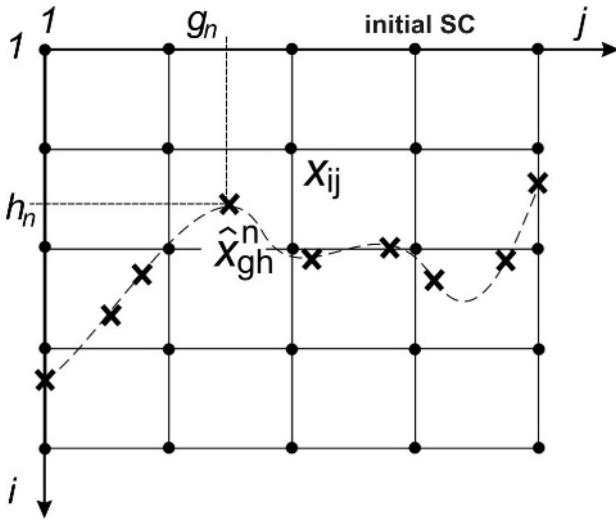


Fig. 1. The scheme of commands-variations modeling along the trajectory on the image $A_{12}(z)$ as a monotonous function of the following sufficient statistics [1]:

$$A(z) = \sum_{i=1}^N \left[\frac{\left(\frac{n_{1i}}{n_1} - \frac{n_{2i}}{n_2} \right)^2}{\left(\frac{n_{1i} + n_{2i}}{n_1 + n_2} \right)} \right], \tag{16}$$

the comparison of which to a threshold gives a required decision rule. Value $A(z)$ coincides with value χ^2 for a well-known criterion χ -square which is based on average quadratic distinction between two selective distributions. In this case (16) becomes an asymptotic approximation of decision (8) if n_{1i}, n_{2i} are large.

4 Definition of SC Belonging to a Standard Class

Let us consider four SC pronunciations: two pronunciations of word "distinction", one pronunciation of "decision" and one pronunciation of "recognition". All words are pronounced by the same announcer. Let's take one of pronunciations of the word "distinction" a recognizing SC, and let other pronunciations form classes of standard SC with the help of model (10)-(15). Using (16) let us define the class to which recognizing SC "distinction" belongs. Let's consider three cases: when classes of SC pronunciations form 5, 10 and 20 pronunciation variants, i.e. $n_1 = n_2 = 5, n_1 = n_2 = 10$ and $n_1 = n_2 = 20$. The frequency charts of SC readouts from a certain class are represented on Fig. 2. Frequencies are tabulated in 30 categories and presented in the form of statistical rows. Fig. 2 (a), (b), (c) represent statistical rows when $n_1 = n_2 = 5$. On Fig. 2 (b) you can see that row charts constructed while comparing classes of SC "distinction" and "distinction" are considerably different, and on Fig. 2 (c) you can see that row charts constructed while comparing classes of SC "distinction" and "recognition" are similar. It means that class definition for SC "distinction" was made

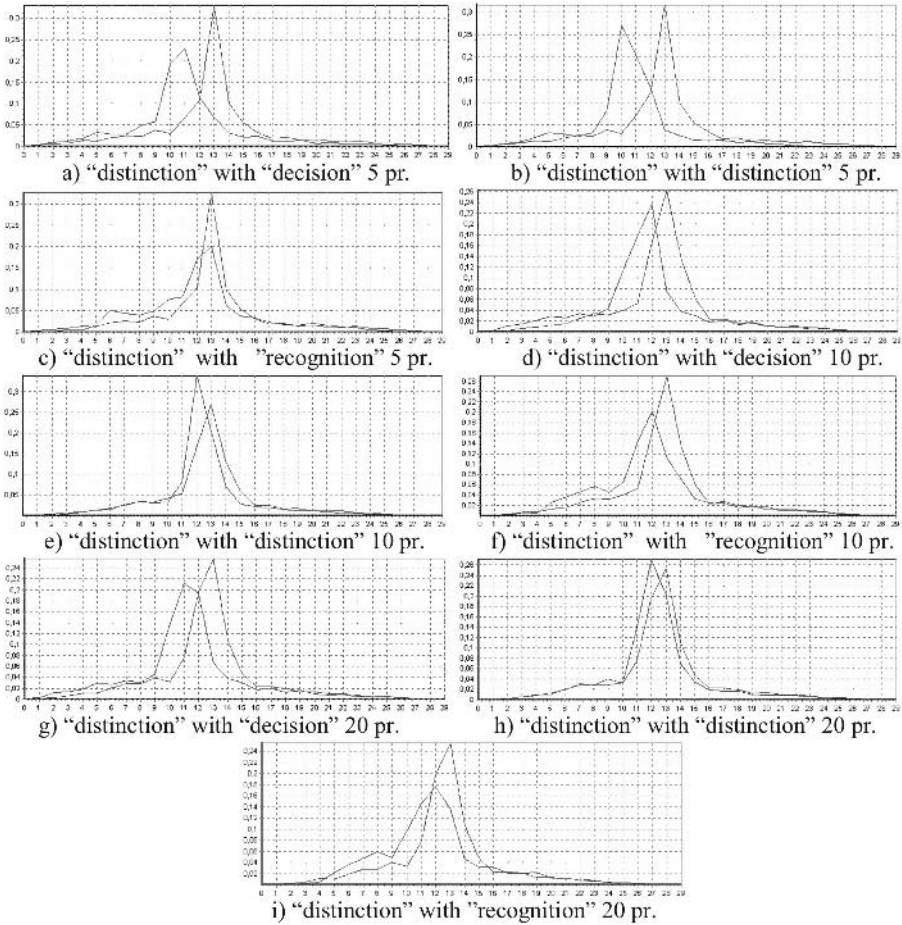


Fig. 2. Statistical rows of SC classes constructed by model (10)-(15)

with a mistake. Fig. 2 (d), (e), (f) represent statistical rows when $n_1 = n_2 = 10$. Here there is no more mistake of a class definition. The most similar rows on Fig. 2 (e) are obtained while comparing SC "distinction" and "distinction". Fig. 2 (g), (h), (i) represent statistical lines when $n_1 = n_2 = 20$. Similarity of rows is more distinctly visible on Fig. 2 (h), this image is obtained while comparing SC "distinction" and "distinction" when $n_1 = n_2 = 20$. Fig. 3 represents value dependencies of likelihood ratio (16) upon number of SC recurrences in a class ($n_1 = n_2 = 5, 10, 20$). As it can be seen from Fig. 3 value (16) decreases if the number of computer modeled recurrences of SC variant observations increases, and if different classes are compared value (16) increases. On Fig 4. you can see the results of the same experiment on definition class of the words pronunciations "simplifying", "simulating" and "modeling" by criterion based on expression (16).

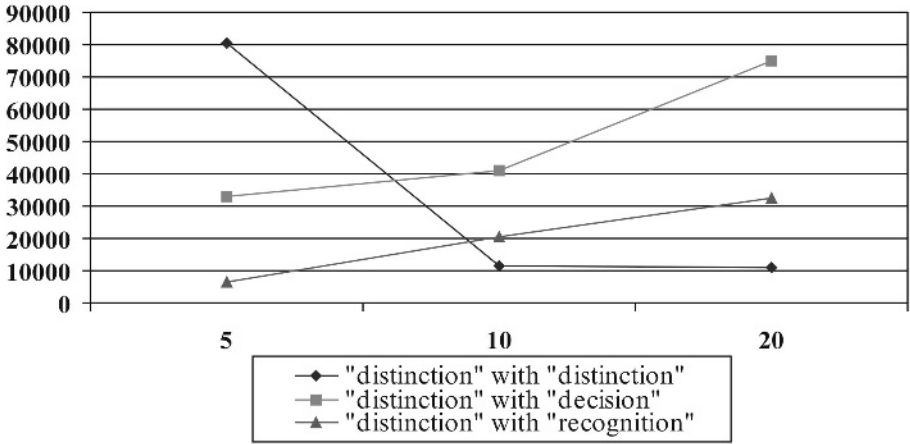


Fig. 3. The chart of likelihood ratio (16) values when $n_1 = n_2 = 5, 10, 20$

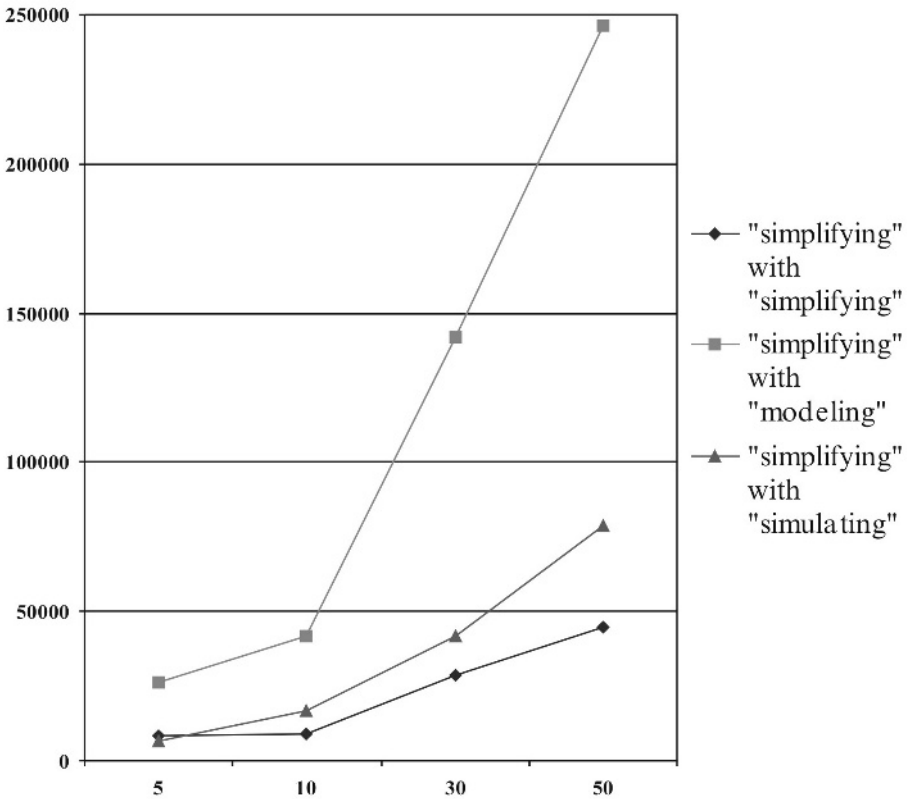


Fig. 4. The chart of likelihood ratio (16) values at $n_1 = n_2 = 5, 10, 30, 50$

The experiment results have shown that beginning with value $n_1 = n_2 = 10$ the definition mistake of SC class "simplifying" by criterion based on expression (16) disappears. If $n_1 = n_2 = 50$ the result becomes more distinct.

5 Conclusion

Thus, application of SC variability models considerably simplifies both the construction procedure of likelihood ratio (8), and the likelihood ratio (8) expression itself, reducing it to (16). Computer modelling allows us to use SC variability models at SC distinction deciding rule synthesis.

However, the considered application of SC variability models has not yet given a certain SC recognition method, but it shows a principle opportunity to simplify the procedure of statistical decision acceptance on SC belonging to some class. Probably, the application of the given models may be useful at algorithms synthesis of SC recognition based on the decision theory positions.

References

1. Repin, V.G., Tartakovskiy, G.P.: The statistical analysis at a priori uncertainty and information systems adaptation. Sovetskoe Radio, Moscow (1977) [*in Russian*]
2. Fant, G.: Acoustic Theory of Speech Production. The Hague, Mouton (1970)
3. Flanagan, J.L.: Speech Analysis, Synthesis and Perception (2nd ed.). Springer-Verlag, New York (1972)
4. Rabiner, L.R., Schafer R.W.: Digital Processing of Speech Signals. Prentice-Hall, Inc., Englewood Cliffs, N.J. (1978)
5. Chuchupal, V., Makovkin K., Gorokhovskiy K., Chichagov A.: A Study of the Acoustic Model Choice for Russian Speech Recognition. In: Proc. of Intern. Workshop "Speech and Computer" SPECOM (2002) 53–57
6. Lucke, H.: Which Stochastic Models Allow Baum-Welch Training? IEEE Trans. Signal Processing, vol. 44, No. 11 (1996) 2746–2756
7. Peinado, A., Segura, J., Rubio, A., Garcia, P., Perez, J.: Discriminative Codebook Design Using Multiple Vector Quantization in HMM-Based Speech Recognizers. IEEE Trans. Speech and Audio Processing, vol. 4, No. 2 (1996) 89–94
8. Shahshahani, B.: A Markov Random Field Approach to Bayesian Speaker Adaptation. IEEE Trans. Speech and Audio Processing, vol. 5, No. 2 (1997) 183–191
9. Krasheninnikov, V.R., Armer, A.I., Derevyankin, V.P., Kozhevnikov, V.I., Makarov, N.N.: The Speech Commands Variability Simulation. In: Proc. of Intern. Conf. on Concurrent Engineering, Lubbock, USA (2005) 387–390
10. Krasheninnikov, V.R., Armer, A.I.: Speech Command Variations Simulation at Different Pronunciations. In: Proc. of the Second IASTED International Multi-Conference on Automation control and information trchnology, Novosibirsk (2005) 155–158
11. Krasheninnikov, V.R., Armer, A.I.: Speech commands variability model. Vestnik UIGTU No. 4/2004, Ulyanovsk (2004) 44–46 [*in Russian*]
12. Habibi, A.: Two-dimensional Bayesian Estimate of Images. In: Proc. of IEEE, vol. 60 (1972) 873–883

u-Table: A Tabletop Interface for Multiple Users

Jangho Lee¹ and Jee-In Kim^{2,*}

¹ Department of Computer Science & Engineering, Konkuk University, Seoul, Korea

`jangho@konkuk.ac.kr`

² CAESIT, Konkuk University, Seoul, Korea

`jnk@konkuk.ac.kr`

Abstract. A tabletop user interface called *u-Table* is proposed in this paper. *u-Table* provides a cooperative place to share multimedia data among portable devices. We developed simple methods for device recognition and fingertip detection. Users can intuitively manipulate data and devices on *u-Table* using their fingertips. We propose new interaction methods for the tabletop interface such as a rotational window, a rotational pop-up menu, an inertial widget, and a transformable tabletop. Then, we developed utility programs for multimedia data communications and application programs. The performance of the fingertip detection algorithm was evaluated.

1 Introduction

A table is a suitable place to work or play with others. People could work on the table with their notebooks, digital cameras, camcorders, PDAs, and other mobile devices. If a tabletop can be used as a large screen and a wireless LAN can convey multimedia data among mobile devices, users can work and play together with the multimedia data more conveniently and more easily. In such a case, proper ways of interactions are required instead of traditional methods using a keyboard and a mouse.

We propose a tabletop-based user interface called *u-Table* as an interface for the cooperative workspace. The users can view multimedia data in mobile devices on the tabletop of *u-Table*. With the tabletop, users can share much larger views of the multimedia data rather than small screens of their mobile devices. They can use *u-Table* as a touch screen. The users can simultaneously use their fingertips to manipulate the interface instead of a mouse. When a user puts a mobile device on the table, a connection to LAN is established automatically without any explicit and manual configuration of devices and systems. The multimedia data of each mobile device can be transferred through the wireless LAN system. The commands of the transfer operations can be issued easily by users' fingertips on the table. Also *u-Table* has new interaction methods. A window widget on the screen can be rotated to the front side of each user so that users can conveniently interact with the window. The users can throw objects on the

* Corresponding author.

tabletop and transform the tabletop itself. It helps each user around *u-Table* to control and manipulate data and devices easily.

We developed three basic technologies for *u-Table*. First, we developed a method of detecting fingertips so that the table could be used as a large touch-screen input device. We used a fingertip as a pointing method because fingertips seem to be the most intuitive interaction method on the table. The fingertip detection must be carried out in real-time, so we had to develop a simple and fast method of detecting fingertips. Second, we need a way to recognize mobile devices on the table. We designed a visual tag to be recognized by *u-Table*. The visual tag is attached to a mobile device. Third, we designed new interaction methods for manipulating objects on the table using fingertips. The table is a cooperative workspace and a number of users can work simultaneously, so the interaction methods must be convenient and natural for users. The new interaction methods were developed in order to satisfy this requirement.

2 Related Works

Over the past few years, there have been much research efforts on a digitalized personal workspace and/or a digitalized cooperative workspace. DigitalDesk[1] used physical documents and digital documents simultaneously. A user could modify physical documents on the desk using a fingertip or a stylus pen. Physical documents can be converted into digital documents. The converted digital documents can be attached to other digital documents on DigitalDesk. Bricks[2] introduced a tangible interface. Bricks used a graspable object as a metaphor to manipulate a virtual object. It used magnetic trackers for the tangible object to support 6 Degree of Freedom(DOF). The trackers can provide a fast and accurate method but expensive. metaDESK[3] and LuminousTable[4] aim to improve it. EnhancedDesk[5] was another research similar to Digital Desk. But it focused more on fast detection of multiple fingertips. It used a thermal camera. The camera can segment accurate skin regions from input images. Some applications such as a drawing tool and a movie sequencer were developed using two-handed interface. HoloWall[6] was a wall display consisting of a rear-projected screen. HoloWall recognize users' input using silhouette occurred by infra-red(IR) illuminators in it. *u-Table* uses a similar method of HoloWall. But, the direction of illuminators is opposite to the direction of the camera and recognition of *u-Table* is more accurate. AugmentedSurfaces[7] was developed in order to exchange physical data and digital data on the table display and the wall display. It introduced a method to point and move data between displays. Also they used visual tags to recognize physical objects like notebooks, books, business cards, etc. Recently, DiamondTouch[8] and SmartSkin[9] used electronic method to sense touch. They show more accurate and fast sensing result. Also, DiamondSpin[10] introduced a circular user interface for a round tabletop display.

3 System

3.1 Hardware Design

u-Table consists of a tabletop, a camera, a projector, a server and a wireless LAN system in order to provide a cooperative workspace as shown in Figure 1. The tabletop is a rear-projected screen and also behaves like a touch-screen input device. The projector and the camera are located under the tabletop. The camera is used to recognize users fingertips and tags of devices on the tabletop. The mobile devices on the table can be connected to the wireless LAN system. The server manages the recognition process and the communication process.

We used a rear-projected screen to present images on the tabletop. The rear-projected screen was chosen because this type of projection does not contaminate images on the screen because of users' hands. Most digitalized desk systems have used a front-projected screen. In such a case, hands of users could contaminate images on the screen because of their shadows. Another point is that the rear-projected screen can be used as a diffuser which blurs the opposite scene. This property can be used to recognize whether users hands touch the screen or not without stereo cameras. Figure 2 shows the implementation of *u-Table*.

3.2 Segmentation

The projected images on the table can disturb the recognition process of fingertips and objects. It is because the camera can not distinguish real objects from the projected images on the tabletop. So, color-based recognition techniques are not helpful in this case. To avoid this type of interference, we used a infra-red(IR) camera for the recognition. The projector was added an IR cut filter, then the images of the project can be easily ignored by the camera.

For the recognition of fingertips and tags, each region must be segmented. We used background subtraction technique for the segmentation as shown in Figure 3. In this case, the background is the image when there is not any obstacle on the table. We assumed the blurred image[11] can be used as image

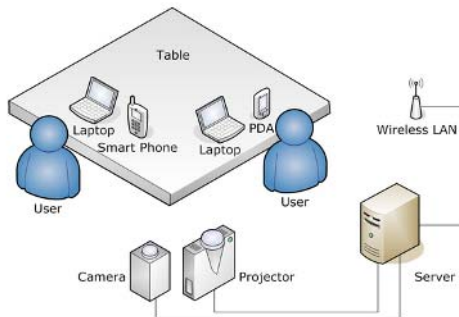


Fig. 1. System overview



Fig. 2. Implementation: a frame, a projector, a camera, and mirrors

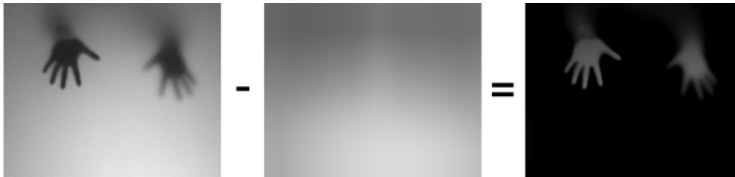


Fig. 3. Background subtraction

of the empty table. This is similar to the adaptive thresholding technique. The segmentation of *u-Table* described as Equation 1 and Equation 2 as shown below:

$$\forall x, \forall y \ S(x, y) = Blur(I(x, y)) - I(x, y) \tag{1}$$

$$\forall x, \forall y \ T(x, y) = \frac{S(x, y)}{Blur(I(x, y)) - S_{min}} \tag{2}$$

$I(x, y)$ is the pixel value of the current image. $Blur(I(x, y))$ is used as a background image. $S(x, y)$ is the result value of background subtraction. S_{min} is the lowest value of shadows and $Blur(I(x, y))$ is regarded as the brightest value. As a result, the touch level from the tabletop, $T(x, y)$ is computed relative to brightness.

3.3 Fingertip Detection

We needed a simple and fast method of fingertip detection because more than one user can use their fingertips simultaneously. We used a template matching technique. [5][12]

A fingertip detection method using a single camera could not recognize the distance of the fingertips from the tabletop. In *u-Table*, images are captured through the screen as a diffuser. So the distance can be easily recognized. We used a feature that the clearness of edge follows the distance of fingertips. Figure 4 shows that the edge of each hand can be interpreted as their corresponding distance. Suppose that one hand is on the table and the other is slightly apart from the table as shown in the right image of Figure 5. The distance can be easily recognized by amount of the edge. We used the Sobel filter to find the edge.

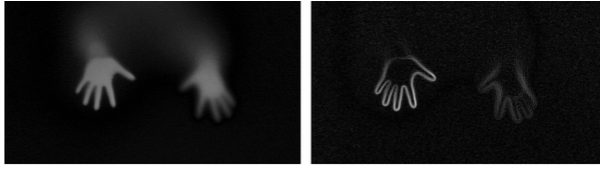


Fig. 4. Edge detection to recognize the distance of the fingertips from the tabletop

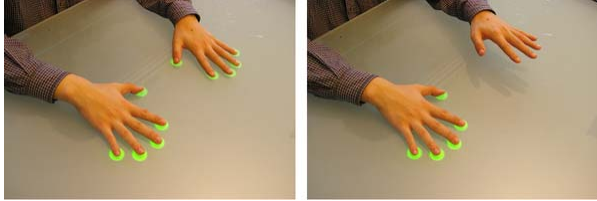


Fig. 5. Results of the fingertip detection

Figure 5 shows the result of the fingertip detection. It demonstrates that only fingertips near the screen are recognized.

3.4 Tag Recognition

We used visual tags to recognize devices on the table. The visual tag is attached to the device. The tag has a unique matrix pattern to identify its corresponding device. The tag has two types of holes. One is the guide hole to recognize position and direction of the tag. The other is the bit hole to identify the tag. It has 9 number of bit holes and it have 512 values whether holes are closed or opened. Figure 6 shows the result of recognizing the tag. The tag is not only the identifier of the device but also the interface for communicating with objects on the tabletop.

3.5 Performance

The performance of fingertip recognition of *u-Table* was tested. The average frame rate was 21 frames per second with Intel Pentium 4, 3.2GHz processor.



Fig. 6. Recognition of a device using its attached tag

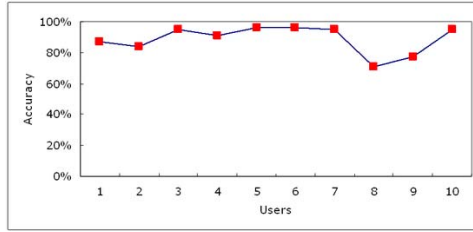


Fig. 7. The accuracy of fingertip detection

The result of fingertip detection was 87.9% of accuracy as shown in Figure 7. We tested 10 users who tried *u-Table* for the first time and each user tried ten times with 10 fingers. Additionally, our experiences with many users in many exhibition events, where *u-Table* was one of major attractions, showed that people really enjoyed and liked the performance of *u-Table*.

4 Interactions for Multiple Users

4.1 Rotational Window

A new interaction method was designed for *u-Table*. It is operated using fingertips. Also, the interaction method must allow multiple users to be able to use their fingertips simultaneously. They can also sit any side of *u-Table*. We developed a window system for *u-Table* by considering this requirements. The window system can provide multiple windows which can be easily and intuitively moved, iconized, resized and rotated by fingertips as shown in Figure 8. All of conventional operations defined in window systems can be exercised in *u-Table* using fingertips. Users can sit in any side of *u-Table*. Thus, the windows must be rotated so that users can view them conveniently. Additionally, the combination of operation is possible. If a user touches the rotation button of the window while dragging the window, the window rotates to the direction of dragging.



Fig. 8. Windows for *u-Table*



Fig. 9. Pop-up menu

4.2 Rotational Pop-Up Menu

To launch applications and change their properties, a rotational pop-up menu is designed for *u-Table*. The menu can be simply popped up using 'double click and drag'. When a user does 'double click', a pivot point for the menu appears. And the menu will be popped up when the user can drag the fingertip to the direction that he wants to rotate. The pop-up menu is more useful than a pull down menu, because users should be able to sit in any side of *u-Table* and access the menu.

4.3 Inertial Widget

When a user transfers an icon or an object on *u-Table* to another user on the other side of the table, gestures for completing the job should be natural. The icon or the object should be easily and conveniently accessed by the other users, as if they send and receive real objects. If a user sends a window widget to the other user by 'fast drag and drop', the window widget will be smoothly arrived to the other user and rotated to the front side of the other user.

4.4 Transformable Tabletop

Imagine a rotational table in a Chinese restaurant. Customers can rotate the table so that they can take dishes on the other side of the table without stretching their arms and/or bodies. Also, imagine a table with a tablecloth and objects on the table. If we transform the table cloath, we can move the objects on the table. We applied the ideas to interaction methods for *u-Table*. A user can transform the tabletop of *u-Table*. A user can activate the transformation mode by 'double



Fig. 10. Inertial widget

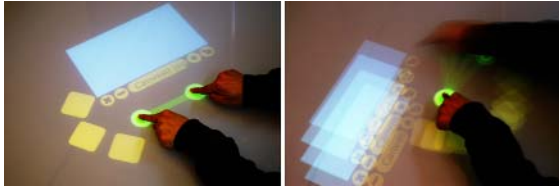


Fig. 11. Transformable tabletop

click’ on *u-Table* using a fingertip of each hand. The fingertips of each hand are used as control points for the following transformations. (i) Translation: The icons and the objects can be moved on the table. The center of the control points is a datum point. The user can move the center point to translate the icons and object on the tabletop. (ii) Rotation: The user can rotate the tabletop around the center point. It is useful to circulate icons and objects on *u-Table* and let users access them without moving themselves. (iii) Scaling: The distance of the fingers is used to scale the tabletop. The user can pull and push icons and objects using scaling operations. (iv) Hybrid operations: When users wants to access icons and objects on *u-Table*, they must use one or more operations of transformation. The operations can simultaneously be combined to transform the icons and the objects on the tabletop.

4.5 Applications

We developed some applications suitable for *u-Table*. Figure 12 show three sample applications: a puzzle, a virtual piano and a drawing tool. The users can sit around the table and can use the applications simultaneously.

4.6 Interactions with Mobile Devices

Figure 13 shows an example of multimedia data transmission between mobile devices. Users can drop their multimedia data on *u-Table* to watch together, modify and move the data to other mobile devices. When the device attached with a tag is put on the tabletop, *u-Table* can recognize what and where device is. The users can download a multimedia data by touch the icon presented near the device. And the users can move the multimedia data on the table to their mobile devices by ‘drag and drop’.

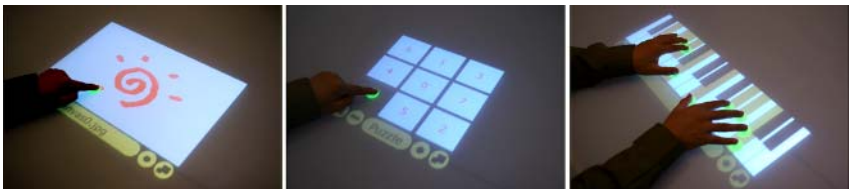


Fig. 12. A drawing tool, a puzzle game, and a virtual piano



Fig. 13. Interaction with a mobile device and manipulation of multimedia data

5 Conclusions

In this paper, we proposed a tabletop based user interface called *u-Table*. This is a tabletop interface for multiple users to share multimedia data. The users can intuitively manipulate the objects on the table using their fingertips. Devices can communicate with other devices conveniently and easily by the fingertips of users. The new interaction methods help the user to interact with the interface easily such as the rotational window, the rotational menu, the inertial widget, and the transformable tabletop. We developed simple and fast recognition methods for fingertip detection and tag recognition.

As a future work, we would like to improve the performance of the fingertip recognition method. Our experiences show that people never use their fingertips if the recognition rates are not satisfactory. Our goal is to make users feel the tabletop of *u-Table* as a real touch screen.

Finally, we have a plan to develop more useful applications and interaction techniques for *u-Table*. Our expectation is that *u-Table* can play important role under a home network environment. This can be a common place to share multimedia data such as images and video clips. Also, *u-Table* can be used as an excellent interface for games. Many board games can be played on *u-Table* by multiple users.

Acknowledgments

This work was supported by the Ministry of Information & Communications, Korea, under the Information Technology Research Center (ITRC) Support Program.

References

1. P. Wellner: The DigitalDesk Calculator: Tangible Manipulation on a Desk Top Display. *UIST* (1991) 107–115
2. George W. Fitzmaurice, Hiroshi Ishii and William Buxton: Bricks: Laying the Foundations for Graspable User Interfaces. *CHI* (1995) 442–449
3. Brygg Ullmer and Hiroshi Ishii: The metaDESK: Models and Prototypes for Tangible User Interfaces. *UIST* (1997) 223–232

4. Eran Ben-Joseph, Hiroshi Ishii, John Underkoffler, Ben Piper and Luke Yeung: Urban Simulation and the Luminous Planning Table: Bridging the Gap between the Digital and the Tangible. *Journal of Planning Education and Research* (2001) Vol. 21 No. 2 196–203
5. Yasuto Nakanishi, Yoichi Sato and Hideki Koike: EnhancedDesk and Enhanced-Wall: Augmented Desk and Wall Interfaces with Real-Time Tracking of Users Motion. *UbiComp Workshop* (2002)
6. Jun Rekimoto and Nobuyuki Matsushita: Perceptual Surfaces: Towards a Human and Object Sensitive Interactive Display. *PUI* (1997)
7. Jun Rekimoto and Masanori Saitoh: Augmented Surfaces: A Spatially Continuous Work Space for Hybrid Computing Environments. *CHI* (1998) 378–385
8. Dietz P. And Leigh D.: DiamondTouch: A Multi-User Touch Technology. *UIST* (2001) 219–226
9. Rekimoto, J.: SmartSkin: An Infrastructure for Freehand Manipulation on Interactive Surfaces. *CHI* (2002) 113–120
10. Shen, C., Vernier, F.D., Forlines, C., Ringel, M.: DiamondSpin: An Extensible Toolkit for Around-the-Table Interaction. *CHI* (2004) 167–174
11. Crow, Frank: Summed-Area Tables for Texture Mapping. *SIGGRAPH* (1984) Computer Graphics 18, 3, 207–212
12. Christian von Hardenberg and François Bérard.: Bare-Hand Human-Computer Interaction. *PUI* (2001) 1–8
13. Richard Hartley and Andrew Zisserman: Multiple View Geometry in Computer Vision. Cambridge University Press (2000) 11–16

Implementation of Embedded System for Intelligent Image Recognition and Processing

Taikyeong Jeong¹, Jinsuk Kang², and Yeon Sung Choi²

¹ Department of Electrical and Computer Engineering,
University of Texas at Austin, Austin, TX 78712-1014, USA
ttjeong@mail.utexas.edu

² Department of Electronics and Information Engineering,
Kunsan National University, Korea
{jkang01, yschoi}@kunsan.ac.kr

Abstract. The main challenges for image recognition in an embedded system design are the uncertainty of the mobile user's location and the limitation of measurement algorithm. This paper demonstrates an implementation of an embedded system which is used for vehicle tracking and license plate recognition. The image of the plate is scanned by the camera attached to a mobile device and then encoded data is transmitted along with the location information to a server that is located in a remote place through a wireless communication network. In order to track a user's location, the image recognition is estimated with spatial and attribute information receiving priority.

In this paper, we present an embedded system for intelligent interface between vehicle and users, employing spatial relative distance algorithm. Comparing the image and location information provides comparable results, and confirms that the embedded system is fairly evaluated by the intelligent image recognition technique.

1 Introduction

Recent efforts in wireless and wired communication technology have brought together an advanced image processing technology which includes an embedded-enabled system. This progress in mobile communication area also generates more demand for the development of embedded systems, for example, mobile devices which include handheld PCs (HPCs), personal digital assistants (PDAs) [1]. Using the mobile device and image processing technology, a system integration for intelligent image recognition is performed to improve image quality as well as automatic tracking and identification.

In order to provide movement and location information of a moving object, it is necessary to identify a simple solution which combines a mobile device and image recognition with the spatial relative distance method. In addition, global positioning system (GPS) technology is a method of finding a location by receiving a broadcasted GPS signal from a satellite moving around the Earth. This is used most often to find out general locations.

By processing with digitized images of vehicle registration numbers which it is sometime difficult to discern with the naked eye, it detects license plates accurately. This can be applied to various areas such as prevention of car robberies, security, and in pursuing location because through this, it is possible to refer to information of vehicles and chase locations [2, 3, 4].

2 Image Recognition Algorithm

This embedded system of image processing technology is implemented to identify the vehicle license plate number of a car and to track its location. The image is scanned by the mobile device camera and then the encoded data is transmitted along with the location information to a remote server through a wireless communication network. The method of identifying a user’s location at actual time is to receive the error revised value from various base stations. The information on clock and the orbit of satellite from satellite provide the information on location [5]. Then, correlative distance is calculated after calculating the revised error. Finally, after performing Kalman filtering, the information is provided through the process of measuring the user’s location [7].

When there are three base stations noted by j , a satellite which provides the information of location, it is necessary to add value through the processes which all the satellites provide, then to divide by the number of satellites, and to perform dispersed processes in a range of time [4]. Using a data window structure, it is necessary to add the relative distance (D_{ij}^k) between reference station (i) and (k) to position for satellite (j), and to divide it by the total number of reference stations. This process can be described in the following Equation (1), assuming the number of reference stations is three.

$$\frac{D_{12}^j + D_{23}^j + D_{13}^j}{3} \tag{1}$$

Then, we discretely conduct the calculation process within certain time. This process can be described in the following Equation (2).

$$D(t) = \frac{\sum_{j=1}^{N_{sat}} \frac{D_{12}^j + D_{23}^j + D_{13}^j}{3}}{N_{sat}} \tag{2}$$

Here, N_{sat} refers to the total number of satellites providing position information. As a next step, we calculate presumed relative distance renewed in window using results from the discretely conducted process. The process to calculate renewed presumed relative distance can be described in the following Equation (3).

$$\hat{D}(t) = \frac{\sum_{i=1}^t D(i) W(i)}{\sum_{i=1}^t W(i)} \tag{3}$$

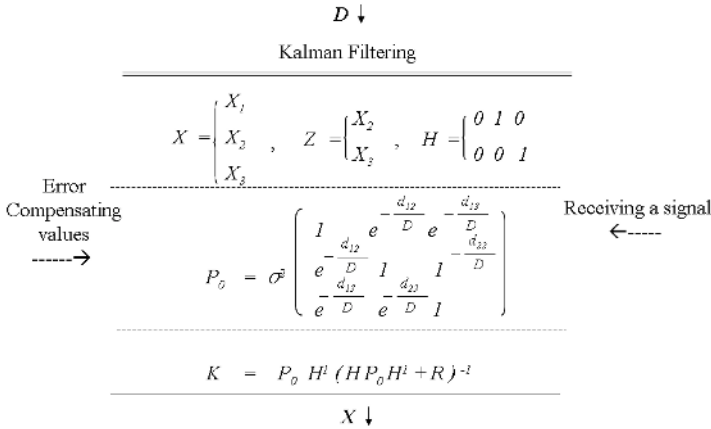


Fig. 1. Modeling of Kalman Filter for Image Recognition Algorithm

$D(t)$ refers to presumed relative distance renewed in a window, and W_i to weighting for each data point. In the meanwhile, a data window that is too large cannot follow the relative distance, and one too small can be perceived incorrectly. In this respect, the proper size of the data window is in accordance with the experimental environment.

Figure 1 shows a measuring process of position information receiver from the Kalman filter modeling using spatial relative method. The Kalman filter receives error compensating values, X_1 , X_2 and X_3 , from the reference station, and then calculates the error compensating value vector $X \cdot [X_1, X_2, X_3]$ presumed with *Raw Data* including clock information and satellite orbit information. Therefore, X_1 , X_2 , X_3 , \hat{X} , D , \hat{D} , D_{ij} , δ and R refer to the error compensating value of the user, the error compensating value of reference station, error compensating value of reference station, presumed X vector, that is $[X_1, X_2, X_3]$, relative distance.

3 Intelligent Image Expression and Processing

We improved the quality of the image through a high-frequency emphasis filter, and extracted the license plate domain through a partial image match using vertical brightness value distribution change and license plate model. During this process, data expression of the transformed image is not memorized in mobile device memory space as a sequential structure, but memorized as an index structure to facilitate more efficient and fast search, extracting characteristics of license plate domain. Figure 2 shows a block diagram of image expression and its processing stage.

An image taken by a PDA camera has resolution of 640×480 , and it requires high quality. Therefore, the quality of the image should be improved first in order to correctly extract the license plate domain. Since the edge of the plate is a high frequency area in image, an emphasis filter is used to improve image quality in the detailed outline part of the image.

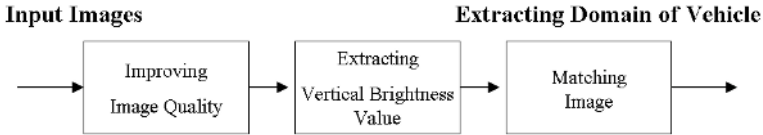


Fig. 2. A Block Diagram of Image Processing Stage



(a) Original Image (b) Improved Image

Fig. 3. Image Quality Comparison

The highest frequency of vertical component is in license plate domain. It means that a binary data on the license plate domain will have a wider brightness value distribution. In this case, a vertical edge should be measured first by applying a vertical filter [8, 9], and the brightness value change distribution in horizontal part of the image should be studied by conducting horizontal search by 20 pixels from the bottom. Equation (4) indicates the image brightness control and relative distance (3 × 5 vertical filter). Therefore, if the brightness value change distribution is higher than the standard, the domain will be a vertical license plate domain. If the vertical domain is more than one, the domain part will be a candidate domain of the license plate.

$$I_v(X,Y) = \sum_{i=0}^4 V_i \cdot I_{(X,Y+1)} + \sum_{i=0}^4 V_{5+i} \cdot I_{(X+1,Y+1)} \sum_{i=0}^4 V_{10+i} \cdot I_{(X+2,Y+i)} \quad (4)$$

4 Experimental Results

The important part of a still image taken by a mobile PDA camera is the spatial relative distance algorithm to identify the license plate domain. There are two general methods in uses: one to detect license plates by using brightness information, and the other to identify characteristics by edge detection and Hough transformation. The first one, however, is overly sensitive to the environment, with a lower recognition rate when there are noises around. The second uses vertical and horizontal components in the license plate domain, with lowered recognition rate and longer processing time in case of damage or noise in plate edge, which is not suitable for real time processing.

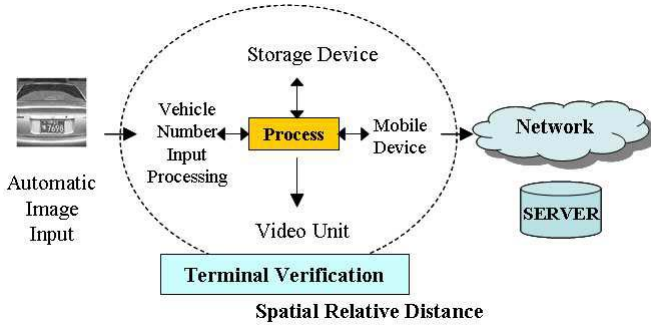


Fig. 4. Image Recognition System Procedure



Fig. 5. Images from Mobile PDA Device using Intelligent Image Recognition

In addition, the processing procedure for thinning of still image data of vehicles obtained through a mobile PDA camera, is a method to obtain wanted image data to perform an operation which removes the boundary pixel on the border without generally destroying the input pattern. The thinning process is performed when the value of a main pixel of $P_1(i, j)$ is 1, and table mapping method is introduced which takes a standard of pixel point in loop-up table (LUT) through a detecting method of framework (letters/numbers of license plates) by applying the operation to a template in order.

On images where paragraphs are inclined from the horizontal direction, we retrieve by dividing areas without concern for size, form, and degrees of inclination of lines, to apply a method of expressing adequate shapes in strong clustering. We calculate the center point for coordinates of a minimally bounded rectangle (MBR), and express the location of connecting factors using a dot.

A simple experimental result can achieve competitive image improvement with a gray image of 320×240 pixels size, taken by a mobile PDA camera (HP iPaq 3630 model) which has Windows CE operating system platform and 32MB memory capacity. The entire image recognition system process is shown in Figure 4.

In particular, we reduce search time by sorting records in a successive index structure in an embedded system with limit of memory, and try to reduce to the utmost the rate of error in information on location of a vehicle through chasing location of spatial relative distance. We prove that it is possible to actualize processing procedures of pattern recognition for numbers and letters from an imputed vehicle through a mobile PDA camera. By matching images of stopped image data from a model license plate, we implemented intelligent image recognition and interface techniques for embedded systems. Figure 5 shows images from a mobile device that identified vehicle's number and letters.

5 Conclusions

In this paper, we have demonstrated an improvement of image quality with a mobile device as intelligent image recognition techniques. Based on the improved image quality, we expressed the record unit of variable length using successive index structure, and presented an efficient method to monitor the vehicle location by matching the result with location information.

Images are recognized by using this intelligent interface technology through wireless communication technology. The embedded system automatically detects the license plate number using the spatial relative distance method. Spatial relative distance is used in real-time and the digitized image of license numbers is transmitted to the remote server, which will figure out a final vehicle location.

Acknowledgment

The author would like to thank the referees for their valuable comments.

References

1. J. Hansson and C. Norstrom, "Embedded database for embedded real-time systems: A component-based approach," *Technical Report, Linkoping University and Malardalen University, Sweden*, 2002.
2. A. Antonacopoulos, D. Karatzas and J. Ortiz Lopez, "Accessing textual information embedded in internet images," *Proc. of SPIE*, vol. 4311, pp.198-205, February. 2001
3. M. G. He, A. L. Harvey and T. Vinary, "Vehicle number plate location for character recognition," *ACCV'95 the 2nd Asian Conference on Computer Vision*, pp. 1425-1428, Dec. 5-8, Singapore
4. T. Chiueh, "Content-based image indexing," *Computer Science Department, State University of New York at Stony Brook, NY 11794 USA*
5. T. Jeong and A. Ambler, "Power efficiency system for flight application (PESFA) mission: Low power dissipation in digital circuit design for flight application/space communications," *IEEE Tran. on Aerospace and Electronics System*, vol. 42, 2006
6. T. Guionnet, C. Guillemost and S. Pateux, "Embedded multiple description coding for progressive image transmission over unreliable channels," *Proc. of IEEE Trans.* pp. 1005-1008, Jun. 2001

7. R. C. Gonzalez and R. E. Woods, "Digital Image Processing," *Addison Wesley*, pp. 447-455
8. Y. Zhang, T. Jeong, F. Chen, R. Niche and G.Gao "A study of the on-chip interconnection network for the IBM Cyclops 64 multi-core architecture," *IEEE 20th International Parallel and Distributed Processing Symposium (IPDPS'06)*, Rhodes Island, Greece, Apr. 2006
9. J. Zhou and D. Lopresti, "Extracting text form WWW images," *Proc. of the 4th International Conference on Document Analysis and Recognition (ICDAR'97)*, Ulm, Germany, Aug. 1997

A Software Reproduction of Virtual Memory for Deeply Embedded Systems

Keun Soo Yim¹, Jae Don Lee¹, Jungkeun Park¹,
Jeong-Joon Yoo¹, Chaeseok Im¹, and Yeonseung Ryu²

¹ Computing Lab., Samsung Advanced Institute of Technology, Yongin 449-712, Korea
keunsoo.yim@samsung.com

² Dept. of Computer Software, Myongji University, Yongin 449-728, Korea

Abstract. Both the hardware cost and power consumption of computer systems heavily depend on the size of main memory, namely DRAM. This becomes important especially in tiny embedded systems (e.g., micro sensors) since they are produced in a large-scale and have to operate as long as possible, e.g., ten years. Although several methods have been developed to reduce the program code and data size, most of them need extra hardware devices, making them unsuitable for the tiny systems. For example, virtual memory system needs both MMU and TLB devices to execute large-size program on a small memory. This paper presents a software reproduction of the virtual memory system especially focusing on paging mechanism. In order to logically expand the physical memory space, the proposed method compacts, compresses, and swaps in/out heap memory blocks, which typically form over half of the whole memory size. A prototype implementation verifies that the proposed method can expand memory capacity by over twice. As a result, large size programs run in parallel with a reasonable overhead, comparable to that of hardware-based VM systems.

Keywords: Embedded system, memory system, and heap management.

1 Introduction

Embedded computer systems are used in home and mobile consumer electronics. Specifically, embedded systems are used not only to control electric motors and LEDs but also to process multimedia data and communication signals. As the electronics are mass produced, it is important to reduce the hardware cost of the embedded systems. An embedded system consists of a microprocessor, code and data memories, and I/O devices. The microprocessor and I/O devices have the irreplaceable capabilities which make us hard to remove them from the system. As a result, memory devices are often directed as an optimization point for lowering the *hardware cost*.

Optimizing the memory size has another benefit in terms of *power consumption*. In near future, the electronics will utilize various physical statuses to work more intelligent. For collecting and controlling the statuses, tiny embedded systems will be used. An example of these tiny systems is micro sensors [1], which are installed in various points where power cable is not reachable. These sensors thus cannot but rely on

battery energy. In contrast, they are requested to work as long as lifetime of the electronics or buildings installed, typically more than ten years. It is sometime impossible to check and replace the battery of all distributed sensors. Thus, efficient management of given battery energy is important. Among the hardware components of a sensor, the energy use of a microprocessor, a code memory (e.g., ROM), and I/O devices can be reduced significantly while they are not being used. On the other hand, a data memory (e.g., DRAM) dissipates a large amount of energy although it is idling due to its refresh operation for all bit lines. Thus, reducing the data memory size is an important design objective in the tiny embedded systems.

There exist many techniques that can reduce the data memory size. Most of them need extra hardware, which are not applicable to the tiny systems. For example, virtual memory (VM) system needs a memory management unit (MMU) and translation lookaside buffer (TLB) [2, 3]. However, MMU and TLB are not supported in a majority of embedded processors (over 90%) [4] due to the following three reasons. One is that the VM hardware is difficult to design as well as forms large silicon area if designed. Another is that as VM hardware checks addresses generated by every instruction, a significant amount of energy is dissipated. The other is that TLB is a source of variable memory access time, making it hard to guarantee real-time constraints. Thus, recently a software reproduction of a portion of VM functionality was presented that is able to check stack overflow and resizes the stack adaptively [5].

Data memory consists of three main areas: global, heap, and stack, and the heap forms over half of total data memory space. Thus, in this paper, we present a software reproduction of VM functionalities specifically for the heap. The reproduced functionalities include heap compaction, compression, and paging. We define a novel heap API used in cooperation with the existing API of *malloc* and *free*. The novel API is designed to achieve the following two. One is abstracting the physical address of an allocated heap block by a logical ID, and the other is identifying unused heap blocks or unused parts of a heap block. When the ratio of free memory space is lower than a specified threshold, the proposed method tries to compact and compress the identified unused memory parts. When both two methods are impossible or inefficient, paging is used that swaps out the least recently used one among the unused to a flash storage. To improve the performance, small size parts are ignored from the compression and paging operations. To verify the effectiveness of the method, we have developed a prototype system on an ARM-based embedded machine [6]. The experimental results verify that the proposed method can expand physical memory capacity significantly so that large size programs run concurrently with a reasonable overhead.

The rest of this paper is organized as follows. Section 2 reviews the previous works in embedded systems area. In Section 3, we describe both the overall organization and specific mechanisms of the proposed method. We then summarize the experimental results in Section 4. Finally, Section 5 makes a conclusion with future directions.

2 Related Work

This section summarizes the prior works reducing data memory size. The prior methods are classified into three categories by the type of memory data: global variable, stack, and heap. First, Biswas *et al.* [6] reused unused parts of *global* variable area as

a stack or a heap. In compile time, they identified dead or used parts of the global area during the execution of specific functions in a program. The dead parts are reused directly when a memory overflow occurs, and the unused parts are reused by preserving the original data through a data compression technique.

Second, Middha *et al.* [5] mimicked a *stack*-related portion of VM functionality in software. They put the inspection codes to the entry and exit points of all functions. In the entry, the codes check whether a stack overflow will occur in the function or not. If it predicts an overflow, it allocates a memory block and extends the stack into the allocated. In the exit point, it tests whether the stack was extended at the entry or not. If the stack was extended, it restores the stack pointer properly and then frees the allocated block. Thus, the stack space is managed in a space-efficient manner while preventing a stack overflow.

Third, in embedded systems, heap area however was seldom managed in a space-efficient manner although heap typically forms over half of the whole memory space. Fundamental methods, which manage heap area in a space-efficient manner, are described as follows. All the followings need a support of VM hardware.

Heap compaction: Heap frequently allocates memory blocks and frees the allocated. As a result, a large portion of heap area is wasted by both internal and external fragmentations [7]. Heap compaction addresses these fragmented areas by compacting the allocated blocks. As the physical address of blocks is changed after compaction, compaction typically requires the address translation mechanism of VM. Specifically, VM translates logical address to physical one. Thus, after the compaction, the virtual address can be modified to direct the changed physical address.

Paging: Embedded systems consist of a small size of data memory. For example, the size is 16KB in a washing machine and is between 512 bytes and 2KB in a sensor node [1]. This severely limits both the capacity and functionality of the systems. Paging can logically expand the memory space by evicting less-frequently used pages to storage and by allocating the obtained space for the other tasks. When the evicted page is accessed, the page is then reloaded into the memory. Typically, VM hardware (e.g., MMU and TLB) is used to implement this paging method [2, 3, 7].

In order to avoid a use of VM hardware, a software method was developed for code memory [10]. It divides a program code in a basic block and replaces all branch instructions that cross two basic blocks by a system call instruction in a similar way that dynamic linking method does [18]. Thus, the program generates a system call whenever it wants to jump another block. Then operating system (OS) checks whether the wanted is loaded in memory or not and loads the wanted to the memory if it is absent. The system call instruction is then changed to an original branch instruction for speed-up. However, it is not appropriate for data memory because data does not have a flow of control that it can intercept as a system call. Thus, this paper presents a software-defined paging system for data memory.

Data compression: Compression reduces the data size and thus expands the memory space. Specifically, OS divides main memory into two parts: uncompressed and compressed [8, 9]. When the physical memory space is not enough, OS compresses a page that has a weak locality and stores it to the compressed part. If compression and decompression can be done quicker than a paging operation to secondary storage, this method improves the overall performance. Since paging is basically needed, this compression method also needs a support of VM. Although compression method was first

developed for high-performance computers, it is also effective at embedded systems that have flash memory storages. This is because if the paging method is used then the lifetime flash memory is seriously shortened. Compression addresses the reduction of flash lifetime.

The above three features are supported in the proposed method without relying on any extra hardware device as described in Section 3.

3 Proposed Software Virtual Memory

This section describes the proposed software virtual memory (SWVM) [12]. Figure 1 shows the overall architecture of a SWVM-based software platform. Legacy applications still use a typical heap allocator. SWVM is based on the same allocator in order to ensure the backward compatibility. At the same time, translated applications use the novel SWVM interface to utilize compaction, compression, and paging features. The interface and detailed mechanism are given in Section 3.1 and 3.2, respectively.

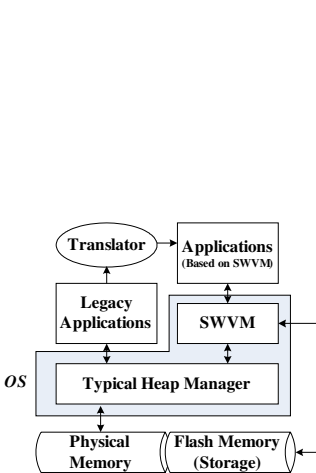


Fig. 1. System architecture

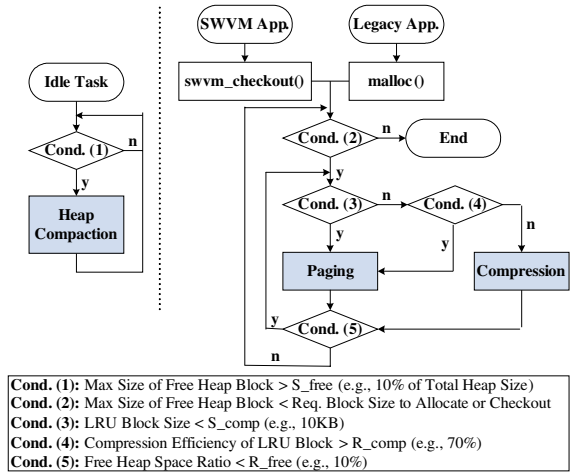


Fig. 2. Algorithm flowchart

3.1 System Interface

The novel interface described in code (1) enables the following two features. One is abstracting the physical address of an allocated heap block by a *handle ID*, and the other is identifying both unused heap blocks and unused parts of a heap blocks.

As an alternative of `malloc()`, `swvm_alloc()` is defined in which *block size* and *option* are used as parameter. *Option* is used to provide extra information to SWVM. For example, it can specify that compression is preferred as the block typically has the high compression efficiency. `swvm_alloc()` returns a *handle ID* of a allocated block instead of a physical address of the block. *Handle ID* is used by `swvm_checkout()` that loads the specific part of the memory block to physical memory. The loaded part is

specified by its *offset* and *length* parameters, and the return value is a *physical address* of the loaded part. In this way, applications access the allocated memory block. When the loaded part will not be used for a specific period of time, the applications can call `swvm_checkin()` that reclaims the loaded part. Repeatedly, `swvm_checkout()` and `swvm_checkin()` can be called in many times. Finally the allocated block is freed by `swvm_free()`.

```

int id; char *pt; int c; /* 0<=c<length */
id = swvm_alloc(size, opt);
pt = (char *) swvm_checkout(id, offset, length);
*(pt + c) += value; /* read & write operations */
swvm_checkin(pt);
swvm_free(id);

```

Conceptually, *handle ID* (*id*) and *physical address* (*pt*) correspond to the virtual and physical addresses in VM, respectively. Thus, a mapping table between *handle ID* and *physical address* is needed in a similar way that VM does. The mapping table can be constructed in two ways according to the granularity of requesting checkout and checkin operations. One is when only whole memory block can be checked out and in. In this case, the mapping table is a one dimensional array whose size is maximum number of *handle ID*. Each element in the array stores both the *status* and loaded *physical address* of a corresponding memory block. The other is when a partial checkout is allowed that can checkout only a part or multiple parts of each memory block. This needs a two dimensional array where first-level array directs a custom data structure for each memory block. The custom data structure keeps the *status* of memory block and the *address* of loaded parts.

The legacy applications and middleware can be translated to SWVM-based applications. Both programmer or source code analyzing tool can change the `malloc()` and `free()` to `swvm_malloc()` and `swvm_free()` as well as insert `swvm_checkout()` and `swvm_checkin()` to the boundary where the heap blocks are used. The boundary can be accurately identified by using the data flow analysis [11]. If translation cost is high, we can selectively apply the translation to programs that need large size memory.

3.2 Management Polices

In the proposed interface, if blocks or parts of blocks are not checked out, this means that they are not in a use (namely, unused state). The unused can be compacted, compressed, or swapped out, and they can be decompressed or swapped in before checking them out. However, when a block or its part is in an unused state for a specific period of time, we classify the block as a least recently used (LRU) block where the above three methods are applied in SWVM. This reduces an overhead of decompression and swap in operations because of the fact that programs typically exhibit a strong tendency in the memory access pattern. For example, a block used in the near past has a high probability to be accessed in the near future (namely, temporal locality). Based on this, `swvm_checkin()` inserts its parameter memory block (or part) to a global LRU queue with the current system time.

SWVM utilizes the LRU queue for expanding the effective memory capacity. Figure 2 gives an overall algorithm. The idle task in OS performs heap compaction if the maximum size of free heap block is lower than the threshold value S_{free} , e.g., 10% of total heap space size. The idle task selects the largest free heap block. It then tries to relocate the two blocks physically adjacent to the free block. This can be done only when the adjacent blocks are in the unused state. The relocated space is selected based on the best-fit policy. It then merges the free block and the space pre-used by the relocated blocks. This repeats the same procedure until the adjacent blocks are being used for other purposes. If the relocation and merging is not possible, the idle task selects next largest free block and repeats the same until it is preempted by another higher priority tasks.

On the other hand, compression and paging operations are triggered on demand if the maximum free heap block size is lower than the size of requested heap block in *swvm_checkout()* and *malloc()* functions. We pop a least recently used block from the LRU queue. If its size is smaller than S_{comp} (e.g., 10KB), it would have a low compression efficiency, degrading the value of compression. Thus, in this case, paging is used. Paging also is used when its compression efficiency is lower than R_{comp} (e.g., 70%). When a heap overflow occurs, we perform both compression and paging until the free space ratio becomes larger than R_{free} (e.g., 10%). Here, we prefer compression than paging by applying paging only if compression results in a low space benefit. This is because paging faces the fore said endurance problem in flash memory. Users can specify their preference of paging and compression for a particular heap block by using *option* in *swvm_alloc()*.

There are many compression algorithms. In SWVM, dictionary-based algorithms (e.g., Ziv-Lempel and X-Match [8]) are used because they provide the high compression efficiency for memory data and perform (de)compression quick. Paging needs a swap area in flash memory, and there are two methods for constructing the swap area. One is directly assigning a physical partition, and the other is using a file provided by flash file systems. The partitioning method typically incurs lower processing overhead than the file system-based method. However, partitioning results in a wear-leveling problem in flash memory because the number of performed erase operations in blocks in the swap partition would be different from that performed in other partitions in the same flash memory.

Figure 3 shows a state transition diagram of a heap block in SWVM. When a block is allocated, it is logically allocated but is not physically neither allocated nor initialized. When it is checked out, SWVM allocates it physically. Then, if it is checked in, it is maintained in an unused state and can be changed to the swapped out or compressed mode when heap overflow occurs. Blocks in the unused state can transit to the used and free states by *swvm_checkout()* and *swvm_free()*, respectively.

In SWVM, checkout granularity is either a whole heap block or parts of a heap block. If a part of a heap block is checked out, we call it a finer-grained checkout, which is based on four basic cases depicted in Figure 4. In Figure 4, a block is allocated in step (1) and a part of it is requested to be checked out in step (2), which is called as ‘subset’ case as a subset of a heap block is checked out. In step (3), the part

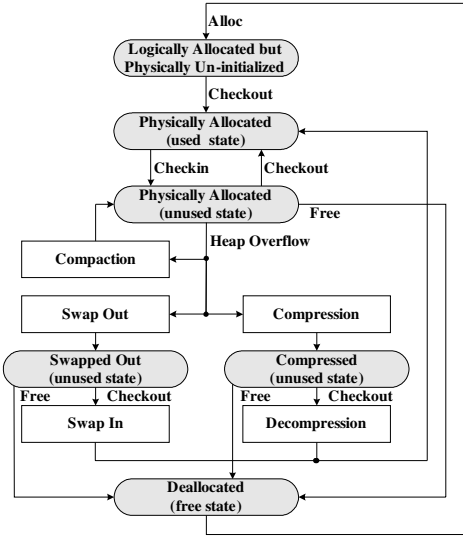


Fig. 3. State transition diagram of a heap block

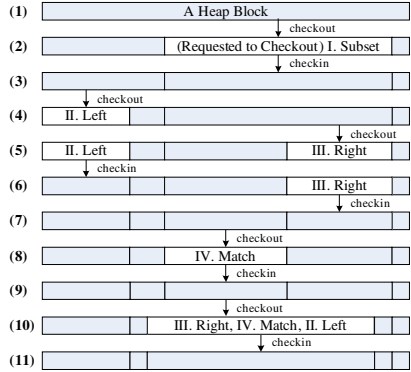


Fig. 4. Example of fine-grained checkout

is checked in and this eventually produces three physical chunks for the heap block. In step (4), another part is checked out, which we call ‘left’ case as it is a left of a physical chunk. Then, in step (5), another part is again checked out, which is the ‘right’ part of a physical chunk. SWVM allows multiple parts of a heap block to be checked out simultaneously. Similarly, in step (8), an exactly matching part of a physical chunk is checked out, and we call this ‘match’ case. Based on these four basic cases ‘subset’, ‘left’, ‘right’, and ‘match’, when a checkout operation is requested to several physical chunks, we divide the operation to each physical chunk, perform individually in each chunk, and finally merges them. Step (10) shows an example where ‘left’, ‘match’, and ‘right’ cases are adopted in a single checkout operation. This is a conceptual description of SWVM management. In practice, SWVM also take into account the state of each physical chunk described in Figure (3).

4 Performance Evaluations

This section describes both the experimental setup and results. In the experiments, we used an ARM9 machine with 64MB of DRAM and 1GB of flash storage. To evaluate the performance accurately, we developed a prototype of SWVM on Samsung Multiplatform Kernel (SMK), a customizable real-time OS for embedded consumer electronics. SMK uses the Doug Lea’s heap allocator [13] and Transactional File System version 4 (TFS4 [14]) as a flash file system. The code size of prototype is 2150 lines.

We designed a benchmark program that emulates various heap usage patterns according to its input parameters. *Total size* means the total size of allocated heap blocks, *init method* means a method used for initializing the blocks (e.g., random, constant, and none), *checkout unit* means the granularity of performing checkout in SWVM (entire block: *coarse-grained*, part of a block: *fine-grained*), *access ratio*

means the ratio of accessed heap block size over *total size*, and *locality* means the access locality of the blocks (e.g., temporal locality).

The benchmark program first allocates heap blocks where the block size is random generated within a value from 40KB to 200KB. It initializes the allocated blocks according to *init method*. Then it randomly accesses the allocated blocks according to the given parameter values, imitating both sequential and random memory access patterns. In this step, SWVM checks out an entire block and the exact part of the block to be accessed if *checkout unit* is coarse and fine, respectively. Finally, it frees all the allocated blocks.

First, we measured the execution time of each step in the benchmark program when *total size* is smaller than the physical memory size. Table 1 compares the execution time of SWVM and a typical method, the Doug Lea’s allocator. Overall execution time of SWVM is comparable to that of the typical method. Specifically, in the allocation step, SWVM provides the faster speed as it logically allocates the requested heap blocks. In the init step, random is used as *init method*. The typical generates random values and writes them to heap blocks, while SWVM checkouts heap blocks, generates random values, writes the values to the blocks, and eventually checkins the blocks. Thus, SWVM works more however its execution time is slightly shorter than that of the typical. This is because both checkout and checkin operations are quite fast (e.g., 27ms if *total size* is 10MB) and in the experiment SWVM faced fewer cache conflict misses. SWVM allocates small metadata blocks in the heap, and this shifts the beginning address of the other heap blocks (like, cache coloring method in slab allocator [16]), potentially lessening the cache conflict misses.

Table 1. Memory system performance under random memory access pattern

Method	Total Size MB (%)	Allocation Time (ms)	Init. Time (ms)	Access Time (ms (%))		Dealloc. T (ms)	
				CU=Coarse	CU=Fine	Coarse	Fine
Typical	1 (2)	1	140	74 (1.0)		1	
	10 (17)	3	1,397	739 (1.0)		2	
	58 (100)	13	8,098	4,275 (1.0)		11	
	59 (101)	Overflow	Overflow	Overflow		Overflow	
SWVM	1 (2)	1	138	73(1.0)	154(2.1)	0	1
	10 (17)	2	1,373	722(1.0)	1,550(2.1)	4	11
	58 (100)	10	7,967	4,202(1.0)	40,618(9.5)	23	198
	64 (110)	11	15,613	27,652(5.8)	61,639(13.0)	30	230
	70 (120)	12	25,322	37,214(7.2)	67,161(13.0)	33	238
	87 (150)	15	53,223	94,512(14.7)	107,497(16.7)	85	285
	116 (200)	20	100,478	149,819(17.4)	186,158(21.7)	118	336

* Init method: random; Checkout unit: *CU*; Access ratio: 100%; Locality: temporal; Overflow handling method in SWVM: Paging; S_{comp} : 10KB.

In the memory access step, when *checkout unit* is *coarse*, SWVM is slightly faster than the typical because of the same reason that it shows a better performance in the init step. However, when *checkout unit* is *fine*, its speed is about twice slower than that of the typical. This is because SWVM repeatedly checks out and in the specific parts of heap blocks, which incur many split and merge operations. Thus, the coarse-

grained checkout has the better performance if the memory access pattern is random. In the deallocation step, SWVM takes a longer time than the typical because it has to reallocate all the physical chunks.

Second, the execution of SWVM was measured when *total size* is larger than the available physical memory size (58MB). The physical memory size was 64MB and about 2MB was used for the code, bss, data, stack, and I/O buffer. Due to fragmentations, 58MB was the maximum allocable heap memory space. In this case, the typical faces a memory overflow as shown in Table 1 and thus the program was not able to run correctly. In the table, ratio in the access time field means the normalized access time against to that of the typical. On the other hand, the SWVM-based program overcomes the overflow problem with a reasonable degradation in the performance. With the coarse-grained *checkout unit*, its speed is degraded by about six to seventeen times when only ninety to fifty percent of the required memory space is available. In hardware-based VM systems, application performance is also dropped by about ten times if only half of the required memory space is available [15]. Thus, this implies that SWVM has a comparable performance to the VM systems.

Third, we measured the performance of SWVM with various parameter configurations of benchmark program. When we set *init method* to be constant, which initializes each heap block by using a unique value, the initialization time almost eliminated (e.g., less than 0.5 millisecond). This is because *swvm_alloc()* marks that the logically allocated block is initialized by a specific value, and the value is actually assigned to the block when *swvm_checkout()* is called. If checkout operation is requested to a particular part of the block, then only that particular part is initialized. Because of this, memory overflow can be significantly lessened in SWVM with constant *init method* as described in Table 2. For example, when *total size* is 87MB and *checkout unit* is coarse, the normalized access time is 1.0, which means that memory overhead was not occupied. Similarly, when *total size* is 64MB and *access ratio* is 200%, the normalized access time is 2.0 and 3.6 for coarse-grained and fine-grained *checkout unit*, respectively. With the random *init method*, the normalized access time was 5.8 and 13.0 when *total size* is 64MB and *access ratio* is 100%. Furthermore, this constant *init method* is also effective for compression method because it has the superb compression efficiency. In practice, several applications typically initialize the heap block by a zero value, strongly confessing the effectiveness of SWVM for real applications.

Table 2. Performance characteristics of SWVM

Default Parameter	Custom Parameter	Value	Total Size MB (%)	Init. Time (ms)	Access Time (ms (%))	
					CU=Coarse	CU=Fine
A,B,C,D1,E	-	-	64 (110)	0	4,870 (1.0)	08,005 (1.7)
		-	87 (150)	0	6,610 (1.0)	11,024 (1.7)
		-	116 (200)	0	54,994 (6.4)	25,359 (2.9)
A,C,D1,E	Access Ratio	130%	64 (110)	0	6,291 (1.3)	10,727 (2.3)
		200%	64 (110)	0	9,568 (2.0)	17,259 (3.6)
		300%	64 (110)	0	29,297 (6.2)	49,161 (10.4)
A,B,C,D2,E	-	-	64 (110)	0	4,870 (1.0)	8,006 (1.7)

* Init method: constant(A); Access ratio: 100%(B); Locality: temporal(C); Overflow handling method: Paging(D1), Compression(D2); S_{comp} : 10KB(E); Checkout unit: CU.

5 Conclusion

In this paper, we have presented a software reproduction of VM functionalities, compaction, compression, and paging. The experimental results have shown that SWVM with the coarse-grained checkout has a comparable performance to a typical heap allocator when the requested memory size is smaller than the physical memory size. Furthermore if the requested is larger than the physical, SWVM-based applications run correctly with a reasonable performance degradation. Thus, SWVM is the most valuable for systems requiring a large memory space only in a short period of time. For future work, we plan to reproduce other VM features, e.g., protection and sharing.

References

1. J. Polastre, R. Szewczyk, C. Sharp, and D. Culler, "The Mote Revolution: Low Power Wireless Sensor Network Devices," *In Proceedings of Hot Chips 16: A Symposium on High Performance Chips*, 2004.
2. U. Vahalia, *UNIX Internals: The New Frontiers*, Prentice Hall, 1996.
3. H. G. Cragon, *Memory Systems and Pipelined Processors*, Jones and Bartlett Pub., 1996.
4. D. Kleidermacher and M. Griglock, "Safety-Critical Operating Systems," *Embedded Systems Programming*, Vol. 14, No. 10, 2001.
5. B. Middha, M. Simpson, and R. Barua, "MTSS: Multi Task Stack Sharing for Embedded Systems," *In Proceedings of the International Conference on Compilers, Architectures, and Synthesis for Embedded Systems (CASES)*, pp. 191-201, 2005.
6. S. Biswas, M. Simpson, and R. Barua, "Memory Overflow Protection for Embedded Systems using Run-time Checks, Reuse and Compression," *Proc. CASES*, pp. 280-291, 2004.
7. A. Silberschatz, P. B. Galvin, and G. Gagne, *Operating System Concepts*, 7th Ed., John Wiley & Sons, 2004.
8. B. Abali, S. Xiaowei, H. Franke, D. E. Poff, and T. B. Smith, "Hardware Compressed Main Memory: Operating System Support and Performance Evaluation," *IEEE Transactions on Computers*, Vol. 50, Issue 11, pp. 1219-1233, 2001.
9. R. S. Castro, A. P. Lago, and D. D. Silva, "Adaptive Compressed Caching: Design and Implementation," *In Proceedings of the 15th Symposium on Computer Architecture and High Performance Computing (HPCA)*, 2003.
10. C. Park, J. Lim, K. Kwon, J. Lee, and S. L. Min, "Compiler-Assisted Demand Paging for Embedded Systems with Flash Memory," *Proc. EMSOFT*, pp. 114-124, 2004.
11. A. V. Aho, R. Sethi, J. D. Ullman, *Compilers: Principles, Techniques, and Tools*, Addison-Wesley, 1986.
12. K. S. Yim *et al.* (Samsung Electronics), "Apparatus and Method for Controlling Virtual Memory," *Republic of Korea Patent*, Filed No. P2005-0107146, 2005.
13. D. Lea, "A Memory Allocator," *Germany UNIX/Mail*, Hanser Verlag, 1996.
14. Samsung Electronics, *TFS4 Programmer's Guide*, TR SEC-TFS4-PG0001, 2004.
15. H. Garcia-Molina and L. R. Rogers, "Performance through memory," *Proc. Intl. Conf. on Measurement and Modeling of Computer Systems (SIGMETRICS)*, pp. 122-131, 1987.
16. J. Bonwick. "The Slab Allocator: An object-caching kernel memory allocator," *In Proceedings of the USENIX Summer Technical Conference*, pp. 87-98, 1994.
17. Samsung Electronics, *S3C2440A Application Notes (Development Kit for ARM9 SoC)*, Product Manual, 2004. (<http://www.samsung.com> and <http://www.mcukorea.com>)
18. J. R. Levine, *Linkers and Loaders*, Morgan Kaufmann Publishers, 2000.

Block-Level Storage Security Architectures

Shichao Ma^{1,2}, Jizhong Han¹, and Zhensong Wang¹

¹Institute of Computing Technology, Chinese Academy of Sciences,
Beijing 100080, PRC

²Graduate School, Chinese Academic of Sciences,
Beijing 100080, PRC
{scma, hjz, zswang}@ict.ac.cn

Abstract. With the unprecedented growth of storage systems in all of today's society, threats on stored sensitive information have become the critical issues that need to be addressed. Further, compared to the transient risks of data in-flight, the risks associated with data-at-rest are more enduring. While there have been many strategies and mechanisms to implement storage security on data-at-rest, these solutions implemented on application level or operating system level have several shortcomings, including weak security and heavy burden on server load. In this paper, we propose two hardware security structures based on block level, namely, store-and-forward architecture and cut-through architecture. In our approach, we design and implement these architectures based on FPGA. Our experimental results show that our schemes achieve transparency and completeness in real time without decreasing performance of system.

1 Introduction

Compared with storage security, there are a number of research results about network security, and a number of network security protocols exist, such as IPSEC [9, 10], SSL [11]. With more and more information need to be stored, especially with the development of SAN and NAS, the importance of storage security has been recognized gradually. Except for performance, capability and reliability, security has become one most important character of storage system [1, 2, 3].

Secure storage system should satisfy confidence, integrity and availability. In [1], Erik Riedel stated that storage security hammer at authentication, authorization, dynamic data encryption, static data encryption, key distribution and key revocation.

Both conventional storage system and network storage system can be described in hierarchy. A common hierarchy of storage system is shown in figure 1.

Based on above hierarchy, current storage security systems are based on operating system layer or based on application layer. For example, Cryptographic File System is based on Unix operating system [5], Encrypting File System is based on Windows operating system [8], etc. Although implementations based on operating system eliminate the complexity of implementation based on application layer, the encryption/decryption speed is low, transparency lost, security is weak and different implementation can not communicate with each other.

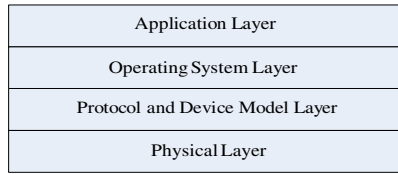


Fig. 1. The hierarchy of storage System

To address this deficiency, the IEEE Computer Society's Security in Storage Working Group is developing Project 1619, Standard Architecture for Encrypted shared storage Media since august 14, 2002 [12]. The group has hoped to complete P1619 standards for the interoperable encryption of storage devices at the physical level by early 2005. But by now, they only produce three drafts: draft proposal for key backup format, draft proposal for tweakable narrow-block encryption and draft proposal for tweakable wide-block encryption.

At present, projects related to encrypt-on-wire include CMU's NASD (Network Attached Secure Disks), PASIS (Survivable Storage) and S4 (Self Securing Storage System); projects related to encrypt-on-disk include MIT's SFS-RO (Secure File System, Read Only), UCSC's SNAD (Secure Network Attached Disks), Stanford's SiRiUS (Securing Remote Untrusted Storage) and HP's PLUTUS [1, 14, 15, 16, 17].

Unlike above projects, we focus on local storage system and local end of network storage system. So we mainly concentrate our attention on static data encryption (encrypt-on-disk), and omit the authentication, authorization and dynamic data encryption (encrypt-on-wire). Erik Riedel stated that static data encryption can provide more performance and security than dynamic data encryption. More details can be found in [1].

The closest research work was done by Enova Tech, which provides storage encryption/decryption chip. However the design uses DES/TDES algorithm as the kernel and system perform is reduced by the encryption/decryption operation.

The novelty of this paper is true transparency. We propose two storage security architecture one of which is cut-through architecture which adopts OFB (output-feedback mode) and achieves high security and completeness (all data including operating system are stored in cipher text) in real time without lowering performance of the system.

The rest of the paper is organized as follows: Section 2 describes the design of two block level architectures and their comparison. The implementation is given in Section 3. The experimental results are presented in Section 4, followed by conclusions.

2 Two Storage Security Architectures

In this section, we details two block-level storage security architectures, namely, store-and-forward architecture and cut-through architecture. Furthermore, the comparison between them is done subsequently.

2.1 Store-and-Forward Architecture

For storage system with encryption/decryption process, because the transmit bus width between processor and storage device is one bit or two bytes and block size of block algorithm is 128 bit (or more), we must buffer the data before we can encrypt/decrypt them, and then retransmit them to next end. All this operations reduce system performance. Figure 2 shows the architecture.

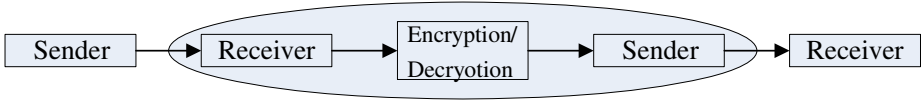


Fig. 2. Store-and-Forward architecture

For storage system without encryption/decryption process, the time to read / write one sector is the time to send and receive data T_{SR} ; for storage system with encryption/decryption process, the time to read/write one sector is the time to encrypt/decrypt and transfer data twice $T_{SR1} + T_{E/D} + T_{SR2}$, here $T_{E/D}$ stands for encryption/decryption time.

Because $T_{SR1} = T_{SR2} = T_{SR}$, the time to read/write one sector for storage system with encryption/decryption operation can be reduced to $2T_{SR} + T_{E/D}$.

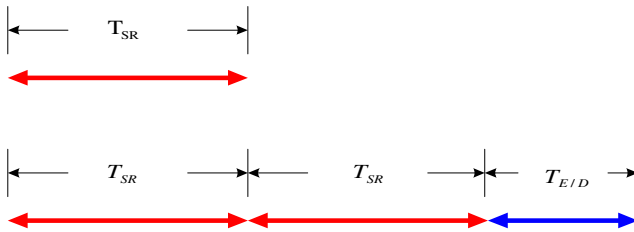


Fig. 3. Timeline of store-and-forward architecture. The top timeline is for system without encryption/decryption operation, and the bottom timeline is for system with encryption/decryption operation.

In figure 3, we can see that this architecture reduce the system performance greatly, and its performance is $\frac{T_{SR}}{(2T_{SR} + T_{E/D})}$ of original system.

Because the block size (128 bit) is less than the size of one sector, we can use pipeline to optimize the above structure, as follow (In figure 4, R_{128} stands for receive of 128 bit data, ED_{128} stands for encryption/decryption of 128 bit data, T_{128} stands for resend of 128 bit).

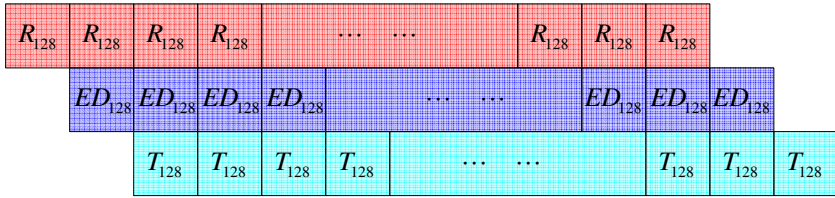


Fig. 4. Pipelining encryption/decryption structure

In above pipeline structure, the read/write time for one sector is $\frac{65}{64}T_{SR} + \frac{1}{64}T_{E/D}$, and the performance ratio is $\frac{T_{SR}}{\frac{65}{64}T_{SR} + \frac{1}{64}T_{E/D}}$.

2.2 Cut-Through Architecture

In this section, we describe all aspects of our Cut-Through architecture design. Cut-Through Architecture

“Buffer the data for encryption/decryption process” is related to encryption mode. In cut-through architecture, we utilize OFB mode to eliminate the limit (buffer the data for encryption/decryption process in Store-and-Forward Architecture) and the architecture is described as follow. In this architecture, the read/write time is same to that of architecture without encryption/decryption, i.e. T_{SR} .

The scheme to generate OfbStream (which is Xored with data for encryption or decryption) is shown in figure 5,

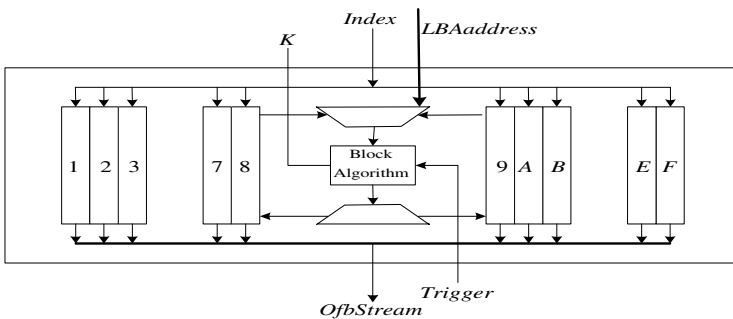


Fig. 5. How to generate OfbStream

The architecture utilize two group 128 bit register (every group include eight register) to form ping-pong structure. Suppose the logic address of the sector we will read/write is LBA , extend it to 64 bit by adding zero at left side, which is noted as LBA_{64} ; Suppose the serial number of the storage device is S_s , extend to 64 bit by

adding zero at left side, and notes as $S_{S_{64}}$. We generate eight vector using following formula, $IV_i = (LBA_{64} \wedge S_{S_{64}}) \ll (i \ll 61), i = 0, 1, \dots, 7$.

The eight IV vector is encrypted by block algorithm and sent to register group one (register one to register eight); when read/write operation takes place, the data on storage data bus is xored with *OfbStream* key stream which is actually data in register group one (indexed by *index*, which is a two bytes counter) and send to storage device (write operation) or processor (read operation). Before the key stream in register group one is used up, algorithm is trigger to encrypt data in register group one and the result is place in register group two (register 9 to register F). When data in register group is used up, we use data in register group two. We continue the operation until the read/write operation finish.

From above analysis, we can see that the encryption and data transmission is parallel.

2.3 Comparison

Storage-and-forward architecture is based on ECB mode or CBC mode, and cut-through architecture is based on CFB mode or OFB mode. In this paper, we select OFB mode as an example.

From above analysis, we can see that cut-through architecture outperform storage-and-forward architecture. Concerning implementation, storage-and-forward architecture is more complex than cut-through architecture, for in storage-and-forward architecture we not only need design sender but also need to design receiver. For write operation, sender is equal to controller, and receiver is equal to device; for read operation, sender is equal to device, and receiver is equal to controller.

3 Implementation

3.1 AES Algorithm Implementation

Storage device is usually divided into fixed-length sector (typical length is 512 bytes), and base unit of read/write operation is the size of a sector. For the out-of-order character of storage, neigh sectors don't own consequential logic relationship, and so the encryption and decryption operation can not span the boundary of sector. This means that cipher text and plain text must have same length and the length must divide the size of sector properly. 192 can not divide 4096, so AES algorithm with length of 192 isn't fit. Although both 128 and 256 can divide 4096 properly, we select 128 bit only since AES with 256 is slower than AES algorithm with 128 and AES algorithm with 128 provide enough security.

The AES algorithm with 128 bit block size has 10 run and every run consists of four steps, so in our design, we use 40 level pipeline to improve the performance the encrypting/decryption operation. The implementation is based on Xilinx XC2VP30 FPGA and gets the performance of 2Gbit/s which is more than the ATA bus speed.

3.2 Architecture Implementation

In our design, we adopt above structure to implement store-and-forward architecture and cut-through architecture. We design a PCB board, which consist of a Xilinx XC2VP30 FPGA and two ATA Interfaces. We call the ATA interface which connects to CPU (motherboard) as M-connect and call the ATA interface which connects to storage device as D-connect, respectively.

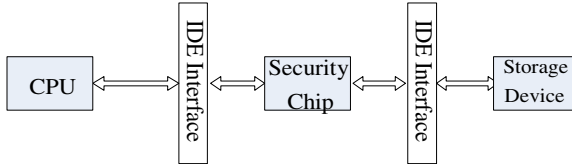


Fig. 6. Implementation Structure of Block-level Storage Security Architecture

ATA controller (for store-and-forward architecture only), CRC fast compute, I2C controller (Interface for key provide) and AES algorithm in Verilog all are placed in XC2VP30. The key is stored in EEPROM with I2C interface in KLV format:

Algorithm Code	Key Length	Key Value	Next Block
----------------	------------	-----------	------------

The Algorithm Code indicates which algorithm the system uses. Just now we only use AES (the algorithm code is 0x02). The algorithm code for DES, 3DES, IDEA and use-defined algorithm is 0x01, 0x03, 0x04 and 0x05 respectively.

4 Results of Experiments

In this section, we describe our experimental testbed and compare the throughput and complexity between store-and-forward and cut-through architecture.

Iometer is an widely used I/O subsystem measurement and characterization tool[13]. We use it to test read speed of storage system for continue read 512B, 1KB, 2KB, 4KB, 8KB, 16KB, and 32KB.

In our experimental testbed, we used one machine with one Pentium4 processor, and installed the Windows2000 Operating System on it. We restricted the hard disk (PATA, WD1200) to work under PIO mode0.

4.1 Throughput Comparision

In following table, IOps stands for command issue times per second, MBps stands for Mbyte per second, CPU% stands for rate of usage of CPU, AIOt stands for average I/O response time (unit is ms), MaxIOt stands for max I/O response time (unit is ms).

We plot data throughout rate (MBps) for store-and-forward architecture and cut-through architecture.

Table 1. Results for store-and-forward architecture

	512B	1KB	2KB	4KB	8KB	16KB	32KB	64KB	128KB
IOps	3322	2538	1538	1408	694.4	349	225	121	66
MBps	1.67	2.43	2.94	3.99	3.90	3.90	5.01	5.21	5.30
CPU %	17.12	15.44	10.53	6.60	3.19	1.72	1.20	0.74	0.42
AIoT	0.301	0.394	0.65	0.71	1.44	2.865	4.44	8.23	15.07
maxIOt	400.3	91.0	65.3	54.5	26.0	40.98	30.01	26.7	23.33

Table 2. Results for cut-through architecture

	512B	1KB	2KB	4KB	8KB	16KB	32KB	64KB	128KB
IOps	9889	7462	4506	2815	1397	698.4	449.4	249	125.5
MBps	4.82	7.29	8.80	11.0	10.92	10.91	15.05	15.58	15.70
CPU %	17.30	15.45	10.55	6.57	3.18	1.72	1.19	0.77	0.44
AIoT	0.101	0.134	0.22	0.355	0.715	1.432	2.223	4.011	7.96
MaxIOt	158.5	46.7	30.32	27.84	13.43	23.89	15.34	13.33	10.22

Table 3. Results without encryption/decryption process

	512B	1KB	2KB	4KB	8KB	16KB	32KB	64KB	128KB
IOps	9880	7462	4500	2825	1395	698.4	449.4	249	125.5
MBps	4.821	7.29	8.81	10.9	10.92	10.91	15.05	15.58	15.70
CPU %	17.30	15.45	10.65	6.5	3.13	1.71	1.20	0.77	0.44
AIoT	0.101	0.134	0.22	0.355	0.715	1.432	2.223	4.011	7.96
MaxIOt	158.6	46.71	30.33	27.8	13.44	23.90	15.34	13.31	10.12

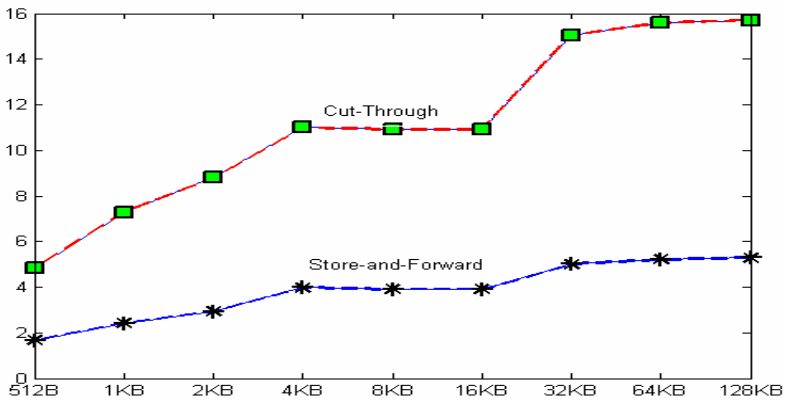


Fig. 7. Throughput comparison for store-and-forward architecture and cut-through architecture. Star-node line stands for test result of store-and-forward architecture and square-node line stand for test result of cut-through architecture, x-coordinate stands for granularity of read/write operation, y-coordinate stands for data throughput (Mbps).

4.2 Complexity Comparison

The logic usage for cut-through architecture based on XC2VP30 of Xilinx Company is as follow,

Table 4. Result for cut-through architecture

Number of Slices	5493 out of 13696	40%
Number of Slice Flip Flops	3831 out of 27392	13%
Number of 4 input LUTs	8179 out of 27392	29%
Number of bonded IOBs	68 out of 416	16%
Number of GCLKs	3 out of 16	18%

The logic usage for store-and-forward architecture based on XC2VP30 of Xilinx Company is as follow,

Table 5. Result for store-and-forward architecture

Number of Slices	12634 out of 13696	92%
Number of Slice Flip Flops	8657 out of 27392	31.6%
Number of 4 input LUTs	18179 out of 27392	66.3%
Number of bonded IOBs	68 out of 416	16%
Number of GCLKs	3 out of 16	18%

4.3 Security Comparison and Analysis

In Store-and-Forward Architecture and Cut-Through Architecture we use same encryption/decryption algorithm, AES, but different operation mode. The modes of operation provide several desirable properties to the cipher text blocks, such as adding randomness to a block cipher algorithm, control of error propagation, generation of key stream for a stream cipher, etc. And the security strength is heavily depend on the encryption/decryption kernel algorithm not operation mode, so we can conclude that the two architecture have same security strength based on AES algorithm.

From above tables, we can see that store-and-forward architecture occupy more resource than cut-through architecture; and that store-and-forward is more complex than cut-through architecture.

5 Conclusion

Storage security has come to be an important issue in today's IT professional. However, existing strategies and mechanisms are mainly implemented on application level and operating system level. This paper proposes two hardware architectures to implement storage security on block level, namely, store-and-forward architecture and cut-through architecture. Our architectures are designed and implemented based on

FPGA. Our experimental results show that the cut-through architecture yields better performance as compared to store-and-forward architecture.

Acknowledgement. This research is partially supported by the National Chinese National 863 project (2003AA135093, 2002AA731146), Chinese National Natural Science Fund (60303017), Chinese 973 Program (2004CB318202), and Faculty Research Grant at Institute of Computing Technology, Chinese Academy of Sciences.

References

1. Paul Stanton, "Security Data in Storage: A Review of Current Research", ACM Computing Research Repository (CORR) Technical Report 0409034, September 2004.
2. Donald Beaver, "Network Security and Storage Security: Symmetries and Symmetry-Breaking", First International IEEE Security in Storage Workshop, December 2002.
3. Shai Halevi, "Draft proposal for tweakable wide-block encryption", First international IEEE security in storage workshop, December 2002.
4. G.R.Blaklay, "Safeguarding Cryptographic Keys", AFIPS Conference Proceedings, vol.48, pp.313-317, 1979.
5. Matt Blaze, "A Cryptographic File System for Unix", First ACM Conference on Communications and Computing Security, Fairfax, VA November, 1993.
6. National Institute of Standards and Technology (NIST), Advanced Encryption Standard (AES), National Technical Information Service, Springfield, VA 22161, Nov. 2001.
7. S.Mangard, M.Aigner, and S.Dominikus, "A highly regular and scalable AES hardware architecture", IEEE trans. Computers, vol. 52, no.4, pp 483-491, April 2003.
8. Mark Russinovich, "Inside Encrypted File System", windowsITPro, <http://www.windowsitpro.com/article>, July 1997.
9. Naganand Doraswamy, Dan Harkins, IPsec-The New Security Standard for the Internet, Intranets, and Virtual Private Networks, Prentice Hall PTR, 2003.
10. S.Kent and R.Atkinson, Security Architecture for the Internet Protocol. RFC2401, November 1998.
11. AbdeNasir Alshamsi, "A technical comparison of IPsec and SSL", Proceedings of the 19th international conference on advanced information networking and applications (AINA'05).
12. Jim Hughes, "IEEE standard for encrypted storage", IEEE computer, November 2004.
13. IOMeter Project, <http://www.iometer.org/>.
14. Garth Gibson, David Nagle, Khalil Amiri, Fay Chang, Howard Gobiuff, Erik Riedel, David Rochberg, Jim Zelenka, "Filesystems for Network-Attached Secure Disks" CMU Computer Science Technical Report, CMU-CS-97-118. July 1997.
15. Eu-Jin Goh, Hovav Shacham, Nagendra Modadugu, and Dan Boneh. SiRiUS: Securing Remote Untrusted Storage. In the proceedings of the Internet Society (ISOC) Network and Distributed Systems Security (NDSS) Symposium 2003.
16. Mahesh Kallahalla, Erik Riedel, Ram Swaminathan, Qian Wang, and Kevin Fu. PLUTUS: Scalable secure file sharing on untrusted storage. In Conference on File and Storage Technology (FAST'03) pp. 29-42 (31 Mar - 2 Apr 2003, San Francisco, CA), Published by USENIX, Berkeley, CA.
17. Ethan L.Miller, Darrell D.E.Long, etc, Strong Security for Network-Attached Storage, Proceedings of the FAST 2002 Conference on File and Storage Technologies, Monterey, California, USA January 28-30, 2002.

An Intelligent Garbage Collection Algorithm for Flash Memory Storages

Long-zhe Han¹, Yeonseung Ryu^{1,*}, Tae-sun Chung², Myungho Lee¹,
and Sukwon Hong¹

¹ Department of Computer Software, Myongji University, Korea

² College of Information Technology, Ajou University, Korea
ysryu@mju.ac.kr, longzhehan@gmail.com

Abstract. Flash memory cannot be overwritten unless erased in advance. In order to avoid having to erase during every update, non-in-place-update schemes have been used. Since updates are not performed in place, obsolete data are later reclaimed by garbage collection. In this paper, we study a new garbage collection algorithm to reduce the cleaning cost such as the number of erase operations and the number of data copies. The proposed scheme automatically predicts the future I/O workload and intelligently selects the victims according to the predicted I/O workload. Experimental results show that the proposed scheme performs well especially when the degree of locality is high.

1 Introduction

Flash memory is becoming important as nonvolatile storages because of its superiority in fast access speeds, low power consumption, shock resistance, high reliability, small size, and light weight [7, 11, 8, 6, 13]. Because of these attractive features, and the decreasing of price and the increasing of capacity, flash memory will be widely used in consumer electronics, embedded systems, and mobile computers.

Though flash memory has many advantages, its special hardware characteristics impose design challenges on storage systems. First, flash memory is organized in terms of *blocks*, where each block is of a fixed number of *pages* [8]. A block is the smallest unit of erase operation, while reads and writes are handled by pages. The size of page is fixed from 512B to 2KB and the size of block is somewhere between 4KB and 128KB depending on the product. Second, flash memory cannot be written over existing data unless erased in advance. Besides erase operation can be performed in a larger unit than the write operation and it takes an order of magnitude longer than a write operation (See Table 1). Third, the number of times an erasure unit can be erased is limited (e.g., 10,000 to 1,000,000 times). Therefore, data must be written evenly to all blocks to avoid wearing out specific blocks to affect the usefulness of the entire flash memory device, that is usually named as *wear leveling*.

* This work was supported by the Korea Research Foundation Grant funded by the Korean Government(MOEHRD)(R08-2004-000-10391-0).

Table 1. Characteristics of different storage media. (NOR Flash: Intel 28F128J3A-150, NAND Flash: Samsung K9F5608U0M).

Media	Access time		
	Read (512B)	Write (512B)	Erase
DRAM	2.56 μ s	2.56 μ s	
NOR Flash	14.4 μ s	3.53ms	1.2s (128KB)
NAND Flash	135.9 μ s	226 μ s	2-3ms (16KB)
Disk	12.4ms	12.4ms	

Since blocks should be erased in advance before updating, updates in place is not efficient. All data in the block to be updated must first be copied to the system buffer and then updated. After the block is erased, all data must be written back from the system buffer to the block. This results in poor update performance. Moreover, the blocks of hot spots would soon be worn out. To solve these problems, data are updated to empty spaces and obsolete data are left at the same place as garbage, which a garbage collector later reclaims.

There have been many researches on garbage collection algorithms (or cleaning policies) for log-structured file systems used on disk-based storages. Recently, some garbage collection algorithms for flash memory file systems are proposed. Garbage collection algorithms should deal with some issues such as how many blocks to erase, which blocks to erase, and where to migrate valid data from erased block. The primary concern of garbage collection algorithms has been to reduce the cleaning cost. But, the number of victim blocks is also a problem for garbage collection policy of flash memory file system. This is because the cost of erase operation is much higher than read/write operations and thus garbage collection could disturb normal I/O operations.

In this paper, we study an intelligent garbage collection algorithm, which predicts I/O workload of the near future and determines the number of victim blocks to be erased according to the predicted I/O workload. If we can predict the I/O workload such as the number of I/O request arrivals during the next garbage collection execution, we can control the number of victim blocks to be erased according to the estimated I/O workload. When the number I/O request arrivals during the next garbage collection is estimated as high, garbage collector selects one or no victim block. Otherwise, garbage collector can select several victim blocks. When garbage collector gathers many valid data from several victim blocks, it can perform data migration efficiently by grouping the data according to their characteristics (i.e., cold data and non-cold data).

The rest of this paper is organized as follows. In Section 2, we review previous works that are relevant for this paper. In Section 3, we present the architecture of proposed garbage collection and deal with the problem of predicting the I/O workload. We also propose a new garbage collection algorithm. Section 4 presents the experimental results to show the performance of proposed scheme. The conclusions of this paper are given in Section 5.

2 Background

2.1 The Cost of Garbage Collection

Flash memory cannot be written over existing data unless erased in advance. Besides erase operation can be performed in a larger unit than the write operation and it takes an order of magnitude longer than a write operation. The erase operation can only be performed on a full block and is slow that usually decreases system performance and consumes power. Therefore if every update is performed in place, then performance is poor since updating even one byte requires one erase and several write operations. In order to avoid having to erase during every update, a *logging approach* has been recommended since it is quite effective in several ways (see Fig. 1). First, logging solves the inability to update *in situ* since an update results in a new write at the end of the log and invalidation of the old. The natural separation of asynchronous erases from writes allows write operations to fully utilize the fixed I/O bandwidth, and thus prevents performance degradation that may occur when writes and erases are performed simultaneously.

When data are updated to empty spaces at the end of the log, obsolete data are left at the same place as *garbage*, which a *garbage collector* process later reclaims. Since garbage collection can be performed in the background, update operation can be performed efficiently. The operation of garbage collection usually involves three stages as Fig. 2. It first selects victim blocks and then identifies valid data that are not obsolete in the victim blocks. And it copies valid data from the victim blocks to the end of log. After that, the victim blocks are erased and available for rewriting.

The cleaning cost and the degree of wear-leveling are two primary concerns of garbage collector. The garbage collector tries to minimize cleaning cost and wear down all blocks as evenly as possible. Sometimes the objective of minimizing cleaning cost conflicts with that of wear-leveling. For example, excessive wear-leveling generates a large number of invalidated blocks, which degrades cleaning performance.

First, we define the cleaning cost. Let MC_i be migration cost and EC_i be erasure cost for i -th garbage collection, respectively. The migration cost denotes the number of copies of valid data from the victim blocks to free space in other

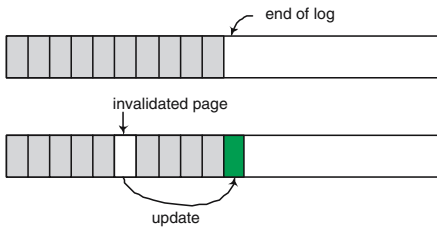


Fig. 1. Log-structured management

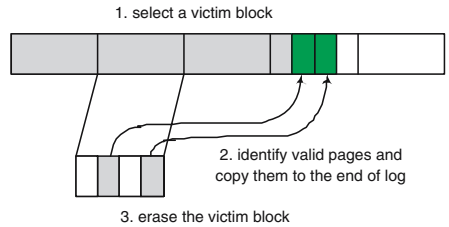


Fig. 2. Three steps of garbage collection

blocks. The erasure cost denotes the number of erasure. Then the cleaning cost of garbage collection can be described as follows:

$$\sum MC_i + EC_i \quad (1)$$

The cost to erase a block is much higher than to write a whole block. The erasure cost dominates the migration cost in terms of operation time and power consumption. Therefore, the number of erase operations determines the garbage collection costs. For better performance and power conservation, the primary goal is to minimize the number of erase operations.

Next, we define the degree of wear-leveling as follows:

$$\epsilon = E_{max} - E_{min} \quad (2)$$

where E_{max} is the maximum erase count and E_{min} is the minimum erase count, respectively. The smaller ϵ is, the longer the lifetime of system is. Since excessive wear-leveling does cleaning performance more bad than good, it is sufficient that ϵ should be below a predefined threshold.

2.2 Garbage Collection Algorithms

There are some issues of garbage collection algorithms:

When. When is garbage collection started and stopped? It usually executes periodically or is triggered when the number of free blocks gets below some threshold.

How many. How many blocks are cleaned at once? The more blocks are cleaned at once, the more valid data can be reorganized. However, cleaning several blocks needs much time, which can disturb normal I/O execution. Thus, most garbage collection algorithms select only one block.

Which. Which block is selected for erasing? One may select a block with the largest amount of garbage or select blocks using information such as age, update time, etc. This is referred to as *victim selection algorithm*.

Where. Where is the valid data written out? This is referred to as *data migration algorithm*. There are various ways to reorganize valid data, such as enhancing the cleaning performance by grouping pages of similar age together or grouping related files together into the same block, etc.

A number of victim selection algorithms based on the *block utilization* have been studied [9, 15, 10, 4, 12]. The *greedy* algorithm selects blocks with the largest amount of garbage for erasure, hoping to reclaim as much as possible with the least cleaning work [12]. The greedy policy tends to select a block in a FIFO order irrespective of data access patterns. It is known that the greedy policy works well for uniform access, but does not perform well for high localities of access [15]. The *cost-benefit* algorithm chooses blocks that maximize the formula [12, 9]: $\frac{age \cdot (1-u)}{u+1}$, where u is the utilization of a block (the fraction of space occupied by valid data) and age is the time since the most recent modification,

respectively. The cost is derived from migration and erasure, which are reflected by the denominator $(u + 1)$. The benefit is given as the space-time product form. The term $(1 - u)$ reflects how much free space it acquires. Because of term *age*, cold blocks can be cleaned at a much higher utilization than hot blocks.

There are several methods to migrate valid data to the cleaned blocks. Most schemes try to gather hot data together to form the largest amount of garbage to reduce garbage collection cost. The *age-sort* algorithm used in Log-Structured File system (LSF) sorts valid data by age before writing them out to enforce the gathering of hot data [12]. For better effect, several blocks are cleaned at once. The *separate block cleaning* algorithm uses separate blocks in cleaning: one for cleaning not-cold blocks and writing new data, the other for cleaning cold segments [9]. The separate segment cleaning was shown to perform better than when only one segment is used in cleaning, since hot data are less likely to mix with cold data. The *dynamic data clustering* algorithm clusters data according to their update frequencies by active data migration [5].

As for wear-leveling, simple swapping approaches have also been proposed. However, swapping data between two blocks requires buffer memory, erasing two blocks and rewriting swapped data. Thus the swapping methods consume a lot of available system resources and time, which could disturb normal I/O execution.

3 Intelligent Garbage Collection

3.1 Motivation

The performance of garbage collection depends on the combination of victim selection policy and data migration policy. The cost-benefit policy, a representative victim selection algorithm, generally performs better than the greedy policy. But it does not perform well for high localities of access without combining efficient data migration policy. We will show it in next section. Under high localities of access, after a large number of logging and cleaning operations, cold data becomes mixed with non-cold data within each block. After that time, cold data moves around uselessly together with non-cold data. For this reason, the utilization of cleaned blocks remains stable at a high value and the amount of free space collected becomes small. In other words, migration cost and erasure cost could be increased. In order to overcome this problem, the cost-benefit policy has to combine data migration policy that separates cold data and hot data when migrating valid data.

Many flash memory file systems are based on Log-Structured File system [14, 1]. But, the separate block cleaning policy and the dynamic data clustering policy cannot be used for log-structured file system. The age-sort policy was used in Log-Structured File system. It sorts the valid pages of victim blocks by the time they were last modified and migrates them at the end of log. For example, it migrates the oldest pages first at the end of log. We use the *cost-benefit with age-sort* algorithm like Log-Structured File system [12].

The problem of this policy is that garbage collector should select several victim blocks for better separation of cold and non-cold data. When it collects valid data

from many victim blocks, there may be high probability of isolating cold data and non-cold data and of migrating them to separated blocks. But, previous garbage collection algorithms choose one victim block since erase operation takes much time and thus erasure of several victims at once can disturb normal I/O operation.

If we can predict the I/O workload such as the number of I/O request arrivals during the next garbage collection execution, we can control the number of victim blocks to be erased according to the estimated I/O workload. When it is predicted that the number I/O request arrivals for the next garbage collection is high, garbage collector selects one or no victim block. Otherwise, garbage collector can select several victim blocks and thus improve its performance.

3.2 Architecture

The proposed garbage collection module consists of three components: (i) a *monitor* that measures the request arrival rate, (ii) a *predictor* that uses the measurements from the monitor module to estimate the workload characteristics in the near future, and (iii) a *garbage collector* that performs garbage collection task.

The monitor is responsible for measuring the request arrival rate. The monitor tracks the number of request arrivals a_i in each measurement interval (I) and records this value. The monitor maintains a finite history consisting of the most recent H values of the number of arrivals. Let A_i be the sequence a_i^1, \dots, a_i^H of values from the measurement history. Let W be the time units to execute garbage collector. The predictor uses the past measurements to predict the number of arrivals \hat{n}_i and the arrival rate λ_i for the W time units.

The garbage collector uses the cost-benefit with age-sort algorithm. It uses the predicted workload to determine the number of victim blocks.

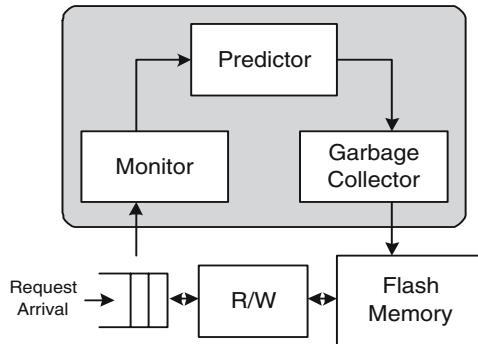


Fig. 3. Proposed garbage collector architecture

3.3 Predicting the Arrival Rate

This section presents a method to predict the I/O arrival rate. In order to predict the number of arrivals \hat{n}_i , we use the model of AR(1) process [3, 2](autogressive of order 1). Using the AR(1) model, a sample value of A_i is estimated as

$$\hat{a}_i^{j+1} = \bar{a}_i + \rho_i(1) \cdot (a_i^j - \bar{a}_i) + e_i^j, \quad (3)$$

where, ρ_i and \bar{a}_i are the autocorrelation function and mean of A_i respectively, and e_i^j is a white noise component. We assume e_i^j to be 0, and a_i^j to be estimated values \hat{a}_i^j for $j \geq H + 1$. The autocorrelation function ρ_i is defined as

$$\rho_i(l) = \frac{E[(a_i^j - \bar{a}_i) \cdot (a_i^{j+l} - \bar{a}_i)]}{\sigma_{a_i}^2}, 0 \leq l \leq H - 1, \quad (4)$$

where, σ_{a_i} is the standard deviation of A_i and l is the lag between sample values for which the autocorrelation is computed.

Let $M = W/I$. Then we estimate $\hat{a}_i^{H+1}, \dots, \hat{a}_i^{H+M}$ using Equ. 3. Then, the estimated number of arrivals in W time units is given by $\hat{n}_i = \sum_{j=H+1}^{H+M} \hat{a}_i^j$ and finally, the estimated arrival rate, $\hat{\lambda}_i = \frac{\hat{n}_i}{W}$.

4 Experiment

We have performed simulations in order to investigate the cost-benefit with age-sort policy by varying the number of victim blocks. There have been no previous works about it. We have also implemented three algorithms for comparison: GR represents the greedy policy with no separation of hot and cold data; CB represents the cost-benefit policy with no separation of hot and cold data; and CBA- x represents the cost-benefit with age-sort policy, where x is the number of victim blocks.

Since at low utilization garbage collection overhead does not significantly affect performance, in order to evaluate the effectiveness, we initialized the flash memory by writing data sequentially to fill it to 90% of flash memory spaces. The created workloads then updated the initial data according to the required access patterns. We used the notation for locality of reference as ' x/y ' that $x\%$ of all accesses go to $y\%$ of the data while $(1-x)\%$ go to the remaining $(1-y)\%$ of data.

We define the number of extra erase operations as the number of erase operations minus the number of erase operations from an ideal scheme. The ideal scheme is defined as a scheme that performs one erase operation for every n -page write requests, where n is the number of pages per block. Similarly, the number of extra write operations is defined as the number of write operations minus the number of writes requested. Performance metrics are the ratio of the number of extra erase operations to the number of erase operations from ideal scheme, the ratio of the number of extra write operations to the number of write requests and the degree of wear-leveling.

Fig. 4 (a) shows the ratio of the number of extra erase operations to the number of erase operations from ideal scheme and (b) shows the ratio of the number of extra write operations to the number of write requests. Both figures illustrate that CBA performed best. As the locality is increased, the performance of CBA-2, CBA-3, and CBA-4 increased rapidly whereas GR, CB, and CBA-1

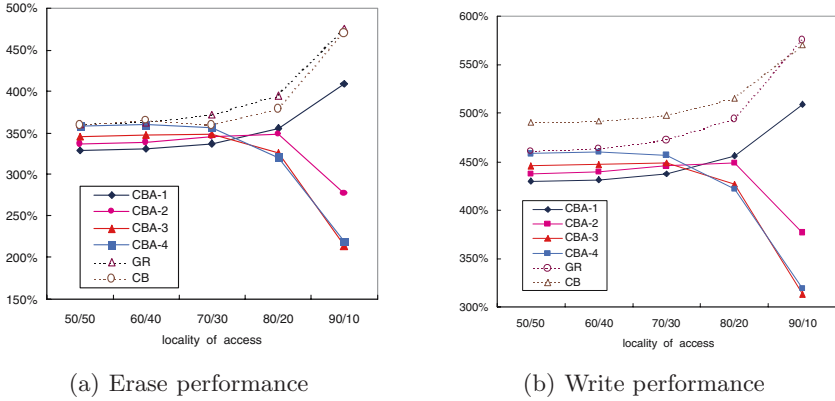


Fig. 4. Comparison of erase and write performance

Table 2. Comparison of wear-leveling degree

	CBA-1	CBA-2	CBA-3	CBA-4	GR	CB
50/50	4	6	11	21	4323	5
60/40	5	11	15	239	4651	6
70/30	6	841	747	11083	6054	6
80/20	7	2387	4215	39513	9515	12
90/10	26	10619	28177	80165	18569	40

deteriorated severely. This is because CBA with several victims can separate data, such that cold data are less likely to mix with hot data as compared with the other policies. This effect is more prominent under higher locality of access. Fig. 4 also shows that the performance of CBA-3 and CBA-4 are nearly the same. Thus, it is sufficient to select at most three victim blocks.

Table 2 shows the simulation results about the degree of wear-leveling. It illustrates that CB and CBA-1 provide stable wear-leveling effects, while the leveling effect of GR and CBA- $\{2|3|4\}$ is not satisfactory especially when the locality is high. In case of CBA with several blocks, hot data and cold data are stored separately on different blocks and hot blocks are much likely to erase frequently. Thus, the wear-leveling degree becomes higher.

5 Concluding Remarks

In this paper, we propose an intelligent garbage collection algorithm, which predicts I/O workload of the near future and determines the number of victim blocks according to the predicted I/O workload. If we can predict the number of I/O request arrivals during the next garbage collection execution, we use this information to control the number of victim blocks so that garbage collector can gather valid data from several victim blocks as much as possible. Proposed

garbage collection scheme can reduce the cleaning cost by performing data migration efficiently. Experimental results show that the proposed scheme performs well especially when the degree of locality is high.

References

1. Yaffs (yet another flash filing system). <http://www.aleph1.co.uk/yaffs/>.
2. G. Box and G. Jenkins. *Time Series Analysis: Forecasting and Control*. Holden-Day, 1976.
3. A. Chandra, W. Gong, and P. Shenoy. Dynamic resource allocation for shared data centers using online measurements, 2002.
4. M. Chiang and R. Chang. Cleaning policies in mobile computers using flash memory. *Journal of Systems and Software*, 48(3):213–231, 1999.
5. M. Chiang, P. Lee, and R. Chang. Using data clustering to improve cleaning performance for flash memory. *Software Practice and Experience*, 29(3):267–290, 1999.
6. T. Chung, D. Park, Y. Ryu, and S. Hong. Lstaff: System software for large block flash memory. *Lecture Notes in Computer Science*, 3398:704–710, 2005.
7. F. Douglis, R. Caceres, F. Kaashoek, K. Li, B. Marsh, and J. Tauber. Storage alternatives for mobile computers. In *Proceedings of the 1st Symposium on Operating Systems Design and Implementation*, 1994.
8. Samsung Electronics. 256m x 8bit / 128m x 16bit nand flash memory. <http://www.samsungelectronics.com>.
9. A. Kawaguchi, S. Nishioka, and H. Motoda. Flash memory based file system. In *Proceedings of USENIX95*, pages 155–164, 1995.
10. H. Kim and S. Lee. An effective flash memory manager for reliable flash memory space management. *IEICE Trans. Information and Systems*, E85-D(6):950–964, 2002.
11. B. Marsh, F. Douglis, and P. Krishnan. Flash memory file caching for mobile computers. In *Proceedings of the 27th Hawaii International Conference on Systems Sciences*, 1994.
12. M. Rosenblum and J. K. Ousterhout. The design and implementation of a log-structured file system. *ACM Trans. Computer Systems*, 10(1):26–52, 1992.
13. Y. Ryu and K. Lee. Improvement of space utilization in nand flash memory storages. *Lecture Notes in Computer Science*, 3820:766–775, 2005.
14. David Woodhouse. Jffs: The journalling flash file system. In *Proceedings of the Ottawa Linux Symposium*, 2001.
15. M. Wu and W. Zwanepoel. envy: A non-volatile, main memory storage system. In *Proceedings of the 6th International Conference on Architectural Support for Programming Languages and Operating Systems*, 1994.

Design and Implementation of a Security Framework Based on the Object-Based Storage Device Standard*

Kwangsun Ko¹, Gu Su Kim¹, June Kim², JungHyun Han³,
Ungmo Kim¹, and Young Ik Eom^{1,**}

¹ School of Information and Communication Eng., Sungkyunkwan University,
300 Cheoncheon-dong, Jangan-gu, Suwon, Gyeonggi-do 440-746, Korea
{rilla91, gusukim, umkim, yieom}@ece.skku.ac.kr

² Digital Home Division, Electronics and Telecommunications Research Institute,
161 Gajeong-dong, Yuseong-gu, Daejeon 305-700, Korea
jkim@etri.re.kr

³ Department of Computer Science and Engineering, Korea University,
Anam-dong, Seongbuk-gu, Seoul 136-701, Korea
jhan@korea.ac.kr

Abstract. Recently, demands on security frameworks adopted for network-based storage mechanisms have considerably increased, as these mechanisms are appointed in important roles within industrial areas. However, there has been minimal research and development of these frameworks. In this paper, the design and implementation of a security framework, based on the Object-based Storage Device (OSD) standard [1], is presented. In the proposed security framework compared with the OSD standard, several different functionalities exist.

1 Introduction

As uses of Internet and intra-net have continuously increased in the social environment, it is required that a considerable quantity of data must be stored and used for various tasks: data mining, ERP (Enterprise Resource Planning), and so on. This social environment has demanded that developments of storage industries must be maintained, and studies of various storage mechanisms must be conducted. Various network-based storage mechanisms, such as Storage Area Network (SAN), Network Attached Storage (NAS), and so on, have important roles in industrial areas, and demands regarding security frameworks adopted by these mechanisms have become considerably more pronounced. Nevertheless,

* This research was supported by Electronics and Telecommunications Research Institute. This research was supported by the MIC(Ministry of Information and Communication), Korea, under the ITRC(Information Technology Research Center) support program supervised by the IITA(Institute of Information Technology Assessment).

** Corresponding author.

there has been minimal research and development of these frameworks. In this paper, the design and implementation of a security framework, based on the Object-based Storage Device (OSD) standard [1], the emerging next generation network-based storage mechanism, is presented.

Our proposed security framework for OSD systems is implemented on Linux systems, using kernel module programming. This framework is characterized by several different functionalities: the credential cache mechanism, the separation of normal and administrative operations, the default capability for GET ATTRIBUTE commands, no key version, and no network faults and no clock synchronization. The details of these different functionalities are described in Section 3. Five test scenarios and results are also verified, in order to confirm proper implementation of the proposed security framework.

2 Related Work

There have been various security frameworks in academic and commercial worlds. In academic worlds, representative research is Network Attached Secure Disks (NASD) [2][3] and Secure Network Attached Disks (SNAD) [2][4]. NASD, developed by Carnegie Mellon University in 1998 is the predecessor of the OSD. The major characteristic of this NASD is providing clients with a legitimate credential, in order for the file accessing bottleneck of file servers to be reduced. This legitimate credential is provided by a file manager server to clients, and consists of a capability and a capability key; the capability is the right to access file servers, and a capability key is a private key used to create a legitimate credential. The full data in the SNAD, developed by UC Santa Cruz University, is encrypted, in order to prevent unauthorized clients from accessing file servers.

In commercial worlds, there have been representative products based on the Linux operating system: the Lustre file system developed by Cluster File Systems, Inc. [5], the ActiveScale Storage Cluster developed by PANASAS, Inc. [6], and the IBM Haifa Laboratory [7]. The Lustre file system supports various environment from small-sized networks to cluster networks and can be used in open and heterogeneous networks. However, the Lustre file system has no security framework individually and is implemented when using the various pre-existing network and security protocols, such as LDAP, Kerberos, POSIX ACS, PKI, and so on. The ActiveScale Storage Cluster supports high performance of data processing in the Linux-based cluster environment, so that clients desiring access to object storage devices request the necessary capability from metadata servers having the authority to manage object storage devices, and then only clients with legitimate capabilities can access desired objects. The IBM Haifa Laboratory particularly proposed the concept of the Object Storage [8][9], however, until now there is no specifically implemented security framework based on this research.

3 Design and Implementation

In this section, the architecture of a security framework based on the OSD standard is designed and this framework is implemented.

3.1 Architecture and Sub-functionalities

A general OSD system, implemented based on the OSD standard, may consist of three subjects: many clients, a few metadata servers, and some OSD servers. Each subject also has several blocks as necessary; the number and the constitution of these blocks is different according to the implementation methods. The simply and conceptually designed architecture, including subjects and several blocks of each subject, of a security framework based on the OSD standard is presented in Figure 1.

As presented in Figure 1, the designed architecture of a security framework consists of three subjects: a client, a metadata server, and two OSD servers. Each subject also has several blocks. Shaded blocks are for a security framework, white blocks for a general OSD system. All subjects operate on Linux systems, connected each other via an IP-based open network, using the Internet Small Computer Systems Interface (iSCSI) mechanism [10][11] and blocks implemented as kernel modules.

In the proposed security framework, similar to the OSD standard [1], there are seven hierarchical keys: master keys (a master authentication key and a master generation key), root keys (a root authentication key and a root generation key), partition keys (a partition authentication key and a partition generation key), and a working key. Each authentication key is used for generating an *integrity check value*, and every generation key is used for generating low-layered hierarchical keys. Furthermore, both the OSD server and the metadata server share

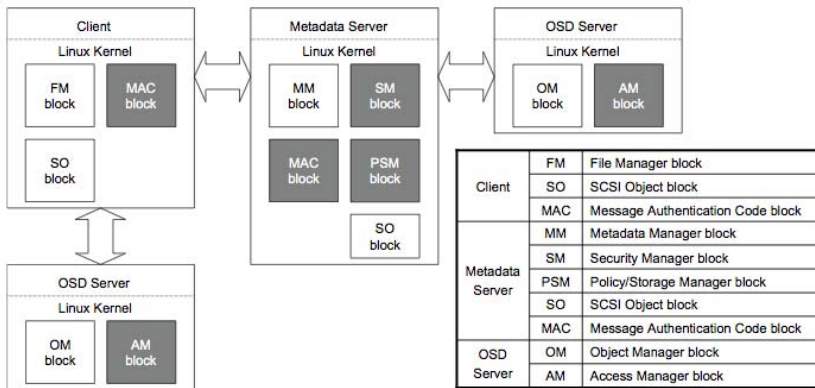


Fig. 1. The architecture of a security framework based on the OSD standard

hierarchical keys; hierarchical keys, managed by each individual OSD server, are also managed in the metadata server. That is, the overall procedures related to hierarchical keys are the same as the OSD standard [1] except for the key version mechanism. The different functionality related to a key version mechanism is described below in the subsection.

3.2 Implementation

The implementation may be divided into six major sub-functionalities: *the creation of a request integrity check value, the validation of request integrity check value, the creation of response integrity check value, the validation of response integrity check value, the creation of a credential, and the creation of a capability key.* The single sequence diagram among sub-functionalities, *the creation of a request integrity check value*, is presented in Figure 2.

As presented in Figure 2, the sequence diagram demonstrates the procedure of client's issuing a credential and generating a Command Descriptor Block (CDB) by function call steps; a user requests a credential for some operations of a particular object in a OSD server (that is, *MAC_set_integrity_check_value()*), the credential cache in a client is looked into (that is, *get_credential_from_cache()*), if not, a credential is requested and delivered from a metadata server (that is, *FMI_get_credential()* and *put_credential_to_cache()*), and a CDB including the credential with a integrity check value is generated by the MAC block (that is, *set_request_integrity_check_value()* or *set_data_out_integrity_check_value()*).

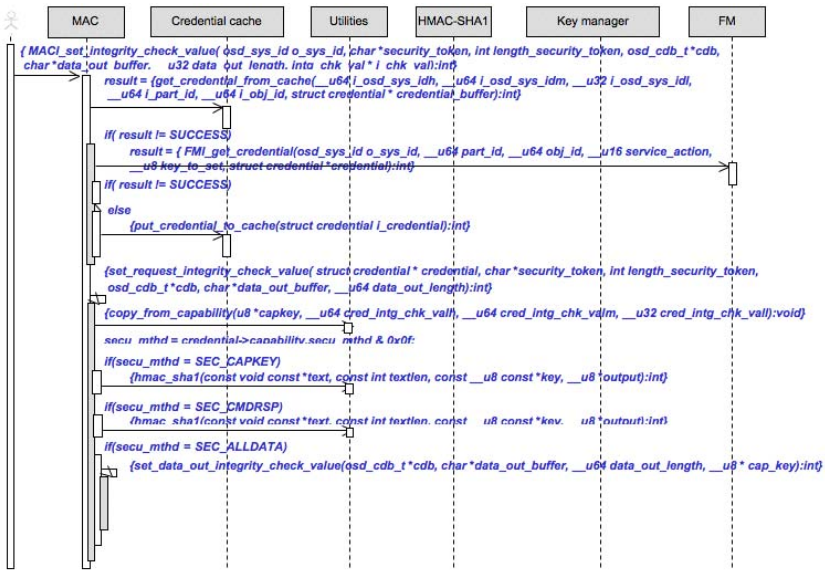


Fig. 2. The sequence diagram of the creation of a request integrity check value

3.3 Different Functionalities

Basic mechanisms and the libraries of our proposed security framework related to cryptography (encryption/decryption), hash function, and etc. are based on the OSD standard [1]. Several different functionalities, implemented on a security framework, are as follows:

- **The credential cache mechanism.** Cache mechanisms are not necessarily good for security. However, a simple cache mechanism, cached only until the expiration date, is adopted for credentials, in order to minimize the cost of issuing a credential from a client's accessing the same objects repeatedly, while there is no credential cache mechanism specified by [1].
- **The separation of normal and administrative operations.** Specified in [1], a client can request normal or administrative operations. However, some restrictions are placed on the implementation of a security framework because clients generally access OSD servers in order to request normal operations, such as read/write/execute a file. Only a metadata server can invoke commands related hierarchical keys, in order to improve the security level of these keys.
- **The default capability for GET ATTRIBUTE commands.** As far as the method of generating capabilities for GET ATTRIBUTE commands, used when issuing a credential, is concerned, there is no detail in [1]. In the proposed security framework implementation, a metadata server creates GET ATTRIBUTE commands using the default capability defined previously when a client issues a credential.
- **No key version.** The OSD standard specify a key version mechanism; the OSD standard specifies what is necessary to support a key version mechanism for the sake of clients' being able to access OSD servers with a previous key for all clients that do not recognize hierarchical keys are updated. The implemented framework does not fundamentally support a key version mechanism; a key version mechanism is used for the separation of clients' accessing OSD servers with either a credential in the cache or a credential issued by a metadata server.
- **No network faults and no clock synchronization.** Assuming that there are no network faults and no clock synchronization, as far as sharing the hierarchical keys between a metadata server and OSD servers is concerned.

4 Test Scenarios and Result

In this section, test scenarios and results are presented. The procedures of test scenarios are mainly based on the functionalities defined by the OSD standard.

4.1 Test Scenarios

Five scenarios are made up of and are achieved: a READ, a WRITE, a GET ATTRIBUTE, a SET KEY, and a SET MASTER KEY command. As an example, one of five scenarios, a READ command, is presented as follows:

1. *Client* initializes credential cache.
2. *OSD server* creates initial master key by using Random Number Generator (RNG) and initializes related data structures. (The initial master key created by the OSD server is delivered to the metadata server offline.)
3. *Metadata server and OSD server* create root key, partition zero key, partition keys, and working keys.
4. *Metadata server* generates the default capability for GET ATTRIBUTE commands. The *Client* constructs the CDB for a READ command. There is, however, no credential in the cache. The *Client* requests the metadata server to issue a credential.
5. *Metadata server* requests a credential for GET ATTRIBUTE commands in order to issue a credential.
6. *Metadata server* sets up related data structures for issuing the credential of GET ATTRIBUTE commands.
7. *Metadata server* creates a request integrity check value of GET ATTRIBUTE commands and transmits these commands to the OSD server. The *OSD server* validates the request integrity check value of the GET ATTRIBUTE commands from the metadata server. The following work is then accomplished.
8. *OSD server* creates a response integrity check value of GET ATTRIBUTE commands' results and transmits it to the metadata server. The *Metadata server* validates the response integrity check value of the responses from the OSD server.
9. *Metadata server* issues the credential and transmits it to the client.
10. *Client* stores the credential in the cache, constructs the CDB for a READ command (including a request integrity check value), and transmits the CDB to the OSD server. The *OSD server* validates the request integrity check value of the READ command from the client. Following works are done.
11. *OSD server* creates a response integrity check value of the READ command's result and transmits to the client. The *Client* validates the request integrity check value of the command from the OSD server.

As described above, this scenario is based on the implemented security framework for an OSD system, formulated differently from the OSD standard.

4.2 Test Result

The result of a READ command is presented in Figure 3.

As presented in Figure 3, a client requesting access to a OSD server firstly has to hold a specific credential, in order to open, write, and execute objects in a OSD server. To achieve this, the client looks up the credential in the credential cache of its MAC block, and if it exists, the client uses this credential, or if not, the client requests the metadata server to issue the legitimate credential. When requested to issue a credential, the metadata server checks access control lists and creates the credential for the client requesting it by supporting PSM and SM blocks. After issuing the credential, the client creates the CDB with

5 Conclusion

In this paper, in order to respond to the demands on security frameworks adopted on various network-based storage mechanisms, the design and implementation of a security framework, based on the OSD standard, is presented. For efficiency, there have been several different functionalities implemented on this security framework: the credential cache mechanism, the separation of normal and administrative operations, the default capability for GET ATTRIBUTE commands, no key version, no network faults, and no clock synchronization. This security framework for a OSD system is implemented based on the Linux kernel using kernel module programming and achieved according to the test scenarios of five commands: a READ, a WRITE, a GET ATTRIBUTE, a SET KEY, and a SET MASTER KEY command.

The main contribution of our proposed paper appears to be the implementation of a OSD security protocol based on Linux systems. In the future work, performance analysis and evaluation is going to be presented for various scenario in order to prove that this framework is effectively implemented compared with the OSD standard.

References

1. American National Standard for Information Technology, SCSI Object-Based Storage Device Commands (OSD), INCITS 400-2004, 2004.
2. P. Stanton, Securing Data in Storage: A Review of Current Research, ACM Computing Research Repository (CoRR) Technical Report 0409034, Sep. 2004.
3. G. A. Gibson and R. V. Meter, "Network Attached Storage Architecture," COMMUNICATIONS OF THE ACM, Vol. 43, No.11, Nov. 2000.
4. E. L. Miller, D. D. E. Long, W. Freeman, and B. Reed, Strong security for distributed file systems, Proc. of the 20th IEEE International Performance, Computing and Communications Conference (IPCCC 01), Phoenix, Apr. 2001, pp. 3440.
5. Cluster File systems, Inc., Lustre: A Scalable, High-Performance File System, <http://www.lustre.org/>.
6. PANASAS, Inc., Panasas White Paper: Object Storage Architecture.
7. IBM Haifa Laboratory, <http://www.haifa.il.ibm.com/projects/storage/objectstore/>.
8. A. Azagury, V. Dreizin, M. Factor, E. Henis, D. Naor, N. Rinetzky, O. Rodeh, J. Satran, A. Tavory, and L. Yerushalmi. "Towards an Object Store." Proc. of the 20th IEEE Symposium on Mass Storage Systems, 2003.
9. M. Factor, K. Meth, D. Naor, O. Rodeh, and J. Satran, "Object Storage: The Future Building Block for Storage Systems." Proc. of the Second International IEEE Symposium on Emergence of Globally Distributed Data, Jun. 2005, pp. 101-105.
10. J. Satran, K. Meth, C. Sapuntzakis, M. Chadalapaka, E. Zeidner, RFC 3720: Internet Small Computer Systems Interface (iSCSI), Apr. 2004.
11. Linux-iSCSI Project, <http://linux-iscsi.sourceforge.net/>.

A Snappy B+-Trees Index Reconstruction for Main-Memory Storage Systems*

Ig-hoon Lee¹, Junho Shim², and Sang-goo Lee¹

¹ School of Computer Science & Engineering, Seoul National University, Seoul, Korea
{ihlee, sglee}@europa.snu.ac.kr

² Department of Computer Science, Sookmyung Women's University, Seoul, Korea
jshim@sookmyung.ac.kr

Abstract. A main memory system employs a main memory rather than a disk as a primary storage and efficiently supports various real time applications that require high performance. The time to recover the system from failure needs to be shortened for real time service, and fast index reconstruction is an essential step for data recovery. In this paper, we present a snappy B+-Tree reconstruction algorithm called Max-PL. The basic Max-PL (called Max) stores the max keys of the leaf nodes at backup time and reconstructs the B+-Tree index structure using the pre-stored max keys at restoration time. Max-PL employs a parallelism to Max in order to improve the performance. We analyze the time complexity of the algorithm, and perform the experimental evaluation to compare its performance with others. Using Max-PL, we achieve a speedup of 2 over Batch Construction and 6.7 over B+-tree Insertion at least.

1 Introduction

Recovery algorithms have two parts: the *backup stage* where information needed for recovery is stored elsewhere during normal operation and the *restoration stage* where the contents are restored after a failure (using the backed up information) [1, 13]. In main-memory systems, the backup information is saved on disks and periodic checkpoints are used extensively with occasional full image dumps for backup [3, 6, 9, 15]. Reducing the time for index reconstruction is important for the speed of recovery since the time to construct the index makes up a greater part in the restoration process [4, 7, 10, 12]. This is especially true for main-memory database systems where fast processing and speedy recovery are critical. By storing a little more information at checkpoint, we attempt to reduce the time for index reconstruction utilizing the additional information. The size of this information needs to be as small as possible in order not to degrade the performance of normal operation. At the same time, the information should be sufficient enough to bring significant reduction in reconstruction time. The overall objective is to obtain the optimal balance between minimizing the

* This research was supported by the Ministry of Information and Communication, Korea, under the College Information Technology Research Center Support Program, grant number IITA-2005-C1090-0502-0016.

amount of information being stored in the backup stage and minimizing the amount of work that has to be done to restore the index.

In this paper, we focus on the B+-Tree index which has shown superior performance over T-tree indexes in main memory databases [11, 14]. We propose to store the maximal key values of each leaf node of an index. At reconstruction time, using the maximum key values, we are able to eliminate the need for node splits and also to introduce a degree of parallelism, thus reducing the overall index restoration time significantly.

The rest of this paper is organized as follows. Section 2 provides the related work. Section 3 illustrates our B+-Tree index reconstruction algorithm, and Section 4 provides the complexity analysis of the algorithm. Section 5 presents an experimental study. And finally, Section 6 provides the conclusion.

2 Related Work

2.1 Main Memory Index Structures

The index structure that has been popular for main memory systems is T-tree [8]. However, it has been shown that B-trees perform better than T-trees in multiprocessing environments with concurrency control [7, 14]. Moreover, B-trees have shown to be more suitable for the cache-conscious structure, which is very important for main memory systems since, with the advancement in CPU speed, a cache miss has become a critical degradation factor of performance [14]. Therefore, we will focus our discussions on B-Trees; particularly the B+-Tree index.

2.2 Reconstruction of the B+-Tree Index

B+-Tree Insertion Method. A simplest way of a B+-Tree is to insert keys one-by-one to the tree using the basic B+-Tree insertion algorithm. It requires a search from the root node to leaf nodes for the position of the given key, and moving keys within the leaf node. If the leaf node is full, the node is split and the split is propagated upwards. Moving keys and node split are serious performance degradation overheads. We call this basic insertion algorithm as B+-Tree Insertion throughout the paper.

Batch Reconstruction Method. Unlike B+-Tree Insertion, the leaf nodes are built first and then the internal nodes, so there are no node splits and moving keys within a node [5]. However, all data records must be reconstructed and the key values sorted before the index construction can start. While time can be saved from eliminating node splits and moving keys, the cost for sorting can be high and parallel processing is limited.

3 Index Reconstruction Algorithm

We propose to store the maximum values of each leaf node of an index at the backup stage and, using this information at the restoration stage, to reconstruct the index structure in a way similar to the batch reconstruction method but without the need to sort the entire list of key values. What we took notice of is the necessary information

for restoration of an index structure is the set of maximum key values of leaf nodes. That is, we can reconstruct the full index structure with only the maximum key values of each leaf node.

3.1 Backup

The checkpoint algorithm for backup employs the step of saving maximal keys of the B+-Tree index, as well as the step to make a backup of data records. The proposed method is independent of how data records are saved, so any of the existing algorithms, such as Fuzzy Checkpointing [4, 12] and log-based backups [1, 6, 13], The module for saving max keys from a B+-Tree index is shown in Fig. 3.1.

```

Max_checkpointBackupIndex()
for( i = 0; i < #INDEX ; i++ )
  tracer=
    index[i].firstTerminalNode;
  for( ; tracer != NULL ; )
    writeMaxKey(tracer.lastkey);
    tracer = tracer.next;
  end for
end for
end

```

Fig. 3.1. Checkpoint algorithm

```

reconstructDataIndex()
Max_constructIdxStructure();
reconstructData();
Max_insertKey2Index();
Max_sortLeafNodes();
end

```

Fig. 3.2. Restoration process

3.2 Restoration

The restoration of a main-memory database includes two stages. The reconstruction of data records and indices from a backup brings the database state up to the last checkpoint. The second stage of reflecting the redo and undo logs is needed to apply changes made up to the failure point. While the second stage is beyond the scope of this paper, we note here that our index reconstruction method is independent to the method employed in the second stage.

The index reconstruction steps of *Max* algorithm are as follows.

- i) Construction of an index structure
- ii) Inserting the record keys to the index structure
- iii) Sorting key values within each leaf node of the index

Construction of an Index Structure. The maximum key values of leaf nodes will be read in from backup and the leaf nodes are constructed. The parent nodes are then constructed from these nodes and the process is repeated until we have the entire index tree structure (Fig. 3.3). At this point, we will have an index structure with only the entries of the leaf nodes missing. While the Batch method must wait for all the key values to be available (thus must wait for data records to be restored first) and sort them to obtain the leaf nodes, we can build the index structure before, during, or after restoration of the data records.

```

Max_constructIdxStructure()
  tracer = terminalHead;
  for( ; (key = readMaxKey()) != NULL; )
    tracer.next = makeNewTerminalNode(key);
    tracer = tracer.next;
  end for
  for(child=terminalHead; child!=NULL; child = child.parent)
    if( child.next == NULL) return;
    parent = makeNewInternalNode();
    child.parent = parent;
    for(tracer=child; tracer!=NULL; tracer=tracer.next)
      if(parent.nKeys > NUM_KEYS_IN_A_NODE) then
        parent.next = makeNewInternalNode();
        parent = parent.next;
      end if
      parent.keys[parent.nKeys++] =
        tracer.keys[tracer->nKeys-1];
    end for
  end for
end

```

Fig. 3.3. Max algorithm: Construct an index structure

```

Max_insertKey2index()
  tracer = root;
  for(i=0;key=getRecordKey();
      i++)
    addr = findLeaf( key );
    memcpy(addr->last, key,
           KEY_REC_SIZE);
  end for
end

```

```

Max_sortLeafNodes()
  for(tracer=firstTerminalNode;
      tracer != NULL; )
    sort( tracer->keys );
    tracer = tracer->next;
  end for
end

```

Fig. 3.4. Max algorithm: (a) Inserting a key to the index (b) Sorting leaf nodes

Inserting Record Keys to the Index Structure. The data records must be reconstructed before the actual key values and record addresses are available. Each key-address pair is inserted into the appropriate leaf node by searching from the root node to leaf nodes as in regular B+-Tree insertions. (Fig 3.4 (a)). Within the leaf node, you could either try to find the correct position for the new entry as it is inserted or simply append it and sort the leaf node later. We propose to postpone the sorting of leaf nodes until no further insertion occurs.

Sorting Key Values in Leaf Nodes. When the insertion for every key-address pair is completed, the entries in each leaf node are sorted (Fig 3.4(b)) Here, you can allocate one or more leaf nodes to each context and process them in parallel.

3.3 Introduction of Parallelism: Max-PL

The purpose of using a main memory database system is for faster transaction processing than a disk-based one. In multi-processor systems, there are a number of ways

to introduce parallelism to main memory data recovery. For example, as soon as some portion of a table is read from the disk, index construction can start on that part of the data [1, 7, 9].

Max-PL is the algorithm that applies a parallelism to the Max algorithm. Fig. 3.5 shows the reconstruction process for the Max-PL algorithm. It uses the pipeline method in which the step of reconstructing a record data and the step of inserting a record key to an index structure are performed simultaneously. The `PL_reconstructData()` and `MaxPL_insertKey2Index()` are the same as the `reconstructData()` and `Max_insertKey2Index()` respectively, except for running as threads in parallel and synchronization between the two threads using the *conditional mutex*. Furthermore, note that `MaxPL_insertKey2Index()` can start after `MaxPL_constructIndexStructure()` constructs an index structure. Also the key in `MaxPL_insertKey2Index()` to be inserted is given from `PL_reconstructData()` and `MaxPL_sortLeafNodes()` is executed on the leaf node which is filled with keys as many as a fit-ratio. If several indexes are declared on a table, the method allocates context to each index declaration and make them take charge of index reconstruction.

```

reconstructDataIndex ()
  thread_create (PL_reconstructData);
  thread_create (MaxPL_constructIndexStructure);
  thread_create (MaxPL_insertKey2Index);
  thread_create (MaxPL_sortLeafNodes);
  thread_join ();
end

```

Fig. 3.5. Restoration process for Max-PL

4 Algorithm Analysis

First, we define terminologies as follows.

n is a number of records, m is number of entries that could be inserted into a node, and h is height of an index.

4.1 Backup Stage

In Max algorithm, maximum values of leaf nodes must be gathered and stored when backing up, unlike the other methods that do not need additional work at the backup stage. We show that the overhead of the additional work is less than 1% of the work needed for the whole data backup.

In our method, the size of the contents to be backed up for an index is,

$$\left(\frac{\text{size of a key}}{\text{size of a leaf node}} \right) \times \left(\frac{\text{number of leaf nodes}}{\text{total number of the index nodes}} \right) \times \text{total size of the index.} \quad (1)$$

The previous equation can be rewritten to

$$\left(\frac{\text{size of a key}}{\text{size of a leaf node}} \right) \times \left(\frac{mh - 1}{(mh - 1)/(m - 1)} \right) \times \text{total size of the index.} \quad (2)$$

For example, when an index node size is 1024 bytes and a key size is 4 bytes, the size of the contents to be backed up is less than 0.4 % of the whole index size.

Since index size is usually smaller than the actual data size, we can conclude that additional work of our method is 1.0 % or less of the work for the whole data backup. Moreover, by processing data backup and index backup in parallel, we may reduce the overhead even further.

4.2 Restoration Stage

The time complexity of Max algorithm can be derived by analyzing the time complexities of three steps, construction of the index structure, inserting record keys to the index, sorting the key values in leaf nodes.

Construction Step of an Index Structure. This step includes creating leaf nodes for every maximal key value. So the number of the created nodes is n/m .

And the number of the operation to compose internal nodes is as follows.

$$\left(\frac{n}{m}\right) \times \sum_{k=0}^{\log_2 n} \left(\frac{1}{m^k}\right) = \frac{nm - 1}{m(m - 1)} \quad (\text{where, } m \geq 2). \tag{3}$$

Therefore, we can get the time complexity, $O(n)$.

Inserting Record Keys to the Index Structure. In this step, we need to traverse from the root to leaf nodes of an index. So, for n records, the number of accesses to index nodes is $n \log_2 m$, and the number of key comparisons within each internal node is $\log_2 m$. Therefore the time complexity for the operation is $O(n \log_2 n)$.

Sorting Key Values in Leaf Nodes. Since a leaf node has m key values and we need to sort n/m leaf nodes, the time complexity of the step would be $((n/m) \times O(m \log_2 m))$. Rearranging, we can get $O(n)$.

So the time complexity of the Max index reconstruction algorithm is

$$O(n) + O(n \log_2 n) + O(n) = O(n \log_2 n). \tag{4}$$

In Table 1, we summarize the performance features of B+-Tree Insertion method, the Batch construction method, and the Max algorithm. The B+-Tree Insertion method incurs overhead of node split and moving keys within a node. A conservative estimate of the number of splits is n/m by assuming that a node split occurs every m

Table 1. Comparison summary

	B+-Tree Insertion	Batch Construction	Max
Elimination of node split & moving keys	No	Yes	Yes
Time complexity	$O(n \log_2 n)$	$O(n \log_2 n)$	$O(n \log_2 n)$
Additional work at backup	No	No	Yes
Parallel processing with data restoration	Yes	No	Yes

insertions. Then the time complexity for node split overhead will be $O((n/m)\log_2 n)$. Furthermore, since node split causes system calls for allocating memory and redistribute keys, the node split overhead is more significant than implied by the time complexity. The overhead of moving keys increases, as the number of entries in a node increases.

On the other hand, the batch construction method has no node split overhead. But, parallel processing is not possible since the whole data part must be reconstructed first. Max algorithm has no node split overhead, and allows for reconstructing data records and reconstructing the related index in parallel.

5 Experimental Evaluation

The experiments were run on Solaris 5.9 with 2 units of Sun UltraSparc III 1.2GHz CPU and 4Gbytes of RAM. All experiment programs were implemented in C, and compiled with cc of the Sun WorkShop 6 update 2 C 5.3, and used *-fast* option to create optimized code.

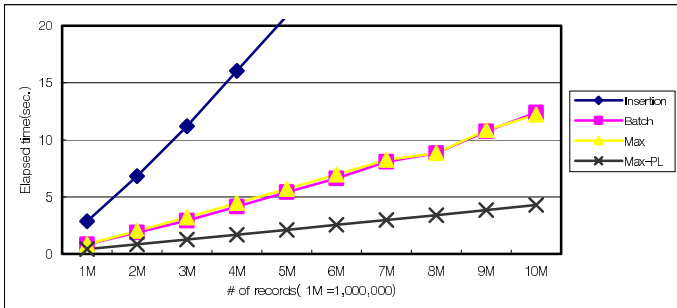


Fig. 5.1. Performance comparisons

The experiment results show the measured reconstruction time for a relation with one index. Size of each record is 128 bytes, and each record has a key value of 4 bytes. An index node size is 1024 bytes. As shown in Fig. 5.1, the total number of record was increased from 1 million to 10 million. It shows the difference of the index reconstruction time taken in accordance with total number of records. The B+-tree Insertion algorithm shows the slowest performance. While the Max algorithm shows similar performance to the batch construction algorithm, the Max-PL algorithm that introduced parallelism shows the best performance among all others. Using Max-PL, we could achieve a speedup of 2.0 to 2.9 over batch construction and 6.7 to 11.7 over B+-tree insertion.

Even when the total reconstruction time (including the time for reading and restoring data records) is considered, Max-PL achieves a speedup of 1.10 to 1.15 over the batch construction and 1.50 to 1.90 over the B+-tree insertion algorithm. We expect that, by reducing the I/O time to read data records from disk using a parallel I/O, the performance difference will increase, because most of total restoration time is spent on I/O.

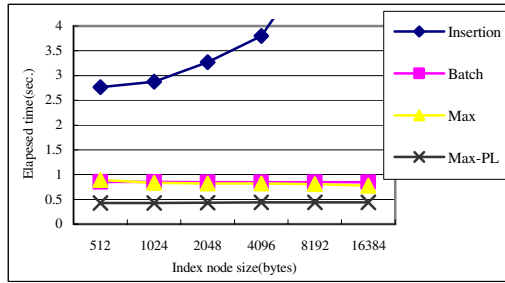


Fig. 5.2. Results on varied node sizes

The experiment results of the index reconstruction time in accordance to the node size is shown in Fig. 5.2 (memory page size= 8K bytes, number of records=1,000,000). For the case of the B⁺-Tree Insertion method, as the size of the node increases, it takes more time because the overhead of moving other keys within the node increases. On the other hand, for the batch and our method, as the node size increases, the height of a tree decreases, thus the index reconstructing time decreases.

6 Conclusion

We have proposed the method of enhancing the reconstruction of B+-Tree indices for main-memory systems. B+-Trees are popularly used in many practical systems, such as Oracle, Microsoft SQL Server, or PostgreSQL on DBMS, or JFS [2], XFS [17] on Linux. The proposed MAX-PL can be used to rebuild B+-Tree indices in those DBMSs or Linux file systems. Moreover, since many modern systems support multi-processor or multi-threading capabilities, the MAX-PL algorithm may benefit better parallelism to improve the performance.

The Max-PL algorithm can also be used with existing checkpoint methods such as the fuzzy checkpoint and the log-based checkpoint. Although the time complexity of Max-PL is $O(n \log_2 n)$, the same as the B+-Tree Insertion method, Max-PL eliminates the overhead of node split and allows for parallel processing in reconstruction process.

For restoration of an index, Max-PL achieves a speedup of 2.0 to 2.9 over the batch construction and 6.7 to 11.7 over the B+-Tree Insertion. Max-PL needs to store maximum keys of leaf nodes of an index at checkpoint time. However, the additional checkpoint data is under about 0.4% compared with the record data to be backed up mostly. So, Max-PL enables the loss of less than 0.4% at the backup stage to bring the gain of 200% or more at the restoration stage in recovery of main-memory systems.

References

- [1] H. Garcia-Molina and K. Salem, "Main memory database systems: an overview", IEEE Trans. on Knowledge and Data Engineering, Vol.4, No.6, pp.509-516, 1992.
- [2] IBM Corporation, <http://www-128.ibm.com/developerworks/linux/library/l-jfs.html>, JFS overview, Jan. 2000.

- [3] H. V. Jagadish, D. Lieuwen, R. Rastogi, and A. Silberschatz, "Dali: A High Performance Main Memory Storage Manager", Proc. 20th conf. on Very Large Databases, 1994.
- [4] H. V. Jagadish, A. Silberschatz, and S. Sudarshan, "Recovering from Main Memory Lapses", Proc. 19th Intl. Conf. on Very Large Databases, pp. 391-404, 1993.
- [5] S. W. Kim and H. S. Won, "Batch-Construction of B+-Trees", Proc. 2001 ACM Symposium on Applied Computing, pp. 231-235, 2001.
- [6] J. C. Lee, K. H. Kim, and S. K. Cha, "Differential Logging: A Commutative and Associative Logging Scheme for Highly Parallel Main Memory Database", 17th Intl. Conf. on Data Engineering, pp. 173-182, 2001.
- [7] S. S. Lee and Y. I. Yoon, "An Index Recovery Method For Real-Time DBMS in Client-Server Architecture", Proc. 4th Intl. Workshop on Real-Time Computing Systems and Applications, pp. 110-117, 1997.
- [8] T. J. Lehman and M. J. Carey, "A Study of Index Structures for Main Memory Database Management Systems", Proc. 12th Intl. Conf. on Very Large Databases, pp. 294-303, 1986.
- [9] E. Levy and A. Silberschatz, "Incremental recovery in main memory database Systems", IEEE Trans. on Knowledge and Data Engineering, Vol.4, No.6, pp.529-540, 1992.
- [10] D. Lomet and B. Salzberg, "Concurrency and recovery for index trees", VLDB Journal, Vol.6, No.3, pp.224-240, 1997.
- [11] H. J. Lu, Y. Y. Ng, and Z. P. Tang, "T-Tree or B-Tree: Main Memory Database Index Structure Revisited", Proc. 11th Australasian Database Conference, 2000.
- [12] J. H. Park, Y. S. Kwon, K. H. Kim, S. H. Lee, B. D. Park, and S. K. Cha, "Xmas: An Extensible Main-Memory Storage System for High-Performance Applications", Proc. 1998 ACM SIGMOD, pp.578-580, 1998.
- [13] R. Ramakrishnan and J. Gehrke, Database Management Systems, 3rd Edition, McGraw-Hill, 2003.
- [14] J. Rao, K. A. Ross, "Making B+ Trees Cache Conscious in Main Memory", Proc. 2000 ACM SIGMOD, pp. 475-486, 2000.
- [15] K. Salem and H. Garcia-Molina, "Checkpointing memory-resident databases", Proc. 5th Intl. Conf. on Data Engineering, pp 452-462, 1989.
- [16] A. Silberschatz, H. F. Korth, and S. Sudarshan, Database system concepts, The McGraw-Hill Companies, Inc. 1997.
- [17] Silicon Graphics, Inc., <http://oss.sgi.com/projects/xfs/>, XFS: A high-performance journaling file system, July 2005.

An Approximate Analytic Performance Model of Object-Based Storage

Qun Liu and Dan Feng

Key Laboratory of Data Storage System, Ministry of Education
School of Computer, Huazhong University of Science and Technology,
Wuhan 430074, China
liliuqun@mail.hust.edu.cn, dfeng@hust.edu.cn

Abstract. The Object-based storage has emerged as an important new field, distinguished from traditional network storage architecture by its focus on large-scale storage resource sharing and high-performance orientation. This paper presents a Stochastic Petri Nets (SPN) model that can be used to evaluate the performance of the object-based storage. But the problem of state space's explosion of SPN limits its ability to analyze complex and large-scale systems. An approximate analysis technique is proposed to replace the complexity model with the performance equivalence simplification model. This simplified model was used to validate the both well scalability and high performance of the OBS as the number of clients and OSD nodes increase.

1 Introduction

Current leading researches in the network storage have proposed using object-based storage (OBS) for increasing demands of bandwidth and capacity. In traditional network storage architectures, there are Storage Area Network (SAN) and Network Attached Storage (NAS). SAN, using block I/O command set, provides high random I/O and data throughput performance via direct access to the data at the level of the disk drive or fiber channel. NAS systems use NFS or CIFS command sets for accessing data with the benefit that multiple nodes can access the data as the metadata on the media is shared [1].

The OBS provides a new command set called object, bringing together the best characteristics of both blocks and files. Like blocks, objects are an original unit of storage that can be directly accessed on a storage device without passing through any metadata servers. Like files, objects are accessed using an interface that abstracts storage applications from the data attributes to store the object, thus making the object easily accessible across different platforms [2]. An object is of variable length and can store data about any kind of application. Just as objects can grow and shrink dynamically, object-based storage device (OSD) is responsible for all internal space management of the object.

The OBS is a promising architecture for high-performance large-scale distributed storage system. Through distributing the storage management, it can provide both scalability and performance. By stripping, replication and parity techniques, it can

also provide high availability and reliability [3]. The goal of object-based storage is to the performance and scalability of the whole system by taking the MDS off the main data path and allowing direct access to the storage devices. Hence, we are interested in questions how to optimize an OBS design and evaluate the performance.

There are a lot of previous works on the performance evaluation of the traditional storage system [4][5] and many analytical models only for disk array performance [6][7]. Analyzing the performance of object-based storage is very few.

In modeling the performance of storage systems, we have to consider two importance aspects: contention for resources and synchronization between various concurrent activities. The former aspect can be described by queuing network modeling, but the latter cannot [8]. The Stochastic Petri Net (SPN) can adequately be satisfied two ways.

The rest of this paper is organized as follows. Chapter 2 is presented bird's eye view of OBS. Then we propose an equivalence simplification model based on SPN model for OBS in Chapter 3. In Chapter 4, we describe useful performance measures and obtain numerical results for the OBS. Finally, we conclude this paper in Section 5.

2 Object-Based Storage

Different from the block, objects are of variable size and it can contain all types of data structures, such as files, database records, medical images and multi-media videos and audios in the OBS. The data structure is determined by the application. It also includes attributes describing characteristics of the data, for example, the creation time, access time, network bandwidth and delay. Moreover, the object can be scalable dynamically.

The OSD maintains storage metadata associated with the space allocation of the objects and the management of the free-space structures. It is built on a “flat” file system, achieving a flat one-dimensional space [9].

An obvious advantage of OBS is that the storage space allocation is managed by the OSD. The traditional block-based file system can be divided into the user component and storage component. The OBS keeps the user component unchanged in the Metadata Server (MDS) and offloads the storage component to the OSD, with the corresponding device interface transformed from block into object. Therefore user component in the MDS is responsible for mapping the logic names like filename to object ID. The storage component in the OSD manages the space allocation and data organization, and realizes flat directory mapping object ID to the block devices. Just owing to benefits of OBS conveniently makes and simplifies the SPN modeling.

According to the T10/SCSI OSD-2 protocol [10], objects can be divided into four types: Root Object, Partition Objects, Collection Object and User Object. Root object is the object of logic unit OSD, and each OSD only has one root object. Its attributes describe global characteristics for the OSD, such as total capacity, the number of partitions that it contains and the attributes associated with the data integrality. Partition object contains a set of collection objects and user objects, with its attributes including the user object number in the partition and the used storage capacity. Collection object is used to realize the quick index of user objects. A partition object may contain zero or more collection objects. A user object may belong to zero or more

collection objects. User objects are the most number, e.g. file and database record are stored in the user objects. Their attributes include the data creation and modification etc. Partition_ID and User_ID identify all the objects. Besides, objects' attributes reside on the OSD, which makes the data sharing between different storage applications become considerably easier. Meanwhile, possessing of the ability of processor, OSD has become an intelligent storage device for self-management. OSD can comprehend some relationships between the blocks on the device, and can use the information to optimize the data layout, prefetch the application data and organize the data.

3 SPN Model

3.1 SPN Introduction

The SPN is a formal model of information flow. It is an effective method for describing and analyzing the flows of information and controls in computer system [11]. And it is used as important tools to evaluate computer system performance.

Firstly, we review the definition of SPN. The SPN is obtained by associating with each transition in a PN an exponentially distributed firing time. It is a 5-tuple (P, T, A, M_0, R) , where

P is the set of places;

T is the set of transitions, and $P \cup T = \emptyset, P \cap T = \emptyset$;

A is the set of input and output arcs, $A \subset (P \times T) \cup (T \times P)$;

M_0 is the initial marking, $M_0 = \{m_1^0, m_2^0, \dots, m_n^0\}$;

$R = \{r_1, r_1, \dots, r_m\}$ is the set of firing rates associated with the SPN transition.

A marking represents the number of tokens in each of the places. A marking may be viewed as a mapping from the set of places P to the natural numbers N . It is said that a SPN is k -bounded if there exists a finite nonnegative integer k such that for every marking M in the reachability set, and for every place P_i , $M(P_i) < k$.

A transition represents a class of possible changes of markings. A change, called transition firing, consists of removing tokens from the input places of the transition and adding tokens to the output places of the transition according to the expressions labeled on the arcs. In SPN models, transitions can be partitioned into two types: timed and immediate transition. The timed transition is used to represent the operations on the request executing or data storing, and is associated with exponential distributed random firing time. The immediate transitions fire in zero time once they are enabled.

The state space of a model makes up of the set of all markings reachable from the initial marking through the occurrence of transition firing. A SPN is isomorphic to continuous time Markov chain (MC), and there is a one-to-one relationship between markings of the SPN and states of the MC[12].

In following section, we will clarify with the modeling for the OBS.

3.2 SPN for OBS

The client is the user in the OBS system. When it sends file request to the system, client firstly sends it to MDS, obtaining file metadata and information associated with

OSD, then it directly interacts with OSD. The MDS is accountable for providing the whole naming space and taking off the main data path. The function of MDS in the OBS is much less than in the traditional network storage systems with block and file I/O interface. So the MDS is not considered in this paper.

The following common assumptions are made in SPN modeling for OBS:

- (1) Data transmission and delay are also not considered in the high-speed network or the OSD;
- (2) The service discipline of each OSD is FIFO;
- (3) There are n OSD nodes working synchronization;
- (4) The OSD nodes are same kind of devices;
- (5) The execution time of object requests in different OSD and the different phase is assumed to be exponentially distributed.

Figure 1 shows the SPN model for OBS. The requests service and data storage are represented by timed transitions associated with exponential distributed firing time. The request sending to the OSD nodes and finishing object service are represented by immediate transitions with zero firing time. In the model the tokens can represent number of object requests. And the meaning of the places and transitions in Figure 1 are described in the following:

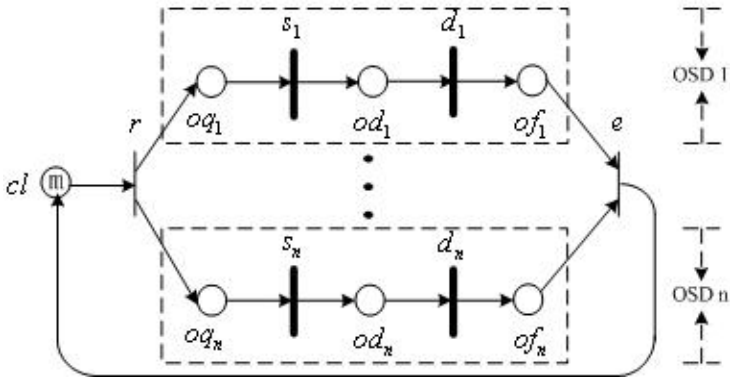


Fig. 1. A SPN model for OBS

• Places

cl : "client requesting" place. It contains m tokens and represents number of requesting client or object requests.

oq_k : "object request queue in the k -th OSD" place. It represents the condition that the request queue is waiting to serve in the k -th OSD when a token is in it.

od_k : "disk I/O request queue in the k -th OSD" place.

of_k : "the k -th OSD finishing disk I/O request" place.

• Transitions

r : "send an object request command" transition.

s_k : "allocate object storage space or lookup object in the k -th OSD" transition.

The transition firing time is related to $1/\alpha$ and the transition rate is α_k .

d_k : "serve disk I/O request in the k -th OSD" transition. The firing rate of the timed transition s_k is β_k .

e : "end disk I/O request" transition.

2.3 Performance Equivalence Simplification Model

To analyze the performance of the SPN model in Figure 1, we can construct the corresponding MC of the model. Based on the MC and state transition rates, we can get the state transition matrix and obtain all the steady state probabilities to calculate the performance measurements. The SPN model with m places of queues is generally equivalent to an m -dimension MC. So the MC of the model in Figure 1 is at least with $m \times n$ dimensions. And the state space of the MC grows exponentially with the increase of m and n . When the state space is large, solving the state equations of the SPN model is impossible for the practical computing systems [13].

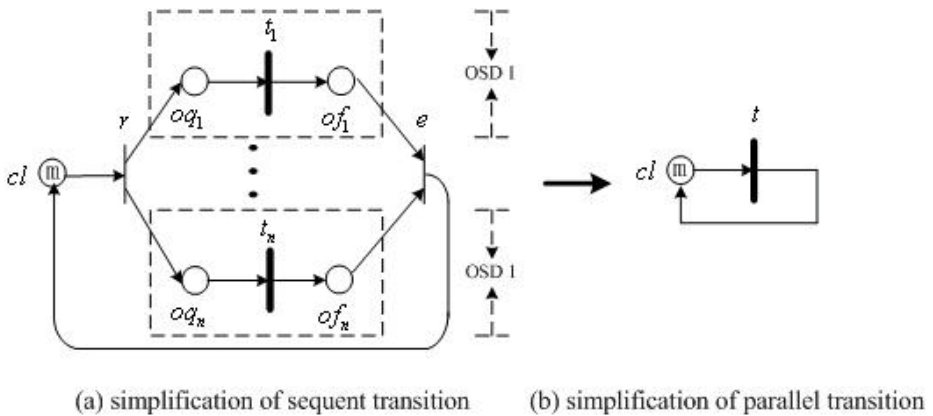


Fig. 2. Performance equivalence simplification model for OBS

In order to reduce the complexity of the model solution, we utilize performance equivalence model [14][15] for simplification of sequent and parallel transition of the SPN model in Figure 2. In this way, a complicated model can be equally transformed into a simplified model. Figure 2 shows the performance equivalence simplification model of Figure 1.

Compared with Figure 1, Figure 2(a) has deleted place od_k , transition s_k , and some relevant arcs. We have replaced transition d_k with t_k ($1 \leq k \leq n$), which is the timed transition modeling the service object at the k -th OSD. The firing rate of the timed transition t_k is λ_k , and

$$\frac{1}{\lambda_k} = \frac{1}{\alpha_k} + \frac{1}{\beta_k}. \tag{1}$$

Figure 2(b) simplifies parallel transitions in figure 2(a) and becomes the simplest equivalence model for OBS. The timed transition rate of the t is λ , and

$$\frac{1}{\lambda} = \sum_{i=1}^n \frac{1}{n\lambda_i} - \sum_{i=1}^{n-1} \sum_{j=i+1}^n \frac{1}{n(\lambda_i + \lambda_j)} + \sum_{i=1}^{n-2} \sum_{j=i+1}^{n-1} \sum_{k=j+1}^n \frac{1}{n(\lambda_i + \lambda_j + \lambda_k)} + \dots + (-1)^{n-1} \frac{1}{n \sum_i \lambda_i} \tag{2}$$

4 Approximate Performance Analysis

In SPN models, the performance measurements can be gotten based on the steady-state probabilities. We introduce the metrics used in this paper for evaluating the performance for OBS.

The system throughput is an important performance measurement. $P[M]$ is the steady state probability for the marking M . The throughput $T(t)$ of transition t is

$$T(t) = \lambda \sum_M P(M). \tag{3}$$

The throughput T of OBS is:

$$T = \sum_{i=1}^m T(t). \tag{4}$$

Response time is another important performance metric. In this paper, we study the response time of the OSD node. $N(p)$ is the average number of tokens in place p . The response time R by transition t_k is

$$R = \max \left[\frac{N(p)}{nT_k} \right], k = 1 \dots n. \tag{5}$$

To avoid the state space explosion and simplify the model solution, without loss of generality, we consider that OBS has one to five OSD nodes in our example. Corresponding to the parameter value is shown in table 1. These service rates are assumed to have been known beforehand by gathering the statistics.

Table 1. Corresponding to the parameter value in the OSD

$n - th$	1	2	3	4	5
α_n	25	20	16	40	25
β_n	40	25	20	16	50

The transition rate of the OBS for different state in equivalence simplification model is shown in table 2.

Table 2. Firing rate in equivalence simplification model

N	1	2	3	4	5
λ_n	15.38	11.11	8.89	11.43	16.67
λ	15.38	17.06	14.43	15.56	16.5

Table 3 and 4 indicate the system throughput and response time of the different client requests in different OSD nodes. These numerical results show that system throughput increases with adding the number of client requests and response time decreases with adding the number of OSD nodes in the same request numeral.

Table 3. System throughput

N	1	2	3	4	5
$T(m = 1)$	15.38	17.06	14.43	15.56	16.5
$T(m = 2)$	30.76	34.12	28.86	31.12	33
$T(m = 4)$	61.52	68.24	57.72	62.24	66

Table 4. System response time (s)

N	1	2	3	4	5
$R(m = 1)$	0.065	0.045	0.0375	0.028	0.0225
$R(m = 2)$	0.13	0.09	0.075	0.056	0.045
$R(m = 4)$	0.26	0.18	0.15	0.112	0.09

5 Conclusions

The SPN is a powerful modeling and analyzing tool for system performance evaluation. This paper presents a modeling and analysis technique based on SPN to research OBS system. But the problem of state space's explosion of SPN limits its ability to analyze complex and large-scale systems. We propose an approximate analysis method called performance equivalence simplification to reduce the complexity of the model solution. This simplified model can validate the both well scalability and high performance of the system when the number of object requests and OSD nodes increase.

Acknowledgements

This work was supported by the National Basic Research Program of China (973 Program) under Grant No.2004CB318201, National Science Re-search Program of China No. 2004CCA07400, Huo Yingdong Education Foundation under Grant No.91068, and the National Science Foundation of China under Grant No.60273074 and No.60303032.

References

1. Panasas Inc. WHITE PAPER: Object Storage Architecture: Defining a new generation of storage systems built on distributed, intelligent storage devices. Rev. 1.0-10/19/2003, www.panasas.com/docs
2. Mike Mesnier, Gregory R. Ganger, Erik Riedel.: Object-Based Storage. IEEE Communications Magazine, pp. 84-90, August 2003
3. Feng Wang, Scott A. Brandt, Ethan L. Miller, and Darrell D. E. Long: OBFS: A file system for object-based storage devices. In Proceedings of the 21st IEEE / 12th NASA Goddard Conference on Mass Storage Systems and Technologies, pages 283-300, College Park, MD, April 2004. IEEE
4. Daniel A. Menascé, Odysseas I. Pentakalos, Yelena Yesha: An Analytic Model of Hierarchical Mass Storage Systems with Network-Attached Storage Devices. SIGMETRICS 1996: 180-189
5. Yao-Long Zhu, Shu-Yu Zhu, Hui Xiong: Performance. Analysis and Testing of the Storage Area Network, 19th. IEEE Symposium on MSST, USA, April 15-18, 2002
6. Dan Feng, Xingrong Zhou, Hai Jin, Jiangling Zhang: Utilization of Disk Drives for RAID. IEEE Proceedings of the 1997 Conference on Advances in Parallel and Distributed Computing, March 19-21, 1997, Shanghai, China, pp.186-189
7. E.K. Lee and R.H. Katz: An analytic performance model for disk arrays. In Proceedings of the 1993 ACM SIGMETRICS, pages 98-109, May 1993
8. K. Kant: Introduction To Computer System Performance Evaluation. McGraw-Hill, 1992.
9. Dan Feng, Ling-jun Qin, Ling-Fang Zeng, Qun Liu: a Scalable Object-based Intelligent Storage Device, Proceedings of the Third International Conference on Machine Learning and Cybernetics, Shanghai, 26-29 August 2004,387-391
10. T10/1731-D Revision 0,October 2004: SCSI Object-Based Storage Device Commands -2 (OSD-2), <http://www.t10.org>
11. M. A. Marsan, G. Balbo, and G. Conte: A class of generalized stochastic Petri nets for the performance evaluation of multiprocessor systems," in Proc. Performance 83, ACM Sigmetrics, Oct. 1983, pp. 198-199
12. G. Ciardo, and K. S. Trivedi: A Decomposition Approach for Stochastic Reward Net Models, Performance Evaluation, 1993, Vol. 18, pp. 37-59
13. Zhiguang Shan, Chuang Lin, and Fengyuan Ren: Modeling and Performance Analysis of a Multiserver Multiqueue System on the Grid. Proceedings of the 9th International Workshop on Future Trends of Distributed Computing Systems (FTDCS 2003), IEEE Computer Society, 28-30 May 2003, San Juan, Puerto Rico, USA, pp. 337-343
14. TIAN Li-qin, LIN Chuang, ZHOU Wen-jiang: Performance Equivalent Simplification of Sequent and Parallel Transitions in Stochastic Petri Nets, CTA ELECTRONICA SINICA, Vol.30, No.8, Aug.2002: 1134-1137
15. Zhangxi Tan, Chuang Lin, Hao Yin, Ye Hong: Approximate Performance Analysis of Web Services Flow Using Stochastic Petri Net. Proceedings of the International Workshop on Grid and Cooperative Computing, LNCS 3251, pp.193-200, 2004

OASIS: Implementation of a Cluster File System Using Object-Based Storage Devices

Young-Kyun Kim, Hong-Yeon Kim, Sang-Min Lee,
June Kim, and Myoung-Joon Kim

Internet Server Group, Digital Home Research Division,
Electronics and Telecommunications Research Institute,
161 Gajeong-dong, Yuseong-gu, Daejeon, 305-350, Korea
{kimyoung, kimhy, sanglee, jkim, joonkim}@etri.re.kr

Abstract. An emerging object-based storage device (OSD) architecture facilitates the creation of self-managed, secure, and shared storage. Despite of its potential of greatly improving the scalability and performance of distributed storage systems, only high-end applications direct their attentions to OSD. Currently, it is necessary for mid/entry-levels applications to employ the OSD technology. In this paper, we present OASIS, a cluster file system using OSD, which is designed to combine the iSCSI protocol with OSD SCSI. Our experiments show that our system matches up to performance of existing systems and achieves linear scalability of performance as the number of clients increased.

1 Introduction

Fundamental advances in storage system architectures and storage device interfaces greatly improve the scalability and performance of storage systems. In the aspect of storage architectures, storage systems focus on the separation of metadata management from the data path, which is a key to the scalability of distributed storage. By this separation, clients directly access to storage devices. It also distributes the system metadata without a central bottleneck. Many systems have been built on this architecture, including IBM Storage Tank, the Lustre File System, and the Panasas Cluster Storage [6, 7, 9, 11].

In the field of storage devices, a new standard interface for a storage device is defined as Object-based Storage Device (OSD) to allow storage devices to manage the layout of object data within the device [12]. OSD differs from standard storage devices such as FC or IDE, with their traditional block-based interface. OSD enables the creation of self-managed, heterogeneous, and secure storage for storage networks. When a variety of storage systems employ OSD, they offload space management into storage devices and reach new levels of scalability.

Although storage systems using OSD have advantages to scalability and performance, there are a few barriers for wide acceptance of OSD technology. Those are already mentioned in [2]. The main barrier is that hosts no longer access blocks of data on disk, rather, they refer to objects and offsets within objects. This requires the changes of basic I/O subsystems in the system stack. Moreover,

clients accessing the storage device should be changed because the hosts do not handle space management anymore.

Up to date, only a few systems using OSD are introduced in the industry. To support large or highly distributed and scalable applications they readily accept the OSD technology and it should be an indispensable component in their systems. The representative systems adopting OSD for highly scalable storage are the PanFS cluster file system, the Lustre SAN file system, and the zFS distributed file system.

Panasas [7] announced the ActiveScale Storage Cluster. It is comprised of the OSDs, the PanFS MetaData Server (MDS), the Panasas File System (PanFS), and Gigabit Ethernet network fabric. PanFS provides direct and parallel access to the OSDs when it needs file data and MDS manages out-of-band metadata operations. While Panasas actively does the standardization effort, OSD is not standard-compliant currently.

Cluster File Systems Inc. developed an open source file system, Lustre [1, 6], in order to be a highly scalable SAN file system. It is built out of three components: clients, Cluster control-system, and Object Storage Targets (OSTs) where a variety of high speed networks such as Quadrics networks, Myrinet, Fibre Channel, Infiniband, and TCP connect them together. As alike as PanFS, Lustre also uses a proprietary OSD to provide very high performance.

zFS [9] is the IBM research project aimed at building a decentralized file system that distributes all aspects of file and storage management over a set of cooperative machines interconnected by a high-speed network. zFS provides applications with a distributed file system. While the Panasas ActiveScale and Lustre share the same concept of the storage architecture, zFS does not. That is, it distributes metadata management into the OSDs instead of the centralized management of meta-data.

All systems as stated above are concentrating their attentions only on highly scalable and high performance storage systems. This means that systems basically require high speed networks including FC, Infiniband, etc. and they use their native protocols accessing the OSDs, which are not standard compliant, and proprietary interfaces of OSD for high performance. As a result, this makes the OSD adoption slower in many applications including small scale storage systems. We think that it is possible for OSD to be more prevalent in many applications by emphasizing conformance of the standard OSD interface and a standard protocol accessing networked storage in the Gigabit Ethernet network that is the most common among storage network fabrics.

In this paper, we present a scalable cluster file system using OSD, OASIS¹, developed for the use of the OSD technology in large-scale distributed storage systems. The basic idea of OASIS is that it is to comply with the T10 OSD specification and to deploy the iSCSI protocol which is widely accepted in the field of the storage industry, for accessing the OSDs. We show the design and implementation of OASIS and describe the experiment results of OASIS so that illustrate the performance implications of OASIS.

¹ OASIS: Object-based storage Architecture for Scalability, Intelligence, and Security.

The rest of this paper is organized as follows: In section 2, we describe the details of OASIS FS, that is, OASIS FS's architecture and the functionality of various components. Section 3 shows various experiments of the implementation result and examines the performance implications of OASIS. Finally, in Section 4, we summarize our work.

2 OASIS Architecture

OASIS is a research prototype that is a cluster file system deploying OSD in an asymmetric file systems environment similar to Lustre and PanFS. The design and implementation of OASIS is aimed at building a highly scalable file system that operates equally well on few or hundreds of machines connected by TCP/IP over Gigabit Ethernet. More specifically, the major objectives of OASIS are as follows.

- To achieve high scalability, it separates storage management from file management and metadata operations from the data path by using the object-based storage device.
- It totally complies with the standard OSD SCSI T10 specification.
- For easy of acceptance of the system, it provides the connectivity infrastructure that binds multiple components of the system over the Gigabit Ethernet network.
- For no single points of failure, it supports the fail-over cluster of metadata servers.
- It leads to an almost linear increase in performance whenever a computing node is added.

OASIS storage devices are network-attached OSDs which provide an object-level interface to the file data and use iSCSI for its SCSI transport. Each OSD manages the layout of objects and autonomously serves and stores objects. Also, the metadata server cluster is in charge of namespace management and authentication, etc. providing clients with the file to objects mapping. Clients with the OASIS client file system module directly communicate with the OSDs in order to retrieve the objects to the file they wish to access.

There are three components in OASIS and Figure 1 demonstrates all the components of it.

- The OASIS OSD Target (OASIS/OST) is a self-managed storage device. It lays out, manages, and serves objects through the OSD command interface. We assume that the OSTs contains a processor, RAM, the Gigabit Ethernet network interface, and disks.
- The OASIS MetaData Server (OASIS/MDS) supports all file system namespace operations including file lookup, file creation, and file and directory attribute manipulation. Also, it allows clients to share file data at the same time of maintaining cache coherency on all clients.

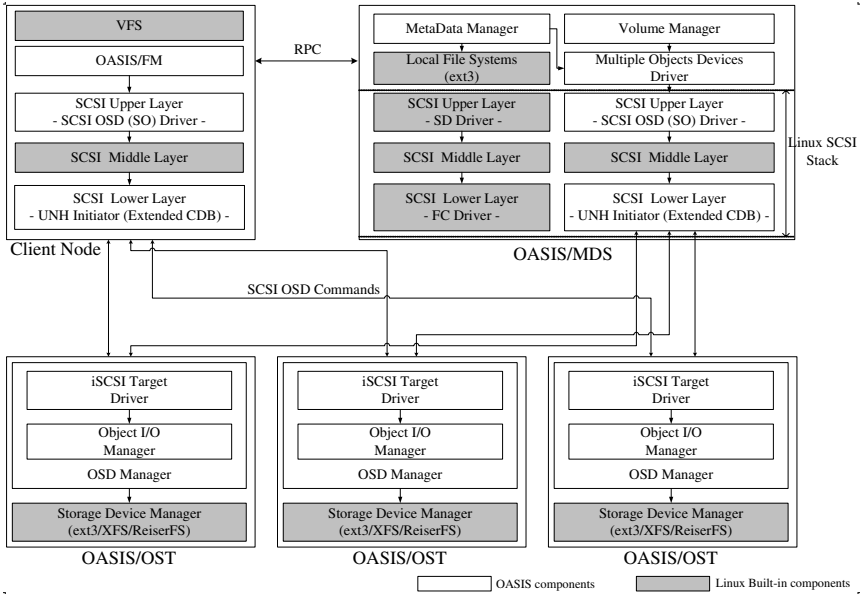


Fig. 1. OASIS components

- The OASIS File System (OASIS/FS) runs on the clients on which they want to use OASIS. It presents to the client the standard POSIX API and provides access to OASIS files and directories. To access file data, it addresses the OSDs directly.

The operation of OASIS is as follows: Applications running on a client machine make file system requests to OASIS/FM on that machine. OASIS/FM preprocesses the requests and queries the clustered metadata servers, OASIS/MDS, to open the files and get information that is used to determine which objects comprise the files. OASIS/FM then contacts the appropriate OASIS/OST to access the objects that contain the requested data, and provides that data to the applications.

2.1 OASIS/OST Satisfying T10 OSD

OASIS/OST is the network-attached storage device on which file data are created, and from where they are retrieved. It provides the standard OSD SCSI T10 protocol and uses iSCSI for its SCSI transport in order to create and delete objects, and write and read byte-ranges to/from the object to the file data.

OASIS/OST is comprised of the OSD manager and the storage device driver. The OSD manager is the kernel-loadable module that implements T10 OSD protocol over iSCSI. On the other hand, the storage device driver is to support data storage within the local file systems, such as ext3, ReiserFS, and XFS. This is similar to the Lustre’s OST, except SCSI OSD commands over TCP/IP.

The OSD manager is divided into the iSCSI target driver and the object I/O manager. The iSCSI target driver is only to support the extensions to iSCSI that are needed to for OSD commands. As a result, OSD commands between clients and targets are transported as SCSI OSD commands over TCP/IP. The object I/O manager is a key component of OASIS/OST. It takes charge of encapsulating and interpreting OSD commands, managing the data layout including the allocation of object data as well as object attributes, executing the security enforcement, and carrying out data I/O with the storage device driver. With this design, we developed it that runs on a Linux platform and is implemented over the local file systems. We think that OASIS/OST provides the flexibility required to adopting new technologies and new types of file systems.

The metadata associated with the objects stored in the OSDs are managed by OASIS/OST and then, the metadata server maintains only one object per OSD, regardless how much data that the object has. This reduces the metadata management burden on the metadata server and greatly increases the metadata server's scalability.

2.2 OASIS/MDS with Reliability and High Availability

OASIS/MDS takes charge of file and directory management and maintains cache consistency for clients of the same file. For the scalability, reliability, and availability of OASIS, OASIS/MDS provides the following key functions:

Basically, OASIS/MDS implements a file structure on the storage system. This includes directory and file creation and deletion and access control. Whenever a client opens a file, the metadata server performs the permission and access control checks associated with the file and returns the inode with the associated map that enumerates the OASIS/OSTs over which the file data is located.

For guaranteed metadata coherency on multiple clients, OASIS/MDS strictly protects all metadata operations. Clients with the OASIS/FMs are guaranteed to always see the same view of the namespace, and will receive consistent results for update operations. In addition to metadata coherency, OASIS/MDS assists client-based data caching by notifying the OASIS/FMs when changes in a cached data impact the correctness of client's cache.

The metadata server provides online storage management by grouping multiple OASIS/OSTs into logical volumes to improve disk utilization and eliminate storage-related downtime. This is done by cooperating with the multiple object devices driver (MOD) that provides virtual devices that are created from one or more independent underlying OASIS/OSTs. It performs functions such as mirroring (RAID1), RAID 0/5, and linear expansions of OASIS/OSTs. Also, the metadata server always monitors the status of the OASIS/OSTs participating in logical volumes. When a certain failure occurred, it detects and executes the recovery.

To eliminate the single points of failure, OASIS supports two metadata servers in an active/standby failover configuration. If the active OASIS/MDS fails, the other node is configured to automatically take over all metadata services. For

achieving MDSs failover, OASIS/MDSs use the shared storage device on which the metadata file system is reside.

To support above mentioned services, OASIS/MDS is comprised of the metadata manager, the volume manager, the MOD driver, and a metadata repository. The metadata manager contains the network interface for communicating with clients through RPC, the namespace manager that is responsible for various namespace operations, and the lock server for cache coherency among multiple clients. Multiple logical volumes can be configured by the combination of the volume manager and the MOD driver that consists of a raid0, a raid1, a raid5, and a linear module. We implement kernel-loadable modules, running on Linux, for OASIS/MDS except the metadata repository. We build the metadata repository of OASIS/MDS on ext3 that resides on the shared storage for easy implementation of failover.

We believe that it is possible for OASIS to increase the scalability of the system including supports of more clients and more storage by both decoupling of the datapath from the control path and supporting the dynamic volume management.

2.3 POSIX-Compliant and Light-Weight OASIS/FM

Whenever a client wants to use OASIS, a kernel-loadable module such as OASIS/FM should be installed on the client. OASIS/FM presents a POSIX file system interface and provides access to OASIS files and directories. It provides the following functions:

OASIS/FM provides the standard POSIX interface for applications to perform operations such as superblock operations, inode operations, and file operations.

It also provides caching in the client for incoming data from OASIS/OSTs as well as metadata from OASIS/MDS. In order to cache all data in OASIS/FM, it uses the Linux buffer/page caches. Hence, OASIS/FM automatically supports the read-ahead cache for prefetching file data and the write-back cache for efficient aggregation of multiple data writes, which seem to be inherent functions of the Linux VFS (Virtual File System).

Clients with OASIS/FM directly access multiple OSTs by the help of the MOD mentioned in Section 2.2. Dissimilar to Lustre, OASIS does not support stripes on a per file basis, but MOD stripes files across multiple OSTs on the file system basis being mounted. Therefore, clients take advantage of utilizing the RAID functions of the system.

OASIS/FM uses the iSCSI protocol so that it can transmit the OSD SCSI commands and the data payload across TCP networks. To enable iSCSI communications, it provides an iSCSI OSD initiator according to the Linux SCSI stack. The iSCSI OSD initiator is comprised of the SCSI OSD (SO) driver that is to construct and parse OSD SCSI commands satisfying the T10 standard and the iSCSI initiator that is to send/receive both OSD SCIS commands and data payload across the network. We use the UNH initiator [10] as the iSCSI initiator and extend it to support the extended CDBs (Command Descriptor Blocks) for OSD commands.

Excluding the MOD driver, OASIS/FM consists of very light-weight modules. We expect that it will be easy to make it portable for other platforms including Windows XP because of its small size and simplicity.

3 Highly Scalable Performance

We implemented all components of the OASIS prototype running on Fedora Core 3 Linux, kernel version 2.6.10. In this chapter, we show the experimental results of the OASIS system by the well-known file system benchmark tools such as IOzone [5] and Iometer [4], demonstrating the scalable performance of our prototype.

3.1 Experimental Setup

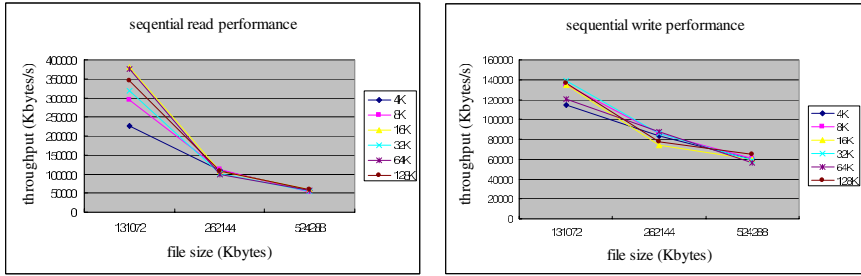
All of the experiments were executed on servers with a Xeon 3.0 GHZ CPU, 512MB of RAM, and a Gigabit Ethernet NIC. More specifically, the test servers include 10 OASIS/OSTs, 2 OASIS/MDS nodes, and 10 client nodes with the OASIS/FMs and all of the them are connected to a Gigabit Ethernet switch. Also, each OASIS/OST equips with two SATA/1.5 disks.

For each experiment, we maintained that the memory size of each client is to be 256 MB and that of each OST to be 512 MB. Also, we unmounted the directory that mounts the OASIS file system to purge the buffer/page cache, then mounted the OASIS file system to run the benchmarks. We repeated these steps ten times and took the average of the performance numbers obtained.

In this experiments, we used two benchmarks. One is to measure the performance of both the sequential read/write and the random read/write of a file in which the file size varies from 128 MB to 512 MB. The other is the aggregated performance benchmark that measures the aggregated read performance of multiple reads requested by clients. During the second experiment, all of clients do not read the same file but each client reads its files in the file system.

3.2 Performance Implications

Figure 2(a) illustrates results of the first benchmark that is performance of single request type such as sequential read or sequential write and allows us to examine the performance of our file system. As seen in Figure 2(a), OASIS exhibits the throughput of about 100 MB/sec for all read operations which access cached data on OASIS/OST. On the other hand, it shows the throughput of 40 MB/sec for the operations that it is necessary to perform physical disk operations in the OASIS/OSTs. From this benchmark, we examined that data caching plays an important role in OSDs to satisfy high performance requirements. As compared with Lustre, our prototype nearly matches up to performance of Lustre for both cache-hits operations and all operations with disk I/Os. Also, Figure 2(b) shows how the performance scales linearly with the number of clients in OASIS. We experimented with 10 clients and 10 OSDs, then identified that performance



(a) Performance on a workload of IOzone



(b) Linear scalability of read performance

Fig. 2. OASIS performance benchmarks

scales linearly for 1 to 10 clients. It illustrates the graph peaks at about 900 MB/sec for sequential read operations on cache-hits data of OSTs. By doing the benchmark, we examined that OASIS continues to provide increased aggregated throughput as the number of clients increases.

In addition to formal tests, we tested OASIS in the hardware environment employing TOE (TCP Offload Engine) hardware accelerators that are installed on clients and OSDs. Through this experiment, we ascertained that OASIS had a little bit performance increase by about 3%. It implies the OASIS system provides enough performance without any hardware accelerator.

4 Conclusions

The emerging technologies based on both of iSCSI and OSD are promising for large-scale and high performance file systems. Not only iSCSI and OSD but the out-of-band metadata operations give storage systems chances for providing high scalability and performance.

For dissemination of object-based storage devices and achievement of the file system using OSD, we have designed and implemented OASIS, a cluster file system targeted for the standard compliant technologies being widely accepted in industries. Currently, OASIS supports the mandatory interface of the T10 OSD specification and transports the OSD commands and data payload through the standard iSCSI protocol.

We have tested the OASIS prototype. In particular, our experiments show that OASIS can provide enough performance for high-end applications and OASIS performance scales linearly to support a large number of clients by distributing the load of a number of clients across OASIS/OSTs. With this results, we believe that OASIS will be a good candidate for highly scalable cluster file systems.

References

- [1] Braam, The Lustre Storage Architecture, Technical reprot, Cluster File System, Inc., 2002. <http://www.lustre.org/docs/lustre.pdf>
- [2] Factor, Meth, Naor, Rodeh, Satran, Object Storage: The Future Building Block for Storage Systems, A Position Paper IBM Labs in Israel, Hifa University, Mount Carmel, <http://www.haifa.il.ibm.com/procject/storage/objectstore>
- [3] IETF, <http://www.ietf.org/html.charters/ips-charter.html>
- [4] Iometer, <http://www.iometer.org/doc/documents.html>
- [5] IOzone Filesystem Benchmark, <http://www.iozone.org>
- [6] Lustre: A Scalable High Performance File System, Cluster File System, Inc. 2003. <http://www.lustre.org/docs.html>
- [7] Nagle, Serenyi, Matthews, The Pansas ActiveScale Storage Cluster - Delivering Scalable High Bandwidth Storage, in Proceedings of the ACM/IEEE SC2004 Conference, Pittsburgh, PA, November 2004.
- [8] Pease, D, Rees, R., Heneman, W, et al., IBM Storage Tank: A Distributed Storage System, in Proceedings of the first USENIX Conference on File and Storage Technologies Work In Progress, Monterey CA, January 2000.
- [9] Rodeh, Teperman, zFS - A Scalable Distributed File System Using Object Disks, Technical report, IBM Labs in Israel, Hifa University, Mount Carmel, 2005, <http://www.haifa.il.ibm.com/procject/storage/zFS/public.html>
- [10] UNH iSCSI, <http://www.iol.unh.edu/consortiums/iscsi/>
- [11] Wang, Brandt, Miller, Long, OBFS: A File System for Object-based Storage Devices, in Proceedings of the 21th IEEE/12th NASA Goddard Conference on Mass Storage Systems and Technologies (MSST2004), College Park, MD, April 2004.
- [12] Weber, SCSI Object-Based storage Device Commands (OSD), Document Number: ANSI/INCITS 4000-2004. InterNational Committe for Information Technology Standard, December 2004. <http://www.t10.org/drafts.html>

G-SCAN: A Novel Real-Time Disk Scheduling Using Grouping and Branch-and-Bound Strategy

Taeseok Kim¹, Eungkyu Song¹, Yunji Koh¹, Youjip Won^{2,*}, and Kern Koh¹

¹ School of Computer Science and Engineering, Seoul National University,
56-1, Shillim-Dong, Kwanak-Ku, Seoul, 151-742, Korea
{tskim, eungkyu, erdbeere2, kernkoh}@oslab.snu.ac.kr

² Division of Electrical and Computer Engineering, Hanyang University,
17, Hangdang-Dong, Seongdong-Ku, Seoul, 133-791, Korea
yjjwon@ece.hanyang.ac.kr

Abstract. For mixed-media workload, disk scheduling strategies have to guarantee the QoS (Quality of Service) of requests with timing constraints while optimizing the disk utilization. In this paper, we present a novel real-time disk scheduling algorithm which optimizes the seek time overhead of all requests while meeting the deadlines of requests with timing constraints. Our algorithm first arranges the requests in the queue by SCAN order and clusters the several adjacent requests into group. And then it finds a feasible schedule which meets the different QoS of each requests using branch-and-bound strategy. Through trace-driven simulation, we show that our algorithm outperforms other algorithms in terms of response time, throughput, and QoS guarantee for real-time requests.

1 Introduction

As multimedia streaming services with timing constraints are rapidly becoming prevalent, the traditional time-sharing operating systems are required to be redesigned for these services. In the data storage and retrieval domain, the next generation file systems should deal with the mixed requests with different QoS. For example, it should efficiently handle the real-time requests such as audio/video playback and in the mean time should be able to handle the best-effort requests which only require the delivery or storage of data. Disk scheduling activity for this mixed workload environment is also a challenging problem.

During the last years, there have been many studies on handling mixed-media workload. Based on traditional period-based strategy, Won et al.[1] and Shenoy et al.[2], etc. proposed mechanisms which allocate a certain fraction of each period to each class of requests. Specially, Shenoy et al. presented the Cello disk scheduling framework[2] using two-level disk scheduling architecture: a class-independent

* Work of this author is supported by grant No. R08-2003-000-11104-0 from the Basic Research Program of the Korea Science & Engineering Foundation.

scheduler and a set of class-specific schedulers. There also have been many approaches that try to integrate EDF (Earliest Deadline First)[3] which focuses on deadline with SCAN which minimizes the seek overhead. SCAN-EDF[4], Mokbel et al.[5], Kamel et al.[6], and SSED0/SSEdV (Shortest Seek and Earliest Deadline by Ordering/Value)[7] are such examples.

In essence, disk scheduling problem is to find an optimal schedule of requests among all the possible schedules. For example, when there are N requests in request queue, the number of all possible combinations of N requests is N factorial. Unfortunately, finding an optimal schedule from this huge solution space is infeasible because of excessive spatial and temporal overhead. Huang et al.[8] presented a new approach called MS-EDF (Minimizing Seek time Earliest Deadline First) which effectively reduces the huge space to a feasible extent for multimedia server system through branch-and-bound strategy. Though they have showed the superior performance of their work, MS-EDF has some limitations for mixed-media workload environment: it handles requests in a batch manner, it considers only real-time requests, etc.

In this paper, we present a novel real-time disk scheduling algorithm called G-SCAN (Grouping-SCAN) for mixed-media workload environment. Our scheduling algorithm resolves the aforementioned problems of MS-EDF by employing on-line mechanism and several techniques. G-SCAN first arranges the requests in the queue by SCAN order and then clusters the adjacent requests without timing constraints into group. Next, G-SCAN reduces the huge solution space to a reasonable extent using several heuristics and branch-and-bound strategy. We demonstrate that G-SCAN is suitable for mixed-media workload since: (i)it is based on on-line request handling mechanism, (ii)it meets the deadline of real-time requests, (iii)it minimizes the seek time costs, and (iv)it has low enough overhead to be implemented.

The remainder of this paper is organized as follows. First, we present the problem definition and assumptions in section 2. And then we illustrate our G-SCAN algorithm in section 3. In section 4, we validate our algorithm through extensive simulation. Finally, we make concluding remarks in section 5.

2 Problem Definition and Assumptions

Our goal is to design a disk scheduling algorithm which is able to meet the deadline of requests with timing constraints and minimize the disk seek time overhead as much as possible. In addition to that, our algorithm should be feasible to be implemented, i.e. it should have justifiable assumptions and reasonable algorithm cost.

To this end, we first classify all requests into two classes: real-time requests and best-effort requests. Real-time requests have their own deadline value and they could be periodic or aperiodic. On the other hand, best-effort requests have no specific deadline, they could be regarded that they have infinite deadline value. We also assume that all requests are independent, i.e., a request does not synchronize or communicate with other requests and all requests are nonpreemptive, i.e. a request could not be preempted by other requests during it is serviced in disk.

3 G-SCAN: An On-Line Real-Time Disk Scheduling Algorithm for Mixed Media Workload Environment

3.1 Motivation

Optimal disk scheduling algorithm is to find a schedule of requests which has optimal cost. For example, given that N requests in the queue, optimal algorithm should search an optimal request schedule among N factorial possible schedules. Searching in this huge solution space is very intricate and it is known as an NP hard problem[9]. In addition to that, in mixed-media workload environment, scheduling algorithm should be able to satisfy the QoS requirements of each request class. For example, soft real-time applications such as audio/video playback require meeting the deadline of each I/O request, while best-effort applications such as database search, file copy, text editing, etc. require low response time or high throughput.

To solve this problem, we employ the branch-and-bound strategy. The branch-and-bound strategy is one of the most efficient solutions to solve the combinatorial problem. In essential, there are a few optimal solutions in searching space, the branch-and-bound strategy tries to find an optimal solution by cutting down the unnecessary space. We cut down the huge solution space using the abovementioned requirements in mixed-media workload environment. For example, we can remove a schedule which has any deadline missed request or a schedule which has too high total seek costs from all possible schedules. Fig. 1 illustrates an example. In this example, we assume that schedule S_a has request R_3 which could not meet its own deadline and S_b has too high total seek costs to be optimal requests schedule. Hence, these schedules and the descendants of those which include S_a or S_b could be removed from the solution space. Level in fig. 1 denotes the number of request in the queue. When level is 2, solution space is $2(= 2 \text{ factorial})$, when level is 3, solution space is $6(= 3 \text{ factorial})$, and so on.

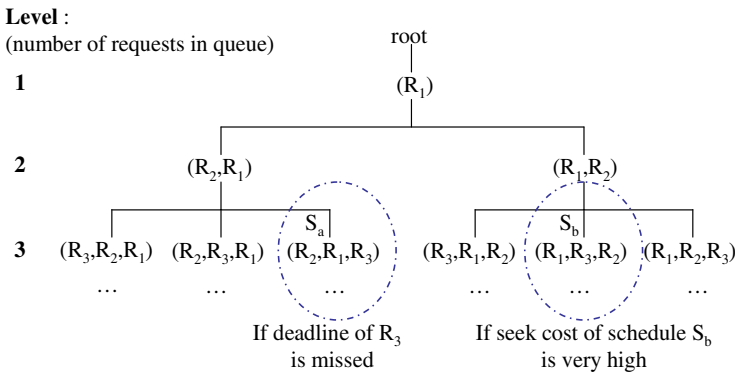


Fig. 1. An example for space reduction. In this example, we assume that R_3 in S_a could not meet its deadline and S_b has very high seek cost.

3.2 Details of G-SCAN (Grouping-SCAN)

In this section, we illustrate the details of our on-line real-time disk scheduling algorithm called G-SCAN. On-line here means that it not only has low overhead, but also should be able to decide a schedule whenever requests arrive at queue or requests leaves from queue. Basically, our algorithm expands the existing schedules whenever the event such as the arrival or the departure of requests is occurred. And then, it cuts down the solution space with criteria which require meeting the deadline of real-time requests, minimizing the seek costs, and so on. Let N and M be the number of requests in the queue and the possible schedules. M is bounded by N factorial, obviously. However, we can reduce this huge solution space to a reasonable extent using two basic strategies: the grouping of adjacent best-effort requests and the branch-and-bound scheme by several heuristics.

To reduce the solution space, we first arrange the requests in the queue by SCAN order. Note that the arrangement by SCAN order is just preliminary procedure for grouping. And then we try to cluster the adjacent best-effort requests one another into group. Since best-effort requests have no deadline, it is justifiable to schedule the best-effort requests in a group by SCAN order. This grouping reduces the huge solution space significantly by removing the unnecessary combination of adjacent best-effort requests.

Fig.2 illustrates an example for grouping of best-effort requests. We assume that there are 11 requests in the queue by SCAN order, and thus the solution space is 11 factorial (fig.2(a)). Fig.2(b) shows the state after grouping the adjacent best-effort requests. G-SCAN basically clusters all the best-effort requests between two real-time requests into a group. However, if the seek distance between any two best-effort requests is too long, they are not put together into single group. It is because any group which has too long seek time may decrease the possibility of finding the best schedule. In fig.2(b), there are two groups between R_4 and R_{11} because the distance between R_6 and R_7 is too long. We put any two best-effort requests which has the seek distance below threshold τ together into a group. If τ is large, the number of all possible schedules is decreased and thus the solution space becomes smaller, but the possibility of finding the best schedule is also decreased. On the other hand, if τ is small, the number of all possible schedules is increased and thus the solution space becomes larger, but the possibility of finding the best schedule is also increased.

Note that there are two requests order within each group: ascending sector number order and descending sector number order. Hence, in fig.2(b), the solution space after grouping is $(8*6 \text{ factorial})$ instead of 6 factorial . Let N_r , N_b , and N_g be the number of real-time requests, the number of best-effort requests, and the number of groups, respectively. The number of schedules before grouping of adjacent best-effort requests is $((N_r + N_b) \text{ factorial})$, while the number of schedules after grouping becomes $((N_r + N_g) \text{ factorial} * 2^{N_g})$. Usually, N_g is much smaller than N_b .

When new request arrives at queue, G-SCAN tries grouping by abovementioned method. If the newly arrived request is best-effort one, it may be merged with the existing group, it may bridge a gap between two groups, or it will create the new group. On the other hand, if the new request is real-time one, it may split the existing group or it is inserted by SCAN order without special action.

Next, with the real-time requests and the grouped best-effort requests, G-SCAN tries to reduce the solution space using the branch-and-bound strategy. To this end, we employ the following heuristics. First two heuristics are adopted in order during new request arrival phase while last heuristic is adopted during request service phase. Since the solution space for scheduling is still huge, it should be reduced as much as possible using following heuristics.

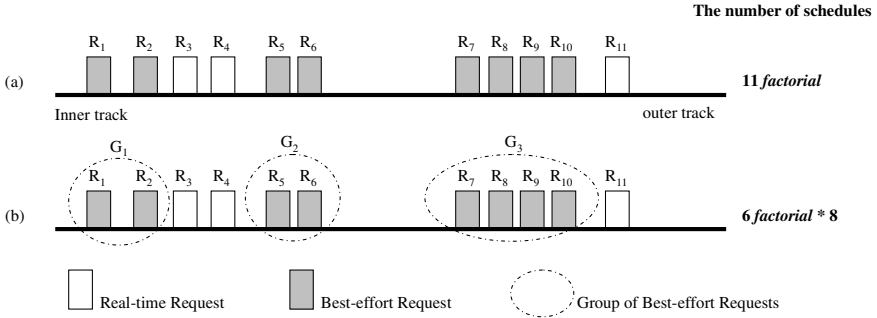


Fig. 2. An example for grouping of best-effort requests located closely each other. In (a), the number of all possible combinations of 11 requests is (11 factorial). On the other hand, in (b), the number of all possible combinations is (6 factorial * 8).

Heuristic 1. Removal of schedule which has any deadline missed request: A schedule with any request which cannot meet its own deadline could be removed.

Since one of our objectives is to meet the deadlines of real-time requests, this heuristic is trivial. If a schedule has any requests which cannot meet the deadline, the new schedule inherited from that schedule by the arrival of new request will also have any requests which cannot meet the deadline. Assume that there is a schedule with the request order (... , R_i , ...), where 1 ≤ i ≤ N, cannot meet the deadline of R_i. When a new request R_k arrives at queue, our scheduler will try to expand the existing schedules by inserting R_k. Since R_i cannot meet the deadline, for the expanded schedules (... , R_k , ... , R_i , ...) and (... , R_i , ... , R_k , ...), R_i still misses the deadline. The number of schedules removed by this heuristic is denoted by K_d.

Heuristic 2. Removal of schedules which have excessive total seek time costs: If the seek cost difference between any schedule S_i(N) and optimal schedule at level N is greater than the disk full sweep cost, S_i(N) could be removed.

Supposed that S_{opt}(N) is the optimal schedule when there are N requests in the queue. And let C_{opt}(N) and C_{sweep} be the seek time cost for S_{opt}(N), the cost for full sweep of disk head, respectively. This heuristic removes a schedule S_i(N) satisfying following inequality.

$$C_i(N) - C_{opt}(N) > C_{sweep} \tag{1}$$

In (1), C_i(N) is the seek time cost for schedule S_i(N). Supposed that optimal schedule after arrival of new request is S_{opt}(N+1) and the seek cost for S_{opt}(N+1) is denoted by C_{opt}(N+1). And then the new schedule S_i(N+1) inherited from S_i(N) which satisfies

inequality (1) cannot have the cost less than that of $S_{opt}(N+1)$. Hence, $S_i(N)$ satisfying (1) could be removed. The number of schedules removed by this heuristic is denoted by K_s .

It is possible that all schedules are removed by above heuristics. For example, when the I/O subsystem is overloaded, all possible schedules may not satisfy the above heuristics. To resolve this phenomenon, even if all possible schedules cannot satisfy the heuristics, G-SCAN does not remove all of them. In other words, G-SCAN leaves one schedule which has minimal seek overhead and this guarantees the completeness of our algorithm.

Heuristic 3. Removal of unselected schedules: When the first request R_i in optimal schedule leaves from queue to be serviced, a schedule which does not begin with R_i could be removed.

This heuristic is trivial. When disk is ready for servicing a request, G-SCAN chooses an optimal schedule at that level. Once optimal schedule is chosen, the first request R_i of that schedule is removed from queue and all schedules which do not begin with R_i are also removed.

Note that our algorithm might not give an optimal schedule in the true sense of the definition. Essentially, optimal algorithm requires knowledge about the request sequence that will arrive at queue in the future. Our goal is just to design an algorithm which could obtain a schedule close to optimum with reasonable cost. The outline of the proposed algorithm is as follows:

When a new request R_i arrives at the queue

1. insert the new request R_i according to the SCAN order.
2. try to group the adjacent best-effort requests.
 - if R_i is a real-time request, it may split the existing group or it is inserted by SCAN order without special action.
 - if R_i is a best-effort request, it may be merged with the existing group, it may bridge a gap between two groups, or it will create the new group.
3. cut down the unnecessary solution space with the branch-and-bound strategy.
 - create a new schedule S_i including R_i .
 - remove S_i which has any deadline missed real-time request.
 - remove S_i which has excessive total seek overhead.

When any request should leave from the queue to be serviced

1. choose the schedule which has minimal seek overhead while meeting the deadlines of all real-time requests.
2. service a request R_i at head position of S_i and remove schedules which do not begin with R_i .

Even if our algorithm reduces the solution space sufficiently, since it essentially deals with a significant amount of schedules, it should be carefully designed. Hence, we employ min-heap data structure in which the key value is the total seek time costs of each schedule.

4 Experimental Evaluation

4.1 Experimental Methodology

In this section, we present the performance analysis of our G-SCAN algorithm. Our goal in this section is to demonstrate that our algorithm outperforms other algorithm and has feasible overhead to be implemented. To this end, we compare our algorithm with other several algorithms such as C-SCAN, EDF, SCAN-EDF, and Kamel's[6] in terms of seek cost, response time, throughput, and deadline miss rate. And then we show the running cost of our algorithm is not excessive. To simulate the various workloads, we arrange four cases in the simulation. They are listed in table 1. Workload 1, workload 2, and workload 3 emulate the mixed-media workload environment, while workload 4 emulates homogeneous workload of multimedia request type. Note that these workloads are somewhat heavy. The reason that we used the heavy workloads is to show that the overhead of our G-SCAN is not very high in heavy load environment.

4.2 Performance Evaluation

Before investigating the performance of our algorithm, we first analyze the effect of grouping. Fig. 3 illustrates the average number of groups after grouping with the average number of requests in the queue as a function of threshold τ . Note that the number of groups illustrated in Fig. 3 includes the real-time requests as well as the grouped best-effort requests. As can be seen, the solution space, i.e. all possible combinations of requests is significantly reduced after grouping. When τ is 100 tracks, the number of requests in the queue is about 16 and thus the size of solution space is 16 *factorial*. After grouping of best-effort requests, the number of groups is about 8, and thus the solution space becomes 8 *factorial* * 2^N . In the worst case, N is 8. As τ is larger, the number of groups becomes smaller.

Table 1. The characteristics of workloads used

Work load	Type of tasks	# of tasks	Bandwidth (if periodic task)	IO size (KB)	File size (MB)
			Inter-arrival time (if random/sequential task)		
1	periodic	1	12 Mbps	64	100
	random	1	20 ms	4-128	200
2	periodic	1	12 Mbps	64	100
	sequential	1	20 ms	64	200
3	periodic	1	10 Mbps	64	100
	random	1	45 ms	4-128	100
	sequential	1	20 ms	64	100
4	periodic	6	4-5 Mbps	64	50-200

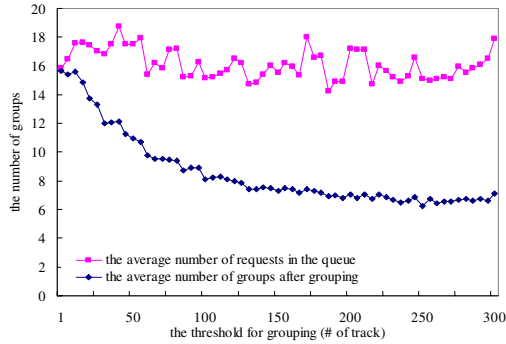
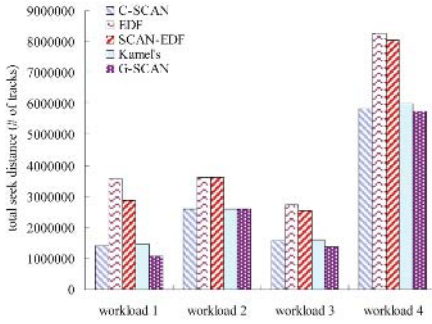


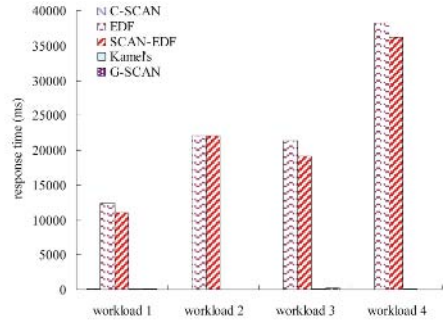
Fig. 3. The number of groups after grouping of adjacent best-effort requests

Next, we present the performance results for various workloads to assess the effectiveness of our scheme. Note that the performance of G-SCAN is measured when τ is 20. First, we investigated the disk head movement behavior of proposed algorithms. As shown in fig. 4(a), C-SCAN, Kamel's, and G-SCAN exhibit relatively low seek overhead. As illustrated, our G-SCAN is a little better than C-SCAN in experiments with workload 1, 3, and 4. It is because C-SCAN handles the requests in one direction and thus it includes unnecessary disk full sweep. Fig. 4(b) and fig. 4(c) show the average response time and the throughput of different algorithms, respectively. For both response time and throughput metrics, our algorithm exhibits superior performance with C-SCAN and Kamel's, too. EDF and SCAN-EDF show the excessive response time in all cases. It is because workloads used in our experiments are heavy. Fig. 4(d) compares different algorithms in terms of deadline miss rate. As expected, EDF and SCAN-EDF shows very low deadline miss rate in experiments with workload 1, 2, and 3. However, we observed that deadline-based scheduling algorithms such as EDF, SCAN-EDF are much worse than C-SCAN in case the workload consists of homogeneous real-time requests (workload 4). All the requests in workload 4 have their own deadlines and thus the deadline-based algorithms which focus only on the deadline value of each request cause too many seek overhead. As can be seen from the fig. 4(d), our G-SCAN algorithm shows relatively low deadline miss rate. When summarizing four performance results, our G-SCAN meets the deadlines of real-time requests as EDF and exhibits so good performance as C-SCAN in terms of disk head movement optimization.

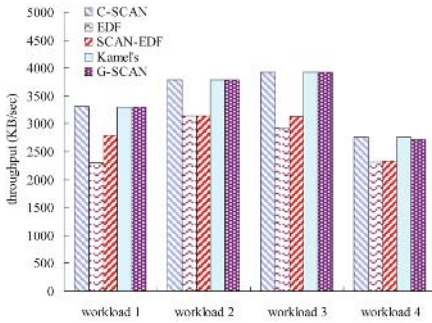
Finally, we show that the overhead of G-SCAN is not excessive. To this end, we measured the number of schedules actually expanded in our experiments. In fig. 5, we compare the total number of schedules in the worst case with the number of schedules actually expanded in experiment with workload 1. Note that the Y axis in fig. 5 is plotted on a log scale. The results show that our G-SCAN generates only a fraction of schedules to obtain the best schedule. In experiment with workload 1, the average number of schedules actually expanded is 1005. And the average of K_d and K_s in abovementioned heuristics are 469, 414, respectively. The overhead in experiments with the other three workloads were negligible. The average number of schedules actually expanded with workload 2, workload 3, and workload 4 are 2, 50, and 4, respectively.



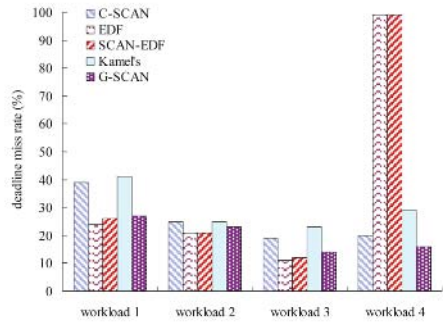
(a) The total seek costs.



(b) The average response time.



(c) The throughput.



(d) The deadline miss rate.

Fig. 4. Performance comparison of C-SCAN, EDF, SCAN-EDF, Kamel's, and G-SCAN

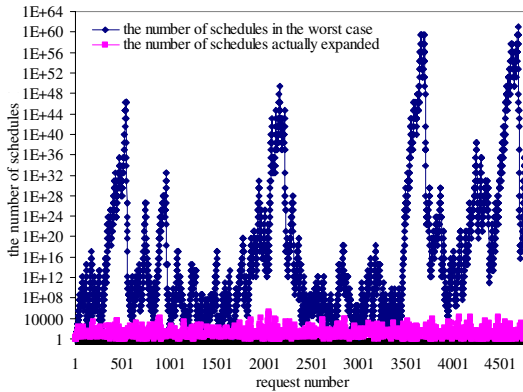


Fig. 5. The number of schedules generated in G-SCAN

5 Conclusions

In this paper, we propose a novel real-time disk scheduling algorithm in support of requests with different QoS requirements. We first recognized the optimal scheduling problem in mixed-media workload as an NP hard problem which finds an optimal solution from very huge space. And then we significantly reduce the huge space to a feasible level by grouping technique and the branch-and-bound strategy. In addition to that, we illustrated that our algorithm is based on on-line method. Through extensive simulation, we demonstrated that our algorithm outperforms other scheduling algorithms in terms of throughput, response time, and deadline miss rate. We also demonstrated that our algorithm has reasonable overhead to be implemented. We anticipate that our algorithm could be equipped with web server with audio/video objects, multimedia servers, ordinary workstation, and home appliances such as set-top box, PVR(Personalized Video Recorder).

References

1. Y. J. Won and Y. S. Ryu: Handling sporadic tasks in multimedia file system. Proc. 8th ACM International Conf. on Multimedia (2000) 462-464.
2. P. Shenoy: Cello: a disk scheduling framework for next generation operating system. Real Time Systems Journal (2002)
3. Liu, C., L, Layland, J., W: Scheduling algorithms for multiprogramming in hard-real-time environment. Journal of the ACM, Vol. 20(1) (1973) 47-61
4. Narasimha Reddy, A., Wyllie, J.: Disk scheduling in a multimedia I/O system. Proc. 1st ACM MM'93, Anaheim, CA, USA (1993) 225-233
5. M.F. Mokbel, W.G. Aref, K. El-Bassyouni, I. Kamel: Scalable Multimedia Disk Scheduling. Proc. 20th IEEE Intl. Conf. on Data Eng. (ICDE), Boston (2004) 498-509
6. I. Kamel, T. Niranjana, and S. Ghandeharizadeh: A Novel Deadline Driven Disk Scheduling Algorithm for Multi-Priority Multimedia Objects. Proc. 16th Int'l Conf. Data Eng. (2000) 349-361
7. Chen, S., Stankovic, J., A, Lurose, J.,F, Towsley, D.: Performance evaluation of two new disk scheduling algorithms for real-time systems. Journal of Real-Time Systems, Vol.3 (1991) 307-336
8. Huang Yin-Fu and Jiing-Maw Huang: Disk Scheduling on Multimedia Storage Servers. IEEE Transactions on Computers, Vol. 53(1) (2004) 77-82
9. M.Andrews, M.A.Bender, and L.Zhang: New algorithms for the disk scheduling problem. 37th Annual Symposium on Foundations of Computer Science, IEEE Computer Society Press (1996) 550-559

A New Key Management Scheme for Distributed Encrypted Storage Systems*

Myungjin Lee, Hyokyung Bahn**, and Kijoon Chae

Dept. of Computer Science & Engineering, Ewha University, Seoul 120-750, Korea
maya012@ewhain.net, {bahn, kjchae}@ewha.ac.kr

Abstract. Data on a storage device are easier targets for malicious attackers. Storing data in an encrypted form is an effective way to improve data security. In an encrypted storage system, key management is one of the most challenging tasks. In this paper, we propose a new key management scheme for distributed encrypted storage that has various salient features. First, in the proposed scheme, encryption keys are not directly known to users. Due to this property, the security of the encrypted data is not deteriorated though some users that have shared the data lose the access right. Second, in the proposed scheme, even if some components of the system are attacked, the security of the system is still guaranteed. Third, the system provides high availability by exploiting the secret sharing scheme.

1 Introduction

Network security has been studied extensively to protect data on transmitting through insecure channels. For example, a large variety of protocols such as IPSec [1], SSH [2], and TLS [3] are developed for secure transmission of data over insecure networks. Recently, storage security has been under serious attention. Data on a storage device are easier targets for malicious attackers than data on transmission because sufficient time is given to the storage attackers. Hence, storage security is an even more challenging problem compared to traditional network security.

In order to protect data in storage devices, some systems use access control mechanisms [4], [5], [6]. However, these mechanisms are not secure when the attacker gets the administrator's account or physical access to the storage system. Once an attacker acquires the access permission, then he/she has controls over the whole system. To reduce this risk, some storage systems store data in an encrypted form [7], [8].

Key management is a difficult problem for sharing encrypted data among users. For example, assume that authorized users have shared the encryption key to access data in the storage, and one of them leaves the system. Then, we should revoke his authority and re-encrypt the data with a new key. In this case, if the volume of data amounts to as large as Gigabytes or Terabytes, too much overhead will be accompanied in decrypting and re-encrypting processes.

* This research was partially supported by University IT Research Center (ITRC) Project and Seoul R&BD Program.

** Corresponding author.

In this paper, we propose a new key management scheme for encrypted storage systems. Our new scheme does not need to re-encrypt data though some users withdraw from the system. This is possible because data encryption keys are not directly known to users in our system. We show how this new scheme efficiently works even though many users join and leave the system frequently.

The remainder of this paper is organized as follows. Section 2 presents the system architecture of the proposed encrypted storage system. The proposed key management scheme is presented in Section 3. We validate the security of the system in Section 4. Finally, Section 5 concludes the paper.

2 The System Architecture

Our system architecture consists of an Administrator, a Key Server, an Integrity Engine, Storage Servers, and Users as shown in Figure 1. This is similar to the architecture proposed by Seitz et al. except the existence of the Integrity Engine [7]. Even though a storage system maintains data in an encrypted form, some malicious user may try to forge the encrypted data in the storage. The Integrity Engine located in front of the Storage Server verifies whether data have been modified while in the storage.

The components of our system and information of each component are listed in Table 1.

Table 1. Components of the system and properties of each component

Component	Property	Function
User	<ul style="list-style-type: none"> • User ID • Key to communicate with Administrator 	<ul style="list-style-type: none"> • Read data
Administrator	<ul style="list-style-type: none"> • Data Access Control Table (DACT) • Key to communicate with User • Key to communicate with Key Server • Key to communicate with Integrity Engine 	<ul style="list-style-type: none"> • Write data • Authenticate users • Manage DACT • Encrypt data
Key Server	<ul style="list-style-type: none"> • Data encryption keys • Key to communicate with Administrator 	<ul style="list-style-type: none"> • Keep encryption keys of data
Integrity Engine	<ul style="list-style-type: none"> • MAC of encrypted data • Key to communicate with Administrator 	<ul style="list-style-type: none"> • Inspect data integrity • Fragment data • Decrypt data
Storage Server(s)	<ul style="list-style-type: none"> • Fragmented encrypted data 	<ul style="list-style-type: none"> • Store fragmented encrypted data

In our system, users have the read-only permission of data and each user can join or leave the system per data or community. This is a common environment at any online streaming sites or community sites. When a User tries to read data, the Administrator authenticates the User if he/she has the access permission to the data. If the authentication process is successfully performed, the User gains authority to

service the requested data from the Administrator. The User then receives the data from the Storage Servers through the Key Server and the Integrity Engine.

We assume that the Administrator is trusted entity and can authenticate users when new user joins the system. The Administrator has several following features. First, it has keys to communicate with each component of the system, i.e., the Key Server, the Integrity Engine, and the Users. Hence, the Administrator can make secure communication with other components of the system. Second, the Administrator has the Data Access Control Table (DACT). When a new user joins or leaves the system, the Administrator updates DACT. If the user requests data, the Administrator verifies whether the user has the access permission of the requested data using DACT. Third, only the Administrator has ability to store data on the Storage Servers. When there are some new data to store, the Administrator creates a new encryption key corresponding to the data. Using this key, the Administrator encrypts the data and stores them on the Storage Servers. Finally, the encryption key of this data is stored on the Key Server.

The Integrity Engine performs data integrity inspection whether the data have been changed while they are in the Storage Server. The Storage Server stores data encrypted by the Administrator.

3 The Proposed Key Management Scheme

In the existing systems, when an authorized user loses his right to access some data, only the access permission of the user is removed. As mentioned in Section 1, however, this may cause serious security problems if some attacker acquires full access permissions. To relieve this problem, the data should be re-encrypted with a new key whenever some user loses his access rights. This may cause extensive computational overhead. In order to solve this problem, we suggest a new key management scheme for encrypted storage systems that does not show the data encryption key itself to the users.

Table 2 lists notations that we use throughout this paper.

Table 2. Notations and their descriptions used throughout this paper

Notation	Description
$E_K(data)$	Encrypt <i>data</i> with key <i>K</i>
K_D	Encryption key for data
K_{AU}	Symmetric key between the Administrator and the User
K_{AK}	Symmetric key between the Administrator and the Key Server
K_{AI}	Symmetric key between the Administrator and the Integrity Engine
S_{UK}	Session key between the User and the Key Server
S_{UI}	Session key between the User and the Integrity Engine
S_{KI}	Session key between the Key Server and the Integrity Engine
\parallel	Concatenation

3.1 User’s Joining and Leaving

When a new user joins the system, the Administrator updates the DACT, and assigns a key between the Administrator and the user. Using this key, the user can request data.

Similarly, when an existing user leaves the system, the Administrator updates the DACT and removes the communication key between the user and the Administrator.

3.2 Storing New Data by the Administrator

When new data should be stored on the Storage Server, the Administrator randomly creates an encryption key and encrypts the data with this key. The encryption key is encapsulated by the communication key between the Administrator and the Key Server. Then, the Administrator sends the encapsulated encryption key to the Key Server. Similarly, the encrypted data are sent to the Integrity Engine. The Integrity Engine, then, calculates and stores the MAC of the encrypted data. The Integrity Engine fragments the encrypted data using a secret sharing scheme [9], and stores them into each Storage Server separately. After all of these steps are finished, the Administrator eliminates both the encrypted data and the encryption key permanently from its local storage.

3.3 Processing User's Request

User's data request can be processed by the following steps. Figure 1 summarizes these processes.

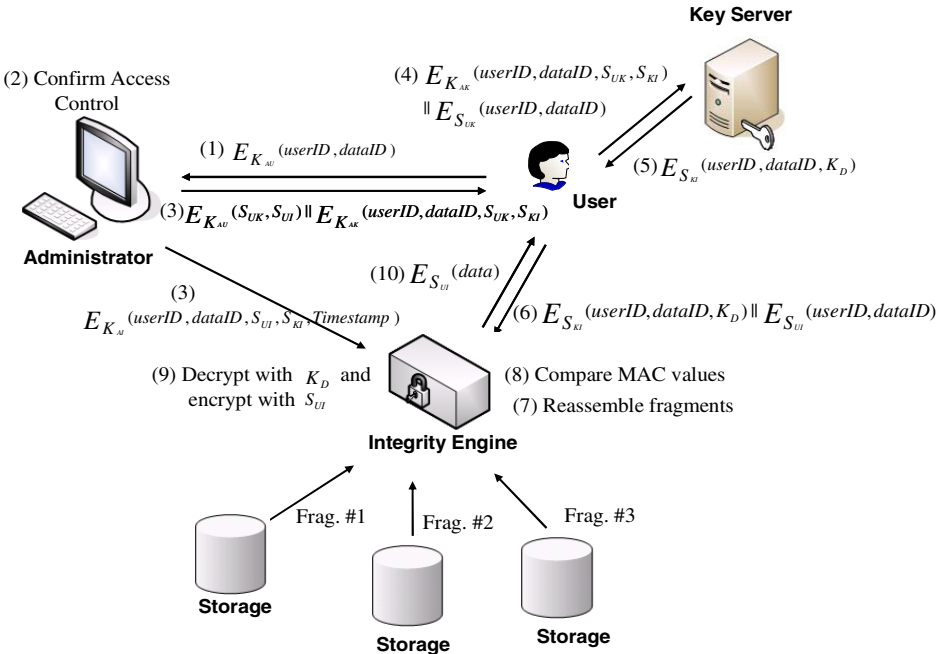


Fig. 1. Processing of data request by a user

Step 1. Request data

To request data, a User sends the following message to the Administrator.

$$E_{K_{AU}}(userID, dataID)$$

The message is encrypted by the key K_{AU} and contains User's ID together with the ID of the requested data.

Step 2. Confirm user's authority on the data access

The Administrator decrypts the received message with the key K_{AU} and confirms the user's authority on the requested data by referencing DACT.

Step 3. Generate session keys and send them to the User and the Integrity Engine

The Administrator creates three session keys S_{UK} , S_{KI} , and S_{UI} , and sends the following message to the User.

$$E_{K_{AU}}(S_{UK}, S_{UI}) \parallel E_{K_{AK}}(userID, dataID, S_{UK}, S_{KI})$$

The User decrypts this message with the key K_{AU} and takes the session keys S_{UK} and S_{UI} from the message. These two session keys are used to communicate securely with the Key Server and the Integrity Engine, respectively, during this session.

At the same time, the Administrator sends the following message to the Integrity Engine.

$$E_{K_{AI}}(userID, dataID, S_{UI}, S_{KI}, Timestamp)$$

In this message, both $userID$ and $dataID$ are included. It also contains the two session keys S_{KI} and S_{UI} together with the *TimeStamp* to protect from replay attacks.

Step 4. Request data encryption key to the Key Server

The User generates the following message by encrypting $userID$ and $dataID$ with the session key S_{UK} and concatenating it with the encrypted message from the Administrator.

$$E_{K_{AK}}(userID, dataID, S_{UK}, S_{KI}) \parallel E_{S_{UK}}(userID, dataID)$$

Then the User sends the generated message to the Key Server. The Key Server decrypts the two parts of the message sequentially and compares $userID$ and $dataID$ in each part. If someone fabricates this information, the Key Server can know it through this process.

Step 5. Send data encryption key

The Key Server searches the encryption key K_D corresponding to $dataID$ and encapsulates it together with $userID$ and $dataID$ using the key S_{KI} . The Key Server then sends the following encapsulated message to the User.

$$E_{S_{KI}}(userID, dataID, K_D)$$

The User cannot decrypt this message because S_{KI} is the communication key between the Key Server and the Integrity Engine, and hence that key is not known to the User. As a result, the User cannot see the data encryption key K_D .

Step 6. *Request data to the Integrity Engine*

Similar to Step 4, the User encrypts $userID$ and $dataID$ using the session key S_{UI} and concatenates it with the message encrypted by the key S_{KI} received from the Key Server in Step 5. Then, the User sends the concatenated message to the Integrity engine.

$$E_{S_{KI}}(userID, dataID, K_D) \parallel E_{S_{UI}}(userID, dataID)$$

Step 7. *Re-assemble data fragmentation*

The Integrity Engine decrypts all the messages from the Administrator and the User, and verifies whether all $userID$ s and $dataID$ s in the messages are identical. It also checks whether the User's request is generated within a bounded time from the *Timestamp* value. If all conditions are satisfied, the Integrity Engine receives the fragmented data from the Storage Servers, and re-assembles them.

Step 8. *Compare two MACs*

The Integrity Engine calculates MAC of the restored data and compares it with the stored one. If the two MACs are not identical, some modifications are made while data are on the Storage Server.

Step 9. *Reply to user*

The Integrity Engine decrypts the data using the key K_D , and sends the following message to the User.

$$E_{S_{UI}}(data)$$

The User can obtain the requested data from this message.

4 Security Analysis

In this section, we validate the proposed key management scheme in terms of resilience and availability. Subsection 4.1 presents the resilience of the system against compromise of system components and Subsection 4.2 presents the availability of the system.

4.1 Resilience Against Compromise of Components

In this subsection, we show that the security of the system is still guaranteed even if some components of the system are attacked. We examine the resilience of the system by analyzing how the compromise of the system components affects the security of the system. Since we assume that the Administrator is the trusted entity, we consider the compromise of each component except the Administrator.

First, if the Key Server is compromised, the attacker may obtain the symmetric key K_{AK} to communicate with the Administrator and also obtain the data encryption keys K_D stored on the Key Server. However, the attacker cannot get the data from the Integrity Engine because the attacker does not have the access permission of the data.

Second, if the Integrity Engine is compromised, the attacker may obtain the symmetric key K_{AI} to communicate with the Administrator and also obtain the encrypted data from the Storage Servers. However, the attacker cannot know the original data because the attacker does not have data encryption/decryption key K_D . Similarly, even if some of the Storage Servers are compromised simultaneously, the attacker cannot obtain the original data without K_D .

In our system, the worst case which may happen with little probability is that both the Key Server and the Integrity Engine are compromised simultaneously by the same attacker. In this case, the proposed system needs some reinforcement. For example, if the system updates the symmetric keys K_{AK} and K_{AI} frequently, the resilience of the system can be improved.

Finally, we assure that compromised users cannot affect the security of the system because the known information to users is just session keys and not data encryption keys. Hence, after a session is over, the keys are useless. Furthermore, in our system, it is not necessary to re-encrypt data with a new key even if some user loses access right to the data. This is because data encryption keys are not directly known to users.

4.2 Availability of the System

Since the proposed system uses the secret sharing scheme in fragmenting the encrypted data to store, it provides high availability. For example, assume that there are n Storage Servers and we use the (n, k) secret sharing scheme. If some of the Storage Servers are not available for several reasons, we cannot retrieve fragmented data from those servers. However, since we use the (n, k) secret sharing scheme, the fragmented data can be restored when k fragments out of n are successfully retrieved. This means that when the number of faulted Storage Servers is less than $n-k$, the system can service the data.

5 Conclusions

We presented a new key management scheme for distributed encrypted storage that has various salient features. First, data encryption keys are not directly known to users in the proposed scheme. As a result, the security of the encrypted data is not deteriorated though some users that have shared the data lose the access right. Second, in the proposed scheme, even if some components such as the Key Server or the Integrity Engine as well as the Storage Servers are attacked, the security of the system is still guaranteed. Finally, we show that the proposed scheme provides high availability by exploiting the (n, k) secret sharing scheme.

References

1. IPsec Working Group: IP Security Protocol (ipsec). Technical report, The Internet Engineering Task Force IETF (2002) <http://www.ietf.org/html.charters/ipsec-charter.html>.
2. Ylonen, T., Kivinen, T., Saarinen, M., Rinne, T., Lehtinen, S.: SSH Protocol Architecture. Technical report, The Internet Engineering Task Force IETF (2002) <http://www.ietf.org/internet-drafts/draft-ietf-secsharchitecture-13.txt>.
3. Dierks, T., Allen, C.: The TLS Protocol Version 1.0. Technical report, The Internet Engineering Task Force IETF (1999) <http://www.ietf.org/rfc/rfc2246.txt>.
4. Zou, X.: Secure Group Communications and Hierarchical Access Control. PhD. Thesis, University of Nebraska-Lincoln, USA (2000)
5. Birget, J-C., Zou, X., Noubir, G., Ramamurthy, B.: Hierarchical-based Access Control in Distributed Environments. International Conference on Communications (2001)
6. Sun, Y., Ray Liu, K. J.: Scalable Hierarchical Access Control in Secure Group Communications. IEEE INFOCOM (2004)
7. Seitz, L., Pierson, J.-M.: Key Management for Encrypted Data Storage in Distributed Systems. Second IEEE International Security in Storage Workshop (2003)
8. Kim, Y., Narasimha, M., Maino, F., Tsudik, G.: Secure Group Services for Storage Area Networks. IEEE Security in Storage Workshop (2002)
9. Shamir, A.: How to Share a Secret. Communications of the ACM, Vol. 22, No. 11 (1979) 612–613

WSRF Services for Composing Distributed Data Mining Applications on Grids: Functionality and Performance

Domenico Talia, Paolo Trunfio, and Oreste Verta

DEIS, University of Calabria,
Via P. Bucci 41c, 87036 Rende, Italy
{talia, trunfio, overta}@deis.unical.it

Abstract. The Web Services Resource Framework (WSRF) has recently emerged as the standard for the implementation of Grid applications. WSRF can be exploited for developing high-level services for distributed data mining applications. This paper describes Weka4WS, a framework that extends the widely-used Weka toolkit for supporting distributed data mining on WSRF-enabled Grids. Weka4WS adopts the WSRF technology for running remote data mining algorithms and managing distributed computations. The paper describes the implementation of Weka4WS using the WSRF libraries and services provided by Globus Toolkit 4. A performance analysis of Weka4WS for executing distributed data mining tasks in two network scenarios is presented.

1 Introduction

In many scientific and business scenarios computational Grids are exploited to access distributed resources and run decentralized applications. Through a service-oriented model, application and system functions can be distributed among several computers or domains. By using this approach, data-intensive and knowledge discovery applications can be developed through the exploitation of Grid technology for delivering high performance and managing data and knowledge distribution. Since Grids emerged as effective infrastructures for distributed high-performance computing and data processing, a few Grid-based data mining systems have been proposed [1, 2, 3, 4]. Our focus here is on distributed knowledge discovery services that allow decentralized teams or virtual organizations accessing and mining data in a high-level, standard and reliable way.

This paper describes *Weka4WS*, a framework that extends the widely-used Weka toolkit [5] for supporting distributed data mining in Grid environments. Weka provides a large collection of machine learning algorithms written in Java for data pre-processing, classification, clustering, association rules, and visualization, which can be invoked through a common graphical user interface. In Weka, the overall data mining process takes place on a single machine, since the algorithms can be executed only locally. The goal of Weka4WS is to extend Weka

to support remote execution of the data mining algorithms. In such a way, distributed data mining tasks can be concurrently executed on decentralized Grid nodes by exploiting data distribution and improving application performance.

In Weka4WS the data mining algorithms for classification, clustering and association rules can be executed on remote Grid resources. To enable remote invocation, all data mining algorithms provided by the Weka library are exposed as a Web Service, which can be easily deployed on the available Grid nodes. Thus, Weka4WS also extends the Weka GUI to enable the invocation of the data mining algorithms that are exposed as Web Services on remote machines. To achieve interoperability with standard Grid environments, Weka4WS has been developed by using the *Web Services Resource Framework (WSRF)* [6] as enabling technology. As WSRF implementations are recent, to the best of our knowledge, *Weka4WS* is the first data mining framework exploiting WSRF Grid services.

The paper describes the design, implementation and performance evaluation of Weka4WS for distributed data mining. To evaluate the overhead introduced by the service invocation mechanisms and their effects on the efficiency of the proposed system, a performance analysis of Weka4WS executing distributed data mining tasks in two different network scenarios is presented. The remainder of the paper is organized as follows. Section 2 describes the architecture and the implementation of the Weka4WS framework. Section 3 presents a performance analysis of the Weka4WS prototype. Finally, Section 4 concludes the paper.

2 Architecture and Implementation

The Web Services Resource Framework defines a family of technical specifications for accessing and managing *stateful resources* using Web Services. The composition of a Web Service and a stateful resource is termed *WS-Resource*. The Globus Alliance recently released the Globus Toolkit 4 (GT4) [7], which provides an open source implementation of the WSRF library and incorporates services implemented according to the WSRF specifications. The Weka4WS prototype described in this paper has been developed by using the Java WSRF library provided by GT4.

In the Weka4WS framework all nodes use the GT4 services for standard Grid functionalities, such as security, data management, and so on. We distinguish those nodes in two categories on the basis of the available Weka4WS components: *user nodes* that are the local machines providing the Weka4WS client software, and *computing nodes* that provide the Weka4WS Web Services allowing for the execution of remote data mining tasks. Data can be located on computing nodes, user nodes, or third-party nodes (e.g., shared data repositories). If the dataset to be mined is not available on a computing node, it can be uploaded by means of the GT4 data management services.

Figure 1 shows the software components of user nodes and computing nodes in the Weka4WS framework. User nodes include three components: *Graphical User Interface (GUI)*, *Client Module (CM)*, and *Weka Library (WL)*. The GUI is an

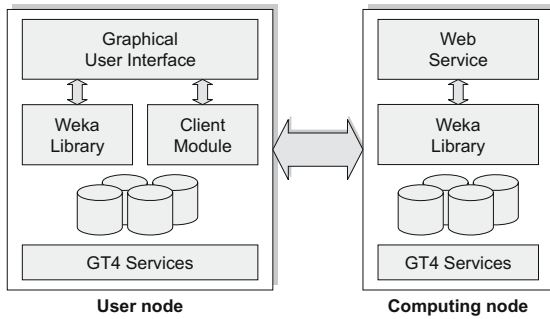


Fig. 1. Software components of user nodes and computing nodes

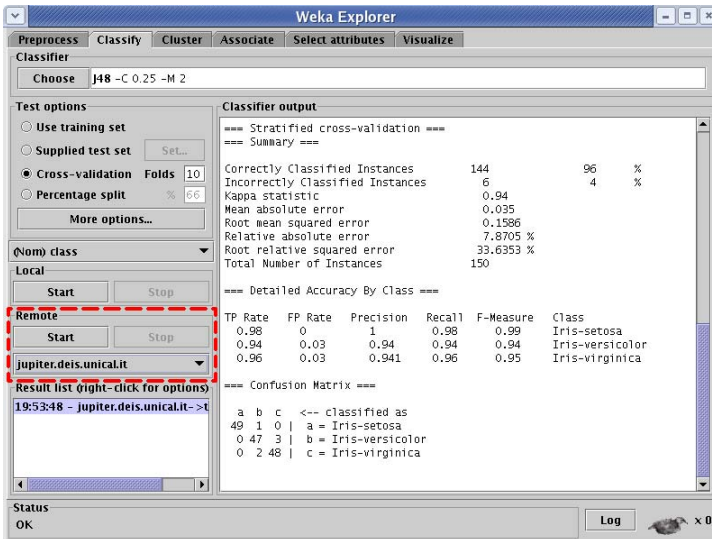


Fig. 2. The GUI: a Remote pane has been added to the original Weka Explorer

extended Weka Explorer environment that supports the execution of both local and remote data mining tasks. Local tasks are executed by directly invoking the local WL, whereas remote tasks are executed through the CM, which operates as an intermediary between the GUI and Web Services on remote computing nodes.

Figure 2 shows a snapshot of the current GUI implementation. As highlighted in the figure, a *Remote* pane has been added to the original Weka Explorer environment. This pane provides a list of the available remote Grid nodes and two buttons to start and stop the data mining task on the selected Grid node. Through the GUI a user can either: *i*) start the execution locally by using the *Local* pane; *ii*) start the execution remotely by using the *Remote* pane. Whenever the output of a data mining task has been received from a remote computing node, it is visualized in the standard *Output* pane (on the right of Figure 2).

Table 1. Operations provided by each Web Service in the Weka4WS framework

Operation	Description
<code>createResource</code>	Creates a new stateful resource.
<code>subscribe</code>	Subscribes to notifications about resource properties changes.
<code>destroy</code>	Explicitly requests destruction of a resource.
<code>classification</code>	Submits the execution of a classification task.
<code>clustering</code>	Submits the execution of a clustering task.
<code>associationRules</code>	Submits the execution of an association rules task.

Computing nodes include two components: a *Web Service (WS)* and the *Weka Library (WL)*. The WS is a WSRF-compliant Web Service that exposes all the data mining algorithms provided by the underlying WL. Therefore, requests to the WS are executed by invoking the corresponding WL algorithms.

2.1 Operations

Table 1 lists the operations provided by each Web Service in the Weka4WS framework. The first three operations are related to WSRF-specific invocation mechanisms (described below), whereas the last three operations - `classification`, `clustering` and `associationRules` - are used to require the execution of a specific data mining task. In particular, the `classification` operation provides access to the complete set of classifiers in the Weka Library (currently, 71 algorithms). The `clustering` and `associationRules` operations expose all the clustering and association rules algorithms provided by the Weka Library (5 and 2 algorithms, respectively).

Table 2. Input parameters of the Web Service data mining operations

Operation	Parameter	Description
<code>classification</code>	<code>algorithm</code>	Name of the classification algorithm to be used.
	<code>arguments</code>	Arguments to be passed to the algorithm.
	<code>testOptions</code>	Options to be used during the testing phase.
	<code>classIndex</code>	Index of the attribute to use as the class.
	<code>dataSet</code>	URL of the dataset to be mined.
<code>clustering</code>	<code>crcValue</code>	Checksum value of the dataset to be mined.
	<code>algorithm</code>	Name of the clustering algorithm.
	<code>arguments</code>	Algorithm arguments.
	<code>testOptions</code>	Testing phase options.
	<code>selectedAttrs</code>	Indexes of the selected attributes.
	<code>classIndex</code>	Index of the class w.r.t. evaluate clusters.
<code>associationRules</code>	<code>dataSet</code>	URL of the dataset to be mined.
	<code>crcValue</code>	Checksum value of the dataset to be mined.
	<code>algorithm</code>	Name of the association rules algorithm.
	<code>arguments</code>	Algorithm arguments.

To improve concurrency, data mining operations are invoked in an asynchronous way, that is, the client submits the task in a non-blocking mode and results are notified to it whenever they are computed.

Table 2 lists the input parameters of the `classification`, `clustering`, and `associationRules` data mining operations. Four parameters are required in the invocation of all the data mining operations: `algorithm`, `arguments`, `dataSet`, and `crcValue`. The `algorithm` argument specifies the name of the Java class in the Weka Library to be invoked (e.g., “*weka.classifiers.trees.J48*”). The `arguments` parameter specifies a sequence of arguments to be passed to the algorithm (e.g., “*-C 0.25 -M 2*”). The `dataSet` parameter specifies the URL of the dataset to be mined (e.g., “*gsiftp://hostname/path/ad.arff*”). Finally, the `crcValue` parameter specifies the checksum of the dataset to be mined.

2.2 Execution Mechanisms

This section describes the steps performed to execute a data mining task on a remote Web Service in the Weka4WS framework.

Figure 3 shows a *Client Module (CM)* that interacts with a remote *Web Service (WS)* to execute a data mining task. In particular, this example assumes that the CM is requesting the execution of a classification task on a dataset located on the user node. Notice that this is a worst case, since in many scenarios the datasets to be mined may be already available (e.g., replicated) on most computing nodes. The following steps are executed in order to perform this task (see Figure 3):

1. **Resource creation.** The CM invokes the `createResource` operation to create a new resource that will maintain the state of the subsequent classification analysis. The state is stored as *properties* of the resource. In this example, a *model* property is used to store the result of the classification task. The WS returns the *endpoint reference (EPR)* of the created resource. Subsequent requests from the CM will be directed to the resource identified by that EPR.
2. **Notification subscription.** The CM invokes the `subscribe` operation that subscribes to notifications about changes that will occur to the *model* resource property. Whenever this property will change its value (i.e., whenever the model has been computed), the CM will receive a notification containing that value, which represents the result of the classification task.
3. **Task submission.** The CM invokes the `classification` operation requiring the execution of the classification task. This operation receives six parameters as shown in Table 2, among which the name of the classification algorithm to be used, the URL of the dataset to be mined and its checksum. If a copy of the dataset is not already available on the computing node, this operation returns the URL where the dataset has to be uploaded.
4. **File transfer.** Since in this example we assume that the dataset is not already available on the computing node, the CM requests to transfer it to the URL specified as a return value by the `classification` operation.

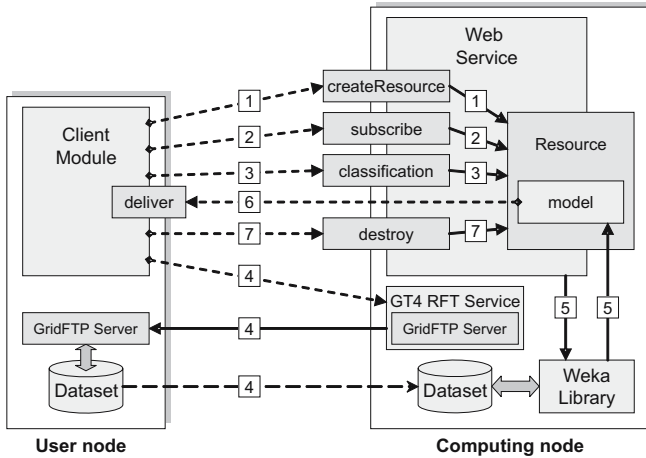


Fig. 3. Execution of a data mining task on a remote Web Service

The transfer request is managed by the GT4 *Reliable File Transfer (RFT)* service running on the computing node, which in turn invokes the *GridFTP* servers [8] running on the user and computing nodes.

5. **Data mining.** The classification analysis is started by the WS through the invocation of the appropriate Java class in the Weka Library. The result of the computation (i.e., the inferred model) is stored in the *model* property of the resource created on Step 1.
6. **Results notification.** Whenever the *model* property has been changed, its new value is notified to the CM by invoking its implicit *deliver* operation. This mechanism allows for the asynchronous delivery of the execution results whenever they are generated.
7. **Resource destruction.** The CM invokes the *destroy* operation, which eliminates the resource created on Step 1.

3 Performance Evaluation

To evaluate the performance of the implemented system, we carried out some experiments where we used Weka4WS for executing data mining tasks in different network scenarios. In particular, here we evaluate the execution times of the different steps needed to perform data classification tasks, as described at the end of the previous section. The main goal of our analysis is to evaluate the overhead introduced by the WSRF mechanisms with respect to the overall execution time.

For our analysis we used the *ad* dataset from the UCI repository [9]. Through random sampling we extracted from it ten datasets, containing a number of instances ranging from 328 to 3280, with a size ranging from 1 to 10 MB. We used Weka4WS to perform a classification analysis on each of these datasets. In particular, we used the *J48* classification algorithm, using cross-validation

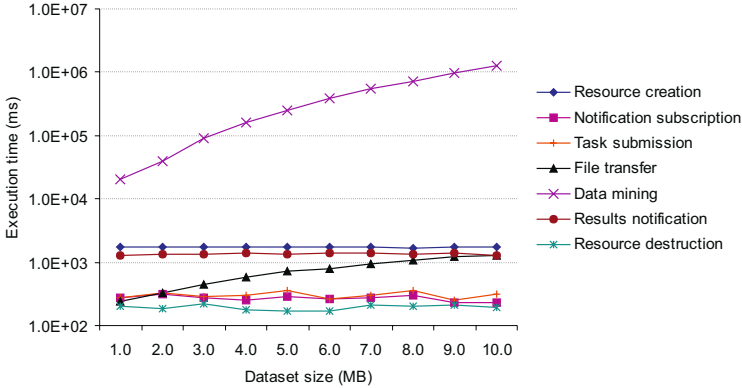


Fig. 4. Execution times of the different steps in the LAG scenario

with 10 folds. Other preliminary results obtained by running clustering tasks are discussed in [10] and are in accordance with the results discussed here.

The classification analysis on each dataset was executed in two network scenarios:

- *Local Area Grid (LAG)*: the computing node and the user node are connected by a local area network, with an average bandwidth of 94.4 Mbps and an average round-trip time (RTT) of 1.4 ms.
- *Wide Area Grid (WAG)*: the computing node and the user node are connected by a wide area network, with an average bandwidth of 213 Kbps and an average RTT of 19 ms.

Figure 4 shows the execution times of the different steps of the classification task in the LAG scenario for a dataset size ranging from 1 to 10 MB. As shown in the figure, the execution times of the WSRF-specific steps are independent from the dataset size, namely: *resource creation* (1732 ms, on the average), *notification subscription* (269 ms), *task submission* (302 ms), *results notification* (1348 ms), and *resource destruction* (194 ms).

On the contrary, the execution times of the *file transfer* and *data mining* steps are proportional to the dataset size. In particular, the execution time of the *file transfer* ranges from 240 ms for 1 MB to 1263 ms for 10 MB, while the *data mining* execution time ranges from 20311 ms for the dataset of 1 MB, to 1262603 ms for the dataset of 10 MB. The total execution time ranges from 24320 ms for the dataset of 1 MB, to 1267620 ms for the dataset of 10 MB.

Figure 5 shows the execution times of the different steps in the WAG scenario. The execution times of the WSRF-specific steps are similar to those measured in the LAG scenario. The only significant difference is the average execution time of the *results notification* step, which increases from 1348 ms in the LAG scenario to 2227 ms in the WAG scenario, due to additional time needed to transfer the classification model through a low-speed network. For the same reason,

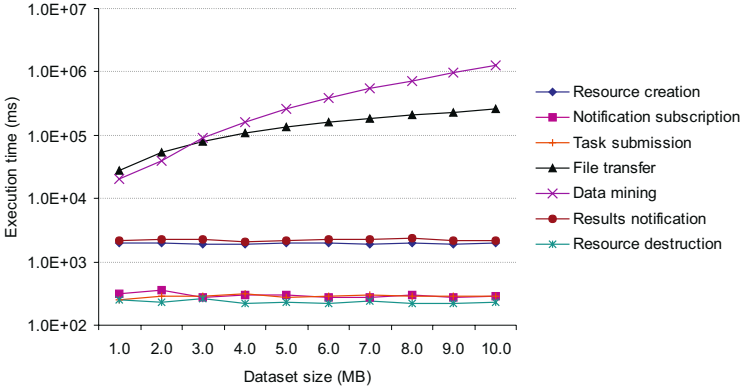


Fig. 5. Execution times of the different steps in the WAG scenario

the transfer of the dataset to be mined requires an execution time significantly greater than the one measured in the LAG scenario. In particular, the execution time of the *file transfer* step in the WAG scenario ranges from 27501 ms for 1 MB to 256021 ms for 10 MB.

The *data mining* execution time is similar to that measured in the LAG scenario, since the classification analysis is executed on an identical computing node. Mainly due to the additional time required by the *file transfer* step, the total execution time is greater than the one measured in the LAG scenario, ranging from 52914 ms for the dataset of 1 MB to 1532678 ms for the dataset of 10 MB. Notice that the *data mining* line crosses the *file transfer* line in correspondence of the dataset of 3 MB. Under this size the *data mining* step is very fast, so the *file transfer* time is the dominant one, whereas for larger datasets the data mining time is larger than the data transfer overhead.

To better highlight the overhead introduced by the WSRF mechanisms and the distributed scenario, Figure 6 shows the percentage of execution times of the *data mining*, *file transfer*, and the other steps with respect to the total execution

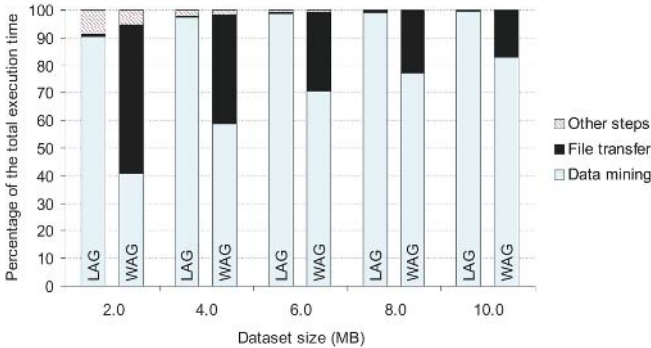


Fig. 6. Percentage of the execution times of the different steps in the LAG and WAG scenarios

time in the LAG and WAG scenarios. For space reasons, the values reported in this figure refer only to the datasets of 2, 6, 4, 8 and 10 MB.

In the LAG scenario the *data mining* step takes the 90.40% of the total execution time for the dataset of 2 MB, whereas it takes the 99.60% of the total execution time for the dataset of 10 MB. At the same time, the *file transfer* ranges from 0.75% to 0.10%, and the other steps range from 8.85% to 0.30%. In the WAG scenario the *data mining* step takes from 40.64% to 82.97% of the total execution time, the *file transfer* ranges from 54.21% to 16.70%, while the other steps range from 5.15% to 0.32%.

We can observe that in the LAG scenario neither the *file transfer* nor the other steps represent a significant overhead with respect to the total execution time. In the WAG scenario the *file transfer* is a critical step only on small datasets, since in this case the *data mining* step is very fast. However, in most scenarios the data mining step is a very time-consuming task, so the *file transfer* step - if needed - is marginal when large datasets must be transferred, as shown in the figure.

As a concluding remark, the performance analysis discussed above demonstrates the efficiency of the WSRF mechanisms as a means to execute data mining tasks on remote resources. By exploiting such mechanisms, Weka4WS can provide an effective way to perform compute-intensive data analysis in Grid environments.

4 Conclusions

Today many data repositories are distributed for necessity and privacy reasons, therefore distributed infrastructures can help in designing data management systems that access and analyze data sources where they are or where it is necessary for functionality and/or performance purposes. To pursue this approach, distributed middleware is a key element and can help users in achieving their goals.

The toolkit described in this paper offers a large set of data mining services for executing knowledge discovery applications in distributed environments. Weka4WS adopts the emerging Web Services Resource Framework (WSRF) for composing knowledge discovery applications that integrate data, algorithms, and resources available from dispersed sites.

The experimental results demonstrate the low overhead of the WSRF invocation mechanisms with respect to the execution time of data mining algorithms, and the efficiency of WSRF as a means for executing data mining tasks on remote resources. By exploiting such mechanisms, Weka4WS can provide an effective way to perform compute-intensive data analysis on Grids. The Weka4WS code is available for research and application purposes. It can be downloaded from <http://grid.deis.unical.it/weka4ws>.

Acknowledgements

This research work is carried out under the FP6 Network of Excellence Core-GRID funded by the European Commission (Contract IST-2002-004265). This

work has been also supported by the Italian MIUR FIRB Grid.it project RBNE01KNFP on High Performance Grid Platforms and Tools.

References

1. Brezany, P., Hofer, J., Tjoa, A. M., Woehrer, A.: Towards an open service architecture for data mining on the grid. Conf. on Database and Expert Systems Applications (2003).
2. Cannataro, M., Talia, D.: The Knowledge Grid. CACM, vol. 46 n. 1 (2003) 89-93.
3. Skillicorn, D., Talia, D.: Mining Large Data Sets on Grids: Issues and Prospects. Computing and Informatics, vol. 21 n. 4 (2002) 347-362.
4. Curcin, V., Ghanem, M., Guo, Y., Kohler, M., Rowe, A., Syed, J., Wendel, P.: Discovery Net: Towards a Grid of Knowledge Discovery. Conf. on Knowledge Discovery and Data Mining (2002).
5. Witten, H., Frank, E.: Data Mining: Practical machine learning tools with Java implementations. Morgan Kaufmann (2000).
6. Czajkowski, K. et al: The WS-Resource Framework Version 1.0 (2004). <http://www-106.ibm.com/developerworks/library/ws-resource/ws-wsrf.pdf>.
7. Foster, I.: Globus Toolkit Version 4: Software for Service-Oriented Systems. Conf. on Network and Parallel Computing, LNCS 3779 (2005) 2-13.
8. Allcock, B., Bresnahan, J., Kettimuthu, R., Link, M., Dumitrescu, C., Raicu, I., Foster, I.: The Globus Striped GridFTP Framework and Server. Conf. on Supercomputing (2005).
9. The UCI Machine Learning Repository. <http://www.ics.uci.edu/~mlearn/MLRepository.html>.
10. Talia, D., Trunfio, P., Verta, O.: Weka4WS: a WSRF-enabled Weka Toolkit for Distributed Data Mining on Grids. Conf. on Principles and Practice of Knowledge Discovery in Databases, LNCS 3721 (2005) 309-320.

On Mining 2 Step Walking Pattern from Mobile Users

John Goh and David Taniar

School of Business Systems, Monash University,
Clayton, Vic 3800 Australia

{Jen.Goh, David.Taniar}@infotech.monash.edu.au

Abstract. Knowledge extraction from mobile user data analyzes data collected from mobile users, such as their user movement data in order to derive useful knowledge. User movement data is stored in a database which records the (x, y) coordinates that users have visited at any given point of time, for each mobile users. In this paper, we present a novel method for mining 2 step walking pattern from mobile users. The result of 2 step walking pattern provides the knowledge of how mobile users walks from one location of interest (*LOI*) to another in any given 2 steps. Case study for Walking-Matrix and Walking-Graph are provided along with performance evaluation.

1 Introduction

Knowledge extraction from mobile user data [23-27, 17-19] is the use of innovative methods for discovering knowledge about mobile users through data gathered from the mobile environment. Knowledge extraction [1, 2, 4, 22] has since been applied into many fields such as discovery from periodic data [7, 8, 9, 12, 13], market basket data [1, 2, 20] and data warehouse [29]. Another part of knowledge extraction research is to improve the performance [28] of mining these data by reducing the cost and time to generate the result. Majority in the population today have a mobile phone. Mobile phone being a mobile device provides communication service to mobile users. Latest invention [21] in mobile phone provides additional services such as global positioning system [3, 14] (*GPS*), radio, email, web services and data services. Therefore, mobile devices can also be location aware [30].

Mobile devices are constantly carried by mobile users, and perform services for them. It can collect useful data for data mining. Some of these data are: location information, parties of communication, date and time of communication [5, 6, 10, 11]. These data could be refined, and prepared for further knowledge discovery. This places mobile data mining in a strategic position for data mining [15, 16] as it carries the data that are closely related to the day to day life of mobile users, such as where they go, what they do. Privacy is an issue when dealing of mobile user data mining, as for many other data mining projects. This paper proposes an innovative method in analyzing how mobile users walks from one location to another in 2 steps, named 2 step walking pattern.

2 Background

The problem of mining 2 step walking pattern is first initiated with a user movement database (*UMD*) which contains a list of (x, y) coordinates that mobile users have visited over every single point in time. Therefore, at any given point, the location of mobile user was tracked and recorded. An example is user movement database, which will be used in the rest of paper is shown in figure 1.

t	u1		u2		u3		u4		u5		u6	
	x	y	x	y	x	y	x	y	x	y	x	y
1	0	0	1	12	0	0	0	0	6	6	6	6
2	0	1	1	13	0	1	0	1	6	7	6	7
3	0	2	1	14	0	2	0	2	6	8	6	8
4	6	6	7	7	6	6	6	6	7	7	12	6
5	6	7	7	8	6	7	6	7	7	8	13	6
6	6	8	7	9	6	8	6	8	7	9	14	6
7	7	7	12	6	7	7	12	6	1	12	15	1
8	7	8	13	6	7	8	13	6	1	13	15	2
9	7	9	14	6	7	9	14	6	1	14	15	3
10	6	6	15	1	12	6	15	1	0	0	0	0
11	6	7	15	2	13	6	15	2	0	1	0	1
12	6	8	15	3	14	6	15	3	0	2	0	2
13	12	6	6	6	15	1	6	6	6	6	6	6
14	13	6	6	7	15	2	6	7	6	7	6	7
15	14	6	6	8	15	3	6	8	6	8	6	8
16	1	12	12	6	6	6	7	7	12	6	7	7
17	1	13	13	6	6	7	7	8	13	6	7	8
18	1	14	14	6	6	8	7	9	14	6	7	9
19	7	7	15	1	7	7	0	0	15	1	15	1
20	7	8	15	2	7	8	0	1	15	2	15	2
21	7	9	15	3	7	9	0	2	15	3	15	3

Fig. 1. User movement database

The next database is to be defined by the data miner, and is called locations of interest (*LOI*) database. *LOI* database consists of the list of location of interest, each defined by a pair of (x, y) coordinates. These coordinates represents the “from position” (x_{from}, y_{from}) and “to position” (x_{to}, y_{to}) in order to define a rectangular area in the two dimensional mobile environment. Figure 2 shows a graphical representation of all the *LOI*.

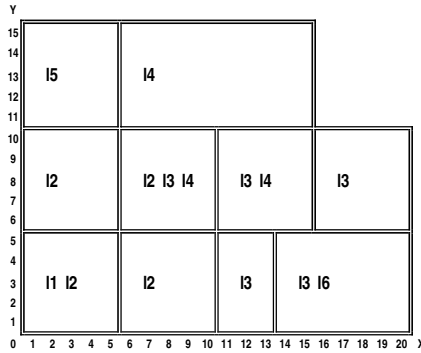


Fig. 2. Graphical representation of location of interest ($l_1, l_2, l_3, l_4, l_5, l_6$)

3 Proposed Method: 2 Step Walking Pattern

The proposed method of 2 step walking pattern is defined as below.

Definition 1: Mobile Environment: Let M be a set of physical coordinates in a two dimensional physical mobile environment, as such $M = \{m_1, m_2, m_3, \dots, m_n\}$. Let I be a set of location of interest, as such $I = \{i_1, i_2, i_3, \dots, i_n\}$, which represents the coordinates of the centre point of a subject in M .

Definition 2: Mobile User: Let U be a set of mobile users in the mobile environment M , as such $U = \{u_1, u_2, u_3, \dots, u_n\}$. Each mobile user in the mobile environment u_j can be identified through a two dimensional coordinates (x, y) , such that location of a mobile user u_j is defined as: $u_j:(u_j;x, u_j;y)$.

Definition 3: We define *location of interest* as a set of pre-defined points (m_n) in the mobile environment (M). These pre-defined points are the location of interest selected by the data miner in order to discover the knowledge of relationship among these locations and the mobile users. Examples of location of interest are *cafés, bookshops, gyms* and *cinemas*.

Definition 4: We define *min-duration* as the minimum duration a mobile user has to present to a location of interest before it is regarded as having an interest in the location. Otherwise, it is deemed that the mobile user have merely passed through the location of interest and was not interested. For t_i to t_j on the same location, if $t_j - t_i \geq min-duration$, then $t_i \rightarrow t_j$ is a valid section, and $t_j - t_i$ is the duration of the valid section.

Definition 5: We further define that mobile user can only be present in *one physical location at any single time*. Therefore, mobile user can only be present in one single point of interest at any single time. $\forall m, t(UMD) : \exists(x, y)$.

Definition 6: We define that location of interest (*LOI*) is represented by a two (x, y) coordinates, namely (x_{from}, y_{from}) and (x_{to}, y_{to}) which represents the starting position and the ending position of two pair of coordinates in order to represent a rectangle.

Definition 7: The location of interest (*LOI*) can be overlapped. This means that at a given position (x, y) , it may represent more than one location of interest, thus $(x, y) \rightarrow 0$ or $\{l_1, l_2, l_3 \dots, l_n\}$.

Definition 8: Minimum weight is stored as *min-weight*. Minimum weight represents the minimum number of occurrence of a candidate 2 step walking pattern over the whole user location database (*ULD*) in order to be qualified as significant enough to be considered as a valid 2 step walking pattern. Minimum weight is defined using a percentage value ranging from 0 to 1, where the actual number required for qualification is equal to $\text{min_weight} * \text{no of mobile users}$.

Definition 9: Candidate walking pattern $(l_x \rightarrow l_y)$ where $x = y$ is not a significant walking pattern because it does not present any sign of movement to another location of interest.

The process of mining 2 step walking pattern is as follows:

Step 1: User movement database (*UMD*) is supplied as the source dataset.

Step 2: Location of interest (*LOI*) are defined in the location of interest database (*LOD*).

Step 3: Minimum duration is defined and stored as *min-duration*. User movement database (*UMD*) is analyzed and converted to relevant location of interest provided that (x, y) stays within the *LOI* boundary for *min-duration*.

Step 4: User location database (*ULD*) is generated based on the analysis from user movement database (*UMD*) and user and location of interest database (*LOD*).

Step 5: Minimum weight is defined and stored as *min-weight*. Analysis is performed on user location database (*ULD*) through using minimum-weight, user location summary database (*ULSD*) is submitted to Walking-Matrix algorithm or Walking-Graph algorithm and final results are displayed. Relevant algorithms follow.

Walking-Matrix Algorithm

Input: User location database (*ULD*), *min_weight*

Output: List of valid 2 step walking pattern

```

01  k = total_mobile_users(ULD);
02  matrix = new Matrix (k, k); // k * k matrix is created;
03  initialize(matrix);
04  for each mobile user u do
05      for each candidate 2 walking pattern (x → y) do
06          matrix(x, y)++;
07      end for
08  end for
09  weight = min_weight * k; // calculate required weight
10  display_matrix(weight); // displays all valid 2 step walking pattern

```

Fig. 3. Algorithm Walking-Matrix

Walking-GraphInput: User location database (*ULD*), *min_weight*

Output: List of valid 2 step walking pattern

```

01 for each mobile user u in ULD do
02   generate_node(graph, u);
03 end for
04 initialize(graph);
05 for each mobile users u do
06   for each candidate 2 walking pattern (x → y) do
07     edge (ux, uy) ++;
08   end for
09 end for
10 k = total_mobile_users(ULD);
11 weight = min_weight * k; // calculate required weight
12 for each node n in graph do
13   for each prefix neighbour p do
14     if p.total > weight then
15       output(p → n);
16     end if
17   end for
18 end for

```

Fig. 4. Algorithm Walking-Graph

Figure 3, 4 represents the snapshots of algorithms used in mining valid 2 step walking patterns. Figure 3 shows how the walking-matrix algorithm is used to determine the output from the user location summary database (*ULSD*). The algorithm uses matrix in order to perform the counting process and output by reading the matrix where *weight* > *min_weight*. Figure 4 shows the algorithm for walking-graph where user location summary database (*USLD*) is converted into graph with nodes and edges. Each node represents the location of interest and each edge represents the relationship between these locations of interests.

4 Case Study

Using the user movement database (*UMD*) and location of interest database (*LOD*) in figure 1 and 2, and pre-defined threshold of *min_duration* = 3, and *min_weight* = 0.5, the following walkthrough provides an insight of how the 2 step walking pattern mining process works.

Step 1: User movement database (*UMD*) is supplied as the source dataset, as per figure 1.

Step 2: Location of interest (*LOI*) are defined in the location of interest database (*LOD*), as per figure 2.

Step 3: Minimum duration is defined and stored as *min-duration*. User movement database (*UMD*) is analyzed and converted to relevant location of interest provided that (x, y) stays within the *LOI* boundary for min-duration. Here, $min_duration = 3$, and $min_weight = 0.5$.

Step 4: User location database (*ULD*) is generated based on the analysis from user movement database (*UMD*) and user and location of interest database (*LOD*). The result of this is as shown in figure 5. Each (x, y) coordinate is converted to $\{l_1, l_2, l_3, l_4, l_5, l_6\}$ location of interest. For example, for user u_1 , at time 1, is l_1 and l_2 . This means that *user 1* at *time 1* is considered to be at both location of interest l_1 and l_2 .

	u_1	u_2	u_3	u_4	u_5	u_6
1	l1, l2	l5	l1, l2	l1, l2	l2	l2
2	l1, l2	l5	l1, l2	l1, l2	l2	l2
3	l1, l2	l5	l1, l2	l1, l2	l2	l2
4	l2	l2, l4	l2	l2	l2, l4	l3
5	l2	l2, l4	l2	l2	l2, l4	l3
6	l2	l2, l4	l2	l2	l2, l4	l3
7	l2, l4	l3	l2, l4	l3	l5	l6, l3
8	l2, l4	l3	l2, l4	l3	l5	l6, l3
9	l2, l4	l3	l2, l4	l3	l5	l6, l3
10	l2	l6, l3	l3	l6, l3	l1, l2	l1, l2
11	l2	l6, l3	l3	l6, l3	l1, l2	l1, l2
12	l2	l6, l3	l3	l6, l3	l1, l2	l1, l2
13	l3	l2	l6, l3	l2	l2	l2
14	l3	l2	l6, l3	l2	l2	l2
15	l3	l2	l6, l3	l2	l2	l2
16	l5	l3	l2	l2, l4	l3	l2, l4
17	l5	l3	l2	l2, l4	l3	l2, l4
18	l5	l3	l2	l2, l4	l3	l2, l4
19	l2, l4	l6, l3	l2, l4	l1, l2	l6, l3	l6, l3
20	l2, l4	l6, l3	l2, l4	l1, l2	l6, l3	l6, l3
21	l2, l4	l6, l3	l2, l4	l1, l2	l6, l3	l6, l3

Fig. 5. User location database (*ULD*)

Step 5: Minimum weight is defined and stored as *min-weight*. Analysis is performed on user location database (*ULD*) through using minimum-weight, and user location summary database (*ULSD*) is submitted to *Walking-Matrix* algorithm or *Walking-Graph* algorithm and final results are displayed.

Through analysis of user location database, the following can be gathered:

u_1	u_2	u_3	u_4	u_5	u_6
$l_1 \rightarrow l_2$	$l_5 \rightarrow l_2$	$l_1 \rightarrow l_2$	$l_1 \rightarrow l_2$	$t_2 \rightarrow t_2$	$l_2 \rightarrow l_3$
$t_2 \rightarrow t_2$	$l_5 \rightarrow l_4$	$t_2 \rightarrow t_2$	$t_2 \rightarrow t_2$	$l_2 \rightarrow l_4$	$l_3 \rightarrow l_6$
$t_2 \rightarrow t_2$	$l_2 \rightarrow l_3$	$t_2 \rightarrow t_2$	$l_2 \rightarrow l_3$	$l_2 \rightarrow l_5$	$t_3 \rightarrow t_3$
$l_2 \rightarrow l_4$	$l_4 \rightarrow l_3$	$l_2 \rightarrow l_4$	$l_3 \rightarrow l_6$	$l_4 \rightarrow l_5$	$l_6 \rightarrow l_1$
$t_2 \rightarrow t_2$	$l_3 \rightarrow l_6$	$t_3 \rightarrow t_3$	$t_3 \rightarrow t_3$	$l_5 \rightarrow l_1$	$l_6 \rightarrow l_2$
$l_4 \rightarrow l_2$	$t_3 \rightarrow t_3$	$l_4 \rightarrow l_3$	$l_6 \rightarrow l_2$	$l_5 \rightarrow l_2$	$l_3 \rightarrow l_1$
$l_2 \rightarrow l_3$	$l_6 \rightarrow l_2$	$l_3 \rightarrow l_6$	$l_3 \rightarrow l_2$	$l_1 \rightarrow l_2$	$l_3 \rightarrow l_2$
$l_3 \rightarrow l_5$	$l_3 \rightarrow l_2$	$t_3 \rightarrow t_3$	$t_2 \rightarrow t_2$	$t_2 \rightarrow t_2$	$l_1 \rightarrow l_2$
$l_5 \rightarrow l_2$	$l_2 \rightarrow l_3$	$l_6 \rightarrow l_2$	$l_2 \rightarrow l_4$	$l_2 \rightarrow l_3$	$t_2 \rightarrow t_2$
$l_5 \rightarrow l_4$	$l_3 \rightarrow l_6$	$l_3 \rightarrow l_2$	$l_2 \rightarrow l_1$	$l_3 \rightarrow l_6$	$t_2 \rightarrow t_2$
	$t_3 \rightarrow t_3$	$t_2 \rightarrow t_2$	$t_2 \rightarrow t_2$	$t_3 \rightarrow t_3$	$l_2 \rightarrow l_4$
		$l_2 \rightarrow l_4$	$l_4 \rightarrow l_1$		$l_2 \rightarrow l_6$
			$l_4 \rightarrow l_2$		$l_2 \rightarrow l_3$
					$l_4 \rightarrow l_6$
					$l_4 \rightarrow l_3$

Fig. 6. Output from analysis of user location summary database (ULSD)

Figure 6 represents the summary of analysis from user location database (ULD). This represents all the 2 steps that each mobile users have went through in the mobile environment. The entire 2 step candidate walking pattern ($l_x \rightarrow l_y$) where $x = y$ are removed because it does not represent a significant move.

Walking Matrix

Figure 7 shows the result of walking matrix algorithm, resulting a walking matrix which consists of all the candidate 2 step walking patterns. The matrix is generated as such where if $l_1 \rightarrow l_2$ is found, it will trace l_1 on the left hand side of the matrix and l_2 on the top side of the matrix and find the exact point for (l_1, l_2) and increment it by 1. The result displays all the candidate 2 step walking patterns where $weight > min_weight$, and thus is also known as valid 2 step walking patterns.

	I1	I2	I3	I4	I5	I6
I1	*	5				
I2	±	*	7	6	±	±
I3	±	4	*		±	6
I4	±	±	3	*	±	±
I5	±	4		±	*	
I6	±	4				*

Fig. 7. Walking-Matrix

Walking Graph

Figure 8 shows the walking graph generated from analysis from *ULSD*. Each node represents a mobile user $\{u_1, u_2, u_3, u_4, u_5, u_6\}$, and each edge represents the total number of occurrences of candidate 2 step walking patterns. Since weight required is 0.5 multiplied by the total number of mobile users, therefore, $weight = 0.5 * 6 = 3$, therefore, anything lesser than 3 is taken out of consideration. The second graph represents the final output where all edges where weight is lesser than 3 are removed.

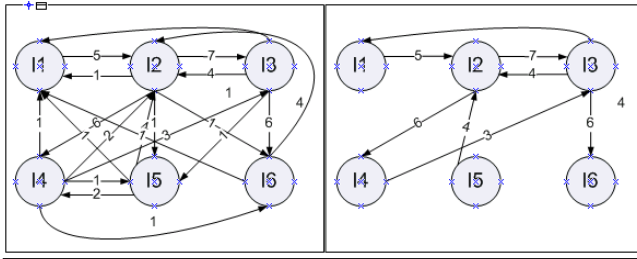


Fig. 8. Walking-Graph

5 Performance Evaluation

We evaluate and compare the performance of *Walking-Matrix* and *Walking-Graph* algorithms based on their execution time and number of walking patterns found. The experiments have been conducted using synthetically generated user movement databases on a Pentium IV machine with a CPU clock rate of 2.4 GHz, and 1 GB of main memory. Algorithms and datasets are implemented to run in main memory to allow direct comparison among them.

In the performance study experiment, we measure the execution times on three synthetic datasets. These three synthetic datasets consists of number of mobile users of 10, 100, 1,000 and total time of 1,000 seconds with 10, 100, 1000 total location of interest. Figure 9 shows the total number of valid 2 step walking patterns found for 10, 100 and 1000 mobile users in this scale up experiment. The total number of valid

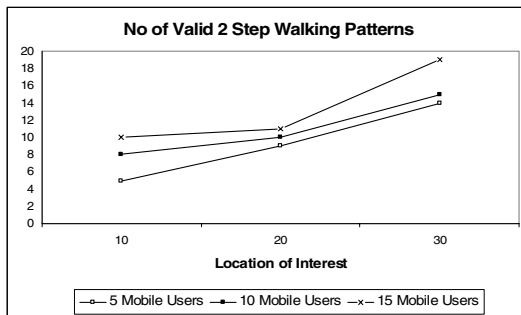


Fig. 9. Execution time

2 step walking patterns found increased when the location of interest increases. The rate of increase is greater between location of interest = 20 to location of interest = 30, compared to location of interest = 10 to location of interest = 20.

6 Conclusions and Future Works

This paper has presented a novel method for mining valid 2 step walking pattern from mobile user data. This provides the ability for the data miner to understand how mobile users walks from one location of interest to another location of interest via two step event. Potential valid 2 step walking patterns are such as mobile users are found to visit café and then directly to library, and this represents a piece of knowledge which is helpful in decision making or understanding more on mobile users.

One of the future works is to further extend the process of mining valid 2 step walking pattern into mining valid 3 step walking pattern. This allows a provision of a transitive location of interest where it is used as a stepping stone to reach the third location of interest from the first location of interest.

References

1. R. Agrawal and R. Srikat. "Fast Algorithms for Mining Association Rules". In *Proc. of the 20th VLDB*, pp. 487-499, 1994.
2. R. Agrawal and R. Srikat. "Mining Sequential Patterns". In *Proc. of 11th ICDE*, pp. 3-14, 1995.
3. B. Hofmann-Wellenhof, H. Lichtenegger, and J. Collins. *Global Positioning System: Theory and Practice*. Springer-Verlag Wien New York, third revised edition, 1994.
4. S. Chakrabarti, S. Sarawagi, and B. Dom. "Mining Surprising Patterns using Temporal Description Length". In *Proc. of 24th VLDB*, pp. 606-617, 1998.
5. L. Forlizzi, R. H. Guting, E. Nardelli, and M. Schneider. "A Data Model and Data Structures for Moving Objects Databases". *ACM SIGMOD Record*, vol. 260, pp. 319-330, 2000.
6. D. R. Forsyth. *Group Dynamics*. Wadsworth, Belmont, CA, 1999.
7. J. Han, G. Dong, and Y. Yin. "Efficient Mining of Partial Periodic Patterns in Time Series Database". In *Proc. of 15th ICDE*, pp. 106-115, 1999.
8. J. Han, J. Pei, and Y. Yin. "Mining Frequent Patterns without Candidate Generation". In *Proc. of ACM SIGMOD*, pp. 1-12, 2000.
9. J. Han and A. W. Plank. "Background for Association Rules and Cost Estimate of Selected Mining Algorithms", In *Proc. of the 5th CIKM*, pp. 73-80, 1996.
10. K. Koperski and J. Han. "Discovery of Spatial Association Rules in Geographical Information Databases". In *Proc of 4th Int Symp. on Advances in Spatial Databases*, vol. 951, pp. 47-66, 1995.
11. J. F. Roddick and B. G. Lees. "Paradigms for Spatial and Spatio-Temporal Data Mining". *Geographic Data Mining and Knowledge Discovery*, Taylor and Francis. Research Monographs in Geographical Information Systems. Miller, H. and Han, J. Eds. pp. 1-14, 2001.
12. J. F. Roddick and M. Spiliopoulou. "A Survey of Temporal Knowledge Discovery Paradigms and Methods". *IEEE Trans. on Knowledge and Data Engineering*, vol. 14, no. 4, pp. 750-767, 2002.
13. W. Wang, J. Yang, and P. S. Yu. "InfoMiner+: Mining Partial Periodic Patterns in Time Series Data". 2nd *IEEE International Conference on Data Mining ICDM 2002*, pp. 725, 2002.

14. P. Zarchan. *Global Positioning System: Theory and Applications*, vol I. American Institute of Aeronautics and Astronautics, 1996.
15. Reed Electronics Research RER – The mobile phone industry – a strategic overview, October 2002.
16. U. Varshney, R. Vetter, and R. Kalakota. “Mobile commerce: A new frontier”. *IEEE Computer: Special Issue on E-commerce*, pp. 32-38, October 2000.
17. Y. Wang, E-P Lim, and S-Y Hwang. “On Mining Group Patterns from Mobile Users”. In *Proc. of the 14th International Conference on Database and Expert Systems Applications DEXA 2003, Lecture Notes in Computer Science*, Springer-Verlag, vol. 2736, pp. 287-296, 2003.
18. Y. Wang, E-P Lim, and S-Y Hwang. “Efficient Group Pattern Mining Using Data Summarization”. In *Proc. of the 15th International Conference on Database and Expert Systems Applications DEXA 2004, Lecture Notes in Computer Science*, Springer-Verlag, vol. 2973, pp. 895-907, 2004.
19. S-Y Hwang, Y-H Loi, J-K Chiu, and E-P Lim, “Mining Mobile Group Patterns: A Trajectory-Based Approach”, In *Proc. of the 9th Pacific Asia Conference of Knowledge Discovery and Data Mining PAKDD 2005, Lecture Notes in Computer Science*, Springer-Verlag, vol. 3518, pp. 713-718, 2005.
20. M. Cho, J. Pei, H. Wang, and W. Wang, “Preference-based frequent pattern mining”, *International Journal of Data Warehousing and Mining* vol. 1, no. 4, pp. 56-77, 2005.
21. M-B Song, S-W Kang, and K-J Park, “On the design of energy-efficient location tracking mechanism in location-aware computing”, *Mobile Information Systems: An International Journal*, IOS Press, vol. 1, no. 2, pp. 109-127, 2005.
22. S. Y. Chen, and X. Loi, “Data mining from 1994 to 2004: an application-oriented review”, *International Journal of Business Intelligence and Data Mining*, vol. 1, no. 1, pp. 4-21, 2005.
23. J. Goh, and D. Taniar, “Mobile user data static object mining (MUDSOM)”, *The IEEE 20th International Conference on Advanced Information Networking and Applications*. (Submitted)
24. J. Goh, and D. Taniar, “Static Group Pattern Mining (SGPM)”, *The 10th Pacific Asia Conference on Knowledge Discovery and Data Mining PAKDD 2006* (Submitted).
25. J. Goh, and D. Taniar. “Mining Frequency Pattern from Mobile Users”, *Knowledge Based Intelligent Information & Engineering and Systems, Lecture Notes in Computer Science Part III*, Springer-Verlag, vol. 3215, pp. 795-801, 2004.
26. J. Goh, and D. Taniar. “Mobile User Data Mining by Location Dependencies”, *5th International Conference on Intelligent Data Engineering and Automated Learning, Lecture Notes in Computer Science*, Springer-Verlag, vol. 3177, pp. 225-231, 2004.
27. J. Goh, and D. Taniar. “Mining Parallel Pattern from Mobile Users”, *International Journal of Business Data Communications and Networking*, vol. 1, no. 1, pp. 50-76, 2005.
28. Y. Xiao, J. F. Yao, and G. Yang, “Discovering Frequent Embedded Subtree Patterns from Large Databases of Unordered Labeled Trees”, *International Journal of Data Warehousing and Mining*, vol. 1, no. 2, pp. 70-92, 2005.
29. H. C. Tjioe, and D. Taniar, “Mining Association Rules in Data Warehouses”, *International Journal of Data Warehousing and Mining*, vol. 1, no. 3, 2005.
30. J. Häkkinä, and J. Mäntyjärvi, “Combining Location-Aware Mobile Phone Applications and Multimedia Messaging”, *Journal of Mobile Multimedia*, vol. 1, no. 1, pp. 18-32, 2005.
31. P. K. C. Tse, W. K. Lam, K. W. Ng, and C. Chan, “An Implementation of Location-Aware Multimedia Information Download to Mobile System”, *Journal of Mobile Multimedia*, vol. 1, no. 1, pp. 33-46, 2005.
32. D. L. Lee, M. Zhu, and H. Hu, “When location based services meet databases”, *Mobile Information Systems*, vol. 1, no. 2, pp. 81-90, 2005.
33. J. Jayaputera, and D. Taniar, “Data retrieval for location-dependent queries in a multi-cell wireless environment”, *Mobile Information Systems*, vol. 1, no. 2, pp. 91-108, 2005.

Effect of Similar Behaving Attributes in Mining of Fuzzy Association Rules in the Large Databases

Zahra Farzanyar¹, Mohammadreza Kangavari², and Sattar Hashemi²

¹ SECOMP Lab., Department of Computer & IT,
Iran University of Science & Technology (IUST), Tehran, Iran
nsfarzan@yahoo.com

² Department of Computer & IT,
Iran University of Science & Technology (IUST), Tehran, Iran
kangavari@iust.ac.ir, s_hashemi@iust.ac.ir

Abstract. Association rule mining is an active data mining research area. Recent years have witnessed many efforts on discovering fuzzy associations. The key strength of fuzzy association rule mining is its completeness. This strength, however, comes with a major drawback. It often produces a huge number of fuzzy associations. This is particularly true for datasets whose attributes are highly correlated. The huge number of fuzzy associations makes it very difficult for a human user to analyze them. Existing research has shown that most of the discovered rules are actually redundant or insignificant. In this paper, we propose a novel technique to overcome this problem. The approach is effective because experiment results show that the set of produced rules is typically very small. Our solution also reduces the size of average transactions and dataset. Our performance study shows that this solution has a superior performance over the other algorithms.

Keywords: Data mining, fuzzy association rules, linguistic terms.

1 Introduction

Data mining is concerned with the nontrivial extraction of potentially useful information from data [1]. The regularities or exceptions discovered from databases through data mining have enabled human decision makers to better make decisions in many different areas [1, 2]. One important topic in data mining research is concerned with the discovery of interesting association rules. Associations allow capturing all possible rules that explain the presence of some items according to the presence of other items in the same transaction. An association rule is an implication of the form $X \Rightarrow Y$, where X and Y are sets of attributes. Association rules can be rated by a number of quality measures, among which support and confidence stand out as the two essential ones [3]. The basic problem of mining association rules is then to generate all association rules $X \Rightarrow Y$ that have support and confidence greater than user-specified thresholds.

The problem of mining association rules was first introduced by Agrawal et al [4], for databases consisting of only categorical attributes. In most real life applications, databases contain many other attribute values besides 0 and 1 such as cardinal or ordinal attributes. Unfortunately, the definition of categorical association rules does

not translate directly to the case of quantitative attributes. It is therefore necessary to provide a definition of association rules for the case of a database containing quantitative attributes. To handle databases with both categorical and quantitative attributes, a quantitative association rule mining method was proposed by Srikant and Agrawal [5]. The method finds association rules by partitioning the quantitative attribute domain and then transforming the problem into binary one.

Apparently, whatever partitioning methods are applied, “sharp boundaries” remain a problem, which may lead to an inaccurate representation of semantics. As a remedy to the sharp boundary problem, the fuzzy set concept has recently been used more frequently in mining quantitative association rules. The fuzzy set theory introduced by Zadeh [6] is better than the interval method because fuzzy sets provide a smooth transition between member and non_member of a set. In these methods, each of quantitative attributes is replaced by a few other attributes that partition the range of the original one using the fuzzy theory. A column belongs to each of these partitions in the table containing transactions. So, the size of each transactions increase which leads to a rising in their scan time. Also in frequent itemsets generation step, the number of candidate itemsets is several times more than when all the exiting attributes are binary forms. It finally causes the definite time to compute the frequency of the candidate itemsets be more.

The other problem emerging here is the huge number of final produced rules. The huge number of associations makes it very difficult, if not impossible, for a human user to analyze them in order to identify those interesting/useful ones. The question is: “Can we preserve the full power of fuzzy association rule mining (i.e., its completeness) without overwhelming the user?”

In this paper, we propose a novel technique to overcome these problems by focusing on similar behaving attributes. The prominent difference of this algorithm efficiency compared to other algorithms is in the number of final produced rules.

This paper is organized as follows. In Section 2, the related works on the mining fuzzy association rules and studies on the interestingness and clustering are outlined. Section 3 investigates the definitions and methodology of mining fuzzy association rules also it introduces a formula to testing strong dependence between attributes and describes a new algorithm of mining fuzzy association rules. Section 4 shows the experimental results. The last section concludes the paper.

2 Related Work

In recent years, some work has been done on the use of fuzzy sets in discovering association rules for quantitative attributes. Miller and Yang [9] applied Birch clustering to identify intervals and proposed a distance-based association rules mining process, which improves the semantics of the intervals. Hirota and Pedrycz [28] proposed a context sensitive fuzzy clustering method based on fuzzy C-means to construct rule-based models. To solve the qualitative knowledge discovery problem, Au and Chan [10] applied fuzzy linguistic terms to relational databases with numerical and categorical attributes. Later, they proposed the F-APACS method [11] to discover fuzzy association rules. Yager [24] introduced fuzzy linguistic summaries on different attributes.

Some work has been done automatically determining the number and intervals of the clusters. Fu et al. [26] proposed an automated method to find fuzzy sets for the mining of fuzzy association rules. Their method is based on CLARANS clustering algorithm [27]. Recently, M. Kaya [30] presented a novel automated clustering method based on multi-objective GA [29].

Hong et al. [12] proposed definitions for the support and confidence of fuzzy membership grades and designed an algorithm to find interesting fuzzy association rules. Ishibuchi et al. [21] and E. Hullermeier [7] illustrated fuzzy versions of confidence and support.

Gyenesei [15, 22] presented two different methods for mining fuzzy quantitative association rules, namely *without normalization* and *with normalization*. The experiments of Gyenesei showed that the numbers of large itemsets and interesting rules found by the fuzzy method are larger than the discrete method defined by Srikant and Agrawal [5]. Hu and Chen [18], the algorithm named FGBRMA, proposed to generate fuzzy association rules from a relational database. Au and Chan [19] developed a fuzzy technique, called FARM II. FARM II is able to handle both relational and transactional data. Chen [13] proposed the fuzziness based fuzzy taxonomies. Some other researchers investigated the mining of weighted association rules. Some approaches by Cai & Fu et al. [14], Gyenesei [15], Shu & Tsang et al. [16], Lee [17] etc. have already been proposed, which are basically similar. Ya et al [20] introduced an algorithm for mining fuzzy association rules by removing redundant fuzzy association rules.

In all the previous algorithms for fuzzy association rules mining, the objective is to find frequent fuzzy itemsets by expanding techniques presented for the binary form and the problems existing in the fuzzy form (that introduced in section 1), remain yet.

3 Fuzzy Association Rules and Proposed Algorithm

Mining fuzzy association rules is the discovery of association rules using fuzzy set concepts such that the quantitative attributes can be handled. In this paper, we view each attribute as a linguistic variable, and the variables divided into various linguistic terms. A linguistic variable is a variable whose terms are linguistic words or sentences in a natural language [31]. Triangular membership functions are used for each linguistic term defined in each quantitative attribute for simplicity. One way of determining membership functions of these linguistic terms is by expert opinion or by people's perception. Yet another way is by statistical methods [32]. Fuzzy clustering based on self-organized learning can also be used to generate membership functions [33]. In this study, we use the presented method in [18].

3.1 Problem Statements

Let $I = \{I_1, I_2, \dots, I_n\}$ be the items set where each I_j ($1 \leq j \leq n$) is an attribute of the original dataset D . Each attribute I_j may have a binary, categorical or quantitative underlying domain Δ_j . Besides, each quantitative attribute I_j is associated with at least two fuzzy sets. If each quantitative attribute I_j is extended by its fuzzy set, we can get the extended attribute set I_f from I . Using the corresponding membership functions defined with each fuzzy set, the original dataset D is changed into a fuzzy

dataset D_f . Given fuzzy dataset $D_f = \{t_1, t_2, \dots, t_N\}$ with I_f , the discovered rules are of the form: $A \Rightarrow B$, where $t_i (1 \leq i \leq N)$ is a transaction in D_f , $A \subseteq I_f, B \subseteq I_f, A \cap B = \phi$, and $A \cup B$ do not contain any two items that are associated with the same attribute (for instance, $A \cup B$ will not contain “income low and income high”). Like Boolean association rules mining, A is called the antecedent of the rule and B is called the consequent of the rule. The standard approach to evaluate the significance of fuzzy association rules is to extend the definition of well-know support and confidence measures to fuzzy association rules [7]. The degree of support of the rule $A \Rightarrow B$ for the whole D_f is defined as:

$$Dsup p(A \Rightarrow B) = \frac{\sum_{i=1}^n A(x) \otimes B(y)}{|D_f|} \quad (1)$$

And the degree of confidence is defined as:

$$Dconf(A \Rightarrow B) = \frac{\sum_{i=1}^n A(x) \otimes B(y)}{A(x)} \quad (2)$$

Where $|D_f|$ is the total number of transactions in D_f , which is equal N, the number of transactions in the quantitative database D. $A(x)$ and $B(y)$ denote the degree of membership of the element x and y with respect to the fuzzy set A and B respectively, \otimes is a t-norm [8]. Based upon the notations of Dsupp and Dconf, a rule $A \Rightarrow B$ is interesting fuzzy association rule if

1. $Dsupp(A \Rightarrow B) \geq \text{Min_supp}$;
2. $Dconf(A \Rightarrow B) \geq \text{Min_conf}$;

Where Min_supp and Min_conf are the thresholds defined by users. Straightforward mining algorithm could be obtained easily. It is basically composed of two phases: generating all frequent itemsets from fuzzy dataset based on Apriori algorithm, then generating all rules from frequent itemsets and calculating confidence for each other. This straightforward algorithm is easy to understand and implement, but the disadvantages are also obvious that introduced in section 1.

Our proposed idea in this algorithm in order to decrease the size of average transactions, data set and the number of fuzzy association rules is fusing the similar behaving attributes. We need a measure of dependency between two items. A widely used one has been introduced in [25]; it is chi-square and is based on support difference.

3.2 Chi-Square Test for Independence and Correlation

Chi-square test statistics (χ^2) is a widely used method for testing independence and/or correlation [25]. In our proposed technique, it is used for testing similar behaving between attributes. Essentially, χ^2 test is based on the comparison of observed frequencies with the corresponding expected frequencies. In other words, χ^2 is used to test the significance of the deviation from the expected values. Let f_0 be an observed frequency, and f be an expected frequency. The χ^2 value is defined as:

$$\chi^2 = \sum \frac{(f_0 - f)^2}{f} \quad (3)$$

A χ^2 value of 0 implies the attributes are statistically independent. If it is higher than a certain threshold value, we reject the independence assumption.

3.3 Proposed Algorithm in Detail

In all the previous algorithms, the objective is to find frequent fuzzy itemsets by expanding techniques presented for the binary form and the problems existing in the fuzzy form, remain. In our proposed algorithm, such procedure is not considered but the fuzzy association rule mining is taken under a novel look. In this method the similar behaving attributes are found and fused. Such attributes have very close and sometimes equal degree of membership in the fuzzy transactions. Finding two similar behaving attributes in one set and separate considering of each is time-consuming and leads to make many similar rules. In our proposed algorithm, we have used Chi-square statistic test to study the similar behavior of attributes. We assume that quantitative attributes have their fuzzy linguistic terms.

At first we construct contingency tables for attributes existing in the I-set two by two. The rows and the columns of these tables are the fuzzy partitions that belong to each of such attributes. We obtain observed frequencies for all of the tables at the same time by scanning once the database, then for each of these tables, we obtain corresponding expected frequencies in case of accepting the independence assumption, and finally we calculate the χ^2 value. The χ^2 value obtained from the chi-square test for each of the contingency tables, is compared to the chi-square table and the similar behaving attributes are determined.

For each of the similar behaving attributes, we consider two partitions which have the most frequency comparing to each other in the contingency table, we candidate them to be fused. After obtaining all the similar behaving attributes, considering the common points between them we deduce the final similar behaving attributes. Then, we fuse the final similar behaving attributes on the primary dataset. We do so by multiplying degrees of membership of partitions related to similar behaving attributes candidate for fusing. Then we put the result in a new column and eliminate the columns related to these partitions. Therefore the size of each transaction is reduced.

Nevertheless, when we fuse similar behaving attributes of each transaction, the chances of finding similar transactions increases. During the writing, a tag is placed in front of every transaction to specify how many times that transaction exists in dataset. While inserting the new transaction, the algorithm checks whether that transaction is already in the memory. If it is, it increases that transaction's counter by one. Otherwise, it inserts the transaction with a count equal to one into the main memory. So this technique reduces the average transaction length and also reduces the dataset size significantly, so we can accumulate more transactions in the main memory. These two reductions in transactions size and dataset size lead to reduction of scan time, which is very effective in increasing the performance of the proposed algorithm.

After fusing similar behaving attributes on dataset, the algorithm iterates through the new fuzzy dataset and generates the frequent itemsets of various lengths by

computing the support counts of candidate itemsets after every pass. It should be noted that the design of this step follows that of the fuzzy version of the Apriori algorithm.

In our algorithm the number of candidate fuzzy itemsets, to be generated, are much less than the previous algorithms and it causes the considerable reduction of the time spent on computing the frequency of candidate itemsets, and therefore it leads to improve the performance of proposed algorithm. Then we produce fuzzy association rules with the found frequent itemsets.

The following shows the details of the proposed algorithm:

Procedure Mining-Algorithm

Input

A set of N transaction data, each with n attribute,
fuzzy linguistic terms for quantitative attributes,
The user-specified minimum fuzzy support,
The user-specified minimum fuzzy confidence,

Output

Phase I: Fuse similar behaving attributes;
Phase II: Generate frequent fuzzy itemsets;
Phase III: Make fuzzy association rules.

Method

Phase I:

Step1. Scan the database, and construct the contingency tables for each of two attributes.

1-1. Compute the χ^2 value.

1-2. Compare obtained χ^2 with chi-square table, if the obtained χ^2 causes to reject independence assumption, announce these two attributes are similar behaving.

Step2. Deduction of final similar behaving attributes.

Step3. Fusing the similar behaving attributes in each transaction and forming a new column.

Phase II: Generate frequent itemsets

Step1. Find the frequent 1-itemsets.

Do

Step2. Produce the frequent k-itemsets L_k

2-1. Produce the candidate k-itemsets C_k from frequent (k-1) itemsets L_{k-1}.

2-2. Compute the support degree for each itemset in k-itemsets by Eq (1).

2-3. Delete the k-itemsets of which support is less than the user-specified minimum fuzzy support.

2-4. Insert the remaining k-itemsets into the frequent itemsets L_k.

Until no more frequent itemset is produced.

Phase III: Make fuzzy association rules with the found frequent itemsets.

Step1. Compute the confidence degree for each rule by Eq (2).

Step2. Remove the rules with the confidence degree less than the user-specified minimum fuzzy confidence.

Step3. Output the remaining fuzzy association rules with their support and confidence degrees and write Meta rules related to each of produced rules.

After finishing the algorithm, we would have all the fuzzy association rules resulting from this new fuzzy dataset. The rules obtained from the proposed algorithm are an exact summary of all the rules made in previous algorithms. We have used Meta rules for them to maintain exactness of the obtained rules. Such rules are the main rules and they show the behavior of similar behaving attributes. In making all the rules we have considered the main rules as the basic ones, and also, we have made the other rules upon them so that they would not break Meta rules. The support degree of these rules is obtained from the related frequencies of contingency tables.

The user can now obtain a complete picture of the domain without being overwhelmed by a huge number of rules. From this summarized information, user can then find some interesting aspects to focus on. So Complexity in phase III of algorithm is reduced.

3.4 Complexity Analysis

Given a database containing N transactions such that each transaction is characterized by n attributes and each attribute is represented by m linguistic terms. The number of contingency tables for chi-square test should be calculated from the following formula:

$$c_n = \sum_{x=1}^{n-1} x = \frac{n(n-1)}{2} \quad (4)$$

Complexity in each of the contingency tables is $O(m^2 N)$, so the complexity of the testing step of the attributes similar behavior is calculated as follows:

$$(m^2 N) \left(\frac{n(n-1)}{2} \right) = (m^2 N)(n^2) = O(m^2 n^2 N) \quad (5)$$

This complexity is indeed desirable.

4 Experimental Results

To illustrate the effect of fusing similar behaving attributes, we will compare the performance of our new algorithm with that of the other method. The only difference between our new algorithm and old algorithm is that the latter do not fuse the similar behaving attributes before scanning the database when generating fuzzy frequent itemsets. In order to evaluate the effectiveness of our new algorithm, we applied it as well as old algorithm to a simulated database. These two algorithms were implemented on pc with CPU 1700-BANIAS, RAM 512M, windows XPPRO-TRAD, and Borland C++ 5.0.

From Figure 1, the experimental results show that the number of rules in our new algorithm is much less than those of old algorithm, which means, with the increasing of the number of attributes, the number of the similar behaving attributes is growing sharply.

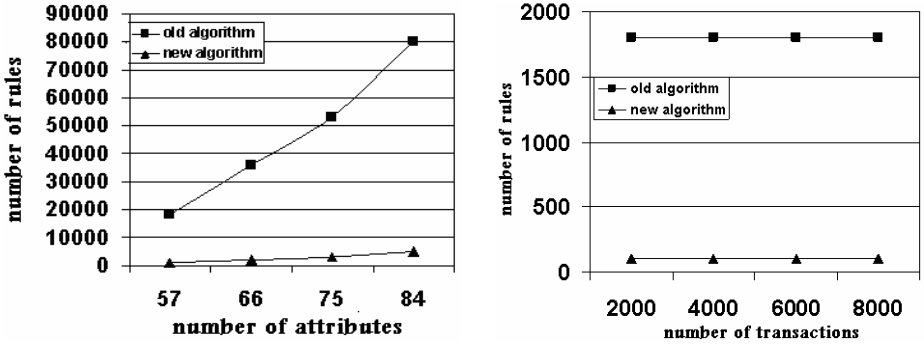


Fig. 1. Rules generated

From Figure 2, we can observe that the executing time of our new algorithm is much less than that of old algorithm.

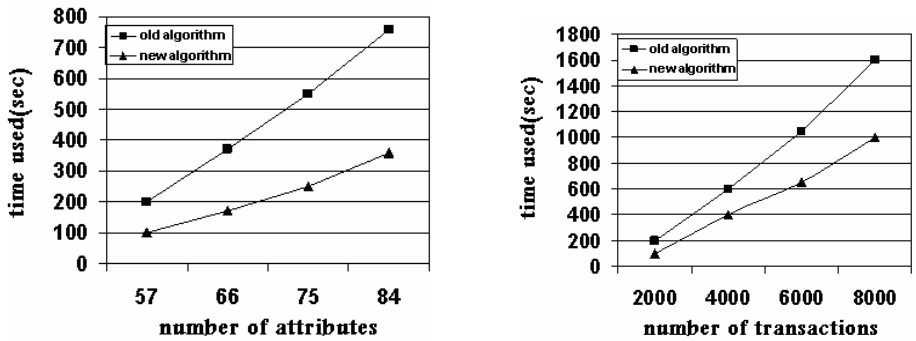


Fig. 2. Execution time

5 Conclusion

Association rule mining is an active data mining research area. Fuzzy association rules described by the natural language are well suitable for the thinking of human subjects. Thus, fuzzy association rules will be helpful to increase the flexibility for the users in making any decisions or designing the fuzzy systems. If mining procedure also produces a huge number of rules, it will be of limited use because a human user does not have the ability to analyze these rules. However, if such a huge number of rules do exist in the data, it will not be appropriate to arbitrarily discard any of them

or to generate only a small subset of them. It is much more desirable if we can summarize them. This paper proposes such a technique. In this way, the fuzzy association rules can be manually inspected by a human user without too much effort.

In our proposed method, the size of average transactions and original dataset is reduced effectively by the recognition and fusion of similar behaving attributes and mining is performed on the reduced dataset that produces a much smaller but richer set of fuzzy association rules which has been approved by experimental results.

References

1. G. Piatetsky-Shapiro, and W.J. Frawley (Eds.), *Knowledge Discovery in Databases*, AAAI/MIT Press, (1991).
2. U.M. Fayyad, G. Piatetsky-Shapiro, P. Smyth, and R. Uthurusamy (Eds.), *Advances in Knowledge Discovery and Data Mining*, AAAI/MIT Press, (1996).
3. J.W. Han, M. Kamber, *Data Mining: Concepts and Techniques*, Morgan Kaufmann, San Francisco, (2001).
4. R. Agrawal, T. Imielinski, A. Swami, Mining association rules between sets of items in large databases, *Proceedings of the ACM SIGMOD International Conference on Management of Data*, May (1993), pp. 207–216.
5. R. Srikant, R. Agrawal, Mining Quantitative Association Rules in Large Relational Tables, *Proc. of ACM-SIGMOD*, Montreal, Canada, (1996).
6. L.A. Zadeh, Fuzzy sets, *Inform. and Control* 8 (1965) 338–353.
7. E. Hullermeier and J. Beringer. Mining implication-based fuzzy association rules in databases, B. Bouchon-Meunier, L.Foulloy, and R.R. Yager, (eds.) *Intelligent Systems for Information Processing: From Representation to Applications*.Elsevier,(2003).
8. D. Ruan, and E.E. Kerre, Fuzzy implication operators and generalized fuzzy method of cases, *Fuzzy Sets and systems*,54(1),pp.23-38,(1993).
9. R.J. Miller, Y. Yang, Association rules over interval data, in: *Proc. ACM SIGMOD Internat. Conf. Management of Data*, (1997), pp. 452–461.
10. K.C.C. Chan and W.-H. Au, “An Effective Algorithm for Mining Interesting Quantitative Association Rules,” in *Proc. of the 12th ACM Symp. on Applied Computing*, San Jose, CA, Feb. (1997), pp. 88-90.
11. K.C.C. Chan and W.-H. Au, “Mining Fuzzy Association Rules,” in *Proc. of the 6th ACM Int’l Conf. on Information and Knowledge Management*, Las Vegas, Nevada, Nov. (1997), pp. 209-215.
12. T.P. Hong, C.S. Kuo, S.C. Chi, Mining association rules from quantitative data, *Intell. Data Anal.* 3 (1999) 363–376.
13. Chen, G. Q.; Wei, Q., (2002). Fuzzy Association Rules and the Extended Mining Algorithms, *Information Sciences*, 147, pp. 201-228.
14. C.H. Cai, W.C. Fu, C.H. Cheng, W.W. Kwong, Mining association rules with weighted items, in: *Proc. IDEAS*, (1998), pp. 68–77.
15. A. Gyenesei, Mining weighted association rules for fuzzy quantitative items, *TUCS Technical Report No: 346*, May (2000).
16. S.Yue, E. Tsang, D.Yeung, D. Shi, Mining fuzzy association rules with weighted items, *Proc. IEEE Internat. Conf. Systems Man Cybernet.* (2000) 1906–1911.
17. K. M. Lee Mining generalized Fuzzy quantitative Association Rules with Fuzzy Generalization Hierarchies, 0-7803-7078-3/01/\$10.00 (C)(2001) IEEE.

18. Y.C. Hu, R.Sh. Chen, G.H. Tzeng Discovering fuzzy association rules using fuzzy partition methods, *Knowledge-Based Systems* 16 (2003) Elsevier, 137–147
19. W.H. Au and K. C. C. Chan Mining Fuzzy Association Rules in a Bank-Account Database, *IEEE TRANSACTIONS ON FUZZY SYSTEMS*, VOL. 11, NO. 2, APRIL (2003)
20. Y. Gao, J. Ma, L. Ma, A new algorithm for mining fuzzy association rules, *Proc. IEEE Internat. Conf. Machine Learning and Cybernetics*.(2004).
21. H. Ishibuchi, T. Nakashima, T.Yamamoto, Fuzzy association rules for handling continuous attributes, in: *Proc. IEEE ISIE*, (2001),
22. A. Gyenesei, A fuzzy approach for mining quantitative association rules, *TUCS Technical Report No: 336*, March (2000).
23. W. Zhang, Mining fuzzy quantitative association rules, *Proc. IEEE Internat. Conf. Tools Artif. Intell.* (1999) 99–102.
24. R.R.Yager, Fuzzy summaries in database mining, *Proc. Conf. Artif. Intell. Appl.* (1995) 265–269
25. Mills, F. *Statistical Methods*, Pitman, (1955).
26. A.W.C. Fu, M.H.Wong, S.C. Sze,W.C.Wong,W.L.Wong,W.K.Yu, Finding fuzzy sets for the mining of association rules for numerical attributes, in: *Proc. IDEL*, October (1998), pp. 263–268.
27. R. Ng, J. Han, Efficient and effective clustering methods for spatial data mining, in: *Proc. Internat. Conf. Very Large Databases*, (1994).
28. K. Hirota, W. Pedrycz, Linguistic data mining and fuzzy modelling, *Proc. IEEE Internat. Conf. Fuzzy Systems*, vol. 2, (1996), pp. 1448–1496.
29. M. Kaya, R. Alhaji, Facilitating fuzzy association rules mining by using multi-objective genetic algorithms for automated clustering, in: *Proc. IEEE Internat. Conf. Data Mining*, November (2003).
30. M. Kaya, R. Alhaji. Genetic algorithm based framework for mining fuzzy association rules , *Fuzzy Sets and Systems* (2004) Elsevier.
31. L.A. Zadeh, The concept of a linguistic variable and its application to approximate reasoning, *Information Science (Part 1)* (1975).
32. M. R. Civanlar and H. J. Trussell, “Constructing membership functions using statistical data,” In *Fuuy Sets und System*, vol. 18, pp.1-14, (1986)
33. R. Kohonen, “Self-Oganization and Associate Memory,” Springer, Berlin, (1988)

The Study on Three Stages in Retinal Mechanism

Sung-Kwan Je¹, Kwang-Baek Kim², Jae-Hyun Cho³, and Eui-Young Cha⁴

¹ Dept. of Computer Science, Pusan National University
jimmy374@pusan.ac.kr

² Dept. of Computer Engineering, Silla University
gbkim@silla.ac.kr

³ Dept. of Computer Information, Catholic University of Pusan
jhcho@cup.ac.kr

⁴ Dept. of Computer Science, Pusan National University
eycha@pusan.ac.kr

Abstract. Recently many researches have been studied in the human vision model to solve the problem of the machine vision. In retina, input data was processed information processing that was data reduction, edge detection, and emphasizing region. The processed image was recognized by brain. Starting from research on the human visual system, we proposed algorithms that process data reduction and edge detection by using wavelet transform and emphasizing region contrast. The proposed retinal model improves sharpening spatial edges in the amacrine outputs. In simulations, the proposed model shows processing the retina outputs in the levels and compares with outputs.

1 Introduction

Recently in the field of optical neural, many researches have been conducted in relation with physiology or biology to solve the problem of information processing of the human. The features of biological visual systems at the retinal level serve to motivate the design of electronic sensors. Along commercially available machine vision sensors are beginning to approach the photoreceptor densities found in primate retinas, they are still outperformed by biological visual systems in terms of dynamic range, and strategies of information processing employed at the sensor level [1-2]. However, most of the retina models have focused only on the characteristic functions of retina by generalizing the mechanisms, or according to researcher's convenience or intuition. Although such a system is efficient to achieve a specific aim in current environment, there are some cases where it is difficult to analyze and understand the visual scene of a human body [3-4]. The current visual systems are used in very restricted ways due to the insufficiency of the performance of algorithms and hardware.

Artificial vision is to develop information processing procedures of the human visual system based on the biological characteristics. Compared with the machine vision technology, it can be effectively applied to industry. The purpose of the artificial vision system has been developed to present vision information to a blind man [4]. Further, we can use this model to developments of the artificial retina prosthesis for recover defective eyesight and clinical diagnosis of an eye. We will

develop the design of such a robot vision system and the new image signal processing algorithms as an example to apply image model [1-3].

Accordingly, it is necessary to the retina model that was integrated functions of the existing other retina models. In this paper, we proposed the computational retinal model that was efficiently integrated the retinal mechanism. Chapter 2 looks into the property of retina through physiological and biological evidence. We propose algorithm based on the mechanism in Chapter 3, and analyze the results of the simulations and conclusions in Chapter 4.

2 Retinal Mechanism

The retina is a highly structured network of neurons that extracts and pre-processes visual information from the image projected upon it by the optics of the eyes. A schematic diagram of the retinal cell structure is shown in Fig. 1. The biological retina is more than just a simple video camera. It not only converts optical information to electrical signals but performs considerable processing on the visual signal itself before transmitting it to higher levels. Various local adaptation mechanisms extend the retina's dynamic range by several orders of magnitude. In order to meet the transmission bottleneck at the optic nerve, the retina extracts only those features required at later stages of visual processing while employing many data reduction strategies such as information processing [3-4].

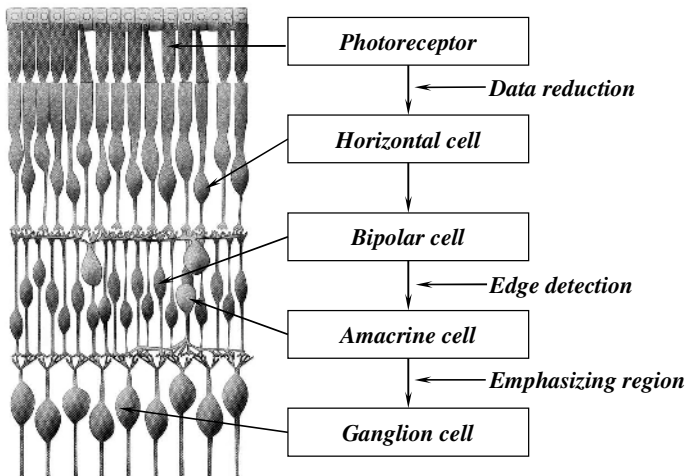


Fig. 1. Retinal Mechanism

Light, entering the eye, passes through the transparent retina and is transformed into an electric signal after being captured by the visual pigment-containing outer segments of the most distal retinal cells, the photoreceptors. However, since ganglion cell is composed with only about 1,000,000 in one eye, a lot of visual information is

compressed for transferring from 125,000,000 receptors to ganglion cell. Actually it is turned into a neural signal by an operation of the retina, but the sampling image is transmitted to primary visual cortex of a brain through optic nerve of the retina which listened to this signal in 125,000,000 rod cells and 6,000,000 con cells [2-3]. It is called data reduction and foveated sampling.

The bipolar cell outputs transmitted information to ganglion cell. The transmitted information was extracted edge to detect motion of an object. Accordingly, the transmitted information was divided into compressed information and edge information. The compressed information was transmitted to P-type ganglion cells (P-cell) and the edge information was transmitted M-type ganglion cells (M-cell). P-cells contain major information of images (what information), whereas M-cells contain edge information of images (where information) [4]. It depends on a mechanism that can minimize the loss of critical information when transmitting information and can maximally minimize the amount of total information. Therefore, human vision is sensitive to 'What' information, but insensitive to 'Where' information.

The edge information was transmitted to amacrine cell before to M-type ganglion cells (M-cell). Amacrine cell was detecting motion of and object at coarse spatial resolution and sharpening edges (emphasizing region). It was effectively detected motion of an object [5].

Shah proposed a computer retina model that integrated the related studies in retina [6]. It variously compared the result on simulation by the singular visual signal level with the high visual acuity of the real retina at each layer according to the illumination level. He was modeled the data reduction of the retina by the center of nonuniform in the photoreceptor using LPM (Log Polar Mapping). Even though his model was reflected biological processing of the real retina well, but wasn't included the characteristics of reaction about detecting motion, one of the most critical peculiarities, that it was the mechanism of the amacrine cell in retina. Generalizing only characteristic functions of the retina, most of the models have been developed in accordance with the researchers facilitate or intuition. Accordingly, it is necessary to consistent and integrate model.

3 Proposed Algorithm

Many of the characteristics of the human visual system are ultimately limited by the fidelity of image sampling within the retina and the strategies used to process the sampled information before its transmission to the cortex. The style of processing performed by the retina is dictated by three main requirements. One is data reduction to reduce the computations required at the retinal level. Two is extracting edge to detect motion of an object by the excitatory-inhibitory synapsing at bipolar cell. Three is emphasizing region contrast to effectively detect motion of an object at amacrine cell.

In this paper, we proposed algorithms that to process the data reduction, edge detection using wavelet transform and emphasizing contrast region in Fig. 2.

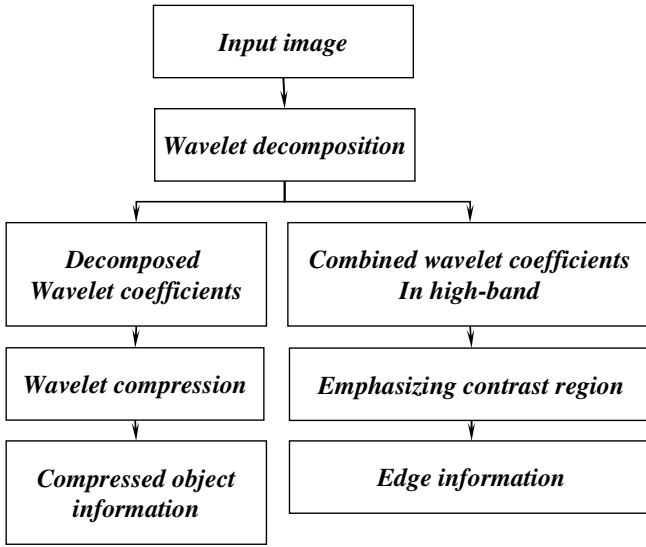


Fig. 2. Proposed Information Processing Model

First, we used wavelet transform to process the data reduction. The information is transmitted by minimizing the loss of important information in ganglion cells and by executing a mechanism that minimizes total amount of information maximally. These mechanisms are very similar to wavelet transform. The information of high-band of wavelet transform has edge information of original image compared to low-band which has a little information. Therefore, P-cell deals with main information of an image like low-band, and M-cell is dealing with edge information of an image like the high-band. M-cell was transmitted the edge of an object information (where pathway) to amacrine cell. The wavelet transform expresses well the local characteristic of spatial or time-frequency, as is MRA. It was adopted in JPEG2000. We used equation (1), (2) to show that wavelet transformed original image and calculated low-frequency, high-frequency filter of wavelet [7].

$$c_k^{J-1} = \sum_{m=0}^{N-1} h(m)c_{M+2k}^J \tag{1}$$

$$d_k^{J-1} = \sum_{m=0}^{N-1} g(m)d_{M+2k}^J \tag{2}$$

We applied low-frequency filter and high-frequency to a vertical direction and shared band with horizontal direction on original image and applied twice of filtering repeatedly again on a low-band section and used 3 level mallat tree to divide high-band section. Because 98% of high-band does division, we considered a diagonal, vertical, horizontal direction and did zigzag scan and did encoding in order to do encoding [8]. We used the image that we passed through a decoding process and a reverse-quantization process again, and it was compressed encoding image to the data reduction.

Second, to extract edge, we decomposed the information using wavelet transform in first level. And we acquired the high-band that was included edge. We used equation (3), (4) to detect edge information.

$$\begin{aligned} Edge_x[i, j] &= 0 + LH_1[i, j] & Edge_y[i, j] &= HL_1[i, j] + HH_1[i, j] \\ Edge_x[i, j + 1] &= 0 - LH_1[i, j] & Edge_y[i, j + 1] &= HL_1[i, j] - HH_1[i, j] \end{aligned} \tag{3}$$

$$\begin{aligned} Edge[i, j] &= Edge_x[i, j] + Edge_y[i, j] \\ Edge[i, j + 1] &= Edge_x[i, j] - Edge_y[i, j] \end{aligned} \tag{4}$$

To calculate the horizontal edge of image ($Edge_x$), we just used the LH_1 and zeros. LH_1 was contained the information of horizontal edge's image and HL_1 was contained the information of vertical edge's image. The same way, to calculate the vertical edge of image ($Edge_y$), we just used the HL_1 and HH_1 in equation (3).

Third, to emphasize contrast region, we proposed the high-boost filter. The high-boost filter was similar to Unsharp mask that sharpened spatial edges. If the image was sharpened edges using unsharp mask, it could add the noise and drastically reduce to the image regions having intensity gradient. To solve the problem, by setting the ganglion cell outputs $G(m, n)$, in equation (5), one obtains the amacrine cell outputs $A(m, n)$.

$$\begin{aligned} A(m, n) &= G(m, n) + HB \\ \text{where, } HB &= -\frac{1}{9} \begin{bmatrix} \alpha & \alpha & \alpha \\ \alpha & w & \alpha \\ \alpha & \alpha & \alpha \end{bmatrix} \end{aligned} \tag{5}$$

HR is a mask filter. It was sharpened the image and added $G(m, n)$. By setting $w = 9\alpha - 1$, in equation (5), one obtains the amacrine cell outputs. The proposed model improves sensitivity to detect motion of an object. Amacrine cell outputs was transmitted the object's edge information (where pathway) to LGN.

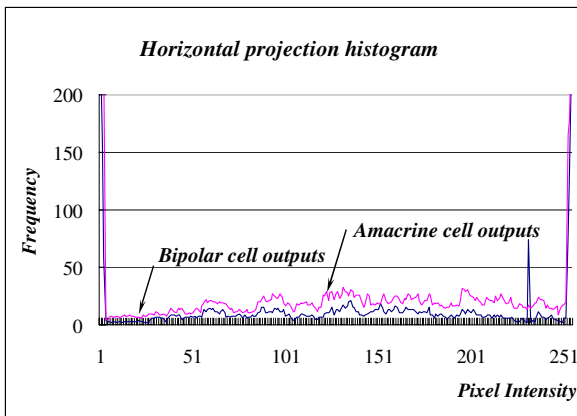
4 Simulations

We used the Visual c++ 6.5 in a Pentium 2.4GHz, 512MB memory, and windows XP environment and implemented the computational retina model based on human visual information processing. We used the SIPI Image Database and HIPR packages which it was used in a lot of paper on image processing at this paper and tested. SIPI is an organized research unit within the School of Engineering founded in 1971 that serves as a focus for broad fundamental research in signal and image processing techniques at USC. It researched in all aspects of signal and image processing and serviced available to SIPI Image Database. The Hypermedia Image Processing Reference (HIPR), a new source of on-line assistance for users of image processing. The HIPR package contains a large number of images which can be used as a general purpose image library for image

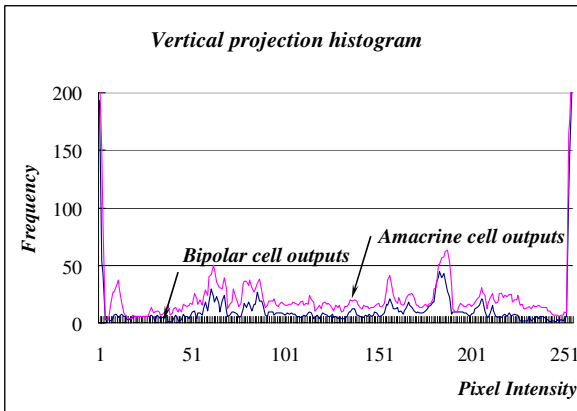
processing experiments. It was developed at the Department of Artificial Intelligence in the University of Edinburgh in order to provide a set of computer-based tutorial materials for use in taught courses on image processing and machine vision.



(a) lena image (b) compressed image (c) bipolar cell output (d) amacrine cell output

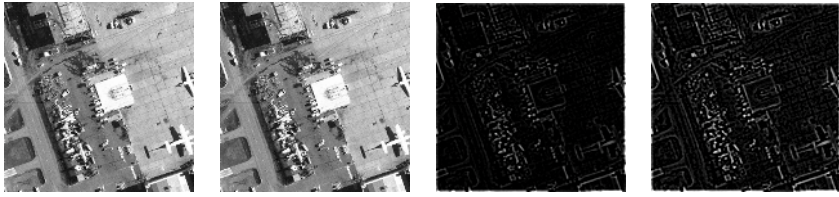


(e) comparison between (c) and (d) in horizontal projection histogram



(f) comparison between (c) and (d) in vertical projection histogram

Fig. 3. Each layer cell's output in the retina



(a) airfield image (b) compressed image (c) bipolar cell output (d) amacrine cell output



(a) crowd image (b) compressed image (c) bipolar cell output (d) amacrine cell output

Fig. 3. (continued)

In this paper, by setting α is 1.2 in Figure (3), we implemented a model to the various images in the visual information processing using wavelet transform. In Figure (3-(b)), the input image (a) was compressed in the photoreceptor using wavelet transform. This mechanism is the data reduction in retina's first processing. The photoreceptor outputs (compressed information-b) transmitted information to bipolar cells. And the compressed image (b) was extracted the edge information by the wavelet decomposition at the first level. The edge information (c) in bipolar cell was modeled using wavelet transform. The edge information is transmitted to amacrine cell. The transmitted information was emphasized edge contrast and was efficiently detected motion of an object. The proposed model was efficiently processed in the retinal levels.

5 Conclusion

In this paper, we proposed algorithms that process data reduction and edge detection by the wavelet transform and emphasize region contrast. It was computational retinal model that efficiently reflect the mechanism of retina and integrated retina model. The purpose of the artificial vision system up to now research is to present vision information to a blind man. Further, we can use this model to developments of the artificial retina prosthesis for recover defective eyesight and clinical diagnosis of an eye. We can also develop the robot vision system and the new image signal processing algorithms as an example to apply electric model.

References

- [1] Firsxhler, M. F., Firschein, O.: Intelligence: The eye, the brain and the computer. Addison-Wesley, (1987)
- [2] Hubel, D.: Eye, Brain, and Vision. Scientific American, (1995)
- [3] Dobelle, W. H.: Artificial Vision for the Blind by Connecting a Television Camera to the Visual Cortex. ASAIO journal, (2000) 3-9
- [4] Brain Science Research Center.: Research on Artificial Audiovisual System based on the Brain Information Processing. Research Paper by the Korea Advanced Institute of Science and Technology. Department of Science Technology, (2001)
- [5] Richter, J., Ullmom, S.: A model for the temporal organization of X and Y type receptive fields in the primate retina. Biological Cybernetics, (1982) 127-145
- [6] Shah, S., Levine, M. D.: Information Processing in Primate Retinal Cone Pathways: A Model. TR-CIM-93-18. Centre for Intelligent Machines. McGill University, Montreal. (Dec. 1993)
- [7] Shapiro, J. M.: Embedded Image coding using zerotrees of wavelet coefficients. IEEE Trans. on Signal Processing. Vol. 41. No. 12. (Dec. 1993) 3445-3462
- [8] Mallat, S. G.: A Wavelet tour of Signal Processing. Academic Press, (1998)
- [9] Gonzalez, R. C. and Woods, R. E.: Digital image processing. Second edition. Prentice Hall, (2001)

Curvature Monotony Condition for Rational Quadratic B-spline Curves

Zhong Li^{1,2}, Lizhuang Ma¹, Dereck Meek³, Wuzheng Tan¹, Zhihong Mao¹,
and Mingxi Zhao¹

¹ Department of Computer Science and Engineering, Shanghai Jiao Tong University,
Shanghai, 200030, China
lizhongzju@hotmail.com

² Department of Mathematics and Science, Zhejiang Sci-Tech University,
Hangzhou, 310018, China

³ Department of Computer Science, University of Manitoba,
Winnipeg R3T 2N2, Canada
ma-lz@cs.sjtu.edu.cn, dmeek@cc.umanitoba.ca,
{Tanwuzheng, mzh-yu, Zhaomx}@sjtu.edu.cn

Abstract. The monotone curvature condition for rational quadratic B-spline curves is studied in this paper. At first, we present the necessary and sufficient conditions of monotone curvature for the uniform rational quadratic B-spline segment and we compare it to the curvature condition of rational quadratic Bezier curve. Then, we give the sufficient condition of monotone curvature for the nonuniform rational quadratic B-spline segment. At last, we obtain the condition of monotone curvature for general rational quadratic B-spline curves with any number of control points.

1 Introduction

For any point along a smooth curve, there is a unique circle that best approximates the curve in the neighborhood of the point. This circle is called the circle of curvature, and the reciprocal of its radius is a non-negative quantity called the curvature at the point. For some applications in the field of Computer Aided Design, it is important to maintain the property of strictly monotone curvature along a curve segment. In Computer Graphics, artists have long been keenly aware of the aesthetic importance of the curvature distribution. Indeed, they often shape a curve by dividing it conceptually into a small number of segments, each of which has monotone curvature [1,5,9].

There have been some researches on the monotone curvature of the curve. Sapidis and Frey [2] studied on quadratic Bezier curves and got the necessary and sufficient conditions of monotone curvature. Based on the research of Higashi et al [4], Mineur et al gave a sufficient condition of monotone curvature for high degree curves [3]. Frey and Field [5] analyzed the curvature distributions of segments of conic sections represented as rational quadratic Bezier curves in standard form. Wang et al [8] also discussed the curvature condition of rational quadratic Bezier curves.

Rational quadratic Bezier curves and rational quadratic B-spline segments belong to the conic segment. These curves have some good properties so that they have been widely applied in the field of CAD [6,8,10-12]. In fact, the rational quadratic Bezier curve is only a special case of rational quadratic B-spline segment. Rational B-spline curves and surfaces, especially nonuniform rational B-spline (NURBS) curves and surfaces have been used as standard tools for representing many geometric entities used in a variety of visualization oriented fields such as Computer Graphics, CAD/CAM, but there seems to be few researches on the curvature condition for them. So the study for rational quadratic B-spline curves with monotone curvature is important and valuable.

In this paper, we first get the necessary and sufficient conditions of monotone curvature for the uniform rational quadratic B-spline segment, and we compare it to the curvature condition of rational quadratic Bezier curve. Then, we give the sufficient condition of monotone curvature for the nonuniform rational quadratic B-spline segment. At last, we obtain the condition of monotone curvature for general rational quadratic B-spline curves with any number of control points.

2 Monotone Curvature Condition for Uniform Rational Quadratic B-spline Segment

The uniform rational quadratic B-spline segment with three control points is written as [7]

$$B(t) = \frac{\sum_{i=0}^3 w_i N_{i,2}(t) B_i}{\sum_{i=0}^3 w_i N_{i,2}(t)}, t \in [0, 1] \tag{1}$$

where B_0, B_1, B_2 are control points, w_0, w_1, w_2 are weights of corresponding control points. Usually $w_i > 0$ and let $w_0 = w_2 = 1, w_1 = w$. $N_{i,2}(t)$ are quadratic B-spline base functions

$$N_{0,2}(t) = \frac{1}{2}(1 - t)^2, N_{1,2}(t) = \frac{1}{2}(-2t^2 + 2t + 1), N_{2,2}(t) = \frac{1}{2}t^2$$

At first, we discuss its sufficient condition of monotone curvature. Change Eq.(1) to

$$B(t) = \frac{Q(t)}{q(t)}$$

where

$$\begin{aligned} Q(t) &= \frac{1}{2}(1 - t)^2 B_0 + \frac{1}{2}(-2t^2 + 2t + 1)w B_1 + \frac{1}{2}t^2 B_2, \\ q(t) &= \frac{1}{2}(1 - t)^2 + \frac{1}{2}(-2t^2 + 2t + 1)w + \frac{1}{2}t^2. \end{aligned} \tag{2}$$

Denote q, q', q'' respectively as the order 0, 1 and 2 derivative of $q(t)$ with respect to t , $B = B(t), Q = Q(t), q = q(t)$, and denote $D(t), N(t)$

$$D(t) = \|qQ' - q'Q\|^2 = (qQ' - q'Q) \cdot (qQ' - q'Q),$$

$$N(t) = qQ' \times Q'' - q'Q \times Q'' + q''Q \times Q'.$$

Here, \times is the scalar cross product of two vectors, \cdot is the dot product of two vectors.

So the curvature equation and its derivative equation can be written as follows

$$k(t) = \frac{B'(t) \times B''(t)}{\|B'(t)\|^3} = \frac{q^3N}{D^{3/2}},$$

$$k'(t) = \frac{q^2}{D^{5/2}}[3q'DN + qDN' - \frac{3}{2}qD'N]. \tag{3}$$

As we know, if $k'(t)$ does not change the sign for all $t \in [0, 1]$, then the curvature of a planar curve is monotone. Let $E = B_1 - B_0, F = B_2 - B_1$, from algebraic computation to know

$$D(t) = \|qQ' - q'Q\|^2 = \frac{1}{4}(1-t)^2((1-w)t + 2w)^2 E \cdot E$$

$$+ \frac{1}{2}t(1-t)((1-w)t + 2w)((w-1)t + 1 + w)E \cdot F + \frac{1}{4}t^2((w-1)t + 1 + w)^2 F \cdot F, \tag{4}$$

$$N(t) = qQ' \times Q'' - q'Q \times Q'' + q''Q \times Q' = wE \times F. \tag{5}$$

From Eq.(5) to know, $N'(t) = 0$, so Eq.(3) becomes

$$k'(t) = \frac{q^2}{D^{5/2}}[3q'DN - \frac{3}{2}qD'N] = \frac{3q^2N}{D^{5/2}}[q'D - \frac{1}{2}qD'].$$

From Eq.(2),(4) and (5), we find $q(t) \neq 0, D(t) \neq 0, N(t) \neq 0, t \in [0, 1]$. So the sign of $k'(t)$ is determined by $q'D - \frac{1}{2}qD'$. Using Bernstein base transformation from t^i to $(1-t)^{4-i}t^i, i = 0, 1, 2, 3, 4, q'D - \frac{1}{2}qD'$ becomes

$$q'D - \frac{1}{2}qD' = \sum_{i=0}^4 \lambda_i(1-t)^{4-i}t^i \tag{6}$$

where

$$\lambda_0 = \frac{1}{4}wa, \lambda_1 = \frac{1}{4}(1+w)b, \lambda_2 = \frac{3}{4}w(1+w)^2c, \lambda_3 = \frac{1}{4}(1+w)d, \lambda_4 = \frac{1}{4}we,$$

$$a = 8w^2E \cdot E - (1+w)^2E \cdot (E + F),$$

$$b = [8w^2E \cdot E - \frac{1}{2}(1+w)^2(E + F) \cdot (E + F)],$$

$$c = (E \cdot E - F \cdot F),$$

$$d = [\frac{1}{2}(1+w)^2(E + F)] \cdot (E + F) - 8w^2F \cdot F,$$

$$e = (1+w)^2F \cdot (E + F) - 8w^2F \cdot F.$$

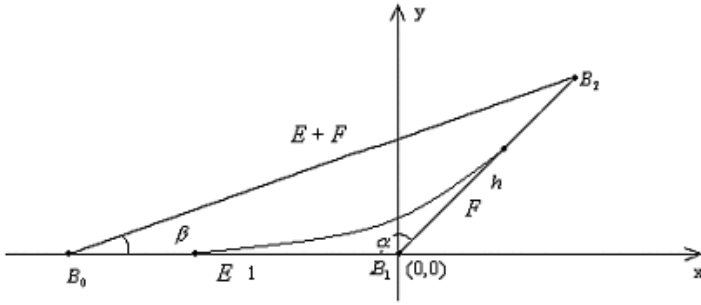


Fig. 1. Uniform rational quadratic B-spline segment

Obviously, if $\lambda_i, i = 0, 1, 2, 3, 4$ do not change the sign when $t \in [0, 1]$, then the sign of $q'D - \frac{1}{2}qD'$ does not change, i.e., $k'(t)$ keeps the same sign, so the curvature is monotone.

Rigid transformations and scaling do not affect the monotonicity of the curvature, so without loss of generality, we denote $B_0 = (-1, 0), B_1 = (0, 0), |B_0B_1| = 1, \alpha = \angle B_0B_1B_2, \beta = \angle B_2B_0B_1, h = |B_1B_2|/|B_0B_1| = |B_1B_2|$, see Fig 1.

Here, we only discuss the case when $h \leq 1$. For $h > 1$, it can be changed to the case of $h < 1$ as long as we reverse the order of their control points.

In Fig 1, we notice that

$$c = E \cdot E - F \cdot F = 1 - h^2 \geq 0.$$

Thus,

$$\lambda_2 = \frac{3}{4}w(1 + w)^2(E \cdot E - F \cdot F) \geq 0.$$

So if $\lambda_i \geq 0, i = 0, 1, 3, 4$, namely, $a, b, d, e \geq 0$, then the curvature is monotone. From the geometry relationship in Fig 1, we find

$$E \cdot (E + F) = |B_0B_2| \cos \beta,$$

$$\frac{1}{2}(E + F) \cdot (E + F) = |B_0B_2| \cos \beta + \frac{h^2 - 1}{2} \leq E \cdot (E + F)$$

We can hold that $b \geq a$. Similarly, $d \geq e$. So when $a \geq 0, e \geq 0, k'(t)$ does not change the sign.

Assume that $\alpha \geq \pi/2$ which guarantees the following calculations.

In order to $a \geq 0$, we can deduce that it must satisfy with

$$\frac{1}{w} \leq 2\sqrt{\frac{2}{1 - h \cos \alpha}} - 1. \tag{7}$$

In order to $e \geq 0$, we can similarly deduce that

$$\frac{1}{w} \geq 2\sqrt{\frac{2}{1 - \cos \alpha/h}} - 1. \tag{8}$$

From Eq.(7) and (8), we notice that when $h \in (-\frac{\cos \alpha}{7}, 1]$,

$$2\sqrt{\frac{2}{1-h \cos \alpha}} - 1 \geq 2\sqrt{\frac{2}{1-\cos \alpha/h}} - 1 \geq 0.$$

Denote

$$w_L = \frac{1}{2\sqrt{\frac{2}{1-h \cos \alpha}} - 1}, w_U = \frac{1}{2\sqrt{\frac{2}{1-\cos \alpha/h}} - 1}.$$

Obviously, when $w \in [w_L, w_U]$, Eq.(7) and (8) can be guaranteed, the curvature is monotone.

When $h \in (0, -\frac{\cos \alpha}{7}]$, we know

$$2\sqrt{\frac{2}{1-\cos \alpha/h}} - 1 \leq 0.$$

Eq.(8) can be guaranteed automatically. In this case, when $w \in [w_L, +\infty)$, the curvature is monotone.

So, if $\angle B_0B_1B_2 \geq \pi/2$ and $w \in [w_L, +\infty)$ (when $h \in (0, -\frac{\cos \alpha}{7})$) or $w \in [w_L, w_U]$ (when $h \in (-\frac{\cos \alpha}{7}, 1]$), then the curvature of uniform rational quadratic B-spline segment is monotone.

In fact, this sufficient condition is also the necessary condition of monotone curvature for the uniform rational quadratic B-spline segment [12].

Hence, the necessary and sufficient conditions of monotone curvature for the uniform rational quadratic B-spline segment is

Theorem 1. *Assume that $B(t)$ is the uniform rational quadratic B-spline segment written as Eq.(1), the curvature is monotone if and only if $\angle B_0B_1B_2 \geq \pi/2$ and $w \in [w_L, +\infty)$ (when $h \in (0, -\frac{\cos \alpha}{7})$) or $w \in [w_L, w_U]$ (when $h \in (-\frac{\cos \alpha}{7}, 1]$).*

Some corollaries can be obtained.

Corollary 1. *For the uniform rational quadratic B-spline segment, when $\angle B_0B_1B_2 < \pi/2$, the curvature is not monotone.*

The proof is omitted.

Corollary 2. *For the uniform rational quadratic B-spline segment, when $w < \frac{2\sqrt{2}+1}{7}$, the curvature is not monotone.*

Proof. By the algebraic deduction, we find if $w < \frac{2\sqrt{2}+1}{7}$, then $\frac{1}{w} > 2\sqrt{2} - 1 > 2\sqrt{\frac{2}{1-h \cos \alpha}} - 1$. Eq.(7) can not be guaranteed, so the curvature is not monotone.

When $w \geq \frac{2\sqrt{2}+1}{7}$, the curvature of uniform rational quadratic B-spline curve may be monotone.

For the rational quadratic Bezier curve and the uniform rational quadratic B-spline segment, we can compare their conditions with monotone curvature.

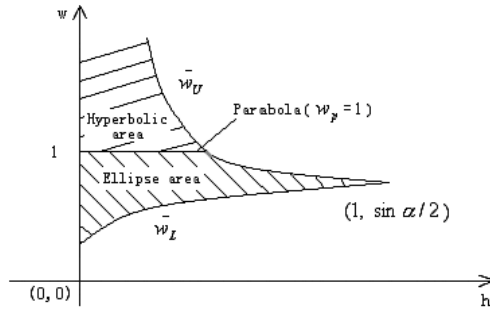


Fig. 2. Monotone curvature region of the rational quadratic Bezier curve

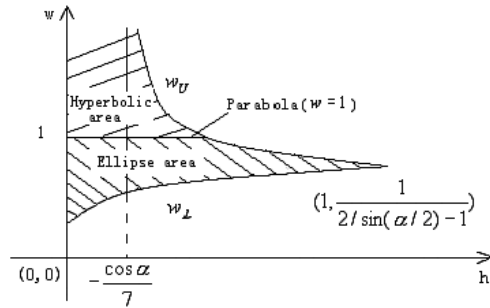


Fig. 3. Monotone curvature region of the uniform rational quadratic B-spline segment

Frey and Field [5] gave the monotone curvature condition of rational quadratic Bezier curve. It can be changed to the following expression [8].

For the standard rational quadratic Bezier curve with control points P_0, P_1, P_2 and weight w_p , the necessary and sufficient conditions with monotone curvature is $\angle P_0P_1P_2 \geq \pi/2$, and $w_p \in [\bar{w}_L, \bar{w}_U]$, where $\bar{w}_L = \sqrt{\frac{1-h \cos \alpha}{2}}, \bar{w}_U = \sqrt{\frac{1-\cos \alpha/h}{2}}, \alpha = \angle P_0P_1P_2, h (h \leq 1)$ is the ratio of two control lines.

The monotone curvature region of rational quadratic Bezier curve is shown in Fig 2. For the uniform rational quadratic B-spline segment, we can also draw its monotone curvature region (Fig 3). From Fig 2 and Fig 3, we find that their expressions with monotone curvature are similar, they both need to satisfy with $\alpha \geq \pi/2$, and when $h \in (-\frac{\cos \alpha}{7}, 1]$, their monotone curvature regions are both in a closed interval $w \in [\bar{w}_L, \bar{w}_U]$ and $w \in [w_L, w_U]$.

But their expressions are different in some extent. When $h \in (0, -\frac{\cos \alpha}{7}]$, the monotone curvature condition for the uniform rational quadratic B-spline segment is $w \in [w_L, +\infty)$ while the condition for the rational quadratic Bezier curve is still $w \in [\bar{w}_L, \bar{w}_U]$. This difference is caused in that for the uniform rational quadratic B-spline segment, w_U is piecewise function (when $h = -\frac{\cos \alpha}{7}$, w_L is $+\infty$).

3 Monotone Curvature Condition for Nonuniform Rational Quadratic B-spline Segment

The nonuniform rational quadratic B-spline segment with three control points is written as

$$B(t) = \sum_{i=0}^2 w_i B_i N_{i,2}(t) / \sum_{i=0}^2 w_i N_{i,2}(t), t \in [t_2, t_3] \tag{9}$$

where B_i are control points, w_i are weights associated with each control point, knot vector $T = \{t_0, t_1, t_2, t_3, t_4, t_5\}$, $N_{i,2}(t)$ are B-spline base functions.

As we know, for the nonuniform rational quadratic B-spline segment, it also belongs to the conic segment. We can obtain its sufficient condition with monotone curvature. Denote

$$\begin{aligned} Q &= w_0 N_{0,2}(t) B_0 + w_1 N_{1,2}(t) B_1 + w_2 N_{2,2}(t) B_2, \\ q &= w_0 N_{0,2}(t) + w_1 N_{1,2}(t) + w_2 N_{2,2}(t), \\ D &= \|qQ' - q'Q\|^2 = (qQ' - q'Q) \cdot (qQ' - q'Q), \\ N &= qQ' \times Q'' - q'Q \times Q'' + q''Q \times Q'. \end{aligned} \tag{10}$$

From algebraic deduction, we find

$$k'(t) = \frac{q^2}{D^{5/2}} [3q'DN + qDN' - \frac{3}{2}qD'N].$$

For Eq.(10), differentiate N and simplify it to get

$$N' = qQ' \times Q''' - q'Q' \times Q''' + q'''Q \times Q'.$$

Since Q, q are quadric equations in t , we can know $N' = 0$, so N is a constant. Then $k'(t)$ becomes

$$k'(t) = \frac{3q^2\|N\|}{D^{5/2}} [q'D - \frac{1}{2}qD'].$$

So the sign of $k'(t)$ is determined by $q'D - \frac{1}{2}qD'$. We have the following theorem.

Theorem 2. For q, D with above definitions, $q'D - \frac{1}{2}qD'$ is a quartic equation in t .

Proof. At first, we prove that $D = \|qQ' - q'Q\|^2$ is a quartic equation in t .

Since Q, q is a quadric equation, we can know that the highest degree of $qQ' - q'Q$ is three. Assume that the coefficient of t^3 in $qQ' - q'Q$ is z and coefficients of t^2 in Q, q are x, y respectively. Obviously, we find

$$z = y \cdot 2x - 2y \cdot x = 0.$$

Hence, the coefficient of t^3 in $qQ' - q'Q$ is zero, so $qQ' - q'Q$ is a quadric equation in t at most, namely, $D = \|qQ' - q'Q\|^2 = (qQ' - q'Q) \cdot (qQ' - q'Q)$ is a quartic equation in t .

For the same reason, we can prove $q'D - \frac{1}{2}qD'$ is a quartic equation in t .

For the quartic equation of $q'E - \frac{1}{2}qD'$, we can use Bernstein base transformation to get the new coefficients λ_i about $(1-t)^{4-i}t^i, i = 0, 1, 2, 3, 4$. Similar to the curvature condition of the uniform rational quadratic B-spline segment, we find when $\lambda_i, i = 0, 1, 2, 3, 4$ do not change the sign for $t \in [t_2, t_3]$, the curvature can be monotone. On the other hand, since the nonuniform rational quadratic B-spline segment belongs to the conic segment, the condition also includes $\angle B_0B_1B_2 \geq \pi/2$. So the sufficient condition with monotone curvature for the nonuniform rational quadric B-spline segment is

Theorem 3. *Assume that $B(t)$ is the nonuniform rational quadratic B-spline segment written as Eq.(9), if $\angle B_0B_1B_2 \geq \pi/2$ and the new coefficients $\lambda_i, i = 0, 1, 2, 3, 4$ do not change the sign for all $t \in [t_2, t_3]$, then the curvature is monotone.*

4 Monotone Curvature Condition for the Rational Quadratic B-spline Curve

For the general rational quadratic B-spline curve with any number of control points, the spline curve can be decomposed to a number of rational quadratic B-spline segments. So the research on curvature condition for general rational quadratic B-spline curves can be changed to the study on the uniform and nonuniform rational quadratic B-spline segment.

Obviously, we can know that if all curvatures of every general rational quadratic B-spline segment are increasing or decreasing simultaneously, then the curvature of the rational quadratic B-spline curve is monotone.

5 Conclusion

In this paper, we first get the necessary and sufficient conditions of monotone curvature for the uniform rational quadratic B-spline segment. Then, we present the sufficient condition of monotone curvature for the nonuniform rational quadratic B-spline segment. At last, we obtain the condition of monotone curvature for the rational quadratic B-spline curve with any number of control points. The advantage of this paper is that our results are directly and conveniently applicable to analyze the curvature condition of rational quadratic B-spline curves.

Acknowledgements

This paper was supported by National Natural Science Foundation of China (No.60373070 and No.60573147), Research Foundation of Microsoft China (Project-2004-Image-01), Postdoctor Foundation of Shanghai (05R214129), Education Foundation of Zhejiang (20050786).

References

1. Farin, G., Sapidis, N.: Curvature and the fairness and surface. *IEEE Computer Graphics & Application*, (1989) 9, 52-57
2. Sapidis, N., Frey, W.: Controlling the curvature of quadratic Bezier curves. *Computer Aided Geometric Design*, (1992) 9, 85-91
3. Mineur, Y., Lichah, T., Castelain, J., et al: A shape controlled fitting method for Bezier curves. *Computer Aided Geometric Design*, (1998) 15, 879-891
4. Higashi, M., Kaneko, K., Hosaka, M.: Generation of high quality curve and surface with smoothing varying curvature. In: *Eurographics'88, Proceedings of the European Computer Graphics Conference and Exhibition*. Amsterdam: North-Holland, (1988) 79-92
5. Frey, W., Field, D.: Designing Bezier conic segments with monotone curvature. *Computer Aided Geometric Design*, (2000) 17, 457-483
6. Lee, E.: The rational Bezier representation for conics. In *Geometric Modeling: Algorithms and New Trends*, ed. G.E. Farin, SIAM, Philadelphia, (1987) 3-19
7. Hoschek, J., Laser, D.: *Fundamentals of Computer Aided Geometric Design*, translated by L.L. Chumaker, A.K. Peters, Wellesley, Massachusetts, (1993)
8. Wang, Y., Wang, S., Li, D., et al: Study of curvature monotony condition for the rational quadratic Bezier curves. *Journal of Computer Aided Design and Computer Graphics*, (2000) 12, 507-511(in Chinese)
9. Walton, D., Meek, D.: A planar cubic Bezier spiral. *Journal of Computational and Applied Mathematics*. (1996) 72, 85-100
10. Meek, D., Walton, D.: Planar G2 Hermite interpolation with some fair, C-shaped curves. *Journal of Computational and Applied Mathematics*, (2002) 139, 141-161
11. Ma, L., Peng, Q.: Smoothing of free-form surfaces with Bezier patches. *Computer Aided Geometric Design*, (1995) 12, 231-249
12. Li, Z., Han, D.: Condition of monotone curvature for the quadratic rational B spline curves. *Journal of Zhejiang University(Science)*, (2003) 1, 23-26(in Chinese)

Estimation of Input Ranking Using Input Sensitivity Approach

Sanggil Kang¹ and Steve Morphet²

¹ Department of Computer, College of Information Engineering,
The University of Suwon, Suwon, Gyeonggi-do, Korea
sgkang@suwon.ac.kr

² Syracuse Research Corporation, Syracuse, NY 13212, U.S.A.
morphet@syrres.com

Abstract. In feed-forward neural networks, all inputs contribute to a greater or lesser extent when calculating the outputs. Therefore, inputs may be ordered from the greatest contributor to the least. Input ranking is non-trivial – cursory examination of the weight and bias matrices fails to reveal ranking. Solving the ranking issue allows the elimination of inputs with little influence on output. This paper presents a new method of determining the input sensitivity of three-layer feed-forward neural networks. Specifically, sensitivity of an input is independent of the magnitudes of the remaining inputs, providing an unambiguous ranking of input importance. Small changes to influential inputs will result in great changes to output. This concept motivated the theoretical approach to input ranking. Examination of theoretical results will demonstrate the correctness of this approach.

1 Introduction

Neural networks are [typically] non-linear systems, as such, the sensitivity of an output with respect to an input i may depend on the magnitude of input i as well as other inputs. The issue of input sensitivity ranking, in one form or another has been addressed in the literature since the late 1980's.

Choi *et al* [1] and Tchaban *et al* [2] address neural network robustness by analyzing weight sensitivity. Engelbrecht *et al* [3] and Belkina *et al* [4] address the difficulty domain experts have identifying input parameters having significant influence on system output. Zurada *et al* [5] and Fu [6] address deleting unimportant inputs from neural network training sets leading to [potentially] smaller neural networks and reduced data vector sizes. Piche [7] attempts to understand the effects of errors on neural networks. He *et al* [8] address improving neural network accuracy and reducing training time. Sung [9] addresses reducing size, shortening training times, and achieving higher accuracy in neural networks. As such, [9] employed input ranking to identify prunable inputs. Specifically, three different input ranking methods are compared – sensitivity analysis; fuzzy curves; and changes in MSE. Sung compared these methods for effectiveness on back-propagation neural networks trained to model simple nonlinear functions. Sung derives a sensitivity analysis formula for back-propagation neural networks with two hidden layers.

Several concerns arise when examining the related literature. Specifically, the sensitivity of an input is dependent on the magnitude of all inputs; thus, the actual ranking becomes problematic. Also, [7] requires neural networks with [statistically] large input to hidden neuron ratios. Many approaches require the omission of bias terms in neural networks. In [1], sensitivity is calculated at specific points in the input space (which will most likely vary when different points are evaluated). Many approaches also require the training of many neural networks in order to evaluate sensitivity.

Our method addresses many of these issues. For instance, in our approach, the sensitivity of an input is independent of the magnitudes of the remaining inputs. Our method decouples the inputs from each other, avoiding problems associated with calculating the joint probability density function. The ratio of hidden neurons to inputs is of no concern, and the derived equations include bias terms. Our method averages input sensitivity across the input range, and requires only one trained neural network to determine input sensitivity. In addition, to identify dependent inputs, only two trained neural networks are required.

The remainder of this paper is organized as follows. Section 2 describes the theoretical description of the input ranking in a partially connected neural network. In Section 3, we derive the input ranking for the hyper-tangent function. In Section 5, we show the simulation results by comparing with another work. We then conclude our paper in Section 5.

2 Input Ranking Using Input Sensitivity

2.1 Architecture Justification

The following is an analytical formulation of input sensitivity in systems whose inputs contribute to the output in a decoupled fashion. Outputs may be thought of as the sum of functions of individual inputs. For instance, $y = y_1(x_1) + y_2(x_2) + \dots + y_n(x_n)$. Such systems may be modeled via feed-forward, partially connected neural networks (PCNNs) in which no hidden neuron is connected to more than one input neuron. The structure of the PCNN is depicted in Fig. 1. Each hidden neuron is assumed to have a non-linear transfer function. Each output neuron is assumed to have a linear transfer

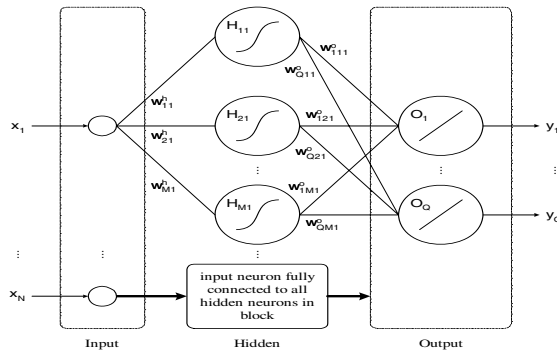


Fig. 1. An example of partially connected feedforward neural network

function. This derivation assumes neural networks with three layers (input, hidden, output).

Fig. 1 implies that the sensitivity of an input is not effected when changes are introduced to the remaining inputs (the input sensitivity of an input i is measured in isolation by adding disturbance to input i only). Thus, calculating input sensitivities in PCNNs is computationally expensive. Also, the joint density function of input and noise is easily derived. Typically, PCNNs will have larger mean squared errors (MSE) than fully connected FFNNs when trained on coupled input/output mappings. However, ranking results from PCNNs and fully connected FFNNs are very similar.

2.2 Derivation of Theoretical Input Sensitivity

Before deriving the theoretical input sensitivity, we summarize the notation and assumptions utilized during the process of the derivation.

- Input i is denoted as x_i ($i=1,2,\dots,N$ (the number of input neurons)).
- x_i is a uniformly distributed random variable in the range $[K_1, K_2]$ ($i=1,2,\dots,N$).
- Input disturbance Δx is normally distributed with zero mean and σ^2 variance.
- Δx is independent of x_i ($i=1,2,\dots,N$).
- σ is assumed small (allowing for approximation in the derivation section).
- M is the number of hidden neurons in each hidden neuron block.
- The output of the j^{th} hidden neuron connected to the i^{th} input neuron is denoted as z_{ji} ($i=1,2,\dots,N$ and $j=1,2,\dots,M$).
- Output q is denoted as y_q ($q=1,2,\dots,Q$ (the number of output neurons)).
- The weight connecting the i^{th} input neuron and the j^{th} hidden neuron is denoted as w_{ji}^h ($i=1,2,\dots,N$ and $j=1,2,\dots,M$).
- The weight connecting the j^{th} hidden neuron and the q^{th} output neuron in hidden block i is denoted as w_{qji}^o ($i=1,2,\dots,N$; $j=1,2,\dots,M$ and $q=1,2,\dots,Q$).
- Biases at the hidden and output layers are denoted as b_{ji}^h and b_q^o respectively.

After training a neural network, the sensitivity of the i^{th} input is calculated by introducing disturbance to [only] input i . The output error of each hidden neuron (denoted as Δz_{ji}) is (t denotes the hidden neuron transfer function)

$$\Delta z_{ji} = t(w_{ji}^h(x_i + \Delta x) + b_{ji}^h) - t(w_{ji}^h x_i + b_{ji}^h) \tag{1}$$

The 2nd moment and the mean of Δz_{ji} (denoted as $E[\Delta z_{ji}^2]$ and $E[\Delta z_{ji}]$ respectively) are obtained using the joint probability density function of x_i and Δx .

$$E[\Delta z_{ji}^2] = \int_{-\infty}^{\infty} \int_{-\infty}^{\infty} \Delta z_{ji}^2 f(x_i, \Delta x) d\Delta x dx_i \tag{2}$$

$$E[\Delta z_{ji}] = \int_{-\infty}^{\infty} \int_{-\infty}^{\infty} \Delta z_{ji} f(x_i, \Delta x) d\Delta x dx_i \tag{3}$$

The output error of the q^{th} output neuron (denoted as Δy_q^i) is

$$\Delta y_q^i = \sum_{j=1}^M w_{qji}^o \Delta z_{ji} \tag{4}$$

Therefore, the mean and 2nd moment of Δy_q^i are

$$E[\Delta y_q^i] = \sum_{j=1}^M w_{qji}^o E[\Delta z_{ji}] \tag{5}$$

$$E[\Delta y_q^{i^2}] = \sum_{j=1}^M w_{qji}^{o^2} E[\Delta z_{ji}^2] + 2 \cdot \left(\sum_{j=1}^{M-1} \sum_{m=j+1}^M w_{qji}^o w_{qmi}^o E[\Delta z_{ji}] E[\Delta z_{mi}] \right) \tag{6}$$

From Eqs. 5 and 6, the standard deviation of the output error is

$$STD(\Delta y_q^i) = \sqrt{E[\Delta y_q^{i^2}] - E[\Delta y_q^i]^2} \tag{7}$$

The sensitivity of output neuron q with respect to input i is

$$S_q(x_i) = STD(\Delta y_q^i) / STD(\text{disturbance}) \tag{8}$$

Thus, the sensitivity of input i (denoted as $S(x_i)$) is

$$S(x_i) = (1/Q) \sum_{q=1}^Q S_q(x_i) \tag{9}$$

3 Derivation for Hyper-Tangent Transfer Function

By replacing the transfer function in Eq. 1 with ‘tanh’ (the hyper-tangent function), the output error of each hidden neuron yields

$$\Delta z_{ji} = \tanh(w_{ji}^h(x_i + \Delta x) + b_{ji}^h) - \tanh(w_{ji}^h x_i + b_{ji}^h) \tag{10}$$

Since Δx is small, Eq. 10 is approximated by

$$\Delta z_{ji} = \tanh(w_{ji}^h(x_i + (\Delta x/2)) + b_{ji}^h) - \tanh(w_{ji}^h(x_i - (\Delta x/2)) + b_{ji}^h) \tag{11}$$

$$\Delta z_{ji} = (2 \sinh(w_{ji}^h \Delta x)) / (\cosh(w_{ji}^h \Delta x) + \cosh(2w_{ji}^h x_i + 2b_{ji}^h)) \tag{12}$$

Assuming $w_{ji}^h \Delta x$ is small, $\sinh(w_{ji}^h \Delta x)$ approximates $w_{ji}^h \Delta x$ and $\cosh(w_{ji}^h \Delta x)$ approximates 1. Rewriting Eq. 12 yields

$$\Delta z_{ji} = (2w_{ji}^h \Delta x) / (1 + \cosh(2w_{ji}^h x_i + 2b_{ji}^h)) \tag{13}$$

Further, the density functions of x_i and Δx are respectively (where $K_1 \leq x_i \leq K_2$; $-\Delta x_i \leq \Delta x \leq \Delta x_i$; and $\sigma \leq 0.01$)

$$f(x_i) = 1/(K_2 - K_1) \tag{14}$$

$$f(\Delta x) = \exp\left(\frac{-\Delta x^2}{2\sigma^2}\right) / \left(\sqrt{2\pi}\sigma\right) \tag{15}$$

Therefore, the joint density function of random variables x_i and Δx is

$$f(x_i, \Delta x) = \exp\left(\frac{-\Delta x^2}{2\sigma^2}\right) / \left((K_2 - K_1)\sqrt{2\pi}\sigma\right) \tag{16}$$

The equation for input sensitivity is derived by simple substitution. Repeat the above calculations for all inputs to obtain the order of input importance.

4 Simulation

Example 1, from Sung's work, presents the input rankings of partially and fully connected neural networks. The networks are trained on the decoupled equation $y = (x_1 + 2)^2 + \sin(2\pi x_2)$, where $0 \leq x_1, x_2 \leq 1$. An additional input (denoted as x_3 , $0 \leq x_3 \leq 1$) having no bearing on the value of y is introduced. Calculating the mathematical input sensitivity using the derivative of the output in terms of the inputs yields $\delta y/\delta x_1=5$, $\delta y/\delta x_2=4.03$ and $\delta y/\delta x_3=0$. Therefore, the ranking is $x_1 > x_2 > x_3$.

Table 1. Statistical and theoretical input sensitivities for example 1

NN Type	Inputs	Statistical Sensitivity			Theoretical Sensitivity			Input Ranking
		x_1	x_2	x_3	x_1	x_2	x_3	
PCNN	x_1, x_2	1.00	0.72	NA	1.00	0.68	NA	$x_1 > x_2$
PCNN	x_1, x_2, x_3	0.96	0.69	0.08	0.93	0.66	0.08	$x_1 > x_2 > x_3$
FCNN	x_1, x_2	0.70	0.58	NA	0.69	0.55	NA	$x_1 > x_2$
FCNN	x_1, x_2, x_3	0.69	0.47	0.05	0.67	0.45	0.05	$x_1 > x_2 > x_3$

Example 2 presents the input rankings of partially and fully connected neural networks. The networks are trained on the coupled equation $y = \log(x_1) \times \exp(x_2)$. The noisy input from example 1 is also introduced. Calculating the mathematical input sensitivity using the derivative of the output in terms of the inputs yields $\delta y/\delta x_1=12.05$, $\delta y/\delta x_2=1.67$ and $\delta y/\delta x_3=0$. Therefore, the ranking is $x_1 > x_2 > x_3$.

Table 2. Statistical and theoretical input sensitivities for example 2

NN Type	Inputs	Statistical Sensitivity			Theoretical Sensitivity			Input Ranking
		x_1	x_2	x_3	x_1	x_2	x_3	
PCNN	x_1, x_2	1.39	0.16	NA	1.34	0.15	NA	$x_1 > x_2$
PCNN	x_1, x_2, x_3	1.39	0.15	0.07	1.35	0.14	0.07	$x_1 > x_2 > x_3$
FCNN	x_1, x_2	0.36	0.61	NA	0.35	0.61	NA	$x_2 > x_1$
FCNN	x_1, x_2, x_3	0.43	0.56	0.03	0.41	0.56	0.03	$x_2 > x_1 > x_3$

In both examples, statistical and theoretical results are in close agreement (a trend that continued with additional experiments). In example 1, the rankings are as anticipated for both the PCNNs and FCNNs. In example 2, the rankings are as anticipated only for the PCNNs. Neither our method nor statistical simulation computes the correct ranking for FCNNs. When FCNNs are trained, the network weight updates are dependent on the magnitude of all inputs. Our equations assume weight updates are dependent only on the magnitude of the considered input (motivating the use of PCNNs). FCNNs violate this essential requirement, resulting in incorrect ranking.

Table 3. Statistical and theoretical input sensitivities for example 3

Case	Inputs	Type	Theoretical Sensitivity				Input Ranking
			x_1	x_2	x_3	x_4	
1	x_1, x_2	Fuzzy	16.39	3.72	NA	NA	$x_1 > x_2$
		Neural	15.63	3.82	NA	NA	$x_1 > x_2$
2	$x_1, x_2 (x_1 = x_2)$	Fuzzy	1.56	1.56	NA	NA	$x_1 = x_2$
		Neural	63.13	25.40	NA	NA	$x_1 > x_2$
3	x_1, x_2, x_3	Fuzzy	15.98	3.93	0.00	NA	$x_1 > x_2 > x_3$
		Neural	15.99	3.33	0.52	NA	$x_1 > x_2 > x_3$
4	x_1, x_2, x_4	Fuzzy	14.97	3.37	NA	0.16	$x_1 > x_2 > x_4$
		Neural	45.60	34.25	NA	30.05	$x_1 > x_2 > x_4$
5	x_1, x_2, x_3, x_4	Fuzzy	15.02	3.85	0.00	0.14	$x_1 > x_2 > x_4 > x_3$
		Neural	62.23	23.59	0.83	22.58	$x_1 > x_2 > x_4 > x_3$
6	x_1, x_2, x_3, x_4	Fuzzy	11.58	3.15	0.01	0.43	$x_1 > x_2 > x_4 > x_3$
		Neural	86.59	12.45	0.51	38.08	$x_1 > x_4 > x_2 > x_3$

Example 3 applies the concept of input ranking to fuzzy logic systems. The training vectors map two inputs (x_1 and x_2) to one output in which x_1 has greater sensitivity than x_2 . Additionally, input x_3 , having no significance on output calculation, is introduced in the cases 3, 5, and 6 (x_3 is randomly generated). Furthermore, input x_4 , dependent on x_1 , is introduced in the cases 4, 5, and 6. Six cases were examined. In all cases, the ranking of a fully connected neural network is provided for comparison. The anticipated input ranking is $x_1 > x_2 > x_4 > x_3$. In Case 1, the fuzzy and neural rankings are in strong agreement. In addition, the ranking is as anticipated. In the fuzzy sub-case of Case 2, x_1 's input sensitivity equals x_2 's (this is intuitively satisfying since the input patterns are identical). This is also consistent with the fuzzy curve approach of [5]. In the neural sub-case, input x_1 is ranked before x_2 . In Case 3, the fuzzy and neural rankings are again in strong agreement and the ranking is as anticipated. In Case 4, the fuzzy and neural rankings agree; however, the numeric values differ greatly. This discrepancy is explained in the fourth example. Also, the numeric rankings of x_1 and x_2 in the fuzzy sub-case are similar to earlier cases. In Case 5, the fuzzy and neural rankings agree; however, the numeric values differ greatly. Also, the numeric rankings of x_1, x_2 , and x_3 in the fuzzy sub-case are similar to earlier cases. In Case 6, the fuzzy and neural rankings do not agree. The fuzzy ranking is as anticipated; however, the numeric rankings of x_1, x_2, x_3 , and x_4 diverge from the numeric rankings of earlier cases.

5 Conclusion

This paper illustrates a new approach for determining input sensitivity ranking. The model has several advantages undisclosed in related literature. Specifically, the sensitivity of an input is independent of the magnitudes of other inputs. Calculating the sensitivity of input i is explicit since only input i is perturbed. Additionally, the derivation of input sensitivity does not stipulate the number of hidden neurons. When removing inputs from fully trained, partially connected neural networks, retraining is unnecessary. Dependent inputs are identified by training [just] two neural networks — large changes in average sensitivity reveal these dependencies. The theoretical model produces reliable input rankings when applied to partially connected neural networks trained on either coupled or decoupled mappings. The input of purely linear, feed-forward neural networks may be ranked with slight adjustments to the derivation. Moreover, the theoretical model strongly agrees with statistical results. Thus, the model provides a reliable, extensible input ranking mechanism.

The model also has disadvantages. Specifically, the theoretical equations have been derived for three-layer, feed-forward neural networks only. Also, ranking the inputs of fully connected neural networks becomes problematic when the inputs are coupled.

References

1. Choi, J.Y., Choi, C.H.: Sensitivity Analysis of Multilayer Perceptron with Differentiable Activation Functions. *IEEE Transactions on Neural Networks*, Vol. 3, No.1 (1992) 101-107
2. Tchaban, T., Taylor, M.J.: Establishing Impacts of the Inputs in a Feed-forward Neural Network, *Neural Comput & Applic*, 7 (1998) 309-317
3. Engelbrecht, A.P., Cloete, I., Zurada, J.M.: Determining the Significance of Input Parameters Using Sensitivity Analysis, *Proceedings of International Workshop on Artificial Neural Networks*, (1995) 382-388
4. Belkina, N.V., Krepets, V.V., Shakin, V.V.: One Stable Estimation of the Parameters of Feed-forward Neural Networks in Dealing with Biological Objects, *Automation and Remote Control*, Vol. 63, No. 1 (2002) 66-75
5. Zurada, J.M., Malinowski, A., Cloete, I.: Sensitivity Analysis for Minimization of Input Data Dimension for Feedforward Neural Network, *Proceedings of IEEE International Symposium on Circuits and Systems*, 6 (1995) 447-450
6. Fu, L., Chen, T.: Sensitivity Analysis for Input Vector in Multilayer Feedforward Neural Network, *IEEE International Conference on Neural Networks 1* (1993) 215-218
7. Piche, S.: Robustness of Feedforward Neural Networks. *International Joint Conference on Neural Networks 2* (1992) 346-351
8. He, F, Sung, A.H., Guo, B.: A Neural Network Model for Prediction of Oil Well Cement Bonding Quality. *Proceedings of IASTED International Conference on Control* (1997) 417-420
9. Sung, A.H.: Ranking Input Importance in Neural Network Modeling of Engineering Problems. *Proceedings of IEEE International Joint Conference on Neural Networks*, 1 (1998) 316-321

A Collaborative Design Environment

Wuzheng Tan, Lizhuang Ma, Zhihong Mao, and Zhong Li

Department of Engineering and Computer Science, Shanghai Jiao Tong University,
200030, China

tanwuzheng@sjtu.edu.cn, ma-lz@cs.sjtu.edu.cn,
mzh_yu@sjtu.edu.cn, lizhongzju@hotmail.com

Abstract. This paper presents a collaborative virtual design environment based on the globally shared product model conforming to STEP Standard. The platform provides an integration environment and changes paradigms between I_DEAS, Smarteam (PDM software) and Conceptual Innovation Design System (CIDS). The platform is illustrated for sugarcane harvester design analysis as an example, and provides a collaborative intelligent environment for the design of products, aiming at integrating people, process and data in the product development.

1 Introduction

Sugarcane is one of the major economical crops in the South of China, and research in small-scale sugarcane harvester is very important for the automation of sugarcane production to sugarcane cultivation. This paper proposes a collaborative virtual design environment that is suitable for product design of sugarcane harvester.

The capability for rapid innovation design is a key factor to enhancing CAD competitiveness. In such an environment, timely access to critical product information by the right people is crucial. This requires appropriate integration platform to include computing methods and programming models that eases product design and streamlines its flow throughout an enterprise.

In recent years, W.He, Q.F.Ni and Ivan B.H.Lee present a model of business information management system [1] for enterprise that is proposed to achieve better process integration and data integrity for lifecycle of the entire product development. Ge Zhengyu and Fan Wenhui present the architecture [2] of product data management (PDM) on product development of the railway rolling stock, and elaborate the definition of system information model and analysis of workflows. Michael Abramovici and Detlef Gerhard bring forward a flexible web-based PDM approach [3] to support virtual engineering cooperation. Tan Wuzheng [4], [5], or [6] took sugarcane harvester design analysis and evaluation as an example, presented some ideas about integrated collaborative environment and provided a conception innovation design system. Ivica Crnkovic, Annita Persson Dahlkvist and Daniel Svensson discuss the integration between PDM and SCM [7]. A new information integration platform for computer integrated manufacturing system (CIMS) is presented, which is based on agent and CORBA [10]. In this paper, we present a

visual collaborative design platform based on the globally shared product model conforming to STEP Standard. The platform provides an integration environment and changes paradigms between I_DEAS, Smarteam(PDM software) and Conceptual Innovation Design System (CIDS). The platform is illustrated for sugarcane harvester design analysis as an example, and provides a collaborative intelligent environment for the design of products, aiming at integrating people, process and data in the virtual product development.

2 State of the Art

2.1 CIDS-State of the Art

CIDS is a tool that helps engineers to smooth the gap between 2D and 3D and accelerate the concept design workflow. It reduces the time required to convert design sketches into 3D models to study form, tests design solutions and makes important creative decisions.

Process of product design is an iterative process from synthesis to analysis, it includes acquiring requirement of product design, analyzing requirement, scheme design, structural design and integer design, as illustrated in Figure.1.

Strategies in Figure.2 can then be used as design references to repeatedly and accurately reproduce designs.

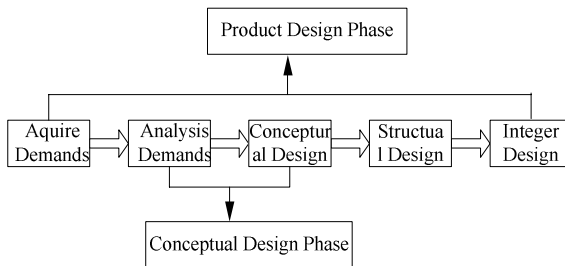


Fig. 1. Process of Design

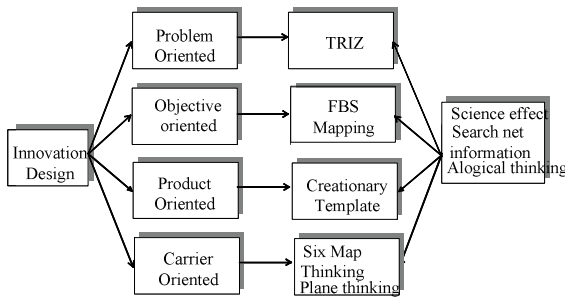


Fig. 2. Strategy of Innovation Design

From concept design to visualization and review, we adopt some new tools [5] and workflow enhancements to advance the process of design.

The final models will be saved in bottom database in PDM and acted as reference for modelling of I_DEAS, as illustrated in Figure.5.

2.2 PDM-State of the Art

“Product Data Management” is a tool that helps engineers and others to manage both data and the product development process. PDM systems keep track of the masses of data and information required to design, manufacture or build, and support and maintain products”[11]. The PDM system used in this paper is Smarteam 4.0, it can manage not only various kinds of documents and product structures, but also development processes. The most important user functions of a PDM system are [11].

- ①Data vault and document management, documents must be stored in an organized manner. Information about documents (meta-data) is stored in a central database, Document management routines are used to manage release and change of documents.
- ②Workflow and Process Management – routine processes can be monitored and controlled by the Smarteam system.
- ③Product Structure Management-product structures, which include description of products parts, are defined and changes in them are controlled.
- ④Part and Component Management (Classification & Retrieval)-standard parts can be classified to support re-use.
- ⑤Project Management-a large project can be broken into sub-projects. The progress of a project can be tracked.
- ⑥Central utility functions.
- ⑦Data Transport and Translation-design is often performed in a heterogeneous environment, with various design tools, on different platforms and at various locations. A PDM system must therefore be able to communicate with various applications and to transfer data between locations. Data created in different applications may need to be translated.
- ⑧Image Services-most design tools, such as CAD, are only used by the designers. An automatic translation to a neutral format possible to view from any desktop PC makes it possible for anyone in a company to view the geometry.
- ⑨ Administration- hardware design involves numerous participants and many document types. Different users have different access rights to documents which must be handled by the PDM system.

A PDM system will have impact on many of the processes in a company. So we must take into account a company’s overall business strategy when introducing a PDM system [12]. A PDM system should have not only efficient customization and usability, but also its internet access and web-based interface to data.

In this paper, we introduce the Smarteam (PDM) system to manage all common data coming from the collaborative design platform.

2.3 I_DEAS-State of the Art

I_DEAS 9.0 is a three-dimensional CAD (Computer Aided Design) software, the most important user functions of I_DEAS system are [13].

- ① Design, Part Modeling.
- ② Design, Surfacing.
- ③ Design, Assembles.
- ④ Drafting.
- ⑤ Simulation.
- ⑥ Test.
- ⑦ Manufacturing.
- ⑧ Geometry Data Translators.
- ⑨ Open I_DEAS.
- ⑩ Others.

Open Architecture (OA) for I-DEAS is a suite of tools that lets you customize, automate, and extend the standard capabilities of I-DEAS software. We use the parametric modeling software I-DEAS as developing platform of virtual products with Open I-DEAS tools [13], as illustrated in section 6.

OA for I-DEAS allows you to:

Customize the user interface.

Automate frequently-used commands with macros and programs. Write programs that directly access model file data.

In fact, the I_DEAS 9.0 software can not only supervise basic I_DEAS data using the shared libraries, but also manage its full I_DEAS data with libraries. However, it can not manage the data of CIDS. In order to manage all common data from CIDS and I_DEAS, we decide to adopt software of Smarteam 4.0 to administer all common data, as shown in Figure.5.

3 Hierarchy for Integration System

Hierarchy model of collaborative platform for CAD/CAE/CAPP/CAM based on PDM is shown in Figure.3 and Figure. 4, the detailed interpretation can be gotten in [4]. Integration system interface adopts agent technology and CORBA [10]. On the basis of this hierarchy model, we introduce a new layer called CIDS [5], the new layer is a multi-layered system architecture which provides capability for conception design process, which is described as following.

CIDS is a visual conception design system based on a PDM framework [5]. The architecture is a multi-layered system model that includes the PDM framework layer, a CIDS-Server layer, an integration layer for I-DEAS and CIDS, a CIDS-Client layer. The PDM framework layer provides a foundation of functional services. The CIDS-Server layer and client layer can be utilized to develop a fully integrated conception innovation design system for managing the entire innovation design and analysis of computing process, from KA (Knowledge Acquirement) and KBM (Knowledge Base Management) to reasoning process, function model optimizing, model solving, simulation analysis and so on. The integration layer for CIDS and I-DEAS is

described in section 6 detailedly. The PDM framework allows product information and development processes to be managed effectively to linking people, products and processes together throughout an entire product development lifecycle [6]. The CIDS model can achieve true process and data integration since a single data and process model is shared by the entire integration system [4], the final models will be saved in bottom database in PDM and acted as reference for modeling of I_DEAS.

GUI of Integration
Integration System Interface about CAD/CAE/CAPP/CAM
Conception Innovation Design System Based on Repository
PDM : Distributed PDM Environment
Web-Database
I-DEAS, ADAMS, VC# , PROE, SQL SERVER 2000

Fig. 3. Hierarchy model of integration system

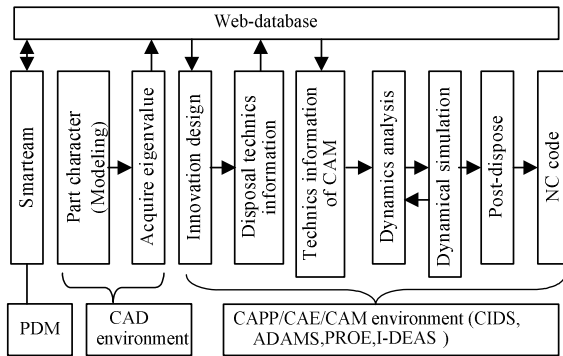


Fig. 4. Hierarchy between web-database and CAPP/CAE/CAM

4 Data Exchange and Collaborative Scheme

What kind of integration or interoperability can be achieved with these three systems? This is a problem which many companies are faced with. Of course, a full integration can be achieved by using a common infrastructure, common interfaces and common data [7], as shown in Figure.5, it needs a common product model, common evolution model and common process model conforming to STEP Standard.

A common support for the process model can be used with the present tools. But other models with today’s functionality are too different to use as common models. So, we should adopt another possibility of integration scheme with separate infrastructures and data, this weak integration needs a well-defined and efficient interface among three systems

Figure.6 shows an ideal integration model [7] that includes an engineering tools layer, a common API layer, the GUI layer, an application software layer, and a

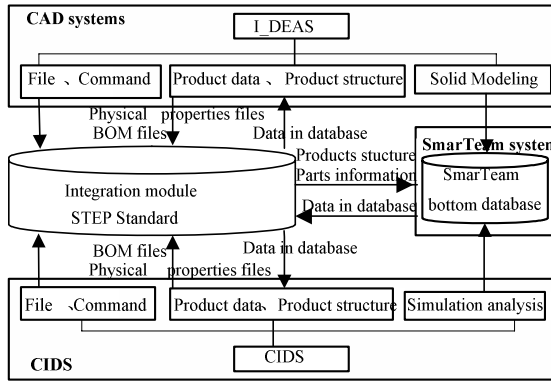


Fig. 5. Integration between PDM, CIDS and CAD systems

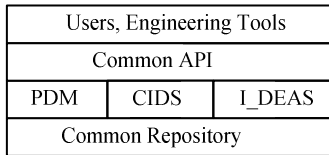


Fig. 6. Common API

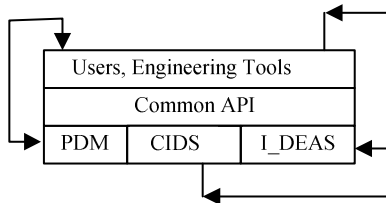


Fig. 7. Direct and indirect use of the tools

common repository layer. The common application user interface exists for both CIDS, I_DEAS and PDM functions, and it is used to present them via common user interface.

Unfortunately, this model cannot work well with the available tools. There are some APIs from these systems which provide incomplete functionality. Another challenge for both tools, independently of each other, is interoperability with other engineering tools. Interoperability requirements will lead to the emergence of better and clearer API's. The new component-based technology also encourages the use of API's.

As an API for I_DEAS, CIDS and PDM tools does not provide full functionality, the solution shown in Figure.6 will appear in practice as shown in Figure.7, there exists many shortcuts to I_DEAS, CIDS and PDM tool without being aware of the integration. This solution may cause problems as certain manual actions may introduce inconsistent states for the I_DEAS, CIDS and PDM combination.

We can end this section with a conclusion that there are certain possibilities of integration of specific parts of CAD, CIDS and PDM, or a use of one from only one domain. These possibilities are however very limited and require much additional efforts of the product.

5 Changing Paradigms in Both CIDS, PDM and I_DEAS

With the nature of the artifacts development, the characteristics of the three systems emerge. In life-cycle models, CIDS is focused more on the requirement phase and later on the phase of simulation analysis and maintenance/support phase. The design phase and production phase as seen from the product development point of view is less significant. On the contrary, in the I_DEAS software product life cycle, the design and development phase are usually the most intensive part, the tools consequently bring into focus support for the corresponding processes. While in life-cycle models of Smarteam, the requirement, design phase and development phase as seen from the software development point of view is less significant, the production and maintenance phase are usually the most intensive part, the tools consequently bring into focus support for the corresponding processes. Figure.8 shows schematically support provided by these tools during the product life-cycle. From the Figure.8, the CIDS and PDM, I_DEAS tools fit together to completely cover the entire product life cycle. Because the trends in three systems are enlargement of the area of control already covered by the other system, a possibility of integration is even more attractive. For example, the innovation design part is becoming more important than pure conception design from the design engineers. CIDS becomes more similar to PDM in the maintenance phase. On the other hand the development phase, due to extensive use of CAD and simulation tools, becomes more important for I_DEAS users.

However, there exist many problems. One is that the sharing or exchanging of data between different tools is not from the same domain but from different phases. There is no scheme yet to solve this problem completely. Another serious problem is the choice of the tools and methods from the overlapping areas. Even if a particular tool

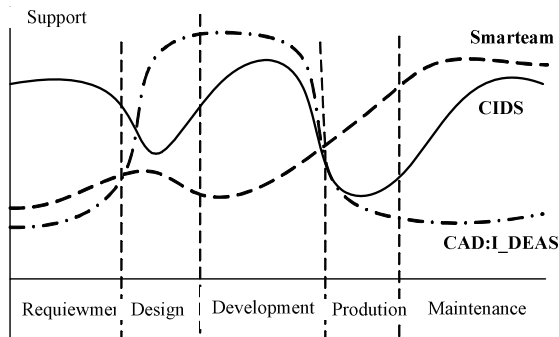


Fig. 8. PDM and CIDS, I_DEAS process support

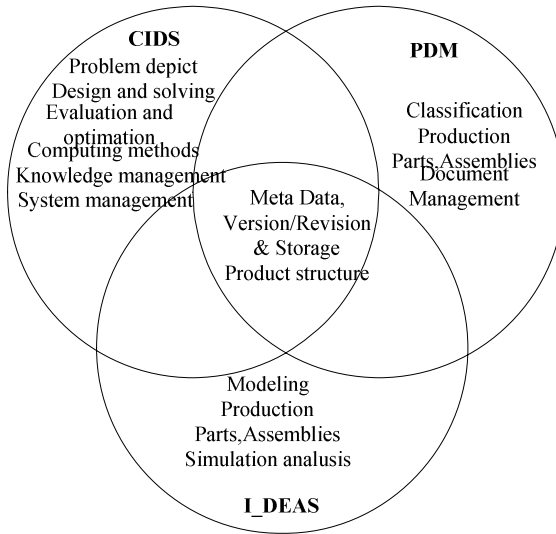


Fig. 9. The main functions of CIDS, PDM and I_DEAS

provides excellent support within one domain, it does not mean that it is suitable or well integrated within the second domain.

Figure.9 depicts the most important functions from three domains. As the figure shows, there are many functions supporting the same or similar process.

When we change paradigms in both CIDS, PDM and I_DEAS, we can gain BOM tables from these three systems, the characteristics of the BOM tables from these three systems are different. As Figure.10 shows, CIDS is focused mainly on 3D

ID	Name	Parent ID	Level	Quantity	Unit	Material	Volume	Weight
1	Assembly		0	1				
2	Part 1	1	1	1				
3	Part 2	1	1	1				
4	Part 3	1	1	1				
5	Part 4	1	1	1				
6	Part 5	1	1	1				
7	Part 6	1	1	1				
8	Part 7	1	1	1				
9	Part 8	1	1	1				
10	Part 9	1	1	1				
11	Part 10	1	1	1				
12	Part 11	1	1	1				
13	Part 12	1	1	1				
14	Part 13	1	1	1				
15	Part 14	1	1	1				
16	Part 15	1	1	1				
17	Part 16	1	1	1				
18	Part 17	1	1	1				
19	Part 18	1	1	1				
20	Part 19	1	1	1				
21	Part 20	1	1	1				
22	Part 21	1	1	1				
23	Part 22	1	1	1				
24	Part 23	1	1	1				
25	Part 24	1	1	1				
26	Part 25	1	1	1				
27	Part 26	1	1	1				
28	Part 27	1	1	1				
29	Part 28	1	1	1				
30	Part 29	1	1	1				
31	Part 30	1	1	1				
32	Part 31	1	1	1				
33	Part 32	1	1	1				
34	Part 33	1	1	1				
35	Part 34	1	1	1				
36	Part 35	1	1	1				
37	Part 36	1	1	1				
38	Part 37	1	1	1				
39	Part 38	1	1	1				
40	Part 39	1	1	1				
41	Part 40	1	1	1				
42	Part 41	1	1	1				
43	Part 42	1	1	1				
44	Part 43	1	1	1				
45	Part 44	1	1	1				
46	Part 45	1	1	1				
47	Part 46	1	1	1				
48	Part 47	1	1	1				
49	Part 48	1	1	1				
50	Part 49	1	1	1				
51	Part 50	1	1	1				
52	Part 51	1	1	1				
53	Part 52	1	1	1				
54	Part 53	1	1	1				
55	Part 54	1	1	1				
56	Part 55	1	1	1				
57	Part 56	1	1	1				
58	Part 57	1	1	1				
59	Part 58	1	1	1				
60	Part 59	1	1	1				
61	Part 60	1	1	1				
62	Part 61	1	1	1				
63	Part 62	1	1	1				
64	Part 63	1	1	1				
65	Part 64	1	1	1				
66	Part 65	1	1	1				
67	Part 66	1	1	1				
68	Part 67	1	1	1				
69	Part 68	1	1	1				
70	Part 69	1	1	1				
71	Part 70	1	1	1				
72	Part 71	1	1	1				
73	Part 72	1	1	1				
74	Part 73	1	1	1				
75	Part 74	1	1	1				
76	Part 75	1	1	1				
77	Part 76	1	1	1				
78	Part 77	1	1	1				
79	Part 78	1	1	1				
80	Part 79	1	1	1				
81	Part 80	1	1	1				
82	Part 81	1	1	1				
83	Part 82	1	1	1				
84	Part 83	1	1	1				
85	Part 84	1	1	1				
86	Part 85	1	1	1				
87	Part 86	1	1	1				
88	Part 87	1	1	1				
89	Part 88	1	1	1				
90	Part 89	1	1	1				
91	Part 90	1	1	1				
92	Part 91	1	1	1				
93	Part 92	1	1	1				
94	Part 93	1	1	1				
95	Part 94	1	1	1				
96	Part 95	1	1	1				
97	Part 96	1	1	1				
98	Part 97	1	1	1				
99	Part 98	1	1	1				
100	Part 99	1	1	1				
101	Part 100	1	1	1				

(A) BOM table of CIDS

ID	Name	Parent ID	Level	Quantity	Unit	Material	Volume	Weight
1	Assembly		0	1				
2	Part 1	1	1	1				
3	Part 2	1	1	1				
4	Part 3	1	1	1				
5	Part 4	1	1	1				
6	Part 5	1	1	1				
7	Part 6	1	1	1				
8	Part 7	1	1	1				
9	Part 8	1	1	1				
10	Part 9	1	1	1				
11	Part 10	1	1	1				
12	Part 11	1	1	1				
13	Part 12	1	1	1				
14	Part 13	1	1	1				
15	Part 14	1	1	1				
16	Part 15	1	1	1				
17	Part 16	1	1	1				
18	Part 17	1	1	1				
19	Part 18	1	1	1				
20	Part 19	1	1	1				
21	Part 20	1	1	1				
22	Part 21	1	1	1				
23	Part 22	1	1	1				
24	Part 23	1	1	1				
25	Part 24	1	1	1				
26	Part 25	1	1	1				
27	Part 26	1	1	1				
28	Part 27	1	1	1				
29	Part 28	1	1	1				
30	Part 29	1	1	1				
31	Part 30	1	1	1				
32	Part 31	1	1	1				
33	Part 32	1	1	1				
34	Part 33	1	1	1				
35	Part 34	1	1	1				
36	Part 35	1	1	1				
37	Part 36	1	1	1				
38	Part 37	1	1	1				
39	Part 38	1	1	1				
40	Part 39	1	1	1				
41	Part 40	1	1	1				
42	Part 41	1	1	1				
43	Part 42	1	1	1				
44	Part 43	1	1	1				
45	Part 44	1	1	1				
46	Part 45	1	1	1				
47	Part 46	1	1	1				
48	Part 47	1	1	1				
49	Part 48	1	1	1				
50	Part 49	1	1	1				
51	Part 50	1	1	1				
52	Part 51	1	1	1				
53	Part 52	1	1	1				
54	Part 53	1	1	1				
55	Part 54	1	1	1				
56	Part 55	1	1	1				
57	Part 56	1	1	1				
58	Part 57	1	1	1				
59	Part 58	1	1	1				
60	Part 59	1	1	1				
61	Part 60	1	1	1				
62	Part 61	1	1	1				
63	Part 62	1	1	1				
64	Part 63	1	1	1				
65	Part 64	1	1	1				
66	Part 65	1	1	1				
67	Part 66	1	1	1				
68	Part 67	1	1	1				
69	Part 68	1	1	1				
70	Part 69	1	1	1				
71	Part 70	1	1	1				
72	Part 71	1	1	1				
73	Part 72	1	1	1				
74	Part 73	1	1	1				
75	Part 74	1	1	1				
76	Part 75	1	1	1				

③ To access the parameterized model storeroom and get the relevant parameter model with OI_CommandServer object of Open I-DEAS by Design parameters, and amend the key dimensions to achieve the part models. Open Architecture capability lets you incorporate your programs into I-DEAS. The following example illustrates how to create a new group from the union of two other groups.

```

OI_ErrorCode      errorCode;
OI_PartGrp_var   gr1, gr2;
OI_Part_var      part;
OI_PartGrpSequence grSeq(1);
grSeq.length(1);
grSeq[OUL] = OI_PartGrp::_duplicate(gr2);
OI_PartGrpMemberSequence_var union
=gr1->PerformBoolean(grSeq, OI_Group::E_
Union, errorCode);
OI_PartGrp_varnewGrp
= part->CreateGroup(union);

```

④ Emulate and analyze all parts to achieve the results. If the results do not fit the demands, then redesign again, else assemble all parts by OI_Assembly object of Open I-DEAS, as shown in Figure. 10 (D).

⑤ Analyze the integral capability, if it fits the demands, the design is over, else it undergoes redesign again.

7 Prototyp Implementation

Based on the principle of a flexible Web-based PDM approach [8], a prototype of web-based collaborative design environment has been developed in which Java is used to demonstrate the conceptions described in this paper. A PDM framework is the center to the platform architecture. The prototype platform is deployed in the Apache-

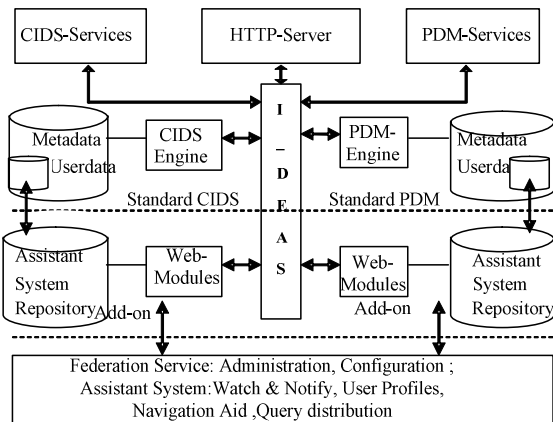


Fig. 12. The prototype of CIDS, I-DEAS and PDM web architecture

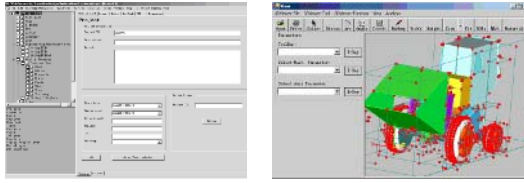


Fig. 13. (left) Prototype CIDS, (right) 3D Viewer

Tomcat environment. Apache and Tomcat are open source software provided by The Apache Software Foundation [9] for deploying web applications. Users can access the system via an Intranet or Internet through a firewall. Figure.12 and Figure.13 show the prototype of CIDS, I_DEAS and PDM web architecture. The standard integration platform consists of CIDS, I_DEAS and PDM engines which provide the basic CIDS, I_DEAS and PDM functions, the database containing metadata and user data. Basic CIDS and PDM functions are e.g. document management, workflow management, or product structure management. A built-in HTTP server allows WWW based client access to the integration system. CIDS and PDM services are for instance visualization modules, data import functions etc.

Acknowledgements

The work is partially supported by national natural science foundation of China (Grand No. 60573147 and No. 60173035) and 863 High Tech Project of China (Grant No. 2003AA411310).

References

1. He W, Ni Q F, Lee I B H. IEEE International Conference on Systems, Man and Cybernetics[C], Nanyang, Singapore, 2003, 20: 1475~1480
2. Ge Zhengyu, Fan Wenhui, Xiong Guangleng. Proceedings of the 4th World Congress on Intelligent Control and Automation[C]. Shanghai, China, [s.n], 2002.
3. Michael Abramovici, Detlef Gerhard. Proceedings of the 33rd Hawaii International Conference on System Sciences [C], [s.l.]:[s.n.], 2000.
4. Tan Wuzheng, Li Shangping, Chen Weixu, Jiang Zhanshi. Modern Manufacturing Engineering, 2004,04:0007
5. W.Tan, L.Ma, L. Luo, and S.Xiao. Study on an Innovation Design System and Its Application. CGIV05. 2005.08.
6. Tan Wuzheng. Research and application of virtual design platform for sugarcane harvester: Master thesis. Guang Xi: Guang Xi University, 2004
7. Ivica Crnkovic, Annita Persson Dahlkvist, Daniel Svensson. Complex Systems Development Requirements-PDM and SCM Integration. 0-7695-1287-9/01 2001.IEEE
8. Michael Abramovici, Detlef Gerhard. A flexible web-based PDM approach to support virtual engineering cooperation[A]. Proceedings of the 33rd Hawaii International Conference on System Sciences [C], [s.l.]:[s.n.], 2000.

9. J. Hunter and W. Crawford, Java Servlet Programming, 2nd Edition, O'Reilly & Associates, Inc., USA, 2001.
10. Felix T.S.Chan, Jie Zhang, H.C.W.Lau and A. Ning. Information Integration Platform for CIMS. Proceedings of the 2000 IEEE International Conference on , Volume: 2 , 12-15 Nov. 2000
11. CIMdata: "Product Data Management: The Definition". CIMdata Inc., Ann Arbor, MI, USA, 1998.
12. S. B. Harris, "Business strategy and the role of engineering data management; a literature review and summary of the emerging research question", Proceedings of the Institution of Mechanical Engineers; Part B; Journal of Engineering Manufacturing, 210;pp.207-220,1996.
13. I_DEAS 9.0 help library.

Towards a High Integrity XML Link Update in Object-Relational Database

Eric Pardede¹, J. Wenny Rahayu¹, and David Taniar²

¹ Department of Computer Science and Computer Engineering, La Trobe University,
Bundoora VIC 3083, Australia

{E.Pardede, W.Rahayu}@latrobe.edu.au

² School of Business Systems, Monash University,
Clayton VIC 3800

David.Taniar@infotech.monash.edu.au

Abstract. With the increasing usage of XML database, XML update has become an important issue in the database community. How updates affect the XML documents need to be investigated further. In this paper we propose a methodology to maintain the integrity of updated XML documents by maintaining the consistency of XML Link. XLink and its subsequent XPointer are W3C standards and used to provide referential purpose among XML documents or nodes.

Since XML Link is embedded as an attribute in an XML instance, our proposal can be used for schema-less documents and for instance-based references. Our proposal is targeted for Object-Relational Storage, one of the most widely used repositories for XML document. While the XML documents are stored as a CLOB XML Type, our update methodologies are implemented as a set of functions that perform checking mechanism before updates.

1 Introduction

Due to the dynamic nature of the web application, we have witnessed a growing number of XML documents that require regular update. XML update methodology has been discussed in a few works [2, 13]. Moreover, the researches on constraints preservation during update operations are even fewer. [9] discussed the issues on capturing semantic constraints during XML update. However, it is applicable to schema-based XML documents.

Unfortunately, very frequently we have to store schema-less XML document in our database repository. For this case, the update methods in [9] face a big problem due to the non-existence of schema. Furthermore, for some cases –even to the XML with schema- the constraints are not schema-based but more to be instance-based.

In this paper we aim to propose a methodology to update XML document without schema bound. The methodology will preserve the referential integrity constraint that exists through some XML linking technologies: *XML Linking Language (XLink)* [15] and *XML Pointer Language (XPointer)* [16].

In this paper we maintain the links if the XML documents stored in XML Enabled-Database that is based on Object-Relational (OR) Repository. In this database family, the XML document is stored as a Character Large Object (CLOB) XML Type.

When we store an XML document in our database, we create a record in a link table. This table will take roles as a lookup repository. Every time we update an XML document, the checking mechanism in forms of PL/SQL will be triggered and access the link table. It will determine whether the update can violate the referential integrity of the database. Based on this decision, the update will be performed or cancelled. Figure 1 illustrates the proposed work.

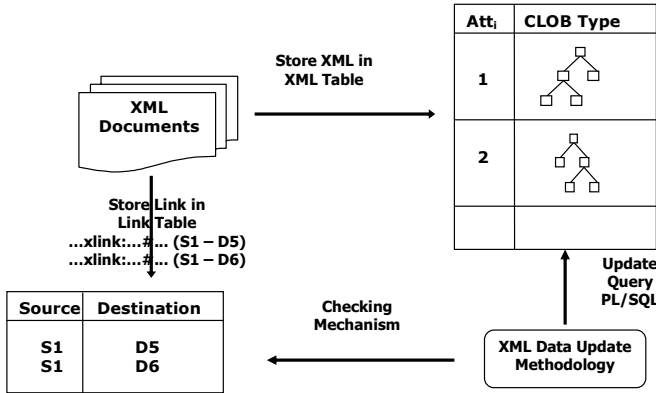


Fig. 1. Proposed Work

In section 2 we provide basic information regarding the XML linking technologies. In this section we also classify the linking based on the sources and destinations of references. In section 3 we briefly introduce the usage of OR Database for storing schema-less XML Document. Section 4 proposes the methodologies for the update operations insertion, deletion and replacement. In section 5 we provide the implementation of our proposed methods and brief analysis. Finally our work will be concluded in section 6.

2 XML Linking Technologies

Linking in XML allows users to create a complexly structured network of distributed resources [17]. W3C has been working on two important linking standards namely XLink and XPointer. While the former has been released as a recommendation [15], the latter is still a candidate for recommendation [16].

XLink is used to describe complex associations between resources identified using Unified Resource Identifiers (URI). Sometimes XLink has added XPointer component for more detailed reference. XPointer, which is built on the *XML Path Language (XPath)* [14], is used as the basis for the fragment identifier for any URI reference that locates a resource. The fragment may be a single XML element or a

collection of elements. The only limitation is that the resources must be an XML Document. Examples of the links are shown as follows.

```
<Article xmlns:xlink="http://www.w3.org/1999/xlink/namespace/"
  title="Linking Language in XML Document">
  <firstchapter>
    <para> (!--.....--) our previous work on <article
      xlink:href="Article2.xml#xpointer(title('Referential Mechanism
        in XML Data Model'))> Referential Mechanism in XML Data Model
      </article>. Our main interest.....</para>
    <para>.....</para>..</firstchapter></Article>
```

We can associate a link in XML with directed labeled graph. The resources are the vertices and the link itself is the edge of the graph. Based on the vertices we can classify the links into three types (see Fig.2): (1) a link between two resources in the same collection, (2) a link between two resources in the same database, but from different collection, and (3) a link between two resources from different database.

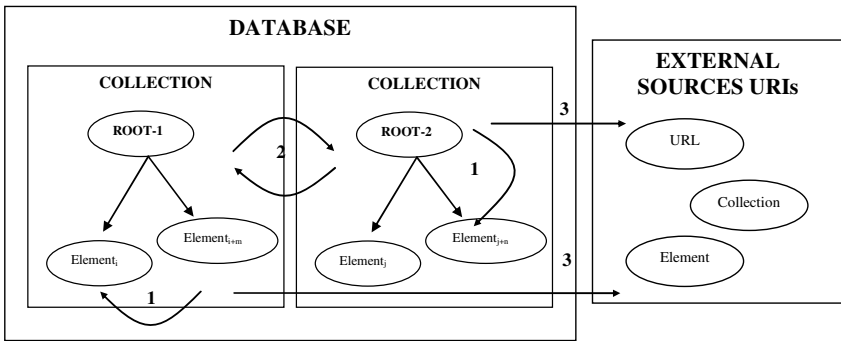


Fig. 2. XML Link Classification based on the Vertices

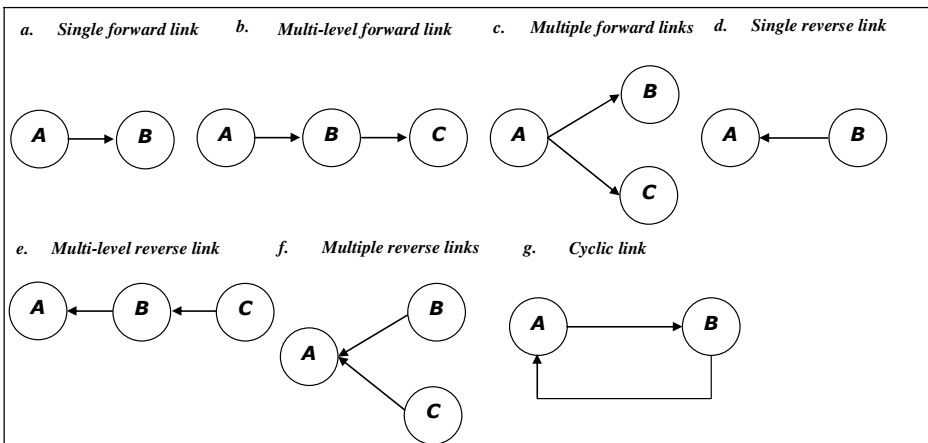


Fig. 3. Internal Link Classification based on Path

Among different links, it is hard to maintain the persistent reference using link type 3. There are current content management systems that contain modules for checking external links regularly. However, it usually draws a high overhead cost and manual intervention and thus, is not desirable [17].

Now we have decided to cover only internal links, we are aware that we need further classification. This is necessary before we can propose the methodology to checking the validity of the update operations.

There are various paths that an XML Link can take to connect XML nodes/documents. We show the paths in this section using the graphs in figure 3. The node depicts the document and the line depicts the link between the documents where the vertex points to destination document.

Having classified the links, we can continue by proposing the update methodology in ORDB as the storage. However, we will first briefly discuss the use of ORDB for schema-less XML storage.

3 Storing Schema-Less XML in Object-Relational Database

ORDB is increasingly popular as XML storage. It is associated with its ability to capture the OO modeling semantic and the maturity of relational implementation. With many new data structures introduced in the current SQL [3, 7], the modeling power of ORDB has increased. In particular, complex data structures such as row type, user-defined type and collection types can be utilized in XML storage.

There are few works that have discussed the usage of ORDB for XML storage. They map different schema languages such as DTD and XML Schema into the OR Schema either by flattening the trees [2, 6, 18] or by maintaining the tree structure of the document [10]. These works are applicable for data-centric XML Document. In other words, we need schema along with the XML documents. In practice, sometimes we have to store a non-schema based XML documents. For this purpose, some ORDB products have extended their products into XML-Enabled Database. This database allows users to store their XML documents even though they do not have a defined schema. The XML documents are usually stored as a Large Object (LOB).

DB2 is one of the major relational products, developed by IBM. It supports the XML by using two extended features: XML Extender and Text Extender [4]. SQL Server 2000 supports the XML in three ways: FOR XML statement, XPath queries based on annotated schema and OpenXML functions [1].

Oracle is a major OR product that has tried to accommodate the XML data in their last three versions. At the time of writing, the latest version of Oracle 10g has supported XML Type. It is a predefined object type that can store an XML document [2]. The XML Type can be implemented as a CLOB or as an object-relational storage [12]. CLOB is mainly used for a document-centric XML. It can be useful if there is no schema available for the document. It supports text indexes for part document search. OR storage is used for data centric document, where some update management is required. For this storage, there are two options that can be followed. We can store the XML as a table or as a column of a table. In this paper we will use the CLOB XML Type in Oracle 10g for implementation of our update methodology.

4 Proposed Methodology

In this section we propose the methodology for different updates (insertion, deletion and replacement). The methodology preserves the referential integrity constraints in the updated documents. The constraints are specified in the linking language attributes of the document.

The link information is stored in a separate table to the actual XML document. The main purpose for this table is not only to store the links but also as a look up reference before an update operation. By doing so, we can prevent broken links in our XML documents. The link table only stores the internal link. These links are link type 1 and type 2 as it is mentioned in section 3. To maintain the external link, we will not have control on the content and therefore some mechanisms that monitor the changes in the content might be required.

The link table also contains a column store the source of the link. This information is necessary during the update process.

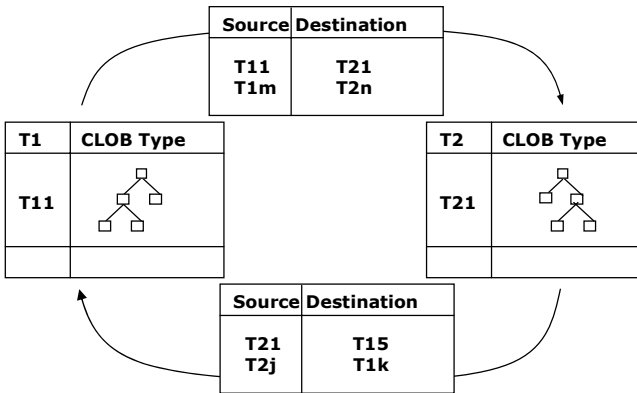


Fig. 4. XML Document and Link Storages

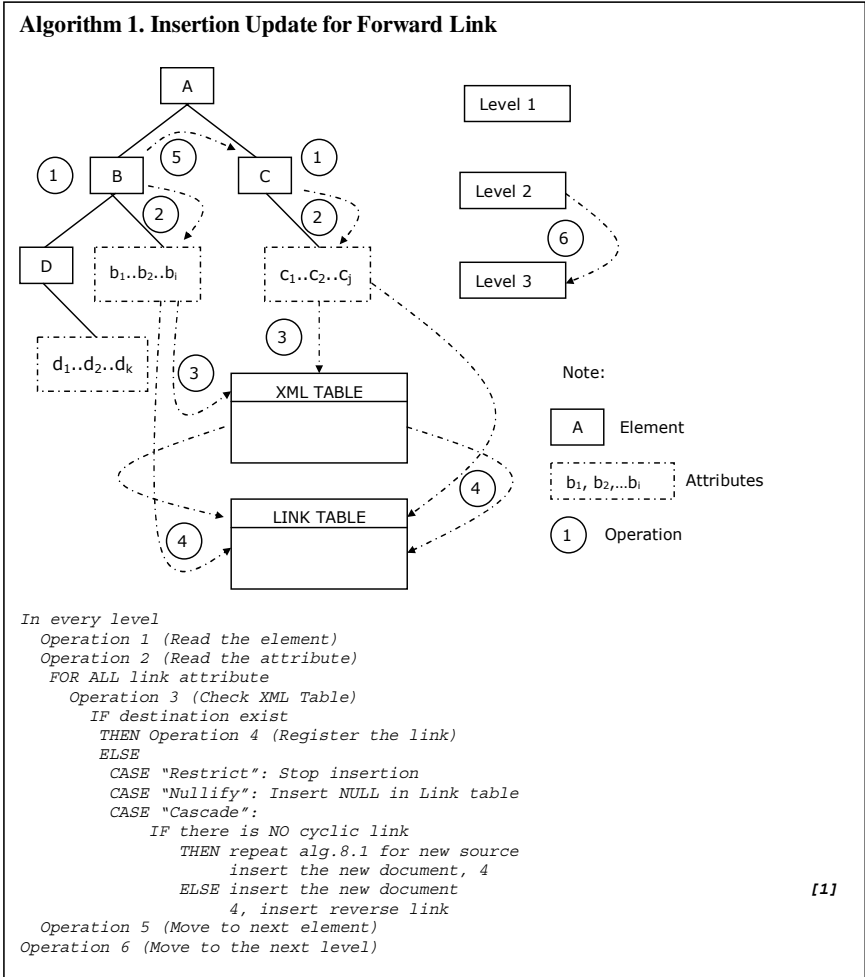
Before we describe the methodology, we show the framework of how these methods will work. In figure 4 we have two tables, each has a CLOB attribute that stores the XML. In addition to the CLOB attribute, they also have an identifier attribute that can be generated every time they are inserted in the database. These identifiers are necessary for defining the source and the destination of the link attribute.

In addition to the storage tables, we need additional tables that store the link information from the source to the destination. For a binary relation, we will need two link tables with different direction of source and destination (see Fig. 4).

4.1 Insertion Methodology

Every time we insert a new XML document as a CLOB in the table, we need to check whether it contains an internal link attribute. If there is an internal link, our proposed method checks the link source and destination.

In algorithm 1 we check whether the actual destination already exists in our database. If the link attribute contains a valid link, we need to register it in the link table. If the link attribute is invalid, we need to follow one of these options: (i) for restrict strategy, the insertion has to be cancelled, (ii) for nullify strategy, remove the link attribute from source document, (iii) for cascade strategy, insert the new document that will become a destination and register the link in the link table. Note that this algorithm is applicable not only for single forward link, but also the other two forward links.



Unlike forward link, there is no specific checking mechanism is required for reserve links. For example in figure 3d, the insertion of A without a B will not raise any referential integrity problem. On the other hand, the insertion of A with B already existed is an unlikely case since during the insertion of B we have already follow algorithm 1.

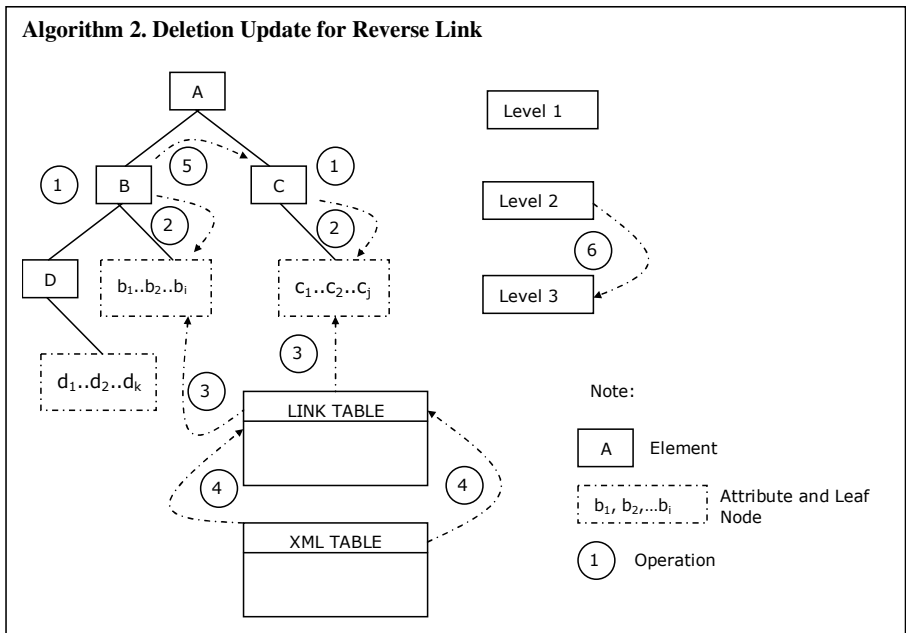
Finally, we can see a cyclic link (see figure 3g) as two single links. However, if we use algorithm 1, we end up with a recursive loop without a stop condition. Therefore, we have different condition [1] as a sub-procedure. Note that we will have a two link tables with reverse values. However, it is very unlikely for us to implement cascade strategy for this one since during insertion of one document we might not have the information for the other document, which is being linked.

4.2 Deletion Methodology

The main concern for deletion is to avoid deleting a target that is referred by other document(s). In our methodology, we perform the checking to the link table before any deletion.

For reverse link we use algorithm 2. We need to check whether there is any internal source actually refers to the target node and perform maintenance operation according to the strategy: (i) for restrict strategy, cancel the deletion, (ii) for nullify strategy, remove the link attribute from the referring document(s), (iii) for cascade strategy, delete all referring document(s) and delete all the links to this target in all link tables.

Algorithm 2 is applicable not only for single reverse link, but also for the other two forward links. For a cyclic link, we need to add an addition checking function [2]. We do not show the algorithm for deletion of forward link due to the page limitation. Note if there is a case where a document has a forward link to a document and reverse link from another document, we need to perform two different checking mechanisms.



Algorithm 2. continued

```

In every level
  Operation 1 (Read the element)
  Operation 2 (Check the attribute and leaf node)
  FOR ALL attribute and leaf node
    Operation 3 (Check the Link Table)
    IF exist as destination
      THEN
        CASE "Restrict": Stop deletion
        CASE "Nullify": Operation 4 (remove the link in Link Table)
        CASE "Cascade":
          IF there is NO cyclic link
            THEN repeat algorithm 8.3 with new source document
              delete the new source document, 4
            ELSE delete the new source document
              4, remove the reverse link
          ELSE ( )
    Operation 5 (Move to next element)
  Operation 6 (Move to the next level)

```

4.3 Replacement Methodology

For replacement operation, we need to ensure that the old value deletion satisfies deletion checking mechanism and the new value insertion satisfies the insertion checking mechanism.

For forward link, we use algorithm, which is very similar to algorithm 1. This algorithm checks whether the new value is a link or not. If it is a link, whether the link refers to a valid link and act according to the predefined strategy. This algorithm also applies for multiple forward link.

While the algorithm for forward link replacement almost resembles the forward link insertion, the algorithm for reverse link replacement almost resembles the reverse link deletion (see algorithm 2). The main concern is whether the old value being replaced is actually being referred by other document(s). We do not show the algorithm for replacement in this paper due to the page limitation.

5 Implementation of Update Methodology

We have fully implemented the proposed update methodology. We use Oracle 10g as the XML-Enabled DBMS. Further release of Oracle can also be used for this implementation. In this product our XML documents are stored in tables as CLOB XML Type. Therefore, schema is optional. The proposed methods are implemented as PL/SQL triggers. Inside these triggers we will use some built-in functions specifically available for CLOB object [11] that are based on standard SQL/XML [5].

For the case study, we use XML documents that contain information of *article*, *person* and *publication*. Before we implement the methodologies, we perform the preparation of the storages. There are three repositories for XML Documents, each for different content. In addition we will need link tables for every set of link direction.

We implement the methodology for each operation and every link type with different maintenance strategy. Not all strategies and operations are implemented. The decision of not implementing some strategies in some operations is based on the usability and practicality of the checking mechanism. For example, we do not need

reverse link insertion check since it will not affect the referential integrity problem. Another example, we do not implement cascade strategy for forward link insertion since in practice we do not always have full information for the referred document.

Due to the page limitation, we do not show the actual implementation in this paper. We only show the summary. Table 1 summarises the implementation of the checking methodologies for insertion (I), deletion (D), and replacement (R) updates. The ones with ticks are those that are likely to be found in practice and thus, are implemented.

Table 1. Insertion Update Methodology Implementation

	Restrict			Nullify			Cascade		
	I	D	R	I	D	R	I	D	R
Single Forward Link	✓	✓	✓	✓	✓	✓	✗	✓	✓
Multiple Forward Link	✓	✓	✓	✓	✓	✓	✗	✓	✓
Multi-Level Forward Link	✓	✓	✓	✓	✓	✓	✗	✓	✓
Single Reverse Link	✗	✓	✓	✗	✓	✓	✗	✓	✗
Multiple Reverse Link	✗	✓	✓	✗	✓	✓	✗	✓	✗
Multi-Level Reverse Link	✗	✓	✓	✗	✓	✓	✗	✓	✗
Cyclic Link	✓	✓	✓	✓	✓	✓	✗	✓	✗

By implementing the update methodology using XML-Enabled Database, we have utilized the technology that is considered mature. Users are also familiar to the implementation and the standard is used by most vendors. It is also backed up with the well-accepted relational model foundation. Nevertheless, it still has a shortcoming. In our implementation, the links in the tables are in document level. Thus, we do not know the element/attribute in the document that actually been referred. In addition, the links need different tables based on the source and destination. If we want to avoid this shortcoming, another option is by storing this XML type using Native XML Database. However, it is still not supported by widely-used standard [8].

6 Conclusion

We propose checking methodology to preserve the referential integrity during an update of XML. The proposal checks the references that are implemented by using XLink and its subsequent XPointer. Since these reference mechanisms do not require a schema, our methods can be used in schema-less XML documents as well as in instance-based reference in XML documents.

We propose a set of checking functions that are triggered before the actual update takes place. The checking functions check the destination of the link, register or remove the link in the database, and perform other operations before deciding whether the update can be proceeded or not. Our methodologies are targeted for XML-Enabled Database as the storage.

Our methodologies avoid the referential integrity violation that can be caused by updating the XML links inside an XML document. These methods have added some new functionality to the current XML data management practice and they are usable both for database and document communities.

References

1. Beauchemin, B. The XML Files, MSDN Library, <http://msdn.microsoft.com/library/> (Setember 2000)
2. Bourett, R.: XML and Databases. <http://www.rpbouret.com/xml/XMLAndDatabases.htm>, (2005)
3. Fortier, P.: SQL3 Implementing the SQL Foundation Standard, McGraw Hill, New York, (1999)
4. IBM DB2. DB2 XML, <http://www-306.ibm.com/software/data/db2/extenders/xmlxt/>, (2006)
5. ISO/IEC. Information Technology – Database Languages – SQL – Part 14: XML-Related Specifications (SQL/XML). ISO/IEC 9075-14 (2003)
6. Klettke, M. and Meyer, H.: XML and Object-Relational Database Systems - Enhancing Structural Mappings Based on Statistics, LNCS 1997, Springer, (2000) pp. 151-170
7. Melton, J. (Ed.): Database Language SQL – Part 2 Foundation. ISO-ANSI WD 9072-2, International Organization for Standardization, Working Group WG3, (August 2002)
8. Pardede, E., Rahayu, J.W., and Taniar, D.: On Maintaining XML Linking Integrity During Update. LNCS 3588, Springer, (2005) pp. 431-440
9. Pardede, E., Rahayu, J.W., and Taniar, D.: Preserving Conceptual Constraints During XML Updates, International Journal of Web Information Systems 1(2), Troubador, (2005) pp. 65-82
10. Pardede, E., Rahayu, J.W., and Taniar, D., "Object-Relational Complex Structures for XML Storage", International Journal of Information and Software Technology, Elsevier Science, to appear (2006)
11. Price, J.: Oracle Database 10g SQL, McGraw Hill Osborne, (2004)
12. Scardina, M., Chang, B., and Wang, J., Oracle Database 10g XML & SQL: Design, Build & Manage XML Applications in Java, C, C++, & PL/SQL, McGraw Hill Osborne, (2004)
13. Tatarinov, I., Ives, Z.G., Halevy, A. Y., Weld, D. S.: Updating XML. ACM SIGMOD (2001) pp.413-424
14. W3C, XML Path Language, <http://www.w3.org/TR/xpath/>, W3C recommendation (November 1999)
15. W3C, XML Linking Language, <http://www.w3.org/TR/xlink/>, W3C recommendation (June 2001)
16. W3C, XML Pointer Language, <http://www.w3.org/TR/xpstr/>, W3C draft (August 2002)
17. Wilde, E., Lowe, D.: XPath, XLink, XPointer, and XML – A Practical Guide to Web Hyperlinking and Transclusion, Addison Wesley, Boston, (2002)
18. Xiaou, R., Dillon, T.S., Chang, E. and Feng, L.: Modeling and Transformation of Object-Oriented Conceptual Models into XML Schema, LNCS 2113, Springer, (2001) pp.795-804

Various Types of Attacks and Solutions Regarding Secure Remote User Access over Insecure Networks

Eun-Jun Yoon and Kee-Young Yoo*

Department of Computer Engineering, Kyungpook National University,
Daegu 702-701, South Korea
Tel.: +82-53-950-5553; Fax: +82-53-957-4846
ejyoon@infosec.knu.ac.kr, yook@knu.ac.kr

Abstract. In 2005, Peyravian-Jeffries proposed secure password-based protocols for remote user authentication, password change, and session key establishment over insecure networks. These protocols, however, are still susceptible to a stolen-verifier attack. Accordingly, the current paper demonstrates the vulnerability of their protocols to a stolen-verifier attack and then, a simple solution to resolve such a problem is presented. In contrast to these protocols, the proposed solution can resist the stolen-verifier attack.

Keywords: Cryptography, Hash function, Network security, Password authentication, Diffie-Hellman, Stolen-verifier attack.

1 Introduction

Remote user authentication over untrusted networks is an important part of security, along with confidentiality and integrity, for servers that allow remote access over untrustworthy networks, like the Internet and the mobile communication environment. As such, a remote password authentication scheme authenticates the legitimacy of users over an insecure channel, where the password is often regarded as a secret shared between the remote server and user. Based on knowledge of the password, a user can use it to create and send a valid login message to a remote server to gain the right to access. Meanwhile, the remote server also uses the shared password to check the validity of the login message and to authenticate the user. Typical user authentication schemes for protecting passwords, while traveling over public networks, encrypt passwords with symmetric-key cryptosystems (such as DES, AES, RC5, etc.) or public-key cryptosystems (such as RSA, DSA, etc.) [1][2][3][4][5]. In 2000, Peyravian-Zunic [7] presented a password change scheme, which does not use any symmetric-key or publickey cryptosystems - they only employ a collision-resistant hash function such as SHA [6]. Their password change scheme, however, is vulnerable to

* Corresponding author.

off-line password guessing attack (i.e., dictionary attack) and denial of service attack [9][10].

In 2005, Peyravian-Jeffries [8] improved the base remote user authentication and password change protocols presented in [7], in order to address the security concerns raised by [9][10][11][12]. They presented two sets of enhanced remote user authentication and password change protocols. Both sets allow parties the option of establishing a session key, which can be used to protect their subsequent communication. The first set fixes the denial of service vulnerability and it only employs a collision-resistant hash function such as SHA, as required in [7]. The first set, however, can not withstand off-line password-guessing attacks if the password is weak. The second set fixes the denial of service vulnerability and it also provides protection against off-line password-guessing attacks. The second set employs the Diffie-Hellman (DH) key agreement scheme [13], in addition to a collision-resistant hash function such as SHA, in order to protect exchanges. Peyravian-Jeffries's protocols, however, are still susceptible to a stolen-verifier attack [10], in which obtaining secret data, which are stored in a server, can allow an illegitimate user to login to a server as a legitimate user. Accordingly, the current paper demonstrates that Peyravian-Jeffries's protocols are vulnerable to a stolen-verifier attack and a simple solution to isolate such a problem is presented. In contrast to Peyravian-Jeffries's protocols, the proposed solution can resist the stolen-verifier attack.

The remainder of this paper is organized as follows: Section 2 briefly reviews Peyravian-Jeffries's protocols, then Section 3 demonstrates the stolen-verifier attack regarding their protocols. Section 4 presents the proposed solution and security measures are discussed. Our conclusions are presented in Section 5.

2 Review of Peyravian-Jeffries's Protocols

This section briefly reviews Peyravian-Jeffries's enhanced hash-based protocols and the DH-based protocols for remote user authentication and password change [8]. Abbreviations used in this paper are as follows:

- *id*: Public user identity of a client.
- *pw*: Secret and possibly weak user password.
- *K*: Strong secret key of a server.
- *p*: Large prime number p .
- *g*: A primitive root in the Galois field $GF(p)$, in which the Diffie-Hellman problem is considered hard.
- *x, y*: Session-independent random exponents $\in [1, p - 1]$, chosen by a client and server, respectively.
- *session_key*: Shared session key computed by a client and server.
- *Hash*(\cdot): Strong collision-resistant one-way hash function such as SHA-1.
- \oplus : Bit-wise XOR operation.

In Peyravian-Jeffries's protocols, the server stores a password digest value, which is referred to as the *idpw_digest*, where $idpw_digest = Hash(id, pw)$.

2.1 Hash-Based Protocols

User Authentication Protocol:

Step 1. Client \rightarrow Server: id, rc

The user submits his/her id and pw to the client. The client generates a random value rc and sends the id and rc to the server.

Step 2. Server \rightarrow Client: rs, ser_auth_token

The server generates a random value rs and computes a one-time token $ser_auth_token = Hash(idpw_digest, rc, rs)$. The server then sends the rs and ser_auth_token to the client.

Step 3. Client \rightarrow Server: id, cli_auth_token

The client first computes the $idpw_digest$ value. Next, it verifies the validity of the received ser_auth_token . The client then generates a one-time $cli_auth_token = Hash(idpw_digest, rc, rs + 1)$. The client sends the id and cli_auth_token to the server.

Step 4. Server \rightarrow Client: Access granted (or denied)

The server verifies the validity of the received cli_auth_token . If it is valid, the server sends a message to the client giving it permission to access the server. If it is not valid, it sends a message denying it access to the server.

Password Change Protocol:

Step 1. Client \rightarrow Server: id, rc

The user submits his/her id , pw , and new_pw to the client. The client generates a random value rc and sends the id and rc to the server.

Step 2. Server \rightarrow Client: rs, ser_auth_token

The server generates a random value rs and computes a one-time token $ser_auth_token = Hash(idpw_digest, rc, rs)$. The server then sends the rs and ser_auth_token to the client.

Step 3. Client \rightarrow Server: $id, masked_idpw_digest_new, mac$

First, the client computes the $idpw_digest$ value. It then verifies the validity of the received ser_auth_token and computes the $idpw_digest_new$ value. Next, the client generates a one-time $mask = Hash(idpw_digest, rc, rs+1)$ and $mac = Hash(idpw_digest, idpw_digest_new, rc, rs)$. Next, the client generates a $masked_idpw_digest_new = mask \oplus idpw_digest_new$. The client sends the id , $masked_idpw_digest_new$, and mac to the server.

Step 4. Server \rightarrow Client: password change accepted (or rejected), $code$

The server verifies the validity of the received mac . If it is valid, the server sends a message to the client accepting the password change. If it is not valid, it sends a message rejecting the password change. The password acceptance or rejection message, that is sent from the server to the client, contains a protected response called $code$ where $code = Hash(idpw_digest, flag, rc, rs)$. The $flag$ here is set to either “accept” or “reject”, depending upon whether the password change is accepted

or rejected. In this step, in order to retrieve $idpw_digest_new$, the server generates the $mask$, as in Step 3 and exclusive-ors it with the received $masked_idpw_digest_new$. If the mac is valid, the server replaces the $idpw_digest$ with the new password digest value (i.e. $idpw_digest_new$). The server verifies the validity of the received mac value by independently computing it using the retrieved $idpw_digest_new$ and its local copies of $idpw_digest$, rc , and rs .

2.2 DH-Based Protocols

User Authentication Protocol:

Step 1. Client \rightarrow Server: id, rc, p, g, g^x

The user submits his/her id and pw to the client. The client generates a random value rc . It also chooses a large prime p and a primitive root g for $GF(p)$. Moreover, the client chooses a large random integer x , where $x < p - 1$, and computes g^x over $GF(p)$. Then, it sends the id , rc , p , g , and g^x to the server.

Step 2. Server \rightarrow Client: $challenge, g^y$

The server generates a random value rs . It also chooses a large random integer y , where $y < p - 1$, and computes g^y and g^{xy} over $GF(p)$. Next, the server generates a one-time $challenge = rs \oplus Hash(g^{xy}, idpw_digest, rc)$. The server then sends the challenge and g^y to the client.

Step 3. Client \rightarrow Server: id, rs

First, the client computes the $idpw_digest$ value. Next, it retrieves the rs from the received challenge token $rs = challenge \oplus Hash(g^{xy}, idpw_digest, rc)$. Then, the client sends the id and rs to the server.

Step 4. Server \rightarrow Client: ser_auth_token , access granted (or denied)

The server verifies that the received rs is the same as the one it generated. If they are different, it sends a message denying the client access to the server. Otherwise, the user is authenticated and the server generates a one-time authentication token $ser_auth_token = Hash(g^{xy}, idpw_digest, rc, rs)$. The server sends ser_auth_token to the client, giving it permission to access the server. Then, the client verifies the validity of ser_auth_token received from the server. If the server's authentication token is valid, the server is authenticated.

In order to establish a symmetric session key to protect (e.g. encrypt) further information exchanged in the session after the initial authentication, (after Step 4 above), the client and server can generate a one-time session key by using the g^{xy} , $idpw_digest$, rc and rs in several ways. For example, the session key can be a hash of g^{xy} , $idpw_digest$, rc , and rs plus some fixed value. That is, $session_key = Hash(g^{xy}, idpw_digest, rc, rs + 1)$. The fixed value, which is added to the rs , makes the session key different from the server's authentication token.

Password Change Protocol:

Step 1. Client \rightarrow Server: id, rc, p, g, g^x

The user submits his/her id , pw , and new_pw to the client. The client generates a random value rc . It also chooses a large prime p and a primitive root g for $GF(p)$. Moreover, the client chooses a large random integer x , where $x < p - 1$, and it computes g^x over $GF(p)$. Then, it sends the id , rc , p , g , and g^x to the server.

Step 2. Server \rightarrow Client: $challenge, g^y$

The server generates a random value rs . It also chooses a large random integer y , where $y < p - 1$, and it computes g^y and g^{xy} over $GF(p)$. Next, the server generates a one-time $challenge = rs \oplus Hash(g^{xy}, idpw_digest, rc)$. Then, the server sends the challenge and g^y to the client.

Step 3. Client \rightarrow Server: id, rs

The client first computes the $idpw_digest$ value. Next, it retrieves the rs from the received $challenge$ token $rs = challenge \oplus Hash(g^{xy}, idpw_digest, rc)$. Then, the client sends the id and rs to the server.

Step 4. Server \rightarrow Client: ser_auth_token

The server verifies that the received rs is the same as the one it generated. If they are different, it sends a message denying the client access to the server. Otherwise, the user is authenticated and the server generates a one-time authentication token $ser_auth_token = Hash(g^{xy}, idpw_digest, rc, rs)$. The server sends ser_auth_token to the client, giving it permission to access the server.

Step 5. Client \rightarrow Server: $id, masked_idpw_digest_new, mac$

The client verifies the validity of ser_auth_token received from the server. If the server's authentication token is valid, the client generates the new password digest value $idpw_digest_new$. Next, the client generates one-time $mask = Hash(g^{xy}, rc, rs)$ and $mac = Hash(g^{xy}, idpw_digest_new, rc, rs)$. Then, the client generates a $masked_idpw_digest_new = mask \oplus idpw_digest_new$. The client sends the id , $masked_idpw_digest_new$, and mac to the server.

Step 6. Server \rightarrow Client: password change accepted (or rejected), $code$

The server verifies the validity of the received mac . If it is valid, the server sends a message to the client accepting the password change. If it is not valid, it sends a message rejecting the password change. The password acceptance or rejection message, which is sent from the server to the client, contains a protected response called code, which is $code = Hash(g^{xy}, idpw_digest, flag, rc, rs)$. The $flag$ here is set to either "accept" or "reject", depending upon whether the password change is accepted or rejected. In this Step, in order to retrieve $idpw_digest_new$, the server generates the $mask$, as in Step 5, and exclusive-ors it with the received $masked_idpw_digest_new$. If the mac is valid, the server replaces $idpw_digest$ with the new password digest value (i.e. $idpw_digest_new$).

The server verifies the validity of the received *mac* value by independently computing it using the retrieved *idpw_digest_new* and its local copies of g^{xy} , *rc*, and *rs*.

3 The Effect of the Stolen-Verifier Attack on Peyravian-Jeffries's Protocols

This section shows that Peyravian-Jeffries's two Hash-Based protocols (user authentication protocol and password change protocol) and two DH-Based protocols (user authentication protocol and password change protocol) are vulnerable to stolen-verifier attacks [10]. In most existing password authentication schemes, the server stores the user's verifier (e.g. hashed passwords), rather than the user's bare password, in order to reduce the security of the breach once the server is compromised. Therefore, servers are always the targets of attacker, because numerous customers' secrets are stored in their databases. The stolen-verifier attack means that an adversary who steals a password-verifier from the server can use it *directly* to impersonate a legitimate user in a user authentication execution. Note that the main purpose of an authentication scheme against the stolen-verifier attack is to reduce the immediate danger to the authenticate user. In fact, an adversary who has a password-verifier may further mount a guessing attack.

In Peyravian-Jeffries's protocols, the hash value $idpw_digest = Hash(id, pw)$ of the user password, which is stored in the server, can be eavesdropped and then used to masquerade as the original user. Peyravian-Jeffries did not explain the stolen-verifier attack, with regard to obtaining the secret data $idpw_digest = Hash(id, pw)$, which is stored in a server. This information can allow an illegitimate user to login to the server as a legitimate user. Suppose an attacker has stolen the password verifier $idpw_digest = Hash(id, pw)$ in the server. Then, he can perform an impersonating attack. For example, the stolen-verifier attack, in Peyravian-Jeffries's DH-Based user authentication protocol is as follows:

- Step 1. Attacker \rightarrow Server: $id, rc', p, g, g^{x'}$
 The attacker generates the rc' and x , and computes $g^{x'}$. Then, it sends the id, rc', p, g , and $g^{x'}$ to the server.
- Step 2. Server \rightarrow Attacker: $challenge, g^y$
 The server will generate the rs and y , and compute g^y and $g^{x'y}$. Next, the server will generate a one-time $challenge = rs \oplus Hash(g^{x'y}, idpw_digest, rc')$. Then, the server will send the challenge and g^y to the attacker.
- Step 3. Attacker \rightarrow Server: id, rs
 By using the stolen $idpw_digest$ value, the attacker retrieves the rs from the received challenge token $rs = challenge \oplus Hash(g^{x'y}, idpw_digest, rc')$. Then, the attacker sends the id and rs to the server.
- Step 4. Server \rightarrow Attacker: ser_auth_token , access granted (or denied)
 The server will verify that the received rs is the same as the one it generated. Since they always hold, the attacker is authenticated and the server will generate a one-time authentication token

$ser_auth_token = Hash(g^{x'y}, idpw_digest, rc', rs)$. The server then will send ser_auth_token to the attacker, thus giving it permission to access the server.

Finally, the attacker verifies the validity of ser_auth_token received from the server. If the server's authentication token is valid, the server is authenticated as well by the attacker. As a result, the attacker can masquerade the original user id , by using the stolen-verifier attack.

In addition, by using the stolen $idpw_digest = Hash(id, pw)$, the attacker can also impersonate the server in order to cheat the legal user as follows:

Step 1. Client \rightarrow Server: id, rc, p, g, g^x

The user submits his/her id and pw to the client. The client generates a random value rc . It also chooses a large prime p and a primitive root g for $GF(p)$. Moreover, the client chooses a large random integer x , where $x < p - 1$, and computes g^x over $GF(p)$. Then, it sends the id, rc, p, g , and g^x to the server.

Step 2. Attacker \rightarrow Client: $challenge, g^{y'}$

Upon intercepting the client's login request messages id, rc, p, g , and g^x , the attacker generates a random value rs' . It also chooses a large random integer y , where $y < p - 1$, and it computes $g^{y'}$ and $g^{xy'}$ over $GF(p)$. Next, by using the stolen $idpw_digest = Hash(id, pw)$, the attacker generates a one-time $challenge = rs' \oplus Hash(g^{xy'}, idpw_digest, rc)$. Then, the attacker sends the challenge and $g^{y'}$ to the client.

Step 3. Client \rightarrow Attacker: id, rs

First, the client will compute the $idpw_digest$ value. Next, it will retrieve the rs from the received challenge token $rs' = challenge \oplus Hash(g^{xy'}, idpw_digest, rc)$. Then, the client will send the id and rs' to the server.

Step 4. Attacker \rightarrow Client: ser_auth_token , access granted (or denied)

After intercepting the client's messages id and rs' , the attacker verifies that the received rs' is the same as the one it generated. If they are different, it sends a message denying the client access to the attacker. If it is not valid, the user is authenticated and the attacker generates a one-time authentication token $ser_auth_token = Hash(g^{xy'}, idpw_digest, rc, rs')$. The attacker sends ser_auth_token to the client, giving it permission to access the attacker. Then, the client will verify the validity of the ser_auth_token received from the attacker. Since the attacker's authentication token is always valid, the attacker is authenticated as well. As a result, the attacker can also masquerade as a legal server, by using the stolen-verifier attack.

4 Simple Solution and Security Analysis

This section proposes a simple solution to overcome the above mentioned security problems inherent in Peyravian-Jeffries's protocols.

4.1 Proposed Solution

In the proposed solution, the server stores $vpw = (idpw_digest \oplus Hash(K)) + Hash(K)$ (or $E_K(idpw_digest)$, where $E(\cdot)$ is the encryption function) by using the server's strong secret key K instead of $idpw_digest = Hash(id, pw)$ for each client in the database. This is done in order to overcome the stolen-verifier attack. For example, we can show that the proposed solution can resist the stolen-verifier attack in Peyravian-Jeffries's DH-Based user authentication protocol. It is as follows:

Step 1. Client \rightarrow Server: id, rc, p, g, g^x

The user submits his/her id and pw to the client. The client generates a random value rc . It also chooses a large prime p and a primitive root g for $GF(p)$. Moreover, the client chooses a large random integer x , where $x < p - 1$, and computes g^x over $GF(p)$. Then, it sends the id, rc, p, g , and g^x to the server.

Step 2. Server \rightarrow Client: $challenge, g^y$

The server generates a random value rs . It also chooses a large random integer y , where $y < p - 1$, and computes g^y and g^{xy} over $GF(p)$. Next, the server retrieves $idpw_digest = (vpw - Hash(K)) \oplus Hash(K)$ (or $D_K(E_K(idpw_digest))$) and generates a one-time $challenge = rs \oplus Hash(g^{xy}, idpw_digest, rc)$. Then, the server sends the challenge and g^y to the client.

Step 3. Client \rightarrow Server: id, rs

The client first computes the $idpw_digest$ value. Next, it retrieves the rs from the received challenge token $rs = challenge \oplus Hash(g^{xy}, idpw_digest, rc)$. Then, the client sends the id and rs to the server.

Step 4. Server \rightarrow Client: ser_auth_token , access granted (or denied)

The server verifies that the received rs is the same as the one it generated. If they are different, it sends a message denying the client access the server. If they are the same, the user is authenticated and the server generates a one-time authentication token $ser_auth_token = Hash(g^{xy}, idpw_digest, rc, rs)$. The server sends ser_auth_token to the client, giving it permission to access the server. Then, the client verifies the validity of ser_auth_token received from the server. If the server's authentication token is valid, the server is authenticated as well.

4.2 Security Analysis

We define the security terms [14] needed for proving the security of the proposed solution. They are as follows:

Definition 1. A weak secret (password pw) is a value of low entropy $W(k)$, which can be guessed in polynomial time.

Definition 2. A strong secret key (K) is a value of high entropy $H(k)$, which cannot be guessed in polynomial time.

Here, we shall only discuss the enhanced security features. The rest of the security features are the same as the original Peyravian-Jeffries's protocols, as described in literature [8].

Theorem 1. *The proposed solution can resist the stolen-verifier attack.*

Proof. An attacker may acquire $vpw = (idpw_digest \oplus Hash(K)) + Hash(K)$ (or $E_K(idpw_digest)$) stored in the server. Without knowing the server's strong secret key K , however, the attacker cannot forge a login request to pass the authentication, as $H(id, pw)$ is hidden in $vpw = (idpw_digest \oplus Hash(K)) + Hash(K)$ (or $E_K(idpw_digest)$), by using the server's strong secret key K . Thus, the validity of the guessed password pw' cannot be verified by checking $(H(id, pw') \oplus Hash(K')) + Hash(K') = vpw$ (or $D'_K(E_K(idpw_digest)) = H(id, pw')$), where pw' is the guessed client's password and K' is the guessed server's strong secret key. Therefore, the proposed solution can resist the stolen-verifier attack.

5 Conclusions

The current paper demonstrated that Peyravian-Jeffries's protocols are vulnerable to the stolen-verifier attack, whereby obtaining secret data stored in a server can allow an illegitimate user to login to a server as a legitimate user. Then, we presented a simple solution to isolate such a problem. In contrast to Peyravian-Jeffries's protocols, the proposed solution can resist the stolen-verifier attack.

Acknowledgements

This work was supported by the Brain Korea 21 Project in 2006.

References

1. Botting, J.: Security on the Internet: Authenticating the User. Telecommunications. Vol. 31. No. 12. (1997) 77-80
2. Halevi, S., Krawczyk, H.: Public Key Cryptography and Password Protocols. Proceedings of Fifth ACM Conference on Computer and Communications Security. (1998) 122-131
3. Jablon, D.P.: Strong Password Only Authenticated Key Exchange. Computer Communication Review. Vol. 26. No. 5. (1996) 5-26
4. Boyko, V., MacKenzie, P., Patel, S.: Provably Secure Password Authenticated Key Exchange Using Diffie-Hellman. Proceedings of Eurocrypt. (2000) 156-171
5. Horng, T.L.: Password Authentication Using Triangles and Straight Lines. Computers and Mathematics Applications. Vol. 30. No. 9. (1995) 63-71
6. National Institute of Standards and Technology.: Secure Hash Standard. FIPS PUB 180-2. (August 2002)
7. Peyravian, M., Zunic, N.: Methods for Protecting Password Transmission. Computers and Security. Vol. 19. No. 5. (2000) 466-469

8. Peyravian, M., Jeffries, C.: Secure Remote User Access over Insecure Networks. *Computer Communications*. In Press. Corrected Proof. Available online 29 (August 2005)
9. Hwang, J.J., Yeh, T.C.: Improvement on Peyravian-Zunic's Password Authentication Schemes. *IEICE Transactions on Communications*. Vol. E85-B. No. 4. (2002) 823-825
10. Lin, C.L., Hwang, T.: A Password Authentication Scheme with Secure Password Updating. *Computers and Security*. Vol. 22. No. 1. (2003) 68-72..
11. Hsieh, B.T., Sun, H.M., Hwang, T.: On the Security of Some Password Authentication Protocols. *Informatica*. Vol. 14. No. 2. (2003) 195-204
12. Ku, W.C., Chen, C.M., Lee, H.L.: Weaknesses of Lee-Li-Hwang's Hash-based Password Authentication Scheme. *Operating Systems Review*. Vol. 37. No. 4. (2003) 19-25
13. Diffie, W., Hellman, M.: New Directions in Cryptography. *IEEE Transaction on Information Theory*. Vol. IT-22. No. 6. (1976) 644-654
14. Menezes, A.J., Oorschot, P.C., Vanstone, S.A.: *Handbook of Applied Cryptograph*. CRC Press. New York. (1997)

Revealing Statistical Independence of Two Experimental Data Sets: An Improvement on Spearman's Algorithm

Bogdan Badea¹ and Adriana Vlad^{1,2}

¹Faculty of Electronics, Telecommunications and Information Technology,
Politehnica University of Bucharest, Romania

²The Research Institute for Artificial Intelligence, Romanian Academy
bogdan_badea@yahoo.com, adriana_vlad@yahoo.com, avlad@racai.ro

Abstract. A high effective statistical independence test procedure derived from Spearman's Rank Correlation Test is presented, applicable to all kind of continuous variables (normal or not, even of unknown probability law). Some relevant practical signal processing test examples as well as a Monte Carlo performance comparison with Spearman's Rank Correlation Test capabilities are explained. Besides describing the test procedure algorithm, the paper reveals, from an engineering point of view, some significant aspects concerning the understanding (perception) of the important and not simple concepts, *i.e.* testing dependence versus statistical independence.

1 Introduction

In many fields (physics, medicine, biology, engineering, psychology), one important task is to verify the statistical independence between various experimental data sets.

The present paper discusses correlation and independence testing on two continuous X and Y random variables (r.v.).

If the experimental data come out from discrete random variables, usual statistical methods can be helpful, *i.e.* by using a Chi Square independence test on the measured frequencies (contingency tables - see [1], [2], [3], [4]).

For continuous random variables, there are well-known statistical tests, applicable only to normal (gaussian) populations.

If the investigated random variables are continuous, but not necessarily normal, Spearman's rank correlation test is usually applied. Constructing contingency tables and testing afterwards the data by a Chi Square independence test is also possible; in this case, some class partitions would be required, leading to a huge data amount for a good test accuracy (because of the great number of required classes).

This paper introduces an improved robust statistical independence test method derived from Spearman's Rank Correlation Test, applicable to all kind of continuous variables (normal or not, even of unknown probability law, see [5]). Our testing procedure differs from Spearman's test by adding a second transform on experimental data, in order to benefit from the Pearson's r independence test on gaussian population.

A statistical correlation test between the continuous r.v. X and Y is always based on the linear regression analysis. Thus, the correlation of the two r.v. is equivalent to the existence of a linear dependence between the two r.v.. To test a linear dependence between the two r.v. means in fact to reveal that there is a significant xy data trend (ascending or descending) - *i.e.* correlation exists if there is a non-zero linear regression slope in xy . The linear regression slope can be also inspected graphically; so scatter diagrams ((x_i, y_i) plots in xy) are very helpful.

One important result of our study is that it makes available some *reference scatter diagrams*, which permits the visual interpretation as well as making decisions referring to the two random variables independence. In fact, our study provides the user with a tool for further independence investigation in the case of non-correlation decision.

Some further contribution is that the test procedure upon statistical independence necessarily implies bivariate gaussian random variables - this aspect is graphically put into evidence. This means that the independence test is applicable if the random variables X and Y are jointly normal distributed (bivariate normal). The jointly normal (gaussian) distribution assumption implies that X and Y are separately normal distributed, but the converse is not always true. The jointly normal distribution assumption is mandatory for this testing and means that the jointly probability density function of the two random variables is a bell shaped curve (Gauss bell).

The two compared methods (Spearman's and our test procedure) are not fundamentally different, as they are both rank correlation based. However, they differ by the test capabilities, by the graphical facilities offered by our method and also by the data sets sizing (*i.e.* how many observations are required for an accurate decision). An important point is that our procedure enables a final decision upon independence which is not possible by means of other tests.

For making an accurate tests capabilities comparison between the two methods, the study evaluates the probability of accepting false data as good (to accept independence when data sets are correlated). That means to apply Monte-Carlo techniques. The error evaluation results indicate that compared to Spearman's, our test is a more effective independence test algorithm (with smaller type two statistical error).

Another important result of this paper resides in the studied examples (for a comparison between the two test methods). An example is taken from the field of chaotic signals.

2 Problem Statement and Test Method

As usual for an independence test, we start by the acquisition of the two experimental data sets of size N , corresponding to the two r.v. X and Y ; each of the two data sets complies with the *i.i.d* statistical model (data come out from independently and identically distributed random variables):

$$x_1, x_2, \dots, x_k, \dots, x_N \quad \text{and} \quad y_1, y_2, \dots, y_k, \dots, y_N.$$

We want to decide whether X and Y are statistically independent.

The proposed independence test operates with some bijective random variable transforms, in order to obtain from X and Y two new normal random variables U and V ,

which preserve the information order coming out from X and Y ; so that the independence of the r.v. U and V is ready to be tested by means of the known tests.

If X and Y are of unknown probability law, we estimate the cumulative distribution functions $F_X(x)$, $F_Y(y)$ by using the well-known probability estimation method (see the estimation of the cumulative distribution function (cdf) for the Kolmogorov-Smirnov test [3], [6], and [7]) *i.e.* by approximating the cdf by stairs function $Fe_X(x)$, $Fe_Y(y)$. It would be important to determine the required data size N in order to have an accurate estimation of $F_X(x)$ and $F_Y(y)$. Here we determine N based on some results implied by the Kolmogorov-Smirnov concordance test. Thus, the absolute maximum difference δ between the theoretical distribution function $F_X(x)$ and the experimental cdf $Fe_X(x)$ is computed: $\delta = \max_x |F_X(x) - Fe_X(x)|$.

The α point value Δ_α for the r.v. Δ (where Δ is the r.v. producing δ values) is $\Delta_\alpha = \sqrt{(\ln(2/\alpha))/(2N)}$, where α is the significance level of the Kolmogorov-Smirnov concordance test. Δ_α can be regarded as maximum admissible absolute difference between the experimental cdf and the theoretical unknown distribution function. In our study, the relation $\delta \leq \Delta_\alpha$ is used to determine N :

$$N \geq (\ln(2/\alpha))/\left(2\Delta_\alpha^2\right). \tag{1}$$

For example, considering $\alpha=0.05$ it results: for $\Delta_\alpha=0.05 \Rightarrow N > 738$; for $\Delta_\alpha = 0.01 \Rightarrow N > 18445$; for $\Delta_\alpha = 0.007 \Rightarrow N > 37642$.

We shall transform the x_k , as well as the y_k , $k = 1 \dots N$ experimental values, into normal distributed data, so that we can apply the known Pearson's independence test by computing the r (Pearson's) correlation coefficient (see [1], [4], [8], [9]) on the normal distributed data sets. This transform preserves the data order.

It is shown (see important remark 5 below), that testing independence between the newly resulted gaussian random variables (after doing the bijective transform) is equivalent to testing independence between the original random variables.

The independence testing method of the two continuous, not necessarily normal distributed r.v. X and Y is presented as follows:

- H0: the r.v. X and Y are statistically independent;
- H1: the alternative hypothesis: r.v. X and Y are dependent.

To perform this test, the N size samples should verify (1). The decision is made with a α statistical significance level. The test algorithm includes the following steps:

1. Obtain the experimental cumulative distribution functions $Fe_X(x)$ and $Fe_Y(y)$.
2. Apply $Fe_X(x)$ transform on the x_k data values and $Fe_Y(y)$ on the values y_k , $k = 1 \dots N$, obtaining the new data x'_k and y'_k , which are uniformly distributed in $(0, 1)$. The data x' and y' are of uniform law, *i.e.* each occurrence of x'_k and y'_k is singular and equally spread in the interval $(0, 1)$. To be noted *the important result* that by this data transform, *Spearman's ranks are revealed*: $N x'_k = Rank(x_k)$; $N y'_k = Rank(y_k)$.
3. Another random variable transform which is the inverse of the distribution function of the standard normal (gaussian) law, computed by numerical methods, is now

applied to data x'_k and y'_k , $k = 1 \dots N$ (obtained according to step 2), generating the new data u_k and v_k . According to the known theory, both u_k and v_k values are standard normal distributed, *i.e.* we generated two random variables U and V , each of them of mean 0 and variance 1.

It is obvious that u_k and v_k take the same values, but in different order.

4. Compute r - the correlation coefficient between U and V and the t test value:

$$r = \frac{\sum_{i=1}^N (u_i - \bar{u})(v_i - \bar{v})}{\sqrt{\sum_{i=1}^N (u_i - \bar{u})^2 \sum_{i=1}^N (v_i - \bar{v})^2}}; \quad t = \sqrt{\frac{r^2}{1-r^2}} (N-2). \quad (2)$$

If the null hypothesis is correct (H_0 : independence), then the t test value is distributed under a Student law with $N - 2$ degrees of freedom.

5. Based on the significance level α , we compute $t_{\alpha/2}$, the $\alpha/2$ point value of the Student law of $N - 2$ degrees of freedom. If $|t| < t_{\alpha/2}$, then the r.v. X and Y could be independent. To decide upon independence, continue with step 6.

Otherwise, that is if $|t| \geq t_{\alpha/2}$, the r.v. X and Y are statistically dependent and no further investigation is required. The test procedure stops.

6. If $|t| < t_{\alpha/2}$, then test if the r.v. U and V are jointly normal distributed. If U and V are proven jointly normal distributed, then X and Y are independent. If U and V are not jointly normal distributed, then X and Y are dependent.

Important remarks:

- 1° By two successive transforms: $x \rightarrow x' \rightarrow u \rightarrow$ and $\rightarrow y \rightarrow y' \rightarrow v$ two *i.i.d.* data sets u_1, u_2, \dots, u_N and v_1, v_2, \dots, v_N are obtained, each being standard normal distributed. The rank information of u is the same as the one of x , and the rank information of v is the same as the one of y .
- 2° It can be easily shown that there is an equality between r (from (2)) and b_1 (from (3)), where r is the correlation coefficient between U and V and b_1 - the linear regression slope (V versus U):

$$b_1 = \frac{\sum_{i=1}^N (u_i v_i - \bar{u} \bar{v})}{\sum_{i=1}^N (u_i^2 - \bar{u}^2)}. \quad (3)$$

This important result is a consequence of step 3, *i.e.* u_k and v_k take the same values, but in different order. As a consequence, the known independence test can be used based on the linear regression slope b_1 .

- 3° In fact, by the first transform $x \rightarrow x'$ and $y \rightarrow y'$ we get Spearman's ranks.
- 4° Especially if the test value satisfies $|t| < t_{\alpha/2}$, for further independence investigation it is of great help to display the scatter diagram of Spearman's ranks and/or the scatter diagram of (u, v) normal distributed data. Our procedure is to test the two r.v. independence by proving that the random variables (U, V) are jointly normal distributed. *Note* that usually scatter diagrams are displayed just for the initial data (x, y) ; here, scatter diagrams are displayed for (u, v) and for Spearman's ranks (on x' and y') as a tool for inspecting data independence.

5° The equivalence of testing the independence of r.v. X and Y based on testing the independence of r.v. U and V can be explained as follows:

U is a function only of X and V is a function only of Y ; if we assume that the r.v. X and Y are independent, it results that the r.v. U and V are independent.

Conversely, because of the two bijective transforms, if U and V are independent, it also results that X and Y are independent (see for example [10], chapter 7).

6° If the two investigated r.v. are of known probability law, then, at step 2 we use the two random variable transforms $F_X(x)$ and $F_Y(y)$. According to the known theory we obtain two uniform r.v. in $(0, 1)$ interval, X' and Y' . Obviously, in this case, we have two bijective functions. If the probability laws are unknown, then a large N is required (see (1)) in order to have a good approximation of the theory.

3 Case Studies

The method can be applied in various test situations. The test examples shown below cover several cases: the reference case (independent random variables - producing *reference scatter diagrams*), some real cases (chaotic signals) and some special cases (as the case of non-correlated but dependent r. v. $Y = X^2$).

An important contribution of the testing procedure is to graphically reveal statistical independence (to enable the use of a visual tool to decide upon independence). Thus, in the same figure, both the scatter diagram (either (u, v) or (x', y') scatter diagrams) and the corresponding linear regression slope are displayed. Remember that in the testing procedure the linear regression slope (3) is equal to Pearson's correlation coefficient (2).

In the examples below, for comparison, the r correlation coefficient and the t test values are computed both for our test and for Spearman's rank correlation test. The Spearman's rank correlation coefficient r_S is computed as in (2), but instead of (u, v) , (x', y') is used (see [3], [7], [9], [11]).

a. Independent random variables. Reference scatter diagrams.

The two independent *i.i.d.* data sets are generated using a uniform random generator in $(0, 1)$; these two independent sets correspond to X and Y , respectively.

After applying the algorithm described above, we obtain the (u, v) scatter diagram displayed in Fig. 1. Our algorithm also provides the x' and y' data sets, which can be assigned to Spearman's ranks. We also displayed a scatter diagram of the Spearman's ranks in Fig. 2. In our illustrations the number of data pairs is $N = 20000$.

In Fig. 1 and Fig. 2, for $N = 20000$ data pairs, the two r.v. are non-correlated:

$$\alpha = 0.05 \Rightarrow t_{\alpha/2} = 1.96$$

$$r = 0.0038 \Rightarrow t = 0.5349 \Rightarrow |t| < t_{\alpha/2} \text{ (our procedure, by means of (2))}$$

$$r_S = 0.0021 \Rightarrow t_S = 0.2944 \Rightarrow |t| < t_{\alpha/2} \text{ (Spearman's test)}.$$

Note that another important aspect revealed by our study is that Fig. 1 and Fig. 2 can be used as *reference scatter diagrams*, serving as a tool for graphical visual interpretation of the independence between the two r.v. X and Y . By using two

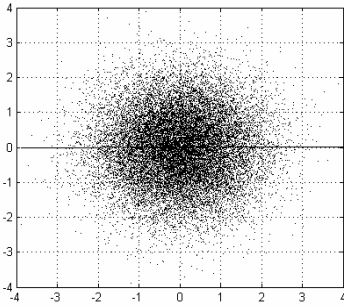


Fig. 1. Reference (u, v) scatter diagram. Scatter diagram (u, v) for uniform independent random variables.

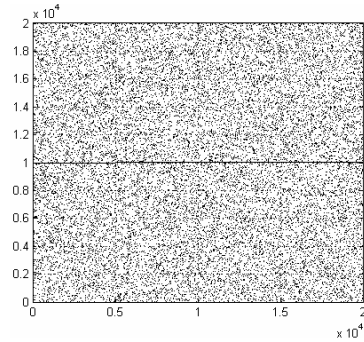


Fig. 2. Reference Spearman's ranks scatter diagram. Scatter diagram of Spearman's ranks for uniform independent random variables.

independent r.v. X and Y of no matter what distribution law, the *reference scatter diagrams* (u, v) and (x', y') should resemble to the one displayed in Fig. 1 and Fig. 2, respectively.

b. Sampling a Chaotic Signal.

Another case study is testing the independence of two random variables sampled at two different iterations from a chaotic signal obtained by (4), with $R = 3.9$ (see [12]):

$$z_k = R z_{k-1} (1 - z_{k-1}); k = 1, 2, \dots \tag{4}$$

The way to construct the two random samples by this recursive function is the following: z_0 is initialized with a uniform random value in $(0, 1)$. The first experimental data set (corresponding to X r.v.) is assigned to the z_k values calculated at a specified number of iterations, $k = k_1$; the second data set (corresponding to Y r.v.) is assigned to the z_k values calculated at another specified number of iteration, $k = k_2$.

Testing independence is based upon a specific distance $k_2 - k_1$ iterations between the first and the second sampling time moment.

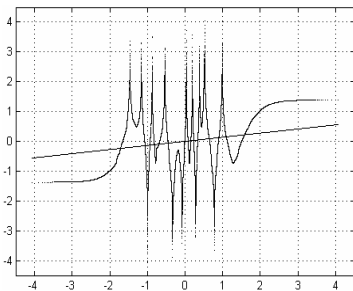


Fig. 3. Scatter diagram (u, v) for a distance 5 sampled chaotic signal

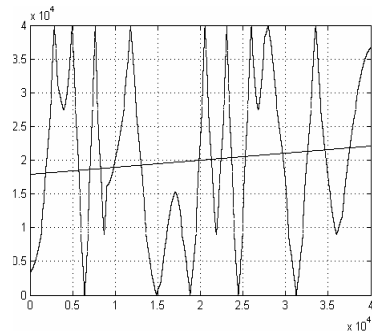


Fig. 4. Scatter diagram for Spearman's ranks for a distance 5 sampled chaotic signal

In Fig. 3 and Fig. 4, for a $k_2 - k_1 = 5$ distance and a number of $N = 40000$ data pairs, both methods reveal dependent samples:

$$\alpha = 0.05 \Rightarrow t_{\alpha/2} = 1.96$$

$$r = 0.1367 \Rightarrow t = 27.5952 \Rightarrow |t| > t_{\alpha/2} \text{ (our procedure, by means of (2))}$$

$$r_S = 0.1047 \Rightarrow t_S = 21.0613 \Rightarrow |t| > t_{\alpha/2} \text{ (Spearman's test).}$$

In Fig. 5 and Fig. 6, for a $k_2 - k_1 = 30$ distance and a number of $N = 40000$ data pairs, both methods reveal independent samples:

$$\alpha = 0.05 \Rightarrow t_{\alpha/2} = 1.96$$

$$r = -0.0001 \Rightarrow t = -0.0216 \Rightarrow |t| < t_{\alpha/2} \text{ (our procedure, by means of (2))}$$

$$r_S = 0.0015 \Rightarrow t_S = 0.2919 \Rightarrow |t| < t_{\alpha/2} \text{ (Spearman's test).}$$

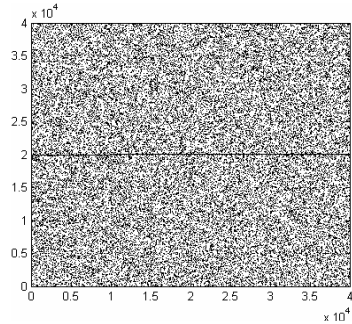
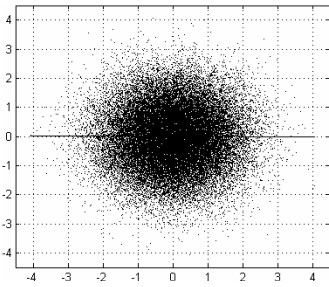


Fig. 5. Scatter diagram (u, v) for chaotic signal and 30 sampling distance

Fig. 6. Scatter diagram for Spearman's ranks for chaotic signal and 30 sampling distance

c. Special case: non-correlated but dependent random variables

If the link between the two random variables is $Y = X^2$, then, by theory, X and Y are non-correlated but still statistically dependent (if the mean of the r.v. X is zero).

Our test procedure, as well as Spearman's correlation test confirms that the two r.v. are non-correlated (see Fig. 7 and Fig. 8). Note that the regression slope (3) is zero.

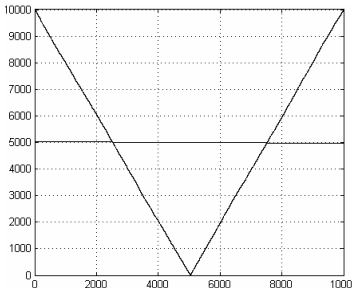
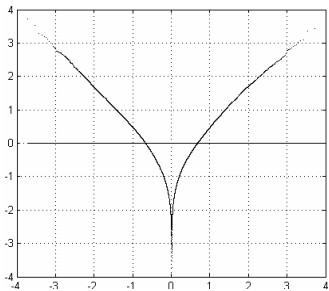


Fig. 7. Scatter diagram (u, v) provided by X and $Y = X^2$

Fig. 8. Scatter diagram for Spearman's ranks. Case study: $Y = X^2$.

Applying the test procedure for $N = 10000$ sample size, it results that X and Y are non-correlated as follows:

$$\begin{aligned} \alpha = 0.05 &\Rightarrow t_{\alpha/2} = 1.96 \\ r = 0.0014 &\Rightarrow t = 0.137 \quad (\text{our procedure, by means of (2)}) \\ r_S = -0.0006 &\Rightarrow t_S = -0.062 \quad (\text{Spearman's test}). \end{aligned}$$

To decide upon statistical independence, we apply our test procedure by comparing Fig. 7 and Fig. 8 with the *reference scatter diagrams*, i.e. Fig. 1 and Fig. 2 respectively. Obviously, dependency is revealed.

d. Testing non-typical distributed data dependencies

For bivariate normal data populations, a Student independence test based directly on Pearson's r correlation coefficient between the two X and Y random variables is applicable. However, unfortunately, some people do use this method, regardless of the experimental data sets distribution; sometimes this works.

We present a counterexample here: a pair of dependent generated data sets which are detected as non-correlated by Pearson's correlation test (wrongly applied here!) and correlated by Spearman's test and by our test procedure.

We use two independent standard normal distributed data sets n_1 and n_2 . We construct the x and y data sets by computing the ratio and the product of n_1 and n_2 , i.e. $x = n_1 / n_2$ and $y = n_1 n_2$ (X and Y are no more gaussian r.v.). Thus, for $\alpha = 0.05$, $t_{\alpha/2} = 1.96$ we obtain:

$$\begin{aligned} r = 0.591 &\Rightarrow t = 103.627 \quad (\text{our procedure, by means of (2)}) \\ r_S = 0.749 &\Rightarrow t_S = 159.623 \quad (\text{Spearman's test}) \\ r_P = 0.004 &\Rightarrow t_P = 0.615 \quad (\text{Pearson's test procedure}). \end{aligned}$$

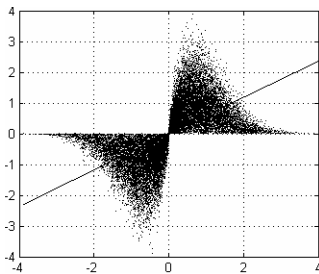


Fig. 9. Scatter diagram (u, v) for the $x = n_1 / n_2$ and $y = n_1 n_2$ data sets

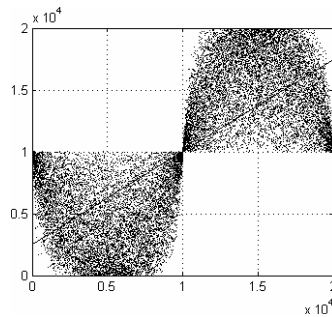


Fig. 10. Scatter diagram for Spearman's ranks for the $x = n_1 / n_2$ and $y = n_1 n_2$ data sets

4 Tests Comparison by Monte Carlo Analysis

Our test procedure and Spearman's rank correlation test procedure are evaluated with respect to their testing capabilities. The comparison method is in fact a Monte Carlo analysis and it is performed in two steps.

First step: we choose a random process, which we know it will generate correlated random variables. For a specific data sample size N we will resume the two tests N_1 times (in our examples $N_1 = 5000$), evaluating the proportion of accepting H_0 (independence decisions found). This proportion does evaluate (in some way) a probability error of accepting correlated data as independent.

Second step: we choose a random process, which we know it will generate independent random variables. For a specific data sample size N we will resume the two tests N_1 times, evaluating the proportion of rejecting H_0 (deciding non-independence) decisions found. This proportion does evaluate a probability error of rejecting correct data sets (deciding the data sets as correlated while in fact they were independent); it should be lower than the chosen statistical significance level α .

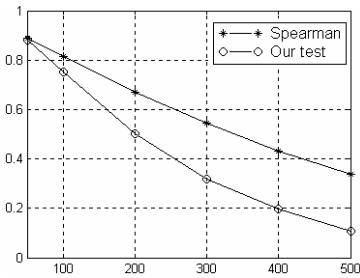


Fig. 11. Vertical axis: Estimated value for the probability of wrongly accepting H_0 ; Horizontal axis: size N . Case study: chaotic signal sampled at a distance $k_2 - k_1 = 5$.

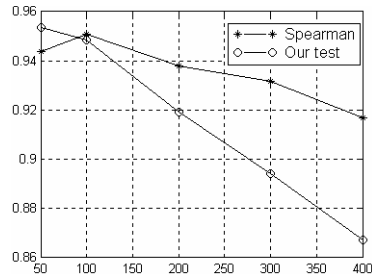


Fig. 12. Vertical axis: Estimated value for the probability of wrongly accepting H_0 ; Horizontal axis: size N . Case study: chaotic signal sampled at a distance $k_2 - k_1 = 10$.

For the **chaotic signal** case study, our method achieves correlation detection more accurately compared to Spearman’s algorithm (our method has a lower probability error of wrongly accepting correlated data). That means that our test procedure needs a less amount of data for detecting dependence. That happens without affecting the probability of rejecting good data (to decide correlation while the two data sets were non-correlated) - see Fig. 13. This probability is lower than α .

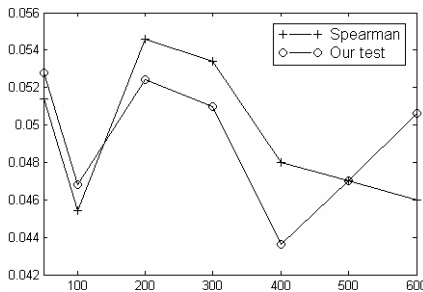


Fig. 13. Estimated probability value of rejecting good data (to decide correlation while data were non-correlated), for $\alpha = 0.05$

Fig. 13 presents the estimated probability error of rejecting H_0 hypothesis (rejecting independent data sets by deciding they were correlated); the two data sets come out from two *independent random variables*.

The probabilities shown in Fig. 13 should be lower than the chosen statistical significance level α (in fact, this is an experimental probability associated with the confidence interval of the theoretical probability, [1], [2], [8]).

5 Conclusions

First of all, this independence test method contributes to a better understanding of the concept of statistical independence, which is connected to the ranks of the sorted data. This method enables testing independence of data pairs - for continuous values of known or unknown statistical distribution. It works because we use bijective transforms applied to the two random variables X and Y .

The entire dependence analysis is shifted by the two bijective transforms from the xy coordinates to the uv coordinates. Testing independence of X and Y is done by applying Person's r correlation test on U and V ; if U and V are dependent then X and Y are dependent. If not (U and V are independent), independence analysis can continue by testing independence on the uv or $x'y'$ coordinates as well, by comparing the scatter diagram to a *reference scatter diagram*.

In the case of lack of data (an accurate estimation of the cumulative distribution function needs a very large amount of data), the only decision to take would be that data "could be independent".

To conclude with, in order to decide whether X and Y are dependent r.v., our test procedure works well. To decide upon independence, of much help is the visual inspection of the UV scatter diagram, which should be similar to the *reference* one.

References

1. Devore, J.: Probability and Statistics for Engineering and the Sciences. 2nd ed., Brooks/Cole Publishing Company, Monterey, Ca. (1987)
2. Walpole, R.E., Myers, R.H.: Probability and Statistics for Engineers and Scientists. 4th ed., MacMillan Publishing, NY (1989)
3. Mood, A., Graybill, F., Boes, D.: Introduction to the Theory on Statistics. Third edition, McGraw-Hill Book Company (1974)
4. Craiu, V.: Verificarea ipotezelor statistice, Ed. Didactică și Pedagogică, București, (1972).
5. Badea, B., Vlad, A.: Testing the Statistical Independence of Continuous Random Variables. A New Robust Algorithm. In: Proc. IEEE Intl. Symp. on Signals, Circuits and Systems-ISSCS 2005, Iași, Romania (July 2005) 171-174
6. Lévine, B.: Fondements Théoriques de la Radiotechnique Statistique. Tome II, Edition Mir, Moscou (1973)
7. Mihoc, Gh., Urseanu, V.: Matematici aplicate în statistică. Ed. Academiei, București (1962)
8. Frieden, B. R.: Probability, Statistical Optics and Data Testing. Springer-Verlag, Berlin, Heidelberg, New York (1983)
9. Iosifescu, M., Moineagu, C., Trebici, V., Ursianu, E.: Mică Enciclopedie de Statistică. Ed. Științifică și Enciclopedică, București (1985)

10. Papoulis, A.: Probability, Random Variables, and Stochastic Processes. McGraw-Hill, NY (1965)
11. Iosifescu, M., Mihoc, Gh., Theodorescu, R.: Teoria probabilităților și statistică matematică. Ed. Tehnică, București (1966)
12. Baptista, M. S.: Cryptography with chaos. Physics Letters A 240 (March 1998) 50-54

Parallelizable Computational Technique for Singularly Perturbed Boundary Value Problems Using Spline

Rajesh Kumar Bawa

Department of Computer Science, Punjabi University,
Patiala - 147 002

Abstract. In this paper, we considered singularly perturbed self-adjoint boundary-value problems and proposed a computational technique based on spline scheme, which is also suitable for parallel computing. The whole domain is divided into three non-overlapping subdomains and corresponding subproblems are obtained by using zeroth order approximations of the solution at boundaries of these subproblems. The subproblems corresponding to boundary layer regions are solved using adaptive spline scheme. Numerical example is provided to show the efficiency and accuracy.

Keywords: adaptive spline, singular perturbation problems, domain decomposition.

Subject Classification: AMS 65L10 CR G1.7.

1 Introduction

Singular perturbation problems (SPPs) arise in several branches of computational science and applications which include fluid dynamics, quantum mechanics, elasticity, chemical reactor theory, gas porous electrodes theory, etc. The presence of small parameter(s) in these problems prevents us from obtaining satisfactory numerical solutions. It is a well known fact that the solutions of SPPs have a multi-scale character. That is, there are thin layer(s) where the solution varies very rapidly, while away from the layer(s) the solution behaves regularly and varies slowly. Various finite difference schemes have been proposed in the literature to guarantee stability of the schemes for all values of the perturbation parameter. Careful examination of numerical results from such schemes on uniform grids shows that, for fixed (small) values of the perturbation parameter, the maximum point-wise error usually increases as the mesh is refined, because of the presence of the boundary or interior layer, until the mesh diameter is comparable in size to the parameter. This behavior is clearly unsatisfactory. Therefore, a separate treatment is necessary to deal with such problems. In this article, we consider the following singularly perturbed self-adjoint boundary-value problem (BVP):

$$Lu(x) \equiv -\varepsilon u''(x) + b(x)u(x) = f(x), \quad x \in D = (0, 1) \quad (1)$$

$$u(0) = A, \quad u(1) = B, \quad (2)$$

where $\varepsilon > 0$ is a small parameter, b and f are sufficiently smooth functions, such that $b(x) \geq \beta > 0$ on $\overline{D} = [0, 1]$. Under these assumptions, the BVP (1)-(2) possesses a unique solution $u(x) \in C^2(\overline{D})$. In general, the solution $u(x)$ may exhibit two boundary layers of exponential type at both end points $x = 0, 1$.

Many sequential techniques are proposed by authors for solving problems of the form (1)-(2), for details one can refer to Miller et. al.[3]. Also, many authors have proposed parallel techniques for solving these type of problems. Paprzycki and Gladwell [6] proposed a mesh chopping algorithm for solving SSP's., Bogloaev [7] proposed an iterative algorithm for domain decomposition applied to singularly perturbed elliptic and parabolic SSP's. Gracia et. al. [2] have devised a HODIE scheme for singularly perturbed reaction-diffusion problems. Very recently, Bawa and Natesan [8] have proposed a quintic spline based computational method for such problems on sequential computer, which is suitable for parallelization. Using similar idea of domain decomposition and exploiting the multiscale nature of solution, we propose a simple and efficient computational domain decomposition based spline technique in such a way that maximum absolute error is reduced to much extent in comparison to applying it on whole domain as proposed in [5]. Further, the present scheme is also well suited for parallel computing.

In [8] we divided the whole domain into three subdomains: two boundary layer subdomains, and one regular subdomain, and converted the boundary layer problems to a regular one by proper transformations using stretching variables, and then applied a quintic spline scheme in all three subdomains. The main advantage of present investigation over this quintic spline based scheme is that no transformation of boundary layer problems and stretching of variables is required. Instead, the original boundary value problem (1)-(2) can be solved directly on subdomains using an adaptive spline scheme to get satisfactory results for small values of the parameter ε . In addition to this, since we are forming three independent boundary value problems after decomposing the domain into three non-overlapping subdomains, the problem can be solved on parallel computer with at least three processors independently to reduce time complexity. This aspect is under investigation of the author.

2 Spline Based Computational Technique

In this section, we describe the proposed technique.

Consider the whole domain $[0, 1]$ with equally spaced knots $x_i = i/N$, $j = 0, \dots, N$,

Using the notation u_i for approximation at mesh point x_i and $S(x_{i-1}, q_{i-1}) = u_{i-1}$, $S(x_i, q_i) = u_i$ as interpolatory constraints and following [5], the adaptive spline function $S(x, q)$ can be defined as solution of the differential equation:

$$\begin{aligned}
 -\varepsilon S''(x, q_i) + p_i S(x, q_i) &= (x - x_{i-1})h^{-1}(-\varepsilon M_i + p_i u_i) + \\
 & (x_i - x)h^{-1}(-\varepsilon M_{i-1} + p_{i-1} u_{i-1})
 \end{aligned}
 \tag{3}$$

where $x_{i-1} \leq x \leq x_i$, $S''(x_i, q_i) = M_i$ and $q_i = \sqrt{p_i/\varepsilon}h$.

Solving this for $S(x, q)$ and using the continuity of its first derivative at mesh point x_i , we get the following equation:

$$u_{i-1} - 2u_i + u_{i+1} = h^2 [q_{i-1}^{-2} M_{i-1} (1 - \frac{q_{i-1}}{shq_{i-1}}) + \tag{4}$$

$$2q_i^{-2} M_i (-1 + q_i chq_i) + q_{i+1}^{-2} M_{i+1} (1 - \frac{q_{i+1}}{shq_{i+1}})] \tag{5}$$

Substituting $M_i = (b_i u_i - f_i) / \varepsilon$ we get the following tridiagonal finite difference scheme:

$$\begin{aligned}
 & [1 - \frac{h^2 b_{i-1}}{q_{i-1}^2 \varepsilon} (1 - \frac{q_{i-1}}{shq_{i-1}})] u_{i-1} + [-2 - 2 \frac{h^2 b_i}{q_i^2 \varepsilon} (-1 + q_i chq_i)] u_i + \\
 & \qquad \qquad \qquad + [1 - \frac{h^2 b_{i+1}}{q_{i+1}^2 \varepsilon} (1 - \frac{q_{i+1}}{shq_{i+1}})] u_{i+1} \\
 = & [-\frac{h^2 f_{i-1}}{q_{i-1}^2 \varepsilon} (1 - \frac{q_{i-1}}{shq_{i-1}}) - 2 \frac{h^2 f_i}{q_i^2 \varepsilon} (-1 + q_i chq_i) - \frac{h^2 f_{i+1}}{q_{i+1}^2 \varepsilon} (1 - \frac{q_{i+1}}{shq_{i+1}})] \\
 & \qquad \qquad \qquad i = 1, \dots, N - 1.
 \end{aligned}$$

We decompose the computational domain $\bar{D} = [0, 1]$ into three subdomains, and then solve the differential equation (1), subject to different boundary conditions in each subdomain. Let $k = 2 * \ln(N) > 0$, and $k\sqrt{\varepsilon}$ be the width of the boundary layer(s) which is near at $x = 0$, and $x = 1$. More precisely, we divide the domain \bar{D} into three non-overlapping subdomains, as $D_1 = [0, k\sqrt{\varepsilon}]$, $D_2 = [k\sqrt{\varepsilon}, 1 - k\sqrt{\varepsilon}]$, and $D_3 = [1 - k\sqrt{\varepsilon}, 1]$, such that $\bar{D} = D_1 \cup D_2 \cup D_3$. The subdomains D_1 and D_3 are called the boundary layer regions, whereas D_2 is known as the regular region.

The BVPs corresponding to the three subdomains are:

$$-\varepsilon u''(x) + b(x)u(x) = f(x), \quad x \in D_1 = (0, k\sqrt{\varepsilon}) \tag{6}$$

$$u(0) = A, \quad u(k\sqrt{\varepsilon}) = \bar{A}, \tag{7}$$

$$-\varepsilon u''(x) + b(x)u(x) = f(x), \quad x \in D_2 = (k\sqrt{\varepsilon}, 1 - k\sqrt{\varepsilon}) \tag{8}$$

$$u(k\sqrt{\varepsilon}) = \bar{A}, \quad u(1 - k\sqrt{\varepsilon}) = \bar{B}, \tag{9}$$

and

$$-\varepsilon u''(x) + b(x)u(x) = f(x), \quad x \in D_3 = (1 - k\sqrt{\varepsilon}, 1) \tag{10}$$

$$u(1 - k\sqrt{\varepsilon}) = \bar{B}, \quad u(1) = B. \tag{11}$$

To determine the boundary conditions at the transition points, we take the zeroth-order asymptotic approximation of the BVP (1-2) given by

$$\tilde{u}(x) = u_0(x) + v_0(\tau) + w_0(\eta),$$

where $u_0(x) = f(x)/b(x)$ is the reduced problem solution, and v_0 , and w_0 are respectively the left, and right boundary layer correction terms

$$v_0(\tau) = [A - u_0(0)] \exp[-\sqrt{b(0)/\varepsilon}x],$$

$$w_0(\tau) = [B - u_0(1)] \exp[-\sqrt{b(1)/\varepsilon}(1 - x)].$$

The values of \bar{A} , \bar{B} are given by

$$\bar{A} = \tilde{u}(k\sqrt{\varepsilon}), \quad \text{and} \quad \bar{B} = \tilde{u}(1 - k\sqrt{\varepsilon}).$$

3 Numerical Illustration

In this section, we provide an example, which is generally taken as test example for these type of problems and implemented the proposed technique. From the numerical tables, one can easily see the accuracy, and performance of the method over other methods.

Example 1. Consider the non-homogeneous self-adjoint SPP

$$-\varepsilon u''(x) + u(x) = -\cos^2(\pi x) - 2\varepsilon\pi^2 \cos(2\pi x), \quad x \in (0, 1)$$

$$u(0) = 0, \quad u(1) = 0.$$

The exact solution is given by

$$u(x) = \frac{[\exp(-x/\sqrt{\varepsilon}) + \exp(-(1-x)/\sqrt{\varepsilon})]}{1 - \exp(-1/\sqrt{\varepsilon})} - \cos^2(\pi x).$$

The transition boundary condition is given by

$$\tilde{u}(x) = -\cos^2(\pi x) + \exp(-x/\sqrt{\varepsilon}) + \exp(-(1-x)/\sqrt{\varepsilon}).$$

The numerical results are given in terms of errors in the tables for various values of ε , and N . Table 1 shows the point-wise error for three values of ε .

For comparison we took the numerical results by applying the spline scheme in whole domain and results are tabulated in Table 2. It is clear that the proposed scheme improves the results significantly.

Table 1. Maximum error by applying spline scheme in whole domain example 1

	Domain	N=32	N=64	N=128	N=256
$\varepsilon = 10^{-06}$	[0, 1]	2.8793e-04	1.3446e-04	5.7463e-05	2.0412e-05
$\varepsilon = 10^{-08}$	[0, 1]	3.0570e-05	1.5223e-05	7.5177e-06	3.6606e-06
$\varepsilon = 10^{-10}$	[0, 1]	3.0748e-06	1.5401e-06	7.6955e-07	3.8384e-07

Table 2. Maximum error of proposed technique for example 1

	Domain	N=32	N=64	N=128	N=256
$\varepsilon = 10^{-06}$	D_1	9.5512e-07	9.8008e-07	9.9223e-07	9.9273e-07
	D_2	0.0	0.0	0.0	0.0
	D_3	9.5512e-07	9.8008e-07	9.9223e-07	9.9273e-07
$\varepsilon = 10^{-08}$	D_1	9.5497e-09	9.7999e-09	9.928e-09	9.9718e-09
	D_2	0.0	0.0	0.0	0.0
	D_3	9.5497e-09	9.7999e-09	9.928e-09	9.9718e-09
$\varepsilon = 10^{-10}$	D_1	9.5498e-11	9.8003e-11	9.9230e-11	9.9711e-11
	D_2	0.0	0.0	0.0	0.0
	D_3	9.5498e-11	9.8003e-11	9.9230e-11	9.9711e-11

4 Conclusions

In this article, we have proposed a spline based computational technique suitable for parallel computing for singularly perturbed reaction–diffusion problems. First, we decompose the domain into three non–overlapping subdomains (two boundary layer regions and one outer region). To determine the boundary conditions, we require the zeroth-order asymptotic approximate solution. We are taking the transition parameter as $k\sqrt{\varepsilon}$, where $k = 2 * \ln(N)$, which is the transition parameter used in the Shishkin–type meshes. It is observed that the maximum error is reduced significantly by the proposed scheme. The implementation of the scheme is simple and it has inherent parallelism as, each subproblem can be solved on three different processors and depending upon availability of no. of processors, the domain D_2 , which is quite large as compared to others, can be further subdivided into appropriate no. subdomains and approach similar to [9], can be applied for parallel computing.

References

1. P.A. Farrell, A.F. Hegarty, J.J.H. Miller, E. O’Riordan, and G.I. Shishkin. *Robust Computational Techniques for Boundary Layers*. Chapman & Hall/CRC Press, 2000.
2. J.L. Gracia, F. Lisbona, and C. Clavero. High order ε -uniform methods for singularly perturbed reaction-diffusion problems. *Lecture Notes in Computer Science*, **1998**:350–358, 2001.
3. J.J.H. Miller, E. O’Riordan, and G.I. Shishkin. *Fitted Numerical Methods for Singular Perturbation Problems*. World Scientific, Singapore, 1996.
4. H.-G. Roos, M. Stynes, and L. Tobiska. *Numerical Methods for Singularly Perturbed Differential Equations*. Springer, Berlin, 1996.
5. M.Stojanovic. Numerical solution of initial and singularly perturbed two-point boundary value problems using adaptive spline function approximation. *Publications de L’institut Mathematique.*, **43**:155-163,1988.
6. M.Paprzycki and I.Gladwell. A parallel chopping method for ODE boundary value problems. *Parallel Computing*, **19**: 651-666,(1993) Elsevier Science Publishers.

7. I. Bogloev, Domain decomposition in Boundary layer for Singular Perturbation problems. *Applied Numerical Mathematics*, **35**: 145-156, (2000). Elsevier Science Publishers.
8. R.K. Bawa and S. Natesan. A computational method for self-adjoint singular perturbation problems using quintic splines, *Computers and Mathematics with Applications*, **50**: 1371-1382 (2005). Elsevier Science Publishers.
9. J. Vigo-Aguiar and S. Natesan, A parallel boundary value technique for singularly perturbed two-point boundary value problems, *The Journal of Supercomputing*, **27**: 195-206 (2004).

Author Index

- Abbas, Cláudia Jacy Barenco V-819
Abraham, Ajith IV-40
Adamidis, Panagiotis V-108
Adolf, David I-711
Ahn, Byung Jun II-77
Ahn, Dong-In III-251
Ahn, Heejune IV-603
Ahn, Jaehoon V-522
Ahn, Jung-Chul IV-370
Ahn, ManKi III-48
Ahn, Sang-Ho III-279
Ahn, Seongjin II-400, II-410, II-487,
V-829, II-1169
Ahn, Sung-Jin II-982
Ahn, Sungsoo V-269
Ahn, Sungwoo II-175
Ahn, Taewook IV-388
Ahn, Yonghak V-1001
Ahn, Youngjin II-661
Akbar, Ali Hammad II-186, II-847
Alam, Muhammad Mahbub II-651
Albertí, Margarita I-721
Alfredo-Badillo, Ignacio III-456
Ali, Hassan IV-217
Ali, Saqib IV-217
Allayear, Shaikh Muhammad II-641
Almendra, Daniel V-819
Al-Mutawah, Khalid I-586
Alvarez, Susana III-1073
Amarnadh, Narayanasetty I-1
Ambler, Anthony P. V-531
An, Kyoungwan II-155
An, Sunshin II-730
Anagun, A. Sermet III-11, III-678
Anan, Yoshiyuki II-40
Andersen, Anders Magnus IV-98
Angelides, Marios C. IV-118
Arce-Santana, Edgar R. V-412
Armer, Andrey I-974
Arteconi, Leonardo I-694

Badea, Bogdan I-1166
Bae, Hae-Young I-914, IV-1126
Bae, Hyo-Jung I-151
Bae, Joonsoo II-379
Bae, Suk-Tae II-309
Bae, Yong-Geun IV-828
Bae, Youngchul III-244
Baek, Jun-Geol V-839
Baek, Myung-Sun V-752
Bagherpour, Morteza III-546
Bahn, Hyokyung I-1072
Bai, Zhang I-885
Baik, Heung Ki V-236
Baixauli, J. Samuel III-1073
Bala, Piotr V-394
Balas, Lale I-547
Balci, Birim I-373
Ban, Chaehoon II-175
Bang, Hyungbin II-319
Bang, Young-Cheol III-1090, III-1129
Bardhan, Debabrata I-10
Bartolotta, Antonino I-821
Bashir, Ali Kashif II-186
Basu, Kalyan I-566
Bawa, Rajesh Kumar I-1177
Bellaachia, Abdelghani V-346
Bentz, Cédric III-738
Berbegall, Vicente V-192
Berkov, Dmitri V-129
Bertoni, Guido III-1004
Biscarri, Félix V-725
Biscarri, Jesús V-725
Blibech, Kaouthar III-395
Boada, Imma I-364
Bohli, Jens-Matthias III-355
Bolze, Raphael V-202
Bories, Benoît I-744
Bravo, Maricela IV-169
Brennan, John K. V-743
Breviglieri, Luca III-1004
Brzeziński, Jerzy IV-1166, V-98
Buiati, Fabio V-819
Burns, John I-612
Byun, Doyoung V-537
Byun, Sang-Seon II-1189
Byun, Sang-Yong III-84
Byun, Sung-Wook I-232

- Byun, Tae-Young III-134
 Byun, Young Hwan V-457
 Byun, Yung-Cheol V-185
 Byun, Yung-Hwan V-512, V-932

 Caballero-Gil, Pino I-577, III-1035
 Caballero, Ismael III-984
 Cáceres, Santos II-18
 Cai, Guoyin IV-1090
 Calderon, Alejandro IV-1136
 Calero, Coral III-984
 Camahort, Emilio I-510
 Camara, José Sierra V-798
 Campos-Delgado, Daniel U. V-412
 Cao, Wenming V-375
 Capacho, Liliana III-554
 Cappelletti, David I-721
 Carballeira, Félix García V-108
 Carlone, Pierpaolo I-794
 Caro, Angelica III-984
 Caron, Eddy V-202
 Carretero, Jesus IV-1136
 Castro, Mildrey Carbonell V-798
 Cattani, Carlo I-785, I-828, I-857
 Cha, Byung-Rae II-1090
 Cha, Eui-Young I-1110
 Cha, Guang-Ho I-344
 Cha, Jae-Sang V-312
 Cha, JeongHee V-432
 Chae, Kijoon I-1072, IV-440
 Chae, Oksam V-1001
 Chae, Young Seok II-760
 Challiol, Cecilia IV-148
 Chan, Yung-Kuan V-384
 Chan, Yuen-Yan I-383, III-309, III-365,
 III-507, IV-406
 Chang, Chung-Hsien I-171
 Chang, Hangbae IV-255, IV-707
 Chang, Hoon IV-577
 Chang, Hoon V-1010
 Chang, Hsi-Cheng V-158
 Chang, Kuo-Hwa III-944
 Chang, Ok-Bae III-188, III-222, IV-893,
 IV-955, V-644
 Chang, Soo Ho II-451
 Chang, Sujeong II-77
 Chang, Yu-Hern III-649
 Chaudhry, Shafique Ahmad II-847
 Chaudhuri, Chitrita II-1
 Chen, Chiou-Nan IV-1107
 Chen, Chun V-39
 Chen, Gencai V-39
 Chen, Huifen III-944
 Chen, Kai-Hung V-384
 Chen, Kaiyun IV-756
 Chen, Ken I-307
 Chen, Lei II-1149
 Chen, Ling V-39
 Chen, Tzu-Yi III-1081
 Chen, Yen Hung III-631
 Cheng, Jingde III-1
 Cheng, Yu-Ming I-171, I-181
 Cheon, Saeng Hoon III-718
 Cheon, SeongKwon III-73
 Cheun, Du Wan II-451
 Cheung, Yen I-586
 Chi, Sang Hoon IV-58
 Chih, Wen-Hai III-668
 Chlebiej, Michał V-394
 Cho, Cheol-Hyung I-101
 Cho, Daerae IV-787
 Cho, Dongyoung IV-491
 Cho, Eun Sook II-1003, IV-985
 Cho, Haengrae V-214
 Cho, Ik-hwan I-326
 Cho, Jae-Hyun I-1110
 Cho, Jong-Rae III-832, III-994
 Cho, Juphil V-236
 Cho, KumWon V-522
 Cho, Kwang Moon IV-1003
 Cho, Mi-Gyung I-904
 Cho, Minju II-760
 Cho, Nam-deok V-546
 Cho, Sang-Hun II-288
 Cho, Sok-Pal II-1082
 Cho, Sung-eon V-600
 Cho, Tae Ho IV-58
 Cho, Yongyun IV-30
 Cho, Yookun II-701, IV-499, IV-549
 Cho, Youngsong I-111
 Cho, You-Ze II-631
 Choi, Bong-Joon V-912
 Choi, Byung-Cheon III-785
 Choi, Byungdo IV-808
 Choi, Byung-Sun II-945
 Choi, Chang IV-567
 Choi, Changyeol II-562, IV-1156
 Choi, Deokjai IV-128
 Choi, Eun Young IV-316
 Choi, Ho-Jin II-796

- Choi, Hwangkyu II-562, IV-1156
 Choi, Hyung-Il V-441
 Choi, Hyun-Seon III-728
 Choi, Jaeyoung IV-11, IV-30
 Choi, Jonghyoun II-525, II-895
 Choi, Jongmyung II-1033
 Choi, Jong-Ryeol IV-893
 Choi, Junho IV-567
 Choi, Junkyun V-829
 Choi, Kuiwon I-335
 Choi, Kyung Cheol IV-659
 Choi, Misook II-49, IV-966
 Choi, Sang-soo V-618
 Choi, Sang-Yule V-312, V-322, V-355
 Choi, Seongman III-222, IV-955, V-644,
 V-675
 Choi, Su-il II-77
 Choi, Sung-Hee IV-937
 Choi, Tae-Young I-307, I-317
 Choi, Wan-Kyoo IV-828
 Choi, Wonjoon IV-279
 Choi, Yeon Sung I-993
 Choi, Yong-Rak IV-432
 Choi, Yun Jeong II-298
 Chon, Jaechoon I-261, III-1172
 Chon, Sungmi II-28
 Choo, Hyunseung II-165, II-288, II-534,
 II-661, II-710, II-856, II-923, II-934,
 II-1121, III-1090, III-1129
 Choo, MoonWon IV-787
 Chun, Junchul I-410
 Chung, Chin Hyun I-929, I-964
 Chung, Chun-Jen III-862
 Chung, Ha Joong IV-549
 Chung, Hyoung-Seog V-491
 Chung, Il-Yong IV-828
 Chung, Jinwook II-487, II-982
 Chung, Kyoil III-375, IV-584, V-251
 Chung, Min Young II-77, II-288, II-534,
 II-856, II-934, II-1121
 Chung, Mokdong IV-1042
 Chung, Shu-Hsing III-610
 Chung, TaeChoong II-390
 Chung, Tae-sun I-1019
 Chung, Tai-Myoung II-135, II-239,
 III-486, V-626, V-655
 Chung, YoonJung III-54, IV-777
 Chung, Younky III-198, III-234
 Ciancio, Armando I-828
 Ciancio, Vincenzo I-821
 Clifford, Raphaël III-1137
 Cocho, Pedro III-964
 Cokuslu, Deniz II-681
 Coll, Narcis I-81
 Cong, Jin I-921
 Cools, Ronald V-780
 Cordero, Rogelio Limón IV-726
 Costantini, Alessandro I-738
 Crane, Martin I-612
 Cruz, Laura II-18
 Culley, Steve J. II-279
 Cumplido, René III-456
 Czekster, Ricardo M. I-202
 Daefler, Simon I-566
 Dagdeviren, Orhan II-681
 D'Anjou, Alicia III-1143
 Darlington, Mansur J. II-279
 Das, Gautam K. II-750
 Das, Sajal I-566
 Das, Sandip I-10, II-750
 David, Gabriel IV-78
 De Cristófolo, Valeria IV-148
 de Deus, Flavio E. V-808
 de Doncker, Elise V-789
 de Oliveira, Robson V-819
 de Frutos-Escrig, David IV-158
 de Ipiña, Diego López IV-108
 de Sousa, Rafael V-819
 Deineko, Vladimir III-793
 Demirkol, Askin V-365
 den Hertog, Dick III-812
 Deo, Puspita I-622
 Derevyankin, Valery I-974
 Desprez, Frederic V-202
 Dévai, Frank I-131
 Diaz, Olivia Graciela Fragoso IV-50
 Doallo, Ramón I-701
 Dogdu, Erdogan IV-88
 Drummond, L.A. V-192
 Duan, Guolin V-450
 Duan, Yucong IV-746
 Durán, Alfonso III-964
 Ekinci, Murat III-1216
 Eksioğlu, Burak III-748
 Eksioğlu, Sandra Duni III-708
 Eom, Jung-Ho II-239
 Eom, Young Ik I-1028
 Erciyas, Kayhan II-681

- Esquivel, Manuel L. III-841
 Eun, He-Jue V-990
 Evangelisti, Stefano I-744

 Fang, Zhijun II-964
 Färber, Gerrit III-638
 Farsaci, Francesco I-821
 Farzanyar, Zahra I-1100
 Fathy, Mahmood V-118
 Fei, Chai IV-179
 Feixas, Miquel I-449
 Feng, Dan I-1045
 Feregrino-Uribe, Claudia III-456
 Ferey, Nicolas I-222
 Fernandez, Javier IV-1136
 Fernández, Marcel III-527
 Fernández, Marcos I-490
 Fernandez, Reinaldo Togores I-30
 Fernández-Medina, Eduardo III-1013,
 III-1024, III-1044
 Fey, Dietmar V-129
 Filomia, Federico I-731
 Fiore, Ugo III-537
 Fleissner, Sebastian I-383, IV-406
 Forné, Jordi IV-1098
 Fort, Marta I-81
 Frausto, Juan IV-169
 Frick, Alexander I-847
 Fu, Xiaolan IV-746
 Fúster-Sabater, Amparo I-577, III-1035

 Gabillon, Alban III-395
 Galindo, David III-318
 Gallego, Guillermo III-822
 Gao, Yunjun V-39
 Garcia, Felix IV-1136
 Garcia, Jose Daniel IV-1136
 García, L.M. Sánchez V-108
 García-Sebastian, M. Teresa III-1143
 Gattiker, James R. III-1153
 Gattton, Thomas M. III-244, IV-947,
 V-665, V-675
 Gaudiot, Jean-Luc IV-622
 Gavrilova, Marina L. I-61, I-431
 Ge, He III-327
 Gerardo, Bobby D. III-144, IV-899,
 V-867
 Gervasi, Osvaldo I-212, I-665
 Gherbi, Rachid I-222
 Ghosh, Preetam I-566
 Ghosh, Samik I-566
 Gil, Joon-Min II-1169
 Go, Sung-Hyun V-867
 Goh, John I-1090
 Goh, Sunbok II-204
 Goi, Bok-Min IV-424
 González, Ana I. III-1143
 Gonzalez, César Otero I-30
 González, J.J. V-772
 González, Juan G. II-18
 González, Luis I-633
 González, Patricia I-701
 Gordillo, Silvia IV-148
 Górriz, J.M. V-772
 Graña, Manuel III-1143
 Gros, Pierre Emmanuel I-222
 Gu, Boncheol IV-499, IV-549
 Gu, Huaxi V-149
 Gu, Yuqing IV-746
 Guillen, Mario II-18
 Guo, Jiang III-974
 Guo, Jianping IV-1090
 Guo, Weiliang I-938
 Gutiérrez, Miguel III-964

 Ha, Jong-Eun III-1163
 Ha, Jongsung II-49
 Ha, Sung Ho III-1110
 Hahn, GeneBeck II-769
 Hamid, Md.Abdul II-866
 Han, Chang-Hyo III-832
 Han, DoHyung IV-594
 Han, Dong-Guk III-375
 Han, Gun Heui V-331
 Han, Hyuksoo IV-1081
 Han, Jizhong I-1010
 Han, Jong-Wook IV-360
 Han, Joohyun IV-30
 Han, JungHyun I-1028
 Han, Jungkyu IV-549
 Han, Ki-Joon II-259
 Han, Kijun II-1159
 Han, Kunhee V-584
 Han, Long-zhe I-1019
 Han, Sang Yong IV-40
 Han, Seakjae V-682
 Han, SeungJae II-359
 Han, Sunyoung II-601
 Han, Youngshin V-260
 Harbusch, Klaus I-857

- Hashemi, Sattar I-1100
 Hawes, Cathy I-644
 He, S. III-934
 Helal, Wissam I-744
 Heng, Swee-Huay III-416
 Heo, Joon II-989, II-1066
 Heo, Junyoung II-701, IV-499, IV-549
 Hérisson, Joan I-222
 Herrero, José R. V-762
 Higdon, David III-1153
 Hinarejos, M. Francisca IV-1098
 Hoesch, Georg V-202
 Hoffmann, Aswin L. III-812
 Hong, Bonghee II-155, II-175
 Hong, Choong Seon II-651, II-866
 Hong, Dong-Suk II-259
 Hong, Dowon IV-584
 Hong, Gye Hang III-1110
 Hong, Jiman II-701, IV-499, IV-558,
 IV-603
 Hong, John-Hee III-832
 Hong, Kwang-Seok I-354
 Hong, Maria II-400
 Hong, In-Hwa IV-245
 Hong, Seokhie III-446
 Hong, Soonjwa III-385
 Hong, Suk-Kyo II-847
 Hong, Sukwon I-1019
 Hong, Sung-Je I-151
 Hong, Sung-Pil III-785
 Hong, WonGi IV-577
 Hong, Youn-Sik II-249
 Horie, Daisuke III-1
 Hosaka, Ryosuke I-596
 Hsieh, Shu-Ming V-422
 Hsu, Chiun-Chieh V-158, V-422
 Hsu, Li-Fu V-422
 Hu, Qingwu IV-746
 Hu, Yincui IV-1090
 Huang, Changqin V-243
 Huang, Chun-Ying III-610
 Huang, Wei I-518
 Huh, Euinam II 390, II-515, II-827,
 II-905, V-717
 Huh, Woong II-224
 Huh, Woonghee Tim III-822
 Hur, Tai-Sung II-224
 Hwang, An Kyu II-788
 Hwang, Chong-Sun II-369, II-816
 Hwang, Ha-Jin V-1018
 Hwang, Hyun-Suk III-115, III-125,
 V-895
 Hwang, InYong II-1140
 Hwang, Jin-Bum IV-360
 Hwang, Jun II-760
 Hwang, Ken III-668
 Hwang, Soyeon IV-344
 Hwang, Suk-Hyung IV-767, IV-937
 Hwang, Sungho III-134
 Hwang, Sun-Myung IV-909
 Hwang, Tae Jin V-236
 Ikeguchi, Tohru I-596
 Im, Chaeseok I-1000
 Im, Eul Gyu III-54, IV-777
 Im, SeokJin II-369
 Im, Sungbin II-806
 Inan, Asu I-547
 Inceoglu, Mustafa Murat I-373
 Iordache, Dan I-804
 Isaac, Jesús Téllez V-798
 Isaila, Florin D. V-108
 Ishii, Naohiro II-40
 Iwata, Kazunori II-40
 Jang, Byung-Jun V-752
 Jang, Hyo-Jong II-106
 Jang, Injoo III-206
 Jang, Jun Yeong I-964
 Jang, Kil-Woong II-671
 Jang, Moonsuk II-204
 Jang, Sangdong IV-1116
 Jang, Taeuk II-760
 Jang, Yong-Il IV-1126
 Je, Sung-Kwan I-1110
 Jeon, Hoseong II-934
 Jeon, Hyung Joon II-974, II-1009
 Jeon, Hyung-Su III-188
 Jeon, Jongwoo III-718
 Jeon, Kwon-Su V-932
 Jeon, Segil V-522
 Jeon, Sung-Eok III-134
 Jeong, Byeong-Soo II-505, II-796
 Jeong, Chang-Sung I-232, II-462
 Jeong, Chang-Won IV-853
 Jeong, Chulho II-430
 Jeong, Dong-Hoon II-996
 Jeong, Dongseok I-326
 Jeong, Gu-Beom IV-1032
 Jeong, Hye-Jin V-675

- Jeong, Hyo Sook V-609
 Jeong, In-Jae III-698
 Jeong, Jong-Geun II-1090
 Jeong, Karpjoo V-522
 Jeong, Kugsang IV-128
 Jeong, KwangChul II-923
 Jeong, Sa-Kyun IV-893
 Jeong, Su-Hwan V-895
 Jeong, Taikyeong T. I-993, V-531
 Jhang, Seong Tae IV-631
 Jhon, Chu Shik IV-631
 Ji, JunFeng I-420
 Ji, Yong Gu IV-697
 Ji, Young Mu V-457
 Jiang, Chaojun I-938
 Jiang, Di I-50
 Jiang, Gangyi I-307, I-317
 Jiang, Yan I-921
 Jianping, Li I-885
 Jin, DongXue III-73
 Jin, Hai IV-529
 Jin, Honggee IV-687
 Jin, Mingzhou III-708, III-748
 Jo, Geun-Sik II-779
 Jo, Jeong Woo II-480
 Jodlbauer, Herbert V-88
 Johnstone, John K. I-500
 Joo, Su-Chong III-251, IV-798, IV-853,
 IV-899
 Joye, Marc III-338
 Juang, Wen-Shenq IV-396
 Ju, Hyunho V-522
 Ju, Minseong IV-271
 Jun, Jin V-839
 Jung, Cheol IV-687
 Jung, Eun-Sun IV-416
 Jung, Hyedong II-691
 Jung, Hye-Jung IV-1052
 Jung, Inbum II-562, IV-1156
 Jung, Jae-Yoon II-379, V-942
 Jung, JaeYoun III-64
 Jung, Jiwon II-155
 Jung, Won-Do II-186
 Jung, Kwang Hoon I-929
 Jung, Kyeong-Hoon IV-448
 Jung, Kyung-Hoon III-115
 Jung, Myoung Hee II-77
 Jung, SangJoon III-93, III-234, IV-1022
 Jung, Seung-Hwan II-462
 Jung, Se-Won II-837
 Jung, Won-Do II-186
 Jung, Won-Tae IV-1052
 Jung, Youngsuk IV-1022
 Jwa, JeongWoo IV-594
 Kabara, Joseph V-808
 Kangavari, Mohammadreza I-1100
 Kang, Dazhou II-1179
 Kang, Dong-Joong II-309, III-1163
 Kang, Dong-Wook IV-448
 Kang, Euisun II-400
 Kang, Euiyoung IV-558
 Kang, Eun-Kwan IV-947
 Kang, Heau-jo V-690
 Kang, Hong-Koo II-259
 Kang, Hyungwoo III-385
 Kang, Jeonil IV-380
 Kang, Jinsuk I-993
 Kang, Maing-Kyu III-898
 Kang, Mikyung IV-558
 Kang, Mingyun V-575
 Kang, Namhi III-497
 Kang, Oh-Hyung III-287, IV-1060
 Kang, Sanggil I-1127
 Kang, Sang-Won II-369
 Kang, Sangwook II-730
 Kang, Seo-Il IV-326
 Kang, Seoungpil II-1066
 Kang, Sin Kuk III-1200
 Kang, Suk-Ho IV-787, V-942
 Kang, Sukhoon II-1060, IV-271, IV-432
 Kang, Wanmo III-777, III-822
 Kang, Yunjeong V-665
 Karsak, E. Ertugrul III-918
 Kasprzak, Andrzej III-1100, III-1119
 Katsionis, George I-251
 Kaugars, Karlis V-789
 Keil, J. Mark I-121
 Képès, François I-222
 Kettner, Lutz I-60
 Key, Jaehong I-335
 Khader, Dalia III-298
 Khonsari, Ahmad V-118
 Khoo, Khoongming III-416
 Kim, Backhyun IV-68, IV-1146
 Kim, Bonghan V-851
 Kim, Bong-Je V-895
 Kim, Byeongchang III-21
 Kim, Byung Chul II-788

- Kim, Byunggi II-319, II-330, II-740,
 II-1033
 Kim, Byung-Guk II-996
 Kim, Byung-Ryong III-476
 Kim, Byung-Soon II-671
 Kim, Chang J. V-932
 Kim, Changmin III-261, IV-787
 Kim, Chang Ouk V-839
 Kim, Chang-Soo III-115, III-125, V-895
 Kim, Cheol Min I-278, I-288, IV-558
 Kim, Chonggun III-64, III-73, III-93,
 III-234, IV-808, IV-818, IV-1022
 Kim, Chulgoon V-522
 Kim, Chul Jin II-1003, IV-985
 Kim, Chul Soo V-185
 Kim, Dai-Youn III-38
 Kim, Deok-Soo I-101, I-111, I-440
 Kim, DongKook II-340, II-349
 Kim, Dong-Oh II-259
 Kim, Dong-Seok IV-853
 Kim, Dongsoo IV-687
 Kim, Donguk I-101, I-111, I-440
 Kim, Duckki II-195
 Kim, Duk Hun II-856
 Kim, Eung Soo III-31
 Kim, Eunhoe IV-11, IV-30
 Kim, Eun Mi III-1190, IV-893
 Kim, Eun Yi III-1200
 Kim, Gil-Han V-284
 Kim, Gui-Jung IV-835
 Kim, Guk-Boh IV-1032
 Kim, Gukboh II-214
 Kim, Gu Su I-1028
 Kim, Gwanghoon IV-344
 Kim, GyeYoung II-106, V-432, V-441
 Kim, Gyoung Bae I-914
 Kim, Hae Geun III-104
 Kim, Haeng-Kon III-84, III-163,
 III-198, IV-844, IV-927, IV-976
 Kim, Haeng Kon IV-873
 Kim, Hak-Jin III-928
 Kim, HanIl IV-558, IV-567, IV-594
 Kim, Hee Taek I-914
 Kim, Hong-Gee IV-937
 Kim, Hong-Jin II-1082
 Kim, Hong Sok V-1010
 Kim, Hong-Yeon I-1053
 Kim, Ho-Seok I-914, IV-1126
 Kim, Ho Won III-375
 Kim, Howon IV-584, V-251
 Kim, Hye-Jin I-955
 Kim, Hye Sun I-288
 Kim, HyoJin II-359
 Kim, Hyongsuk III-1172
 Kim, Hyun IV-466
 Kim, Hyuncheol V-829
 Kim, Hyung-Jun IV-483
 Kim, Hyunsoo III-852
 Kim, Iksoo IV-68, IV-1146
 Kim, IL V-912
 Kim, Ildo II-87
 Kim, InJung III-54, IV-777
 Kim, In Kee V-1
 Kim, Intae IV-21
 Kim, Jaehyoun II-934
 Kim, Jae-Soo II-572
 Kim, Jae-Yearn III-590
 Kim, Jaihie II-96
 Kim, Jee-In I-983
 Kim, Je-Min II-1219
 Kim, Jeong Hyun II-996, II-1066
 Kim, Jin-Geol IV-288
 Kim, Jin Ok I-929, I-964
 Kim, Jin Suk II-480
 Kim, Jin-Sung V-968, V-979
 Kim, Jin Won IV-499, IV-509
 Kim, John II-114
 Kim, Jong-Hwa V-503
 Kim, Jongik II-552
 Kim, Jongsung III-446
 Kim, Jongwan II-369
 Kim, June I-1028, I-1053
 Kim, Jungduk IV-255, IV-707
 Kim, Jung-Sun V-922
 Kim, Junguk II-760
 Kim, Kap Hwan III-564
 Kim, Kibom III-385
 Kim, Ki-Chang III-476
 Kim, Ki-Doo IV-448
 Kim, Ki-Hyung II-186, II-847
 Kim, Ki-Uk V-895
 Kim, Ki-Young IV-612
 Kim, Kuinam J. II-1025
 Kim, Kwang-Baek I-1110, III-172,
 III-279, V-887
 Kim, Kwangsoo IV-466
 Kim, Kwanjoong II-319, II-1033
 Kim, Kyujung II-28
 Kim, Kyung-Kyu IV-255
 Kim, Kyung Tae IV-519

- Kim, LaeYoung II-1131
 Kim, Min Chan IV-669
 Kim, Min-Ji V-932
 Kim, Minsoo III-154, IV-697, V-269,
 V-922
 Kim, Minsu III-134
 Kim, Min Sung III-31
 Kim, Misun II-420, III-154
 Kim, Miyoung II-885
 Kim, MoonHae V-522
 Kim, MoonJoon IV-577
 Kim, Moonseong II-710, III-1054,
 III-1090, III-1129, V-626
 Kim, Myeng-Ki IV-937
 Kim, Myoung-Joon I-1053
 Kim, Myoung-sub V-700
 Kim, Myung Keun I-914
 Kim, Nam-Gyun I-241
 Kim, Pankoo IV-567
 Kim, Sangbok II-515
 Kim, Sangho V-491
 Kim, Sang-II III-728
 Kim, Sangjin IV-388
 Kim, Sangki II-87
 Kim, Sangkuk II-11
 Kim, Sangkyun IV-639, IV-716
 Kim, Seki III-1054
 Kim, Seoksoo II-1060, IV-271, V-565,
 V-575, V-584, V-591, V-700
 Kim, Seok-Yoon IV-612
 Kim, Seong Baeg I-278, I-288, IV-558
 Kim, Seungjoo II-954, V-858
 Kim, Seung Man I-480
 Kim, Seung-Yong IV-612
 Kim, Sijung V-851
 Kim, SinKyu II-769
 Kim, Soo Dong II-451, IV-736
 Kim, Soo Hyung IV-128
 Kim, Soon-gohn V-690
 Kim, Soon-Ho III-172
 Kim, So-yeon V-618
 Kim, Su-Nam IV-448
 Kim, Sungchan I-459
 Kim, Sung Jin V-609
 Kim, Sung Jo IV-669
 Kim, Sung Ki II-876
 Kim, Sung-Ryul III-1137
 Kim, Sung-Shick III-928
 Kim, SungSoo I-904
 Kim, Sungsuk IV-567
 Kim, Tae-Kyung II-135
 Kim, Taeseok I-1062
 Kim, Tai-hoon V-700
 Kim, Ung Mo II-165, IV-456
 Kim, Ungmo I-1028, V-139
 Kim, Won II-106
 Kim, Woo-Jae II-720
 Kim, Wu Woan IV-1116
 Kim, Yang-Woo II-905
 Kim, Yeong-Deok IV-271
 Kim, Yong-Hwa V-968
 Kim, Yong-Min II-340, II-349
 Kim, Yongsik IV-687
 Kim, Yong-Sung V-958, V-968, V-979,
 V-990
 Kim, Yong-Yook I-241
 Kim, Yoon II-562, IV-1156
 Kim, Young Beom II-515, II-827
 Kim, Youngbong IV-226
 Kim, Youngchul II-319, II-1033
 Kim, Younghan III-497
 Kim, Younhyun II-611
 Kim, Young-Kyun I-1053
 Kim, Youngrag III-64
 Kim, Young Shin V-457
 Kim, Youngsoo II-545
 Kim, Yunkuk II-730
 Knauer, Christian I-20
 Ko, Eung Nam IV-475
 Ko, Hyuk Jin II-165
 Ko, Il Seok V-331, V-338
 Ko, Kwangsun I-1028
 Ko, Kyong-Cheol IV-1060
 Kobusińska, Anna IV-1166
 Koh, Byoung-Soo IV-236, IV-245
 Koh, Kern I-1062
 Koh, Yunji I-1062
 Kohout, Josef I-71
 Kolingerová, Ivana I-71
 Kong, Jung-Shik IV-288
 Koo, Jahwan II-487
 Kosowski, Adrian I-141, I-161
 Koszalka, Leszek V-58
 Koutsonikola, Vassiliki A. II-1229
 Kozhevnikov, Victor I-974
 Krasheninnikova, Natalia I-974
 Krasheninnikov, Victor I-974
 Kreveld, Marc van I-20
 Krusche, Peter V-165
 Ku, Chih-Wei II-1210

- Ku, Hyunchul II-827
 Kurzynski, Marek III-1210
 Kwak, Jae-min V-600
 Kwak, Jin II-954
 Kwak, Jong Min V-338
 Kwak, Jong Wook IV-631
 Kwak, Keun-Chang I-955
 Kwon, Dong-Hee II-720
 Kwon, Dong-Hyuck III-38
 Kwon, Gihwon IV-1081, V-905
 Kwon, Jang-Woo II-309, V-887
 Kwon, Jungkyu IV-1042
 Kwon, Oh-Cheon II-552
 Kwon, Oh-Heum IV-306
 Kwon, Seungwoo III-928
 Kwon, Soo-Tae III-767
 Kwon, Taekyoung II-769, II-915
 Kwon, Tae-Kyu I-241
 Kwon, Yoon-Jung V-503
- Laganà, Antonio I-212, I-665, I-675,
 I-694, I-721, I-738, I-757
 Lago, Noelia Faginas I-731
 Lai, Jun IV-179
 Lai, Kin Keung I-518
 Lan, Joung-Liang IV-1107
 Laskari, E.C. V-635
 Lawrence, Earl III-1153
 Lazar, Bogdan I-779
 Lazzareschi, Michael III-1081
 Le, D. Xuan IV-207
 Lee, Amy Hsin-I III-610
 Lee, Bo-Hee IV-288
 Lee, Bongkyu IV-549, V-185
 Lee, Byung-kwan III-38, III-172,
 III-261
 Lee, Byung-Wook I-946, II-495
 Lee, Chae-Woo II-837
 Lee, Changhee I-440
 Lee, Changhoon III-446
 Lee, Changjin V-537
 Lee, Chang-Mog IV-1012
 Lee, Chang-Woo IV-1060
 Lee, Chien-I II-1210
 Lee, Chilgee V-260
 Lee, Chulsoo IV-777
 Lee, Chulung III-928
 Lee, Chung-Sub IV-798
 Lee, Dan IV-994
 Lee, Deok-Gyu IV-326, IV-370
- Lee, Deokgyu IV-344
 Lee, Dong Chun II-1017, II-1051,
 II-1082
 Lee, Dong-Ho III-728
 Lee, Dong Hoon III-385, IV-316
 Lee, DongWoo IV-197, IV-491
 Lee, Dong-Young II-135, III-486, V-626,
 V-655
 Lee, SungYoung II-390
 Lee, Eun Ser IV-1070, V-546, V-555
 Lee, Eung Ju IV-187
 Lee, Eunseok II-430, II-621, V-49
 Lee, Gang-soo V-618
 Lee, Gary Geunbae III-21
 Lee, Geon-Yeob IV-853
 Lee, Geuk II-1060
 Lee, Gigan V-952
 Lee, Gueesang IV-128
 Lee, Gun Ho IV-659
 Lee, Hanku V-522
 Lee, Ha-Yong IV-767
 Lee, Hong Joo IV-639, IV-716
 Lee, HoonJae III-48, III-269
 Lee, Hosin IV-255
 Lee, Ho Woo III-718
 Lee, Hyewon K. II-214
 Lee, Hyobin II-96
 Lee, Hyun Chan I-111
 Lee, Hyung Su II-691, IV-519
 Lee, Hyung-Woo V-284, V-294
 Lee, Ig-hoon I-1036
 Lee, Im-Yeong IV-326, IV-370
 Lee, Inbok III-1137
 Lee, Jaedeuk V-675
 Lee, Jae Don I-1000
 Lee, Jae-Dong IV-1126
 Lee, Jae-Kwang II-945
 Lee, Jae-Seung II-945
 Lee, Jaewan III-144, III-178,
 IV-899, V-867
 Lee, Jae Woo V-457, V-512, V-932
 Lee, Jaewook II-487
 Lee, Jae Yeol IV-466
 Lee, Jaeyeon I-955
 Lee, Jae Yong II-788
 Lee, Jangho I-983
 Lee, Jang Hyun II-1199
 Lee, Jeong Hun III-600
 Lee, Jeonghyun IV-21
 Lee, JeongMin IV-577

- Lee, Ji-Hyun III-287, IV-994
 Lee, Jin Ho III-875
 Lee, Joahyoung II-562, IV-1156
 Lee, Jongchan II-1033
 Lee, Jong Gu III-1190
 Lee, Jong Sik V-1
 Lee, Jong-Sool III-564
 Lee, Jong-Sub III-898
 Lee, Jongsuk II-49
 Lee, Jungho I-326
 Lee, Junghoon IV-558, V-185
 Lee, Jungsuk V-269
 Lee, Junsoo V-175
 Lee, Kang-Hyuk II-309
 Lee, Kang-Woo IV-466
 Lee, Kang-Yoon II-827
 Lee, Keun-Ho II-816
 Lee, Keun Wang II-1074
 Lee, Kihyung II-175
 Lee, Kil-Hung II-572
 Lee, Kilsup IV-917, V-877
 Lee, Ki-Young II-249
 Lee, Kunwoo I-459
 Lee, Kwang Hyoung II-1074
 Lee, Kwangyong IV-499
 Lee, Kwan H. I-480
 Lee, Kwan-Hee I-151
 Lee, Kyesan II-905, V-708, V-717,
 V-952
 Lee, Kyujin V-708
 Lee, Kyu Min IV-483
 Lee, KyungHee IV-380
 Lee, Kyung Ho II-1199
 Lee, Kyunghye II-410
 Lee, Kyungsik III-777
 Lee, Kyung Whan IV-873
 Lee, Malrey III-244, IV-947, V-644,
 V-665, V-675
 Lee, Mun-Kyu IV-584
 Lee, Myungho I-1019
 Lee, Myungjin I-1072
 Lee, Na-Young V-441
 Lee, Samuel Sangkon II-231
 Lee, Sangjin IV-245
 Lee, Sang-goo I-1036
 Lee, Sang Ho IV-1070, V-555, V-609
 Lee, Sang-Hun II-239
 Lee, Sang Hun I-459
 Lee, Sangjin III-446, IV-236
 Lee, Sang Joon V-185
 Lee, Sang-Jun V-503
 Lee, Sangjun IV-549
 Lee, Sang-Min I-1053
 Lee, Sangyoung II-87, II-96
 Lee, Seojeong IV-966
 Lee, Seok-Cheol III-115
 Lee, Seon-Don II-720
 Lee, SeongHoon IV-491
 Lee, Seonghoon IV-197
 Lee, Seong-Won IV-622
 Lee, Seoung-Hyeon II-945
 Lee, Seoung-Soo V-503
 Lee, SeoungYoung II-1140
 Lee, Seungbae V-467
 Lee, Seung-Heon II-495
 Lee, Seunghwa II-621, V-49
 Lee, Seunghwan III-64, III-93
 Lee, Seung-Jin V-512
 Lee, Seungkeun IV-21
 Lee, Seungmin V-476
 Lee, Seung-Yeon II-905
 Lee, SeungYong V-922
 Lee, Se Won III-718
 Lee, SooCheol II-552
 Lee, SuKyoung II-1131
 Lee, Su Mi IV-316
 Lee, Sungchang II-923
 Lee, Sung-Hyup II-631
 Lee, Sung Jong IV-917
 Lee, Sung-Joo IV-828
 Lee, SungYoung II-390
 Lee, Sungkeun II-204
 Lee, Tae-Dong II-462
 Lee, Taehoon IV-1081
 Lee, Tae-Jin II-288, II-534, II-661,
 II-710, II-856, II-923, II-1121
 Lee, Vincent I-586
 Lee, Wankwon IV-491
 Lee, Wansuk II-954
 Lee, Wongoo II-11, V-851
 Lee, Won-Hyuk II-982
 Lee, Wookey IV-787, V-942
 Lee, Woongho I-326
 Lee, Yang-sun V-600
 Lee, Yongjin IV-197
 Lee, Yongseok V-665
 Lee, YoungGyo III-54
 Lee, Young Hoon III-875
 Lee, Young-Koo II-505
 Lee, Youngkwon II-915

- Lee, Young-Seok III-144
 Lee, Youngsook III-517, V-858
 Lee, YoungSoon V-675
 Lee, Yun Ho III-875
 Lee, Yun-Kyoung I-232
 Leininger, Thierry I-744
 León, Carlos V-725
 Leong, Chee-Seng IV-424
 Lho, Tae-Jung II-309, III-1163, V-887
 Liang, Yanchun I-938
 Liang, Zhong III-928
 Liao, Yuehong III-974
 Li, Fucui I-317
 Li, Haisen S. V-789
 Li, Jie II-59
 Li, Jin III-309, III-365, IV-406
 Li, Kuan-Ching IV-1107
 Li, Li I-895
 Li, Lv V-32
 Li, Qu I-393
 Li, Sheng I-420
 Li, Shiping I-317
 Li, Shujun V-789
 Li, Xun I-895
 Li, Yanhui II-1179
 Li, Yunsong V-149
 Li, Zhanwei V-450
 Li, Zhong I-1118, I-1134
 Lim, Andrew III-688
 Lim, Chan-Hyoung III-832
 Lim, Hyotaek IV-380
 Lim, Hyung-Jin II-135, II-239, III-486,
 V-626, V-655
 Lim, Jeong-Mi IV-679
 Lim, JiHyung IV-380
 Lim, Jiyoung IV-440
 Lim, Sungjun IV-707
 Lim, Taesoo IV-687
 Lim, Younghwan II-28, II-400,
 II-410, II-487
 Lin, Ching-Fen III-944
 Lin, Chuen-Horng V-384
 Lin, Hon-Ren V-158
 Lin, Hung-Mei III-338
 Lin, Kung-Kuei V-158
 Lin, Woei II-1111
 Ling, Yun IV-649
 Lísal, Martin V-743
 Lisowski, Dominik V-58
 Liu, Chia-Lung II-1111
 Liu, Fuyu IV-88
 Liu, Guoli III-659
 Liu, Heng I-528
 Liu, Joseph K. IV-406
 Liu, Jun IV-649
 Liu, Kai III-748
 Liu, Qun I-1045
 Liu, Shaofeng II-279
 Liu, Xianxing II-59
 Liu, XueHui I-420
 Loke, Seng Wai IV-138
 Lopes, Carla Teixeira IV-78
 López, Máximo IV-169
 Lu, Jiahui I-938
 Lu, Jianjiang II-1179
 Lu, Jiqiang III-466
 Lu, Xiaolin I-192, I-875
 Luna-Rivera, Jose M. V-412
 Luo, Ying IV-1090
 Luo, Yuan I-431
 Lv, Xinran V-450

 Ma, Hong III-688
 Ma, Lizhuang I-1118, I-1134
 Ma, Shichao I-1010
 Madern, Narcis I-81
 Magneau, Olivier I-222
 Mah, Pyeong Soo IV-509
 Makarov, Nikolay I-974
 Małafiejski, Michał I-141, I-161
 Mamun-or-Rashid, Md. II-651
 Manos, Konstantinos I-251
 Manzanares, Antonio Izquierdo V-798
 Mao, Zhihong I-1118, I-1134
 Markiewicz, Marta I-684
 Markowski, Marcin III-1119
 Marroquín-Alonso, Olga IV-158
 Martín, María J. I-701
 Mateo, Romeo Mark A. III-178, V-867
 Matte-Tailliez, Oriane I-222
 Maynau, Daniel I-744
 McLeish, Tom I-711
 McMahan, Chris A. II-279
 Mecke, Rüdiger I-268
 Meek, Dereck I-1118
 Mehlhorn, Kurt I-60
 Meletiou, G.C. V-635
 Mellado, Daniel III-1044
 Meng, Qingfan I-938
 Merabti, Madjid IV-352

- Mercorelli, Paolo I-847, I-857
 Miao, Zhaowei III-688
 Mijangos, Eugenio III-757
 Mikołajczak, Paweł V-394
 Millán, Rocío V-725
 Min, Byoung Joon II-270, II-876
 Min, Hong IV-499, IV-549
 Min, Hong-Ki II-224
 Min, Hyun Gi IV-736
 Min, Jun-Ki II-67
 Min, Kyongpil I-410
 Min, So Yeon II-1003, II-1074, IV-985
 Mitra, Pinaki I-1, II-1
 Moet, Esther I-20
 Moh, Chiou II-1111
 Mohades, Ali V-735
 Moin, M. Shahram III-1180
 Mok, Hak-Soo III-832, III-994
 Molinaro, Luis V-808
 Monedero, Íñigo V-725
 Moon, Aekyung V-214
 Moon, Il Kyeong III-600
 Moon, Ki-Young II-945
 Moon, Kwang-Sup III-994
 Moon, Mikyeong II-441, IV-226
 Moon, Young Shik V-404
 Morarescu, Cristian I-771, I-779,
 I-804, I-814, I-839
 Moreno, Anna M. Coves III-638
 Moreno, Ismael Solís IV-50
 Morillo, Pedro I-490
 Morimoto, Shoichi III-1
 Morphet, Steve I-1127
 Mouloudi, Abdelaaziz V-346
 Mouriño, Carlos J. I-701
 Mu, Yi III-345
 Mukhopadhyay, Sourav III-436
 Mukhtar, Shoab II-847
 Mun, Gil-Jong II-340
 Mun, YoungSong II-195, II-214, II-319,
 II-400, II-410, II-420, II-471, II-487,
 II-525, II-611, II-740, II-885, II-895
 Murzin, Mikhail Y. I-605
- Na, Yang V-467, V-476
 Na, Yun Ji V-331, V-338
 Nah, Jungchan IV-440
 Nakashima, Toyoshiro II-40
 Nam, Do-Hyun II-224
 Nam, Junghyun III-517, V-858
 Nam, Taekyong II-545
 Nandy, Subhas C. II-750
 Naumann, Uwe I-865
 Navarro, Juan J. V-762
 Neelov, Igor I-711
 Neumann, Laszlo I-449
 Ng, Victor I-383
 Niewiadomska-Szynkiewicz, Ewa I-537
 Nilforoushan, Zahra V-735
 Noh, Bong-Nam II-340, II-349, V-922
 Noh, Hye-Min III-188, IV-893
 Noh, Min-Ki II-1169
 Noh, Sang-Kyun II-349
 Noh, Seo-Young II-145
 Noh, SiChoon II-1051
 Noh, Sun-Kuk II-582
 Noori, Siamak III-546
 Noruzi, Mohammadreza III-1180
 Nowiński, Krzysztof V-394
 Nyang, DaeHun IV-380
- Ogryczak, Włodzimierz III-802
 Oh, Am-Suk II-309, V-887
 Oh, Hayoung IV-440
 Oh, Heekuck IV-388
 Oh, Hyukjun IV-603
 Oh, Inn Yeal II-974, II-1009
 Oh, Jaeduck II-471
 Oh, Jehwan V-49
 Oh, Juhyun II-760
 Oh, June II-1199
 Omary, Fouzia V-346
 Onosato, Masahiko I-469
 Orduña, Juan Manuel I-490
- Ortiz, Guillermo Rodríguez IV-50
 Ould-Khaoua, Mohamed V-118
- Paar, Christof III-1004
 Pacifici, Leonardo I-694
 Pahk, Cheryl Soo III-1190
 Paik, Juryon IV-456
 Pak, Jinsuk II-1159
 Palazzo, Gaetano Salvatore I-794
 Palmieri, Francesco III-537
 Pamula, Raj III-974
 Papadimitriou, Georgios I. II-1229
 Pardede, Eric I-1146, IV-207
 Park, Chang Mok IV-296

- Park, Chang-Seop IV-679
 Park, Chang Won IV-549
 Park, Chiwoo IV-697
 Park, Choung-Hwan II-1043
 Park, Dae-Hyeon V-958
 Park, DaeHyuck II-400
 Park, Dea-Woo IV-883
 Park, DongSik V-260
 Park, Eun-Ju IV-927
 Park, Geunyoung IV-549
 Park, Gilcheol V-565, V-591
 Park, Gi-Won II-631
 Park, Gyungleen II-760, IV-558, V-185
 Park, Hee-Un V-700
 Park, HongShik II-1140
 Park, Hyeong-Uk V-512
 Park, Ilgon IV-509
 Park, Jaehyung II-77
 Park, Jaekwan II-155
 Park, Jaemin IV-549
 Park, Jang-Su IV-370
 Park, Jea-Youn IV-835
 Park, Jeongmin II-430
 Park, Jeong Su IV-316
 Park, Jeung Chul I-480
 Park, Jong Hyuk IV-236, IV-245
 Park, Jongjin II-525
 Park, Joon Young I-111
 Park, Jungkeun I-1000
 Park, Jun Sang V-457
 Park, Ki-Hong IV-1060
 Park, Kisoeb III-1054
 Park, Ki Tae V-404
 Park, Kyoo-Seok III-125, V-912
 Park, Kyungdo III-928
 Park, Mee-Young V-512
 Park, Mi-Og IV-883
 Park, Namje V-251
 Park, Neungsoo IV-622
 Park, Sachoun V-905
 Park, Sangjoon II-319, II-1033
 Park, Sang Soon V-236
 Park, Sang Yong IV-1
 Park, SeongHoon V-68
 Park, Seungmin IV-499
 Park, Seung Soo II-298
 Park, Soo-Jin IV-432
 Park, Soon-Young IV-1126
 Park, Sung Soon II-641
 Park, Taehyung II-806
 Park, Wongil II-330
 Park, Woojin II-730
 Park, Yong-Seok IV-370
 Park, Young-Bae II-224
 Park, Young-Jae II-515
 Park, Young-Shin IV-432
 Park, Youngsup I-402
 Park, Young-Tack II-1219
 Parpas, Panos III-908
 Pastor, Rafael III-554
 Paun, Viorel I-779, I-804
 Pazo-Robles, Maria Eugenia I-577
 Pazos, Rodolfo II-18, IV-169
 Pegueroles, Josep III-527
 Pérez, Jesús Carretero V-108
 Pérez, Joaquín IV-169
 Pérez-Rosés, Hebert I-510
 Perrin, Dimitri I-612
 Petridou, Sophia G. II-1229
 Phillips, Robert III-822
 Piao, Xuefeng IV-549
 Piattini, Mario III-984, III-1013,
 III-1024, III-1044
 Pillards, Tim V-780
 Pineda-Rico, Ulises V-412
 Pion, Sylvain I-60
 Pirani, Fernando I-721, I-738
 Poch, Jordi I-364
 Pont, Michael J. V-22
 Pontvieux, Cyril V-202
 Porrini, Massimiliano I-721
 Porschen, Stefan I-40
 Pozniak-Koszalka, Iwona V-58
 Prados, Ferran I-364
 Puchala, Edward III-1210
 Pulcineli, L. V-819
 Puntonet, C.G. V-772
 Pusca, Stefan I-763, I-771, I-779,
 I-804, I-839
 Puttini, Ricardo Staciariini V-808
 Qin, Xujia I-393
 Qu, Xiangli V-224
 Qu, Zhiguo I-921
 Quintana, Arturo I-510
 Quirós, Ricardo I-510
 Rabenseifner, Rolf V-108
 Rahayu, J. Wenny I-1146, IV-207
 Rahman, Md. Mustafizur II-866

- Ramírez, J. V-772
 Rao, Imran II-390
 Reed, Chris I-644
 Rehfeld, Martina I-268
 Reitner, Sonja V-88
 Reyes, Gerardo IV-169
 Rhee, Choonsung II-601
 Rhee, Gue Won IV-466
 Rhee, Yang-Won III-287, IV-1060
 Rico-Novella, Francisco III-527
 Riganelli, Antonio I-665
 Rigau, Jaume I-449
 Rim, Kiwook IV-21
 Rodionov, Alexey S. I-605
 Roh, Byeong-hee IV-279
 Rosa-Velardo, Fernando IV-158
 Rossi, Gustavo IV-148
 Roy, Sasanka I-10
 Rubio, Monica I-510
 Ruskin, Heather J. I-612, I-622
 Rustem, Berç III-908
 Ryba, Przemyslaw III-1100
 Ryu, Jong Ho II-270
 Ryu, Yeonseung I-1000, I-1019
- Sadjadi, Seyed Jafar III-546, III-574
 Safaei, Farshad V-118
 Sakai, Yutaka I-596
 Salavert, Isidro Ramos IV-726
 Salgado, René Santaolaya IV-50
 Samavati, Faramarz I-91
 Sarac, T. III-678
 Sarkar, Palash III-436
 Saunders, J.R. I-556, III-934
 Sbert, Mateu I-449
 Schirra, Stefan I-60
 Schizas, Christos N. IV-118
 Schoor, Wolfram I-268
 Schurz, Frank V-129
 Ścisło, Piotr V-394
 Sedano, Iñigo IV-108
 Segura, J.C. V-772
 Sellarès, J. Antoni I-81
 Semé, David V-10
 Seo, Dae-Hee IV-326
 Seo, Dong Il II-270
 Seo, Dongmahn II-562, IV-1156
 Seo, JaeHyun III-154, V-922
 Seo, Jeongyeon I-101
- Seo, Kyu-Tae IV-288
 Seo, Manseung I-469
 Seo, Won Ju III-718
 Seo, Young-Jun IV-864
 Seo, Yuhwa III-954
 Severiano, José Andrés Díaz I-30
 Severn, Aaron I-91
 Shao, Feng I-307
 Shi, Qi IV-352
 Shi, Wenbo III-213
 Shibasaki, Ryosuke I-261
 Shim, Choon-Bo II-114
 Shim, Donghee IV-491
 Shim, Jang-Sup V-968, V-979, V-990
 Shim, Junho I-1036
 Shim, Young-Chul II-125, II-591
 Shimizu, Eihan I-261
 Shin, Chang-Sun III-251, IV-798
 Shin, Chungsoo II-740
 Shin, Dae-won III-261
 Shin, Dong-Ryeol IV-483
 Shin, Dong Ryul II-165
 Shin, Dongshin V-467
 Shin, Hayong I-440
 Shin, Ho-Jin IV-483
 Shin, Jeong-Hoon I-354
 Shin, Kee-Young IV-509
 Shin, Kwangcheol IV-40
 Shin, Myong-Chul V-312
 Shin, Seung-Jung II-487
 Shin, Woochul I-895
 Shin, Yongtae III-954
 Shuqing, Zhang I-885
 Siem, Alex Y.D. III-812
 Singh, David E. IV-1136
 Skouteris, Dimitris I-757
 Śliwiński, Tomasz III-802
 Smith, William R. V-743
 Sobaniec, Cezary V-98
 Sofokleous, Anastasis A. IV-118
 Soh, Ben IV-179
 Soh, Wooyoung V-682
 Sohn, Hong-Gyoo II-989, II-1043
 Sohn, Sungwon V-251
 Sohn, Surgwon II-779
 Soler, Emilio III-1024
 Soler, Josep I-364
 Son, Jeongho II-1159
 Son, Kyungho II-954
 Son, Seung-Hyun III-590

- Song, Eungkyu I-1062
 Song, Eun Jee II-1051
 Song, Ha-Joo IV-306
 Song, Hyoung-Kyu V-752
 Song, Jaekoo V-575
 Song, Jaesung I-469
 Song, JooSeok II-359, II-769, II-1131
 Song, Jungsuk IV-245
 Song, Ki Won IV-873
 Song, Sung Keun V-139
 Song, Wang-Cheol V-185
 Song, Yeong-Sun II-1043
 Song, Young-Jae IV-835, IV-864
 Soriano, Miguel III-527
 Sosa, Víctor J. II-18, IV-169
 Souza, Osmar Norberto de I-202
 Stanek, Martin III-426
 Stankova, Elena N. I-752
 Sterian, Andreea I-779, I-804
 Stewart, Neil F. I-50
 Storch, Lorian I-675
 Suh, Young-Ho IV-466
 Suh, Young-Joo II-720
 Sun, Jizhou V-450
 Sun, Lijuan V-450
 Sun, Youxian IV-539
 Sung, Jaechul III-446
 Sung, Sulyun III-954
 Susilo, Willy III-345
 Syukur, Evi IV-138
- Tae, Kang Soo II-231
 Takagi, Tsuyoshi III-375
 Talia, Domenico I-1080
 Tan, Pengliu IV-529
 Tan, Wuzheng I-1118, I-1134
 Tang, Chuan Yi III-631
 Tang, Lixin III-659
 Tang, W.J. I-556
 Taniar, David I-1090, I-1146
 Tarantelli, Francesco I-675
 Tasan, Seren Özmehmet V-78
 Tasoulis, D.K. V-635
 Tasso, Sergio I-212
 Tate, Stephen R. III-327
 Teng, Lirong I-938
 tie, Li V-32
 Tiskin, Alexander III-793, V-165
 Toma, Alexandru I-839
 Toma, Cristian I-779
- Toma, Ghiocel I-804
 Toma, Theodora I-771
 Torabi, Torab IV-98, IV-217
 Torres-Jiménez, José IV-726
 Tragha, Abderrahim V-346
 Trujillo, Juan III-1024
 Trunfio, Paolo I-1080
 Tsai, Cheng-Jung II-1210
 Tsai, Chwei-Shyong III-406
 Tsai, Yuan-Yu I-171, I-181
 Tunali, Semra V-78
- Uhm, Chul-Yong IV-448
- Vafadoost, Mansour III-1180
 Vakali, Athena I. II-1229
 Val, Cristina Manchado del I-30
 Vanhoucke, Mario III-621
 Varnuška, Michal I-71
 Vazquez, Juan Ignacio IV-108
 Vehreschild, Andre I-865
 Verdú, Gumersindo V-192
 Verta, Oreste I-1080
 Vidal, Vicente V-192
 Vidler, Peter J. V-22
 Villalba, Luis Javier García V-808,
 V-819
 Villarroel, Rodolfo III-1024
 Villarrubia, Carlos III-1013
 Villecco, Francesco I-857
 Virvou, Maria I-251
 Vlad, Adriana I-1166
 Voss, Heinrich I-684
 Vrahatis, M.N. V-635
- Walkowiak, Krzysztof II-1101
 Wan, Wei IV-1090
 Wan, Zheng II-964
 Wang, Bo-Hyun I-946
 Wang, Chung-Ming I-171, I-181
 Wang, Gi-Nam IV-296
 Wang, GuoPing I-420
 Wang, K.J. III-885
 Wang, Kun V-149
 Wang, Kung-Jeng III-668
 Wang, Shoujue V-375
 Wang, Shouyang I-518
 Wang, Weihong I-393
 Wang, Yanming III-309
 Wang, Zhengyou II-964

- Wang, Zhensong I-1010
 Watson, Mark D. I-121
 Wawrzyniak, Dariusz V-98
 Wee, Hui-Ming III-862, III-885
 Weidenhiller, Andreas V-88
 Wei, Guiyi IV-649
 Wei, Tao IV-262
 Wen, Chia-Hsien IV-1107
 Wheeler, Thomas J. I-654
 Wild, Peter J. II-279
 Wollinger, Thomas III-1004
 Won, Dong Ho II-165
 Won, Dongho II-545, II-954, III-54,
 III-517, IV-777, V-251, V-858
 Won, Youjip I-1062
 Woo, Sinam II-730
 Woo, Yo-Seop II-224
 Woo, Young-Ho II-224
 Wu, Chaolin IV-1090
 Wu, Chin-Chi II-1111
 Wu, EnHua I-420
 Wu, Hsien-Chu III-406
 Wu, Mary III-93, IV-818, IV-1022
 Wu, Q.H. I-556, III-934
 Wu, Qianhong III-345
 Wu, Shiqian II-964
 Wu, Xiaqing I-500
 Wu, Zhaohui II-1149
- Xia, Feng IV-539
 Xia, Yu III-1064
 Xiao, Zhenghong V-243
 Xiaohong, Li V-32
 Xie, Mei-fen V-375
 Xie, Qiming V-149
 Xie, Xiaoqin IV-756
 Xu, Baowen II-1179
 Xu, Fuyin V-243
 Xue, Yong IV-1090
- Yan, Jingqi I-528
 Yang, Byounghak III-581
 Yang, Ching-Wen IV-1107
 Yang, Hae-Sool IV-767, IV-937, IV-976,
 IV-1052
 Yang, Hwang-Kyu III-279
 Yang, Hyunho III-178
 Yang, Jong S. III-1129
 Yang, Kyoung Mi I-278
 Yang, Seung-hae III-38, III-261
- Yang, Xuejun V-224
 Yang, Young-Kyu II-495
 Yang, Young Soon II-1199
 Yap, Chee I-60
 Yeh, Chuan-Po III-406
 Yeh, Chung-Hsing III-649
 Yeo, So-Young V-752
 Yeom, Hee-Gyun IV-909
 Yeom, Keunhyuk II-441, IV-226
 Yeom, Soon-Ja V-958
 Yeun, Yun Seog II-1199
 Yi, Sangho II-701, IV-499, IV-549
 Yi, Subong III-144
 Yildiz, İpek I-547
 Yim, Keun Soo I-1000
 Yim, Soon-Bin II-1121
 Yoe, Hyun III-251
 Yoh, Jack Jai-ick V-484
 Yoo, Cheol-Jung III-188, III-222,
 IV-893, IV-955, V-644
 Yoo, Chuck II-1189
 Yoo, Chun-Sik V-958, V-979, V-990
 Yoo, Giljong II-430
 Yoo, Hwan-Hee V-1010
 Yoo, Hyeong Seon III-206, III-213
 Yoo, Jeong-Joon I-1000
 Yoo, Kee-Young I-1156, V-276, V-303
 Yoo, Ki-Sung II-1169
 Yoo, Kook-Yeol I-298
 Yoo, Sang Bong I-895
 Yoo, Seung Hwan II-270
 Yoo, Seung-Jae II-1025
 Yoo, Seung-Wha II-186
 Yoo, Sun K. I-335
 Yoon, Eun-Jun I-1156, V-276, V-303
 Yoon, Heejun II-11
 Yoon, Hwamook II-11
 Yoon, Kyunghyun I-402
 Yoon, Won Jin II-856
 Yoon, Won-Sik II-847
 Yoon, Yeo-Ran II-534
 Yoshizawa, Shuji I-596
 You, Ilsun IV-336, IV-416
 You, Young-Hwan V-752
 Youn, Hee Yong II-691, III-852,
 IV-1, IV-187, IV-456, IV-519,
 V-139, V-185
 Young, Chung Min II-534
 Yu, Jonas C.P. III-885
 Yu, Jun IV-649

Yu, Ki-Sung II-525, II-982
Yu, Lean I-518
Yu, Mei I-307, I-317
Yu, Sunjin II-87, II-96
Yu, Tae Kwon II-451
Yu, Young Jung I-904
Yu, Yung H. V-932
Yuen, Tsz Hon I-383
Yun, Jae-Kwan II-259
Yun, Kong-Hyun II-989

Zeng, Weiming II-964
Zhai, Jia IV-296
Zhang, David I-528
Zhang, Fan II-59
Zhang, Fanguo III-345
Zhang, Jianhong IV-262

Zhang, JianYu IV-262
Zhang, Jie V-149
Zhang, Minghu IV-529
Zhang, Xinhong II-59
Zhang, Zhongmei I-921
Zhao, Mingxi I-1118
Zheng, He II-954
Zheng, Lei IV-1090
Zheng, Nenggan II-1149
Zhiyong, Feng V-32
Zhong, Jingwei V-224
Zhou, Bo IV-352
Zhou, Yanmiao II-1149
Ziaee, M. III-574
Zongming, Wang I-885
Zou, Wei IV-262
Żyliński, Paweł I-141, I-161